Thomas Bortfeld
Rupert Schmidt-Ullrich
Wilfried De Neve
David E. Wazer
Editors

Image-Guided IMRT

Springer

Image-Guided IMRT

Thomas Bortfeld · Rupert Schmidt-Ullrich
Wilfried De Neve · David E. Wazer (Eds.)

Image-Guided IMRT

With 124 Figures, 96 in Color and 44 Tables

Springer

Thomas Bortfeld
Dept. of Radiation Oncology
Massachusetts General Hospital
30 Fruit Street
Boston, MA 02114
USA

Rupert Schmidt-Ullrich
Dept. of Radiation Oncology
Virginia Commonwealth University
401 College Street
Richmond, VA 23298–0058
USA

Wilfried De Neve
Dept. of Radiotherapy
Ghent University Hospital
De Pintelaan 185
9000 Ghent
Belgium

David E. Wazer
Dept. of Radiation Oncology
Tufts University
750 Washington Street
Boston, MA 02111
USA

Library of Congress Control Number 2005925670

ISBN-10 3-540-20511-X Springer Berlin Heidelberg 2006
ISBN-13 978-3-540-20511-1 Springer Berlin Heidelberg 2006

Springer-Verlag is a part of Springer Science+Business Media
springeronline.com

Printed in Germany

Editor: Dr. Ute Heilmann
Desk Editor: Meike Stoeck
Production and Typesetting: LE-TEX Jelonek, Schmidt & Vöckler GbR, Leipzig
Cover: Frido Steinen-Broo, EStudio Calamar, Spain
Printing and binding: Stürtz, Würzburg

Printed on acid-free paper 21/3150/YL 5 4 3 2 1 0

Preface

Intensity-modulated radiotherapy (IMRT) has widened the horizons of radiation therapy due to its ability to conform radiation dose distributions to complex tumor target volumes while sparing nearby critical structures as much as physically possible. IMRT has also led to paradigm shifts in all elements of the chain of radiotherapy, from treatment prescription over treatment planning ("inverse" planning) to treatment delivery and verification. Although IMRT and inverse planning have the potential to streamline and simplify radiotherapy, at the current stage of the development IMRT is still significantly more involved than conventional radiotherapy.

This book is meant to help the reader understand the concepts and components of IMRT, to give a topical overview of advanced image-guided and biologically guided approaches, and to provide useful hints on how to master IMRT in clinical practice. Reading this text alone is not sufficient to start a clinical IMRT program. The book will rather provide up-to-date theoretical and practical information about IMRT that should be consulted in addition to other sources that are listed as references. We highlight not only the strengths of IMRT but discuss also the weaknesses, limitations, and unique challenges such as the prolonged treatment times and increased leakage radiation. All this, we hope, will be useful for clinicians and physicists who are interested in exploring the potential of IMRT, as well as a reference for those who already apply IMRT in clinical practice.

The book has been written by an international group of authors with an international readership in mind. Some IMRT aspects, such as quality assurance, have different flavors in different countries, because of national regulations and reimbursement issues. We tried to take this into account by covering the American and the European perspectives on quality assurance in two separate chapters. This also emphasizes the importance of the topic. The authors of all chapters are distinguished experts in their field and we are grateful that they devoted some of their precious time to the writing of their chapters.

The material has been organized into three major parts: (I) Foundations, (II) Advanced Image-Guided and Biologically Guided Techniques, and (III) Clinical Applications. Part I lays the foundation for state-of-the-art IMRT. As for image guidance (part II), it has been said that radiotherapy, and in particular IMRT, has always been image-guided and that the current hype about image guidance is not justified. While there is some truth to this statement, there have been recent developments in image-guided IMRT that deserve separate coverage. The developments with the biggest potential impact are probably the inclusion of functional imaging information into target segmentation and dose prescription, and the advancement of adaptive "4D" radiotherapy techniques, which incorporate temporal changes into the treatment scheme. These developments, which are currently being pursued at only a few centers, will most likely find their way into broader clinical application in the near future.

The Clinical Applications section (III) reviews the use of IMRT for individual anatomic sites and common clinical applications. Each chapter is presented in a similar format: Clinical problem – Potential benefits of IMRT – Unique challenges – Target and organ-at-risk definition – Planning – Delivery issues – Clinical studies and trials – Future directions. We have drawn upon experienced practitioners of IMRT to summarize the current literature as well as provide their personal insights as to how they approach the specifics of treatment planning and delivery including required imaging, anatomic segmentation, normal tissue dose-volume relationships, and target dose. The section is designed to provide detailed and practical information to the clinician and medical physicist as they implement IMRT under a broad set of clinical circumstances.

In closing, we must make special mention of our coeditor, Rupert K.A. Schmidt-Ullrich. Dr. Schmidt-Ullrich was one of the early pioneers in the development of IMRT and has fostered within his department at the Virginia Commonwealth University one of the most distinguished research programs in the world. His overriding passion in recent years was to produce a textbook for IMRT that would be broadly recognized for its comprehensiveness, quality, and readability. The effort, as reflected in these pages, is a testament to his vision, insight, and commitment to excellence. Sadly, Rupert will

not see his vision fulfilled as he died from metastatic colon cancer just weeks prior to the completion of this volume. It is nonetheless important to note that as a measure of both the strength of his spirit and his commitment to this important task, he continued to actively work on completing this book until days before his death. As such, we respectfully dedicate this work to the memory of Rupert K.A. Schmidt-Ullrich.

Boston and Ghent
August 2005

Thomas Bortfeld
Wilfried De Neve
David E. Wazer

Contents

List of Contributors

Douglas W. Arthur
Dept. of Radiation Oncology
Virginia Commonwealth University
Richmond, USA

Stanley H. Benedict
Dept. of Radiation Oncology
Virginia Commonwealth University
Richmond, USA

Margaret Bidmead
Head and Neck Unit
Royal Marsden Hospital and
Institute of Cancer Research
London, UK

Thomas Bortfeld
Dept. of Radiation Oncology
Massachusetts General Hospital
Boston, USA

Don Brabbins
Dept. of Radiation Oncology
William Beaumont Hospital
Royal Oak, USA

Kristy K. Brock
Radiation Physics
Princess Margaret Hospital
Toronto, Canada

David Buck
Dept. of Radiation Oncology
Virginia Commonwealth University
Richmond, USA

Mark K. Buyyounouski
Dept. of Radiation Oncology
Fox Chase Cancer Center
Philadelphia, USA

Eric L. Chang
Dept. of Radiation Oncology
MD Anderson Cancer Center
Houston, USA

George T.Y. Chen
Dept. of Radiation Oncology
Massachusetts General Hospital
Boston, USA

William W. Chou
Dept. of Radiation Oncology
Memorial Sloan-Kettering Cancer Center
New York, USA

Cynthia Chuan
Dept. of Radiation Oncology
University of California at San Francisco
San Francisco, USA

Catherine H. Clark
Head and Neck Unit
Royal Marsden Hospital and
Institute of Cancer Research
London, UK

Emmanuel E. Coche
Cliniques Universitaires Saint-Luc
Université Catholique de Louvain
Brussels, Belgium

Wilfried De Neve
Dept. of Radiotherapy
Ghent University Hospital
Ghent, Belgium

Carlos De Wagter
Dept. of Radiotherapy
Ghent University Hospital
Ghent, Belgium

David P. Dearnaley
Head and Neck Unit
Royal Marsden Hospital
and Institute of Cancer Research
London, UK

Nesrin Dogan
Dept. of Radiation Oncology
Virginia Commonwealth University
Richmond, USA

Thierry P. Duprez
Cliniques Universitaires Saint-Luc
Université Catholique de Louvain
Brussels, Belgium

Wim Duthoy
Dept. of Radiotherapy
Ghent University Hospital
Ghent, Belgium

Patricia J. Eifel
Dept. of Radiation Oncology
M.D. Anderson Cancer Center
Houston, USA

Natia Esiashvili
Dept. of Radiation Oncology
Emory University and Clinic
Atlanta, USA

Gary Ezzell
Dept. of Radiation Oncology
Mayo Clinic Scottsdale
Scottsdale, USA

Steve J. Feigenberg
Department of Radiation Oncology
Fox Chase Cancer Center
Philadelphia, USA

Maria T. Guerrero Urbano
Head and Neck Unit
Royal Marsden Hospital and
Institute of Cancer Research
London, UK

Kevin J. Harrington
Head and Neck Unit
Royal Marsden Hospital and
Institute of Cancer Research
London, UK

Eric M. Horwitz
Department of Radiation Oncology
Fox Chase Cancer Center
Philadelphia, USA

David A. Jaffray
Radiation Physics
Princess Margaret Hospital
Toronto, Canada

Steve B. Jiang
Dept. of Radiation Oncology
Massachusetts General Hospital
Boston, USA

Jeffrey Kapatoes
TomoTherapy
Madison, USA

Paul J. Keall
Dept. of Radiation Oncology
Virginia Commonwealth University
Richmond, USA

Mary Koshy
Dept. of Radiation Oncology
Emory University and Clinic
Atlanta, USA

Jerome C. Landry
Dept. of Radiation Oncology
Emory University and Clinic
Atlanta, USA

Nancy Y. Lee
Dept. of Radiation Oncology
Memorial Sloan-Kettering Cancer Center
New York, USA

David Lockman
Dept. of Radiation Oncology
William Beaumont Hospital
Royal Oak, USA

Max Lonneux
Cliniques Universitaires Saint-Luc
Université Catholique de Louvain
Brussels, Belgium

Weiguo Lu
TomoTherapy
Madison, USA

Gig S. Mageras
Dept. of Medical Physics
Memorial Sloan-Kettering Cancer Center
New York, USA

Anita Mahajan
Dept. of Radiation Oncology
MD Anderson Cancer Center
Houston, USA

Alvaro Martinez
Dept. of Radiation Oncology
William Beaumont Hospital
Royal Oak, USA

Radhe Mohan
MD Anderson Cancer Center
University of Texas
Houston, USA

Jean M. Moran
Dept. of Radiation Oncology
University of Michigan Medical Center
Ann Arbor, USA

Monica Morris
Dept. of Radiation Oncology
Virginia Commonwealth University
Richmond, USA

Andrzej Niemierko
Dept. of Radiation Oncology
Massachusetts General Hospital
Boston, USA

Simeon Nill
Dept. of Medical Physics
DKFZ Heidelberg
Heidelberg, Germany

Christopher M. Nutting
Head and Neck Unit
Royal Marsden Hospital and
Institute of Cancer Research
London, UK

Uwe Oelfke
Dept. of Medical Physics
DKFZ Heidelberg
Heidelberg, Germany

Gustavo Hugo Olivera
TomoTherapy
Madison, USA

Andrea Pirzkall
Dept. of Radiation Oncology
University of California at San Francisco
San Francisco, USA

Alan Pollack
Department of Radiation Oncology
Fox Chase Cancer Center
Philadelphia, USA

Robert A. Price Jr.
Department of Radiation Oncology
Fox Chase Cancer Center
Philadelphia, USA

John Purviance
Dept. of Radiation Oncology
Tufts University
Boston, USA

Peter Remeijer
The Netherlands Cancer Institute
Antoni van Leeuwenhoek Ziekenhuis
Amsterdam, The Netherlands

Eike R.M. Rietzel
Dept. of Radiation Oncology
Massachusetts General Hospital
Boston, USA

Thomas Rockwell Mackie
Medical Radiation Research Center
Madison, USA

Benjamin D. Rosenbluth
Dept. of Radiation Oncology
Memorial Sloan-Kettering Cancer Center
New York, USA

Kenneth E. Rosenzweig
Dept. of Radiation Oncology
Memorial Sloan-Kettering Cancer Center
New York, USA

Kenneth Ruchala
TomoTherapy
Madison, USA

Rupert Schmidt-Ullrich
Dept. of Radiation Oncology
Virginia Commonwealth University
Richmond, USA

Michael B. Sharpe
Radiation Physics
Princess Margaret Hospital
Toronto, Canada

Jeffrey V. Siebers
Dept. of Radiation Oncology
Virginia Commonwealth University
Richmond, USA

Danny Song
Dept. of Radiation Oncolgy
Virginia Commonwealth University
Richmond, USA

Daniel M. Spielman
Dept. of Radiology, Stanford University
School of Medicine
Stanford, USA

Christophe Van de Wiele
Dept. of Nuclear Medicine
University Hospital Ghent
Ghent, Belgium

Marcel van Herk
The Netherlands Cancer Institute
Antoni van Leeuwenhoek Ziekenhuis
Amsterdam, The Netherlands

Dirk Verellen
Dept. of Radiotherapy
AZ-VUB
Brussels, Belgium

Lynn J. Verhey
Dept. of Radiation Oncology
University of California at San Francisco
San Francisco, USA

Frank A. Vicini
Dept. of Radiation Oncology
William Beaumont Hospital
Royal Oak, USA

David E. Wazer
Dept. of Radiation Oncology
Tufts University
Boston, USA

Steve Webb
Joint Dept. of Physics
Institute of Cancer Research
And Royal Marsden NHS Trust
Sutton, UK

Jan J. Wilkens
Dept. of Medical Physics
DKFZ Heidelberg
Heidelberg, Germany

Christopher G. Willett
Dept. of Radiation Oncology
Duke University
Durham, USA

Jeffrey F. Williamson
Dept. of Radiation Oncology
Virginia Commonwealth University
Richmond, USA

John Wong
Dept. of Radiation Oncology
Johns Hopkins University
Baltimore, USA

Yan Wu
Dept. of Radiation Oncology
Virginia Commonwealth University
Richmond, USA

Ping Xia
Dept. of Radiation Oncology
University of California at San Francisco
San Francisco, USA

Lei Xing
Dept. of Radiation Oncology
Stanford University
School of Medicine
Stanford, USA

Di Yan
Dept. of Radiation Oncology
William Beaumont Hospital
Royal Oak, USA

Yong Yang
Dept. of Radiation Oncology
Stanford University
School of Medicine
Stanford, USA

Ellen Yorke
Dept. of Medical Physics
Memorial Sloan-Kettering Cancer Center
New York, USA

Part I
Foundations

Rationale of Intensity Modulated Radiation Therapy: A Clinician's Point of View

Wilfried De Neve

1

Contents

1.1 Introduction

IMRT is used in many radiotherapy departments for a variety of tumor sites. A thorough review of clinical experience with IMRT as it has been applied to treat common tumors is given in part 3 of this book. Using intensity modulated rather than uniform intensity beams, the planner has far more control to structure the shape of the dose distribution as a function of the shape of the planning target volume (PTV) and its anatomical relations to organs-at-risk (OARs). Some dose distributions cannot be obtained with uniform intensity beams and have suitable characteristics to increase the therapeutic ratio of radiotherapy for certain tumor sites. This introductory chapter will focus on the specific dose distributions that can be generated with reasonable ease using intensity modulation and will briefly discuss the clinical rationale.

1.2 Historical Perspective

Within a year of discovery, more than a century ago, X-rays were used therapeutically. During the following years, pioneers of radiotherapy observed that ionizing radiation was harmful to healthy tissues. Many technological developments took place that aimed to reduce the toxicity of radiation to healthy tissues and to increase the anti-tumor effects. For many decades, improvements in radiotherapy were hampered by the inability to determine accurately the geometrical location of tumors. In so-called conventional radiotherapy, bony landmarks, air-soft tissue edges, skin-topography or contrast materials (liquid, surgical clips) related to the location of the tumor were used to define roughly shaped fields. With the development of medical CT-scanners, progress in radiotherapy was boosted. In conformal radiotherapy, fields from which the aperture was conformed to the edges of the tumor replaced roughly shaped fields. Treatment machines were designed to deliver flat and wedged beams. Spatial combinations of uniform and wedged beams collimated to the projection of the target create a convex high-dose volume (i.e., it cannot create high-dose volumes with concave surfaces). Using uniform beams, the treatment of tumor volumes with concave surfaces would over-dose sensitive tissues in the concavities. In the 1980s, Brahme demonstrated the unique potential of intensity modulated (IM) beams to create homogeneous concave dose distributions [1]. Inside IM-beams, the radiation fluence (intensity) was not equal but had a value that was a function of its geometrical location inside the cross section of the beam [2]. As a possible strategy to make the design of IM-beams feasible, the concept of inverse planning was also proposed by Brahme [3]. In inverse planning, computer algorithms are used to convert a (medically) desired dose distribution into beam intensity maps that can be delivered by a treatment machine.

IMRT remained a research topic mainly in physics laboratories until, in 1993, Carol proposed an integrated planning and delivery system (NOMOS MiMiC) capable of clinical IMRT tomotherapy [4]. Since 1993, much has

happened. Inverse planning for delivery with a multileaf collimator (MLC) was developed. The major vendors of linear accelerators developed MLC control systems to deliver IMRT. A variety of methods to plan and deliver IMRT are available. Now the field of IMRT application is not only the generation of concave dose distributions but includes many other situations as discussed below.

1.3 Clinical Rationale of Concave Dose Distributions

Tumors acquire irregular shapes by invading contiguous structures or lymph node regions. If the tumor bends around organs at risk (OARs), the drawing of the gross tumor volume (GTV) or clinical target volume CTV may exhibit a concave or invaginated surface leading to a concave PTV. The dose inside the concavity may be limited by the OAR to a dose level below the acceptable range of the PTV prescription dose. An acceptable planning strategy involves the creation of a concave dose distribution matching the PTV shape with sufficiently low dose inside the concavity to spare the OAR. Table 1 shows a list of tumor sites for which a concave PTV is often a planning challenge.

The list of tumor sites in Table 1 suggests that concave PTV(s) may be more common than convex PTV(s). Actually, true convex PTV shapes are rare and occur mostly for small, early stage tumors. If such tumors are flanked by or located inside organs of parallel functional unit architecture, concave dose distributions are not needed. I expect that flat beams will be rarely used when, in the future, the application of intensity-modulated beams becomes less cumbersome.

Using simplified models of photon beams and phantom anatomy, the intensity patterns to create homogeneous concave dose distributions have been calculated analytically for arc therapy [1]. To obtain a homogeneous dose inside the PTV, the intensity of the arcing beam must increase steeply towards the cavity. This principle is also true for multiple static beams as explained in Fig. 1a. Some systems like the Nomos MiMiC or the Tomotherapy machine are designed to deliver IMRT by arc therapy. Most other systems use static beams. During the planning phase, the number of beams and their directions must be defined upfront. The definition of the beam assembly to create a concave dose distribution is not trivial and the planner should be aware of some general principles. Reducing the number of beams (Fig. 1b) or increasing the wanted dose ratio between OAR and target (Fig. 1c) will cause a loss of target dose-homogeneity.

Another issue of concern involves the dose gradients near the PTV-concavity. Often little space is available to obtain the wanted dose difference between the surface of the PTV concavity and the OAR and the steepness of dose gradients must be maximized. Steep dose gradients are created by the penumbra of segment edges (see chapter I. 7). Proper choice of beam directions is important to optimally exploit segment edges in the creation of steep dose gradients. If steep gradients are required along the curvature of a concavity, a sufficient number of beams with appropriate orientation (roughly orthogonal to the direction of the gradient directions) must be used.

Table 1. Tumor sites featuring concave PTV

Tumor site	Extension (s)	Critical organ(s)
Pharynx, larynx, oral cavity	Lymph node regions	Spinal cord
Sinonasal	Neighboring anatomical spaces, skull base	Optic pathway structures
Skull base	Foramina, septa, arachnoidal space	Optic pathway structures, brainstem
Paraspinal	Foramina, arachnoidal space	Spinal cord
Mediastinum, lung	Lymph node regions	Spinal cord, esophagus
Pleura	Pleura, septa	Lung, liver
Ovarium	Peritoneum	Liver, kidneys
Retro-peritoneum	Connective tissue spaces	Kidney, liver, spinal cord
Prostate	Seminal vesicles	Rectum
Prostate (advanced)	Lymph nodes	Small bowel
Rectum	Lymph nodes	Small bowel
Cervix	Parametria, lymph nodes	Small bowel, rectum, bladder
Breast	Medial and lateral edges	Lung, heart

Column 1: Tumor sites exhibiting concave PTV. Column 2: Tumor extensions or regions of invasion bending around critical organs. Critical organ(s): Organ(s) inside the PTV-concave regions that – due to dose-volume-toxicity characteristics – require the creation of a concave dose distribution

1.4 Intentionally Inhomogeneous Dose Distributions

In conventional radiotherapy, intentionally inhomogeneous dose distributions are usually delivered in successive phases of the treatment, e.g., by shrinking field techniques. The delivery of different prescription dose levels during the same fraction involves intensity-modulated beams. By simultaneous use of multiple

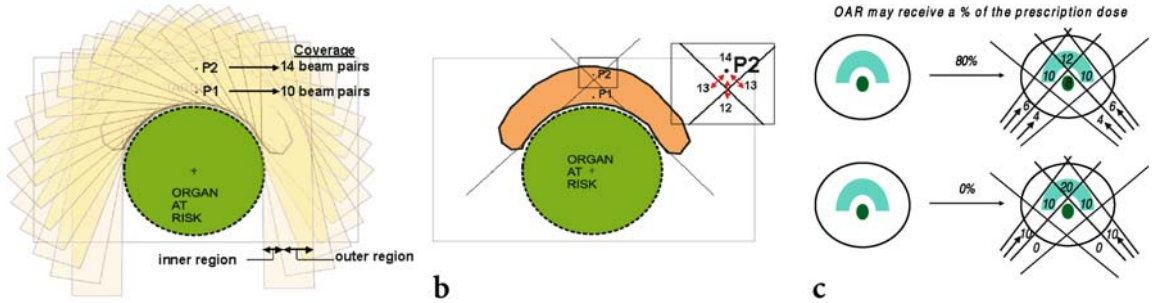

Fig. 1. (a) Irradiation of a concave PTV by many static beams that are tangential to the OAR. Let us assume that each rectangle represents a pair of opposed beams and that for each pair the variation of dose deposition with depth is negligible. Inside the PTV, point P1 is located closer to the concavity than point P2. The figure shows that P1 is exposed to fewer beams than P2 and in general, the closer a point is located nearby the concavity, the fewer the number of beams it is exposed to. If the intensity across the beam pair cross section is equal (unmodulated) then the dose to a point is proportional to the number of beam pairs that it is exposed to. Thus, the dose to P1 is 10/14th of the dose of P2. Let us divide all beam pairs in an inner (close to the concavity) and an outer region. Analysis of the figure shows that point P1 is never exposed to the outer region. Point P2 is exposed to the inner region of some beam pairs and to the outer region of other beam pairs. Thus by reducing the intensity in the outer region of the beam pairs, the dose to P2 can be lowered selectively. By repeating this procedure for pairs of points inside the PTV, we can show that the intensity inside the beam pair increases with decreasing distance to the concavity. (b) Let us consider point P2. Point P2 is embedded at the intersection of 2 beam pairs. The *insert* shows that P2 receives dose from these 2 beam pairs on top of dose from 12 beam pairs. At the beam edges inhomogeneities occur as indicated by the *arrows*. Note that the beam edges nearby the highest intensity are concerned. The *vertical arrow* crosses an inhomogeneity by exposure to n vs $n-2$ beam pairs, n being 14 in this example. The *oblique arrows* cross inhomogeneity by exposure to n vs $n-1$ beam pairs. The inhomogeneity will be roughly proportional to $n/n-a$, the value of a being dependent on the intersections of beam edges. Thus, with decreasing n, the inhomogeneity will increase. As a consequence the regional inhomogeneity inside the target will be larger closer to the concavity. (c) Example of a decreasing in-PTV inhomogeneity forced by increasing the requested dose ratio between the OAR and the concave PTV. In the upper panel, the OAR may receive 80% of the median prescription dose and the inhomogeneity is smaller than in the lower panel where the OAR may receive 0% of the prescription dose

prescription doses, dose and overall treatment time are tailored to indices of disease control like cancer cell density and proliferation rate while the normal tissue toxicity is reduced by restricting the volume exposed to high doses, and through fractionation. A discussion regarding the advantages of simultaneous use of multiple dose levels can be found elsewhere [5]. For many solid tumors, most loco-regional relapses occur inside the GTV. The highest dose level is therefore applied to the GTV region. Lower prescription doses may be prescribed to parts of the PTV for two main reasons; these parts are regions at risk for subclinical disease or regions of overlap between PTV and OAR(s). For subclinical disease ample evidence exist that high control rates can be achieved with relatively modest doses. Lowering the dose to regions of overlap is a consequence of dose-priority ranking. Dose constraints needed to avoid complications are given priority to the application of a higher dose that would possibly improve local control. The strategy is shown in Fig. 2a that shows a PTV with two OARs located peripherally (OAR1 and OAR2) and one located centrally (OAR3). OAR1 and OAR2 have part of their volumes inside the expansion margin for motion and set-up uncertainty around the CTV. OAR3 is located inside the CTV. At the overlap regions, the dose is limited by priority ranking of the OARs. Assuming that MTD(OAR1) < MTD(OAR2) < MTD(OAR3), MTD being the maximum tolerated dose, then different maximum dose limits exist for different regions of the PTV as shown in Fig. 2b. This 'avoidance' strategy of dose escalation has been applied in prostate [6] and head and neck cancer [7]. The degree of toxicity was consistent with the dose level in the overlap regions. However, the strategy may be questionable. If the region of the PTV, which is at highest risk for relapse, resides inside an overlap region where dose constraints to the OAR are prioritized, then delivering higher doses to other areas of the PTV may be senseless. These considerations question a nowadays-popular IMRT strategy in early prostate cancer. It is known that 60–70% of primary prostate tumors arise in the peripheral zone, close to the anterior rectal wall. By priority ranking the dose is restricted to the overlap region between the PTV and the rectal wall while higher doses are applied in the PTV part outside this overlap region. As a result, the gross tumor volume (as defined by T2-weighted MRI imaging or MRI spectroscopy) is often located in a relatively under-dosed region, namely the dose gradient near the overlap region (Fig. 2c).

From a radiobiology viewpoint, it seems self-evident to direct dose escalation to the regions inside the PTV that are supposed to be the most radiation resistant [8]. To achieve tumor control, a higher dose must be applied to GTV than to subclinical disease. In terms of radio-resistance, GTV is heterogeneous. Novel biological imaging techniques, mostly based on PET, MRI and MRS, may have the potential to construct three-dimensional maps of radio-biological parameters related to radio-resistance [9–11] (see chapters II. 2, II. 3, II. 4). These maps can be fused with high-resolution CT and

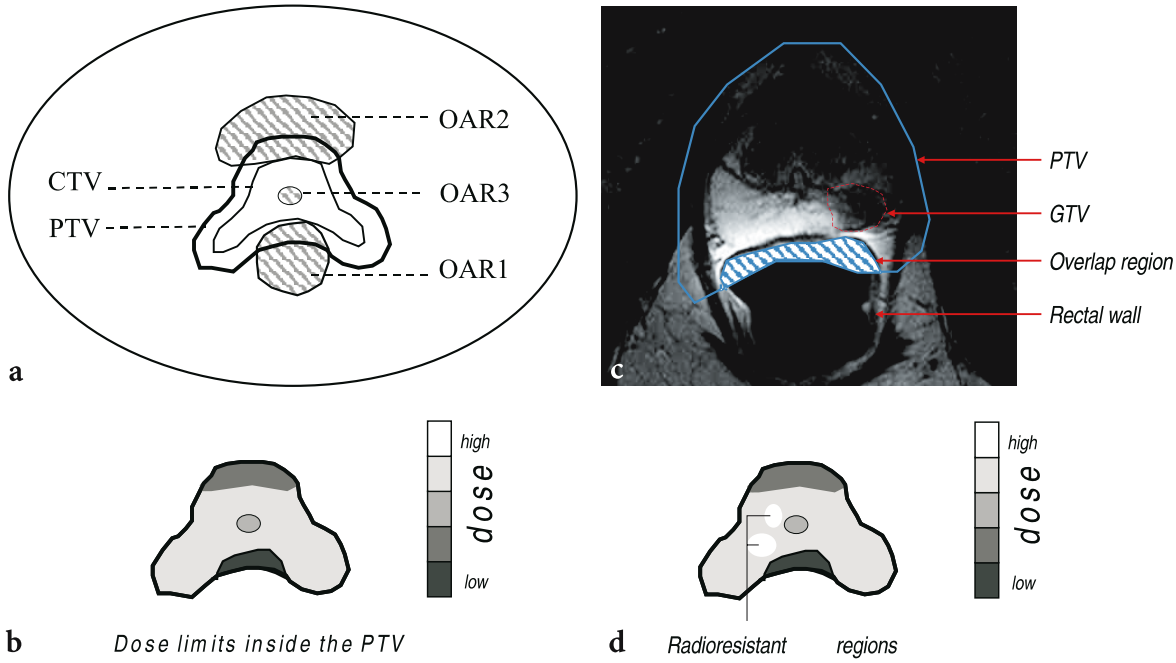

Fig. 2. **(a)** CTV: clinical target volume; PTV: planning target volume; OAR: organ at risk. Partial overlap between the OAR1 and OAR2 with PTV. OAR3 is located entirely inside the PTV. OAR1 is most sensitive to radiation, OAR3 most resistant. **(b)** Dose to the overlap regions must be kept below tolerance of the respective OARs. Dose to the non-overlapping part of the PTV is restricted by tissues that are usually not considered as dose-limiting. For "structural" tissues inside tumors or invaded by tumors, the dose/volume/toxicity relationships are usually not known since prescription doses close to their tolerance may not have been explored. **(c)** T2-weighted MRI image. GTV located in the peripheral zone, adjacent to the overlap region between rectal wall and PTV. Maximum dose constraint to the overlap region will restrict dose to the GTV because dose gradients have limited steepness (figure from G. Villeirs). **(d)** Identification of the most radiation resistant regions by biological imaging. Dose escalation focused to these regions is hypothetically safer than to the whole non-overlapping region of the PTV and maybe as efficient to increase local control. Clinical studies are needed to investigate this hypothesis

MRI for treatment design and optimization with a strategy of small-volume focused dose escalation to radiation resistant foci (Fig. 2d). The maximum dose that can be given to small volumes of the PTV is unknown. A variety of tissues including connective, vascular, muscular and other tissues may have to be considered as dose limiting. If the tissues inside the PTV have parallel functional unit architecture and if dose escalation is focused to small sub-volumes, highly increased doses may be tolerable. This hypothesis is supported by stereotactic radiosurgery [12] or brachytherapy [13, 14] boosts on top of conventional dose levels that allowed the safe delivery of remarkably high doses if individual high-dose volumes were kept small. IMRT-based focused dose escalation guided by biological imaging techniques is becoming an area of intense translational and clinical research.

1.5 Compensating Unwanted Effects of Loss of Electron Equilibrium

When photon beams traverse heterogeneous tissues, several effects occur near the interface between low-density media (lung, sinonasal, pharyngeal, tracheal or bronchial air cavities) and tissues of higher density (including tumors). These effects are due to a loss of electron equilibrium: arriving electrons are not completely balanced in number by the produced (leaving) electrons. In addition, the secondary electrons after single and multiple scattering can deposit their energy at a relatively large distance in low-density tissues, i.e., their path-lengths are longer. Three types of effects may be counteracted by the use of intensity modulation:

1. A local dose decrease where the beam re-enters the higher density tissue (rebuild-up: Fig. 3). This rebuild-up is caused by the lower density of production of secondary electrons in the low-density tissue and can be important for beams that traverse low-density tissue before hitting the tumor. In case of small beam width, the under-dosage in the rebuild-up region is deepened by loss of secondary electrons outside the boundaries of the beam [15].
2. Lateral dose spread in low-density tissue beyond the geometrically expected beam boundaries (Fig. 3). The reason is that, even for modest photon energies, the electron path length in low-density tissue is of the order of centimeters. This implies that the

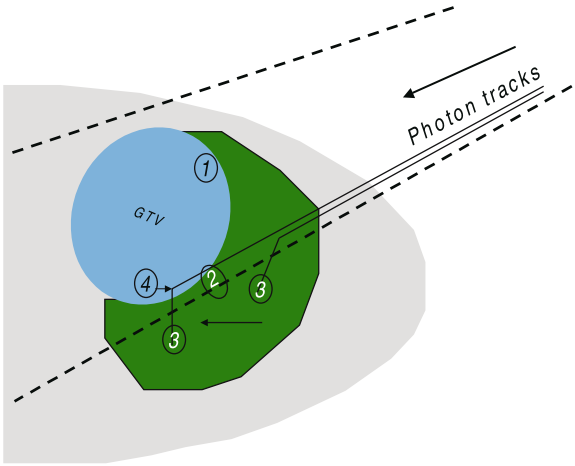

Fig. 3. Loss of electron equilibrium (see main text for explanation) leading to under-dosage at the interface between tumor and low-density tissue (*shown in green*) because of: 1: re-build-up at the tumor edge upstream of the photon beam; 2: penumbra broadening; 3: secondary and multiple scattered electrons deposit dose far outside the beam edge in low-density tissue; 4: leaving electrons not fully compensated by arriving electrons because insufficient electrons are generated in the small slit of low-density tissue nearby the beam edge

beam edges become dosimetrically blurred and that larger volumes of low-density tissue are exposed to significant doses [16, 17].

3. Under-dosage where the tumor flanks low-density tissue at beam edges since more electrons leave the tumor interface zone than arrive from the low-density tissues (Fig. 3) [16, 17].

1.5.1 IMRT to Counteract Re-buildup

The use of intensity modulation to correct under-dosage by re-buildup looks obvious. By the use of beams from other directions, it is theoretically possible to design intensity peaks that give additional dose to a rebuild-up region. In practice, motion, deformation and variability during the course of fractionated radiotherapy and small size of the re-buildup region are serious difficulties to apply IMRT for this purpose. Beam direction optimization might allow to avoid beams that cause re-buildup in the tumor altogether. The use of lower photon energies also reduces the re-buildup effects.

1.5.2 IMRT to Counteract Effects of Beam-edge Degradation

A margin is included in the beam apertures surrounding the PTV to account for the dose fall-off at the beam edges (i.e., "penumbra"). For higher energy beams and for low-density tissues adjacent to the PTV, the beam aperture margin should be increased to account for the beam-edge blurring. However, increased margins also increase the volume of normal tissue irradiated. An elegant IMRT technique to reduce the beam aperture margin involves the use of compensating rinds of increased beam intensity [18, 19]. These compensation techniques were evaluated for 6- and 18-MV X-rays by calculating penumbral widths as a function of the increased beam intensity in the rind, the rind width, and tissue density [20]. Results of calculations and film dosimetry showed that the distance between the 95%–50% isodose lines was reduced from 11 mm to 4 mm for 6-MV X-rays in a lung phantom, when the beam intensity is increased by 20% in a 10 mm wide rind. At 18 MV, this distance is reduced from 16 mm to 6 mm with a 20% increase in rind intensity, but a 15 mm wide rind is required. In all cases, penumbra compensation did not result in any appreciable increase in scatter dose outside the field boundaries.

Clearly, intensity modulation can be used to counteract some of the unwanted effects of loss of electron equilibrium but this capability cannot be routinely exploited yet. Most IMRT planning systems are not able to produce the appropriate modulation patterns due to the use of conventional dose computation algorithms during the optimization process. In these algorithms secondary electron transport is not (well) modeled and phenomena due to loss of electron equilibrium are neglected. These issues are discussed in chapter I. 6.

1.6 Missing Tissue Compensation

A simple and straightforward use of intensity-modulated beams is missing tissue compensation that inherently results from the plan optimization process. IMRT has been used for this purpose in head and neck [21] and breast cancer [22, 23] amongst other sites. In modern applications, missing tissue compensation is rarely the only goal of IMRT.

1.7 Anecdotal Applications of IMRT and Combinations with other Treatment Modalities

Korevaar et al. [24] reported on mixed intensity modulated high-energy electron and photon beams to create dose distributions that feature: (a) a steep dose fall-off at larger depths, similar to pure electron beams, (b) uniform beam profiles and sharp and depth-independent beam penumbras, as in photon beams, and (c) a selectable skin dose that is lower than for pure electron beams. The intensity modulated electron beam com-

ponent consisted of two overlapping concentric fields with optimized field sizes, yielding broad, fairly depth-independent overall beam penumbras. The matched intensity modulated photon beam component has a high intensity rind to sharpen this penumbra. The combination of the electron and the photon beams yields dose distributions with the characteristics (a)–(c) mentioned above. Although the use of electron beams can be avoided by using photon IMRT, it is often at the expense of larger volumes irradiated at low doses. Examples include avoidance of electron beams in head and neck to treat the posterior neck or in breast cancer to treat the internal mammary chain. The IMRT 'dose bath' to the contra-lateral breast, intra-thoracic organs or head-and neck structures may be cumbersome. Routine availability of beams with the characteristics described by Korevaar would allow decreasing the dose bath in many IMRT applications as well as for conventional techniques like cranio-spinal axis irradiation or in anatomical sites like the retro-peritoneal region in which sharper dose falloff in depth is needed.

Clinical situations exist in which the PTV consists of a region for which the treatment involves brachytherapy while another region is best treated by external beam only. An example is loco-regionally advanced cervical cancer with clinically positive lymph nodes. A proper match between the dose distributions delivered by both modalities is a technical challenge that – intuitively – can be solved by IMRT. Literature on the use of IMRT to match the dose distribution obtained by brachytherapy is scarce (see chapter III. 11).

1.8 Conclusion

Intensity-modulated photon beams can be used to obtain homogeneous concave dose distributions. They allow the creation of intentionally non-homogeneous dose distributions for the prescription of multiple dose levels to be delivered during the same fraction. Dose gradients can be delivered with controlled steepness and location. Unwanted dosimetrical effects of loss of electron equilibrium near interfaces between lower and higher density tissues can be counteracted by IMRT but the appropriate planning technology is not generally available yet. Simple and straightforward is the use of intensity-modulated beams for missing tissue compensation. Dose distributions can be generated to match brachytherapy or electron beam plans. Mixed intensity and energy modulated electron-photon beams with steep dose-fall off and sharp depth-independent penumbra can be created.

Acknowledgements. The project "Conformal Radiotherapy Ghent University Hospital" is supported by the Belgische Federatie tegen Kanker and by grants from the Fonds voor Wetenschappelijk Onderzoek Vlaanderen (grants FWO G.0049.98, G.0039.97), the Ghent University (GOA 12050401, BOF 01112300, 011V0497, 011B3300) and the Centrum voor Studie en Behandeling van Gezwelziekten.

References

1. Brahme A, Roos JE, Lax I (1982) Solution of an integral equation encountered in rotation therapy. Phys Med Biol 27:1221–1229
2. Lax I, Brahme A (1982) Rotation therapy using a novel high-gradient filter. Radiology 145:473–478
3. Eklof A, Ahnesjo A, Brahme A (1990) Photon beam energy deposition kernels for inverse radiotherapy planning. Acta Oncol 29:447–454
4. Carol M, Grant WH III, Pavord D, Eddy P, Targovnik HS, Butler B, Woo S, Figura J, Onufrey V, Grossman R, Selkar R (1996) Initial clinical experience with the Peacock intensity modulation of a 3-D conformal radiation therapy system. Stereotact Funct Neurosurg 66:30–34
5. Mohan R, Wu Q, Manning M, Schmidt-Ullrich R (2000) Radiobiological considerations in the design of fractionation strategies for intensity-modulated radiation therapy of head and neck cancers. Int J Radiat Oncol Biol Phys 46:619–630
6. Zelefsky MJ, Fuks Z, Hunt M, Yamada Y, Marion C, Ling CC, Amols H, Venkatraman ES, Leibel SA (2002) High-dose intensity modulated radiation therapy for prostate cancer: early toxicity and biochemical outcome in 772 patients. Int J Radiat Oncol Biol Phys 53:1111–1116
7. Claus F, Boterberg T, Ost P, De Neve W (2002) Short term toxicity profile for 32 sinonasal cancer patients treated with IMRT. Can we avoid dry eye syndrome? Radiother Oncol 64:205–208
8. Gregoire V (2002) Target-volume selection and delineation in the cervico-maxillo-facial region: beyond the concepts of the ICRU. Cancer Radiother 6(1):29s–31 s
9. Ling CC, Humm J, Larson S, Amols H, Fuks Z, Leibel S, Koutcher JA (2000) Towards multidimensional radiotherapy (MD-CRT): biological imaging and biological conformality. Int J Radiat Oncol Biol Phys 47:551–560
10. Van de Wiele C, Lahorte C, Oyen W, Boerman O, Goethals I, Slegers G, Dierckx RA (2003) Nuclear medicine imaging to predict response to radiotherapy: a review. Int J Radiat Oncol Biol Phys 55:5–15
11. Chao KS, Bosch WR, Mutic S, Lewis JS, Dehdashti F, Mintun MA, Dempsey JF, Perez CA, Purdy JA, Welch MJ (2001) A novel approach to overcome hypoxic tumor resistance: Cu-ATSM-guided intensity-modulated radiation therapy. Int J Radiat Oncol Biol Phys 49:1171–1182
12. Tate DJ, Adler JR Jr, Chang SD, Marquez S, Eulau SM, Fee WE, Pinto H, Goffinet DR (1999) Stereotactic radiosurgical boost following radiotherapy in primary nasopharyngeal carcinoma: impact on local control. Int J Radiat Oncol Biol Phys 45:915–921
13. DeNittis AS, Liu L, Rosenthal DI, Machtay M (2002) Nasopharyngeal carcinoma treated with external radiotherapy, brachytherapy, and concurrent/adjuvant chemotherapy. Am J Clin Oncol 25:93–95
14. Rudoltz MS, Perkins RS, Luthmann RW, Fracke TD, Green TM, Moye L, Wludyka P, Choi YK, Ackerman SN (1999) High-dose-rate brachytherapy for primary carcinomas of the oral cavity and oropharynx. Laryngoscope 109:1967–1973

15. Martens C, Reynaert N, de Wagter C, Nilsson P, Coghe M, Palmans H, Thierens H, De Neve W (2002) Underdosage of the upper-airway mucosa for small fields as used in intensity-modulated radiation therapy: a comparison between radiochromic film measurements, Monte Carlo simulations, and collapsed cone convolution calculations. Med Phys 29:1528–1535
16. Dirkx ML, Heijmen BJ, Korevaar GA, van Os MJ, Stroom JC, Koper PC, Levendag PC (1997) Field margin reduction using intensity-modulated X-ray beams formed with a multileaf collimator. Int J Radiat Oncol Biol Phys 38:1123–1129
17. Miller RC, Bonner JA, Kline RW (1998) Impact of beam energy and field margin on penumbra at lung tumor-lung parenchyma interfaces. Int J Radiat Oncol Biol Phys 41:707–713
18. Mohan R, Wu Q, Wang X, Stein J (1996) Intensity modulation optimization, lateral transport of radiation, and margins. Med Phys 23:2011–2021
19. Brugmans MJ, van der Horst A, Lebesque JV, Mijnheer BJ (1999) Beam intensity modulation to reduce the field sizes for conformal irradiation of lung tumors: a dosimetric study. Int J Radiat Oncol Biol Phys 43:893–904
20. Sharpe MB, Miller BM, Wong JW (2000) Compensation of X-ray beam penumbra in conformal radiotherapy. Med Phys 27:1739–1745
21. Nutting CM, Normile PS, Bedford JL, Harrington KJ, Webb S (2003) A systematic study of techniques for elective cervical nodal irradiation with anterior or opposed anterior and posterior beams. Radiother Oncol 69:43–51
22. Evans PM, Hansen VN, Mayles WP, Swindell W, Torr M, Yarnold JR (1995) Design of compensators for breast radiotherapy using electronic portal imaging. Radiother Oncol 37:43–54
23. Kestin LL, Sharpe MB, Frazier RC, Vicini FA, Yan D, Matter RC, Martinez AA, Wong JW (2000) Intensity modulation to improve dose uniformity with tangential breast radiotherapy: initial clinical experience. Int J Radiat Oncol Biol Phys 48:1559–1568
24. Korevaar EW, Heijmen BJ, Woudstra E, Huizenga H, Brahme A (1999) Mixing intensity modulated electron and photon beams: combining a steep dose fall-off at depth with sharp and depth-independent penumbras and flat beam profiles. Phys Med Biol 44:2171–2181

The Potential and Limitations of IMRT: A Physicist's Point of View

R. Mohan, T. Bortfeld

2

Contents

2.1 Introduction, Basic Concept, Short History

The basic idea underlying intensity-modulated radiotherapy (IMRT) is that, in complex cases (and also in some not so complex cases, as we will discuss below), one needs radiation fields with optimized *non-uniform spatial intensity distributions* from different directions of incidence in order to achieve the desired dose distribution in the tumor target volume with adequate sparing of the near-by critical structures. IMRT may be considered as a generalization of 3D conformal radiotherapy (3D CRT) in which multiple (sometimes non-coplanar) non-uniform radiation fields are used and shaped according to the projection of the tumor target volume, taking into consideration dose-volume constraints of the intervening and surrounding normal tissues. The two techniques are compared in Fig. 1.

That radiation fields with highly non-uniform intensities are sometimes needed to create the desired uniform dose to the target volume was first recognized and described by Brahme et al. in 1982 [1]. They considered the irradiation of a ring-shaped target volume around a circular critical structure (organ at risk, OAR); see Fig. 2. This could be a model of a tumor surrounding the spinal cord. The example could serve as a general motivation of IMRT. At first glance, an obvious treatment technique for such a tumor would be a rotation technique with a central block as schematically shown in Fig. 2. However, this does *not* produce a uniform dose distribution in the ring-shaped target. In fact, the resulting dose profile through the center of the ring falls off gradually toward the OAR, where the dose is almost zero, as desired (solid line at the bottom of Fig. 1). The considerable target dose inhomogeneity resulting from blocking the central part of the beam can be understood with the geometrical argument presented in the previous chapter.

The idea of using IMRT in this example is that the dose distribution in the target can be made *homogeneous* by applying an *inhomogeneous* beam intensity distribution (beam profile) in the unblocked part of the beam as shown schematically by the dashed line in Fig. 2. In this way the dose deficit in the target can be "filled up". In reality the resulting dose distribution is of course not as perfect as depicted by the dashed line at the bottom of Fig. 2. There will be some scatter dose in the OAR, and the dose profile deviates somewhat from the rectangular shape due to the penumbra. Nevertheless, IMRT allows us to push the dose conformation potential to the physical limits. This means in particular that

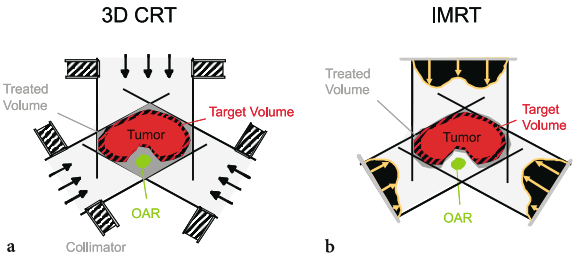

Fig. 1. Comparison of the principles of 3D conformal radiotherapy and IMRT. The use of conformal uniform fields generally yields a convex dose distribution. If the tumor "wraps around" a critical structure, as shown in this example, the latter will get the full treatment dose. With IMRT one varies the intensity across each treatment field and can deliver more intensity to those rays that hit the target volume only, and reduce the intensities of the rays that pass through both the target and critical structures. Intensities within each beam are adjusted so that, when multiple beam are superimposed, the combination produces the desired dose coverage of the target volume and sufficient sparing of the critical structure(s)

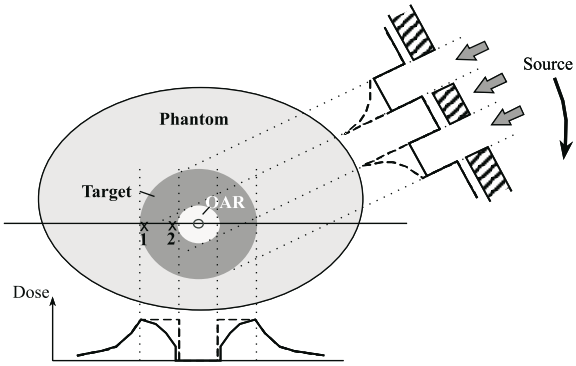

Fig. 2. The original example of Brahme [1] representing an abstract case of a ring-shaped target volume around a critical structure (say, the spinal cord). The rotation with a centrally blocked beam produces an inhomogeneous dose distribution in the target. This is depicted by *the solid line at the bottom*, which is a dose profile through the isocenter. Only through the modulation of the intensity within the open part of the beam (*dashed curve*) can the missing dose be filled up (*dashed curve at the bottom*)

the dose gradient between the target and the OAR can be made as steep or even somewhat steeper than the dose gradient at the edge of a conventional uniform beam.

Based on this basic motivation we can give a definition of IMRT as follows:

Definition of intensity modulated radiotherapy (IMRT):
IMRT is a radiation treatment technique with multiple beams incident from different directions in which at least some of the beams are intensity-modulated so that each beam intentionally delivers a non-uniform dose to the target. The desired dose distribution in the target is achieved after superimposing such beams. The additional degrees of freedom to adjust intensities of individual rays are utilized to achieve a better target dose conformality and/or better sparing of critical structures.

Of the various alternatives proposed for the delivery of IMRT, two dominant but significantly different approaches have emerged. Based on the original ideas of Brahme et al., Mackie et al. [2] have proposed a rotational approach called "Tomotherapy" in which intensity-modulated photon therapy is delivered using a rotating slit beam. Intensity (or rather fluence) modulation is achieved through the use of a dedicated system that incorporates a temporally modulated slit multi-leaf collimator whose leaves move rapidly in or out of the slit. Like a CT scanner, the radiation source and the collimator revolve around the patient. Either the patient is translated between successive rotations (serial tomotherapy) or continuously during rotation (helical tomotherapy). For the latter, the system looks like a conventional CT scanner and includes a megavoltage portal detector to provide for the reconstruction of megavoltage CT images. The first clinical helical tomotherapy machines have recently been implemented.

In the second approach, a set of intensity-modulated fields incident from fixed gantry angles and a standard multileaf collimator (MLC) are used to deliver the optimized intensity (or rather fluence) distribution in either dynamic mode, in which the leaves move while the radiation is on [3–5], or static or "step-and-shoot" mode, in which the sequential delivery of radiation sub-portals is combined to achieve the desired fluence distribution [6]. Every major commercial treatment planning system manufacturer has implemented one or both of these modes. This approach is a relatively straightforward extension of existing technology. It is facilitated by the fact that in most cases one does not need more than about nine intensity-modulated beams to achieve a dose distribution that is close to optimal [7]. In today's practice MLC-based IMRT often uses not more than seven beams [8].

The first clinical IMRT was delivered with a serial tomotherapy device in 1994 [9], shortly followed by MLC-based IMRT, which was first implemented into clinical use at Memorial Sloan-Kettering Cancer Center in 1995 [10] and rapidly gained wide acceptance. Some other variants of IMRT delivery techniques have been described and brought into clinical practice. They are described elsewhere in this volume (chapter 7).

For physical reasons it is clear that IMRT will not be able to achieve an ideal dose distribution that delivers dose to the tumor only and no dose to the surrounding healthy tissues. However, the greater flexibility of IMRT, which is due to the large number of degrees of freedom, will allow us to come closer to the ideal distribution than any other conventional photon radiotherapy method. It is also clear that, because of the great number of degrees of freedom, IMRT requires computer-aided tools, not only for the computation of the dose distributions that result from a given set of treatment parameters (the "forward problem"), but also for the inverse problem of determining treatment parameters based on the clinical objectives. Solution to the inverse problem may be achieved with specially designed optimization techniques (see chapter 4, this volume). This process is also often referred to as "inverse planning."

2.2 Potential of IMRT

Most of the advantages of IMRT are based on its ability to manipulate optimally intensities of individual rays (beamlets) within each beam. This ability permits greatly increased control over radiation fluence, enabling custom-design of optimum dose distributions. Potential advantages of IMRT are described in the following paragraphs.

2.2.1 Higher Conformality and Margin Reduction

The ability to control fluence can be used to produce sharper fall-off of dose at the PTV boundary and to produce dose distributions that are far more conformal than those possible with standard 3D CRT. (While the achievement of sharper boundaries is considered to be one of IMRT's benefits, it should be noted that, if desired, a gradual fall off could also be accomplished.) Conceptually, the ability to achieve sharper boundaries has been addressed in the previous chapter and is further explained below.

When a photon beam traverses the body, it is scattered, depositing dose not only along the path of each ray of the beam but also at points away from it. The electrons knocked out by the incident photons travel laterally to points in the neighborhood of each ray, depositing dose along the way. Near the middle of a uniform beam, incoming electrons offset outgoing electrons and equilibrium exists. However, at and just inside the boundaries of the beam, there are no incoming electrons to balance electrons flowing out of the beam. Therefore, a "lateral disequilibrium" exists and leads to a dose deficit inside the boundaries of beams. For lower energy beams and at large depths, scattered photons also contribute significantly to this effect. The conventional approach to overcome this deficiency is to add a margin for the beam penumbra to the PTV so that the tumor dose is maintained at the required level. For IMRT plans there is another method to counterbalance the dose deficit. The intensity of rays just inside the beam boundary may be increased. Since some of the increased energy must also flow out, a very large increase would be required if the margin for the penumbra were set to zero or to a very small value. Therefore, an increase in boundary fluence alone is not enough. A combination of an increased fluence and the addition of a margin, albeit a much smaller one, is a better solution [11, 12].

The sharpening of beams and higher conformality means smaller margins. A reduction of the margins attributable to the penumbra by as much as 8 mm has been found to be feasible for prostate treatments [12]. High conformality means that the volume of normal tissues exposed to high doses may be reduced significantly, which, in turn, may allow escalation of tumor dose or reduction of normal tissue dose or both, leading presumably to improved outcome. A lower rate of complications may also mean lower cost of patient care following the treatment.

2.2.2 Target Dose Homogeneity

Dose distributions within the PTV, in theory, can be made more homogeneous with IMRT. The PTV dose homogeneity is traditionally considered to be a highly desirable feature of dose distributions.

> Experience with current IMRT systems has led to an impression among many that IMRT inherently produces inhomogeneous dose distribution within the target volume. If all things were equal, the IMRT plan should always produce more homogeneous dose distribution than a plan made with uniform beams. The inhomogeneity commonly observed is due to the overriding need to partially or wholly protect one or more critical organs, as well as due to the limitations of some inverse planning systems.

The degree of dose heterogeneity depends upon the severity of constraints on normal structures and their proximity to the PTV. If the dose-volume tolerances of the normal structure in the immediate vicinity of the PTV are much lower than the prescription dose, and if unobstructed paths for sufficient number of beams cannot be found, the PTV dose distributions are likely to be inhomogeneous. Furthermore, dose inhomogeneity may become more significant when dose is escalated. Dose homogeneity also depends upon the complexity of anatomy. For a simple case, for instance, if all normal tissues outside the target volume were to be avoided equally and all had identical constraints, then PTV dose can be made nearly perfectly homogeneous. Another factor that affects target dose inhomogeneity is the number of beams. The larger the number of beams, the larger the number of rays passing through each volume element and, thus, the greater the ability to compensate for PTV dose deficits caused when some of the rays must be blocked due to normal tissue constraints.

2.2.3 IMRT and Integral Dose

It is commonly believed that IMRT has a tendency to spread low, but still potentially damaging, doses to large volumes of normal tissues and that integral doses for IMRT are higher than for 3D conformal radiotherapy. In fact, this has been one of the concerns inhibiting the application of IMRT to lung and esophagus treatments. Preclinical treatment design studies indicate that such concerns may be unwarranted. Two recent studies, one for lung and the other for esophagus, showed that volumes receiving higher than 10 Gy as well as the integral dose are reduced with IMRT [13–16]. Figure 3 shows data for lung patients. The volumes receiving doses above 20 and 30 Gy were reduced with IMRT as compared to 3D-CRT. Volumes at 10 Gy were about the same and, in many cases, volumes receiving higher than 5 Gy increased. Figure 4 shows integral dose for 3D-CRT and IMRT plans for the same group of lung patients. In all cases the IMRT integral dose is less than or equal to the 3D-CRT integral dose. It should be mentioned that all IMRT plans

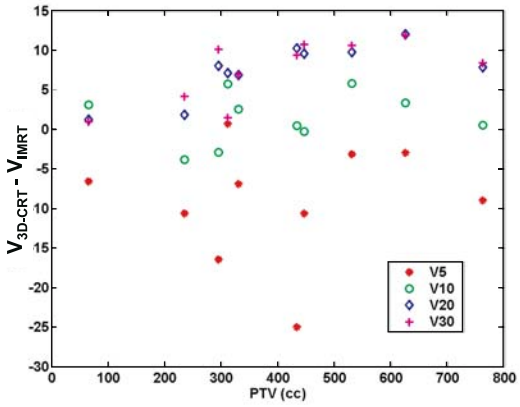

Fig. 3. Comparison of healthy non-target volumes treated at small dose levels with 3D CRT and IMRT for a group of lung patients. Similar amounts of volume are treated at or above 10 Gy with both modalities. At higher dose levels IMRT provides better sparing, while 3D CRT is better at the lowest dose level of 5 Gy. (From Liu et al. [13])

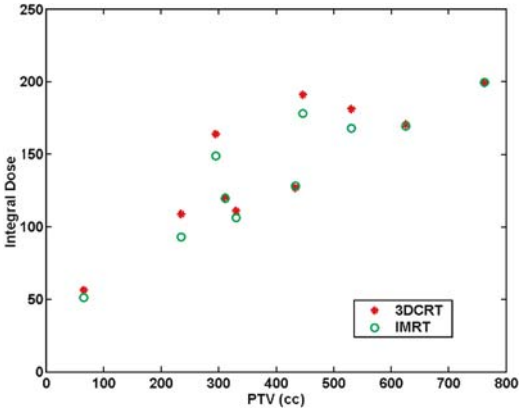

Fig. 4. Comparison of the overall integral dose delivered with 3D CRT and IMRT for the same group of lung patients as in Fig. 3. IMRT delivers similar or somewhat lower integral doses than 3D CRT. (From Liu et al. [13])

of Figs. 3 and 4 used nine beams. Liu et al. also found that the use of a smaller number of beams (five or seven) reduced the 10 Gy volumes to below the 3DCRT levels without perceptibly compromising the target dose. Furthermore, the differences of 5 Gy volumes between the IMRT and 3D-CRT plans was found to be statistically insignificant.

2.2.4 Potential for Efficiency

IMRT has the potential to be more efficient with regard to treatment planning and delivery than standard 3DCRT, although this potential has not yet been widely recognized or realized due to the evolving nature of the field.

The treatment design process is relatively insensitive to the choice of planning parameters, such as beam directions. There are no secondary field shaping devices other than the computer-controlled multi-leaf collimator (MLC). Furthermore, large fields and boosts can be integrated into a single treatment plan and, in many cases, electrons can be dispensed with, permitting the use of the same integrated boost plan for the entire course of treatment. An integrated boost treatment may offer an additional radiobiological advantage in terms of lower dose per fraction to normal tissues while delivering higher dose per fraction to the target volume. Higher dose per fraction also reduces the number of fractions and hence lowers the cost of a treatment course. In general, the automation of various aspects of planning, quality assurance and delivery of IMRT should lead to considerable improvement in efficiency.

Clinical Sites Where IMRT may be Most Advantageous: In principle, IMRT could be used to treat just about any treatment site. However, the extra effort and time required, at least in the current way IMRT is practiced, may not justify its use unless significant potential for clinical benefit exists. IMRT is considered to be of value primarily for concave target volumes. The most prominent example is that of the prostate planning target volume when the PTV overlaps the rectum and especially when seminal vesicles are involved. As illustrated in Fig. 5, blocking the rectum (dotted magenta line) from receiving unacceptable doses without blocking the target volume (dotted cyan line), especially when escalating prescription doses, is one of the initial successes of IMRT.

In addition, IMRT has been shown to be effective when arbitrarily shaped targets (including convex ones) may be surrounded by or be in the vicinity of complex normal tissue anatomy (Fig. 6). In this respect, the advantage of IMRT is being exploited for head and neck cancers. Another key advantage of IMRT is its capacity to deliver the same or different doses per fraction to different targets simultaneously. An example of the former is the simultaneous stereotactic radiotherapy of multiple brain nodules [17, 18]. Figure 7 illustrates

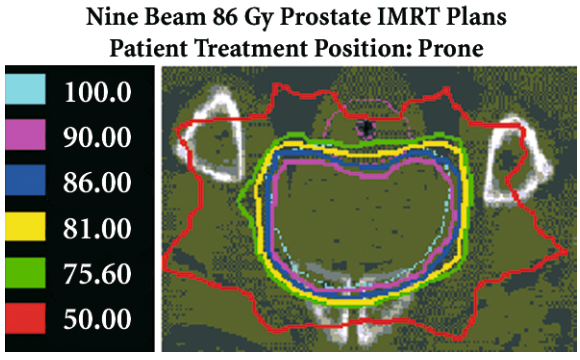

Fig. 5. IMRT dose distribution for a prostate treatment with good sparing of the rectum

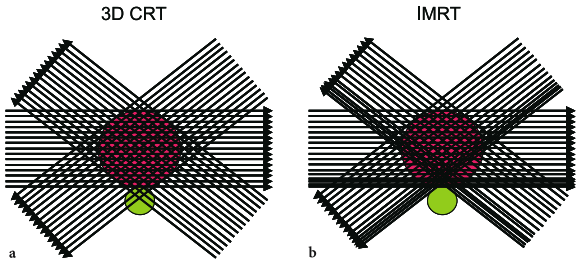

Fig. 6. IMRT provides a potential advantage not only for the treatment of concave target volumes, but also for simple convex target volumes if critical structures are nearby. This illustration shows that 3D CRT leads to some dose load in the critical structure (*shown in green*) unless only the lateral beam is used (which would lead to unacceptably high entrance and exit doses). IMRT allows one to spare the critical structure completely while maintaining good target coverage through intensity modulation

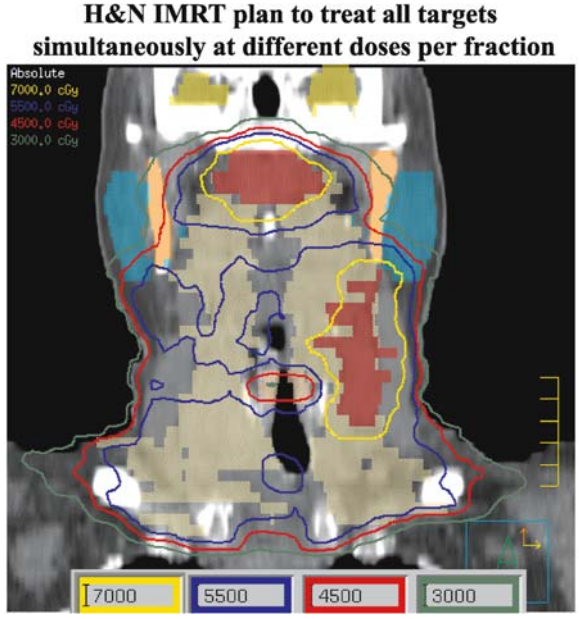

Fig. 7. Simultaneous treatment of different target areas with different doses for a head and neck case. (From Wu et al. [19])

simultaneous treatment of gross target volume, microscopic extensions and nodes to 2.33, 2 and 1.8 Gy per fraction respectively for 30 fractions.

2.3 Limitations of IMRT

We should, however, recognize that IMRT has limitations. There are certain dose distributions (or dose-volume combinations) that are simply not physically achievable. The optimization of IMRT plans involves tradeoffs that balance specified normal tissue objectives against each other and against tumor objectives. Generally, improvement in the benefit to any one of the anatomic structures cannot be achieved without increasing the cost to another [20,21]. Furthermore, our knowledge about what is clinically optimal and achievable and how best to define clinical and dosimetric objectives of IMRT is limited. Moreover, the best solution may elude us because of the limitations of the mathematical formalism and methods used to find it or due to the practical limits of computer speed and the time required. For instance, the optimization process may get trapped in a local minimum in the space of solutions that may be far from acceptable or, if acceptable, may be far from optimum. Furthermore, the direction of incident beams (in MLC-based IMRT from a predefined set of beams) are generally chosen to be equispaced or based on intuition or convention. These directions may be good enough but not necessarily optimum.

Uncertainties of various types, e.g., those related to daily (inter-fraction) positioning, displacement and distortions of internal anatomy, intra-fraction motion and changes in physical and biological characteristics of tumors and normal tissues during the course of treatment, may limit the applicability and efficacy of IMRT.

Figure 8 shows that when a prostate IMRT plan designed based on the planning CT (left panel) is applied to one of the CT images obtained during the course of radiotherapy, there is a significant loss of target coverage. Blue, red, yellow and green regions represent prostate, seminal vesicles, bladder and rectum respectively.

Dosimetric characteristics of a delivery device, such as radiation scattering and transmission through the MLC leaves, introduce some limitations in the accuracy and deliverability of IMRT. For instance, leakage through the MLC and the large number of monitor units typically required for IMRT may make it difficult to achieve very low doses. In addition, the limited accuracy of the current IMRT dosimetric verification systems (based principally on radiographic film) diminishes the confidence in the delivered dose. Furthermore, most current dose calculation models are limited in their accuracy, especially for the small, complex shapes required for IMRT. It is quite conceivable that inaccuracies in dose calculations may yield a solution different from the one if dose calculations were accurate [22]. Perhaps the most important factor that may limit the immediate success of IMRT is the inadequacy of imaging to define the true extent of the tumor, its extensions and the radiobiological characteristics and geometric, dose-response and functional characteristics of normal tissues.

2.4 Potential Risks of IMRT

We should also be aware of the potential risks of IMRT. The effect of the large fraction sizes used in integral boost IMRT on tissues embedded within the GTV is un-

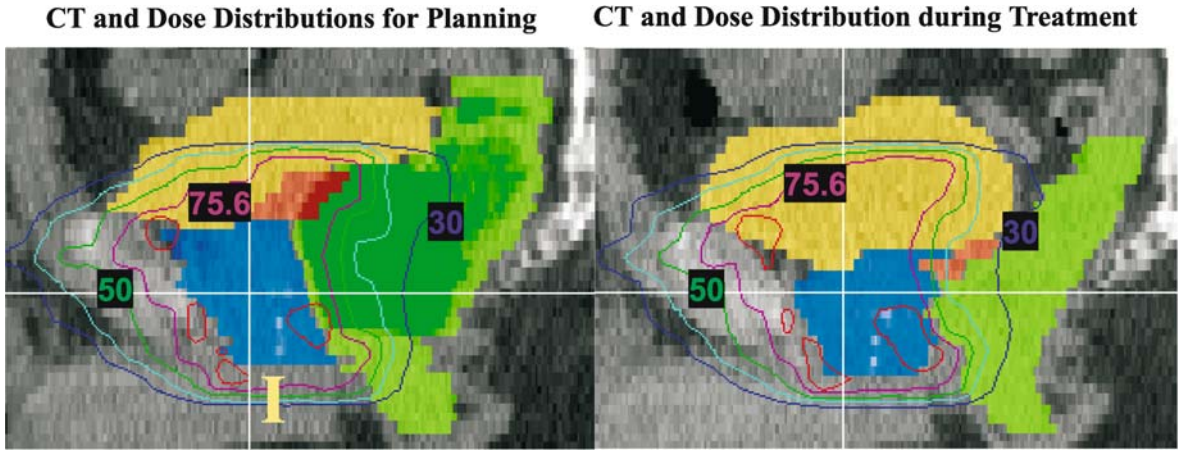

Fig. 8. For this illustration a prostate IMRT plan was designed using the planning CT (*left panel*) and was then applied to one of the CT images obtained during the course of radiotherapy. The variation of the anatomy from day to day can lead to a significant loss of target coverage. *Blue, red, yellow and green regions* represent prostate, seminal vesicles, bladder and rectum respectively. (Dong, unpublished)

certain and may present an increased risk of injury [23]. There may also be an increased risk that the high degree of conformation with IMRT may lead to geographic misses of the disease and recurrences especially for disease sites where positioning and motion uncertainties play a large role or where there are significant changes in anatomy and biology during the course of radiotherapy. Similarly, high doses in close proximity of normal critical structures may pose a greater risk of normal tissue injury. In addition, IMRT dose distributions are unusual and highly complex and existing experience is too limited to interpret them properly and evaluate their efficacy and may lead to unforeseen sequelae. Figure 9a compares a 3D-CRT lung plan with an IMRT plan and Fig. 9b shows the corresponding DVHs. While it is clear that the IMRT plan produces a more homogeneous dose distribution in the target volume and spares more lung above 10 Gy, it is not clear what the consequences of larger volumes receiving less than 5 Gy might be.

These limitations and risks point to the need for continued investigations to improve the methodology and to minimize the uncertainties. Such investigations are essential to exploit the full power of IMRT. Even in its current form, however, IMRT has a significant potential to improve outcome.

2.5 Outlook

In spite of the fact that IMRT is already in clinical use in several institutions in Europe and many in the USA, much needs to be done to integrate it more efficiently and seamlessly into the clinical workflow environment. This is essential to make full use of its potential without getting trapped in the shortcomings of the implementation. The first hurdle is the initial implementation and the commissioning of the IMRT system. Turnkey IMRT solutions have been advertised but the reality is different. Often, the interfacing of the different components of the imaging, IMRT planning, leaf sequence generation and delivery chain together turns out to be a major problem. Current developments aim at more streamlined and integrated solutions. Some recent approaches

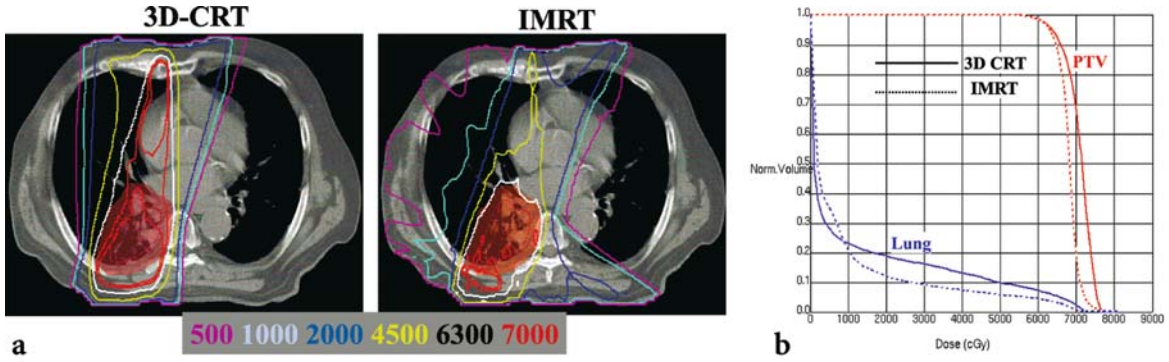

Fig. 9. Comparison of 3D CRT and IMRT lung plans. While IMRT provides better sparing at or above the 10 Gy dose level, it treats bigger volumes at doses around 5 Gy. The biological consequences of this have yet to be determined

try to optimize the sequence of MLC shapes directly, without using the intermediate stage of the intensity maps [24, 25].

Another practical IMRT issue is that it has become common practice to require resource-intensive patient-specific verification of IMRT. One of the arguments for this is that IMRT is more complex than 3D-CRT, and therefore it is more error-prone. Whether this assertion is true or not, there is no doubt that more efficient tools are needed to make the process of IMRT verification less labor-intensive and less time-consuming. Later chapters in this book will deal with these issues in detail (see chapters 10 and 11, this volume).

Other research and development activities aim at improving the planning of IMRT. In most systems, IMRT planning is considered as an optimization problem. The goal is to find the parameters (intensity maps, sometimes also beam orientations, energy, etc.) that yield the best possible treatment plan taking into account various clinical, technical, and physical prescriptions and constraints. Even though the IMRT planning systems claim to yield the optimal treatment plan, treatment planners often find the result of the first optimization run unacceptable. Significant tweaking of optimization parameters and re-runs of optimization are then necessary. In difficult cases it may be necessary to cycle through this "human iteration loop" more than ten times, which is unsatisfactory and involves trial and error as in conventional planning.

The fundamental limitation of current optimization approaches is that a clinician often finds it difficult to formulate a complete set of optimization criteria in the quantitative mathematical terms required by the optimization systems, even though he/she is capable of ranking individually the prepared plans. Clinicians, optimization experts, and physicists have recently started to work together to find ways out of this dilemma [26].

Current IMRT planning systems optimize the intensity maps for a number of beams with given orientations. In fully rotational approaches such as in tomotherapy, individual beams do not exist and therefore it is not necessary or even possible to select beam angles. However, in MLC-based IMRT with multiple beams, the orientations have to be manually pre-selected. There has been an on-going debate as to whether or not there is merit in automatically optimizing beam angles in addition to beam intensities, and what the optimum number of beams is [27]. From a mathematical point of view, optimization of beam angles is a very difficult problem, much more difficult than the optimization of intensity maps. In the current practice the most common approach is to use "class solutions." Based on experience or published work, one first determines appropriate beam angles for different classes of cases (i.e., disease sites), and these beam angles and numbers are then used for future treatments of cases of this class. The question still remains as to what to do in new cases, especially since it is known that the most suitable beam angles in IMRT can be drastically different from the best 3D-CRT beam angles [28]. Therefore, beam angle optimization could play an important role in IMRT.

The degree of dose conformality that is achievable with IMRT is beginning to challenge the accuracy and precision with which the target volume and critical structures can be localized, especially in extra-cranial treatments. Day to day setup errors, internal organ motion, and outlining errors can compromise the achievable dose localization by a larger degree than the finite dose gradient due to the remaining physical and technical limitations in IMRT. Several chapters in this book address issues of image guided targeting, control of internal organ motion, and time-adaptive radiotherapy strategies.

IMRT is probably the ultimate radiotherapy technique using photon beams. Nevertheless, as mentioned above, it still has limitations that are based on the physical properties of the interaction of photons with matter. Among those limitations are the relatively high integral dose and the inability to spare simultaneously multiple critical structures surrounding the target volume. Complex critical treatments such as pediatric treatments therefore leave something to be desired in terms of both target coverage and critical structure sparing. The more fundamental physical limitations can only be avoided by going to a different treatment modality such as proton therapy. It has recently been shown that intensity modulation can play an important role in proton therapy as well [14, 29].

References

1. Brahme A, Roos JE, Lax I (1982) Solution of an integral equation in rotation therapy. Phys Med Biol 27:1221–1229
2. Mackie TR, Holmes TW, Swerdloff S, Reckwerdt PJ, Deasy JO, Yang J, Paliwal BR, Kinsella TJ (1993) Tomotherapy: a new concept for the delivery of conformal radiotherapy. Med Phys 20:1709–1719
3. Convery DJ, Rosenbloom ME (1992) The generation of intensity-modulated fields for conformal radiotherapy by dynamic collimation. Phys Med Biol 37(6):1359–1374
4. Stein J, Bortfeld T, Doerschel B, Schlegel W (1994) Dynamic X-ray compensation for conformal radiotherapy by means of multi-leaf collimation. Radiother Oncol 32:163–173
5. Svensson R, Kallman P, Brahme A (1994) An analytical solution for the dynamic control of multileaf collimators. Phys Med Biol 39:37–61
6. Bortfeld T, Kahler DL, Waldron TJ, Boyer AL (1994) X-ray field compensation with multileaf collimators. Int J Radiat Oncol Biol Phys 28:723–730
7. Bortfeld T, Burkelbach J, Boesecke R, Schlegel W (1990) Methods of image reconstruction from projections applied to conformation radiotherapy. Phys Med Biol 35:1423–1434
8. Palta JR, Mackie TR (eds) (2003) Intensity-modulated radiation therapy – the state of the art. Medical Physics Publishing

9. Woo SY, Sanders M, Grant W, Butler EB (1994) Does the "peacock" have anything to do with radiotherapy? Int J Radiat Oncol Biol Phys 29(1):213–214
10. Ling CC, Burman C, Chui CS, Kutcher GJ, Leibel SA, LoSasso T, Mohan R, Bortfeld TR, Reinstein L, Spiro S, Wang X-H, Wu Q, Zelefsky M, Fuks Z (1996) Conformal radiation treatment of prostate cancer using inversely-planned intensity-modulated photon beams produced with dynamic multileaf collimation. Int J Radiat Oncol Biol Phys 35(4):721–730
11. Chen Z, Wang X, Bortfeld T, Mohan R, Reinstein LE (1995) The influence of scatter on the design of the optimized intensity modulators. Med Phys 22(11):1727–1733
12. Mohan R, Wu Q, Wang X-H, Stein J (1996) Intensity modulation optimization, lateral transport of radiation and margins. Med Phys 23(12):2011–2022
13. Liu HH, Wang X, Dong L, Wu Q, Liao Z, Stevens CW, Guerrero TM, Komaki R, Cox JD, Mohan R (2004) Feasibility of sparing the lung and other thoracic structures with intensity-modulated radiation therapy (IMRT) for non-small cell lung cancer (NSCLC). Int J Radiat Oncol Biol Phys 58(4):1268–1279
14. Oelfke U, Bortfeld T (2003) Optimization of physical dose distributions with hadron beams: comparing photon IMRT with IMPT. Technol Cancer Res Treat 2(5):401–412
15. Murshed H, Liu HH, Liao Z, Barker JL, Wang X, Tucker SL, Chandra A, Guerrero T, Stevens C, Chang JY, Jeter M, Cox JD, Komaki R, Mohan R (2004) Dose and volume reduction for normal lung using intensity-modulated radiation therapy for advanced-stage non-small cell lung cancer. Int J Radiat Oncol Biol Phys 59(4):1258–1267
16. Chandra A, Liu H, Tucker SL, Liao Z, Stevens C, Chang J, Jeter M, O'Reilly M, Mohan R, Cox JD, Komaki R, Guerrero T (2003) IMRT reduces lung irradiation in distal esophageal cancer over 3D CRT. Int J Radiat Oncol Biol Phys 57(2 Suppl):S384–S385
17. Benedict SH, Cardinale RM, Wu Q, Zwicker RD, Broaddus WC, Mohan R (2001) Intensity-modulated stereotactic radiosurgery using dynamic micro-multileaf collimation. Int J Radiat Oncol Biol Phys 50(3):751–758
18. Mohan R, Cardinale RC, Wu Q, Benedict S (2000) Intensity-modulated stereotactic radiosurgery. In: Molls M (ed) Three-dimensional radiation treatment, technological innovations and clinical results. S Karger AG, Basel, Switzerland, Munich, Germany, pp 40–48
19. Wu Q, Mohan R, Morris M, Lauve A, Schmidt-Ullrich R (2003) Simultaneous integrated boost intensity-modulated radiotherapy for locally advanced head-and-neck squamous cell carcinomas. I: Dosimetric results. Int J Radiat Oncol Biol Phys 56(2):573–585
20. Yu Y (1997) Multiobjective decision theory for computational optimization in radiation therapy. Med Phys 24(9):1445–1454
21. Küfer K-H, Scherrer A, Monz M, Alonso F, Trinkaus H, Bortfeld T, Thieke C (2003) Intensity modulated radiotherapy – a large scale multi-criteria programming problem. OR Spectrum 25:223–249
22. Siebers JV, Mohan R (2003) Monte Carlo and IMRT. In: Mackie TR (ed) Intensity-modulated radiotherapy – the state of the art. Medical Physics Publishing, Madison, WI, pp 531–560
23. Mohan R, Wu Q, Manning M, Schmidt-Ullrich R (2000) Radiobiological considerations in the design of fractionation strategies for intensity-modulated radiation therapy of head and neck cancers. Int J Radiat Oncol Biol Phys 46(3):619–630
24. De Meerleer G, Vakaet L, De Gersem W, Villeirs G, De Neve W (2004) Direct segment aperture and weight optimization for intensity-modulated radiotherapy of prostate cancer. Strahlenther Onkol 180(3):136–143
25. Shepard DM, Earl MA, Li XA, Naqvi S, Yu C (2002) Direct aperture optimization: a turnkey solution for step-and-shoot IMRT. Med Phys 29(6):1007–1018
26. Langer M, Lee EK, Deasy JO, Rardin RL, Deye JA (2003) Operations research applied to radiotherapy, an NCI-NSF-sponsored workshop February 7–9, 2002. Int J Radiat Oncol Biol Phys 57(3):762–768
27. Soderstrom S, Brahme A (1996) Small is beautiful – and often enough (Letter to the Editor). Int J Radiat Oncol Biol Phys 34(3):757–758
28. Stein J, Mohan R, Wang X-H, Bortfeld TR, Wu Q, Preiser K, Clifton Ling C, Schlegel W (1997) Number and orientations of beams in intensity-modulated radiation treatments. Med Phys 24(2):149–160
29. Lomax AJ, Boehringer T, Coray A, Egger E, Goitein G, Grossmann M, Juelke P, Lin S, Pedroni E, Rohrer B, Roser W, Rossi B, Siegenthaler B, Stadelmann O, Stauble H, Vetter C, Wisser L (2001) Intensity modulated proton therapy: a clinical example. Med Phys 28(3):317–324

Imaging for IMRT

Peter Remeijer, Marcel van Herk

3

Contents

3.1 Application of Images in IMRT

IMRT planning is based on a model of the patient that describes location and shape of normal structures and target. Because of the high degree of geometrical optimization that is possible with IMRT (for instance, beams can have a lower intensity when passing through a critical structure or avoid them all together), it is important that the patient model is accurate and representative for the patient during treatment. For this reason, imaging is an essential part of intensity-modulated radiotherapy (IMRT). Typically, IMRT plans (like conformal plans) are based on a CT scan of the patient in treatment position. With the advent of more advanced imaging modalities like multi-slice CT, dynamic and functional magnetic resonance imaging (MRI), magnetic resonance spectroscopy (MRS), and positron emission tomography (PET), the scope of possibilities for defining the target volume has increased beyond mere anatomical data.

In IMRT, images are acquired for the following purposes:

1. Treatment planning, i.e., delineation of target and normal structures. Typically the patient model that is used for treatment planning is created once prior to treatment. Because this patient model, however, will become outdated due to changes or variations in the anatomy, multiple techniques for image guidance have been developed.
2. Image guidance and/or treatment verification, i.e., for determination and correction of variations. The classical example is electronic portal imaging, which allows correction of the setup of the bony anatomy and/or markers. Adaptive strategies, such as the one developed by Yan et al. [1], apply multiple data sets acquired before or during the treatment on a normal scanner. The newest development is to use a scanner integrated with the treatment machine, such that information for both on- and off-line corrections can be acquired just prior to treatment.
3. Follow-up studies, i.e., for determining the response during and after treatment. Often PET scans are taken to estimate the degree of tumor response, and CT is used to estimate tumor regression based on geometrical measures.

For these tasks, various image modalities are available:

1. X-ray images – used for bony anatomy and marker based setup when the X-ray imaging set is integrated with the linear accelerator [2,3], and for determining tumor motion in lung [4]. X-ray images are also well suited for gating the linear accelerator [4].
2. MV images – used widely for setup based on the bony anatomy and on markers, e.g., [5].
3. CT – used typically for treatment planning since it combines high geometrical accuracy with a measure of electron density. During recent years CT has evolved from a rather crude slice-based quasi-3D modality to a stage where slice distances can be as small as the individual pixel size, combined with a very short scan time. CT is also used on a small scale for in-room imaging [6]. However, patient motion is required to move the patient from the linear accelerator to the CT gantry, requiring rigid immobi-

lization of the patient and QA. By using information on patient breathing, it has now become possible to obtain respiratory correlated CT scans [7, 8]. Respiration correlated (4D) CT is the technique of choice for accurate determination of lung tumor motion for treatment planning. An alternative is to use slow scanning [9], where a more representative CT scan is acquired, compared to a free breathing CT, at the cost of image resolution.

4. MV cone-beam CT (CB CT) has been proposed for image guidance application on conventional accelerators (with moderate success). However, using a special detector system, MVCT with sufficient quality can be acquired on the Tomotherapy system, allowing soft-tissue based setup.
5. kV CBCT: recently introduced in clinical practice [10]: used for bony anatomy, prostate, bladder, lung. Respiration correlated technique has been developed [11].
6. MRI – used as primary image modality for some stereotactic techniques in the head. Otherwise matched with CT for better delineation of target and critical structures. Used widely for brain, nasopharynx, head and neck, and on a smaller scale for prostate. Has also been used to obtain 4D information for the lung [12].
7. PET: widely used for lung [13], little for nasopharynx and neck [14]. Recently, respiration gated PET has been developed [15, 16].
8. US: used for prostate localization, limited accuracy [17].
9. SPECT: use for lung perfusion measurement: both during follow-up and planning [18, 19].

One common factor in the application of these new possibilities is the necessity to relate the information to a well defined geometrical reference, in general the coordinate system of the planning CT scan. Hence registration tools for, for example MRI-CT or PET-CT matching will be invaluable in the radiotherapy department of the future.

3.2 Image Administration, Archiving, Communication and DICOM-RT

Regardless of whether one only uses a CT scan for planning, or multiple modalities with advanced registration tools for an exact definition of the target volume, the data need to be stored and moved around in the department between the various programs and stations. Typically a hospital contains several databases to serve this purpose. For example, there may be an image archive in the radiology department, one or more treatment planning systems in the radiotherapy department (each with its own database), and a patient administrative database. This situation is sub-optimal: different versions of data may exist in different places, it is difficult to find information, each system has independent backups, information is duplicated on several locations, and information may get lost due to accidental wrong input (e.g., storage of a scan under the wrong patient number).

A much better approach is the use of a single central archive on which all patient data is stored with close links to all related software. This will facilitate easy retrieval of the data and will enable long-term access to the patient data. This approach can nowadays be facilitated to a large extent by a central PACS (Picture Archiving and Communications System), which stores image data, keeps a database of the images, and supplies the images to, for example, viewers.

The basic requirements for an image archive should be: space for at least five years of image data, although by legal requirements storage over a longer period may be needed; high speed access to recent data; medium speed access to historic data; limited maintenance requirements; extendible; safe. An aspect that needs to be addressed is the expected lifetime of both the actual hardware equipment and the media used for the image archive.

Although standardization has come a long way, connections to all imaging modalities and the storage of radiotherapy specific information can still be problematic. Therefore, compatibility checks should play a large role when acquiring and implementing a PACS or a new imaging modality.

3.2.1 DICOM

The basis of most current imaging networks is DICOM, which stands for "Digital Imaging and Communications in Medicine". It is a complex standard that addresses the following aspects:

- It defines a network protocol for exchange of medical data.
- It defines the logical format for images from a large variety of sources, such as CT, MRI, PET, and many others and a physical file format on how images may be stored on disk.
- It defines the structure of a database to store these images.

These topics will now be discussed in a highly simplified way. For more details, one should refer to the official DICOM standard [20].

First of all, DICOM defines a network protocol, not unlike, for example, the FTP (file transfer protocol) protocol. It describes a way to transmit images and patient data of any type over a network. DICOM distinguishes servers (for example, a central image archive) and clients (for example, a planning system that retrieves images, or a CT scanner that sends images).

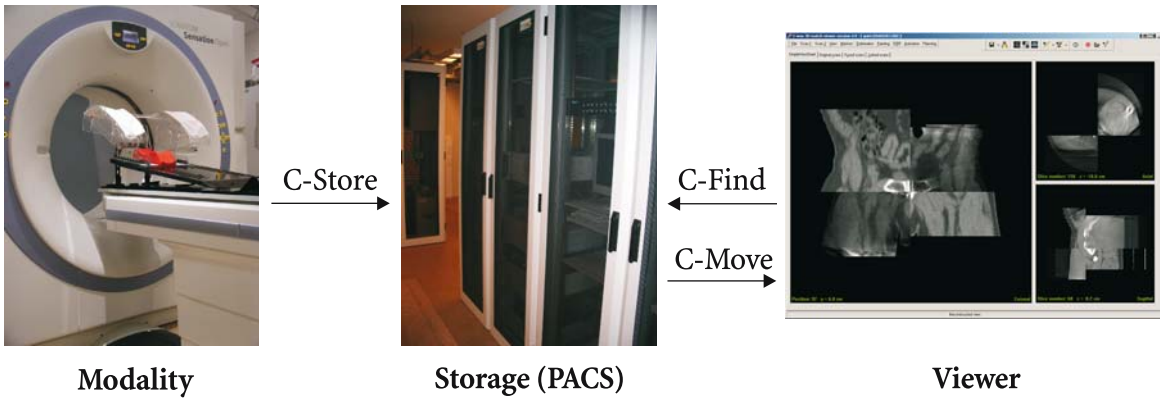

Fig. 1. A simple DICOM network, consisting of one modality, a storage utility and a viewer. In reality, one has to deal with many more modalities and viewing applications, but the basic structure stays the same. C-Store, C-Find and C-Move are DICOM commands and are used to move data from around and to query systems

Figure 1 shows a simplified DICOM network. Because the C-Store and C-Move commands can only be used to push data or to move data from one server to another, the viewer application needs to have both client and server functionality; It's a client when performing patient queries (using C-Find) and issuing C-Move commands, and a server when receiving the data.

To identify DICOM-capable machines on the network, the so-called Application Entity (AE) is used. An application entity defines the combination of the address or host name of a machine (i.e., computer) together with a port number. The port number is needed to select a communication channel on the machine, a bit like channels on a television. Because the port number is part of the AE, multiple DICOM applications can co-exist on a single machine. AEs are very important in DICOM because in communication between servers only the AE is used to specify a destination server of, for example, a C-Move command.

DICOM stores and transmits most image data in a 2D format (i.e., slice by slice for a CT or MRI scan). An exception is some nuclear medicine data, where a single object can contain 3D or 4D (time resolved) data. The components of each image are rigidly defined by the DICOM standard. An image consists of large numbers of items that are defined by a group number, an element number, and the data contents. The interpretation and type of the data is defined in a data dictionary that defines all possible group/element number pairs (there are thousands defined, but many are optional or vendor specific). These data contain (amongst others): generic image information, patient information, acquisition information, orientation information, image information, and pixel data.

DICOM also specifies a hierarchical database organization for an image archive and that it should contain the following elements: patients, studies, series and images. A study usually contains all scans made on a particular patient visit on a given scanner. A series usually contains all slices to form one 3D volume. Note that the interpretation of a series and a study may differ between manufacturers and modalities. For example, proton density and T2 image pairs acquired simultaneously are often combined in a single series.

3.2.2 DICOM-RT

The addition of radiotherapy data to DICOM is relatively recent. This means that the number of systems supporting DICOM-RT or parts thereof is still changing. The main difference between DICOM for radiology and DICOM-RT is the addition of many new types of data objects. The database organization, network protocol and data formats are the same. The following radiotherapy data objects are officially defined by the DICOM standard (more will be added in the future):

- *RT Structure Set*, containing information related to patient anatomy, for example structures, markers, and reference points. These entities are typically identified on devices such as CT scanners, physical or virtual simulation workstations or treatment planning systems.
- *RT Plan*, containing geometric and dosimetric data (MUs) specifying a course of external beam and/or brachytherapy treatment. The RT Plan entity may be created by a simulation workstation, and subsequently enriched (copied and modified) by a treatment planning system before being passed on to a record and verify system or treatment device. An RT Plan usually references a RT Structure Set to define a coordinate system and set of patient structures.
- *RT Image*, specifying radiotherapy images, which have been obtained on a conical imaging geometry, such as those found on conventional simulators and portal imaging devices. It can also be used for calculated images using the same geometry, such as digitally reconstructed radiographs (DRRs).

- *RT Dose*, containing dose data generated by a treatment planning system in one or more of several formats: three-dimensional dose data, isodose curves, DVHs, or dose points.
- *RT Treatment record*, data about a delivered treatment, i.e., from a record and verify system.

Quality Assurance

The DICOM protocol ensures that data is transmitted without corruption. However, this does not mean that things cannot go wrong. In particular, one should pay attention to the orientation of the images. Serious incidents may occur due to reversal of left and right side of the patient. In particular, feet first scans tend to cause reverse orientations for some combinations of scanners and viewers. Note that an operator may also forget to enter the correct patient orientation in the scanner's console. Another problem is that patient IDs can be incorrectly entered. The result is that images can no longer be found or worse that, for example, images of the wrong patient are used for planning.

3.3 Image Registration, Fusion and Viewing

Image registration is used widely for treatment planning, organ motion studies, image guidance, and follow up. The purpose of image registration is to find the transformation (translation, rotation, deformation) that maps one scan onto another. In this way, scans can be combined and fused on a pixel-by-pixel basis (e.g., for target volume delineation), or differences can be quantified (for image guidance and follow up). In radiotherapy, image registration is mostly used to align rigid structures, e.g., bone, in multiple scans. Bone acts as a frame of reference for treatment (verified by means of X-ray images) relative to which the position of organs of interest is determined. For deformable organs, an alternative could be to use elastic registration. In such a case one scan would be considered as a golden standard to which the other scan would be warped. In radiation treatment planning such a procedure frequently is undesirable since both scans are equally valid samples of the changing anatomy. By visualizing the organ motion, the physician is able to average both scans visually. Combining scans made at different times therefore potentially reduces the effects of organ motion and delineation variation, which are important error sources in radiotherapy [21]. Elastic or deformable registration does play a role in tracking dose delivery to deforming organs [22] and to a smaller level to remove distortions introduced by the imaging equipment (e.g., a probe in the rectum). A limited overview of registration algorithms used for radiation therapy is given in Table 1. Some recent overviews in literature are given by Hutton [21], Pluim [24] and Hill [25]. If one looks at the author's impression of the advantages and disadvantages of the algorithms, it is obvious that not all algorithms are suitable for all applications. A complete system, therefore, should implement more than one algorithm. However, most commercial planning systems and virtual simulation systems provide only limited support for image registration: usually only landmark or one volume based algorithms (typically using mutual information) are available.

Besides good algorithms, an image registration package requires database tools: access to image archives and possibility to store the match results (e.g., as a view). Useful matching tools include tools to crop mobile anatomy, perform interactive pre-matching. Good evaluation tools are 'sliding window' and overlay views in

Table 1. Overview of the classes of registration algorithms used in radiotherapy. Each of these algorithms is suitable for specific types of applications. A comprehensive system should therefore provide multiple of these algorithms

Algorithm	Advantages	Disadvantages	Typical application
Landmarks [26, 27]	Simple and robust. Unbiased in absence of distortion	Accuracy depends on the number of landmarks. Good internal landmarks difficult to find. External landmarks are sensitive to MRI distortion	General purpose. Gold standard for evaluation of other algorithms
Interactive [28, 29]	Easy to use	Slow and not very accurate	General purpose
Frame-based [30]	Highly accurate with CT	Invasive procedure. Frame is very sensitive to MRI distortion	Stereotactic RT
Contours [31–33]	Fast and accurate	Contouring required	Soft tissues
Chamfer matching (based on automatic segmentation) [34–37]	Fast and accurate	Automatic segmentation requires careful tuning	Bone (i.e., skull, pelvis, lung)
Volume matching [38–40]	Little preprocessing required. Works extremely well for same modality registration	Slow. Highly sensitive to organ motion	Brain

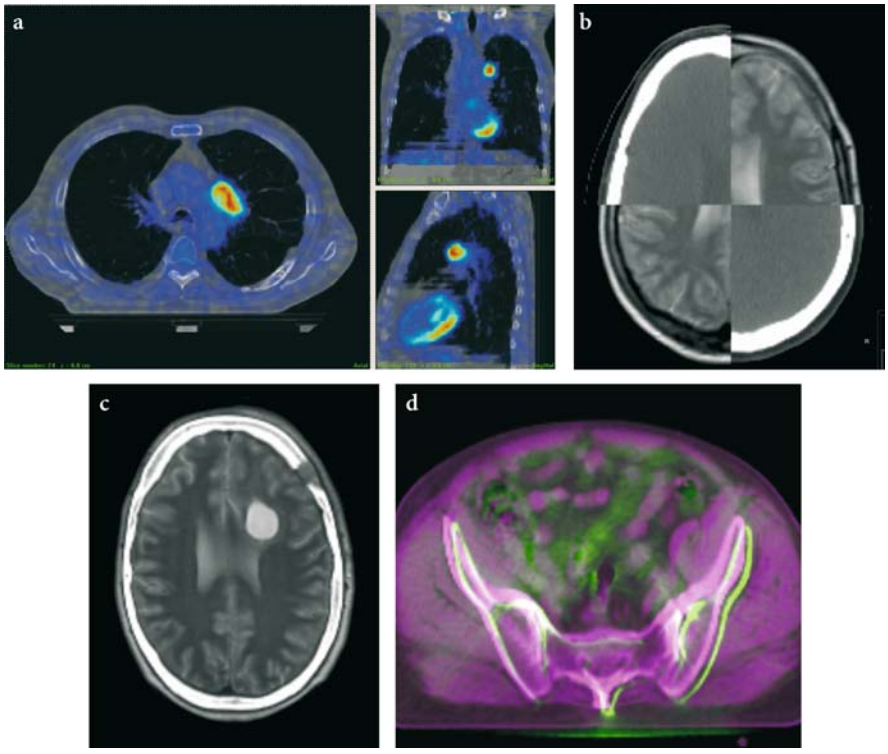

Fig. 2a–d. A few examples of image fusion possibilities: **(a)** a CT scan fused with PET information in three planes with linked level and window settings; **(b)** a cut view to show CT and MRI information simultaneously; **(c)** the local maximum of a matched CT and MRI pair. The result is that bone information from CT is shown on top of tissue information from the MRI scan; **(d)** a fusion of two CT scans where one is shown in *purple* and the second in *green*. This method is very suitable for verifying bony anatomy registrations

any orientation, the possibility to apply the transformation from one scan pair to another scan pair, and tools for quantitative and visual comparison of match results. A few examples of these tools are given in Fig. 2. An overlay of CT bone on MR is often used during interactive pre-matching or as a quick inspection of the registration accuracy, which is then performed in axial, sagittal and coronal reconstructions throughout the scan volume. The sagittal reconstruction is particularly important for verifying brain cases. Finally, the reliability of the registration depends strongly on the followed protocols for image acquisition. For example, the reliability of a matching procedure often reduces if the head is not completely scanned.

3.4 Tools for Image Segmentation and Contouring

All planning systems allow slice-by-slice delineation of structures of interest such as GTV, CTV and organs at risk. A number of tools exist to improve the delineation quality. First, by providing orthogonal cuts or projections with the delineated contours overlaid, the operator can ensure that the contours are continuous in 3D, it is important; However, to make the contours visible in the orthogonal cuts that contours are connected, e.g., based on triangulation software. Similarly, a tool that projects contours delineated on surrounding slices allows verification of the continuity of the contours in 3D. A number of planning systems have integrated tools for semi-automatic delineation of healthy organs. Generally these tools use gray value segmentation, optionally followed by clean-up operations based on connectivity and shape. The quality of the automatic contouring is generally quite good, but some manual editing remains necessary. The most advanced tools use shape models of the healthy organs that are deformed to follow the planning scan.

With the advent of image registration, tools such as a colorwash overlay (typically used for PET) and specially linked cursor tools are very useful to allow delineation in matched image modalities. Considering that prior to matching, the slices of the different modalities are not coincident, it is always problematic to delineate both in CT and MRI at the same time. For instance, if one draws along a slice of the CT, MRI slices will be shown resampled or vice-versa.

3.5 Geometric Uncertainties and Margins

IMRT aims at maximizing tumor control while minimizing damage to the surrounding tissues. To increase the therapeutic range, smaller and smaller margins are being used between the clinical target volume (CTV), and

the planning target volume (PTV) [41], and thus a much higher conformality is attained. Since high precision is essential, each step in the IMRT procedure must be image guided and roughly based on the three following steps:

1. CT scanning while aligning the patient with lasers to external radio-opaque skin marks.
2. Treatment planning, delineation of the tumor and planning beams relative to the skin marks as visible on the CT scan.
3. Treatment, with patient alignment based on the skin marks.

3.5.1 Geometric Uncertainties in Radiotherapy

Figure 3 shows the above radiotherapy procedure in 17 detailed steps.

The patient enters the diagram on the left. Going to the top of the diagram we follow the physical patient: the skin marks are aligned on the lasers, the lasers being aligned with the CT room coordinates. Then the patient is moved to the treatment room, where lasers are used to align the patient's skin marks again. However, the patient's bony anatomy may have moved with respect to the skin marks and the tumor may have moved with respect to the bony anatomy. Going to the bottom of the diagram, we follow the patient's CT scan through the planning process, to beam setup, and beam delivery.

Each of the steps in this diagram will incur a small error. These errors can be categorized as follows:

1. Delineation errors: misplacement of the delineated contour with respect to the tumor [42–44]. This error occurs only once. Recent data have shown that the error in target volume delineation may be the single largest one in the whole radiotherapy chain in a modern radiotherapy department.
2. Planning errors: these errors may be caused by a wrong beam setup, expansion of the CTV with wrong margins, etc. These errors can and should be avoided by the use of quality assurance protocols, and verification of the plans by a second dosimetrist.
3. Organ motion: movement of the tumor with respect to the bone [2,3,45]. Note that this error occurs twice in the diagram! – first during treatment planning, and second during treatment execution. Even though no movement occurs as such in the CT scan, the organ movement is frozen by the action of taking the CT image. The beam will be targeted at the 'arbitrary' position the moving organ had during the scan [46].
4. Setup errors: deviation between the CT room coordinate system or the treatment room coordinate system and the patient's bony anatomy, e.g., [47–51]. This error also occurs twice, one of which is the 'arbitrary' position of the moving patient during CT scan.

Each of the errors in the diagram is small, but it is not unrealistic that the errors in each step are on the order of a millimeter. Because there are so many steps, it is *unavoidable* that large errors (geographical misses) occur in some cases. Just imagine what would happen, if, on a bad day, all errors were 1 mm and all in the same direction! So, even though the standard radiotherapy procedure is intended to be highly accurate, it is important to take additional measures to determine and correct errors in clinical practice.

Because the total error is built out of many small errors, the total error has most likely a *normal distribution*. This follows from the central limit theorem, which roughly states that the distribution of the sum of many variables with an arbitrary distribution will tend to be normally distributed. The above-mentioned geographical misses correspond with the tail of that normal distribution.

Some of these errors occur for each treatment fraction, while others occur only once. We will call the former *random errors*, because they can be different for each new fraction, while the latter will be called *systematic errors*, because they will give rise to identical errors for each treatment fraction. In Fig. 4,

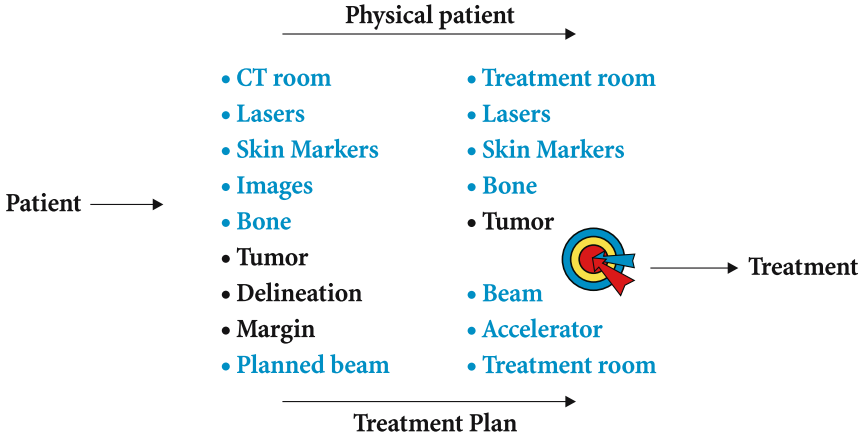

Fig. 3. A schematic diagram of the radiotherapy chain. All *blue steps* can be checked with portal imaging!

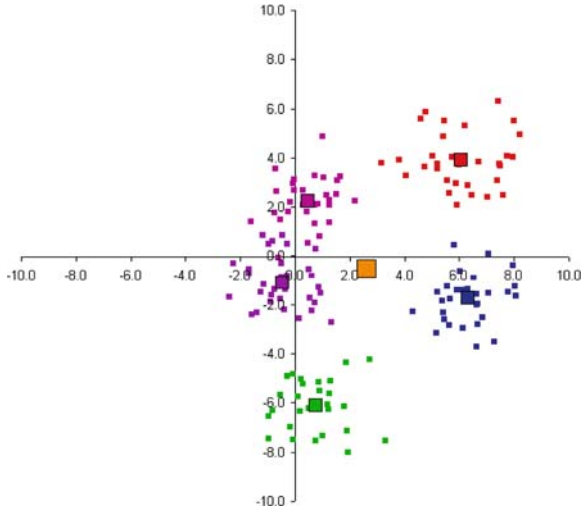

Fig. 4. Random and systematic errors. Each group of points represents the fractions of a patient. The scatter within a group is the day-to-day variation. The group average (*the five larger squares*) is the systematic error of a patient. The mean of all patient averages is indicated by the *large orange square*. This is the overall mean

the random errors are all located on the right side. Note that systematic errors are also stochastic in nature; if the same patient would be CT scanned and planned twice, different systematic errors would be found.

Because the errors are most likely normally distributed, it follows naturally that an analysis in terms of mean and standard deviation (SD) will most accurately describe them. A basic approach to deal with these errors is to consider a group of P patients, a number of F_p measured fractions for each patient 'p', and a measurement x_{pf} for each measured fraction (e.g., a measurement of a setup error in the AP direction) [52]. The average patient error can then be written as

$$m_p = \sum_{f=1}^{F_p} \frac{x_{pf}}{F_p} \tag{1}$$

and the total number of measured fractions, N and their overall mean, M, as

$$N = \sum_{p=1}^{P} F_p\,, \quad M = \frac{1}{N} \sum_{p=1}^{P} \sum_{f=1}^{F_p} x_{pf} \tag{2}$$

The variation around this mean has two components. The first component is the random error, or day-to-day variation. For a single patient p, the standard deviation of the random errors is given by

$$\sigma = \sqrt{\frac{1}{N-P} \sum_{p=1}^{P} \sum_{f=1}^{F_p} \left(x_{pf} - m_p\right)^2} \tag{3}$$

The second component is the systematic, or average, patient error. The standard deviation, Σ, of the systematic errors is given by

$$\Sigma = \sqrt{\frac{P}{N(P-1)} \sum_{p=1}^{P} F_p \left(m_p - M\right)^2} \tag{4}$$

The most important quantities are M, Σ and σ. In general the overall mean M should be close to zero. If it is not, it means that a systematic error is introduced somewhere in the radiotherapy chain which is equal for all patients, e.g., a misaligned laser. The standard deviation of the mean patient errors (Σ) tells us how large the systematic errors for individual patients can become, while the standard deviation of the random errors (σ) quantifies the magnitude of the day-to-day variations. Note that intra-fraction errors are not part of this analysis.

3.5.2 Measurement and Correction of Geometrical Errors

Measurement of geometrical errors is of great importance for the definition of margins. Since systematic errors will have the largest impact on their magnitude, it is most important to reduce these errors as much as practically possible. The methods for determining and correcting errors from the abovementioned categories are quite diverse:

1. Target volume delineation – target volume delineation errors may be measured by multi-observer studies and may be reduced by clear protocols, training and consultation and multi-modality imaging (e.g., MRI). For example, in a multi-observer study with 18 patients and 3 physicians, Rasch et al. [43] found the following differences between observers: 1.5 mm SD where the prostate is clearly visible and up to 3.5 mm SD at the seminal vesicles and the apex. One physician systematically delineated larger target volumes than the others. Prostates delineated on MR were about 30% smaller in volume than on CT. The MR defined prostate was systematically 8 mm smaller at the posterior aspect (seminal vesicles) and 6 mm at the apex.
2. Organ motion – motion of the tumor may be measured by repeat CT or by implanting markers that are traced by X-ray or portal imaging. Recently, studies have reported ultrasound and (cone beam) CT tracking of the tumor. Reduction of organ motion is possible to some degree by good CT scan protocols (make your CT scan representative as possible for treatment), by internal patient setup (breathing control, gating), by external patient setup (external patient motion may influence internal motion), and by good treatment protocols (e.g., visit a toilet before treatment [45]). A more advanced way to reduce the effects of organ motion is the use of adaptive strategies [21]; based on image data acquired over the first few fractions of the treatment, the treatment plan is adapted to aim for smaller systematic deviations.

3. Setup errors – a very effective technique to measure and reduce setup errors is portal imaging. In the last decade hundreds of publications have appeared about the use of portal imaging. It is common to compare the portal images made with simulation images. However, in light of the previous description of the treatment process, it should be clear that the best way to use portal images is to compare them with a *Digitally Reconstructed Radiograph*. In this way, the location of the beam with respect to the bony anatomy, which is visible on the portal image, is compared directly with the planned situation that is documented on the DRR. The measured errors may be reduced by on-line or off-line decision/correction protocols.

It is important to realize that by determining the patient's bony anatomy relative to the beam with portal imaging a large number of steps in the radiotherapy chain are verified. In relation to Fig. 3, 13 of the 17 steps will be verified and corrected to a large extent, and the only remaining errors will be organ motion and delineation errors (and possibly planning errors).

In recent years, many groups have published data on these error sources. However, we would like to emphasize that the magnitude of these errors will be institute or physician dependent. This is especially true for setup errors and delineation uncertainties. For organ motion this is less the case, although different patient preparation and setup protocols may still lead to different results. In order to be able to estimate the margin size, the total geometric uncertainty of the tumor position needs to be known. This error includes all abovementioned errors (delineation errors, organ motion and setup errors) and its standard deviation can be computed using $\Sigma_{\text{total}} = \sqrt{\Sigma^2_{\text{delineation}} + \Sigma^2_{\text{organmotion}} + \Sigma^2_{\text{setup}}}$ for the systematic errors and $\sigma_{\text{total}} = \sqrt{\sigma^2_{\text{organmotion}} + \sigma^2_{\text{setup}}}$ for the random errors. Note that this is in contrast with the concept of internal target volume, which implies adding margins linearly [53].

Since delineation errors are only systematic, the total random error does not contain that component. Table 2 shows prostate data that were analyzed in this way. Note that all errors are similar in magnitude. Therefore, correcting, for example, setup errors only will not be sufficient. In order to reduce the total geometrical uncertainty of the location of the tumor, *all errors* will have to be addressed.

3.5.3 Margins

As stated in the previous section, the margin size will depend on the geometrical uncertainties. But how large should the margin be chosen, once the magnitude of these uncertainties are known?

In general, a margin will be a compromise between the risk of complications and the risk of local failure. In the literature, many different recipes have been given for margin generation, but no consensus has been achieved [54–61]. This means that the statistical methods required for choosing treatment margins are still unclear. A number of authors have performed simulations using real patient data to determine the impact of geometrical variations on the dose delivery, but these simulations are specific to one treatment and are less suitable to determine general rules [46, 62, 63].

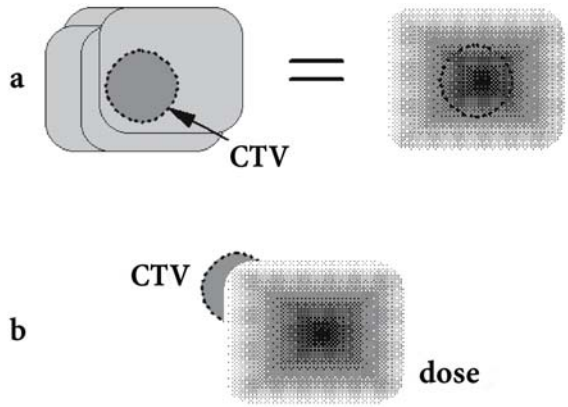

Fig. 5a,b. Schematic drawing of the impact of geometrical deviations on the dose distribution: **(a)** random errors lead to blurring of the dose distribution; **(b)** systematic errors lead to a (unknown) shift of the cumulative dose distribution relative to the CTV

	Random errors (mm SD)			Systematic errors (mm SD)		
	LR	SI	AP	LR	SI	AP
Target delineation				1.7	2.0...3.5[a]	2.0
Organ motions	0.9	1.7	2.7	0.9	1.7	2.7
Setup errors[b]	2.0	1.8	1.7	2.6	2.4	2.4
Total error	2.2	2.5	3.2	3.2	3.6...4.5[a]	4.1

LR = left-right, SI = superior-inferior, AP = anterior-posterior
[a] Due to the larger uncertainty in target volume delineation near the apex and the seminal vesicles
[b] Estimates of the systematic error without the use of a correction protocol

Table 2. Overview of prostate irradiation uncertainties (standard deviations of translations) as obtained by different studies from the Amsterdam (NKI) group

We have developed a simple analytical description of the influence of random and systematic geometrical deviations on the dose delivery in radiotherapy and we have used this methodology to derive rules for selecting margins [64].

For this methodology, the cumulative dose distribution delivered to the clinical target volume, CTV (i.e., the anatomical volume containing tumor cells) is computed analytically for a smooth CTV treated with an idealized dose distribution. Geometrical deviations are separated into random and systematic error components. First, the dose distribution is convolved with all random errors (Fig. 5a) [47, 48, 65]. In general this will shrink the 95% dose volume by some extent. Next, the convolved dose distribution is shifted by a possible systematic error (Fig. 5b) [57, 66] and the dose delivered to the CTV is determined.

The occurrence of systematic errors is related to the *probability distribution* of those errors. Therefore, the probability that a systematic error is below a certain level can be linked to a confidence interval dictated by the probability distribution of those errors. In three dimensions, for example, 90% of all systematic errors (with standard deviation Σ) will have a vector length smaller than 2.5Σ. This also means that if a margin of 2.5Σ is taken, 90% of all systematic errors will be within that margin.

Table 3 shows confidence intervals for other confidence levels and dimensions. Note that for AP-PA treatments there will be no dose effect for an AP movement. Therefore the 2D numbers may be more appropriate for those cases. However, since IMRT treatments are generally highly conformal, the 3D case will be most appropriate for IMRT.

In summary, a simple margin based on statistical principles can thus be constructed in three steps:

1. Express the required minimum CTV dose for a fraction of patients. For example, 90% of all patients should receive a CTV dose of 95% or more.
2. Add a margin for the systematic errors, such that 90% of them are covered.
3. Add a margin to compensate for the penumbra widening effect of the random errors.

For the specific case where the requirement is a minimum CTV dose of 95% to 90% of the patients a simple equation can be given:

$$\text{PTV margin} = 2.5\Sigma + 0.7\sigma \quad (5)$$

Because of the spheroid shape of a confidence interval, the margin should be added using a rolling-ball like algorithm [67]. If the margins are not equal in all directions, the expansion should be done using an ellipsoid shape instead. Stroom et al. provided an alternative margin recipe based on coverage probability. A margin should be used that is 2 times the total SD of systematic errors plus 0.7 times the total SD of random errors to ensure that, on average, 99% of the target volume receives 95% of the prescribed dose or more. A fundamental problem of coverage probabilities is that they tend to undervalue narrow tumor extensions, which are smeared out to very low probability levels and will not be included in the margin.

In summary:

- The first step in determining a margin for a specific patient group is to obtain estimates of the random and systematic components of the total radiotherapy chain. This will include delineation, organ motion and setup errors.
- Combine the errors by adding them quadratically, yielding a standard deviation for both systematic and random errors. Subsequently, a margin can be computed using these standard deviations.
- Systematic errors require three to four times more margin than random errors. To reduce the required margin it is therefore most efficient to focus on reducing the systematic errors first, by using clear delineation protocols, multi-modality imaging and setup correction protocols.

3.6 Future Developments

Because of the importance geometrical uncertainties play in the quest for smaller margins, imaging will become more and more important for IMRT. Future developments will be aimed at the two weakest links in radiotherapy: Accurate definition of the target, and precise image guided delivery of the treatment plan to reduce the influences of organ motion as much as possible.

Table 3. Overview of the mathematically derived margins for systematic (Σ) and random errors (σ). The margin for random errors is a first order approximation under the assumption that the penumbra of the dose profile has a 6 mm width from 20–80%. The underlined numbers were used in the simplified margin prescription

Margin for systematic errors				Margin for random errors	
Confidence level	1D margin	2D margin	3D margin	Dose level	Margin
85%	1.44Σ	1.95Σ	2.31Σ	85%	0.5σ
90%	1.64Σ	2.15Σ	$\underline{2.50\Sigma}$	90%	0.6σ
95%	1.96Σ	2.45Σ	2.79Σ	95%	$\underline{0.7\sigma}$

Towards a better definition of the target, many studies are looking at combining information from multiple modalities. However, none of these provide a true 'golden standard' of the tumor extent. Possibly, the solution lies in the inclusion of pathology information into those studies.

Furthermore, the inclusion of functional information in treatment planning may provide important information in relation to normal tissue complications. For example, geographical knowledge about lung perfusion may favor certain beam directions. The use of biological information is already starting to play an important role in radiotherapy treatment planning and will do more so in the near future. For many institutions FDG-PET is already a standard means of determining active tumor regions. Promising techniques in this respect are MR spectroscopy and contrast enhanced MRI.

On the other side of the radiotherapy chain, high precision is still limited by organ motion. By using image guidance, large improvements can be obtained here. For some treatment sites, markers can be used to determine the position of the target volume. Note that these are always surrogate for the actual tumor position. So verification of marker position vs tumor position will remain necessary at some stage.

Other new directions are the use of more advanced imaging modalities on the treatment machine (US, MRI, CT).

References

1. Yan D, Wong JW, Vicini F, Michalski J, Pan C, Frazier A, Horwitz E, Martinez A (1997) Adaptive modification of treatment planning to minimize the deleterious effects of treatment setup errors. Int J Radiat Oncol Biol Phys 38:197–206
2. Balter JM, Sandler HM, Lam K et al. (1995) Measurement of prostate movement over the course of routine radiotherapy using implanted markers. Int J Radiat Oncol Biol Phys 31:113–118
3. Balter JM, Lam KL, Sandler HM, Littles JF, Bree RL, Ten Haken RK (1995) Automated localization of the prostate at the time of treatment using implanted radiopaque markers: technical feasibility. Int J Radiat Oncol Biol Phys 33(5):1281–1286
4. Shimizu S, Shirato H, Ogura S, Akita-Dosaka H, Kitamura K, Nishioka T, Kagei K, Nishimura M, Miyasaka K (2001) Detection of lung tumor movement in real-time tumor-tracking radiotherapy. Int J Radiat Oncol Biol Phys 51:304–310
5. Nederveen AJ, Dehnad H, van der Heide UA, van Moorselaar RJ, Hofman P, Lagendijk JJ (2003) Comparison of megavoltage position verification for prostate irradiation based on bony anatomy and implanted fiducials. Radiother Oncol 68(1):81–88
6. Court L, Rosen I, Mohan R, Dong L (2003) Evaluation of mechanical precision and alignment uncertainties for an integrated CT/LINAC system. Med Phys 30:1198–1210
7. Ford EC, Mageras GS, Yorke E, Ling CC (2003) Respiration-correlated spiral CT: a method of measuring respiratory-induced anatomic motion for radiation treatment planning. Med Phys 30:88–97
8. Vedam SS, Keall PJ, Kini VR, Mostafavi H, Shukla HP, Mohan R (2003) Acquiring a four-dimensional computed tomography dataset using an external respiratory signal. Phys Med Biol 48:45–62
9. Lagerwaard FJ, Van Sornsen de Koste JR, Nijssen-Visser MR, Schuchhard-Schipper RH, Oei SS, Munne A, Senan S (2001) Multiple "slow" CT scans for incorporating lung tumor mobility in radiotherapy planning. Int J Radiat Oncol Biol Phys 51:932–937
10. Jaffray DA, Siewerdsen JH, Wong JW, Martinez AA (2002) Flat-panel cone-beam computed tomography for image-guided radiation therapy. Int J Radiat Oncol Biol Phys 53(5):1337–1349
11. Sonke JJ, Zijp L, Remeijer P, van Herk M (2005) Respiratory correlated cone beam CT. Med Phys 32:1176–1186
12. Shimizu S, Shirato H, Aoyama H, Hashimoto S, Nishioka T, Yamazaki A, Kagei K, Miyasaka K (2000) High-speed magnetic resonance imaging for four-dimensional treatment planning of conformal radiotherapy of moving body tumors. Int J Radiat Oncol Biol Phys 48:471–474
13. Caldwell CB, Mah K, Ung YC, Danjoux CE, Balogh JM, Ganguli SN, Ehrlich LE (2001) Observer variation in contouring gross tumor volume in patients with poorly defined non-small-cell lung tumors on CT: the impact of 18FDG-hybrid PET fusion. Int J Radiat Oncol Biol Phys 51(4):923–931
14. Daisne JF, Duprez T, Weynand B, Lonneux M, Hamoir M, Reychler H, Gregoire V (2004) Tumor volume in pharyngolaryngeal squamous cell carcinoma: comparison at CT, MR imaging, and FDG PET and validation with surgical specimen. Radiology Aug 18
15. Nehmeh SA, Erdi YE, Pan T, Pevsner A, Rosenzweig KE, Yorke E, Mageras GS, Schoder H, Vernon P, Squire O, Mostafavi H, Larson SM, Humm JL (2004) Four-dimensional (4D) PET/CT imaging of the thorax. Med Phys 31:3179–3186
16. Wolthaus JW, van Herk M, Muller SH, Belderbos JS, Lebesque JV, de Bois JA, Rossi MM, Damen EM (2005) Fusion of respiration-correlated PET and CT scans: correlated lung tumour motion in anatomical and functional scans. Phys Med Biol 50:1569–1583
17. Langen KM, Pouliot J, Anezinos C, Aubin M, Gottschalk AR, Hsu IC, Lowther D, Liu YM, Shinohara K, Verhey LJ, Weinberg V, Roach M III (2003) Evaluation of ultrasound-based prostate localization for image-guided radiotherapy. Int J Radiat Oncol Biol Phys 57(3):635–644
18. Seppenwoolde Y, Engelsman M, De Jaeger K, Muller SH, Baas P, McShan DL, Fraass BA, Kessler ML, Belderbos JS, Boersma LJ, Lebesque JV (2002) Optimizing radiation treatment plans for lung cancer using lung perfusion information. Radiother Oncol 63(2):165–177
19. Marks LB, Spencer DP, Sherouse GW, Bentel G, Clough R, Vann K, Jaszczak R, Coleman RE, Prosnitz LR (1995) The role of three dimensional functional lung imaging in radiation treatment planning: the functional dose-volume histogram. Int J Radiat Oncol Biol Phys 33(1):65–75
20. DICOM homepage: http://medical.nema.org/
21. Yan D, Lockman D, Brabbins D, Tyburski L, Martinez A (2000) An off-line strategy for constructing a patient-specific planning target volume in adaptive treatment process for prostate cancer. Int J Radiat Oncol Biol Phys 48:289–302
22. Yan D, Jaffray DA, Wong JW (1999) A model to accumulate fractionated dose in a deforming organ. Int J Radiat Oncol Biol Phys 44:665–675
23. Hutton BF, Braun M (2003) Software for image registration: algorithms, accuracy, efficacy. Semin Nucl Med 33:180–192

24. Pluim JP, Maintz JB, Viergever MA (2003) Mutual-information-based registration of medical images: a survey. IEEE Trans Med Imaging 22:986–1004
25. Hill DL, Batchelor PG, Holden M, Hawkes DJ (2001) Medical image registration. Phys Med Biol 46:R1–R45
26. Schad LR, Boesecke R, Schlegel W, Hartmann GH, Sturm V, Strauss LG, Lorenz WJ (1987) Three dimensional image correlation of CT, MR, and PET studies in radiotherapy treatment planning of brain tumors. J Comput Assist Tomogr 11:948–954
27. Hemler PF, Napel S, Sumanaweera TS, Pichumani R, van den Elsen PA, Martin D, Drace J, Adler JR, Perkash I (1995) Registration error quantification of a surface-based multimodality image fusion system. Med Phys 22:1049–1056
28. Kessler ML, Pitluck S, Petti P, Castro JR (1991) Integration of multimodality imaging data for radiotherapy treatment planning. Int J Radiat Oncol Biol Phys 21:1653–1667
29. Rosenman JG, Miller EP, Tracton G, Cullip TJ (1998) Image registration: an essential part of radiation therapy treatment planning. Int J Radiat Oncol Biol Phys 40:197–205
30. Yan CH, Whalen RT, Beaupre GS, Sumanaweera TS, Yen SY, Napel S (1998) A new frame-based registration algorithm. Med Phys 25:121–128
31. Pelizzari CA, Chen GT, Spelbring DR, Weichselbaum RR, Chen CT (1989) Accurate three-dimensional registration of CT, PET, and/or MR images of the brain. J Comput Assist Tomogr 13:20–26
32. Brunie L, Lavallee S, Troccaz J, Cinquin P, Bolla M (1993) Pre- and intra-irradiation multimodal image registration: principles and first experiments. Radiother Oncol 29:244–252
33. Turkington TG, Hoffman JM, Jaszczak RJ, MacFall JR, Harris CC, Kilts CD, Pelizzari CA, Coleman RE (1995) Accuracy of surface fit registration for PET and MR brain images using full and incomplete brain surfaces. J Comput Assist Tomogr 19:117–124
34. van Herk M, Kooy HM (1994) Automatic three-dimensional correlation of CT-CT, CT-MRI, and CT-SPECT using chamfer matching. Med Phys 21:1163–1178
35. Kooy HM, van Herk M, Barnes PD, Alexander E III, Dunbar SF, Tarbell NJ, Mulkern RV, Holupka EJ, Loeffler JS (1994) Image fusion for stereotactic radiotherapy and radiosurgery treatment planning. Int J Radiat Oncol Biol Phys 28:1229–1234
36. Mangin JF, Frouin V, Bloch I, Bendriem B, Lopez-Krahe J (1994) Fast nonsupervised 3D registration of PET and MR images of the brain. J Cereb Blood Flow Metab 14:749–762
37. Kwa SL, Theuws JC, van Herk M, Damen EM, Boersma LJ, Baas P, Muller SH, Lebesque JV (1998) Automatic three-dimensional matching of CT-SPECT and CT-CT to localize lung damage after radiotherapy. J Nucl Med 39:1074–1080
38. Maes F, Collignon A, Vandermeulen D, Marchal G, Suetens P (1997) Multimodality image registration by maximization of mutual information. IEEE Trans Med Imaging 16:187–198
39. Hajnal JV, Saeed N, Soar EJ, Oatridge A, Young IR, Bydder GM (1995) A registration and interpolation procedure for subvoxel matching of serially acquired MR images. J Comput Assist Tomogr 19:289–296
40. Studholme C, Hill DL, Hawkes DJ (1997) Automated three-dimensional registration of magnetic resonance and positron emission tomography brain images by multiresolution optimization of voxel similarity measures. Med Phys 24:25–35
41. ICRU (1993) Prescribing, recording and reporting photon beam therapy. ICRU Report 50, Bethesda, MD
42. Fiorino C, Reni M, Bolognesi A et al. (1998) Intra- and inter-observer variability in contouring prostate and seminal vesicles: implications for conformal treatment planning. Radiother Oncol 285–292
43. Rasch C, Barillot I, Remeijer P et al. (1999) Definition of the prostate in CT and MRI: a multi-observer study. Int J Radiat Oncol Biol Phys 43:57–66
44. Remeijer P, Rasch C, Lebesque JV et al. (1999) A general methodology for three-dimensional analysis of variation in target volume delineation. Med Phys 26:931–940
45. van Herk M, Bruce A, Kroes AP et al. (1995) Quantification of organ motion during conformal radiotherapy of the prostate by three dimensional image registration. Int J Radiat Oncol Biol Phys 33:1311–1320
46. van Herk M, Remeijer P, Rasch C, Lebesque JV (2000) The probability of correct target dosage: dose-population histograms for deriving treatment margins in radiotherapy. Int J Radiat Oncol Biol Phys 47:1121–1135
47. Bel A, Vos PH, Rodrigus PT et al. (1996) High-precision prostate cancer irradiation by clinical application of an offline patient setup verification procedure, using portal imaging. Int J Radiat Oncol Biol Phys 35:321–332
48. Bel A, van Herk M, Lebesque JV (1996) Target margins for random geometrical treatment uncertainties in conformal radiotherapy. Med Phys 23:1537–1545
49. el-Gayed AA, Bel A, Vijlbrief R et al. (1993) Time trend of patient setup deviations during pelvic irradiation using electronic portal imaging. Radiother Oncol 26:162–171
50. Greer PB, Jose CC, Matthews JH (1998) Set-up variation of patients treated with radiotherapy to the prostate measured with an electronic portal imaging device. Australas Radiol 3:207–212
51. Hanley J, Lumley MA, Mageras GS et al. (1997) Measurement of patient positioning errors in three-dimensional conformal radiotherapy of the prostate. Int J Radiat Oncol Biol Phys 37:435–444
52. Remeijer P, Geerlof E, Ploeger L, Gilhuijs K, van Herk M, Lebesque JV (2000) 3-D portal image analysis in clinical practice: an evaluation of 2-D and 3-D analysis techniques as applied to 30 prostate cancer patients. Int J Radiat Oncol Biol Phys 46 1281–1290
53. Aaltonen P, Brahme A, Lax I et al. (1997) Specification of dose delivery in radiation therapy. Recommendation by the Nordic Association of Clinical Physics (NACP). Acta Oncol 36 Suppl 10:1–32
54. Mageras GS, Fuks Z, Leibel SA, Ling CC, Zelefsky MJ, Kooy HM, van Herk M, Kutcher GJ (1999) Computerized design of target margins for treatment uncertainties in conformal radiotherapy. Int J Radiat Oncol Biol Phys 43:437–445
55. Austin-Seymour M, Kalet I, McDonald J et al. (1995) Three dimensional planning target volumes: a model and a software tool. Int J Radiat Oncol Biol Phys 33:1073–1080
56. Ekberg L, Holmberg O, Wittgren L et al. (1998) What margins should be added to the clinical target volume in radiotherapy treatment planning for lung cancer. Radiother Oncol 48: 71–77
57. Hunt MA, Kutcher GJ, Burman C et al. (1993) The effect of setup uncertainties on the treatment of nasopharynx cancer. Int J Radiat Oncol Biol Phys 27:437–447
58. Jones D, Hafermann MD, Rieke JW et al. (1995) An estimate of the margin required when defining blocks around the prostate. Br J Radiol 68:740–746
59. Roach M, Pickett B, Rosenthal SA et al. (1994) Defining treatment margins for six field conformal irradiation of localized prostate cancer. Int J Radiat Oncol Biol Phys 28:267–275
60. Rudat V, Schraube P, Oetzel D et al. (1996) Combined error of patient positioning variability and prostate motion uncertainty in 3D conformal radiotherapy of localized prostate cancer. Int J Radiat Oncol Biol Phys 35:1027–1034

61. Stroom JC, de Boer HC, Huizenga H et al. (1999) Inclusion of geometrical uncertainties in radiotherapy treatment planning by means of coverage probability. Int J Radiat Oncol Biol Phys 43:905–919
62. Mageras GS, Kutcher GJ, Leibel SA, Zelefsky MJ, Melian E, Mohan R, Fuks Z (1996) A method of incorporating organ motion uncertainties into three-dimensional conformal treatment plans. Int J Radiat Oncol Biol Phys 35: 333–342
63. Killoran JH, Kooy HM, Gladstone DJ et al. (1997) A numerical simulation of organ motion and daily setup uncertainties: implications for radiation therapy. Int J Radiat Oncol Biol Phys 37:213–221
64. van Herk M, Remeijer P, Rasch C, Lebesque JV (2000) The probability of correct target dosage – dose population histograms for deriving treatment margins in radiotherapy. IJROBP 2000 (submitted)
65. Leong J (1987) Implementation of random positioning error in computerised radiation treatment planning systems as a result of fractionation. Phys Med Biol 32:327–334
66. Pickett B, Roach M (1996) The impact of isocenter placement errors associated with dose distributions used in irradiating prostate cancer. Med Dosim 21:61–68
67. Stroom JC, Storchi PR (1997) Automatic calculation of three-dimensional margins around treatment volumes in radiotherapy planning. Phys Med Biol 42:745–755

Physical Optimization

4

Uwe Oelfke, Simeon Nill, Jan J. Wilkens

Contents

4.1 Introduction

One of the two prerequisites for the clinical application of IMRT was the development of inverse planning strategies – simply because the available forward planning strategies could not be applied to the optimization of the enormous number of treatment parameters suddenly required for the efficient delivery of intensity modulated treatment fields. The concept of 'physical optimization' was the first strategy implemented in commercial inverse planning systems and still currently is the 'working horse' of most available planning platforms. Even the modifications of the original concept often referred to as 'biological optimization', described below, basically keep the same logical structure of the optimization while only the mathematical formulation of the objectives of the optimization is modified. One common factor of both approaches is the selection of the energy fluence profiles for a pre-selected set of beam ports as the only treatment parameters to be optimized in the planning process. We consider the respective physical optimization as the current 'standard model' of IMRT optimization and review some of its detailed features later. The more recent extensions of this concept that attempt to include further physical degrees of freedom in the optimization process are described. The reader should be aware that the following brief discussion cannot aim to reflect all aspects of the physical optimization approach for IMRT. A by far more complete review about inverse planning and IMRT optimization and their details can be found in the papers of T. Bortfeld [1, 2] and S. Webb [3, 4].

Before we start to review the methods mentioned above, we want to discuss briefly a few of the uncertainties or 'weak' conceptual points of current treatment plan optimization strategies, which mostly can be traced back to our quite limited knowledge of the correlation between delivered dose patterns and their induced clinical impact. First, there arises the obvious difficulty of what should be considered the optimal clinical treatment plan. IMRT allows for an enormous variety of achievable dose patterns whose merits have to be derived from mostly a few more or less clearly defined clinical endpoints. This fact requires a reduction of our complete 3D dose distributions to a few 'global' indicators which are assumed to represent the quality of its related treatment plans. This aspect will shortly be addressed. Finally, the lack of detailed knowledge of the correlation between dose and clinical response allows and demands for a certain 'subjectivity' about what is the best clinical compromise achievable with IMRT, i.e., each treatment plan optimization has to introduce a certain 'steerability' for the physician to achieve his preferred plan. New strategies related to new approaches like multi-criteria optimization [5–7] are briefly mentioned later.

4.1.1 What Is an 'Optimal' Treatment Plan?

The task of IMRT optimization, or more precisely the task to generate an *optimal clinical* treatment plan for an IMRT treatment of a specific patient, is a conceptually and to some extent also mathematically challenging problem. Ideally, the goal of the optimization effort should be uniquely defined and be quite clear before the development of respective optimization strategies. Unfortunately, the definition of *clinical optimal* is by no means clear for the detailed level of dose painting achievable with IMRT. As soon as one goes beyond the paradigm of 3D-conformal therapy – maximum dose concentration within the tumor combined with minimal doses in organs at risk – one has to face far more difficult decisions about the *optimal clinical* plan. Subtle decisions on clinical compromises between tumor dose distributions and doses in several partially irradiated organs at risk require additional knowledge about the importance of dose homogeneity in the target, dose volume effects in organs at risk, radio-sensitivity of patient specific tissues and many more so called 'biological' parameters. The current lack of a solid 'a priori' knowledge of respective therapy relevant parameters is one of the intrinsic problems of IMRT optimization.

One key issue is the correlation of current clinical experience with a set of physical treatment parameters responsible for the observed clinical effect. Considering that usually the number of clinically relevant indicators for the assessment of success, failure or specific risks of a treatment is fairly small compared to the number of employed treatment parameters, this process naturally involves quite a reduction of the available physical information. For instance sets of complete 3D-dose distributions have to be reduced to a few, mostly organ averaged, quantities which serve as indicators for the quality of an achieved treatment plan. One of the advantages of 'physical optimization' concepts is that they are based on quality indicators derived completely from verifiable physical quantities like dose levels and irradiated volumes while the 'biological approach' assumes additional knowledge – mostly in terms of phenomenological parameters – to characterize an observed clinical effect. Both strategies are successfully implemented in clinical practice. While the 'biological optimization' approach can be considered as an extension to the purely 'physical concept' both of them naturally suffer from the fact that our detailed knowledge about the response of complexly organized tissues to radiation fields with complicated variations in space and time is quite limited.

4.1.2 Physical Parameters and Indicators

Let us now consider the basic physical parameters–quantities which can be determined by a well-defined measurement without any additional assumptions – and discuss their role for the optimization process. The primary physical quantity available for characterizing a radiation treatment is the three-dimensional dose distribution for a patient anatomy specified by its electron densities obtained from a CT scan. This simple physical representation of the anatomy is further reduced by specifying volumes of interest (VOI), whose definitions especially for tumor targets is of crucial importance for the optimization. Current routinely employed diagnostic procedures usually cannot specify any further spatial discrimination of the VOIs with respect to their functionality or radio-sensitivity.

This lack of information seemed to justify the well-accepted reduction of complete 3D-dose distributions within VOIs to the respective dose volume histograms (DVHs), which form the basis of all currently employed optimization strategies. The loss of intrinsic spatial dose information induces a certain amount of 'blindness' to the optimization procedure, which might well be clinically relevant. As example one can just think of analyzing a correlation between minimal dose values in a target and related tumor control. Not knowing whether a peripheral region of the target VOI, usually carrying a higher probability of not being tumor tissue, or an actual central tumor voxel receives that minimal dose almost prevents any meaningful analysis of this type. Furthermore, our current fixation on optimization procedures based on global DVHs may be seriously questioned in the future as the increased application of biological imaging modalities in radiation oncology [8] may reveal the importance of a spatially correlated 'fine structure' within the traditional VOIs.

Global organ DVHs are the essential quantities from which all quality indicators of treatment plans are derived. They therefore form the basis of current IMRT optimization approaches employed for inverse planning. The definition of quality indicators constitutes a further reduction of the information about the initially available dose distributions. Physical indicators are simply determined in terms of doses and irradiated volumes, e.g., minimal and maximal dose, global dose averages like mean or median dose or selected coordinate pairs of dose and irradiated volume to restrict the shape of a specific DVH. The definition of 'biological' indicators additionally requires further parameters, e.g., the assumed radiosensitivity of a tissue, which is necessary for the definition of the equivalent uniform dose (EUD) [9]. Common to both sets of indicators is their 'global' definition for an entire VOI, i.e., they do not allow the control of any local dose features within a certain region of interest.

Finally, we just would like to note that one specific physical parameter so far has not been explicitly considered in IMRT optimization strategies: *time*. Neither global dose rate effects nor the influence of different fractionation schemes seemed to be a first order effect

relevant for the optimization of IMRT. In comparison to effects of spatial dose inhomogeneities, specifically addressed in almost every optimization strategy, temporal dose inhomogeneities are always assumed either to be non-existent or of minor relevance. Now that time adapted radiotherapy based on new linac-integrated imaging technologies might actually provide us with the combined spatial and temporal dose information, the issue of time dependent effects may need to be addressed explicitly in the future.

4.1.3 Clinical Compromises and Steerability

After a set of global quality indicators for various tissues is identified, there is still the open question how these should be combined for the evaluation of a treatment plan. Moreover, the planner or physician usually needs a 'steering wheel' for the optimization process, which allows him to put more emphasis on one or several quality indicators for selected tissues of interest. This practical procedure of finding the best clinical compromise is one of the most difficult planning tasks and currently available planning systems can address this problem only insufficiently. There are basically three intrinsic problems of the current planning approach.

First, as discussed earlier, current optimization procedures rely on global dose indicators, which do not allow the control of any local dose feature within a volume of interest, i.e., currently the planner will be forced to introduce 'artificial' VOIs in order to manipulate this specific feature of the plan. Second, and more profound, the planning system does not provide any information about the physical limits which can be reached for a selected set of treatment parameters. Third, and probably of most practical consequence, is the fact that the planning system does not have 'prior' information about 'efficient compromises' between conflicting goals of the optimization. For instance, information like "how much more would the average dose in organ 'y' increase if the dose homogeneity in the target is improved by 5%" can only be obtained by a lengthy manual trial and error planning process.

At least the last two problems mentioned above could be adequately addressed by new planning strategies based on multi-criteria optimization methods. A key feature of this approach is that the optimization process will be separated in two steps. First, new mathematical strategies will be employed to create an entire set of clinically relevant treatment plans for which the 'efficient compromises' between different conflicting objectives are well known. Second, a new navigation tool will allow an easy and efficient search for the optimal treatment plan preferred by the individual planner. More details and first applications about these new planning strategies can be found in [5–7, 10].

4.2 The "Standard Model" of IMRT Optimization

While the potential benefit of intensity modulated treatment fields was first demonstrated by mathematical inversion of the relationship between energy fluence and its resulting dose patterns for idealized geometries [11], current practical approaches are all based on an iterative optimization scheme as schematically displayed in Fig. 1. The starting point of the optimization is a selected set of variable treatment parameters x whose values have to be adjusted to their optimal setting x_{opt}. First, the 3D-dose distribution D is calculated for the starting, non-optimal values of x. Next, this complete 3D-dose pattern is reduced to a single number via the objective function $OF(x)$. The value of $OF(x)$ represents the quality of the current plan and therefore allows a ranking of different plans, i.e., the optimization of the treatment plan corresponds in mathematical terms to a search for the minimal (in most cases preferred) or maximal value of OF. This is achieved with the help of the optimization algorithm, which calculates

an up-dated set of x-values, labeled as x' in Fig. 1, for the next iteration of the optimization process. Often, the convergence of this 'optimization loop' is stopped when a certain threshold value for the relative change of $OF(x)$ between two subsequent iterations is not exceeded. The parameter set x found at that time is considered the result of the optimization process and will be used for the final assessment of the plan quality.

In the following, we will describe in detail the main components of the optimization loop employed for the standard IMRT optimization that uses only physical quantities for the specification of the plan quality.

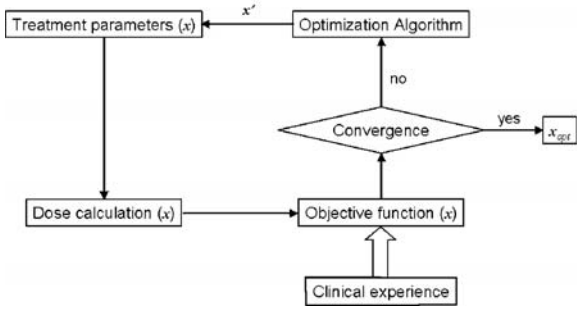

Fig. 1. The optimization loop for iterative IMRT optimization. From a set of initial treatment parameters x (usually the intensity amplitudes) a 3D-dose distribution is derived. Then, the respective treatment plan is evaluated and ranked by the objective function, which is based on current clinical experience. If the quality of the treatment plan is considered to be sufficient the current value x is chosen as the optimum x_{opt}. If no convergence towards the optimal value is detected new fluence amplitudes x' are suggested by the optimization algorithm and a new iteration of the optimization is initiated

4.2.1 What is Optimized?

In the standard approach of IMRT plan optimization [1, 12, 13] the 2D-fluence profiles for all beam ports are chosen as the only free treatment parameters. Obvious other choices, like the number of beams, the beam entry angles, the beam energy or even the radiation type are preselected by the planner and remain fixed during the optimization process. The subdivision of each treatment field into small independent spatial sub-units, labeled by numbers from 1 to N_b and usually referred to as 'bixels', allows one to define a set of related fluence amplitudes x_i, $i = 1 \ldots N_b$ as optimization parameters. The number of these parameters naturally depends on the size of the lesion being irradiated and the choice of the spatial resolution of the fluence maps. In most cases the spatial extension of the bixel is chosen to correlate closely with the leaf width of the multi-leaf collimator (MLC) to be used for the actual treatment, e.g., for a standard MLC with 10 mm leaf width (projected at the plane of the isocenter) a bixel size of 10 mm × 10 mm is employed. The use of finer bixel resolutions seems to be advantageous for the irradiation of complex shaped smaller lesions with micro- or mini-MLCs [14, 62]. The respective gain in spatial precision results in an increased number of treatment parameters and most likely also in extended overall treatment times. It has been shown that bixel resolutions in the range of 2 – 5 mm square can be beneficial for selected clinical cases, and that a further increased bixel resolution will however, fail to yield even more improved results [63].

The choice of fluence amplitudes as the only optimization parameters facilitates the solution of the optimization problem considerably if a simple mathematical formulation of the optimization task in terms of physical parameters is chosen. One obvious reason is the linear relationship between fluence and dose. How this optimization problem is set up and which methods can be used for its solution will be described in the following paragraphs of this section. Approaches, which extend the standard optimization to other treatment parameters than fluence amplitudes are discussed separately below.

The concept described so far aims to optimize the so called 'ideal' intensity maps, i.e., the optimization process is based on the chosen 'bixel' configuration without considering the next practical step for the delivery of IMRT treatment fields: the conversion of the ideal intensity map into patterns of leaf sequences. Naturally, this step involves a re-grouping of the elementary bixels into larger, practically deliverable treatment fields, which can only approximate the ideal intensity profiles and therefore usually leads to a reduced quality of the treatment plan. The size of these effects was for instance demonstrated by [15] and there are several approaches to include these effects into the original optimization scheme [15–17]. Another attempt to overcome the 'sequencer problem' in IMRT optimization is the method of direct aperture optimization also discussed below.

4.2.2 Dose Constraints and Quality Indicators

Dose and DVH Constraints

The specification of dose constraints for the tissues of interest is the first step for the mathematical formulation of the optimization problem. Ideally, the constraints should be derived directly from clinical experience, i.e., they should rely on a direct correlation between clinical observation and characteristic dose values.

For targets, usually global thresholds for the tolerable minimal and maximal doses ($D_{\min}$ and $D_{\max}$) are set for the entire volumes, i.e., for a tumor VOI whose voxels are labeled with an index i ranging from $1 \ldots N_T$, the respective doses D_i should all satisfy the constraint: $D_i > D_{\min}$ and $D_i < D_{\max}$. The doses $D_{\min}$ and $D_{\max}$ are usually chosen close to the prescribed dose D_{pres} and the respective dose window allows for some flexibility if conflicting goals in organs at risk have to be satisfied simultaneously. The values of $D_{\min}$ and $D_{\max}$ in this approach represent the 'clinical' experience, i.e., they characterize the biological dose response although they are purely physical quantities. If both tolerance dose values are chosen to be close to each other and if both dose constraints are enforced with high priority, the use of $D_{\min}$ and $D_{\max}$ should also lead to sufficient dose homogeneity. However, the feature of dose homogeneity in the target can also be addressed explicitly by imposing a constraint on the dose variance for target structures.

Dose Volume Constraints

For the remaining $k = 1 \ldots N_k$ organs at risk (OARs), composed of N_i^k voxels, the natural expansion of the dose constraints described above is to employ a maximal tolerance dose $D_{\max}^k$ for all voxels. For OARs, however, one wants to include not only global constraints for the entire organ. Observed or predicted dose volume effects for certain OARs can be accounted for by imposing one or several maximal dose limits $D_{\max}^{k,l}$ only if the dose exceeds this tolerance dose for a fraction v_l of the organ's volume [18, 20]. These dose-volume histogram constraints, i.e., $\text{DVH}(D_{\max}^{k,l}) < v_l$, can be visualized directly as shown in Fig. 2 where the two points $(D_{\max}^{k,l}; v_l)$ $l = 1, 2$ in the dose-volume plane should all be above the actual DVH-curve. The respective points identify 'forbidden' zones in the DVHs as indicated.

Quality Indicators for Physical Constraints

Next, the previously defined clinical dose constraints are employed to define a mathematical measure which in-

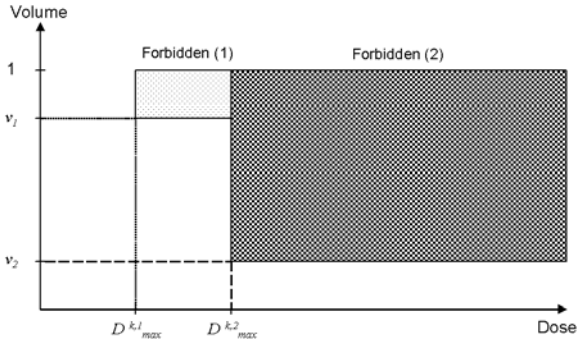

Fig. 2. Dose volume histogram constraints. Two typical DVH constraints are indicated by the two data points $(D^{k,1}_{\max}, v_1)$ and $(D^{k,2}_{\max}, v_2)$, i.e., no volume greater than v_1 (v_2) should be irradiated with a dose higher than $D^{k,1}_{\max}(D^{k,2}_{\max})$. As a consequence the DVH constraints mark the indicated regions in the volume-dose plane as 'forbidden zones', i.e., if a DVH crosses these areas the DVH constraint is violated

dicates its quality for a given treatment plan. Usually, this is done by assigning a numerical value to a specific violation of the given constraint. These quality indicators refer to one individual constraint and tissue, e.g., the standard measure is the sum of the quadratic dose deviations found for all voxels of the considered organ. In mathematical terms, the related function $OF^{(-)}_T$ for the avoidance of an under-dosage of the target takes the form

$$OF^{(-)}_T(x) = \frac{1}{N_T}\sum_{i=1}^{N_T}\left[C_+\left(D^T_{\min} - D^T_i(x)\right)\right]^2 . \quad (1)$$

The analogue term for the avoidance of global overdosage effects for either target or OARs reads

$$OF^{(+)}_k(x) = \frac{1}{N_k}\sum_{i=1}^{N_k}\left[C_+\left(D^k_i(x) - D^k_{\max}\right)\right]^2 . \quad (2)$$

The operator $C_+(x)$ defined by $C_+(x) = x$ for $x \geq 0$ and $C_+(x) = 0$ for $x < 0$ ensures that only constraint violations contribute to the quality indicators $OF^{(+)}$ and $OF^{(-)}$. These most prominent quality indicators of objective functions – the measure of square deviations form given dose constraints – introduces new parameters into the optimization problem, which are not based on clinical experience but which instead are required for the mathematical formulation of the optimization problem. The 'square' terms were mostly chosen because the resulting full objective functions are still mathematically convex [4], which allows the employment of very fast gradient techniques for the solution of the optimization problem (for more details see section later). The definition of quality indicators for the more general DVH constraints is done similarly and can for instance be found in [19]. Unfortunately, DVH constraints lead to non-convex objective functions [21,22] However, it was shown [23] that the resulting local minima in the overall objective function are of minor practical relevance.

Objective Functions

For the final mathematical formulation of the optimization problem, the individual quality indicators which each represent the merit of a particular plan for one clinical constraint have to be combined to yield a single valued quality measure of the complete treatment plan. Naturally, the given indicators for target structures OF_T and organs at risk OF_k refer to mutually conflicting goals of the optimization, i.e., the combination of these individual constraints is crucial for the clinical compromise achievable with that particular optimization scheme. Furthermore, and maybe even more important, the design of the overall objective function has to introduce 'steering parameters' such that the planner can efficiently derive the clinically acceptable plan of his choice. Simplicity of the objective function, combined with the request that the overall objective function remains convex, leads to the well known weighted sum of individual quality indicators, i.e.,

$$OF(x) = w^{(+)}_T OF^{(+)}_T(x) + w^{(-)}_T OF^{(-)}_T(x) + \sum_k w_k OF^{(+)}_k(x) . \quad (3)$$

With the introduced weighting factors w for each constraint the planner can now 'steer' the result of the optimization towards the optimal treatment plan of his preference. As already mentioned, the parameters w unfortunately do not have any intuitive meaning and it is unknown how sensitive the outcome of an optimization is coupled to variations of the respective weighting factors. Both features make the manual determination of these parameters a cumbersome planning task, which is one of the reasons why there is increasing interest in the already mentioned approaches of multicriteria optimization (see above). An extension of this introduction of global penalty factors with the aim to improve local dose features of a plan was introduced in [24].

Technical Criteria – Plan Degeneracy

As already mentioned, the standard model of inverse planning for IMRT optimizes an ideal fluence profile, independent of the sub-sequent translation into MLC-sequences required by the dose delivery system. Features of this important practical step directly prior to the dose delivery can be additionally optimized without significantly reducing the plan quality. This is due to the fact that the solution of the IMRT optimization problem is not unique and that numerous sets of fluence amplitudes yield treatment plans of comparable quality. This degeneracy of the optimal fluence profiles, e.g., discussed in [4,25,26], allows one to account for further technical constraints that facilitate the practical dose delivery.

One of these additional technical criteria is the 'smoothness' of the intensity maps. Intensity maps that avoid patterns of clinically unmotivated high fluence gradients can be delivered faster and safer. The smoothing of these discontinuities can be either achieved by applying a median filter (cf. [27]) to the fluence profiles or by adding a respective term to the objective function [28].

Another important technical aspect is the conversion of the derived continuous fluence modulations into a spectrum of discrete fluence values, e.g., this number of intensity levels determines the number of subfields being used for the step-and shoot technique. It has been shown that for most cases a moderate number (5–7) of intensity levels seems to be adequate [29] which leads to a number of IMRT segments in the order of 100 which can be efficiently delivered with current IMRT technology.

4.2.3 Optimization Algorithms

To calculate the beam weights for a given set of constraints and a selected objective function, an optimization algorithm is required. Not all optimization algorithms can be used for all objective functions due to the mathematical properties of the objective functions. Over the last decades numerous optimization approaches for different problems haven been published and applied to problems within the field of radiation therapy [3, 30]. In general, these algorithms can be divided into two categories. First, there are the deterministic algorithms like the gradient approach. These techniques are applied to optimization problems where the objective functions are convex and therefore only a global minimum and no local minima exist [1]. For these convex objective functions like the standard quadratic objective function the deterministic algorithms can calculate the optimal solution very fast and are therefore currently used in most commercially available IMRT treatment planning systems [3]. Second, there are the stochastic methods, like simulated annealing or genetic algorithms. They have the advantage that even for non-convex objective functions based on biological objectives or DVH-constraints the global minimum can be found even if local minima exist.

In this section we only briefly discuss the rationale of the most frequently used algorithms. First, as examples for deterministic algorithms, simple gradient methods and the conjugate gradient approach are described. Second, the basic ideas of stochastic algorithms like simulated annealing and genetic algorithms are discussed. More detailed information about optimization algorithms used in radiotherapy can for instance be found in [31].

Deterministic Approaches

Steepest Descent This method is mostly used for finding the global minimum of a convex objective function $OF(x)$, where x represents the set of variable treatment parameters which have to be adjusted to their optimal value. The objective function can be visualized as a multi-dimensional surface given in terms of the coordinates x. For a general non-convex objective function a one-dimensional example is shown in Fig. 3. A key role in the optimization plays the first derivative of this function or its generalization for N-dimensions – the gradient of $OF(x)$. The gradient $\nabla OF(x)$ determines the steepest direction along the surface of the objective function. Finding the minimum of $OF(x)$ via an iterative method requires that the values of the intensities x are updated at each step of the iteration i. The update of x while advancing from the iteration i to $i+1$ is for the gradient approaches given by the rule

$$x(i+1) = x(i) - \alpha \cdot \nabla OF\left(x(i)\right) \ . \tag{4}$$

This iterative search can be visualized as a ball rolling downhill into the valley along the steepest direction (see Fig. 3) until the minimum of the valley is reached. The constant factor α, often referred to as the damping factor, determines the step size of the iterative process. One problem with the steepest descent method is that many small steps in the calculated direction are performed even if the valley is of perfect quadratic form. The different methods of gradient approaches mostly differ by the determination of α and therefore the step size. For the steepest descent method the value of α is set to a fixed value independent of the position and the iteration step.

Newton's Method The Newton methods take into account the second order derivatives of the objective function for the determination of the damping factor, which controls the speed and success of the optimization. Employing a Taylor expansion of $OF(x(i))$ up to the second order derivatives one can show that a new damping factor for each iteration step is a promising alternative choice for α.

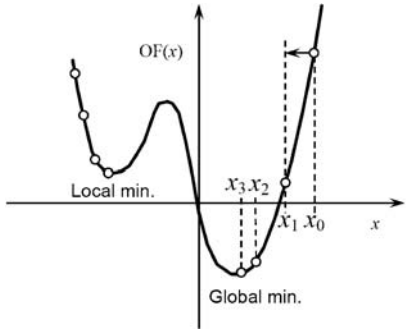

Fig. 3. The steepest descend algorithm starts from position x_0 and always walks with a predefined step size towards the global minimum. If the algorithm started on the *left side*, the algorithm would be trapped in the local minimum

For the multi-dimensional optimization problem encountered in radiation therapy (several hundred fluence amplitudes have to be simultaneously optimized) the damping factor can be expressed in terms of the inverse Hessian H^{-1} of the second derivatives of $OF(x)$ [32], i.e.,

$$x(i+1) = x(i) - H^{-1}\left(x(i)\right)\nabla OF(x(i)) = x(i) - \alpha_{\text{Newton}}\nabla OF\left(x(i)\right) . \quad (5)$$

One problem within the Newton approach is that for each step the complete inverse Hessian has to be calculated, which is a complex and time-consuming process. One possible solution of this problem is not to recalculate the inverse Hessian at each iteration step but to use approximations for the inverse Hessian [30]. If these methods are applied, the optimization algorithms are called "Quasi Newton" approaches. For example the treatment planning system *KonRad* uses a "Quasi Newton" algorithm for the optimization of the fluence patterns [19]. There are other possible solutions and implementations for this problem, which can be found in [32]. The "steepest descent" method can be viewed as a special case of the "Quasi Newton" approach.

Conjugated Gradient Approach The problem with the "steepest descent" or Newton methods is that the directions of the moves towards the unknown minimum in two successive iterations are not mutually orthogonal, i.e., the gain of approaching the minimum value of $OF(x)$ achieved in one step of the iteration might get partially lost in the next step [32]. This is not the case for the "conjugated gradient" approach. Mathematically, there are two different methods to determine the global minimum of the objective function with that approach. The first approach calculates the Hessian at each step of the iteration and it can be shown that this version of the "conjugated gradient" approach finds the global minimum after N iterations where N is the number of optimization parameters x [32]. However, since the Hessian cannot always be calculated in a reasonable amount of time, an alternative approach is used more often for applications in radiation therapy [33].

Starting from an arbitrary point $x(0)$ the objective function is evaluated, at different positions along the line through the starting point $x(0)$ in the direction of the encountered 'steepest descent' $h(0) = -\nabla OF\left(x(0)\right)$. This is done until the position of the minimum of $OF(x)$ along that line is found. At the position of the line minimum $x_{\min}$ the gradient $g(1) = -\nabla OF(x)_{x_{\min}}$ is calculated and used for the determination of the next direction in which the global minimum will be approached. The new direction for this 'line minimization' approach is given by various iterative rules, i.e., $h(i+1) = g(i+1) + \gamma(i)h(i)$ where the factor $\gamma(i)$ can be calculated according to Fletcher–Reeves or after Polak and Ribiere [32].

A detailed mathematical description and instructions on how the conjugated gradient approach is effectively implemented can for instance be found in [32]. One of the main problems with conjugated gradient algorithms can be the speed of the line minimization. An example for a successful application of the conjugated gradient method in inverse IMRT planning is the HELIOS (Varian) IMRT treatment planning system.

One potential concern with deterministic algorithms is that the iterative process may get trapped in a local minimum (see Fig. 3) such that the desired global minimum is never discovered. Local minima can be encountered for example if DVH constraints are added to the objective function. Several investigations by different groups have come to somewhat different conclusions about this problem. Deasy [21] argues that the IMRT algorithm should include methods to deal with the problem of local minima, whereas others like Wu and Mohan [23] or Llacer et al. [22] have shown that even in the presence of local minima acceptable solutions for a given IMRT problem can be found. A study concerning the speed and the convergence properties of different gradient algorithms used for the optimization of IMRT can be found in [21].

Stochastic Methods

Stochastic optimization algorithms offer the advantage that they can find the optimal treatment parameters even for complex objective functions with potential local minima. The price to pay for this nice feature is a significantly increased optimization time in comparison to the discussed deterministic algorithms. Historically the method of simulated annealing was introduced as one of the first algorithms by S. Webb [34] in radiation therapy planning. More recently, even more complex optimization engines based on 'genetic algorithms' are employed for treatment plan optimization. In the following we introduce the basics of these concepts without referring to mathematical details which can be found in the given references.

Simulated Annealing There are basically two strategies as to how the method of 'simulated annealing' escapes from the trap of local minima – 'climbing uphill' and 'tunneling'. Both methods were illustrated by Webb [35] with a nice example.

Imagine a walker is instructed to find a well in a hilly landscape. The well is assumed to be at the lowest point of the landscape and therefore coincides with the 'global minimum'. Since the walker has no a priori knowledge on where to go he starts his task by walking downhill since he is aware that the mountains are higher then the well. Using the potential energy (V) as the objective function it is clear that $V_{\text{Well}} < V_{\text{Hill}}$. His task is therefore to minimize $|V - V_{\text{Well}}|$. Consequently, he walks in the direction of the steepest descent until he encounters a valley. Unfortunately, the walker can see only the nearest surroundings due to some fog and therefore he

does not know if the valley is the local or the global minimum. The only way to find out is to walk 'uphill' for some time and to further explore the whole landscape. In mathematical terms the 'simulated annealing' algorithm provides some probability of searching in the 'uphill direction' so that the search for a global minimum continues even if a local one is encountered.

Alternatively, the walker could have enlarged his step size so enormously that he leaves the valley in one step. This process is equivalent to a "tunneling" through the walls of that valley (see Fig. 4).

Mathematically, both described strategies involve the sampling of distributions. First, the step size $\Delta x(i)$ after i iterations ($i \geq 1$) is randomly chosen from a displacement distribution $D(\Delta x(i))$. The width of this distribution is dynamically decreasing so that smaller steps are preferred when one approaches the optimal solution. The sampling of $D(\Delta x(i))$ allows the inclusion of the 'tunneling' strategy. Next, the decision whether that iteration step was a good move toward the optimal solution has to be made. This is done by random sampling of a probability distribution $P(i)$. If the difference of the objective function $\Delta OF(i) = OF\left(x(i) + \Delta x(i)\right) - OF\left(x(i)\right)$ is negative, then the new set of treatment parameters is accepted. However, in contrast to the gradient methods, the new position is also accepted with a probability $P(i)$ if the difference is positive. The probability distribution $P(i)$ for all displacement distributions is given as

$$P(i) = \exp\left(\frac{-\Delta OF(i)}{k_B T(i)}\right) . \tag{6}$$

With the temperature $T(i)$ the width of $P(i)$ is dynamically adjusted to smaller values during the optimization process. How this 'cooling' of the 'up-hill' climbing is done best depends also on the complexity of the objective function. Different combinations of $P(i)$ and $D(\Delta x(i))$ define various types of simulated annealing algorithms. The most prominent ones are discussed below.

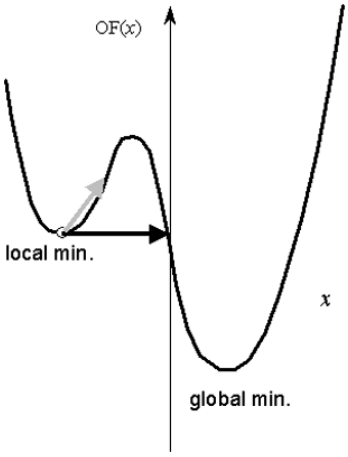

Fig. 4. Simulated annealing: To avoid the local minimum the algorithm can either tunnel through (*black arrow*) or climb (*gray arrow*) the barrier

The concept of using the temperature to describe the simulated annealing process is taken from the area of solid physics. If, for example, a metal is heated until a phase transition occurs from solid to liquid then the molecules are moving randomly. If now the system is slowly cooled down a regular crystal structure is formed [36]. This procedure ensures that the internal energy of the solid is minimized.

Boltzmann Annealing

For the classic simulated annealing process the starting temperature $T(0)$ is very large which leads to a higher probability to accept uphill steps. During the iteration process, the temperature is reduced and $T(i)$ must satisfy the condition $T(i) \geq T(0)\frac{1}{\log(i)}$ [37]. For the Boltzmann annealing the step size $\Delta x(i)$ is sampled from a Gaussian distribution:

$$D_{\text{Boltzmann}}\left(\Delta x(i)\right) = \left(2\pi T(i)\right)^{-N/2} \times \exp\left(-\frac{\Delta x(i)^2}{k_B T(i)}\right) . \tag{7}$$

Fast Simulated Annealing

Another method is the "fast simulated annealing" algorithm which has been frequently used for the optimization of IMRT treatment plans [38, 39]. For "fast simulated annealing" the temperature change is given as $T(i) = T(0)/i$ and the displacement vectors are sampled from a Cauchy distribution [40]:

$$D_{\text{Fast}}\left(\Delta x(i)\right) = \frac{T(i)}{\left(\Delta x(i)^2 + T(i)^2\right)^{(N+1)/2}} \tag{8}$$

Compared to the classical "Boltzmann annealing" the temperature is changed faster for the "fast simulated annealing" and the displacement vectors are chosen from a wider distribution. Fast simulated annealing is used for example in the Corvus treatment planning system [38].

Genetic Algorithms Genetic algorithms (see [64, 65]) have also been used recently for the optimization of IMRT plans based on highly complex objective functions [41, 42]. They emulate basic principles found in evolutionary biological systems to identify the 'most likely survivor' in a given pool of potential solutions. This is done by applying genetic principles such as inheritance, mutation, recombination and natural selection. Genetic algorithms are normally used if the search space is complex and large and traditional hill climbing algorithms like simulated annealing are likely to encounter difficulties.

In the following we will use a very simple example to illustrate a few of the basic features of genetic algorithms. Let us consider the problem of finding the minimum of the one-dimensional objective function $OF(x) = x^2$ with the help of a genetic algorithm, which can for example be divided into the following processes: Encoding, Evaluation, Crossover, Mutation and Decoding.

Encoding and Decoding

First, the original optimization problem has to be formulated in such a way that the processes responsible for the genetic evolution can be mathematically simulated. One of the most critical tasks is to find a good representation of the solution space, a step which is often referred to as 'Encoding'. An inappropriate encoding could lead to a very slow, practically useless optimization algorithm. For our example, one possible solution is to use a binary representation of the values of $OF(x)$. Due to a priori knowledge we can for instance limit the solution space to a range of $0-15$ and therefore we can use a four-bit representation. Different candidates for a solution, e.g., $A(x=2)$ and $B(x=13)$ are then encoded as $A=\{0010\}$ and $B=\{1101\}$. These strings can be compared to genetic strings where the bits (0/1) are the genes. Decoding simply denotes the process of reversing the solutions back into the original representation.

Next, one has to create a "first generation pool" of solutions. These solutions are created either with the help of prior knowledge or by assuming a random distribution for a likely range of parameters. In case of IMRT, a single solution is described by the weights of the beamlets used for the optimization or by MLC shapes.

Evaluation

The next step is to evaluate the current generation pool and rank the solutions according to their fitness with the help of the objective function. In our example solution A has a higher rank than solution B since we are searching for the global minimum of $OF(x)$. This ranking determines a normalized probability distribution which specifies the likelihood that a solution will be part of the next generation pool of solutions. At this stage of the optimization process one also decides whether the best solution of the considered pool is of sufficient quality such that the optimization can be stopped. New solutions not available in the current genetic pool can be created by processes like 'crossover' and 'mutation'.

Crossover

By using the probability distribution calculated from the evaluation of the gene pool, two arbitrary solutions are selected and a 'crossover' process is performed at an arbitrary position within the 'chromosome' of these solutions. For our example a crossover of solution A and B at position 2 would lead to two new solutions. $C=\{0001\}$ (corresponding to $x=1$) and $D=\{1110\}$ (corresponding to $x=14$) which are then added to the second generation pool. This process is repeated until a sufficient number of solutions is available in the second generation pool. Since the crossover process is done preferably between two high rank solutions, the application of crossover processes alone bears the risk of being trapped within a local minimum. This can be avoided by additionally using the 'mutation process' as a second method of creating new solutions in the next genetic pool.

Mutation

The mutation process offers an analogue to the 'hill climbing' strategy applied in the 'simulated annealing' algorithm. The mutation procedure is done by changing one bit at a random position within a considered solution. For example a mutation of C could lead to $\{1001\}$ (corresponding to $x=9$) if the first bit is changed. After the application of a well defined number of mutations and cross-over processes the newly created pool of solutions is evaluated again. When the desired convergence of the algorithm is reached the final solution is decoded back into the space of treatment parameters.

Summary

The advantage of deterministic approaches like the steepest descent, Quasi Newton or the conjugated gradient approach in contrast to the stochastic approaches is the optimization speed. For a highly complex IMRT case with over 1,000 degrees of freedom, a typical optimization time for one solution takes about 1 min on a standard PC, whereas the times for stochastic optimization algorithms are significantly higher. If complex non convex objective functions with extreme local minima are employed, there is no alternative than to use stochastic algorithms like simulated annealing or genetic algorithms.

There are other optimization algorithms applied for IMRT optimization that were not considered in this section. For example, one other promising optimization method is linear programming. Especially for multi criteria optimization problems this technique seems to be advantageous [31]. A comprehensive review of optimization techniques applied in radiotherapy can be found in [43].

4.3 Optimization of Other Degrees of Freedom

The previous sections dealt mainly with the "standard approach" of IMRT, i.e., with the optimization of intensity maps for predefined beam configurations. This means that the planner specifies the general irradiation conditions (e.g., to use photons at 6 MV with five given beam directions using this specific hardware etc.), and all that is left to the planning software is to compute "optimal" intensity maps for every beam. However, there are a lot of other degrees of freedom that could in principle be included into the optimization process in order to improve the treatment plan. Generally speaking, every parameter that can modify the energy fluence in the patient is a potential candidate for optimization. In addition to the optimization of intensity maps, the following degrees of freedom could be exploited: the *number of beams* (or arcs) and their *directions of incidence*, usually given by gantry and couch angles; the

treatment modality (photons, electrons, protons etc., alone or in combination); the *beam energy*; the *delivery technique* (compensators, various multi-leaf collimators (MLC) with different leaf widths, the number of intensity levels per beam etc.) and finally the *patient position* or *setup* (supine/prone, use of a balloon, bolus etc.). Although an experienced planner can make an educated guess to find almost optimal values for many of these parameters, several attempts have been made to include some of these variables, e.g. the beam directions, into the optimization loop.

The influence of the beam energy is rather small in photon IMRT, and it has been suggested that one relatively low photon energy (e.g., 6 MV) is sufficient for intensity modulated treatment plans since the dose fall-off and the depth of the maximum are less important in IMRT than in conventional radiotherapy, especially if a high number of modulated beams is used. For example, Sternick et al. [44] found no significant difference in the dose distribution of a rotational IMRT plan when they increased the beam energy from 4–15 MV. This situation is of course different for charged particle beams (electrons, protons etc.), where the energy is an important parameter that controls the range of the particles.

If the quality of the treatment plan is assessed in terms of the biological outcome rather than the physical dose, different *fractionation schemes* might also offer additional degrees of freedom in the optimization process. However, this is beyond the scope of this chapter.

There is another class of degrees of freedom that becomes important when the treatment plan does not involve the "classic" intensity maps. It is obvious that inverse planning techniques can be used in conventional radiotherapy to optimize *blocks*, *wedge angles* and *directions*, *weighting factors* and *MLC shapes* for conformal fields. If more than one aperture per beam direction is used, one can even create IMRT plans without optimizing an abstract intensity map. Instead, the weights and sometimes even the shapes of these apertures are optimized directly in the planning process, thereby rendering any leaf sequencing steps after the optimization unnecessary. These techniques are called *"aperture-based" inverse planning*.

In the following sections, we will concentrate on two of the points mentioned above, namely on the optimization of beam directions and on aperture-based optimization techniques, since they enjoy considerable interest and were studied by many research groups.

4.3.1 Optimization of Beam Directions

Over the last few years there have been numerous discussions as to whether it is advantageous or necessary to optimize beam directions in IMRT. It seems that this question has not yet been answered completely, at least not to everybody's satisfaction. Although one is tempted to think that treatment plans will become much better if optimal beam directions are chosen (as it is the case in conventional radiotherapy), this is not so clear for IMRT. The general expectation is that the more modulated beams one is using, the less important are their directions of incidence.

There are basically two reasons why the optimization of beam directions was less frequently investigated than for example the optimization of intensity maps: first, there is often not much to gain in this additional step (compared to the much bigger benefit when one moves from three-dimensional (3D) conformal radiotherapy to IMRT), and second, the optimization of beam directions is mathematically difficult, since it is a non-convex problem [45]. This means the optimization algorithm might get trapped in local minima if one uses fast gradient descent techniques, and one has to employ more time consuming algorithms like simulated annealing or exhaustive search.

The potential impact of the optimization of beam directions certainly depends on the individual case, and it is strongly connected to the number of beams that are used. The "best" dose distribution can of course be achieved with a very high (in fact infinite) number of beams. However, above a certain number of beams, the quality of the plan "saturates" and is only marginally improved when additional beams are considered. The number of beams required for an acceptable plan depends on the anatomy, on the desired level of dose homogeneity in the target volume, on the architecture and tolerance of organs at risks and on the prescribed dose (cf. [46]). In general, no more than nine beams are needed to get acceptable results. For seven to nine beams, it is often sufficient to spread them evenly in one plane without compromising the dose distribution, i.e., not much can be gained when the beam directions are optimized [45, 46]. However, this is case dependent, and especially complex head and neck cases might benefit from beam angle optimization. Pugachev et al. [47] found an improvement in the dose distribution for a nasopharynx case when nine noncoplanar beams with optimized angles were used instead of nine equally spaced coplanar beams. On the other hand, a prostate case in their study did not benefit from a respective beam angle optimization.

The situation is different for small numbers of beams. Stein et al. [46] found that the optimization of beam directions is most valuable for less than six beams. Söderström and Brahme [48] suggested that three beam portals could be sufficient to achieve reasonable outcomes in terms of the tumor control without severe complications, provided that the orientations of these three fields are optimally selected. This is supported by a study of Das et al. [49], where three to five opti-

mized beam directions gave similar results as a large number of evenly spaced beams. In clinical practice of IMRT, however, five to seven evenly spaced coplanar beams are frequently used, and the optimization of their incident angles is considered not to be an important issue.

Techniques for the Optimization of Beam Directions

If one attempts to optimize the angles of incident beams in IMRT, one is confronted with a mathematically difficult task. The main reason for this is that the beam directions and the respective intensity maps are coupled, i.e., they cannot be optimized independently from each other. It is a complex and non-convex optimization problem with local minima in the objective function [45]. Depending on the chosen resolution of gantry and couch angles (e.g. 5° or 10°) the search space can also become very large, even if angles where the gantry can collide with the patient or the couch are excluded. In order to avoid local minima, stochastic optimization algorithms like simulated annealing have to be chosen for the optimization of beam directions. To reduce the optimization time, hybrid techniques have often been used that employ simulated annealing for the optimization of the beam angles in an outer loop, while for every beam configuration the intensity maps are optimized in an inner loop using faster gradient descent techniques (cf. [46, 47, 50]; for a similar hybrid approach with different optimization techniques see [51]). The concept of hybrid techniques is illustrated in Fig. 5.

Due to the strong coupling between beam directions and intensity maps in IMRT it is very difficult to predict "good" beam directions. This is different in 3D conformal radiotherapy, where the most important issue for suitable beam angles is to avoid organs at risks. The concept of the beam's-eye-view proved to be very helpful in this context. In IMRT, it is not necessary to avoid beam directions through organs at risk, because they can be spared in the intensity map [45]. In fact, it may even be favorable to include such beam orientations in order to find the best possible trade-off between target and organs at risk in the dose distribution (cf. [46]). For optimal sparing of the normal tissue, the beams should be separated as much as possible (cf. [52]). This is the reason why – in a coplanar configuration – the beams should be evenly spaced. Since not much can be gained in IMRT from opposing fields, the number of beams in such a situation will very often be odd. There have been attempts to develop methods for the computer-assisted selection of beam orientations in IMRT, which utilize score or cost functions to rank potential beam directions (e.g. [53]). However, the optimization of beam directions is still a difficult task and an evenly spaced configuration of coplanar beams continues to be the most frequent form of IMRT.

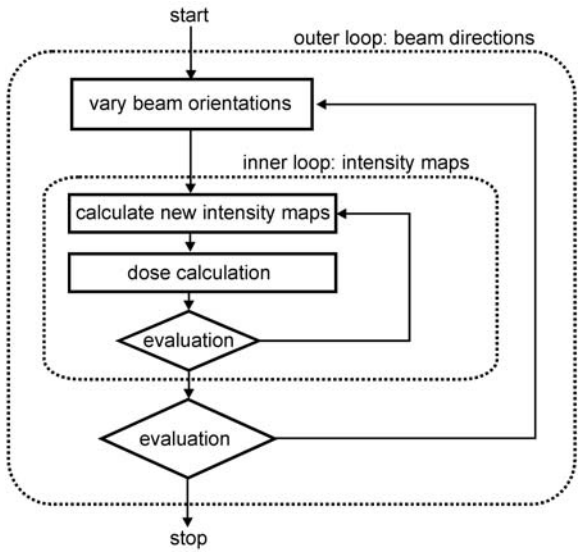

Fig. 5. Flowchart for a hybrid optimization approach: the beam directions are optimized in the outer loop (e.g., using a stochastic optimization algorithm), while the intensity maps for every beam configuration are optimized in the inner loop, where fast algorithms like the gradient technique can be employed

4.3.2 Aperture-based Optimization

Aperture-based optimization (for a review see [54]) is a technique for IMRT that is designed to reduce the complexity of intensity modulated treatment plans and to facilitate the application of IMRT in clinical practice. In short, this is achieved by avoiding the optimization of intensity maps, since their delivery by a multi-leaf collimator requires sophisticated post-processing methods ("leaf-sequencing"). Instead, the planning process is based on a small, preset number of apertures (i.e., MLC shapes) per beam direction. The optimization is then either limited to calculate optimal weights for predefined apertures (which can, for example, be derived from the patient's anatomy), or it can be extended to a simultaneous optimization of the shapes and weights of the apertures (cf. Fig. 6). The first approach is called contour-based aperture optimization, while the second one is termed direct aperture optimization (DAO). Both techniques will be described in more detail below.

One of the main advantages of aperture-based optimization compared to beamlet-based optimization is that many problems that are related to the leaf-sequencing can be avoided. Depending on the individual case and on the specific multi-leaf collimator used, the translation from intensity maps to deliverable MLC patterns can introduce considerable deviations between the planned and the delivered dose. This can be attributed to the discretization of intensity levels, to head scatter and leaf transmission/leakage, to the tongue-and-groove-effect and to dosimetric problems with small off-axis segments or segments with very low monitor units. Ide-

ally, these sequencing issues as well as any constraints given by the MLC (interdigitation etc.) should be integrated into the optimization loop, but this is not always possible in practical applications. In aperture-based IMRT, no sequencer is necessary and the beams are often relatively smooth, consisting of a small number of segments per beam, which are more similar to conventional fields and therefore easier to verify. Since MLC constraints can be included into the optimization process, the resulting apertures are ready to deliver without any further processing.

Contour-based Optimization

In contour-based aperture optimization, several aperture shapes per beam direction are defined in a pre-processing step before the optimization. They are then kept constant, and the individual weights of these segments are optimized according to given dose constraints as described in the section about the standard optimization techniques. Following the classification by Shepard et al. [54], contour-based inverse planning can be divided in two subgroups depending on how the apertures are defined. This can be done either based on the patient's anatomy ("anatomy-based"), i.e., on the outlined structures like planning target volume and organs at risk, or the apertures can be defined according to certain isodose-lines achieved with an open field ("isodose-based").

Anatomy-based definition of apertures was investigated mainly by the research groups at the University Hospital Ghent (e.g., [55, 56]) and at the Thomas Jefferson Hospital in Philadelphia (e.g., [57, 58]). Xiao et al. described an intuitive method to obtain suitable aperture shapes: for every beam direction, the first segment is defined in the beam's-eye-view (BEV) to match the planning target volume (PTV) surrounded by an appropriate margin. For every organ at risk (OAR) that overlaps the PTV in the BEV, additional segments are then added which conform to the PTV but block the respective organ at risk. In principle, forward planning techniques can then be applied to obtain the weights of the individual segments. However, it is of course much more effective to employ inverse planning methods to optimize the weights of the segments according to given dose constraints for PTV and organs at risk as in standard inverse treatment planning. Several optimization algorithms were used in this context, e.g. Cimmino's algorithm [57] or mixed-integer programming [58]. The latter has the advantage that dose-volume-constraints can easily be integrated. In both cases, treatment plans that were comparable to conventional beamlet-based IMRT plans could be generated with aperture-based optimization techniques.

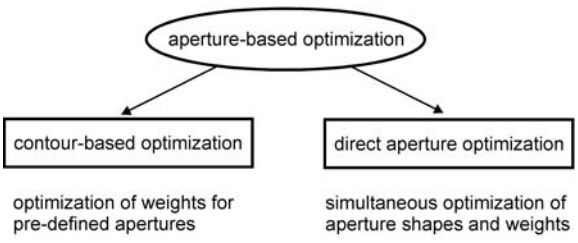

Fig. 6. Aperture-based optimization techniques can be divided in two groups: "contour-based optimization" and "direct aperture optimization"

De Neve et al. [55] and De Gersem et al. [56] pursued a somewhat different approach to define the aperture shapes. Their "anatomy-based segmentation tool" (ABST) does not only use the projections of PTV and organs at risk in the beam's-eye-view, but it additionally takes into account the distance to the nearest OAR in the BEV projection. Instead of one single segment that conforms to the PTV "minus" the OAR, it is subdivided into a series of smaller segments that allow boosting those regions of the PTV that are close to the OAR, since these region are often underdosed if only one segment blocking the OAR is used.

Isodose-based definition of apertures was described by the group at the William Beaumont Hospital in Royal Oak [60] for tangential breast irradiation. They first calculated 3D dose distributions for open tangential fields, and used the projections of the 3D isodoses in the beam's-eye-view to define additional segments that conform to certain isodose levels (from 100% to 120% in steps of 5%). These new segments as well as the open fields and two segments that blocked the lung were then fed into an optimization engine to obtain the respective weighting factors. By choosing only the segments with the highest values for the weighting factor, they ended up with typically six to eight segments for the total treatment plan. They showed that this approach is an efficient and effective method to improve the dose distribution compared to conventional wedged fields.

An important advantage of contour-based aperture definition is that the optimization itself can be based on very accurate dose calculations: since the aperture shapes are defined before the optimization, effects like head scatter or leaf transmission/leakage can easily be accounted for, which is much more difficult in beamlet-based optimization. Another advantage is that the leaf positions are not restricted to the resolution of the beamlet grid (which is often 1 cm in the direction of leaf travel). This means that the dose gradient between PTV and OAR might be placed more accurately at the desired position.

Direct Aperture Optimization

The name of direct aperture optimization (DAO) was proposed at the University of Maryland in Baltimore [39] for a technique developed by De Gersem [59] and originally called leaf-position optimization. Its main feature is that the weights and shapes of apertures are opti-

mized simultaneously, thereby adding more degrees of freedom to the aperture-based planning approach. The aperture definition step before the optimization (as described above for the contour-based techniques) is of course not needed here. Instead, the user specifies the number of beams, their directions of incidence and the number of apertures n per beam. This means that the planner can increase the complexity of the plan by increasing n from one (which would yield a 3D conformal plan) to any desired degree of modulation, since n apertures can yield up to $2^n - 1$ intensity levels [39]. The optimization algorithm then varies the weights of the apertures as well as the leaf positions on a predefined grid, e.g., in steps of 5 mm. Any MLC constraints as well as further restrictions like a minimum aperture size or a minimum number of monitor units per aperture can be accounted for. Since the optimization of the aperture shapes is a mathematically difficult, nonconvex problem, stochastic algorithms like simulated annealing were used for this purpose. This provides the additional advantage of complete freedom in the choice of the objective function, i.e., biological objectives can be integrated easily. The resulting plan is ready for delivery, and no further sequencing steps are necessary. In particular, the continuous weights (i.e., intensity levels) of the segments do not have to be discretized as in beamlet-based planning.

Shepard et al. [39, 54] found a significant reduction of the total number of segments and the total number of monitor units when comparing DAO plans to standard IMRT plans. In many cases, not more than five apertures per beam are needed for highly conformal IMRT plans. They concluded that direct aperture optimization is a very efficient technique that maintains the dosimetric advantages of IMRT while reducing the complexity of the treatment plan.

Direct aperture optimization was also applied to intensity modulated arc therapy (IMAT) [54, 61]. It can account for all delivery constraints in the optimization, and no additional sequencing step is required, which makes it a robust tool to create treatment plans for IMAT.

References

1. Bortfeld T (1999) Optimized planning using physical objectives and constraints. Semin Radiat Oncol 9:20–34
2. Bortfeld T (2003) Physical optimization. In: Palta JR, Mackie TR (eds), Intensity modulated radiation therapy – the state of the art, Medical Physics Monograph No. 29, pp 51–75
3. Webb S (2001) Intensity modulated radiation therapy. Bristol (IOP) Publishing
4. Webb S (2003) The physical basis of IMRT and inverse planning. Br J Radiol 76:678–689
5. Romeijn HE, Dempsey JF, Li JG (2004) A unifying framework for multi-criteria fluence map optimization models. Phys Med Biol 49:1991–2013
6. Lahanas M, Schreibmann E, Baltas D (2003) Multiobjective inverse planning for intensity modulated radiotherapy with constraint-free gradient-based optimization algorithms. Phys Med Biol 48:2843–2871
7. Küfer KH, Hammacher HW, Bortfeld T (2000) A multicriteria optimization approach for inverse radiotherapy planning. In: Schlegel W, Bortfeld T (eds), XIII International Conference on the Use of Computers in Radiation Therapy. (XIII ICCR). Springer, Berlin Heidelberg New York
8. Ling CC, Humm J, Larson S, Amols H, Fuks Z, Leibel S, Koutcher JA (2000) Towards multidimensional radiotherapy (MD-CRT): biological imaging andbiological conformality. Int J Radiat Oncol Biol Phys 47:551–560
9. Niemierko A (1997) Reporting and analyzing dose distributions: a concept of equivalent uniform dose. Med Phys 24:103–110
10. Thieke C (2003) Multicriteria optimization in inverse radiotherapy planning. University of Heidelberg
11. Brahme A, Roos JE, Lax I (1982) Solution of an integral equation encountered in rotation therapy, Phys Med Biol 7:1221–1229
12. Fraass BA, Kessler ML, McShan DL, Marsh LH, Watson BA, Dusseau WJ, Eisbruch A, Sandler HM, Lichter AS (1999) Optimization and clinical use of multisegment intensity-modulated radiation therapy for high-dose conformal therapy. Semin Radiat Oncol 9:60–77
13. Oelfke U, Bortfeld T (2001) Inverse planning for photon and proton beams. Med Dosim Summer 26:113–124
14. Kubo HD, Wilder RB, Pappas CT (1999) Impact of collimator leaf width on stereotactic radiosurgery and 3D conformal radiotherapy treatment plans. Int J Radiat Oncol Biol Phys 44:937–945
15. Siebers JV, Lauterbach M, Keall PJ, Mohan R (2002) Incorporating multi-leaf collimator leaf sequencing into iterative IMRT optimization. Med Phys 29:952–959
16. Alber M, Nüsslin F (2001) Optimization of intensity modulated radiotherapy under constraints for static and dynamic MLC delivery. Phys Med Biol 46:3229–3239
17. Litzenberg DW, Moran JM, Fraass BA (2002) Incorporation of realistic delivery limitations into dynamic MLC treatment delivery. Med Phys 29:810–820
18. Langer M, Brown R, Urie M, Leong J, Stracher M, Shapiro J (1990) Large scale optimization of beam weights under dose-volume restrictions. Int J Radiat Oncol Biol Phys 18:887–893
19. Bortfeld T, Stein J, Preiser K (1997) Clinically relevant intensity modulation optimization using physical criteria. In: Leavitt DD, Starkschall G (eds) XII International Conference on the Use of Computers in Radiation Therapy (XII ICCR), Salt Lake City, USA. Medical Physics Publishing, Madison, WI, pp 1–4
20. Spirou SV, Chui CS (1998) A gradient inverse planning algorithm with dose-volume constraints. Med Phys 25:321–333
21. Deasy JO (1997) Multiple local minima in radiotherapy optimization problems with dose-volume constraints. Med Phys 24:1157–1161
22. Llacer J, Deasy JO, Bortfeld TR, Solberg TD, Promberger C (2003) Absence of multiple local minima effects in intensity modulated optimization with dose-volume constraints. Phys Med Biol 48:183–210
23. Wu Q, Mohan R (2002) Multiple local minima in IMRT optimization based on dose-volume criteria. Med Phys 29:1514–1527
24. Cotrutz C, Xing L (2003) IMRT dose shaping with regionally variable penalty scheme. Med Phys 30:544–551

25. Alber M, Meedt G, Nüsslin F, Reemtsen R (2002) On the degeneracy of the IMRT optimization problem. Med Phys 29:2584–2589
26. Llacer J, Agazaryan N, Solberg TD, Promberger C (2004) Degeneracy, frequency response and filtering in IMRT optimization. Phys Med Biol 49:2853–2880
27. Webb S, Convery DJ, Evans PM (1998) Inverse planning with constraints to generate smoothed intensity-modulated beams. Phys Med Biol 43:2785–2794
28. Alber M, Nüsslin F (2000) Intensity modulated photon beams subject to a minimal surface smoothing constraint. Phys Med Biol 45:N49–52
29. Keller-Reichenbecher MA, Bortfeld T, Levegrun S, Stein J, Preiser K, Schlegel W (1999) Intensity modulation with the "step and shoot" technique using a commercial MLC: a planning study. Multileaf collimator. Int J Radiat Oncol Biol Phys 45:1315–1324
30. Holmes T, Mackie TR (1994) A comparison of three inverse treatment planning algorithms. Phys Med Biol 39: 91–106
31. Censor Y (2003) Mathematical optimization for the inverse problem of intensity modulated radiation therapy. In: Palta JR, Mackie TR (eds) Intensity-modulated radiation therapy: the state of the art. American Association of Physicists in Medicine. Medical Physics Publishing, Madison, pp 25–49
32. Press WH, Flannery BP, Teukolsky SA, Vetterling WT (1992) Numerical recipes in C: the art of scientific computing. Cambridge University Press, Cambridge
33. Zhang X, Liu H, Wang X, Dong L, Wu Q, Mohan R (2004) Speed and convergence properties of gradient algorithms for optimization of IMRT. Med Phys 31:1141–1152
34. Webb S (1989) Optimisation of conformal radiotherapy dose distributions by simulated annealing. Phys Med Biol 34:1349–1370
35. Webb S (1997) The physics of conformal radiotherapy: advances in technology. Institute of Physics Publishing, Bristol Philadelphia
36. Kirkpatrick CD, Gelatt CD, Vecchi MP (1983) Optimization by simulated annealing. Science 220:671–680
37. Geman S, Geman D (1984) Stochastic relaxation, Gibbs distribution and the Bayesian restoration in images. IEEE Trans Patt Anal Mac Int 6:721–741
38. Carol MP, Nash RV, Campbell RC, Huber R, Sternick E (1997) The development of a clinically intuitive approach to inverse treatment planning: partial volume prescription and area cost function. In: Leavitt DD, Starkschall G (eds) Proceedings of the XIIth International Conference on the Use of Computers in Radiation Therapy. Medical Physics Publishing, Madison, pp 317–319
39. Shepard DM, Earl MA, Li XA, Naqvi S, Yu C (2002) Direct aperture optimization: a turnkey solution for step-and-shoot IMRT. Med Phys 29:1007–1018
40. Szu H, Hartley R (1987) Fast simulated annealing. Phys Lett A 122:157–162
41. Cotrutz C, Xing L (2003) Segment-based dose optimization using a genetic algorithm. Phys Med Biol 48:2987–2998
42. Li Y, Yao J, Yao D (2003) Genetic algorithm based deliverable segments optimization for static intensity-modulated radiotherapy. Phys Med Biol 48:3353–3374
43. Shepard DM, Ferris MC, Olivera GH, Mackie TR (1999) Optimizing the delivery of radiation therapy to cancer patients. SIAM Rev 41:721–744
44. Sternick ES, Bleier AR, Carol MP, Curran BH, Holmes TW, Kania AA, Lalonde R, Larson LS (1997) Intensity modulated radiation therapy: what photon energy is best? In: Leavitt DD, Starkschall G (eds) Proceedings of the XIIth International Conference on the Use of Computers in Radiation Therapy. Medical Physics Publishing, Madison, pp 418–419
45. Bortfeld T, Schlegel W (1993) Optimization of beam orientations in radiation therapy: some theoretical considerations. Phys Med Biol 38:291–304
46. Stein J, Mohan R, Wang XH, Bortfeld T, Wu Q, Preiser K, Ling CC, Schlegel W (1997) Number and orientations of beams in intensity-modulated radiation treatments. Med Phys 24: 149–160
47. Pugachev A, Li JG, Boyer AL, Hancock SL, Le QT, Donaldson SS, Xing L (2001) Role of beam orientation optimization in intensity-modulated radiation therapy. Int J Radiat Oncol Biol Phys 50:551–560
48. Söderström S, Brahme A (1995) Which is the most suitable number of photon beam portals in coplanar radiation therapy? Int J Radiat Oncol Biol Phys 33:151–159
49. Das S, Cullip T, Tracton G, Chang S, Marks L, Anscher M, Rosenman J (2003) Beam orientation selection for intensity-modulated radiation therapy based on target equivalent uniform dose maximization. Int J Radiat Oncol Biol Phys 55:215–224
50. Rowbottom CG, Nutting CM, Webb S (2001) Beam-orientation optimization of intensity-modulated radiotherapy: clinical application to parotid gland tumours. Radiother Oncol 59:169–177
51. Hou Q, Wang J, Chen Y, Galvin JM (2003) Beam orientation optimization for IMRT by a hybrid method of the genetic algorithm and the simulated dynamics. Med Phys 30:2360–2367
52. Webb S (1995) The problem of isotropically orienting N converging vectors in space with application to radiotherapy planning. Phys Med Biol 40:945–954
53. Pugachev A, Xing L (2001) Pseudo beam's-eye-view as applied to beam orientation selection in intensity-modulated radiation therapy. Int J Radiat Oncol Biol Phys 51:1361–1370
54. Shepard DM, Earl MA, Yu CX, Xiao Y (2003) Aperture-based inverse planning. In: Palta JR, Mackie TR (eds) Intensity-modulated radiation therapy: the state of the art. Medical Physics Publishing, Madison, pp 115–137
55. De Neve W, De Wagter C, De Jaeger K, Thienpont M, Colle C, Derycke S, Schelfhout J (1996) Planning and delivering high doses to targets surrounding the spinal cord at the lower neck and upper mediastinal levels: static beam-segmentation technique executed with a multileaf collimator. Radiother Oncol 40:271–279
56. De Gersem W, Claus F, De Wagter C, De Neve W (2001) An anatomy-based beam segmentation tool for intensity-modulated radiation therapy and its application to head-and-neck cancer. Int J Radiat Oncol Biol Phys 51:849–859
57. Xiao Y, Galvin J, Hossain M, Valicenti R (2000) An optimized forward-planning technique for intensity modulated radiation therapy. Med Phys 27:2093–2099
58. Bednarz G, Michalski D, Houser C, Huq MS, Xiao Y, Anne PR, Galvin JM (2002) The use of mixed-integer programming for inverse treatment planning with pre-defined field segments. Phys Med Biol 47:2235–2245
59. De Gersem W, Claus F, de Wagter C, Van Duyse B, De Neve W (2001) Leaf position optimization for step-and-shoot IMRT Int J Radiat Oncol Biol Phys 51:1371–1388
60. Kestin LL, Sharpe MB, Frazier RC, Vicini FA, Yan D, Matter RC, Martinez AA, Wong JW (2000) Intensity modulation to improve dose uniformity with tangential breast radiother-

apy:initial clinical experience. Int J Radiat Oncol Biol Phys 48:1559–1568
61. Earl MA, Shepard DM, Naqvi S, Li XA, Yu CX (2003) Inverse planning for intensity-modulated arc therapy using direct aperture optimization. Phys Med Biol 48:1075–1089
62. Fiveash JB, Murshed H, Duan J, Hyatt M, Caranto J, Bonner JA, Popple RA (2002) Effect of multileaf collimator leaf width on physical dose distributions in the treatment of CNS and head and neck neoplasms with intensity modulated radiation therapy. Med Phys 29:1116–1119
63. Bortfeld T, Oelfke U, Nill S (2000) What is the optimum leaf width of a multileaf collimator? Med Phys 27:2494–2502
64. Goldberg DE (1989) Genetic algorithms in search, optimization and machine learning. Addison-Wesley
65. Falkenauer E (1998) Genetic algorithms and grouping problems. Wiley, New York

Practical IMRT Planning

Wilfried De Neve, Yan Wu, Gary Ezzell

5

Contents

5.1 Introduction

Introduction of IMRT in clinical practice remains a challenge. The delivery of IMRT is usually of lesser concern, as reliable MLC-equipped linear accelerators that allow IMRT delivery in step & shoot or dynamic mode are available. Other parts in the chain of IMRT procedures remain to be improved, especially planning and quality assurance. This chapter focuses on pitfalls in planning. Ideally, the IMRT planning system creates a desired dose distribution as a sequence of treatment machine-states and monitor unit values (often called control point sequence). In reality, the present IMRT planning systems are not yet capable of achieving this goal autonomously. The systems are interactive and

many machine parameters have to be set upfront by a skilled planner. Also, the desired dose distribution may be impossible to achieve and the systems then need expert guidance to achieve an *acceptable dose distribution* as a realistic goal. We define as acceptable a dose distribution that differs from the desired dose distribution 1) within preset limits of dose and 2) only in regions where the desired dose distribution cannot be physically achieved.

It is considered good practice to define key elements of the desired dose distribution in writing as dose prescription guidelines of a protocol. For IMRT planning, the dose prescription guidelines often need to be complemented by additional parameters to obtain acceptable dose distributions. The definition of such parameters as dose-to-volume prescriptions is the subject of this chapter. Other chapters deal with other forms of prescription including EUD, TCP, NTCP and P+.

This chapter offers guidelines and techniques to avoid most of the pitfalls encountered in IMRT planning. Not all commercial IMRT planning systems have all the tools to implement the proposed techniques and the reader who tries to follow the guidelines may get stuck. A discussion with the vendors regarding possible upgrades or even the purchase of a new planning system may be the only way out. We have added an appendix to this chapter, structured as a series of questions and answers, which deals with properties and defaults of commercial planning systems. These questions and answers may be useful as back-up information for a discussion with vendors or for comparative evaluation of different IMRT planning systems.

5.2 The Desired Dose Distribution in Clinical Guidelines and Protocols

5.2.1 Dose Prescription

The desired dose distribution for IMRT is often described in guidelines that are part of a clinical protocol. These guidelines typically describe the desired dose to contoured volumes that represent the tumor (CTV), and set dose constraints to contoured structures that represent normal tissues. The PTV is a construct which helps us to ensure that the desired dose can be anatomically achieved in the CTV. A construct, similar to PTV was proposed by ICRU (ICRU Report 62) for Organ(s)-At-Risk (OAR(s)), namely the Planning Risk Volume (PRV). The use of a margin around an OAR to define a PRV is somewhat controversial. Toxicity to OARs with serial functional unit (FU) architecture is correlated with the maximum dose. The use of a maximum dose constraint to the PRV rather than to the unexpanded OAR will lower the risk of exceeding the maximum dose constraint by motion of the OAR into nearby dose gradients. The value of adding a margin to an OAR with parallel FU architecture is not obvious and the subject of research. We recommend using a positive margin to create the PRV for an OAR with serial FU architecture. No recommendations can be given for an OAR with parallel FU architecture. Further, we will use the term PRV in the context of IMRT planning irrespective of the size of the margin applied to the OAR and we will use the term *dose prescription* for the definition of desired doses as well as for the application of dose constraints.

5.2.2 Dose Provisional Prescription

The authors of clinical guidelines formulate a dose prescription for a group of patients from whom the selection criteria are specified. They cannot foresee all aspects of anatomy and biology of the individual patient who will be treated according to the guidelines. In practice, the dose prescription in a clinical protocol may be irrelevant, physically impossible to achieve or internally conflicting in some regions of the planning image set. For example, by implementing a margin around the CTV, part of the PTV may extend outside the patient contour. The part of the PTV outside the patient is important to define beam aperture and intensity but dose prescription to the ambient air is *irrelevant*. Present optimization engines are not capable of solving this problem. Tricks are needed to secure intensity in the air region of the PTV. When the PTV extends close to a PRV, the dose prescription may be *impossible* to achieve if the difference between the minimum and maximum dose requirements to PTV and PRV respectively would imply a dose gradient of such steepness that it cannot be physically achieved. Dose prescriptions may be *conflicting* in regions of overlap between PTV and PRV. Mainly for these reasons, the dose prescription in clinical protocols is a tentative or provisional prescription (Fig. 1) and therefore we will further use the term *dose provisional prescription*.

5.2.3 Dose Values to Contoured Volumes in the Dose (Provisional) Prescription

Analysis of treatment outcome as a function of dose and dose distribution provides us with dose-to-volume indices on local control and organ toxicity that can be used for the dose provisional prescription. Using dose-volume indices that result from scientific evidence may be the best strategy to improve the accuracy of the dose prescription (i.e., to guarantee that the dose-volume indices are suitable to obtain the clinical goals). Using the ICRU (ICRU Report 50 and 62) recommendations as

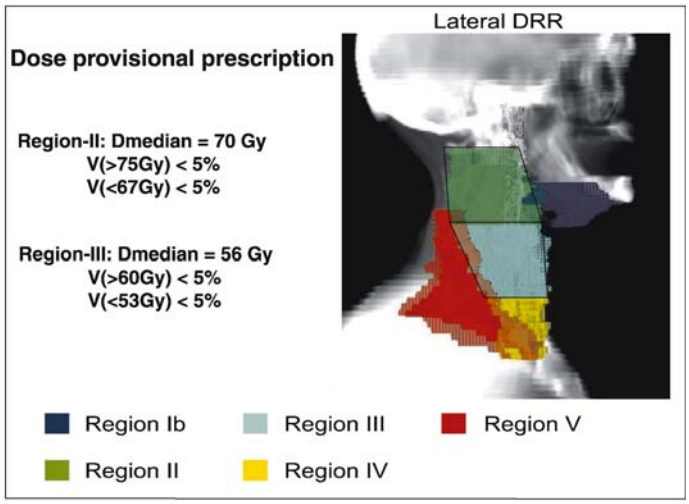

Fig. 1. Dose provisional prescription. Example of a dose provisional prescription to the CTVs of cervical lymph node regions II and III at the right side of the neck. The objective for region II is to achieve a median dose of 70 Gy (Dmedian = 70 Gy) with less than 5% of the volume receiving more than 75 Gy ($V(> 75\,\text{Gy}) < 5\%$) and with less than 5% of the volume receiving less than 67 Gy ($V(< 67\,\text{Gy}) < 5\%$). For region III, a median dose of 56 Gy with ($V(> 60\,\text{Gy}) < 5\%$) and ($V(< 53\,\text{Gy}) < 5\%$) is the objective

paradigm, the *dose provisional prescription* for the PTV should consist of a desired physical dose (D) at a specification point complemented by an acceptable dose range ($D-5\%$ as minimum to $D+7\%$ as maximum). Due to intentionally inhomogeneous dose distributions or when the location of the isocenter is outside the PTV (for example when irradiating a concave PTV), the definition of a suitable geometrical location for one or more specification point(s) is less trivial in IMRT than in conventional radiation therapy. Therefore, D is often prescribed to a dose index of central tendency (Dmedian, the median or Dmean, the mean dose) or to a reference isodose surface (for example D95, the isodose surface which covers 95% of the volume) in the PTV and not to a geometrical dose specification point [1–4]. In either case, an index of the acceptable dose range should be added, preferentially, the minimum and the maximum dose. In a contoured volume, planning systems may calculate the minimum and maximum doses very differently for different voxel sizes or for different numbers of dose points seeded in the volume. Surrogates for the minimum or maximum dose as respectively D98 or D2, the dose levels on the dose-volume histogram (DVH) below or above which lays 2% of the contoured volume, are preferred because they are more stable estimates of the extremes [5].

We could argue over selection of a reference isodose like D98 or D95 for prescribing dose to gross tumor and Dmedian for prescribing dose to subclinical disease. The radiobiological rationale is that the dose-local control probability curve for gross tumor is threshold-sigmoid for gross tumor while it is hypothetically linear with dose for subclinical disease [6]. Considering the shape of the dose-response curves, lowering the minimum dose to the PTV of gross tumor would be much less desirable than to PTV of subclinical disease. If trade-off has to be made during optimization, which involves lowering the minimum dose to the PTV, D98 or D95 will be affected earlier than Dmedian.

For PRV with serial functional unit architecture, the maximum dose correlates with toxicity and therefore a maximum-dose constraint like D2 is a logical choice for the *dose provisional prescription*. For PRV with parallel functional unit architecture, the minimum percentage of the volume below a threshold dose, the maximum percentage of the volume above a threshold dose or the mean dose is often used for the *dose provisional prescription* since these parameters correlate with toxicity.

The use of multiple dose indices for each contoured structure enhances the precision of dose prescription and is preferred over a single index.

5.3 From Dose Provisional Prescription to Planning Dose Objectives

The analysis of treatment outcome as a function of dose and dose distribution provides us with suitable parameters for the *dose provisional prescription* as well as for assigning dose objectives to contoured volumes in IMRT planning. Commercial IMRT planning systems allow specifying *planning dose objectives* as single dose values, as multiple dose-to-volume values or as a whole DVH. For many OARs, multiple dose-to-volume values have been derived from clinical data and it can be recommended to use these as *planning dose objectives* rather than a single value. For example, in radiotherapy of prostate cancer, a combination of dose-volume (or dose-area) constraints for the rectum (no more than 50% of the volume should exceed 65 Gy AND no more than 30% should exceed 70 Gy AND no more than 5% should exceed 75 Gy [7]) to avoid late rectal bleeding has been derived from clinical observations. If the planner would set a single dose objective, for example no more than 5% should exceed 75 Gy, the planning system may be too loosely guided towards

a desired dose distribution. In this example, a plan in which 100% of the rectum receives 70 Gy would fulfill the planning dose objective but may be clinically unacceptable. When using *planning dose objectives*, the planner should avoid setting objectives that are irrelevant to pursue or impossible to achieve, as these may not guide optimization in a good direction. The section on "build-up and in-air PTV regions" describes how to remove irrelevant and impossible dose objectives. In this chapter, the section "Overlap volumes and dealing with conflicting dose objectives" has a title, which is self-evident. Finally the problem of "dose littering" is addressed.

5.3.1 Build-up and In-air PTV Regions

By invasion of tumor in the skin or by applying a margin, the PTV may reach close to or even outside the patient's skin outline. An example is the PTV associated with the neck nodal regions II–VI that are located beneath the skin. The superficial part of the PTV may extend in the buildup region of incoming photon beams or even in the surrounding air. Most dose computation algorithms cannot accurately compute dose in buildup regions, which will lead to convergence errors when such algorithms are used in optimization [8]. Optimizing the physical dose in air is irrelevant but the part of the PTV outside the skin contour is not irrelevant, as it should secure sufficient coverage of surrounding air to prevent CTV from reaching outside the beam edge by deformation, movements or setup error. In tangential breast irradiation, the region of the beam that bypasses the skin surface is called the *flash* region [9]. We will use the term *flash* also for other anatomical sites in which extension of the PTV outside the skin surface imposes the creation of fluence outside the skin.

In inverse plan optimization, at least three problems must be considered regarding build-up and in-air PTV regions. First, it is usually physically impossible to achieve the minimum prescription dose to the regions of the PTV close to or outside the patient's outline, respectively in buildup areas or in air. Second, the optimization algorithm might attempt to increase the dose in these PTV regions by creating intensity peaks in beams with suitable directions. This often leads to unacceptable inhomogeneous PTV dose distributions or hot dose spots elsewhere. Third, removing the part of the PTV in air or bounding the PTV expansion by the skin contour (for which some planning systems have automated algorithms) avoids irrelevant optimizing of dose in air but is not an advisable solution since *flash* will not be created during optimization. No turnkey solution exists for IMRT planning of dose in buildup regions or for securing *flash*. Procedures involving PTV-fragmentation, relaxing the dose objectives and creation of flash are described in the following sections.

PTV-fragmentation and Relaxing the Dose Objectives

If under-dosage of the CTV nearby the skin is unacceptable, apply bolus. If under-dosage in the buildup region is acceptable, two different planning strategies types could be followed. One method is based on fragmentation of the PTV while in the other method the acceptable range of the PTV prescription dose is relaxed. In the fragmentation method, the PTV is divided in two or more sub-volumes so that the region as well as degree of acceptable underdosage can be described. The part of the PTV that is closer than 4–6 mm to the skin or bolus surface is defined as a sub-volume separate from the remaining part of the PTV. To each sub-volume the wanted dose and the acceptable and physically achievable dose range are set as planning dose objectives. Relaxing the acceptable range of the dose provisional prescription to the whole PTV, as only measure, has the drawback of lacking spatial control regarding the underdosed region.

Flash

PTV fragmentation and relaxed planning dose objectives aim at allowing an under-dosage of a controlled volume inside the PTV where buildup occurs but does not solve the problem of *flash*. In published studies on IMRT for breast irradiation, beam apertures and intensities for treating *flash regions* were manually defined or solutions in research-based systems were proposed [9–11].

Inverse planning was used in the study of Hong. After optimization, the intensity profiles were extended in the anterior direction 2 cm beyond the skin surface to provide adequate margin for patient breathing and set-up uncertainty [11].

In the segmental IMRT technique described by Kestin, the superficial edge of the beam aperture allowed 2 cm of flash beyond the breast [10]. Based on dose computation using the full beam aperture, smaller segments were conformed to avoid the BEV projection of the high isodose surfaces at dose-increments of 5%.

Evans proposed two methods to set the intensities in the flash region [9]. Method 1 involved setting the intensities to the lowest value required inside the breast, which is often a point in the breast periphery close to the flash region. The flash region of the beam aperture is unmodulated. Method 2 involved extrapolation of intensity values from the breast periphery in the ventral direction (similar to Hong's method [11]). The flash region is modulated if the beam region projected to the breast periphery is modulated.

These procedures to secure flash share the drawback that optimized intensity patterns are restricted to regions of the beam outside the flash region. A solution to optimize the flash region was proposed by Löf and considers the stochastic process of patient positioning in fractionated radiotherapy [12]. It has been implemented in UM-Plan as MIGA optimization (MIGA:

Multiple Instances of Geometry Approximation). The MIGA method simulates the expected distribution of patient geometries (location, anatomy, positioning), and then optimizes a single IMRT plan using a weighted sum of the behavior over all the simulated geometry instances (McShan at the XIVth ICCR, May 10–13, 2004, Seoul, Korea). The method uses a probability distribution of position and shape of CTVs and OARs for plan optimization, making the PTV and PRV constructs obsolete.

5.3.2 Overlap Volumes and Dealing with Conflictual Dose Objectives

Margins may result in overlap volumes between different PTVs, between PTV and PRV and between different PRVs. Each overlap leads to a volume, which is shared by two or more contoured volumes. A conflict of the dose provisional prescription may occur in the overlapping volume if the acceptable doses of the contoured volumes lack a common dose range. To secure that the conflict does not exist in the planning dose objectives at least two different methods can be applied. One method is based on fragmentation of the contoured volumes. Dose objectives are set for the fragments, some of which contain the overlap volumes while others contain non-overlapping volumes. In the other method the dose objective is a relaxation of acceptable range of the prescription dose. Both methods aim at the same result being a controlled under-dosage of a volume inside the PTV, a controlled over-dosage of a volume inside the PRV or both. Both methods may be used simultaneously in the same planning case. Both methods require priority ranking, which is a clinical decision and should, ideally, be specified in the clinical protocol.

Overlap Between PTVs

In head and neck cancer, two or more adjacent or overlapping PTVs with different dose prescriptions are common. The CTV of lymph node regions I to VI share borders. Let us take the example of the border between the CTV of lymph node regions II (CTV-II) and III (CTV-III) in Fig. 2. By applying a margin to the CTV of both regions to obtain PTV-II and PTV-III, a region of overlap between both PTV occurs. If the minimum of the dose provisional prescription of one PTV is higher than the maximum of the dose provisional prescription of the other PTV a conflict of prescription occurs in the overlap area.

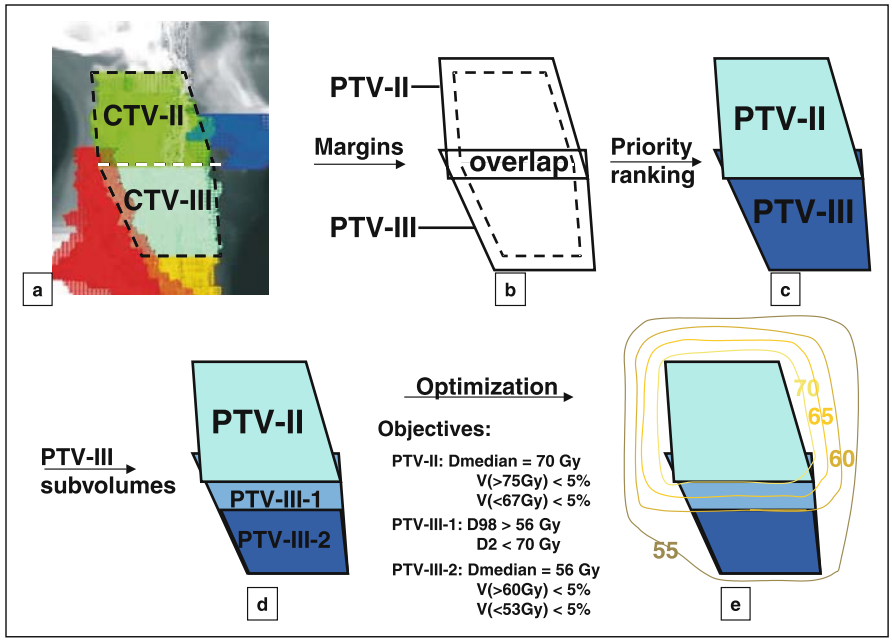

Fig. 2a–e. Overlap volumes and priority ranking: **(a)** dose provisional prescription to the CTV-II and CTV-III as shown in Fig. 1; **(b)** PTV-II and PTV-III are constructed to help securing that the dose objectives to CTV-II and CTV-III can be met. CTV-II and CTV-III share a common border. By adding margins, PTV-II and PTV-III overlap. The overlap volume is such that the dose provisional prescription to CTV-II and CTV-III would be conflictual for PTV-II and PTV-III. Priority ranking is required; **(c)** priority is assigned the dose provisional prescription of CTV-II that is planned to the entire PTV-II. The overlap volume is removed from PTV-III. In the reduced PTV-III, the physical limitations of dose gradient steepness make it impossible to achieve the dose provisional prescription of CTV-II. Possible solutions to secure that the dose gradient between PTV-II and PTV-III is forced outside PTV-II include: 1. Assigning a much higher importance weight to PTV-II than to PTV-III at optimization; 2. Relaxing the maximum dose objective for PTV-III; 3. Fragmentation of the PTV-III volume (panel d) and relaxing the maximum dose objective for a subvolume of PTV-III or a combination of 1–3; **(d)** fragmentation of PTV-III to create a subvolume for relaxing the maximum dose constraint; **(e)** unambiguous dose objectives for plan optimization

To obtain clean planning dose objectives, a possible solution involves priority ranking of the PTVs and allowing a gradient zone in one or both PTV(s). For the example in Fig. 2, protocols at Ghent University Hospital rank priority to the PTV with the highest prescription dose, in this case region II. As a result, the overlap volume of PTV-III on PTV-II is discarded while the overlap volume of PTV-II on PTV-III receives a planning dose objective similar to PTV-II. The conflict of prescription is removed from the planning dose objectives but they remain impossible to achieve because the planning dose objective would imply an infinitely steep dose gradient at the border between PTV-II and PTV-III. The planning dose objectives can be made possible by fragmentation of one or both of the PTV. In Fig. 2, the aim was to place the gradient inside PTV-III since priority is given to the PTV with the highest prescription dose. The planning dose objectives to the gradient volume (PTV-III-1) are such that a common dose range exists with both PTV-II and PTV-III.

The procedure used at Virginia Commonwealth University is slightly different. In the optimization system, all the regions-of-interest (ROIs) are classified into three types, TARGET, OAR and OVERLAP. In terms of priorities, the setting on the optimization system is OVERLAP-OAR-TARGET in descending order. With everything else being equal, when it comes to ray-weight adjustments in the optimization process, if a ray passes through both an OAR and target(s), the ray-weight will not be increased if the dose to the OAR has reached its limit regardless of effect to the targets. In other words, the OARs have higher priorities. If you do want the overlapping regions to be treated, just assign the type of the region to be OVERLAP, which is of the highest priority – the dose or dose-volume constraints prescribed to it will be met first. The optimization will almost always find a more sensible solution when the overlapping regions are dissected or singled out with its dose objectives clearly given, compared with that of a conflicting prescription and letting the optimization make the choice based purely on the scores.

Overlap Between PTV and PRV

Dealing with overlap between PTV and PRV follows similar procedures. An example is the PTV of paranasal sinus cancer that may intersect the PRV of the optic nerves (PRV-ON) that we assume to be structures of serial functional unit architecture. Avoidance of optic nerve toxicity is imperative in the protocol implemented at Ghent University Hospital [4] and therefore the maximal dose to the volume of intersection must be lower than the maximum tolerated dose (MTD) of the optic nerves. If overlap occurs, the minimum acceptable PTV dose (66 Gy) exceeds the maximum dose constraint of 60 Gy to the optic nerves. A conflict exists in the dose provisional prescription. To obtain a feasible planning dose objective, the volume-fragmenting method is used, which involves the creation of PTV sub-volumes. The PTV prescription dose of 70 Gy (range 66 – 75 Gy) is retained as a planning dose objective to the sub-volume of the PTV from which all voxels are located at a distance of 3 mm or more from the PRV-ON. A distance of 3 mm is required to achieve a dose difference of 6 Gy between a maximum dose of 60 Gy in the PRV-ON and a minimum dose of 66 Gy in the non-overlapping sub-volume of the PTV. In the PTV, including the overlap with PRV-ON, a minimum dose of 60 Gy, equal to the maximum allowed dose to PRV-ON, can be set – theoretically – as dose objective. In practice, clinical experience showed that a minimum dose of 57 Gy could be achieved for the part of the PTV, which overlaps the PRV-ON, when the hard constraint of 60 Gy maximum dose to the PRV-ON is imposed. Thus, a possible planning dose objective for the minimum dose in the overlap volume between PTV and PRV-ON is 57 Gy. To plan the same case, the procedure at Virginia Commonwealth University would be slightly different. The shared volume between PTV and PRV-ON is of type OVERLAP that has the highest priority and receives a dose prescription with an acceptable range of 57 Gy to 60 Gy. Since OVERLAP has highest and OAR (to which to non-overlapping part of PRV-ON belongs) has second highest priority, the dose gradient imposed by the PTV dose prescription is forced outside the PRV-ON.

Overlap Between PRVs

In mutually overlapping PRV, the constraints of all PRV apply simultaneously. In practice, the dose constraints of a PRV of serial functional unit architecture limit the maximum dose in the overlap volume while integral dose to the overlap volume is limited by a PRV of parallel functional unit architecture.

5.3.3 Avoidance of Dose Littering Outside PTV and PRV/OAR

The region of the patient imaged for IMRT planning is composed of contoured volumes, representing tumor and non-tumor tissues. The contours of the PTVs are considered to contain all tumor cells of interest for the radiotherapy plan. Of the non-tumor tissue, one part is contoured as PRV while another part is not contoured. When dose objectives are imposed for PTVs and PRVs only, dose littering may occur in the volume of non-tumor tissue where a dose prescription is lacking. This happens because IMRT planning systems exploit many degrees of freedom to optimize a dose distribution according to the dose objectives. If the acceptable range of doses is undefined in certain regions of the virtual patient, these regions may be used by the system as a waste box for dose. Not surprisingly, high doses, even the dose maximum of the plan, may be found in these unde-

fined regions (Fig. 3a). Further, we will use the name Unspecified Imaged Volume (UIV) for part of the imaged volume outside the contours of PTVs and PRVs. Absence of dose prescription to UIV results in two types of problem, namely high-dose spots (Fig. 3a) and poor dose gradients outside the PTV (Fig. 3b). Four methods for constraining dose to UIV will be described in the next paragraphs: 1. The use at Washington University (WU) of the UIV [13]; 2. The use at Loyola University Chicago (LUC) of *virtual critical structures* at sites of expected hot spots [14]; 3. The use at VCU of a transitional zone immediately outside the PTV and a shell outside the transitional zone; 4. The use at GUH of all surrounding tissue of the PTV with stepwise centrifugal increase of severity regarding the dose maximum constraint [15].

Dose Objectives to the UIV

IMRT planning for cervical carcinoma with positive para-aortic lymph nodes involved setting prescription parameters for several PTVs and PRVs [13]. PRVs were created using a 0.4–2.0 cm margin around spinal cord, kidneys, colon, liver, small intestine and stomach. The UIV (tissues outside the PTVs and PRVs, called "tissue" or "patient" by the authors) received a maximum dose provisional prescription of 40 Gy, with a relatively low importance weight and the lowest overlap priority. This procedure has the advantage that the UIV does not need to be defined as a contoured structure. By giving the lowest overlap priority to the imaged volume of the patient, the constraints of PTVs and PRVs are secured in the overlap regions but a maximum dose constraint remains in the UIV region. A drawback of the procedure is related to the large size of the UIV that must be controlled by a threshold of dose. The method is not efficient to improve conformality of intermediate dose levels since a dose slightly inferior to the threshold could be spilled throughout the UIV.

Virtual Critical Structures or Pseudo-OARs

A *virtual critical structure* or *pseudo-OAR* is an arbitrary region of interest where you don't want the dose to be dumped to. In practice, the planner or a software tool generates the contours of the *virtual critical structure* or *pseudo-OAR* to which planning dose constraint are imposed. The main purpose is the prevention of hot dose spots in well-defined places. Drawbacks of the method are protection of only user-selected UIV parts against dose littering and tumor-site specificity.

Shell Outside PTV Complemented with Pseudo-OARs

A couple of regions of interest as shown in Fig. 4c are created. The first is a region of interest, the so-called transitional zone(s) (TZs) and the second is termed as normal tissue (NT). The TZ is a shell around the PTV with a user-defined thickness (often 0.5 ~ 1.0 cm). There are no dose (or dose volume) constraints specified in the TZs, and the purpose of having such a buffer region is to allow the dose to fall off gracefully (hopefully) while insuring the coverage of prescribed dose to the targets. We could have intuitively defined the whole body excluding the target volume(s) and the TZ(s) as normal tissue, which would have been a rather big volume most of the time. The main problem with a structure of large volume in the subsequent optimization is that it is often not very efficient to control the possible dose spillage using such a structure as a small percentage of a big volume could still be too big without mentioning it is not easy to gauge the exact volume of the normal tissue included in the dose grid specified. So instead, the definition of the normal tissue (NT) is simply a shell structure around the

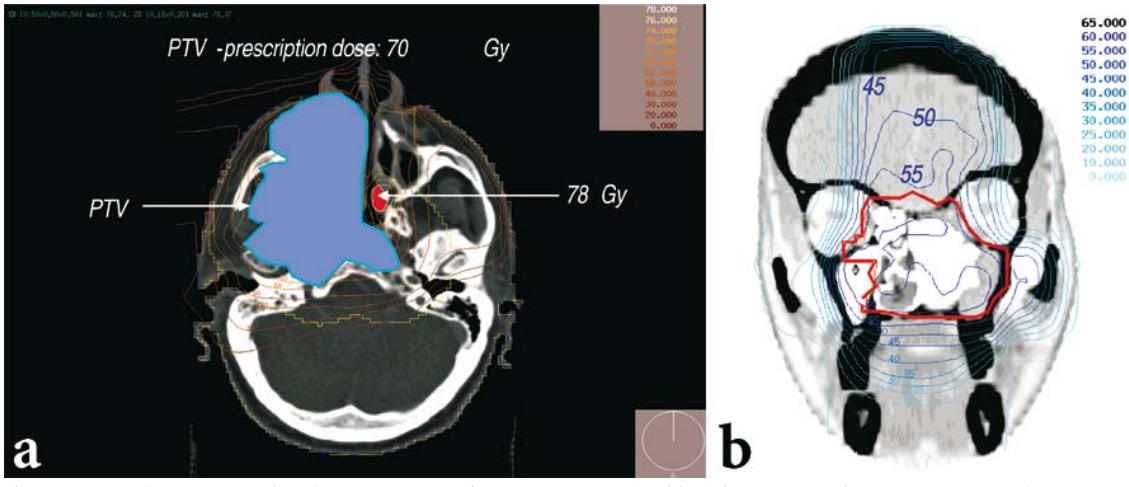

Fig. 3a,b. Dose littering: **(a)** plan dose maximum of 78 Gy outside the PTV in unconstrained region "mole in the backyard"; **(b)** large-volume dose littering cranially from the PTV (*red contour*) although respecting the 60 Gy maximum dose constraint of brain

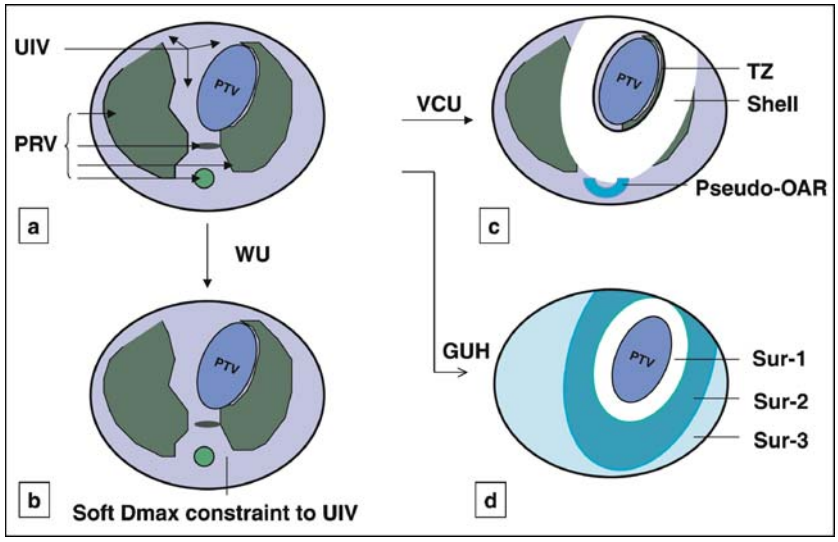

Fig. 4a–d. Methods to prevent dose littering: **(a)** volume containing a PTV, 4 PRV and the remaining of the imaged volume called UIV: Unspecified Imaged Volume; **(b)** method described by investigators from WU: Washington University. A soft Dmax (dose maximum) constraint is assigned the whole UIV; **(c)** method used at VCU: Virginia Commonwealth University. No constraints are imposed to a narrow TZ (transitional zone) immediately outside the PTV. Dose constraints are imposed to a shell surrounding the TZ. Inside the remaining UIV, one or more Pseudo-OAR(s) are constructed from which the location and shape is experience-based; **(d)** "Matroska" method described by investigators from GUH: Ghent University Hospital. Several shell structures inside each other (like Russian matroskas) leave no UIV. Outer shells have more severe dose maximum constraints than inner shells

TZs with a user-defined thickness (often 0. 5 ∼ 1.0 cm). The dose-volume constraint is typically set to be a no more than small percentage of volume (e.g., 5%) receiving 95% of the lowest prescribed dose of the PTVs. Obviously, the primary purpose of the NT is to ensure the dose conformality to the targets. The combination of the NT so constructed and pseudo-OARs to prevent dose littering often works well.

Stepwise Constraints with Distance from PTV (Matroska Method)

Soft maximum dose constraints are imposed to shell shaped volumes (called surroundings (Sur) in Fig. 4d) outside the PTV. Outer shells are created to enclose inner shells (like Russian matroskas) until no UIV is remaining. Outer shells have more severe dose maximum constraints than inner shells [16]. The method is very efficient to secure conformality and to avoid high dose spots outside the PTV. The drawback is that interesting dose distributions may be rendered physically impossible by the global maximum dose constraints to the shells. If these constraints are unnecessarily severe in certain regions, the search space for optimization is narrower than it should be.

5.4 Dose Prescription for the Individual Patient

After IMRT planning and conversion of deliverable beams to an instruction file (control point sequence) for the treatment machine, all elements of the *dose prescription* are embedded in the instruction file. If the plan is accepted for clinical delivery, the machine instruction file implicitly contains the *dose prescription*. The explicit *dose prescription* that is calculated from the absolute dose distribution associated to the machine instruction file is the closest in-silico prediction of the absorbed dose in the patient.

As described elsewhere, differences between the *dose provisional prescription* and the *dose prescription* may be unavoidable. If the dose prescription is consistent with the *planning dose objectives*, the differences are not caused by poor planning techniques. Differences, which are inconsistent with the *planning dose objectives*, should be investigated. To evaluate the value of an IMRT plan, a comparison between the *planning dose objectives* and the *dose prescription* is more informative than a comparison between the planning dose objectives and the *dose provisional prescription*.

5.5 Future Directions

IMRT dose distributions are strongly affected by both the constraint parameters and target-normal tissue geometry of the individual patient. Standard site-specific constraint templates can serve as a starting point for optimization or even as the final constraints in non-challenging situations. The final constraints for patient-specific optimization in

challenging situations must still be determined iteratively. An example of a strategy for the specific situation of concave dose distributions is discussed in-length by Hunt et al. [16]. Algorithms for patient-specific determination of constraints are needed.

In conventional radiation therapy using flat beams, issues like flash, overlap and dose littering were relatively easily addressed using ICRU guidelines 52 and 60. With the advent of IMRT with its inherent need for optimization, the use of concepts like PTV and PRV to account for motion and set-up uncertainty is less obvious. PTV is probably not the best approach for securing flash. Similar considerations can be made regarding dose-to-contoured-volume prescriptions, which are not the best approach to deal with overlap and dose littering. The use of probability distributions of the CTV and OAR location, including models for anatomical deformation in IMRT planning, will make the concepts of PTV and PRV obsolete and will solve many of the problems associated with build-up flash and overlap during optimization. However, substantial research and development is still ahead and unsolved questions as the parameters of probability distributions and deformations, or the incorporation of changing anatomy during fractionated IMRT need to be investigated.

In radiotherapy planning, it was common practice to consider the biology distribution within the contoured structures being uniform and to aim for a homogeneous dose distribution inside the tumor contours. An invariant biology distribution inside the normal tissue contours translated to dose constraints that were not a function of the spatial location. In reality, it has long been recognized that the spatial distribution of biological properties in most tumors and normal tissues is heterogeneous. With the advent of various molecular and functional imaging techniques, it may become possible to map out the biology distribution on a patient-specific basis. To use the spatially heterogeneous biology information derived from the new imaging modalities new concepts of dose prescription need to be considered. Contour-based dose prescriptions may become cumbersome to optimize the dose distribution as function of the biology distribution. Voxel-based dose prescriptions based on biological properties may be necessary and are advantageous, as they will guide optimization engines to avoid dose littering. Again, substantial research is ahead regarding biological and functional imaging and regarding the use of this information in IMRT planning. For these reasons, we hypothesized that a chapter dealing with practical issues in basic dose-to-contoured-volume IMRT planning still had its place in a book on IMRT.

Acknowledgements. GOA 12050401, BOF 01112300, 011V0497, 011B3300

Appendix: Properties of Commercial IMRT Planning Systems

The companies selling radiation therapy planning systems all recognize that supporting IMRT is a commercial imperative, and their products are undergoing rapid development. Any inventory of current systems and their capabilities would become rapidly out of date. However, there is value in discussing the most important aspects of the IMRT planning process and how different systems have approached them. Readers can use this information in specifying their requirements and evaluating alternative vendors.

This appendix is structured as a series of questions that might be posed to a vendor, each followed by a discussion of why it is relevant and what answers one might expect.

A General System Design Questions

A.1 Is the IMRT Capability Provided by a Stand-alone System or Is It Integrated into a 3D RTP System?

The first commercially available IMRT product used a stand-alone planning system that supported specialized hardware added to an accelerator. Providers of general-purpose treatment planning systems have since developed IMRT modules that are integrated into their products. Integration has several potential advantages. Inverse planning is a process that has much in common with conventional planning. Tasks such as defining the patient, registering different image datasets, outlining targets and structures, displaying dose distributions, and comparing competing plans occur with both. In an integrated system, a user need only learn one method for accomplishing them and the physicist need only validate those processes. A stand-alone system will have its own interface and concomitant need for training and validation.

Beyond the matter of convenience, there are also clinical needs to be considered. IMRT fields may be delivered in conjunction with conventional fields, and so there is the need to combine them in a single dose display. There is also a frequent desire to develop alternative plans, both IMRT and non-IMRT, for a given patient and compare them. This can best be accomplished within an integrated environment so that the anatomy segmentation is identical, the dose computation is comparable, and the display tools are equivalent.

All that being said, a stand-alone system can deal with many of these issues if it has adequate DICOM-RT connectivity with a clinic's conventional planning system. In the ideally connected world, the ability to move datasets between planning systems would allow separate systems to behave like interconnected modules of a larger struc-

ture. In the current real world, these connections are sometimes partial or unidirectional. Nevertheless, such tools are becoming more prevalent and robust.

A.2 How Can IMRT Fields Be Combined with Non-IMRT Fields?

This is relevant, for example, for an IMRT head and neck treatment that includes a conventional supraclavicular field. Or an initial treatment with conventional fields followed by an IMRT boost.

A.3 How Can a Planner Compare an IMRT Plan to a Non-IMRT Alternative?

B Questions About the Optimization Objectives and the Optimization Engine

B.1 How Are the Treatment Goals Parameterized?

Each inverse planning system has its own method of quantifying the competing goals of treatment, and they have different levels of sophistication and complexity. It may be useful to consider that all treatment planning is a form of numerical modeling. We are familiar with how patients, beams, and radiation interactions are modeled and devote considerable energy to validating those models and knowing their limitations. Inverse planning introduces another element: a numerical model of what the treatment is to accomplish. It is difficult to devise tools that are intuitive to use and adequately represent clinical thinking, and there is no consensus yet as how best to proceed.

The simplest systems allow planners to assign each structure a single dose value and a relative weight. Others allow a desired dose volume histogram (DVH) to be defined to different levels of detail (e.g., three points only or multiple points, perhaps with different weights assigned to different points). The relative importance of a structure might be expressed using a numerical weight, or associating a descriptor such as "critical" or "expendable" to a structure may indicate the clinical intention. Some systems allow absolute constraints to be applied (e.g., dose the cord cannot exceed 45 Gy). How the numerical representation of clinical intent influences the optimization leads to the next set of questions.

B.2 Is the Form of the Objective Function Available, or Is It a Commercial Secret?

The parameters associated with the treatment goals are combined into an objective function. At each iteration during optimization, the relevant doses are determined and the value of the objective function calculated. The optimization algorithm alters the modulation patterns to minimize (or perhaps maximize) the objective function, iterating many times through the process until a stopping criterion is reached. For a planner, it is very useful to understand the form of the objective function and how the user-defined parameters (e.g., goal doses and weights) are used in the function. It is useful because the planner has to modify those parameters in order to drive the optimizer in a desired direction, and it is much easier to develop a feel for the process if the underlying structure is known.

The details of the optimization process are often treated as trade secrets, however, and vendors differ in how much information they give their users. Planning would be easier if inverse planning algorithms were revealed in the detail that dose calculation algorithms are.

B.3 Can the User Observe the Objective Function Overall Score?

Related questions: Can the user see subscores for different structures? Is the objective function value displayed during the optimization? The most common problem facing users of inverse planning systems is looking at the result of an optimization run and trying to decide what parameter(s) to change to drive that result in a desired direction. It is helpful if the system reports the overall objective function score for the plan and the subscores associated with the different treatment goals. That information can often show which goal is hardest to satisfy and so indicate the most fruitful change to make.

B.4 What is the Basic Optimization Method?

Related question: Can the user test the reproducibility of the optimizer, such as by using different random number seeds or initial intensity patterns?

Some commercial implementations employ random search schemes, such as fast simulated annealing, while others use deterministic gradient descent methods. In either case, planners would like to know if the optimization method is reliably finding a plan with an objective function score that is very nearly the best possible. One way of testing that is to run the optimization multiple times from different starting positions (e.g., different initial intensity patterns) or with different random number seeds. As part of the commissioning process, users should be able to test the reproducibility in such a fashion.

B.5 Can Volumes Overlap? If Volumes Overlap, How Are Competing Goals Handled? Related Question: What Tools Are Available to Grow Volumes, e.g., from a CTV to a PTV?

Consider a common IMRT situation such as a prostate treatment. The prostate as CTV and organs such as rectum and bladder are outlined on the planning CT. The

PTV for the prostate is of course larger than the CTV, and frequently overlaps part of the anterior rectal wall as seen on the planning CT. Will dose to that overlap region be considered as applying to the PTV, the rectum, or both during the optimization? How will the dose be apportioned to DVHs for plan evaluation? Different planning systems handle these questions differently.

B.6 How Can a User "Fine-Tune" an Inverse Plan?

It is common for an inverse plan to be almost acceptable, with perhaps a localized hotspot that should be removed. In some systems, the only way to modify the plan is to redefine the problem (change plan goals, define new structures, ...), reoptimize, and hope for an improvement. Others permit the user to indicate how the localized isodose lines should be reshaped, and then the system adjusts the plan accordingly.

Another approach used by some systems allows the user to make changes in the delivery instructions directly (reshape segments, reweigh segments, remove segments ...). Then the system recomputes the resulting dose distribution. With sufficient care and insight, such direct action can improve a plan, or simplify it without significantly diminishing its quality.

B.7 Is "Forward-Planning" Supported?

(User defines beam segment shapes, optimizer decides relative weights.)

Systems that allow the user to directly modify the delivery sequence can often be used for a modified form of IMRT in which the user defines the shapes of the beam segments directly. The optimizer then determines the MU/segment to best accomplish the treatment goals. This is sometimes termed "forward-planned" IMRT, and is useful for breast treatments, for example. In such cases, the mobility of the target requires the fields to extend beyond the patient as visualized on the planning CT. Suitably designed segments can be combined to produce better plans than can be obtained with simple wedges. A pure inverse planning system designs segments to treat defined targets, and it is difficult to define a target that is outside of a patient. Targets that extend into shallow buildup regions are also problematic (see section 5.3.1, this chapter).

B.8 How Long Does an Optimization Run Take? Can Optimization Runs Be Queued?

The practical issue of calculation time is significant for inverse planning. It is also changing rapidly as hardware speeds and software design advance. Presently, calculation times for a typical head and neck case vary from several minutes to over one hour, depending on the vendor. Several trials are usually necessary to develop an acceptable plan, so the calculation time is a practical concern. It is very useful if calculations can be queued to run in the background. A user can then prepare several trials with different optimization parameters and then view the results later after all have completed, while moving on to other productive work in the meanwhile.

C Question About the Support of Various Delivery Techniques

C.1 What is the Spatial Resolution of the Ideal Intensity Map? What is the Spatial Resolution of the MLC Positions During Delivery?

IMRT planning systems calculate an intensity pattern that is quantized spatially. For delivery with an MLC, the quantization in the direction perpendicular to leaf motion generally corresponds to the leaf width, e.g., 10 mm. In the direction parallel to leaf motion there is more variability. Many commercial systems divide the irradiated area into beamlets, e.g., $10 \times 10\,mm^2$, and calculate the desired intensity pattern on that scale. Then, during treatment, the MLC leafs move in steps no smaller than 10 mm. (This type of planning lends itself to step-and-shoot type of delivery.) In this approach, both the planning and delivery is quantized spatially to the size of the beamlets.

The beamlets do not necessarily need to be square. Some systems allow the size of the beamlet width to be adjusted by the user. Having narrower beamlets (e.g., $5 \times 10\,mm^2$ or $2 \times 10\,mm^2$) potentially allows finer control of dose gradients at the borders of structures, but there can be a cost in calculation and delivery time. If each beamlet is treated independently in the optimization, then more beamlets means more variables to be optimized and more segments to be delivered. The dose calculation for each beamlet size also needs to be validated; a system that accurately calculates the doses from $10 \times 10\,mm^2$ beamlets may fail for smaller ones.

Another approach used by some vendors is to calculate first a desired intensity pattern on a fine grid, say at a 2 mm spacing in the direction of leaf travel. Then, the MLC leaf motions can be selected to produce an intensity pattern that matches the design as closely as possible. This approach is well-suited for dynamic delivery in which the MLC motion is continuous.

C.2 Can Minimum Segment Widths Be Set? Do Users Find this Necessary to Achieve Accurate Dose Predictions?

This question is related to the previous one. Some systems allow the user to specify a minimum field opening that will be used in delivery, thus reducing uncertainty about the dosimetric accuracy of very small fields. For example, one might specify that the distance between leaf pairs be at least 20 mm. If the intensity pattern were first calculated on a 2 mm grid, then this would mean

that a given segment might position a leaf end anywhere along a line at 2-mm intervals, but the opposing leaf would need to be at least 20 mm distant. Is such a specification necessary? This relates to the dose calculation algorithm and its ability to accurately model very small fields. Some systems are better than others in this regard. In principle, this should affect the ability of the system to produce sharp dose gradients.

C.3 Can a Minimum Be Set for the Number of MU per Segment?

Users may have concerns about the ability of the linear accelerator to accurately deliver segments that have very few (or fractional) monitor units. Some planning systems allow the user to specify a minimum number of MU that will be used in the delivery sequence.

The previous two questions allude to the problem of relating the intensity pattern needed to produce the desired dose to the pattern that can actually be produced by the machine. A more general question getting to that relationship is:

C.4 What is the Relationship Between the Desired Intensity Pattern, the Deliverable Sequence, and the Final Dose Display?

The inverse planning problem requires many iterations and dose calculations, and many systems employ simplified dose calculation algorithms to speed the optimization process. Here again is the usual tradeoff between speed and accuracy, and various approaches to dealing with that tradeoff. For example, at least one system uses a simplified algorithm for several iterations to move quickly to a partial solution, and then uses a more accurate algorithm to refine the solution. Commonly, the optimizer produces a desired set of intensities that may not actually be deliverable in practice. Each planning system needs to create a delivery sequence for the actual treatment device, and the sequence needs to respect the mechanical limitations of the device and any additional limitations (e.g., minimum field size or MU/segment) imposed by the planner. So it is best if the planning system ultimately calculates the dose that would be delivered by the actual treatment sequence using the best available dose calculation algorithm. Not all systems do that, and there can be systematic differences between the dose predicted by the system and that delivered to the patient.

C.5 Are Different Dose Calculation Algorithms Used During Optimization?

Is there a final dose calculation based on the actual delivery sequence? Are there situations in which the calculated dose can be expected to differ from the delivered dose?

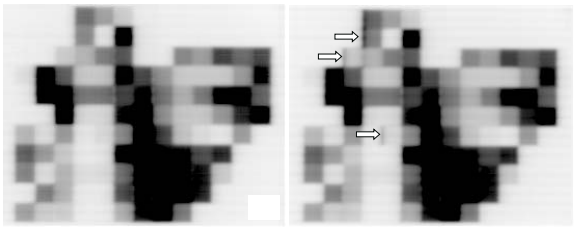

Fig. 5a,b. An IMRT field delivered with two different leaf segmentation algorithms: (a) closed leaf pairs are moved under a jaw; (b) the closed leaf pairs remain in the irradiated area. Since the leaf ends are rounded (and in this case are prevented from actually touching), additional dose is given to localized spots.

C.6 What Delivery Systems Will the Planning System Support? For the Systems that Are Supported, Are all the Limitations/Capabilities Taken into Account?

A planning system by itself is impotent. It needs to produce delivery instructions that will work with an accelerator/MLC combination. Each delivery system has its own capabilities, limitations, and constraints, and planning systems may not account for all of them.

Related questions: Are the limitations of MLC leaf movement, such as central axis overtravel, total leaf extension, and interdigitation accounted for? If the MLC has rounded leaf ends, is that accounted for? If leaves are to be totally closed for some MU, are they moved under a jaw for better shielding? If dynamic delivery is supported by the MLC, is it supported by the planning system? If dynamic arc delivery is supported by the MLC, is it supported by the planning system?

Figure 5 shows an example of a problem that can occur if a planning system does not move closed leaf pairs under a jaw. These films were taken on an accelerator with an MLC that has rounded leaf ends. Each film is of one IMRT field used for a head and neck treatment. During some of the treatment segments, at least one leaf pair is to be totally closed. The films were taken using two segmentation algorithms. In Fig. 5a, closed leaf pairs are moved under a jaw. In Fig. 5b, the closed leaf pairs remain in the irradiated area. Since the leaf ends are rounded (and in this case are prevented from actually touching), additional dose is given to localized spots.

D Other Questions

D.1 What Future Directions Are Being Explored?

This open-ended question relates to on-going developments in the field that will likely be of clinical use.

D.2 What Was Fixed or Added in Your Last Software Release?

This question can help establish how mature the software product is.

References

1. Zelefsky MJ, Fuks Z, Hunt M, Yamada Y, Marion C, Ling CC, Amols H, Venkatraman ES, Leibel SA (2002) High-dose intensity modulated radiation therapy for prostate cancer: early toxicity and biochemical outcome in 772 patients. Int J Radiat Oncol Biol Phys 53:1111–1116
2. Eisbruch A, Ship JA, Dawson LA, Kim HM, Bradford CR, Terrell JE, Chepeha DB, Teknos TN, Hogikyan ND, Anzai Y, Marsh LH, Ten Haken RK, Wolf GT (2003) Salivary gland sparing and improved target irradiation by conformal and intensity modulated irradiation of head and neck cancer. World J Surg 27:832–837
3. Munter MW, Karger CP, Hoffner SG, Hof H, Thilmann C, Rudat V, Nill S, Wannenmacher M, Debus J (2003) Evaluation of salivary gland function after treatment of head-and-neck tumors with intensity-modulated radiotherapy by quantitative pertechnetate scintigraphy. Int J Radiat Oncol Biol Phys 58:175–184
4. Claus F, Boterberg T, Ost P, De Neve W (2002) Short term toxicity profile for 32 sinonasal cancer patients treated with IMRT. Can we avoid dry eye syndrome? Radiother Oncol 64:205–208
5. Wu Q, Mohan R, Morris M, Lauve A, Schmidt-Ullrich R (2003) Simultaneous integrated boost intensity-modulated radiotherapy for locally advanced head-and-neck squamous cell carcinomas. I: Dosimetric results. Int J Radiat Oncol Biol Phys 56:573–585
6. Withers HR, Suwinski R (1998) Radiation dose response for subclinical metastases. Semin Radiat Oncol 8:224–228
7. Boersma LJ, van den Brink M, Bruce AM, Shouman T, Gras L, te Velde A, Lebesque JV (1998) Estimation of the incidence of late bladder and rectum complications after high-dose (70–78 Gy) conformal radiotherapy for prostate cancer, using dose-volume histograms. Int J Radiat Oncol Biol Phys 41:83–92
8. Jeraj R, Keall P (2000) The effect of statistical uncertainty on inverse treatment planning based on Monte Carlo dose calculation. Phys Med Biol 45:3601–3613
9. Evans PM, Donovan EM, Partridge M, Childs PJ, Convery DJ, Eagle S, Hansen VN, Suter BL, Yarnold JR (2000) The delivery of intensity modulated radiotherapy to the breast using multiple static fields. Radiother Oncol 57:79–89
10. Kestin LL, Sharpe MB, Frazier RC, Vicini FA, Yan D, Matter RC, Martinez AA, Wong JW (2000) Intensity modulation to improve dose uniformity with tangential breast radiotherapy: initial clinical experience. Int J Radiat Oncol Biol Phys 48:1559–1568
11. Hong L, Hunt M, Chui C, Spirou S, Forster K, Lee H, Yahalom J, Kutcher GJ, McCormick B (1999) Intensity-modulated tangential beam irradiation of the intact breast. Int J Radiat Oncol Biol Phys 44:1155–1164
12. Lof J, Lind BK, Brahme A (1998) An adaptive control algorithm for optimization of intensity modulated radiotherapy considering uncertainties in beam profiles, patient set-up and internal organ motion. Phys Med Biol 43:1605–1628
13. Esthappan J, Mutic S, Malyapa RS, Grigsby PW, Zoberi I, Dehdashti F, Miller TR, Bosch WR, Low DA (2004) Treatment planning guidelines regarding the use of CT/PET-guided IMRT for cervical carcinoma with positive paraaortic lymph nodes. Int J Radiat Oncol Biol Phys 58:1289–1297
14. Dogan N, Leybovich LB, King S, Sethi A, Emami B (2002) Improvement of treatment plans developed with intensity-modulated radiation therapy for concave-shaped head and neck tumors. Radiology 223:57–64
15. Claus F, De Gersem W, De Wagter C, Van Severen R, Vanhoutte I, Duthoy W, Remouchamps V, Van Duyse B, Vakaet L, Lemmerling M, Vermeersch H, De Neve W (2001) An implementation strategy for IMRT of ethmoid sinus cancer with bilateral sparing of the optic pathways. Int J Radiat Oncol Biol Phys 51:318–331
16. Hunt MA, Hsiung CY, Spirou SV, Chui CS, Amols HI, Ling CC (2002) Evaluation of concave dose distributions created using an inverse planning system. Int J Radiat Oncol Biol Phys 54:953–962

Dose Calculations for IMRT

Jeffrey V. Siebers

6

Contents

6.1 Introduction

The prediction of the patient dose distribution is central to IMRT optimization and beam delivery processes. The predicted dose for a candidate set of plan parameters is used to evaluate the plan objective function during the iterative optimization, to adjust and determine the beamlet intensities required to produce an optimal plan, and to judge the clinical acceptability of a plan. These tasks require accurate prediction of the IMRT dose distribution.

In competition with dose accuracy is IMRT dose calculation speed. IMRT plan optimization involves probing the solution space of beamlet intensities, number and angle of beams, beam energies, and other free parameters for an optimal solution. The iterative optimization process can require from ten or fewer iterations to converge for simple bounded problems with a limited solution space to thousands of iterations for complex multiple-parameter optimization problems with complex objective functions. The time to predict the dose for an individual candidate parameter set is often the rate-limiting component affecting the overall optimization time. Hence, severe approximations are often imbedded in the calculation algorithm used within the optimization loop in order to allow the optimization to be completed in an acceptable time frame. These approximations degrade the accuracy of the dose prediction.

This chapter focuses on the issues related to the calculation of dose for photon beam IMRT. The general dosimetric characteristics of IMRT beams and algorithms used for IMRT dose calculation algorithms are described, as are methods of incorporating dose calculations into the plan optimization loop. The balance and tradeoffs of dose calculation accuracy and dose calculation speed are considered throughout, with special attention paid to the consequences of inaccurate dose calculations on clinical dose distributions and the optimality of the final treatment plan. To aid the reader with respect to commercial systems, Table 1 summarizes the properties of several commercial IMRT systems with respect to the issues discussed in this chapter.

6.2 Dosimetric Characteristics of IMRT Beams

IMRT makes use of non-uniform radiation fluence distributions incident upon a patient from numerous beam directions to create a desired three-dimensional dose distribution. Non-uniform fluence patterns are created by using a continuous or discrete sequence of small beam apertures formed using a multi-leaf collimator (MLC). The consequences of this type of beam delivery method on the accuracy of the computed dose distribution are:

- Small beam apertures: most dose calculation algorithms exhibit the greatest inaccuracies for small treatment fields, particularly in regions of tissue heterogeneities [1–3]. For IMRT, the effects of small-field dose calculation heterogeneity errors on the overall dose distribution will depend on the intensity modulation in the vicinity of the dose sampling. Errors can be expected to be largest in regions that have large in-

Table 1. Comparison of commercial treatment planning system dose calculation algorithms and optimization strategies

System	Optimization dose algorithm	Deliverable optimization	Post optimization dose algorithm	Delivery method	Segment weight re-optimization
Corvus 5.0	PB	No	MC (optional)	sMLC and DMLC	No
Eclipse 7.1.67	Fast 3D superposition	No	PB	sMLC and DMLC	No
CMS XiO 4.2	PB-based fast 3D superposition	No	SC	sMLC	No (but can reopt beam weight)
KonRad 2.1	PB	Optional	PB	sMLC and DMLC	No
Pinnacle 7.4	PB with SC corrections	Optional (direct leaf position optimization)	SC	sMLC and DMLC	Yes
Plato	PB	No	PB	sMLC and DMLC	No
Oncentra 1.3	PB	No	PB or SC	sMLC	Yes

tensity gradients (spikes or dips) since the gradients behave like small fields superimposed on the main field. Conversely, in large regions of near uniform fluence, the heterogeneity correction induced error will be expected to be similar to that for 3DCRT algorithms. Dose calculation algorithm output factor errors are also typically greatest for small field sizes, which also contributes to IMRT dose errors.

- MLC leakage radiation: the dose delivered to a given point in a patient consists of components due to fluence transmitted through the sequence of open MLC apertures and that due to MLC radiation leakage, where leakage includes radiation transmitted through and scattered from the MLC and the MLC leaf tips. Figure 1 shows a profile through the fluence maps generated for a head and neck IMRT treatment plan delivered with the dynamic MLC (DMLC) technique, with the fluence from indirect sources (MLC leakage radiation) separated out from the total. Within the narrow intensity spike at $x = 1$ cm, 50% of the fluence is from indirect sources; in the intensity valley at $x = 2$ cm, 100% of the fluence is from indirect sources; and in the relatively flat fluence portion from $x = 4$ to $x = 9$ cm, the indirect component accounts for $> 10\%$ of the fluence [4]. The MLC leakage radiation sets the lower limit of the dose that can be delivered within the jaw boundaries. It has a harder energy spectrum than an open beam, with the percent depth-dose at 10 cm depth being 5% greater for an MLC blocked beam than for an open beam [5]. Most IMRT dose calculation algorithms approximate the effects of MLC leakage radiation on the total dose distribution.

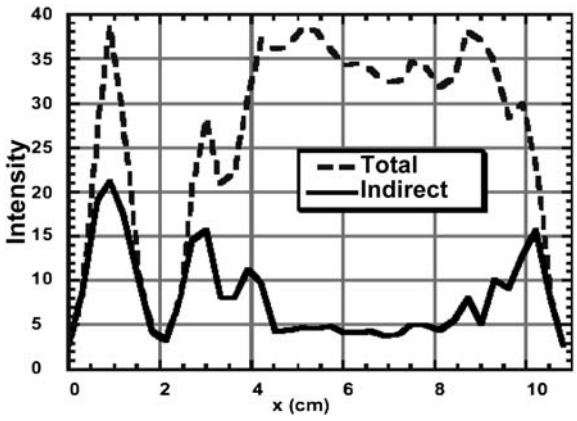

Fig. 1. Sample profiles of the total and indirect (MLC leakage and scatter) fluence contributions for a typical head and neck IMRT treatment plan. Indirect sources consist of a substantial fraction of the total fluence in intensity valleys and in narrow intensity spikes

Evidence of dose calculation errors in IMRT can be found in routine IMRT quality assurance in which computed and measured dose distributions in a phantom are compared. Such experimental checks of IMRT fields routinely show discrepancies between the planned (desired) and actual dose, independent of the treatment-planning platform [6], particularly in regions of large dose gradients. Oftentimes, IMRT QA measurements are, however, made in low dose gradient regions, precisely where the dose calculation error is expected to be smallest, possibly miss-leading the user regarding the accuracy of their dose calculation algorithm.

6.3 IMRT Dose Calculation Algorithms

The prediction of the absorbed dose delivered to a given individual patient is a general problem encountered in radiation therapy. For externally directed photon beams, the problem can be stated as: for a given radiation fluence incident upon the patient geometry, determine the energy absorbed (the absorbed dose) within the patient as a function of position. This simple formulation shows that dose calculation problem consists of two distinct components: fluence prediction and the determination

of the dose from that incident fluence. Each of these components plays an important role in an IMRT dose calculation.

Dose calculation algorithms are generally classified as correction-based algorithms or model-based algorithms [7]. In correction-based algorithms, the dose computation effectively first computes dose to a homogeneous water phantom, then applies various correction strategies to account for source to patient surface distance (SSD) changes and tissue heterogeneities within the patient. Model-based algorithms, on the other hand, generally perform the dose calculation directly in the patient geometry. The IMRT collaborative working group of AAPM and ASTRO has separated IMRT dose calculation algorithms into four categories [8], correction-based broad beam algorithms, correction-based pencil-beam algorithms, and model-based kernel-based and Monte Carlo algorithms.

- Broad beam algorithms are correction-based dose calculation algorithms [7] that utilize measured dose distributions to generate a parameterization of dose distributions in a homogeneous water phantom as function of field size, depth, off-axis distance, and surface to source distance. For a patient specific dose calculation, dose for the treatment conditions are first reconstituted for a homogeneous water phantom, and then patient anatomy specific corrections are applied to account for surface contours and tissue heterogeneities. Broad-beam algorithms are designed for use with radiation beams that have nominally uniform fluence distributions, such as for an open or simply blocked field, or for fields in which the fluence is a simple, smoothly varying function, such as that produced by a wedge. Broad beam algorithms rely on the fact that within a homogeneous patient or phantom, radiation equilibrium is approximated within the field boundaries. Heterogeneity corrections for broad beam algorithms, when used, are based upon density scaling equivalent path-length methods. Broad beam algorithms are not applicable to the variable intensity conditions of IMRT due to the lack of radiation equilibrium within IMRT fields, and are not recommended to be used, in general, for IMRT optimization. They are, however, occasionally used for aperture based IMRT optimization [9] and can also be utilized as a secondary monitor unit checking programs for IMRT QA [10, 11].
- Pencil-beam (PB) algorithms are correction-based algorithms [7] that utilize parameterized measured data from a limited number of irradiation conditions in addition to pencil beam energy deposition kernels in a water phantom derived from Monte Carlo calculations [12] or measurements [13, 14] to reconstitute dose distributions in a homogeneous phantom. Patient specific contours and heterogeneities are then accounted for as corrections to the homogeneous dose distribution [12, 15]. PB models account for beam intensity modulations and field shapes, but utilize radiological path length scaling methods to account for heterogeneities and patient contours. PBs account for the radiation disequilibrium due to lateral transport of secondary radiation for modulated intensity distributions in homogeneous media, but not for internal heterogeneities and surface irregularities. PB algorithms have significant speed advantages over kernel-based approaches (below) since they effectively pre-convolve the point kernels over the depth dimension. PB algorithms are the most commonly used algorithms for IMRT optimization due to their fast dose calculation speed. However, their accuracy is dependent upon the heterogeneity of the patient geometry.
- Kernel-based algorithms are model-based algorithms [7] which can be used to compute directly the dose in a patient or phantom. Kernel-based approaches, typically called superposition or convolution algorithms (SC), separate the effects of primary photons incident upon the patient from the effects of secondary radiations generated within the patient. In SC algorithms, the total energy released per unit mass (TERMA) from primary photon interactions in the patient is computed and the effect of secondary radiations generated in the patient are accounted for using pre-computed secondary energy spread kernels which are superimposed over or convolved with the TERMA to yield the total dose distribution [16–18]. SC algorithms account for tissue heterogeneities in the TERMA calculation, but typically use radiological path length methods to scale the secondary energy spread kernels. They are much more accurate than PB in heterogeneous geometries and can accurately compute dose in regions of electronic disequilibrium; hence they are applicable to IMRT dose calculations. SC dose calculation times are relatively long compared to PB approaches [19,20] and, although they can be used within the IMRT optimization loop [21], SC algorithms are usually only used after the end of optimization to compute the final deliverable dose distribution.
- Monte Carlo (MC) algorithms are model based algorithms and can be used to compute directly the dose to the patient. In the MC method, individual photon and electron tracks through the accelerator treatment head, multi-leaf collimator, and patient are simulated. Since MC algorithms simulate a stochastic process, the results have an inherent statistical imprecision (noise) which generally decreases with the square of the dose calculation time, but is independent of the number of beams simulated, a distinct advantage when many treatment angles are used for patient treatment. MC algorithms are considered the most accurate dose calculation algorithms since they directly account for tissue heterogeneities and make no assumptions regarding radiation equilibrium. For

IMRT, MC has the additional advantage that particles can be directly transported through the multi-leaf collimator segments or through a moving multi-leaf collimator, hence, radiation leakage and scatter effects can be directly taken into account [22]. The major deterrent to implementation of MC for IMRT dose calculation, particularly during optimization, is the time required to complete the dose calculation process. Additional discussion on MC dose algorithms is given at the end of this chapter.

In addition to the dose calculation algorithm type, a major factor influencing dose calculation accuracy is the user specific commissioning and tuning of the dose calculation model to match IMRT dose distributions for their particular accelerator. Both initial dosimetric quality assurance under carefully controlled test conditions and routine patient specific quality assurance are useful to ensure dose calculation accuracy and determine the limits of a user's specific implementation.

6.4 Dose Calculation Within the IMRT Optimization Loop

The choice of the dose calculation algorithm and how it is incorporated into the IMRT optimization loop affects the speed, accuracy, and optimality of the final dose distribution. The amount of realism used during the fluence optimization in terms of the whether the optimized fluences used by the dose calculation algorithm can be delivered by the accelerator hardware or not also affects the optimality of the plan.

6.4.1 IMRT Optimization Process

A flow diagram for a typical IMRT optimization process is shown in Fig. 2. Dose calculation algorithms appears twice in this flow diagram, once during the optimization process (Box 2) and once following the creation of MLC leaf sequences in computing the deliverable dose distribution (Box 9). In many planning systems, these are different dose calculation algorithms. The Box 2 dose calculation, which is repeated multiple times during optimization, is normally a fast dose calculation algorithm, such as a fast PB algorithm, to enable rapid completion of the optimization. Approximations utilized within the Box 2 algorithm to achieve the dose calculation speed can result in dose inaccuracies. To minimize the impact of these inaccuracies, the Box 9 dose calculation algorithm, which is executed only once per optimization, is often performed with a slower, more accurate algorithm (such as an SC algorithm) to determine the post-optimization deliverable dose distribution. The differences in dose calculation accuracy between the Box 2 and Box 9 dose calculation algorithms

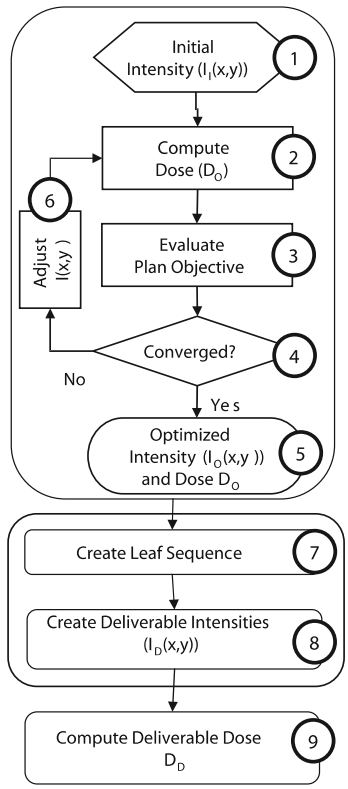

Fig. 2. In the typical IMRT optimization process, dose calculation occurs both with the optimization loop (Box 2) and following conversion of the optimized intensities to MLC leaf sequences (Box 9). These may be the same, or different dose calculation algorithms

combined with the inability of the MLC to achieve the optimal fluence patterns results in differences between optimized (Box 5) and deliverable (Box 9) dose distributions for an IMRT plan, often with deterioration in the plan quality between Box 5 and Box 9. An example of this is shown in Fig. 3, which shows a T2N3M0 base-of-tongue cancer patient who was treated with dynamic MLC-IMRT from nine equiangle, coplanar beams. The original plan (computed with SC) showed good target coverage and dose uniformity, while the deliverable plan that considered the MLC delivery showed a substantial hot spot in the target volume and higher doses to critical structures. Furthermore, the cord is spared by the 40 Gy line in the optimized plan, but is transected by the 45 Gy line for the deliverable plan. This type of deviation between optimized and deliverable results is typical in routine IMRT practice.

In clinical practice, techniques used to improve a deliverable treatment plan when the optimized and deliverable dose distributions disagree to such an extent that the deliverable dose distribution is clinically unacceptable include:

- Adjusting the plan monitor units so as to produce an acceptable plan.
- Re-optimizing the IMRT beam segment weights for multi-segmental (sMLC) IMRT.
- Modifying the plan objectives and re-optimizing the plan. This requires the planner to modify or over-specify planning objectives for the optimized dose

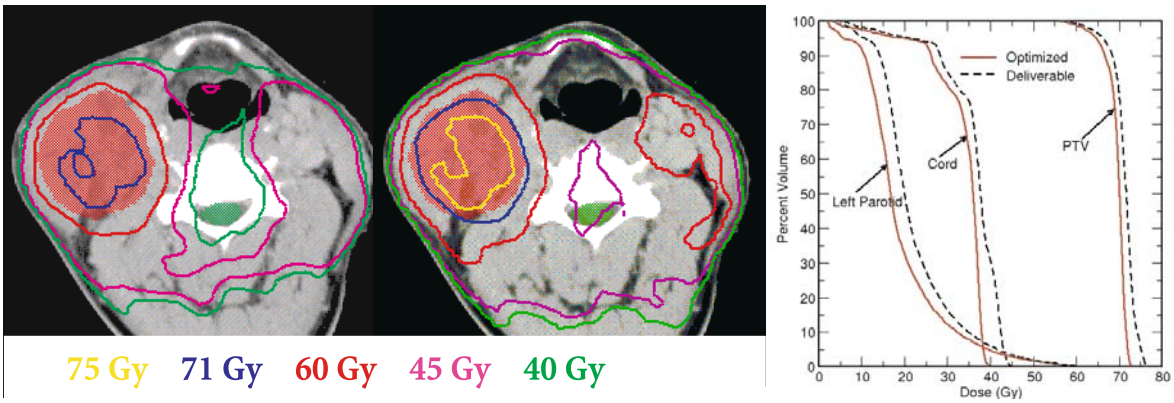

Fig. 3. a–c Isodose profiles and DVH comparison for an optimized intensity distribution and the corresponding deliverable dose distribution for DMLC delivery to a patient. Note the differences to in the target coverage (*red* PTV) and normal tissue sparing (*green* cord)

distribution (D_O, Fig. 2, Box 5) in order to achieve an acceptable deliverable (D_D, Fig. 2, Box 9) dose distribution.

Optimization techniques that avoid the post-optimization plan degradation include:

- Using an accurate dose calculation throughout the optimization process, or for the final iterations of the plan optimization process [19].
- Including the MLC leaf sequencing within the optimization loop. This is termed deliverable-based optimization (DBO). DBO does not require post-optimization conversion to leaf sequencing, thereby avoiding plan the degradation from the post-optimization leaf conversion step. DBO can accomplished by including the full leaf sequencing process within the optimization loop [22, 23] or by directly optimizing MLC leaf positions [24].

6.4.2 Dose Computation at Each Iteration

Most IMRT planning systems compute the entire 3D dose distribution during each optimization iteration (Fig. 2, Box 2). To account for the intensity modulation during the dose calculation, for each IMRT beam, the intensity variations are modeled as a 2D matrix of energy fluence or energy fluence modifiers incident on the patient. This energy fluence is then used by the dose calculation algorithm to compute the 3D dose distribution for each optimization iteration. A variety of algorithms can be used when the entire dose distribution is computed at each iteration. A major advantage of this method is it is straight forward to implement into a treatment planning system since the intensity modulation can be considered as a transmission compensator matrix by the treatment planning system [21].

Since the time required to complete an optimization is proportional to the product of the number of iterations and the dose calculation time per iteration, to minimize optimization time, fast, approximate dose calculation algorithms are often used such as those based on ray-tracing the primary beam or those based upon fast PB algorithms [12, 25, 26]. Techniques such as using adaptive dose grids, [27] random sampling of dose points within structures of interest, [28, 29] and pre-computation of radiological path-lengths and other quantities that do not change from one iteration to the next are often used to reduce the dose calculation time [19]. Each of these methods has the potential to reduce dose calculation accuracy; however, the goal of proper implementation of these techniques is to have the accuracy reductions become clinically insignificant. Post-optimization dose recalculation with and an accurate algorithm is used to reduce the clinical consequences of the approximations used during the optimization.

6.4.3 Precomputation of Sub-field or Bixel Dose Distributions

Instead of computing the entire dose distribution during each iteration in the optimization, an alternative method is to perform individual dose calculations for sub-components of the radiation field prior to optimization and then use weighted summations of these sub-components to compute the dose at each optimization iteration. The simplest of these approaches is to pre-compute large sub-divisions of the radiation field in what is called *aperture-based* optimization [9, 30–32], in which beams are sub-divided into multiple (possibly overlapping) MLC apertures to be used for beam delivery. The number of segments used limits the number of possible intensity levels and the complexity of the delivery. The simplified IMRT planning technique, in which a few segments are manually adjusted, is called

forward IMRT. Arbitrary 3D dose calculation algorithms are suitable for both forward and inverse aperture-based approaches, subject to the field-size and heterogeneity limitations of the algorithm. The pre-selected MLC leaf positions can be used to incorporate head scatter or even MLC scatter radiation effects on the dose distribution, depending on the algorithm.

An alternative pre-calculation approach is to subdivide an individual beam into a matrix of small (1 cm×1 cm or smaller) equal-sized pencil-beam like elements, each with a corresponding intensity value [33, 34]. For each individual beam element, the contribution to the total dose distribution is computed and stored in what is termed a *bixel*. Since bixels are small, only PB, SC, or MC algorithms are suitable for computing them. The dose computation during plan optimization consists of summing the doses of the individual pre-computed bixels weighted by their respective intensities, which are varied from one iteration to the next.

In the bixel approach, the time required to precompute the individual bixel dose distributions depends strongly on the algorithm used to create them. However, the bixel dose distributions are computed only once, and therefore the dose computation typically consumes only a small fraction of the total optimization time. Depending on the beam size, substantial quantities of computer memory are necessary to store the bixel dose distributions. For a typical IMRT case with 500 beamlets per beam, 9 treatment angles, and 200,000 2-byte integer dose volume elements in the dose scoring grid, 1.8 GB of memory is required to store the dose matrices. In early IMRT implementations, this memory requirement was a substantial barrier to implementation of bixel-based optimization. Although modern computers are now capable of utilizing this much high speed RAM, alternative methods have been developed to reduce the memory requirements and reduce the overall computation time. These include (1) storing and computing doses only for regions of interest (targets and critical structures), (2) computing dose only for a sub-set of points within regions of interest [28, 29], (3) specifying a cut-off radius for pencil beams, beyond which the contribution is set equal to zero [35], and (4) sparsely sampling the bixels (pencil beams) in the low dose region in such a way that the total energy deposited is conserved [36].

Unlike the aperture-based pre-computation approach, the bixel-based approach inherently is a non-deliverable IMRT optimization approach. In the bixel-based approach, the MLC beam delivery and the effects of MLC leakage and scatter radiation are not incorporated into the optimization process. It may be possible to add in bixels representing the blocked beam (with a contributing fraction of F_{closed} where F_{closed} is the fraction of time that the MLC is closed for that bixel) for radiation passing through the closed MLC. However, even in this case, the effect of radiation passing through the rounded MLC leaf tips will not be incorporated.

6.5 Effects of Dose Accuracy on IMRT Plans

Approximations used in IMRT dose calculation optimization algorithms and in post-optimization dose computations affect both the accuracy and the optimality of IMRT treatment plans. The following sub-sections describe the accuracy component in terms of their effect on the dose distribution used for plan evaluation using what is called a dose prediction error and of the loss in optimality in terms what is called an optimization convergence error.

6.5.1 Plan Dose Distributions: Dose Prediction Error

The accuracy of a treatment planning systems' dose calculation algorithm is a measure of agreement between the dose distribution predicted by the treatment planning system and that that would be achieved in a patient. The difference between the actual and predicted dose distributions can be called a dose prediction error (DPE). DPE is a measurable quantity for phantoms in which 3D dose distributions can be measured. DPE, however, can not be determined under circumstances where the full 3D dose distribution cannot be measured, such as within a patient. For practical purposes, in such cases, the DPE of a given algorithm can be estimated by comparing its dose calculation results with those of a dose calculation algorithm that is known to be superior (more accurate) based upon measurable DPEs.

There are several sources of DPEs for radiation therapy dose calculations. The major sources of inaccuracies and hence DPEs for IMRT dose calculations are:

1. Heterogeneities: due to improper or incomplete handling of patient heterogeneities by the dose-calculation algorithm. Heterogeneity errors can be estimated by comparing calculations with measurements in an anthropomorphic phantom, or by comparing with another algorithm that more accurately accounts for heterogeneities such as SC or MC. In general, sites in which tissues are nearly homogeneous (brain, prostate) little heterogeneity error would be expected independent of the dose calculation algorithm. For heterogeneous geometries (lung, head and neck), on the other hand, the heterogeneity errors would expected to be larger for dose calculation algorithms that use radiological path-length corrections to account for heterogeneities. The use of multiple beam angles may dilute the dose errors from individual beams such that the error in the total dose distribution is acceptable, however, this has not been shown to be true for all cases.
2. Fluence: due to improper or incomplete prediction of the fluence incident upon the patient or phantom. Dose calculation algorithms require accurate predic-

tion of the fluence to predict dose accurately. Fluence errors can be due to approximations or inaccuracies in the conversion from MLC leaf-sequences to fluence or intensity-maps to be used by the dose calculation algorithm, or due to errors in the treatment machine delivery of the fluence. In phantom geometries, fluence errors can be measured by comparing calculated dose distributions with ones measured with films or portal images on a plane normal to the beam central axis. This is often completed as a part of routine IMRT QA. The impact of fluence errors on patient dose distributions can be estimated by transferring measured fluence values back into the treatment planning system to be used as input for dose re-calculation [37]. Alternatively, this can be done by re-computing doses using the leaf sequences reported by treatment machine (from their log files) with an algorithm that has been verified to have minimal fluence errors. Generally, it is the purview of the IMRT quality assurance process (whether measurement or calculation based) to detect gross errors caused by fluence errors.

3. Patient geometry: due to improper or incomplete accounting for the patient set-up uncertainties, intra-fraction motion, or other patient anatomical changes in the dose calculation. Most dose calculation algorithms consider the patient to be a static geometry, with the single CT data set acquired at the beginning of treatment accepted to be representative of the geometry throughout the treatment. Margins are used to account for patient set-up uncertainties and intra-fraction motion. The adequacy of margins to ensure target coverage and normal tissue sparing for IMRT is the subject of on-going investigations. Recomputing doses for multiple patient set-ups [38], convolving dose distributions [39] or fluences [40] with expected patient setup errors is also being applied to estimate the impact of these errors. Also, multiple patient imaging studies are being applied to be able to better estimate the variability of patient setups and their impact of patient setup errors on IMRT dose distributions. It may be difficult or impossible to evaluate the dose errors caused by patient geometry changes since patient setup-errors and day-to-day anatomic variations are impossible to predict, however, the user should be aware of such errors and avoid using IMRT in situations in which probable patient geometry changes would result in unacceptable patient outcomes, such as in treatment of moving targets such as a mobile lung tumor with only a static planning image.
4. Other: there can be other contributors to dose errors. These can be specific to the calculation algorithm and to individual users' commissioning of a treatment planning algorithm. It is generally the role of routine and patient specific quality assurance measurements to detect such errors.

Clinically, DPEs depend upon both the algorithms used for the dose calculation, the treatment site, and the beam configuration. Uncorrected DPEs will result in the dose delivered to a patient to differ from that which is predicted by the treatment planning algorithm. An example of a DPE is shown in Fig. 4, in which a lung IMRT treatment plan that was optimized using a fast PB algorithm that used a radiological path-length correction method to account for the tissue heterogeneities is compared with the same plan recalculated with SC and MC dose calculation algorithms which inherently account for tissue heterogeneities. The PB algorithm which was used for optimization predicted the PTV D_{95} to be 59.5 Gy, while the SC algorithm predicts 55.5 Gy and the MC predicts 54.7 Gy. The cord DVHs for the three algorithms, however, are all very similar. Had the PB plan been used for the dose prescription, the target would have been underdosed by 4–5 Gy.

Clinical consequences of many DPEs can be reduced by performing a final dose calculation with the most accurate dose calculation algorithm available in the planning system prior to plan evaluation and modifying the plan monitor units to meet the clinical goals. For the lung plan above, this would have involved increasing the monitor units to deliver the prescription dose. This, however, would also have increased the cord dose.

6.5.2 Plan Optimality: Optimization Convergence Error

The optimality of an IMRT plan is a measure of how well the plan satisfies (minimizes or maximize) the objective function used during optimization. The difference between the plan that best satisfies the plan objective function and the plan that is delivered to the patient can be called the optimization convergence error (OCE). Determination of OCEs have some of the

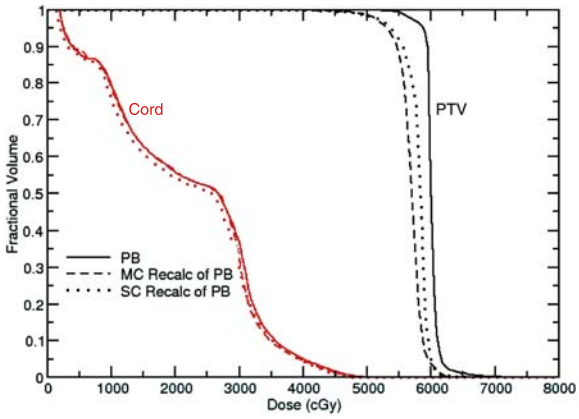

Fig. 4. Example of a dose prediction error (DPE) on dose-volume histograms for a sample lung treatment plan which was optimized with a PB algorithm and recomputed with SC and MC dose algorithms. DVHs for the PTV and the cord are shown

same limitations as determination of DPEs since it may be impossible to determine the true optimal plan; however, OCEs can be estimated by comparing plans with those in which a source of the OCE has been minimized or eliminated.

One source of OCE is DPEs during the iterative IMRT optimization. When a dose calculation algorithm with a DPE is used during optimization, the optimization can converge to a different intensity solution than the one that it would converge to if an algorithm without the DPE was used [41]. Consider the lung example previously shown in Fig. 4. The PB algorithm used during optimization used a radiological path-length method to account for heterogeneities, a method known to overestimate dose in lung tissue and at lung-tumor interfaces. The optimizer, therefore, was misguided in its attempt to adjust intensities to correct for heterogeneity induced dose perturbations; hence, when the plan was re-computed with SC or MC, the PTV dose was underestimated. When the lung plan is optimized using an SC algorithm (Fig. 5), the optimizer is guided to account more properly for the heterogeneity induced dose perturbations. Interestingly, the dose distribution and DVHs for the SC-optimized and PB-optimized plans are very similar, but with different intensity distributions for each beam. This indicates that the IMRT optimization process can account for heterogeneity induced dose perturbations.

Non-dose calculation related sources of OCE include post-optimization conversion of optimized intensity patterns to deliverable MLC leaf sequences (Fig. 2) and failures of the optimizer to find the global minimum, either because of becoming trapped in a local minima or failing to run to convergence.

Clinically, OCEs result in a sub-optimal plan being delivered to a patient. Provided that DPEs are eliminated by performing a final dose calculation with an accurate dose calculation algorithm, the dose distribution used to evaluate the plan can be accurate and the sub-optimal plan may be found to be clinically acceptable. The advantages to reducing OCEs are that better plans may be found, often with reduced dose to critical structures [22]. Furthermore, using planning techniques such as deliverable optimization which minimizes OCE, the optimizer deals with realistic plan objectives. This can reduce the trial and error procedure of adjusting (over-specifying) the objective function and re-optimizing the plan often used in IMRT planning.

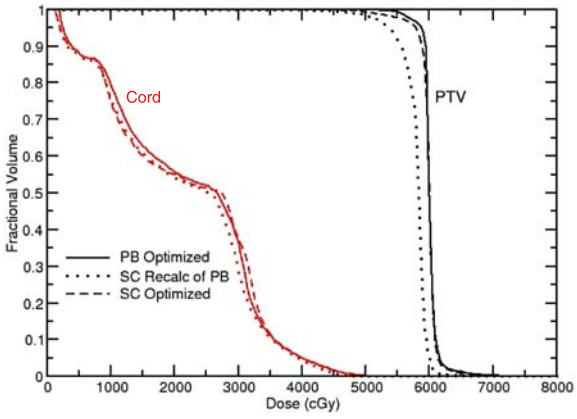

Fig. 5. Optimization convergence error for the lung IMRT example of Fig. 4. When the PB optimized DVH (*solid lines*) is re-computed with SC (*dotted lines*), the DPE of the PB dose calculation is observed. When the plan is optimized using the SC algorithm (*dot-dash lines*), the OCE (the difference between the SC recalc and the SC optimized) is observed

6.6 Reduce IMRT Dose Calculation Time by Interlacing Accurate and Fast Algorithms

Using accurate dose calculations for all iterations of an optimization process to minimize OCE is impractical due to the excessive dose calculation time required by accurate dose calculation algorithms. A solution to the dose calculation speed vs accuracy dilemma is to interlace the use of fast and accurate dose calculations during the plan optimization process. Fast but less accurate algorithms can be used for most of the optimization iterations and slower accurate methods for a smaller number of final iteration.

One of the simplest approaches is to use sequentially the different algorithms during the IMRT optimization. For example, fast PB dose computations can be used in the initial stages of the optimization, with the results being provided to a slower, more accurate SC algorithm. Because the PB is very fast, it can be used for any initial optimization tasks such as selection of the number of beams and of gantry, couch, and collimator angles. Following determination of the optimal beam configuration and convergence of the PB optimization, resultant intensity distributions can be used as input to an optimization which uses SC dose algorithms. Because the initial PB calculation provides a good initial guess to the SC-based optimization, the number of SC iterations is reduced, thus, reducing the optimization time compared to an optimization using only the SC algorithm. It has been demonstrated that this technique yields plans that are equivalent to using the accurate algorithm throughout the optimization [19].

More efficient processes utilize fast algorithms throughout the optimization process. These are termed hybrid dose computation approaches since they entail combining or mixing of dose calculation algorithms. One such approach uses an SC dose algorithm to calculate an approximate scatterless dose kernel based upon the ray-traced dose for each element of the intensity matrix, then uses this kernel, implemented as a fast table look-up, for subsequent dose calculations to compute

dose during the optimization. The kernel is periodically updated by re-computing with the SC calculation to reduce the inaccuracies of using the scatterless kernel [20]. The scatterless kernel dose calculation is more than 100 times faster than the SC dose computation, thus the speed is dominated by the number of SC dose computations required.

Other hybrid methods use a periodically updated beam-by-beam dose correction matrix to correct dose values computed with a fast algorithm. The dose correction matrix has the same dimensions as the patient dose matrix and is used to describe the deviation between the fast dose algorithm results and the accurate dose algorithm results at a fixed point during optimization. Both multiplicative and additive correction matrices have been used. A flow diagram for the corrective additive dose-correction method is given in Fig. 6 using PB as the fast algorithm and SC as the slower, more accurate algorithm, although other algorithms could be used in this loop. At the beginning of the optimization, all elements in the dose correction matrix are set equal to zero (Box 1). The optimization process (Fig. 6 Box 2), which consists of an optimization process such as one from Fig. 2, proceeds using the fast PB algorithm with the corrected dose $D_C = D_{PB} + C$. Following optimization convergence, the dose is recomputed with the more accurate algorithm (Box 4, D_{SC}) and results are compared with D_C. If the results differ by more than the convergence criteria, then the correction matrix is updated using $C = D_{SC} - D_{PB}$ and the optimization continues. Otherwise, the correction matrix has converged and the optimization is completed.

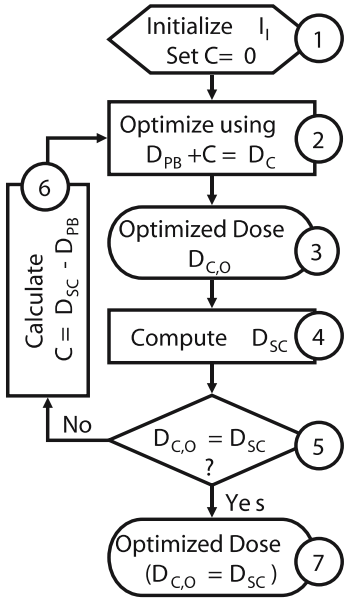

Fig. 6. Flow diagram for a correction-based dose scheme for use in IMRT optimization

It is important to note that for the correction based methods, immediately after the correction matrix is set to $C = D_{SC} - D_{PB}$, the initial dose in the optimization loop (Box 2) is computed with $D_C = D_{PB} + C = D_{SC}$, that is, the optimization occurs with the SC as the basis dose. It can be shown that, using the correction methods, the fast (PB) algorithm only effectively operates on the change in the fluence (or intensity) ΔI; thus, as the outer loop converges (as $\Delta \ln \rightarrow 0$), $D_C \rightarrow D_{SC}$. The equivalence of plans developed using the correction methods and using an accurate algorithm throughout optimization has been empirically demonstrated [42].

6.7 Outlook: Monte Carlo for IMRT Dose Calculations

The desire for highly accurate optimized IMRT dose distributions will likely lead to widespread clinical implementation of MC algorithms into IMRT systems in the future. To date, the major use of MC for IMRT has been to verify plans developed with non-MC algorithms [43–45]. Although general agreement between the treatment planning systems dose calculation algorithm and MC is observed in these studies, dose differences of 10–20% for some patients have been observed.

For IMRT plan optimization, even though MC has been used for plan optimization in a test study [46], it is currently considered too slow for routine IMRT optimization. Within the next few years, several key components are coming into place which will enable future MC-based IMRT optimization including:

- Fast, new generation of fast MC dose computation algorithms such as XVMC [47,48], VMC++ [49], and DPM [50], which reduce the MC by factors of 4–20.
- Denoising techniques [51, 52], in which the statistical noise inherent in MC dose computations can be reduces, reducing the MC dose calculation time to by a factor of 4–10.
- Hybrid dose calculation strategies, which can reduce the number of MC dose computations required to be three or less per optimization.

Combinations of these techniques should allow accurate MC dose calculation during optimization, which was previously considered too time consuming. MC optimized plans should minimize dose prediction and optimization convergence errors, resulting in improvement in the quality of deliverable IMRT plans.

References

1. Mackie TR et al. (1985) Lung dose corrections for 6- and 15-MV X-rays. Med Phys 12(3):327–332

2. Yu CX, Mackie TR, Wong JW (1995) Photon dose calculation incorporating explicit electron transport. Med Phys 22(7):1157–1165
3. Arnfield MR et al. (2000) The impact of electron transport on the accuracy of computed dose. Med Phys 27(6):1266–1274
4. Mohan R et al. (2000) The impact of fluctuations in intensity patterns on the number of monitor units and the quality and accuracy of intensity modulated radiotherapy. Med Phys 27(6):1226–1237
5. Kim JO et al. (2001) A Monte Carlo study of radiation transport through multileaf collimators. Med Phys 28(12):2497–2506
6. Low DA (2002) Quality assurance of intensity-modulated radiotherapy. Semin Radiat Oncol 12(3):219–228
7. Mackie TR et al. (1996) Photon beam dose computations. In: Mackie TR, Palta JR (eds) Teletherapy: present and future. Advanced Medical Publishing, Madison, WI
8. Intensity Modulated Radiation Therapy Collaborative Working Group (2001) Intensity-modulated radiotherapy: current status and issues of interest. Int J Radiat Oncol Biol Phys 51(4)880–914
9. De Meerleer G et al. (2004) Direct segment aperture and weight optimization for intensity-modulated radiotherapy of prostate cancer. Strahlenther Onkol 180(3):136–143
10. Yang Y et al. (2003) Independent dosimetric calculation with inclusion of head scatter and MLC transmission for IMRT. Med Phys 30(11):2937–2947
11. Xing L et al. (2000) Monitor unit calculation for an intensity modulated photon field by a simple scatter-summation algorithm. Phys Med Biol 45(3):N1–N7
12. Mohan R, Chui CS (1987) Use of fast Fourier transforms in calculating dose distributions for irregularly shaped fields for three-dimensional treatment planning. Med Phys 14(1): 70–77
13. Ceberg CP, Bjarngard BE, Zhu TC (1996) Experimental determination of the dose kernel in high-energy X-ray beams. Med Phys 23(4):505–511
14. Storchi P, Woudstra E (1996) Calculation of the absorbed dose distribution due to irregularly shaped photon beams using pencil beam kernels derived form basic beam data. Phys Med Biol 41(4):637–656
15. Bourland JD, Chaney EL (1992) A finite-size pencil beam model for photon dose calculations in three dimensions. Med Phys 19(6):1401–1412
16. Mackie TR, Scrimger JW, Battista JJ (1985) A convolution method of calculating dose for 15-MV X-rays. Med Phys 12(2):188–196
17. Boyer A, Mok E (1985) A photon dose distribution model employing convolution calculations. Med Phys 12(2):169–177
18. Ahnesjo A (1989) Collapsed cone convolution of radiant energy for photon dose calculation in heterogeneous media. Med Phys 16(4):577–592
19. Siebers JV et al. (2001) Acceleration of dose calculations for intensity-modulated radiotherapy. Med Phys 28(6):903–910
20. Wu Q et al. (2003) A fast dose calculation method based on table lookup for IMRT optimization. Phys Med Biol 48(12):N159–N166
21. Wu Q, Mohan R (2000) Algorithms and functionality of an intensity modulated radiotherapy optimization system. Med Phys 27(4):701–711
22. Siebers JV et al. (2002) Incorporating multi-leaf collimator leaf sequencing into iterative IMRT optimization. Med Phys 29(6):952–959
23. Seco J, Evans PM, Webb S (2002) An optimization algorithm that incorporates IMRT delivery constraints. Phys Med Biol 47(6):899–915
24. Cho PS, Marks RJ II (2000) Hardware-sensitive optimization for intensity modulated radiotherapy. Phys Med Biol 45(2):429–440
25. Bortfeld T, Schlegel W, Rhein B (1993) Decomposition of pencil beam kernels for fast dose calculations in three-dimensional treatment planning. Med Phys 20(2 Pt 1):311–318
26. Chui CS, Mohan R (1988) Extraction of pencil beam kernels by the deconvolution method. Med Phys 15(2): 138–144
27. Niemierko A, Goitein M (1989) The use of variable grid spacing to accelerate dose calculations. Med Phys 16(3): 357–366
28. Niemierko A, Goitein M (1990) Random sampling for evaluating treatment plans. Med Phys 17(5):753–762
29. Lu XQ, Chin LM (1993) Sampling techniques for the evaluation of treatment plans. Med Phys 20(1):151–161
30. Shepard DM et al. (2002) Direct aperture optimization: a turnkey solution for step-and-shoot IMRT. Med Phys 29(6):1007–1018
31. Chen Y et al. (2002) A deterministic iterative least-squares algorithm for beam weight optimization in conformal radiotherapy. Phys Med Biol 47(10):1647–1658
32. De Gersem W et al. (2001) An anatomy-based beam segmentation tool for intensity-modulated radiation therapy and its application to head-and-neck cancer. Int J Radiat Oncol Biol Phys 51(3):849–859
33. Webb S, Oldham M (1996) A method to study the characteristics of 3D dose distributions created by superposition of many intensity-modulated beams delivered via a slit aperture with multiple absorbing vanes. Phys Med Biol 41(10):2135–2153
34. Jeraj R, Keall P (1999) Monte Carlo-based inverse treatment planning. Phys Med Biol 44(8):1885–1896
35. Cho PS, Phillips MH (2001) Reduction of computational dimensionality in inverse radiotherapy planning using sparse matrix operations. Phys Med Biol 46(5)N117–N125
36. Thieke C et al. (2002) Acceleration of intensity-modulated radiotherapy dose calculation by importance sampling of the calculation matrices. Med Phys 29(5):676–681
37. Renner WD et al. (2003) A dose delivery verification method for conventional and intensity-modulated radiation therapy using measured field fluence distributions. Med Phys 30(11):2996–3005
38. Vineberg K et al. (2002) IMRT plans robust to setup error and motion: Explicit incorporation of clinical setup data using the multiple instance of geometry approximation (MIGA). Int J Radiat Oncol Biol Phys 54(2S):255
39. Leong J (1987) Implementation of random positioning error in computerised radiation treatment planning systems as a result of fractionation. Phys Med Biol 32(3):327–334
40. Beckham WA, Keall PJ, Siebers JV (2002) A fluence-convolution method to calculate radiation therapy dose distributions that incorporate random set-up error. Phys Med Biol 47(19):3465–3473
41. Jeraj R, Keall PJ, Siebers JV (2002) The effect of dose calculation accuracy on inverse treatment planning. Phys Med Biol 47(3):391–407
42. Siebers JV et al. (2002) Reducing dose calculation time for accurate iterative IMRT planning. Med Phys 29(2):231–237
43. Ma CM et al. (2000) Monte Carlo verification of IMRT dose distributions from a commercial treatment planning optimization system. Phys Med Biol 45(9):2483–2495
44. Wang L, Yorke E, Chui CS (2002) Monte Carlo evaluation of 6 MV intensity modulated radiotherapy plans for head and neck and lung treatments. Med Phys 29(11):2705–2717

45. Pawlicki T, Ma CM (2001) Monte Carlo simulation for MLC-based intensity-modulated radiotherapy. Med Dosim 26(2):157–168
46. Laub WU, Bakai A, Nusslin F (2001) Intensity modulated irradiation of a thorax phantom: comparisons between measurements, Monte Carlo calculations and pencil beam calculations. Phys Med Biol 46(6):1695–1706
47. Fippel M (1999) Fast Monte Carlo dose calculation for photon beams based on the VMC electron algorithm. Med Phys 26(8):1466–1475
48. Fippel M et al. (2000) Inverse treatment planning for radiation therapy based on fast Monte Carlo dose calculation. In: Monte Carlo 2000 Conference, Lisbon. Springer, Berlin Heidelberg New York
49. Kawrakow I, Fippel M (2000) VMC++, a fast MC algorithm for Radiation Treatment planning. In: XIII International Conference on the Use of Computers in Radiation Therapy. Springer, Berlin Heidelberg New York
50. Sempau J, Bielajew AF (2000) Towards the elimination of Monte Carlo statistical fluctuation from dose volume histograms for radiotherapy treatment planning. Phys Med Biol 45(1):131–157
51. Deasy JO (2000) Denoising of electron beam Monte Carlo dose distributions using digital filtering techniques. Phys Med Biol 45(7):1765–1779
52. Kawrakow I (2002) On the de-noising of Monte Carlo calculated dose distributions. Phys Med Biol 47(17):3087–3103

IMRT Delivery Techniques

Steve Webb

7

Contents

7.1 Introduction

When a patient is first diagnosed with cancer their hope is to be cured with a minimum of side effects. When treatment comprises radiotherapy these words translate in the doctor's mind to the goal of maximising tumour control probability whilst simultaneously minimising normal tissue complication probability. The physicist further translates to a goal of obtaining a high dose within the tumour and as low a dose as reasonably achievable (ALARA principle) elsewhere. After these two translations most patients would no longer understand the language describing their hopes.

The goal of creating a high-dose in the tumour, specified as wrapping the 95% isodose shell around the volume like a piece of clingfilm, has itself been known and understood for over a century. There is nothing new with the goal; rather it is our current ability to *achieve or closely approximate* the goal which has lent to the phrase conformal radiation therapy (CFRT) an unwarranted novelty. Intensity-modulated radiation therapy (IMRT) is the latest in a long chain of developments in improving the physical basis of radiotherapy that comes closer to the goal [1–4].

The success of IMRT is a consequence of improvements and developments in all the links of the radiotherapy chain. This starts with 3D imaging, identifying and contouring targets and structures to avoid, deciding the treatment goals in terms of dose or some biological substitute, planning and optimising planning, delivery and clinical evaluation, trial and assessment. As the reader studies IMRT, here in this book conveniently divided into chapters on individual links in the chain, it is important to remember the strength of the chain lies in the linkages. Hence IMRT delivery should not be studied in isolation; indeed in recent years it specifically requires to enter into the planning considerations as we shall see below.

No committee or Society adopted or defined the nomenclature "IMRT". Hence there is some debate what it strictly means. Didactically a beam with a block is "modulated" in that the primary fluence is either "off" or "on", ignoring leakage. Additionally, or alternatively, pieces of metal in the field, generating wedge-shaped dose distributions, also modulate fluence. I choose to *not* describe these as IMRT. To me IMRT implies the use of several fields, each with a modulated intensity, specified as a matrix of beam elements (bixels) of different fluence, probably on a fine spatial scale and with either a coarse or fine fluence increment scale. If I had been writing a few years ago I would have said that IMRT requires inverse planning, but now this is not strictly true and there are many modifications of forward planning that serve to generate modulated beams. An example is Direct Aperture Optimisation [5].

Let us consider that some planning technique has led to a set of two-dimensional field shapes each with modulated intensity within bixels (see chapter I. 4). A convenient representation is shown in Fig. 1 where

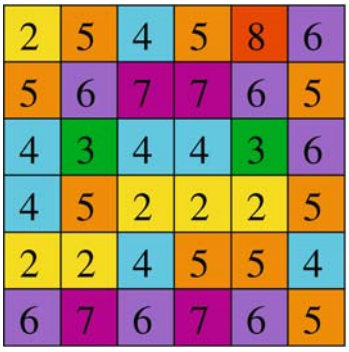

Fig. 1. IMRT is the delivery of modulated fields. Planning systems generate maps of varying MUs per beam element (bixel); e.g. CORVUS might generate something like this which is to be viewed as an example rather than the outcome of a specific planning case. Delivery can be colloquially regarded as "painting by numbers"

IMRT is literally "painting by numbers". Mathematically the problem of delivery is now to arrange irradiation so the combined effects of direct primary radiation, transmitted leakage and scatter add up to the defined pattern. This may be either through irradiating bixels for different times or by placing attenuating materials in the path of otherwise unattenuated rays.

In general it is a somewhat intractable problem to solve for the full irradiation physics so instead workers tend to find solutions which will reproduce the pattern of primary intensities. A variety of *a-posteriori* "fixes" are then introduced to cater for the complete physics. This would enrage a pure mathematician but it is common practice largely because the solution of the complete problem may be very difficult or even impossible. Most practices in radiation therapy are approximations to what is really required together with elaborate investigations of the consequences.

With this in mind the main methods to deliver a modulated field as part of an IMRT treatment are:

- The metal compensator
- A multileaf collimator (MLC) operating in multiple-static-field (MSF) mode
- A MLC operating in dynamic mode (the DMLC technique)
- Intensity modulated arc therapy (IMAT)
- Slice-based tomotherapy with a *m*ultivane *i*ntensity *m*odulat*i*ng *c*ollimator (MIMiC)
- Spiral tomotherapy
- The Cyberknife
- Non-MLC-based techniques (concepts)

The following sections examine each of these in turn.

7.2 The Metal Compensator

The metal compensator is the Cinderella of IMRT, somewhat overlooked but still with much potential. It relies on placing in an otherwise uniform beam an absorber of varying thickness in the direction of the ray propagation. Generally it is made of just one material of linear attenuation coefficient μ_E depending on energy E such that the primary intensity after rays pass through a thickness d becomes $I = I_0 \exp(-(\mu_E d))$ where I_0 is the target-side intensity. By varying the thickness d, the intensity is thus modulated. What could be simpler? There is no limitation due to the finite size of any collimator leaves. There is no limitation due to the accuracy of leaf placement. There are no tongue-and-groove artefacts. There is no quantisation of fluence increment as there would be with a multiple-static-field technique (see later). The compensator has almost unit monitor unit efficiency (defined as the ratio of the peak MUs in a modulated field to the number of MUs required to deliver the field). Little can go wrong. Quality assurance is straightforward. One can actually see a representation of the intensity distribution (well: one actually sees the metal thickness which is related to the natural logarithm of the intensity variation). Although the compensator was invented, as its name suggests, to compensate for the fact that a patient surface is not flat, it effectively performs IMRT. So why replace it? Many workers do not want to [73, 74]. They are happy with this way of realising an intensity distribution and they need read little further in this chapter.

The main urge to replace the compensator centred on its equally obvious disadvantages. It has to be made for each field and for each treatment fraction. At one time this was time consuming, messy, hazardous and tedious. This may be less so now. Once made, the compensator has to be stored along with all the others for patients on treatment. They are bulky and storage equates to money in a busy hospital. They are heavy and have to be manipulated into the blocking tray. Moving large chunks of metal on a regular basis is not the best Health and Safety at Work Practice. In principle they could be misused (wrong patient, wrong field, wrong orientation) but this is unlikely because compensators can be coded mechanically to interact with checking software in the beam files. The spatial resolution is not in practice ultrafine – it depends on either the radius of the cutting tool (if machining metal) or the size of poured spheres and the width of the cutting wire of the machine making a mould for pouring. There is clearly a maximum sensible dynamic range if the compensator is not to be too thick.

It might be said that the urge to replace the compensator lies more with its somewhat anachronistic image. Surely in an era when one can use a computer to repeatedly generate field patterns that combine to give the required intensity variation then one should be doing this? We live at a time when we expect the electronic versions of everything to be better than their manual counterparts. This is a very modern and miniaturised industrial revolution analogous to the replacement of

Fig. 2. The basic building blocks of an Ellis compensator with some arranged to make a 1D modulated profile by the compensation technique

the cottage weavers with the Jacquard loom. And just as the mechanised Jacquard loom misbehaved from time to time and delivered the wrong pattern and the manual weaver temporarily was fêted as more reliable so the analogy with the compensator holds. At conferences, after every talk on quality assurance of a MLC someone in the audience will say "and what about the compensator?"

There are many ways to make a compensator. The earliest way was to make what is called an Ellis compensator (named after the British radiotherapist Frank Ellis), simply a stack of LEGO-like bricks of varying thickness. The number of bricks stacked vertically defined the dynamic range. The width of the bricks defined the spatial resolution and their height the intensity resolution (Fig. 2). Generally they were not focused to the source. To do so would have been very difficult and required several planes of bricks with the size varying from plane to plane [6]. Another way to make a compensator is to mill a metal block to the required shape. Another way to make a compensator is to cut out sheets of lead of different shapes and to glue them together (Fig. 3) to make a pattern [7]. A fourth way is to use a hot-wire

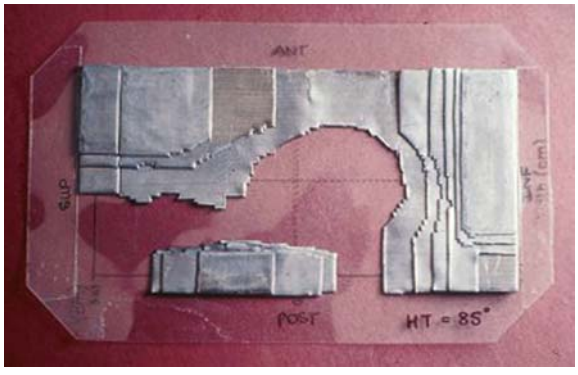

Fig. 3. How a compensator was constructed from thin lead sheets glued together in order to modulate the intensity of a tangential beam for improving the homogeneity of dose in breast radiation therapy (Courtesy of the Breast Technology Group, Royal Marsden NHS Foundation Trust)

cutting device to cut a mould of the required compensator shape out of tough Styrofoam and then to fill this with either lead or tungsten balls or a hot liquid melt which cools to the required shape. Yet another technique has been to use a series of pistons to stamp a pattern in a kind of heavy alloy putty [8]. This latter method is effectively reusable. Other workers have constructed carousels with several compensators per carousel [9]. Some compensators have been single per field.

7.3 Modulation Achieved Using the Jaws of the Accelerator

7.3.1 Dynamic Modulation

Intensity modulation (or more correctly fluence modulation [10]) can be achieved using just the jaws of an accelerator either in static or dynamic mode. This was done in the 1970s before the use of a MLC became commonplace [11]. In dynamic mode the longitudinal size of the modulated field could be fixed using one pair of jaws. Then a modulation would be created by dynamically sweeping the other pair of jaws with the radiation switched on. The "trailing jaw" chases the "leading jaw". Suppose that point x represents position across the field in the direction of the sweep. If the leading jaw uncovers this point at time $t_2(x)$ and the trailing jaw covers it at time $t_1(x)$, then the primary intensity at x is given simply by

$$I(x) = t_1(x) - t_2(x) \tag{1}$$

since this simply represents the period for which point x is exposed to the primary radiation from the source. The time "t" and the number M of monitor units (MU) are directly proportional for constant accelerator output. Hence sometimes one sees expressions such as

$$I(x) = M_1(x) - M_2(x) \tag{1a}$$

instead, equivalently. "Intensity" is often represented by MUs. Now by varying the speed of the leading and trailing jaw velocities a suitable modulation may be achieved [12].

Simple differentiation gives

$$\frac{\mathrm{d}I(x)}{\mathrm{d}x} = \frac{\mathrm{d}I}{\mathrm{d}t} \cdot \frac{\mathrm{d}t}{\mathrm{d}x} = \frac{\mathrm{d}I}{\mathrm{d}t} \Big/ \frac{\mathrm{d}x}{\mathrm{d}t} \tag{1b}$$

which indicates that, when the gradient $\mathrm{d}I(x)/\mathrm{d}x$ is large, the velocity $\mathrm{d}x/\mathrm{d}t$ of jaws is small. Conversely, for a small spatial gradient $\mathrm{d}I(x)/\mathrm{d}x$, the velocity $\mathrm{d}x/\mathrm{d}t$ of jaws is large. Hence, given that the jaws must have a maximum velocity $\updownarrow$, some modulations with small spatial gradients may not be achievable if $\mathrm{d}I/\mathrm{d}t$ is fixed.

From (1),

$$\frac{\mathrm{d}I(x)}{\mathrm{d}x} = \frac{\mathrm{d}t_1}{\mathrm{d}x} - \frac{\mathrm{d}t_2}{\mathrm{d}x} = \frac{1}{V_1(x)} - \frac{1}{V_2(x)} \,. \tag{2}$$

It can be shown that when $\mathrm{d}I(x)/\mathrm{d}x > 0$ the leading jaw should move at maximum velocity. Then the modulation of the velocity of the trailing leaf is

$$V_1(x) = \frac{\overset{\wedge}{\vee}}{1 + \overset{\wedge}{\vee} \frac{\mathrm{d}I(x)}{\mathrm{d}x}} \quad \text{and} \quad V_2(x) = \overset{\wedge}{\vee} \,. \tag{3}$$

Conversely, when $\mathrm{d}I(x)/\mathrm{d}x < 0$ the trailing jaw should move at maximum velocity $V_1(x) = \overset{\wedge}{\vee}$ and the modulation of the velocity of the leading jaw is

$$V_2(x) = \frac{\overset{\wedge}{\vee}}{1 - \overset{\wedge}{\vee} \frac{\mathrm{d}I(x)}{\mathrm{d}x}} \,. \tag{4}$$

These equations ensure that the delivery is completed in minimum time. The proof of these can be found in [13–15]. These relationships were independently and simultaneously discovered in Heidelberg, New York and Stockholm in 1994 (Fig. 4).

Consider the case when $\mathrm{d}I(x)/\mathrm{d}x > 0$ and $V_2(x) = \overset{\wedge}{\vee}$ and $V_1(x) = \overset{\wedge}{\vee} / \left(1 + \overset{\wedge}{\vee} \frac{\mathrm{d}I(x)}{\mathrm{d}x}\right)$.

Clearly $V_1(x)$ must be $\leq \overset{\wedge}{\vee}$, i. e.

$$\frac{\overset{\wedge}{\vee}}{1 + \overset{\wedge}{\vee} \frac{\mathrm{d}I(x)}{\mathrm{d}x}} \leq \overset{\wedge}{\vee} \,, \tag{5}$$

which can always be met. So the use of two jaws would permit all modulations to be achieved. A similar argument holds for $\mathrm{d}I(x)/\mathrm{d}x < 0$ when

$$V_2(x) = \frac{\overset{\wedge}{\vee}}{1 - \overset{\wedge}{\vee} \frac{\mathrm{d}I(x)}{\mathrm{d}x}} \leq \overset{\wedge}{\vee} \tag{6}$$

is always satisfied.

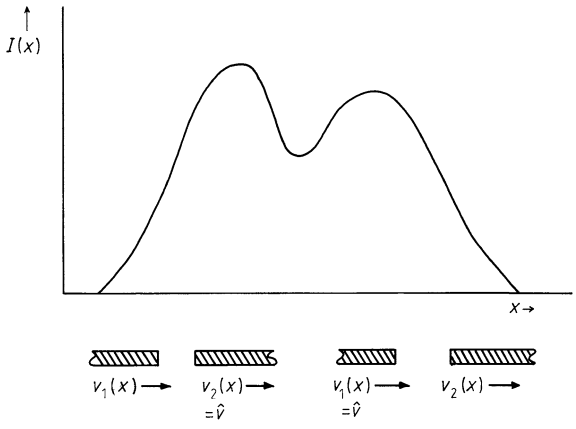

Fig. 4. When the gradient $\mathrm{d}I/\mathrm{d}x$ of the intensity profile $I(x)$ is positive, the leading leaf (2) should move at the maximum velocity $\overset{\wedge}{\vee}$; conversely when the gradient $\mathrm{d}I/\mathrm{d}x$ of the intensity profile $I(x)$ is negative the trailing leaf (1) should move at the maximum velocity $\overset{\wedge}{\vee}$. The velocity equations ((6) and (7)) are illustrated by showing a schematic of the pair of leaves in two separate locations delivering the IMB profile shown in the *upper part* of the figure

These are not the only equations that would lead to a particular specified modulation. It is clear that any arbitrary time can be added to both $t_1(x)$ and $t_2(x)$ without affecting the modulation. Also if the requirement for one jaw to move at maximum speed $\overset{\wedge}{\vee}$ were relaxed, other equations of motion would arise, e.g. suppose $\mathrm{d}I(x)/\mathrm{d}x > 0$ and $V_2(x) = \overset{\wedge}{\vee}/a$ were selected with $a > 1$. Then the trailing jaw requires to move at speed

$$V_1(x) = \frac{\overset{\wedge}{\vee}}{a + \overset{\wedge}{\vee} \frac{\mathrm{d}I(x)}{\mathrm{d}x}} \tag{7}$$

and the condition that $V_1(x) \leq \overset{\wedge}{\vee}/a$ is still satisfied and the modulation can still be achieved. However, with $a > 1$ the overall delivery time would be longer.

Modulation by jaw movement was rarely performed clinically because accelerator jaws were not computer controlled in the 1970s. Hence deliveries were performed in just a few research centres such as the Joint Centre for Radiation Therapy, Boston, USA [11].

These expressions also only relate to the experimental realisation of the primary fluence. If the jaws have transmission τ and the total irradiation time is T then an additional leakage intensity at point x of

$$L(x) = \big(T - I(x)\big)\,\tau \tag{8}$$

will arise.

However, this apparent nuisance can be overcome by defining a modified intensity profile $i(x)$ and fitting the jaw motion instead to this: i. e. we arrange that

$$L(x) + i(x) = I(x) \,, \tag{9}$$

i. e.

$$[T - i(x)]\,\tau + i(x) = I(x) \,, \tag{10}$$

i. e.

$$i(x) = \frac{I(x) - T\tau}{1 - \tau} \,. \tag{11}$$

It is then this *modified* intensity profile $i(x)$ which is used on the l.h.s. of (1) and all deduced equations for leaf velocity. Hence the leakage can be used positively and is not a major problem. However, it should be noticed that this means that zero and certain low intensities cannot be obtained. Clearly we require that $i(x) \geq 0$ i. e. $I(x) \geq T\tau$. In this sense leakage *is* a problem. It can be minimised by keeping the total irradiation time T as short as possible and using thick jaws to keep τ as small as possible.

Additionally, the head scatter is a function of field size and this requires an iterative correction loop to ensure that, as far as possible, the sum of primary fluence, leakage fluence and head-scatter fluence is the required overall planned fluence.

Modulation with moving jaws is one-dimensional. As described, the modulation is transaxial to the patient if the couch is normal to the face of gantry rotation. If

instead the roles of the two jaw sets were reversed, the modulation could be made longitudinal instead.

7.3.2 Static Modulation

Jaws can also be used to create an intensity modulation in multiple-static-field mode. Following the same principles as above, the transaxial jaws could take up different locations whilst the radiation beam is switched off and the beam switched on for variable time with the jaws set to be at each location. The sum of the open area irradiations then create the modulation. Suppose there are M rectangular open fields with the left (or trailing) jaw location L_m and right (or leading) jaw location R_m for the m-th sub-field ($m = 1, 2 \ldots M$). Let t_m be the time (or monitor units) of the m-th sub-field. Then the primary intensity at x is

$$I(x) = \sum_{m=1}^{M} t_m \delta(L_m, R_m) \tag{12}$$

where

$$\delta(L_m, R_m) = \begin{cases} 1 & \text{if } L_m < x < R_m \\ 0 & \text{otherwise.} \end{cases}$$

Additionally the transmission leakage is

$$L(x) = \tau \sum_{m=1}^{M} t_m \left(1 - \delta(L_m, R_m)\right) \tag{13}$$

Head scatter also contributes. In general it is not now possible to perfectly obtain the required intensity pattern but small adjustments can be made in an iterative way to minimise the difference between the required planned modulation and that delivered. The principles are discussed (in a somewhat different context) in [16]. Two-dimensional MSF jaw IMRT can also be achieved by varying the position of all four jaws for each field component (call the other two superior (S_m) and inferior (I_m) jaws).

Then

$$I(x, y) = \sum_{m=1}^{M} t_m \delta(L_m, R_m, S_m, I_m) \tag{14}$$

where $\delta(L_m, R_m, S_m, I_m) = 1$ if $L_m < x < R_m$ and $S_m < y < I_m$ where the y coordinate is orthogonal to x and increasing from superior to inferior orientations. Correspondingly, the leakage is *not* simply an extension of (13) since

$$L(x, y) \neq \tau \sum_{m=1}^{M} t_m \left(1 - \delta(L_m, R_m, S_m, I_m)\right) \tag{15}$$

because for some sub-fields *one* jaw will shield (x, y) whereas for others *both* jaws will shield (x, y). The required expression is more complicated, as follows.

If the L, R jaws have leakage transmission τ_{LR} and the S, I jaws have leakage transmission τ_{SI} then

$$L(x, y) = \sum_{m=1}^{M} t_m \left(1 - \delta(L_m, R_m, S_m, I_m)\right) \tau_m \tag{16}$$

where $\tau_m = \tau_{LR}$ if $S_m < y < I_m$ and either $x < L_m$ or $x > R_m$ and $\tau_m = \tau_{SI}$ if $L_m < x < R_m$ and either $y < S_m$ or $y > I_m$ and $\tau_m = \tau_{LR} \times \tau_{SI}$ if both of (either $x < L_m$ or $x > R_m$) and (either $y < S_m$ or $y > I_m$) are true. Again in 2D it is not possible to perfectly deliver any specified modulation without recourse to iteration to account for the scatter physics.

Whilst it is inherently obvious that jaws can create a modulated intensity in principle, would anyone do this in practice? First a "decomposition algorithm" or "stripping algorithm" would be required to compute the subfields and their intensities which sum to the required modulation. There is no single set of subfields that generate any given modulated intensity pattern and the exact set that emerge would depend on the algorithm. A convenient choice is to strip off from the required pattern, at each cycle of decomposition, the largest area subfield to create a residual pattern, continuing the process until the residual field is empty. Of course, this only creates the subfields whose primary intensities sum to what is required. Dai and Hu [17] investigated the efficiency of this process for random integer patterns of different spatial dimensions and of different peak value. The results were confirmed by Webb [18,19]. Plots of the mean number of monitor units and mean number of subfields were created for decompositions of a large number of such random patterns. The conclusion of such studies was somewhat surprising namely that jaw-only (JO) – IMRT was possible with an efficiency about four times worse than using an MLC (depending on peak intensity and area of pattern). It was, however concluded [18–21], that this would effectively rule out JO IMRT in practice and an additional mechanism was proposed, the use of a tertiary mask to improve the delivery efficiency. We shall return to this later. In passing, one should comment that, in principle, each bixel could be sequentially delivered, one by one, but no one would do this as it would be ludicrously inefficient. As far as is known no one has yet solved the stripping problem with transmission leakage factored in, nor with head scatter. Clearly the larger the number of components the larger the overall treatment time and the more problematic leakage becomes.

7.4 IMRT Using an MLC

The reader may wonder why the jaw-only method of delivering IMRT has been discussed at such length given that the technique is negligibly used clinically. There are several reasons. First, it was historically first. Second,

this approach nicely de-emphasises the phenomenological improvement from use of the MLC. The techniques of using the MLC for IMRT are fundamentally identical, per leaf pair, to those using the jaws (and so will not be repeated here). Instead we shall emphasise the differences and the reasons why IMRT with an MLC is a clinical reality whereas with jaws it is not.

7.4.1 MSF–MLC Static IMRT

This technique goes under the names "step and shoot" or "stop and shoot". The multileaf collimator (MLC) is conceptually the outcome of sawing up one pair of jaws into a set of adjacent and independently controllable "jaw-lets". It was never designed nor intended for IMRT so in this sense is a remarkable implementation for an important clinical purpose of an undesigned-for-purpose piece of equipment. It was designed as a field shaper to replace the use of blocks. Because each finger (leaf) of the MLC can be independently moved, a field pattern with stepped edges can be created. Because of scatter and electron transport these sharp steps become blurred with depth in tissue. The MLC was patented in 1959 [22], first commercially developed by Scanditronix in the mid-1980s and did not come into widespread clinical use until the early to mid 1990s. I like to cite this to emphasise to impatient observers that there is often a long period between invention and refined clinical implementation and that this is necessarily so. In fairness, it should be said that modern MLCs as available from Elekta, Siemens and Varian *have* been re-engineered with IMRT in mind (Table 1).

If we consider the single transaxial slice corresponding to the projection of just one leaf pair, then a modulated 1D field can be created by superimposing sub fields created by a series of left (L_m) and right (R_m) leaf positions. All the expressions presented earlier for jaws identically apply for this leaf pair, track or channel and again for all such leaf pairs. The easiest way to visualise this process is to imagine the 1D fluence profile as a series of M equal-fluence-increment steps (Fig. 5). There will be M "up steps" and of course M "down steps". There is a very large number of ways of experimentally realising such a modulation. If there is a single peak there are $(M!)^2$ ways [23] and, if multiple peaks, the number of permutations and combinations is more complicated. The expressions were derived and discussed by Webb [24, 25]. Suffice it here to say this number is still very large. This is because for each subfield any "up step" can be paired with any "down step" which is further to its right and with one or more peaks between them. Despite this flexibility a popular (and historically the first used) choice is to pair the first "up step" with the first "down step" and so on sequentially. This ensures the leaf pair always travels unidirectionally. Figure 6 illustrates this. The method is often referred to as the Bortfeld and Boyer technique

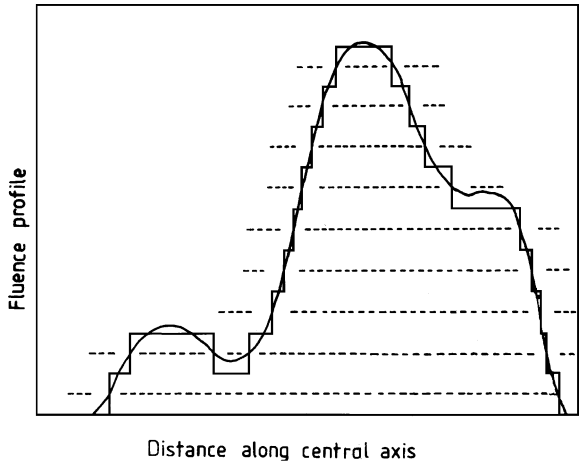

Fig. 5. How a 1-D intensity modulation may be created for a radiotherapy beam profile. The *horizontal axis* is the distance along the direction of travel of the leaf, measured at the isocentre of the beam (called a central axis in the transaxial cross-section of the patient). The *vertical axis* is X-ray fluence. The *solid line* is the intensity modulation expressed as a continuous function of distance, interpolated from the discrete modulation resulting from some method of inverse planning. The *horizontal dotted lines* are the discrete intervals of fluence. *Vertical lines* are created where the *dotted lines* intersect the continuous profile thus giving a set of discrete distances at which discrete fluence increments or decrements take place. These are realised by setting the left and right leaves of a MLC leaf-pair at these distances in either "close-in" or "leaf-sweep" technique. Note all left leaf settings occur at positions where the fluence is increasing and all right leaf settings occur at positions where the fluence is decreasing

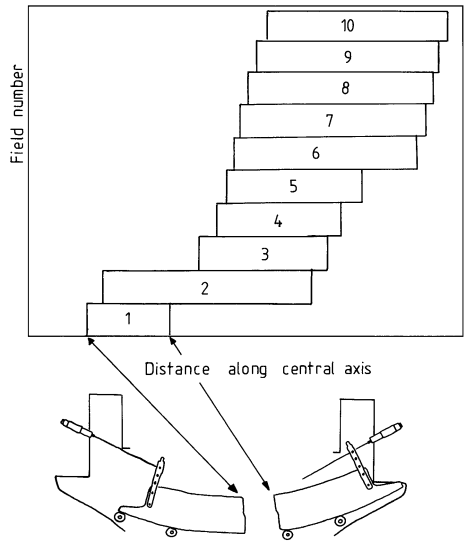

Fig. 6. The ten separate fields which when combined would give the distribution of fluence shown in Fig. 5. Each rectangle represents a field and the *left vertical edge* is the position of the left leaf and the *right vertical edge* is the position of the right leaf. This method of setting the leaves is known as the "leaf-sweep" technique. A schematic of a pair of MLC leaves is shown below the fields with *arrows* indicating the correspondence with the field edges

Table 1. Properties of commercial MLCs in Summer 2004

Manufacturer	Name of MLC	Number of leaves	Maximum field size at isocentre (cm^2)	Leaf width at isocentre	Leaf over-center travel (cm)	Leaf height (cm)	Max leaf speed (cm/s)	Weight (kg)	Suits which accelerator	Focus
Elekta (1)	Integrated MLC	80	40 × 40	1 cm	12.5		None specified		Elekta	Single
Elekta (2)	Beam modulator	80	16 × 22	4 mm	11.0		3	50	Elekta	Tilted
Siemens	Integrated MLC	58	40 × 40	1 cm; outer-most leaves 6.5 cm	10		2		Siemens	Double
Varian	Millennium MLC-120	120	40 × 40	Central 20 cm of field 0.5 cm	19.5		2.5		Varian	Single
				Outer 20 cm of field 1.0 cm	Max. leaf separation on each bank of leaves is 14.8					
	Millennium MLC-80	80	40 × 40	1 cm			2.5		Varian	Single
	Millennium MLC-52	52	26 × 40	1 cm			2.5		Varian	Single
BrainLab	m3	52	10 × 10	3.0 mm, 4.5 mm and 5.5 mm	5		1.5	35	Varian	Single
Radionics	MMLC	62	10 × 12	4.0 mm	5	7	2.5	38	All	Single
MRC Leibinger/ Siemens	Mini MLC	80	7.3 × 6.4 on a Siemens	1.6 mm	1.4	9	1.2	40	All	Parallel
MRC/Siemens	Moduleaf	80	12 × 10	2.5 mm	5.5	7	2.0	39.7	All	Single
3D Line (Wellhöfer)	Mini MLC	48	11 × 10	4.5 mm	2.5	8	1	35		Double
Direx	Acculeaf	72	11 × 10				1.5	27		Two sets of leaf pairs at 900

because Art Boyer and Thomas Bortfeld were first to describe this [26, 27]. They delivered such fields from several gantry angles to create a conformal dose to the representation of prostate in a "sliced bread phantom" comprising films sandwiched between water-equivalent patient shaped slabs. They digitised the films, plotted contours and compared these with the planned dose distributions. The delivery of each field component had to be done without the aid of a computer and was pioneering. Today we would recognise that this experiment is essentially the key tool in assuring the IMRT quality and it has been repeated in many centres, patient by patient [28]. This IMRT technique goes under the name "leaf sweep". It is the way in which IMRT is effectively delivered today by all three of the major MLC providers.

An alternative method is to "close in" on the peaks with leaves moving bi-directionally. Yet another is to deliver the first component by pairing the furthest-left "up step" with the furthest right "down step" and then the remaining (M-1) steps by leaf sweep. This has the advantage that a portal image of the whole delivery area could be taken with the first component for position verification.

A distinguishing feature of the step and shoot technique is that the transmitted leakage fluence will vary depending on the leaf pairing choices made. This might be exploited. For example one could seek the pattern which minimises this.

A key complication with MSF-MLC IMRT is that the 2D field delivery problem is only equal to the sum of 1D field delivery problems to first order. With a practical MLC there are limitations on the behaviour of individual leaf pairs and coupled adjacent leaf pairs. The earlier Elekta MLC prohibited any left leaf from coming closer than 1 cm to the paired right leaf or adjacent right leaf and also prohibited interdigitation (illustrated in Fig. 7). The Siemens leaves could just touch but not interdigitate whilst the Varian leaves could fully interdigitate. The newer Elekta MLC will be able to interdigitate. Thus the "solutions" for the field-pattern set for one leaf pair cannot be blindly joined to the solutions for the adjacent pair. In general "interpreters" are required. These are algebraic "recipes" whereby a modulated 2D field can be decomposed into a set of 2D MLC field patterns which do not violate the equipment constraints. Hence the interpreters tend to be manufacturer specific. Indeed it has been commonplace for each manufacturer to further develop and market one interpreter emanating from a collaborating university centre. Moreover once the problem was posed as a 2D decomposition problem, rather than a set of 1D problems, other algorithms have emerged based on stripping off areal patterns. An efficient one in terms of the number of patterns is the "power of 2 areal decomposition" of Xia and Verhey [29]. Plenty of others have been described. Indeed a kind of cottage industry subspecialty has grown up of theoreticians attacking this optimisation problem. The algorithms are intercompared with worst-case scenarios of random fluence patterns of varying size and varying number of fluence levels or peak value [30]. However it is now recognised their behaviours depend on the pattern being decomposed. The original Bortfeld–Boyer method generates the smallest number of MUs but not the lowest number of components. Webb [3] has reviewed this topic. Recently Langer et al. [31] have used integer arithmetic algorithms to create the "best ever" interpreter, which simultaneously minimises both the number of field components *and* the total number of MUs (which translates to minimising to overall treatment time). Note, however, that these are all methods to manipulate primary fluence maps. The reader might by now construe that here may be a case of the law of diminishing returns and it may not be useful to overdo further research in this area.

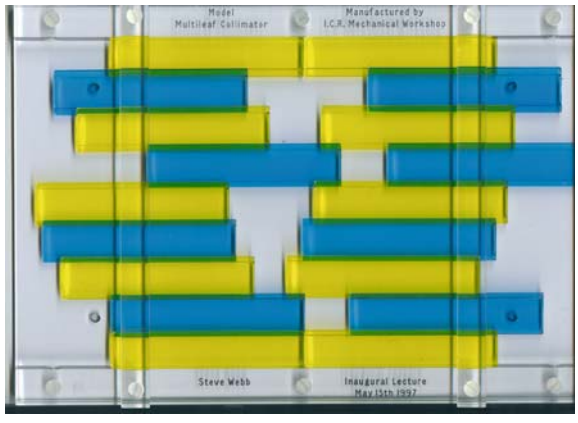

Fig. 7. Interdigitation using a plastic model MLC. The MLC comprises nine leaf pairs with alternate pairs shown in *yellow* and *blue*. The tongue and groove regions show *green*. Some leaf pairs are here arranged to demonstrate interdigitation

The leaf sides of MLC leaves have tongues and grooves (T-G) so when subfields are joined, tongue-and-groove artefacts (underdoses) can arise in the beam's-eye-view of these less-than-full-height leaf pairs [75–77]. This caused quite a stir a few years ago and it was shown that in general (although not necessarily for specific cases) it was not possible to solve the problem of finding a solution with zero T-G underdose [25]. Recently the T-G problem has been de-emphasised because, by suitable rotation of the collimator between fields at different gantry angle and by factoring in electron transport and patient motion the problem is, although still present, clinically insignificant [32]. Also, field decomposition algorithms have been proposed employing collimator rotation between subfields for any one field [33].

Mostly everything written here so far has assumed that IMRT is strictly compartmentalised into an equipment-independent planning stage followed

by a delivery-equipment-dependent interpretation for delivery. This is traditionally how IMRT has been conducted between its inception around 1988 and until the late 1990s. However, the problem of factoring in the effects of transmission leakage and head scatter have already been alluded to and so it was natural that, as time passed, the delivery constraints were built into the planning stage. This avoids any corruption of the otherwise optimised modulated field patterns. Then "what you plan is what you get" (WYPIWYG). Such planning properly accounts for the full physics of the process (so far as modelling the photon transport is accurate) and, since equipment constraints are built in, the plans are deliverable [34–36]. This is discussed in detail in chapter I. 4.

Before leaving this subject we should note that one of the main concerns about the step and shoot technique, especially in the early years of development, was the over-long intersegment deadtime; hence the desire to minimise the number of field components. Originally some 5 s or so long for the equipment of some manufacturers, this has been reduced to a second or so by the development of the fast tuning magnetron for Elekta IMRT [37]. Varian uses a gridded gun, which interrupts the beam when the leaf positions are adjusted. This leads to the appearance of the technique as almost dynamic and in this author's opinion the nomenclature/terminology is somewhat ill defined. I prefer MSF-MLC to refer to clearly definable segments with a recognisable finite time interval between them. The terminology also lends itself well to those clinical methods in which just a few subfields are added to "top up" the main delivery as appropriate to some forms of breast IMRT [38]. It also describes "field within a field" as originally proposed independently by Boyer et al. [39] and Webb [40] and as used clinically at (e.g.) NKI [41], Ghent [42], U Michigan [43] and William Beaumont Hospital [44].

Finally a quite new concept has recently emerged of Direct Aperture Optimisation (DAO) in which the shape and intensity increment of a geometrically shaped patch became the planning optimisation variables. The sub fields so planned are directly deliverable by the MSF-MLC technique [5].

7.4.2 Dynamic MLC (DMLC) IMRT

Just as the MSF-MLC static IMRT technique is to first order the sum of the 1D static deliveries so, once again, the 2D DMLC delivery technique is to first order the sum of the 1D dynamic deliveries and the equations specified for dynamic jaw delivery apply. This technique necessarily sequentially follows planning. For some accelerations and modulation patterns the limitations of the equipment geometry mean that the leaves cannot alone deliver the modulation and an interpreter combining the use of leaves and jaws is required (e.g. [45]). Historically this was the first MLC technique available from Elekta who now, like the other manufacturers, offer step and shoot. The interpreter needs to include an iterative loop to factor in the transmission leakage and the head scatter [46]. Interestingly, the tongue-and-groove problem is completely soluble for the DMLC technique because leaf synchronisation achieves a situation in which the fluence in the BEV of the tongues and grooves is always between that in adjacent leaf tracks at each and every position x [47,48]. The dosimetry of the DMLC methode particularly for small field components was disscussed by [78]. Large modulated fields must be addressed by field splitting [80, 88, 89].

7.4.3 IMAT

Intensity-modulated arc therapy (IMAT) invented by Yu [23] is a logical development of the MSF-MLC method. Suppose that, for each of A gantry angles, each modulated field comprises M subfield components. IMAT rotates the gantry M times delivering just one component from each gantry angle at each rotation. The principle is that the components are chosen to minimise the leaf movement from one gantry location to the next. This exploits the huge degeneracy in field decomposition mentioned earlier and the linearity of delivery whereby the order of delivering components is immaterial. The novelty of IMAT was somewhat held back initially due to the absence of a matched planning technique, a problem now solved [49]. Both for IMAT (now offered commercially by Elekta) and the MSF-MLC method studies have been done to attempt to reduce the number of fluence levels or components and (for IMAT) in some circumstances as few as three rotations have been sufficient [50].

7.4.4 The MLC Itself

As mentioned earlier the MLC was initially designed as an attempt to make an automatic field shaper. In fact the patented design from Gscheidlen [22] had four sets of leaves all in one plane (Fig. 8). A template was offered up and assorted wheels, cams and push rods swung into action to move the leaves until they just touched the template which was then removed and the leaves locked, very much the "steam age" of the MLC with not a computer in sight. Even 30 years later, when the first motorised MLCs started to be commercially manufactured, their controlling electronics was not linked to the computer control of the accelerator and certainly not linked to that of the planning system. Such MLCs were press-ganged into service for IMRT (but worked). Today we are seeing MLCs truly designed for IMRT with appropriate tongue-and-groove design

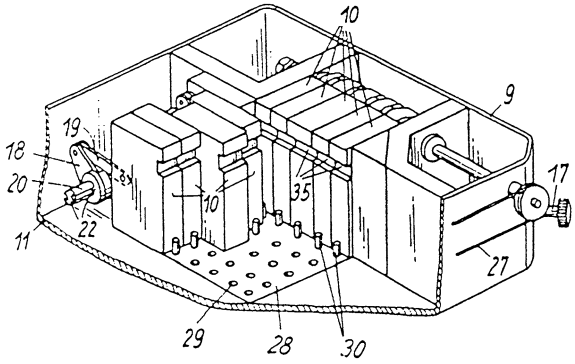

Fig. 8. Schematic view of Gscheidlen's multileaf collimator patented in 1959, showing just two of the four sets of leaves. The manual actuating mechanism and the template for setting the field shape may be seen, as well as some of the guide bars (from [22])

to minimise interleaf leakage, appropriate thickness to minimise interleaf transmission leakage, appropriate interdigitation facility, suitable maximum leaf speeds, some with narrower leaves for finer definition of fields, leaves that can overtravel the midline and all with computer control integrated into the main computer control of the accelerator. Generally, although not always, the driving instructions can be generated by, or at least interfaced to, the planning system computer. MLCs are, like cars, continually being refined. My earlier reviews [1–3] benchmarked the situation at those dates. Table 1 is the most up to date compilation. Other useful reviews are those by Galvin [51] and Bortfeld et al. [52] and the subject of MLC leaf width has been discussed by [79, 81–83, 87].

7.5 Tomotherapy

Historically, clinical IMRT by tomotherapy preceded clinical IMRT by any MLC-based technique by about four years and well into the twenty-first century the number of patients treated worldwise by tomotherapy exceeded that by MLC-based-methods. At the time of writing it has become impossible to continue counting (early on companies knew and issued statistics of number of "installed bases" and patients treated) but my guess would be that now the situation has reversed and MLC-based methods have the greater "market share of clinical IMRT". It may then seem unusual to have reviewed MLC-based methods first but this was because they naturally linked to the much older jaw-based methods and also because this is not intended to be strictly historically chronological (see [53] for historical review). Several IMRT delivery methods were being developed in parallel. Certainly they did not grow out of each other (see further comment later).

7.5.1 Slice-based "Static" Tomotherapy

In "slice-based" or "static" or "step and shoot" tomotherapy the patient and couch are static with respect to the gantry, which rotates continuously through 270° with the radiation beam on. The radiation is collimated to a narrow fan defining a transaxial slice of the patient assuming the couch is in its default position. The fan presents as a narrow rectangular slit aperture much wider transaxially than longitudinally. The thin rectangle of radiation is divided into two further rectangular

Table 2. Features of IMRT delivery techniques

Technique	First research use	First clinical use	Spatial resolution is limited by (as well as focal spot)	Delivering MU efficiency ∝ 1/delivery time	Dynamic range
Compensator	1930s	1930s	Cutter and/or ball size and or drill size	Close to 1	Continuous
MLC step & shoot or MSF	1993	1997	Across leaf: leaf width; along leaf: precision of leaf setting	Typically 0.3	Depends on number of levels/segments
MLC dynamic	1994	1995	Across leaf: leaf width; along leaf: precision of leaf setting		Effectively continuous
MIMiC tomotherapy	1992	1994	Vane size across field; slit width along field	Typically 0.1	10%
IMAT	1995	2001	Across leaf: leaf width; along leaf: precision of leaf setting	Typically 0.3	Depends on number of rotations
Helical tomotherapy	1993	2002	Vane size across field. None longitudinally	Typically 0.1	1.5%
Cyberknife	1994	1994	Smallest collimator size	Typically <0.05	Effectively continuous

slices of the same transaxial width and each half the longitudinal length of the main aperture. Each of these is further divided into 20 beam elements. 2×20 small fingers of attenuators, 8 cm in height, can be driven into and out of the field by electropneumatic action and the variable dwelltime of each creates the spatial modulation. Each of these two slices is separately modulated by its set of 20 attenuators. As the gantry rotates over 270° the status of each modulator ("in" or "out") can be adjusted every 0.5° and so over 5° the fluence profile can be built in increments which are 10% of maximum. From the view of the tumour the effect is as if a static modulation had been delivered every 5° at fixed midpoint positions (i.e. 2.5°, 7.5°, 12.5° etc.). This collimator, the *m*ultivane *i*ntensity *m*odulat *i*ng *c*ollimator (MIMiC) was designed by the NOMOS Corporation (previously called MEDCO) to retrofit to any accelerator (Fig. 9). The vane motion is controlled by instructions from an onboard computer which itself accepts a disc of vane-driving instructions generated by the planning system CORVUS (formerly called PEACOCKPLAN). There is no interface to the outside room. The gantry orientation is sensed by gravity-driven inclinometers. Both subslices are delivered simultaneously and automatically. The positions of the vanes is recorded for a posteriori review and any departure from plan leads to radiation-off status from which subsequent recovery is possible. The only additional controls are the high-pressure umbilicals and the power umbilical. The slice width can be adjusted by a factor of 2. After irradiation of two slices the patient must be incremented on the couch with respect to the gantry, and repeatedly so, until the full longitudinal extent of the tumour has been treated. The accuracy of this matchline has been an issue and the CRANE device ensures longitudinal incremental accuracy to 0.1 mm.

The MIMiC and PEACOCKPLAN were first announced at the 1992 Calgary ASTRO conference and at the conference at the World Health Organisation in Geneva in October 1992 [54]. A striking feature was that the system, when announced, was almost ready for use and the first patient was treated in March 1994 at Baylor College of Medicine, Houston, Texas. In the following three years over a hundred such installations were brought into clinical use. The world's first conference on IMRT was held in Durango, Colorado in May 1996 with the proceedings published as the first book with IMRT in its title [55]. The conference was filmed with videotape sets distributed to users. The planning system was based on the work of Webb [56] using simulated annealing although it was independently developed and, as all planning systems, underwent many significant modifications. A 2D MIMiC comprising inflatable mercury-fillable balloons was engineered in the factory and a prototype constructed but it was never marketed [57]. In time the NOMOS Corporation became less of a one-product company and diversified into the planning of IMRT by the DMLC technique. For reasons that are hard to determine the MIMiC-based IMRT did not really take off clinically outside of the

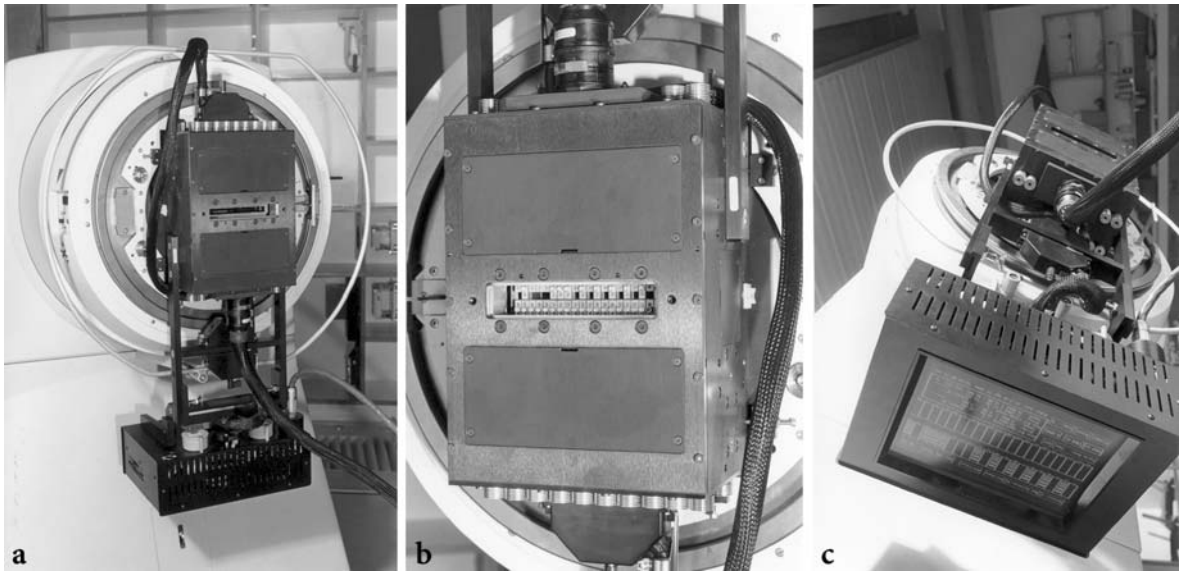

Fig. 9. a,c General views showing the NOMOS MIMiC collimator plus the computer which controls the movement of the leaves. The computer is mounted on two arms which protrude from the MIMiC. The computer is controlled via a touch-screen and has a floppy disk drive for the disk which contains the information for changing the leaf positions, determined by the CORVUS planning system. The two cables which can be seen are the airline and the electrical links to the equipment. These two cables rotate with the equipment. **b** The NOMOS MIMiC collimator attached to an Elekta SL25 linear accelerator at the Royal Marsden NHS Trust, Sutton, UK. The two sets (banks) of leaves (or vanes) can be seen with some open and some shut (loan of MIMiC courtesy of the NOMOS Corporation)

USA. The competition from MLC-based methods probably did not help because in the early years NOMOS concentrated on its US installed base and by the time diversification to Europe was attempted many European centres were developing DMLC IMRT or MSF-MLC IMRT.

7.5.2 Helical Tomotherapy

Helical tomotherapy is similar in that the radiation is collimated to a similarly narrow form defining a single slit of radiation with long axis transaxial to the patient. Within this single slice a single MIMiC with 64 not 20 elements modulates the field. As it does so, with the gantry continuously rotating, the patient is slowly translated through the field. So, in the frame of the patient, this is as if the slit beam executes a helical spiral trajectory. This is much more forgiving of any unwanted longitudinal movement of the patient. As with static tomotherapy, the modulation is determined from a matched planning system.

Additionally the use of a continuously rotating gantry combined with a megavoltage detector allows on-board MVCT. Sinograms so formed could also be compared with planned sinograms to allow some assessment and correction for patient mispositioning.

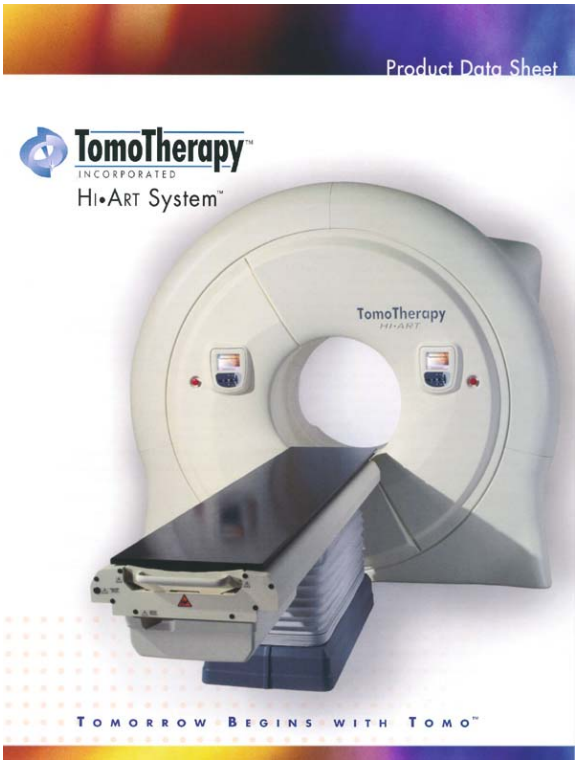

Fig. 10. The front cover of the brochure for the HI.ART Tomotherapy machine

The concept of spiral tomotherapy was announced in 1993 [58] and for ten years the development of research systems and the clinical prototype has taken place in the full gaze of the research community. A system treated the first patient in August 2002 and the originating University of Wisconsin spun off Tomotherapy Inc, a company that has built several more machines (Fig. 10) and at the time of writing is beginning to install these [59]. At the AAPM Summer School in 2003 on IMRT there was a great emphasis on spiral tomotherapy and some conjecture that this may replace other techniques (see later discussion). Although it was viewed once as a specialist tomotherapy tool, its supporters are now emphasising its ability to perform conventional radiotherapy and even multi focal whole body radiotherapy [60].

The concept of the MIMiC delivery device originated in the University of Wisconsin [61, 62] and its patents are licensed to the NOMOS Corporation. The two IMRT delivery techniques are generally reviewed together although there are distinctive differences.

7.6 The Cyberknife

The most recent arrival on the scene for clinical IMRT is the Accuracy Cyberknife (Fig. 11). This is an X-band short linear accelerator mounted on a robotic arm that has six degrees of freedom. In this way the beam from the accelerator can point into 1.6π of solid-angle space. The accelerator can be fitted with one of a set of collimators providing a circular beam. The diameter of this beam can be as small as 5 mm and as large as

Fig. 11. The Accuracy Cyberknife

60 mm. The design purpose of the machine was to deliver stereotactic radiotherapy with high precision, initially for intracranial sites and subsequently for extracranial corporal sites such as for paraspinal tumours. The delivery equipment is paired with a planning system, which commences with 1200 possible trajectories (100 "nodes" on the surface of a sphere each with 12 potential entry directions). Planning determines the minimum-number best set from these consistent with the conformality goals. The intensity for each beam can be adjusted.

By definition therefore the Cyberknife is a system for delivering a number of pencil beams of different fluence and from a set of directions such that the result is a highly conformal 3D dose distribution i. e. IMRT. In principle it is the most flexible of IMRT systems in that it does *not* predetermine a few fixed directions, compute the modulations and subsequently interpret these into a set of subfield patterns. However its initial clinical purpose perhaps shows the way the Cyberknife is viewed. Also, at the time of writing, there are a very few such systems compared with the scale of use of C-arm linacs. One potential major advantage of the Cyberknife is its coupling to the imaging systems which continuously monitor organ movement and feed this back to the robot [63] (see later).

7.7 Other IMRT Delivery Techniques

Not surprisingly, a number of other ways to deliver IMRT have been conceptualised. It is important to distinguish that these have in general not been turned into prototypes (with some exceptions) and certainly have not been adopted by manufacturers and brought into clinical service. For this reason they will not be reviewed in as much detail.

A 1D modulation can be formed by scanning an attenuating bar across the field with the bar dwelling at different locations x for a variable dwell time. Clearly the bar can only create a 1D modulation so it is analogous to the use of linac jaws. The spatial resolution relates to the width of the bar, hence there is a compromise between the width of the bar and the ability to generate any modulation at all. This concept has led to an engineering prototype [64].

When discussing the option to deliver IMRT with just the accelerator jaws mention was made of the improvement consequent on the use of a tertiary mask. This concept [18–20] aims to group bixels for simultaneous delivery, a grouping which could not be performed with jaws alone. The grouping would also not be possible with an MLC although the intention was to explore IMRT *without* the use of a MLC. It has been shown that this concept significantly reduces the number of field subcomponents and the treatment monitor units. Three concepts were explored, the use of a binary chequer-board mask, a pseudorandom binary mask and a set of relocatable single-bixel attenuators. The papers provide detail. These systems are not yet engineered. A further proposal is the variable aperture collimator (VAC) in which single bixel attenuators may be placed in variable parts of an otherwise open field to form components [20]. A prototype is being constructed [21].

Several groups have considered concepts of performing IMRT using one or more cobalt sources. Schreiner [65] has built a laboratory prototype on first-generation CT principles. Warrington and Adams [9] are building an automatic compensator carousel for IMRT on a cobalt machine. Barthold et al. [66] are developing a machine called CORA using a scanned arc of multiple cobalt sources. A possible application for the VAC is attached to a cobalt source machine (or even to the Cyberknife) to improve efficiency.

Finally in this section is mentioned the Scanditronix Racetrack Microtron with its scanned pencil beam of radiation of variable intensity. The system is not in widespread clinical use now.

7.8 Verification of IMRT Delivery Techniques

A much discussed concern with advanced conformal radiotherapy techniques is whether the delivered fluence is the planned fluence. This will be discussed in detail elsewhere in this book (see de Wagter and Moran/Xia chapters, this volume) but some comment is offered here and essential features of each technique are discussed. A distinction must be drawn between quality assurance of the equipment in general and quality assurance of an individual patient treatment delivery. This section mainly concerns the latter.

7.8.1 Compensator

The compensator is a clearly visible item so the only concern is to ensure it is the correct one for the particular patient and particular field. This can be ensured by providing locking pins which operate microswitches on the blocking tray where the compensator is located. The signals coded by these pins are then checked with the instructions in the file specifying the beam and agreement flags that delivery will be correct. If confirmation of the delivered fluence is required a film or EPID can record this for comparison with the prediction of the planning system. If conformation of the full 3D delivered dose is required then a "Bortfeld–Boyer experiment" (see above) can be done. Supporters of the compensator argue that its simplicity with no parts moving in time nor space ensures a safe, verifiable delivery for each frac-

tion. It could be argued that dosimetric verification of each fraction is unnecessary.

The main QA issues with compensators concern their fabrication and since these are so varied the QA techniques are specific to each method.

7.8.2 Jaws IMRT and MLC IMRT

If the delivery is via a series of multiple-static-sub-fields then each of these could be separately recorded by film or EPID. Scanned film data or electronic pictures can be summed to give a measure of the overall fluence map for comparison with the planning prediction. Alternatively if one subcomponent spans the whole irradiated field just this could be delivered. This should show enough anatomical detail to compare with a simulator film or a CT scout view. This will *not* of course verify the total delivered fluence.

If the delivery is dynamic then the goal is to measure a map of the overall fluence pattern and to compare it with that planned. This requires some form of integrating detector capable of rapid frame acquisition and integration. At least one group has also developed a way to calibrate such a 2D patient-attenuated fluence map with a second 2D map of patient-*un*attenuated fluence to reveal anatomical data for comparison with a simulator film or scout view [67, 68].

An alternative for both static and dynamic IMRT is to strap a film to the gantry head and/or to have some electronic monitor in the blocking tray to measure the fluence passing into the patient. All the above methods can provide hard copy to store in the patient's file. Moreover a "Bortfeld–Boyer experiment" could be performed to QA the whole IMRT process.

What can be done if an error at a particular fraction were detected? In principle the "dose delivered so far" could be computed, subtracted from the planned 3D dose and the patient replanned for the residual 3D dose [69]. The QA of the equipment is a large topic discussed elsewhere [84–86], see chapters I. 10 and I. 11.

7.8.3 Tomotherapy

For both static and dynamic tomotherapy QA focuses on a priori delivering the total fluence to a phantom for comparison with the plan. Additionally, during treatment, the movement of the vanes is monitored and gross error can initiate shutdown from which recovery is possible. During irradiation for spiral tomotherapy the delivered sinogram could be compared with that planned.

It is fashionable to talk about the QA of IMRT as a paradigm shift because whereas, for conventional radiotherapy with a few fixed fields, it has always been possible to check a light field to patient tattoos and reposition if necessary, there is more fear and other emotion attached to treatment techniques during which the attenuators move and spend variable amounts of time in different locations. Possibly this fear stems from a feeling of loss of control. However if the goal is to assure the overall quality of a treatment then there is no need to understand the detailed delivery mechanisms. This is somewhat analogous to flying a plane. No one checks every aeroplane function for every eventuality every flight. Instead key checks are made and the total confidence stems from process control at manufacture and service. A huge amount has been written about verification of IMRT fractions. Far less has been said about what exactly to do if delivery does *not* match planned expectations. This aspect should be studied more.

7.9 Final Observations

Three-dimensional medical imaging is an essential adjunct to all the components in the IMRT chain. Its use for planning and verification of IMRT has been covered elsewhere in this book. However, one other use deserves including in a chapter on delivery methods. This is the use of 3D imaging at the time of treatment to first measure organ movement and then feedback this information into the IMRT delivery. The flagship approach is the Cyberknife. A pair of stereoscopic X-ray detectors measure the position of internal markers in the tumour. However, they cannot do this continuously because too much radiation dose would ensue. So this is performed very briefly periodically, say every 10 s. An infrared tracking system monitors the positions of external markers continuously. Provided the mathematics linking the movements of internal and external markers is known [63] this generates a pseudomeasurement of the continuous movement of the internal markers (Fig. 12). This can be fed back to the robotic IMRT delivery so that the delivery tracks the tumour movement. This is vital because one then can, in principle, treat just the clinical target volume (CTV) rather than the planning target volume (PTV) with its unwanted artificial man-made margins. The Cyberknife technology lends itself to this but again, in principle, measurement of tumour movement could be fed back to make the DMLC technique track too. Some intriguing movies of "breathing DMLC motions" have been made [70]. One can conceptualise how this could work for IMAT and other dynamic tomotherapy methods. All this points to the emerging field of image-guided IMRT (IG-IMRT or IGRT) so we cease to become a "major treater of stationary plastic", to quote one critic, and start to move usefully to treat the moving, breathing, alive patient.

The path to today's practical realisation of IMRT delivery has been nonlinear, non-sequential and diverse. By this is meant that one practical technique has not

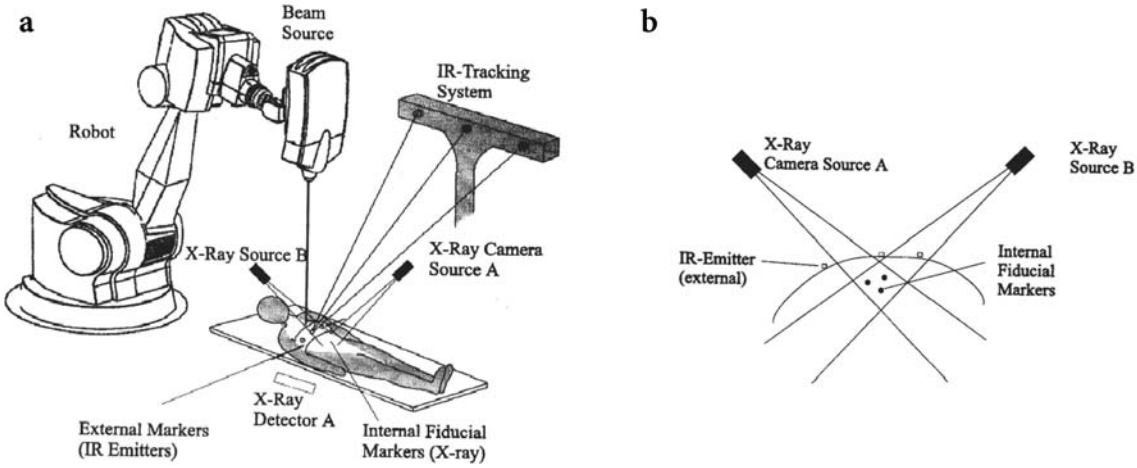

Fig. 12. How online imaging guides the Cyberknife: The motion of internal markers is detected by X-rays; motion of external markers is detected by infrared. Motions are correlated every 10 s. Monitor of external markers by infrared then translates to movement of internal tumour markers in almost real-time and this is fed back to the robot

grown out of another in a neat serial fashion. A series of disconnected inventions, discoveries, concepts and commercial developments took place in parallel simultaneously. Yet neither was there any deliberate competition from some single starting place, no race to the goal. Since most of the developments took place in university hospital departments with good communication via courses, conferences and the internet, the developments were public, peer reviewed and open. In general companies have encouraged as much as possible, and as consistent with commercial enterprise, an understanding of their products, which have grown from this research. Indeed many companies formed development consortia with such university hospitals. Despite the fact that companies make money from cancer therapy, which may have added a glitzy atmosphere in the exhibition hall which some may find uncomfortable, it should be firmly acknowledged that without company involvement – call it support or collaboration or whatever – widespread clinical IMRT would not have been possible. The heroic one-off historical attempts at forms of modulated therapy (the gravity oriented devices, the tracking cobalt unit, rotating shielding devices etc.) all died out through lack of such support [53].

Other chapters in this book will address clinical implementation. We might observe that most clinical IMRT, though driven by the clinical holy grail of complication-free tumour control, now over a century old, has been process driven. That is to say, physicists, computer scientists and engineers created these approaches with the *expectation* of clinical gain. The subject is now truly interdisciplinary with radiographers, oncologists and radiologists all playing roles. Some have argued that the excitement far outweighs the clinical evidence [71]. This is probably true – IMRT may well be the "Emperor's new isodose curves" [72] but whilst IMRT physics outweighs the clinical *evidence* it certainly does not outweigh the clinical *need*. A feature of European clinical IMRT is the establishment of clinical trials designed to demonstrate clinical benefit. So far all the evidence is favourable for further clinical refinement [4].

References

1. Webb S (1993) The physics of three-dimensional radiation therapy: conformal radiotherapy, radiosurgery and treatment planning. IOPP, Bristol
2. Webb S (1997) The physics of conformal radiotherapy: advances in technology. IOPP, Bristol
3. Webb S (2000) Intensity modulated radiation therapy. IOPP, Bristol
4. Webb S (2004) Contemporary IMRT: Developing Physiks and Clinical Implementation. IOP Publishing, Bristol, UK
5. Shepard DM, Earl MA, Yu CX, Xiao Y (2003) Aperture-based inverse planning. In: Palta JR, Mackie TR (eds) Intensity-modulated radiation therapy – the state of the art. Medical Physics Publishing, Madison, Wisconsin, USA, pp 115–137
6. Ellis F, Hall EJ, Oliver R (1959) A compensator for variation in tissue thickness for high energy beams. Br J Radiol 32:421
7. Donovan EM, Johnson U, Shentall G, Evans PM, Neal AJ, Yarnold JR (2000) Evaluation of compensators in breast radiotherapy – a planning study using multiple static fields. Int J Rad Oncol Biol Phys 46:671–679
8. Xu T, Shikhaliev PM, Al-Ghazi M, Molloi S (2002) Reshapable physical modulator for intensity modulated radiation therapy. Med Phys 29:2222–2228
9. Warrington AP, Adams EJ (2002) Cobalt-60 teletherapy for cancer – a revived treatment modality for the 21st century. Proc Sem on Appropriate Medical Technology for Developing Countries. Feb 6th 2002, IEEE, London, pp 21.1–21.19
10. Webb S, Lomax A (2001) There is no IMRT? Phys Med Biol 46:L7–L8
11. Kijewski PK, Chin LM, Bjärngard BE (1978) Wedge-shaped dose distributions by computer controlled collimator motion. Med Phys 5:426–429

12. Convery DJ, Rosenbloom ME (1992) The generation of intensity-modulated fields for conformal therapy by dynamic collimation. Phys Med Biol 37:1359–1374
13. Stein J, Bortfeld T, Dörschel B, Schlegel W (1994) Dynamic X-ray compensation for conformal radiotherapy by means of multileaf collimation. Radiother Oncol 32:163–173
14. Spirou SV, Chui CS (1994) Generation of arbitrary intensity profiles by dynamic jaws or multileaf collimators. Med Phys 21:1031–1041
15. Svensson R, Källmann P, Brahme A (1994) Analytical solution for the dynamic control of multileaf collimators. Phys Med Biol 39:37–61
16. Webb S (2001) Concepts for shuttling multileaf collimators for intensity-modulated radiation therapy. Phys Med Biol 46:637–651
17. Dai J-R, Hu Y-M (1999) Intensity-modulation radiotherapy using independent collimators: an algorithm study. Med Phys 26:2562–2570
18. Webb S (2002) Intensity-modulated radiation therapy using only jaws and a mask. Phys Med Biol 47:257–275
19. Webb S (2002) Intensity-modulated radiation therapy using only jaws and a mask – 2: A simplified concept of single bixel attenuators. Phys Med Biol 47:1869–1879
20. Webb S, Hartmann G, Echner G, Schlegel W (2003) Intensity modulated radiation therapy using a variable aperture collimator. Phys Med Biol 48:1223–1238
21. Webb S, Hartmann G, Echner G, Schlegel W (2003) Intensity modulated radiation therapy using a variable aperture collimator (VAC). ESTRO, Geneva, Sept 2003. Radiother Oncol 68(Supplement 1):S97
22. Gscheidlen W (1959) Device for collimation of a ray beam. US Pat 2904692
23. Yu C (1995) Intensity modulated arc therapy with dynamic multileaf collimation: An alternative to tomotherapy. Phys Med Biol 40:1435–1449
24. Webb S (1998) Configuration options for intensity-modulated radiation therapy using multiple-static fields shaped by a multileaf collimator. Phys Med Biol 43:241–260
25. Webb S (1998) Configuration options for intensity-modulated radiation therapy using multiple-static fields shaped by a multileaf collimator: 2. Constraints and limitations on 2D modulation. Phys Med Biol 43:1481–1495
26. Bortfeld T, Kahler DL, Waldron TJ, Boyer AL (1994) X-ray field compensation with multileaf collimators Int J Radiat Oncol Biol Med Phys 28:723–730
27. Bortfeld T, Boyer AL, Schlegel W, Kahler DL, Waldron TJ (1994) Realisation and verification of three-dimensional conformal radiotherapy with modulated fields. Int J Radiat Oncol Biol Med Phys 30:899–908
28. Adams EJ, Convery DJ, Warrington AP, Webb S (2001) IMRT planning at the Royal Marsden NHS Trust using TMS. Insights 3(1):1–2
29. Xia P, Verhey L (1998) Multileaf collimator leaf-sequencing algorithm for intensity modulated beams with multiple static segments. Med Phys 25:1424–1434
30. Que W (1999) Comparison of algorithms for multileaf collimator field segmentation. Med Phys 26:2390–2396
31. Langer M, Thai V, Papiez I (2001) Improved leaf sequencing reduces segments or monitor units needed to deliver IMRT using multileaf collimators. Med Phys 28:2450–2458
32. Deng J, Pawlicki T, Chen Y, Li J, Jiang SB, Ma C-M (2001) The MLC tongue-and-groove effect on IMRT dose distributions. Phys Med Biol 46:1039–1060
33. Otto K, Clark BG (2002) Enhancement of IMRT delivery through MLC rotation Phys Med Biol 47:3997–4017
34. Cho PS, Marks RJ II (2000) Hardware-sensitive optimisation for intensity modulated radiotherapy. Phys Med Biol 45:429–440
35. Seco J, Evans PM, Webb S (2001) Analysis of the effects of the delivery technique on an IMRT plan: comparison for multiple static field, dynamic and NOMOS MIMiC collimation. Phys Med Biol 46:3073–3087
36. Seco J, Evans PM, Webb S (2002) An optimisation algorithm that incorporated IMRT delivery constraints. Phys Med Biol 47:899–915
37. Budgell GJ, Martens C, Claus F (2001) Improved delivery efficiency for step and shoot intensity modulated radiotherapy using a fast-tuning magnetron. Phys Med Biol 46:N253–N261
38. Evans PM, Donovan EM, Partridge M, Childs P, Convery DJ, Eagle S, Hansen VN, Suter B, Yarnold JR (2000) The delivery of intensity modulated radiotherapy to the breast using multiple static fields. Radiother Oncol 57:78–89
39. Boyer AL, Desobry GE, Wells NH (1991) Potential and limitations of invariant kernel conformal therapy. Med Phys 18:703–712
40. Webb S (1991) Optimisation by simulated annealing of three-dimensional conformal treatment planning for radiation fields defined by a multileaf collimator. Phys Med Biol 36:1201–1226
41. Wittkämper FW, Brugmans MJP, Lebesque JV, van der Horst A, Mijnheer RJ (1998) Clinical implementation of IMRT in the Netherlands Cancer Institute. Proc. Elekta Oncology Systems First Users Conf (Palm Springs, CA 2988), pp 76–83
42. De Neve W, de Wagter C, de Jaeger K, Thienpont M, Colle C, Derycke S, Schelfhout J (1996) Planning and delivering high doses to targets surrounding the spinal cord at the lower neck and upper mediastinal levels: static beam-segmentation technique executed by a multileaf collimator. Radiother Oncol 40:2171–2179
43. Fraass BA, Kessler ML, McShan DL, Marsh LH, Watson BA, Dusseau WJ, Eisbruch A, Sandler HM, Lichter AS (1999) Optmization and clinical use of multisegment intensity-modulated radiation therapy for high-dose conformal therapy. Semin Radiat Oncol 9:60–77
44. Vicini FA, Sharpe M, Kestin L, Martinez A, Mitchell CK, Wallace MF, Matter R, Wong J (2002) Optimising breast cancer treatment efficacy with intensity modulated radiotherapy. Int J Rad Oncol Biol Phys 54:1336–1344
45. Convery DJ, Webb S (1998) Generation of discrete beam-intensity modulation by dynamic multileaf collimation under minimum leaf separation constraints. Phys Med Biol 43:2521–2538
46. Convery DJ, Cosgrove VP, Webb S (2000) Improving dosimetric accuracy of a dynamic MLC technique. In: Schlegel W, Bortfeld T (eds) Proc 13th Int Conf on the Use of Computers in Radiation Therapy, pp 277–279
47. Van Santvoort JPC, Heijmen BJM (1996) Dynamic multileaf collimation without "tongue-and-groove" underdose effects. Phys Med Biol 41:2091–2105
48. Webb S, Bortfeld T, Stein J, Convery D (1997) The effect of stair-step transmission on the "tongue-and-groove problem" in dynamic radiotherapy with a multileaf collimator. Phys Med Biol 42:595–602
49. Shepard D, Earl M, Naqvi S, Yu CX (2002) An inverse planning tool for intensity modulated arc therapy. Med Phys 29(6):1336
50. Yu CX, Li XA, Ma L, Chen D, Naqvi S, Shepard D, Sarfaraz M, Holmes TW, Suntharalingam M, Mansfield CM (2002) Clinical implementation of intensity-modulated arc therapy. Int J Rad Oncol Biol Phys 53(2):453–463

51. Galvin JM (1999) The multileaf collimator – a complete guide. Proceedings of the 1999 Annual Meeting of the AAPM (see also Medical Physics 26:1092–1093)
52. Bortfeld T, Schlegel W, Höver K-H, Schulz-Ertner D (1999) Mini and micro multileaf collimators. Handout material, 41st annual meeting of the American Association of Physicists in Medicine, Nashville, Tennessee, July 1999. www: http://www.aapm.org/meetings/99AM/pdf/2796–50260.pdf
53. Webb S (2003) Historical perspective on IMRT. In: Palta JR, Mackie TR (eds) Intensity modulated radiation therapy – the state of the art. Medical Physics Publishing, Madison, Wisconsin, USA, pp 1–23
54. Carol MP, Targovnik H, Campbell C, Bleier A, Strait J, Rosen B, Miller P, Scherch D, Huber R, Thibadeau B, Dawson D, Ruff D (1993) An automatic 3D treatment planning and implementation system for optimised conformal therapy. In: Minet P (ed) Three-dimensional treatment planning. Pierre Minet, Liege, pp 173–187
55. Sternick ES (1997) (ed) The theory and practice of intensity modulated radiation therapy. Advanced Medical Publishing, Madison, WI, USA
56. Webb S (1989) Optimisation of conformal dose distributions by simulated annealing. Phys Med Biol 34:1349–1370
57. Carol MP (1997) Where we go from here: on person's vision. In: Sternick ES (ed) The theory and practice of intensity modulated radiation therapy. Advanced Medical Publishing, Madison, WI, pp 243–252
58. Mackie TR, Holmes T, Swerdloff S, Reckwerdt P, Deasy JO, Yang J, Paliwal B, Kinsella T (1993) Tomotherapy: A new concept for the delivery of dynamic conformal radiotherapy Med Phys 20:1709–1719
59. Mackie TR, Olivera GH, Kapatoes JM, Ruchala KJ, Balog JP, Tomé WA, Hui S, Kissick M, Wu C, Jeraj R, Reckwerdt PJ, Harari P, Ritter M, Forrest L, Welsh J, Mehta MP (2003) Helical tomotherapy. In: Palta JR, Mackie TR (eds) Intensity modulated radiation therapy – the state of the art. Medical Physics Publishing, Madison, WI, USA, pp 247–284
60. Welsh JS, Olivera GH, Mackie TR (2003) Novel uses and applications of IMRT. In: Palta JR, Mackie TR (eds) Intensity modulated radiation therapy – the state of the art. Medical Physics Publishing, Madison, WI, USA, pp 875–882
61. Swerdloff S, Mackie TR, Holmes T (1994) Analytical solution for the dynamic control of multileaf collimators. US Pat 5317616
62. Swerdloff S, Mackie TR, Holmes T (1994) Multi-leaf radiation attenuator for radiation therapy. US Pat 5351280
63. Schweikard A, Glosser G, Bodduluri M, Murphy M, Adler JR (2000) Robotic motion compensation for respiratory motion in radio-surgery. Comput Aided Surg 5(4):263–277
64. Fiorino C, Fossati V, Ardesi A, Cattaneo GM, del Vecchio A, Fusca M, Longobardi B, Signorotto P, Calandrino R (1993) Development of a computer controlled moving bar (CCMB) conformal technique for neck irradiation. Radiother Oncol 27:167–170
65. Schreiner LJ (2001) The potential for intensity modulated radiation therapy with cobalt 60. NORDION Insights 3(1):3
66. Barthold S, Echner G, Hartmann G, Pastyr O, Schlegel W (2002) CoRA – A new cobalt radiotherapy arrangement with multiple sources – a feasibility study. Phys Med 19:13–26
67. Fielding AL, Evans PM (2001) The use of electronic portal images to verify the delivery of intensity modulated radiotherapy beams produced with dynamic multi-leaf collimation. Radiother Oncol 61 Supplement 1, S26
68. Fielding AL, Evans PM, Clark CH (2002) The use of electronic portal imaging to verify patient position during intensity modulated radiotherapy delivered by the dynamic MLC technique. Int J Radiat Oncol Biol Phys 54(4):1225–1234
69. Wu C, Jeraj R, Olivera GH, Mackie TR (2002) Re-optimization in adaptive radiotherapy. Phys Med Biol 47:3181–3195
70. Keall P, Wu Q, Wu Y, Kim JO (2003) Dynamic MLC IMRT. In: Palta JR, Mackie TR (eds) Intensity-modulated radiation therapy – the state of the art. Medical Physics Publishing, Madison, WI, USA, pp 319–371
71. Schulz RJ, Kagan (2002) On the role of intensity modulated radiation therapy in radiation oncology. Med Phys 29(7):1473–1480
72. Kavanagh BD (2003) The emperor's new isodose curves. Med Phys 30:2559–2560
73. Chang SX, Cullip TJ, Deschesne KM, Miller EP, Rosenman JG (2004) Compensators: an alternative IMRT delivery technique. J Appl Clin Med Phys 5(3):15–36 PMID: 15753937
74. Xu T, Al-Ghazi MS, Molloi S (2004) Treatment planning considerations of reshapeable automatic intensity modulator for intensity modulated radiation therapy. Med Phys Aug; 31(8):2344–2355 PMID: 15377101
75. Kamath S, Sahni S, Palta J, Ranka S, Li J (2004) Optimal leaf sequencing with elimination of tongue-and-groove underdosage. Phys Med Biol 49(3):N7–19 PMID: 15012015
76. Que W, Kung J, Dai J (2004) 'Tongue-and-groove' effect in intensity modulated radiotherapy with static multileaf collimator fields. Phys Med Biol 49(3):399–405 PMID: 15012009
77. Haryanto F, Fippel M, Bakai A, Nusslin F (2004) Study on the tongue and groove effect of the Elekta multileaf collimator using Monte Carlo simulation and film dosimetry. Strahlenther Onkol 180(1):57–61 PMID: 14704846
78. Chow JC, Seguin M, Alexander A (2005) Dosimetric effect of collimating jaws for small multileaf collimated fields. Med Phys 32(3):759–765 PMID: 15839348
79. Burmeister J, McDermott PN, Bossenberger T, Ben-Josef E, Levin K, Forman JD (2004) Effect of MLC leaf width on the planning and delivery of SMLC IMRT using the CORVUS inverse treatment planning system. Med Phys 31(12):3187–3193 PMID: 15651601
80. Kamath S, Sahni S, Palta J, Ranka S (2004) Algorithms for optimal sequencing of dynamic multileaf collimators. Phys Med Biol 49(1):33–54 PMID: 14971771
81. Dvorak P, Georg D, Bogner J, Kroupa B, Dieckmann K, Potter R (2005) Impact of IMRT and leaf width on stereotactic body radiotherapy of liver and lung lesions. Int J Radiat Oncol Biol Phys 61(5):1572–1581 PMID: 15817364
82. Jin JY, Yin FF, Ryu S, Ajlouni M, Kim JH (2005) Dosimetric study using different leaf-width MLCs for treatment planning of dynamic conformal arcs and intensity-modulated radiosurgery. Med Phys 32(2):405–411 PMID: 15789586
83. Leal A, Sanchez-Doblado F, Arrans R, Capote R, Lagares JI, Pavon EC, Rosello J (2004) MLC leaf width impact on the clinical dose distribution: a Monte Carlo approach. Int J Radiat Oncol Biol Phys 59(5):1548-1559 PMID: 15275743
84. Chauvet I, Petitfils A, Lehobey C, Kristner JY, Brunet Y, Lembrez R, Gaboriaud G, Mazal A, Zefkili S, Rosenwald JC (2005) The sliding slit test for dynamic IMRT: a useful tool for adjustment of MLC related parameters. Phys Med Biol 50(4):563-80 PMID: 15773620
85. Venencia CD, Besa P (2004) Commissioning and quality assurance for intensity modulated radiotherapy with dynamic multileaf collimator: experience of the Pontificia Universidad Catolica de Chile. J Appl Clin Med Phys 5(3):37-54 PMID: 15753938

86. Stell AM, Li JG, Zeidan OA, Dempsey JF (2004) An extensive log-file analysis of step-and-shoot intensity modulated radiation therapy segment delivery errors. Med Phys 31(6):1593-602 PMID: 15259664
87. Wang L, Movsas B, Jacob R, Fourkal E, Chen L, Price R, Feigenberg S, Konski A, Pollack A, Ma C. Stereotactic IMRT for prostate cancer: dosimetric impact of multileaf collimator leaf width in the treatment of prostate cancer with IMRT. J Appl Clin Med Phys. 2004 Spring;5(2):29-41. Epub 2004 Apr 1. PMID: 15738911 [PubMed - in process]
88. Kamath S, Sahni S, Ranka S, Li J, Palta J. Optimal field splitting for large intensity-modulated fields. Med Phys. 2004 Dec;31(12):3314-23. PMID: 15651614 [PubMed - indexed for MEDLINE]
89. Abdel-Hakim K, Nishimura T, Takai M, Sakahara H. Review of monoisocentric split-field technique for conventional and IMRT treatment in head and neck cancers: technical limitations and approaches for optimization. Technol Cancer Res Treat. 2005 Feb;4(1):107-13. PMID: 15649094 [PubMed - in process]

Biological Aspects of IMRT Planning and Delivery

Andrzej Niemierko

8

Contents

8.1 Rational for Biological Considerations

Planning and delivery of IMRT differs from planning and delivery of conventional conformal radiotherapy, and this is well illustrated in this book. IMRT has a potential to deliver superior dose distributions. The impact of those improved dose distributions on clinical outcomes (i.e., local control, survival, complications etc.) needs to be estimated. For example, it is not enough to know that the maximum dose to the parotid gland is 3 Gy less with IMRT than it is with conventional radiotherapy while the minimum dose to the CTV is 2 Gy less, and the delivery of each IMRT fraction is twice as long. The biological effect of these well-defined dosimetric differences might be clinically important, or it might not be important at all. Although our understanding of the underlying biological mechanisms is incomplete there is enough accumulated data and clinical experience to make the discussion of these issues meaningful.

Several aspects of biological considerations in planning IMRT are described in detail in part II, chapter 5. In this chapter other radiobiological considerations that need to be taken into account while planning and delivering IMRT are considered. Specifically, the following subjects are discussed: the consequences of sublethal radiation damage repair for dose rate and fraction time considerations, phenomenon of radiation-induced cancers, and dose rate and tissue proliferation issues in designing fractionation schemes for a boost technique.

8.2 Sublethal Damage Repair

Radiation damage to cells is not always lethal. It is well documented that sublethal damage caused by radiation can be repaired within hours after irradiation [1, 2]. The molecular mechanisms of cell damage, repair and radioresistance are still not fully understood but the clinical consequences of sublethal damage repair are profound and have been evident for decades. Namely, splitting the dose into fractions reduces the cumulative effect of total dose. The magnitude of the effect depends on several factors among those the most important are: the interfractional interval, dose per fraction, type of cells, hypoxia, and radiation modality. Sublethal damage repair occurs not only in normal tissues but also in tumors, both in vitro and in vivo. The half-time of sublethal damage repair in most mammalian cells is about 1 h. For late responding normal tissues in vivo it can be substantially longer. The actual rate of repair is not easy to estimate directly. The most common indirect method to examine the sublethal damage repair is to observe the cell survival fraction in split-dose experiments. Figure 1 shows an example of cell survival curves described using the LQ model (see chapter II. 5.6.1) with the alpha parameter of 0.1 and beta of 0.2. The cell surviving fraction after a single fraction of 4 Gy is about 0.09. However, when this dose is split into two equal fractions of 2 Gy separated by enough time to allow full sublethal damage repair, the overall cell surviving fraction is about 0.20. The rate of sublethal damage repair appears to be the greatest immediately after irradiation because the pool of cells that can be repaired is the largest. Due to the repair effect the cell survival curves plotted on a log-linear scale have charac-

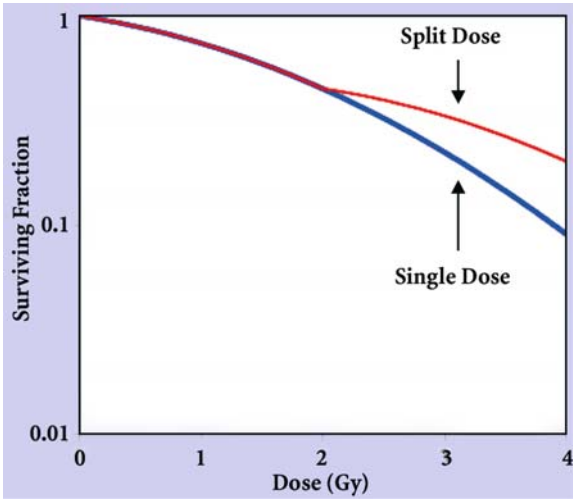

Fig. 1. Schematic representation of cell survival for a single dose of 4 Gy and in a split dose experiment where the total dose of 4 Gy is delivered in two fracti ons of 2 Gy each separated by enough time to allow full repair of sublethal damage

teristic shoulder. The more pronounced repair effect the curvier is the shoulder of the corresponding cell survival curve.

8.3 Clinical Consequences of Sublethal Damage Repair

Naturally, the sublethal damage repair takes place not only between the fractions but also during the irradiation. Therefore, the treatment time of each fraction impacts the level of cell survival and, consequently, the clinical outcome of radiation treatment. Namely, as the treatment time is extended the biological effect of a given dose is generally reduced. In conventional radiotherapy, a dose of 2 Gy can be delivered using three fields in about 6 min total. In IMRT with static fields, the total treatment time to deliver 2 Gy to the target volume can be as long as 30 min (or more). This difference in the delivery time is significant and needs to be taken into consideration in IMRT planning and delivery. It is important to recognize that the clinical protocols specifying total dose and dose per fraction are based on clinical experience with non-modulated beams and shorter treatment times. When the same prescribed doses are delivered with extended treatment times the clinical results might be worse than the outcomes in standard non-modulated radiotherapy techniques. That is, despite delivering superior dose distributions the local control rates may suffer. On the other hand, the extended treatment times are beneficial for the critical normal structures reducing the probability of complications. This differentiating effect of sublethal damage repair should be taken into account in optimizing IMRT delivery.

There is not yet much clinical experience with extended treatment times with external beams albeit there is plenty of data from small animal experiments and from cell survival experiments (e.g., [1]) and, obviously, there are data from brachytherapy studies (e.g., [3]). An interesting study of the effect of treatment time in gamma-ray stereotactic radiosurgery versus protracted intermittent exposures during accelerator-based radiosurgery with multiple arcs was reported by Benedict [4]. In their experiment, the human malignant glioma cells were irradiated using a 6-MV linear accelerator. The intermittent radiation delivery with arc of SRT was simulated by dividing the total dose (6, 9, 12, and 18 Gy) into equal fractions (1.5, 2.0, 3.0, and 6 Gy). To simulate the treatment times required for SRT the delivery times ranged from 16 min to 3 h. As expected, for a given total dose cell survival increased with increasing total irradiation time. The increase in survival was more pronounced at higher doses. For example, at a total dose of 12 Gy the level of cell survival increased by 64% when irradiation time was increased from 16 to 48 min and increased almost fivefold when irradiation time was increased from 16 to 112 min. Note that these delivery times are of the same order of magnitude as estimates of sublethal damage repair half-times for several tissues.

The impact of prolonged delivery times of IMRT treatments on tumor control has been studied by Wang [5]. Specifically, the effects of delivery times ranging from 0 to 45 min were estimated using the LQ-based EUD and TCP models (see chapter II. 5.6.1) using the LQ model parameters derived from the clinical data for prostate cancer ($\alpha = 0.15\,\mathrm{Gy}^{-1}$, $\alpha/\beta = 3.1$ Gy, repair half-time of 16 min). The results were compared with the EUDs and TCPs calculated for the same prescribed doses and delivered using conventional external beam radiotherapy. For example, for a prescribed dose of 81 Gy in 1.8 Gy per fraction the EUD (normalized to 2 Gy per fraction) for conventional delivery is 78 Gy but it drops to 69 Gy for an IMRT with a fraction delivery time of 30 min. This more than 10% decrease in the EUD corresponds to about 20% decrease in the corresponding probability of local control (assuming the slope of the dose-response curve of 2). Obviously, the magnitude of the effect depends on the values of the model parameters. For example, the effect would be smaller for larger α/β ratios or for longer repair half-times.

8.4 Radiation-induced Cancers

Cells that are not killed by radiation may undergo a completely successful repair process or may suffer a permanent change or mutation. The occurrence of mutation is a stochastic effect with, probably, no dose

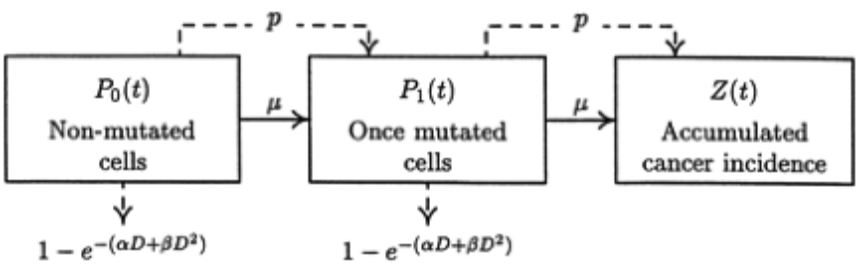

Fig. 2. Two-stage model of carcinogenesis is based on populations $P_0(t)$ of non-mutated stem cells and $P_1(t)$ of one-mutant stem cells. Cells survive dose D with probability $exp(-\alpha D-\beta D^2)$ and, independently, are not mutated with probability $exp(-\gamma D-\delta D^2)$. *Dashed lines* show pathways that are active as a result of irradiation

threshold. In other words, a single photon or electron can cause a base change leading to a mutation. There is a long history of a link between radiation exposure and an elevated incidence of cancer. For example, about 120,000 of the Japanese survivors of the atomic bomb attacks on Hiroshima and Nagasaki have been carefully monitored for over 50 years and the amassed data have been critically assessed by several committees. However, it is still difficult to predict the relative risk of radiation-associated second tumors among patients treated by radiotherapy [6, 7]. There are two important reasons why this is difficult. First, the latent period for most malignancies is relatively long. The shortest latent period, about 7 to 12 years, is for leukemia. For solid tumors, it can be as long as 20 to 50 years. Cancer patients may not live long enough to experience secondary cancer associated with radiation therapy. Second, patients with cancer may be at higher risk of a second cancer because of their lifestyle (say, smoking) or because of genetic predispositions to cancer.

Even very low doses (< 2 Gy) have been associated with second tumor formation. For example, between 1948 and 1960, 10,834 children in Israel were irradiated to the scalp to induce alopecia for the purpose of aiding the topical treatment of tinea capitis [8]. The mean doses to the neural tissue in these children were estimated to be 1.5 Gy. The relative risk of tumor formation at 30 years compared to the general population was as high as 18.8 for schwannomas, 9.5 for meningiomas, and 2.6 for gliomas. A clear-cut dose-response effect was observed, with the relative risk approaching 20 after doses of approximately 2.5 Gy.

The mechanism of radiation-associated carcinogenesis is multifaceted and not well understood. It is typically assumed that cell proliferation is the consequence of signals (positive or negative) affecting cell division and cell differentiation. Radiation can change these signals. For example, a cell can become malignant as a result of activation of an oncogene or, as a result of losing a suppressor gene, or both. In any case, radiation, like hormones and cytotoxic drugs, can be a trigger not only a treatment for cancer. Although no dose is too small to induce mutation, the severity of cancer is not dose related. That is, a cancer induced by a small dose of radiation is not less harmful than a cancer induced by a large dose.

There is growing evidence that second tumors are more likely following combined modality treatment (radiation and chemotherapy), which is increasingly common. The risk of radiation-associated cancer varies considerably with age at the time of irradiation. In some cases, younger patients may be especially vulnerable, because of developmental "window of opportunity" for second tumor development. For example, Bhatia [9] following a cohort of 1,380 children with Hodgkin's disease observed that breast cancer was the most common solid tumor with an estimated actuarial incidence in women that approached a whopping 35% by 40 years of age.

The toxicity of therapeutic doses of radiation is mainly acute. However, the carcinogenic effects are not restricted to those tissues manifesting clinical toxicity. In fact, the opposite may be more accurate, since high doses of radiation may sterilize the carcinogenetic potential of a tissue by killing cells. Only those cells that are not killed delay growth to repair damage, and only in those cells DNA repair errors may lead to transforming mutations. The efficiency of tumor induction varies inversely with repair capacity that in turn depends on the integrity of cell-cycle checkpoints [10]. The general form of the dose-response curve for radiation-associated second tumors is not clear, but several experiments on small animals suggest that the incidence increases with dose up to a maximum usually occurring between 3 and 10 Gy (delivered in single dose) followed by a subsequent monotonic decrease. Clinical evidence supports this biphasic relationship. For example, breast exposures of 20–50 cGy can induce tumors whereas doses exceeding 10 cGy (in fractionated radiotherapy) seem to be less carcinogenic [11]. There are also studies reporting highest incidence of radiation-associated second tumors occurring at field peripheries where dose is less than at the field center [10].

Mathematical models of radiation carcinogenesis usually assume that cells progress towards malignant change by accumulating a series of mutations [12]. Figure 2 illustrates a two-stage model used by Lindsay. In this model cells that are mutated by dose D have, by default, also survived

irradiation. This dual event occurs with probability $p = \exp\left(-\alpha D - \beta D^2\right)\left[1 - \exp\left(-\gamma D - \delta D^2\right)\right]$ where α and β are the intrinsic cellular radiosensitivities, μ is the spontaneous mutation rate, and γ and δ are the mutational radiosensitivities. The functions $P_0(t)$ and $P_1(t)$ are, respectively, the number of non-mutated stem cells (i.e. normal stem cells) and one-mutant stem cells at time t, while $Z(t)$ is the probability that at least one malignant transformation has occurred in the time interval $[0, t]$ when irradiation was administered at time $t = 0$. Normal stem cells are subjected to ongoing spontaneous mutation at rate μ, causing an accumulation of one-stage pre-malignant mutant cells. These one-stage mutants are also subjected to the same risk of mutation and at the same rate μ. When a cell has received a second mutation, this results in a malignant transformation. However, as radiation modulates a variety of interdependent short- and long-term outcomes influenced by the balance between growth, apoptosis, mutations, repair and genetic instability, the mechanism of carcinogenesis is complex and cannot be described by a simple mechanistic model. Indeed, it has been proposed to apply the formalism of chaos and complexity theory to carcinogenesis, which leads to considering cancer as a complex adaptive system [13]. There is also strong evidence that biological response to radiation involves contributions from unirradiated "bystander" cells that respond to signals from the irradiated cells [14].

There is an important practical implication of the biphasic relationship between dose and the probability of second tumor induction as illustrated in Fig. 3 from Lindsay [12]. Depending on the position of the turning point (i.e., the maximum probability) there is no guarantee that dose reduction is an appropriate strategy for second tumor avoidance. For example, if the dose in some irradiated region were higher than the dose corresponding to the turning point, a dose reduction would lead to an increase of the probability of second tumor. This situation may happen in the vicinity of the target volume. Of course, lowering dose in this region may significantly reduce the probability of acute toxicity and this is usually more important than considerations of second tumors.

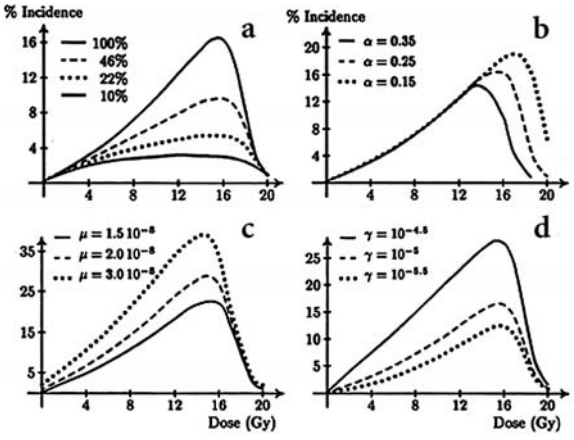

Fig. 3a–d. Percentage incidence of carcinogenesis 20 years after irradiation is illustrated in: (a) for various levels of cell repopulation; (b) for various values of the intrinsic cellular radiosensitivities α and β with $\beta = \alpha/10$; (c) for various values of the spontaneous mutation rate μ; (d) for various values of the mutational radiosensitivities γ and δ with $\gamma = \delta/10$

8.5 Strategies for Delivering Boost Dose

The ability to modulate the intensity profile of radiation beams dramatically increases the flexibility of shaping or sculpting dose distributions. This flexibility is most often utilized to create dose distributions that maximally conform to the exact shape of the target volume and conformally avoid critical normal structure. By creating steep dose gradients outside the target volume, the dose to the surrounding normal tissues is minimized. In this approach, it is assumed that the target volume should receive a uniform dose. However, intensity modulation can also be used to create nonuniform dose distributions within the target volume or volumes, if so desired. The simples nonuniform target dose prescription occurs when there is a specified region of subclinical disease that requires doses lower than the gross tumor volume. For example, in the head and neck carcinoma the prescription for the gross tumor volume might be 70 Gy while the dose for the lymph node region at risk might be 50 Gy. In conventional radiotherapy this dose prescription is often delivered in two phases. In the first phase (up to 50 Gy) both target volumes are simultaneously irradiated with larger fields. In the second, "boost" phase, the remaining 20 Gy is delivered to the gross tumor target volume.

There are three modes of implementing IMRT to deliver the boost technique. Namely, 1) using IMRT to deliver the boost dose only while the gross tumor volume (phase 1) is irradiated using a conventional technique; 2) using IMRT to deliver both phases of the treatment independently; and 3) using IMRT to deliver the desired nonuniform dose distribution at each fraction, that is, irradiate all targets simultaneously. The latter technique has been named "simultaneous integrated boost" (SIB-IMRT) [15] or "simultaneous modulated accelerated radiation therapy" (SMART) [16]. The dose distributions that can be achieved with IMRT are clearly superior to those achievable with conventional radiotherapy as indicated in Fig. 4 from Mohan [7]. In addition, the IMRT technique has been reported to be safer and more efficient for planning and delivery than a conventional technique.

When planning inhomogeneous dose distributions for the target volume one needs to consider biological implications. Specifically, since all subvolumes of a target or targets are irradiated during all fractions, the dose

per fraction is different for different regions with different prescribed doses. Of course, this accounting for dose per fraction effect is necessary because: a) we want to be able to compare the SIB-IMRT (or SMART) plan with the conventional plan, and b) the dose prescriptions are based on previous clinical experience with conventional treatment. For example, in a conventional protocol the prescribed dose per fraction might be 2 Gy for both phases of the treatment. As a result, the gross tumor volume receives 2 Gy per fraction for all fractions and the nodes receive 2 Gy per fraction during the first phase of the treatment but less than 2 Gy during the subsequent boost phase. In addition to differences in dose per fractions the total number of fractions might be smaller and, subsequently, the overall treatment time might be shorter for IMRT. These effects need to be considered especially for tumors with relatively short doubling times. Naturally, the normal tissues are also affected by modified fractionation scheme. The most commonly used method for accounting for biological implications of different doses per fraction and different overall treatment time for both tumors and normal structures is based on the LQ model. Assuming a constant rate of cell repopulation, the overall cell surviving fraction, SF, over time T can be expressed as follows:

$$\ln \mathrm{SF} = -nd\left(\alpha + \beta d\right) + \frac{T - T_k}{T_{\mathrm{pot}}} \ln 2\,, \tag{1}$$

where T_k is the time at which repopulation begins after the start of treatment (often assumed to be about two to three weeks), and T_{pot} is the potential doubling time. The value T_{pot} can be as short as two days for a rapidly growing squamous cell carcinoma and it determines the importance of the overall treatment time (Fig. 5). The parameters α and β (or rather their ratio α/β) determine the importance of dose per fraction effect. When proliferation is slow or can be ignored a simple formula can be derived from (1) that is often used to account for dose per fraction effect alone. That is, for a total dose D delivered in d Gy per fraction an equivalent total dose delivered in 2 Gy per fraction is calculated as follows:

$$D_2 = D\frac{\left(\frac{\alpha}{\beta} + d\right)}{\left(\frac{\alpha}{\beta} + 2\right)}\,. \tag{2}$$

The dose D_2 in (2) is often termed a normalized total dose (NTD).

Using (1) and (2) Mohan evaluated radiobiological consequences of simultaneous integrated boost technique (SIB) for IMRT of head and neck cancers [7]. They confirmed that IMRT dose distributions are most conformal when designed to be delivered as SIB. They also established that there is an additional important benefit of SIB. Namely, biologically effective dose for normal tissues outside the target volumes is lower because the dose per fraction within the normal structures is also lower than that in the conventional techniques. On the other hand, the dose per fraction within the target volume is higher than during conventional radiotherapy. This is beneficial tumor-wise but may pose a problem for normal tissues embedded within the target volume.

8.6 Implications of Biological Considerations

The examples of biological considerations discussed in this chapter clearly indicate that "biology matters" and should be well thought out when designing new treatment plans, new fractionation protocols, or when

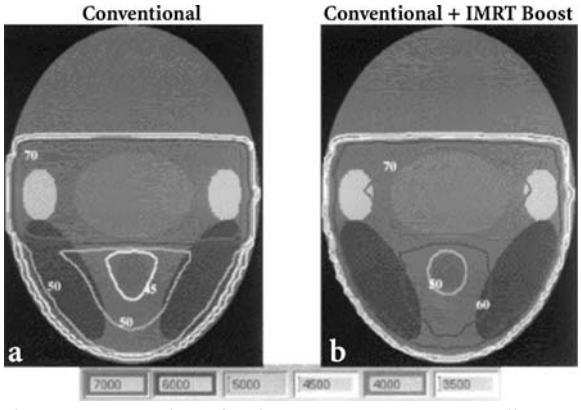

Fig. 4. Treatment plans of a schematic HD carcinoma case illustrating the superiority of SIB dose distributions. Isodose distributions are in terms of nominal dose

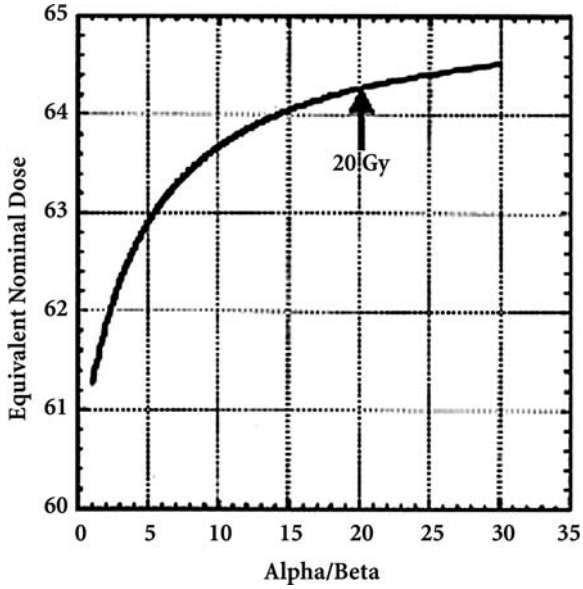

Fig. 5. Dependence of the biologically equivalent dose delivered in 28 daily fractions on the α/β value for T_pot value of 4 days (calculated based on formula 1). The plotted dose delivered in 28 fractions is biologically equivalent to 70 Gy delivered in 35 daily fractions.

introducing new technologies that may alter the way that radiation treatment is delivered. There is no doubt that our understanding of the underlying complex biological mechanisms is rudimentary and our models describing these mechanisms are simplistic. However, as the examples provided elsewhere in this volume demonstrate, even those simplistic models have a potential to improve the quality of planning and delivery of radiation therapy. As more clinical and experimental data are accumulated the biological models will be refined, validated, and will gain predictive power necessary for expending their acceptance by practitioners of radiation therapy.

References

1. Thames HD, Hendry JH (1987) Fractionation in radiotherapy. Taylor & Francis
2. Hall EJ (2000) Radiobiology for the radiologist, 5th edn. J.B. Lippincott, Philadelphia
3. Fowler JF, Van Limbergen EF (1997) Biological effect of pulsed dose rate brachytherapy with stepping sources if short half-times of repair are present in tissues. Int J Radiat Oncol Biol Phys 37(4):877–883
4. Benedict SH, Lin PS, Zwicker RD, Huang DT, Schmidt-Ullrich RK (1997) The biological effectiveness of intermittent irradiation as a function of overall treatment time: development of correction factors for linac-based stereotactic radiotherapy. Int J Radiat Oncol Biol Phys 37(4):765–769
5. Wang JZ, Li XA, D'Souza WD, Stewart RD (2003) Impact of prolonged fraction delivery times on tumor control: a note of caution for intensity-modulated radiation therapy (IMRT). Int J Radiat Oncol Biol Phys 57(2):543–552
6. Loeffler JS, Niemierko A, Chapman PH (2003) Radiation-associated second tumors following radiosurgery: tip of an iceberg or bump on the road? Neurosurgery 52(6): 1436–1442
7. Mohan R, Wu Q, Manning M, Schmidt-Ullrich R (2000) Radiobiological considerations in the design of fractionation strategies for intensity-modulated radiation therapy of head and neck cancers. Int J Radiat Oncol Biol Phys 46(3): 619–630
8. Ron E, Modan B, Boice JD, Alfandary E, Stovall M, Chetrt A, Katz L (1988) Tumors of the brain and nervous system after radiotherapy in childhood. N Engl J Med 319:1033–1039
9. Bhatia S, Robison LL, Oberlin O, Greenberg M, Bunin G, Fossati-Bellani F, Meadows AT (1996) Breast cancer and other second neoplasms after childhood Hodgkin's disease. N Engl J Med 334:745–751
10. Epstein R, Hanham I, Dale R (1997) Radiotherapy-induced second cancers: are we doing enough to protect young patients? Eur J Cancer 33:526–530
11. Boice JD Jr, Land CE, Shore RE, Norman JE, Tokunaga M (1979) Risk of breast cancer following low-dose radiation exposure. Radiology 131:589–597
12. Lindsay KA, Wheldon EG, Deehan C, Wheldon TE (2001) Radiation carcinogenesis modelling for risk of treatment-related second tumours following radiotherapy. Br J Radiol 74:529–536
13. Schwab ED, Pienta KJ (1996) Cancer as a complex adaptive system. Med Hypotheses 47:235–241
14. Brenner DJ, Little JB, Sachs RK (2001) The bystander effect in radiation oncogenesis: II. A quantitative model. Radiat Res 155:402–408
15. Wu Q, Mohan R, Morris M, Lauve A, Schmidt-Ullrich R (2003) Simultaneous integrated boost intensity-modulated radiotherapy for locally advanced head-and-neck squamous cell carcinomas. I: Dosimetric results. Int J Radiat Oncol Biol Phys 56(2):573–585
16. Butler EB, Teh BS, Grant WH III, Uhl BM, Kuppersmith RB, Chiu JK, Donovan DT, Woo SY (1999) Smart (simultaneous modulated accelerated radiation therapy) boost: a new accelerated fractionation schedule for the treatment of head and neck cancer with intensity modulated radiotherapy. Int J Radiat Oncol Biol Phys 45(1):21–32

Image Guided Patient Setup

D. Verellen

9

Contents

9.1 Introduction

Improper knowledge of the patient's anatomy and position during the course of therapy has always been a major source of concern in radiation therapy potentially compromising the clinical results by insufficient dose coverage of the target volume and/or overdosage of normal tissues. The management of target localization emanates in the concept of treatment margins (gross target volume or GTV; clinical target volume or CTV; set-up margin or SM; internal margin or IM; planning target volume or PTV; and planning risk volume or PRV [34, 35]). Image-guided radiation therapy (IGRT) aims at reducing these margins without compromising the clinical outcome. It is a category mistake in claiming that new techniques such as 3D conformal radiation therapy (CRT) and intensity modulated radiation therapy (IMRT) allow reduction of the treatment margins. These margins (in particular PTV) should ideally reflect the geometrical uncertainty of the target localization and, consequently, CRT techniques allow realization of dose distributions that match the PTV. In this chapter IGRT will be reviewed as a tool to detect and correct for patient set-up errors, patient movement errors, organ movement and organ changes. In fact with the introduction of the IGRT concept we move from patient oriented positioning towards target volume oriented positioning.

The introduction of IMRT, however, opens an additional challenge with respect to image-guidance, in particular the intent to deliver a higher dose to the site of primary disease whilst simultaneously giving a lower dose to subclinical or electively treated regions. This so-called simultaneous integrated boost (SIB) [53] is receiving increased attention in clinical literature and was first proposed by Pickett et al. [68] and Ling et al. [48]. With IMRT it is now possible to produce inhomogeneous dose distributions in an intentional and systematic manner. SIB will only be feasible with the introduction of biological or functional imaging modalities in the treatment planning process, providing geometric integrity amongst various imaging modalities can be preserved. Preparation of radiation treatments has always been more or less image-guided and indeed the introduction of CT-imaging in the late 1970s [99] for the treatment planning process can be considered to be a major step in improvement of treatment quality. This is a process of continuous evolution with improvements (both on sensitivity and specificity) in morphological (e.g., fast CT and MR-imaging) and functional (e.g., MR-spectroscopy [40] and PET imaging [28]) imaging modalities that help the radiation oncologist in accurate defining the target volume and organs at risk during the pre-treatment phase (or treatment planning), creation of the earlier discussed SIB, and even assessment of organ motion. In fact, image registration techniques, whether deformable or not, and automated segmentation of structures are gaining interest in the community.

Moreover, image-based follow-up correlated to the treatment plan can provide the necessary information on distributions of failure in and near the treatment volume. The latter may provide useful insight on failures either due to inadequate dose or inadequate margins. The latter use of imaging in radiotherapy is often referred to as multi modality imaging (MMI) and although extremely important and essential in the determination of the target volume it will not be explored further in this chapter.

The latest developments in radiotherapy (such as stereotactic body radiotherapy or SBRT, dynamic field shaping arc therapy or DAT and IMRT) have allowed surgical precision of radiation dose distributions with the intent to cure the patient without damaging healthy tissue, and indeed, with the clinical implementation of IMRT the attention is shifting from dosimetric feasibility studies towards patient-based studies and investigation of treatment efficiency. Yet, the current positioning techniques do not match the accuracy needed to perform CRT/IMRT adequately. In fact, difficulties with accurate target localization have represented the most significant obstacles to full exploitation of the capabilities of CRT/IMRT treatments. Some of the latest developments in IGRT will be highlighted in this chapter. As this is a rapid evolving field inevitably some techniques might not get the attention they deserve, for which the author apologizes and takes full responsibility.

Two ways exist in presenting the available solutions for image-guided radiotherapy: one can either review the existing commercial and customised solutions with respect to their appropriate usage, or one can identify different problems and review possible solutions within this particular topic. The latter approach has been followed in this chapter separating image-guided radiotherapy in (a) solutions for reduction of SM (to account for uncertainties in patient position and beam alignment) only for those cases that present small or negligible intra-treatment organ movement, and (b) IGRT solutions that aim for reduction of both SM and IM (to account for variations in size, shape and position of the CTV) for those cases that present important intrafractional organ movement. To the reader who looks for a summary concerning a particular technology this approach will not give straightforward answers. However, a revision of commercially available techniques (representing technical status at the time of writing) is summarized in Table 1. A third category might be the assessment of the amount of tumor response and to adapt the treatment accordingly during the course of treatment. As this is more related on how to use images as opposed to the technology itself, this subject will also be omitted in the current review.

9.2 IGRT for Management of Interfraction Geometric Uncertainties (Reduction of SM)

9.2.1 Rationale

A myriad of studies have been published on the subject and it is difficult (not the scope of this paper) to summarize the set-up accuracies that can be realized with the different technologies let alone compare the different systems. The proper way to proceed for a center, once an IGRT system has been selected and installed is to determine the clinical set-up accuracy that can be realized on-site for each particular pathology, and apply treatment margins accordingly. The choice of the technology to be introduced into a particular department largely depends on the patient flow, immobilization and treatment protocols. Clearly, the system requirements for single fraction or hypofractionated treatments will

Table 1. Overview of existing commercially available technologies in image-guidance

	Interfractional (reduction of SM)	Intrafractional (reduction of SM and IM)
Planar imaging, EPID (available on most commercially available linacs)	Requires surrogate, difficult to assess 3D information	NOT possible
Stereoscopic X-ray imaging (independent of linac manufacturer)	Requires surrogate, 6 DOF possible	Requires surrogate, 6 DOF possible, real-time target localization possible
Ultrasound imaging (independent of linac manufacturer)	NO surrogate required, limited to pathologies that can be imaged with US	NOT possible
kVCBCT (only available on Varian and Elekta)	Requires no surrogate, 6 DOF possible	NOT possible
MVCBCT (only available on Siemens)	Requires no surrogate, 6 DOF possible	NOT possible
MVCT (only available on helical Tomotherapy)	Requires no surrogate, 6 DOF possible	NOT possible
Optical tracking, video, ...	If used in stand-alone mode, not able to visualize target volume	If used in stand-alone mode, not able to visualize target volume

DOF: "degrees-of-freedom", referring to three translational and three rotational set-up corrections that can be calculated

be entirely different from those for hyperfractionated treatment protocols. Basically, the treatment procedure should be *effective* as well as *efficient*. Acquisition of an IGRT system should be guided by the department's treatment philosophy, not the other way around. As stated earlier, these systems are in continuous evolution and many constructors rely on input from treatment centers on how to further develop these products.

The treatment plan for external beam radiotherapy is typically based on the anatomy presented in the planning CT scan data set (either with or without additional imaging modalities) being no more than a snapshot in time. In fact, the traditional simulation process will gradually become less important if not obsolete with the introduction of more sophisticated treatment techniques such as IMRT and DAT, and the need for classical simulators has been called into question [16]. During the course of radiotherapy, the position of the anatomic structures relative to the treatment beam can be different from this initial situation owing to variations in patient position and internal organ motion. Again, these differences vary largely from center to center and patient to patient, and depend on the procedure for patient set-up, with or without immobilization, as can be seen from an excellent overview by Langen et al. [43]. For prostate patients, to give a typical example, it has been well established that this gland moves considerably between fractions, mainly because of differential filling of the rectum with faecal matter or gas [117]. Average movements due to positioning uncertainties of 3 to 4 mm have been reported [109]. In addition, the day-to-day prostate mobility due to organ motion is about 4 mm (SD) in the antero-posterior (AP) and cranio-caudal (CC) directions and 2 mm (SD) in the latero-lateral directions [74, 110]. However, important prostate displacements of 14 mm and more have been reported [73, 77, 100]. To account for these potential movements, margins are added to the clinical target volume to create a statistical volume that envelopes the true CTV ensuring correct coverage of the latter by the treatment beam with a high confidentiality. In this chapter we will evaluate different solutions that help reducing this PTV margin by reducing interfraction geometric uncertainties (often referred to as the set-up margin or SM, which takes into account uncertainties in patient position and beam alignment). This patient set-up error can have a systematic and a random component. The former can originate at different phases during the treatment planning process (the data transfer from CT to treatment planning, misregistration of different imaging datasets, target definition during treatment planning, data transfer to treatment machine, the use of immobilization systems, ...) and propagates to the final patient set-up. This error will be systematically identical for all treatment fractions and can be represented as the distance of the mean of daily positions to a predefined ideal point in space. The random component, as its name suggests, varies from day-to-day and is represented by the range of different positions for every treatment fraction. Van Herk et al. [102] identified 17 potential sources of errors in the treatment chain that will result in a geometrical set-up error for the patient, see chapter I. 3. Based on a statistical analysis these investigators [101] derived rules (other formalisms and many adaptations have been published since) for selecting margins illustrating this idea nicely following:

$$\text{margin CTV} \rightarrow \text{PTV} = 2.5\Sigma + 0.7\sigma - 3\,\text{mm} \quad (1)$$

with Σ representing the systematic and σ the random component of the set-up errors observed in a certain patient population. This formula suggests that the systematic error is more important and that efforts in reducing treatment margins should focus on this component. The latter is the basis for the so-called off-line approach. This approach, however, should not be generalized as the example of obese patients clearly illustrates that the random component can be more prominent than the systematic component [19]. Therefore the clinical application of IGRT for patient set-up verification/correction can generally be classified in two approaches: off-line [7, 8, 100, 115, 116] and on-line [1, 6, 19–21, 25, 31, 66, 92, 94–97, 103]. The former monitors the position of the patient during a limited number of fractions and adapts the safety margins and/or treatment plan accordingly, also coined adaptive radiation therapy (ART). This approach does not allow for decreasing the treatment margins sufficiently for aggressive CRT. The on-line approach offers the possibility of reducing most geometric errors (both systematic and random), yet is considered to be time consuming and requiring automated control of the treatment couch to make it efficient in clinical routine [6, 94, 95, 108]. As mentioned in the introduction the proper way to proceed is to define the set-up accuracy with a particular IGRT system realized for a particular patient population and consequently derive the appropriate PTV margins. This procedure is illustrated in the AZ-VUB experience with the introduction of a real-time tracking infrared system in combination with stereoscopic kV-imaging (see paragraph on intrafraction geometric uncertainty) [108] for treatment of the prostate. Figure 1 summarizes the results from three studies [85, 86] that have been pooled into one data base and re-analyzed [Verellen, unpublished data, March 2004] yielding an overall 3D residual error equal to 1.1 mm (SD: 11.7 mm), 1.4 mm (SD: 7.1 mm), 0.5 mm (SD: 4.6 mm) and 1.2 mm (SD: 3.8 mm) respectively for positioning based on room lasers, infrared tracking, automated image fusion of bony structures from DRRs and X-ray images or matching of implanted markers respectively. For the first three results the comparison was based on bony references, whereas the last figure results from the actual marker coordinates and as such the only indication of the actual target positioning including organ movement. These re-

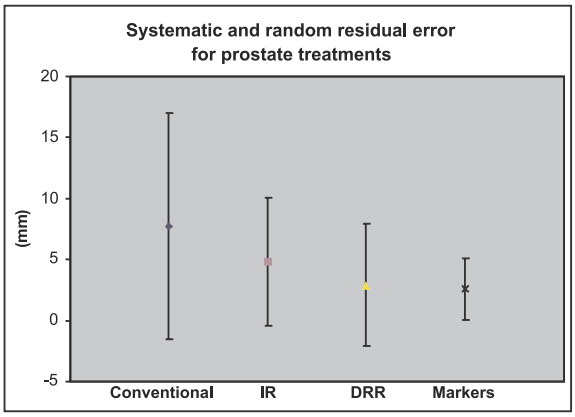

Fig. 1. An estimate of the distribution (AZ-VUB) of set-up errors for prostate treatments resulting from positioning with respectively skin markers and room-laser alignment, infrared tracking, automated fusion between DRR and actual X-ray images, and matching of implanted markers. The systematic error is calculated as the standard deviation of the mean deviation of individual patients. The random error is defined as the standard deviation of the individual deviations of all patients after subtraction of the corresponding mean

sults show a striking reduction in the spread of data (SD) going from conventional to marker matching method. To obtain an estimate of the distribution of systematic errors in set-up for all patients, the standard deviation (SD) of the mean deviation of individual patients was calculated. The random component was determined by calculating the SD of the individual deviations (pooled data) after subtractions of their corresponding mean. Based on these results the following (conservative) rules for PTV margin have been proposed at the AZ-VUB for this particular patient population: 6.0 mm latero-lateral, and 10.0 mm antero-posterior and cranio-caudal when DRR-fusion is used for positioning; 5.0 mm antero-posterior and cranio-caudal, and 3.0 mm latero-lateral when implanted markers are used for target positioning.

The latter example touches another issue that deserves special attention with respect to image-guidance, which is the visualization (or more general: assessment of geometric localization) of the target volume. Ideally, IGRT systems should enable visualization of the actual target volume, yet for practical reasons many systems rely on surrogates. Often bony structures are used as a surrogate (portal films, EPIDs, ...) yet if the target volume is likely to move independently of the bony landmarks, alternatives are called for such as implanted radio-opaque markers [1, 3, 4, 24] or even wireless electromagnetic transponders [113]. The implanted markers raise the issue of marker migration. Reports on pulmonary seed migration (i.e., 0.3%) in seed implantation for prostate brachytherapy have often been referred to as major disadvantage of this approach [52, 62, 82]. Recent studies however, have shown negligible migration observing SD in inter-marker position of the same magnitude as the uncertainty of the measuring system [18, 70].

9.2.2 EPIDS

Electronic portal imaging devices (EPIDs) [11, 32, 57] have been embraced with great expectation to increase accuracy in patient set-up. A comprehensive overview of existing EPID techniques has been published by Herman et al. [32] in 2001. This report also acknowledges that the initial promise has not led to widespread clinical application of EPIDs. Most studies presented developments by research centers (in collaboration with manufacturers) to cover their individual needs, and many commercial systems are often (arguably) limited to digital replacements for portal film and do not allow fully automated correction of set-up errors. As mentioned before, the clinical application of EPIDs for patient set-up can generally be classified in the off-line and on-line approach. A general limitation of EPID is that it is restricted to two-dimensional assessment of set-up errors (it is a planar radiography system) and the concept requires a surrogate for the target volume (either bony landmarks or implanted radio-opaque fiducial markers). Balter et al. clearly illustrated the potential of megavoltage portal imaging to investigate interfractional prostate motion introducing radio-opaque markers and orthogonal portal films in 1995 [4]. First reports of on-line positioning prior to treatment required manual adjustment of the treatment couch (entering the treatment room [21] or installation of a hand-pendant outside the treatment room [20]) and comparison of reference and daily portal by eye. Since then the major improvements have been on the use of (semi) automated alignment of reference and daily image, yet automation of the patient set-up is still not a standard option in most commercially available systems. Recently some commercial systems have introduced on-board kV-imaging allowing stereoscopic or orthogonal imaging in combination with the beam-EPID system allowing 3D assessment of set-up errors without the need of rotating the treatment gantry for assessment of 3D information (see also paragraph on intrafraction geometric uncertainties). Nevertheless, planar radiographs are difficult to interpret and out-of-plane rotations are not as evident to cope with as translations.

A general advantage of EPIDs is that the image is created with the megavoltage beam that is used to treat the patient. It is generally accepted that the quality of the images acquired using these megavoltage X-rays is inherently poorer than that acquired with kilovoltage X-rays. Besides the well-known decrease in subject contrast as the energy of the beam increases, many other factors will contribute to the poor quality of portal images (such as performance of the image receptor, X-ray

scatter in the patient, size of the X-ray source, . . .) [32]. Yet, in many cases, and especially with the latest developments, the image quality can be good enough to visualize the surrogate structures (bone or implanted markers) that are used to localize the target. The technology and history of megavoltage imaging has been described in detail by Herman et al. [32], and the most frequent systems are based on matrix ion chamber, combinations of camera and metal plate with phosphor screens and active matrix flat panels (photo diode arrays such as amorphous silicon or photoconductor arrays such as amorphous selenium). The latter technology generally produces improved image quality in comparison to the other approaches and is becoming a standard in most commercial systems. A word of caution is in its place in that the longevity of these flat panels (or camera's) is still not established. Based on initial experience with EPIDs, Wong et al. [32] calculated that the total annual cost for imaging is less expensive with EPIDs than with film if portal imaging is performed frequently. This model however, may not be true if the camera or electronics needs annual replacement to ensure excellent image quality. The additional advantage of EPIDs in that it utilizes the actual treatment beam allows as such direct verification of the alignment of target volume and treatment beam (as opposed to other systems that require an additional calibration – hence additional source of errors – to register with the treatment machine's isocenter). Moreover, EPIDs have the potential to verify other treatment settings (hence offering a more comprehensive approach) such as intensity profiles in intensity modulated therapy, field sizes, and can be used to assess exit dosimetry [38, 64], to mention but a few applications. The major disadvantage is to generate three-dimensional set-up information [26, 27, 42, 49, 59, 65, 66, 69] and to integrate this in automated positioning on existing equipment [6, 92, 94–96].

9.2.3 Stereoscopic kV-Imaging and Real-time Imaging

A solution to the inherent 2D limitation of EPIDs for target localization has been offered with the introduction stereoscopic kilovoltage imaging devices [14, 39, 60, 61, 80, 81, 108]. The approach of using diagnostic X-rays for verifying treatment set-up is not new [6, 9, 82] and offers a twofold advantage: (a) image quality (a well-documented problem in EPIDs) is no longer an issue, especially in combination with AmSi detectors [32, 58]; (b) patient dose becomes less important compared to daily megavoltage images acquired with EPIDs. Dose measurements performed at the AZ-VUB [108] with an appropriate ionization chamber resulted in 0.513 mSv per image for a typical clinical setting. Moreover, the combination with real-time monitoring of patient positioning independent of linac gantry position is not limited to target observation, but also offers the possibility of controlling the treatment beam based on that information (see paragraph on intrafraction geometric uncertainty). In principle two approaches exist: one uses the image guidance to align the target volume with respect to the treatment beam [39, 80, 81, 108] using a remote couch control, the other in turn, uses the imaging information to guide the treatment beam [14,59–61] using a robotic linac (CyberKnife, Accuray Oncology, Sunnyvale, CA). The latter has the potential of true real-time tumor tracking, whereas the former can be used to gate the treatment in case of organ motion (see later). Millimeter accuracy has been reported for both approaches [14, 108].

The ExacTrac 3.0/NOVALIS BODY system (BrainLAB, Heimstetten, Germany) resides in the former classification in that it combines visualization of internal structures based on stereoscopic X-ray imaging with real-time infrared tracking of the patient's surface. The system is designed to be a positioning tool ensuring accurate positioning a priori fulfilling the following basic requirements: (a) being integrated in the treatment planning process, (b) performing as a fully automated positioning tool (not verification tool) allowing high accurate positioning of the target volume based on treatment planning data, (c) not increasing the number of actions required for patient set-up compared to conventional methodologies (believed to be one of the major reasons for the limited clinical use of EPIDs to date), and (d) performing this task within an acceptable time frame (i.e., a typical treatment including positioning should not exceed 15 min) [85, 86, 108]. As this system is commercially available and compatible with most commercial systems, it will be used as an example to illustrate the principle of stereotactic X-ray imaging. A detailed description has been given by Verellen et al. [108].

Automated positioning of the patient (or robotic movement of the treatment couch) is realized with the real-time infrared (IR) tracking device by detecting IR-reflective/CT markers placed on the patient's surface, comparison of marker location with stored reference information, and instructing the treatment couch to move the patient to a preplanned position. The markers are visible by two IR cameras and one video camera that are mounted to the ceiling of the treatment room (Fig. 2). The patient's movements can be monitored in 3D real-time with the IR cameras in the room, and consequently the patient's position can be controlled on-line either using a hand-pendant or computer assisted commands.

The X-ray imaging system is fully integrated into the IR tracking device described above and consists of a generator, two X-ray tubes (MP 801 X-ray generator and comet X-ray tubes: K&S Röntgenwerk, Bochum, Germany) embedded to the floor, and two amorphous silicon (AmSi) detectors (PerkinElmer Optoelectronics GmbH, Wiesbaden, Germany) mounted to the ceiling (Fig. 2). The angle between both X-ray tube – detec-

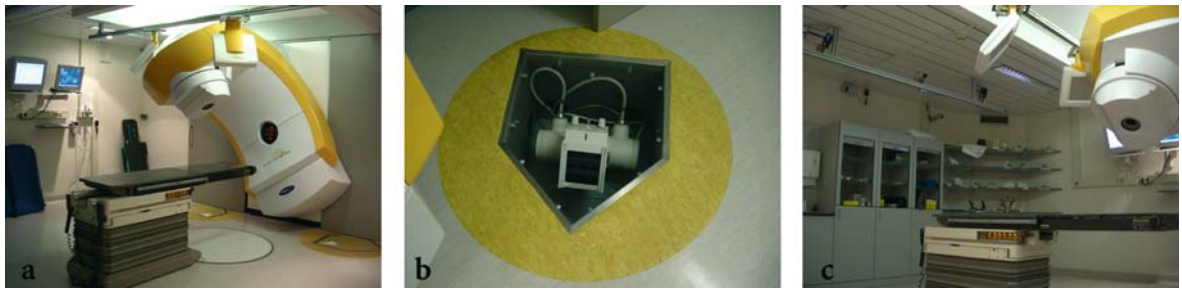

Fig. 2. a-c Room view with NOVALIS system (at the AZ-VUB), note the video cameras, IR-cameras and AmSi detectors mounted to the ceiling and the X-ray tubes embedded in the floor (ExacTrac 3.0/NOVALIS BODY)

tor pairs is approximately 90°, and approximately 42° tilted from the horizontal. In addition a key-board controlled interface has been developed allowing remote computer-assisted control of patient movement to predefined positions (final treatment position) from outside the treatment room. The X-ray system produces diagnostic photon beams ranging from 40 keV to 150 keV in exposure mode and from 40 keV to 125 keV in fluoroscopic mode, and projects a field size of approximately $20 \times 20\,cm^2$ on the AmSi-detector. The detectors have an active area of $22 \times 22\,cm^2$. A calibration is needed to define the spatial relationship between X-ray tubes and AmSi detectors on one hand and the relationship with respect to the treatment machine's isocenter on the other hand. The spatial relationship with respect to the treatment isocenter is established by defining a relationship between the X-ray system and the IR tracking system with radio-opaque markers inside and IR-reflective markers outside a specially designed calibration phantom. Patient and treatment couch movements are controlled by real-time tracking of the IR-reflective markers.

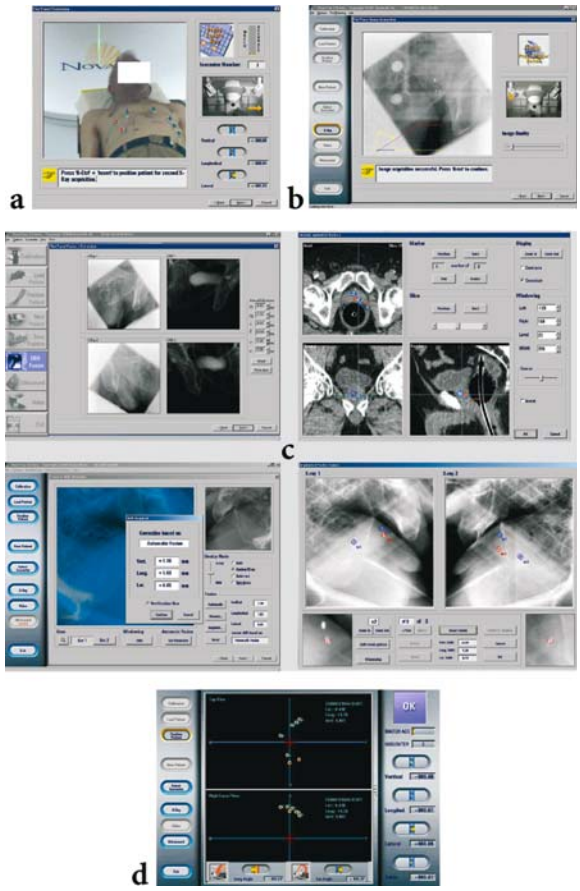

Fig. 3a–d. Flowchart illustrating the different steps in the positioning procedure using ExacTrac 3.0 /NOVALIS BODY. *From top to bottom*: (a) Patient on the treatment couch with IR reflective markers. (b) Acquisition of X-rays (only one shown). (c) Calculation of 3D correction vector based on either automated fusion of X-ray images with DRRs representing the ideal position (*left*) or matching of implanted radio-opaque markers (*right*). (d) Automated patient positioning

Once both X-ray images have been acquired, two options are provided: automated fusion of the actual X-ray images and DRRs representing the ideal patient position, and matching implanted radio-opaque markers. The former procedure is considered to be an improvement in patient set-up compared to conventional methods, yet not able to cope with internal organ movements and therefore still requiring a substantial internal target margin (IM) [35]. The implanted markers offer a more realistic assessment of the target volume's actual position and therefore enables reduction of treatment margins suitable for CRT/IMRT/SBRT. An illustration of the procedure is given in the flowchart (Fig. 3).

Automated Fusion of kV-Imaging and DRRs

In this set-up a 2D/3D co-registration algorithm is applied to align a 3D CT patient data set with two X-ray images. Assuming that all components of the system are properly calibrated (i.e., the exact position of the X-ray tubes and detectors are known with respect to the machine's isocenter) it is possible to generate digitally reconstructed radiographs (DRRs) from the planning CT (representing the ideal patient position) and compare these with the acquired X-ray images. For an accurate positioning both the location and orientation of the patient need to be assessed taking into account all six degrees-of-freedom (6 DOF) for the im-

age co-registration (translations as well as rotations). An automated fusion algorithm based on gradient correlation is used, which optimizes a similarity measure for each image pair [65]. The similarity measure relies primarily on edges and gives a high response if strong edges are visible in the same place. In a first phase the two pairs of corresponding X-rays and DRRs are fused and the amount of 2D translations necessary to register the image pairs can be used to compute a first coarse 3D correction vector (this is possible since the spatial relations and magnification factors between X-ray tubes and patient are known). This 2D/3D correction vector is then used as a starting value for the second phase, being the 6 DOF co-registration. The latter is obtained from an iterative optimization cycle to determine values for the rotation and the translation of the 3D CT data set as to maximize the similarity measure between the corresponding DRRs (each time re-calculated from the previous values for rotations and translations) and the actual X-ray images. The latter requires an efficient algorithm for rendering DRRs (since some hundred DRRs will be used in the registration process), an efficient optimization, and automated fusion algorithm. If the automated fusion should fail a back-up procedure is offered to manually shift the DRR images until an acceptable registration is obtained; the user can define regions of interest in the images (eliminating regions of high contrast that are not related to the patient's anatomy such as patient immobilization devices that may influence the automated fusion); adapting the tissue-bone contrast in the DRR; or limit the search area (avoiding that the system drifts off to find an unrealistic solution).

Matching Implanted Markers

Assuming a calibrated X-ray system, implanted radiopaque markers previously located in the planning CT volume set will be projected on the X-ray images (Fig. 3). When the initial patient set-up is correct these projections will coincide with the images of the markers on the X-ray image. In case of a set-up error, each marker projection can be clicked and dragged by mouse to coincide with the corresponding image of the actual position. The combined marker translations/rotations in each X-ray projection allow for calculation of a full 6 DOF correction assuming a rigid configuration. If the marker configuration deviates too much from the expected configuration (indicating possible marker migration), the system will fail to match the markers and the "migrated" marker will have to be eliminated in the software. An algorithm for automated marker detection is currently under investigation.

Based on phantom studies, Verellen et al. [108] have shown sub-millimeter accuracy with the system when using implanted markers. Soete et al. [86] have validated the system for clinical use and adopted appropriate treatment margins for treatment of the prostate (see earlier). On-going work is currently focusing on using the 6 DOF information to control a so-called "tilt-box" that will enable rotational adjustment of the treatment table top. Yin et al. [119] is using the same technology for single fraction treatment of spinal tumors in combination with an immobilization device, and performing CT-imaging and treatment planning the same day as treatment.

9.2.4 Ultrasound-based Systems

Whereas both previous IGRT solutions suffer from the need for a surrogate to localize the target volume (bony structures or implanted markers) ultrasound-based solutions aim at visualizing soft tissue and in particular the target volume prior to treatment. Holupka et al. [33] reported a feasibility study on the use of a transrectal ultrasound probe in 1996, the advantage being to localize the prostate within 2 mm and to reproducibly fix the prostate gland relative to the probe eliminating target motion. The initial commercial systems used a less invasive approach in applying an external ultrasound probe and required the acquisition of two ultrasound images, onto which the patient's CT contours are overlaid. After the user aligns the CT contours with the ultrasound images, the software calculates the respective couch shifts to align the organ in the treatment field [46]. The system is non-invasive and its commercial availability has created some excitement in the radiotherapy community (in particular for prostate localization), mainly in the US where each localization procedure could be charged as an ultrasound study, suggesting that the system's popularity was more economically driven as to improvement of target localization.

The first commercial systems (BAT, former NOMOS corporation now North American Scientific, Cranberry Township, PA, USA; and ExacTrac, BrainLAB, Heimstetten, Germany) were based on two ultrasound images to generate 3D information. The device is typically a portable system situated adjacent to the treatment couch. The import of patient-specific CT structures is required, as well as the isocenter localization from the treatment planning system, prior to target volume alignment. A system to track the ultrasound probe's position in space is introduced (i.e., a mechanical arm for the BAT system [54] or an optical tracking such as infrared LEDs [10] or reflectors that are monitored by stereoscopically mounted infrared cameras as for the ExacTrac system [Verellen, unpublished data, 2000]). After registering the probe with respect to the treatment machine's isocenter, two ultrasound images are acquired (transverse and sagittal suprapubic). Since both the CT structure and ultrasound image location relative to the isocenter are known, the CT structures corresponding to a particular ultrasound plane can be generated and overlaid onto the ultrasound images acquired on that particular treatment session. If the target volume is properly positioned

with respect to the treatment beam, the CT structures will match the respective structures on the ultrasound images. If the target volume is displaced, the CT structures can be manoeuvred manually in three dimensions until a best match is realized with the ultrasound images. The corresponding couch shifts in three directions to realign the target volume with the treatment beam are calculated (rotations are not taken into account).

Initial studies reported on ultrasound "real-time" positioning of the prostate showed promising results [90]. Recent studies comparing these initial ultrasound devices with EPIDs in combination with implanted radio-opaque markers or daily CT scans revealed some drawbacks for prostate localization [44–46, 98]. The ultrasound-based alignments were systematically different from the marker-based alignments in some directions (depending on the study) and the remaining random variability of the prostate position after the ultrasound-based alignment was similar to the initial variability without the use of any alignment other than room lasers. Van den Heuvel et al. reported residual set-up errors after ultrasound positioning of 2.5 ± 5.7, -2.6 ± 5.4 and -0.4 ± 4.3mm in the AP, CC and lateral direction respectively comparing BAT alignment with prostate marker alignment [98]. These researchers concluded that the margins needed for compensation of geometric uncertainty are comparable to a program that does not perform position adjustment. Langen et al. observed directed differences of respectively 0.2 ± 3.7, 2.7 ± 3.9 and 1.6 ± 3.1mm [44]. The random variations reported in these studies vary from 2–3 to 3–4 to 0–5 mm and difference up to 9 mm have been observed [45]. Possible sources for the differences in systematic errors as identified by Langen et al. were as follows. (1) Ultrasound alignment assumes that the CT contour of the prostate is similar in shape and size to the prostate as seen on the ultrasound image. This assumption may not be valid, as different imaging modalities are known to yield differences in the prostate definition. (2) A possible correlation between ultrasound image quality and the amount of prostate that is obstructed by the pubic bone on an AP projection. (3) Calibration of the ultrasound system (i.e., determination of the probe's position with respect to the machine's isocenter). Another possible source of systematic errors that was not identified by these investigators may be a deformation of the patient's anatomy during the ultrasound investigation, which was not present during initial CT-acquisition and is no longer present at the time of treatment. A possible source of patient movement between the CT scan and BAT alignment was eliminated by Lattanzi et al. [46] by performing the ultrasound alignment directly in the CT room. This study reported a directed average difference of -0.1 ± 2.8, 0.0 ± 2.3 and -0.2 ± 2.4mm in the AP, CC and lateral directions respectively. These last results have, however, been the subject of some debate [98]. Finally, Langen et al. showed an important inter-user variability, where among eight users, the average range of couch shifts due to contour alignment variability was 7, 7, and 5 mm in the AP, CC, and lateral direction respectively [44].

More recently, 3D systems have been introduced (e.g. SonArray, Zmed Inc., Ashland, MA; and the newer BAT system, North American Scientific, Cranberry Township, PA) to overcome the limitation of using a spatially flexible 2D imaging technique to view 3D anatomy. The latter system generates 3D ultrasound data sets through optical tracking of free hand acquired 2D ultrasound images (Fig. 4). The operator holds the ultrasound probe and manipulates it over the anatomical region of interest. The 2D images are transferred to a control computer using a standard video link. The position and angulation of the ultrasound probe are determined using an array of four infrared light-emitting diodes (LED) attached to the probe. Two charged coupled device camera's (CCD) are used to determine the position of the LEDs, and this information is input to the control computer. The position of each image plane can therefore be determined

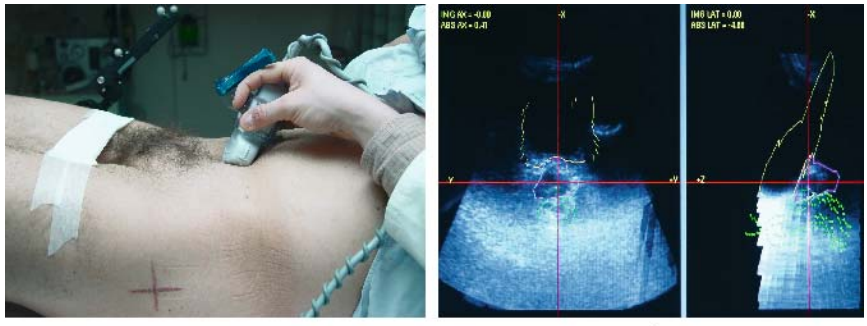

a b

Fig. 4. a,b Three-dimensional ultrasound guidance (SonArray). The system generates 3D ultrasound data through optical tracking of free hand acquired 2D ultrasound images (*left*). Since both the CT structure and ultrasound image location relative to the treatment machine's isocenter are known, the CT structures corresponding to a particular ultrasound plane can be generated and overlaid onto the ultrasound images (*right*). The CT structures can be moved in three dimensions until a best match is realized and the corresponding couch shifts in 3D to realign the target are calculated. (Images courtesy of De Meerleer et al. 2004)

using the LEDs, and an ultrasound volume can be reconstructed by coupling the positional information with the images. The optical guidance system is also used to determine the absolute position of the ultrasound image volume in the treatment room coordinate system and as such the position of the image volume relative to the linac's isocenter is known. Tomé et al. [89] emphasized that while there has been a proliferation for image (ultrasound)-guided systems, little attention has been given to quality assurance for these systems. These investigators performed a detailed commissioning and quality assurance showing an average accuracy within 1 mm on phantom studies, however, proper clinical confirmation is still required. A common drawback of these systems remains the need for human interaction to acquire the ultrasound images in the treatment room prior to treatment and the manual alignment of CT and ultrasound structures. The commercial systems calculate the required shifts but do not allow for an automated correction of the treatment couch. These issues compromise efficiency (workflow) for accuracy, increasing the overall treatment time.

9.2.5 Computed Tomography

To overcome the 2D limitation of planar detection systems in assessing 3D localization problems, several investigators have proposed the use of CT scans prior to treatment (also coined volumetric imaging). In addition, tomographic slices through the patient remove the problem of overlaying anatomy in 2D imaging and the pre-treatment CT-data can be compared directly with the planning CT-data. The reported solutions can be classified into two distinct classes: (a) using kV X-ray quality or (b) using the megavolt treatment beam to acquire CT data. There are a number of advantages of CT for target localization prior to treatment: the CT data set offers full 3D information, CT has better soft-tissue contrast than planar radiographs, and the positioning CT is easier to compare with the planning CT.

Kilovolt CT

Again, two solutions have been reported in literature: A first option is to place a conventional CT scanner in the treatment room. The scanner may be positioned over the treatment couch using rails and/or the treatment couch may be used to transport the patient into the bore of the CT gantry [2, 15, 41, 83, 91], or even the use of a C-arm CT system can be considered. A second option is installation of a kV X-ray tube and detector array onboard the linac. Because the gantry rotation of a linac is much slower than a CT ring gantry flat-panel detectors are introduced to acquire so-called cone-beam CT or volume CT imaging (kV cone beam CT–kVCBCT) [36]. Both Elekta (Synergy) and Varian (On-Board Imager) are being released commercially in 2004.

An illustration of the in-room CT system is given by Court et al. [15] reporting mechanical precision and alignment uncertainties for this integrated CT/linac system. The system described integrates a high-speed CT scanner on rails and a linac. The couch base can be rotated to position the patient for either treatment or scanning, without having to move the patient from the treatment table to the CT couch. They have identified the following sources of uncertainties with their system: (1) the patient couch position on the linac side after a rotation, (2) the patient couch position on the CT side after a rotation, (3) the patient couch position as indicated by the digital read-out, (4) the difference in couch sag between CT and linac positions, (5) the precision of the CT coordinates, (6) the identification of fiducial markers from CT images, (7) the alignment of contours with structures in the CT images, and (8) the alignment of set-up lasers. The largest single uncertainty (1 SD) was found in the couch position on the CT side after a rotation (0.5 mm in the lateral direction) and the alignment of contours with the CT images (0.4 mm in the craniocaudal direction). All other sources of uncertainty were less than 0.3 mm (1 SD).

Jaffray et al. have proposed the kVCBCT system [36] that has recently be commercialised by Elekta. The approach was to integrate a kV X-ray source and a large-area flat panel detector on a standard linac allowing fluoroscopy, radiography, and cone beam volumetric CT (kVCBCT). The kVCBCT allows a volumetric CT image to be reconstructed from data collected during a single gantry rotation [22]. The X-ray tube – detector axis is orthogonal to the treatment beam. A conventional X-ray tube (Eureka Rad-92, Varian Sapphire Housing) has been mounted on a retractable arm that extends from the accelerator's drum structure (Elekta SL 20, Elekta Oncology Systems, Crawley, UK). A $41 \times 41\ cm^2$ flat-panel X-ray detector (Perkin Elmer Optoelectronics, Wiesbaden Germany) is mounted opposite the kV-tube at a nominal detector-to-focal spot distance of 155 cm. These investigators identified two major geometric non-idealities (variations in the angular velocity of the gantry by a factor of 2 through rotations over 360°, and variability in the geometric relationship between the kV focal spot and the flat-panel detector attributed to flex in the detector motion) that in the end have been taken into consideration during reconstruction by adjusting the back-projection to be consistent with the geometry of acquisition.

Based on phantom studies, Jaffray et al. [36] illustrated the fully volumetric nature of the cone-beam CT data, showing excellent spatial resolution in all three dimensions (as opposed to conventional CT where the cranio-caudal resolution depends on the slice thickness and pitch). The system provided submillimeter spatial resolution (approximately 0.7 mm full-width at half maximum of the line spread function) and a lowest readily detectable contrast at 47 Hounsfield units.

So far no clinical studies have been published that utilize this information for automated alignment of the target volume with respect to the machine's isocenter.

Megavolt CT

Again, two solutions have been proposed: First the use of EPIDs available on a conventional linac to produce megavolt cone beam CT image data (MVCBCT) [23, 56, 71], and second the unique and specific helical scanning that is provided with the tomotherapy system (TomoTherapy Inc, Madison, WI) [51]. The application of megavolt for CT has both an inherent advantage as well as disadvantage. As with EPIDs, contrast is poorer compared to diagnostic X-ray quality, on the other hand high-Z artefacts are not present. The latter not only reduces imaging artefacts caused by (dental) prosthesis or even bone but also improves the unique identification of implanted radio-opaque markers.

Application of the EPID to generate MVCBCT has the advantage that no additional hardware is required. Again, alignment of target and treatment beam is straightforward as the actual treatment beam is used to generate the images. Feasibility studies on megavolt CT scanning had been performed in the 1980s and were typically based on a single slice tomogram per gantry rotation [84]. A major problem with these approaches was accurate table indentation. Nakagawa et al. proposed to use a pretreatment MVCT slice to verify the patient set-up for stereotactic radiosurgery of the lung [63]. To overcome the problem of table indentation Mosleh-Shirazi et al. [56] reported a feasibility study on 3D MVCBCT using a scintillation detector – CCD camera based EPID on the linac, with the image frame acquisition synchronized with the radiation pulses. A first prototype required approximately 40 cGy and 2 h reconstruction time on a Sun SPARC 2 to obtain a density resolution of 2% and spatial resolution of 2.5 mm. Ford et al. investigated the use of gated image acquisition to reduce motion artifacts and defining a limited region of interest [23], their system required 2.5 MU/projection and 100 projections (approx. 7 min) to yield 2% contrast resolution and 2 mm spatial resolution. A major concern in MVCBCT is the extra-target dose introduced by the target localization process due to the challenge posed by the poor detection efficiency of X-ray detectors in the MV energy range. This low efficiency results in poor signal-to-noise performance for clinical acceptable doses [36]. Current "low dose" solutions are possible with frame acquisitions during beam-off and a trigger mode yielding 0.08 MU/image frame or 15 MU in total for a volumetric MVCBCT [71]. These investigators [71] showed the possibility of using a standard linac with stable low dose rate and an EPID to obtain clinically useful images. An interesting feature of MVCT is the linear relationship between electron density and megavoltage Hounsfield units due to the almost dominance of Compton scatter as the attenuation mechanism for clinical megavolt beams (4 – 6 MV) for the tissue materials encountered in clinic [23, 56].

A completely novel approach is presented with helical tomotherapy, which is a fusion of a linac with a helical CT scanner. This system uses a fan beam to acquire an MVCT of the patient prior to and potentially even during treatment [51]. For treatment a dedicated binary MLC is used to modulate the fan beam to provide rotational IMRT, not unlike the add-on device for sequential tomotherapy (MIMiC, NOMOS, Sewickly, PA) [13, 104, 105]. The beam rotation is synchronized with continuous longitudinal movement of the couch through the bore of the gantry, performing a helical beam pattern. When operating as a helical MVCT system, the leaves are fully retracted to the open state. The on-board CT option offers a number of verification processes as follows. (a) The MVCT scan can be fused with the planning CT scan for automated target localization and positioning prior to treatment. Verification of the automated fusion routine on an anthropomorphic phantom showed correct translations and rotations to an accuracy of less than 1 mm or 1° [51]. The set-up correction (involving rotations and translations) can be implemented either by moving the patient or, in principle, by modifying the IMRT delivery to account for the patient's actual geometric offset. (b) The CT detector system can be operated during the treatment to compare the detector signal with the expected signal and as such detect deviations, or alternatively, to reconstruct the dose delivered to the patient from exit dose measurements. The energy fluence distribution and the CT representation can be used to compute the actual dose distribution in the patient. This reconstructed dose distribution represents the dose the patient actually received, and it may be superimposed on the CT representation just obtained to realize a new form of in vivo dosimetry.

9.2.6 Others

As already stated in the introduction the concept of target localization is as old as radiotherapy and in continuous evolution. Many solutions have been sought to improve both the efficacy as well as the efficiency of this process. The previous paragraphs highlighted some of the most recent and promising solutions to reduce the SM based on image-guidance of internal structures. One solution that has not been covered in detail is the use optically-guided or video-based positioning systems. These systems, although image-based and having the potential to fully automate the positioning process, do not allow visualization of internal structures, but allow for high-precision repositioning of the skin surface. As

such, these systems are well fitted to increase the efficiency of the patient set-up procedure in comparison with the manual set-up procedure based on alignment of skin markers and room lasers. Concerning increasing the efficacy, these systems have a limited potential for extracranial lesions. Soete et al. [85] have shown a decrease of the SD in patient set-up errors in both the lateral and antero-posterior directions for prostate patients using an optical tracking system with infrared reflecting skin markers (ExacTrac, BrainLAB), but observed no significant improvement in the longitudinal direction compared to conventional skin-marker – laser alignment. A near real-time prototype opto-electronic dynamic 3D surface sensor has been introduced by Moore et al. [55] designed to match the patient contour to a digital body surface generated from CT-data. Yan et al. [118] investigated a video-based repositioning technique designed to use skin features obtaining 1.0 mm (SD 0.3 mm) and 0.2° (SD 0.5°) on phantoms. Other solutions such as immobilization devices should also be considered when in search for reduction of treatment margins, preferably in combination with an image-guided system.

9.3 IGRT for Management of Intrafraction Geometric Uncertainties (Reduction of Both SM and IM)

9.3.1 Rationale

As most treatments require a beam-on time of 1 min or more (especially with the introduction of IMRT where efficiency often is compromised for efficacy [67, 107]) tumor motion introduces a fourth dimension in the problem of target localization, being time. The tumor position and the beam fluence pattern both have a time dependence in IMRT. Internal organ and tumor movement during treatment not only introduces an added risk of missing the target, but also introduces errors in the dose delivery, which in itself may have become a modulation in time for most IMRT techniques. Especially the DMCL techniques making use of temporal modulation of the beam are susceptible to increased uncertainties as both the target and the leaves are moving (not necessary in phase). One can envisage a worst case scenario in that the tumor "escapes" the treatment window that slides over the target volume. SMLC and in particular the so-called close-in technique (as opposed to the sweeping or sliding window technique) might be considered less influenced by this time dependence, and the use of physical compensators may as well be considered to be the most efficient in this respect [78]. However, the dynamic techniques seem to be more popular emphasizing the need for appropriate image-guided techniques to assess the localization of the target volume at all times during the treatment delivery, preferably tailored to the pathology and or individual patient. Depending on the tumor's location and the degree of fixation to other structures the degree and direction of motion is tumor-specific. As CT-simulation has replaced conventional fluoroscopic simulation for 3D CRT and IMRT, image-guidance is not limited to the moment of actual treatment, but needs to be incorporated at the time of imaging for treatment planning. In other words, the image-guidance procedure chosen for a certain tumor location needs to be considered at each step in the entire chain of events from initial imaging for treatment planning on. Based on the IGRT approach that will be used, all imaging techniques should be adapted to cope with internal organ movement accordingly.

Langen et al. [43] recently published a comprehensive overview on organ motion and its management, emphasizing the importance of the knowledge on the amount and nature of CTV motion for the determination of the IM (especially interesting for liver and lung treatment where increasing knowledge suggest the use of hypofractionated treatment schedules). Again, several solutions can be identified to account for individualized physiologic movements and variations in geometry of the CTV during therapy.

In a first approach, one can try to eliminate the IM from the SM, establish a procedure for optimal reduction of the SM, and measure the actual extent of motion to incorporate an individualized and tumor specific IM in the PTV. This procedure would suggest using "slow" imaging techniques, multiple sets of fast imaging techniques or fluoroscopic techniques (conventional simulation or fast MRI [79]) to assess the individualized internal organ movements during the treatment planning process. An illustration of this idea is given by Caldwell et al. [12] in that PET images are used to improve knowledge of the IM for moving tumors. These investigators make a point on the limitations of fast, helical and multi-slice CT scans that provide a "snapshot" only of a tumor that might be mobile. The tumor may be frozen by fast image acquisition at a geometric extreme position and the resulting images may not correctly represent either the time-averaged position or the shape of the tumor. Even slow CT-images of a moving object do not represent the stationary object nor do they include information of the total extent of motion. Unlike CT, PET imaging does not provide a snapshot of the target's position, but rather a time-averaged image representing a summed representation of the tumor in all its locations. PET therefore, defines the statistical volume through which the tumor moves and subsequently defines an individualized IM (provided threshold and uptake are properly accounted for). Based on phantom studies, Caldwell et al. showed that PET images closely resemble the capsular shape expected of the time-averaged motion of a sphere, and in all cases the PET-imaged volume

was larger than the true motion volume [12]. Van de Steene et al. [93] have adopted this approach in the treatment of small primary lung tumors or metastasis in fusing PET-images (requiring approximately 6 min per couch position) with the planning CT, and using the former for determination of the IM. This approach in combination with applying implanted radio-opaque markers [18] and stereoscopic kV-imaging enabled the following rules for the SM applied in a hypofractionated treatment schedule using dynamic field shaping arc therapy: 4 mm isotropic margin for primary lung tumors in case of implanted markers and 6 mm latero-lateral and antero-posterior, and 8 mm cranio-caudal in the absence of markers.

A second approach is to "freeze" the target in a certain location that is known both during the treatment planning process (i.e., initial imaging) and during treatment. Basically this requires some kind of body immobilization (stereotactic body frame) and imaging prior to treatment [30, 114, 119].

A third approach is to track to movement of the target (during free or shallow breathing of the subject, or breath hold), which requires a breathing synchronized radiotherapy technique (an example is given in the chapter on stereoscopic kV-imaging) or a robotic linac that actually follows the moving target. In both cases the image-guidance technology is quite similar, the difference being that one approach utilizes the motion information to trigger the beam the other utilizes the information to guide the machine. These methods are discussed in detail in chapter II. 11. Different technologies have been proposed in literature for either of the two last solutions that all require a so-called "breathing synchronized radiotherapy system" or "gating" and especially focuses on reducing the IM for targets that show considerable motion due to breathing or cardiac related movements. Again several option have been reported in the literature: (a) use of a stereotactic body frame [30, 114], (b) a spirometer to monitor the lung volume and possibly guide the patient's breathing or train the patient as to allow triggering of the beam at a certain moment in the breathing cycle [72, 112], (c) a video camera system or infrared system to capture the vertical motion of reflective markers placed on the patient's body, and (d) the use of a wrap-around inductive transducer placed around the abdomen to determine the change in a cross-sectional area.

The last two approaches also require fast CT-data acquisition for treatment planning established or "triggered" at a known position during the moving cycle of the target volume and this position, in turn, is reproduced during treatment delivery. This is the so-called "prospective" approach. The so-called "retrospective" approach, in turn, is based on acquisition of multiple "gated" CT-data sets that correlate each with a specified moment in the moving cycle. And a specific set is chosen during treatment planning that represents to the ideal moment in the breathing cycle that can be reproduced during treatment (some discussion exists on whether this should be at deep inhalation, deep exhalation or plain free breathing).

9.3.2 Stereoscopic kV-ray Imaging

Two possibilities have been investigated to eliminate the margin for tumor motion using this approach of stereotactic kV-imaging: gating or tumor tracking. The former uses a treatment window at the time of treatment that can be created where the target is allowed to dwell during beam-on, and consequently the beam is turned off when the target moves outside this window (gated treatment). This approach requires either real-time imaging of the actual target (technically difficult) or real-time tracking of external moving features that can be correlated to the internal movements. Provided an appropriate correlation can be established, the latter approach not only allows for the so-called "gated" treatment (where the beam is switched on and off when the target respectively moves in- or outside the treatment window), but also allows robotic movement of the linac following (tracking) the assumed position of the target [14, 59–61]. As both technologies apply a similar approach in image guidance the gating technique as it is used with the NOVALIS BODY/ExacTrac 3.0 system at the AZ-VUB for primary lung lesions or liver metastasis will be used as an illustration of the concept.

Treatment planning is based on a fast CT-scan acquired during free breathing of the patient and the PTV margin is defined based on registration with PET images (see earlier). Two kinds of markers are used that are present at the time of planning-CT acquisition: infrared reflective markers allowing real-time monitoring of the patient's position and breathing cycle (see also the earlier description of the NOVALIS BODY system) and implanted radio-opaque markers that can be visualized using the stereoscopic kV-system. At the time of treatment planning both markers are identified and registered with respect to the planning isocenter for this particular phase of the breathing cycle (defined by the CT data set). The following procedure will now be repeated at each treatment fraction (Fig. 5). Prior to treatment the patient is positioned using the infrared positioning system to align the treatment isocenter approximately with the machine's isocenter. The patient is allowed free breathing and during several seconds the breathing signal is monitored in 3D. The user then defines an image acquisition level at which kV-images (one pair of images taken at the same point in the breathing cycle) will be taken (triggered by the IR system). Usually this imaging level will be defined at the phase that will be used as a window for treatment (at expiration or inhalation whichever has preference), but additional imaging levels can be defined at any time

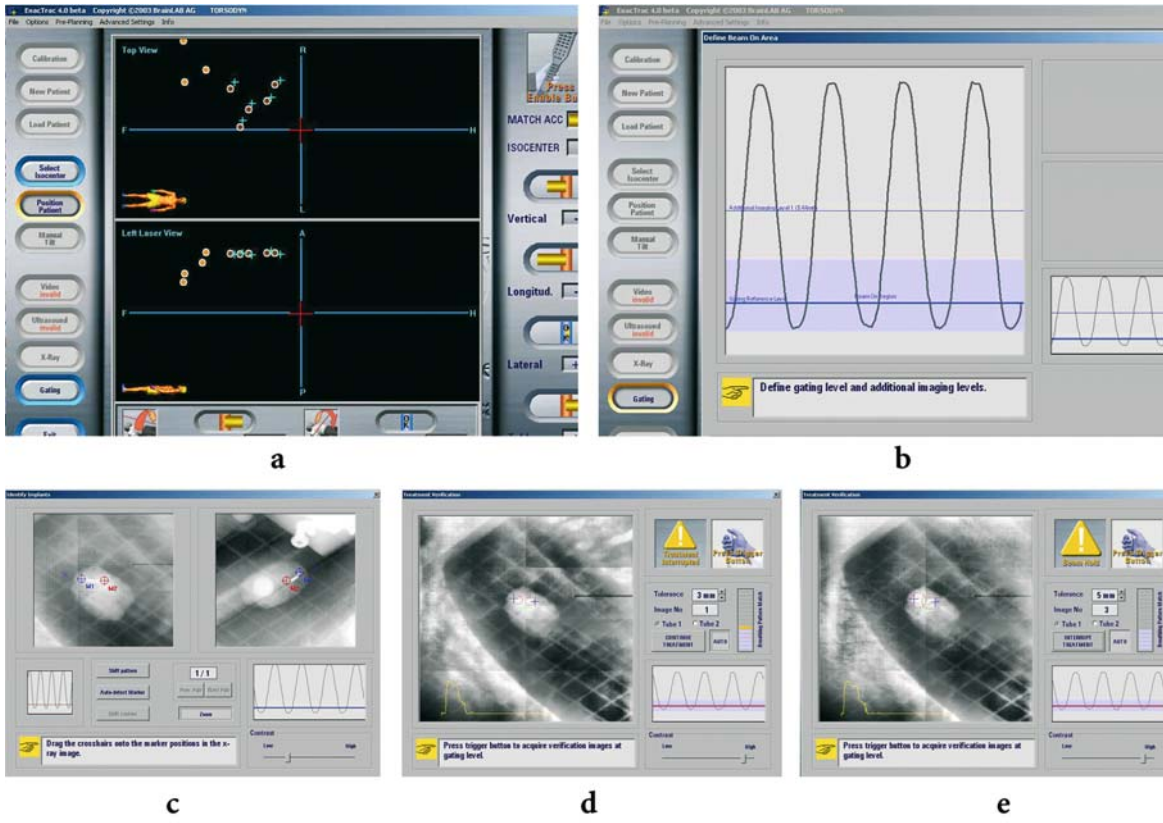

Fig. 5a–e. Illustration of gating interface at the ExacTrac/NOVALIS BODY console: **(a)** the real-time IR tracking window during initial set-up; **(b)** the breathing signal as measured with the IR system with definition of the imaging level inside the gating window (*blue area*). The gating window can be customized by the user. The kV image acquisition will be triggered whenever the breathing signal crosses this line. An additional verification imaging level is set outside the treatment window or gate. The beam will be on whenever the breathing signal is inside the *blue area* and turned off whenever the signal is outside this window; **(c)** the auto detection of the internal marker images at the treatment level. This information will be used to position the target at this breathing level with respect to the treatment machine's isocenter; **(d)** verification images where the implanted marker is outside the pre-defined tolerance region and the beam will be automatically turned off; **(e)** a verification image with an accepted position of the implanted marker suggesting the correlation between internal and external marker is maintained and treatment will proceed

of the breathing cycle. The user then defines a treatment window determining the beam-on time allowed before and after this phase of the cycle. At this stage there exists no correlation between the internal and external markers apart from the initial identification from the CT-data set that has been acquired at an unknown phase of the breathing cycle. Consequently, one pair of kV-images is acquired (triggered by the IR system at identical moments in the breathing cycle) and auto-detection of the implanted markers is performed. This establishes the initial correlation between the IR monitoring system and the implanted markers (i.e., the target volume). The treatment couch position is automatically adjusted as to align the treatment isocenter (at that particular phase of the breathing cycle) with the machine's isocenter, and treatment can start. The gantry is placed in position and the beam will be triggered by the IR-system through a connector to the treatment machine's console stopping or starting both irradiation and leaf motion immediately. The treatment beam will be on when the breathing signal monitored by the IR system is inside the predefined treatment window and off when the signal is outside this window. The former approach assumes a stable correlation between internal and external markers, which of course need not be true. Therefore, the user can predefine an allowed uncertainty around the implanted markers in the initial images and during treatment multiple pairs of stereoscopic kV-images may be acquired at the predefined imaging levels. Each time the implanted markers will be automatically detected and if the marker position is within the allowed region, treatment will proceed as planned. If, on the contrary, the implanted markers are not in the allowed region of uncertainty, the treatment will be aborted and the user will be asked to re-establish the correlation between internal en external markers.

Absolute dose measurements [Verellen D. et al., unpublished data, 2004] with the ionization chamber (IC) mounted to a moving phantom (the top of the IC

Fig. 6a–d. Megavolt portals illustrating the "gated" approach to cope with internal organ motion: **(a)** a daily QA-pattern used for verification of the miniMLC-linac combination for DMLC-IMRT treatment acquired on a X-OMAT V film (Kodac, Rochester); **(b)** the result of the same pattern acquired with the film fixed, but the linac delivery gated following a breathing cycle of 16 cycles/min; **(c)** the resulting fluence pattern with the film mounted to a moving phantom (again following a 16 cycles/min breathing pattern, with 3 cm longitudinal distance between the two extreme positions) and a non-gated treatment delivery. Note that the leaf-motion is perpendicular to the motion of the film; **(d)** the resulting fluence pattern on a moving film mounted to the phantom from a gated treatment [D. Verellen et al., unpublished results, 2004]

described an ellipse with a 3-cm projection in the gantry-target direction, simulating a breathing cycle with 16 cycles/min) and irradiated with a $3 \times 3\text{cm}^2$ small field with static gantry showed 0.44 Gy (SD: 0.01 Gy), 0.95 Gy (SD: 0.00 Gy) and 0.98 Gy (SD: 0.00 Gy) for a 1.00 Gy treatment in air for non-gated irradiation and gated irradiation with a default window and tight window, respectively. The same cyclic motion was performed with a radiographic film mounted to the phantom and irradiated with a QA-test pattern for IMRT (Fig. 6), showing some residual blurring in the pattern when irradiated in gating mode with a default gating window.

The beam tracking approach as proposed with the CyberKnife system [14, 59–61] is based on a similar correlation – and updated correlation – between external markers (to monitor the breathing signal) and internal markers to enable the linac in actually following the target's internal motion (Fig. 7). Rigid phantom tests based on TLD dosimetry showed a sub-millimeter accuracy in the system's performance in fiducial guided targeting [61]. These investigators [Schweikard et al., unpublished data, 2003] observed a systematic lag in tracking a linear motion of a needle pointer that was correlated to the velocity (i.e., an RMS between 0.9 mm and 2.8 mm for linear velocities between respectively 3 mm/s and 10 mm/s). Based on these results, inspiration breath-hold was introduced clinically with a reported 3D reproducibility within 1.8 mm and 2.5 mm for lung tumors and pancreas tumors respectively [60].

Fig. 7. The CyberKnife (Accuray Oncology, Sunnyvale, CA) concept, consisting of a linac mounted to a robotic arm able to track organ motion. The latter is realized through a combination of optical tracking of surface markers and correlation with internal structure based on stereoscopic kV-images acquired on 2 kV-flatpanel detectors mounted at an oblique angle behind the patient couch. (image by Karl H. Blohm)

9.3.3 EPIDs in Combination with On-board kV-systems

The on-board kV-systems that have been explained in the chapter on kVCBCT can in principle also be used to establish a correlation between internal and external motion. Again, several approaches are possible: applying an external monitoring system similar to the IR system as described earlier and trying to establish a correlation between internal and external information and applying the external signal to trigger the beam, or applying the on-board kV-system in fluoroscopic mode and using this information to trigger the beam. The latter has the disadvantage that only information in a plane parallel to the treatment beam can be obtained during treatment and consequently 1D is lost. In principle this could be solved with the usage of the EPID, which again will be technically difficult when DMLC techniques are used in IMRT. So far, no publications have been found on this approach, but several groups are investigating these possibilities.

9.3.4 MegaVolt Imaging

The helical tomotherapy system as described previously also offers a possible solution for image guided treatment of moving lesions. The concept that MVCT imaging can be performed during treatment provides information on motion of the target. The system has the potential to vary both the treatment slice thickness and the pitch (ratio of table increment and slice thickness). This flexibility allows for instance usage of

a relative large slice thickness (e.g., 2.50 cm) and a fine pitch (e.g., 0.25 cm) and assigning separate treatments that related to different moments in the breathing cycle (i.e. to different positions of the target) to consecutive gantry rotations. This option and others are still under investigation and will be reported in literature shortly.

9.4 Patient Immobilization

When it can be guaranteed that the representation of the patient at the time of delivery is the same as at the time of imaging, the use of these primary images to define extremely tight margins is justified. The latter is true in stereotactic radiosurgery (SRS) where the brain is relatively fixed to the cranium, and the cranium in turn fixed to a rigid external device and coordinate system. Which brings us to the concept of immobilization, with SRS as the ultimate example. In fractionated stereotactic radiotherapy for cranial lesions and head-and-neck treatment, immobilization can also reduce the need for image guidance prior and during each particular treatment session, albeit with less accuracy than in the previous example [37, 105, 106, 111]. The use of immobilization devices for thoracic or abdominal lesions is a matter of debate [85, 87], yet the combination of immobilization (e.g., the stereotactic body frame or SBF [114]) with the proper tools for target localization can largely help in reducing the PTV margins [30, 114, 119]. The rationale is that a well-constructed immobilization device will aid in patient repositioning and help the patient maintain the treatment position. These techniques can vary from relatively simple tools (e.g., a knee roll for prostate treatments) towards elaborate body casts with or without devices to limit the effects of breathing related motion. Again, there is no general rule and each center is advised to weigh the extra efforts against the advantages in positioning, and investigate the geometric precision obtained with the tools available on-site.

Immobilization techniques for intracranial targets can be classified in minimally invasive (typically for single fraction stereotactic radiosurgery) and non-invasive or relocatable systems (typically for multi fraction stereotactic radiotherapy). The introduction of linac-based radiosurgery has introduced a large variety of such systems aiming at set-up precision that could compete with the gamma-knife technology. The stereotactic frame was original developed as a device for accurate positioning of instruments such as probes and biopsy needles into predefined locations in the brain. Generally the frame consists of a ring which is rigidly attached with pins to the patient's skull and defines a coordinate system is such a way that any point in the brain can be described with a unique set of coordinates. A target localizer assembly is added that in combination with an imaging system can be used in determination of the target coordinates. The basic frame is also used for patient set-up and immobilization at the treatment machine utilizing a so-called couch docking device. Reports on geometrical uncertainty in stereotactic radiosurgery usually describe the entire procedure's accuracy (both mechanical accuracy and patient relocation) and vary from sub-millimeter for gamma-units to the order of 1 mm for linac-based systems [17, 75, 106]. Non-invasive stereotactic frames typically obtain geometric precision in the order of millimeters [37, 111].

Immobilization for the head and neck region usually consists of a support under the head and a facial fixation mask (with or without inclusion of shoulders), both attached to a base-plate on top of the treatment couch. The thermoplastic cast is considered to be a standard allowing reproducibility in patient set-up with standard deviations in the order of 2 mm to 4 mm [5]. Despite immobilization large set-up variations can occur [29] and an increased accuracy can be realized by separating the immobilization system from the positioning technique, one example of which has been described by Verellen et al. [105] (Fig. 8), introducing customized ear moulds and a bite block with imbedded radio-opaque markers in combination with a thermoplastic cast. Other systems have been proposed that evolved from the so-called relocatable frames for stereotactic radiosurgery [17]. As such the immobilization system is exclusively used to reduce patient motion during treatment, and target localization is performed by means of image-guidance techniques as discussed earlier.

Immobilization for the thorax and abdominal region is more complicated and as mentioned in the introduction, the use of thermoplastic body casts is a controversial issue both for breast and pelvic irradiation. Tight fixation of the patient's body is impossible and the targets and organs at risk are still mobile due to breathing motion or change in organ fillings. Additional marks at the patient's body surface are less accurate than marks attached to a mask system, yet the latter may not be as representative as should be and might even introduce an additional systematic error. However, the use of effective immobilization devices may improve the probability that the patient

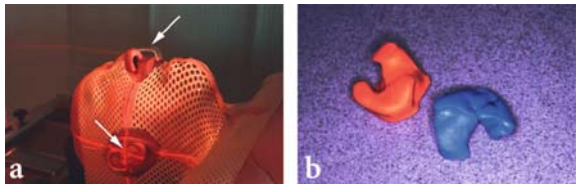

Fig. 8. (a) Image of facial mask system illustrating the usage of fiducial markers (0.2 cm diameter lead beads) fixed to the customized earmoulds and bite block for target localization. (b) Image of the customized earmoulds with a 0.2 cm lead bead as fiducial marker for target localization (visual, CT, and portal imaging)

will return repeatedly to the same position and maintains that position during treatment. In addition these devices might reduce possible introduction of errors in image co-registration (especially when using rigid fusion algorithms) in establishing quasi-identical patient positions at different imaging acquisitions (Fig. 9). A general consensus is that, in order to be effective, an immobilization device needs to extend well beyond the treatment site; it requires a thorough understanding of anatomy and physiology; and its efficacy depends on the care with which it is fabricated and used. The most stringent specifications are met with the so-called body frames for stereotactic body radiosurgery first introduced by Lax and Blomgren [47], where the device is used for patient fixation, external reference system for determination and localization of the stereotactic coordinates, and a mechanical tool for reduction of breathing mobility. Using a similar SBF Wulf et al. [114] analyzed 32 targets in thoracic and abdominal treatment sites, yielding standard deviations of 3.4 mm antero-posterior (mean 1.1 mm), 3.3 mm latero-lateral (mean 0.7 mm) and 4.4 mm cranio-caudal (mean 1.5 mm), with maximal deviations of 12 mm. If a security margin for target variability of 5 mm (antero-posterior and latero-lateral) and 10 mm (cranio-caudal) was used their results indicated that about 12–16% of the targets might be missed partially in the antero-posterior and lateral direction, and 9% of the targets in the cranio-caudal direction. Therefore, the conclusion was drawn to recommend CT-verification prior to irradiation to detect these targets with decreased reproducibility. A treatment session usually lasted for 30–60 min. While patient set-up and repositioning in the SBF could be performed within 5 min, target verification and control of isocenter coordinates relative to the target was more time consuming. As described above, these investigators preferred CT-verification to isocenter verification relative to bony landmarks. The former was performed at the CT-scanner with subsequent transport of the patient in the SBF to the treatment room, with additional isocenter verification at the linac to detect patient dislocation due to transport. Again, separating immobilization from localization and hence trying to increase both efficacy as well as efficiency.

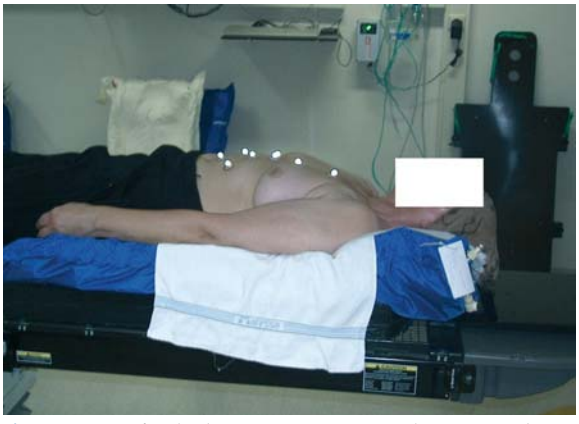

Fig. 9. Image of a body cast system in combination with IR-reflective markers mounted on the patient's surface for target localization

A final remark with respect to immobilization devices concerns dose absorption and ideally the device should be included in the dose calculations process. The effect on the patient's surface dose in particular, can be important especially if beam energies lower than 6 MV are used and the beam traverses several cm of foam and additional casts.

9.5 Conclusions

With the introduction of IMRT and SBRT we have reached a point where the radiation dose can be shaped to the target volume with surgical precision. However, these new treatment techniques introduce an enormous inherent risk, to quote J. Rosenman: "We are at increased risk of missing very precisely." Inter observer variability in target delineation is a well known problem and improper knowledge of the target volume and the most likely microscopic spread may introduce improper identification of the CTV. These issues, although being of utmost importance and not to be neglected, may be covered appropriately with the introduction of complementary imaging techniques during the process of target delineation in the treatment planning. Misalignment of the target volume with respect tot the treatment beam, on the other hand, belongs to an entirely different class of treatment errors. The latter is translated in the introduction of SM and IM in defining the PTV margin. In addition to geometric miss, the temporal creation of fluence patterns inherent to most IMRT techniques introduces yet another uncertainty in the dose delivery process. In this chapter some of the most common techniques to enable reduction of both the SM and IM have been reviewed in view of IMRT. The issue of internal motion and imaging in real-time is a matter of debate and most the techniques that have been reviewed in this chapter have not yet been validated clinically, and many adaptations will surely follow. Again, the reader is advised to define the department's philosophy clearly prior to choosing a solution that fits in this approach and avoid being caught in a so-called fashion in radiotherapy.

The author would like to quote D. Jaffray to close this chapter with a final comment that closely voices his own opinion: "... Finally, an area of critical importance for clinical implementation of this technology [...] is in the seamless integration of the imaging system within the control system of the linear accelerator. It is clear that clumsy imaging procedures will not succeed in today's

busy treatment centers, and only through the development of a highly integrated imaging and delivery system will this technology begin to make clinical inroads. An unfortunate case in point can be found in the very slow acceptance of portal imaging technology. Although this technology has been available in one form or another for many years, it has yet to be adopted in the mainstream. This is a consequence of the lack of appropriate tools for image interpretation and failure to fully integrate these systems into clinically acceptable practice. It is hoped that we can learn from this experience and not have the technology developed here suffer a similar fate".

References

1. Alasti H, Petric MP, Catton CN et al. (2001) Portal imaging for evaluation of daily on-line setup errors and off-line organ motion during conformal irradiation of carcinoma of the prostate. Int J Radiat Oncol Biol Phys 49(3):869–884
2. Aoki Y, Akanuma A, Karasawa K et al. (1987) An integrated radiotherapy treatment system and its clinical application. Radiat Med 5(4):131–141
3. Balter JM, Lam KL, Sandler HM et al. (1995) Automated localization of the prostate at the time of treatment using implanted radiopaque markers: technical feasibility. Int J Radiat Oncol Biol Phys 33(5):1281–1286
4. Balter JM, Sandler HM, Lam K et al. (1995) Measurement of prostate movement over the course of routine radiotherapy using implanted markers. Int J Radiat Oncol Biol Phys 31(1):113–118
5. Bel A, Keus R, Vijlbrief RE et al. (1995) Setup deviations in wedged pair irradiation of parotid gland and tonsillar tumors, measured with an electronic portal imaging device. Radiother Oncol 37:153–159
6. Bel A, Petrascu O, Van de Vondel I et al. (2000) A computerized remote table control for fast on-line oatient repositioning: implementation and clinical feasibility. Med Phys 27(2):354–358
7. Bel A, van Herk M, Lebesque JV (1996) Target margins for random geometrical treatment uncertainties in conformal radiotherapy. Med Phys 23:1537–1545
8. Bel A, Vos PH, Rodrigus PT et al. (1996) High-precision prostate cancer irradiation by clinical application os an offline patient setup verification procedure, using portal imaging. Int J Radiat Biol Phys 35:321–332
9. Biggs PJ, Goitein M, Russell MD (1985) A diagnostic X ray field verification device for a 10 MV linear accelerator. Int J Radiat Oncol Biol Phys 11:635–643
10. Bouchet LG, Meeks SL, Goodchild G et al. (2001) Calibration of three-dimensional ultrasound images for guided radiation therapy. Phys Med Biol 46:559–577
11. Boyer AL, Antonuk L, Fenster A et al. (1992) A review of electronic portal imaging devices (EPIDs) Med Phys 19(1):1–16
12. Caldwell CB, Mah C, Skinner M et al. (2003) Can PET provide the 3D extent of tumor motion for individualized internal target volumes? A phantom study of the limitations of CT and the promise of PET. Int J Radiat Oncol Biol Phys 55(5):1381–1393
13. Carol M (1995) Peacock: A system for planning and rotational delivery of intensity-modulated fields. Int J Imaging Syst Technol 6:56–61
14. Chang SD, Main W, Martin DP et al. (2003) An analysis of the accuracy of the CyberKnife: a robotic frameless stereotactic radiosurgery system. Neurosurgery 52(1):140–146
15. Court L, Rosen I, Mohan R et al. (2003) Evaluation of mechanical precision and alignment uncertainties for an integrated CT/LINAC system. Med Phys 30:1–13
16. De Boer HCJ, van Sornsen de Koste JR, Senan S et al. (2001) Analysis and reduction of 3D systematic and random setup errors dusirn the simulation and treatment of lung cancer patients with CT-based external beam radiotherapy dose planning. Int J Radiat Oncol Biol Phys 49:857–868
17. Delannes M, Daly NJ, Bonnet J et al. (1991) Fractionated radiotherapy of small inoperable lesions of the brain using a non-invasive stereotactic frame. Int J Radiat Oncol Biol Phys 21:749
18. De Mey J, Van de Steene J, Vandenbroucke F et al. (2005) Percutaneous placement of marking coils before stereotactic radiation therapy of malignant lung lesions. J Vasc Interv Radiol 16:51–56
19. De Neve W, Van den Heuvel F, Coghe M et al. (1993) Interactive use of on-line portal imaging in pelvic radiation. Int J Radiat Oncol Biol Phys 25:517–524
20. De Neve W, Van den Heuvel F, De Beukeleer M et al. (1992) Routine clinical on-line portal imaging followed by immediate field adjustment using a tele-controlled couch. Radiother Oncol 24:45–54
21. Ezz A, Munro P, Porter AT et al. (1992) Daily monitoring and correction of radiation field placement using a video-based portal imaging system: a pilot study. Int J Radiat Oncol Biol Phys 22(1):159–165
22. Feldkamp LA, Davis LC, Kress JW et al. (1984) Practical cone-beam algorithm. J Opt Soc Am A 1:612–619
23. Ford EC, Chang J, Mueller K et al. (2002) Cone-beam CT with megavoltage beams and an amorphous silicon electronic portal imaging device: potential for verification of radiotherapy of lung cancer. Med Phys 29(12):2913–2924
24. Gall KP, Verhey LJ (1993) Computer-assisted positioning of radiotherapy patients using implanted radiopaque fiducials. Med Phys 20(4):1153–1159
25. Gildersleve J, Dearnaley DP, Evans PM et al. (1994) A randomised trial of patient repositioning during radiotherapy using a megavoltage imaging system. Radiother Oncol 31(2):161–168
26. Gilhuijs KG, van de Ven PJ, van Herk M (1996) Automatic three-dimensional inspection of patient setup in radiation therapy using portal images, simulator images and computed tomography data. Med Phys 23(3):389–399
27. Gilhuijs KGA, Drukker K, Touw A et al. (1996) Interactive three dimensional inspection of patient setup in radiation therapy using digital portal images and computed tomography data. Int J Radiat Oncol Biol Phys 34(4):873–885
28. Gross MW, Weber WA, Feldmann HJ et al. (1998) The value of F-18-fluorodeoxyglucose PET for the 3-D radiation treatment planning of malignant gliomas. Int J Radiat Oncol Biol Phys 41:989–995
29. Halverson KJ, Leung TC, Pellet JB et al. (1991) Study of treatment variation in the radiotherapy of head and neck tumors using a fiber-optic on-line radiotherapy imaging system. Int J Radiat Oncol Biol Phys 21:1327–1336
30. Herfarth KK, Debus J, Lohr F et al. (2000) Extracranial stereotactic radiation therapy: set-up accuracy of patients treated for liver metastases. Int J Radiat Oncol Biol Phys 46(2):329–335
31. Herman MG, Abrams RA, Mayer RR (1994) Clinical use of on-line portal imaging for daily patient treatment verification. Int J Radiat Oncol Biol Phys 28(4):1017–1023

32. Herman MG, Balter JM, Jaffray DA et al. (2001) Clinical use of electronic portal imaging: report of AAPM Radiation Therapy Committee Task Group 58. Med Phys 28(5):712–737
33. Holupka EJ, Kaplan ID, Burdette EC et al. (1996) Ultrasound image fusion for external beam radiotherapy for prostate cancer. Int J Radiat Oncol Biol Phys 35(5):975–984
34. International Commission on Radiation Units and Measurements (1993) Prescribing, recording and reporting photon beam therapy. ICRU Report 50, ICRU, Bethesda, Maryland
35. International Commission on Radiation Units and Measurements (1999) Prescribing, recording and reporting photon beam therapy. ICRU Report 62, ICRU, Bethesda, Maryland
36. Jaffray DA, Siewerdsen JH, Wong JW et al. (2002) Flat-panel cone-beam computed tomography for image-guided radiation therapy. Int J Radiat Oncol Biol Phys 53(5):1337–1349
37. Karger CP, Jäkel O, Debus J et al. (2001) Three-dimensional accuracy and interfractional reproducibility of patient fixation and positioning using a stereotactic head mask system. Int J Radiat Oncol Biol Phys 49:1493–1504
38. Kirby MC, Williams PC (1995) The use of electronic portal imaging devices for exit dosimetry and quality control measurements. Int J Radiat Oncol Biol Phys 31:593–603
39. Kitamura K, Shirato H, Shimizu S et al. (2002) Registration accuracy and possible migration of internal fiducial gold marker implanted in prostate and liver treated with real-time tumor-tracking radiation therapy. Radiother Oncol 62:275–281
40. Kurhanewicz J, Dahiya R, Macdonald JM et al. (1993) Citrate alterations in primary and metastatic human prostate adeno-carcinoma – 1H magnetic resonance spectroscopy and biochemical study. Magn Reson Med 29:149–157
41. Kuriyama K, Onishi H, Sano N et al. (2003) A new irradiation unit constructed of self-moving gantry-CT and linac. Int J Radiat Oncol Biol Phys 55(2):428–435
42. Lam KL, Ten Haken RK, McShan DL et al. (1993) Automated determination of patient setup errors in radiation therapy using spherical radio-opaque markers. Med Phys 20(4):1145–1152
43. Langen KM, Jones TL (2001) Organ motion and its management. Int J Radiat Oncol Biol Phys 50(1):265–278
44. Langen KM, Pouliot J, Anezinos C et al. (2003) Evaluation of ultrasound-based prostate localization for image-guided radiotherapy. Int J Radiat Oncol Biol Phys 57(3):635–644
45. Lattanzi J, McNeely S, Pinover W et al. (1999) A comparison of daily CT localization to a daily ultrasound-based system in prostate cancer. Int J Radiat Oncol Biol Phys 43(4):719–725
46. Lattanzi J, McNeely S, Hanlon A et al. (2000) Ultrasound-based stereotactic guidance of precision conformal external beam radiation therapy in clinically localized prostate cancer. Urology 55:73–78
47. Lax I, Blomgren H, Näslund I et al. (1994) Stereotactic radiotherapy of malignancies in the abdomen. Methodological aspects. Acta Oncol 33:677–683
48. Ling CC, Humm J, Larson S et al. (2000) Towards multidimensional radiotherapy (MD-CRT): Biological imaging and biological conformality. Int J Radiat Oncol Biol Phys 47:551–560
49. Lujan AE, Balter JM, Ten Haken RK (1998) Determination of rotations in three dimensions using two-dimensional portal image registration. Med Phys 25(5):703–708
50. Lutz W, Winston KR, Maleki N (1988) A system for stereotactic radiosurgery with a linear accelerator. Int J Radiat Oncol Biol Phys 14:373–381
51. Mackie TR, Kapatoes J, Ruchala K et al. (2003) Image guidance for precise conformal radiotherapy. Int J Radiat Oncol Biol Phys 56(1):89–105
52. Merrick GS, Butler WM, Dorsey AT et al. (2000) Seed fixicity in the prostate/periprostatic region following brachytherapy. Int J Radiat Oncol Biol Phys 46(1):214–220
53. Mohan R, Wu Q, Manning M et al. (2000) Radiobiological consideration in the design of fractionated strategies for intensity modulated radiotherapy of head and neck cancers. Int J Radiat Oncol Biol Phys 46:619–630
54. Mohan DS, Kupelian PA, Willoughby TR et al. (2000) Short-course intensity-modulated radiotherapy for localized prostate cancer with daily transabdominal ultrasound localization of the prostate gland. Int J Radiat Oncol Biol Phys 46(3):575–580
55. Moore CJ, Graham PA (2000) 3D dynamic body surface sensing and CT-body matching: a tool for patient set-up and monitoring in radiotherapy. Comput Aided Surg 5(4): 234–345
56. Mosleh-Shirazi MA, Evans PM, Swindell W et al. (1998) A cone-beam megavoltage CT scanner for treatment verification in conformal radiotherapy. Radiother Oncol 48:319–328
57. Munro P (1995) Portal imaging technology: past, present, and future. Semin Radiat Oncol 5(2):115–133
58. Munro P, Bouius DC (1998) X-ray quantum limited portal imaging using amorphous silicon flat-panel arrays. Med Phys 25(5):689–702
59. Murphy MJ (1997) An automatic six-degree-of-freedom image registration algorithm for image-guided frameless stereotaxic radiosurgery. Med Phys 24(6):857–866
60. Murphy MJ, Adler JR, Bodduluri M et al. (2000) Image-guided radiosurgery for the spine and pancreas. Comp Aided Surg 5:278–288
61. Murphy JM, Martin D, Whyte R et al. (2002) The effectiveness of breath-holding to stabilize lung and pancreas tumors during radiosurgery. Int J Radiat. Oncol Biol Phys 53(2): 475–482
62. Nag S, Vivekanandam S, Martinez-Monge R (1997) Pulmonary embolization of permantly implanted radioactive palladium-103 seeds for carcinoma of the prostate. Int J Radiat Oncol Biol Phys 39(3):667–670
63. Nakagawa K, Aoki Y, Tago M et al. (2000) Megavoltage CT-assisted stereotactic radiosurgery for thoracic tumors: original research in the treatment of thoracic neoplasms. Int J Radiat Oncol Biol Phys 48:449–457
64. Pasma KL, Heijmen BJM, Kroonwijk M et al. (1998) Portal dose image prediction for dosimetric treatment verification in radiotherapy: an algorithm for open beams. Med Phys 25(6):830–840
65. Penney GP, Weese J, Little JA et al. (1998) A comparison of similarity measures for use in 2-D–3-D medical image registration. IEEE Trans Med Img 17(4):586–595
66. Petrascu O, Bel A, Linthout N et al. (2000) Automatic on-line electronic portal image analysis with a wavelet-based edge detector. Med Phys 27(2):321–329
67. Pirzkall A, Carol M, Lohr F et al. (2000) Comparison of intensity-modulated radiotherapy with conventional conformal radiotherapy for complex-shaped tumors. Int J Radiat Oncol Biol Phys 48(5):1371–1380
68. Pickett B, Vignault E, Kurhanewicz J et al. (1997) Static field intensity modulation to treat a dominant intra-prostatic lesion to 90 Gy compared to seven field 3-dimensional radiotherapy. Int J Radiat Oncol Biol Phys 39:863–873
69. Plattard D, Soret M, Troccaz J et al. (2000) Patient set-up using portal images: 2D/2D image registration using mutual information. Comput Aided Surg 5(4):246–262
70. Pouliot J, Aubin M, Langen KM et al. (2003) (Non)-migration of radio-opaque prostate markers. Int J Radiat Oncol Biol Phys 56:862–866

71. Pouliot J, Xia P, Aubin M et al. (2003) Dose-guided radiation therapy using low-dose megavoltage cone-beam CT. Med Phys 30(6):1337–1338
72. Reboul F, Mineur L, Paoli JB et al. (2002) Thoracic radiotherapy and control of respiration: current perspectives. Cancer Radiother 6:135–139
73. Roach M III, Faillace-Akazawa P, Malfatti C (1997) Prostate volumes and organ movement defined by serial computerized tomographic scans during three-dimensional conformal radiotherapy. Radiat Oncol Invest 5:187–194
74. Rudat V, Schraube P, Oetzel D et al. (1996) Combined error of patient positioning variability and prostate motion uncertainty in 3D conformal radiotherapy of localized prostate cancer. Int J Radiat Oncol Biol Phys 35:1027–1034
75. Schell MC, Bova FJ, Larson DA et al. (1995) AAPM Report No. 54, Stereotactic radiosurgery: Report of AAPM task group 42
76. Schewe J, Lam K, Balter J et al. (1995) Development of a room-based diagnostic imaging system for use in radiotherapy. Med Phys 22:939–940
77. Schild SE, Casale HE, Bellefontaine LP et al. (1993) Movements of the prostate due to rectal and bladder distension: implication for radiotherapy. Med Dosim 18:13–15
78. Sherouse GW (2001/2002) In regard to intensity-modulated radiotherapy collaborative working group. IJROBP (2001) 51:880–914; Int J Radiat Oncol Biol Phys (2002) 53(4):1088–1089
79. Shimizu S, Shirato H, Aoyama H et al. (2000) High-speed magnetic resonance imaging for four-dimensional treatment planning of conformal radiotherapy of moving body tumors. Int J Radiat Oncol Biol Phys 48(2):471–474
80. Shirato H, Shimizu S, Kitamura K et al. (2000) Four-dimensional treatment planning and fluoroscopic real-time tumor tracking radiotherapy for moving tumor. Int J Radiat Oncol Biol Phys 48(2):435–442
81. Shirato H, Shimizu S, Kuneida T et al. (2000) Physical aspects of a real-time tumor-tracking system for gated radiotherapy. Int J Radiat Oncol Biol Phys 48(4):1187–1195
82. Shiu AS, Hogstrom KR, Janjan NA (1987) Technique for verifying treatment fields using portal images with diagnostic quality. Int J Radiat Oncol Biol Phys 13:1589–1594
83. Shiu AS, Chang EL, Ye JS et al. (2003) Near simultaneous computed tomography image-guided stereotactic spinal radiotherapy: an emerging paradigm for achieving true stereotaxy. Int J Radiat Oncol Biol Phys 57(3):605–613
84. Simpson RG, Chen CT, Grubbs EA et al. (1982) A 4-MV CT scanner for radiation therapy: the prototype system. Med Phys 9:574–579
85. Soete G, Van de Steene J, Verellen D et al. (2002) Initial clinical experience with infrared reflecting skin markers in the positioning of patients treated by conformal radiotherapy for prostate cancer. Int J Radiat Oncol Biol Phys 52(3):694–698
86. Soete G, Verellen D, Michielsen D et al. (2002) Clinical use of stereoscopic X-ray positioning of patients treated with conformal radiotherapy for prostate cancer. Int J Radiat Oncol Biol Phys 54(3):948–952
87. Song PY, Washington M, Vaida F et al. (1996) A comparison of four patient immobilazation devices in the treatment of prostate cancer patients with three dimensional conformal radiotherapy. Int J Radiat Oncol Biol Phys 34(1):213–219
88. Tapen EM, Blasko JC, Grimm PD et al. (1998) Reduction of radioactive seed embolization to the lung following prostate brachytherapy. Int J Radiat Oncol Biol Phys 42(5): 1063–1067
89. Tomé WA, Meeks SL, Orton NP et al. (2002) Commissioning and quality assurance of an optically guided three-dimensional ultrasound target localization system for radiotherapy. Med Phys 29(8):1781–1788
90. Trichter F, Ennis RD (2003) Prostate localization usinf transabdominal ultrasound imaging. Int J Radiat Oncol Biol Phys 56(5):1225–1233
91. Uematsu M, Shioda A, Suda A et al. (2000) Intrafractional tumor position stability during computed tomography (CT)-guided frameless stereotactic radiation therapy for lung or liver cancers with a fusion of CT and linear accelerator. Int J Radiat Oncol Biol Phys 48(2):443–448
92. Van de Steene J, Van den Heuvel F, Bel A et al. (1998) Electronic portal imaging with on-line correction of setup error in thoracic irradiation: Clinical evaluation. Int J Radiat Oncol Biol Phys 40(4):967–976
93. Van de Steene J, Van Acker S, Vinh-Hung V et al. (2004) Hypofractionated stereotactic radiotherapy in the thoracic region. Radiother Oncol 73(Suppl):S428
94. Van de Vondel I, Coppens L, Verellen D et al. (1998) Microprocessor controlled limitation system for a stand-alone freely movable treatment couch. Med Phys 25(6):897–899
95. Van de Vondel I, Coppens L, Verellen D et al. (2001) Remote control for a stand-alone freely movable treatment couch with limitation system. Med Phys 28(12):2518–2521
96. Van de Vondel I, Coppens L, Van Acker S et al. (2005) Graphical user interface for semi-automatic patient positioning: technical aspects and clinical features. Radiother Oncol(submitted)
97. Van den Heuvel F, De Neve W, Verellen D et al. (1995) Clinical implementation of an objective computer-aided protocol for intervention in intra-treatment correction using electronic portal imaging. Radiother Oncol 35:232–239
98. Van den Heuvel F, Powell T, Seppi E et al. (2003) Independent verification of ultrasound based image-guided radiation treatment, using electronic portal imaging and implanted gold markers. Med Phys 30(11):2878–2887
99. Van Dyk J, Mah K (1993) CT scanners for treatment planning. In: Williams JR, Thwaites DI (eds) Radiotherapy physics in practice. Oxford Medical Publication, Oxford, pp 125–131
100. van Herk M, Bruce A, Kroes AP et al. (1995) Quantification of organ motion during conformal radiotherapy of the prostate by three dimensional image registration. Int J Radiat Oncol Biol Phys 33:1311–1320
101. van Herk M, Remeijer P, Lebesque JV (2002) Inclusion of geometric uncertainties in treatment plan evaluation. Int J Radiat Oncol Biol Phys 52:1407–1422
102. van Herk M, Barrilot I, Bel A et al. (2000) Geometric uncertainties in conformal radiotherapy and how to deal with them. Sixth International Workshop on Electronic Portal Imaging (Brussels, 5–7 June 2000, Van de Steene J (ed)
103. Verellen D, De Neve W, Van den Heuvel F et al. (1993) On-line portal imaging: Image quality defining parameters for pelvic fields – a clinical evaluation. Int J Radiat Oncol Biol Phys 27:945–952
104. Verellen D, Linthout N, Van den Berge D et al. (1997) Initial experience with intensity-modulated conformal radiation therapy for treatment of the head and neck region. Int J Radiat Oncol Biol Phys 39(1):99–114
105. Verellen D, Linthout N, Storme G (1998) Target localization and treatment verification for intensity modulated conformal radiation therapy of the head and neck region: The AZ-VUB experience. Strahlenther Onkol 174(Suppl):19–27
106. Verellen D, Linthout N, Bel A et al. (1999) Assessment of the uncertainties in dose delivery of a commercial system for Linac-based stereotactic radiosurgery. Int J Radiat Oncol Biol Phys 44(2):421–433

107. Verellen D, Linthout N, Soete G et al. (2002) Considerations on treatment efficiency of different conformal radiation therapy techniques for prostate cancer. Radiother Oncol 63: 27–36
108. Verellen D, Soete G, Linthout N et al. (2003) Improved target localization and patient set-up by combining real-time infrared tracking and stereoscopic X-ray imaging. Radiother Oncol 67:129–141
109. Verhey LJ (1995) Immobilization and positioning patients for radiotherapy. Semin Radiat Oncol 5:100–114
110. Vigneault E, Pouliot J, Laverdière J et al. (1997) Electronic portal imaging device detection of radiopaque markers for the evaluation of prostate position during megavoltage irradiation: a clinical study. Int J Radiat Oncol Biol Phys 37(1):205–212
111. Willner J, Flentje M, Bratengeier K et al. (1997) CT simulation in stereotactic brain radiotherapy – analysis of isocenter reproducibility with mask fixation. Radiother Oncol 45: 83–88
112. Wong JW, Sharpe MB, Jaffray DA et al. (1999) The use of active breathing control (ABC) to reduce margin for breathing motion. Int J Radiat Oncol Biol Phys 44(4):911–919
113. Wong J, Wright N, Dimmer S et al. (2003) Theory of operation for a novel electromagnetic system for precise target localization and continuous tracking. Med Phys 30(6):1415
114. Wulf J, Hadinger U, Oppitz U et al. (2000) Stereotactic radiotherapy of extracranial targets: CT-simulation and accuracy of treatment in the stereotactic body frame. Radiother Oncol 57(2):225–236
115. Yan D, Wong JW, Gustafson G et al. (1995) A new model for "accept or reject" strategies in off-line and on-line megavoltage treatment evaluation. Int J Radiat Oncol Biol Phys 31:943–952
116. Yan D, Wong J, Vicini F et al. (1997) Adaptive modification of treatment planning to minimize the deleterious effects of treatment setup errors. Int J Radiat Oncol Biol Phys 38:197–206
117. Yan D, Xu B, Lockman D et al. (2001) The influence of interpatient and intrapatient rectum variation on external beam treatment of prostate cancer. Int J Radiat Oncol Biol Phys 51:1111–1119
118. Yan Y, Song Y, Boyer AL (2002) An investigation of a video-based patient repositioning technique. Int J Radiat Oncol Biol Phys 54(2):606–614
119. Yin FF, Ryu S, Ajlouni M et al. (2002) A technique of intensity-modulated radiosurgery (IMRS) for spinal tumors. Med Phys 29(12):2815–2822

QA-QC of IMRT: European Perspective

Carlos De Wagter, Ph.D.

10

Contents

10.1 Introduction

The quality of IMRT is closely related to the physical quantity of absorbed dose and can therefore be elegantly expressed and tested quantitatively. Particularly the distribution of absorbed dose, being a scalar function in the 3D patient coordinate space, is fundamental in quality assurance (QA). The concept of a distribution inherently combines the positional and intrinsically dosimetric endpoints of IMRT. Absorbed dose also acts as an intermediate quantity between medicine and physics. More biological quantities, e.g., tumor control probability or normal tissue complication probability, are more elusive and less accessible for QA.

IMRT is an integrated process involving imaging, treatment planning and treatment delivery. Logically, QA activities are spread out of over the links of the treatment chain. Apart from IMRT-dedicated delivery systems, the majority of IMRT treatments are delivered using linear accelerators, which technically evolved quite slowly over the past decade, equipped with multileaf collimators that were at the onset basically designed to replace shielding blocks. Interestingly, computer control was the most important evolutionary development. By this, the treatment chain has become longer and QA should therefore be focused on machine performance characteristics that are rarely rigorously specified and usually receive little attention during maintenance and periodic quality control.

The end product of IMRT is a 3D dose distribution, the planned dose distribution that the radiation oncologist wants to be deposited in the patient at a specific site. A direct assessment through measurement of dose absorbed in the patient is generally impossible. In *in vivo* dosimetry, a related quantity, such as entrance dose or exit dose in a point or plane, is measured and compared to the quantity predicted from the planned dose distribution through a computational model, which preferentially is *independent* of the model used to design and compute the planned dose distribution. The alternative approach is to deliver the planned dose distribution to an anthropomorphic phantom and to compare the phantom measured dose distribution to the dose distribution that is recomputed for the phantom from the treatment plan using the *same* computational model. An almost philosophical reflection is that quality assurance then aims at tracking errors in the treatment process rather than in the actual clinical treatment delivery to the patient.

What is Quality Assurance in general terms? QA is a procedure within a paradigm, that is process oriented and that demonstrates the extent to which quality

has been or will be controlled. For QA, one will conduct "checkpoints" along the way to detect where the process may be introducing errors or uncertainties. At these checkpoints Quality Control (QC) examines the intermediate or final process output for minimum levels of quality. QC on itself does not actually try to improve the quality. QA does and attempts to ensure quality upstream by anticipating problems before they occur. QA should also cover the "people" part of the process. Although QC of the end product should be balanced against QC at the intermediate "checkpoints", end-product QC remains important especially in long process chains. Let us consider the production line of a motorbike that ultimately seems to suffer from wobbling and weaving, notwithstanding that the individual parts and subprocesses have been strictly quality assured. Then, it is the task of QA to move QC upstream and to tighten up tolerances or to suggest conceptual modifications to the production process so that errors are no longer amplified nor propagated throughout the production process.

Current IMRT practice and reimbursement in Northern America seems to call for treatment plan verification for the individual patient. This is not only a burden to the physics team, but is not very efficient: a considerably long patient-*aspecific* part of the treatment chain is retested for every patient. Alternatively, we propose a thorough class-solution QA strategy that is only intensively applied pre-clinically or after a modification of the class solution, in combination with a tuned periodic equipment QA program and a patient-specific QA approach that only tracks for gross errors.

Quality assurance in IMRT is mainly founded on quantitative comparisons between computed and/or measured dose distributions. Differences between measurement and calculation are principally caused by an error in planning, positioning, delivery or measurement technique. An agreement between the two distributions, on the contrary, is in itself not a proof of satisfying quality. Indeed, the distributions that are compared may both contain uncertainty or bias, so that an agreement may be reached by chance. This consideration may serve as an argument to include many degrees of freedom, i.e., many measuring points, in the comparison. This is saying that comparing dose distributions is better than comparing doses measured in a limited set of points.

10.2 The Paradigm of Quality Assurance (QA) in IMRT

QA in a non-IMRT context is traditionally divided in two categories: periodic equipment QA and routine patient-specific QA. As indicated by Williams [1], with IMRT a new category has come up: pre-treatment QA, which however is still closely connected to patient-specific QA. Therefore, we would like to add a third category, i.e., class-solution QA. Indeed, each class solution has its own planning and delivery techniques that have to be quality assured within the class solution. As we will see in this chapter, these three QA categories do not remain isolated but effectively interact as schematically represented in Fig. 1. The clinical introduction or update of a class-solution, for instance, may affect the QA activities in the other two categories of the triad. Patient-specific QA and equipment QA are parallel procedures and should not interfere directly. In the remainder of the chapter, we will further focus on the interaction between class-solution QA and equipment QA.

10.2.1 Patient-specific QA

Verification of patient positioning and machine output may be treated as independent problems, at least for patient-specific QA. The verification of patient position before and during the treatment delivery belongs to the growing and promising field of image guided radiation therapy, which falls beyond the scope of this chapter that will further focus on dose-based QA.

Although a multitude of methods can be used for patient-specific dose-based QA, individual treatment plans must be checked using time-effective and simple methods, realizing that this QA workload is proportional to the number of patients. As argued above, patient-specific QA should only be able of detecting gross errors, e.g., of more than 5% in absolute dose relative to the prescribed dose.

In-treatment Dose Verification

Ideally, the dose delivered should be verified during the actual patient treatment. In the advent of clinical IMRT, Essers and Mijnheer [2] concluded that patient dose verification had to be an essential part of a QA program

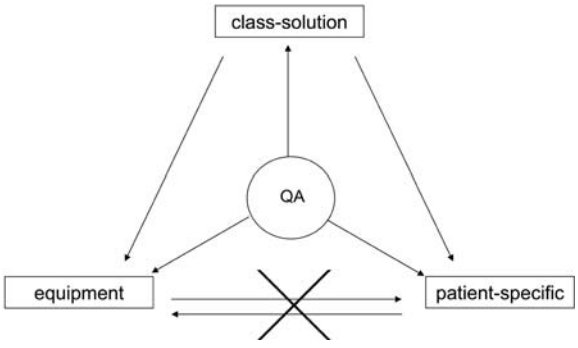

Fig. 1. The quality assurance (QA) program considered as a triad of three QA categories. Class-solution QA, typically applied pre-clinically, determines the QA procedures and tolerances in periodic equipment QA and routine patient-specific QA. The latter two categories both depend on the class solution but should not directly interact

and had to play a complementary role to treatment-sheet double checking. The classical *in vivo* surface dosimetry using point detectors is impractical in IMRT due to high gradients in fluence or dose and the variability of beam size and incidence during IMRT delivery. However, electronic portal imaging (EPID) allows checking separate intensity modulated (IM) beams [3] and principally allows reconstructing the dose distribution in the patient by relating the intensity of the transmitted beam to the dose in the patient [4]. This development of *transit dosimetry* in combination with patient setup verification is widely stimulated by the recent technological progress in amorphous silicon EPID.

Patient-specific Pre-treatment QA

The most commonly applied approach is to deliver the original patient treatment plan to a representative standard phantom that contains one or more point detectors. Figure 2a displays such a phantom setup for monitor unit (MU) verification of prostate IMRT using an ionization chamber mounted at treatment isocenter, as applied at Ghent University Hospital (GUH). The method assumes that the treatment isocenter lies in a uniform high-value portion of the dose distribution, a condition satisfied at GUH for prostate IMRT. Figure 2b presents the measured difference to the prescribed isocenter dose for a contiguous series of 111 prostate IMRT patients treated at GUH (unpublished data). The linear regression vs patient weight explains 64% of the variance. If the residual difference was higher than 5%, the MU verification measurement was repeated. If the difference remained higher than 5%, the dose distribution in the standard phantom was computed using the patient treatment plan and the same planning system. In any of the eight cases, the recomputed dose was within 5% of the measured dose.

Although MU verification by direct measurement remains the standard in IMRT, independent software can be developed to verify a treatment plan [5]. It has to be remarked that an experimental MU verification checks a longer part of the clinical treatment chain than the computational MU verification.

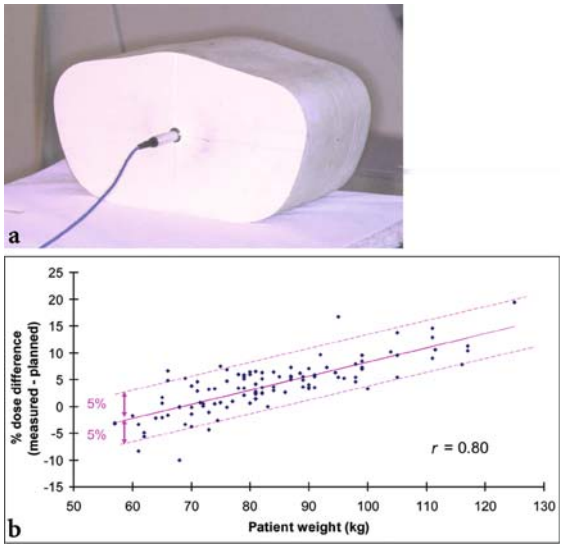

Fig. 2. (a) Pelvic phantom for MU verification of prostate IMRT. The unmodified patient treatment plan is delivered to the phantom that contains an ionization chamber at isocenter. (b) Linear regression analysis of the measured dose difference vs patient weight. Resulting coefficient of correlation is 0.80. Only 8 of the 111 patients (7%) deviate by more than ±5% from the regression line

10.2.2 Equipment QA

Equipment QA is intended to follow the acceptance testing and commissioning phase of radiation equipment and treatment planning systems. Equipment QA should have a periodic character and is ideally synchronized with the maintenance and upgrade activities applied to the equipment.

The laser alignment system, the positional stability of the treatment isocenter and the integrity of machine mechanical movements are subject of periodic QA. Machine dependent features that are dosimetrically relevant for IMRT include the dose characteristics of narrow,

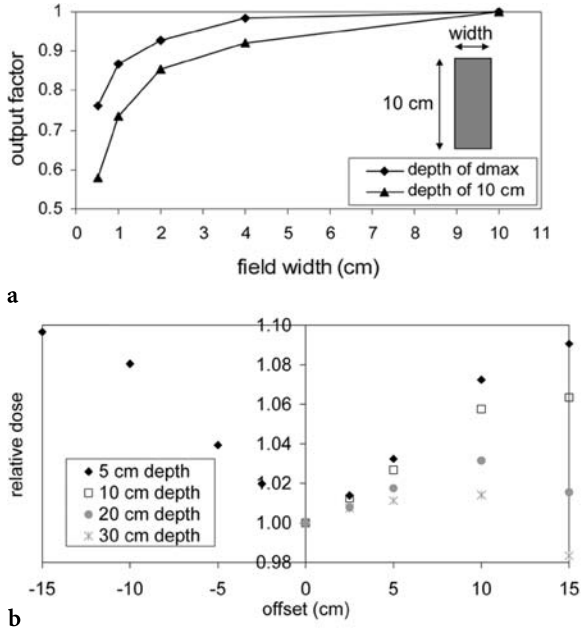

Fig. 3a,b. Output factor (OF) of small and offset fields. Data measured from an Elekta SL18 accelerator at 6 MV: (a) OF as function of field width for fields of fixed length of 10 cm, at depth of maximum dose (1.5 cm) and 10 cm. The elongated fields were collimated in width using the standard MLC in combination with the backup collimator jaws. OF strongly decreases with field width for fields narrower than 2 cm. The difference between both curves is due to the lower depth penetration of smaller fields; (b) relative output of a (5 × 5 cm)-field as a function of field offset in the direction of leaf travel for various measurement depths. The curves are normalized to the output of the central (5 × 5 cm)-field at the respective depths

offset and low-monitor-unit beams and the geometric accuracy of the multileaf collimator (MLC).

Dosimetric Characteristics of Small Fields

Small fields, especially narrow elongated centered and off-axis fields, may contribute considerably to IMRT dose. Small fields, however, are experimentally and computationally hard to assess. The output factor of typical elongated fields is given in Fig. 3a as a function of field width. The curve obtained at a depth of 10 cm shows a higher variation due to the effect that field size has on the depth dose curve. At higher-energy photon beams (> 10 MV), there is an additional effect by contaminant electrons [38]. This underlines the importance of reporting the depth at which output factors are defined ([6], p 104). The output factor of small fields is critically dependent on the actual field size: at a depth of 10 cm, the dose of a 9 mm wide field is 7% lower than the dose of a 10 mm wide field for the same number of MUs. Figure 3a demonstrates that MLC QA is important in IMRT techniques that use many small subfields, e.g., inversely planned IMRT.

Dosimetric Effects of Field Offset

The effect of a field offset in the direction of leaf travel is shown in Fig. 3b. The central local minimum is caused by the flatness filter and the lack of phantom scatter in case of a small field. At deeper depth, the effect is counteracted at extended offsets by the softer photon energy spectrum at off-axis positions. Interestingly, the effect of field offset on the output is largely independent of field size and shape (Martens and De Wagter, unpublished data).

Dosimetric Characteristics of Low-monitor-unit Fields

The higher the number of beam segments, the lower their average number of MUs is. Stabilizing control mechanisms during beam start-up may introduce dosimetric uncertainties. Output measurements, however, are commonly performed for 50 or more MU and profiles are measured in continuous radiation mode. Therefore, the dose per MU as a function of MU count must be assessed [7]. Also the initial beam profiles should be investigated, possibly in combination with a motion of the focal spot at the start of irradiation [8]. The linac should also be investigated for spurious dark current radiation [9].

Multileaf-collimator QA

MLC QA is a major part of equipment QA. As outlined by Williams [1], IMRT implies interdependence between dosimetric and geometric accuracy, that requires careful consideration. QC tests must be carefully designed to ensure that the leaves are in the required positions at the required times. Conventional QA tests for static MLCs are not sufficiently sensitive for this purpose. A simple leaf-positioning QC test being used at Ghent University Hospital consists in delivering abutting similar elongated segments and visually inspecting the patching of the segments on a dosimetric film. An example of such a test film is shown in Fig. 4. This film reveals that the segments on the left were slightly too narrow, while the overlap to the right indicates that segments were too wide there. Careful analysis of the MLC log file data for can also contribute to equipment QA, especially in dynamic IMRT delivery. For dynamic MLC, additional tests and ingenious QC procedures can be found in literature [10].

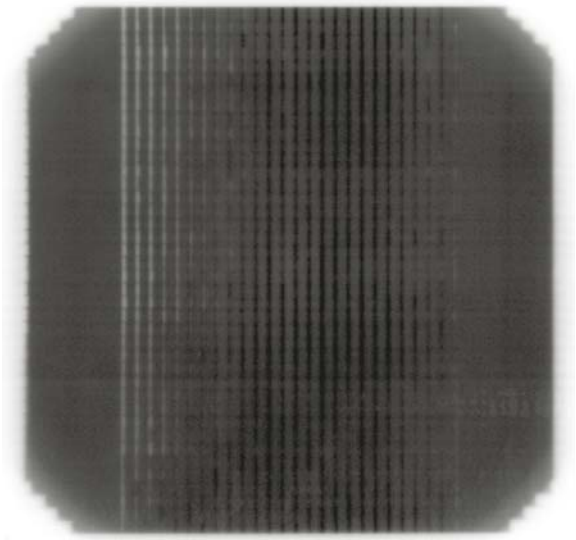

Fig. 4. MLC test pattern for MLC QA. The lateral film was exposed to 27 1 cm wide strips in a step-and-shoot fashion. The strips are intended to abut at the 50% dose lines. Data from an Elekta SL18 accelerator at 6 MV. The MLC has a rounded leaf ends. Due to the leaf overtravel restriction to 12.5 cm, the outer segments are wider. In this film, the zones of prominent overlap and underlap clearly ask for a mechanical recalibration of the MLC.

QA of the Treatment Planning System

The full treatment of QA of planning systems is beyond the scope of this chapter and is not presented here. We will restrict ourselves to enumerate some critical QC tests for IMRT treatment planning systems (computations against measurements):

- Output factor of elongated fields as a function of field width (e.g., Fig. 3a)
- Relative output as a function of field offset in the direction of leaf travel for various measurement depths (e.g., Fig. 3b)
- Collimator exchange effect of elongated field, i.e., the difference in output factor of rectangular fields if the upper and lower collimators are interchanged
- Effect of the position of the (backup) collimator jaws on the output factor of (irregular) MLC collimated fields
- 2D dose distribution of an MLC test plan for geometric leaf positioning (e.g., Fig. 4)

10.2.3 Class-solution QA

From a holistic perspective, QA should focus on the end result of the entire treatment chain: the 3D dose distribution that results from the complete IMRT treatment. Verellen et al. [11] were one of the first to verify inversely planned entire-treatment dose distributions with patient-specific anthropomorphic phantom measurements using analine dosimeters, TLDs and radiographic film. To measure directly dose in 3D, gel dosimetry is the only candidate [12]. A more complete treatment of dosimetry methods follows below.

Although a concrete patient case can serve as an ideal starting condition, class-solution QA has not to be applied to individual patient treatments. 3D dosimetry is too complex and laborious for patient-specific QA. In that view, class-solution QA is to be considered as pre-clinical rather than pre-treatment.

Also the planning approach followed within the class solution will determine the required number of clinical cases that will be investigated within a given class solution. The complex fluence maps derived form inverse planning make the plans more prone to delivery errors and require hence more QA than the few relatively large subfields from forward planning.

10.2.4 How Much QA Is Enough?

There are basically two strategies to ensure the quality of the IMRT treatment process.

Strategy 1 Realizing that each link in the treatment chain has its own potential sources of error, the physics team can develop QC checks for each link. Most of these checks are equipment related, involving i) the irradiation and imaging hardware and ii) the planning computational system. These two levels of QA are depicted as level 1 and level 2 in Fig. 5.

Strategy 2 The rationale of this strategy is that the end product of IMRT consists of a 3D dose distribution that the radiation oncologist wants to be deposited in the patient at a specific site. The quality of the end product can be assessed by an experimental 3D dosimetry, as denoted symbolically in the top of the pyramid in Fig. 5a. In practice, the treatment plan is delivered to a representative anthropomorphic phantom that allows 3D dosimetry. A quantitative comparison between the acquired dose distribution and the dose distribution recomputed for the phantom is a powerful method in the quality assessment. When this comparison reveals intolerable dose discrepancies we descend the pyramid down to level 3 and will perform a separate dosimetry of the IM-beams themselves. Strictly, 3D dosimetry of the entire treatment delivery has to be considered as a redundant QA procedure. Descending the pyramid after finding discrepancies can be informative but is time-costly. For this reason, the 3D measuring procedure, planning system and delivery system must have been commissioned and quality assured thoroughly (the latter two according to Strategy 1) before. However, descending the pyramid through level 3 may be worthwhile, especially if it leads to an improvement of the Strategy-1 QC tests of levels 1 to 2 for the class solution under validation.

It is clear that a reasonable balance between equipment QA (Strategy 1) and class-solution QA (Strategy 2) has to be found. The advantage of Strategy 1 is that

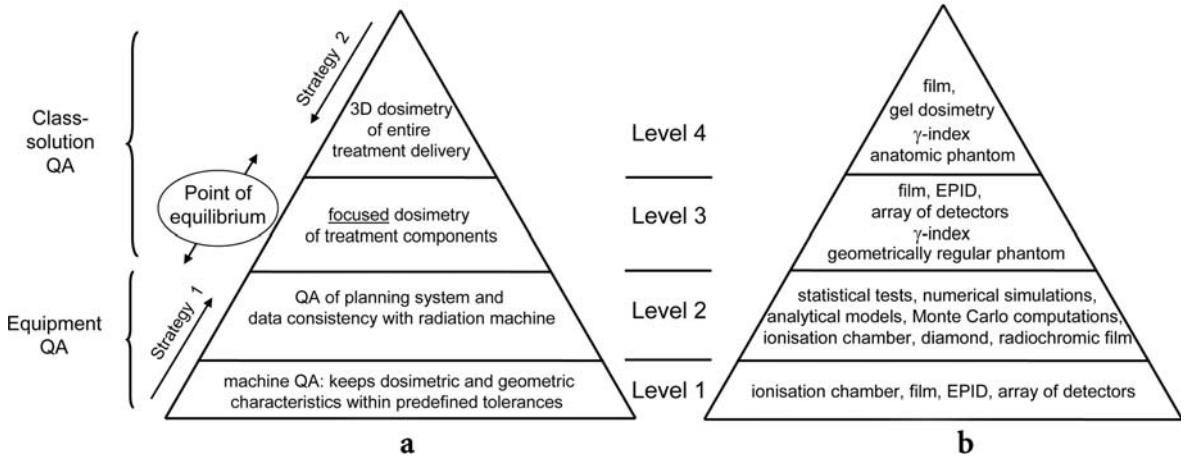

Fig. 5. (a) Conceptual pyramid that correlates the various levels of patient-*aspecific* dosimetric QA in IMRT. Like in a real pyramid, each level of QA is based on the stability of the underlying levels. In equipment QA (Strategy 1), one ascends from the base; in class-solution QA (Strategy 2), one descends from the top by applying a 3D dosimetry of an entire treatment that belongs to the class solution to be validated. Class-solution QA decreases in frequency when the class solution matures in the clinic. The point of equilibrium, representing the optimal balance, depends on the treatment technique and may further evolve with the experience gained by the IMRT team. (b) Methodology and tools appropriate for each of the levels

IMRT QA can be integrated into the traditional routine machine QA. Strategy 2, on the contrary, offers a unique dosimetric verification of the IMRT treatment, even when it was not a priori clear whether the tolerances used in Strategy 1 would effectively lead to an accurate treatment (as a matter of fact, Strategy 2 allows to identify the weakest link in the treatment chain and to fine-tune the tolerances and frequency of the QC tests needed in Strategy 1 for the class solution under validation). Indeed, a 3D dose verification is capable of revealing computational errors, inadequate beam data or malfunction of the accelerator, errors in transfer of data, and critical combinations or amplifications of deviations that could have been tolerated in a pure Strategy-1 approach. Each class solution has its own delivery technique and unique planning technique that give rise to different QA considerations. It is prudent to test frequently at first and reduce the frequency as experience builds. As the confidence in the class solution grows and the quality control tests in Strategy 1 become optimized and streamlined with the patient-specific QA, one may expect that the frequency of Strategy-2 procedures will decrease. Each IMRT team is challenged to determine the dynamics of the optimum equilibrium between equipment QA and treatment-plan-specific QA. See also caption of Fig. 5.

10.2.5 Phantoms for QA

The phantom needed depends on the level of QA. For the dosimetric verification of entire IMRT treatments, an anthropomorphic phantom allows to extend the controlled part of the treatment chain close to the patient. Such a phantom should at least have the 3D shape of the irradiated region of a "standard" patient. In addition, the phantom should be treated as the patient throughout the treatment chain, from CT-imaging to the actual treatment delivery using the actual gantry angles. Reference markers are important since structural landmarks might be useless or absent. The treatment plan to be validated has to be recomputed for the phantom. Heterogeneous phantoms, which contain air cavities or simulate lung tissue, are justified if the tissue heterogeneities may affect the quality and fate of the class solution. The evaluation of the planning system's ability to correctly compute dose in heterogeneous situations, however, belongs to the commissioning of the planning system and is beyond the scope of IMRT QA.

For the dosimetric verification of IM beams, a regular slab phantom suffices, as indicated in Fig. 5b. These phantoms have a geometrically clean design and allow an easier and more reliable placement of the detector, e.g., film. The IM fields are delivered perpendicular to the film (straight down). At this stage, we are interested in the 2D lateral dose distribution at a certain depth that should not be too deep. Dose distributions measured at too large depths become blurred by radiation interactions with the phantom (the quality of the computational modeling of these interactions does not need to be checked at this stage). Reasonable depths are 5 cm and 10 cm, depending on whether the quality index of the photon beam is lower or higher than 0. 75.

10.3 Dosimetry for IMRT

QA of IMRT has driven a paradigm shift in radiation dosimetry: the three-dimensional spatial accuracy has become as important as the intrinsic dosimetric accuracy. This has started the development of new radiation detectors next to systems for the verification of patient position.

The character of IMRT dose distributions and the delivery techniques indeed complicate dose measurements. Dose gradients that often occur in IM-beams lead to important volume effects for many detectors, and the possibly dynamic delivery of IM-beams requires integrating dosimeters when complete IM-beams or treatments must be analyzed.

In IMRT, shielded organs at risk may be surrounded by sharp dose gradients, and their unintended dose is mainly due to leakage transmission through the collimators and scatter, implying an important contribution of low-energy photons. Therefore a detector used to analyze intensity-modulated (IM) beams must have a good spatial resolution and a response which is independent

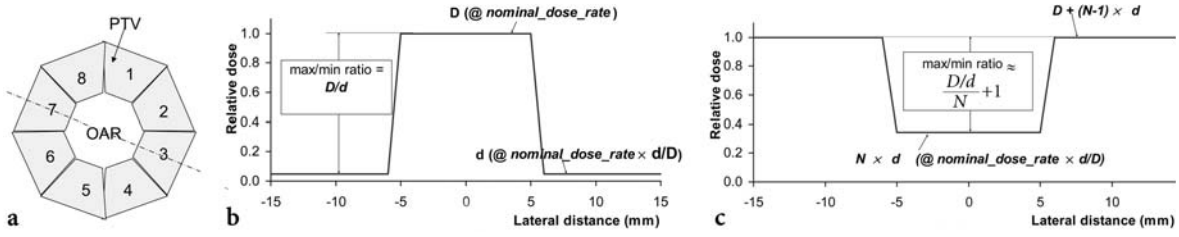

Fig. 6. (a) Fictive annular PTV around OAR in beam's eye view of an IM beam that consists of eight abutting segments. (b) Hypothetical lateral dose profile of one segment. (c) Resulting dose profile along *dot-dashed line in panel* (a). The maximum/minimum dose ratio is decreased considerably in (c), but the ratio of delivery dose rates (PTV vs OAR) has remained about the same as for a single segment

of the energy spectrum. In addition, the dose rate at any measurement point must be integrated over the entire exposure, preventing the use of traditional field scanners that use a single detector.

In complete-treatment or composite IMRT dose distributions, dose-rate effects in the detector might have higher impact than expected at first sight. Indeed, consider in Fig. 6a an annular PTV and central OAR in beams' eye view from an IM beam. The PTV is irradiated by N non-overlapping but abutting segments. Each segment delivers a dose D at the depth considered, but also a stray dose d (scatter and leakage does) outside the segment's penumbra, as denoted in Fig. 6b. Assuming that the stray dose simply cumulates in the OAR and PTV, we obtain a doses $(D + (N-1) \times d)$ and $(N \times d)$ in the PTV and OAR respectively. As explained in Fig. 6c and its legend, the ratio of *delivery dose rates* (PTV vs OAR) has remained about the same as to that of the segments themselves but is substantially lower than the *dose* ratio (PTV vs OAR). It is, of course, the low dose rate that has to be taken into consideration to estimate possible dose rate effects in the detector. In conclusion, this simple case demonstrates that a composite distribution is not enough to analyze dose rate effects, details about the dose accumulation are required.

10.3.1 Point Detectors (0D)

For dosimetry in narrow beams (level 2 in Fig. 5), the diamond detector (PTW-Freiburg, Germany) is a suitable detector [13]. The diamond is water equivalent and energy independent for megavoltage photon beams, and has an excellent spatial resolution but a correction for the dose rate dependence must be performed.

The Farmer-type chamber is the best detector in regions of shallow dose gradient and for measuring low doses. In fact, the accuracy of the ionization chamber may be affected during IMRT as there are moments that the ionization chamber is outside the actual beam or is partially irradiated. From an experimental study, Laub and Wong [14] concluded that for ionization chambers, the role of the volume effect is small compared to the effect of lateral electron disequilibrium. The possible impact of this on absolute dosimetry has been investigated in terms of Monte Carlo computed stopping-power ratios [15] and ion chamber perturbation [16, 39] at 6 MV. These studies indicate that the measuring error may amount to a few percent for individual beamlets, but that the overall error is IMRT-plan-dependent.

10.3.2 Detector Arrays (1D, 2D) and EPID (2D)

As these devices have to be irradiated with the beam axis perpendicular to the surface, they are only suited for dosimetry of IM beams. Compared to film, these level-3 or level-1 detectors (Fig. 5b) have the advantage of short acquisition time. Some pointers to relevant literature are [3, 17, 18].

10.3.3 Film (2D)

For dosimetry of individual IM beams (level 3 in Fig. 5b), film is oriented perpendicular to the beam axis at a depth of typical 5 or 10 cm. In this orientation, film dosimetry is generally considered reliable in both the high-dose and low-dose portions of the field. Martens et al. [19] found that for equivalent field sizes up to 15×15 cm, the accuracy was within 3% for XV-2 film (Eastman Kodak, Rochester, NY, USA) at 6 MV and 18 MV. Yeo et al. [20], on the contrary, found that both XV-2 and EDR2 film (Eastman Kodak, Rochester, NY, USA) exhibit considerable energy dependence at 6 MV. They could reduce the over response in and outside penumbra regions from 9% to 3% by using thin lead foils parallel to the film.

Although radiographic film is widely used as "composite film" dosimeter for entire-treatment dose verification (level 4 in Fig. 5b), its validity is still subject of controversy in literature and conflicting data have been reported. When film is considered as an 2D dosimeter for IMRT entire treatment verification, a number of unavoidable problems occur. The essential point is that film response is not constant with energy, and film becomes increasingly sensitive at low photon/electron energies. As discussed in [21], the various beam orientation differently affect the photon spectrum along the film. Both the XV-2 film [22, 23] and EDR2 film [24] show a higher sensitivity in the region around dose maximum, typically by 4%, when the film is oriented perpendicular rather than parallel to the incoming radiation. At depth of 10 cm, Robar and Clark [25], in contrast, did not find differences higher than 1.5% for both 6 MV and Kodak XV-2. Another problem is that film outside the actual beam edge has a higher sensitivity. A possible remedy for "composite film", could be lateral scatter filtering by using thin lead foils parallel to the film [20].

In an inter-center QA network for IMRT verification, the European QUASIMODO group used a pelvic phantom that contained seven EDR2 films that were basically oriented parallel to the beam axes [24]. The original intention was to interpret the "composite film" dosimetry absolutely, i.e., without normalization using another detector. However, due to the above mentioned problems, the QUASIMODO group had to adopt a two-parameter linear conversion that they applied to the "film-measured dose".

GORTEC, a French inter-center group specifically joined to define a common program for head-and-neck IMRT has also reported QA activities using film dosimetry in a homogeneous cylindrical phantom [26].

Radiochromic film, on the other hand, is an appropriate 2D detector for special applications like dose measurements near interfaces [27]. By virtue of its tissue-equivalence [28], there are no concerns about a possible induced electronic disequilibrium. Radiochromic films however are more expensive, and their application is time consuming and labor-intensive, especially when following the double-exposure calibration method [28]. Therefore, their usage is limited to levels 2 and 4 (Fig. 5b).

A word of concern about the future of film dosimetry (and hope for nature). Under pressure of environmental regulations, most hospitals convert to filmless imaging. So radiographic film might disappear in the next decade.

10.3.4 Gel Dosimetry (3D)

The most viable method of gel dosimetry that will be discussed briefly is based on gelatin gel that is doped with monomers that polymerize by absorption of dose [29]. Magnetic resonance imaging (MRI) allows to acquire quantitatively the dose distribution according to the relationship between $R2 = 1/T2$ and dose, which has to be obtained for each gel production. This calibration includes MRI of a number of test tubes containing gel and exposed to different dose levels typically between 0 and typically 8 Gy. Quantitative MRI of $T2$ has been especially optimized for gel dosimetry. A vacuum technique can be used to model the gel cast after a specific patient or anthropomorphic phantom. The resulting gel phantom is irradiated completely according to the treatment plan except for the absolute dose: in order to fully exploit the dynamic range of about 8 Gy, all the beam MU-counts are scaled up or several treatment fractions are delivered. Gel dosimetry is fully 3D and allows to simultaneously integrating the dose rate distribution in the whole phantom during the whole treatment. For relative dosimetry, an accuracy of 3% for an in-slice spatial resolution of 1.56 mm and a slice thickness of 5 mm has been reported [30].

10.4 Quality Management of QA Procedures and QA Tools

The computed or planned dose distribution often serves as the gold standard in QA. The reason is that it conforms to the therapeutic objectives and has sometimes evolved in conjuncture with the objectives used in the planning process, rather than it would have a predictive value. This means that the computed dose distribution is thought to be inseparably associated with the clinical intent of the IMRT treatment. One could say that the planned dose distribution contains the quality that has to be realized and ensured by the QA activities. Therefore, the comparison of the evaluated dose distribution to the planned distribution is essential.

Coincidental agreement should be avoided by providing sufficient independent measured data. Agreement can be coincidental, for instance, the lack of accounting for lateral electron disequilibrium may be counteracted by the neglect of accounting for longitudinal electronic disequilibrium. This is an argument to also include depth-dose comparisons at off-axis positions.

The more critical parts of the dose distributions should be involved in the comparison, e.g., dose to PTV, dose to OARs, dose gradients, dose near and in low-density tissues (if modeled in the phantom or planning).

10.4.1 Comparison Between Two Dose Distributions

First, the geometric correlation between the two distributions is established by using reference landmarks, ranging from pinprick marks in film to fiduciary markers containing CT- or MR-contrast that are placed on the phantom or patient. This geometric correlation is mathematically achieved by a coordinate transformation to a coordinate system common to both voxel grids. One of the distributions will serve as the reference, the other one is denoted as evaluation distribution.

As both geometric and dosimetric accuracy are important in IMRT, Low et al. [31] cleverly introduced the gamma (γ) index method. This evaluation method is based on a 4D distance concept: the three spatial (normalized) dimensions are supplemented with a dosimetric (normalized) dimension. In each evaluation grid point, the 4D distance is computed to all reference grid points. The γ-value in that evaluation grid point is defined as the minimum of all these 4D distances. By respective normalization of the dimensions to the spatial tolerance criterion, e.g., 3 mm, and the dosimetric tolerance criterion, e.g., 4% difference between evaluated and reference dose, the evaluated voxels where $\gamma < 1$ can be considered to fall within tolerance and to be acceptable with regard to the reference dose distribution.

Conceptually, the gamma approach may be assessed in a different way. Around any evaluation point, a fictive sphere is constructed with radius equal to the set spatial tolerance criterion. The γ-value will be lower than 1, i.e., the evaluation dose will be accepted, if a reference position can be found within that sphere where the dose is within a tolerance that decreases with distance (Fig. 7a). The gamma tool inherently allows comparing flat dose as well as steep dose gradient regions. Further refinements of the γ-concept and clarifying applications can be found in [32].

The gamma evaluation method is also applicable when one the distributions has a lower dimensionality.

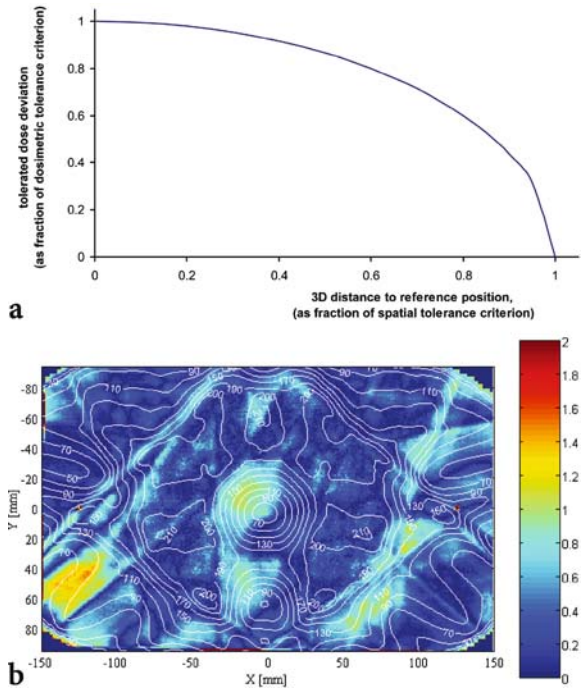

Fig. 7. (a) The gamma (γ) concept allows to compare dose distributions in dosimetric and positional terms. Tolerated dose deviation as a function of 3D distance of the evaluation point to the reference position in order to keep $\gamma < 1$. (b) Example of film-measured γ-distribution in the transverse slice of a pelvic phantom that contained a fictive horse-shoe shaped PTV. A (3%, 3 mm) tolerance criterion was used, the dosimetric criterion (3%) being expressed relative to the prescribed dose. The isodose lines of the computed dose distribution have been superposed. Apparently, the regions where $\gamma \geq 1$ (indicating $> 3\%$ dose difference and > 3 mm spatial shift between computation and measurement) are situated in the lower-dose regions

Gillis et al. [24] used the gamma method in a European QA multi-center study to compare 2D "composite film" (evaluate) dose to 3D computed (reference) dose. The gamma software routines were developed in the Matlab Version 6.1 (The MathWorks Inc., Natick, MA, USA) environment and the DICOM-RT and Image Processing toolboxes were used. Figure 7b displays the γ-distribution in the central transverse slice of the pelvic phantom used. By expressing dose differences relative to the prescribed dose, rather than relative to local dose, the analysis is more tolerant in low-dose regions.

A gamma analysis may also be useful to evaluate computed dose distributions against measured reference dose distributions for QA of treatment planning systems [37].

10.4.2 Validation of QA Procedures and QA Tools

Any QA tool or procedure must be reliable (precision) and valid (accuracy). Both performances have to be demonstrated prior to integration as a QA tool in IMRT QA.

Validation of a QA procedure requires that its output is sensitive to the characteristic, quantity or parameter being assessed. To optimize these sensitivities, numerical perturbation analysis methods and Monte Carlo simulations listed as methodologies in level 2 of Fig. 5b can be helpful.

Interestingly, complex methods like gel and film dosimetry themselves can be considered as a chain of procedures to which the concepts of the current chapter might be applied. For gel dosimetry, for instance, too many scientific works make a combination of i) validation of gel dosimetry and ii) application to the dose verification of complex dose distributions. The combination of these two objectives is too ambitious, i.e., a substantial deal of the validation work can be performed in known or even uniform dose distributions where the calibrated ionization chamber is the gold standard. This fact was painfully demonstrated by MacDougall et al. [33] in a topical review that, however, did not offer any valid comparable alternative for 3D dosimetry.

10.5 Practical Examples of Class-solution QA

10.5.1 Step-and-shoot IMRT for Nasopharynx

The first example is that of an IMRT treatment of a nasopharynx tumor extensively described in [34]. Figure 8a summarizes the treatment plan. The computed dose distribution reveals a secondary hot spot in the occipital region of the brain. This hot spot was due to an unintended intersection of the interior segments of the 165°-beam and 195°-beam.

Figure 8b illustrates the gel dosimetry and quantitatively compares the gel-measured dose distribution to the computed one in the sagittal mid-plane. The MRI-slice thickness was 10 mm while the pixel size was (1.2×1.2 mm). The difference found in the PTV is practically below 5%. However, the difference map demonstrates an important shift of the posterior hot spot. A plausible geometric explanation for the shift is given in Fig. 8c. The position of the posterior hot spot is critically dependent on the angular separation of the posterior beams: a deviation of two times 1° can reproduce the effect measured in Fig. 8b. This high sensitivity to the gantry angle accuracy was taken into account by tightening the tolerance for the mechanical equipment QA within the class solution. This rectifying feedback is an illustration of a descent from the pyramid top down to level 1 in Fig. 5. This level-4 experimental observation underlines the clinical importance of positioning the treatment isocenter in or near the PTV and avoiding small angular beam separations.

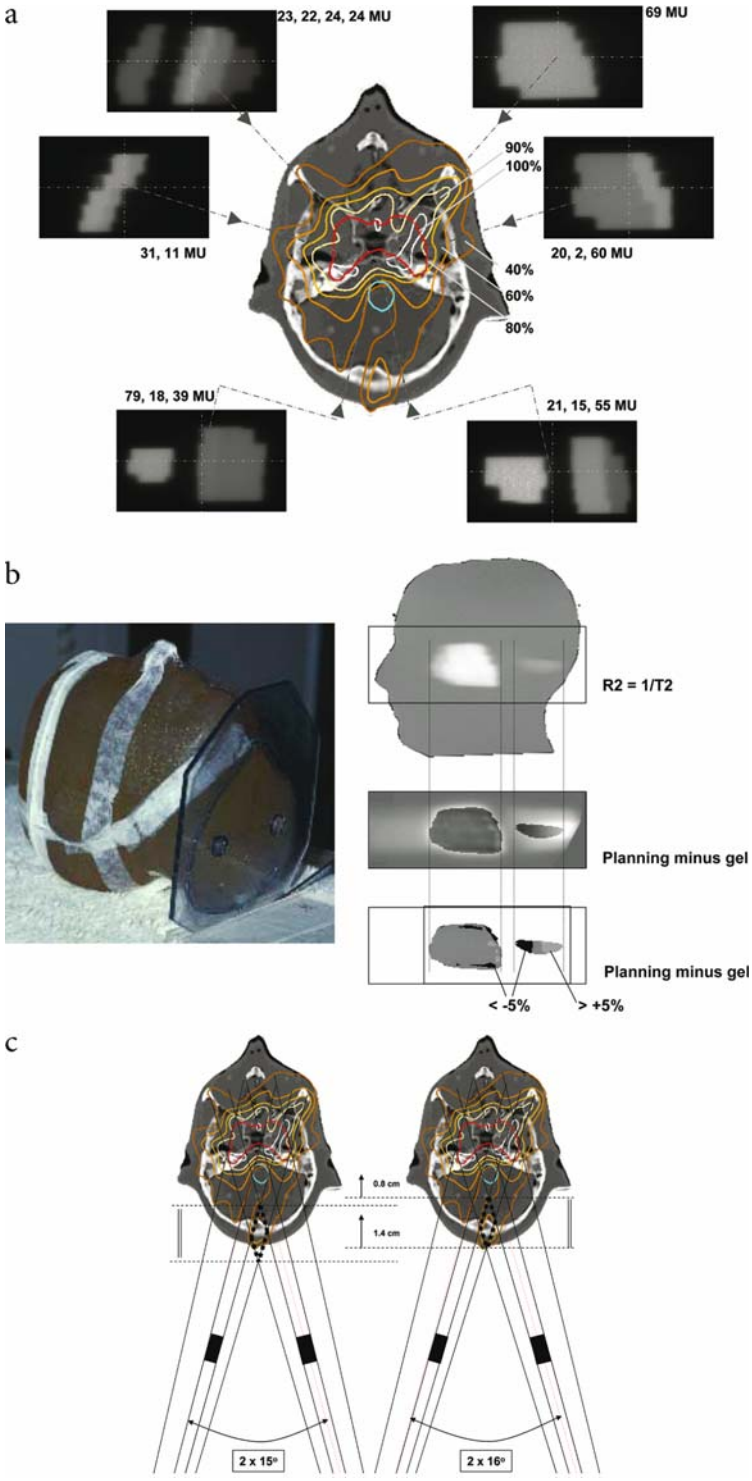

Fig. 8a–c. 3D-dose class-solution verification of a step-and-shoot IMRT treatment at 6 MV for a concave PTV in the nasopharynx region: **(a)** layout of the treatment plan and normalized dose distribution recomputed in the Alderson-Rando phantom. The intensity maps (in positive) obtained by film dosimetry, gantry angles and segment weights (in MU) are indicated for each of the six coplanar IM-beams. The treatment isocenter lies between the PTV and the brain stem; **(b)** *Left panel:* gel phantom vacuum molded after the Alderson-Rando phantom. The laser lines drawn on the adhesive tape ensure positioning reproducibility. *Right panel:* MRI-measured R2 distribution and derived dose distribution in the sagittal mid-plane as obtained by gel dosimetry. Comparison to planning reveals that dose differences higher than 5% mainly occur in the secondary hot spot where they suggest a shift; **(c)** *Left panel* illustrates the intended configuration of the 165°- and 195°-beams. *Right panel* displays the geometric simulation of the effect of an imprecision of the gantry angle: two deviations of 1° easily explain the measured shift of the hot spot

10.5.2 Intensity Modulated Arc Therapy (IMAT) for Whole Abdominopelvic Region

In [35] polymer gel dosimetry was used for a level-4 dosimetric verification of whole abdominopelvic intensity modulated arc therapy (IMAT). As remarked by Williams [1], IMAT is perhaps the most demanding in terms of the equipment performances. Therefore, a full Strategy 2 for the first treatment plans to be validated is mandatory. One of the challenges for gel dosimetry [36] was the large gel volume that was incorporated in the hy-

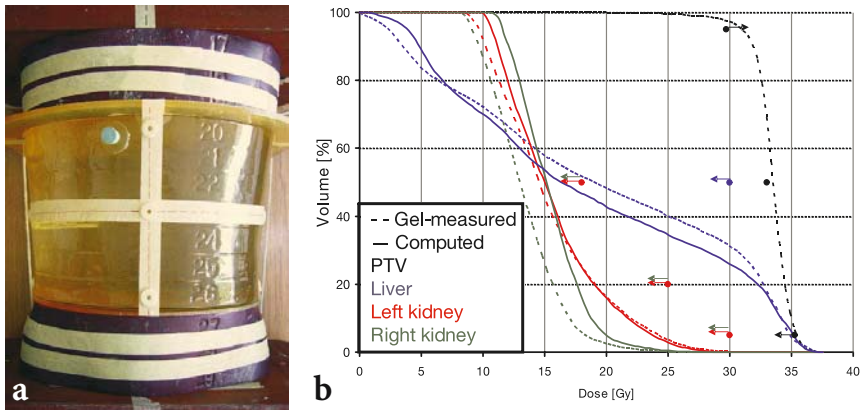

Fig. 9. (a) Hybrid gel phantom, based on the Alderson-Rando phantom, used for the 3D-dose verification of an IMAT (intensity modulated radiation therapy) treatment for whole abdominopelvic irradiation. The Barex cast contains a 9 l volume of polymer gel. The *seven reference markers*, which are attached to the phantom on the laser lines, contain CT- and MRI-contrast. (b) Resulting dose-volume histograms (DVHs) from the gel dosimetry (*dashed lines*) compared to the computations (*solid lines*) in terms of clinical dose after 22 fractions. In order to have maximum precision in gel dosimetry, the MUs of the treatment plan had been scaled up in order to obtain 7.5 Gy as median dose in the PTV, instead of the class-solution fraction dose of 1.5 Gy. The gel dosimetry ascertains that all DHV constraints had been met.

brid phantom displayed in Fig. 9a. The 3D capabilities of gel dosimetry allowed the construction of gel-measured dose–volume histograms (DVHs), which are compared to the computed (planned) DVHs in Fig. 9b. Although the DVHs of liver and right kidney reveal discrepancies between gel measurements and computations, the gel dosimetry confirms that all the clinical planning objectives have been satisfied. This positive level-4 QA result has stimulated the physician's confidence in the class solution.

10.6 Conclusion

Routine QA in traditional radiation therapy involves numerous redundancy checks that are sometimes repeated for every patient. Extrapolation of this 'attitude' to IMRT is untenable. Instead, focused QA procedures that test the vulnerable links, are needed in the triad of routine patient-specific QA, periodic equipment QA and thorough class-solution QA. The physics team is encouraged to aim at a balance between the triad using the conceptual approach that has been presented to optimize and streamline QA procedures within class solutions, rather than proliferating redundant QA checks. Multi-center co-operation and QA networking can be helpful and stimulating.

Rather than a burden to the physics team, QA should be a passionate professional activity of combining the appropriate instruments and strategy to ensure or even manage the radiation physics quality of the implemented IMRT planning and delivery processes.

One might expect that new dedicated delivery technologies like tomotherapy and image guided robotic IMRT have the potential of shortening the loop of planning and delivery, and hence will allow the QA activities to be condensed and further streamlined. In the mean time, QA of the longer treatment chain remains mandatory and will further stimulate familiarization with IMRT and keep the level of alertness and vigilance.

Acknowledgements. Grant 36.0183.03 of the Fund for Scientific Research Flanders (FWO) and GOA grant 12050401 of Ghent University

References

1. Williams PC (2003) IMRT: delivery techniques and quality assurance. Br J Radiol 76:766–776
2. Essers M, Mijnheer B (1999) In vivo dosimetry during external photon beam radiotherapy. Int J Radiat Oncol Biol Phys 43:245–259
3. Van Esch A, Depuydt T, Huyskens DP (2004) The use of an aSi-based EPID for routine absolute dosimetric pre-treatment verification of dynamic IMRT fields. Rad Oncol 71:223–234
4. Louwe RJW, Damen EMF, van Herk MB, Minken AWH, Törzsök O, Mijnheer BJ (2003) Three-dimensional dose reconstruction of breast cancer treatment using portal imaging. Med Phys 30:2376–2389
5. Spezi E, Lewis DG, Smith CW (2002) A DICOM-RT-based toolbox for the evaluation and verification of radiotherapy plans. Phys Med Biol 47:4223–4232
6. Dutreix A, Bjärngard BE, Bridier A, Mijnheer B, Shaw JE, Svensson H (1997) Monitor unit calculation for high energy photon beams. ESTRO Booklet no 3 (Physics for radiotherapy). Garant Publishers, Leuven
7. Hansen VN, Evans PM, Budgell G, Mott J, Williams P, Brugmans M, Wittkämper FW, Mijnheer B, Brown K (1998) Quality assurance of the dose delivered by small radiation segments. Phys Med Biol 43:2665–2675

8. Sonke JJ, Brand B, van Herk M (2003) Focal spot motion of linear accelerators and its effect on portal image analysis. Med Phys 30:1067–1075
9. Cheng CW, Das IJ, Ndlovu AM (2002) Suppression of dark current radiation in step-and-shoot intensity modulated radiation therapy by the initial pulse-forming network. Med Phys 29:1974–1979
10. Van Esch A, Bohsung J, Sorvari P, Tenhunun M, Fagundes M, DiPetrillo T, Kramer B, Koistinen M, Engler MJ (2002) Acceptance tests and quality control (QC) procedures for the clinical implementation of intensity modulated radiotherapy (IMRT) using inverse planning and the sliding window technique: experience from five radiotherapy departments. Radiother Oncol 65:53–70
11. Verellen D, Linthout N, Berge DVD, Bel A, Storme G (1997) Initial experience with intensity-modulated conformal radiation therapy for treatment of the head and neck region. Int J Radiat Oncol Biol Phys 39:99–114
12. De Deene Y, De Wagter C, Van Duyse B, Derycke S, Merseman B, De Gersem W, Voet T, Achten E, De Neve W (2000) Validation of MR-based polymer gel dosimetry as a preclinical three-dimensional verification tool in conformal radiotherapy. Magn Reson Med 43:116–125
13. Westermark M, Arndt J, Nilsson B, Brahme A (2000) Comparative dosimetry in narrow high-energy photon beams. Phys Med Biol 45:685–702
14. Laub WU, Wong T (2002) The volume effect of detectors in the dosimetry of small fields used in IMRT. Med Phys 30:341–347
15. Sánchez-Doblado F, Andreo P, Capote R, Leal A, Perucha M, Arráns R, Núñez L, Mainegra E, Lagares JI, Carrasco E (2003) Ionization chamber dosimetry of small photon fields: a Monte Carlo study on stopping-power ratios for radiosurgery and IMRT beams. Phys Med Biol 48:2081–2099
16. Capote R, Sánchez-Doblado F, Leal A, Lagares JI, Arráns R, Hartmann G (2004) An EGSnrc Monte Carlo study of the microionization chamber for reference dosimetry of narrow irregular IMRT beamlets. Med Phys 31:2416–2422
17. Martens C, De Wagter C, De Neve W (2001) The value of the LA48 linear ion chamber array for characterization of intensity-modulated beams. Phys Med Biol 46:1131–1148
18. Letourneau D, Gulam M, Yan D, Oldham M, Wong JW (2004) Evaluation of a 2D diode array for IMRT quality assurance. Radiother Oncol 70:199–206
19. Martens C, Claeys I, De Wagter C, De Neve W (2002) The value of radiographic film for the characterization of intensity-modulated beams. Phys Med Biol 47:2221–2234
20. Yeo IJ, Beiki-Ardakani A, Cho Y, Heydarian M, Zhang T, Islam M (2004) EDR2 film dosimetry for IMRT verification using low-energy photon filters. Med Phys 31:1960–1963
21. Childress NL, Dong L, Rosen II (2002) Rapid radiographic film calibration for IMRT verification using automated MLC fields. Med Phys 29:2384–2390
22. Oldham M, Webb S (1997) Intensity-modulated radiotherapy by means of static tomotherapy: planning and verification study. Med Phys 24:827–836
23. Danciu C, Proimos BS, Rosenwald JC, Mijnheer BJ (2001) Variation of sensitometric curves of radiographic films in high energy photon beams. Med Phys 28:966–974
24. Gillis S, De Wagter C, Bohsung J, Perrin B, Williams P, Mijnheer BJ (2004) An inter-centre quality assurance network for IMRT verification: Results of thze ESTRO QUASIMODO project. Radiother Oncol 76. In press.
25. Robar JL, Clark BG (1999) The use of radiographic film for linear accelerator stereotactic radiosurgical dosimetry. Med Phys 26:2144–2150
26. Marcié S, Aletti P, Lefkopoulos D, Tomsej M et al. (2003) Quality assurance program for intensity-modulated radiotherapy (IMRT) treatments of head and neck carcinomas. Cancer/Radiother 7:172–178
27. Paelinck L, Reynaert N, Thierens H, De Wagter C, De Neve W (2003) The value of radiochromic film dosimetry around air cavities: experimental results and Monte Carlo simulations. Phys Med Biol 48:1895–1905
28. Niroomand-Rad A, Blackwell C, Coursey B, Gall K, Galvin J, McLaughlin W, Meigooni A, Nath R, Rodgers J, Soares C (1998) Radiochromic film dosimetry: recommendation of AAPM radiation therapy task group 55. Med Phys 25:2093–2115
29. Maryanski MJ, Ibbott GS, Eastman P, Schulz RJ, Gore JC (1996) Radiation therapy dosimetry using magnetic resonance imaging of polymer gels. Med Phys 23:699–705
30. De Deene Y, De Wagter C, Van Duyse B, Derycke S, De Neve W, Achten E (1998) Three-dimensional dosimetry using polymer gel and magnetic resonance imaging applied to the verification of conformal radiation therapy in head-and-neck cancer. Radiother Oncol 48:283–291
31. Low DA, Harms WB, Mutic S, Purdy JA (1998) A technique for the quantitative evaluation of dose distributions. Med Phys 25:656–661
32. Low DA, Dempsey JF (2003) Evaluation of the gamma dose distribution comparison method. Med Phys 30:2455–2464
33. MacDougall ND, Pitchford WG, Smith MA (2002) A systematic review of the precision and accuracy of dose measurements in photon radiotherapy using polymer and Fricke MRI gel dosimetry. Phys Med Biol 47:R107–R121
34. De Neve W, De Gersem W, Derycke S, De Meerleer GMM, Bate MT, Van Duyse B, Vakaet L, De Deene Y, Mersseman B, De Wagter C (1999) Clinical delivery of intensity modulated conformal radiotherapy for relapsed or second-primary head and neck cancer using a multileaf collimator with dynamic control. Radiother Oncol 50:310–314
35. Duthoy W, De Gersem W, Vergote K, Coghe M, Boterberg T, De Deene Y, De Wagter C, Van Belle S, Neve W (2003) Whole abdominopelvic radiotherapy (WAPRT) using intensity modulated arc therapy (IMAT): first clinical experience. Int J Radiat Oncol Biol Phys 57:1019–1032
36. Vergote K, De Deene Y, Duthoy W, De Gersem W, De Neve W, Achten E, De Wagter C (2004) Validation and application of polymer gel dosimetry for the dose verification of an intensity-modulated arc therapy (IMAT) treatment. Phys Med Biol 49:287–305
37. Mijnheer B, Olszewska A, Fiorini C, Hartmann G, Knoös T, Rosenwald JC, Welleweerd H (2004) Quality assurance of treatment planning systems – practical examples for non-IMRT photon beams. ESTRO (European Society for Therapeutic Radiology and Oncology), Booklet no. 7 (Physics for radiotherapy), ESTRO, Brussels
38. Venselaar J, Heukelom S, Jager N, Mijnheer B, van der Laarse R, van Gasteren H, van Kleffens H, Westermann C (1999) Effect of electron contamination on scatter correction factors for photon beam dosimetry. Med Phys 26:2099–2106
39. Bouchard H, Seuntjens J (2004) Ionization chamber-based reference dosimetr y of intensity modulated radiation beams. Med Phys 31:2454–2465

QA-QC of IMRT: American Perspective

Jean M. Moran, Ping Xia

11

Contents

11.1 The Paradigm of Quality Assurance

In the United States, the professional societies of the American Association of Physicists in Medicine and the American Society of Therapeutic Radiologists have collaborated within their organizations and between organizations to provide guidance in determining the appropriate use of IMRT, beginning an IMRT program, and maintaining the appropriate quality assurance to safely use IMRT [1–3]. The complex beam intensity modulation in each IMRT field has required new systems for treatment planning and delivery and therefore, a paradigm shift has occurred in quality assurance. Each institution should have a comprehensive quality assurance program tailored to their software, delivery system, and patient planning and treatment process for IMRT. Such a program typically involves a team approach to quality assurance including physicians, physicists, dosimetrists, therapists, and nurses. This chapter focuses on system, machine, and patient-specific quality assurance requirements in IMRT delivery.

11.1.1 Verification of Patient Position

For IMRT to fulfill its promise to reduce normal tissue complications while improving local control, verification of target position is critical. Verification methods may vary by institution and depend on the specific disease site and whether or not the tumor volume involves organ motion. Other chapters in this book address adaptive approaches to patient positioning and the development and potential of image-guided therapy. Therefore, this section focuses on how patient immobilization and verification should be addressed within a comprehensive quality assurance program.

As in conventional conformal radiotherapy, the patient model for IMRT is developed based on image data such as CT scans, additional diagnostic scans, and information about patient setup and organ motion. A well-defined process should be used for patient immobilization prior to acquisition of the treatment planning CT scan. For each treatment site, it is helpful to develop and follow a checklist prior to the CT scan with details such as slice thickness, region of interest, and immobilization aids clearly listed.

The degree of positioning accuracy depends on the immobilization, localization method, and motion of the organ. When using thermoplastic materials, the manu-

facturer instructions for heating and cooling should be followed carefully. An improperly cooled patient mask may shrink after the CT scan and be uncomfortable for the patient during the entire course of treatment. For head and neck patients, it may be necessary to cut regions out of the mask material to reduce skin reactions because of increased surface dose due to the mask material [4].

At the treatment unit, patient anatomy can be verified with orthogonal images using electronic portal imagers or film [5]. For head and neck patients, bony landmarks are sufficient as reference points for the location of the tumor. When a mask is used over the head and shoulders along with other immobilization aids (such as bite blocks), a setup accuracy of 1 – 3 mm is possible [6]. For prostate, organ motion has been shown to be significant with respect to the pelvis bony structure and therefore, another method is required for accurate target positioning. Daily localization with gold implanted markers [7] or ultrasound [8] are methods that are used in the US and permit localization to within 2 – 3 mm. Use of such a daily positioning method allows for a reduction in dose delivered to the bladder and rectum when treating prostate cancer.

For other organs that move significantly with respiration (lung, liver, breast), gating and active breathing control methods that limit respiratory motion while the beam is on allow for significant improvements in target positioning [9–11]. Prior to using such methods, additional QA is required on the immobilization method (see chapter II. 11).

Other improvements have been made to the treatment couch. Patient immobilization devices that can be fixed directly to the treatment couch improve the precision and efficiency of the patient setup process. Treatment table tops made of carbon fiber permit beam delivery at multiple angles without metal parts in the beam. Measurement of attenuation through such treatment couches should be conducted to determine whether the attenuation should be taken into consideration or can be safely ignored. While published data from other institutions provide a guideline of what is achievable, it is important that each institution assess its immobilization and localization method to determine the accuracy of its own immobilization and positioning process for each treatment site [11]. It may be necessary to change the process prior to the start of an IMRT program if the positioning accuracy does not meet the treatment goals. The positioning and organ motion information is used in the treatment planning system to expand target and organ-at-risk volumes [12, 13]. This information sets the limits of what is achievable for normal tissue sparing with IMRT. Additional checks, such as comparing measured patient treatment SSDs with the treatment planning system, can also be an effective part of a QA program.

11.1.2 Dosimetric Verification as Validation of IMRT Plans

AAPM Task Group 40 report recommends an independent check of monitor units prior to patient treatment [14]. In conventional therapy, this can be done through hand calculations based on measurements in water. For IMRT plan verification, the situation is more complicated due to the hardware and software involved in IMRT planning and delivery. Individual fields are composed of many small segments (ranging from a few to several hundred) of varying intensity located on and off the central axis of the beam. Therefore, hand calculations are unreasonable for verification of IMRT plans. The main approaches used for verification of IMRT plans are dosimetric measurements and monitor unit calculations.

Dosimetric measurements typically encompass two types of checks for pre-treatment quality assurance. One measurement is a composite delivery of all IMRT fields at the correct delivery angles on a phantom (often cylindrical or cubic) with an ion chamber or other detectors to verify the dose at a single point or multiple points [15,16]. The chamber position (and hence the phantom position in plastic phantoms) may need to be adjusted to determine an appropriate high dose, shallow gradient region for the measurement. At many centers, additional verification is performed of individual fields with film or other 2D imaging systems. Verification can be a qualitative visual check of the intensity patterns or it can be done in a phantom with dosimetric measurements to provide additional information on the delivery [16].

Measurements of individual patient treatment fields test the transfer of patient information from the planning system to the record-and-verify system, the deliverability of individual fields, and dosimetric evaluation of the delivery compared to the dose calculation in the phantom geometry. However, a limitation of dosimetric measurements in a homogeneous phantom is that errors from the planning process are not checked. For example, if the table top in the CT scanner is improperly contoured as part of the patient surface that error would not be caught with dosimetric measurements. A careful review of the patient CT scan and contoured structures is still necessary.

11.1.3 Computational vs Experimental Dosimetry

No single quality assurance check provides enough information to verify that IMRT delivery for a patient will be accurate. Dosimetric measurements are time-consuming and only verify the dose in a phantom geometry. Also, discrepancies between planar measurements and calculations may be difficult to interpret in

terms of the clinical significance on a patient by patient basis. Independent monitor unit calculations provide a complementary verification of the dose to a single point at isocenter in the patient when compared to the treatment planning system calculation.

Methods based on a Clarkson integration for individual segments or on scatter calculations have been developed for dynamic, step-and-shoot delivery, MIMiC, and mMLC delivery methods [17–19]. The user should understand the method of calculation and approximations in the algorithm. Approximations include ignoring the contour of the patient surface or limited modeling of scatter interactions resulting in less accurate calculations in regions where the contribution of dose from scatter is high [18]. Prior to clinical use, the calculation method should be verified against phantom measurements and the treatment planning system algorithm. Once a calculational method is properly verified, significant time can be saved when compared to measurements. However, additional QA checks are needed to verify accurate transfer of patient data and accurate delivery.

11.1.4 Reliability and Validity of Tests for QA

Quality assurance tests should be designed to ensure that the sensitivity is appropriate to the impact of potential errors [2, 15, 16]. Standard plans should be developed and validated for testing during commissioning and after software upgrades of the treatment planning and inverse planning systems, data transfer software, and the record and verify system. For MLC-based IMRT systems, accuracy of delivery depends on the number of segments, leaf sequencing (with or without leaf synchronization to minimize tongue-and-groove) and machine-related parameters such as leaf position tolerance, delivery method (SMLC, DMLC), leaf speed (for DMLC) and dose rate [2]. For serial tomotherapy with the MIMiC collimator, positional problems with the alignment of the MIMiC collimator with the linear accelerator or with the couch indexing can lead to significant treatment delivery errors and therefore must be checked [20].

11.1.5 QA of Total Treatment Chain

The entire treatment chain for IMRT must be verified. When compared with 3D conformal therapy, stricter requirements may be placed on frequency of testing and accuracy because of new planning and delivery methods. Thorough commissioning of individual components should be followed with checks of the entire process from the CT scan and derivation of the patient model (including setup and motion) to treatment planning and delivery.

The first part of the QA chain is information from the CT-simulation. The beam angles and sharp gradients within fields require accurate models of the patient. As fields become more conformal, organ motion can degrade the delivered dose distribution. As discussed above, proper immobilization is required for the CT scan. Setup uncertainty and organ motion must be considered for input into the treatment planning process [21, 22]. As with 3D conformal therapy, CT and other image datasets must be transferred accurately to the treatment planning system and the spatial and density information must be verified. The expansion of surfaces from generated contours can be verified using phantom tests.

The second part of the treatment chain is the treatment planning system. Tools, such as dose volume histograms, beam placement, dose calculation, and digital reconstructed radiograph generation, should all be verified following published guidelines [2, 3, 14, 23]. The user should assess how dose changes with increased intensity modulation. In addition to standard checks, the generation of leaf sequences from the inverse planning system for delivery must be checked. Some systems allow for recalculation of the dose using the sequenced MLC files. Tools should be readily available to transfer the patient plan to a phantom geometry, recalculate the doses, and import measured 2D distributions.

The final part of the chain is patient treatment. This step relies on accurate transfer of patient treatment data. Data should be transferred digitally from the planning system to the record-and-verify system. All IMRT fields should be delivered with the level of accuracy considered to be acceptable and achievable during commissioning of the IMRT process. Beam angles through the table top should be evaluated to determine if attenuation through the table top is modeled correctly in the planning process. The patient position should be evaluated on the first few days of treatment using EPIDs or film [24].

11.1.6 QA as a Familiarization Tool when Starting IMRT

When first beginning an IMRT program, quality assurance is an important part of determining the limits of a planning and delivery system. QA tests can be run more frequently to determine the reproducibility of leaf positioning. Process QA should begin with simple geometric fields measured in a flat phantom geometry and progress to more complicated intensity modulated fields. In addition to simple checks, treatment planning studies should be done on patient models prior to treating with IMRT. Target and normal structures in the treatment fields should be contoured, the dosimetrist should gain experience in adjusting the objective functions in the inverse planning system to meet the physician needs. Once an acceptable plan is reached,

the delivery should be tested along with dosimetric measurements and verification calculations if appropriate. At each step, the process should be verified. For example, the structures derived from the drawn contours should be evaluated in 3D to make sure that the contours are drawn consistently. Because the output of the inverse planning system is dependent on the treatment objectives and prescribed dose, each new treatment site should be commissioned from treatment planning, optimization, to delivery. Mechanical checks should also be in place to evaluate reproducibility of mechanical systems over time. Finally, it is important that all members of the implementation team understand how long each part of the process takes so that the expectations of the IMRT program are reasonable, achievable, and safe.

11.1.7 How much QA Is Enough?

Each institution's QA program should be designed to encompass the entire IMRT process. The checks should be divided into hardware, software, and data transfer checks. Procedures should be in place to modify the institution's existing daily, weekly, monthly, and annual QA to include appropriate tests for IMRT. The physicist should be prepared with the appropriate tests to run after software and hardware upgrades. As an institution gains more experience with the IMRT process, hardware, and software, it may be appropriate to adapt the process accordingly.

The frequency of tests depends on the significance of errors as well as institution's experience, equipment, and frequency of software and hardware upgrades. For example, since errors in leaf positioning and leaf gap affect all IMRT patients, routine tests should evaluate the accuracy of both parameters. Later sections address the QA checks in detail.

The QA program must also be designed considering the software and hardware at the institution. For example, individual pre-treatment QA measurements are a critical part of a QA program if the institution does not verify patient monitor unit calculations with an independent dose calculation algorithm. If an institution does use an independent dose calculation algorithm, then it also needs specific tests to verify data transfer from the planning system to the record-and-verify system. If limitations are set on the smallest monitor unit fraction, number of segments, or segment size, it is important that checks are in place to adhere to those limits.

After gaining years of experience, several centers have decreased their individual patient-specific QA measurements. The decrease in patient-specific measurements was possible because the system was thoroughly tested and appropriate individual QA tests are in place to identify specific problems [16].

11.2 Treatment-Method Specific QA

Quality assurance tests of an inverse treatment planning system, leaf sequencing algorithm, and delivery technique involves a subset of checks from the commissioning process [2, 3]. The tests outlined in this section focus primarily on SMLC-IMRT, DMLC-IMRT, and sequential tomotherapy since these are the main delivery methods currently in clinical use.

For SMLC-IMRT and DMLC-IMRT, fields are composed of many small segments superimposed during delivery at a fixed gantry angle. For sequential tomotherapy, a special multileaf intensity modulating collimator (MIMiC, NOMOS Corp., Sewickley, Pennsylvania) consisting of two banks of 20 tungsten vanes with a leaf length of 1 or 2 cm and leaf width of 1 cm when projected 100 cm from the X-ray target to the isocenter for a maximum field size of 2×20 cm at isocenter for a single arc. The beam intensity is usually modulated every 5 or 10 degrees of gantry rotation by moving leaves into and out of the fan beam. The beam intensity produced at each leaf position is proportional to the fraction of time the leaf is held in the open position. Prior to verifying individual IMRT fields, it is important to verify the separate parts of the planning system that will affect the overall accuracy. It is important that QA includes the following checks:

1. Penumbra modeling
2. On- and off-axis small field collimator scatter factors
3. Leaf offset factor to correct discrepancies between the light field and radiation field
4. Transmission through the MLC leaves or vane collimator – inter-leaf leakage, intra-leaf leakage, and leaf-end leakage
5. Leaf sequencer accuracy
6. Additional checks for sequential tomotherapy

11.2.1 Penumbra Modeling

For conventional therapy, the impact of the modeling inaccuracies in the penumbra is typically limited to the region encompassing the outside of the target volume. For IMRT delivery, fields are composed of many subfields. Therefore, modeling inaccuracies affect multiple regions across the target volume and normal tissues. Measurements with ionization chambers that have an inner diameter greater than 3 mm will over-estimate the penumbra width [2, 15]. Care should be taken that measurements are made with an appropriate detector for determining the penumbra width such as film or small detector with high spatial resolution such as a diode, diamond detector, or pinpoint ionization chamber [2].

11.2.2 Small Field Scatter Factors

The small sub-fields that make up IMRT fields affect the output factor of the beam on and off the central axis. As sub-fields decrease in size to less than $3 \times 3\ cm^2$, the output sharply decreases due to lack of electronic equilibrium [25]. These fields are often irregularly shaped as well. It is important to verify the dose calculation algorithm against reliable beam measurements made with an appropriate small field detector. Special care must be taken to verify that leaf positioning is accurate because of sensitivity of the output factor on leaf positioning for small fields. For example, a 2 mm deviation in field size changes the dose per monitor unit by 2% for a $2 \times 2\ cm^2$ field and 15% for a $1 \times 1\ cm^2$ field for a 6-MV photon beam [25]. Discrepancies between measurements and calculations off-axis can be due to lack of inclusion of off-axis softening of the photon energy spectrum in the model [25]. The commissioning process should include determining the minimum acceptable segment size for IMRT and QA tests based on these results and then setting this limit in the treatment planning system if possible. This should be coupled closely with determination of the necessary leaf position accuracy for delivery along with the appropriate QA that the accuracy requirement is met.

11.2.3 Radiation Field Offset

Leaf position accuracy not only affects the machine output, but also affects the dose delivery in the overlap and underlap regions of sub-fields within an IMRT field. A systematic leaf position error may be introduced if differences between the radiation field and the light field are not taken into account in the planning system. The dosimetric effect of the differences depends on how the radiation and light field are calibrated. The radiation field offset is a significant factor for MLC designs that have curved leaf-ends and move linearly with respect to the radiation beam instead of moving divergently with the beam. The radiation field offset is also found in double-focused MLCs (where the motion of MLC leaves follows the divergence of the radiation beam) [26]. Several institutions have studied the radiation field offset and found values ranging from of 0.7 to 1 mm depending on the characteristics of multi-leaf collimators, beam energy, and gantry angles [27, 28]. Ignoring the radiation field offset in IMRT delivery has been shown to result in significant discrepancies between calculations and measurements of IMRT fields, especially in the vicinity of critical structures [28, 29]. Ideally, this issue will be addressed more directly in future versions of commercial treatment planning systems. The radiation field offset should be determined by measurement of the radiation field over multiple gantry angles (e.g., 0, 90, and 270°) with film. An average correction value should be chosen.

11.2.4 Leakage and Transmission: Interleaf, Intraleaf, Leafend

For MLC-based systems, leakage and transmission are important factors that should be modeled directly when possible. The main types of transmission for MLC systems are interleaf leakage, intraleaf transmission, and transmission between opposed leafends. The values for the different systems are dependent on the design, position in the collimator head, and whether or not the leaf ends are double-focused, moving in an arc with respect to the beam or curved, moving linearly. The amount of leakage per field can also vary with the leaf sequencing algorithm and the maximum beamlet intensity of a field.

Figure 1 shows the leakage patterns for the three major MLC collimators [30]. The inter-leaf and the intra-leaf leakage are represented by the crests and troughs of the graphs, respectively. Table 1 shows the values for Siemens, Elekta, and Varian accelerators [30]. Notice that the most significant difference is in the values of the leaf-end leakage. Siemens has a double focused de-

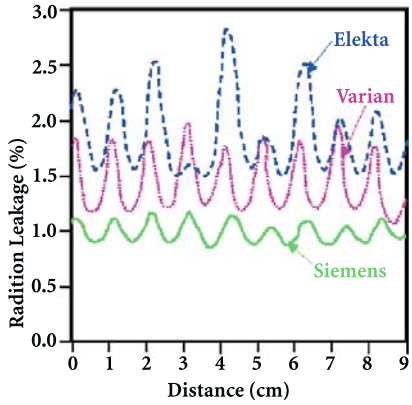

Fig. 1. Leakage patterns for the major MLC collimators. From: Huq MS, Das IJ, Steinberg T, Galvin JM (2002) A dosimetric comparison of various multileaf collimators. Phys Med Biol 47(12):N159–N170. Reprinted with permission

Manufacturer	Inter-leaf (%)	Intra-leaf (%)	Leaf-end (%)
Siemens	1.1	0.8	1.6
Elekta	2.5	1.6	> 20%
Varian	1.8	1.2	> 20%

Table 1. Values of inter-leaf, intra-leaf, and leaf-end transmission for a 6-MV beam

sign where the leaves more in an arc with respect to the beam resulting in leakage similar to that between adjacent leaves. Because the Elekta and Varian leaves are curved, the leakage between opposed leaves is approximately 20% [31]. The Elekta system also has a backup jaw immediately above the MLC. Users should measure their machine's transmission values with film and compare the results to published values.

For all MLCs, the percent transmission value for conventional treatment is better than the leakage of a conventional cut block. However, the low delivery efficiency ratio (defined as the MU for a physical compensator to the MU for MLC-IMRT field) for IMRT fields can result in a significant portion of the total dose being contributed from the MLC transmission, particularly as the IMRT field complexity increases [32]. At this time, many treatment planning systems only model the transmission with an average value. More sophisticated models which take into account the different types of transmission are actively under investigation.

11.2.5 Leaf Sequencer

The optimization system derives intensity maps for each treatment angle based on the input objectives in the planning system. These intensity maps can be continuous profiles or discretized into beamlets of specific size (e.g., $0.5 \times 0.5\,cm^2$ or $1 \times 1\,cm^2$). Hardware and software delivery constraints may or may not be accounted for in the derivation of the intensity maps. The leaf sequencer (or leaf motion calculator) converts the intensity profile into a series of control points for delivery by the MLC that include all leaf positions and fractional monitor units based on delivery restrictions such as MLC leaf width, MLC step size, and intensity level.

As part of treatment planning commissioning for IMRT, the physicist should understand the basic principles of converting intensity profiles into a deliverable set of leaf sequences. The constraints for leaf sequencing are dependent on the MLC design such as leaf width, over-travel distance, maximum field size, and interdigitation of leaves. User options in leaf sequencing algorithms typically include the MLC step size and the number of intensity levels. As the step size is decreased and the number of intensity levels is increased, the leaf sequenced file will more closely resemble the continuous profile. However, for some delivery systems, the number of control points or segments of the field is directly proportional to the delivery time. For these delivery systems, one has to consider the practical delivery time when choosing these parameters and determine the accuracy limits of the chosen leaf sequencing parameters. Another potential drawback of using a finer MLC step size and increased number of intensity levels, especially for SMLC-IMRT delivery, is the inclusion of many segments with small monitor units and/or small field sizes. As noted earlier, the delivery accuracy for such small segments with low (or fractional) monitor units is much more strongly dependent on positioning accuracy due to machine and modeling limitations of these small segments.

For DMLC-IMRT delivery, some algorithms synchronize leaves to minimize tongue-and-groove effects while others minimize total travel time. The significance of effects such as tongue-and-groove depends on the modulation within the field. Developing an efficient leaf sequencer that can minimize total delivery MUs, total number of segments, and total MLC leaf travel distance, remains an active research area [33, 34].

11.3 Machine Specific QA

Tests for accelerator quality assurance of IMRT delivery should verify proper functioning of delivery equipment at an appropriate level of accuracy and reproducibility. Individual patient pre-treatment QA measurements do not serve as a valid substitute for routine evaluation of the delivery equipment since those checks are designed to validate the overall process and treatment planning system/leaf sequencer output. To aid in problem-solving, delivery system checks should be kept distinct from process checks involving delivery of files from the treatment planning system and leaf sequencer algorithm. The tests in this section focus on QA for MLC-based IMRT systems (SMLC-IMRT and DMLC-IMRT) and sequential tomotherapy IMRT delivery systems.

11.3.1 MLC-based Systems

The frequency of tests depends on the impact of an error on patient planning and on the likelihood of an error occurring. Several tests are an important part of acceptance testing and annual quality assurance. Also, verification may be required after service if parts of the delivery system have been affected. Physical constraints of the MLC should be verified such as the maximum IMRT field width, software-controlled opposed leaves gap, and leaf inter-digitation (if allowed). The specific tests will depend on the design of the MLC [35]. For MLC-based systems, mechanical and dosimetric checks should verify the alignment and positioning of the MLC carriage and leaves to the central axis of the beam and to opposing leaves. The carriage skew affects the orientation of all leaves with respect to the central axis of the beam and should be measured with film [16]. Another check of the carriage involves checking the physical gap between the carriages with feeler gauges [16]. Because carriage adjustments are needed infrequently, the physicist may want to make any changes with a service

engineer. Any adjustments should then be verified and documented.

MLC-related quantities that are incorporated into the treatment planning system are inter- and intra-leaf transmission/leakage, leaf end transmission, the radiation field offset, and small field output factors as described in Section 11.2. Tests of those parameters were described in Section 11.2. Figure 2a shows an example film for a 6 MV photon beam from a Siemens accelerator. To test the leakage and the gap between leaves, all leaves are closed at different locations across the field with the Y jaws held open by creating a small opening with the top and bottom mega-leaves (specific to the Siemens MLC design). If there is additional leakage dose between opposed leaves, unnecessary dose may be delivered in SMLC-IMRT where closed leaf pairs may appear in the middle of the field (if the closed leaves cannot be placed under a backup jaw). The position of closed leaves may also depend on the leaf sequencing algorithm. Another example test film for a Siemens 6 MV photon beam is shown in Fig. 2b to determine the radiation field offset. A series of abutting strips were delivered at a 0 degrees gantry angle resulting in a radiation field offset of 0.5 mm for this example. In addition to film tests, the special case of small fields on and off the central axis should be investigated. The machine output, beam flatness, and symmetry should be measured for small fields with few (or fractional) monitor units to set the limits in the planning and leaf sequencing system.

More frequent tests should be conducted on leaf positioning accuracy and leaf gap in both static and DMLC- or SMLC-IMRT modes. Figure 2c depicts a film exposed to a test pattern consisting of eight strips with 2 cm width separated by 1 cm gaps. This test pattern can be used for numerical analysis of leaf position accuracy across the field by measuring the full width at half maximum for each strip. A sensitive visual test of leaf positioning and gap accuracy and gap is the band test where a 1-mm field is delivered every few cm over the MLC range [16, 36]. Similar test patterns can be used for all manufacturers. The effect of gravity on leaf positioning should be evaluated by measuring the test fields at multiple gantry angles. Such tests can be part of a routine QA program by alternating the gantry angle on a regular basis.

Additional tests are required for DMLC-IMRT. Leaf pair speed can be evaluated using a simple ramp test where strips of different doses are delivered [36]. The effect of dose rate on leaf position accuracy should be evaluated at multiple dose rates if more than one dose rate is used clinically. The effects of leaf acceleration and deceleration can be evaluated using machine log files when available [37]. The effect of the leaf position tolerance value on the dosimetric accuracy should be tested or an appropriate value investigated and used [28, 37].

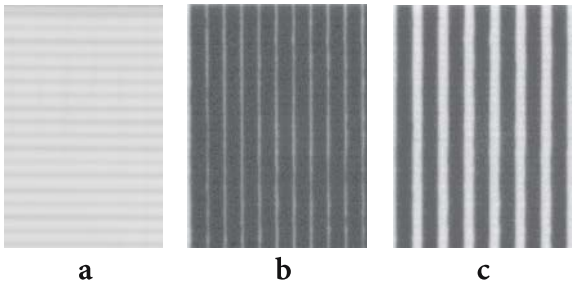

Fig. 2a–c. Three MLC patterns designed to test for static MLC leaf position accuracy: **(a)** MLC leaves closed at various locations across the IMRT field; **(b)** an MLC pattern with a series of abutting strips; **(c)** an MLC pattern with a series of 2-cm strips and 1-cm gaps in between

11.3.2 Sequential Tomotherapy

Because the MIMiC collimator is an add-on device to the linear accelerator, additional quality assurance checks are required to verify that it is correctly positioned. The collimator fits into a block tray slot of a linear accelerator with its long axis oriented along the patient's transaxial direction. Positional adjustment screws and bolts enable the collimator slit to be aligned accurately with the cross-wires. Figure 3a shows an example alignment verification of the radiation field along the inplane direction (parallel to the axis of rotation of the gantry) obtained with film positioned 15 cm off the isocenter and parallel to the inplane. Two exposures were delivered at gantry angles of 90 and 270 degrees with the MIMiC vanes fully open (2×20 cm field size at isocenter). The amount of misalignment of the MIMiC in the inplane direction is the distance between the lines in the Fig. 3a. This is a sensitive test because it amplifies the effect caused by both gantry and collimator sag. A test of the collimator alignment in the crossplane direction is shown in Fig. 3b. A film was positioned at isocenter (parallel to the axis of the gantry) with every other leaf of the MIMiC open and then two exposures were delivered at gantry angles of 90 and 270 degrees. When the two exposures are superimposed, the result is a checkerboard as shown in Fig. 3b. Misalignments are seen by evaluating the matchline. In this example, the checkerboard is not perfectly matched at the field edge due to the amplified effect of gantry and collimator sag.

Another important aspect of QA for sequential tomotherapy involves verification of the couch indexing.

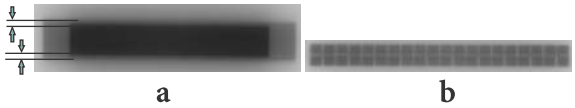

Fig. 3a,b. Quality assurance films to verify the alignment of the MIMiC collimator when it is attached to the accelerator: **(a)** alignment verification of the radiation field in the inplane direction (parallel to the axis of rotation of the gantry); **(b)** alignment verification of the radiation field in the crossplane direction

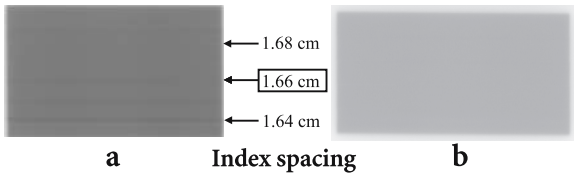

Fig. 4a,b. Film dosimetry used to determine the cranial-caudal increments: **(a)** multiple abutting fields superimposed on a single film with all leaves open at nominal index spacing from 1.64 cm to 1.70 cm; **(b)** uniform field from a film taken by superimposing five abutting fields with 1.66 cm index spacing

Because each gantry rotation about a patient treats two 1 cm slices, the treatment couch must be indexed craniocaudally to treat targets with dimensions greater than 2 cm. It is critical that the fields treated by each successive arc are matched precisely. The actual field size projected at 100 cm SAD may vary slightly for different accelerators since the field width depends on the beam penumbra and the distance from the radiation source to the block tray slot. As shown in Fig. 4a, the actual index spacing between successive treatment fields can be measured by abutting multiple fields on a single film (at isocenter and a depth of 5 cm) with all leaves open at nominal index spacing ranging from 1.64 to 1.70 cm. For this example, the index spacing for successive treatment fields was determined to be 1.66 cm. Then, the index spacing can be verified by superimposing multiple fields on a single film as shown in Fig. 4b. Five fields with 1.66 cm index spacing were delivered and resulted in a fairly uniform field.

Additional quality assurance checks are required each time the couch indexing device, the Crane, is attached. The Crane consists of a large vertical column that supports two arms each equipped with an electronic digital micrometer that has a precision of 0.01 mm. The crane is locked to the side rail of the treatment couch by two clamps which are mounted on one of the arms. If the clamps are not mounted correctly on the rail, the control of the couch movement will be inaccurate. Since the Crane is installed and removed daily, a simple daily QA procedure assures correct mounting of the Crane device to the couch. In addition, a quarterly check of the treatment indexing may be performed using the same film method mentioned above.

With respect to accuracy of the MIMiC collimator, leaf position accuracy and the leaf switch rate should be evaluated.

11.3.3 Record and Verify System

At each institution, the interface between information used by the accelerator and the record-and-verify system for all IMRT delivery systems should be tested. The value of the leaf position tolerance and limits on gantry, collimator, and table position accuracy should be tested.

11.4 Patient Specific Quality Assurance

Individual patient quality assurance should take place at each step of the treatment planning and delivery process as discussed in Section 11.1. When possible, procedures or checklists should be followed to ensure consistency in the overall process.

Patient quality assurance begins with immobilization of the patient for the CT scan. Patients should be set up in a comfortable position since IMRT treatment may take longer than conventional treatment. Stringent patient immobilization is required for IMRT treatments because the plans are highly conformal and often include high dose gradient regions at the boundaries between the tumor and sensitive structures. The dosimetric effect of patient movement and setup uncertainties in IMRT treatment is greater than those in conventional treatment. Any treatment aids that are used should be noted in the patient chart. The isocenter is usually placed at the center of the tumor volume if IMRT is delivered with conventional multi-leaf collimators. If IMRT is delivered with an add-on collimator, placement of the isocenter must also consider clearance between the patient and the add-on collimator.

In treatment planning CT acquisition, a thinner image slice (i.e., 3 mm) is preferred for IMRT treatment so that radiation oncologists and treatment planners can outline the tumor volume and sensitive structures more accurately. Furthermore, thinner image slices result in better quality digital reconstructed radiographs (DRRs).

After the patient CT scan is transferred, the target and structures of interest should be drawn by the radiation oncologist and dosimetrist. Any structure that will be assigned an objective function in the inverse planning system must be contoured. Target and organ-at-risk structures should then be expanded based on the institution's organ motion and setup data. All structures and expansions should be reviewed by a physicist, dosimetrist, or oncologist in 3D prior to beginning the optimization process. The number of beams should be selected and the beam angles reviewed. The cost or objective functions that are used for treatment planning should also be reviewed. Ideally, clinical protocols will be used to derive the values of the cost or objective function.

After an optimized plan has been accepted by the radiation oncologist, the dosimetrist or physicist should use the planning system to sequence the fields. The transfer of patient treatment data, such as gantry angle, collimator angle, and jaw positions, from the planning system to the record-and-verify system should be verified. The plan should also be validated to make sure that no collisions will take place. After the patient information is downloaded, the institution's pre-treatment QA program should be followed. This will involve

either a monitor unit verification check or dosimetric measurements as discussed in Section 11.1. For dosimetric measurements, the beam technique data are then used for dose calculations in the phantom geometry. Proper export of the dose calculation information or import of the measured data should be verified. The physicist should then determine if the QA fits within the institution's criteria for acceptability. The AAPM guidance document suggests an action level of 3 to 4% in high dose, low gradient regions for verification in a phantom compared with measurements [2]. If the measurement exceeds the action level, then it is the responsibility of the physicist to identify the problem. Additional measurements may be required along with a thorough review of the patient plan.

Once a plan successfully passes the pre-treatment QA, the patient setup should be verified on the first day of treatment. If the treatment isocenter is different from the isocenter marked at the time of the CT-simulation, special care must be taken to make sure that the correct shift is made when setting up the patient. To verify patient position, a set of orthogonal images should be acquired and compared with digitally reconstructed radiographs. If a patient move is required, then an additional set of images should be acquired and verified by the radiation oncologist. The institution should follow its individual site protocol to determine if an adaptive approach will be used for patient setup (multiple measurements over the first few days to determine an average displacement) or if the precision of daily imaging is required.

The AAPM guidance document on IMRT recommends verification of individual ports on the first day of treatment when supported by the delivery and verification system. Individual ports may be constructed from the outline of the IMRT field and acquired with film or an EPID [2]. In addition, some EPIDs allow for acquisition of images during IMRT delivery. These fields can be superimposed on the patient anatomy seen in the portal image. It may be difficult to interpret such results apart from clearly defining the borders of the field and large differences in field intensity. Additional QA checks on the first day include verification of the IMRT field delivery without anatomic information. One method is to measure the fluence intensity patterns by taping a piece of film to the reticule during the patient's delivery for comparison to the intensity patterns from the treatment plan. This method shows gross errors in the treatment delivery. Another method is to record the machine log files which track the MLC position and review the reconstructed delivery of the intended vs actual position [37]. Weekly physics checks should verify that the correct dose is delivered for every treatment. Tools in record-and-verify systems can be used to look for anomalies in the patient treatment such as variations in table position.

11.5 Methods of Dosimetry of IM Beams

As described in many publications, individual IMRT fields have typically been verified with film. An accurate film program requires stringent quality assurance and the process is very time consuming for film delivery (plus acquisition of the dose response curve), processing, digitizing, and data analysis. Digital approaches are therefore desirable. Electronic portal imager devices (EPIDs) and 2D diode arrays offer the potential to significantly reduce the time it takes to do individual field dosimetry by digital acquisition. Appropriate software tools are essential for quantitative evaluation of the accuracy between dose calculations and measurements. It is important to make sure that any dosimetry system has proper quality assurance associated with it since decisions about patient care are made based on the results. This section addresses the use of film, EPIDs, and 2D diode arrays for 2D evaluation of individual IMRT fields.

11.5.1 Film

Film is an essential part of commissioning an IMRT system because of its excellent spatial resolution and is used by many centers for a number of daily, weekly, and monthly quality assurance tests. Components of a film dosimetry program include film, water equivalent phantom, processor, digitizer (or scanner), and analysis software. For a reliable film dosimetry program, all aspects must be quality assured.

In the U.S., Kodak XV and EDR (extended dose range) film are primarily used. The response of each film type has been compared for energy and depth dependence [38–40]. When compared to XV film, EDR film shows less dependence on the processor and field size, and less response to low energy photons. EDR film also has been found to have better reproducibility and agreement with ion chamber measurements than XV film. Because of the decreased sensitivity of EDR film, it can be used to measure a complete fraction of an IMRT delivery.

Radiochromic film has also been investigated in a limited way for IMRT field dosimetry. The advantage of radiochromic film is that it changes color as a result of radiation and therefore no processing is required. However, great care must be taken when using radiochromic film as well to achieve accurate results [41, 42].

Due to the number of measurements required, ready pack film is often used. Ready pack film can conveniently be placed at any depth between slabs in a plastic phantom. Air trapped in the package can be removed by placing a pinhole in the package and forcing the air out. The phantom should be easy to use and to set up reproducibly for dosimetric measurements. When the

phantom is set up, fiducial marks should be placed on the film. These are built in to some phantom designs. If they are not, fiducial marks can be added using a jig and placing pinholes with a specific orientation outside of the beam. When using slabs of water equivalent material perpendicular to the beam, a jig can be used which allows placement of fiducials with pinholes. The pinholes allow for alignment of the film image independent of the dose distribution. This is critical for evaluating the accuracy of MLC leaf position. Failure to use fiducials could lead to missing a systematic error in either MLC leaf positioning or introduction of a position offset in the leaf sequencer compared with the intended field. The depth in water equivalent material and source-to-surface distance should be verified for all measurements. The measurement depth should be chosen based on the depth of primary clinical interest.

A characteristic curve to convert the film response to dose should be measured at the same time as IMRT fields are measured and all films should be processed at the same time after verification of processor performance. The characteristic curve should be measured over the range of expected doses. An unexposed film is required to determine the fog level of each film batch. Because a characteristic curve must be acquired each time, methods have been published in the literature to record multiple levels on a single film to save time and film [43]. The over-response of film to low energies must be considered when evaluating individual field measurements. To more accurately evaluate regions outside the field, multiple sensitometric curves can be used [44].

Quality assurance of the film processor is important since the gray level is dependent on the temperature of the chemicals and the concentration of developer and fixer. Processor stability should be assessed regularly. The temperature of the chemicals should be recorded. Fluctuations in the temperature are an indicator that maintenance should be called. To evaluate the effect of the processor on film, a light sensitometer can be used. On a regular basis, an unexposed film should be exposed to the sensitometer in the dark room, processed, and the optical density should be determined using a densitometer. The processor stability and ranges of acceptable values can be determined by plotting the film response over time from the sensitometer [28]. The system should be assessed after running several unprocessed films through the processor. The amount of fixer and developer should be checked to make sure that additional chemicals are not required while processing films for data analysis. Another concern about processor performance relates to the number of film processed on a regular basis. As many institutions replace their film verification program with EPIDs, the processor performance may become instable and adversely affect a film dosimetry program.

The next part of a film dosimetry program is the digitizer or scanner system. The digitizer response should be evaluated regularly for spatial intensity, characteristic response, and noise when there are large changes in optical density. Data transfer should be evaluated for accuracy where the pixel size and dimensions are assessed. There are additional concerns with the digitizer for radiochromic film analysis such as the light source of the digitizer [45].

Finally, the user should have a means of applying the measured characteristic curve to the IMRT field measurements through analysis software. The software should be evaluated for accuracy of transformations of the data when aligning, correct application of dosimetric curve, import of calculations (if applicable) and analysis tools such as dose difference displays, profile extraction, gradient evaluation, and other tools for comparing measurements with calculations.

11.5.2 EPID

Film is used at many centers for IMRT dosimetry because of its availability and flexibility of placement in a phantom. However, film is time-consuming to use, requires additional hardware, and involves a multi-step process to determine the results. Once an IMRT program has been commissioned and started with ion chamber and film measurements, it may be appropriate to use another device for individual beam verification measurements.

As mentioned earlier, electronic portal imaging devices (EPIDs) have been mounted on linear accelerators at many centers for verification of patient position. It is a logical extension of EPID technology to investigate applying such systems to IMRT dosimetry. Dosimetric applications have been investigated for charge-coupled camera devices (CCD), scanning liquid ionization chamber (SLIC) imagers, and active matrix flat panel imagers (AMFPI). In applying these systems for dosimetry, the systems may need to be operated in a mode different from that used clinically for patient position verification (radiographic or continuous acquisition modes). Additional software may also be required which is not available commercially yet.

To use an EPID for dosimetric verification, the EPID response must be characterized for dose, dose rate, field size, and leaf speed (if DMLC delivery) dependence. Corrections are required and depend on the construction of the system. In addition, a portal dose prediction or portal dose image must be calculated to evaluate the measurements.

CCD EPIDs have been applied to DMLC dosimetric measurements using a modified system that includes a 1 mm thick stainless steel slab in addition to the fluorescent layer [46]. Corrections are applied for the dark frame, the system's non-linear response, non-uniform spatial response, and optical cross talk. The application of a convolution kernel to correct for differ-

ence in absolute dose and penumbra for small fields has improved the response of the system for fields less than $3 \times 3\,cm^2$ [47]. Agreement between the CCD-EPID and measurements was within 2% for large fields measured with an ion chamber and for small fields measured with a linear diode array.

Commercial SLIC EPIDs have also been characterized for dosimetric measurements for SMLC-IMRT and DMLC-IMRT [48–50]. Different acquisition modes have been used for SMLC and DMLC delivery [48–50]. A problem with using this device for dosimetry is the need for equilibrium in the iso-octane layer of the device which led to measurements of only one segment per minute in one experiment [48]. Multiple investigators have found the agreement within about 2% with ion chamber and film data except in steep gradient regions.

The final EPID systems that have recently been characterized for dosimetric applications are active matrix flat panel imagers (AMFPIs). Commercially, the systems have a fluorescent layer above the imager area which adversely affects the dosimetric response [51]. The imager response has been modeled with Monte Carlo, deconvolution, and empirical methods for SMLC and DMLC delivery and agreement of approximately 2% has been measured by multiple investigators [52–54]. Further application of EPIDs for individual IMRT field verification is expected to continue. Commercial systems, including software, are still under development. Once such systems are in place, they offer great potential for saving time for verification of individual IMRT fields.

11.5.3 2D Arrays

Two-dimensional detector arrays are commercially available for individual IMRT field verification. In the currently available system, 445 n-type diodes are distributed over an area of $22 \times 22\,cm^2$ (Sun Nuclear, Melbourne, FL). The spatial resolution is 7.07 mm in the central $10 \times 10\,cm^2$ region of the detector array and 14.14 mm in the outside area and the array is designed solely for perpendicular beam measurements. Similar to EPIDs, such arrays should only be used after an IMRT program has been commissioned.

Before measurements, the diode array is calibrated at depth. Each detector has its own sensitivity factor with respect to the diode on the central axis. After measurement, the dose calibration factors are applied for comparison to calculations (or measurements with another detector). The response of the array has been characterized as a function of dose, dose rate, reproducibility, and temperature. Overall, the diode array was determined to have a reproducible and linear response (up to 295 cGy) and a dependence on temperature [55, 56]. Measurements of output factors agreed to within 2% for field size ranging from $2 \times 2\,cm^2$ to $25 \times 25\,cm^2$ [56]. Additional studies have found diode arrays to be sensitive enough to measure the effect of segments that are dropped during IMRT delivery [57]. While the overall response is very good, the current diode arrays are limited by their size and coarse spatial resolution. These systems only verify a representative sample of delivered IMRT fields.

11.6 Methods of Dosimetry of Complete IMRT Treatments

While individual field checks are essential for determining the cause of errors in IMRT delivery, verification of the complete IMRT treatment allows for assessment of plan delivery at the proper gantry, collimator, and couch angles that are used for patient treatment. The patient's IMRT plan is transferred to a phantom and calculations are done at the points or depths of interest. The phantom can be cylindrical, cubic, or anthropomorphic. Cylindrical and cubic phantoms of water equivalent material are often used because the phantoms and detectors can be set up reproducibly. Ion chamber measurements are often used to verify the absolute dose at a single point. Some phantoms have been designed that accommodate multiple detectors such as film, ionization chambers, TLDs, and MOSFETs [58, 59]. The advantage of such phantoms is that absolute dose can be verified at multiple points in both high and low dose regions.

11.6.1 2D Film

Complete IMRT treatments can be verified in two dimensions using film placed between water equivalent material or in an anthropomorphic phantom [28]. In the US, EDR film, or less commonly, radiochromic film can be used for such measurements. The issues with a film dosimetry program were discussed in Section 11.5.1. The dose response curve should be measured at the same time as the phantom measurement. To properly verify a plan, the calculated monitor units that are to be delivered for the patient treatment should be used. Monitor unit scaling or a change in dose rate can result in small differences in delivery of the fields. When doing composite film dosimetry, it can be difficult to determine the cause of differences between the measurement and calculation. Therefore, individual field measurements (with film and/or ionization chamber) may be required if unacceptable results are obtained with a 2D composite film.

11.6.2 3D Gel

Methods of 1- and 2D dosimetry provide an incomplete evaluation of accuracy of delivery for a complete

IMRT treatment. Ideally, IMRT verification would be done in 3D when beginning an IMRT program and as a check of the overall treatment and delivery process. Gel dosimetry offers the potential to do this plus the flexibility of varying gel density to measure dose throughout heterogeneous regions [60].

Gels can be made in a lab or purchased as a package to be mixed on site. Great care and specialized readout equipment (optical CT scanner or MR scanner) are required to do accurate gel dosimetry (MGS, Guildford, New Haven, CT). The response of polymer gels is dependent on exposure to light and oxygen, the gel composition, and the temperature of the gel during readout [61]. A few investigators have explored plan verification for IMRT delivery [60, 62–64]. Accuracy of gel dosimetry is typically on the order of 3–5% with a spatial resolution of 2–5 mm.

At this time, gel dosimetry is very time-intensive process and dependent on environmental conditions. Even with off-the-shelf gel dosimetry kits, it is difficult to obtain accurate results without prior experience. Further development of more robust polymer gels is required before gel dosimetry can be used reliably at multiple centers. There are also still technical challenges in the readout by optical CT or MR scanners which are under investigation [65]. Until these issues are overcome, an appropriate approach might be the use of gel dosimetry in a phantom by credentialing institutions, such as the Radiation Therapy Oncology Group (RTOG) and the Radiological Physics Center (RPC) in the US for participation in national protocols as has been done with radiochromic film [29]. Multiple centers would benefit from the information that can be learned about their patient treatment process for a specific IMRT test case without needing to develop in-house expertise and a full-scale research program.

References

1. IMRT Collaborative Working Group (2001) Intensity-modulated radiotherapy: current status and issues of interest. Int J Radiat Oncol Biol Phys 51:880–914
2. Ezzell GA, Galvin JM, Low D et al. (2003) Guidance document on delivery, treatment planning, and clinical implementation of IMRT: report of the IMRT Subcommittee of the AAPM Radiation Therapy Committee. Med Phys 30:2089–2115
3. Galvin JM, Ezzell G, Eisbruch A et al. (2004) Implementing IMRT in clinical practice: A joint document of the American Society for Therapeutic Radiology and Oncology and the American Association of Physicists in Medicine. Int J Radiat Oncol Biol Phys 58:1616–1634
4. Lee N, Chuang C, Quivey JM et al. (2002) Skin toxicity due to intensity-modulated radiotherapy for head-and-neck carcinoma. Int J Radiat Oncol Biol Phys 53:630–637
5. Herman MG, Balter JM, Jaffray DA et al. (2001) Clinical use of electronic portal imaging: report of AAPM Radiation Therapy Committee Task Group 58. Med Phys 28:712–737
6. Lee N, Zhu N, Baker L et al. (2003) Intra-fraction patient motion in head/neck cancer patients undergoing intensity-modulated radiation therapy (IMRT). Int J Radiat Oncol Biol Phys 57:409
7. Vigneault E, Pouliot J, Laverdiere J et al. (1997) Electronic portal imaging device detection of radioopaque markers for the evaluation of prostate position during megavoltage irradiation: a clinical study. Int J Radiat Oncol Biol Phys 37:205–212
8. Mohan DS, Kupelian PA, Willoughby TR (2000) Short-course intensity-modulated radiotherapy for localized prostate cancer with daily transabdominal ultrasound localization of the prostate gland. Int J Radiat Oncol Biol Phys 46:575–580
9. Wong JW, Sharpe MB, Jaffray DA et al. (1999) The use of active breathing control (ABC) to reduce margin for breathing motion. Int J Radiat Oncol Biol Phys 44:911–919
10. Ramsey CR, Scaperoth D, Arwood D, Oliver AL (1999) Clinical efficacy of respiratory gated conformal radiation therapy. Med Dosim 24:115–119
11. Dawson LA, Balter JM (2004) Interventions to reduce organ motion effects in radiation delivery. Semin Radiat Oncol 14:76–80
12. ICRU (1993) Prescribing, recording and reporting photon beam therapy. Report 50. International Commission on Radiation Units and Measurements, Washington DC
13. ICRU (1999) Prescribing, recording and reporting photon beam therapy. Supplement to ICRU Report 50. Report 62. International Commission on Radiation Units and Measurements, Washington DC
14. Kutcher GJ, Coia L, Gillin M et al. (1994) Comprehensive QA for radiation oncology: report of AAPM Radiation Therapy Committee Task Group 40. Med Phys 21:581–618
15. Low DA, Mutic S, Dempsey JF et al. (1998) Quantitative dosimetric verification of an IMRT planning and delivery system. Radiother Oncol 49:305–316
16. LoSasso T, Chui CS, Ling CC (2001) Comprehensive quality assurance for the delivery of intensity modulated radiotherapy with a multileaf collimator used in the dynamic mode. Med Phys 28:2209–2219
17. Xing L, Chen Y, Luxton G et al. (2000) Monitor unit calculation for an intensity modulated photon field by a simple scatter-summation algorithm. Phys Med Biol 45:N1–N7
18. Chen Z, Xing L, Nath R (2002) Independent monitor unit calculation for intensity modulated radiotherapy using the MIMiC multileaf collimator. Med Phys 29:2041–2051
19. Zhu J, Yin FF, Kim JH (2003) Point dose verification for intensity modulated radiosurgery using Clarkson's method. Med Phys 30:2218–2221
20. Low DA, Mutic S (1997) Abutment region dosimetry for sequential arc IMRT delivery. Phys Med Biol 42:1465–1470
21. Balter JM, Lam KL, McGinn CJ et al. (1998) Improvement of CT-based treatment-planning models of abdominal targets using static exhale imaging. Int J Radiat Oncol Biol Phys 41:939–943
22. Jaffray DA, Yan D, Wong JW (1999) Managing geometric uncertainty in conformal intensity-modulated radiation therapy. Semin Rad Onc 9:4–19
23. Fraass B, Doppke K, Hunt M et al. (1998) American Association of Physicists in Medicine Radiation Therapy Committee Task Group 53: Quality assurance for clinical radiotherapy treatment planning. Med Phys 25:1773–1829
24. Yan D, Ziaja E, Jaffray D et al. (1998) The use of adaptive radiation therapy to reduce setup error: a prospective clinical study. Int J Radiat Oncol Biol Phys 41:715–720
25. Sharpe MB, Miller BM, Yan D, Wong JW (2000) Monitor unit settings for intensity modulated beams delivered using a step-and-shoot approach. Med Phys 27:2719–2725

26. Chuang C, Woodruff D, Verhey L, Xia P (2002) Investigation of the dosimetric consequences of leaf setting uncertainties for a double-focused MLC in IMRT delivery. Med Phys 29:1269
27. Boyer AL, Li S (1997) Geometric analysis of light-field position of a multileaf collimator with curved ends. Med Phys 24:757–762
28. LoSasso T, Chui CS, Ling CC (1998) Physical and dosimetric aspects of a multileaf collimation system used in the dynamic mode for implementing intensity modulated radiotherapy. Med Phys 25:1919–1927
29. Cadman P, Bassalow R, Sidhu NP et al. (2002) Dosimetric considerations for validation of a sequential IMRT process with a commercial treatment planning system. Phys Med Biol 47:3001–3010
30. Huq MS, Das IJ, Steinberg T, Galvin JM (2002) A dosimetric comparison of various multileaf collimators. Phys Med Biol 47:N159–N170
31. Galvin JM, Smith AR, Lally B (1993) Characterization of a multi-leaf collimator system. Int J Radiat Oncol Biol Phys 25:181–192
32. Mohan R, Arnfield M, Tong S et al. (2000) The impact of fluctuations in intensity patterns on the number of monitor units and the quality and accuracy of intensity modulated radiotherapy. Med Phys 27:1226–1237
33. Xia P, Hwang AB, Verhey LJ (2002) A leaf sequencing algorithm to enlarge treatment field length in IMRT. Med Phys 29:991–998
34. Seco J, Evans PM, Webb S (2002) An optimization algorithm that incorporates IMRT delivery constraints. Phys Med Biol 47:899–915
35. Xia P, Verhey LJ (2001) Delivery systems of intensity-modulated radiotherapy using conventional multileaf collimators. Med Dosim 26:169–177
36. Chui CS, Spirou S, LoSasso T (1996) Testing of dynamic multileaf collimation. Med Phys 23:635–641
37. Litzenberg DW, Moran JM, Fraass BA (2002) Incorporation of realistic delivery limitations into dynamic MLC treatment delivery. Med Phys 29:810–820
38. Dogan N, Leybovich LB, Sethi A (2002) Comparative evaluation of Kodak EDR2 and XV2 films for verification of intensity modulated radiation therapy. Phys Med Biol 47:4121–4130
39. Chetty IJ, Charland PM (2002) Investigation of Kodak extended dose range (EDR) film for megavoltage photon beam dosimetry. Phys Med Biol 47:3629–3641
40. Esthappan J, Mutic S, Harms WB et al. (2002) Dosimetry of therapeutic photon beams using an extended dose range film. Med Phys 29:2438–2445
41. Niroomand-Rad A, Blackwell CR, Coursey BM et al. (1998) Radiochromic film dosimetry: recommendations of AAPM Radiation Therapy Committee Task Group 55. American Association of Physicists in Medicine. Med Phys 25: 2093–2115
42. Dempsey JF, Low DA, Mutic S et al. (2000) Validation of a precision radiochromic film dosimetry system for quantitative two-dimensional imaging of acute exposure dose distributions. Med Phys 27:2462–2475
43. Childress NL, Dong L, Rosen II (2002) Rapid radiographic film calibration for IMRT verification using automated MLC fields. Med Phys 29:2384–2390
44. Stern RL, Kurylo J, Siantar CH et al. (2004) Film dosimetry in the peripheral region using multiple sensitometric curves. Med Phys 31:327–332
45. Gluckman GR, Reinstein LE (2002) Comparison of three high-resolution digitizers for radiochromic film dosimetry. Med Phys 29:1839–1846
46. Pasma KL, Dirkx ML, Kroonwijk M et al. (1999) Dosimetric verification of intensity modulated beams produced with dynamic multileaf collimation using an electronic portal imaging device. Med Phys 26:2373–2378
47. Vieira SC, Dirkx MLP, Pasma KL, Heijmen BJM (2003) Dosimetric verification of X-ray fields with steep dose gradients using an electronic portal imaging device. Phys Med Biol 48:157–166
48. Curtin-Savard AJ, Podgorsak EB (1999) Verification of segmented beam delivery using a commercial electronic portal imaging device. Med Phys 26:737–742
49. Van Esch A, Vanstraelen B, Verstraete J et al. (2001) Pretreatment dosimetric verification by means of a liquid-filled electronic portal imaging device during dynamic delivery of intensity modulated treatment fields. Radiother Oncol 60:181–190
50. Chang J, Mageras GS, Ling CC (2003) Evaluation of rapid dose map acquisition of a scanning liquid-filled ionization chamber electronic portal imaging device. Int J Radiat Oncol Biol Phys 55:1432–1445
51. El-Mohri Y, Antonuk LE, Yorkston J et al. (1999) Relative dosimetry using active matrix flat-panel imager (AMFPI) technology. Med Phys 26:1530–1541
52. McCurdy BM, Luchka K, Pistorius S (2001) Dosimetric investigation and portal dose image prediction using an amorphous silicon electronic portal imaging device. Med Phys 28:911–924
53. Warkentin B, Steciw S, Rathee S, Fallone BG (2003) Dosimetric IMRT verification with a flat-panel EPID. Med Phys 30:3143–3155
54. Van Esch A, Depuydt T, Huyskens DP (2004) The use of an aSi-based EPID for routine absolute dosimetric pre-treatment verification of dynamic IMRT fields. Radiother Oncol 71:223–234
55. Jursinic PA, Nelms BE (2003) A 2-D diode array and analysis software for verification of intensity modulated radiation therapy delivery. Med Phys 30:870–879
56. Letourneau D, Gulam M, Yan D et al. (2004) Evaluation of a 2D diode array for IMRT quality assurance. Radiother Oncol 70:199–206
57. Li JG, Dempsey JF, Ding L et al. (2003) Validation of dynamic MLC-controller log files using a two-dimensional diode array. Med Phys 30:799–805
58. Low DA, Gerber RL, Mutic S, Purdy JA (1998) Phantoms for IMRT dose distribution measurement and treatment verification. Int J Radiat Oncol Biol Phys 40:1231–1235
59. Chuang CF, Verhey LJ, Xia P (2002) Investigation of the use of MOSFET for clinical IMRT dosimetric verification. Med Phys 29:1109–1115
60. Gum F, Scherer J, Bogner L et al. (2002) Preliminary study on the use of an inhomogeneous anthropomorphic Fricke gel phantom and 3D magnetic resonance dosimetry for verification of IMRT treatment plans. Phys Med Biol 47:N67–N77
61. McJury M, Oldham M, Cosgrove VP et al. (2000) Radiation dosimetry using polymer gels: methods and applications. Br J Radiol 73:919–929
62. Oldham M, Baustert I, Lord C et al. (1998) An investigation into the dosimetry of a nine-field tomotherapy irradiation using BANG-gel dosimetry. Phys Med Biol 43:1113–1132
63. Low DA, Dempsey JF, Venkatesan R et al. (1999) Evaluation of polymer gels and MRI as a 3-D dosimeter for intensity-modulated radiation therapy. Med Phys 26:1542–1551
64. De Deene Y (2002) Gel dosimetry for the dose verification of intensity modulated radiotherapy treatments. Z Med Phys 12:77–88
65. Oldham M, Siewerdsen JH, Kumar S et al. (2003) Optical-CT gel-dosimetry I: basic investigations. Med Phys 30:623–634

Part II
Advanced Image-Guided and Biologically Guided Techniques

Imaging Lymph Nodes Using CT and MRI, Imaging Cancer by PET

Th. Duprez, E.E. Coche, M. Lonneux

1

Contents

1.1 Introduction

Dramatic improvements in both radiation planning methods and imaging techniques during the past two decades have led to the synergistic concept of imaging-supported three-dimensional (3D) conformal and intensity modulated radiation therapy (CRT & IMRT) [1]. By combining up-to-date three dimensional techniques giving precise anatomical information and molecular tests yielding metabolic information, better precision is achieved in tumoral volumes targeting through which higher radiation doses could be delivered to high-risk sub-volumes of the gross tumoral volume (GTV), lower doses could be delivered to the lower-risk sub-volumes, and through which non-tumoral areas included into the clinical tumoral volume (CTV) could be spared [2]. Precise and accurate 3D delineation of the different tumoral sub-volumes within CTV is obviously crucial and relies on the capabilities of the different imaging modalities to give higher tissue contrast and to become more sensitive and (ideally)

specific to the metabolic activity of the CTV components. Computed tomography (CT) and magnetic resonance imaging (MRI) are well established imaging modalities for the three-dimensional contouring of the lesions [3]. As demonstrated in the next II. 2 and II. 3 chapters, intrinsic metabolic and/or molecular information allowing the classification of the sub-volumes may be now achieved by either magnetic resonance spectroscopy (MRS), or by isotopic positron-emission tomography (PET) or single-photon emission computed tomography (SPECT) imaging using tracers of variable specificity tailored to the metabolic and/or antigenic characteristics of the target tissue. Functional MR techniques such as free water diffusion-weighted imaging (DWI) and perfusion-weighted imaging (PWI) may add but still remain investigational for assessing the lymph node involvement with neoplastic processes [4, 5]. Including malignant lymph nodes into the CTV and excluding benign ones appears mandatory to optimize the treatment planning. But accurate characterization of the false-negative normal-sized nodes harboring metastatic micro-deposits, and of the false-positive ones which are enlarged only by benign reactive changes remains unsolved issue in spite of major recent improvements of structural imaging modalities. Both CT and MRI have overall similar and unsatisfactory diagnostic accuracy for malignant lymph nodes detection using either size criterion [6], or necrosis criterion [7]. The co-registration of the anatomic and of the metabolic/molecular information in a composite image appears as a key-progress to lower inappropriate upgrading of benign large nodes and to decrease missing of nodal micro-metastases when delineating the GTV and the CTV for radiation therapy planning. This initial II. 1 chapter gives an overview of the equipment and clinical techniques of the three main modalities for lymph node imaging.

1.2 Computed Tomography Imaging

1.2.1 Hardware/Software Requirements for High-Quality CT

Computed tomography technology has continued to improve over the past decades. The first CT mode introduced in the early 1970s by Godfrey Hounsfield was *sequential*, i.e., the patient remained stationary while transverse slices were acquired but with a spatial table incrementation between slice acquisitions [8]. The main limitations to this initial approach were the time required to perform the examination and the gap between two slices, possibly resulting in lesion misregistration. For several years, *spiral/helical* [9] or *volumetric* CT has been used in clinical practice; data recording is obtained during the continuous rotation of a set of detectors while the table undergoes continuous motion at a predetermined speed [140, 141]. This new approach has several advantages when compared to the conventional CT mode. Among these, the following should be emphasized: shortened acquisition time (under 1 min to obtain a complete volume of 30 cm FOV in the *z*-axis with intermediate spatial resolution), optimization of the intravenous injection of iodinated contrast medium, acquisition of an uninterrupted volume of data which can subsequently be post-processed, and a substantial decrease in patient irradiation. It has recently been demonstrated that for a given X-ray dose and using overlapping reconstruction, the spiral CT technique has a better longitudinal resolution than the conventional CT technique [10–12]. Recently spiral CT technology has further improved with the incorporation of multiple rows of detectors instead of a single row ("*multislice*" or "*multirow*" CT) [13, 14]. With the recent decrease in gantry rotation time, multislice helical CT is now up to eight times faster than conventional single-slice helical CT. The concurrent acquisition of multiple slices results in a significant reduction in scanning time, permitting one-step acquisition of large volumes, a procedure which was previously unfeasible. In a similar manner, given volumes can be scanned using narrower beam collimation, resulting in a higher transverse spatial resolution without additional time loss. Both high-resolution and standard images can be reconstructed in the so-called "*combi-mode*" from data acquired using narrow collimation. On the one hand, patient dose exposure is reduced because repeated scanning is no longer required. On the other hand, narrow collimation is beneficial to standard reconstructions, as partial volume artifacts are drastically reduced.

1.2.2 Basic Tissue Contrast on CT Images

Spontaneous tissue contrast on CT images is directly related to the X-ray characteristics. Only thin tissue slices are irradiated, without subsequent deleterious superimposition or blurring of structures located outside the selected slice planes [15]. Each detector rotating around the patient during data acquisition receives a variable amount of X-rays depending on the physical parameters of the incidental beam (kilovoltage (kV), milliamperes per second (mA s)), and on the specific attenuating characteristics (tissue volume, physical composition) of the patient's tissues. The CT system measures the tissue attenuation coefficient which has a diagnostic value. Attenuation is quantified by a numerical value ranging from approximately −1000 to 3000 Hounsfield units (HU). The system is calibrated so that water has an attenuation value of 0 HU, and air an attenuation value

of −10,000 HU. A normal lymph node is a soft tissue structure with spontaneous intermediate density of 30–50 HU. The node hilum density may be negative when it contains fatty tissue. However, calcifications have a high attenuation value and therefore appear very bright on CT images. The CT technique is far more sensitive than MRI in depicting calcifications [16]. When necrosis occurs, the lymph node may show low attenuation values due to the fluid content. To characterize better a normal or abnormal structure and differentiate it from its environment, intravenous contrast medium may be injected before or during the CT procedure. Most CT contrast media contain iodine (I). After a rapid intravenous bolus injection, contrast medium molecules rapidly diffuse through most capillary membranes from the intravascular to the extravascular space, allowing the detection of necrotic areas within the nodes and/or tumor (Figs. 1,3a) which contain less contrast medium-filled blood vessels than the surrounding normally vascularized tissues. The intensity of nodal contrast enhancement after contrast medium perfusion depends on the degree of vascularization [17]. Nodal enhancement is a non-specific finding, as inflammatory or tumoral nodes may have similarly higher attenuation values due to contrast medium uptake by the feeding vessels.

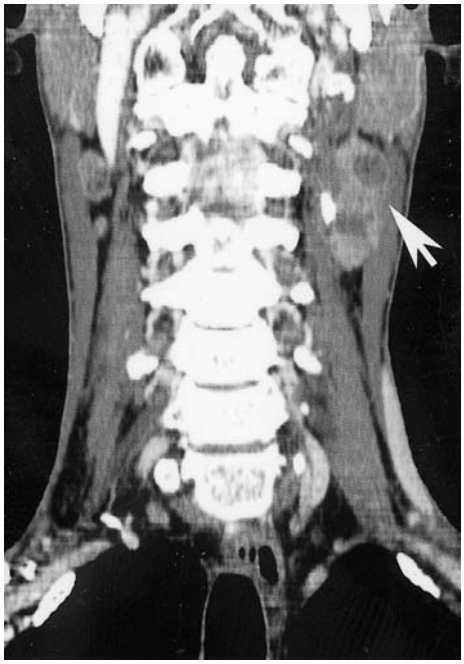

Fig. 1. Coronal CT reformatted image of the cervical area: 40-year-old man with an ulcerated epiglottis tumor. Data were obtained by contrast-enhanced MSCT using the following parameters: FOV: 230 mm; slice thickness: 2 mm; reconstruction interval: 1 mm; table speed: 6.7 mm/s; kV: 120; mA s: 150; matrix: 512 × 512. Frontal reformation demonstrated the posterior location of necrotic lymph nodes (*arrow*) between the posterior scalene and the sterno-cleido-mastoid muscles on the left side

1.2.3 CT Image Acquisition Parameters

Kilovoltage, Milliamperes per Second

The kV reflects the energy level of the incidental X-ray beam. Higher energies result in an increased penetration through the tissues so that a greater number of photons can reach the detectors on the opposite side. Subsequent reduction in quantum noise leads to smoother images. The mA s value quantifies the number of emitted X-ray photons. The quantum noise value is inversely proportional to the mA s number. Increasing the mA s decreases the quantum noise value and increases contrast resolution. In selecting the mA s value, the radiologist must take into account the overall image quality, the radiation dose, and ultimately the impact of the image quality on the final diagnosis. The standard values used at our institution are 120 kV and 150 mA s for cervical region imaging and 100 kV and 165 mA s for the chest and abdomen imaging. The mA s value must be significantly increased for conformal radiotherapy (CRT) planning. For example, in the case of whole-body scanning, imaging must be performed at 120 kV and at around 300 mA s.

Beam Collimation

Beam collimation designates the actual width of the incidental X-ray beam. In sequential CT, the basic slice thickness is defined as follows: a 5-mm wide beam leads to the acquisition of a 5-mm thick section, and a 10-mm wide beam to a 10-mm thick section. In spiral CT, slice thickness is increased by image distortion due to the continuous motion of the patient through the gantry during scanning. Selecting the beam collimation (the nominal slice thickness) is one the first parameters to define, since it has a major impact on the sensitivity of lesion detection. For detecting small nodes, it would be inappropriate to choose a thick slice section since a thin lesion could be missed because of the partial volume averaging effects. Usually, lymph node staging using CT requires a 3–5 mm slice thickness in the neck area [18] and 5–10 mm in the chest and abdomen.

Rotation Time

Rotation time designates the length of time necessary for the beam source to complete one full 360° rotation. Until recently, this took 1 s for all spiral scanners. Nowadays the *multislice* CT (MSCT) mode has enabled this to be reduced to a sub-second rotation time [14], i.e., 0.5 s. With this kind of CT system, four contiguous slices may be obtained during one rotation with eight images acquired in 1 s. For oncology patients, this new approach limits the time the patient has to spend in an uncomfortable position, and reduces the need for repeated breath-holding and for repeated contrast medium injections [19]. The image quality of spiral CT with a sub-second gantry rotation period is better than

that obtained with a one-second rotation time, particularly for mediastinal examinations [20]. In the near future, MSCT systems will be introduced with a rotation time of less than 0.5 s, enabling the acquisition of 38 images per second.

Pitch

In sequential scanning, the patient remains stationary during acquisition of the multiple projections needed to reconstruct the transaxial image. In spiral CT, the patient is continuously moved through the gantry during data acquisition. In single-slice spiral scanning, the pitch is determined by the ratio of the table movement per single 360° gantry rotation to the beam collimation. The pitch equals 1 if the beam collimation is 10 mm and the patient is moved into the gantry by 10 mm during every 360° rotation. If the beam collimation is 10 mm, with the patient being passed through the gantry at a speed of 20 mm/rotation, the pitch value increases to 2. Increasing the pitch leads to an overall decrease in the delivered radiation dose (with all other imaging parameters remaining unchanged), since the overall scanning time is shortened as a result of the faster passage of the patient through the gantry. A pitch value greater than 1 can be selected if the area of interest is too large to be covered by the prescribed collimation when using a pitch of 1. The use of a greater pitch increases the distortion along the *z*-axis and also increases the noise. This distortion may impact on the delineation of the target volume in CRT. Image quality in this case would be preserved with a pitch value of around 2 [21].

Matrix and Field of View

The image matrix quantifies the number of pixels of the image grid. The spatial volume represented by an individual pixel depends on the size of the field of view (FOV). Current spiral CT scanners reconstruct standard images with a 512×512 display matrix. As the total number of pixels in each image is limited, the selection of a larger FOV results in a larger volume of each pixel with a concomitant loss of spatial resolution. The optimal FOV depends on the size of the region being explored, with the most appropriate FOV being around 230–250 mm for the neck, and about 400–500 mm for the chest and abdomen.

Contrast Medium

All intravenous contrast agents currently approved for CT imaging contain iodine atoms bound within complex organic vector molecules. The protocol for contrast medium injection varies according to the explored area.

For *neck* examination, most authors [22, 23] recommend biphasic injection. At our institution, the first 50–60 cc of contrast medium (300–350 mg I/ml) are injected as a drip perfusion to impregnate the interstitial compartment. The other 50–60 cc of contrast medium are injected at a rate of 2 cc/s approximately 2 min after the first drip perfusion injection. The delay before imaging is 30 s after administering the second injection. This protocol usually provides an adequate opacification of the different vascular structures, thereby allowing an accurate interpretation of head and neck CT images. A recent report has highlighted the value of delayed scans in head and neck spiral CT examination [24]. The latter authors have demonstrated a greater definition of some neck lesions on images obtained 10–15 min after contrast medium injection. Although slightly less spatial resolution is obtained with spiral CT than with the conventional serial CT due to the reduced scanning times, the spiral technique usually permits better vessel opacification. When using a faster CT technique and a power injector, asymmetric or heterogeneous opacification of the internal jugular veins is frequently observed, which may mimic venous thrombosis or nodal necrosis when viewed as a single slice [25].

For *chest* imaging, 80–120 cc of a concentrated iodinated agent (100–150 mg I/ml) are injected through an antecubital vein at a rate of 1–2 cc/s. The delay before imaging is 35–50 s depending on the circulation time. Leung has recommended the intravenous injection of 100 ml of 150 mg I/ml contrast medium at a rate of 2.5 ml/s with a delay before scanning of 25 s [26]. For abdominal examination, the maximum contrast enhancement of the vessels mainly relies on the volume of the contrast medium injected and on the time to peak enhancement, which is determined by the injection rate [27]. Our current abdominal injection protocol for lymph node assessment consists of the perfusion of 100 ml of contrast agent (300 mg I/ml) at a rate of 2 ml/s and a delay before scanning of 35 s.

1.2.4 Post-processing of CT Images

Window Setting

The full range of attenuation values cannot be displayed on the CT images due to the limitation in the number of gray scale levels detectable by the human eye. A single window setting cannot properly display all the information contained in the CT image. The optimal window width and window level (W/L) settings for soft tissues such as lymph nodes may vary according to the CT system, the monitor, the printer and the type of film. The optimal window setting is approximately 400/50 HU for soft tissue and lymph node analysis. However, a bone window setting of 1700/300 HU may be used to identify nodal calcifications better.

Reconstruction Interval

Data are volumetrically acquired by the spiral CT technique, and axial transverse images may be subsequently reconstructed at any point throughout the

volume. Images may be reconstructed at intervals which are smaller than the initial nominal slice thickness. When images are reconstructed at smaller increments than the beam collimation, they "overlap" one another. The creation of overlapping sections improves the longitudinal resolution of reformatted images in the *z*-axis [10]. This property allows the reconstruction of high-resolution 2D or 3D images. Overlapping slices also improve the detection of small structures.

2D and 3D Reconstructions

Both kinds of reconstruction require the acquisition of only one data set, thus avoiding additional examination time and/or an increase in radiation exposure. High-quality orthogonal and 3D reconstructions are obtainable without the step borders artifact observed in standard incremental scans. The topographical relationships between the lymph nodes and any other tissues or vessels can then be evaluated in sagittal, axial, coronal, or oblique views. Multiplanar reformation (MPR) creates images along arbitrary straight or curved planes of at least one voxel in thickness. MPR images can be created in any plane with the same spatial resolution as the original axial transverse sections ("*isotropic*" viewing). MPR ignores all data except those along the single voxel path defining the reformation plane. This technique is easy to use and facilitates the assessment of the relationship between lymph nodes, vessels and other anatomical structures (Fig. 1). True 3D rendering techniques consider the entire data set or an edited subset of data for the generation of images. Shaded surface display (SSD) and volume rendering (VR) are the two existing algorithms for 3D image rendering using spiral CT. With the VR technique, the processing method is based on the use of a linear projection of virtual rays through the data set to create a projectional image of the pixel of interest. The relative density information is preserved by this technique, since it is not surface-dependent. The other technique, i.e. the SSD, uses intensity thresholding of the CT data so that all values within a defined range are selected for rendering and the remainder are removed from the data set [28, 29]. These two 3D reconstruction techniques are rarely used in clinical practice because the nodal density is too close to that of the surrounding muscles or viscera to obtain accurate nodal definition. Further software improvements are needed before an accurate 3D nodal display can be obtained.

1.2.5 Normal Lymph Nodes on CT Images

Computed tomography imaging permits an adequate assessment of the lymphatic system in almost all parts of the body. The high tissue contrast between the lymph nodes and the surrounding fatty tissue is usually sufficient to delineate normal or enlarged lymph nodes. The injection of intravenous iodinated contrast medium usually helps to differentiate the lymphatic structures from the adjacent vascular structures. Its use is mandatory for lymph node assessment in the cervical region because of the poor fatty interfaces in this area. On unenhanced CT images, normal lymph nodes display the same intermediate density as the muscles at 30–40 HU. Normal nodes are elliptic, round or triangular in shape [17]. The node hilum may contain small amounts of fat which are sometimes detectable on thin collimation CT images. After intravenous contrast medium perfusion, normal nodes become slightly more enhanced than the muscles. Both CT and MR modalities are suited to nodal status assessment in most parts of the body. MRI performance is highest in the neck and abdomen, and to a lesser extent in the chest where it is restricted by the presence of a large quantity of air. In terms of cost effectiveness, the use of CT for nodal status assessment seems to be a more attractive proposition than MRI which is expensive, time-consuming and more often used for parenchymal examination than for "pure" nodal status assessment.

The *cervical lymph nodes* are divided into four to five groups, all being contiguous to one another. Most classification systems are based on the studies of Rouviére [30]. The TNM system divides the head and neck lymph nodes into 12 groups. In recent studies [31, 32] the neck has been divided into six levels including eight nodal groups (Fig. 2a,b).

The *thoracic lymph nodes* are usually classified into parietal and visceral groups. Different classifications based on location and drainage routes have been proposed by various authors. For the past 10 years, two systems of nodal classification for lung cancer staging have been commonly used [33]: that of the American Joint Committee on Cancer [34] and that of the American Thoracic Society (ATS) together with the North American Lung Cancer Study Group [35] (Fig. 2c).

The *abdominal lymph nodes* are usually classified either according to the course of the major vessels and the ligaments, or to their location within the peritoneal or the retroperitoneal cavities. Lymph nodes are located, e.g., within the subdiaphragmatic area, the gastrohepatic ligament, the retrocrural space, the upper paraaortic area (from the celiac to the renal arteries), the lower paraaortic area (from the renal arteries to the iliac bifurcation), the porta hepatis, the portacaval space, and the internal or external iliac area (Fig. 2d–f).

1.2.6 Pathological Lymph Nodes on CT Images

Many different radiological criteria are used to assess the presence or absence of metastatic tissue within the lymph nodes. These include the axial diameter, the pattern of enhancement, the spheroid shape and the grouping of the nodes. The size and shape of normal

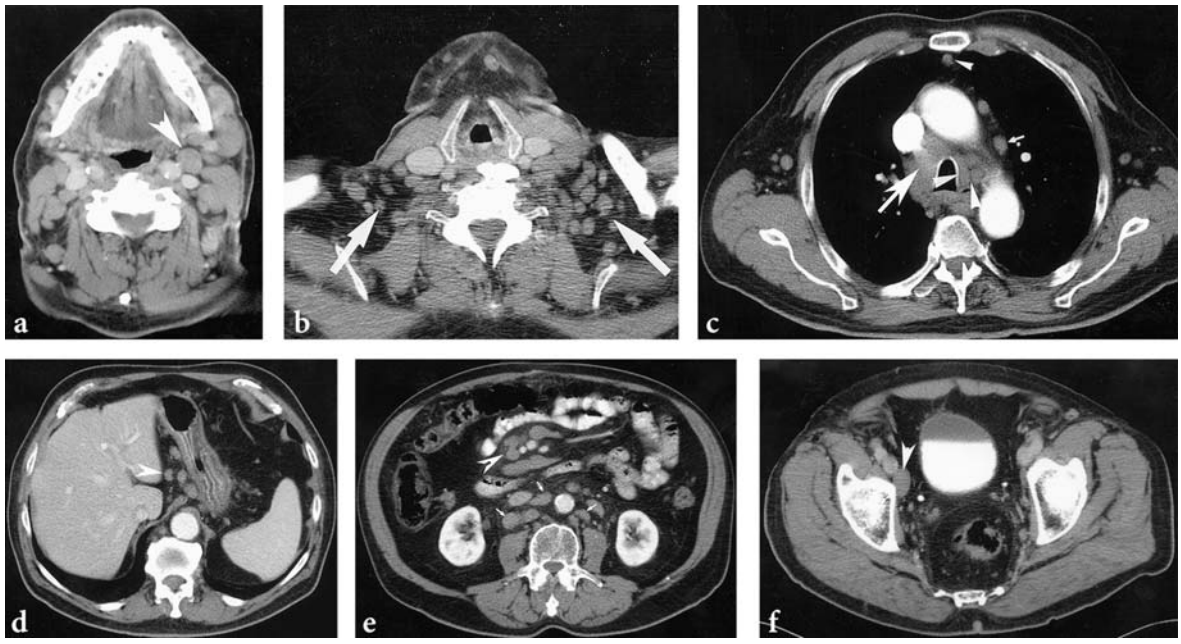

Fig. 2. The ability of spiral CT to depict accurately lymph nodes in almost all areas of the body: examples of lymph nodes within the neck, the chest and the abdomen. **(a)** Axial contrast-enhanced MSCT view at upper neck level in a 73-year-old man with a lymphoma. The following parameters were used: FOV: 250 mm; slice thickness: 3.2 mm; table speed: 16.7 mm/s; kV: 120; mA s: 214; matrix: 512 × 512. Bilateral homogeneous lymph nodes are visible, mainly in zone II (*arrow*). **(b)** Axial CT view at lower neck level shows numerous small lymph nodes in zone V (*arrows*). **(c)** Axial contrast-enhanced MSCT view at lower tracheal level using the following parameters: FOV: 430 mm; slice thickness: 5 mm; table speed: 17.5 mm/s; kV: 120; mA s: 149; matrix: 512 × 512. A homogeneous lymph node of 12 mm in the short axis is depicted on station nr 4 R (*arrow*). Small lymph nodes are visible on station nr 4 L (*arrowhead*), 5 (*short arrow*), 6 (*small arrowhead*) and in both axillae. **(d)** Axial contrast-enhanced MSCT view obtained at upper abdominal level using the following parameters: FOV: 430 mm; slice thickness: 5 mm; table speed: 16.7 mm/s; kV: 120; m As: 214; matrix: 512 × 512. Small sub-centimeter lymph nodes are seen in the left gastric artery area (*arrowhead*). **(e)** Axial CT image at mid-abdomen level showing numerous lymph nodes located in the mesenterium (*arrowhead*) and in the retroperitoneal spaces (*short arrows*). **(f)** A lymph node measuring 15 mm in the short axis was present in the right external iliac vein area (*arrowhead*)

lymph nodes vary according to their different locations in the body, and therefore different criteria must be used for each location to characterize nodes as benign, normal sized or abnormally enlarged.

In the *head and neck*, any combination of shape and minimum or maximum axial diameter seems to be a less valid indicator than minimum axial diameter alone [36]. Cervical lymph nodes with a diameter greater than 10 mm in the short axis should be considered as abnormal. The dimension in the axial plane should not exceed 11 mm in the jugulodigastric subanatomy and 10 mm in the other locations [22, 36, 37]. In a recent study, CT was reported to perform slightly better than MRI in the detection of squamous cell carcinoma (SCC) nodal metastases in neck nodes on the basis of the size of the nodes and the presence of central necrosis [6]. With the use of a 1-cm cut-off size or the presence of an internal abnormality to indicate a positive node, CT had a negative predictive value of 84% and a positive predictive value of 50%.

On *chest* CT, a short-axis nodal diameter exceeding 1 cm is considered abnormal, except in the subcarinal space [16]. The diameter of the node usually parallels its likelihood of harboring active disease. For example, in patients with bronchogenic carcinoma, the likelihood of mediastinal node involvement is directly proportional to nodal size. In a prospective study including 143 patients with bronchogenic carcinoma, the sensitivity of CT in detecting a malignant lymph node on a per patient basis was 64%, with a specificity of 62% [38]. In this study a lymph node measuring 1–1.9 cm and 2–2.9 cm was found to be malignant in 25% and 62% of cases, respectively.

On *abdominal* CT scans, reports on the upper limits of normal node size vary from 6 to 20 mm, also depending on their location. Some authors have found that a short-axis nodal diameter exceeding 6 mm in the retrocrural space, 8 mm in the paracardiac and gastrohepatic ligament areas, 10 mm in the porta hepatis, 9 mm in the upper paraaortic region, and 11 mm in the lower paraaortic area is indicative of abnormality, particularly if multiple nodes are present [39].

It should be emphasized that the simple assessment of lymph node size is not in itself a sufficiently accurate method for determining whether nodes are normal or abnormal. During the early stages of various pathological processes, significant nodal involvement may be

present in the absence of macroscopic enlargement of the nodes. Other morphological criteria may help the radiologist to classify accurately the type of lymph nodes. It has also been reported that the nodal enhancement pattern may be helpful in differentiating benign from malignant nodes. On contrast-enhanced CT, until proven otherwise, a central zone of low attenuation within the node reveals the presence of tumoral cells and/or necrosis, regardless of nodal size [17, 40] (Figs. 1,3a). The presence of extranodal tumor extension is depicted on contrast-enhanced CT as an irregular and usually thick enhanced rim infiltrating the adjacent fatty planes (Fig. 3b). The presence of nodal calcification is indicative of disease, which may be at an active stage or not. Nodal calcification is common in many non-malignant conditions such as sarcoidosis, tuberculosis, histoplasmosis, coccidioidomycosis and other infectious diseases [17]. Inflammatory diseases such as rheumatoid arthritis, scleroderma and amyloidosis may also result in nodal calcium deposits. Pneumoconiosis used to be the most common cause of benign lymph node calcification in previous decades. Nodal calcifications are also present in neoplastic conditions such as Hodgkin's lymphoma, treated metastatic nodes arising from primary prostate carcinoma, testis, colon, thyroid primary neoplasms, and neuroblastoma [41–43]. Calcifications may appear in the metastatic nodes before any therapeutic intervention takes place, i.e., in patients with malignancies originating from primary lung, testicular, breast, colonic, ovarian neoplasms, and head and neck SCC [42].

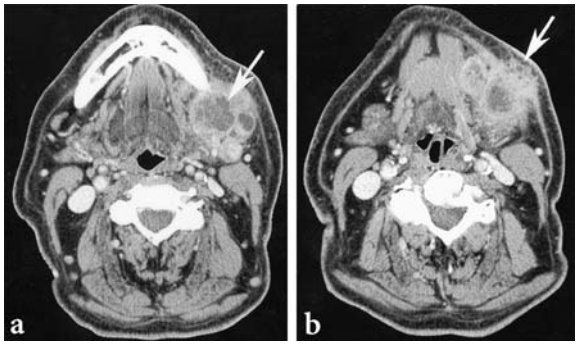

Fig. 3. Central necrosis and extracapsular spread of tumoral nodes on CT images. **(a)** Contrast-enhanced axial CT section at sub-mandibular level in a 75-year-old man with oropharyngeal carcinoma. The examination was performed using the following parameters: FOV: 230 mm; slice thickness: 2 mm; table speed: 6.7 mm/s; kV: 120; mA s: 150; matrix: 512 × 512. A large nodular mass consistent with clustered lymph nodes is well depicted on the left side, at level I. The central area of the mass shows low attenuation (*arrow*), indicative of necrosis. **(b)** Contrast-enhanced axial CT section obtained 2 cm below the level of the previous view (**a**) using the same parameters. The margins of the lymph nodes show an irregular, thick enhanced rim which infiltrates the adjacent fatty tissue. This findings reflects macroscopic extracapsular tumoral spread

1.3 Magnetic Resonance Imaging

1.3.1 Hardware/Software Requirements for High-Quality MRI

Strength of the Basic Magnetic Field

In an MR system the strength of the basic magnetic field is expressed in Tesla (T), with 1 T being equivalent to 10^4 Gauss. The higher the magnetic field, the higher the signal-to-noise ratio (SNR) of the images ("higher, faster, stronger"). 1.5-T systems are currently standard for "high-field" MR scanners, although others use "intermediate" to "low" fields at 1, 0.5, or even 0.2 T. "Ultra-high" whole-body 3-T systems are now entering clinical practice. Higher SNR can be of value in four ways when examining patients with neoplastic disease:

A reduction in examination time for patients who are intolerant to the MRI procedure: images of diagnostic quality can more easily be obtained within shortened acquisition times when using higher-field systems.

An increase in spatial resolution of the images either by increasing the matrix size or decreasing the slice thickness, or incorporating both for a similar acquisition time, with only one restriction to time-saving: the need to increase the number of slices when decreasing the slice thickness to cover a similar volume.

An increase in temporal resolution of serial images after intravenous bolus injection of paramagnetic contrast agent: analysis of the temporal pattern of contrast enhancement has been applied to nodal imaging with promising results [44]. In this respect, higher-field systems allow repeated acquisitions within shortened time periods, resulting in an improved analysis of the enhancement profile.

Motion artifacts "*freezing*" is a critical measure when examining severely ill patients who are unable to remain immobile and/or refrain from swallowing for a few minutes while under examination. The higher the strength of the basic field, the better the quality of the image obtained with ultra-short acquisition times: about 150 ms/slice in echo-planar imaging (EPI) and 6–7 s/slice by gradient-recalled echo (GRE) technique using start-of the-art systems. However, the fastest sequences are also the most sensitive to many artifacts (e.g., field inhomogeneity, magnetic susceptibility, chemical shift, motion). Freezing may therefore be obtained at the expense of clarity, and critical image degradation may occur when examining small structures such as the lymph nodes. Physiological motion, e.g., that of the heart and lungs or the bowels, are other aspects of the same issue, and can be partially managed by pharmacological means or by breath-holding for short acquisition periods, by cardiac gating, or by respiratory triggering. Finally, motion freezing is more effectively achieved by ultra-short spiral CT acquisition

than by MRI, which still suffers from significant limitations in speed/quality correlation, in spite of recent technological advances.

Significant material drawbacks paralleling an increase in field strength limit recourse to increasingly higher strengths, i.e.:

- An increase in all hardware and software constraints and requirements
- An increase in all artifacts (e.g., motion, magnetic susceptibility, chemical shift)
- An increase in the T1 relaxation time in all tissues, which results in slightly degraded fatty tissue contrast on T1-weighted images

A level of 1.5 T has become the standard value in oncological imaging, an excellent trade-off between the pros and cons of field strength increase. For several months the major manufacturers of MR systems have been advocating the use of their new 3-T whole-body system and have indicated that it could well replace older systems, but this new technology needs to be fully evaluated.

Magnetic Field Gradients

Magnetic field gradients are additional magnet coils which are repeatedly switched during data acquisition to generate spatial encoding of the magnetic resonance signal. Major improvements in gradient technology, i.e., strength (nowadays up to 60 mT/m) and technical performance (e.g., decreased rise times, active shielding, non-resonant properties) have led to a marked improvement in image quality, both as regards spatial resolution and acquisition speed at all fields.

Anatomically Adapted Coils

Since the intensity of the MR signal decreases with the square of the distance between the explored (or "emitting") area and the receiving device (or "coil"), the design of receiving coils has been adapted as closely as possible to the anatomy of the investigated areas. Additional refinements in coil technology (e.g., preamplification, quadrature design, phased-array multiple components) have led to improved signal reception and processing. All MRI manufacturers currently propose a wide variety of anatomically adapted coils. The use of a specifically designed neck phased-array coil and a thoraco-abdominal phased array multi-coil system is currently advocated for lymph node imaging, instead of the outdated "body-coil" included in the system.

Access to Off-line Workstations

Image data acquisition, image reconstruction and image post-processing – serial steps in the MR procedure – can be performed at different times and locations. The imaging system usually acquires raw data and performs standard image reconstruction online to allow real-time optimized management of the current examination. The transfer of images (or even the raw data) to an independent workstation should then be made to avoid time-wasting interference with the ongoing examinations on the clinical imager. Powerful workstations are required to perform complex image processing, e.g., 3D/multiplanar reformation, segmentation, parametric quantitative analysis, or image fusion to other imaging modalities such as CT, PET and others.

The Fast Spin Echo Technique

The fast spin echo (FSE) technique, based on the rapid acquisition with relaxation enhancement (RARE) approach defined by Jürgen Hennig in 1986, made a major contribution to the clinical application of MRI in the early 1990s, not only because of increased acquisition speed and subsequent time-saving, but also because of the specific characteristics of the technique which allow a significant reduction of many artifacts [45]. This became the standard technique in T2-weighted imaging of the cervical nodal regions shortly after its introduction in clinical practice [46–48]. FSE is currently included in all clinical imagers at all field strengths and has replaced conventional spin echo (CSE) in the investigation of almost all parts of the body, including the nodal areas.

1.3.2 Basic Tissue Contrast on MR Images

Introduction

The tissue signal intensities on MR images reflect their differences in physico-chemical composition and magnetic properties. A vast number of intrinsic (tissue) and extrinsic (e.g., magnetic field properties, pulse sequence data, etc.) parameters influence MRI rendering of tissue contrast. The main parameters, however, are the density of hydrogen nuclei (protons) and the relative proportion of the latter with free-water properties (a long longitudinal "T1" relaxation time and a long transversal "T2" relaxation time), or bound properties (short T1 and T2 relaxation times) such as the fatty tissue protons [49]. As water and fat are the main components of the body and contain a large number of hydrogen nuclei, it can be said that MRI is the hydrogen nucleus ("proton") imaging of these major components. The pulse sequence parameters may be optimized to express either the short T1 relaxation times of the bound protons as a high signal intensity ("T1-weighted" sequences), or the long T2 relaxation times of the free-water protons as a high signal intensity ("T2-weighted" sequences). T1- and T2-weightings provide the basic contrasts in MR images. CSE, FSE, GRE, or EPI are only different technical modalities by which T1- and T2-weightings are obtained [50].

The Lymph Nodes on T1-weighted MR Images

The adipose tissue which contains a majority of bound protons appears very bright on T1-weighted images. In turn, tissues which contain a majority of free-water protons with longer T1 and T2 relaxation times display intermediate to low signal intensity. Normal pathological but non-necrotic nodes display this low/intermediate T1 signal intensity (Fig. 4a,c). As most of the nodes are embedded within a fatty environment, the spontaneous contrast between the nodes and the surrounding tissues is excellent. Although the delineation of the nodal contours is extremely clear on T1-weighted images, the low/intermediate signal intensity of normal nodes may be similar to that of numerous other normal (e.g., muscles) or abnormal tissues (e.g., metastatic or reactive inflammatory nodes). The only determinant feature is that necrotic-cystic nodes have a very low T1 signal intensity due to an increase in free-water proton content.

The Lymph Nodes on T2-weighted MR Images

The fatty tissue usually displays a lower signal intensity on T2-weighted than on T1-weighted images, but to a lesser degree when FSE is utilized which results in a significant residual T1-weighting responsible for high signal intensity of the fat despite overall T2-weighting of the image (Fig. 4b,d). The major difference between T1- and T2-weightings is that water-containing tissue displays a higher signal intensity in the latter which is proportional to the amount of free-water protons present. Tumoral tissues with a high degree of cellularity and a high nucleo-cytoplasmic ratio with a resulting low "cytoplasmic water" content but a high density of lipidic membrane interfaces display a low T2 signal intensity. Normal nodes usually display a low to intermediate T2 signal intensity. Tumoral nodes may exhibit a low to high signal intensity depending on the balance between cellular density (decrease in signal intensity) vs stromal inflammatory changes and necrosis (increase in signal intensity) (Fig. 5).

Standard Contrast Procedures

T1 Contrast-enhancement by Paramagnetic Contrast Agent Perfusion Paramagnetic contrast agents are in standard use for the routine MR examination of patients with neoplastic diseases. These agents consist of macromolecular chelates carrying a few gadolinium (Gd) atoms with a strong paramagnetic effect, resulting in a marked decrease in T1 and T2 relaxation times of the surrounding free-water and fat protons. Reducing the T1 relaxation time has a major impact on the T1-weighted images, as an increase in signal intensity is observed in the vascularized areas the permeative vasculature of which allows interstitial leakage of the contrast medium

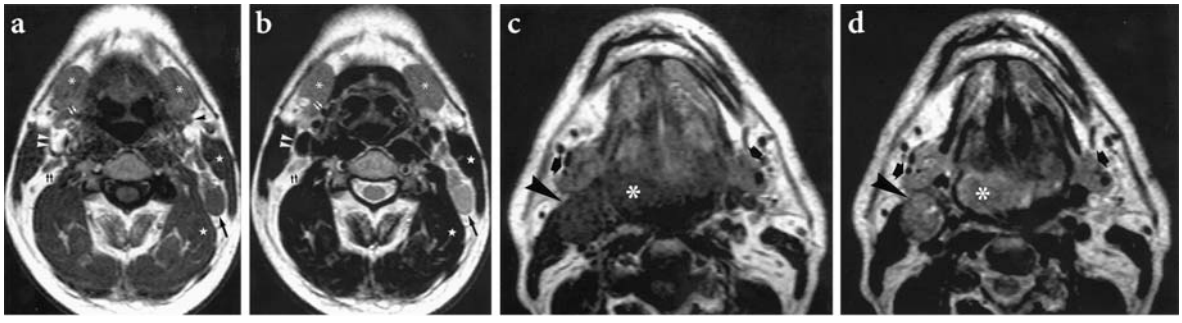

Fig. 4. The potential of unenhanced MRI to differentiate lymph nodes from muscles, vessels, and glands by comparing "native" (unenhanced) T1- and T2-weighted images. (a), (b) Posterior jugular node involv ement in a case of oropharyngeal SCC (the primary tumor is not seen on these views). (a) Precontrast CSE transverse T1-weighted image without FS at a threefold level displays tumoral lymph node involvement (*black arrow*) with a similar low signal intensity to muscles (*white stars*), some vessels (*thin black arrowhead*) and submandibular glands (*white notches*), contrasting well with the bright signal intensity of the surrounding fatty tissue. Vessels may display either low signal intensity due to the "flow void" phenomenon (*double thin white arrows*) or very bright signal intensity due to flow artifacts (*double white arrowheads*). Bright artifacts within the flow vessel lumen are increased when using the GRE technique, which has been advocated for differentiating nodes from vessels. (b) FSE transverse T2-weighted image without FS in a similar slice location to **Fig. 1a** clearly differentiates the different structures, with an intermediate signal intensity shown by the tumoral node, and a very low signal intensity of the muscles and all the vessels due to the flow-void phenomenon. Fatty tissue remains very bright on these T2-weighted images obtained via the FSE technique without FS, due to the "shine-through" effect of residual T1-weighting. An almost isosignal intensity between the enlarged node (*black arrow*) and normal sized contralateral nodes (*thin black double arrows*) on both weightings may be observed. (c), (d) SCC of the base of the tongue with jugular lymph node involvement. (c) Precontrast CSE transverse T1-weighted image without FS through the level of the primary tumor (*white notch*) and that of a homolateral jugular lymphadenopathy (*black arrowhead*). Both sites display a similar low signal intensity. In turn, the submandibular glands exhibits slightly higher signal intensity due to physiological fatty infiltration in this elderly patient (*black arrows*). (d) FSE T2-weighted transverse image without FS in a similar slice location: all three structures display a similar intermediate signal intensity. Contrary to the previous case, the T2-weighting seems more "confusing" as all three structures exhibit a similar signal intensity, but the comparison of both weightings allows an accurate identification of the nodes

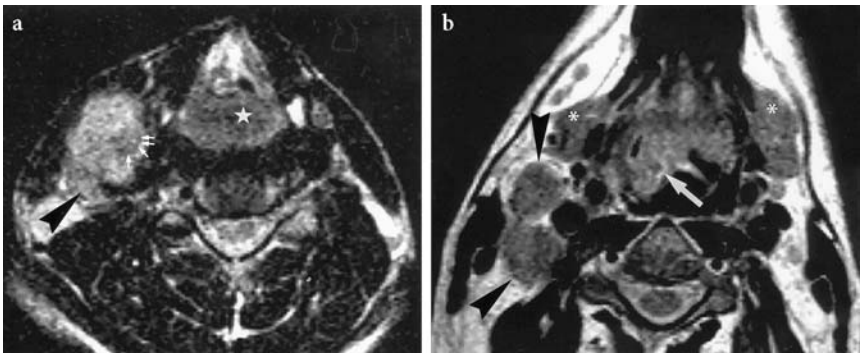

Fig. 5. Variability in the pretreatment T2 signal intensity of the primary neoplasm and the metastatic nodes. (a) FSE T2-weighted transverse image without FS in a case of posterior laryngeal SCC where the primary tumor (*white star*) displays a lower signal intensity than the metastatic homolateral jugular nodes (*black arrowhead*); however, sub-areas of lower signal intensity are present within the nodes (*thin white arrows*). Low SNR due to the use of a head coil to explore the neck results in the "noisy" appearance of this image (obtained seven years ago). Currently available specifically adapted neck coils ensure routine optimized image quality. (b) FSE T2-weighted transverse image without FS in a case of SCC of the base of the tongue (*white arrow*) where the primary tumor displays a slightly higher signal than the metastatic jugular nodes (*black arrowheads*). As in **Fig. 1d**, the isointensity between node metastases and submandibular glands (*white notches*) may be confusing

molecules. However, contrast enhancement suffers from certain limitations and drawbacks:

- Contrast enhancement highlights the lesional vasculature and permeable properties of the vessel walls, but this feature is non-specific with respect to the inflammatory or tumoral nature of the lesion.
- If the lesion is embedded within the fatty tissue – as in the vast majority of lymph nodes – the contrast between the lesion and the surrounding adipose tissue decreases on post-contrast T1-weighted images, since white on white provides a lower contrast than gray on white. This drawback may be overcome by using the fat saturation (or fat suppression) option – designated by the acronym "FS" – which decreases the brightness of the fat on MRI without decreasing that due to contrast enhancement (see below).

Paramagnetic agents reduce the T1 and the T2 relaxation times of the surrounding protons. The reduction in T2 relaxation time only has a theoretical impact on the image, since the decrease in signal intensity due to T2 reduction is not visible to the human eye on T2-weighted images with a standard window setting, and the pre- and post-contrast T2-weighted images therefore look similar. Our approach, like that of many others, is as follows: we first acquire the pre-contrast T1-weighted images, perfuse the paramagnetic contrast agent (always at a standard dose of 0.1 mM Gd/kg), then immediately after perfusion acquire the T2-weighted images which are unaffected by the contrast agent. As sufficient time for T2-weighted image acquisition has elapsed, high-quality T1-weighted post-contrast images are obtained with adequate contrast diffusion and deposition within the tissues due to a sufficient time lapse between perfusion and image acquisition. If additional T1-weighted sequences are acquired later, the interpretation of these images must take into account the time lapse between contrast agent perfusion and image acquisition, as contrast enhancement characteristics evolve over time.

Suppression of Fat Signal Intensity The high signal intensity of fatty tissue both on T1-weighted and on FSE T2-weighted images may hinder the detection of small enhanced foci (on T1-weighted images), or small amounts of abnormally hydrated tissue (on T2-weighted images) within the fat. By decreasing the "flashy" brightness of the adipose tissue, the detection of small structures embedded within it can be improved. In the early 1990s, FS prepulses with a specific frequency-selective spectral saturation of the fatty protons were introduced in clinical imagers, and could be combined with all kinds of sequences independently of the weighting (T1/T2) or the technique used (CSE, FSE, GRE, EPI). These procedures have rapidly replaced the short tau inversion recovery (STIR) sequence aimed at suppressing fat signal intensity. However, the significant drawbacks of the FS prepulses must be considered:

- FS prepulse application requires time within the time of repetition (TR) of pulse sequence data. Therefore prolonged TRs are necessary, few of which have an impact on long TR sequences (such as T2-weighted sequences), but which nevertheless have a marked effect on short TR sequences (such as the T1-weighted sequences) both as regards the decreased number of slices obtainable within a defined TR or the need to increase the latter so that the number of slices remains unchanged, thereby prolonging the acquisition times and modifying the T1-weighting characteristics of the sequence.
- FS may be heterogeneous throughout the image, to a higher degree if large FOVs are used which include a number of air/bone/soft tissue interfaces and structures of different shape/size (e.g., the neck vs the shoulder).

- Theoretically the comparison between pre- and post-contrast T1-weighted images should be made between strictly similar images except for contrast agent perfusion, which means that a comparison should be made between pre- and post-contrast T1-weighted FS images. As "native" unenhanced pre-contrast T1-weighted images without fat saturation seem mandatory, fat saturated pre-contrast images should be obtained in addition to "normal" T1-weighted images, resulting in a significant increase in examination time.

In our experience, the FS option is invariably activated for the T2-weighted sequences (exclusively using the FSE technique). Pre- and post-contrast T1-weighted images are obtained in the reference plane (usually transverse) without FS. If a specific question remains unanswered regarding these "standard" post-contrast images which could be addressed by using FS, then an additional FS sequence – similar to the unsuppressed pre- and post-contrast sequences – is obtained in the reference plane. In the second (usually coronal) or even third (usually sagittal) "extra" planes (in addition to the reference plane), only FS post-contrast T1-weighted images are acquired.

1.3.3 Clinical Trade-offs in MR Nodal Imaging

Nodal Imaging as Ancillary to Primary Tumor Staging

Magnetic resonance nodal status is frequently interpreted as an "extra" item of information displayed on images which are aimed at the optimal depiction of the primary tumor. This means that node depiction may be limited to fewer incidences and/or weightings than the primary neoplasm, since optimized tumoral investigation requires specifically adapted and centered sequences (e.g., thin slices, limited FOVs). The complete set of pre- and post-contrast T1-weighted and T2-weighted images is thus rarely available for all nodal areas. At our institution, we include an additional large FOV coronal sequence at the end of the examination if all nodal areas have not been covered by the initial primary-targeted sequences. Post-contrast T1-weighting is the method of choice for this ultimate "nodal" sequence (Fig. 6c), but coronal large FOV pre-contrast T1-weighted images obtained at the beginning of the examination could constitute a viable alternative to this approach.

Reduction of Acquisition Times

Reducing the duration of the MR sequences leads to a reduction in patient discomfort and in a decreased risk of motion artifacts. However, reduced acquisition times may result in critical image degradation. In turn, long acquisition times may result either in unnecessary pictorial quality of the images or in insufficient quality due to motion artifacts introduced by patients who are unable to keep still, refrain from swallowing, or hold their breath. Finding the optimal trade-off between time and diagnostic relevance is the most commonly encountered challenge in MRI clinical practice, and is a crucial factor in examining oncology patients.

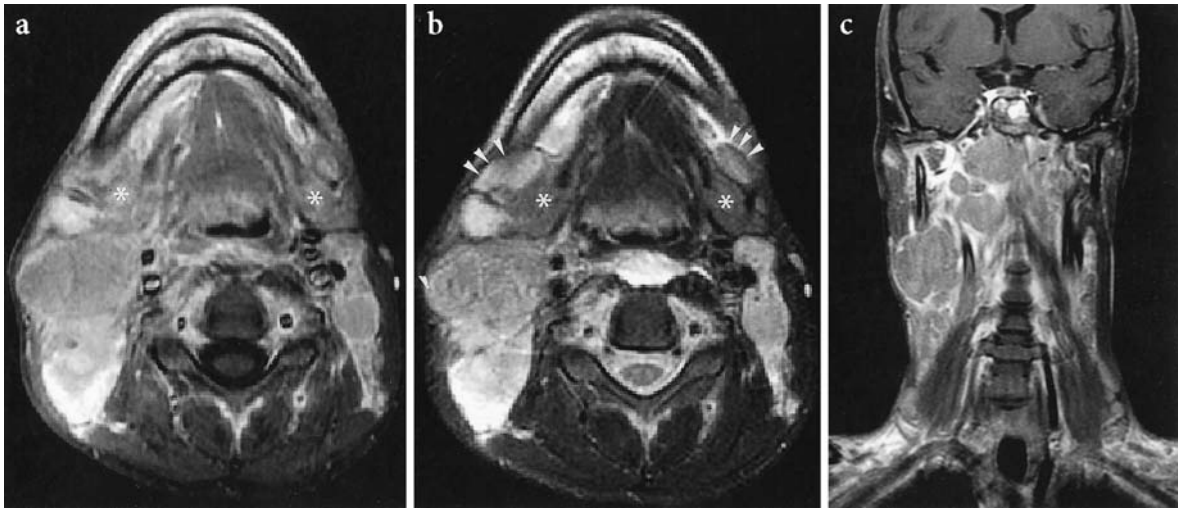

Fig. 6. The fat suppression option: undifferentiated carcinoma of the rhinopharynx with diffuse nodal involvement. (a) Post-contrast CSE T1-weighted transverse image with FS: the suppression of the fat signal results in good delineation of enhanced nodal masses and inflammatory/infiltrative environment (i.e., in the right spinal area) (b) FSE T2-weighted transverse image with FS in a similar slice location to Fig. **5a:** lymph node contours appear more accurately delineated (*white arrowheads*), and the differentiation between nodes and salivary glands (*notches*) seems better than on the previous image even though a global similarity between both is obvious, except for the discriminating signal intensity of the cerebrospinal fluid (CSF) surrounding the spinal cord. (c) Post-contrast CSE T1-weighted coronal image with FS: adenomegalies are well delineated and surrounded by highly enhanced areas. The high-quality image has been obtained using an up-to-date specifically adapted phased-array neck coil

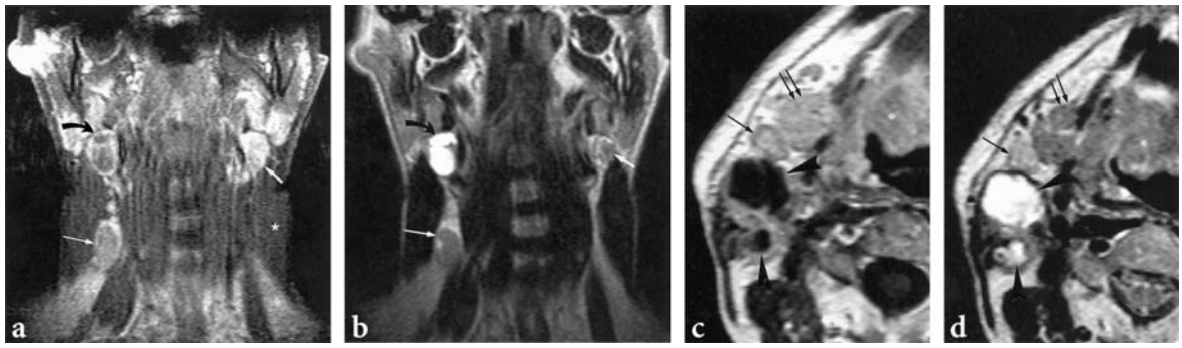

Fig. 7. Central necrosis of metastatic lymph nodes. **(a)**, **(b)** Bilateral nodal metastases of oropharyngeal SCC. **(a)** Post-contrast CSE T1-weighted coronal image with FS shows three different metastatic nodal patterns: (1) an area of low signal intensity surrounded by an intensely contrast-enhanced rim (*black curved arrow*); (2) an area of intermediate signal intensity with a bright rim (*thin white arrow*); (3) an area of intermediate signal intensity partially "obscured" by an intensely "flashing" rim (*thick white arrow*). Fat is well suppressed at the level of the *white star*, but less satisfactorily so at the level of the *white notch*. **(b)** FSE T2-weighted coronal image without FS in a strictly similar slice location to Fig. **3a** clearly reveals central necrosis as a very bright cystic area within the node displaying the lowest T1 signal intensity (*black curved arrow*), whereas the other nodes are not necrotic-cystic. **(c)**, **(d)** Close-ups of metastatic jugular nodes of an infiltrating SCC of the right vallecula (*white notch*). **(c)** Post-contrast CSE transverse T1-weighted image without FS. Necrotic areas within the nodes display very low signal intensity (*arrowheads*). A non-necrotic lymph node (*arrow*) and submandibular gland (*double arrows*) exhibit similar signal intensity. **(d)** FSE T2-weighted transverse image without FS in a similar slice location to that in Fig. **3c** shows very bright signal intensity of the nodal necrotic-cystic areas. Signal intensities of the non-necrotic node and the submandibular gland are significantly different

MR Nodal Staging with or Without Contrast Agent Perfusion?

The comparison of T1- and T2-weighted images in the same plane provides relevant information on tissue characteristics (Figs. 4,5). The "basic" unenhanced images allow a clear delineation of the nodes and their differentiation from other structures such as vessels and muscles, thereby avoiding the need for contrast agent perfusion even for head and neck imaging. However, improved MRI performance in nodal examination when paramagnetic contrast agents are used has repeatedly been reported [37, 51, 52]. Post-contrast images of the nodal areas are frequently available, since accuracy in the delineation of the primary tumor requires contrast agent perfusion. However, information on the high or low degree of vascularization per se does not result in significantly increased specificity regarding the normal, inflammatory or neoplastic nature of the nodes. The true advantage of post-contrast T1-compared to T2-weighted images appears to lie in the depiction of non-cystic nodal necrosis. By interpreting only unenhanced images there is a risk that non-cystic nodal necrosis may remain undetected [53]. However, in our experience this seems to occur less frequently than cystic necrosis which is well depicted on T2-weighted images (Fig. 7).

3D Acquisition vs 3D Post-processing

Routine MR images are contiguous (or not) 2D slices. These images can be subsequently loaded in a 3D post-processing program which can reformat views in all planes. Acceptable image quality of the reformatted views may be obtained if the original slices were acquired without interslice gaps, and were not excessively thick when compared to the FOV and the matrix size, the main parameters of final voxel size. In cases of excessive voxel volume and/or a discrepancy between the three main parameters (thickness, FOV, matrix), the reformatted images exhibit the well-known "staircase" phenomenon. In true 3D mode, the area of interest is acquired as a volume and the raw data are processed using volumetric reconstruction algorithms which result in better multidirectional reformatting possibilities. However, 3D acquisition suffers from a major drawback, as it demands an excessive amount of time. The GRE technique introduced in the late 1980s has resulted in a significant increase in acquisition speed, thereby allowing 3D acquisition within an acceptable time frame. Up to now, the GRE technique still remains the method of choice for 3D volume imaging, albeit with an accompanying increase in artifacts connected with its use (e.g., motion and flow sensitivity, magnetic susceptibility) which limit image quality in heterogeneous regions such as the head and neck, where numerous interfaces are present between the bone, soft tissue and air. For large volume imaging, the time-saving GRE technique should be used. However, the unavoidable trade-offs involved in maintaining acquisition time within an acceptable range could affect optimal spatial resolution, which is too high a price to pay when analyzing structures as small as nodes. Therefore 3D MRI is only of limited interest for nodal imaging, except for co-registration purposes. Three-dimensional GRE imaging of brain or neck volumes requiring 10 min (or more) acquisition time were used during the initial period when we co-registered MR and PET data at our institution. At present, usual FSE 2D sequences utilizing

standard parameters (5 mm slice thickness, no interslice gap, matrix 256 × 512, FOV 24 × 24 cm) and requiring less than 3 min are co-registered with PET data with sufficient spatial resolution and anatomical depiction to identify structures with increased amounts of glucose uptake.

1.3.4 In the Research Field

Lymphophilic Experimental MR Contrast Agents

MR contrast agents with preferential uptake within the reticular tissues are currently under investigation. MR "lymphography" involves the use either of "negative" contrast agents (dark areas on T2-weighted images), or "positive" contrast agents (bright areas on T1-weighted images) for the normal nodes which take up the contrast agent. The most frequently investigated negative contrast agent introduced in clinical practice contains dextran-coated ultra-small super-paramagnetic iron oxide (USPIO) particles, and has shown promising early results, i.e., increased sensitivity and specificity in nodal metastases detection [54–56, 150–153]. Gadofluorine 8, tyrosine-GDTA, and perfluorinated Ga chelates are positive contrast agents that have been experimentally evaluated in animal models, again with promising early results [57–59]. However, whether the crucial goal of detecting small metastatic deposits within unenlarged nodes could be truly addressed by this technique is uncertain as long as MRI spatial resolution remains such a limiting factor.

In Vivo Measurements of Intrinsic Physical Properties of the Tissues

Different magneto-physical properties of the tissues can be determined using the MR technique. Multi-echo sequences allow precise measurements in milliseconds of the *T1 and T2 relaxation times* [60]. Adequate comparative measurements and mathematical treatment of the voxel signal intensities with and without application of an off-resonance prepulse saturating the restricted water proton pool included into water molecules closely surrounding macromolecules allow the calculation of the *magnetization transfer ratio* (MTR) [61]. The *apparent diffusion coefficient* (ADC) which can be calculated after the application of diffusion-sensitizing gradients in the so-called "diffusion-weighted" (DW) sequences reflects the restriction of free-water molecular movement [62]. Attempts have been made to measure the relaxation times [60, 63] and the MTR [64], and the ADC [154] within the nodes. The time parameters may have a low impact on differentiating tumoral from non-tumoral nodes since a wide overlap between normal, reactive and tumor categories has been observed. MTR measurements within the nodes have demonstrated a better performance, with statistically significant differences in mean MTR between malignant and benign adenopathies [65, 66]. However, these studies suffered from certain weaknesses such as the absence of comparison between MTR values and size criteria in the same nodes, or the presence of a wide standard deviation in MTR values within malignant nodes due to the inclusion of necrotic-cystic nodes. However, the accuracy of statistically significant thresholds issued from large normative databases suffers from limited power in individual cases due sensitivities and specificities of less than 100%. Moreover, the limited spatial resolution of MRI techniques does not enable accurate analysis or biophysical measurements to be made within very small volumes, which restricts the applicability of this method to only a limited number of nodal areas. However most promising results in the purpose of differentiating benign from malignant enlarged nodes have been obtained by measuring the ADC [154].

Perfusion-weighted Imaging

Perfusional parameters may be obtained using different MRI techniques such as the dynamic contrast-enhanced (DCE) imaging using the bolus tracking T2* susceptibility effect imaging or such as the arterial spin labeling (ASL) technique [67]. Again, the node size may restrict the applicability of this technique to a limited number of nodal areas. Recently published papers have highlighted the potential value of nodal perfusion imaging in the purpose of detecting metastatic disease within nodes [155–158].

1.3.5 Neoplastic Lymph Nodes: Specific MR Targets

Introduction

Detecting malignant lymph nodes still remains a major challenge due to two inherent limitations present in all morphological imaging techniques: (a) the failure to detect small metastatic deposits within macroscopically unenlarged nodes; and (b) the inability to differentiate between inflammatory nodal response and tumor invasion within enlarged nodes. Improved criteria for the semiological evaluation of nodal images have been developed which, however, remain limited to probabilities without giving a 100% confidence level [6]. Critical evaluation of the nodal images must be made by including the normal range of size and number for each location to reach the best confidence level in lymph node status interpretation [68]. Basic concepts regarding nodal size, shape, site, number, fatty core and central necrosis are applicable to both MRI and CT with minor differences between the two techniques, such as the unsurpassed ability of CT in detecting calcium deposits

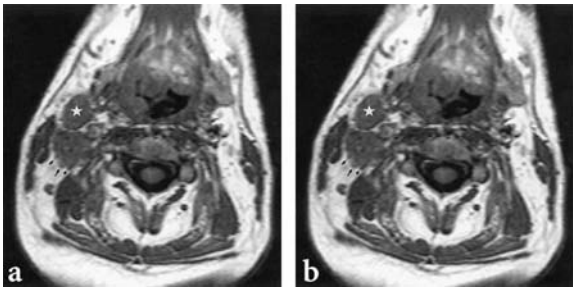

Fig. 8. Suspected extracapsular tumoral spread. Contiguous pre-contrast CSE T1-weighted transverse images without FS in a case of SCC of the base of the tongue and the right vallecula. (a) Lower slice: two enlarged tumoral nodes are present in the homolateral jugular area. The anterior node (*white star*) has smooth contours, suggesting the absence of extranodal spread. The posterior node exhibits suspicious irregularities in its posterior aspect (*thin black arrows*). (b) Contiguous slice in upper location: pseudopodal tumoral extrusion (*arrowhead*) reinforces the suspicion for extranodal tumoral spread

within (or outside) nodes. The specific features of the MR technique have been described below.

Extracapsular Tumoral Spread

The irregular margins of an enlarged node suggest tumoral spread beyond the nodal capsule. It has generally been considered that CT is more accurate in depicting extracapsular spread [40, 51]. In our experience, however, we have found that MRI performs well in this respect (Fig. 8) although experienced investigators have stated that preoperative imaging techniques may only detect the presence of major macroscopic extranodal spread. As even pathologists do not always agree on the presence of microscopic nodal spread, the radiological assessment of extracapsular spread should be considered as being unreliable, even when using MRI [53].

Contrast Enhancement

All nodes become enhanced after perfusion of paramagnetic contrast medium. Tumoral nodes may become enhanced to a different degree which is not predictive of the histological content of the involved nodes. By whitening the nodes, the administration of contrast agent decreases the spontaneous contrast between the nodes and the fatty environment. The FS option must therefore be used, with the subsequent drawbacks of time loss and increase in artifacts. Moreover, post-contrast T1-weighted and T2-weighted information is often redundant, except in the specific case of non-cystic necrosis within the nodes which remains undetected or is only poorly detected on T2 images [53]. The incidence of this condition seems low in our clinical experience. Whether paramagnetic contrast agent perfusion is an absolute requirement in a "pure" nodal MR setting is open to question. In routine practice the issue does not arise, since MR examination addresses both aims of primary and nodal staging.

Post-treatment Nodal Status

Increased accuracy in the assessment of post-treatment nodal status is obtained when strictly similar images are compared, both as regards weightings and slice locations (Fig. 9). In our clinical approach, the pretreatment examination is always reviewed before planning the follow-up to ensure optimal reproducibility between examination protocols. Adequate timing of the first "baseline" post-treatment examination is a controversial issue, with the contradictory demands of detecting tumor residue/relapse as soon as possible, and waiting for the resolution of disturbing inflammatory post-treatment reactions. However, there seems to be a general consensus that a delay of three to four months after completion of radiation therapy (RT) is optimal to perform control imaging [53]. The main observations on post-therapeutic examination have been listed below:

- *Complete disappearance:* in Fig. 9, enlarged nodes suspected of harboring macrometastases on the basis of pretreatment images are no longer detectable.
- *Normalized appearance:* enlarged nodes exhibit a normalized size. They usually appear to be intensely vascularized, possibly indicative of inflammatory changes (not illustrated).
- *Evolution to shrunk fibrous scar:* the nodes appear to be shrunk, hypovascularized on post-contrast T1-weighted images and hypointense on T2-weighted images. which is considered to reflect fibrotic evolution. This pattern usually takes more time than the standard three to four months delay after treatment completion (Fig. 10).

Nodal Relapse

Neither CT nor MRI have performed well in the early detection of recurrent/residual disease due to confusing post-therapeutic inflammatory changes in the treated areas. The results of meticulous attempts at the early detection of nodal relapse have been frustrating [69, 70]. However, recent studies have demonstrated the impact of the PET technique in determining disease-free post-treatment status in patients with head and neck neoplasms [71].

1.4 Positron Emission Tomography Imaging

1.4.1 Physical Principles of PET Imaging

Positrons are electron anti-particles. A positron is produced during the decay of a nuclide having an excess

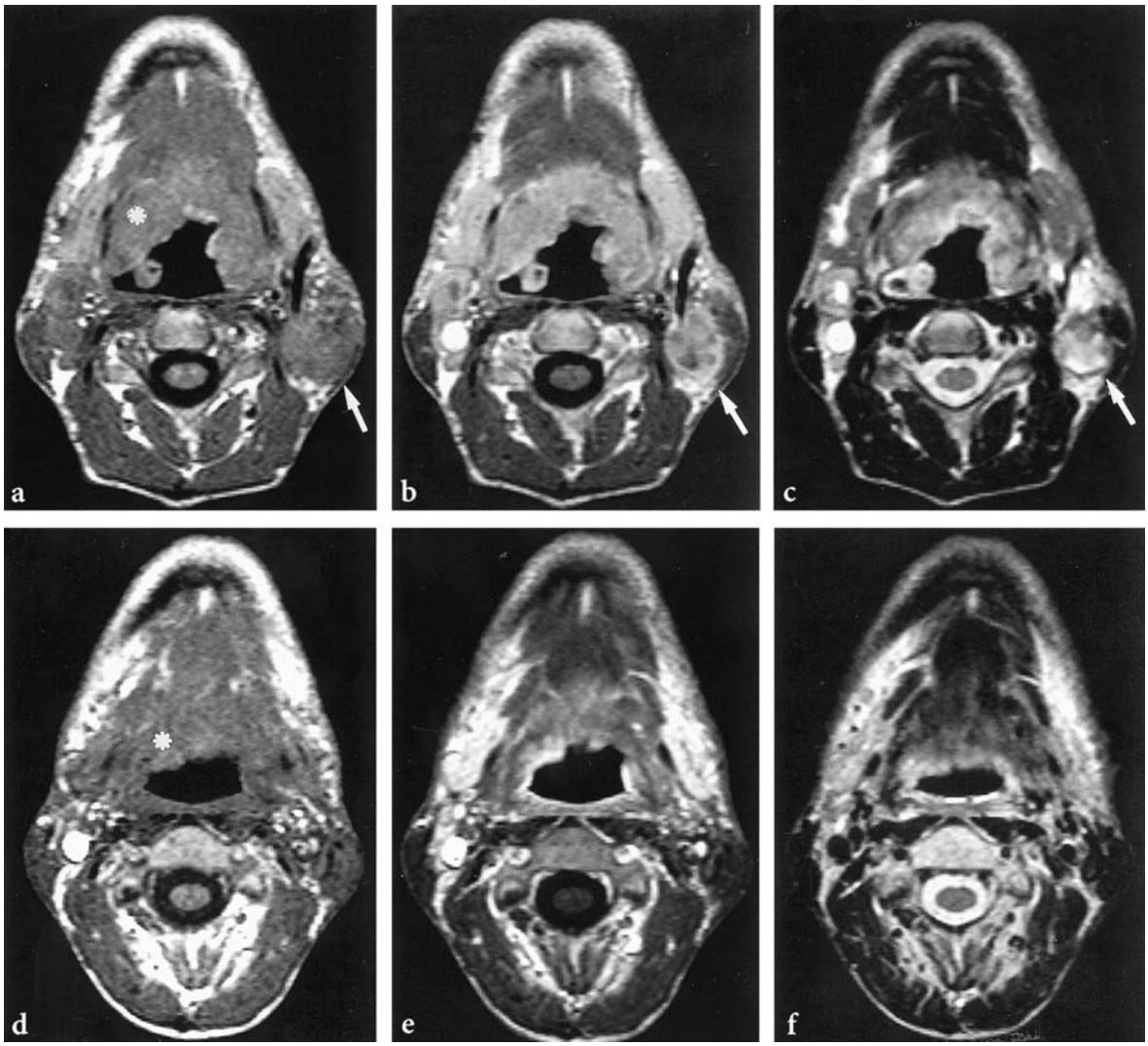

Fig. 9. Comprehensive MR setting of pre- and post-treatment status. All slice locations are similar in all weightings in both studies to ensure accurate intra- and inter-examination comparison. **(a)**-**(c)** *Upper row*: pre-contrast T1 **(a)**, post-contrast T1 **(b)**, and T2 **(c)**images prior to RT. **(d)**- **(f)** Similar views three months after completion of RT. Both the vallecular primary tumor (*white notches*) and the nodal metastases (*arrows*) completely disappeared after treatment. The availability of the three "colors" (pre- and post-contrast T1, and T2) in strictly similar plane and slice locations on the pre- and post-therapeutic examination allows confirmation of the complete disappearance of the lesions

of protons within the nucleus when compared to the number of neutrons. Positron emitters are obtained by bombarding nuclides with a cyclotron-generated proton beam. Like the electrons, the positrons may have different energy levels, ranging from 0 to a specific value. After emission, the positron is slowed down by interaction with the surrounding matter and ultimately hits an electron, which results in the "*annihilation*" reaction. This occurs after a short distance of a few millimeters, the precise length of which depends on the positron energy. For example, the average traveling distance of a positron is 0.35 mm for ^{18}F (maximum distance: 2.3 mm) and 1.1 mm for ^{15}O (maximum distance: 8.1 mm). The annihilation reaction results in the production of a pair of photons both energized at 511 keV. Positron emitters allow the labeling of biomolecules without modifications in their chemical and biological properties, e.g., ^{15}O, ^{11}C or ^{13}N can be used as direct substitutes for ^{16}O, ^{12}C or ^{14}N, and ^{18}F can replace ^{1}H. Another characteristic of positron emitters is their short physical half-life compared to other nuclides used in nuclear medicine imaging such as ^{99m}Tc or ^{201}Tl. Their half-lives range from 2 minutes for ^{15}O to 110 minutes for ^{18}F, which reduces their availability for PET systems not equipped with an on-site cyclotron.

The detection of radioactivity within the patient's body is carried out by scintillators which produce visible light when hit by an incident photon. Photons resulting

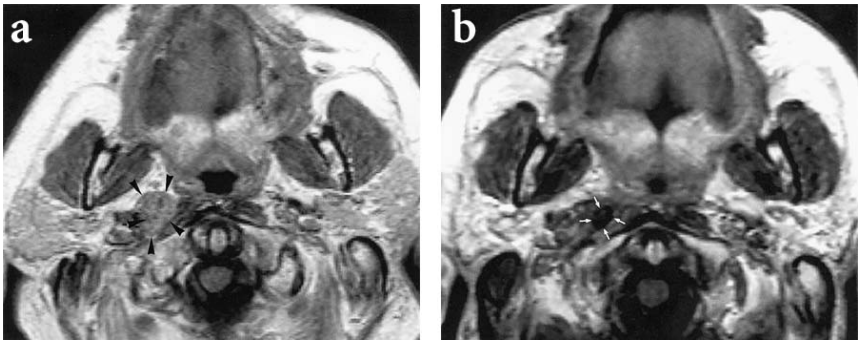

Fig. 10. Post-RT metastatic lymph node scarring. **(a)** Post-contrast CSE T1-weighted transverse image of the pre-RT MR examination: a right lateral-retropharyngeal lymph node metastasis can be clearly seen (*arrowheads*). **(b)** Post-contrast CSE T1-weighted transverse image in a similar slice location eight months after completion of RT: a residual nodule exhibits very low signal intensity without contrast enhancement (*arrows*), corresponding to fibrous scarring

from the annihilation reaction have two major characteristics: first a high energy level of 511 keV, which requires crystals with a high stopping power for detection. If the stopping power is too low, the probability of detecting a photon by interaction with the crystalline material will be lessened and the event may not be detected. Sodium iodide (NaI) is the most commonly used scintillation material in nuclear medicine, with a high photon yield at 40 scintillation photons/keV when compared to other materials such as bismuth germanium oxide (BGO) with 4.8 scintillation photons/keV. In spite of a lower photon yield, BGO is better suited for 511 keV photon detection because of its higher stopping power. PET detectors are typically made of BGO crystals 4 mm in cross-section and 20–30 mm in length, arranged in groups and connected to photomultiplier tubes. Blocks of detectors are arranged in rings, covering an axial FOV of 10–16 cm. The second major characteristic of the annihilation photons is that they are emitted in opposite directions, and therefore require a pair of crystals placed at an angle of 180° so they can be detected. A given pair of detectors selectively detects events occurring along a single line connecting them. The site of photon production (annihilation reaction) can be localized by analyzing multiple lines of response crossing each other at the production point. Only photons that hit the pair of detectors within a definite time frame are taken into account by the PET system (the "true" coincidences), and coincidental events occurring too late in time from one another are rejected. Both constraints of coincidental emission and time frame ensure the accurate spatial localization of the radioactivity within the body (electronic collimation), without the need for external collimators which would reduce the sensitivity of the system.

Up to 80% of the gamma radiation can be absorbed by the patient's body: the so-called "attenuation" phenomenon. In PET imaging, attenuation does not depend on the location in depth of the decay event, since event detection relies on a pair of photons traveling along a line. Attenuation can be quantified by measuring the absorption of the 511 keV photons produced by an external radiation source through each line of response. This is commonly obtained by rotating a ^{68}Ge external radiation source around the patient. Correction for attenuation allows the measurement of quantitative indexes, which are ancillary for diagnostic purposes but necessary for the assessment of the tumoral response to therapy.

1.4.2 Metabolic Imaging of Tumors

Tumoral cells undergo changes involving many metabolic pathways. A particular metabolic function within the cells can be measured in vivo by detecting specific radio-labeled molecules. A large number of metabolic characteristics of tumoral cells have been studied using radiotracers labeled with positron emitters: blood flow (with $H_2{}^{15}O$ as tracer), protein synthesis (with labeled amino acids such as ^{11}C-methionine or ^{11}C-tyrosine), DNA synthesis (with labeled DNA precursors such as ^{11}C thymidine) and glucose consumption (with labeled glucose analogs). Static (after a period of radiotracer incorporation) as well as dynamic (during radiotracer incorporation) images can be obtained, depending on which clinical issue has to be investigated. Functional imaging has become the necessary complement to anatomical imaging in a number of medical domains, especially in oncology where glucose metabolism imaging using 2-[^{18}F]-fluoro-2-deoxy-d-glucose (FDG) combined with PET has proven to be a powerful diagnostic and staging tool. Several changes in glucose metabolism are responsible for the increased accumulation of labeled glucose in tumoral cells [72]. The increase in lactate production within tumors is first evidenced by an increase in tumoral anaerobic glycolysis, as observed by Warburg in the 1930s [73]. The overexpression of glucose transporters on the cell membrane, mainly subtypes 1 and 3 [74–78], as well as their upregulation by hypoxia which is frequently observed in tumors [79] first account for increased glucose

uptake. Moreover, intracellular enzyme characteristics are altered: hexokinase, the first-step phosphorylating enzyme, is overexpressed in tumoral cells [80] and becomes less sensitive to downregulation. Glucose-6-phosphatase, the reverse enzyme of hexokinase, is underexpressed or absent in tumors [81], so that incoming glucose is rapidly phosphorylated and further metabolized. An increase in glucose uptake and consumption is observed in tumoral cells compared to adjacent cells. This metabolic phenomenon is related to cell multiplication and therefore is also present in non-neoplastic proliferative cells, e.g., inflammatory cells [82] such as macrophages or granulocytes. Malignant transformation leads to a permanent dysregulation of the rate of proliferation, which boosts the mechanisms of increased glucose uptake. FDG is the analog of choice for PET imaging since, contrary to native glucose which is rapidly metabolized into CO_2, deoxyglucose is trapped in its monophosphorylated form after the action of hexokinase. The next glycolytic enzyme, glucose-6-isomerase, does not recognize FDG as substrate. This leads to the accumulation of labeled deoxyglucose in the tumoral cell, with the result that tumoral foci are easily detected throughout the body (high tumor-to-background ratio) apart from the brain where the normal high cortical glucose uptake hampers the detection of tumoral lesions within the gray matter.

1.4.3 FDG-PET Acquisition Protocols in Oncology

Specifically adapted PET scanners are BGO-based systems (see above) with a resolution of 5 mm in the axial plane. Since they are expensive, alternative methods for FDG imaging have been developed using modified but standard gamma cameras with NaI crystals and electronic or external collimators, or incorporating specific electronics for the detection of coincidence photons. Such modified systems suffer from lower sensitivity for the detection of annihilation photons, and thus have a lower diagnostic capacity, especially for small lesions (< 1.5 cm) and/or abdominal foci [83–87]. Although the clinical usefulness of modified systems has been established in lung [88, 89] and in head and neck cancers [90], more studies are needed before the equivalence of modified and PET-specifically adapted systems for cancer detection and staging can be determined. This point is crucial for nodal staging, since the cut-off size of positive nodes is often close to or less than 1.5 cm.

Patient Preparation

Patients must have fasted for at least 6 h prior to examination to ensure that they are in a euglycemic state (no competition between labeled and native glucose) with normal insulin levels. This is of importance, since elevated insulin levels result in increased muscular and cardiac glucose uptake at the expense of tumoral uptake [91, 92]. For imaging cervical malignancies (head and neck SCCs, thyroid tumors or lymphomas), the oral administration of 10 mg diazepam 30 min before injection of the tracer is advisable to decrease the cervical muscular uptake occurring in some patients, which interferes with the interpretation of the cervical lymph node stations [93] (Fig. 11).

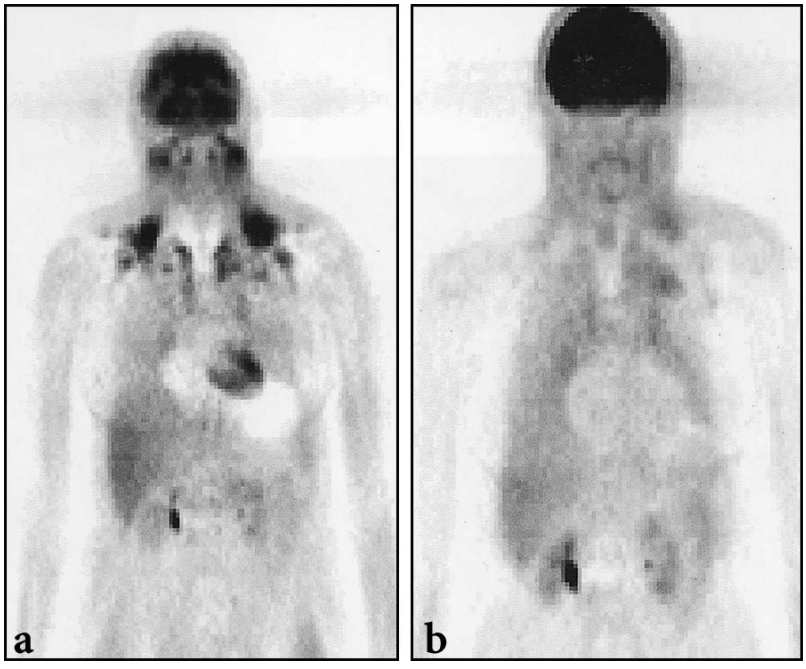

Fig. 11. Coronal whole-body FDG-PET view. High muscular uptake is observed in the cervical area precluding the detection of metastatic lymph nodes (*left*). A similar view in the same patient obtained one week later, after the administration of 10 mg diazepam 30 min before FDG injection (*right*): pre-medication with diazepam is advisable when assessing head and neck tumors

Tracer Injection

370 MBq (10 mCi) FDG are injected intravenously. Oral or intravenous hyperhydration is necessary to accelerate urinary excretion of the unbound fraction of tracer, thereby reducing the radioactive load and increasing the tumor-to-background ratio, especially in the abdomen and pelvis. Urinary excretion can be further stimulated by intravenous administration of diuretic drugs 15 min after tracer injection. During the 1-h incorporation period, patients are instructed to remain quiet and calm to minimize uptake by the laryngeal and skeletal muscles.

Imaging and Data Processing

Immediately after the bladder has been emptied, the patient is positioned in the PET system. The standard FOV usually covers the upper part of the body from the pelvis to the top of the head. This common procedure is referred to as a *"whole-body"* examination. If necessary, e.g., in the case of melanoma or sarcoma, the lower limbs are included in the FOV. Consecutive emission scans of 5 min each over seven bed positions are acquired in 2D mode followed by transmission scans of 1 min each for attenuation correction purposes. Specifically adapted regional acquisition protocols can be introduced for particular clinical problems, such as for the staging of the head and neck region where a longer acquisition time in 3D mode increases the image quality. At our institution, images are reconstructed by iterative algorithm [94] and segmented attenuation correction. The advantages of whole-body attenuation correction are the following: better spatial localization, accurate lesion geometry (essential for further image co-registration with CT or MRI), and the possibility of quantifying tracer uptake, which can be helpful in some instances (see above). The sensitivity is also increased by correction for attenuation, especially for abdominal lesions [95].

1.4.4 FDG-PET Imaging of Cancer

A unique feature of FDG-PET imaging is the possibility of obtaining information on both locoregional and distant tumoral spread in a single imaging procedure. FDG-PET is therefore viewed as a sensitive tool for cancer staging in many clinical situations: the initial staging of cancer (lung cancer, lymphoma, melanoma), restaging after induction therapy (lung cancer, lymphoma, breast cancer), evaluation of residual mass (lymphoma, testicular cancer) or the detection of recurrence (colorectal, breast, head and neck cancer). As far as RT is concerned, the potential value of FDG-PET imaging is twofold. First, PET could help in better delineating the active fraction of the tumor in order to deliver an extra dose to this region or reduce the total target field. This approach needs further validation, since only preliminary results have been reported so far. Second, the ability of PET to correct the pretreatment staging of tumors obviously has a major impact on patient management. For example, PET represents a breakthrough in nodal staging since it allows the characterization of lymph nodes as benign or malignant independent of their size, although one should not forget that this technique has limitations as regards spatial resolution. PET findings may change tumoral N staging by detecting increased metabolism within normal-sized lymph nodes (upstaging) or conversely, by showing that enlarged benign lymph nodes do not concentrate FDG (downstaging). Of course PET sensitivity and specificity are not totally satisfactory, as the limited spatial resolution of the system impedes the detection of micrometastases, and since benign but highly inflammatory lymph nodes can display increased FDG uptake. In many instances, structural imaging should be considered as a complement to FDG-PET, because multimodal image registration allows a more accurate localization of highly metabolic foci (Fig. 12).

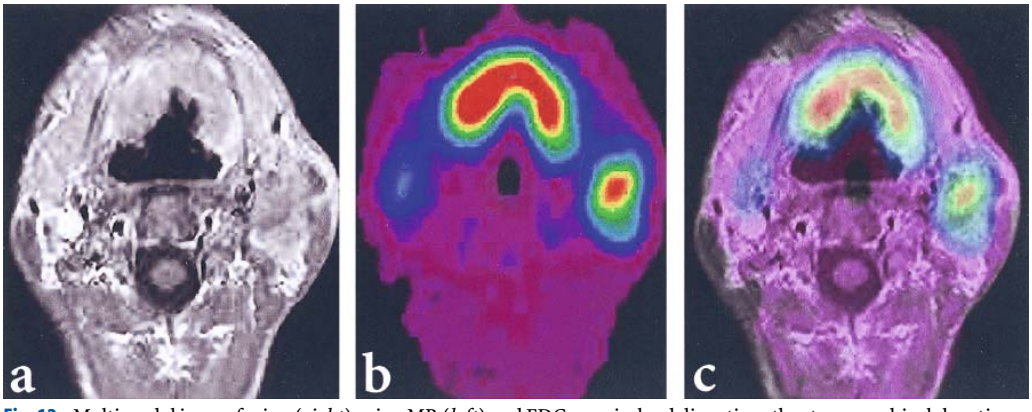

Fig. 12. Multimodal image fusion (*right*) using MR (*left*) and FDG-PET (*middle*) images of a hypopharyngeal SCC with metastatic cervical lymph nodes. Anatomical data are of assistance in precisely delineating the topographical location of the hot spots observed on the FDG-PET images

Lung Cancer

The use of FDG-PET in the examination of lung tumors has significantly increased the accuracy of the preoperative staging of patients with non-small cell carcinoma. Table 1 summarizes the published data.

PET leads to a significant increase in the sensitivity and specificity of preoperative N staging, resulting in a 50% reduction of invasive staging procedures, e.g., mediastinoscopy [96]. As PET has a very high negative predictive value, a PET-negative mediastinum allows curative surgery to be performed without prior mediastinoscopy. In turn, PET-positive homolateral mediastinal involvement (N_2 disease) requires invasive confirmation to avoid refusal of surgery by a patient with a false-positive PET scan. The lack of anatomical landmarks on PET images often interferes with the precise localization of the most appropriate nodal station to be sampled. Therefore, PET-CT image co-interpretation or fusion increases the diagnostic accuracy of the imaging examination [97] by indicating the best-suited nodal site for biopsy (Fig. 13).

In the field of RT, some reports have suggested that the metabolic information provided by PET could help in delineating the active fraction of the tumor, resulting in narrowed irradiation fields [98, 99]. Similarly, it has been also stated that PET could help in differentiating tumoral tissue from benign atelectasis in central lung neoplasms [100]. However, published studies in the field have mainly been retrospective, and further data are needed to validate these promising hypotheses. Correction for tumor movement during breathing is also being developed at the technical level, which would increase the accuracy of the metabolic data provided by PET examination [101].

Head and Neck Tumors

The advantage of FDG-PET in the N staging of SCC tumors of the head and neck region is not clearly established when compared to morphological CT and MR modalities (Table 2).

It has been suggested that PET is of greater accuracy in predicting the absence of nodal involvement (higher negative predictive value than CT-MR), which could reduce the indications for bilateral neck dissection [102, 103]. One of the most interesting applications of PET is that concerning the detection of the primary tumor in the presence of cervical metastatic adenopathy from unknown SCC. Indeed, with an identification rate of up to 40% in patients with a previously negative standard examination (including CT, US and panendoscopy) PET contributes positively to patient management by allowing selective treatment of the primary, instead of irradiating large volumes if the primary tumor remains unidentified [104–106] (Fig. 14).

Lymphomas

PET-FDG has proven to be very effective in the staging of both Hodgkin's and non-Hodgkin's lymphomas. PET is

Reference	No. of patients	PET		CT	
		Sensitivity	Specificity	Sensitivity	Specificity
[124]	30	78	81	56	86
[125]	42	83	82	43	85
[126]	29	76	98	65	87
[127]	32	100	100	81	56
[128]	27	100	98	60	93
[129]	47	89	99	57	94
[130]	76	83	94	63	73
[131]	23	82	81	64	44
[132]	68	93	95	75	63
[133]	50	90	86	72	81
[134]	32	80	100	50	75
Total	456	7	92	62	76

Table 1. Comparison of FDG-PET and CT for the nodal staging of non-small-cell lung cancer

	n	PET		MRI or CT	
		Sensitivity	Specifity	Sensitivity	Specifity
[135]	22	89	100	72	56
[102]	12	91	88	36	94
[136]	60	90	94	82	85
[137]	48	72	99	67	97
[90]	54	96	90	85	86
[138]	37	83	91	86	97
[139]	25	50	100	40	100

Table 2. Comparison of FDG-PET and CT/MRI for the nodal staging of head and neck squamous-cell carcinoma

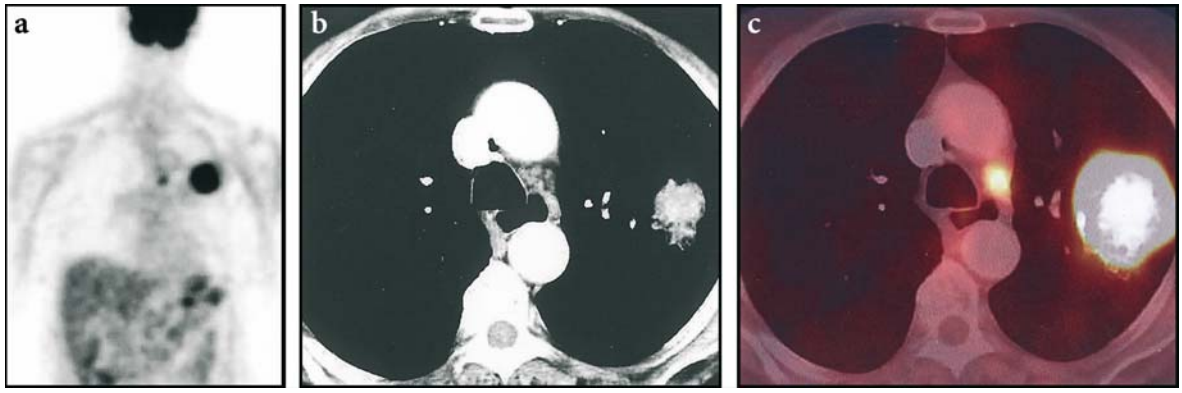

Fig. 13. Coronal FDG-PET reformatted view of a patient with lung carcinoma of the left upper lobe presenting with a hypermetabolic focus consistent with left mediastinal adenopathy (*left*). Normal-sized (less than 10 mm) lymph nodes are visualized on CT images (*top right*). Image fusion (*bottom right*) demonstrates that positive lymph nodes on PET imaging are located within the left mediastinum, which was confirmed by mediastinoscopy

highly sensitive in detecting nodal and bone marrow involvement, resulting in disease upstaging in about 10% of patients [107–109]. Again, the ability of PET to detect active disease in unenlarged lymph nodes explains these results. PET has been shown to modify patient management in about 25% of cases [110], e.g., by indicating a switch from RT to systemic chemotherapy in patients initially classified as stage I and who were subsequently upstaged by PET (Fig. 15).

Esophageal Cancer

PET has demonstrated promising results in the pretreatment evaluation of esophageal tumors. The sensitivity of PET in tumoral node detection is similar to that of CT and endoscopic ultrasound, but its specificity is higher [111, 112]. It is also useful in detecting distant lymph node or non-nodal metastases [113], but nodal involvement adjacent or close to the primary tumor cannot be differentiated from uptake within the latter. The detection by PET of non-palpable metastases within the jugular lymph nodes can be of major importance in treatment planning (Figs.16, 17).

Testicular Tumors

No data are currently available on the use of FDG-PET in the preoperative staging of testicular tumors, although its use in the assessment of viable tumor tissue after therapy has been recognized [114]. In the pretreatment setting, the sensitivity of this method for nodal involvement detection is close to that of CT (around 60%). In non-seminomatous tumors, PET information could avoid retroperitoneal lymph node resection if high sensitivity was demonstrated, which has not been observed in the few published cases. In seminomatous tumors,

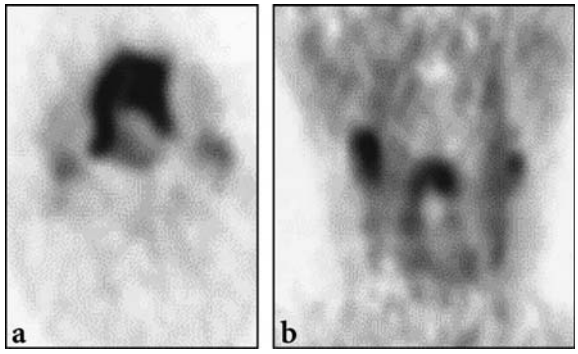

Fig. 14. Whole-body FDG-PET: axial (*left*) and coronal (*right*) views of bilateral nodal metastases of hypopharyngeal SCC. The right adenopathy measured less than 10 mm and was therefore incorrectly rated as benign on the CT images

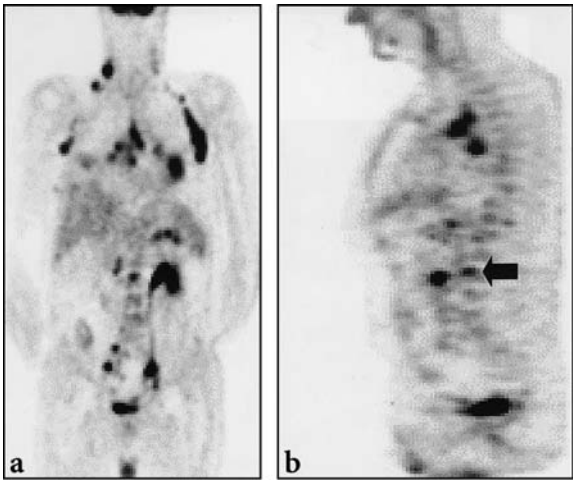

Fig. 15. FDG-PET coronal (*left*) and sagittal (*right*) reformatted views in a patient with non-Hodgkin's lymphoma. PET depicts tumoral lymph nodes on both sides of the diaphragm, as well as a bone lesion within a vertebral body (*arrow*). Blind bone marrow biopsy performed in the posterior left iliac crest was negative. Vertebral bone marrow involvement was later confirmed by MR examination (not illustrated)

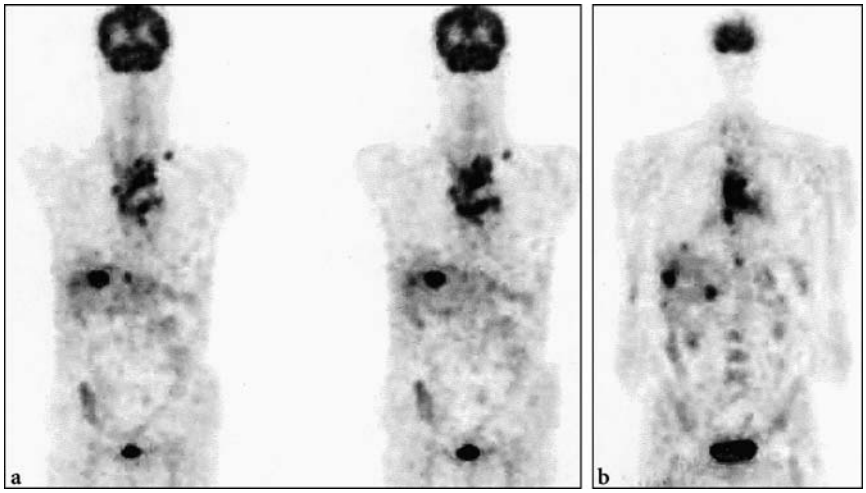

Fig. 16. Three adjacent coronal reformatted views featuring typical FDG-PET findings in esophageal carcinoma with bulk nodal metastases in the mediastinum, liver, and left supra-clavicular nodal area

RT of the lymph outflow is an established standard procedure in early tumoral stages which does not require positive imaging.

Breast Tumors

The detection of micrometastases within axillary lymph nodes is not possible by FDG-PET due to the limitations in spatial resolution of this method. Therefore, PET cannot replace conventional surgical exploration of the axilla using the sentinel node technique. Reported sensitivities for N staging were initially good (80–95%) [115, 116] but it was further shown that sensitivity dropped to 33% for nodal metastases from small primary tumors (pT1) [116]. A potential advantage of PET is its ability to detect nodal metastases in the internal mammary chain, as illustrated in Fig. 18. However, the clinical impact of this aspect on delineation of the radiation field has to be prospectively studied.

Other Cancers

The results of FGD-PET in the assessment of locoregional extension of digestive tract tumors have been disappointing, although the overall sensitivity for the detection of distant metastases has remained very high. A sensitivity of only 25% has been reported for the diagnosis of nodal involvement in colorectal cancer [117]. As the metastatic nodes were located in the immediate vicinity of the primary tumor, they could not be identified as separate hot spots due to the limitations in spatial resolution. The use of FDG-PET can reasonably be advocated for the preoperative staging of rectal tumors when enlarged lymph nodes are visualized on CT or EUS, since this could influence the therapeutic decisions. In pancreatic cancer, a sensitivity of 49% and a specificity of 63% have been reported for metastatic lymph node detection, while the sensitivity for detection of metastases is about 80% [118].

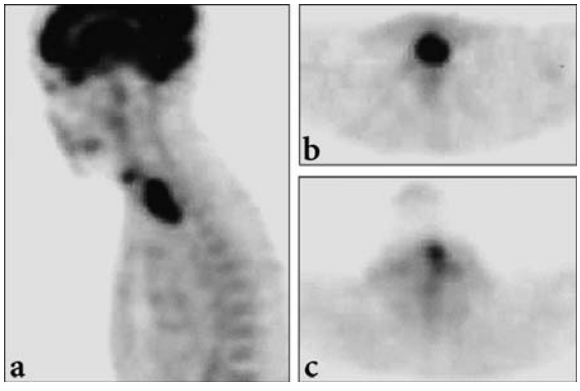

Fig. 17. Sagittal view (*left*) and axial views (*right*) at the level of the esophageal primary tumor (*top*) and left paratracheal metastatic lymph node (*bottom*), found to be negative on CT examination but later confirmed as positive by ultrasound and biopsy

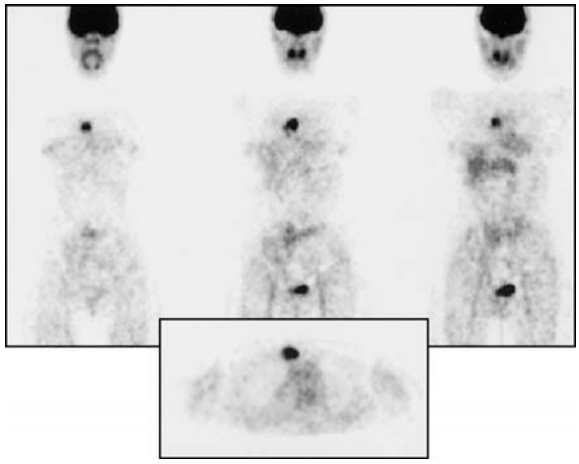

Fig. 18. High FDG uptake in the right parasternal region corresponding to breast cancer nodal metastases in the internal mammary chain; coronal view (*top*) and axial view (*bottom*)

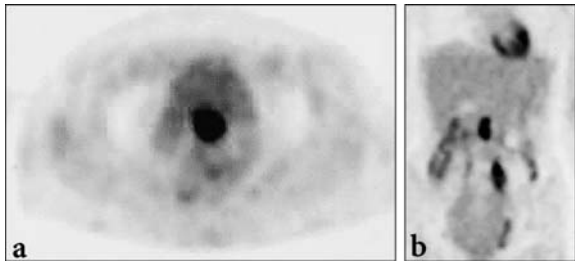

Fig. 19. Preoperative whole-body FDG-PET in a case of uterine cervix SCC showing the primary tumor (*axial view; left*) and the metastatic lymph nodes in the left iliac and lumbo-aortic chains (*coronal view; right*)

In the gynecological domain, PET has recently been proposed as a technique for assessing the lymphatic extent of uterine cervical cancers, and has shown higher sensitivity and specificity than CT [119]. By detecting metastatic lymph nodes, PET could play a role in indicating adjuvant RT (Fig. 19).

1.5 Conclusion

Both CT and MRI are high-performing cross-sectional imaging modalities of which anatomic information can be appropriately processed in a three-dimensional way to enable optimal target delineation for RT planning. MRI provides better tissue contrast than CT in some areas of the body. But CT has the major advantages of suffering lower geometric distortion, and of carrying indispensable information on density mapping which is integrated into the algorithms for RT dose calculation. The two techniques are thus far suited to give the radiotherapist the anatomic depiction of the target area. They maybe used exclusively to each other, or complementarily in the figure that lower soft tissue contrast on CT images impairs the accurate delineation of the targeted volume. But both techniques suffer the major limitation of overestimating the true tumoral volume [120]. The combination of CT/MR-based structural information together with metabolic-physiologic information compensating for overestimates of the former appears mandatory to optimize the delineation of the target. The initial step in the purpose has been obtained by the co-registration between CT/MR and FDG-PET information in a 'fused' composite image [121]. It has been now validated for many neoplastic conditions. But new investigational eras are being explored in the field of tumoral metabolic imaging. The two next chapters highlight the potential of MR spectroscopy to indicate which tumoral sub-volumes require higher irradiation and how more specific radiopharmaceuticals than FDG could be able to depict hypoxia, angiogenesis, apoptosis, and receptors status. The application of the technique to the malignant lymph node has already given preliminary but encouraging results [122, 123]. The multimodal approach of tumor imaging combining structural and physiologic/metabolic information, and the co-registration in three-dimensional space of the different kinds of information through image fusion are keys for improving both precision and efficiency of conformal radiotherapy.

References

1. Suit H (2002). The Gray Lecture 2001: coming technical advances in radiation oncology. Int J Radiat Oncol Biol Phys 53:798–809
2. Enami B, Sethi A, Petruzelli GJ (2003) Influence of MRI on target delineation and IMRT planning in nasopharyngeal carcinoma Int J Radiat Oncol Biol Phys 57:481–488
3. Intensity-Modulated Radiation Therapy Collaborative Working Group (2001) Intensity-modulated radiotherapy: current status and issues of interest. Int J Radiat Oncol Biol Phys 53:1088–1089
4. Fischbein NJ, Noworolski SM, Henry RG, Kaplan MJ, Dillon WP, Nelson SJ (2003) Assessment of metastatic cervical adenopathy using dynamic contrast-enhanced MR imaging. AJNR – Am J Neuroradiol 24:301–311
5. Sumi M, Sakihama N, Sumi T, Morikawa M, Uetani M, Kabasawa H, Shigeno K, Hayashi K, Takahashi H, Nakamura T (2003) Discrimination of metastatic cervical lymph node with diffusion-weighted MR imaging in patients with head and neck cancer. AJNR – Am J Neuroradiol 24:1627–1634
6. Curtin HD, Ishwaran H, Mancuso AA, Dalley RW, Caudry DJ, McNeil BJ (1998) Comparison of CT and MR imaging in staging of neck metastases. Radiology 207:123–130
7. King AD, Tse GM, Ahuja AT, Yuen EH, Vlantis AC, To EW, van Hasselt AC (2004) Necrosis in metastatic neck nodes: diagnostic accuracy of CT, MR imaging, and US. Radiology 230:720–726
8. Hounsfield GN (1973) Computerized transverse axial scanning (tomography). Description of system. Br J Radiol 46:1016–1022
9. Towers JM (1993) Spiral or helical CT? Am J Roentgenol 161(4):901–902
10. Kalender WA et al. (1994) A comparison of conventional and spiral CT: an experimental study on the detection of spherical lesions. J Comput Assist Tomogr 18:167–176
11. Wang G, Vannier MW (1994) Longitudinal resolution in volumetric X-ray CT-analytical comparison between conventional and helical CT. Med Phys 21:429–433
12. Wang G et al. (1994) Theoretical FWTM values in helical CT. Med Phys 21:753–754
13. Fuchs T et al. (2000) Technical advances in multi-slice spiral CT. Eur J Radiol 36:69–73
14. Klingenbeck-Regn K et al. (1999) Subsecond multi-slice computed tomography: basics and applications. Eur J Radiol 31:110–124
15. Petterson H (1995) The NICER centennial book. A global textbook of radiology. Nicer Institute, Oslo
16. Naidich DP et al. (1999) Computed tomography and magnetic resonance of the thorax. Lippincott-Raven, Philadelphia
17. Sakai O et al. (2000) Lymph node pathology. Benign proliferative lymphoma, and metastatic disease. Radiol Clin North Am 5:979–998

18. Van den Brekel MWM, Castelijns JA (2000) Imaging of lymph nodes in the neck. Semin Roentgenol 1:42–53
19. Rydberg J et al. (2000) Multisection CT: scanning techniques and clinical applications. Radiographics 20:1787–1806
20. Rubin GD et al. (1998) Thoracic spiral CT: influence of subsecond gantry rotation on image quality. Radiology 208:771–776
21. Wang G, Vannier MW (1997) Optimal pitch in spiral computed tomography. Med Phys 24:1635–1639
22. Mancuso AA et al. (1983) Computed tomography of cervical and retropharyngeal lymph nodes: normal anatomy, variants of normal, and application in staging head and neck cancer. Radiology 148:715–723
23. Som PM (1987) Lymph nodes of the neck. Radiology 165:593–600
24. Harris EW et al. (1996) Enhanced CT of the neck: improved visualization of lesions with delayed imaging. Am J Roentgenol 167:1057–1058
25. Sakai O et al. (1997) Asymmetrical or heterogenous enhancement of the internal jugular veins in contrast-enhanced CT of the head and neck. Neuroradiology 39:292–295
26. Leung AN (1997) Spiral CT of the thorax in daily practice: optimization of the technique. J Thoracic Imag 12:2–10
27. Han JK et al. (2000) Factors influencing vascular and hepatic enhancement at CT: experimental study on injection protocol using a canine model. J Comput Assist Tomogr 24:400–406
28. Cline HE et al. (1991) 3D surface rendered MR images of the brain and its vasculature. J Comput Assist Tomogr 15:344–351
29. Magnusson M et al. (1991) Evaluation of methods for shaded surface display of CT volumes. Comput Med Imaging Graphics 15:247–256
30. Rouviére H (1948) Anatomie humaine descriptive et topographique, 6th edn. Masson, Paris
31. Grégoire V et al. (2000) Selection and delineation of lymph node target volumes in head and neck conformal radiotherapy. Proposal for standardizing terminology and procedure based on the surgical experience. Radiother Oncol 56:135–150
32. Som PM et al. (1999) An imaging-based classification for the cervical nodes designed as an adjunct to recent clinically based nodal classifications. Arch Otolaryngol Head Neck Surg 125:388–396
33. Cymbalista M et al. (1999) CT demonstration of the 1996 AJCC-UICC regional lymph node classification for lung cancer staging. Radiographics 19:899–900
34. American Joint Committee on Cancer (1992) Lung. In: Beahrs OH, Henson DE, Hutter RVP et al. (eds) Manual for staging cancer, 4th edn. Lippincott, Philadelphia, pp 115–121
35. American Thoracic Society (1983) Medical Section of the American Lung Association. Clinical staging of primary lung cancer. Am Rev Respir Dis 127:659–664
36. Van den Brekel MWM et al. (1990a) Cervical lymph node metastasis: assessment of radiologic criteria. Radiology 177:379–384
37. Som PM (1992) Detection of metastasis in cervical lymph nodes: CT and MR criteria and differential diagnosis. Am J Roentgenol 158:961–969
38. McLoud TC et al. (1992) Bronchogenic carcinoma: analysis of staging in the mediastinum with CT by correlative lymph node mapping and sampling. Radiology 182:319–323
39. Dorfman RE et al. (1991) Upper abdominal lymph nodes: criteria for normal size determined with CT. Radiology 180:319–322
40. Yousem DM et al. (1992) Central nodal necrosis and extracapsular neoplastic spread in cervical lymph nodes: MR imaging versus CT. Radiology 182:753–759
41. Dolan PA (1963) Tumor calcification following therapy. Am J Roentgenol 89:166–174
42. Eisenkraft BL, Som PM (1999) The spectrum of benign and malignant etiologies of cervical node calcification. Am J Roentgenol 172:1433–1437
43. Ghahremani GG, Straus FH (1971) Calcification of distant lymph node metastases from carcinoma of colon. Radiology 99:65–66
44. Laissey JP et al. (1994) Enlarged mediastinal lymph nodes in bronchogenic carcinoma: assessment with dynamic contrast-enhanced MR imaging. Radiology 191:263–267
45. Hennig J et al. (1986) RARE-imaging. A fast imaging method for clinical MR. Magn Reson Med 3:829–833
46. Fullbright et al. (1994) MR of the head and neck: comparison of fast spin-echo and conventional spin-echo sequences. Am J Neuroradiol 15:767–773
47. Held P, Breit A (1994) MRI and CT of tumors of the pharynx: comparison of two imaging procedures including fast and ultrafast MR sequences Eur J Radiol 18:81–89
48. Yousem DM, Hurst RW (1994) MR of cervical lymph nodes: comparison of fast spin echo and conventional T2 W scans. Clin Radiol 49:670–675
49. Mitchell DG (1999) MRI principles. Saunders, Philadelphia
50. Rinck PA (1993) Magnetic resonance in medicine – the basic textbook of the European MR forum, 3rd edn. Blackwell Scientific, London
51. Chong VFH et al. (1996) MR features of cervical node necrosis in metastatic disease. Clin Radiol 51:103–109
52. Van den Brekel MWM et al. (1990b) Detection and characterization of of metastatic cervical adenopathies by MR imaging: comparison of different MR techniques. J Comput Assist Tomogr 14:581–589
53. Van den Brekel MWM, Castelijns JA (1999) New developments in imaging of neck node metastases. In: Mukherji SK, Castelijns JA (eds) Modern head and neck imaging. Springer, Berlin Heidelberg New York
54. Anzaï Y, Prince MR (1997) Iron-oxide enhanced MR lymphography: the evaluation of cervical lymph node metastases in head and neck cancer. J Magn Reson Imag 7:75–81
55. Harika et al. (1996) Macromolecular intravenous contrast agent for MR lymphography: characterization and efficacy studies. Radiology 198:365–370
56. Hoffman HT et al. (2000) Functional magnetic resonance imaging using iron oxide particles in characterizing head and neck adenopathy. Laryngoscope 110:1425–1430
57. Fujimoto Y et al. (2000) Magnetic resonance lymphography of profundus lymph nodes with liposomal gadolinium diethylenetriamine pentaacetic acid. Biol Pharm Bull 23: 97–100
58. Misselwitz B et al. (1999) Gadoflurorine 8: initial experience with a new contrast medium for interstitial MR lymphography. MAGMA 8:190–195
59. Staatz G et al. (2001) Interstitial T1-weighted MR lymphography: lipophilic perfluorinated gadolinium chelates in pigs. Radiology 220:129–136
60. Dooms GC et al. (1985) Characterization of lymphadenopathy by magnetic resonance relaxation times: preliminary results. Radiology 155:691–697
61. Grossman RI et al. (1994) Magnetization transfer: theory and applications in neuroradiology. Radiographics 14:279–90
62. Lebihan D, Turner R (1991) Intravoxel incoherent motion imaging using spin echoes. Magn Reson Med 19:211–227
63. Wiener JI et al. (1986) Breast and axillary tissue MR imaging: correlation of the signal intensities and relaxation times with pathological findings. Radiology 160:299–305

64. Yousem DM (1999) Magnetization transfer imaging of the extracranial head and neck. In: Mukherji SK, Castelijns JA (eds) Modern head and neck imaging. Springer, Berlin Heidelberg New York
65. Gillams et al. (1996) Magnetization transfer contrast MR in lesions of the head and neck. Am J Neuroradiol 17:355–360
66. Sheppard LM, Yousem DM (1994) MTI of cervical adenopathies. ASNR, paper 130
67. Petrella J, Provenzale J (2000) MR perfusion of the brain: techniques and applications. Am J Roentgenol 175:207–19
68. Carrington B (1998) Lymph nodes. In: Husband JHS, Reznek RH (eds) Imaging in oncologic. Isis Medical Media, Oxford, pp 729–748
69. Dillon WP, Harnsberger HR (1991) The impact of radiologic imaging on staging of cancer of the head and neck. Semin Oncol 18:64–79
70. Gussack GS, Hudgins PA (1991) Imaging modalities in recurrent head and neck tumors. Laryngoscope 101:119–124
71. Mukherji SK et al. (2000) The ability of dual camera coincidence tomography 18F fluorodeoxyglucose imaging to differentiate recurrent head and neck SCC from post-treatment changes. The Radiological Society of North America, 88th annual scientific assembly, Chicago, paper 473
72. Vuillez JP (1998) Métabolisme glucidique des cellules tumorales: conséquences pour l'utilisation de radiopharmaceutiques analogues du glucose. Med Nucl Imag Fonct Metab 22:9–29
73. Warburg O (1930) The metabolism of tumors. Arnold Constable, London, pp 75–327
74. Brown R, Wahl R (1993) Overexpression of GLUT-1 glucose transporter in human breast cancer. An immunohistochemical study. Cancer 72:2979–2985
75. Brown R et al. (1996) Intratumoral distribution of tritiated FDG in breast carcinoma: correlation between Glut-1 expression and FDG uptake. J Nucl Med 37:1043–1047
76. Mellanen P et al. (1994) Expression of glucose transporters in head and neck tumors. Int J Cancer 56:622–629
77. Reske S et al. (1997) Overexpression of glucose transporter and increased FDG uptake in pancreatic carcinoma. J Nucl Med 38:1344–1348
78. Younes M et al. (1995) GLUT1 expression in human breast carcinoma: correlation with known prognostic markers. Anticancer Res 15:2895–2898
79. Burgman P et al. (2001) Hypoxia-induced increase in FDG uptake in MCF7 cells. J Nucl Med 42:170–175
80. Bustamente E, Pedersen P (1977) High aerobic glycolysis of rat hepatoma cells in culture: role of mitochondrial hexokinase. Proc Natl Acad Sci USA 74:3735–3739
81. Weber G, Cantero A (1955) Glucose-6-phosphatase activity in normal, precancerous, and neoplastic tissues. Cancer Res 15:105–108
82. Kubota R et al. (1992) Intratumoral distribution of fluorine-18-fluorodeoxyglucose in vivo: high accumulation in macrophages and granulation tissues studied by microautoradiography. J Nucl Med 33:1972–1980
83. Delbeke D et al. (1999) FDG PET and dual-head gamma camera positron coincidence detection imaging of suspected malignancies and brain disorders. J Nucl Med 40:110–117
84. Landoni C et al. (1999) Comparison of dual-head coincidence PET versus ring PET in tumor patients. J Nucl Med 40:1617–1622
85. Lonneux M et al. (1998) Can dual-headed 18F-FDG SPECT imaging reliably supersede PET in clinical oncology? A comparative study in lung and gastrointestinal tract cancer. Nucl Med Commun 19:1047–1054
86. Martin W et al. (1995) FDG-SPECT: correlation with FDG-PET. J Nucl Med 36:988–995
87. Shreve P et al. (1998) Oncologic diagnosis with 2-[fluorine-18]fluoro-2-deoxy-d-glucose imaging: dual-head coincidence gamma camera versus positron emission tomographic scanner. Radiology 207:431–437
88. Tatsumi M et al. (1999) Feasibility of fluorodeoxyglucose dual-head gamma camera coinidence imaging in the evaluation of lung cancer: comparison with FDG PET. J Nucl Med 40:566–573
89. Weber W et al. (1999) Assessment of pulmonary lesions with 18F-fluorodeoxyglucose positron imaging using coincidence mode gamma cameras. J Nucl Med 40:574–578
90. Stokkel M et al. (2000) Preoperative evaluation of patients with primary head and neck cancer using dual-head 18-fluorodeoxyglucose positron emission tomography. Ann Surg 231:229–234
91. Langen K et al. (1993) The influence of plasma glucose levels on fluorine-18-fluorodeoxyglucose uptake in bronchial carcinomas. J Nucl Med 34:355–359
92. Torizuka T et al. (1998) Effect of insulin on uptake of FDG by experimental mammary carcinoma in diabetic rats. Radiology 208:499–504
93. Barrington S, Maisey M (1996) Skeletal muscular uptake of fluorine-18-FDG: effect of oral diazepam. J Nucl Med 37:1127–1129
94. Lonneux M et al. (1999) Attenuation correction in whole body FDG oncological studies: the role of statistical reconstruction. Eur J Nucl Med 6:591–598
95. Hustinx R et al. (2000) Impact of attenuation correction on the accuracy of FDG-PET in patient with abdominal tumors: a free-response ROC analysis. Eur J Nucl Med 27:1365–1371
96. Vansteenkiste JF, Mortelmans L (1999) FDG-PET in the locoregional lymph node staging of non-small cell lung cancer: a comprehensive review of the Leuven lung cancer group experience. Clin Pos Imaging 2:223–231
97. Vansteenkiste JF et al. (1998b) FDG-PET scan in potentially operable non-small cell lung cancer: do anatomometabolic PET-CT fusion images improve the localisation of regional lymph node metastases? Eur J Nucl Med 25:1495–1501
98. Giraud P et al. (2001) CT and (18)F-deoxyglucose (FDG) image fusion for optimization of conformal radiotherapy of lung cancers. Int J Radiat Oncol Biol Phys 49:1249–1257
99. Vanuystel L, Vansteenkiste JF, Stroobants S et al. (2000) The impact of (18)F-fluoro-2-deoxy-d-glucose positron emission tomography (FDG-PET) lymph node staging on the radiation treatment volumes in patients with non-small cell lung cancer. Radiother Oncol 55:317–324
100. Nestle U et al. (1999) 18F-deoxyglucose positrom emission tomogrpahy (FDG-PET) for the planning of radiotherapy in lung cancer: high impact in patients with atelectasis. Int J Radiat Oncol Biol Phys 44:593–597
101. Nehmeh SA, Ford E, Rosenzweig K et al. (2001) Gated positron emission tomography: a technique for reducing lung tumor motion effect. J Nucl Med 42:34P
102. Braams J et al. (1995) Detection of lymph node metastases of squamous-cell cancer of the head and neck with FDG-PET and MRI. J Nucl Med 36:211–216
103. Myers L et al. (1998) Positron emission tomography in the evaluation of the N0 neck. Laryngoscope 108:232–236
104. Aassar et al. (1999) Metastatic head and neck cancer: role and usefulness of FDG PET in locating occult primary tumors. Radiology 210:177–181
105. Bohuslavizki KH et al. (2000) FDG PET detection of unknown primary tumors. J Nucl Med 41:816–822

106. Hanasono MM et al. (1999) Uses and limitations of FDG positron emission tomography in patients with head and neck cancer. Laryngoscope 109:880–885
107. Moog F et al. (1997) Lymphoma: role of whole-body 2-deoxy-2-[F-18]fluoro-d-glucose (FDG) PET in nodal staging. Radiology 203:795–800
108. Moog F et al. (1998a) 18-F-fluorodeoxyglucose-positron emission tomography as a new approach to detect lymphomatous bone marrow. J Clin Oncol 16:603–609
109. Moog F et al. (1998b) Extranodal malignant lymphoma: detection with FDG PET versus CT. Radiology 206:475–481
110. Shah N et al. (2000) The impact of FDG positron emission tomography imaging on the management of lymphomas. Br J Radiol 73:482–487
111. Flamen P et al. (2000) Utility of positron emission tomography for the staging of patients with potentially operable esophageal carcinoma. J Clin Oncol 18:3202–3210
112. Lerut T et al. (2000) Hitopathologic validation of lymph node staging with FDG-PET scan in cancer of the esophagus and gastroesophageal junction. A prospective study based on primary surgery with extensive lymphadenectomy. Ann Surg 232:743–752
113. Block M et al. (1997) Improvement in staging of esophageal cancer with the addition of positron emission tomography. Ann Thorac Surg 64:770–776
114. Cremerius U et al. (1998) FDG-PET for detection and therapy control of metastatic germ cell tumor. J Nucl Med 39: 815–822
115. Adler L et al. (1997) Axillary lymph node metastases: screening with [F-18]2-deoxy-2-d-glucose (FDG) PET. Radiology 203:323–327
116. Avril N et al. (1996) Assessment of axillary lymph node involvement in breast cancer patients with positron emission tomography using radiolabelled 2-(fluorine-18)-fluoro-2-deoxy-d-glucose. J Natl Cancer Inst 88:1204–1209
117. Abdel-Nabi H et al. (1998) Staging of primary colorectal carcinomas with fluorine-18 fluorodeoxyglucose whole-body PET: correlation with histopathologic and CT findings. Radiology 206:755–760
118. Diederichs C et al. (2000) Values and limitations of 18F-fluorodeoxyglucose-positron-emission tomography with preoperative evaluation of patients with pancreatic masses. Pancreas 20:109–116
119. Sugawara Y et al. (1999) Evaluation of FDG PET in patients with cervical cancer. J Nucl Med 40:1125–1131
120. Daisne JF, Duprez Th, Weynand B, Lonneux M, Hamoir M, Reychler H, Grégoire V (2004) Tumor volume in pharyngolaryngeal squamous cell carcinoma: comparison at CT, MR imaging, and FDG PET and validation with surgical specimen. Radiology 233:93–100
121. Schwartz DL, Ford E, Rajendran J, Yueh B, Coltrera MD, Virgin J, Anzai Y, Haynor D, Lewellyn B, Mattes D, Meyer J, Phillips M, Leblanc M, Kinahan P, Krohn K, Eary J, Laramore GE (2005) FDG-PET/CT imaging for preradiotherapy staging of head-and-neck squamous cell carcinoma. Int J Radiat Oncol Biol Phys. 61:129–36
122. Star-Lack JM, Adalsteinsson E, Adam MF, Terris DJ, Pinto HA, Brown JM, Spielman DM (2000) In Vivo 1H MR spectroscopy of human head and neck lymph node metastasis and comparison with oxygen tension measurements. AJNR – Am J Neuroradiol 21:183–193
123. King AD, Yeung DK, Ahuja AT, Leung SF, Tse GM, van Hasselt (2004) In vivo proton MR spectroscopy of primary and nodal nasopharyngeal carcinoma. AJNR – Am J Neuroradiol 25:484–490
124. Chin R et al. (1995) Mediastinal staging of non-small-cell lung cancer with positron emission tomography. Am J Respir Crit Care Med 152:2090–2096
125. Patz E et al. (1995) Thoracic nodal staging with PET imaging with 18FDG in patients with bronchogenic carcinoma. Chest 108:1617–1621
126. Sazaki M et al. (1996) The usefulness of FDG positron emission tomography for the detection of mediastinal lymph node metastases in patients with non-small cell lung cancer: a comparative study with X-ray computed tomography. Eur J Nucl Med 23:741–747
127. Sazon D et al. (1996) Fluorodeoxyglucose positron emission tomography in the detection and staging of lung cancer. Am J Respir Crit Care Med 153:417–421
128. Scott W et al. (1996) Mediastinal lymph node staging of non-small cell lung cancer: a prospective comparison of computed tomography and positron emission tomography. J Thorac Cardiovasc Surg 111:642–648
129. Steinert H et al. (1997) Non-small cell lung cancer: nodal staging with FDG PET versus CT with correlative lymph node mapping and sampling. Radiology 202:441–446
130. Valk P et al. (1995) Staging non-small cell lung cancer by whole-body positron emision tomographic imaging. Ann Thorac Surg 60:1573–1582
131. Wahl RL et al. (1994) Staging of mediastinal non-small cell lung cancer FDG PET, CT, and fusion images: preliminary prospective evaluation. Radiology 191:371–377
132. Vansteenkiste JF et al. (1998a) Lymph node staging in non-small cell lung cancer with FDG-PET scan: a prospective study on 690 lymph node stations from 68 patients. J Clin Oncol 16:2142–2149
133. Bury T et al. (1996) Staging of the mediastinum: value of positron emission tomography imaging in non-small cell lung cancer. Eur Respir J 9:2560–2564
134. Guhlmann A et al. (1997) Lymph node staging in non-small cell lung cancer: evaluation by [F]FDG positron emission tomography (PET). Thorax 52:438–441
135. Laubenbacher C et al. (1995) Comparison of fluorine-18-fluorodeoxyglucose PET, MRI and endoscopy for staging head and neck squamous-cell carcinomas. J Nucl Med 36:1747–1757
136. Adams S et al. (1998) Prospective comparison of 18F-FDG PET with conventional imaging modalities (CT, MRI, US) in lymph node staging of head and neck cancer. Eur J Nucl Med 25:1255–1260
137. Benchaou M et al. (1996) The role of FDG-PET in the preoperative assessment of N-staging in head and neck cancer. Acta Otolaryngol 116:332–335
138. DiMartino E et al. (2000) Diagnosis and staging of head and neck caner. Arch Otolaryngol Head Neck Surg 126:1457–1461
139. Paulus P et al. (1998) 18FDG-PET for the assessment of primary head and neck tumors: clinical, computed tomography and histopathological correlation in 38 patients. Laryngoscope 108:1578–1583
140. Brink J (1995) Technical aspects of helical (spiral) CT. Radiol Clin North Am 33:834–851
141. Kalender WA et al. (1990) Spiral volumetric CT with single-breath-hold technique, continuous transport, and continuous scanner rotation. Radiology 176:181–183
142. Ruehm SG, Schroeder T, Debatin JF (2001) Interstitial lymphography with gadoterate meglumine: initial experience in humans Radiology 220:816-821
143. Mack MG, Balzer JO, Straub R, Eichler K, Vogl TJ (2002) Superparamagnetic iron oxide-enhanced MR imaging of head and neck lymph nodes. Radiology 222:239–44

144. Sigal R, Vogl T, Casseman J et al. (2002) Lymph node metastases from head and neck squamous cell carcinoma : MR imaging with ultrasmall superparamagnetic oxide particles (Sinerem MR) Results of Phase-III multicenter clinical trial. Eur Radiol 12:957–8
145. Bulte JW, Kraitchmann DL (2004) Iron oxide MR contrast agents for molecular and cellular imaging. NMR Biomed 17:484–99
146. Fischbein NJ, Noworolski SM, Henry RG, Kaplan MJ, Dillon WP, Nelson SJ (2003) Assessment of metastatic cervical adenopathy using dynamic contrast-enhanced MR imaging. AJNR - Am J Neuroradiol 24:301–11
147. Noworolski SM, Fischbein, NJ, Kaplan MJ, Lu Y, Nelson SJ, Carvajal L, Henry RG (2003) Challenges in dynamic contrast-enhanced MRI imaging of cervical lymph nodes to detect metastatic disease. JMRI - J Magn Reson Imaging 17:455–62
148. Shah GV, Fischbein NJ, Patel R, Mukherji SK (2003) Newer MR imaging techniques for head and neck. Magn Reson Imaging Clin N Am 11:449–69
149. Shah GV, Fischbein NJ, Gandhi D, Mukherji SK (2004) Dynamic contrast-enhanced MR imaging. Top Magn Reson Imaging 15:71–77
150. Ruehm SG, Schroeder T, Debatin JF (2001) Interstitial lymphography with gadoterate meglumine: initial experience in humans Radiology 220:816–821
151. Mack MG, Balzer JO, Straub R, Eichler K, Vogl TJ (2002) Superparamagnetic iron oxide-enhanced MR imaging of head and neck lymph nodes. Radiology 222:239–244
152. Sigal R, Vogl T, Casseman J et al. (2002) Lymph node metastases from head and neck squamous cell carcinoma : MR imaging with ultrasmall superparamagnetic oxide particles (Sinerem MR) Results of Phase-III multicenter clinical trial. Eur Radiol 12:957–958
153. Bulte JW, Kraitchmann DL (2004) Iron oxide MR contrast agents for molecular and cellular imaging. NMR Biomed 17:484–499
154. Sumi M, Sakihama N, Sumi T, Morikawa M, Uetani M, Kabasawa H, Shigeno K, Hayashi K, Takahashi H, Nakamura T (2003) Discrimination of metastatic cervical lymph node with diffusion-weighted MR imaging in patients with head and neck cancer. AJNR – Am J Neuroradiol 24:1627–1634
155. Fischbein NJ, Noworolski SM, Henry RG, Kaplan MJ, Dillon WP, Nelson SJ (2003) Assessment of metastatic cervical adenopathy using dynamic contrast-enhanced MR imaging. AJNR – Am J Neuroradiol 24:301–311
156. Noworolski SM, Fischbein, NJ, Kaplan MJ, Lu Y, Nelson SJ, Carvajal L, Henry RG (2003) Challenges in dynamic contrast-enhanced MRI imaging of cervical lymph nodes to detect metastatic disease. JMRI – J Magn Reson Imaging 17: 455–462
157. Shah GV, Fischbein NJ, Patel R, Mukherji SK (2003) Newer MR imaging techniques for head and neck. Magn Reson Imaging Clin N Am 11:449–469
158. Shah GV, Fischbein NJ, Gandhi D, Mukherji SK (2004) Dynamic contrast-enhanced MR imaging. Top Magn Reson Imaging 15:71–77

PET and SPECT in IMRT: Future Prospects

Christophe Van de Wiele

2

Contents

2.1 Introduction

Intensity modulated radiotherapy is characterized by the high-precision application of radiation to an exactly defined target and by very rapid dose falloff to spare normal tissue. Improvement in the physical dose distribution obtained by IMRT has raised the issue of accuracy of target volume selection and delineation on a 3D basis. For both technical and logistic reasons, computed tomography (CT scan) has become the reference imaging modality for 3D tumor delineation in IMRT. CT does not suffer from geometric distortion and inherently contains information on the density mapping which is used by the algorithms for dose calculation. As compared to CT, MRI allows better target volume definition compared with CT in some specific sites and provides multi-plane images, facilitating the assessment of tumor extension. On the other hand, MRI images may be degraded by geometric distortion at the edge of the field of view, do not allow precise delineation of the external contour of the body and the bony structures and lack information on tissue density. Whilst CT-MRI image fusion is feasible and may overcome some of the abovementioned limitations, both techniques have difficulties in detecting lymph node metastases when they show a normal appearance. Additionally, primary tumor boundaries on CT and MRI images may be vague when there are inflammatory changes around the tumor or when metal artifacts hamper image interpretation. PET (positron emission tomography) and SPECT (single photon emission tomography) may offer a solution to solve these problems for certain clinical situations. As opposed to CT and MRI, SPECT and PET imaging provides biological information. Using this information, a more specific, biological target volume rather than morphological target may be delineated which may help to guide customized dose delivery. For instance, the use of specific markers to visualize biological pathways known to influence response to ionizing radiation (e.g. tumor hypoxia and proliferation) could lead to delineation of sub-target volumes for delivering an extra boost dose.

2.2 Basic Technology: SPECT and PET Imaging

The gamma camera is an imaging device that is able to detect scintillations (flashes of light) produced when gamma rays, resulting from radioactive decay, interact with a thallium doped sodium iodide crystal at the front of the camera [1]. The scintillations are detected by photomultiplier tubes (PMTs), and whilst the areas of crystal seen by tubes overlap, the location of each scintillation can be computed from the relative response in each tube. The energy of each scintillation is also measured from the response of the tubes, and the electrical signal to the imaging computer consists of the location and photon energy. In front of the crystal resides a collimator, which is made of lead and usually manufactured with multiple elongated holes (parallel-hole collimator). The holes allow only gamma rays that are traveling perpendicularly to the crystal face to enter. In conventional planar gamma camera imaging the gamma photons absorbed by the crystal therefore form a projection of the distribution of the radiopharmaceutical

in front of the camera. In SPECT imaging the camera is rotated around the patient and several projections at different angles are acquired, tomographic images can be generated through the use of specific reconstruction algorithms [2].

As with SPECT, positron emission tomography (PET) relies on computerized reconstruction procedures to produce tomographic images, however, by means of indirectly detecting positron-emission [3]. Positrons when emitted by radioactive nuclei will combine with an electron from the surroundings and annihilate. Upon annihilation both the positron and the electron are then converted to electromagnetic radiation in the form of two high-energy photons which are emitted 180° away from each other. It is this annihilation radiation that can be detected externally and is used to measure both the quantity and the location of the positron emitter. Simultaneous detection of two of these photons by detectors on opposite sides of an object places the site of the annihilation on or about a line connecting the centers of the two opposing detectors. At this point mapping the distribution of annihilations by computer is allowed. If the annihilation originates outside the volume between the two detectors, only one of the photons can be detected, and since the detection of a single photon does not satisfy the coincidence condition, the event is rejected.

Since radioisotopes suitable for PET have a short half-life (e.g., 110 min for ^{18}F, an on-site cyclotron is needed for production of such isotopes [4]. Also, special radiosynthesis facilities are required restricting the availability of non-commercially available PET-radiopharmaceuticals to specialized centers. Opposed to PET, the synthesis of SPECT radiopharmaceuticals is mostly less expensive. As the half-lives of the isotopes used in SPECT are longer than those of isotopes used in PET (hours vs minutes), longer acquisition times are also possible in SPECT. This may, for instance, allow receptor imaging at equilibrium, a prerequisite in order to obtain reliable information with respect to relative receptor density measurements. On the other hand, the resolution of a conventional PET camera is twice as good as that of a conventional gamma camera and PET allows for more accurate quantification when compared to SPECT.

2.3 PET and SPECT Tracers of Interest for 3D-image Characterization of Tumors for IMRT Planning

2.3.1 FDG

The most widely used PET tracer in oncology imaging is 2-^{18}fluoro-2-deoxy-glucose (FDG) [5]. The rationale behind its use is the finding of an increased rate of glucose consumption in malignant tissues, due to an increase of glycolytic enzymes and of the number of glucose transporters expressed on malignant cells [6–8]. After injection, FDG is transported by facilitated diffusion into neoplastic cells where it is phosphorylated by hexokinase and subsequently trapped as it is not a substrate for the subsequent enzymatic driven pathways for glucose metabolism. As the neoplastic cells accrue larger amounts of FDG due to their increased metabolism, increased activity is detected that delineates the hypermetabolic tumor from the surrounding normal tissues. Since its first application in the detection of primary brain tumors, FDG PET has been increasingly used for its ability to detect primary malignant tumors, but also for its ability to detect both regional and distant metastases, distinguish benign from malignant tissue or recurrent cancer from treatment-related scarring, and document response to therapy [9]. A major limitation of FDG PET is the limited spatial resolution, approximately 5–8 mm for ^{18}F with current PET machines [10]. Below a threshold of twice this resolution, due to partial volume effect, tracer activity will be underestimated eventually leading to false-negative results. On the other hand, as leucocytes and macrophages also accumulate FDG, when selecting for FDG PET, data obtained in patients presenting with inflammatory conditions should be closely correlated to conventional imaging as to avoid false-positive findings [11].

Several, mainly retrospective studies, have provided evidence that the detection of hypermetabolic tumor tissue by means of FDG PET may lead to a better definition of the clinical target volume, i.e. the local and regional extension of the neoplastic disease. Available data on FDG PET and IMRT are scarce and limited to patients suffering from cervical cancer, non- small cell lung cancer (NSCLC) and squamous cell carcinoma of the head and neck (SCCHN).

Mutic et al. evaluated a treatment planning method for dose escalation to the para-aortic lymph nodes (PALNs) based on FDG PET with IMRT in four cervical cancer patients with PALN involvement [12]. The treatment plans for the four patients revealed that escalated prescription doses could be delivered to target volumes while maintaining acceptable doses to the surrounding critical structures. More specifically, radiation doses could be escalated from the conventional 45 Gy to 59.4 Gy for the gross target volume (positive PALNs defined on FDG PET) and 50.4 Gy for the clinical target volume (para-aortic bed). The data indicate that PET-guided IMRT could be used in a clinical trial in an attempt to escalate doses delivered to patients with cervical cancer who have positive PALNs. The guidelines regarding the selection of the appropriate treatment parameters (e.g., number of beams, beam geometry) and organ specific parameters (e.g., importance weighting

and tolerance dose) for IMRT planning when aiming for a goal dose of 50.4 Gy to the clinical target volume and of 59.4 Gy to the gross volume where described in a separate paper.

Grills et al. evaluated four different techniques of radiation therapy, respectively IMRT, limited and optimized three-dimensional conformal radiotherapy (3D-CRT) and traditional radiotherapy, used to treat non-small cell lung cancer and also determined their efficacy in meeting multiple normal-tissue constraints while maximizing tumor coverage and achieving dose escalation [13]. In this series the target volume was delineated using information from both the treatment planning CT and the treatment planning PET scan to create a composite tumor/nodal volume. The primary tumor volume ($GTV_{primary}$) was defined on the PET scan using a previously defined formula, respectively [(0.3069 × mean standardized uptake value) + 0.583]. GTV_{nodal} included all lymph nodes larger than 1 cm on CT scan and all lesions smaller than 1 cm on CT scan that were positive on FDG PET. The clinical target volume (CTV) was defined as 0.5 cm 3D expansion of the $GTV_{primary}$ + the GTV_{nodal}. The planning target volume was defined as the CTV with appropriate margin to compensate for variability in internal target motion due to respiration or other internal motion, as well as variability in patient set-up. Their data show that whereas IMRT is of limited additional value (compared to 3D-CRT) in node-negative cases, it is beneficial in node-positive patients and in patients with target volumes close to the esophagus. When meeting all normal- tissue constraints in node-positive patients, IMRT can deliver RT doses 25–30% greater than 3D-CRT and 130–140% greater than traditional radiotherapy.

Scarfone et al. defined conventional GTVs, FDG PET GTVs and final FDG PET/CT GTVs, based on co-registered images, in six patients suffering from SCCHN [14]. The resulting PET/CT GTV was larger than the original CT GTV volume by an average of 15% with the CT GTV being modified in five out of six patients.

2.3.2 Proliferation Markers

A non-invasive, reliable and repeatable technique allowing assessment of tumor proliferation would constitute a useful tool to the radiotherapist to estimate the potential of repopulation of clonogens during radiotherapy. Information obtained by such techniques would allow for a customized "dynamic" dose delivery to "clonogenic" subvolumes when performing IMRT.

Radiolabeled Thymidines and Derivatives

Tumor cell proliferation has been studied extensively using autoradiography to detect uptake of tritiated thymidine into cellular DNA. The proportion of labeled cells at a short interval after administration of tritiated thymidine (the labeling index) is a measure of the proportion of cells that were in S-phase and thus actively dividing [15, 16]. Unfortunately, assessment of the labeling index requires invasive biopsy and is invariably subject to sampling errors. Accordingly, radiolabeled thymidines, respectively 2-[^{11}C]-thymidine, [methyl-^{11}C]thymidine and ^{18}F-fluorothymine, as well as halogenated deoxyuridines, respectively ^{76}Br-deoxyuridine, ^{123,131,124}I-deoxyuridine and ^{18}F-fluorodeoxyuridine, were developed for imaging tumor proliferation [17]. Out of these, both 2-[^{11}C]-thymidine and [methyl-^{11}C]thymidine as well as ^{76}Br-deoxyuridine and ^{123,131,124}I-deoxyuridine are rapidly metabolized, resulting in high background activity and low tumor uptake. In contrast, ^{18}F-fluorothymidine is much more resistant to in vivo degradation and is more avidly taken up by tumor tissues. As initial clinical results suggest ^{18}F-fluorothymidine tumor uptake values significantly correlate with tumor proliferative status, this tracer may prove of interest for IMRT planning.

Radiolabeled Amino Acids

Amino acids uptake by cells is largely mediated by carriers that are either sodium dependent, e.g. system A, ASC and Gly that transport amino acids with short, polar or linear side chains such as alanine, serine and glycine, or sodium independent, e.g. system L, $B^{o,+}$ and system y^+ that are transporters of branched chain and aromatic amino acids, such as leucine, valine, tyrosine and phenylalanine [18–21]. Tumors generally show increased pooling of amino acids, amongst others by up- regulation of carriers, e.g. system A [22, 23]. Although part of the pooled amino acids in tumor tissue is shuttled into protein synthesis, a fraction will be used for other purposes, e.g. metabolic fuel. In general, the fraction of radiolabeled amino acids that is incorporated into proteins is small as compared to the total amount that is taken up by the cell [24, 25]. Nevertheless, despite the fact that imaging shows the sum of both fractions, usually the total amino acid signal generated relates to tumor proliferation. Furthermore, as inflammatory cells have a low protein metabolism as compared to glucose metabolism, radiolabeled amino acid uptake in tumor tissue is less obscured by interfering uptake in concomitant inflammatory tissues than is the case for FDG [26–28]. As a result, radiolabeled amino acid imaging could allow for a better discrimination between tumor tissue and inflammatory tissue and thus also in a more appropriate tumor volume delineation when considering radiation treatment planning.

To date, virtually all amino acids have been radiolabeled for tumor imaging by means of PET. However, given their ease of synthesis and limited metabolite formation following intravenous injection in man, ^{11}C-methyl-methionine (MET) and ^{11}C-tyrosine (TYR) have

been most extensively studied. Evidence that their uptake reflects tumor proliferation in vivo in humans has so far only been provided for ^{11}C-methyl-methionine. Changes in ^{11}C-methyl-methionine uptake were shown to reflect response to radiotherapy treatment in patients suffering from a wide variety of tumors. Studies implementing ^{11}C-methione for IMRT planning may prove worthwhile.

2.3.3 Hypoxia Markers

For a number of tumors, radiotherapeutic treatment may fail due to the presence of tumor hypoxia ($pO_2 < 5$ mm). For instance, approximately 80% of head and neck squamous cell carcinoma have significant hypoxic fractions ($pO_2 < 2.5$ mm Hg) while the figure for carcinoma of the uterine cervix is around 50% [29–31]. One approach to overcome hypoxic tumor resistance is to escalate radiation dose. However, increasing radiation indiscriminately may increase normal tissue complication rates in areas where critical structures are in close proximity of gross tumor or a high-risk surgical bed, e.g. head and neck cancer. PET or SPECT-guided imaging of hypoxia could provide a novel avenue to escalate radiation doses, without compromising normal tissue function.

Several investigators have focused on the development of radiolabeled compounds that are selectively retained in hypoxic areas and can be visualized non-invasively and repetitively by means of SPECT or PET. The chemical basis for most of these compounds has been to incorporate a 2-nitroimidazole moiety to act as a bioreductive molecule accepting a single electron and producing a free radical anion which, after further reduction, is then incorporated into cell constituents under hypoxic conditions. To date, four of these radiopharmaceuticals have been injected in oncological patients, respectively the N-1 substitute 2-nitroimidazole derivatives ^{1}8F-misonidazole (^{18}F-MISO) and ^{123}I-iodoazomycin arabinoside (123-IAZA) and the bioreductive non imidazole moiety containing ^{99m}Tc-2,2′-(1,4-diaminobutane)bis(2-methyl-3-butanone)dioxime (^{99m}Tc HL91) and ^{60}Cu-diacetyl-bis(N-4-methylthiosemicarbazone) (^{60}Cu-ATSM) [32–40]. Although the mechanisms of tumor accumulation of both ^{99m}Tc HL91 and ^{60}Cu ASTM have yet to be clarified, it is believed that the ^{99m}Tc and ^{60}Cu complexes are bio-reducible groups by themselves [40, 41]. Out of these four tracers, ^{60}Cu ASTM has the best tracer kinetics, allowing imaging as early as 10 min following tracer injection with high enough contrast to identify hypoxic tumor sub-volumes. Importantly, ^{60}Cu-ASTM retention occurs only in cells with intact mitochondria, allowing straightforward discrimination of necrotic from hypoxic cells. The feasibility of ^{60}Cu-ASTM guided IMRT was recently demonstrated in a patient suffering from head and neck carcinoma [42].

2.3.4 Apoptosis Markers

Since its recognition as a major form of cell death after radiation, apoptosis is being increasingly studied as a marker of cellular radiosensitivity and prognosis for radiotherapy treatment outcome. The positive correlation of tumor response to radiation and the background level of apoptotic cells seen in murine systems raises the possibility of developing the in-vivo visualization of apoptosis as an assay for defining subvolumes for IMRT planning. If the spontaneous level of apoptosis plays a similar role in tumor responsiveness to radiation in humans, then patient tumor subvolumes whose pretreatment biopsy specimens exhibit low levels of apoptosis may benefit from higher local treatment doses.

Annexin V binds to membrane-bound phosphatidyl serine (PS), a constitutive anionic membrane phospholipid that is normally restricted to the inner leaflet of the plasma membrane lipid bilayer but is selectively exposed on the surfaces of cells as they undergo apoptosis (programmed cell death) [43]. To date, Annexin V has been fluorinated for PET and radioiodinated and coupled to a wide variety of linker molecules such as diamide dimercaptide (N_2S_2) or hydrazino nicotinamide for complexation with ^{99m}Tc for SPECT. In particular in vivo uptake of ^{99m}Tc-radiolabeled annexin V as assessed by means of SPECT imaging was shown to allow for non-invasive monitoring of cell death dynamics and effectiveness of therapies aimed at reducing cell death in patients suffering from myocardial infarction and reperfusion injury as well as in viral and auto-immune myocarditis and nonischemic cardiomyopathies [44–47]. Studies assessing in vivo quantitative ^{99m}Tc-Annexin V uptake in human tumors and their relationship to radiotherapy outcome as well as its potential to modulate radiation treatment planning are underway.

2.3.5 Others

Advances in fundamental radiobiology suggest that improvements in tumor control can be achieved through strategies that combine radiation and molecular targeting. One approach which is currently being clinically evaluated is to target specific molecules involved in tumor cell survival after irradiation, using inhibitors of EGFR or Ras [48]. Because of tumor heterogeneity and the existence of multiple tumor radio-resistance pathways, an extension of this approach being investigated at the pre-clinical level is to use Hsp90 inhibitors as a means of reducing the levels of multiple radioresponse

regulatory proteins. In addition, it may also be possible to target normal tissue processes, such as angiogenesis, to enhance the radioresponse of tumors. Finally, an alternative approach to combining radiation and molecular targeting is to exploit radiation-induced gene expression to induce targets for other modalities or to increase their effectiveness. Several studies have demonstrated that radiosensitivity of cells may be influenced by the addition of a wide variety of exogenous growth factors or hormones in receptor positive cells before or after irradiation. The tissue radiation interactions resulting in the increase of radiosensitivity are complex and still poorly understood. PET and SPECT tracers allowing in vivo assessment of the local tumor distribution of these molecular targets may help to delineate subvolumes of interest for dose-increase. For instance, when administering EGFR-blocking antibodies as radiotherapeutic adjuvant, areas of low or absent EGFR expression may benefit from higher dose-delivery in IMRT planning.

2.4 Discussion and Future Prospects

Till recently, traditional radiation treatment planning relied solely on density imaging such as chest radiographies and CT in order to obtain anatomic information of structures of interest for treatment, including target and normal tissue. The advent of FDG PET has now made it possible to exclude or include particular areas based on their level of glucose metabolism. A limited number of studies, respectively in NSCLC-, cervix- and head and neck carcinoma suggest that integration of information obtained by means of FDG PET in intensity modulated radiotherapy is feasible. In these patient populations, recurrences following radiotherapy are mainly located in the high- dose-prescription regions, suggesting the need for even higher doses in these areas. Inclusion of areas of increased FDG tumor uptake in the target definition process for these malignancies may provide information that is complementary to conventional CT and may result in target volumes that contain proliferating tumor burden. If these volumes are small, focused dose escalation of large magnitude can be attempted which might result in improved local control by IMRT. The medical significance of including these additional data in the original treatment plan on final patient outcome will than need to be determined prospectively.

Aside from FDG, in the future new and more specific radiopharmaceuticals are likely to become routinely available that may permit a more accurate imaging of tumor clonogen density to complement the information gained by FDG and CT. Of special interest are SPECT and PET radiopharmaceuticals for the evaluation of tumor hypoxia, angiogenesis, apoptosis and receptor status, variables that play an important role in determining the outcome of radiation therapy. In this regard, the study by Chao et al. demonstrating the feasibility of ^{60}Cu-ATSM-guided IMRT following co-registration of hypoxia ^{60}Cu-ATSM PET images to the corresponding CT images for IMRT planning is worth mentioning.

To the degree that PET provides physiologic data not available on CT, hybrid PET/CT treatment volumes may reduce the risk of geographic misses, particularly when using IMRT to constrict treatment volumes. When reviewing differences between CT and PET target volumes, however, careful consideration will need to be given to the quality of the co-registration and its potential role in these differences.

References

1. Eberl S, Zimmerman RE (1998) Nuclear medicine imaging instrumentation. In: Muray IPC, Ell PJ (eds) Nuclear medicine in clinical diagnosis and treatment. Churchill Livingstone, Edinburgh, pp 1559–1569
2. Bailey DL, Parker JA (1998) Single photon emission computed tomography. In: Muray IPC, Ell PJ (eds) Nuclear medicine in clinical diagnosis and treatment. Churchill Livingstone, Edinburgh, pp 1589–1601
3. Meikle SR, Dahlbom M (1998) Positron emission tomography. In: Muray IPC, Ell PJ (eds) Nuclear medicine in clinical diagnosis and treatment. Churchill Livingstone, Edinburgh, pp 1603–1616
4. Boyd RE, Silvester DJ (1998) Radioisotope production. In: Muray IPC, Ell PJ (eds) Nuclear medicine in clinical diagnosis and treatment. Churchill Livingstone, Edinburgh, pp 1617–1624
5. Jones T (1996) The imaging science of positron emission tomography. Eur J Nucl Med 23:807–813
6. Som P, Atkins HL, Bandoypadhyay D et al. (1980) A fluorinated glucose analogue, 2-fluoro-2-deoxy-D-glucose (F-18): non-toxic tracer for rapid tumour detection. J Nucl Med 21:670–675
7. Warburg O (1956) On the origin of cancer cells. Science 123:309–314
8. Flier JS, Mueckler MM, Usher P, Lodish HF (1987) Elevated levels of glucose transport and transporter messenger RNA are induced by ras or src oncogenes. Science 235:1492–1495
9. Weber WA, Avril N, Schwaiger M (1999) Relevance of positron emission tomography (PET) in oncology. Stralenther Onkol 175:356–373
10. Dahlbom M, Hoffman E, Hoh CK, Schiepers C, Rosenqvist G, Hawkins RA, Phelps ME (1992) Whole- body positron emission tomography: part I. Methods and performance characteristics. J Nucl Med 33:1191–1199
11. Strauss LG (1996) Fluorine-18 deoxyglucose and false-positive results: a major problem in the diagnostics of oncological patients. Eur J Nucl Med 23:1409–1415
12. Mutic S, Malyapa RS, Grigsby PW et al. (2003) PET-guided IMRT for cervical carcinoma with positive para-aortic lymph nodes-a dose-escalation treatment planning study. Int J Radiat Oncol Biol Phys 55:28–35
13. Grills IS, Yan D, Martinez AA, Vicini FA, Wong JW, Kestin LL (2003) Potential for reduced toxicity and dose escalation in the treatment of inoperable non-small-cell lung cancer: a comparison of intensity-modulated radiation therapy (IMRT), 3D

conformal radiation, and elective nodal irradiation. Int J Radiat Oncol Biol Phys 57:875–890
14. Scarfone C, Lavely WC, Cmelak AJ, Delbeke D, Martin WH, Billheimer D, Hallahan DE (2004) Prospective feasibility trial of radiotherapy target definition for head and neck cancer using 3-dimensional PET and CT imaging. J Nucl Med 45:543–552
15. Mendelsohn ML (1960) The growth fraction: a new concept applied to tumours. Science 132:1496–1503
16. Slingerland JM, Tannock IF (1987) Cell proliferation and cell death. In: Tannock IF, Hill RP (eds) The basic science of oncology, 3rd edn. McGraw- Hill, New York, pp 134–165
17. Van de Wiele C, De Bondt P, Peeters M, Vermeersch H, Dierckx RA (2002) Radiolabelled thymidines and deoxyuridines for measuring cellular proliferation in tumours – an update. Nucl Med Commun 23:925–931
18. Souba WW, Pacitti AJ (1992) How amino acids get into cells: mechanisms, models, menus and mediators. J Parenter Enteral Nutr 16:569–578
19. Christensen HN (1990) Role of amino acid transport and countertransport in nutrition and metabolism. Phys Rev 70:43–77
20. Oxender DL, Christensen HN (1963) Distinct mediating systems for the transport of neutral amino acids by the Ehrlich cell. J Biol Chem 238:3686– 3699
21. Shotwell A, Jayme DW, Killberg M et al. (1981) Neutral amino acid transport systems in Chinese hamster ovary cells. J Biol Chem 256:5422–5427
22. Isselbacher KJ (1972) Sugar and amino acid transport by cells in culture: differences between normal and malignant cells. N Engl J Med 286:929–933
23. Busch H, Davis JR, Honig GR et al. (1959) The uptake of a variety of amino acids into nuclear proteins of tumors and other tissues. Cancer Res 19:1030–1039
24. Argiles JM, Costelli P, Carbo N et al. (1999) Tumour growth and nitrogen metabolism in the host. Int J Oncol 14:479–486
25. Souba WW (1993) Glutamine and cancer. Ann Surg 218:715–728
26. Kubato K, Yamada S, Kubota R et al. (1992) Intratumoral distribution of fluorine-18-fluorodeoxyglucose in vivo: high accumulation in macrophages and granulation tissues studied by microautoradiography. J Nucl Med 33:1972–1980
27. Kubota R, Kubota K, Yamada S et al. (1995) Methionine uptake by tumor tissue: a microautoradiographic comparison with FDG. J Nucl Med 36:484–492
28. Kubota K, Matsuzawa T, Fujiwara T et al. (1989) Differential diagnosis of AH109A tumor and inflammation by radioscintigraphy with L-[methyl-11C]-methionine. Jpn J Cancer Res 80:778–782
29. Fyles AW, Milosevic M, Wong R et al. (1998) Oxygenation predicts radiation response and survival in patients with cervix cancer. Radiother Oncol 48:149–156
30. Hockel M, Schlenger K, Hockel S, Vaupel P (1999) Association between tumor hypoxia and malignant progression: the clinical evidence in cancer of the uterine cervix. In: Vaupel P, Kelleher DK (eds) Tumour hypoxia. Wissenschaftliche Verlagsgesellschaft mbH., Stuttgart, pp 65–74
31. Nordsmark M, Overgaard M, Overgaard J (1996) Pretreatment oxygenation predicts radiation response in advanced squamous cell carcinoma of the head and neck. Radiother Oncol 41:31–39
32. Koh WJ, Rasey JS, Evans ML et al. (1992) Imaging of hypoxia in human tumors with (F-18)fluoromisonidazole. Int J Radiat Oncol Biol Phys 22(1):199–212
33. Koh WJ, Bergman KS, Rasey JS et al. (1995) Evaluation of oxygenation status during fractionated radiotherapy in human non-small cell lung cancers using (F-18)fluoromisonidazole positron emission tomography. Int J Radiat Oncol Biol Phys 33(2):391–398
34. Rasey JS, Koh WJ, Evans ML et al. (1996) Quantifying regional hypoxia in human tumors with positron emission tomography of (F-18)fluoromisonidazole: a pretherapy study of 37 patients. Int J Radiat Oncol Biol Phys 36(2):417–428
35. Parliament MB, Chapman JD, Urtasun RC et al. (1992) Non-invasive assessment of human tumour hypoxia with 123I-iodoazomycin arabinoside: preliminary report of a clinical study. Br J Cancer 65:90–95
36. Urtasun RC, Parliament MB, McEwan AJ et al. (1996) Measurement of hypoxia in human tumors by non-invasive spect imaging of iodoazomycin arabinoside. Br J Cancer 74:S209-S212
37. Groshar D, McEwan AJB, Parliament MB et al. (1993) Imaging tumor hypoxia and tumor perfusion. J Nucl Med 34:885–888
38. Cook GJR, Houston S, Barrington SF, Fogelman I (1998) Technetium-99m-labeled HL91 to identify tumor hypoxia: correlation with Fluorine-18-FDG. J Nucl Med 103:39–99
39. Van de Wiele C, Versijpt J, Dierckx RA, Moerman M, Lemmerling M, D'Asseler Y, Vermeersch H (2001) Technetium-99m-labelled HL91 versus CT and biopsy for the visualisation of tumour recurrence of squamous head and neck carcinoma. Nucl Med Commun 22:269–275
40. Takahashi N, Fujibayashi Y, Yonekura Y et al. (2000) Evaluation of Cu-62 labeled diacetyl- bis(N-4-methoylthiosemicarbazone) as a hypoxic tissue tracer in patients with lung cancer. Ann Nucl Med 14(5):323–328
41. Siim BG, Laux WT, Rutland MD, Palmer BN, Wilson WR (2000) Scintigraphic imaging of the hypoxia marker (99m)technetium-labelled 2, 2′-(1,4-diaminobutane)-bis(2-methyl-3-butanone)dioxime (Tc-99m-labeled HL-91; Prognox): Noninvasive detection of tumor response to the antivascular agent 5.6-dimethylxanthenone-4-acetic acid. Cancer Res 60(16):4582–4588
42. Chao KS, Bosch WR, Mutic S et al. (2001) A novel approach to overcome hypoxic tumor resistance: Cu-ATSM-guided intensity-modulated radiation therapy. Int J Radiat Oncol Biol Phys 49(4):1171–1182
43. van Engeland M, Nieland LJW, Ramaekers FCS et al. (1998) Annexin-V-affinity assay: a review on an apoptosis detection system based on phosphatidylserine exposure. Cytometry 31:1–9
44. Narula J, Acio ER, Narula N et al. (2001) Annexin-V imaging for noninvasive detection of cardiac allograft rejection. Nature Med 7:1347–1352
45. Hofstra L, Liem IH, Dumont EA et al. (2000) Visualisation of cell death in vivo in patients with acute myocardial infarction. Lancet 356:209–212
46. Blankenberg FG, Vriens PW, Tait JF et al. (1998) Non-invasive detection and quantification of acute heart transplant rejection using 99mTc radiolabeled annexin V (Abstr). Radiology 1337
47. Narula J, Acia ER, Narula N et al. (2000) Phase-I Tc99m-Annexin-V imaging study in heart transplant rejection: can noninvasive detection of apoptosis in cardiac allografts obviate the need for endomyocardial biopsy (Abstr). Circulation 102:3714
48. Harari PM, Huang SM (2004) Combining EGFR inhibitors with radiation or chemotherapy: will preclinical studies predict clinical results? Int J Radiat Oncol Biol Phys 58:976–983

Magnetic Resonance Imaging for IMRT

Lynn J. Verhey, Cynthia Chuang, Andrea Pirzkall

3

Contents

3.1 Introduction

The planning of radiotherapy has evolved rapidly in the past 10 to 15 years, from two-dimensional treatment planning based on projection images, to three-dimensional planning based on thin-section computerized tomography (CT) and, more recently, to computer-optimized planning using CT anatomical images combined with other imaging information from modalities such as MR, PET and SPECT. These other modalities can add information about tissue identification, tissue boundaries and tissue function that can be extremely important in both the diagnosis and treatment of cancer.

Methods of radiation treatment delivery have also evolved rapidly in recent years. The linear accelerator control systems are now primarily digital and are capable of delivering and controlling large numbers of patient-specific beams in a short period of time. The introduction and nearly universal adoption of the multileaf collimators for two-dimensional beam shaping, combined with computer-controlled beam delivery, has virtually eliminated the need for radiation therapists to enter the room during a patient treatment, thereby making the daily treatments much more efficient. Finally, the introduction of intensity modulated radiotherapy (IMRT) in the mid-1990s makes possible the delivery of higher doses to defined tumors while keeping constant, or reducing, the dose to surrounding sensitive tissues.

These new capabilities for sophisticated treatment planning and treatment delivery can be effectively used only if the target volumes and critical normal tissues can be accurately defined on the treatment planning CT study. In particular, magnetic resonance imaging (MRI) is capable of providing excellent soft tissue definition, unrestricted multiplanar and volumetric imaging data as well as functional information with the addition of spectroscopy (MRSI).

This chapter will concentrate on the use of MR data in the planning of precision radiotherapy, especially IMRT and conformal radiotherapy (3DCRT), technical aspects of MRI and MRSI including potential and limitations, current clinical applications of MRI and MRSI and future directions for research and development. The role of PET and SPECT in IMRT is discussed elsewhere in this volume [1].

3.2 Use of MR Data in IMRT and 3DCRT Treatment Planning

Clearly, MRI provides soft tissue contrast that can be critically important for the definition of target and sensitive organs for precision radiotherapy. There are technical issues, however, that need to be considered before these images can be used. First, the spatial accuracy of the MRI data needs to be assured. This accuracy is a function of the linearity of the magnetic field gradients in the MR magnet as well as eddy currents [2]. These system distortions tend to be larger at the edges of the magnet than in the center, so are a larger problem when imaging the pelvis than the head and neck. With good quality assurance, the distortions should be no larger than the basic uncertainty of the MR pixel

location, which is typically less than 3 mm [3]. System distortions can be measured and corrected through the use of phantoms of known geometry. Such a system can reduce the uncorrected distortions to less than the imaging uncertainty of 1–2 mm. Second, the MR data must be registered relative to the CT data that are needed for dose calculations. This process is called image fusion [4, 5]. Three-dimensional image fusion is relatively easy in areas such as brain [6] and head and neck, where there are numerous anatomical landmarks and where structures can be considered fixed in position. It becomes much more difficult in areas such as the pelvis and thorax, where organs move due to variable filling of neighboring organs or breathing. In some cases, such as the pelvis, only qualitative image fusion might be possible [7]. Powerful imaging tools make it possible to verify the accuracy of the image fusion prior to the radiotherapy planning process [8]. In some cases, such as stereotactic irradiation of intracranial targets, MRI images can be used as primary planning data, because the approximation of uniform water-equivalent tissue density along each beam path is quite good in the brain.

The use of MRI to augment CT in treatment planning for head and neck tumors has become rather routine [9]. This is due to the critical importance of accurate delineation of sensitive normal organs within the head and neck region. Often the gross tumor volume (GTV) can be observed either with contrast-enhanced CT or with gadolinium-enhanced MRI. The clinical target volume (CTV), however, is often a large volume containing nodal volumes and many tissues not explicitly defined as normal tissues. MRI is capable of defining sensitive normal tissues within the image that can be critical in the definition of a treatment plan. Typically, treatment plans are created by selecting beam directions that avoid most of the sensitive normal tissues defined with the assistance of MR, although for IMRT, inverse planning methods are capable of creating excellent dose plans simply by defining the desired doses to defined targets and normal tissues.

3.3 Technical Aspects of MRI and MRS

Magnetic resonance imaging (MRI) is a non-invasive imaging technique that makes use of the fact that certain atomic nuclei, such as ^{1}H, ^{31}P, ^{19}F, and ^{13}C, have inherent spin properties that allow them to acquire discrete amounts of energy in the presence of a static magnetic field. The application of electromagnetic fields (non-ionizing radiofrequency radiation) at right angles to a static magnetic field causes these nuclei to jump to higher energy levels. After removal of the electromagnetic fields, the nuclei subsequently drop back to their original spin states by emitting electromagnetic radiation at a rate that can be characterized by their T1 (spin-lattice) and T2 (spin-spin) relaxation times. A receiver coil detects the emitted radiation and records the time domain of the MR signal that, once processed using a Fourier transform, reveals the spectrum of intensities and frequencies of the nuclei from different chemical species within the excited volume. The location of peaks in the spectrum defines the chemicals within the sample; the peak intensity reflects their concentration. Conventional MRI uses the properties of the protons from water to obtain information about their spatial distribution in different tissues. Specialized radiofrequency pulses and magnetic field gradients are used to label the water signal as a function of space and, after appropriate post-processing, provide an anatomic image of the changes in proton density and relaxation properties.

MR spectroscopic data are typically acquired by suppressing the large signal from water and allowing the properties of other compounds to be recorded and analyzed. Water suppressed 1H spectroscopy techniques are commercially available for obtaining spectra from selected regions within the brain and prostate and can be combined with additional localization techniques to produce either a single spectrum from a region of interest (single-voxel MRS) or a multidimensional array of spectra from the region of interest (3D multivoxel MRS, MRSI, chemical shift imaging (CSI)). The peaks in individual spectra reflect the relative concentrations of cellular chemicals within that spatial location. The peak heights and/or areas under the curve relate to the concentration of the respective metabolites; differences in these concentrations can be used to distinguish "normal/healthy" tissue from neoplastic or necrotic tissue. As an efficient method for obtaining arrays of spatially localized spectra at spatial resolutions of 0.2 to 1 cc, 3D multivoxel MRSI is of greater potential value than single-voxel MRS in target delineation and monitoring response to therapy and allows the generation of maps of the spatial distribution of cellular metabolites. This is an ideal representation for integrating the information into RT treatment planning. Fig. 1 shows 3D-MRSI superimposed on an axial T1 post-contrast MRI for a patient with GBM.

A significant advantage of ^{1}H-MRSI over other metabolic imaging techniques is that the data can be obtained as part of a conventional MRI and the data can be directly overlaid upon each other. This enhances the display of metabolic data and allows it to be correlated with the anatomy as revealed by MRI, thereby allowing areas of anatomic abnormality to be directly correlated with the corresponding areas of metabolic abnormality. As will be described below, the combination of conventional MRI imaging with MRSI metabolic data and with anatomic CT, promises to vastly improve the definition of both tumor volumes and normal tissues as required

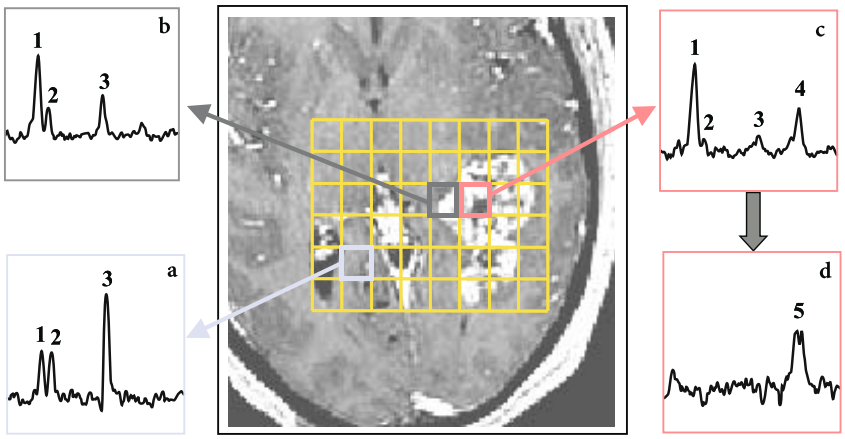

Fig. 1a–d. Patient with left temporo-occipital GBM. Axial T1 post contrast MRI shows typical contrast enhancement (CE) with central necrosis. 3D-MRSI performed within a defined area using short-echo point-resolved spectroscopy (referred to as PRESS box), represented by gridlines, reveals metabolic signature of examined brain tissue. Four examples of spectral patterns are given detecting the following metabolites: 1) choline (Cho), 2) creatine (Cr), 3) *N*-acetylaspartate (NAA), 4) lipid (Lip), and 5) lactate (Lac). **(a)** Normal brain tissue marked by high peak of NAA and low peak of Cho. The resulting Cho-to-NAA ratio is therefore low (about 1 : 2). Cho and Cr are exhibiting similar peak heights. **(b)** Tumor spectrum characterized by an increase of Cho and a decrease in NAA as compared to the normal tissue voxel **(a)**. The Cho-to-NAA ratio is high (about 1 : 0.5). (Note that the spectrum is derived from a single voxel that contains only partially CE.) **(c)**, **(d)** Mix of tumor and necrosis revealed by lactate edited sequences which are postprocessed to separate Lip and Lac that overlap due to resonating at the same frequency. **(c)** Summed spectrum shows peaks of high Cho and extremely diminished NAA (Cho-to NAA ratio is about 1 : 0.3), and in addition, the presence of Lip. (Note that the spectrum is derived from a single voxel that contains partially CE and macroscopic necrosis.) **(d)** Difference spectrum allows quantification of Lac as a marker of hypoxia. The Cho-to-NAA-Index (CNI) values for the above voxels are: **(a)** −0. 6, **(b)** 3.6, **(c)**+ **(d)** 3.4

for full exploitation of highly conformal radiotherapy delivery methods such as IMRT.

3.4 Clinical Applications of MRI/MRS

Accurate delivery of the prescribed dose to target volumes is essential for successful local control of diseases. Technological advancement has led to the widespread use of three-dimensional conformal radiation therapy and intensity modulated radiation therapy (IMRT) in recent years. The goal of IMRT is to tailor radiation dose to be highly conformal to the three- dimensional shape of the tumor target, and to minimize radiation damage to the surrounding sensitive tissues. This high conformality of IMRT plans often allows dose escalation of the tumor target while keeping the critical normal tissue dose within tolerance.

3.4.1 Recent Advances in MR Imaging

To be truly able to realize the potential offered by IMRT, accurate target delineation is essential. Recent advances in magnetic resonance imaging and magnetic resonance spectroscopy imaging have the potential to offer better target delineation in multiple tumor sites and for different tumor types, thus facilitating the use of IMRT and other highly conformal radiotherapy methods for those tumors.

One of the recent advances in MR is Dynamic Contrast Enhanced MRI (DCE-MRI), which has made the successful transition from methodological development to clinical validation, and is now rapidly becoming a mainstream clinical tool [10]. DCE-MRI was developed in the mid-1990s, in which fast spoiled gradient echo sequences are performed with rapid sampling, approximately 5 – 10 s per image after the administration of a bolus of intravenous contrast medium. It allows the study of the microcirculation of tumors and normal tissues. Enhancement of a specific body tissue depends on a wide variety of factors, including vascularity, capillary permeability, renal clearance and volume, and composition of extracellular fluid [11].

After the intravenous administration of paramagnetic, low-molecular-weight contrast medium, the contrast will pass through the capillary bed and be confined transiently within the vascular space. The contrast then passes rapidly into the extravascular-extracellular space at a rate determined by the permeability of the microvasculature, its surface area and blood flow [10]. Therefore, tumor will be visualized with high contrast, due to greater microvascular permeability and diameter, increased blood flow and volume. The contrast enhancement will eventually appear in the normal tissue. Both T1 and T2* weighted MR sequences can be used to detect the initial vascular phase, thus enabling tissue perfusion and blood volume estimation.

The tracer kinetic principle-based two-compartment pharmacokinetic model has been used to study blood volume, permeability or extraction flow effects, provid-

ing estimates of relative blood volume (rBV), relative blood flow (rBF), and mean transit time (MTT) [10]. Methods using time-signal intensity curves (TIC) and parameters, such as Time of peak enhancement (Tpeak), initial and mean gradient of the rise of enhancement curves, rate of enhancement, maximum signal intensity and washout ratio (WR) have also been used to semi-quantitatively [11] study the dynamic contrast enhanced effects as a means of differentiating between tumor and benign lesions.

3.4.2 Applications in Head and Neck Cancer

DCE-MRI has been used recently for differentiating between malignant and benign lesions for salivary gland tumors [12] and solitary pulmonary nodules [13], diagnosis and screening of breast lesions [14–19], assessment of metastatic cervical lymph nodes [20], staging of urinary bladder cancer [21], and possible identification of malignant lymphoma of the head and neck [22].

Yabuuchi et al. used DCE-MRI to examine 33 salivary gland tumors in 29 patients. Time of peak enhancement (Tpeak) and washout ratio (WR) were correlated with microvessel count and cellularity-stromal grade obtained from histopathological evaluation. It was determined that a Tpeak of 120 s and a WR of 30% had high sensitivity and specificity for differentiation between malignant and benign salivary gland tumors, demonstrating that DCE-MRI could be very effective for these tumors [12].

Asaumi et al. conducted a small study of DCI-MRI of lymphoma of head and neck in which they studied 18 lymphoma lesions in 8 patients. It was found that the contrast intensity curves showed a relatively rapid increase, reaching a maximum at 45–120 s, and a relatively rapid decrease in most lesions. These patterns may suggest characteristic features useful for distinguishing malignant lymphomas from other lesions [22].

3.4.3 Applications in Breast Cancer

Many studies have utilized DCE-MRI for breast cancer diagnosis and screening. In the study done by Heinisch et al., in which 40 lesions in 36 patients were studied, MRI was more sensitive than FDG-PET in disclosing malignant breast tumors. DCE-MRI was also more accurate than FDG-PET in the assessment of multifocal disease. Although the authors did speculate that the lower sensitivity of FDG-PET compared to MRI seems to be due to difficulties in reliably imaging lobular carcinomas [17] and carcinomas smaller than 10 mm.

The most significant and largest study is from a collaborative study by the Magnetic Imaging Screening Study Group. 1909 eligible women, including 358 carriers of germ-line mutations, were screened. During the study, 51 tumors (44 invasive cancers, 6 ductal carcinomas in situ, and 1 lymphoma) and 1 lobular carcinoma in situ were detected within a median follow-up period of 2.9 years. The sensitivity of clinical breast examination, mammography, and MRI for detecting invasive breast cancer was 17.9, 33.3, and 79.5%, respectively, and the specificity was 98.1, 95.0, and 89.8%, respectively. The overall discriminating capacity of MRI was significantly better than that of mammography ($P < 0.05$) [16].

3.4.4 Applications in Lung and Elsewhere

Schaefer et al. studied 51 solitary 5–40 mm pulmonary nodules, out of which 27 were malignant. It was found that stronger enhancement, higher maximum peak and faster slope characterized malignancy for solitary pulmonary nodules. Malignant nodules also exhibited more significant washout [13].

Fischbein et al. used time to peak enhancement, peak enhancement, maximum slope and washout slope for their study of DCE-MRI of cervical lymph nodes of 21 patients with newly diagnosed squamous cell carcinomas. It was found that Tpeak was longer, the peak enhancement and the maximum slope of wash-in were lower, and that washout was slower in tumor-involved lymph nodes [20].

Barentsz et al. stated that DCE-MRI results in improved local and nodal staging, aided in improved separation of transurethral granulation tissue and edema from tumor, and also helped in monitoring and evaluating the effects of chemotherapy [21].

There are other technical advances in the acquisition pulse sequencing that are enabling better detection and characterization of other types of tumors. Ohno et al. have used short inversion time inversion-recovery (STIR) turbo spin-echo (TSE) MR imaging in 110 patients with non-small cell lung cancer for the detection and differentiation of metastases in Mediastinal and Hilar lymph nodes. By using lymph node to saline ratios (LSR), it was found that metastases have higher LSR. Quantitative analysis of LSR showed that sensitivity was 93%, and specificity was 87% [23]. Plathow et al. have used dynamic MRI to examine intrathoracic tumor mobility during breathing cycle in 20 patients. They used three images per second and measured positions of the diaphragm, upper, middle, and lower lung regions, and the tumor in three dimensions for both the deep inspiratory and expiratory breathing positions. It was found that lower lung regions move more significantly than the upper regions, and that tumor motion shows a high variability during quiet respiration [24].

Although the above-described applications of MR are very useful for screening and diagnosis of cancer, they are also of great potential value for the quantitative defi-

nition of the gross tumor volume required for precision radiotherapy.

3.4.5 Potential Applications of MRSI in Treatment Planning for Radiotherapy

Two major disease sites will be discussed with respect to the potential and actual incorporation of MRS imaging into the treatment planning process for RT: prostate cancer and brain gliomas. Imaging protocols for both disease sites are described in detail elsewhere [25–27].

3.4.6 MRSI for Brain Gliomas

High-grade gliomas (HGG) comprise up to 86% of newly diagnosed primary CNS tumors in the adult population

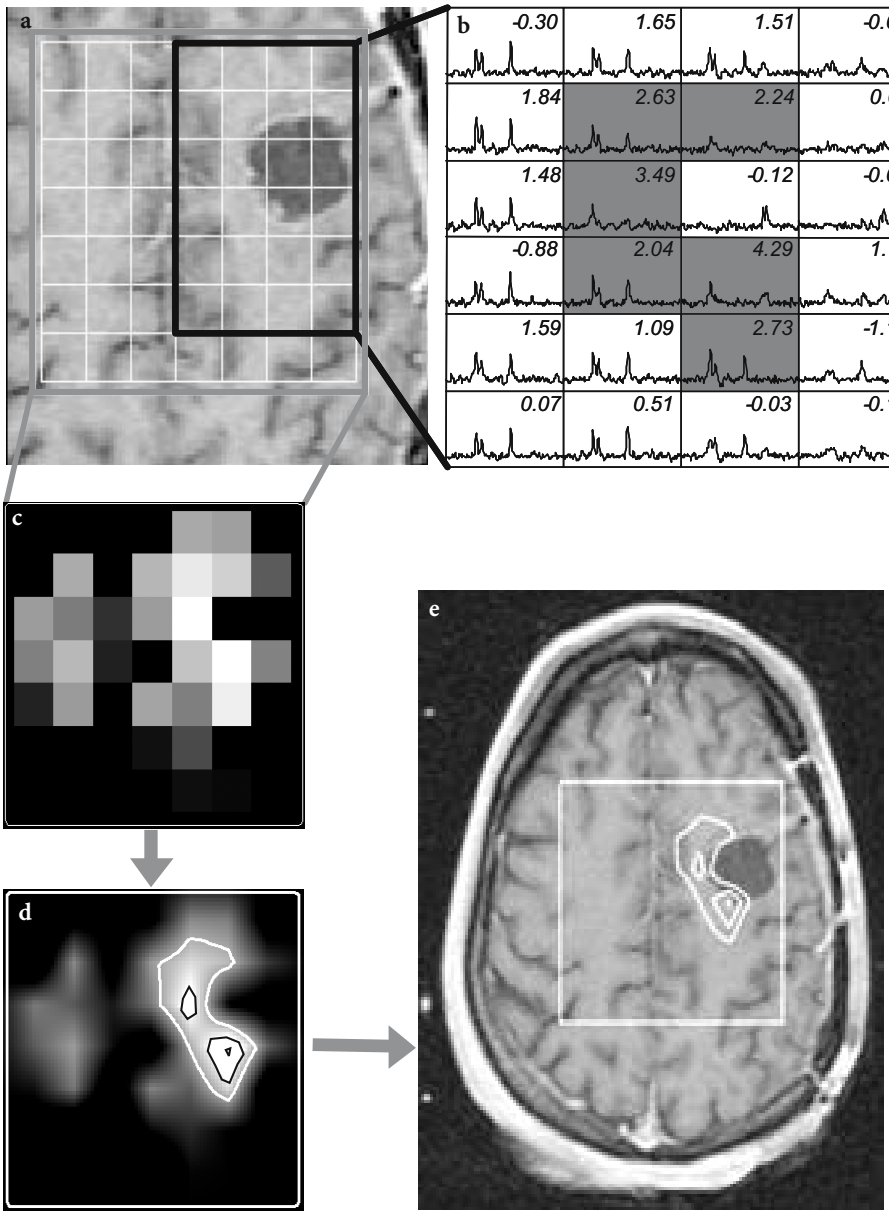

Fig. 2a–e. Patient with recurrent, initially low-grade, glioma; status post resection and fractionated RT with 59.4 Gy. A subsequent boost with Gamma Knife (GK) radiosurgery was planned based upon MRI/MRSI: **(a)** T1 weighted axial MRI with superimposed MRSI PRESS box; **(b)** enlarged spectra and actual Cho-to- NAA Index (CNI) for a subset of voxels in immediate vicinity of the resection cavity. *Shaded voxels* highlight those with a CNI of ≥ 2; **(c)** gray scale CNI image; the brighter the voxels the higher the respective CNI; **(d)** high resolution CNI image resulting from sampling the low resolution CNI image to match the resolution of the MR image. Superimposed are CNI contours of 2 (*bright line*), 3 (*dark middle contour*) and 4 (*dark inner contour*) as a result of interpolation; **(e)** CNI contours of 2, 3 and 4 superimposed onto the respective MRI slice in preparation for treatment planning

age 35 to 64 years, with an increasing percentage in advanced ages [28]. Despite multimodality treatment approaches including surgery, radiation therapy and chemotherapy, the prognosis for patients with HGG remains dismal. Median survival averages 9–12 months for patients with grade IV (glioblastoma multiforme, GBM) and 20–36 months for patients with grade III (anaplastic astrocytoma, AA) gliomas [29]. Dose escalation appears to be needed because the local failure rate remains very high after treatment using conventional doses of 60 Gy with conformal radiation therapy (CRT) [30]. One possible reason for this continued failure could be the use of inappropriate target volumes for high dose delivery.

The current target definition for RT of brain gliomas encompasses the extent of abnormality on MRI (contrast enhancement on T1 weighted images and hyperintensity seen on the T2 weighted images) enlarged by several centimeters [31]. Using this definition, a rather large volume of uninvolved brain tissue may be exposed unnecessarily and the dose that can be safely delivered may be limited by the risk of complications. This suggests that there would be value in restricting the dose prescription to the tumor extent only and possibly direct higher doses to smaller subregions of more aggressive tumor, a targeting and dose prescription process that is ideally realized through the use of IMRT.

Several studies have been performed to quantify the difference of spatial extent derived from MRI vs MRSI, respectively, in patients with high-grade and low-grade gliomas. A measure for metabolic abnormality based on ratios of metabolite levels (CNI) was used to compare the spatial extent and heterogeneity of metabolic (MRSI) and anatomic (MRI) information in patients with newly diagnosed [32] and surgically resected [33] gliomas in order to explore the value that MRSI might have for defining the target for radiation therapy in brain gliomas. Significant differences have been found between anatomic and metabolic determinants of volume and spatial extent of the neoplastic lesion for patients with newly diagnosed HGG [32]. These findings suggest that MRSI-derived volumes are likely to be more reliable in defining the location and volume of microscopic and actively growing disease when compared to conventional MRI.

Preliminary evaluation of MRSI follow-up exams that were performed post-RT has shown a predictive value for MRSI with respect to focal recurrence [33]. For ten patients without contrast enhancing residual disease following surgical resection we have been able to establish a spatial correspondence between areas of new CE, developed during follow-up, and areas of CNI abnormality, as assessed after surgery but prior to RT. We found a very strong inverse correlation between the volume of the CNI abnormality and the time to onset of new contrast enhancement; the greater the volume of CNI, the shorter the time to recurrence. Fig. 2 shows a patient with low grade glioma post-resection with areas of high CNI adjacent to the surgical cavity. This information can be used to define a boost target volume for radiotherapy. MRSI has also proved to be of value in predicting overall survival in patients with GBM; the larger the volume of the CNI abnormality the shorter the survival [33].

Additional metabolic indices have been evaluated by Li et al. [34]. These studies suggest that tumor burden, as measured with either the volume of the metabolic abnormalities or the maximum magnitude of the metabolic indices, correlates with the degree of malignancy. The spatial heterogeneity within the tumor, and the finding that metabolic disease activity appears to extend beyond MRI changes, may be responsible for the continuing failure of current treatment approaches.

3.4.7 MRI Combined with MRSI for Prostate Cancer

Conventional MRI of the prostate relies on signal intensities that are due to morphological changes within the gland that can help define the presence and extent of cancer [35]. The optimal current technique uses a combination of an endorectal coil and a pelvic external coil array to produce high resolution T2-weighted images that can be used to differentiate prostatic zonal anatomy, prostate cancer and surrounding soft tissues [27]. Unfortunately, these images are still lacking metabolic information that can accurately define the presence and spatial extent of active tumor. By combining metabolic information from MRSI with the excellent morphological information of MRI, it becomes possible to obtain a clear picture of the location of active foci of tumor cells within the prostate, with a high degree of confidence [27]. The quantity of the metabolites choline, citrate, creatine, which can be independently determined by MRSI, is considered an indicator of cellular activity that can be used to demonstrate the location and extent of active tumor with a high degree of specificity [36]. In particular, the ratio of the metabolites (choline + creatine)/citrate has proven to be a reliable marker of active disease. Figure 3 shows a T2-weighted axial MRI of the prostate gland with a superimposed proton spectral array identifying a focus of tumor within the left midgland. Such displays of information are now becoming routinely available at some institutions [27].

3.4.8 Other Potential Applications of MRSI for Cancer

As shown above, Magnetic Resonance Spectroscopy Imaging offers a more precise, biochemical-based tumor definition for GBM and for the prostate. Recent advances in identifying biochemical markers in other types of tumor have also emerged, and could possibly

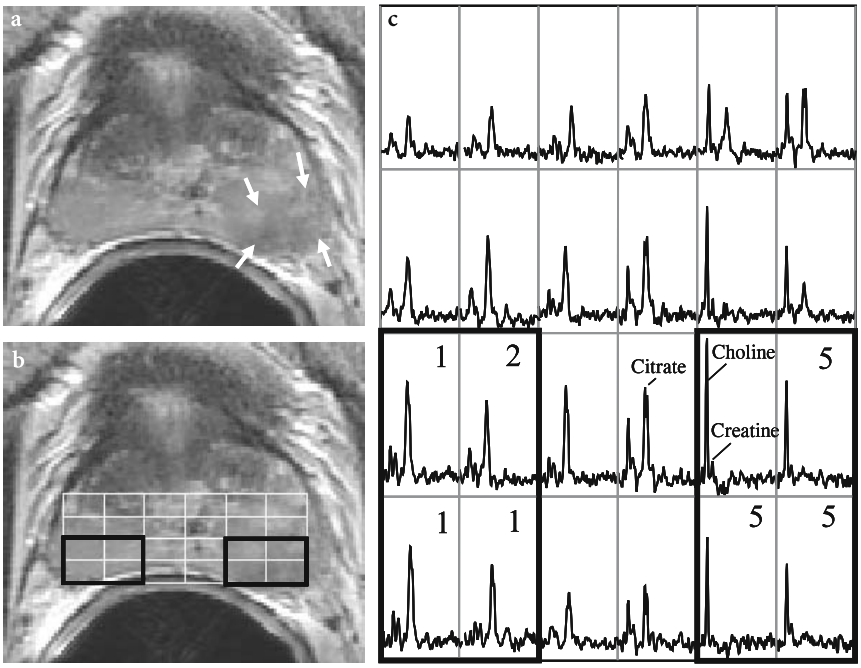

Fig. 3. (a) A representative reception-profile corrected T2 weighted Fast Spin Echo (FSE) axial image demonstrating a tumor in the left midgland to apex. (b) Superimposed PRESS selected volume encompassing the prostate with the corresponding axial 0.3 cm^3 proton spectral array. (c) Corresponding individual voxels with spectral pattern and their overall spectroscopic grading along the peripheral zone. Marked voxels suggest "definitely healthy" (1) and "probably healthy" (2) prostate metabolism on the right side but "definitely cancer" (5) on the left side in spatial agreement with the anatomic abnormality

aid in better delineation of tumor extent, most notably in breast cancer, in which spectroscopic studies of the breast have confirmed that high levels of choline- containing compounds at 3.2 ppm accumulate mostly in malignant lesions [18, 37–39].

Huang et al. studied 50 breast cancer patients using DCE-MRI and MRSI. It was determined that although DCE-MRI has great sensitivity (100%), a combined T1-weighted DCE-MRI with 1H MR spectroscopy of choline-containing compounds could increase the specificity of breast cancer detection from 62.5 to 87.5%. Further addition of perfusion MR imaging could increase the specificity up to 100% [18].

Yeung et al. used 1H MR spectroscopy to characterize different breast histopathologic subtypes and also studied the feasibility of using 1H MRS to assess axillary lymph node involvements. They found that for most cases of DCIS, the choline-to-creatine ratio was less than 1.7, which is similar to the ratio in normal breast tissue and benign lesions. However, for invasive breast cancers, choline level is consistently elevated, unless there is an extensive in situ component. The study also found that choline-containing compounds can be reliably detected in metastatic nodes in patient with breast cancer, therefore, in vivo 1H MRS of axillary lymph nodes appears to be feasible [38].

In addition to using choline for breast cancer detection, there is a report of using 1H MRS to characterize bone and soft-tissue tumors. Pui et al. performed MRS imaging in 36 patients with bone and soft-tissue tumors larger than 1.5 cm in diameter. It was found that choline was detected in 18 out of 19 patients with malignant tumors, and not detected in 14 out of 17 patients with benign tumors. The sensitivity is 95% and specificity is 82%, with accuracy of 89% [40]. This initial result is encouraging for the use of MRS imaging to accurately characterize musculoskeletal tumors.

3.4.9 Potential of MRSI for Targeting IMRT

The use of MRI/MRSI imaging data in radiotherapy treatment planning for prostate cancer has been demonstrated [7]. In particular, these investigators developed a simple IMRT treatment plan that irradiated the MRSI-positive regions within the prostate to a high dose of 90 Gy or above while simultaneously irradiating the entire prostate to a conventional dose of 72–75 Gy using conventional irradiation. Figure 4 shows a dose distribution designed with IMRT to satisfy this goal [7]. Such an application of MR methods to IMRT planning demonstrates the power of this technology, although the clinical benefit of this targeted dose escalation has not yet been proven.

The difference in spatial extent of gliomas as seen on MRSI vs MRI and the spatial heterogeneity within gliomas as assessed on MRSI in patients with a newly

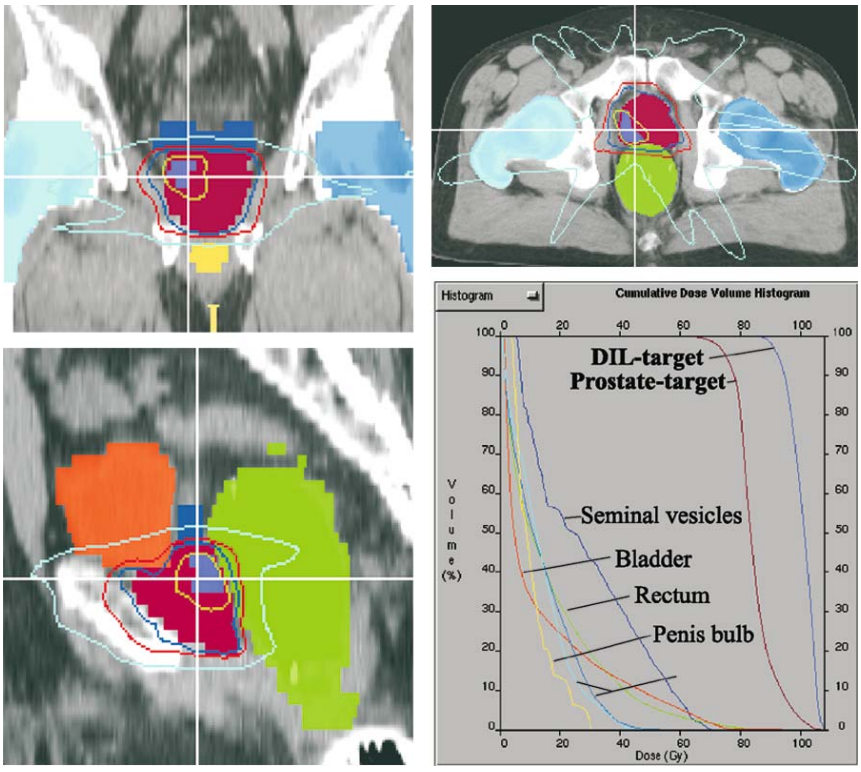

Fig. 4. Intensity modulated radiation therapy prescribing 92 Gy (*green*) to the DIL (Dominant Intraprostatic Lesion) and 73.8 Gy (*blue*) to the entire prostate while sparing surrounding normal structures (*red:* 60 Gy, *turquoise:* 25 Gy)

diagnosed brain glioma, are forcing a reassessment of our targeting and dosing concepts for the delivery of RT to malignant gliomas. IMRT offers the potential to simultaneously deliver differential doses to user-defined regions. It is critical that the regions identified for differential dose distributions be defined accurately; areas suitable for high dose must be identified separately from areas that are appropriate for lower dose. Therefore, what is required is a means of determining which region requires which dose.

The MRSI-derived CNI index, since it has been shown to correlate with active disease and to patterns of failure, appears to have potential as a guide for defining high-dose appropriate regions. However, it is not yet clear how the CNI should be used to delineate these regions. On first pass it might be assumed that regions with a high metabolic activity, indicating active disease, should be targeted. However, it also could be argued that it is the regions with a lower metabolic activity that will require a higher dose of radiation; these regions may have suffered from poor oxygenation, thus requiring a higher dose of radiation in order for the radiation to be effective in controlling the cell population. An in-depth analysis of other MRSI metabolites, such as creatine and lactate, may help differentiate regions of aerobic from regions of anaerobic metabolism, thus detecting hypoxic areas. In addition, MR-based perfusion and diffusion measuring techniques such as cerebral blood volume (CBV) and apparent diffusion coefficient (ADC) may allow an indirect determination of oxygen rich (or oxygen starved) areas. By combining the values of these indices that look at different metabolites, it may be possible to enhance interpretation of each individual component.

Applying metabolic and physiologic MR-based imaging for target guidance and utilizing the powerful capability of IMRT to increase dose selectively to appropriate areas while simultaneously prescribing a conventional dose to areas at lower risk seems an appropriate goal. The feasibility of incorporating MRSI data into the IMRT treatment planning process has been tested and methods have been established for necessary image data analysis and transfer [41, 42]. Recent studies have suggested, however, that the use of CNI abnormalities to enlarge the definition of the GTV may not be the optimal approach. These showed that the addition of CNI abnormality to the volume of contrast enhancement would increase its average volume by 60% (CNI $\geq$ 3) and 50% (CNI $\geq$ 4), relative to contrast enhancement alone [32]. Treatment of such large volumes to very high doses might not be feasible.

3.5 Future Directions

More recently, other forms of MR-based physiologic imaging have been developed, such as perfusion (PWI) and diffusion weighted imaging (DWI). Combining the

information from these imaging techniques with MRSI is likely to be of value for defining differential dose requirements for treating high-grade gliomas, and GBM in particular. MRSI seems to be more sensitive to the detection of microscopic tumor infiltration and residual disease after surgical resection as compared to MRI, PWI contributes superior information on tumor vascularity and DWI on the water content and cell density within a neoplastic lesion. We anticipate that incorporating all of these data into the treatment planning process will provide a more reliable description of the biological properties of the tumor that will be important for improving the target definition and possibly the efficacy of RT.

New, higher strength magnetic fields (7 T) are now becoming available for MR and are expected to lead to improved spatial resolution of spectroscopy data as well as improved ability to identify specific metabolites. These promising new developments in imaging promise to revolutionize our ability to define tumor cell distributions in the patient which are required for full exploitation of IMRT.

Efforts are now underway to define metabolic/physiologic imaging parameters that are indicating areas at higher risk for tumor recurrence and subsequently to consider those for higher dose prescription. Although the clinical application of MRSI for precision radiotherapy is most developed for gliomas and prostate cancer, there is every reason to believe that MRS will provide critical information on the location and tumor cell density within the defined target volumes in many other areas of the body. The superposition of metabolic information on the morphological MRI data and in turn, on the CT data needed for treatment planning, promises to provide the capability of using IMRT to "paint" 3D dose distributions that are appropriate for the local tumor cell density. Ideally, this will lead to improved local tumor control.

References

1. Van de Wiele C (2005) PET and SPECT in IMRT: Future prospects. In: Bortfeld T, Schmidt-Ullrich R, De Neve W, editors. IMRT Handbook: Concepts & Clinical Applications. Springer, Berlin Heidelberg New York (this volume)
2. Khoo VS, Dearnaley DP, Finnigan DJ et al. (1997) Magnetic resonance imaging (MRI): considerations and applications in radiotherapy treatment planning. Radiother Oncol 42:1–15
3. Hill D, Hawkes D, Gleeson M et al. (1994) Accurate frameless registration of MR and CT images of the head: applications in planning surgery and radiation therapy. Radiology 191:447–454
4. Barillot C, Lemoine D, Le Briquer L et al. (1993) Data fusion in medical imaging: merging multimodal and multipatient images, identification of structures and 3D display aspects. Eur J Radiology 17:22–27
5. Treves S, Mitchell K, Habboush I (1998) Three dimensional image alignment, registration and fusion. J Nucl Med 42:83–92
6. Graves EE, Pirzkall A, Nelson SJ et al. (2001) Registration of magnetic resonance spectroscopic imaging to computed tomography for radiotherapy treatment planning. Med Phys 28:2489–2496
7. Xia P, Pickett B, Vigneault E et al. (2001) Forward or inversely planned segmental multileaf collimator IMRT and sequential tomotherapy to treat multiple dominant intraprostatic lesions of prostate cancer to 90 Gy. Int J Radiat Oncol Biol Phys 51:244–254
8. Van den Berge DL, De Ridder MD, Storme GA (2000) Imaging in radiotherapy. Eur J Radiology 34:41–48
9. Chung N-N, Ting L-L, Hsu W-C et al. (2004) Impact of magnetic resonance imaging versus CT on nasopharyngeal carcinoma: Primary tumor target delineation for radiotherapy. Head Neck 26:241–246
10. d'Arcy JA, Collins DJ, Rowland IJ et al. (2002) Applications of sliding window reconstruction with cartesian sampling for dynamic contrast enhanced MRI. NMR Biomed 15: 174–183
11. Shah GV, Fischbein NJ, Gandhi D et al. (2004) Dynamic contrast-enhanced MR imaging. Top Magn Reson Imaging 15:71–77
12. Yabuuchi H, Fukuya T, Tajima T et al. (2003) Salivary gland tumors: diagnostic value of gadolinium-enhanced dynamic MR imaging with histopathologic correlation. Radiology 226:345–354
13. Schaefer JF, Vollmar J, Schick F et al. (2004) Solitary pulmonary nodules: dynamic contrast-enhanced MR imaging-perfusion differences in malignant and benign lesions. Radiology 232:544–553
14. Liu P-F, Debatin J, Caduff R et al. (1998) Improved diagnostic accuracy in dynamic contrast enhanced MRI of the breast by combined quantitative and qualitative analysis. Br J Radiol 71:501–509
15. Brix G, Kiessling F, Lucht R et al. (2004) Microcirculation and microvasculature in breast tumors: pharmacokinetic analysis of dynamic MR image series. Magn Reson Med 52:420–429
16. Kriege M, Brekelmans CTM, Boetes C et al. (2004) Efficacy of MRI and mammography for breast-cancer screening in women with a familial or genetic predisposition. N Engl J Med 351:427–437
17. Heinisch M, Gallowitsch HJ, Mikosch P et al. (2003) Comparison of FDG-PET and dynamic contrast-enhanced MRI in the evaluation of suggestive breast lesions. Breast 12:17–22
18. Huang W, Fisher PR, Dulaimy K et al. (2004) Detection of breast malignancy: diagnostic MR protocol for improved specificity. Radiology 232:585– 591
19. Esserman L, Wolverton D, Hylton N (2002) Magnetic resonance imaging for primary breast cancer management: current role and new applications. Endocr Relat Cancer 9:141–153
20. Fischbein N, Noworolski S, Henry R et al. (2003) Assessment of metastatic cervical adenopathy using dynamic contrast-enhanced MR imaging. Am J Neuroradiol 24:301–311
21. Barentsz JO, Engelbrecht M, Jager GJ et al. (1999) Fast dynamic gadolinium-enhanced MR imaging of urinary bladder and prostate cancer. J Magn Reson Imaging 10:295–304
22. Asaumi J-I, Yanagi Y, Hisatomi M et al. (2003) The value of dynamic contrast-enhanced MRI in diagnosis of malignant lymphoma of the head and neck. Eur J Radiol 48: 183–187
23. Ohno Y, Hatabu H, Takenaka D et al. (2004) Metastases in mediastinal and hilar lymph nodes in patients with non-small

cell lung cancer: quantitative and qualitative assessment with STIR turbo spin-echo MR imaging. Radiology 231:872–879
24. Plathow C, Ley S, Fink C et al. (2004) Analysis of intrathoracic tumor mobility during whole breathing cycle by dynamic MRI. Int J Radiat Oncol Biol Phys 59:952–959
25. Nelson SJ (2001) Analysis of volume MRI and MR spectroscopic imaging data for the evaluation of patients with brain tumors. Magn Reson Med 46:228–239
26. Nelson SJ, McKnight TR, Henry RG (2002) Characterization of untreated gliomas by magnetic resonance spectroscopic imaging. Neuroimaging Clin N Am 12:599–613
27. Kurhanewicz J, Swanson MG, Nelson SJ et al. (2002) Combined magnetic resonance imaging and spectroscopic imaging approach to molecular imaging of prostate cancer. J Magn Reson Imaging 16:451–463
28. Velema JP, Percy CL (1987) Age curves of central nervous system tumor incidence in adults: variation of shape by histologic type. J Natl Cancer Inst 79:623–629
29. Laramore GE, Martz KL, Nelson JS et al. (1989) Radiation Therapy Oncology Group (RTOG) survival data on anaplastic astrocytomas of the brain: does a more aggressive form of treatment adversely impact survival? Int J Radiat Oncol Biol Phys 17:1357–1358
30. Hochberg FH, Pruitt A (1980) Assumptions in the radiotherapy of glioblastoma. Neurology 30:907–911
31. Nakagawa K, Aoki Y et al. (1998) High-dose conformal radiotherapy influenced the pattern of failure but did not improve survival in glioblastoma multiforme. Int J Radiat Oncol Biol Phys 40:1141–1149
32. Pirzkall A, McKnight T, Graves E et al. (2001) MR-spectroscopy guided target delineation for high-grade gliomas. Int J Radiat Oncol Biol Phys 50:915–928
33. Pirzkall A, Li X, Oh J et al. (2004) 3D MRSI for resected high-grade gliomas before RT: tumor extent according to metabolic activity in relation to MRI. Int J Radiat Oncol Biol Phys 59:126–137
34. Li X, Lu Y, Pirzkall A et al. (2002) Analysis of the spatial characteristics of metabolic abnormalities in newly diagnosed glioma patients. J Magn Reson Imaging 16:229–237
35. Yu KK, Hricak H (2000) Imaging prostate cancer. Radiol Clin North Am 38:59–85
36. Kurhanewicz J, Vigneron DB, Hricak H et al. (1996) Three-dimensional H-1 MR spectroscopic imaging of the in situ human prostate with high (0.24–0.7) spatial resolution. Radiology 198:795–805
37. Kvistad KA, Bakken IJ, Gribbestad IS et al. (1999) Characterization of neoplastic and normal human breast tissues with in vivo 1H MR spectroscopy. J Magn Reson Imaging 10:159–164
38. Yeung DK, Yang W-T, Tse GM (2002) Breast cancer: in vivo proton MR spectroscopy in the characterization of histopathologic subtypes and preliminary observations in axillary node metastases. Radiology 225:190–197
39. Yeung DK, Cheung HS, Tse GM (2001) Human breast lesions: characterization with contrast-enhanced in vivo proton MR spectroscopy – initial results. Radiology 220:40–46
40. Pui M, Wang Q, Xu B et al. (2004) MRI of gynecological neoplasm. J Clin Imaging 28:143–152
41. Graves E, Pirzkall A, Nelson S et al. (2001) Registration of magnetic resonance spectroscopic imaging to computed tomography for radiotherapy treatment planning. Med Phys 28:2489–2496
42. Nelson SJ, Graves E, Pirzkall A et al. (2002) In vivo molecular imaging for planning radiation therapy of gliomas: an application of 1H MRSI. J Magn Reson Imaging 16:464–476

Molecular/Functional Image-guided Intensity Modulated Radiation Therapy

Lei Xing, Yong Yang, Daniel M. Spielman

4

Contents

4.1 Introduction

4.1.1 Molecular and Functional Imaging

For much of the last century, medical imaging has been focused on faster and more detailed anatomic pictures of the human body. The accomplishment of the visible human project of the National Library of Medicine (http://www.nlm.nih.gov/research/visible) represents perhaps one of the most important milestones in these developments. With the goal of producing a system of knowledge structures that transparently links visual knowledge forms to symbolic knowledge formats such as the names of body parts, a complete, anatomically detailed, 3D representations of the normal male and female human bodies were rendered based on transverse CT, MR and cryosection images of male and female cadavers. Medical imaging has been an integral part of radiation therapy since the discovery of X-rays and the imaging techniques, such as X-ray, CT, MRI and ultrasound (US) imaging, are the foundation for the modern radiation therapy modalities that are routinely used in clinics, such as 3D conformal radiation therapy, intensity modulated radiation therapy (IMRT), stereotactic radiosurgery, and brachytherapy. Indeed, the development of radiation therapy has strongly relied on the imaging technology and, historically, almost every major advancement in imaging science would bring radiation therapy to a new level.

In general, medical imaging is involved in all key steps of radiation treatment (Fig. 1). One of the most important uses of imaging techniques is the delineation of a tumor target. Despite the tremendous successes, the anatomic imaging techniques such as CT/MRI/US are inherently deficient in that they can only reveal spatial changes in physical properties and fail to provide basic biological information that is much needed for the optimal management of the patients. Clinically, tumor biology plays an important role in the diagnosis, treatment decision-making, and assessment of therapeutic response of various diseases. It is thus highly desirable to develop imaging techniques capable of revealing the spatial biology distribution of the patients. Toward this goal, a new branch of science, referred to as molecular imaging, is emerging as a result of research efforts in cellular biology and imaging techniques over the years. The development of cellular and molecular imaging provides significant opportunities for the radiation discipline to take the patient's biological information into the radiation therapy treatment decision-making process and to truly individualize cancer radiotherapy.

4.1.2 IMRT as a Means of Producing Biologically Conformal Dose Distributions

IMRT is an advanced form of external beam irradiation and represents a radical change in radiation oncology

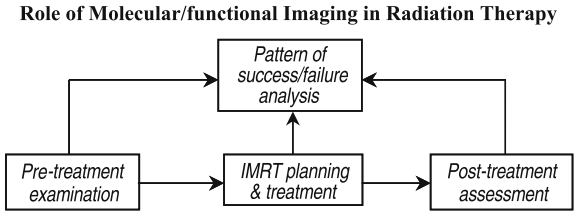

Fig. 1. A schematic of radiation treatment process. Molecular/functional imaging plays an important role in each of the key steps (represented by *blocks*) of the radiation treatment process

practice [1–3]. This new process of treatment planning and delivery shows significant potential for improving the therapeutic ratio and offers a valuable tool for dose escalation and/or radiation toxicity reduction. Preliminary published results and unpublished results from several institutions indicate that with IMRT, radiation doses to sensitive structures can be reduced significantly while maintaining adequate target dose coverage [4–15]. Because in many clinical situations the dose to the tumor volume is limited by the tolerance doses of the sensitive structures, it is considered likely that IMRT will improve local control and lead to an increase in survival rate for certain cases through dose escalation. In addition, IMRT has the potential to improve the efficacy of treatment planning and delivery in routine clinical practice with the use of computerized planning and treatment process. For details about IMRT inverse treatment planning, delivery and quality assurance, we refer the readers to the related chapters of this book.

In IMRT, each incident beam is divided into a number of beamlets (typically, the size of a beamlet is in the order of 1×1 cm), allowing us to modify the dose distribution on an individual beamlet level. Using IMRT, it is possible to produce not only spatially uniform but also non-uniform dose distributions. Recently, Ling et al. and several other researchers [16–21] have emphasized the technical capability of "dose painting" and "dose sculpting" offered by IMRT, which allows customized dose delivery to the target volume(s) with centimeter or even sub-centimeter spatial resolution. Using functional and molecular imaging techniques to identify spatial metabolic distribution and hence guide the delivery of radiation represents a paradigm shift in radiation oncology and this type of "biologically" conformal radiation therapy may provide a significant opportunity to improve conventional IMRT treatment. A timely question is how to integrate the state-of-the-art functional imaging technologies into radiation therapy techniques such as IMRT to positively impact clinical cancer management. The purpose of this chapter is to review recent progress in this endeavor and identify the important issues in the development of biologically conformal radiation therapy.

4.2 Functional and Molecular Imaging and Biologically Conformal Radiation Therapy

Current IMRT treatment plan optimization is based on the assumption of uniform biology distribution within the target volume and is aimed at achieving geometrically conformal dose distributions under the guidance of CT/MRI images. In reality, it has long been recognized that the spatial distribution of biological properties in most tumors and normal tissues are heterogeneous. With the advent of various molecular and functional imaging techniques, it is now possible to map out the biology distribution on a patient specific basis. To use the spatially heterogeneous biology information derived from the new imaging modalities to guide IMRT dose painting and sculpting process, several key problems need to be resolved. In general, the molecular/functional imaging-guided IMRT generally favors non-uniform dose distributions and requires a plan optimization formalism in voxel domain to deal with the biological heterogeneity. In addition, new methods of specifying the desired doses and a mechanism for inter- and intra-structural tradeoff, which will be explained below, must be introduced to efficiently produce metabolically/functionally conformal doses. In Fig. 2 we list the general steps of biologically conformal IMRT treatment. Each of the steps in Fig. 2 is discussed below.

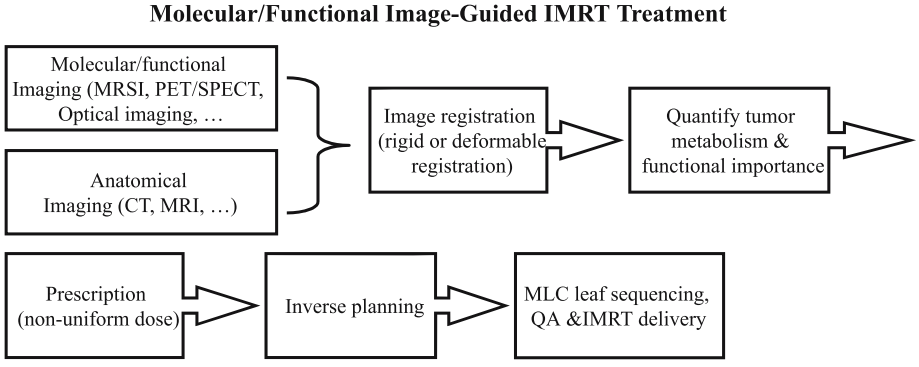

Fig. 2. Procedure of biologically conformal IMRT treatment

4.2.1 Integration of Functional and Molecular Imaging into IMRT Planning

The area of molecular/functional imaging is rapidly evolving [22–24]. Many of the molecular imaging modalities (such as fluorescent and bioluminescent imaging, optical imaging, SPECT/PET with novel isotopes/contrast agents targeting some specific molecular markers, MR spectroscopic imaging (MRSI)) are being developed for tumor specific imaging and deployed into clinical practice. Presently, MRSI, PET/SPECT and micro-bubble based ultrasound are perhaps the most mature modalities and available for guiding radiation therapy treatment. Details on various molecular and functional imaging modalities have been given elsewhere in this volume (see Verhey and van de Wiele chapters) and will not be repeated here. The remainder of this chapter will be focused on the issues related to the integration of the new imaging modalities into radiation treatment planning.

4.2.2 Image Registration

Radiation therapy treatment planning is mainly CT image-based because it provides complete geometric data and electron density information for accurate dose calculation. To utilize the biological information derived from the new image modalities, we must map the imaging data onto treatment planning CT images. The level of complexity of image coregistration depends on the imaging techniques involved and specific software tools often need to be developed in order to use some of the new imaging modalities, such as fluorescent images, endoscopic images and endorectal images. Sometimes, deformable model-based image registration is required if the shape(s) of the involved organs are deformed from its normal shape.

Let us take endorectal MRSI as an example. The introduction of endorectal surface coils significantly improves spatial resolution and signal-to-noise ratio (SNR) of prostate MR imaging and allows evaluation of tumor location, tumor volume, capsular penetration, invasion of neurovascular bundle, and seminal vesicle involvement, which is crucial for accurate treatment planning. Endorectal-coil based MRSI has also been shown effective in distinguishing between areas of cancer and normal prostatic epithelium through differences in [choline + creatine]/citrate ratio [25–28]. However, the use of endorectal probe inevitably distorts the prostate and other soft tissue organs, making it impossible to fuse directly the acquired image data onto treatment planning CT. In Fig. 3 we show the difference between endorectal coil-based MRI defined and CT-defined prostate volume [29]. In order to fuse MRI/MRSI with treatment planning CT, it is necessary to develop an effective deformable image registration procedure. Otherwise, the gain from the use of the state-or-the-art imaging techniques may be lost due to the inferior performance of image registration.

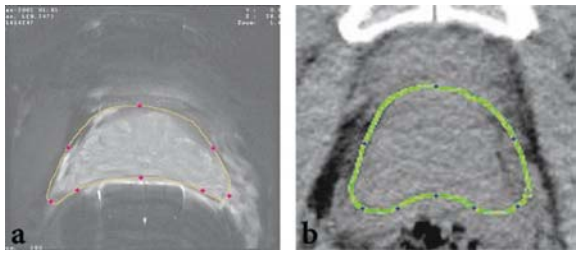

Fig. 3. Difference between endorectal coil-based MRI defined and treatment planning CT-defined prostate volumes

Zaider et al. [30] have reported a translation and scaling based registration method to map MRS positive volumes onto the CT and ultrasound images. In their approach, the coordinates of the boundary and the center of mass were used to linearly interpolate the positions of the mapped voxels. A larger discrepancy was found for regions with more severe distortion (4 mm). Lian et al. [29, 31] have developed an effective deformable image registration algorithm to map the MRI/MRSI information obtained using a rigid or inflatable endorectal probe onto CT images and to verify the accuracy of the registration by phantom and patient studies. For this purpose, a thin plate spline (TPS) transformation first introduced by Bookstein [32] was implemented to establish voxel-to-voxel correspondence between a *reference* image and a *floating* image with deformation. The idea is to find a continuous transformation to minimize the landmark difference in two images. The detailed description of the TPS transformation can be found in Bookstein's original paper [32]. To access the quality of the registration, an elastic phantom with a number of implanted fiducial markers was designed. Radiographic images of the phantom were obtained before and after a series of intentionally introduced distortions. After mapping the distorted phantom to the original one, the displacements of the implanted markers were measured with respect to their ideal positions and the mean error was calculated. Phantom studies showed that using the deformable registration method the mean landmark displacement error was 0.62 ± 0.39 mm when the distortion was of the order of 23.07 mm. A deformable model seems to be necessary to map faithfully the metabolic information onto the treatment CT images. When a non-deformable method based on a rigid-body transformation and scaling was used for the same distortion, the mean displacement of the fiducials with respect to their actual positions was found to be as large as 12.95 ± 0.57 mm. In patient studies, CT images of two prostate patients were acquired, followed by

3-Tesla (3 T) MR images with a rigid endorectal coil. For both patient studies, significantly improved registration accuracy was achieved. The prostate centroid position displacement was 0.58 ± 0.10 mm and the coincidence index was $92.6 \pm 5.1\%$ when a TPS transformation was used. Different from the non-deformable approach, the TPS-based registration accommodates the organ distortion and enables us to achieve significantly higher MRI/MRSI and CT image registration accuracy. More advanced finite element method is also developed to attack the problem [33].

4.2.3 Quality Assurance of Molecular and Functional Imaging Modalities

Any new imaging modality requires validation and quality assurance to ensure that the obtained images faithfully reflect the reality. In anatomical imaging, surrogate phantoms have been widely used for assessing the geometric and physical (e.g., electron density) properties of the images. For radiation therapy application, Mutic et al. have reported a simple design of a PET phantom to validate the image registration of PET and CT images [34]. Generally speaking, for a biological imaging modality, validation of geometric accuracy represents only one facet of the problem. The accuracy of the pixel values of the imaging modality also needs our attention. While the specific meaning of the pixel values depends on the modality, let us take an MRSI phantom (Fig. 4) constructed by Hunjan et al. as an example to illustrate the basic idea. The multi-modality, multi-purpose phantom is suitable for quality assurance testing of fusion data from MRI, MRSI and CT images [35]. The phantom contains fiducial markers that are simultaneously MR, MRS, and CT-visible. To examine the accuracy of MRSI for brain tumor, the phantom was filled with a brain-mimicking solution with an insert holding eight vials containing calibrated solutions of precisely varying metabolite concentrations that emulated increasing grade/density of brain tumor. Metabolite ratios calculated from fully relaxed 1D, 2D and 3D MRS data for each vial were compared to calibration ratios acquired in vitro using a 9.4-Tesla MR spectrometer. Figure 5 shows an axial scout scan of the MRS metabolite ratio quantitation standard showing the calibration vials 1–8. The resulting single voxel MR spectra are shown inset next to corresponding vials and a linear fit between the Choline/NAA ratio (NAA: *N*-acetyl-aspartate, see Verhey chapter, this volume) of the calibration solutions obtained at 9.4 T vs the calibration-solution-filled vials inside the phantom obtained at 1.5 T. For detailed information on the design of the phantom and measurements, please refer to [35,36].

4.2.4 Inverse Treatment Planning

In general, molecular/functional imaging could impact the current radiation therapy treatment in two fundamental aspects [16, 20, 37]. First, it offers an effective means for us to delineate more accurately the tumor and define better the treatment volume. Second, it provides valuable spatial metabolic information in the tumor and sensitive structures. While it is straightforward to modify the radiation portals to accommodate any changes in treatment volume, new methods of dose optimization and medical decision-making must be developed

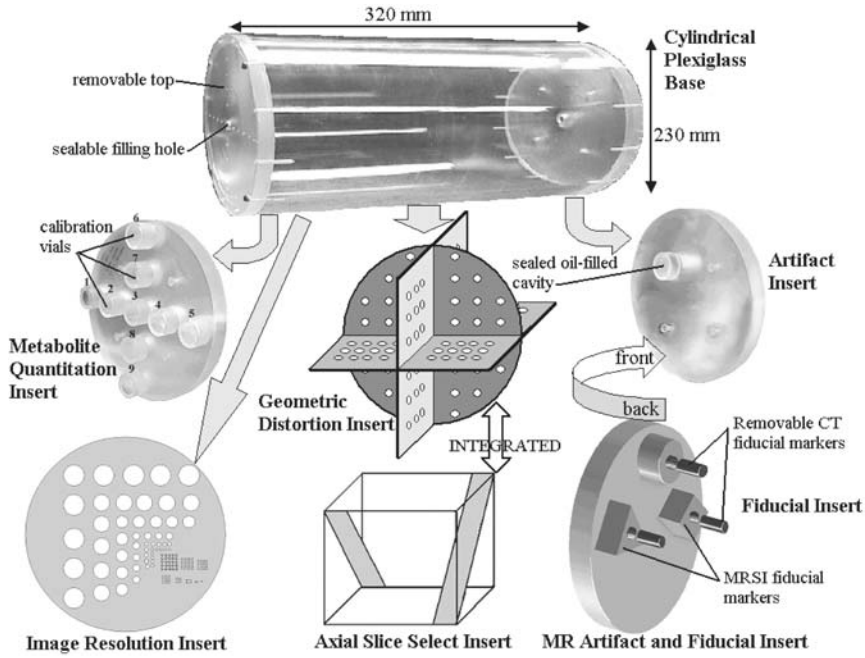

Fig. 4. A photo of quality assurance phantom built for testing/validating the geometric and metabolic accuracy of the endorectal coil-based MRI/MRSI (from Hunjan S et al. (2003) IJROBP 57:1159–1173, with permission)

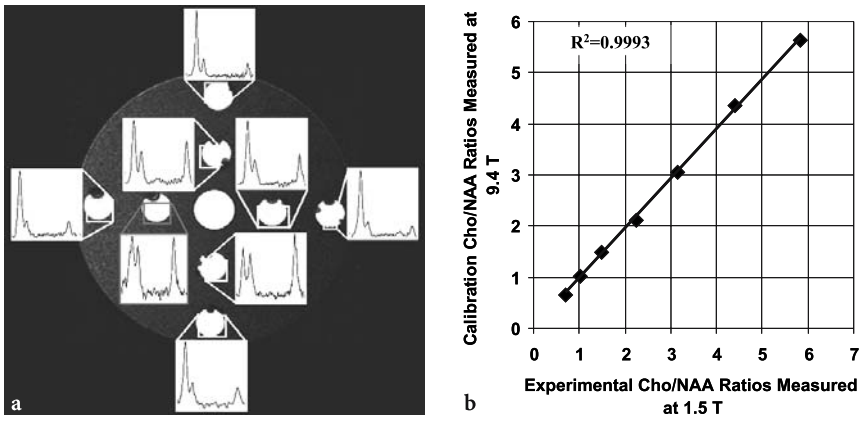

Fig. 5. (a) An axial scout scan of the MRS metabolite ratio quantitation standard showing the calibration vials 1–8. The resulting single voxel MR spectra are shown *inset* next to corresponding vials. (b) Linear relationship between the choline/NAA ratio of the calibration solutions obtained at 9.4 T vs the calibration-solution-filled vials inside the phantom obtained at 1.5 T (from Hunjan S et al. (2003) IJROBP 57:1159–1173 with permission)

to take full advantage of the metabolic information and IMRT. We have recently introduced the concept of 3D geometric plus 1D metabolic/functional inverse planning and demonstrated the integration of MRSI into IMRT planning. The goal of this type of treatment scheme is to achieve biologically conformal doses, instead of the geometrically conformal dose distribution sought by conventional radiation therapy planning. We showed that, under the guidance of MRSI metabolic maps, it is possible to prescribe a higher dose where there is resistance and/or where there are dense tumor cell populations. Similarly, the technique also allows for differential sparing of sensitive structures accounting for functionally important regions. A few important issues related to new inverse planning schemes are outlined in the following.

Relation Between Metabolic Abnormality Level and Radiation Dose

An important task in biologically conformable radiation therapy is to quantify the tumor burden and relate the metric to the radiation dose. We will derive such a relation based on a radiobiologal model under the assumption that all necessary model parameters are known. At present, the radiobiology parameters are sparse and one should perhaps take a less precise yet more practical approach. Generally speaking, the relation between the abnormality level and radiation dose can in principle be determined experimentally or through analysis of animal and hypothesis-driven clinical data, which is similar to the establishment of the empirical radiation dose prescriptions for different disease sites in our current clinical practice. A linear relation between the dose and metabolic abnormality levels [20]

$$D^t(n) = D_0^t + \kappa M(n) \tag{1}$$

was assumed in our previous study, where $D^t(n)$ is the prescribed target dose at voxel n, $M(n)$ is the abnormality level at the voxel, κ is an empirical coefficient, D_0^t can be regarded as the conventional prescription dose when functional imaging information is not available or when the abnormality level is minimum, $M(n) = 0$. The bottom line is that no subvolume in the tumor should receive a dose less than conventionally prescribed dose D_0^t unless it is clinically justifiable. For a given organ, we postulated that the tolerance dose is related to the functional importance by

$$D^c(n) = D_0^c - \alpha K(n) \tag{2}$$

where $D^c(n)$ is the tolerance dose at voxel n, $K(n)$ is the functional importance at the voxel, α is an empirical coefficient, D_0^c represents the tolerance dose corresponding to the situation when functional distribution information is not available or when the functional importance is minimum, $K(n) = 0$.

We emphasize that the above two relations are somewhat ad hoc and may need to be refined as more knowledge is gained. For treatment of prostate cancer, it seems to be a good strategy to attempt to escalate the dose to those high tumor burden points as high as possible while keeping the normal tissue complications below a certain level. In this case, the linear relations at Eqs. 1 and 2 serve as a reasonable starting point for fine-tuning or optimization.

Implementation

Some preliminary studies of incorporating metabolic information into the IMRT inverse planning has been reported by our group [20] and others and the technical feasibility of planning deliberately non-uniform dose distributions in accordance with functional imaging requirements has been demonstrated. In our preliminary study, a conventional quadratic objective function was

used with an iterative inverse planning algorithm for the optimization of the system with inhomogeneous dose prescription specified according to the method described above. The generalized quadratic objective function used for the metabolic/functional optimization problem reads [20]

$$F = \sum_{\sigma=1}^{n_\sigma} \left[\frac{r_\sigma}{N_\sigma} \sum_{n=1}^{N_\sigma} r_n \cdot \left[D_c(n) - D^p(n) \right]^2 \right] \tag{3}$$

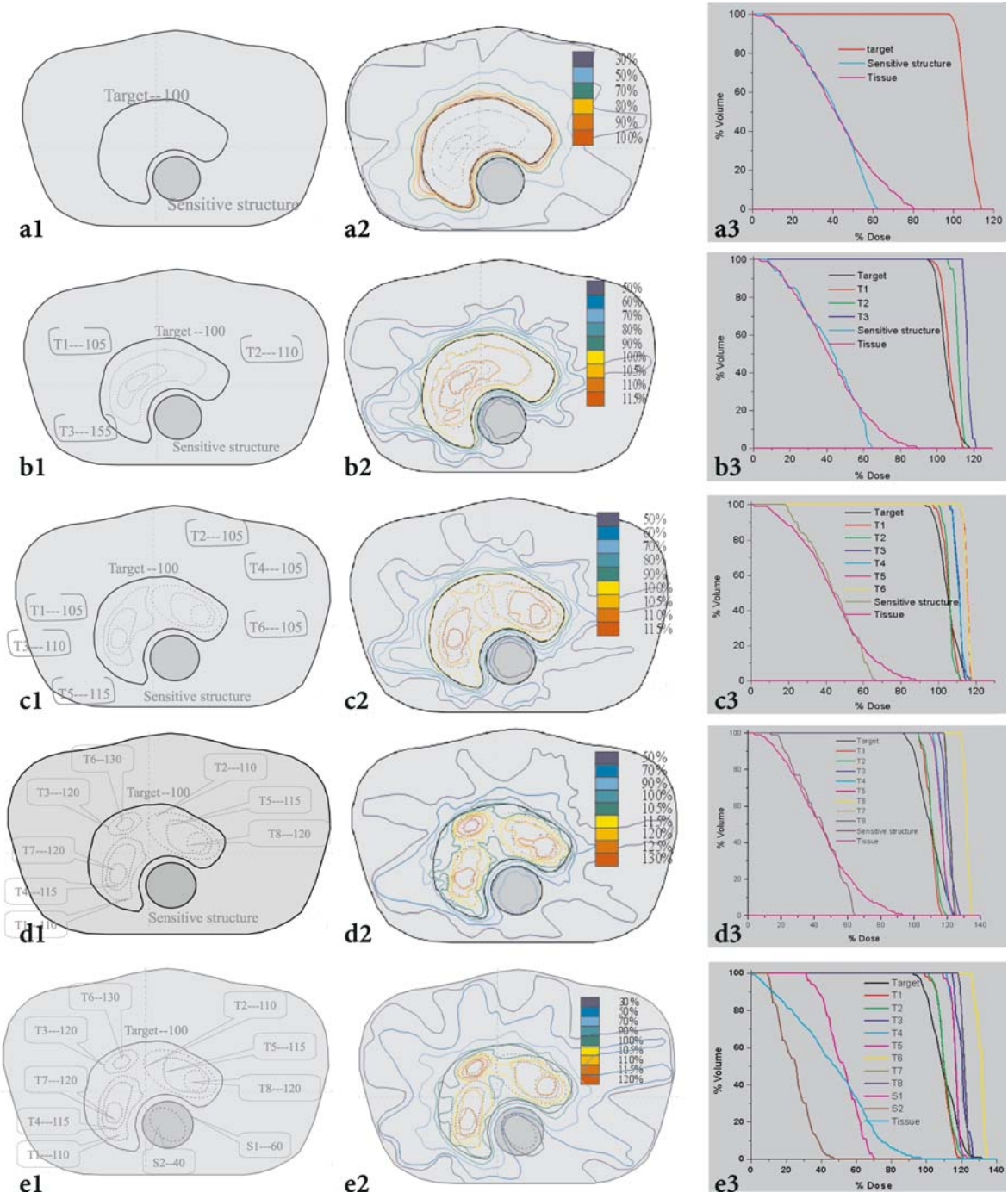

Fig. 6. An elliptical phantom case with a C-shaped target and an abutting circular sensitive structure. A few hypothetical metabolic and functional distributions are assumed: (Al) conventional case with uniform or unknown metabolic distribution; (Bl) unifocal tumor; (Cl) two foci tumor; (D1) three foci tumor; and (E1) three foci tumor and a sensitive structure with two different regions of functional importance. The second row (A2, B2, C2, D2, and E2) shows the IMRT dose distribution for each metabolic map. The corresponding DVHs for each region enclosed by two incremental abnormality levels are presented in the third row

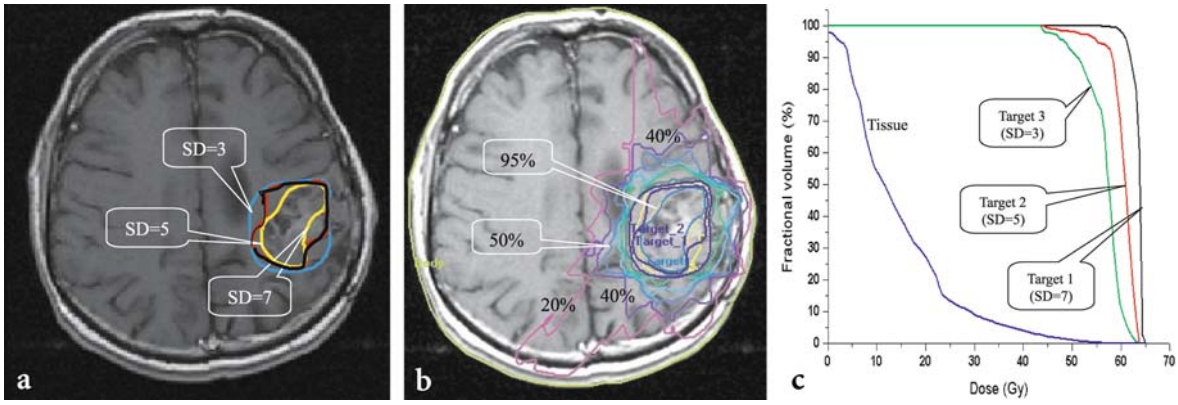

Fig. 7a–c. IMRT treatment plan for a malignant glioma case: **(a)** three abnormality levels; **(b)** the isodose distribution; **(c)** the sensitive structure and target DVH for different metabolic abnormality levels

where N_σ represents the total number of voxels of a structure, $D_c(n)$ is the calculated dose at voxel n, $D^p(n)$ is the prescribed dose given by Eqs. 1 or 2 depending on whether the voxel n belongs to the target or normal tissue. The weighting factor at a voxel n is a product of two factors, an overall factor specific to the structure σ, r_σ, and a voxel dependent component [40], r_n, describing the relative weighting of different voxels inside the structure. For voxels of organ-at-risk, for which the computed dose is lower than the tolerance dose, r_n is set to zero.

For testing purpose we constructed a phantom with a few hypothetical metabolic distributions in the tumor and functional importance distributions in the sensitive structure, as shown in top row of Fig. 6. The use of a phantom case with hypothetical functional data allows us to test systematically the performance of the algorithm effectively without going into the technical details of functional imaging modalities. In Fig. 6 we show the IMRT plans obtained for these hypothetical situations. Figure 7 shows a six-field (0°, 55°, 135°, 180°, 225° and 305° in IEC convention) IMRT glioma case. The MRSI metabolic map was discretized into three discrete levels (Fig. 7a). The level of abnormality at a point is characterized by an index based on the number of standard deviations (SD) from normal values of the choline/NAA ratio. The tumor was unifocal and 44 Gy was prescribed to the volume between the tumor boundary and the first abnormality level (AL=3) and 64 Gy was prescribed to the highest abnormal region (AL between 5 and 7).

Role of Intra-structural Tradeoff

Even in the conventional inverse planning scheme, voxels within a target or a sensitive structure volume are generally not equivalent in achieving their dosimetric goals in IMRT planning. Depending on the patient's geometry, beam modality and field configuration, some regions may have better chance to meet the prescription than others, and vice versa. It has been shown [41] that the proposed modulation of spatial penalty distribution is more advantageous over the conventional inverse planning technique with structurally uniform importance factors, leading to significantly improved IMRT treatment plans that would otherwise be unattainable. An example is given in Fig. 8, in which the isodose curves are "pushed" toward the target volume and the dose gradient at the tumor boundary is greatly increased. The significant improvement is also demonstrated in the DVH plots. It is remarkable that simply by modulating the spatial importance distribution an almost uniform reduction of $\sim$ 20% (normalized to the maximum sensitive structure dose) in the sensitive structure dose was accomplished. Conversely, the target dose can often be escalated by $\sim$ 10% while keeping the radiation toxicity at its current IMRT level.

The intra-structural tradeoff plays a more important role when dealing with biologically heterogeneous systems since non-uniform dose prescription often aggregates the competition among the voxels. The approach proposed by Shou and Xing can easily be extended for the determination of an adequate set of voxel dependent importance factors to model the intra-structural tradeoff. Briefly, once the prescription dose is given, it is possible to quantify the degree for a voxel to achieve its dosimetric goal by introducing the concept of dosimetric capability for each voxel in a target or sensitive structure. As an example, in Fig. 9 we show the capability maps obtained for a uniform dose prescription when five incident beams are involved. The capability of a voxel represents a priori dosimetric knowledge of the system. The intra-organ tradeoff is then modulated purposely using a heuristic relationship between the inherent dosimetric capability and the voxel-based weighting factors. In such a way, we can impose a differential penalty scheme and allow the system to suppress potential overdosing spots and boost the potential underdosing spots, leading to

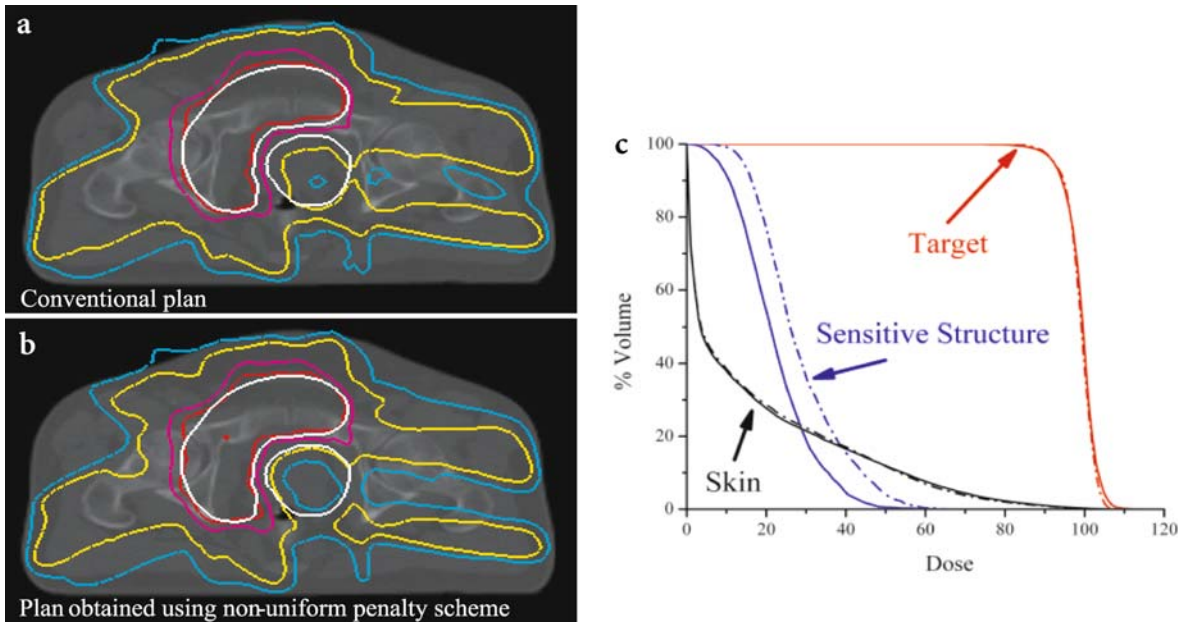

Fig. 8. Isodose distributions for plans obtained with and without penalty modulation and DVH curves. The isodose curves labeled in the plots are 105% (*red*), 100% (*pink*), 80% (*yellow*), and 40% (*blue*), respectively. In the DVH plot, the *dashed* and *solid* lines represent the results obtained without and with spatial penalty modulation, respectively

a solution that is more consistent to our clinical expectation.

The voxel based penalty scheme can also be used as a means to fine-tune the regional doses. Clinically, it happens frequently that, after optimization, the dose at all but just one or a few small regions are satisfactory and thus prevent the plan from being acceptable. The difficulty is that the location of the hot/cold region in inverse planning is generally not known until the "optimal" plan is obtained. Consequently, an "on-the-fly" mechanism is highly desirable to adaptively fine-tune the dose distribution after a solution close to the optimum is obtained. Currently, the modification can only be achieved through adjusting structure dependent system parameters (e.g., prescription, importance factors), which influence not only the dose at the region of interest but also at other areas. In order to modify the dose at a specific region, in principle, one can use ray-tracing to find the beamlets that intercept the area and adjust their intensities accordingly. But there are numerous ways to change and the optimal arrangement of the beamlet intensities is not obvious. In biologically conformal IMRT, the issue becomes more urgent. The voxel dependent penalty scheme provides a practical solution for us to modify the local dosimetric behavior effectively, as has been demonstrated in recent studies of our group [42, 43] and Wu et al. [44].

Spectral Uncertainty

In practice, molecular/functional imaging data do not always accurately reflect the actual metabolic level over the entire imaging volume because of some technical limitations (in MRSI, for example, shimming can be problematic near air-filled cavities and may strongly depend on the surface coil SNR on the spatial position). To utilize fully the metabolic information, it is desirable to develop an algorithm to incorporate numerically the spectral uncertainties (confidence map) into IMRT treatment planning. A statistical analysis-based inverse planning seems to be ideally suitable for this purpose. Assuming that the fluctuation of the spectral activity or the prescribed dose $D^p(n)$ at voxel n is specified by a probability distribution $P_n(D^p)$, we incorporate the $P_n(D^p)$ by using a statistical inference technique. Considering that currently available functional image data are not completely reliable and that missing or incomplete spectral data may occur frequently, such type of technique should be useful to minimize the effect and generate statistically optimal treatment plans. When there is no uncertainty in the spectral data, the algorithm reduces to the conventional inverse planning scheme.

Biological Model for Molecular/Functional Image-guided IMRT

Dose-based, and more recently, clinical knowledge-based models provide an immediately applicable technique for generating spatially non-uniform dose distributions. However, a biological model-based approach is more fundamental and logical in dealing biological imaging data and is worth of a detailed investigation. Two important questions in the biological

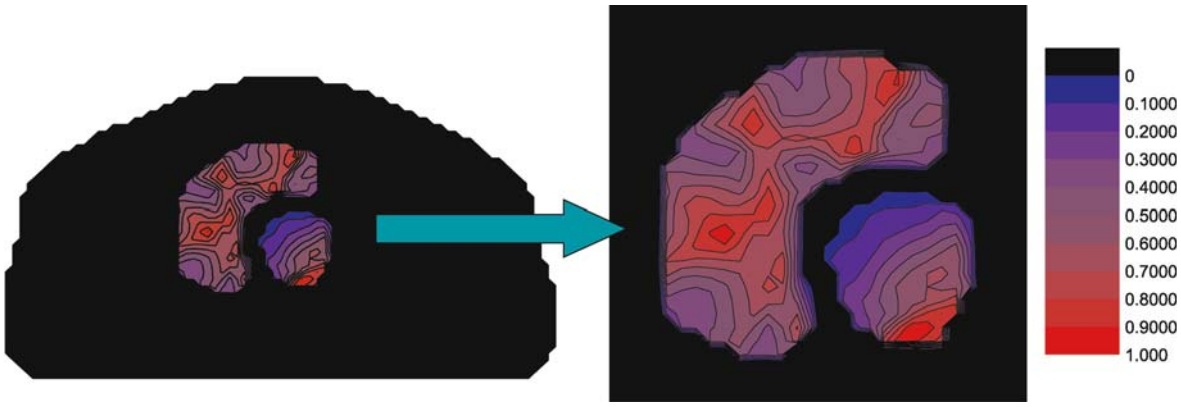

Fig. 9. Dosimetric capability map of the target and sensitive structure for a hypothetical case with five equally spaced beams. The data for each structure is normalized to unity. The *left panel* shows the complete geometry of the hypothetical structures. The capability maps of the target and sensitive structure are enlarged and shown in the *right panel*

modeling of the system are [45]: (i) how to determine the non-uniform dose prescription provided that the biology distribution is known; and (ii) how to find the optimal solution. While the latter problem is similar to that in conventional IMRT inverse planning, the solution to the first problem entails some theoretical considerations. Earlier we used the metabolic abnormality index to characterize phenomenologically the tumor burden. Using a radiobiological model, it is possible to relate the prescription dose to the more fundamental radiobiology parameters to optimize the cell killing.

Let us start with the linear quadratic (LQ) model. We include the effect of tumor cell proliferation but ignore the quadratic term. The model parameters include clonogen density (ϱ), radiosensitivety (α), and proliferation rate (γ). The time dependence of the parameters are ignored. The tumor control probability, TCP_i, for a tumor voxel i, can be expressed as

$$TCP_i = \exp\left[-\varrho_{0i} V_i \exp\left(-\alpha_i D_i + \gamma_i \Delta T\right)\right] \tag{4}$$

where V_i is the volume of voxel i, ϱ_{0i}, α_i and γ_i represent the initial clonogen density, radiosensitivety and proliferation rate in voxel i, respectively, D_i is the dose received by voxel i, and ΔT is the overall treatment time. In Eq. 4, $\gamma_i = \ln 2/T_{pi}$ where T_{pi} is the potential doubling time in voxel i. TCP for the tumor is given by

$$TCP = \prod_i TCP_i \tag{5}$$

A constraint from the normal cells within the tumor volume given by

$$\sum_i m_i D_i = E_t \tag{6}$$

should be applied to determine the tumor dose prescription, where m_i is the mass of voxel i, E_t is the integral dose in tumor. The problem now becomes to maximize the TCP under the constraint of Eq. 6, which can be solved using the method of Lagrange multipliers [46]. When the mass and volume are equal for all tumor voxels, the desired prescription dose of a voxel is given by

$$D_i = \frac{\alpha_r}{\alpha_i} D_r - \frac{1}{\alpha_i}\left(\gamma_r - \gamma_i\right)\Delta T - \frac{1}{\alpha_i}\ln\left(\frac{\alpha_r \varrho_{0r}}{\alpha_i \varrho_{0i}}\right) \tag{7}$$

where D_r is the reference dose for the voxel with reference radiobiological parameters ($\varrho_{0r}, \alpha_r, \gamma_r$). In general, D_r should be set to a value that yields a clinical sensible TCP at the reference voxel. For a given disease site, the radiation dose used in current clinical practice with "intent to cure" can be used as a good starting point in selecting the value of D_r. Once the desired dose prescription distribution is determined, IMRT inverse planning optimization can proceed by numerically maximizing the TCP while maintaining the NTCP below a certain limit. One can also take a "hybrid" approach by using the conventional objective function with the above dose prescription.

Plan Review Tools

The sheer volume of information inherent in 3D treatment designs and the corresponding dose distributions make display and objective assessment problematic. Details of a dose-distribution's spatial characteristics can be obtained by examining 2D isodose curves in a slice-by-slice fashion; however, this is a quasi-quantitative, time-consuming process and is not an efficient way to compare competing plans even for conventional IMRT. In the presence of an additional degree of freedom (metabolic abnormality), the problem is exacerbated by the breakdown of uniform dose assumption within the target volume. One of the commonly used approaches is the reliance on data reduction techniques in the quantitative assessment of alternative plans. DVH is one of the most widely used data reduction techniques. This technique enables the ready reduction of the complex 3D data set of a treatment design into the 2D display

of the fractional volume of a given structure receiving doses within a particular range. Unfortunately, this tool becomes invalid for metabolic/functional plan evaluation because of possibly non-uniform biological status of the involved structures. Metabolic/functional IMRT techniques require new plan review tools to facilitate the quantitative comparison of plans. The following are a few tools that are potentially useful for the plan review of molecular/functional image guided IMRT plans:

1. Effective dose ratio distribution: The effective dose ratio at a voxel is defined as the ratio of the physical dose and the prescribed dose. This distribution considers both the spatial dose distribution and the metabolic map and provides intuitive information on the geometric location of underdosing or overdosing regions. In this way, we can use conventional wisdom to evaluate a metabolic/functional based dose distribution. The DVH corresponding to the effective dose ratio distribution is also useful.
2. DVH clusters: In practice, not all underdosing/overdosing are equally significant and underdosing/overdosing at a certain metabolic level maybe more acceptable than at other metabolic levels. A cluster of DVHs, each corresponding to an incremental range of metabolic activity of interest, may provide useful tool to address the issue. The cluster of DVHs can be used to check the overall dosimetric behavior at an individual metabolic level. Figure 7 represents an example of a three-level DVH cluster. For a sensitive structure with functional data available, similar techniques apply.
3. Functional dose-volume histogram (FDVH): Distribution of functional importance appears to be heterogeneous in some normal organs and functional imaging modalities such as MRSI or PET/SPECT may provide valuable information about the spatial distribution of the functional importance. The FDVH, originally introduced by Lu et al. [47], Marks et al. [48], and Alber and Nusslin [49] may prove to be a useful plan review tools. A similar histogram function can be introduced for the tumor, but its usefulness needs to be justified.
4. Modified TCP and NTCP calculation tools: The conventional TCP and NTCP formula [38, 39, 50, 51] need to be modified to take into account the heterogeneous biology distribution [52–54]. This modification should be straightforward if the spatial distributions of radiobiological parameters are known. Although it is difficult to obtain quantitative results from the model calculation because of the uncertainties in the parameters, qualitative conclusions regarding the deliberately non-uniform irradiation scheme can be drawn and may shed useful insight into the problem [54].

4.3 Conclusion

The success of radiotherapy critically depends on the imaging modality used for treatment planning and the level of integration of the available imaging information. The use of functional/metabolic imaging provides us much more than a tool to delineate better the boundary of a tumor target. Together with anatomical CT or MRI images, functional imaging affords valuable 3D structural plus 1D metabolic data for both tumor and sensitive structures, valuable for guiding us to design spatially non-uniform dose distributions to deliver high doses to where the tumor burdens are high and differentially spare the sensitive structures according to the functional importance distributions. The integration and utilization of the functional data in radiation therapy treatment planning become increasingly important to improve clinical cancer management. While it is straightforward to modify the radiation portals to accommodate any changes in treatment volume, new methods of dose optimization and medical decision-making must be developed to take full advantage of the metabolic information and IMRT. How to achieve biologically conformal doses, instead of the geometrically conformal dose distribution, presents a new challenge to radiation oncology discipline. Hopefully, with the efforts from multiple institutions, the new approach of imaging, planning and decision-making will be resolved. Ultimately, whether using deliberately inhomogeneous dose distributions obtained under the guidance of functional imaging such as MRSI can improve patient survival and reduce the side effects associated with radiation treatment should be established through extensive clinical trials.

Acknowledgements. We would like to thank Drs. A. Boyer, S. Hunjan, J. Lian, C. Cotrutz, Z. Shou, P. Maxim, E. Schreibmann, Q. Le, S. Hancock, I. Gibbs, K. King, B. Daniel, D. Kim and E. Adalsteinsson for many useful discussions. We also wish to acknowledge grant support from the National Cancer Institute (1 R01 CA98523-01), National Institute of Health (P41 RR09784), the Department of Defense (DAMD17-03-1-0023), and the Vadasz Family Foundation. The authors are also grateful to the publishers of Physics in Medicine and Biology, Medical Physics, and International Journal of Radiation Oncology, Biology and Physics for their permission for using the copyrighted figures.

References

1. Webb S (2001) Intensity-modulated radiation therapy. Institute of Physics Publishing, Bristol, pp xv, 633

2. IMRT Collaborative Working Group (2001) Intensity-modulated radiotherapy: current status and issues of interest. Int J Radiat Oncol Biol Phys 51:880–914
3. AAPM IMRT Sub-committee (2003) Guidance document on delivery, treatment planning, and clinical implementation of IMRT: Report of the IMRT subcommittee of the AAPM radiation therapy committee. Med Phys 30:2089–2115
4. Carol M, Grant WH III, Pavord D et al. (1996) Initial clinical experience with the Peacock intensity modulation of a 3D conformal radiation therapy system. Stereotactic Functional Neurosurg 66:30–34
5. Ling CC, Burman C, Chui CS et al. (1996) Conformal radiation treatment of prostate cancer using inversely-planned intensity-modulated photon beams produced with dynamic multileaf collimation. Int J Radiat Oncol Biol Phys 35:721–730
6. Woo SY, Grant WH III, Bellezza D et al. (1996) A comparison of intensity modulated conformal therapy with a conventional external beam stereotactic radiosurgery system for the treatment of single and multiple intracranial lesions. Int J Radiat Oncol Biol Phys 35:593–597
7. Le QT, Xing L, Boyer AL (1999) Head and Neck IMRT – The Stanford Experience, International Symposium: 3D Conformal Radiation Therapy and Intensity Modulated Radiation Therapy in New Millenium, vol 42. Medical Physics Publishing, Houston
8. Hancock S, Luxton G, Chen Y, Xing L, Boyer AL (2000) Intensity modulated radiotherapy for localized or regional treatment of prostate cancer: clinical implementation and improvement in acute tolerance, Annual meeting of ASTRO, Boston, MA
9. Teh BS, Mai WY, Uhl BM et al. (2001) Intensity-modulated radiation therapy (IMRT) for prostate cancer with the use of a rectal balloon for prostate immobilization: acute toxicity and dose-volume analysis. Int J Radiat Oncol Biol Phys 49:705–712
10. Huang E, Teh BS, Strother DR et al. (2002) Intensity-modulated radiation therapy for pediatric medulloblastoma: early report on the reduction of ototoxicity. Int J Radiat Oncol Biol Phys 52:599–605
11. Mundt AJ, Lujan AE, Rotmensch J et al. (2002) Intensity-modulated whole pelvic radiotherapy in women with gynecologic malignancies. Int J Radiat Oncol Biol Phys 52:1330–1337
12. Mundt AJ, Roeske JC, Lujan AE et al. (2001) Initial clinical experience with intensity-modulated whole-pelvis radiation therapy in women with gynecologic malignancies. Gynecol Oncol 82:456–463
13. Chao KS, Deasy JO, Markman J et al. (2001) A prospective study of salivary function sparing in patients with head-and-neck cancers receiving intensity-modulated or three-dimensional radiation therapy: initial results. Int J Radiat Oncol Biol Phys 49:907–916
14. Lee N, Xia P, Quivey JM et al. (2002) Intensity-modulated radiotherapy in the treatment of nasopharyngeal carcinoma: an update of the UCSF experience. Int J Radiat Oncol Biol Phy 53:12–22
15. Eisbruch A (2002) Intensity-modulated radiotherapy of head-and-neck cancer: encouraging early results. Int J Radiat Oncol Biol Phys 53:1–3
16. Ling CC, Humm J, Larson S et al. (2000) Towards multidimensional radiotherapy (MD-CRT): biological imaging and biological conformality. Int J Radiat Oncol Biol Phys 47:551–560
17. Goitein M, Niemierko A (1997) Intensity modulated therapy and inhomogeneous dose to the tumor: a note of caution. Comment in: Int J Radiat Oncol Biol Phys 38(5):1138–1139; (1996) Int J Radiat Oncol Biol Phys 36:519–522
18. Macklis R, Weinhous M, Harnisch G (2000) Intensity-modulated radiotherapy: rethinking basic treatment planning paradigms. Int J Radiat Oncol Biol Phys 48:317–318
19. Rosenman J (2001) Incorporating functional imaging information into radiation treatment. Semin Radiat Oncol 11:83–92
20. Xing L, Cotrutz C, Hunjan S, Boyer AL, Adalsteinsson E, Spielman DM (2002) Inverse planning for functional image-guided IMRT. Phys Med Biol 47:3567–3578
21. Alber M, Paulsen F, Eschman SM, Machulla HJ (2003) On biologically conformal boost dose optimization. Phys Med Biol 48:N31–N35
22. Contag CH, Ross BD (2002) It's not just about anatomy: in vivo bioluminescence imaging as an eyepiece into biology. J Magn Reson Imag 16:378–387
23. Seltzer M, Schiepers C, Silverman DH et al. (2001) Recent advances in imaging endogenous or transferred gene expression utilizing radionuclide technologies in living subjects: applications to breast cancer. J Nucl Med 42:586–590
24. Cheery SR (2003) In vivo molecular and genomic imaging: new challenges for imaging physics. Phys Med Biol 49:R13–R48
25. Kurhanewicz J, Vigneron DB, Hricak H et al. (1996) Three-dimensional H-1 MR spectroscopic imaging of the in situ human prostate with high (0.24–0.7 cm^3) spatial resolution prostate carcinoma: MR imaging findings after cryosurgery. Radiology 198:795–805
26. Zaider M, Zelefsky MJ, Lee EK et al. (2000) Treatment planning for prostate implants using magnetic-resonance spectroscopy imaging. Int J Radiat Oncol Biol Phys 47:1085–1096
27. DiBiase SJ, Hosseinzadeh K, Gullapalli RP et al. (2002) Magnetic resonance spectroscopic imaging-guided brachytherapy for localized prostate cancer. Int J Radiat Oncol Biol Phys 52:429–438
28. Kim D, Mayer D, Xing L, Daniel D, Spielman D (2005) In vivo detection of citrate for prostate cancer at 3 Tesla. Magn Reson Med (in press)
29. Lian J, Xing L, Hunjan S et al. (2004) Mapping of the prostate in endorectal coil-based MRI/MRSI and CT: a deformable registration and validation study. Med Phys 31:3087–3094
30. Zaider M, Minerbo GN (2000) Tumour control probability: a formulation applicable to any temporal protocol of dose delivery. Phys Med Biol 45:279–293
31. Lian J, Hunjan S, Dumoulin C, Levin J, Watkins R, Rohling K, Giaquinto R, Kim D, Lo A, Spielman D, Daniel B, Xing L (2003) Integrating deformable MRI/MRSI and CT image registration into the prostate IMRT treatment planning. Int J Radiat Oncol Biol Phys 57:S207
32. Bookstein FL (1989) Thin plate splines and the decomposition of deformations. IEEE Trans Pattern Anal Mach Intell 11:567–585
33. Wu X, Yu C, DiBiase SJ, Gullapallib R (2003) The application of deformable image registration for MRS in prostate treatment planning. Int J Radiat Oncol Biol Phys 57:S208
34. Mutic S, Dempsey JF, Markman J, Chao KS, Purdy JA (2001) Multimodality image registration quality assurance for conformal three-dimensional treatment planning. Med Dosim 26:79–82
35. Hunjan S, Adalsteinsson E, Kim DH et al. (2003) Quality assurance of magnetic resonance spectroscopic imaging-derived metabolic data. Int J Radiat Oncol Biol Phys 57: 1159–1173
36. Hunjan S, Spielman DM, Adalsteinsson E, Boyer AL, Xing L (2002) Phantom for quality assurance testing of MRSI data

incorporated into radiation treatment planning. In: Proceeding of Annual Meeting of International Associate of Magnetic Resonance in Medicine, Honolulu, Hawaii
37. Xing L, Cotrutz C, Hunjan S, Boyer AL, Adalsteinsson E, Spielman D (2002) Inverse planning for functional image-guided IMRT. Oral Presentation in 2002 Annual Meeting of ASTRO, New Orleans, LA
38. Niemierko A (1997) Reporting and analyzing dose distributions: a concept of equivalent uniform dose. Med Phys 24:103–110
39. Lyman JT, Wolbarst AB (1987) Optimization of radiation therapy, III: A method of assessing complication probabilities from dose-volume histograms. Int J Radiat Oncol Biol Phys 13:103–109
40. Xing L, Li JG, Donaldson S, Le QT, Boyer AL (1999) Optimization of importance factors in inverse planning. Phys Med Biol 44:2525–2536
41. Shou Z, Xing L (2003) Improve IMRT dose distribution by using spatially non-uniform dose importance factors. Proceeding of the 14th ICCR. Seoul, Korea
42. Cotrutz C, Xing L (2002) Using voxel-dependent importance factors for interactive DVH-based dose optimization. Phys Med Biol 47:1659–1669
43. Cotrutz C, Xing L (2003) IMRT dose shaping using regionally variable penalty scheme. Med Phys 30:544–551
44. Wu C, Olivera GH, Jeraj R, Keller H, Mackie TR (2003) Treatment plan modification using voxel-based weighting factors/dose prescription. Phys Med Biol 48:2479–2491
45. Yang Y, Xing L (2005) Towards biologically conformal radiation therapy (BCRT): selective IMRT dose escalation under the guidance of spatial biology distribution. Med Phys (in press)
46. Crooks S, Xing L (2002) Constraint least square method for inverse treatment planning. Int J Radiat Oncol Biol Phys 54:1217–1224
47. Lu Y, Spelbring DR, Chen GT (1997) Functional dose-volume histograms for functionally heterogeneous normal organs. Phys Med Biol 42:345–356
48. Marks LB, Sherouse GW, Munley MT, Bentel GC, Spencer DP, Scarfone C (1999) Incorporation of functional status into dose-volume analysis quantitative pulmonary single photon emission computed tomography for radiotherapy applications. Med Phys 26:196–199
49. Alber M, Nusslin F (2002) Tools for the analysis of dose optimization: I. Effect-volume histogram. Phys Med Biol 47:2451–2458
50. Martel MK, Ten Haken RK, Hazuka MB, Turrisi AT, Fraass BA, Lichter AS (1994) Dose-volume histogram and 3D treatment planning evaluation of patients with pneumonitis. Int J Radiat Oncol Biol Phys 28:575–581
51. Martel MK, Ten Haken RK, Hazuka MB et al. (1999) Estimation of tumor control probability model parameters from 3D dose distributions of non-small cell lung cancer patients. Lung Cancer 24:31–37
52. Webb S, Nahum AE (1993) A model for calculating tumour control probability in radiotherapy including the effects of inhomogeneous distributions of dose and clonogenic cell density. Phy Med Biol 38:653–666
53. Niemierko A, Goitein M (1993) Implementation of a model for estimating tumor control probability for an inhomogeneously irradiated tumor. Radiother Oncol 29:140–147
54. Popple RA, Ove R, Shen S (2002) Tumor control probability for selective boosting of hypoxic subvolumes, including the effect of reoxygenation. Int J Radiat Oncol Biol Phys 54:921–927

Biological Optimization

Andrzej Niemierko

5

Contents

hard the planner tries, he or she is often left with a residual conviction that it might be possible to do better and this has led, over the years, to many efforts to develop computer-aided techniques to optimize plans. The desire for such techniques has intensified in recent years with the advent of IMRT, which allows novel superior dose distributions to be achieved but can pose quite difficult design problems.

It is helpful to distinguish between plan selection, plan improvement, and plan optimization. Plan selection implies some scheme that will find a plan that satisfies certain stated goals – without requiring any starting plan. Plan improvement involves finding a plan that is better than some initial plan. Plan optimization means the identification of that plan which is better than any other by virtue of having a maximum value of some score, subject possibly to certain constraints. Plan improvement and optimization are sometimes confused with one another, but the term optimization has a strict mathematical meaning that should be respected.

In each case, the problem can be divided into two parts: 1) the definition of the criteria by which a plan is to be judged; and 2) the design or selection of a procedure to search for the desired plan. The latter problem is a very difficult one because the enormously large number of possibilities leads to a daunting computational problem if results must be obtained fast enough to be clinically useful. For this reason, the search problem tends to receive the lion's share of attention. However, efforts to achieve any of the above forms of plan enhancement have not met with wide acceptance or even success, and this is largely due, in our opinion, to grave inadequacies in the way the criteria for plan acceptance have been formulated.

5.1 Rationale for Biological Considerations in IMRT Optimization

Designing good radiation treatments is a difficult and complex art. Many considerations must be balanced to arrive at a satisfactory plan of treatment. No matter how

5.2 Defining Objectives for IMRT Planning and Optimization

An appropriate definition of the criteria for plan evaluation and optimization (i.e., the statement of our clinical objectives) is a prerequisite for the success of IMRT.

Defining the objectives may be a more difficult task than may appear to be at first glance. An "objective function" is the quantitative mathematical definition of the clinical objectives whether they are in terms of a desired pattern of radiation dose or in terms of the desired overall clinical outcome. The value of the objective function is the putative index of the goodness of the treatment plan. The term score is often used to denote the value of the objective function. The criteria of optimization must be clinically relevant in that it should attempt to represent the clinician's judgment as closely as possible but nonetheless not be bound entirely by conventional thinking. The criteria should, thus, allow extrapolation of conventional experience to novel and unusual dose distributions, if only in small incremental steps.

One of the difficulties in defining what is best (and yet achievable) for the patient arises from the fact that the clinical reasoning that a physician applies to judge the merits of a treatment plan is multifarious and subjective. Furthermore, despite many decades of experience, knowledge of the radiation response of tumors and of radiation-induced normal tissue sequelae is inadequate and not well documented. This deficiency exists due partly to the shortcomings of conventional radiotherapy including the lack of tools previously for the imaging, planning and delivery of precise 3D conformal radiation treatments and to the various sources of uncertainties (e.g., positional, motion, dosimetric, etc.). Furthermore, the functional response of organs and tumors to radiation dose is highly complex and may depend upon numerous as yet poorly understood factors. Examples of these factors include the volume effect, inter-patient variation of sensitivity, intra-tumor variation in clonogenic cell density and cell sensitivity, the impact of other treatment modalities such as chemotherapy, hormonal therapy or surgery, the paired organ and interdependent organ effects, histology, age, diabetes, hypertension, history of smoking, to name just a few that have been documented to modify radiation response. Thus, a complete and unambiguous statement of what is in the best interest of a patient is difficult.

5.3 Insufficiency of Dosimetric Considerations Alone

The goal of radical radiation therapy is to eliminate the tumor tissue while minimizing the unavoidable damage to surrounding normal tissues and organs. Therefore, it is reasonable that the treatment planning process, including the optimization component, should address this goal as directly as possible. Whether the irradiated tumor is eradicated or not and whether the surrounding normal tissues suffer from excessive radiation-induced damage depends on many dosimetric and biological factors. The dosimetric factors such as volumetric and temporal distribution of dose are relatively easier to define, measure and control, as opposed to more complex biological factors. For these reasons, they have been commonly used to prescribe, record, verify, and optimize radiation treatments. However, it is the biological mechanisms that are ultimately responsible for expressing radiation-induced damage to a tumor and normal cells.

5.3.1 Dose Criteria

Traditionally, most of the tools and criteria that have been applied to designing radiation treatment plans involve constraints on the dose delivered to selected points or regions within the patient. These criteria indeed parallel some of those used by clinicians in evaluating plans. Some of the earlier attempts to optimize radiation treatment plans employed objective functions based on features of dose distributions [1–7]. For example, one could choose to maximize the minimum dose to the tumor subject to a constraint on the maximum dose to certain normal structures. For simplicity, many investigators have utilized purely dose-based criteria for optimizing intensity distributions as well. A simple but often used example of an objective function based on dose considerations is

$$F = \sum_i \left(T - D_i\right)^2 + \sum_j w_j \sum_k H\left(D_k - N_j\right)\left(N_j - D_k\right)^2 \tag{1}$$

where F is the treatment plan score that needs to be minimized, T is the desired dose to the target volume and N_j is the tolerance dose of the n-th normal structure. D_i is the computed dose in the i-th voxel of the target and D_k is the computed dose at the k-th voxel of the j-th normal structure. The Heaviside operator $H(x)$ is defined by $H(x) = 1 \text{for} x \geq 0 \text{and} H(x) = 0 \text{for} x < 0$. It ensures that only those normal tissue voxels in which the dose is too high contribute to the objective function. See chapter I. 4 for a more in depth discussion. The quantity w_j is the weight or relative penalty for exceeding the tolerance dose for normal structures.

However, for many cases, purely dose-based criteria may not be sufficient. Moreover, it is easy to demonstrate that dose-based criteria can produce completely incorrect results. Let us consider, for instance, the quadratic criteria defined by (1) applied to a $10 \times 10 \times 10$ cc tumor with a voxel size $0.4 \times 0.4 \times 0.4$ cc (15,625 voxels). Let us also assume that the normal tissue term satisfies the constraints fully and does not contribute to the score. Let us also assume that the probability of controlling the tumor is 50% for dose of 60 Gy and for 75 Gy it is 55%. The desired target dose is 75 Gy. Note that according to (1), the lower the score the better the plan. Let us consider two plans. In the first one, the target volume is perfectly uniformly irradiated to 60 Gy, that is, all 15,625 voxels

receive 60 Gy leading to a score of 3,515,625 and a probability of local control of 50%. In the second plan, one voxel receives zero dose and the remaining 15,624 voxels receive 75 Gy. The latter score is 5625, which is much better. However, a common definition of local control is that all tumor cells need to be killed and this is not the case for a voxel that received no dose. In fact, in the latter case the probability of tumor control is zero[1].

It is possible that (i) local control may be achieved without killing all tumor cells, and that (ii) voxels near the tumor boundary, where cold spots typically occur, may not contain any tumor cells.

Thus, a plan judged considerably superior based on dose limits criteria is totally unacceptable based on the tumor control criteria.

5.3.2 Dose-volume Criteria

Generally, the response of the tumor and normal tissues is a function not only of radiation dose, but also of the volume subjected to each level of dose. Thus, at the next level of refinement, the optimization criteria could be expressed in terms of dose-volume combinations, e.g., the limit on the volume of an organ that may be allowed to receive a certain dose or higher. This has been typically the highest level of sophistication that is used in conventional planning of radiation treatments. Often this is not sufficient. Let us consider the illustration in Fig. 1a of a normal structure for which a constraint has been specified that no more than 25% of the volume is to receive 50 Gy [52]. All three DVHs shown meet this criterion. However, the DVH represented by the solid curve clearly causes the least damage. One can argue that we can overcome this limitation by specifying the entire DVH. However, as illustrated in Fig. 1b, this would be too limiting. Multiple DVHs, in fact, an infinite number of them, could lead to an equivalent damage to a particular organ, but each DVH may produce different effects on other organs and the tumor. When this happens, DVHs usually cross each other as shown in Fig. 1b. Only one of them is optimal if the tumor and other organs are considered simultaneously. Therefore, the use of only dose-volume criteria to describe the response of a tissue to radiation may also be inadequate under many circumstances.

These considerations have led to an interest in developing quantitative models that attempt to predict the likely biological response of organs and tissues to any arbitrary pattern of irradiation. The need to assess inhomogeneous dose distributions comes from two sources. First, even if the goal is to achieve uniform irradiation of the target volume, any scheme that is used in an automated procedure must be able to evaluate a non-uniform pattern of irradiation, if only to ensure that, by giving it a low score, a more uniform dose distribution will be preferred. It is also possible that a somewhat non-uniform target volume irradiation may lead to an overall more satisfactory plan than one in which there is an entirely uniform target coverage but which is associated with a higher dose to an adjacent critical organ. The second reason to assess inhomogeneous dose distributions is that these are the norm when it comes to the normal tissues outside the target volume – and there is thought to be a sometimes quite strong volume dependence of normal tissue tolerance of which clinicians wish to take advantage.

5.4 Implementation of Biological Indices

The next step forward may be to supplement dose and dose-volume criteria with biological (or dose-response-based) criteria. A suitable way to cast the objective

[1] Here we assume that all the voxels of the outlined target volume contain tumor cells.

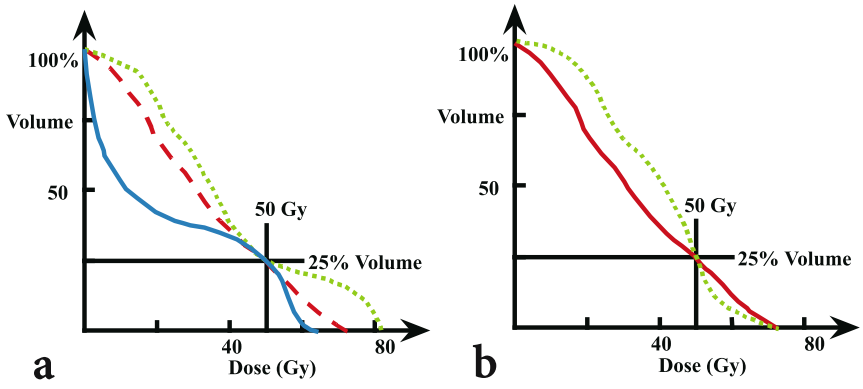

Fig. 1. (a) Schematic representation of a normal structure DVH for which a constraint has been specified that no more than 25% of the volume is to receive 50 Gy. All three DVHs meet the criterion. The DVH represented by the solid line clearly causes the least damage. (b) Multiple DVHs can lead to an equivalent damage to a particular organ, but each DVH may produce different effects on other organs and the tumor

function in terms of clinical and biological criteria is to employ such indices as tumor control probability (TCP), Normal Tissue Complication Probability (NTCP), and equivalent uniform dose (EUD). A number of investigators [8–25, 53] have proposed models for predicting biological and dose-response indices. Although these models and the models for combining them into an objective function are being refined continually as additional dose-response data become available, they remain simplistic and open to criticism. However, if used judiciously, they can be useful for comparing rival plans and for modest extrapolation of conventional experience. Supplementing them with constraints on dose and dose-volume combinations may also alleviate concerns regarding the unreliability of the predictions of biological and dose-response-based objective functions. Such a step will keep the results of optimization from deviating significantly from conventional experience and make them consistent with the judgment of the physician.

A typical objective function consists of a combination of sub-scores. Each sub-score quantifies a particular feature of a particular end point of interest. A frequently suggested score function, S, based on biological indices is the so called "probability of uncomplicated control", defined as

$$S = TCP \prod_i \left(1 - NTCP_i\right) \tag{2}$$

This form of the objective function represents maximizing the probability of local control, TCP, while minimizing the probabilities of adverse effects on normal tissues, $NTCP_i$. Although maximizing the probability of uncomplicated control represents almost direct statement of the goals of radical radiotherapy, it is not without evident flaws. The most important one is the explicit assumption that all complications are of equal consequence and that each additional percentage point of tumor control exactly offsets each additional percentage point of normal tissue complication. This is contrary to clinical practice. Consequently, it is essential that the severity of the complications is taken into account in developing a numerical score.

A modified version of (2) has been proposed by Brahme and his collaborators [54]. Based on the analysis of clinical data for head and neck tumors they concluded that there is a proportion of patient population where the probability of tumor control is correlated with the probability of complication. This can be accounted for by modifying (2) and defining the score function, P_+, as follows:

$$P_+ = TCP - NTCP + \delta(1 - TCP)NTCP \tag{3}$$

Here, δ is the proportion of patients for whom there is no correlation between the TCP and $NTCP$. This formulation of the score function does not account for the severity of complications either.

Another example of the objective function was proposed by the Memorial Sloan Kettering Cancer Center group and is defined as

$$S = \prod_i s_i \tag{4}$$

Here, s_i are the tumor, normal anatomic structure and end point-specific sub-scores. Sub-scores may be functions of the TCP, EUD, $NTCPs$ and other dose-response-based quantities. A suitable sub-score function has been suggested by Kutcher [15, 26] and is illustrated in Fig. 2. The sub-score decreases linearly and slowly from unity with increase in the $NTCP$. When the $NTCP$ reaches the limit of acceptability P_a, the sub-score begins to drop rapidly, reaching a value of zero when the $NTCP$ exceeds a critical limit P_c. The limits P_a and P_c are chosen based on the physicians' judgment of the merits of treatment plans. Other sub-scores may represent dose or dose-volume based constraints. An example of a commonly used dose-based constraint would be a limit on the target dose inhomogeneity.

We should indicate that there is considerable debate about the choice of criteria of optimization. There are some who believe that specifying criteria in terms of dose or dose-volume limits is adequate, while others believe that it is also important to include dose-response information. Those who favor the former argue that the current dose-response data are so sparse and unreliable that they will not yield dependable results. The opponents argue that, at the very least, we should use what we know. While dose response data for specific tumors and normal tissues are limited, we do know that dose-response of a tumor is a non-linear, typically sigmoidal, function of dose and the size of the tumor. The response of a normal structure is a non-linear function of dose and the volume receiving each level of dose, and that different anatomic structures exhibit different degrees of volume effect. Incorporation of even such limited in-

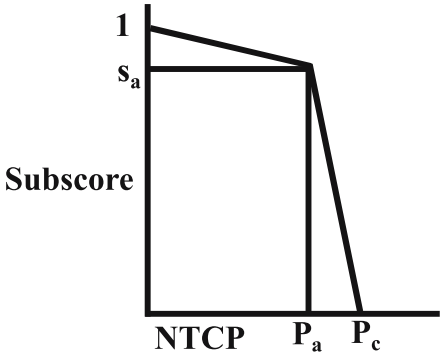

Fig. 2. A sub-score function suggested by Kutcher [15]. The sub-score decreases linearly and slowly from unity with increase in the NTCP. When the NTCP reaches the limit of acceptability P_a, the sub-score begins to drop rapidly, reaching a value of zero when the NTCP exceeds a critical limit P_c. The limits P_a and P_c are chosen based on the physicians' judgment of the merits of treatment plans

formation is likely to lead to improved treatment plans and possibly outcomes. However, the treatment plans thus obtained may be so different from conventional plans that it may sometimes be difficult to judge their quality. Therefore, as indicated above, incorporation of biological and dose-response indices may best be done in incremental steps.

5.4.1 Combination of Individual TCPs and NTCPs

The computation of TCPs or NTCPs for individual organs or tissues is a necessary but insufficient condition for computing a score by which a plan may be judged. After computing individual TCPs and NTCPs (which may be considered as sub-scores) they must be combined, together possibly with other evaluations, into an overall numerical score. As has been alluded to already, the combination of sub-scores is a difficult matter. Some of the problems associated with the combination of sub-scores are discussed below. One "solution", however, is worth mentioning right away.

The very act of ranking two or more plans establishes, implicitly or explicitly, a scale of "goodness" on which plans are ordered and can therefore be assigned numerical positions. Thus, since clinicians must ultimately pick a "best" plan, even in subjective evaluations there is the possibility of assigning a one-dimensional score. However, judging a plan is a multi-faceted problem with many considerations being entertained; in guiding a clinician in the assessment of a plan it may be counterproductive to boil all the information down into a single scalar quantity – the "score". Rather, it may be better to provide multidimensional information which would, in particular, include the individual TCPs and NTCPs together with other information such as the dose distributions and dose statistics and allow the clinician to evaluate a plan or compare alternative plans from this vectorial representation. A high NTCP, for example, would alert the clinician to a potential problem; a low NTCP might allow him or her to gloss over the evaluation of some region or tissue. Used in this way, TCPs and NTCPs would provide a very useful tool to facilitate plan evaluation without presuming to provide an overall judgment.

Multiple End-points

There is generally not one but several potential end-points for a particular organ or tissue. This issue can be addressed by computing a separate NTCP for each end-point. Their relative weightings are, however, difficult to provide since there may be interactions between them (a severe reaction may mask a lesser reaction). The computation of separate NTCPs for separate endpoints is more difficult if there is a continuous and graded response of the tissues, as might be the case with skin reactions, for example.

Range of Severity of a Given End-point

A particular end-point may be relatively minor in its implications, or may represent a major complication. A skin ulceration could be small and easily controlled, or it could involve a large area and be a serious source of infection.

Complexity of Correlated Conditions

The response to radiation of a particular patient may well not be the same as that of the general population. For example, the clinical effect of radiation on lung function may depend on the patient's history of substance abuse and on his lung function before treatment. The clinician readily incorporates such considerations into the analysis of a plan; it is much less easy for the computer to do so.

Interactions Between Complications

Two or more independently computed complications may interact with one another. This may be in a mechanistic sense, as when the presence of one complication makes the other more likely, or it can be functionally, as when the loss of function in one kidney makes the loss of function in the second a more grave situation. (However, the latter example could also be an example of the first consideration, since it is possible that loss of function in one kidney would affect the sensitivity to radiation of the other.)

Tumor Considered as Normal Tissue

It is an obvious point that the target volume contains a matrix of tissue, damage to which may represent a complication to the patient. One cannot irradiate the target volume to arbitrarily high dose; any optimization scheme will need a mechanism to avoid this. One good solution is to associate a second endpoint, other than tumor control, for the target volume.

"Other Tissue"

Just because the planner specifically identifies certain organs and tissues for special consideration does not mean that the unidentified tissues feel no pain. These must be considered as well. One mechanism for this is to construct a dose-volume histogram for "other" tissues – those that are within the patient's external contour and outside all explicitly identified volumes of interest. One can then evaluate an NTCP for these tissues and include it in the score.

Complexity of the Plan

It is generally agreed that, other things being equal, clinicians will prefer a simple plan which is easy to implement over one that is complex and may be difficult to set up. While the time to implement the plan is a consideration, the main motivation comes from the belief that delivery of the more complex plans may be more prone to mistakes. The availability of

automated treatment verification and some treatment verification aids may affect these judgments. In any event, these considerations must be accommodated; a sub-score to quantify plan complexity is therefore needed.

Combination of Sub-scores

One must first decide whether the correct algorithm for computing a score from a set of sub-scores is a linear addition of the sub-scores with appropriate weighting factors, a product of sub-scores with weighting exponents, or some other expression. Both additive and multiplicative approaches have been employed. The latter has the advantage that an unacceptable complication, presumably leading to a sub-score of zero, will force the overall score for the plan to be zero (i.e. unacceptable), whereas, in a linear addition, an unacceptable complication could be inappropriately counterbalanced by many high sub-scores.

One question, addressed implicitly above is whether there are "cross terms" in the score. In the case of the additive score, for example, should there be terms that include the product of two or more sub-scores? Such questions might seem more complex than the models would support. However, it is important that the models reflect clinical judgment, and it seems at least possible that such correlations are sometimes made in clinical practice.

Weighting Factors

The central problem in combining sub-scores is in the assignment of weighting factors. These exemplify the relative importance assigned to the various endpoints assessed. It is clearly essential that the severity of the complications is taken into account in developing a numerical score. In this connection, it is worth pointing out that the frequently stated assertion that the goal of therapy planning is to maximize the likelihood of uncomplicated tumor control is unequivocally wrong. Such a statement implies that all complications are of equal consequence and that each additional percentage point of tumor control exactly offsets each additional percentage point of normal tissue complication. This is patently contrary to clinical practice.

Sub-scores have often been based on physical dose considerations (dose homogeneity, difference between the delivered and tolerance doses, etc.). The relative weighting of such sub-scores is very difficult and rapidly comes to seem arbitrary. The great advantage of biologically based models is that they define scores of direct clinical relevance and meaning; their combination should be easier and more intuitive – and should admit more readily of patient involvement in planning decisions.

All this having been said, there is little data or experience for how to assign weights. This is clearly an important area for future research.

5.5 IMRT Optimization Using the Concept of EUD

The group at the Medical College of Virginia used the concept of EUD (Equivalent Uniform Dose) as an argument of dose-response function [27] for IMRT optimization study. The concept of EUD is described in detail later. In short, EUD represents dose that is equivalent (in terms of the same level of the probability of local control or complication) to a given non-uniform dose distribution.

The EUD-based optimization of IMRT plans for prostate and head and neck cancer patients was done and compared with the corresponding plans optimized with dose-volume based criteria. In all cases it was clear that, for the same minimum target dose, sparing of organs-at-risk was greatly improved in the EUD-based plan. Furthermore, a sharp dose gradient at the interface between the target and organs at risk was also produced. The maximum target dose was also increased significantly, implying a hot spot inside the target. Such a result is expected if no constraints on the maximum target dose are imposed. That is, the objective function can be insensitive to hot spots within only a part of the target volume. The EUD continues to increase during successive optimization iterations, although by very small amounts, when dose to any portion of the target volume is increased. While excess dose to a part of the target may be considered beneficial in some clinical situations, it is generally not desirable. Therefore, the target volume was also treated as a normal structure with its own dose-response characteristics. This approach lead to much-improved target dose homogeneity with a small degradation in normal structure sparing. Figure 3 illustrates the effectiveness of EUD-based objective function for the example of head and neck tumor. Three dose distributions are shown corresponding to three optimization approaches: 1) based on dose and dose-volume considerations only, 2) EUD-based without constraints on target dose inhomogeneity, 3) EUD-based with constraints on target dose inhomogeneity. The corresponding DVHs for the target volume, parotid glands and for the spinal cord are also shown. An important additional advantage of EUD-based objective functions is that they allow exploration of a larger solution space than dosimetry-based objective functions. This can be demonstrated by showing that there are solutions violating one or more dosimetry-based constraints that, nevertheless, are clearly superior biology-wise.

Inference one can draw from the work published so far is that, while for certain treatment sites and associated normal anatomy where volume effect is negligible, it may be sufficient to state objectives purely in terms of dose-limits. Generally, it is important to incorporate the volume effect and perhaps biology into optimization in

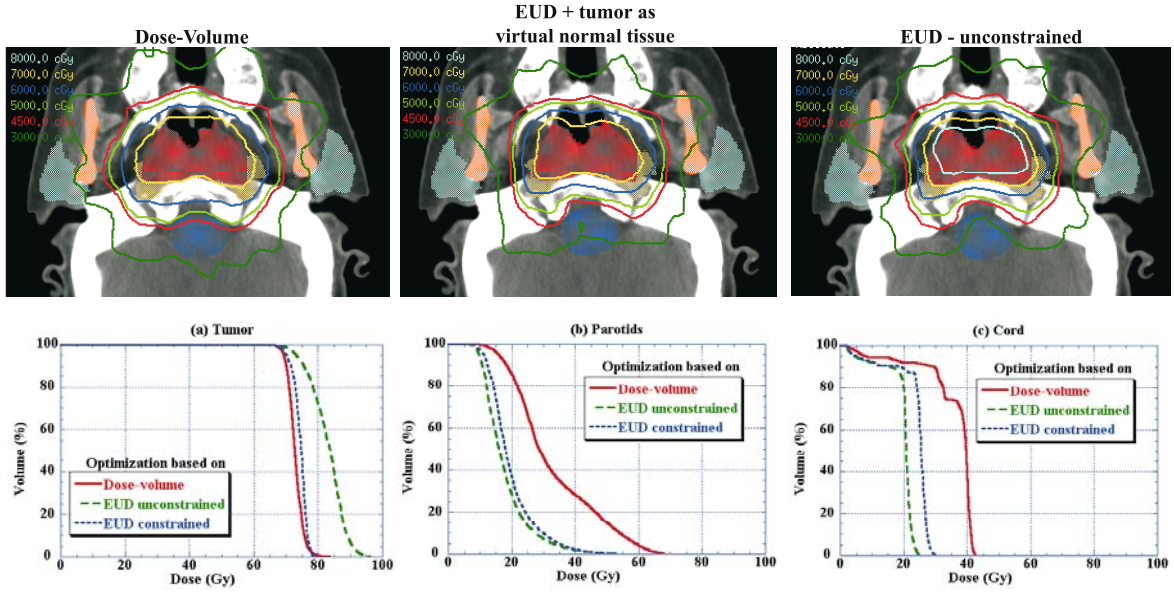

Fig. 3. Comparison of dose distributions and the corresponding DVHs for conventional and EUD-based IMRT dose distributions for head and neck carcinoma

a clinically relevant manner. While the results favor the use of dose-response-based objectives, they cannot be called conclusive and further studies are required. One thing, however, is clear. The choice of dose-response-based criteria must be made intelligently and with great caution. A good choice can steer the solution in the direction of better outcome. A poor choice may lead to bad plans and erroneous conclusions. A case in point is the unconstrained use of the probability of uncomplicated control of (2) above. To illustrate the potential problem, let us consider, for instance, a treatment plan in which *TCP* is 60% and *NTCP* of spinal cord is 1%, producing a treatment plan score of 0.54. Let us compare that with a plan in which *TCP* is 80% but *NTCP* of cord is 10%, yielding a score of 0.72. According to (2), therefore, the second plan would be superior but would definitely not be acceptable clinically. (Note that for this type of objective function a higher score corresponds to a better plan.)

Generally, whether dose-, dose-volume or dose-response-based criteria are needed may depend upon the tissue architecture of the anatomic structure. For spinal cord, for example, purely dose-based criteria may be adequate. For lung, on the other hand, dose-volume based or dose-response-based criteria would be necessary.

5.6 Models of Tissue Response to Radiation

This section describes in more detail the models of Tumor Control Probability (TCP), Normal Tissue Complication Probability (NTCP) and Equivalent Uniform Dose (EUD) that are introduced as black-box indices in the previous sections.

Models of tissue response to radiation can be classified into two broad categories. One category includes mechanistic models developed based on our best understanding of the underlying biological processes. The second category includes phenomenological models based on the observed phenomena and general laws governing these phenomena. Although these two categories are based on quite different philosophical approaches, they offer complimentary views. Mechanistic models are highly reductionist and have been considered by many investigators as the ultimate models. This view has a strong historical backing as essentially for the last 400 years science has advanced by reductionism. The idea of reductionism is that you could understand the world, all of nature, by examining smaller and smaller pieces of it. When assembled, the small pieces would explain the whole. This view has been challenged recently by pointing out that "more is different" and that radiation response of large and complex aggregates of elementary entities (e.g., cells, molecules, proteins) is unlikely, a priori, to be understood in terms of a simple extrapolation or scaling of a specific response of these entities.

An important argument for using phenomenological models and against the reductionistic models is based on the observation that many essential properties of a living system are properties of the whole, which none of the parts have. These properties arise from the interactions and relationships between the parts or elementary entities. It is also important to note that these

properties are often destroyed when the system is dissected, either physically (e.g., by analyzing only small biopsy samples of actual tumor cells in vivo) or theoretically (e.g., by building a reductionist model), into elements. It has been noted that, generally, there is a causal gap between one level of description and the next.

In empirical sciences, the ultimate test of model quality is the level of agreement of the model predictions with the corresponding experimental data. No preference of one model category over the other can be given at this point. Whether this inconclusiveness stems from the weakness of the available clinical data unable to differentiate the models or, from their actual equivalence is an important scientific question worth a thorough investigation.

5.6.1 Mechanistic Models Based on Target-cell Hypothesis

Most of the mechanistic models are based on the so-called "target-cell hypothesis". That is, it is assumed that the response of interest (such as local control or complication) of an organ or tissue is determined by the survival of the target cells of that organ/tissue. It follows then that the fundamental underlying mechanism is that of the cell kill. The most prevalent model describing cell kill is the Linear-Quadratic (LQ) model [28, 55] described in the next section. The phenomenological models are described in the following section.

The Linear-Quadratic (LQ) Model

According to the LQ model the natural logarithm of the surviving fraction of cells, SF, after a course of n fractions and dose per fraction d is given by

$$\ln SF = -nd(\alpha + \beta d) \tag{5}$$

where α and β are the LQ model parameters that are tissue and end-point specific.

This basic LQ model can easily be extended to include the effects of repopulation, redistribution, reoxygenation, accelerated repopulation, and repair [29–32]. For example, to account for repopulation, and assuming a constant rate of repopulation, the overall surviving fraction, SF, over time T can be expressed as follows:

$$\ln SF = -nd(\alpha + \beta d) + \frac{T - T_k}{T_{\text{pot}}} \ln 2 \tag{6}$$

Here, T_k is the time at which repopulation begins after the start of treatment, and T_{pot} is the potential doubling time.

Repair can be accounted for by using an "incomplete-repair" model proposed by Thames [29]. The idea is that after a dose d the injury induced by some fraction θ of the dose is still unrepaired by the time an additional dose is given. This fraction is assumed to decay exponentially in time, according to $\theta = \exp(-\mu \Delta t)$, where μ is the tissue specific repair constant and Δt is the inter-fractional interval. Thames proposed that, under these conditions, the logarithm of cell surviving fraction could be expressed as

$$\ln SF = -nd\left[\alpha + \beta d\left(1 + h_n(\theta)\right)\right] \tag{7}$$

where

$$h_n(\theta) = \left[\frac{2}{n}\right]\left[\frac{\theta}{1-\theta}\right]\left[n - \frac{1-\theta^n}{1-\theta}\right]$$

A convenient extension of the LQ model to account for redistribution and reoxygenation can be found in Brenner's paper [32].

Of course, there is a price to pay for using more complex biological models that try to account for several effects. In addition to using more complicated and less intuitive mathematical formulae, the number of free model parameters that need to be estimated from experimental and clinical data is increasing. Unfortunately, these parameters have not been estimated with satisfying accuracy for most organs or tissues in vivo. Therefore, the quantitative model predictions have large uncertainties and should be viewed with a critical eye.

Tissue Architecture

The LQ model can be applied to tumors and normal tissues in a very similar manner. That is, the LQ model can be interpreted as a dose modifying function describing survival of the hypothetical target cells. However, the LQ model does not deal at all with the fact that cells are organized structurally or functionally into Functional Sub-Units – FSUs (term coined by Withers [33]) which in turn are organized into organs and tissues. For example, the kidney can be thought of as being composed of nephrons with each nephron being composed of tubule cells. Normal tissues and organs in particular differ markedly from one another in their architecture, and these differences likely result in very different observed responses to radiation. One can envision three fundamentally different types of organization of normal organs, described in terms of the FSUs they describe – see Table 1 and Fig. 4.

It has been suggested and experimentally verified for some organs [34] that structurally organized FSUs can regenerate from one surviving cell. For organs without structurally defined FSUs, the FSU can be defined as the largest area or volume that can be regenerated by a single surviving or immigrating cell. Clearly the tolerance of a tissue to radiation therapy depends not only upon the radiosensitivity of its critical "target" cells, but also upon how those cells are organized into FSUs,

Table 1. Three different types of normal tissue architecture and the proposed corresponding mechanisms of their response to radiation treatment

Type	Description	Examples	Model
Critical Element (CE)	The structure is composed of many FSUs and irreparable damage to any one will cause a complication	Spinal cord	Chain made up of many friable links
		Nerves	
		Peritoneum	
Critical Volume (CV)	Damage to a substantial fraction of the FSUs is necessary to cause a complication	Kidney	Rope made up of many strands which will hold until many are broken
		Liver	
		Lung	
Graded Response (GR)	Response occurs on a continuous scale	Skin	Granular clump of "dosimeters"
		Mucosa	

upon the number of cells per FSU, and upon the number of FSUs necessary to maintain a specified level of function.

Dose-volume Relationship

The dependence of complication probability on the irradiated volume (under conditions of constant dose) is central to the issue of choosing an optimum plan. The models presented below all make predictions concerning this relationship, although often these are not made explicit.

Models which are based on the *critical element* assumption, and which further assume that the response of one element is not correlated with that of any other, lead to a *linear complication probability* vs *volume relationship* for small (with respect to unity) complication probabilities – see Fig. 5.

The integral response model can support almost any complication probability vs volume relationship. It certainly does not have to be linear and, in the model's intended application in which an organ is considered to retain function until some critical proportion of its functional units are inactivated, the integral response model has a *non-linear complication probability* vs *volume relationship* and, in particular, can exhibit a threshold effect.

The *graded response model shows a complete absence of a complication probability* vs *volume relationship*. That is, the dose to give a given complication (grade of response) is independent of volume.

According to the classification presented in the table tumors can be regarded as the Critical Element type of structures. That is, a complication (tumor recurrence) occurs when at least one clonogen survives. This is based on the prevalent assumption that to control a tumor all clonogens need to be destroyed.

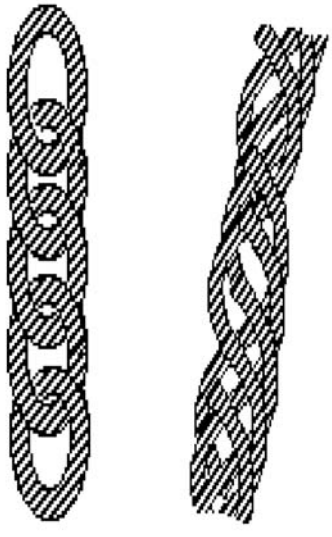

Fig. 4. Schematic illustration of tissue architecture for the Critical Element and Critical Volume NTCP models

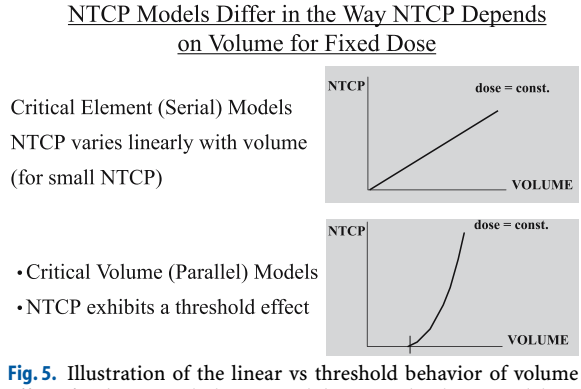

Fig. 5. Illustration of the linear vs threshold behavior of volume effects for the Critical Element and the Critical Volume models

The following sections describe mechanistic models of Equivalent Uniform Dose (EUD), Tumor Control Probability (TCP) and Normal Tissue Complication Probability (NTCP), which have been proposed for 3D and IMRT treatment planning.

Equivalent Uniform Dose (EUD)

Dose distributions throughout organs and volumes of interest are never exactly uniform, and may often be far from it, especially for normal tissues. Brahme proposed that, for relatively small dose nonuniformity, the dose effectively delivered to the target can be approximated by the mean target dose [35]. For large dose inhomogeneities, Brahme suggests using the minimum target dose. The mean target dose approach assumes that doses above the mean target dose compensate for doses less than the mean target dose. That is, the (unspecified) clinical effect of irradiation is a near-linear function of dose. On the other hand, the minimum target dose approach assumes that a cold spot cannot be compensated by any dose delivered to the rest of the target volume. That is, the dose in excess of the minimum target dose is ignored. Both Brahme's propositions are the first-order approximations that reveal the difficulty and importance of adequate reporting and evaluating of inhomogeneous dose distributions.

It is obvious that an oversimplification is made when the dosimetric aspects of a complex three-dimensional treatment plan are reduced in the patient's records to a dose or a few doses at the reference point or points. Such an oversimplification has important consequences for subsequent statistical analysis of the clinical trials. For example, by assuming that all patients received the same (prescribed) dose, the underlying dose-response relationship is flattened out, and a possible finer structure of the dosimetric data of the trial's arm can be lost.

It is intuitively logical that, for a given end-point, for any inhomogeneous dose distribution delivered to a volume of interest (VOI) according to a certain fractionation scheme, there exists a unique uniform dose distribution delivered in the same number of fractions, over the same total time, which causes the same radiobiological effect. The important feature of this equivalent dose distribution would be its uniformity, which allows one to use a single number to describe the entire VOI dose distribution.

The simplest EUD model for tumors was proposed to be based on the assumption that two target dose distributions are biologically equivalent if they cause the survival of the same number of clonogens [24]. For example, if one uses surviving fraction at 2 Gy (SF_2) as a measure of the clonogen radiosensitivity than the overall survival fraction after dose D would be

$$SF(D) = \left(SF_2\right)^{\frac{D}{2\,\mathrm{Gy}}} \tag{8}$$

For any inhomogeneous dose distribution the overall survival fraction is

$$SF\left(\{D_i\}\right) = \frac{1}{N}\sum_{i=1}^{N}\left(SF_2\right)^{\frac{D_i}{2\,\mathrm{Gy}}} \tag{9}$$

where the sum is taken over N dose calculation points within the target volume. The same fraction of cells survive if the target is irradiated uniformly to a certain unknown dose, which was proposed to be called the Equivalent Uniform Dose (EUD). In Fig. 6 an inhomogeneous dose distribution on the left kills certain number of clonogens (dark dots). There are more dark dots in the D_2 region because dose D_2 is larger than dose D_1. When the same volume is irradiated uniformly to dose EUD, the number of dark dots is the same as the total number of dark dots in the inhomogeneously irradiated volume on the left. Therefore, based on cell survival considerations one could obtain the following formula for EUD:

$$EUD(Gy) = 2Gy\frac{\ln\left[\frac{1}{N}\sum_{i=1}^{N}(SF_2)^{\frac{D_i}{2Gy}}\right]}{\ln\left[SF_2\right]} \tag{10}$$

If one prefers to use the LQ formalism the EUD formula becomes

$$EUD(Gy) = -\frac{\ln\left[\frac{1}{N}\sum_{i=1}^{N}\exp(-\alpha D_i)\right]}{\alpha} \tag{11}$$

It was shown that the EUD in (10) or (11) is not a very sensitive function of the SF_2 or α for most clinically relevant dose distributions [24]. Since the precise values of SF_2/α in vivo are not known for any tumor, setting the SF_2 to 0.5 or α to 0.35 has been recommended as a reasonable, albeit somewhat arbitrary, pick.

It is fairly straightforward to extend the EUD model to account for dose per fraction effects, clonogen proliferation, repair or reoxygenation. Since this EUD model is based on the survival analysis, the arguments and formulae presented in the section describing the LQ model apply.

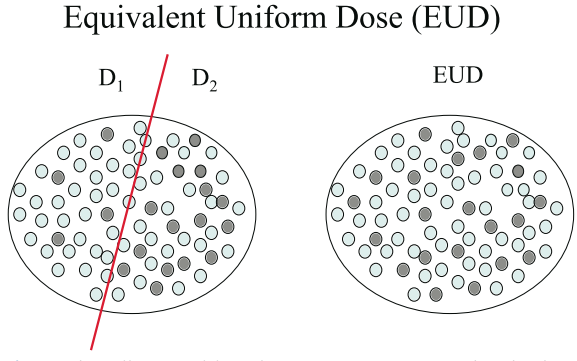

Fig. 6. The cell survival-based EUD concept assumes that the dose distributions are biologically equivalent if the number of killed cells (*illustrated as dark dots*) are identical

According to a simple mechanistic model of tumors (and in agreement with some clinical data), larger tumors contain more clonogens and therefore, larger doses are necessary to eradicate them [36]. When analyzing and comparing doses received by tumors of different sizes one may wish to relate the doses to the same reference absolute volume V_{ref}. For example, V_{ref} might be the average volume of tumors in a particular study or, any reasonable arbitrary chosen volume. Assuming that the number of clonogens is proportional to volume, the EUD can be calculated as follows:

$$EUD\left(V_{ref}\right) = EUD(V) + 2\text{Gy}\frac{\ln\left(\frac{V}{V_{ref}}\right)}{\ln\left(SF_2\right)} \tag{12}$$

where V is the absolute tumor volume and $EUD(V)$ is calculated using (10).

The practical value of the EUD concept has been confirmed in several analyses of the clinical data. For example, a study of chordoma of the base of skull cases treated by a combination of proton and photon beams revealed that EUD was significantly associated with the observed outcomes (local control) [38]. In this study, several dosimetric and treatment related parameters were analyzed using the Cox proportional hazards model. Table 2 shows the results of the analysis. Gender was the most significant predictor of local control with the prognosis in males being significantly better than that in females. EUD was found to be a significant predictor (at the 0.05 P-level) along with the target volume, the minimum target dose, and the dose to the coolest 5% of the target volume. Note that the prescribed dose or the mean target dose was not significant.

Models of Tumor Control Probability (TCP)

The dose-response curve of tumors is found to have a sigmoidal shape in a wide variety of animal experiments and in many clinical studies. Any model of tumor control would be expected to have such a characteristic, implicitly or explicitly. A corollary finding, which any such model must deal with, is that the slope of the dose-response curve observed clinically is more shallow (half the observed values of γ_{50} defined as the percentage increase in TCP per percent increase in dose near $TCP = 50\%$ are in the range of from 1.2 to 3.4 with a modal value of 2) than that predicted from simple cell-survival models. Two types of explanation have been advanced: 1) there may be only a very small number of clonogenic cells within tumors (compared to the total number of cells); and 2) there may be significant inter-patient heterogeneity of tumor sensitivities. (Intra-patient heterogeneity has a much less strong influence on the slope of the dose-response curve but could lead to a shallow dose-response through the preceding mechanism if there were a resistant compartment containing only a small number of cells.) We favor the second explanation because models in which a shallow slope is obtained through a small clonogen number: 1) have to resort to *very* small clonogen numbers indeed; and 2) predict an unrealistic dose-volume relationship for tumor control. Models which take into account inter-patient heterogeneity, on the other hand, can explain the shallow dose-response relationship and can give reasonable values for the dose-volume relationship with entirely reasonable inter-patient variations in cell sensitivities (and, possibly, variations in cell number and dosimetry).

Assuming that the number of surviving clonogens follows the Poisson statistics, and that a tumor is controlled if none of the clonogens survive the treatment, the probability of local control is

$$TCP = \exp(-N') \tag{13}$$

where N' is the expected number of surviving clonogens. If the tumor cells do not proliferate during the treatment, the N' depends on the initial number of clonogens, N_0, and their radiosensitivity which determines the overall fraction, SF, of the clonogens surviving a total dose D:

$$N' = N_0 SF(D) \tag{14}$$

Using the LQ model described in this chapter, the overall surviving fraction is

$$SF(D) = \exp(-\alpha D - \beta d D) \tag{15}$$

Table 2. Summary of univariate analysis using Cox proportional hazards model with stratification by gender (except for the analysis of gender). Hazard ratios and their 95% confidence intervals are shown for the parameters significant at the 0.05 P-level only

Parameter	P-value	Hazard ratio	Standard error	95% Confidence Interval
Gender	0.009	0.43	0.14	0.23–0.82
Minimum dose	0.011	0.93	0.03	0.88–0.98
Target volume	0.014	1.01	0.004	1.002–1.018
EUD	0.016	0.91	0.04	0.84–0.98
$D_{5\,cc}$	0.033	0.92	0.04	0.85–0.99
$D_{90\%}$	0.10			
Prescribed dose	0.14			
Mean dose	0.27			
Histology	0.27			

where d is the dose per fraction, and α and β are the parameters of the LQ model.

Assuming that the clonogens respond to radiation independently, and that they are uniformly distributed within the tumor volume, we can extend the model to any inhomogeneous dose distribution and to different absolute tumor volumes. The expression for calculating the TCP for a tumor volume V irradiated non-uniformly according to a differential $DVH\ \{D_i, v_i\}$ can be derived as follows:

$$TCP\left(V, \{D_i, v_i\}\right) = \exp\left(-\sum_{i=1}^{N} N_i'\right) = \exp\left(-\rho V \sum_{i=1}^{N} v_i \times \exp(-\alpha D_i - \beta d_i D_i)\right) \quad (16)$$

where ρ is the density of clonogens. If dose inhomogeneity is not too large, and the α/β ratio is 10 Gy or more, the quadratic component of the LQ model is much smaller than the linear component and (16) reduces to

$$TCP\left(V, \{D_i, v_i\}\right) = \exp\left(-\rho V \sum_{i=1}^{N} v_i \exp(-\alpha D_i)\right) \quad (17)$$

For an individual patient the values of the parameters of the TCP model (α, β, and ρ) are unknown. They also vary from patient to patient. Therefore, one can only calculate the expected value of TCP taken over a population. For example, assuming that the inter-patient variation in β and ρ is either much smaller than the variation in α or, that these variations can be embedded into the variation in α, the expected value of TCP is calculated as follows:

$$\langle TCP \rangle = \int g(\alpha) TCP(\alpha) d\alpha \quad (18)$$

where $g(\alpha)$ is the probability density function (pdf) for α that describes variation in α over a population. It is commonly assumed that α follows a normal (Gaussian) distribution with mean $\bar{\alpha}$ and variance σ^2:

$$g(\alpha) = \frac{1}{\sigma\sqrt{2\pi}} \exp\left(-\frac{(\alpha - \bar{\alpha})^2}{2\sigma^2}\right) \quad (19)$$

Equation (18) can only be solved numerically although the calculations are easy to perform.

This model of TCP has been tested on several clinical data sets. As an example, Fig. 7 shows the results of fitting the model to the data set of base of skull chordoma patients treated at the Massachusetts General Hospital in Boston [38]. The analysis revealed a fairly steep dose-response relationship for both female and male patients – the slope γ_{50} of 3.7. However, the two dose-response curves are significantly separated with

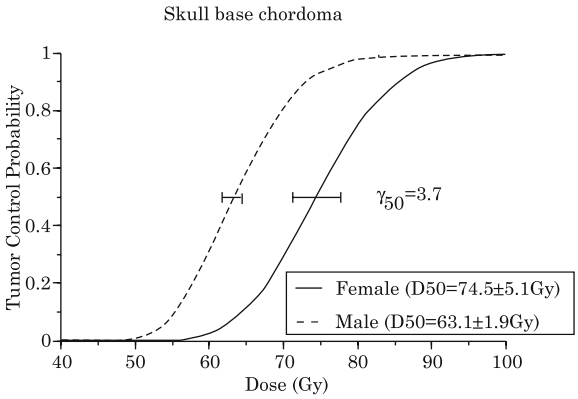

Fig. 7. Dose-response curves for chordoma of the base of skull for male and female patients treated with protons at MGH

the corresponding doses D_{50} of 74. 5 ± 5.1 Gy for females and D_{50} of 63. 1 ± 1.9 Gy for males. The error bars on the D_{50} doses indicate one standard deviation.

Several investigators developed TCP models roughly along the lines presented in this section [13, 17, 19, 35, 36, 39, 40].

Non-uniform Cell Burden and Expectation

Conventionally defined target volumes are represented as discrete volumes circumscribed by closed surfaces. This representation fails to take into account both the likely variations of cell density and sensitivity in different parts of the tumor – especially in its periphery – and the varying levels of confidence that malignant cells are actually present – especially in regions of (only) possible microscopic extension. Some, even very early, models have included such effects. Graffman included variation of the fraction of hypoxic cells in the tumor periphery [41]; Fisher has considered the importance of a graded cell density [42]. The possibility that a portion of the target volume is not malignant was considered by Goitein and Schultheiss [39] and has been incorporated in the formalism of the dose-response model. Any realistic model of tumor control has to take these effects into account.

Models of Normal Tissue Complication Probability (NTCP)

The response of normal tissues to radiation seems to us to be a far more complicated phenomenon than the response of tumors. Given that modeling the latter is difficult and controversial, it is hard to be optimistic about our ability to model the former. Nevertheless, clinicians daily make judgments about the likely consequences to normal tissues of a given treatment scheme. The goal of modeling normal tissue response is to capture some of that knowledge, where it exists, and to provide a framework within which new knowledge and understanding may be stimulated.

As we have already mentioned in the section on tissue architecture, most normal organs and tissues can

be described as being composed of functional subunits (FSUs) defined either structurally (for example nephrons in the kidney), or functionally (for example as the largest volume that can be repopulated by one clonogenic cell). If the end-point of interest can be triggered by a single lesion, the "critical element" (other term - "serial") architecture is considered. If the end-point occurs only when a substantial subvolume of the irradiated structure is damaged, the "critical volume" (other term - "parallel") architecture is considered.

Assuming that an organ consists of N FSUs, the probability that M or more of them is destroyed is given by the cumulative binomial probability [17, 43, 44]:

$$P = \sum_{t=M}^{N} \binom{N}{t} P_{\mathrm{FSU}}^{t} \left(1 - P_{\mathrm{FSU}}\right)^{N-t} \tag{20}$$

where P_{FSU} is the probability of killing one FSU. For the critical element architecture, the M is one and (20) reduces to

$$\begin{aligned} P(M=1) &= \sum_{t=1}^{N} \binom{N}{t} P_{\mathrm{FSU}}^{t} \left(1 - P_{\mathrm{FSU}}\right)^{N-t} \\ &= 1 - P_{\mathrm{FSU}}^{0}(1 - P_{\mathrm{FSU}})^{N} = 1 - (1 - P_{\mathrm{FSU}})^{N} \end{aligned} \tag{21}$$

Equation (21) is analogous to the Schultheiss's probability model [12, 45]. P_{FSU} can be calculated using either the logistic function (as was proposed by Schultheiss) or using the LQ cell survival models described earlier:

$$P_{\mathrm{FSU}} = [1 - \exp(-\alpha D - \beta d D)]^{K} \tag{22}$$

where K is the number of cells per FSU and $\exp(-\alpha D - \beta d D)$ is the probability that a cell survives dose D. Equation (22) assumes that an FSU is capable of regenerating from one clonogenic cell.

For large number of FSUs (say, N larger than 100) and for M larger than a few, the cumulative binomial probability is accurately approximated by a step function:

$$\sum_{t=M}^{N} \binom{N}{t} P_{\mathrm{FSU}}^{t} (1 - P_{\mathrm{FSU}})^{N-t} \approx \begin{cases} 1 & \text{for} \quad P_{\mathrm{FSU}} \geq \frac{M}{N} \\ 0 & \text{for} \quad P_{\mathrm{FSU}} < \frac{M}{N} \end{cases} \tag{23}$$

The ratio $M/N(\mu)$ corresponds to a partial volume of an organ which is destroyed by radiation. Therefore, one can interpret μ as a "functional reserve" of an organ [43, 46]. That is, the Critical Volume (Parallel) model states that the organ exhibits the end-point of interest if the damaged volume exceeds the "critical volume" or exceeds the "functional reserve" for that end-point.

The value of μ is, ordinarily, not known for an individual patient. Therefore, using a similar logic to that used for the TCP modeling, we can calculate the expected value of NTCP taken over a population. Assuming that all sources of inter-patient variation can be embedded into the variation of μ, the expected value of NTCP is

$$\langle NTCP \rangle = \int g(\mu) NTCP(\mu) d\mu \tag{24}$$

where $g(\mu)$ is the pdf for μ. Note that in clinically relevant situations $NTCP(\mu)$ is a step function, and (24) can be simplified:

$$\langle NTCP \rangle = \int_{-\infty}^{P_{\mathrm{FSU}}} g(\mu) d\mu \tag{25}$$

If μ follows a normal distribution with mean $\overline{\mu}$ and variance σ^2 (25) reduces to standard normal distribution function:

$$\begin{aligned} \langle NTCP \rangle &= \frac{1}{\sigma\sqrt{2\pi}} \int_{-\infty}^{P_{\mathrm{FSU}}} \exp\left[-\frac{(t-\overline{\mu})^2}{2\sigma^2}\right] dt \\ &= \Phi\left(\frac{P_{\mathrm{FSU}} - \overline{\mu}}{\sigma}\right) \end{aligned} \tag{26}$$

where Φ is the error function.

The extension of this model to an inhomogeneously irradiated structure is straightforward [17, 43]. Following the assumption that FSUs are uniformly distributed, and that they respond to radiation independently, P_{FSU} in (26) should be substituted by the average value of P_{FSU}, $\overline{P}_{\mathrm{FSU}}$, calculated over the entire volume of interest:

$$\overline{P}_{\mathrm{FSU}} = \sum_{i=1}^{N} v_i P_{\mathrm{FSU}}\left(D_i\right) \tag{27}$$

where $\{D_i, v_i\}$ correspond to bins of the differential DVH.

The most consequential difference between the CV and the CE models is in the very different dose-volume relationships they predict. Figure 8 shows an example of the probability of complication as a function of partial volume irradiated. Model predictions with and without taking into account inter-patient variability are shown. It is apparent that the CV model exhibits a volume threshold effect whereas the CE model does not. Indeed, the CE model has a characteristic linear dependence of NTCP on volume for small values of NTCP.

As an example of using the NTCP models in clinical studies, we analyzed the risk of late rectal wall bleeding as a function of the dose and absolute volume irradiated, using our Critical Volume (CV) model. The analysis was performed for 41 patients with a minimum follow-up of 4 years (no censoring) [47]. The volume of anterior rectum at risk was identified on each individual patient's transverse CT scans extending from the superior limit of the anus inferiorly to 2 cm superior to the prostate tumor volume superiorly, and extending laterally and posteriorly to a mid-coronal plane dividing anterior from posterior rectum. Long-term anterior

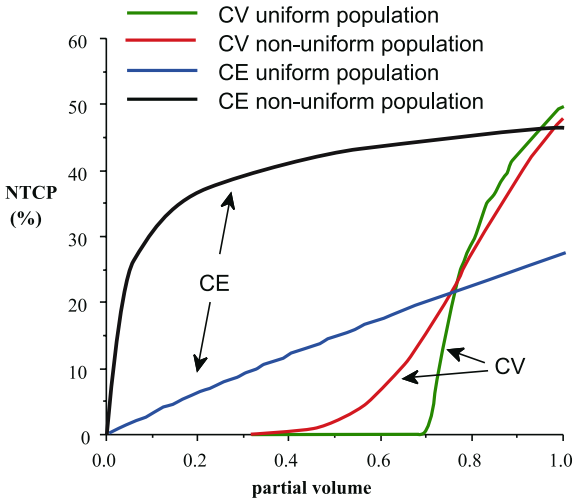

Fig. 8. The effect of population heterogeneity on the model predictions for Critical Element and Critical Volume models

rectal bleeding occurred in 14 of 41 patients. The maximum likelihood method was used to obtain the best parameters of the CV model. Using these parameters the probability of complication was calculated for each patient. To compare visually the model's predictions with the observed rates of complication we divided patients into four quartiles according to their calculated NTCP. Figure 9 shows the model's predictions and the observed rates of complication. The error bars for the observed NTCPs were calculated using binomial statistics. The good agreement between the model's predictions and the observed rates of complication suggests that the CV model might be a useful tool in planning radiotherapy of the prostate.

Källman et al. developed a "relative seriality" model that has the elements of both Critical Element and Critical Volume models [13].

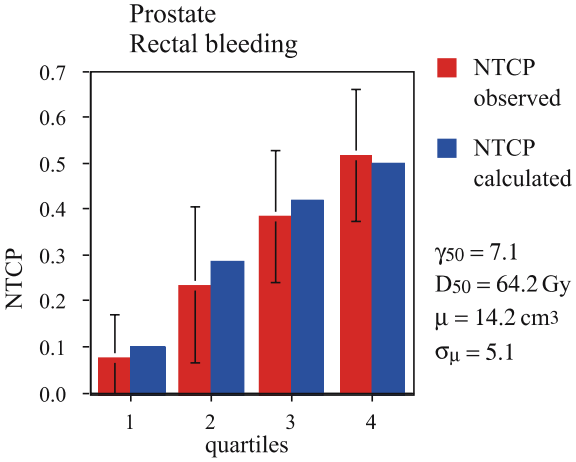

Fig. 9. Comparison of the observed and predicted rectal bleeding rates for prostate patients treated at MGH [47]

Phenomenological and Statistical Models of TCP and NTCP

One can argue that because the underlying biological mechanisms responsible for tissue damage are enormously complex it is practically impossible to develop a comprehensive and useful biological model of tissue response to radiation. Therefore, it might be better to use models driven by the data not by our incomplete understanding of the biological mechanisms. Phenomenological and statistical models make minimal assumptions about the underlying biology. This is a good approach if there is enough good data covering a wide spectrum of doses, volumes, and fractionation schemes. For example, both TCP and NTCP (labeled in (28)–(30) as p) can be modeled using a generalized linear model with the logit or probit link function [48, 49]:

$$\eta = \beta_0 + \beta_1 \ln(D) + \beta_2 \ln(V) + \beta_3 \ln(T) \tag{28}$$

$$\text{Logit:} \quad \ln\left(\frac{p}{1-p}\right) = \eta \quad \text{that is:} \quad p = \frac{\exp(\eta)}{1+\exp(\eta)} \tag{29}$$

$$\text{Probit:} \quad \Phi^{-1}(p) = \eta \quad \text{that is:} \quad p = \Phi(\eta) \tag{30}$$

$$= \frac{1}{\sqrt{2\pi}} \int_{-\infty}^{\eta} \exp\left(-\frac{t^2}{2}\right) dt$$

D is the total dose, V is the irradiated volume, T is the overall treatment time, β_i are the model parameters, and Φ is the standard normal distribution function. The Probit and Logit models are statistically indistinguishable on practically all real data sets.

The error function, Φ, was used in the phenomenological NTCP model proposed by Lyman [8]. The original Lyman model does not take into account the fractionation effects, and assumes that the tolerance dose, TD, changes with partial irradiated volume, v, according to the power law:

$$\text{NTCP} = \Phi(\eta) \quad \eta = \frac{D - TD(v)}{mTD(v)} \quad TD(v) = TD(1)v^{-n} \tag{31}$$

$TD(1)$, m, and n are the model parameters. The parameter m controls the slope of the dose-response curve, and the parameter n controls the dose-volume effects. Burman [50] estimated these parameters for several normal structures based on the estimates of tolerance doses provided by Emami [51].

Note that neither (28) nor the Lyman model (31) take into account dose inhomogeneity. For inhomogeneous dose distributions Lyman [9] and later Kutcher [10] proposed a dose-volume histogram (DVH) reduction scheme using the power law relationship with the same parameter n as it is used in (31). According to the Kutcher's DVH reduction scheme, a differential DVH

composed of N bins $\{D_i, v_i\}$ is reduced to a one bin histogram $\{D_{\text{ref}}, v_{\text{eff}}\}$ as follows:

$$v_{\text{eff}} = \sum_{i=1}^{N} v_i \left(\frac{D_i}{D_{\text{ref}}}\right)^{\frac{1}{n}} \tag{32}$$

The "effective volume", v_{eff}, is then substituted for v in (31). To assure that v_{eff} is always less than, or equal to, the volume of the whole organ, D_{ref} is commonly set to the maximum dose. The choice of D_{ref} does not matter for calculating the NTCP using (31), because D_{ref} cancels out. Equations (31) and (32) are often referred to as the "Lyman–Kutcher" model.

Phenomenological Model of EUD

Recently, a model of Equivalent Uniform Dose (EUD) loosely based on the mid-nineteenth century Weber-Fechner law describing a relationship between a stimulus and response has been proposed [56]. It has been found that for many natural and complex systems the response obeys a power-law distribution. In relation to radiation treatment one can assume that the level of response of a tissue or organ to radiation is proportional to a power function of the stimulus. There are different components of the stimulus beyond the obvious one, that is the total dose. In principle, the influence of other components of radiation treatment such as dose per fraction, time between fractions, or the total treatment time can be also well approximated by a power-law distribution. Here, we describe only the application of the power-law to modeling the inhomogeneity of the dose distribution. It has been proposed that for any inhomogeneous dose distribution within a volume of interest (VOI) (targets and normal organs and tissues) the EUD is described as follows:

$$\text{EUD} = \left[\frac{1}{N}\sum_{i=1}^{N} D_i^a\right]^{\frac{1}{a}} \tag{33}$$

where the sum is over all (N) voxels within the VOI and a is a tissue and end-point specific parameter. Value of the parameter a should be extracted from the clinical data. It should be noted that because the proposed model corresponds to a global and approximated functional relationship between the dose distribution and the response, the value of the parameter cannot be derived from mechanistic considerations. The EUD can be also calculated from a differential dose-volume histogram (DVH). From a general (33) it follows that

$$EUD = \left[\sum_{i=1}^{N} v_i D_i^a\right]^{\frac{1}{a}} \tag{34}$$

where pairs $\{v_i, D_i\}$ correspond to volume and dose bins of the DVH.

For tumors, the parameter a is always negative and for normal tissues and organs it is always positive. It can be shown that this is a consequence of a very general dose-volume relationship for tumors and normal tissues. Namely, it follows an observation that cold spots are bad for tumors and hot spots are bad for normal tissues. The extent of this effect is governed by the parameter a. It is logical that the EUD for any inhomogeneous dose distribution should be bounded by the minimum dose and the maximum dose within the VOI. It can be shown that for tumors the EUD is bounded by the minimum target dose and the mean target dose. For most normal tissues, the EUD is bounded by the mean dose and the maximum dose. Figure 10 and Fig. 11 show a hypothetical DVH (Fig. 10) corresponding to an inhomogeneous dose distribution with the minimum dose of 30 Gy, the average dose of 50 Gy, and the maximum dose of 70 Gy. Figure 11 shows the EUD for this histogram as a function of the value of the parameter a.

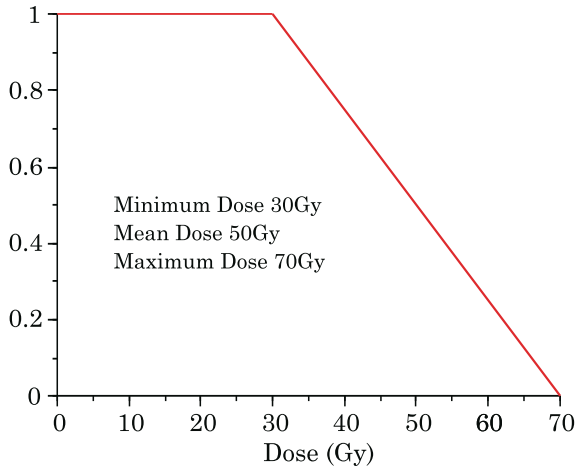

Fig. 10. A DVH corresponding to a nonuniform dose distribution with the range of doses (30 – 70 Gy)

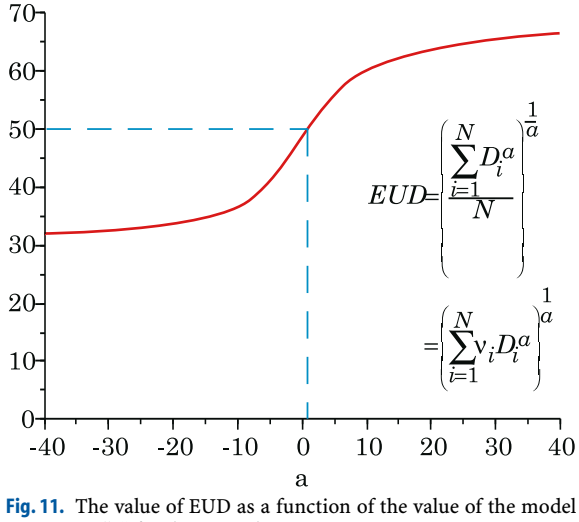

Fig. 11. The value of EUD as a function of the value of the model parameter "a" for the DVH shown in Fig. 10

Table 3. The estimated values of the EUD parameter "a" for a few tumors and normal structures

Structure (Source)	End-point	a
Chordoma base of skull (MGH)	Local control	–13
Squamous cc (Brenner)	Local control	–13
Melanoma (Brenner)	Local control	–10
Breast (Brenner)	Local control	–7.2
Parotids (Eisbruch)	Salivary function (< 25%)	< 0. 5
Parotids (Chao)	Salivary function (< 25%)	0.5
Liver (Lawrence)	Liver failure	0.6
Liver (Dawson)	Liver failure	0.9
Lung (Kwa)	Pneumonitis	1.0
Lung (Emami)	Pneumonitis	1.2
Kidney (Emami)	Nephritis	1.3
Liver (Emami)	Liver failure	2.9
Heart (Emami)	Pericarditis	3.1
Bladder (Emami)	Symptomatic contracture	3.8
Brain (Emami)	Necrosis	4.6
Colon (Emami)	Obstruction/perforation	6.3
Spinal cord (Powers)	White matter necrosis	13
Esophagus (Emami)	Perforation	18
Spinal cord (Schultheiss)	Paralysis	20

Figure 11 clearly demonstrates that the EUD for tumors approaches the minimum target dose for the values of *a* approaching the negative infinity. The EUD for normal organs approaches the maximum dose for the values of the parameter *a* approaching the positive infinity. Note that for an equal to 1 (one) the EUD is just the mean dose.

Table 3 shows the values of the parameter *a* for a few tumors and normal structures. Some of the values have been extracted from clinical or experimental data by fitting a logistic model of dose-response to data using the maximum likelihood methodology. Some of them were calculated from the consensus normal tissue tolerance data published by Emami et al. It must be emphasized that for most structures these values are rather uncertain and should not be used without full understanding of the model.

The structures in Table 3 are listed in the order of increasing value of *a*. The order suggests that structures with functional end-points tend to have low values of *a*(i.e., around 1). These are also structures with relatively large functional reserve. For these organs (such as lung, liver, or kidney) the maximum dose matters less and the mean dose taken over the entire structure matters more. These structures are said to exhibit large volume effects. That is, roughly speaking, it matters how much of the structure volume is irradiated (or spared). On the other spectrum of dose-volume effects are the so-called serial or critical element structures (such as spinal cord or esophagus) which are characterized by larger values of *a*. The relevant end-points for these structures seem to correspond to, or be the results of, structural damage. These structures are more sensitive to the maximum dose even if only a relatively small volume is irradiated to that high dose.

5.7 The Role of Models of Tissue Response to Radiation

Without a doubt, the most telling criticism of the various biological models outlined above is that they affect to represent what are surely extremely complex and at best poorly understood systems with very simplistic models which use very few parameters. Can such models have any hope of success or be of any value? If the goal were to predict in an absolute sense the response of human tissues to radiation, one would have to respond in the negative. However, fortunately this is not the case. To a certain extent one is interested in the relative impact of two or more dose distributions on each organ or tissue and here there is perhaps a reasonable chance for at least correctly ranking plans in terms of their impact on a given organ and, perhaps, some quantitative measure of their relative impact.

It is worth emphasizing that a dose specification is also, implicitly, a biological model in that it carries the implication that, for example, an unacceptable biological response would result if that dose were exceeded within the specified organ. Such a "model" is even more simplistic and is certainly less likely to be correct than the biological models described above. On the other hand, dose prescriptions have the advantage of explic-

itness and stability over time. The danger in biological modeling is that the models can become so complex that their content is not understood or agreed upon among experts.

The great advantage of these biological models is that they report scores of direct clinical relevance. Probabilities of complication or tumor control are of direct interest to the clinician and patient. Their combination into an overall score is certainly very difficult, but at least the parameters are in the correct space. Anyone who has attempted to develop a scoring scheme using dose criteria will have come squarely against the near impossibility of allocating reasonable relative weights to the several dose comparisons which go to make up the plan evaluation.

Biological models seem to us to have potential value, both for plan evaluation (where TCPs and NTCPs can be reviewed as independent values and used to highlight regions of concern or unconcern) and for plan selection, improvement or optimization. Their development has highlighted the dearth of clinical data that the models attempt to represent, particularly as regards the dose-volume effect, and may promote much needed research into both tumor and normal tissue responses to inhomogeneous patterns of irradiation.

References

1. Hope CS, Laurie J et al. (1967) Optimization of X-ray treatment planning by computer judgement. Phys Med Biol 12(4):531–542
2. Bahr GK, Kereiakes JG et al. (1968) The method of linear programming applied to radiation treatment planning. Radiology 91(4):686–693
3. Hodes L (1974) Semiautomatic optimization of external beam radiation treatment planning. Radiology 110(1):191–196
4. McDonald SC, Rubin P (1977) Optimization of external beam radiation therapy. Int J Radiat Oncol Biol Phys 2(3/4):307–317
5. Starkschall G (1984) A constrained least-squares optimization method for external beam radiation therapy treatment planning. Med Phys 11(5):659–665
6. Powlis WD, Altschuler MD et al. (1989) Semi-automated radiotherapy treatment planning with a mathematical model to satisfy treatment goals. Int J Radiat Oncol Biol Phys 16(1):271–276
7. Morrill SM, Lane RG et al. (1991) Treatment planning optimization using constrained simulated annealing. Phys Med Biol 36(10):1341–1361
8. Lyman JT (1985) Complication probability as assessed from dose-volume histograms. Radiat Res Suppl 8(9):S13–S19
9. Lyman JT, Wolbarst AB (1987) Optimization of radiation therapy, III: A method of assessing complication probabilities from dose-volume histograms. Int J Radiat Oncol Biol Phys 13(1):103–109
10. Kutcher GJ, Burman C (1989) Calculation of complication probability factors for non-uniform normal tissue irradiation: the effective volume method [see comments]. Int J Radiat Oncol Biol Phys 16(6):1623–1630
11. Lyman JT, Wolbarst AB (1989) Optimization of radiation therapy, IV: A dose-volume histogram reduction algorithm. Int J Radiat Oncol Biol Phys 17(2):433–436
12. Niemierko A, Goitein M (1991) Calculation of normal tissue complication probability and dose-volume histogram reduction schemes for tissues with a critical element architecture. Radiother Oncol 20(3):166–176
13. Kallman P, Agren A et al. (1992) Tumour and normal tissue responses to fractionated non-uniform dose delivery. Int J Radiat Biol 62(2):249–262
14. Lyman JT (1992) Normal tissue complication probabilities: variable dose per fraction. Int J Radiat Oncol Biol Phys 22(2):247–250
15. Mohan R, Mageras GS et al. (1992) Clinically relevant optimization of 3-D conformal treatments. Med Phys 19(4):933–944
16. Niemierko A, Urie M et al. (1992) Optimization of 3D radiation therapy with both physical and biological end points and constraints. Int J Radiat Oncol Biol Phys 23(1):99–108
17. Niemierko A, Goitein M (1993) Implementation of a model for estimating tumor control probability for an inhomogeneously irradiated tumor. Radiother Oncol 29(2):140–147
18. Niemierko A, Goitein M (1993) Modeling of normal tissue response to radiation: the critical volume model. Int J Radiat Oncol Biol Phys 25(1):135–145
19. Webb S (1993) The effect on tumour control probability of varying the setting of a multileaf collimator with respect to the planning target volume. Phys Med Biol 38(12):1923–1936
20. Mohan R, Wang X et al. (1994) The potential and limitations of the inverse radiotherapy technique. Radiother Oncol 32(3):232–248
21. Wang XH, Mohan R et al. (1995) Optimization of intensity-modulated 3D conformal treatment plans based on biological indices [see comments]. Radiother Oncol 37(2):140–152
22. Kutcher GJ (1996) Quantitative plan evaluation: TCP/NTCP models. Frontiers Radiat Ther Oncol 29:67–80
23. Mohan R, Wang X et al. (1996) Optimization of 3-D conformal radiation treatment plans. Front Radiat Ther Oncol 29:86–103
24. Niemierko A (1997) Reporting and analyzing dose distributions: a concept of equivalent uniform dose. Med Phys 24(1):103–110
25. Niemierko A (1998) Radiobiological models of tissue response to radiation in treatment planning systems. Tumori 84(2): 140–143
26. Kutcher G (1990) Quantitative plan evaluation. AAPM Summer School. American Institute of Physics, J Purdy, Woodbury, NY
27. Wu Q, Mohan R et al. (2002) Optimization of intensity-modulated radiotherapy plans based on the equivalent uniform dose. Int J Radiat Oncol Biol Phys 52(1):224–235
28. Douglas BG, Fowler JF (1976) The effect of multiple small doses of X rays on skin reactions in the mouse and a basic interpretation. Radiat Res 66(2):401–426
29. Thames HD (1985) An 'incomplete-repair' model for survival after fractionated and continuous irradiations. Int J Radiat Biol 47(3):319–339
30. Thames HD, Hendry JH (1987) Fractionation in radiotherapy. Taylor & Francis
31. Hall EJ (1994) Radiobiology for the radiologist. J.B. Lippincott, Philadelphia
32. Brenner DJ, Hlatky LR et al. (1995) A convenient extension of the linear-quadratic model to include redistribution and reoxygenation. Int J Radiat Oncol Biol Phys 32(2): 379–390
33. Withers HR, Taylor JM et al. (1988) Treatment volume and tissue tolerance. Int J Radiat Oncol Biol Phys 14(4):751–759

34. Withers HR (1986) Predicting late normal tissue responses. Int J Radiat Oncol Biol Phys 12(4):693–698
35. Brahme A (1984) Dosimetric precision requirements in radiation therapy. Acta Radiol Oncol 23(5):379–391
36. Brenner DJ (1993) Dose, volume, and tumor-control predictions in radiotherapy. Int J Radiat Oncol Biol Phys 26(1):171–179
37. Okunieff P, Morgan D et al. (1995) Radiation dose-response of human tumors. Int J Radiat Oncol Biol Phys 32(4):1227–1237
38. Terahara A, Niemierko A et al. (1999) Analysis of the relationship between tumor dose inhomogeneity and local control in patients with skull base chordoma. Int J Radiat Oncol Biol Phys 45(2):351–358
39. Goitein M (1985) Calculation of the uncertainty in the dose delivered during radiation therapy. Med Phys 12(5):608–612
40. Zagars GK, Schultheiss TE et al. (1987) Inter-tumor heterogeneity and radiation dose-control curves. Radiother Oncol 8(4):353–361
41. Graffman S, Groth T et al. (1975) Cell kinetic approach to optimising dose distribution in radiation therapy. Acta Radiol Ther Phys Biol 14(1):54–62
42. Fisher ER, Fisher B (1969) Effects of X-irradiation on parameters of tumor growth, histology, and ultrastructure. Cancer 24(1):39–55
43. Jackson A, Kutcher GJ et al. (1993) Probability of radiation-induced complications for normal tissues with parallel architecture subject to non-uniform irradiation. Med Phys 20(3):613–625
44. Stavreva N, Niemierko A et al. (2001) Modelling the dose-volume response of the spinal cord, based on the idea of damage to contiguous functional subunits. Int J Radiat Biol 77(6):695–702
45. Schultheiss TE, Orton CG et al. (1983) Models in radiotherapy: volume effects. Med Phys 10(4):410–415
46. Jackson A, Ten Haken RK et al. (1995) Analysis of clinical complication data for radiation hepatitis using a parallel architecture model. Int J Radiat Oncol Biol Phys 31(4):883–891
47. Hartford AC, Niemierko A et al. (1996) Conformal irradiation of the prostate: estimating long-term rectal bleeding risk using dose-volume histograms. Int J Radiat Oncol Biol Phys 36(3):721–730
48. Herbert ED (ed) (1993) Quality assessment and improvement of dose-response models: some effects of study weaknesses on study findings. "c'est magnifique?" A report of Task Group 1 of the AAPM Biological Effects Committee. AAPM Report No. 43, Med Phys Pub, Madison
49. Lindsey JK (1997) Applying generalized linear models. Springer, Berlin Heidelberg New York
50. Burman C, Kutcher GJ et al. (1991) Fitting of normal tissue tolerance data to an analytic function. Int J Radiat Oncol Biol Phys 21(1):123–135
51. Emami B, Lyman J et al. (1991) Tolerance of normal tissue to therapeutic irradiation. Int J Radiat Oncol Biol Phys 21(1): 109–122
52. Mohan R, Niemierko A (2002). Intensity modulated radiation therapy. ASTRO Syllabus, New Orleans
53. Kutcher GJ et al. (1991) Histogram reduction method for calculating complication probabilities for three-dimensional treatment planning evaluations. Int J Radiat Oncol Biol, Phys 21(1):137–146
54. Brahme A (1996) Recent developments in radiation therapy planning and treatment optimization. Australas Phys Eng Sci Med 19(2):53–66
55. Barendsen GW (1982) Dose fractionation, dose rate and iso-effect relationships for normal tissue responses. Int J Radiat Oncol Biol Phys 8(11):1981–1997
56. Niemierko A (1999) A generalized concept of Equivalent Uniform Dose. Proceedings of the 41th AAPM Annual Meeting, Nashville, Tennessee. Med Phys 26(6):1100

Advanced Imaging and Guidance System for Use in Intensity Modulated RT

D.A. Jaffray, K.K. Brock, M.B. Sharpe

6

Contents

6.1 Introduction

The advent of advanced volumetric imaging technologies combined with rapid visualization tools is set to have a profound impact on the practice of radiation oncology. The role of these technologies in the accurate identification and localization of diseased and normal structures remains to mature. A great deal of effort has been invested in the development of novel imaging signals for target characterization (see Chapter II. 2). However, as yet very few of these signals have been used in the clinical process as standard determination of target structures. The challenges associated with validation of these surrogates for disease extent are not insignificant. Large-scale clinical investigations must be pursued to validate the merits of these biological target volumes [1]. The importance of developing a robust infrastructure to support these investigations should not be underestimated if these evaluations are to be achieved in a timely fashion.

Currently, the vast majority of target and normal structures are defined using computed tomography (CT), the development of which has taken almost 15 years to become the standard of care in radiation therapy. The gradual introduction of structural magnetic resonance (MR) imaging into the simulation process is encouraging [2–4]. The merits of MR in characterization of diseased and normal structures throughout the body are not debated (see Chapter I. 3). Clearly, a first step toward improved determination of radiation therapy targets should include adoption of the mature imaging signals achieved through MR imaging methods. Leveraging the substantial experience with MR in the radiology environment would permit an accelerated validation of MR-based structural imaging in the design of targets and normal structures. Furthermore, the adaptation of the treatment to the dynamic changes in these structural signals would be more readily adopted, given that the original target definitions were based on these same signals.

The development of a robust system for image signal integration and treatment design is a focus of our research program. The system is being developed in conjunction with the development of a program for volumetric image-guidance of radiation field placement using cone-beam CT imaging integrated with the treatment unit. Figure 1 illustrates the conceptual elements of a comprehensive and integrated program for image-guided radiation therapy. In this program, geometric guidance and dose delivery is satisfied through a cone-beam CT equipped medical linear accelerator while dynamic re-evaluation of target and normal structures is performed off-line using the novel imaging signals that are being developed through functional and molecular imaging approaches. In current investigations, the focus is placed on the development of a methodology of integrating MR image signals into a process for target definition and evaluation that interfaces with the volumetric imaging capabilities of a cone-beam CT equipped medical linear accelerator. In this chapter, two novel technologies that will significantly impact the radiation simulation and treatment process are introduced – a cone-beam CT guided medical linear accelerator and an MR simulator. Critically important software systems that are being developed for integration of these de-

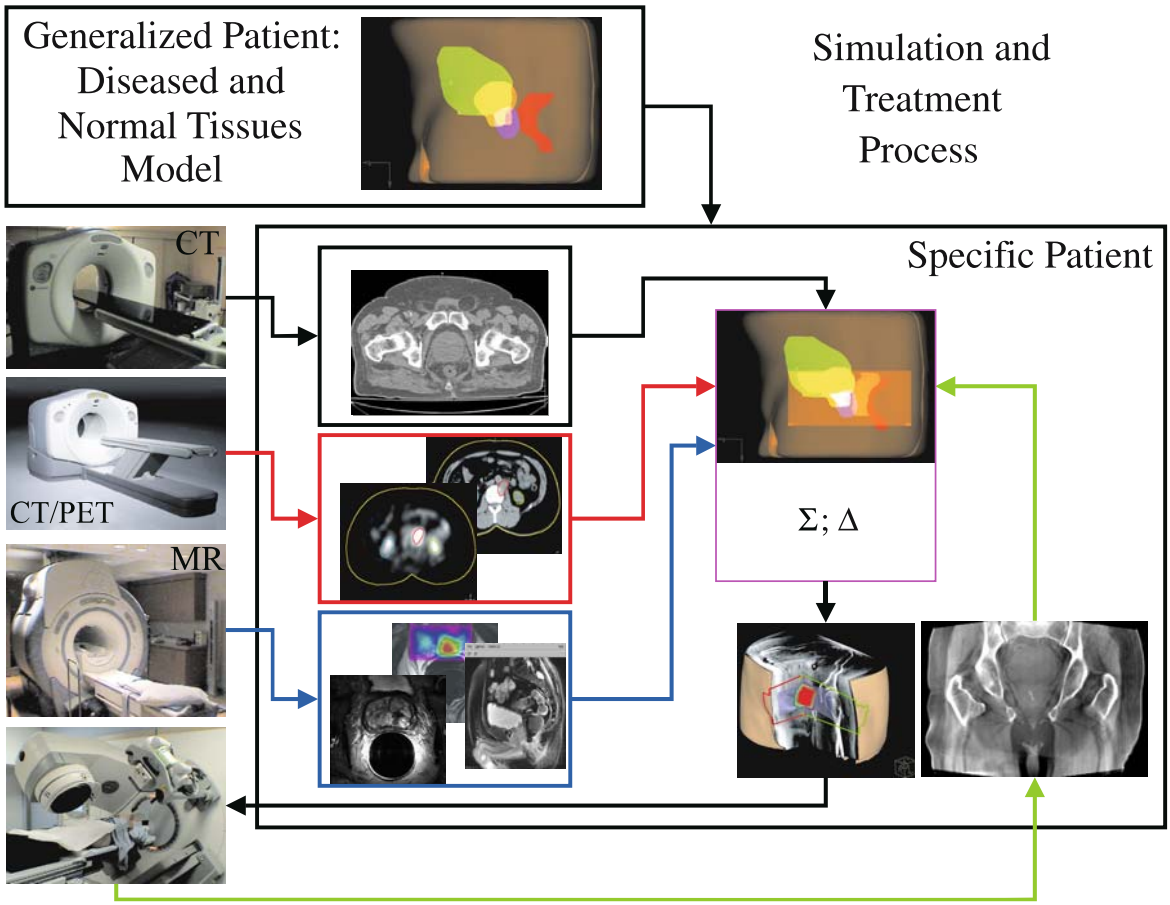

Fig. 1. The development of numerous imaging modalities for the guidance and monitoring of radiation therapy requires the creation of a robust software system for integration of these various image signals and determination of appropriate actions. The development of MR-simulators combined with volumetric imaging at the treatment unit is a key ingredient in the creation of such a simulation and treatment process. The expanding use of structure-derived inverse treatment plans combined with images of changing anatomy will instigate changes in the desired daily dose distribution leading to dynamic refinement over the course of therapy. Methods of monitoring response and verifying the delivery geometry are prerequisites of this type of advanced process

vices into the radiation therapy clinical process are also described.

6.2 Image-guided Radiation Therapy Using Cone-beam CT

The deleterious effects of imprecision in the daily placement of the radiation dose include increased dose to surrounding normal structures and significant restrictions to dose escalation in those diseases for which higher doses are associated with higher control rates. In current radiotherapy practice, the residual geometric uncertainties require planning target volume (PTV) margins in the range of 5–20 mm depending on the location of the target volume and methods of assuring the geometric quality of the delivery process. Margins such as these result in dose limiting complications in surrounding structures and require prolonged fractionation schedules. The development of a method of precise radiation delivery through daily localization of the target and normal structures would be of significant benefit.

Over the past eight years, a novel imaging method has been developed for adaptation to a conventional medical linear accelerator. The method employs CT principles in conjunction with a large area flat panel detector to generate a volumetric computed tomography dataset through a single rotation of the system about the patient. The need for only a single rotation makes it readily adapted to the structure of the conventional gantry systems employed in radiation therapy. Significant effort has gone into characterizing this technology over the past five years [5–12]. Overall, the systems are capable of producing high-resolution volumetric images of soft-tissue structures within the patient at reasonable doses (< 5 cGy). A current prototype is shown in Fig. 2. This system has been employed in a variety of clinical sites to

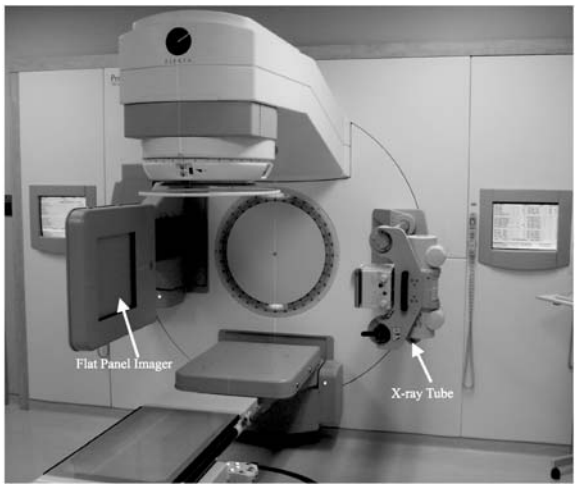

Fig. 2. The Elekta Synergy system for volumetric image-guided radiation therapy. This system permits kilovoltage cone-beam CT images to be acquired of the patient prior to radiation delivery for on-line assessment of internal target position. At present, this system will generate a volumetric CT dataset (512^3) from 330 projections acquired over 100 s. The volumetric images are available for on-line adjustment within minutes. This technology is being evaluated for image quality and accuracy of guidance

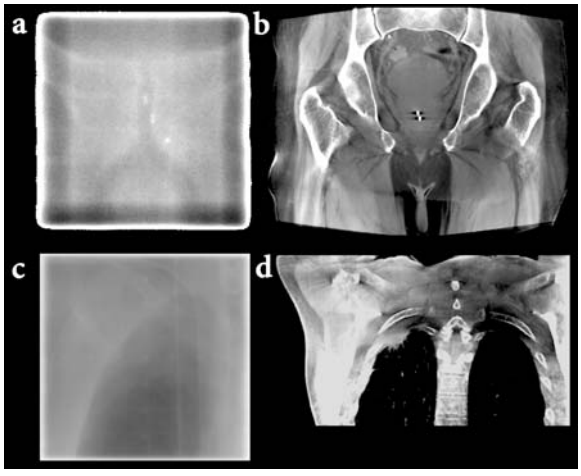

Fig. 3a–d. A comparison of: **(a)**, **(c)** megavoltage portal images; **(b)**, **(d)** kilovoltage cone-beam CT images of the same patient for prostate **(a)**, **(b)** and lung **(c)**, **(d)**. The doses used to form the portal and cone-beam CT images are comparable. The difference in information contained in the two different modalities is significant. The prostate images contain gold markers currently used as the 'gold standard' to guide field placement. Both image sets were acquired on the unit shown in Fig. 2

explore its utility in targeting radiation field placement. Figure 3 shows a comparison of the type of data the system generates in contrast to the conventional portal imaging (flat panel detector) approaches. The advantage of volumetric imaging over projection imaging in the interpretation of patient positioning is under evaluation. The elimination of the ambiguity associated with the projected geometry contained in radiographs (MV or kV) seems to be of significant merit (see Fig. 4). This may be an advantage in the rapid evaluation required in an on-line guidance model, in which the patient position would be adjusted on a daily basis based upon images of their internal anatomy. Figure 5 presents the kind of feedback models that can be pursued with the availability of this type of volumetric data at each treatment fraction.

The establishment of the system's geometric positioning accuracy and precision is critical for these image sets to be of value in the guidance of treatment. To this end, a comprehensive guidance system has been constructed to allow the images generated with this system to be directly imported into a three-dimensional (3D) treatment planning system with image fusion capabilities. A calibration method has also been developed to relate the coordinate systems of the imaging and delivery systems, such that image signals within each cone-beam CT dataset can be used to estimate the target position with respect to isocenter. Using portal localization as the ground truth, the cone-beam CT system was employed to position a spherical target at the treatment isocenter of the accelerator. The spherical target was imaged using cone-beam CT images and compared to a planning CT dataset for which the target's center had been set as isocenter. A contour of the spherical target was aligned to the on-line image using the fusion capabilities of a 3D planning system. The resulting displacements were then applied to the patient positioning couch and a second set of portal images were acquired. The residuals over a three month period of daily trials is shown in Fig. 6. The system demonstrates an excellent precision of 1 mm over the prolonged period of these investigations. The study of accuracy of the system in these tests demonstrates a slight miscalibration in the initial commissioning of the device. This is illustrated by the noticeable 2 mm systematic error in the left-right dimension of the plot in Fig. 6. This systematic error has since been corrected through the development of a more robust method of calibrating the treatment isocenter that employs portal images from multiple gantry angles (over 360°).

Overall, the cone-beam CT device is showing its capacity to generate volumetric images of radiation therapy patients in the treatment position at acceptable imaging doses. The resulting images are of excellent spatial detail and moderate soft-tissue contrast. Depending on the anatomical site, the soft-tissue images are more than sufficient to guide the placement of the radiation treatment field. The geometric guidance precision studies to date demonstrate the devices stability and suitability for guidance. The volumetric images have the added advantage of being very easy to evaluate in comparison to projection radiographs of either megavoltage or kilovoltage energies. This is further illustrated in Fig. 4. The imaging performance of the system will be influenced significantly by peristalsis in some anatomical sites (liver, stomach, upper GI). The issue

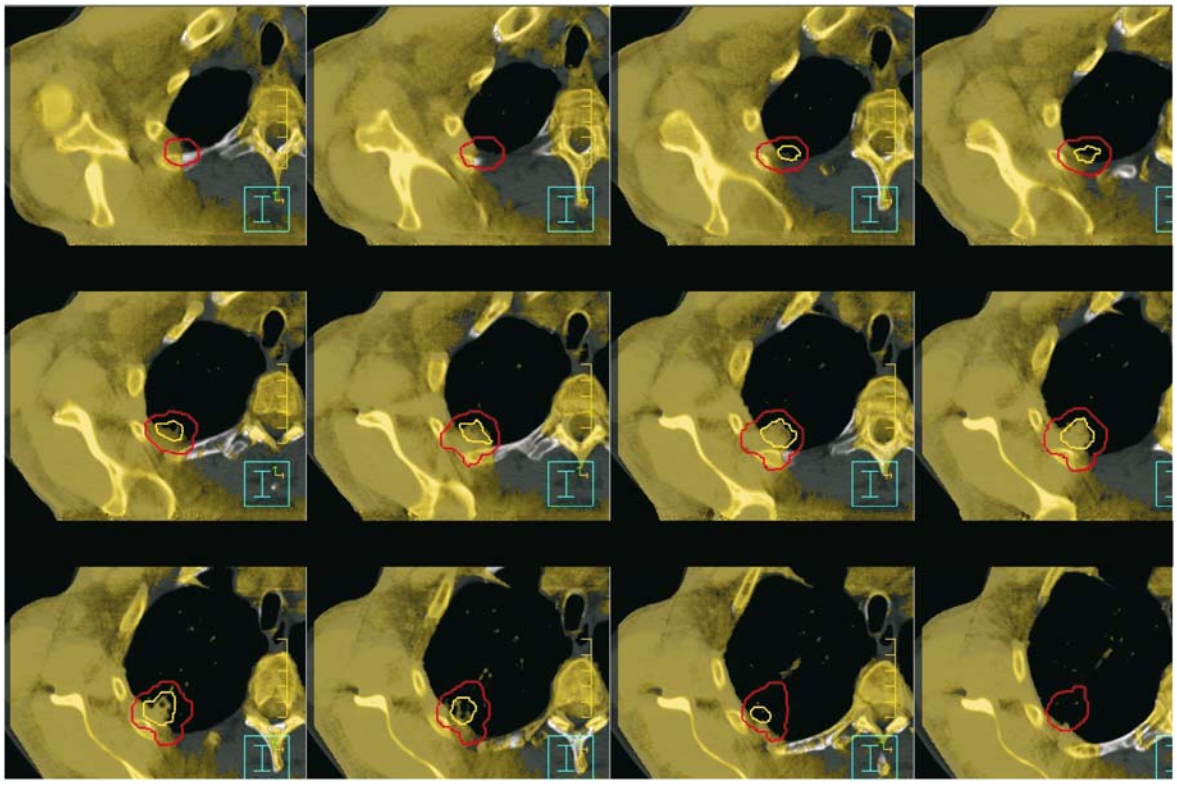

Fig. 4. A series of axial slices through a cone-beam CT dataset of a patient under treatment for lung cancer. The image set in *yellow* is the cone-beam CT and the image set in *gray scale* is the planning CT. The two contours are the CTV and PTV volumes used in the planning process. The confirmation of target location in this geometrically calibrated cone-beam CT is easily interpreted

of breathing motion has been addressed through the development of retrospective respiratory correlated reconstructions [13]. This approach has been applied by multiple investigators and shows excellent results for lesions in the lung where contrasts are quite high. The success of this approach in improved imaging of liver, for example, remains to be proven.

Besides the technical elements of the cone-beam CT system, there are many logistic issues that are raised by this technology. The presentation of a substantial quantity of readily interpreted imaging information about the geometric position of the patient with respect to the treatment beam creates both opportunity and challenges when introduced to conventional practice. Each image presents both predictable and unpredictable deviations from that outlined in the treatment plan and treatment planning CT. In this context, the justified selection of PTV margins comes under significant scrutiny. The employment of appropriate margins may appear to be excessive when an estimate of the dose

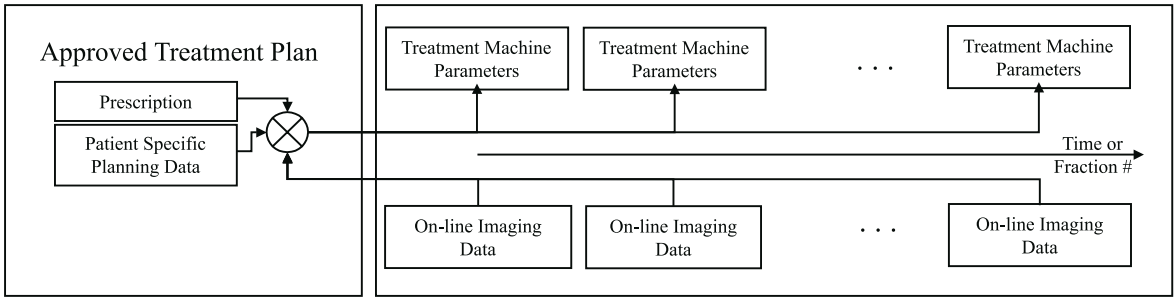

Fig. 5. The establishment of a robust and accurate source of information regarding the target and normal structures at the time of treatment permits exploration of a feedback model the can be refined to accommodate uncontrolled or treatment-induced changes in these structures. The explicit dependencies of IMRT- based plans on these structures will make feedback a feasible objective. The calculation of appropriate treatment machine parameters can be performed at the time of therapy depending upon that fraction's image as well as any previous data collected for that patient. In this way, the treatment plan becomes a method of reacting to the on-line data instead of a fixed set of pre-approved parameters

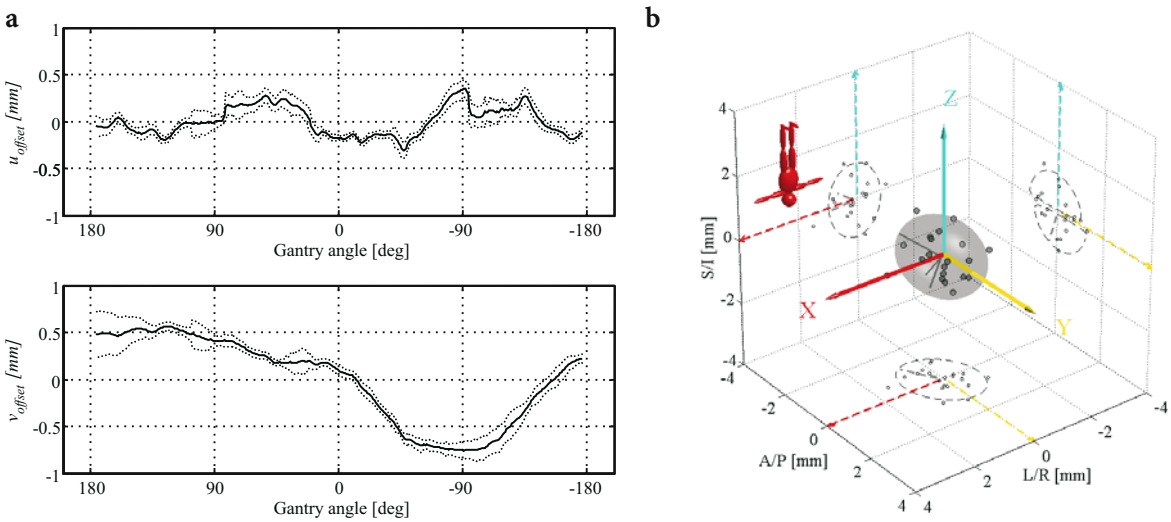

Fig. 6a,b. The geometric accuracy and precision of the imaging information generated by the cone-beam CT systems needs to be validated for guidance to be possible: (a) a prolonged study of the geometric stability of the kilovoltage imaging subcomponents has demonstrated the mechanical assembly is capable of delivering sub-mm precision; (b) the accuracy and precision of the system compared to portal imaging based methods. The overall guidance precision is 1 mm with a systematic error detected in the left-right dimension. This has since been resolved through a more robust determination of treatment isocenter

distribution is overlaid upon the daily image of the normal and targeted anatomy. The decision to intervene needs to be carefully managed and needs to be consistent with the margins employed to avoid gross errors or gross inefficiencies in the treatment process. Of critical importance is the development of appropriate tools and decision rules for the appropriate utilization of this technology. The radiation equipment manufacturers need to make every effort to create systems that do not inhibit appropriate use of this information. The level of integration required to capitalize fully on this new data at the treatment unit will challenge the currently accepted standards of integration in the radiation therapy environment.

The introduction of volumetric data into the delivery guidance, verification, and evaluation process will lead to the demand for tools that permit these activities to be performed in a quantitative fashion. Over the past five years, numerous investigators have been exploring the development of methods of dealing with deformations in anatomy [14–16]. Careful quantification of these daily imaging data can lead to a dramatic improvement in the quality assurance processes employed in radiation therapy. The presentation of each day's treatment to the responsible clinician will provide a level of accuracy that has not been previously attainable. The concise volumetric format of these results will also serve to minimize the time required for the clinician to perform this evaluation.

In addition to providing an accurate record of the treatment process, the volumetric datasets provide a reference for which other imaging data can be referenced. The revolution that is ongoing in the radiotherapy simulation process with respect to MR imaging is well supported by the introduction of volumetric cone-beam CT over the treatment course. Geometrically accurate images that permit accurate dose calculations to be performed are critical for radiation therapy. The advancement of an integrated system for simulation and treatment that employs CT for robust geometric characterization and attenuation coefficient estimation while integrating MR imaging results for tissue characterization and measurement of target and normal structure mobility may be the radiation oncology practice of the future. Of course, as shown conceptually in Fig. 1, further augmentation with additional imaging modalities should also be expected.

6.3 The Development of MR Simulators

Since its invention in 1973, MR imaging has been improving the ability to visualize both normal and diseased tissues [17]. Its integration into radiotherapy treatment planning process began in the mid-1980s when treatment planning began to integrate 3D imaging techniques [18–21]. However, not until recently, with the advent of dedicated MR scanners in the radiation oncology setting (referred to as an MR-Simulator), has MR imaging truly began to integrate into the imaging, planning, treatment, and monitoring of cancer patients treated with radiation. There are very few dedicated MR simulators in current practice. The MR simulator installed at the Fox Chase Cancer Center [2] was one of the first to be installed and it operates at a low field strength (0.23 T). The majority of MR scanners installed in clinics today are 1.5 T, closed-bore scanners, with the

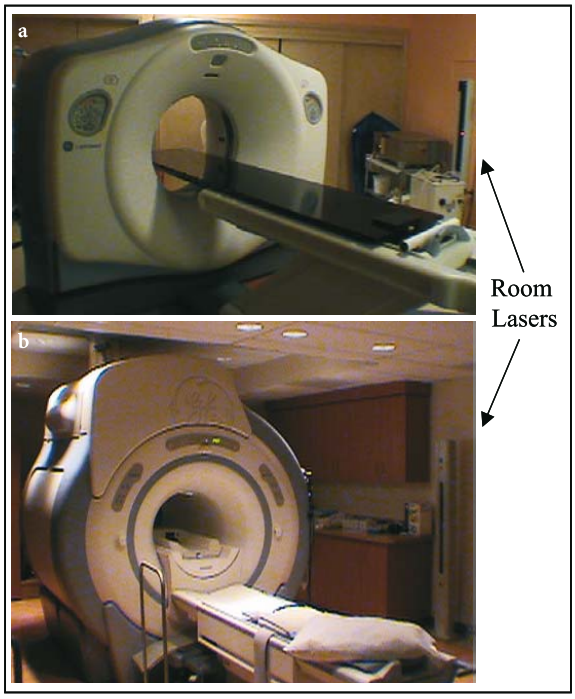

Fig. 7a,b. Photographs of: (a) the CT-simulator; (b) a MR-simulator in the Radiation Medicine Program of the Princess Margaret Hospital. The MR simulator is based upon the GE 1.5 T Excite System (four channel). Lasers have been installed in the room to permit better replication of the setup conditions employed in CT-simulation prior to the MR imaging. The room is equipped with a power injector for contrast enhanced and perfusion studies. A flat table insert was constructed to improve further the similarity of positioning between the CT and MR simulators. This system is equipped with a GE AdvantageSim workstation

introduction of 3 T scanners on the rise. The slow acceptance of low-field open bore scanners in radiation therapy is likely to continue. The advantages of higher field strength, 1.5 T or more, are driving other radiation oncology programs to adopt these higher field strength scanners in the role of MR-simulator. Figure 7 shows an MR-simulator and CT-simulator installation at Princess Margaret Hospital. The radiation oncology practice will benefit from the continued advancements in MR technology. A variety of specialized coils are now available to provide enhanced imaging of the head and neck, spine, thorax, abdomen, and extremities. In addition, the technical advances in parallel imaging are allowing a reduction in image acquisition time while retaining a high image quality. In parallel imaging, the amount of *k*-space data acquired is reduced and the remainder of the data is interpolated allowing for a large reduction in imaging time at a cost of only a small reduction in image quality [22]. This faster imaging can be extremely useful for monitoring motion using cinematographic (cine) MR as well as for full volume scans at breath hold [23]. Both are of great value in the design of appropriate margins in the radiation therapy process.

6.3.1 The Potential of MR Imaging for Radiotherapy

MR imaging offers outstanding soft tissue contrast as well as the ability to perform functional imaging via MR spectroscopy. The most common sites for MR integration into treatment planning are the brain and prostate. MR imaging has been shown to significantly improve the ability to define both tumor and normal structures in the brain [24–26]. Its integration into treatment planning is straightforward, as rigid registration will accurately align the MR to the planning CT scan in the majority of cases. MR spectroscopy also provides valuable functional information of the brain [27,28]. MR imaging has also demonstrated value in the treatment of prostate cancer. The soft tissue contrast in MR makes the prostate, especially at the posterior apical prostate border, which is difficult to decipher on CT imaging, much easier to visualize and therefore contour. Studies have shown that inter-observer variations are smaller for MR-based contours of the prostate than CT-based contours [29, 30]. A variety of MR sequences are also available to provide optimal imaging of implanted seeds (i.e. GRE) as well as prostate anatomy (i.e. T2 FSE), which can further aid in prostate MR to CT registration. MR spectroscopy can provide functional information of the prostate, indicating diseased areas as well as response to treatment [31–34].

Definition, staging, and delineation of tumors in the liver also benefit from the soft tissue contrast of MR imaging. Spoiled gradient and fast spin echo sequences can also be enhanced using MR contrast agents (e.g. gadolinium). Tumor delineation can then be compared between MR and CT, following the appropriate image registration. Figure 8 shows the corresponding planes of an MR and CT scan for a patient treated for primary colangiocarcinoma. The patient had contraindication to IV contrast, so IV contrast was not permitted. The tumor is barely visible on the CT scan, shown on the left, compromising the ability to define the tumor region. T2 weighted fast spin echo MR imaging, middle image, shows the excellent definition between the tumor and normal tissue, without additional contrast. The image on the right illustrates the rigid body registration that was performed to align the MR to the CT scan for treatment planning. Notice the good agreement of the liver near the tumor, but discrepancies farther from the tumor, near the stomach, for example, that indicate the necessity for deformable image registration.

The utilization of MR imaging for breast cancer staging, response, and detection has been increasing, with research indicating that radiation effects, small tumor detection, and recurrence may be better imaged using MR [35–39]. The benefits of MR for lung cancer are being actively investigated and are indicating that MR can assist with determining risk factors of radiation pneumonitis, tumor response, and staging [40–42]. Cervical

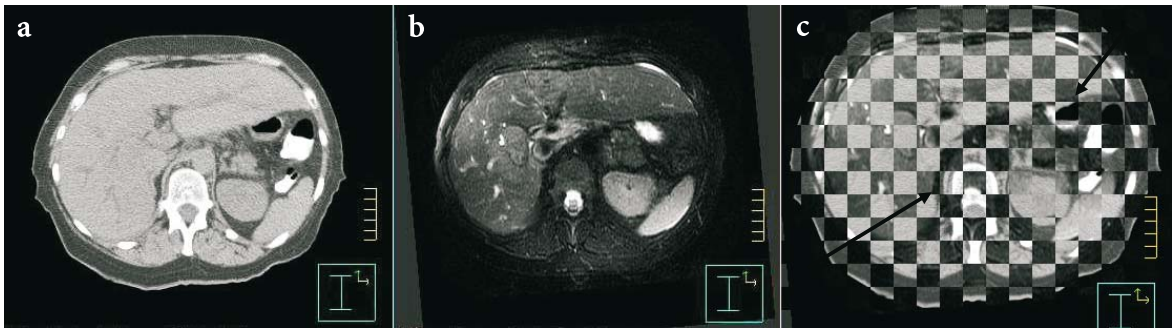

Fig. 8. CT and MR images of the liver in a patient suffering from primary colangiocarcinoma. The tumor is barely visible on the CT scan (*left*) compromising the ability to define the tumor region. T2 weighted fast spin echo MR imaging (*center*) shows the excellent definition between the tumor and normal tissue, without additional contrast. The image on the right illustrates the rigid body registration that was performed to align the MR to the CT scan for treatment planning. Notice the good agreement of the liver near the tumor, but discrepancies farther from the tumor (designated by *black arrows*), indicating the necessity for deformable image registration

cancer staging and diagnosis, tumor response and recurrence, and normal tissue complications detection has also been shown to improve with the addition of MR imaging [43–46].

6.3.2 Imaging of Moving Organs

MR imaging offers a unique method to quantify the motion and deformation of tumors and regions of interest. Multiple imaging sessions and continuous, cine, imaging can be performed to determine a patient's inter- and intra-fractional motion, as no ionizing radiation is delivered. This can to be useful for monitoring pelvic (prostate, bladder, rectum, and cervix), liver, and lung motion. Continuous sagittal cine loops of the prostate, rectum, and bladder have shown prostate motion, patterns of bladder filling, and effects of rectal gas [47]. Monitoring of pelvic organs over a time scale of a treatment fraction can provide insight into the correct PTV margins for regions of interest. Prostate motion on the order of 1–2 cm has been shown as a result of bladder filling and for rectal fluctuation [47]. Sudden motion of the prostate has been demonstrated due to rectal gas motion, with potential implications for image-guided radiation treatments. MR cine imaging can assist in determining the average time that the prostate can be assumed to stay in one position, the associated confidence interval, as well as the effects of bowel and bladder regimens on prostate motion. Figure 9a–c shows three frames of a half-hour cine MR sequence for a prostate patient, indicating significant prostate motion and deformation due to rectal gas, shown in the middle image. Similar studies of motion have been performed to examine intra- and inter-fraction motion of the cervix and uterus in patients being treated for cancer of the cervix. The rapid response of the disease to the course of radiation therapy is easily visualized in sagittal MR images (Fig. 9d–g).

Lung and liver tumor motion can also be assessed using cine MR [48]. Rapid, 2D images through the coronal, sagittal, and axial plane of the tumor can allow patient specific PTV margins to be calculated during normal breathing. This can be especially useful for liver tumors,

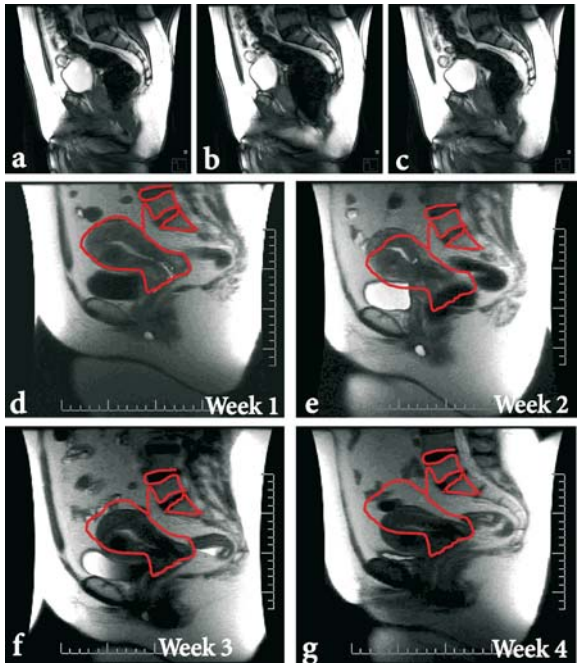

Fig. 9a–g. The role of MR in characterizing inter and intra-fraction motion is growing. The inter- and intra-fraction motion of the prostate has been well- studied using sagittal cine-MR: **(a)** - **(c)** images of the prostatic anatomy show how the motion of a gas pocket through the rectum can induce significant displacements in the gland within a short time period (few seconds to a few minutes); **(d)** - **(g)** panel of images demonstrating inter-fraction displacement of the cervix and uterus over four weeks of external beam radiation therapy. The intra-fraction motion was small in comparison to these excursions and deformations. This combination makes on- line guidance a feasible solution in conformal irradiation for localized cancer of the cervix

which are often only visible on contrast-enhanced CT, limiting the ability to directly track the tumor on 4D CT. Continuous monitoring over several breathing cycles is also possible to evaluate periodicity of the patient's respiratory cycle. Full, 3D data sets at breath hold can also aid in determining the deformation and correlation between organ motion in different regions of the treatment field.

6.3.3 Limitation of MR Imaging – Distortion

One limitation of MR imaging is the presence of distortion due to non-linearities in the magnetic field and the magnetic susceptibility of human tissue. Numerous investigators have characterized this distortion and proposed methods to correct for it, either by aligning the MR image to a geometrically robust CT image, or by characterizing the field-induced distortion and numerically correcting for it, which does not account for the differences in the distortion when patients are present. The magnitude of the distortion also depends on the imaging sequence, applied gradient strengths, and phase-encoding direction. Typically, distortion increases with distance from the magnet field center and varies with patient imaging subject, indicating that phantom tests can specify the extent of the distortion, but a patient-specific correction may be necessary for the accuracy required for treatment planning and target definition.

Mizowaki et al. [49] reported on image distortion using a $24 \times 24 \times 20$ cm grid-pattern acrylic phantom in a 0.2-T magnet using both T1- and T2-weighted spin-echo pulse sequences, with each sequence repeated three times. The maximum displacements of the 432 intersections were 15 mm for both sequences. The mean ranged from 1.65 to 1.74 mm (SD: 2.4 – 2.42 mm) for the T1-weighted sequence and from 1.58 to 1.67 mm (SD 2.14 – 2.4 mm) for the T2-weighted sequence. The distortion was less at the isocenter of the magnet, intersections within 120 mm of the center of the image had an average displacement of 0.73 to 0.80 mm (SD: 0.76 – 0.79 mm) for both imaging sequences. Wang et al. [50] reported on assessment and correction for 3D distortion using $310 \times 310 \times 310$ mm phantom containing 10,830 control points imaged on a Siemens Sonata 1.5-T MR scanner in clinical use with an inversion recovery gradient echo 3D imaging sequence (TR = 1,540 ms, TE = 1.53 ms). The differences, mean (SD, max), in the x, y, and z direction between the measured coordinates of the control points in the image and the physical locations were 1.46 mm (SD: 1.47 mm, max: 8.14 mm), 1.44 mm (SD: 1.39 mm, max: 7.03 mm), and 1.36 mm (SD: 1.35 mm, max: 9.33 mm), respectively. The continued presence of geometric distortions present in MR images will challenge wide-spread acceptance as a complete replacement to CT-simulation. Post-fusion comparison of CT and MR images is the current standard in evaluating the geometric accuracy of MR images and will likely remain until confidence in distortion correction schemes are proven in the clinical setting. CT imaging remains the established primary imaging modality for radiotherapy, offering relatively affordable imaging that is geometrically robust and contains electron density information required for dose calculations. Although it has been proposed to replace CT imaging in some cases, MR imaging will continue to be integrated into the radiotherapy process as an augmentative imaging technique used to enhance the target and normal structure identification currently achieved through CT imaging alone. It is therefore necessary to develop robust methods of relating these images of the patient. Setting up the patient similar in both scanning modalities will assist in this endeavor, however image registration is necessary to obtain the accurate results necessary for treatment planning.

The implementation of an MR scanner into the radiotherapy department as a MR simulator has included the addition of lasers, similar to those found in the standard CT-simulator and treatment room, see Fig. 7. The use of lasers allows the technologist to place the patient in a position that resembles the treatment position as closely as possible, and that captured by the CT-simulator. Although helpful, lasers are not fundamental as image registration techniques can align the MR image with the CT image. The use of lasers creates a closer starting point for the registration to begin, reducing registration time by eliminating an initial global alignment.

6.3.4 Multi-modality Imaging

As multi-modality imaging becomes increasingly integrated into the treatment planning process, for target delineation, quantification of tumor motion, and measure of functionality, the ability to relate the regions of interest from multiple, multi-modality scans, to the planning CT scan, to pre-treatment cone-beam CT scan necessitates a multi-modality deformable image registration technique for extracranial sites. This registration method must be accurate and robust, and ideally quick and have an inherent method to track functionality, classification, motion of ROIs, dose, and response. Figure 10 outlines a schematic for the integration of multi-modality, multiple instance of geometry imaging into image-guided radiotherapy. As CT will likely remain the standard imaging modality, and the one imaging modality that is consistent across all imaging sites, it will serve as the base (or primary) model of the patient to which all future images will be aligned. An accounting system can be developed from this image, which will store all future information. The scale of this system can vary from very small, at regions of in-

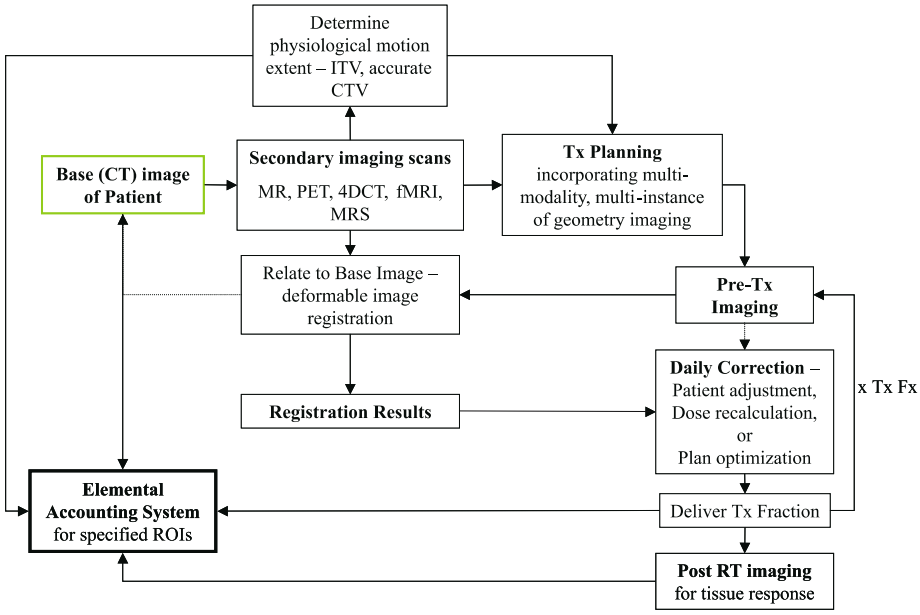

Fig. 10. A system is being developed for model-based tracking of the structures of interest during the course of radiation therapy. This system provides a means of integrating the image signals and applied therapy dose distributions for re-evaluation of appropriate intervention. The basis of this approach is common surrogates within the various imaging modalities and the employment of mechanical models for interpolation and extrapolation of anatomy between or beyond robust surrogates. In this approach, the CT signals play an important role providing the reference surrogates in the overall process

terest (ROIs) that are very important, i.e. the tumor, to larger, at peripheral organs which are receiving a low, heterogeneous dose.

Secondary imaging scans (MR, PET, MRS, 4DCT, etc.) can be aligned to the base scan using deformable image registration, to relate anatomical information such as tumor classification, staging, and functional information [51–58]. Motion extent and the relationship between the tumor and soft tissue surrogates (e.g. liver tumor as a function of liver position) can also be determined from the secondary imaging scans, by intra-modality registration, i.e. 4DCT, cine MR, etc. This information can then be related back to the base image, and transferred to the accounting system for treatment planning purposes. The treatment planning process can then incorporate all information from the accounting system related to the base scan, from which the patient will be planned. This will allow all information to be included in the treatment planning process: accurate gross tumor volume (GTV) classification will be obtained from comparing the 'tumor' designation on the multiple imaging modalities and the motion and deformation of both tumor and normal structures will allow for accurate PTV and PRV margins.

Pretreatment cone-beam CT imaging will then be related back to the ideal patient position, either by direct registration of the tumor or soft tissue surrogates. Any discrepancies between the cone-beam CT representation of the patient and the ideal patient position can be accounted for by patient adjustment, dose recalculation, or plan re-optimization. The treatment fraction can be delivered and the dose recorded in the accounting system to monitor any residual differences between the planned and delivered dose. The march towards multiple imaging modalities and on-line volumetric tracking of the applied therapy will drive the radiation therapy process toward a more integrated simulation and treatment process, in which, the term 'simulator' will fade and imaging modalities will be drawn upon as needed to establish the information of relevance for each patient's treatment.

6.4 Summary

The creation of a comprehensive system for simulation is being driven by both the advancements in imaging tools for characterization of the patient's diseased and normal anatomy and by the introduction of volumetric imaging systems for daily guidance and verification of delivery. Such a comprehensive system will (i) accelerate the introduction of further developments in imaging to the simulation process, (ii) provide an appropriate infrastructure to support the vast quantity of imaging information that will be streaming from image-guidance approaches such as cone-beam CT systems. Genuine opportunity to bring accurate disease and normal structure characterization together with daily accounting of the dose delivered for better understanding of disease control and complication induction, as well as, permit

re-optimization of the treatment's parameters as therapy progresses.

Acknowledgements. The authors would like to acknowledge the contributions of Dr. Laura Dawson, Dr. Alan Nichol, Dr. Charles Catton, Dr. David Payne, Dr. Jeffrey Siewerdsen, Dr. Douglas Moseley, and Dr. Philip Chan. The assistance of Mr. Cameron Chiarot in the preparation of this manuscript is greatly appreciated.

References

1. Ling CC, Humm J, Larson S, Amols H, Fuks Z, Leibel S, Koutcher JA (2000) Towards multidimensional radiotherapy (MD-CRT): biological imaging and biological conformality. Int J Radiat Oncol Biol Phys 47:551–560
2. Mah D, Steckner M, Palacio E, Mitra R, Richardson T, Hanks GE (2002) Characteristics and quality assurance of a dedicated open 0.23 T MRI for radiation therapy simulation. Med Phys 29:2541–2547
3. Mah D, Freedman G, Milestone B, Hanlon A, Palacio E, Richardson T, Movsas B, Mitra R, Horwitz E, Hanks GE (2002) Measurement of intrafractional prostate motion using magnetic resonance imaging. Int J Radiat Oncol Biol Phys 54:568–575
4. Mah D, Steckner M, Hanlon A, Freedman G, Milestone B, Mitra R, Shukla H, Movsas B, Horwitz E, Vaisanen PP, Hanks GE (2002) MRI simulation: effect of gradient distortions on three-dimensional prostate cancer plans. Int J Radiat Oncol Biol Phys 53:757–765
5. Jaffray DA, Chawla K, Yu C, Wong JW (1995) Dual-beam imaging for online verification of radiotherapy field placement. Int J Rad Oncol Biol Phys 33:1273–1280
6. Jaffray DA, Drake DG, Moreau M, Martinez AA, Wong JW (1999) A radiographic and tomographic imaging system integrated into a medical linear accelerator for localization of bone and soft-tissue targets. Int J Radiat Oncol Biol Phys 45:773–789
7. Jaffray DA, Siewerdsen JH, Wong JW, Martinez AA (2002) Flat-panel cone-beam computed tomography for image-guided radiation therapy. Int J Radiat Oncol Biol Phys 53:1337–1349
8. Jaffray DA, Siewerdsen JH (2000) Cone-beam computed tomography with a flat-panel imager: initial performance characterization. Med Phys 27:1311–1323
9. Siewerdsen JH, Jaffray DA (1999) A ghost story: spatio-temporal response characteristics of an indirect-detection flat-panel imager. Med Phys 26:1624–1641
10. Siewerdsen JH, Jaffray DA (1999) Cone-beam computed tomography with a flat-panel imager: effects of image lag. Med Phys 26:2635–2647
11. Siewerdsen JH, Jaffray DA (2000) Optimization of X-ray imaging geometry (with specific application to flat-panel cone-beam computed tomography). Med Phys 27:1903–1914
12. Siewerdsen JH, Jaffray DA (2001) Cone-beam computed tomography with a flat-panel imager: magnitude and effects of X-ray scatter. Med Phys 28:220–231
13. Sonke J, Remeijer P, van Herk M (2003) Respiration-correlated cone-beam CT: obtaining a four-dimensional data set. Med Phys 30:1415
14. Brock KK, McShan DL, Ten Haken RK, Hollister SJ, Dawson LA, Balter JM (2003) Inclusion of organ deformation in dose calculations. Med Phys 30:290–295
15. Joshi S, Pizer S, Fletcher PT, Yushkevich P, Thall A, Marron JS (2002) Multiscale deformable model segmentation and statistical shape analysis using medial descriptions. IEEE Trans Med Imaging 21:538–550
16. Yan D, Jaffray DA, Wong JW (1999) A model to accumulate fractionated dose in a deforming organ. Int J Radiat Oncol Biol Phys 44:665–675
17. Lauterbur PC (1973) Image formation by induced local interactions: examples of employing nuclear magnetic resonance. Nature 242:190–191
18. Curran WJ, Hackney DB, Blitzer PH, Bilaniuk L (1986) The value of magnetic resonance imaging in treatment planning of nasopharyngeal carcinoma. Int J Radiat Oncol Biol Phys 12:2189–2196
19. Fraass BA, McShan DL, Diaz RF, Ten Haken RK, Aisen A, Gebarski S, Glazer G, Lichter AS (1987) Integration of magnetic resonance imaging into radiation therapy treatment planning: I. Technical considerations. Int J Radiat Oncol Biol Phys 13:1897–1908
20. Glatstein E, Lichter AS, Fraass BA, Kelly BA, van de Geijn J (1985) The imaging revolution and radiation oncology: use of CT, ultrasound, and NMR for localization, treatment planning and treatment delivery. Int J Radiat Oncol Biol Phys 11:299–314
21. Schad LR, Boesecke R, Schlegel W, Hartmann GH, Sturm V, Strauss LG, Lorenz WJ (1987) Three dimensional image correlation of CT, MR, and PET studies in radiotherapy treatment planning of brain tumors. J Comput Assist Tomogr 11:948–954
22. Carlson JW, Minemura T (1993) Imaging time reduction through multiple receiver coil data acquisition and image reconstruction. Magn Reson Med 29:681–687
23. McKenzie CA, Lim D, Ransil BJ, Morrin M, Pedrosa I, Yeh EN, Sodickson DK, Rofsky NM (2004) Shortening MR image acquisition time for volumetric interpolated breath-hold examination with a recently developed parallel imaging reconstruction technique: clinical feasibility. Radiology 230:589–594
24. Hawighorst H, Schreiber W, Knopp MV, Essig M, Engenhart-Cabilic R, Brix G, van Kaick G (1996) Macroscopic tumor volume of malignant glioma determined by contrast-enhanced magnetic resonance imaging with and without magnetization transfer contrast. Magn Reson Imaging 14:1119–1126
25. Khoo VS, Dearnaley DP, Finnigan DJ, Padhani A, Tanner SF, Leach MO (1997) Magnetic resonance imaging (MRI): considerations and applications in radiotherapy treatment planning. Radiother Oncol 42:1–15
26. Schad LR, Boesecke R, Schlegel W, Hartmann GH, Sturm V, Strauss LG, Lorenz WJ (1987) Three dimensional image correlation of CT, MR, and PET studies in radiotherapy treatment planning of brain tumors. J Comput Assist Tomogr 11:948–954
27. Nelson SJ, Graves E, Pirzkall A, Li X, Chan AA, Vigneron DB, McKnight TR (2002) In vivo molecular imaging for planning radiation therapy of gliomas: an application of 1H MRSI. J Magn Reson Imaging 16:464–476
28. Pirzkall A, McKnight TR, Graves EE, Carol MP, Sneed PK, Wara WW, Nelson SJ, Verhey LJ, Larson DA (2001) MR-spectroscopy guided target delineation for high-grade gliomas. Int J Radiat Oncol Biol Phys 50:915–928
29. Dubois DF, Prestidge BR, Hotchkiss LA, Prete JJ, Bice WS Jr (1998) Intraobserver and interobserver variability of MR imaging- and CT-derived prostate volumes after transper-

ineal interstitial permanent prostate brachytherapy. Radiology 207:785–789
30. Parker CC, Damyanovich A, Haycocks T, Haider M, Bayley A, Catton CN (2003) Magnetic resonance imaging in the radiation treatment planning of localized prostate cancer using intra-prostatic fiducial markers for computed tomography co-registration. Radiother Oncol 66:217–224
31. Coakley FV, Qayyum A, Kurhanewicz J (2003) Magnetic resonance imaging and spectroscopic imaging of prostate cancer. J Urol 170:S69–S75
32. Menard C, Smith IC, Somorjai RL, Leboldus L, Patel R, Littman C, Robertson SJ, Bezabeh T (2001) Magnetic resonance spectroscopy of the malignant prostate gland after radiotherapy: a histopathologic study of diagnostic validity. Int J Radiat Oncol Biol Phys 50:317–323
33. Mizowaki T, Cohen GN, Fung AY, Zaider M (2002) Towards integrating functional imaging in the treatment of prostate cancer with radiation: the registration of the MR spectroscopy imaging to ultrasound/CT images and its implementation in treatment planning. Int J Radiat Oncol Biol Phys 54:1558–1564
34. Pickett B, Kurhanewicz J, Fein B, Coakley F, Shinohara K, Roach M (2003) Use of magnetic resonance imaging and spectroscopy in the evaluation of external beam radiation therapy for prostate cancer. Int J Radiat Oncol Biol Phys 57:S163–S164
35. Gibbs P, Liney GP, Lowry M, Kneeshaw PJ, Turnbull LW (2004) Differentiation of benign and malignant sub-1 cm breast lesions using dynamic contrast enhanced MRI. Breast 13:115–121
36. Hathaway PB, Mankoff DA, Maravilla KR, Austin-Seymour MM, Ellis GK, Gralow JR, Cortese AA, Hayes CE, Moe RE (1999) Value of combined FDG PET and MR imaging in the evaluation of suspected recurrent local-regional breast cancer: preliminary experience. Radiology 210:807–814
37. Muuller RD, Barkhausen J, Sauerwein W, Langer R (1998) Assessment of local recurrence after breast-conserving therapy with MRI. J Comput Assist Tomogr 22:408–412
38. Sardanelli F, Lozzelli A, Fausto A (2003) MR imaging of the breast: indications, established technique, and new directions. Eur Radiol 13(Suppl 3):N28–N36
39. Viehweg P, Heinig A, Lampe D, Buchmann J, Heywang-Kobrunner SH (1998) Retrospective analysis for evaluation of the value of contrast-enhanced MRI in patients treated with breast conservative therapy. MAGMA 7:141–152
40. Muryama S, Akamine T, Sakai S, Oshiro Y, Kakinohana Y, Soeda H, Toita T, Adachi G (2004) Risk factor of radiation pneumonitis: assessment with velocity-encoded cine magnetic resonance imaging of pulmonary artery. J Comput Assist Tomogr 28:204–208
41. Takenaka D, Ohno Y, Hatabu H, Ohbayashi C, Yoshimura M, Ohkita Y, Sugimura K (2002) Differentiation of metastatic versus non-metastatic mediastinal lymph nodes in patients with non-small cell lung cancer using respiratory-triggered short inversion time inversion recovery (STIR) turbo spin-echo MR imaging. Eur J Radiol 44:216–224
42. Yankelevitz DF, Henschke CI, Batata M, Kim YS, Chu F (1994) Lung cancer: evaluation with MR imaging during and after irradiation. J Thorac Imaging 9:41–46
43. Jeong YY, Kang HK, Chung TW, Seo JJ, Park JG (2003) Uterine cervical carcinoma after therapy: CT and MR imaging findings. Radiographics 23:969–981
44. Lyng H, Vorren AO, Sundfor K, Taksdal I, Lien HH, Kaalhus O, Rofstad EK (2001) Assessment of tumor oxygenation in human cervical carcinoma by use of dynamic Gd-DTPA-enhanced MR imaging. J Magn Reson Imaging 14:750–756
45. Schoeppel SL, Ellis JH, LaVigne ML, Schea RA, Roberts JA (1992) Magnetic resonance imaging during intracavitary gynecologic brachytherapy. Int J Radiat Oncol Biol Phys 23:169–174
46. Wachter-Gerstner N, Wachter S, Reinstadler E, Fellner C, Knocke TH, Potter R (2003) The impact of sectional imaging on dose escalation in endocavitary HDR-brachytherapy of cervical cancer: results of a prospective comparative trial. Radiother Oncol 68:51–59
47. Ghilezan M, Siewerdsen JH, van Herk M, Martinez A, Jaffray DA (2002) Assessment of prostate and seminal vesicles motion/deformation using sagittal cinneMRI for margin determination in on-line Image-Guided Radiation Therapy (IGRT) for prostate cancer. Int J Radiat Oncol Biol Phys 54:182–182
48. Koch N, Liu HH, Olsson LE, Jackson EF (2003) Assessment of geometrical accuracy of magnetic resonance images for radiation therapy of lung cancers. J Appl Clin Med Phys 4:352–364
49. Mizowaki T, Nagata Y, Okajima K, Kokubo M, Negoro Y, Araki N, Hiraoka M (2000) Reproducibility of geometric distortion in magnetic resonance imaging based on phantom studies. Radiother Oncol 57:237–242
50. Wang D, Doddrell DM, Cowin G (2004) A novel phantom and method for comprehensive 3-dimensional measurement and correction of geometric distortion in magnetic resonance imaging. Magn Reson Imaging 22:529–542
51. Bharatha A, Hirose M, Hata N, Warfield SK, Ferrant M, Zou KH, Suarez-Santana E, Ruiz-Alzola J, D'Amico A, Cormack RA, Kikinis R, Jolesz FA, Tempany CM (2001) Evaluation of three-dimensional finite element-based deformable registration of pre- and intraoperative prostate imaging. Med Phys 28:2551–2560
52. Brock KK, Hollister SJ, Dawson LA, Balter JM (2002) Technical note: creating a four-dimensional model of the liver using finite element analysis. Med Phys 29:1403–1405
53. Brock KM, Balter JM, Dawson LA, Kessler ML, Meyer CR (2003) Automated generation of a four-dimensional model of the liver using warping and mutual information. Med Phys 30:1128–1133
54. Joshi S, Pizer S, Fletcher PT, Yushkevich P, Thall A, Marron JS (2002) Multiscale deformable model segmentation and statistical shape analysis using medial descriptions. IEEE Trans Med Imaging 21:538–550
55. Liang J, Yana D (2003) Reducing uncertainties in volumetric image based deformable organ registration. Med Phys 30:2116–2122
56. Meyer CR, Boes JL, Kim B, Bland PH, Zasadny KR, Kison PV, Koral K, Frey KA, Wahl RL (1997) Demonstration of accuracy and clinical versatility of mutual information for automatic multimodality image fusion using affine and thin-plate spline warped geometric deformations. Med Image Anal 1:195–206
57. Rohlfing T, Maurer CR Jr, O'Dell WG, Zhong J (2004) Modeling liver motion and deformation during the respiratory cycle using intensity-based nonrigid registration of gated MR images. Med Phys 31:427–432
58. Yan D, Jaffray DA, Wong JW (1999) A model to accumulate fractionated dose in a deforming organ. Int J Radiat Oncol Biol Phys 44:665–675

External Beam Adaptive Radiation Therapy (ART) on a Conventional Medical Accelerator

John Wong, Di Yan, David Lockman, Don Brabbins, Frank Vicini and Alvaro Martinez

7

Contents

7.1 Introduction

The advent of inverse planning and IMRT has allowed the delivery of radiation dose that conforms tightly to the target but which falls off sharply to minimize irradiation of surrounding structures. The exquisite dose distributions, however, have their misgivings as they often lure the clinicians into prescribing a smaller treatment margin which may not be valid.

Treatment margins, or more specifically, planning target volume (PTV) and clinical target volume (CTV) are our acknowledgements that there are uncertainties associated with the patient treatment setup and disease extension, respectively. They are prescribed to minimize the risk of geometric misses. The conventional approach in radiation therapy is to employ a generic margin for the patient population, which will vary depending on anatomic site. The generic margin is based on the clinical experience and is meant to accommodate the patient population. Often overlooked, however, is that this generic margin is institution-specific, as the nature of treatment variation depends very much on the treatment technique and personnel. One needs to be vigilant in validating the efficacy of a published margin if it were to be adopted for a new treatment method, such as IMRT.

7.2 Stratification of Treatment Strategies Based on Adaptive Radiation Therapy for Prostate Cancer

In reality, generic treatment margin is wasteful because much of its expanse is used to account for the variations of the systematic treatment error (say setup) between patients (see Fig. 1a). A common population-based margin recipe would assign more than three times the weight to the margin for the systematic error than that for random error [1, 2], i.e. margin $= 2.5\Sigma + 0.7\sigma$, where Σ is the standard deviation (SD) of the systematic error distribution and σ the root-mean-square of the random error distribution. It follows then, significant reduction in margin can be achieved if effort is directed toward measuring and correcting for systematic error. Correspondingly, much gain can be achieved by optimizing the treatment margin for the individual patient.

The process of Adaptive Radiation Therapy (ART) at William Beaumont Hospital was developed with the goal of deriving an optimal patient-specific PTV [3]. Over the years, we have applied the general principles of acquiring repeat imaging information to determine an appropriate, individual or population, PTV for treatment of cancer in the breast [4,5], lung [6], and colorectal region [7]. However, our largest experience is with treatment of prostate cancer [8–11] which will be the focus of this chapter.

Figure 1 shows a schematic presentation of the stratification of adaptive treatment strategies. Each cluster of same-colored points symbolizes the geometric deviations of each patient from the prescribed position at the center. In the conventional treatment with generic margin as shown in Fig. 1a, a significant portion is used to account for the inter-patient variation. With the conventional practice of weekly imaging, there is insufficient information to make further refinement. However, with additional imaging information, it is possible to model the systematic (mean) and random (standard deviation) of the treatment variation for the individual patient

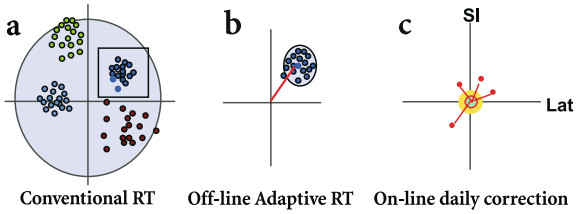

Fig. 1a–c. A schematic presentation of strategies to optimize margin for setup variation. Each *like-colored dot* represents the daily setup position of an individual patient with respect to the treatment isocentre at the cross-hair: **(a)** a large generic margin (*shaded circle*) prescribed to accommodate the variations between patients; **(b)** the off-line ART correction for the estimated systematic setup error based on a limited number of measurements. The smaller patient-specific margin can be prescribed to accommodate the random setup variation; **(c)** the patient setup is measured and corrected daily, and allows for the prescription of the smallest margin

as shown in Fig. 1b, such that the appropriate correction can be made for the former. For most patients, the re-optimized margin would also be significant smaller since the impact of random error is less deleterious than systematic error [1, 2, 9]. Thus, the general principle of ART is to characterize the variation early on in the treatment course using appropriate imaging information, such that an optimal PTV can be customized for the individual patient. More importantly, the ART process forms the foundation for making appropriate treatment decision. For those patients whose treatment variations are large and required unacceptably large margins, or when an aggressive short course treatment involves high dose per fraction, then a more proactive on-line strategy of daily intervention based on daily imaging information can be adapted, as shown in Fig. 1c.

7.3 Adaptive Radiation Therapy and Methods of Radiation Delivery

Implementation of ART requires commitment to perform repeat imaging. In terms of measurement, it is convenient to consider the PTV being comprised of a component pertaining to setup variation, PTV_s, and a component pertaining to internal organ motion, PTV_o. The former can be quantified based on bony structures exposed on portal images. Quantification of internal organ motion is more involved, and can be obtained using simple radiographic surrogates, such as implanted radio-opaque markers, or more advanced imaging techniques, such as ultra-sound or X-ray computed tomography (CT). In theory, PTV_s and PTV_o do not need to be separated. This is particularly the case when volumetric imaging information of the patient can be acquired in treatment position [12], where a subsequent correction would account for both setup variation and organ motion. However, the availability of electronic portal imaging devices or films in the conventional clinic allows optimization of PTV_s for many disease sites to be more readily achieved. The reduction in margin for setup margin contributed significantly to the overall reduction of the PTV.

With ART, a balance is struck between the amount of daily information acquired and the robustness of the estimated systematic and random errors. For prostate patients treated with a four-field box conformal treatment technique, a retrospective analysis was performed on the 15–20 daily portal images and CTs acquired from 30 patients to determine the necessary but reasonable number of daily measurements [9]. It was also desired that only one PTV adjustment would be performed for most patients. With knowledge of the variability of the treatment error, a trade-off can be made between the extent of the PTV and the risk of dose deficit in the CTV, as a function of dose gradient, i.e. treatment technique. Such soft margin design would not be possible without repeat imaging information. In our retrospective study, we accepted a risk of maximum 1% dose deficit to the CTV due to setup variation, and maximum 2% dose deficit due to prostate motion. We identified that by using the imaging information acquired in the first week of treatment, a patient-specific PTV reduction about one-fourth that of the generic PTV would be possible.

Since 1996, all prostate patients at our institute have been treated with an ART protocol that requires five days of portal (or open field) projection images for determining setup variation. In addition to the planning CT, four daily CT scans are acquired of the patient immediately after treatment in the first week on a conventional single slice helical scanner. Figure 2 shows the schematic of the ART workflow. The patients are setup without any immobilization device. No special dietary instructions are given, except the patients are advised to maintain daily routine during the course of treatment. In our earlier experience with ART, additional weekly, then bi-weekly CTs were also acquired during the course of treatment for verification purposes. The practice was discontinued after roughly 300 patients when we observed that

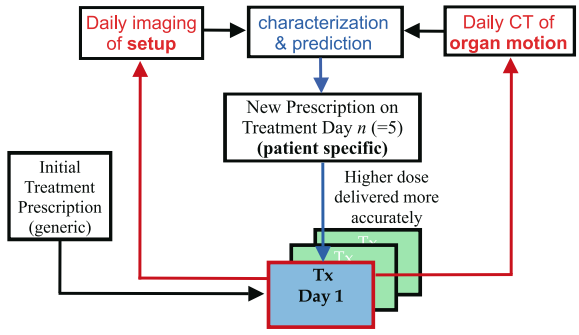

Fig. 2. Schematic of the ART workflow where data for setup and organ motion for the first five days of generic treatment are acquired and analyzed to derive a patient-specific PTV

PTV adjustments were seldom made based on variation of organ motion. Instead, taking advantage of our standard practice that electronic portal images are acquired daily, setup variations are evaluated for three treatment days immediately after PTV re-optimization; and periodically thereafter. That information would trigger a re-evaluation of the efficacy of the re-optimized PTV.

Until the beginning of 2004, all prostate ART patients were treated with the four-field box conformal technique. Patients were divided into two groups, depending on whether the seminal vesicles would be treated or not. The dose volume histogram (DVH) constraints for normal tissues published from Memorial Sloan Kettering Cancer Center [13, 14] were adopted for dose escalation. Depending on the extent of the patient-specific PTV, it was possible to stratify each patient to a different prescription dose level. Dose levels of 70.2 to 79.2 Gy as minimum dose to the PTV [10] were used. On average, the patient-specific PTV was 25% smaller than a generic PTV based on 1 cm uniform margin expansion around the CTV. This roughly translates to a reduced expansion of about 6 to 7 mm. The reduced PTV allowed dose escalation for significant number of patients even with the simple four-field box conformal technique. Figure 3 shows an interim histogram analysis of the percentage of first 206 patients that were treated to the different dose levels at 1.8 Gy per fraction. Fifty percent of the patients were treated to a minimum dose of 77.4 Gy to the PTV, rivaling the dose delivered with IMRT at other institutes. Early toxicity data are encouraging and not different than those published in the literature [11]. Equally important, the ART process also identified that for some patients that PTV reductions were not possible, and provided indication that more proactive on-line image guided adjustment would be necessary to facilitate dose escalation. After these initial ART patients, it was decided that Group 1 patients with favorable prognosis who did not require treatment of the seminal vesicles would not be treated to higher than 75.6 Gy.

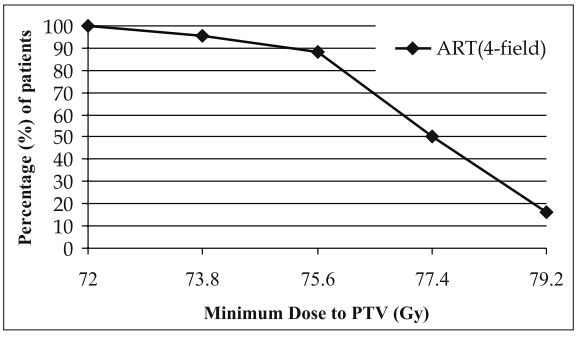

Fig. 3. Distribution of the prescription dose for the 206 ART patients treated with the four-field conformal box technique. Group 1 patients consisted of 55% patients who required treatment only to the prostate only. Group 2 patients consisted of remaining 45% patients who required treatment to the prostate and the seminal vesicles. The DVH constraints for rectal wall were 75.6 Gy to 30% of the volume and 82.0 Gy to 5% of the volume. The DVH constraints for the bladder were 75.6 Gy to 50% of the volume and the maximum dose less than 85.0 Gy. The minimum dose to the PTV in Group 1 patients was not limited to 75.6 Gy in these early data

In 2004, the strong perception in the community that IMRT represents superior treatment has spurned direct requests from prostate patients at our institute for the treatment. We have since incorporated five-field IMRT in our ART protocol, i.e. IMART. Four-field box conformal treatments are delivered in the first week while measurements of setup variation and organ motion are made. The patient-specific PTV is then derived for the ensuing IMRT for the rest of treatment course. The PTV is slightly larger than that for the four-field box in order to accommodate the risk of dose deficit due to the sharper, and less forgiving, dose gradient associated with IMRT [9]. Because there is no strong indication for further dose escalation, IMART is designed primarily to deliver less dose to the rectal wall, as well as to strike a better compromise between PTV coverage and bowel sparing for the 15% patients with bowel proximal to the PTV. As such, each IMRT plan must meet a new constraint – no more than 40% of the rectal wall is to receive 70 Gy [15]. As of August 2004, more than 100 patients have been treated with IMRT using the ART protocol. The follow-up period is too short for making any statement about clinical outcome.

7.4 Infrastructure for Adaptive Radiation Therapy

Questions have often been raised as to whether the ART process, which requires daily imaging, can be impractical. Fundamental to successful implementation of ART is the establishment of a network infra-structure with software tools and the training of the treatment personnel to perform image analysis. This seems logical as treatment simulation, planning and electronic portal imaging review are increasingly being performed on remote workstations, and often in the "virtual" world. The off-line nature of ART reduces the burden of the physician and the personnel on the treatment machine in making adjustment on a per image session basis [16]. The modification based on ART is more effective by alleviating the larger impact of systematic error. In addition, the ART process lends itself to improving efficiency as the re-optimized PTV translates to changing beam aperture which can be made via network using the MLC, as shown in Fig. 4. At William Beaumont Hospital, a standard time allocation for a four-field prostate ART is 10 min, and a five-field IMART is 12 min.

It should be noted that in the ART process for prostate cancer, much gain in margin reduction can be achieved with the simpler correction of the setup

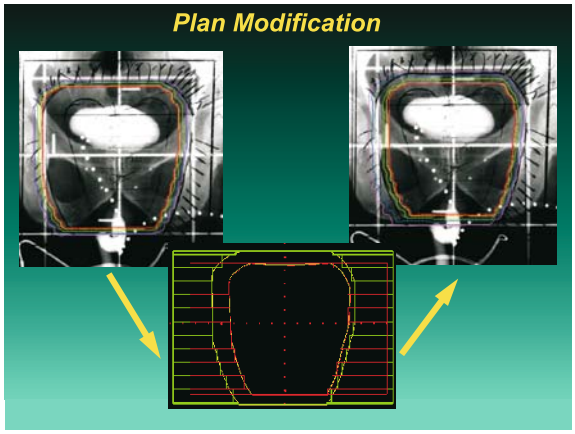

Fig. 4. A schematic showing the plan modification in the ART process for a prostate patient can be made via the MLC. In the *bottom panel*, the *green lines* denote the MLC configuration before modification, and *red* after modification

error. Figure 5 shows a retrospective analysis of the modified PTV margin for 300 ART patients treated with the four-field box technique. The extensions of the margin in the anterior-to-posterior, right-to-left, and superior-to-inferior directions, respectively, are plotted as cumulative histogram distributions. More than 70% of the patients can be treated with a setup margin of less than 3 mm, significantly less than the margin prescribed with conventional treatment. The reduction of margin for organ motion is roughly the same magnitude as that for setup error. Adaptive correction of setup error using repeat portal images can be readily performed in most clinics equipped with electronic portal imaging systems, and should not be overlooked. However, it should also be noted that the magnitude of the reduction is dependent on the technique and clinical site. A thorough examination of the setup variation in the clinic is needed prior to implementing the adaptive process.

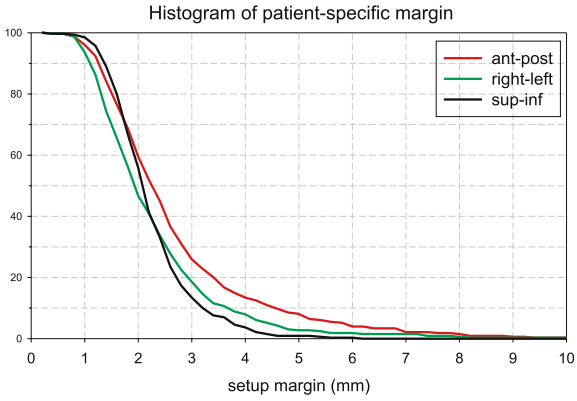

Fig. 5. The cumulative histogram distributions of the modified PTV margin for 300 ART patients treated with the four-field box technique. The margin extensions in the anterior-to-posterior (*red*), right-to-left (*green*), and superior-to-inferior (*black*) directions, respectively, are shown. More than 70% of the patients can be treated with a setup margin of less than 3 mm

Certainly, characterization of organ motion using repeat CTs is by far the more involved procedure. The logistics of acquiring the scans, fusing the CTs based on bony structures, contouring the daily CTV for PTV optimization and replanning are non-trivial. On the other hand, the hurdles are diminishing rapidly with the advent of new technologies that support image guided radiation therapy. The advent of multi-slice CT scanners and treatment units with on-board CT capabilities, such as the Tomotherapy HiART and the Elekta Synergy systems, will greatly simplify image acquisition. In addition, advanced software tools for 2D and 3D image registration [17–19], organ deformation [20–23] and workflow schemes [24,25] are being developed to replace the present procedures of manual image processing. It appears that, more than ever before, time is ripe for general embrace of ART in the community.

7.5 Discussions

Impressive advances have been recently made in many areas of radiation therapy. The most noticeable are the use of IMRT delivery methods and multiple modality images for target definition. Yet, the overall treatment process remains virtually unchanged. Treatment planning, delivery and verification are mostly performed as independent functions. It appears often that new hardware dictates the method of treatment, as in the case of the MLC and IMRT. A more desirable approach is to have the treatment objective and patient information guide the selection of an appropriate treatment strategy.

Deeply entrenched in the radiation treatment process is the use of population average parameters, such as the PTV, in the optimization of patient treatment. Such an approach is wasteful and undermines the effectiveness of advanced delivery methods. The emergence of technologies to support image guidance offers great potential to overcome such shortcomings, making it easier to derive patient-specific treatment parameters. However, one must still be cognizant of the magnitude of improvement required and achievable with respect to the amount of efforts spent. It was with this intent when we first introduced the concept of ART to improve treatment setup by tackling the underutilization of electronic portal imaging devices [8]. It soon evolved to include organ motion [9]. With ART, the patient information is evaluated and aligned with the appropriate treatment strategies, whether aggressive or conservative. The methodology is well poised to incorporate exciting new patient-specific information from biological to functional information to improve the overall quality, efficiency and efficacy of radiation therapy.

References

1. van Herk M, Remeijer P, Rasch C, Lebesque JV (2000) The probability of correct target dosage: dose-population histograms for deriving treatment margins in radiotherapy. Int J Radiat Oncol Biol Phys 47(4):1121–1135
2. van Herk M (2004) Errors and margins in radiotherapy. Semin Radiat Oncol 14(1):52–64
3. Yan D, Vicini F, Wong J, Martinez A (1997) Adaptive radiation therapy. Phys Med Biol 42(1):123–132
4. Baglan KL, Sharpe MB, Jaffray D, Frazier RC, Fayad J, Kestin LL, Remouchamps V, Martinez AA, Wong J, Vicini FA (2003) Accelerated partial breast irradiation using 3D conformal radiation therapy (3D-CRT). Int J Radiat Oncol Biol Phys 55(2):302–311
5. Remouchamps VM, Letts N, Yan D, Vicini FA, Moreau M, Zielinski JA, Liang J, Kestin LL, Martinez AA, Wong JW (2003) Three-dimensional evaluation of intra- and interfraction immobilization of lung and chest wall using active breathing control: a reproducibility study with breast cancer patients. Int J Radiat Oncol Biol Phys 57(4):968–978
6. Liang J, Yan D, Kestin LL, Martinez AA (2003) Minimization of target margin by adaptive treatment planning to target respiratory motion. Int J Radiat Oncol Biol Phys 57(2)Suppl:S233–S234
7. Nuyttens JJ, Robertson JM, Yan D, Martinez A (2002) The variability of the clinical target volume for rectal cancer due to internal organ motion during adjuvant treatment. Int J Radiat Oncol Biol Phys 53(2):497–503
8. Yan D, Ziaja E, Jaffray D, Wong J, Brabbins D, Vicini F, Martinez A (1998) The use of adaptive radiation therapy to reduce setup error: a prospective clinical study. Int J Radiat Oncol Biol Phys 41(3):715–720
9. Yan D, Lockman D, Brabbins D, Tyburski L, Martinez A (2000) An off-line strategy for constructing a patient-specific planning target volume in adaptive treatment process for prostate cancer. Int J Radiat Oncol Biol Phys 48(1):289–302
10. Martinez AA, Yan D, Lockman D, Brabbins D, Kota K, Sharpe M, Jaffray DA, Vicini F, Wong J (2001) Improvement in dose escalation using the process of adaptive radiotherapy combined with three-dimensional conformal or intensity-modulated beams for prostate cancer. Int J Radiat Oncol Biol Phys 50(5):1226–1234
11. Brabbins D, Martinez A, Yan D, Lockman D, Wallace M, Gustafson G, Chen P, Vicini F, Wong J (2005) A dose escalation trial using the adaptive radiotherapy process (ART) as a delivery system in localized prostate cancer: analysis of chronic toxicity. Int J Radiat Oncol Biol Phys 61(2):400–408
12. Jaffray DA, Siewerdsen JH, Wong JW, Martinez AA (2002) Flat-panel cone-beam computed tomography for image-guided radiation therapy. Int J Radiat Oncol Biol Phys 53(5):1337–1349
13. Zelefsky MJ, Fuks Z, Happersett L, Lee HJ, Ling CC, Burman CM, Hunt M, Wolfe T, Venkatraman ES, Jackson A, Skwarchuk M, Leibel SA (2000) Clinical experience with intensity modulated radiation therapy (IMRT) in prostate cancer. Radiother Oncol 55(3):241–249
14. Zelefsky MJ, Fuks Z, Hunt M, Yamada Y, Marion C, Ling CC, Amols H, Venkatraman ES, Leibel SA (2002) High-dose intensity modulated radiation therapy for prostate cancer: early toxicity and biochemical outcome in 772 patients. Int J Radiat Oncol Biol Phys 53(5):1111–1116
15. Vargas C, Kestin LL, Yan D, Brabbins DS, Liang J, Gustafson GS, Chen PY, Vicini FA, Wong JW, Martinez AA (2003) Dose-volume analysis of predictors for chronic rectal toxicity following treatment of prostate cancer with high-dose conformal radiotherapy. Int J Radiat Oncol Biol Phys 57(2)Suppl:S398–S399
16. Herman MG, Balter JM, Jaffray DA, McGee KP, Munro P, Shalev S, Van Herk M, Wong JW (2001) Clinical use of electronic portal imaging: report of AAPM Radiation Therapy Committee Task Group 58. Med Phys 28(5):712–737
17. van Herk M, de Munck JC, Lebesque JV, Muller S, Rasch C, Touw A (1998) Automatic registration of pelvic computed tomography data and magnetic resonance scans including a full circle method for quantitative accuracy evaluation. Med Phys 25(10):2054–2067
18. Birkfellner W, Wirth J, Burgstaller W, Baumann B, Staedele H, Hammer B, Gellrich NC, Jacob AL, Regazzoni P, Messmer P (2003) A faster method for 3D/2D medical image registration – a simulation study. Phys Med Biol 48(16):2665–2679
19. Park H, Bland PH, Meyer CR (2003) Construction of an abdominal probabilistic atlas and its application in segmentation. IEEE Trans Med Imaging 22(4):483–492
20. Brock KM, Balter JM, Dawson LA, Kessler ML, Meyer CR (2003) Automated generation of a four-dimensional model of the liver using warping and mutual information. Med Phys 30(6):1128–1133
21. Liang J, Yan D (2003) Reducing uncertainties in volumetric image based deformable organ registration. Med Phys 30(8):2116–2122
22. Christensen GE, Carlson B, Chao KS, Yin P, Grigsby PW, Nguyen K, Dempsey JF, Lerma FA, Bae KT, Vannier MW, Williamson JF (2001) Image-based dose planning of intracavitary brachytherapy: registration of serial-imaging studies using deformable anatomic templates. Int J Radiat Oncol Biol Phys 51(1):227–243
23. Schaly B, Kempe JA, Bauman GS, Battista JJ, Van Dyk J (2004) Tracking the dose distribution in radiation therapy by accounting for variable anatomy. Phys Med Biol 49(5):791–805
24. Mackie TR, Kapatoes J, Ruchala K, Lu W, Wu C, Olivera G, Forrest L, Tome W, Welsh J, Jeraj R, Harari P, Reckwerdt P, Paliwal B, Ritter M, Keller H, Fowler J, Mehta M (2003) Image guidance for precise conformal radiotherapy. Int J Radiat Oncol Biol Phys 56(1):89–105
25. Wong J, Watt L, Yan D, Lockman D, Brabbins D, Gustafson G, Martinez A (2004) In: Yi B, Ahn S, Choi E, Ha S (eds) ARTIST: Work flow for image guided radiotherapy. Proceedings of the XIV International Conference on the Use of Computers in Radiation Therapy. Jeong Publishing, Seoul

Adaptive Radiation Therapy (ART) Strategies Using Helical Tomotherapy

Gustavo Hugo Olivera, Thomas Rockwell Mackie, Kenneth Ruchala, Weiguo Lu, Jeffrey Kapatoes

8

Contents

8.1 Introduction

Tomotherapy is intensity-modulated rotational radiotherapy utilizing a photon fan beam [1–6]. In helical tomotherapy the gantry and couch are in continuous motion and, from the patient's point of view, the source describes a helical trajectory. Helical tomotherapy was designed around a ring gantry similar to a helical CT scanner. The constraints of a ring gantry are minimal since few patients are treated with non-coplanar radiation fields and IMRT diminishes the need for these types of field arrangements. Most importantly, a ring gantry is a very stable platform for CT scanning. The original helical tomotherapy concept had kV and MV beams for imaging and treatment respectively [1]. On the current version megavoltage photons from the treatment linac are used to generate the CT scans [7,8]. The same detector can also be used to detect the exiting treatment beam in order to provide the data for dose reconstruction [9].

Figure 1 is a labeled photograph of the TomoTherapy (Madison WI) Hi-Art tomotherapy unit with its covers off. The helical tomotherapy beam line was designed for image-guided IMRT treatments.

The linac and gantry systems of the tomotherapy system are highly favorable for CT. The gantry sag of the tomotherapy system is negligible so that no sag corrections are required. The size of the electron beam on the target is about 1 mm so that the resolution is about 1.2 mm to 1.6 mm which is comparable to a conventional CT scanner for high contrast objects. Operating with typical patient doses of 1 cGy, the soft tissue contrast is about 2–3% which is higher than a modern CT scanner. Nevertheless, the images have sufficient quality for adaptive radiotherapy processes.

The tomotherapy unit's xenon gas detector elements have tungsten septa separating ionization cavities. In addition to the ionization collectors, the tungsten plates are embedded photon converters intercepting the megavoltage photons and yet are thin enough to let an appreciable fraction of the electrons set in motion to deposit energy in the xenon gas. The interception of the beam by the tungsten means that the quantum efficiency of the system is about 25%, which is much more than the few percent collection efficiency of modern portal imaging systems, and decreases necessary imaging dose proportionally.

8.2 Treatment Plan Generation

Currently helical tomotherapy optimization is based on physical (dose-based) objective functions [10]. However, biological estimators to rank plans and biological optimization for treatment planning will be included in the future. The flexible delivery capabilities of tomotherapy will enable simple implementation of such novel techniques. Helical tomotherapy can deliver the complex radiation patterns that may result from biologically based optimizations. With helical tomotherapy, since all beam directions are available, it is not necessary to choose specific beam directions. A large number of beam directions are very beneficial to simultaneously achieving target dose uniformity and normal tissue

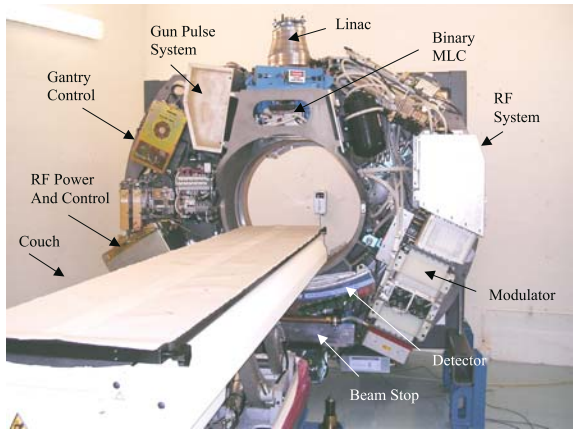

Fig. 1. Helical tomotherapy unit in a factory test cell. Major components are labeled

sparing as well as possible. However, if desired, dose from any number of beam directions can be minimized, by partially or even completely blocking those beam directions to meet specific doses constraints.

Contributions from any beam direction and fluence intensities through the binary MLC are optimized for conformal dose distribution. However, the use of a binary MLC does not prevent the optimization of dose distributions in the superior-inferior direction. Due to the simultaneous couch motion, there is an effectively continuous range of beamlet positions in the S/I direction. Additional beamlet options can be added by using narrower jaw thicknesses and/or reducing the pitch, as this will allow the beam to pass through a particular point several times; the optimizer can then select the most appropriate beamlets given the beamlets at different angles and longitudinal positions that impinge upon the desired target. In practice, pitch values in the range of 1/4 to 1/2 commonly provide a good balance between delivery time and beamlet availability.

Figure 2 is an example of a head and neck case. The number of beamlet intensities that needs to be optimized for this type of case is on the order of 40,000. As can be observed, target dose conformity and uniformity are excellent. There are no hot spots in the target region. Both left and right parotid sparing is achieved, as can be seen in the DVH. Moreover, there are no hot streaks or other areas of high dose in the normal tissue regions.

8.3 CT-Based Patient Setup Verification

The verification CT serves as the basis for all of the patient-specific quality assurance processes; however, the patient setup verification may be the most important. The CT verification representation of the patient indicates the anatomy of the patient just minutes before the treatment begins. Setup verification directly com-

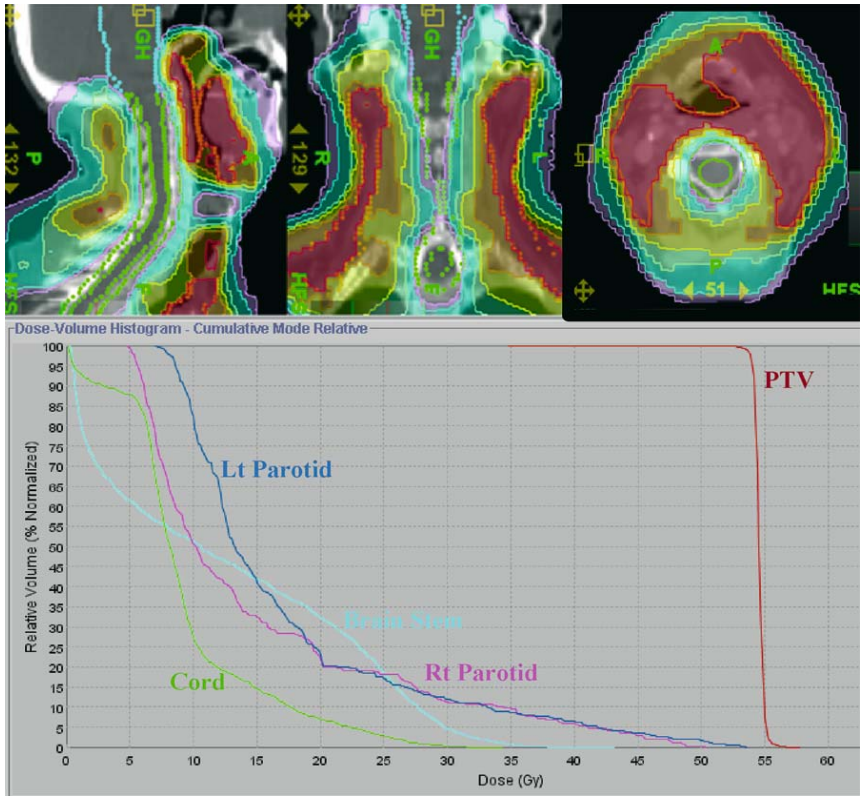

Fig. 2. Dose distribution and DVHs generated for a head and neck plan. The level of target conformity and sensitive structure sparing is very good. The number of beams directions as well as the modulation capabilities plays an important role in obtaining good quality plans for this type of case

pares the planning CT with the verification CT using image registration and fusion.

This section will describe the verification CT capability and compare and contrast this system with a contemporary kilovoltage fan beam and cone-beam CT scanner systems.

8.3.1 Verification CT Image Quality

The reliability of a verification representation is directly related to its image quality including the absence of artifacts. The detector resolution of the Hi-Art unit is 1.2 mm in the transverse direction and equal to the slice width in the longitudinal direction. Typically, 4 mm is used for the jaw width for CT scanning; however, a small slice width (example 2 mm) could be used for the fine resolution needed for small target volumes. The unit takes about 800 projection views per rotation. At the center of a CT image the pixel resolution is dominated by the detector and focal spot resolution but peripheral resolution can be degraded if too few projections are used. Figure 3 indicates that the Hi-Art is capable of resolving 1.2 to 1.6 mm objects near the edge of a 30 cm diameter phantom. A cone-beam detector resolution is approximately 0.25 mm which can clearly support a pixel resolution of 1 mm at the axis but only 285 projections [11] are used which does not support a resolution of 1 mm at the edge of its 40 cm field of view. This resolution limitation of cone beam CT at the edge of the field of view will be more evident in transverse views and less evident in sagital or coronal views.

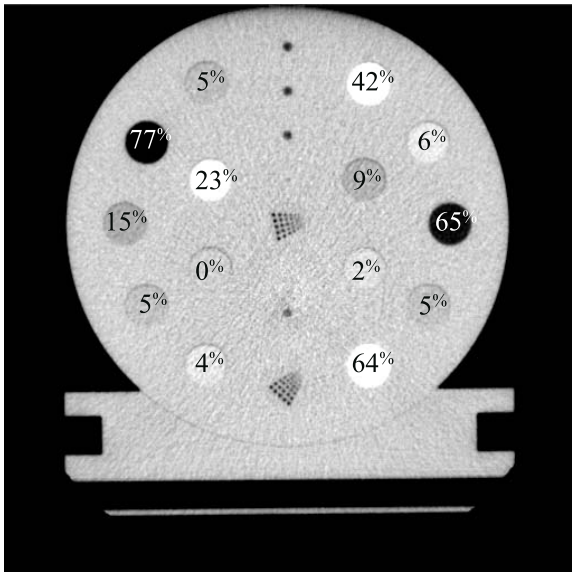

Fig. 3. Verification CT at megavoltage (MV) energies of an RMI Solid Water CT phantom. The 2% contrast plug is clearly seen as are the 1.2 and 1.6 air holes in the solid water phantom. The dose was estimated at 1 cGy at the center of the phantom

Figure 4 illustrates that bone has less contrast than a conventional CT scan but it is still clearly discernable on the Hi-Art unit. The boundary of lung with internal major airways and vascular structures are evident. The boundary between fat and muscle is clearly distinguished which means that the breast and prostate are discernable.

Many organ and tissue structures are visible in the verification CT scans. Organ boundaries such as the kidney and bladder are clearly visible. The lens of the eye is discernable. Unlike the highest quality conventional CT scanners, the contrast between white and grey matter in brain is not visible.

The verification CT uses approximately a 3.5-MV beam which means that the photons interact almost exclusively by Compton interactions so that the attenuation coefficient is linear with the electron density of the medium. Metal artifacts arise in conventional CT scanners because the attenuation of the metal is greatly enhanced due to the photo-electric effect. In helical CT, the beam is penetrating enough to eliminate artifacts arising from metal objects like hip prostheses and dental filings. This means that the representation supplied

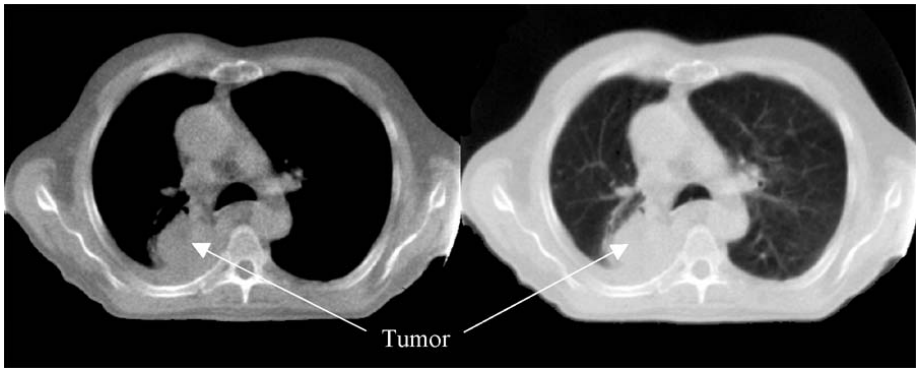

Fig. 4. Verification CT of a lung patient. The panel on the *left* is a soft-tissue window and the panel on the *right* is a lung window. The difference between muscle and fat and bone and soft tissue is clearly distinguishable. Some of the vascular structures are visible in the lung. The tumor boundary in the lung is discernable but its extension into the mediastinum is not visible. The dose to the patient was approximately 3 cGy

by a verification CT is a more reliable CT system for patients with implanted metal appliances.

8.3.2 Setup Verification and Adjustment

Patients are not rigid bodies and anatomical changes may impact patient positioning. Translations and rotations adjustments assume that the patient transformation from their position at the time of the verification scan to the time of planning CT is rigid. Rigid transformations do not take into account many relevant alternations such as bending, twisting, organ filling, tumor volume changes, or periodic motion like respiration. The verification CT scan can assess all of these representation alterations except those, like respiration, that occur at the time scale of the CT exam itself. However, most of the time only rigid body transformations need be applied to the patient to detect for most setup problems. The rigid assumption implies that only translations and rotations offsets can be applied. This subsection will describe how the offsets can be determined and corrected.

If, at the time of treatment, the patient is setup exactly as they were for the planning CT, the anatomy will be exactly registered between the verification and planning image sets. The patient is positioned by aligning the patient's skin marks with lasers located outside of the bore of the unit. A sagittal representation of the patient's planning CT is shown on the operator console to aid in selecting the slices to be scanned. A verification scan is taken and reconstructed during the acquisition. The verification image set is registered onto the planning image set and the translation and rotation offsets are reported. Typically the image fusion is usually first done automatically using a mutual information algorithm [12–15]. Since yaw and pitch are difficult offset angles to correct, automated registration can include any of the combinations of rigid movements:

1. Translations only (x-direction is left-right, y-direction is in-out, z-direction is up-down)
2. Translations plus roll (rotation about y-axis)
3. Translations plus roll, and yaw (rotation about z-axis)
4. Translations plus roll, yaw, and pitch (rotation about x-axis)

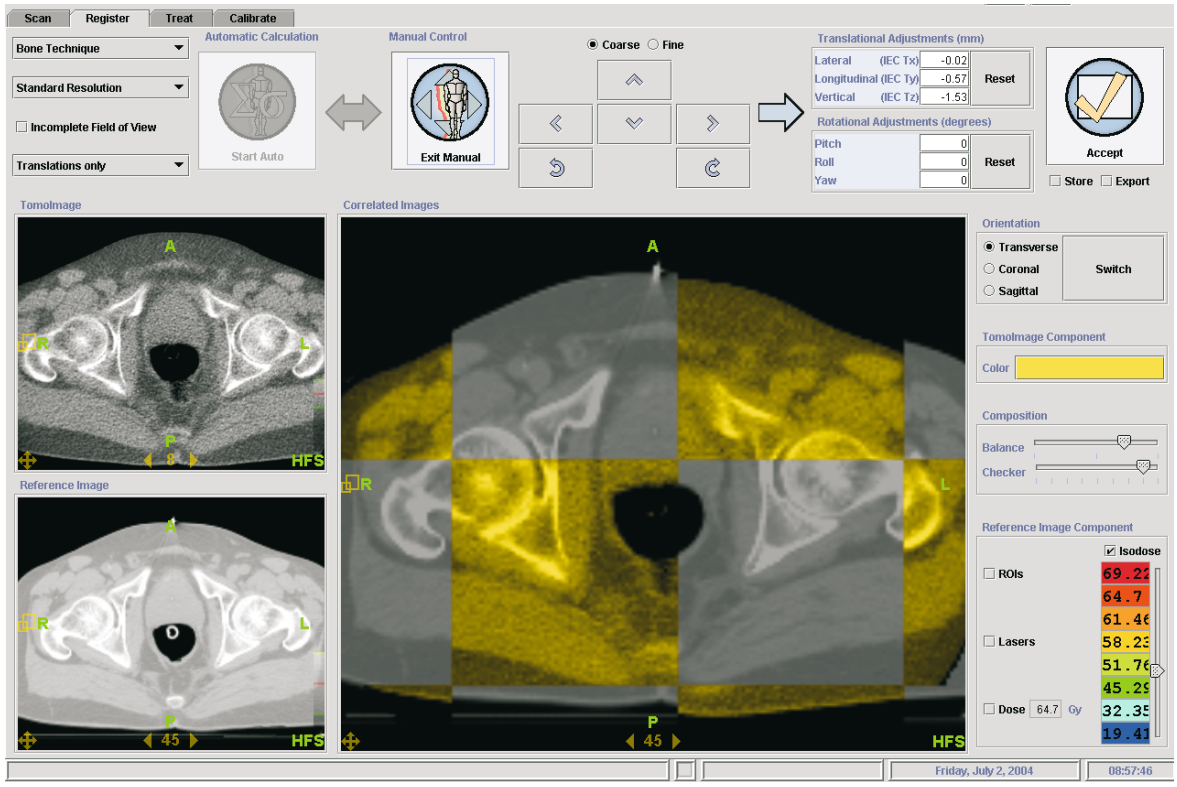

Fig. 5. The registration window for a prostate patient. The *grey squares* are from the planning CT. The verification CT used less than 1 cGy and is shown in the *upper left* and the planning CT is in the *lower left*. The *yellow squares* in the large panel are from the tomotherapy verification CT. The rectal boundary and the fat pad surrounding the prostate is clearly aligned on these transverse images. It should be noted that the skin boundary and the leg bones are not as well aligned as the prostate. Regions of interest and the dose distribution obtained from the planning system can be superimposed on the images but these capabilities have been turned off in this presentation. The translational alignments suggested were 0.0 mm lateral, −0.6 mm longitudinal, and −1.5 mm vertical

Following automated registration the patient registration can be fine-tuned manually. This allows the operator to take into account, as best as possible, the non-rigid nature of the transformation. Once the image registration is completed, the offsets also describe how the patient must be adjusted. Figure 5 shows an example of the graphical user interface for the registration utility being used to register a prostate patient.

If the patient requires adjustment the patient can be translated accordingly. The Hi-Art CT couch has automated vertical (elevation) and longitudinal translations. An automated gantry start angle adjustment accounts for patient roll. The couch top can be manually adjusted in the lateral direction (x-direction). Yaw and pitch rotations can be accommodated using angularly calibrated immobilization and positioning aids, which are especially useful for the head and neck. The Hi-Art unit tomotherapy unit includes a set of moveable CT-simulator lasers so that the modified position of the patient can be confirmed.

8.3.3 Process Time for Verification CT

A major difference between the Hi-Art helical tomotherapy unit and a cone-beam CT attached to a linac is the use of a ring instead of a C-arm gantry. Ring gantries have no rotation collision issues and so may rotate much faster than the IEC restriction of once per minute imposed on C-arm gantries. The rotation period of the Hi-Art helical tomotherapy unit is 10 s and the typical slice thickness that is used is 4 mm. For each rotation, two CT slices can be obtained. Pitches of 1.0, 2.0, and 3.0 are typically available so that up to 1.2 cm length can be scanned in 10 s. A typical tumor of 8 to 10 cm long would take as little as 2 min to acquire 25 CT slices. Longer lengths and smaller pitches take more time proportionately. Acquisition occurs on the fly so there is little delay following acquisition for the images to be analyzed. By contrast, Moseley [11] reported that a kilovoltage cone beam CT took 1.7 min to acquire 285 projections and few minutes to reconstruct; however, this effort would yield 256 slices, almost twice as many slices per minute as the Hi-Art unit. The original concept for a tomotherapy unit suggested that it be equipped with a conventional CT scanner [1]. Currently four-row conventional CT scanners are in common use. A four-row CT detector system with 4 mm slice widths would allow about 100 slices to be acquired in 2 min which would be at a faster rate than a cone-beam CT scanner. It is interesting to note that conventional CT vendors first invested in making their gantries rotate faster and only later invested in having more rows of detectors.

Whether or not a CT scan is done every day depends on the reliability of setup. Likely a CT scan will be done every day for a pelvic irradiation on an obese patient. However, a CT scan would likely be done only weekly on a cooperative head and neck patient. Between these extremes the frequency of acquisition will likely be highly patient and practice-specific.

8.4 Hierarchy of Adaptive Processes

The possibility to choose between many imaging modalities and delivery techniques before, during or after each radiotherapy fraction has opened many new possibilities in the management of radiotherapy planning. This continuous flow of information can be used in an adaptive fashion to provide feedback for future deliveries. The adaptive radiotherapy concept was initially introduced by Di Yan [16, 17]. The following section explains the extension and application to helical tomotherapy. In helical tomotherapy, multimodality images can be used for target and sensitive structure delineation as usual. Moreover, any of these image modalities can also be used in conjunction with daily images obtained at the time of treatment, to perform either on-line or off-line processes. The use of on-line imaging in adaptive radiotherapy is illustrated in Fig. 6.

8.4.1 On-line Processes

On-line images, in particular CT, can be used for patient positioning based on anatomical information. Modern CT capabilities allow identification of not only high contrast landmarks such as bone or implanted markers, but also soft tissue information. Such images can be used to determine appropriate adjustments to pa-

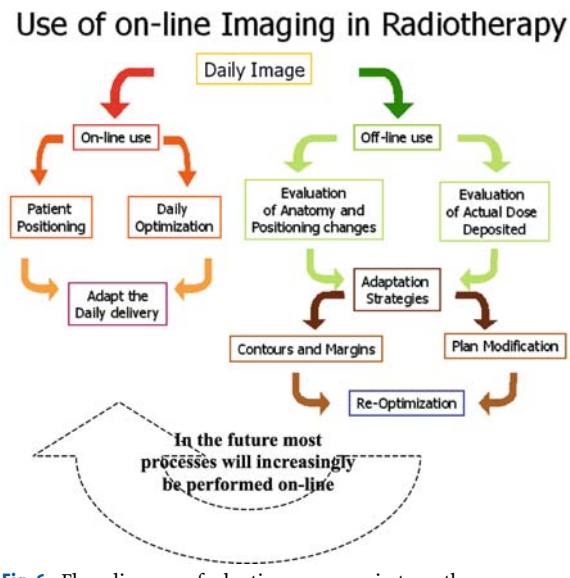

Fig. 6. Flow diagram of adaptive processes in tomotherapy

tient positioning. In some cases it may be necessary to correct for imperfections in the setup. However, visualizing internal anatomy and facilitating changes in patient position may also help remedy inter-fraction anatomical changes. For example, if target structures, organs-at-risk, bony anatomy, and external boundaries all move relative to one another, a patient position may be selected that best reflects the dose distribution of the original plan.

The limitations of using patient adjustments to account for anatomical changes are that possible position adjustments are typically limited to rigid-body assumptions, and that the more the anatomy changes, the more difficult it may be to appropriately situate the patient for the delivery of the original treatment plan. In principle, re-planning might be the best option, but this is not currently feasible on-line. Therefore, an alternative method is proposed in which pre-treatment patient imaging facilitates a choice between several available plan variations for delivery of each fraction. The key benefit of this process is that it provides many of the benefits of on-line re-optimization, in that anatomical changes can be accounted for, but with all of the necessary computations performed ahead of time.

If anatomical changes can be predicted or at least bounded within certain limits, plans can be prepared beforehand. The process begins with the creation of several sets of contours and/or PTV margins, and the subsequent preparation of plans appropriate for each of these margins or anatomical scenarios. At the time of treatment, the plan that best fits the daily anatomy can be delivered. Such an approach is referred to as Multi-Margin Optimization with Daily Selection (MMODS) [18–20]. In a prostate cancer case PTV expansions with 3, 5, 7.5, and 10 mm margins were generated and optimizations were obtained for each case. It would also be feasible to include multiple contours for sensitive structures, accounting for different fillings of structures like the bladder and rectum.

At the time of treatment, once the images are registered, the necessary target margin to encompass the entire target can be selected. With this information a plan is chosen and delivered.

Figure 7 is a DVH comparison between (1) the original plan generated with an original CT with a PTV margin of 5 mm (full line), (2) the total accumulated dose from delivery of the 5 mm PTV plan with daily evaluation of the dose via daily CT (dotted line), and (3) the total accumulated dose from the delivery of a selected plan for each fraction based on the daily CT (dashed line). For the last curve (dashed line), the selected plan was the one with the smallest margin that best fit the target. As can be observed, since adequate margins were used, in all cases the target has good coverage. However, the level of avoidance that is achieved for the sensitive structures is remarkably different showing the advantages of this simple approach.

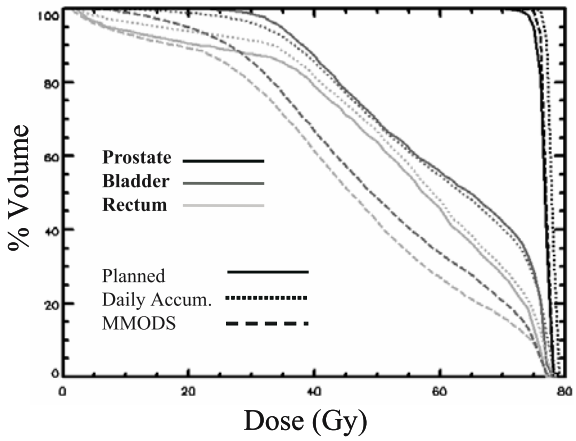

Fig. 7. DVH comparison between (1) the original plan generated with a planning CT with a PTV margin of 5 mm (*full line*), (2) the total accumulated dose from delivery of the 5 mm PTV plan with daily evaluation of the dose via daily CT (*dotted line*), and (3) the total accumulated dose from delivery of a selected plan for each fraction based on the daily CT (*dashed line*)

A complementary on-line approach is to define the patient position based on target dose coverage and sensitive structure avoidance. A possible way to do this is on-line re-computation of dose using the CT just taken so as to represent both the patient's setup position and daily anatomical information. With this dosimetric information, positioning can be adjusted by looking at the dose that will be delivered to different anatomical sites.

Still another approach that can be used is on-line optimization based on the on-line CT. One of the drawbacks of this technique is the need for daily generation of accurate contouring for IMRT. As will be shown later, for certain anatomical sites, creating deformation maps between the plan CT and the daily CT can automatically generate target and sensitive structures. These deforma-

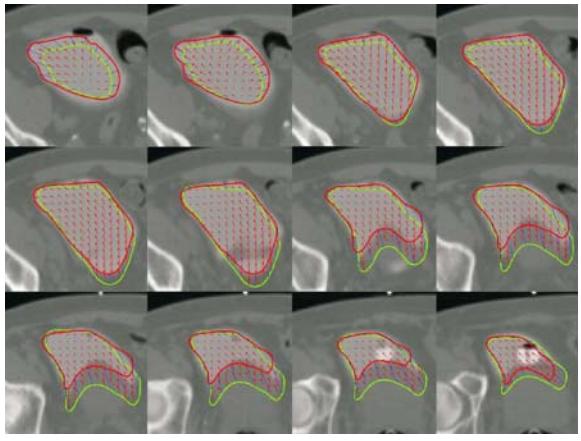

Fig. 8. Illustration of deformation maps generated for the bladder. Original shape and position is contoured in *green* and deformed position and shape is shown in *red*

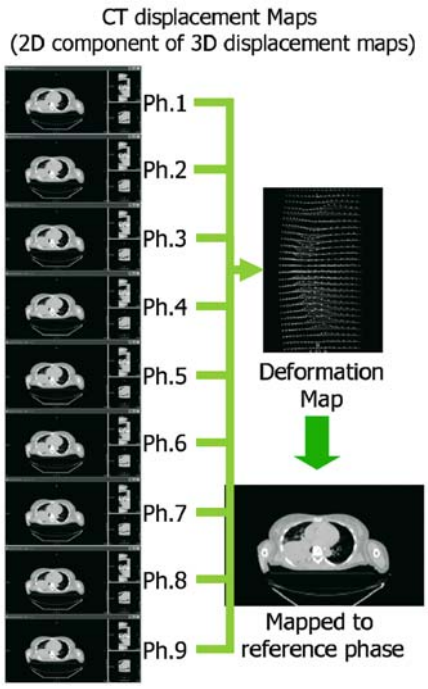

Fig. 9. Flow diagram describing the deformable registration to a reference phase by applying deformation maps generated from the different phases

tion maps can be applied to the original plan contours to generate daily contours. Figure 8 shows a reference organ (in this case the bladder is contoured by the green lines) deformed to its present location and anatomical shape (contoured by red lines). Arrows indicate the direction and amount of deformation. The daily contours can be used to create on-line plans. However, in many cases, such as in prostate, it is not easy to daily delineate the CTV, especially in the inferior-superior direction.

The availability of on-line capabilities and processes provide not only the possibility of performing image guided adaptive radiotherapy (IGRT), but potentially enable the re-definition of the standards of clinical radiotherapy treatment. If the optimization technique is fast and flexible enough to generate quick on-line plans, the vision of daily "scan, plan and treat" will eventually become reality.

8.4.2 Off-line Processes

Daily images can be used off-line to determine how the daily positioning and anatomy changes of each fraction, or a set of fractions, affect the target coverage and normal tissue avoidance. For instance, patient specific contours can be created after a few fractions defining the level of movement and anatomy change that are associated to that particular patient. Also, in cases like lung or head and neck, daily images help to keep track of tumor reduction that may be significant after few fractions. The images obtained after each fraction can be used to delineate new contours and re-optimization if necessary.

Daily images obtained in the treatment position also allow computation of the dose delivered to the patient. To analyze a plan as a whole is necessary to add together the dose distribution from multiple fractions and comparing the sum with the desired planning dose distribution. This can be easily achieved if patients are rigid bodies, then doses can be added voxel by voxel in physical space. Unfortunately, in the majority of cases where the rigid body assumption do not hold, it would be more appropriate to add doses based on the biological content of each voxel. In those cases, it is necessary to generate deformation maps and use a process called deformable dose registration [21]. This is a two-step process. First, by using the frame of the reference CT and a fraction CT, a three-dimensional deformation map is obtained. Second, the same deformation map is applied to the fraction dose (either the predicted or reconstructed dose) in order to map the dose distribution to the reference CT (Fig. 8). By mapping all the fraction dose distributions to the reference CT (and therefore to a common framework), dose can be added voxel by voxel in a more meaningful way.

Using daily CTs to obtain actual patient positioning, anatomical changes, deformation maps and dose distribution after each fraction; decisions can be made regarding if, how, and when the plan needs to be adapted. Changes may include generation of new contours to define regions of interest, new margins for previously defined structures, etc. In general, adaptation will result in the generation of a new plan that we will refer to as re-optimization.

In the future, as computers get faster and more automatic on-line processes are developed, most of the processes will be on-line even when analysis of data and some level of decision making will remain off-line either to gather enough information to make decisions or to avoid disruption of patient throughput.

8.4.3 Dose Prediction, Dose Verification, Dose Reconstruction and Re-optimization

Thus far it has been shown that helical tomotherapy provides a means to image the patient immediately prior to treatment, the opportunity to register and reposition the patient, and many additional avenues for on-line or off-line adaptive therapy. One common component of these adaptive therapy techniques is the evaluation of the dose deposited in the patient each fraction at different stages of the treatment. In this section the methods that can be used in tomotherapy to evaluate patient dose will be described. The scope of all of these techniques is to provide the dose that was actually deposited to the

patient considering positional and anatomical changes. The different methods allow one to balance the desired level of accuracy with data collection and processing requirements.

One basic requirement for the dose reconstruction process is the acquisition of a patient CT that represents the anatomy at the time of treatment. Ideally, this CT will be collected during the treatment; the longer the temporal separation between collection and treatment, the less likely it is to be an accurate representation. Additionally, it is extremely important that the CT provides information such as Hounsfield number as a function of tissue density in order to compute dose. Given these requirements, this section describes several possibilities for calculating dose and provides examples of how plans can be analyzed and re-optimized based on the results.

To evaluate patient dose after each fraction different approaches can be taken:

- Dose prediction: while the patient is on the couch, a CT is taken. This CT is then located at a position that describes a tentative position where the treatment will be delivered. After that, 'on-line' evaluation of the dose that will be deposited to the patient is computed using the planned energy fluence. This technique allows the dose that will be deposited to the patient to be predicted if the delivery proceeds according to plan. This technique is useful to evaluate on-line patient positioning based on the dose that will be delivered.
- Dose verification: uses the CT that was taken at the time of treatment to evaluate patient dose. The evaluation of the dose that was deposited to the patient is computed using the planned energy fluence. The difference with regards to dose prediction is that dose verification is an off-line process; therefore, information that described what happened during the actual treatment, such as linac output, etc., can be incorporated to correct the planned energy fluence.
- Dose reconstruction: Dose reconstruction is a determination of the dose delivered at the time of treatment [9, 22]. The CT detector runs at the time of treatment recording the treatment beam exiting through the patient and couch. Using the CT image set acquired just before or during treatment, the energy fluence incident on the patient can be computed. Using the incident fluence, the dose distribution is computed in the patient.

All of these methods account for patient anatomy and position provided that the CT adequately represents the patient. Dose verification can include some hardware components of the delivery to be a more accurate representation of the actual dose delivered. The most accurate is dose reconstruction since it includes not only anatomical information but also linac output, MLC behavior, and synchrony between couch and gantry.

After daily dose verifications or dose reconstructions are computed, comparisons between planned and delivered dose can be performed. If all went as planned, dose distributions and DVHs will show excellent agreement. If, on the other hand, larger discrepancies exist between the planned and delivered doses and the decision is made to re-optimize a plan, several alternatives are possible. Quadratic objective functions can be simplistic approximations that are far from representing an ideal clinical situation. However, they can still be a very useful tool solving and understanding radiotherapy optimization problems. If the objective function is a weighted quadratic objective function, simple expressions can be derived to re-optimize a plan after a number of fractions were delivered [23, 24].

Two common approaches to re-optimization are:

- Single-fraction based re-optimization
- Multiple-fraction based re-optimization

In the single fraction re-optimization, a goal can be to re-optimize in such a way that, in each fraction, the new plan delivers a dose distribution as close as possible to the original prescribed dose. It can be demonstrated [24] that the dose that needs to be re- optimized in this case is

$$d_K^P = Kd^P - \sum_{m=1}^{K-1} d_m \tag{1}$$

where d_K^P is the re-optimization dose prescription for the K-th fraction, d^P is prescribed dose per fraction and d_m with $(m = 1, 2, \ldots, K-1)$ is the dose delivered in fraction m.

Alternatively, the re-optimization the goal can be to deliver a dose distribution as close as possible to the total dose of Nd^P after all N fractions. If $K-1$ fractions were delivered, a decision was taken to perform a re-optimization and a new plan is generated for all of the subsequent fractions (indexed from K to N), it can be shown [24] that the prescription dose should be

$$d_K^P = \frac{Nd^P - \sum_{m=1}^{K-1} d_m}{N - K + 1} \tag{2}$$

This section described how several techniques can be used to evaluate the dose deposited on the patient. This information is essential to define how to adapt patient plans. Each one of these techniques may have different levels of accuracy and relies on different assumptions. That information in conjunction with deformable dose registration allows comparing plan and delivery (either fraction to fraction or plan as a whole). Based on this information it may be decided to generate a new plan (re-optimization). As can be observed, the process of adaptive radiotherapy can, in principle, be done automatically. Still more research need to be done to define reasonable action levels for undertaking reoptimization and thereby altering subsequent treatments.

8.5 Considerations for Adaptive Optimization

Plan generation based on 4D patient representation is a key component for adaptive tomotherapy. Intrinsically treatment planning optimization should be a four-dimensional (4D) process. The dimension of time should be considered when positioning and/or anatomy varies over the course of the treatment. These changes may occur within a fraction (intra-fraction anatomy/positioning changes), or between fractions (inter-fraction anatomy/positioning changes). Traditionally, treatment planning has been performed by having a 3D representation of the patient, typically a CT, and assuming that this representation will remain the same during the course of the treatment. Using this approach, the common technique to account for possible anatomy and/or positioning changes is the addition of margins to the targets and/or sensitive structures. Even though this approach can be adequate in certain cases, it may not always provide the best possible tradeoff between target coverage and sensitive structure/normal tissue avoidance and increases the integral dose to the patient. With the availability of images and processes that provide a temporal evolution of the patient representation, as well as the actual dose deposited, treatment planning optimization has essentially acquired a new dimension. Either in the inter- or intra-fraction case, time can be incorporated as one of the variables to determine how and when to adapt a treatment.

8.5.1 Intra-Fraction Considerations

In the case where breathing motion can be obtained from a 4D data set, tomotherapy enables a 4D treatment plan that will generate a 4D delivery that accounts for positional and anatomical changes simultaneously. The final aspect of the problem is generating a plan that uses information regarding where the patient is in the breathing cycle. Then, the optimized 4D plan that accounts for cyclically changing patient position and anatomy will be delivered. The plan should be generated in such way that, when the dose delivered for different phases is added (considering anatomical changes), a very good tradeoff between tumor control and complications is achieved.

An important consideration is that when dose is added anatomical changes should also be included by using deformable dose registration. Therefore, before specific implementations for 4D planning and delivery is discussed, some deformable registration capabilities necessary to achieve this goal will be described.

Consider a lung case where the 4D CT representation describes position and anatomy changes using ten different breathing phases. The first step is to choose an arbitrary reference phase where the plan will be analyzed (dose distributions, DVHs, etc.). The deformable registration maps all other phases back to this reference phase. Figure 9 describes the processes for deformable registration where each phase is mapped back to a reference phase, in this case, the first phase.

In this case, the deformable registration technique developed by Lu et al. [25] was used. That methodology is very efficient and provides excellent results in cases such as lung.

The simplest implementation of a 4D planning and delivery for helical tomotherapy techniques had been described by Zhang et al. [26] as breathing synchronized delivery (BSD). However, several other more elaborate implementations are also possible.

BSD relies on the patient reproducing a breathing pattern. Several approaches can be used for patient coaching and for verifying the breathing reproducibility such as, spirometry, external markers, laser positioning devices, implanted beacons, etc. Each one of these techniques will have different pros and cons that are out of the scope of this chapter. We will assume that the patients can reproduce their breathing cycle and that they are perfectly monitored using a convenient device.

As was already mentioned, the first step in performing BSD optimization is to choose a phase representation where the plan will be evaluated. Once that phase is chosen, deformation maps from each phase to the reference phase are generated.

By knowing the breathing period, a start breathing phase, delivery start angle, pitch and gantry period (typically 15 to 20 s) can be chosen. These parameters provide all the information that is necessary to give the relationship between breathing cycles, gantry angle and couch position for the whole delivery.

From the planning point of view the information needed is which CT phase is to be used to compute the dose for each part of the delivery. Then all the beamlets are computed for the whole treatment. Next, the deformation maps are used to map back the dose from all the different phases to the reference phase (deformable dose registration). Figure 10 shows the processes of deforming a beamlet from a phase to the reference phase.

Subsequently, after all the beamlets are on the reference phase framework, the plan optimization can be started as a 3D problem using any available optimization technique. Therefore, the use of deformation and

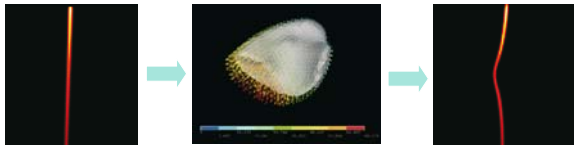

Fig. 10. For a beamlet in one particular phase a deformation map is applied to be mapped to the reference phase (figure courtesy Tieshi Zhang)

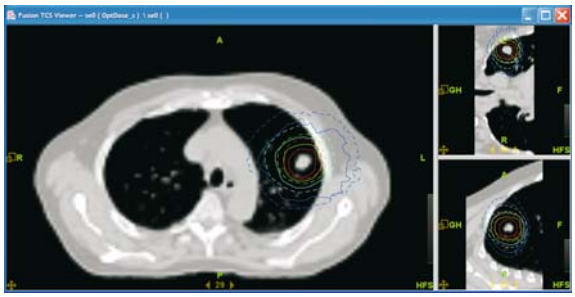

Fig. 11. Isodose comparison between a plan that was generated using 3D optimization but also evaluating the dose distribution considering the 4D CT characteristics during delivery (*dash line*) and one with 4D optimization analyzing also the 4D characteristics of the delivery (*full line*)

mapping techniques allows transformation of a 4D optimization problem into a more tractable 3D optimization problem.

As an example, Fig. 11 is an isodose comparison between the plan that was generated using 3D optimization but also evaluating the dose distribution considering the 4D CT characteristics during delivery (dash line) and one with 4D optimization analyzing also the 4D characteristics of the delivery (full line). A 4D plan optimization will have, in principle, the possibility to have target definition such that a PTV will be smaller with respect to the one obtained from a 3D CT patient representation. This is because if only 3D CT is used for target delineation, the structures will in principle be an average over the different phases on the 4D CT (provided that the 3D CT is slow enough and the 4D CT fast enough with respect to the breathing cycle). Another advantage is also shown on this figure. When the plan was generated a 3D CT patient representation was used, but the actual dose was delivered to the patient while breathing. If the dose is computed considering patient breathing during delivery the dose is blurred and, therefore, less conformal to the target. Under these conditions, 4D optimization may provide (depending on the level of motion and anatomy change, position, motion, etc., of the target and sensitive structures) remarkable advantages compared to 3D optimizations.

8.5.2 Inter-Fraction Considerations

During a fractionated treatment, adequate margins can certainly provide a good trade-off for tumor coverage and sensitive structure sparing. However, the tumor and sensitive structures may not always have the same shape, receive the same dose or be located in the same position. From these considerations it is clear that the dose deposited will be time dependent and will be compared with a plan which in general assumes time independence. In this section, the type of consideration that applies to inter-fraction changes will be exemplified for prostate cases.

By having daily on-line imaging, a retrospective analysis for prostate patients with daily CT can be performed. A particular feature for this study should be that the influence of anatomy deformations on the setup and treatment planning should be analyzed using a deformable dose registration approach.

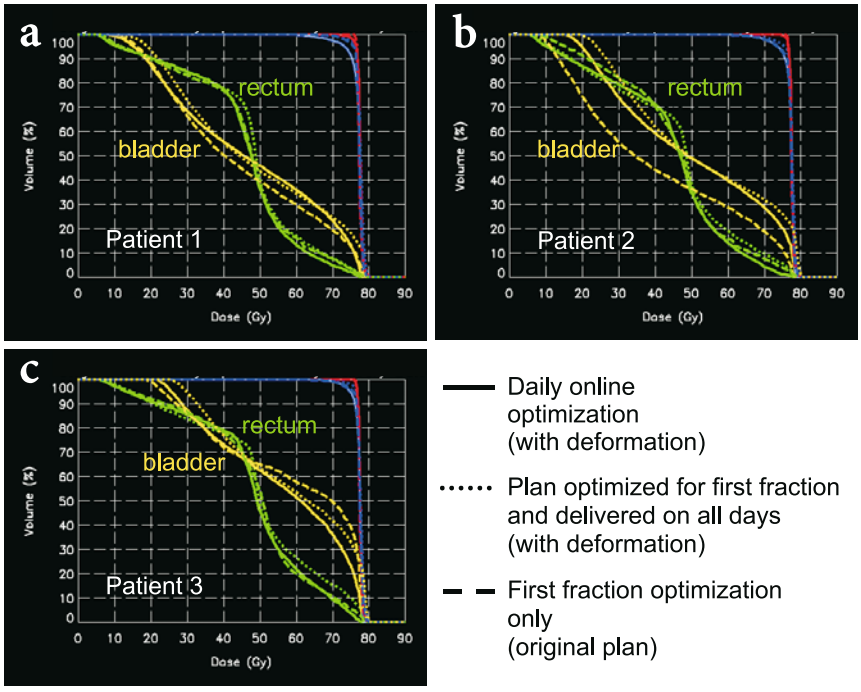

Fig. 12. DVH plan comparisons for three prostate patients. The dose distribution is added using d eformable dose registration. *Blue:* PTV; *red:* CTV

The present study was performed for three prostate patients having at least 17 daily positioning CTs. For all cases the margin considered for the PTV was a 0.5 cm three-dimensional expansion.

To study the importance of daily optimization the following plans were compared:

- The plan obtained by optimizing on the first planning CT.
- The plan obtained by optimizing on the first planning CT is delivered on each fraction, but the dose distribution is analyzed by re-computing on the daily CT and the total dose is added using deformable dose registration.
- The plan is obtained by optimizing on each daily CT, and the total dose is added using deformable dose registration.

Figure 12 is the DVH comparison for the three patients. As can be observed, provided that the margins are big enough, good coverage of the CTV will be achieved in all cases. However, for the regions at risk, some differences can be found between the original plan and either optimization with daily dose verification and daily optimization. In particular the bladder is different as can be observed in Fig. 12b,c. From these results it can be concluded that accurate estimation of the daily fractions can only be achieved by using daily images with dose verification and/or dose reconstruction. Also the evaluation of the plan as a whole should be done by adding the dose with deformable dose registration. It is also interesting to note that no appreciable differences can be observed on the DVHs corresponding to the daily plan optimization (that in principle should be the best plan that we can be obtained) and the one that is obtained by delivering always the same plan generated using the planning CT when in both cases the dose is added using deformable dose registration. The results seem to indicate that – at least in this case – little more will be achieved by expending extra time and resources performing daily online optimization.

8.6 Summary

The development of helical tomotherapy has introduced a platform that is capable of delivering precise IMRT treatments while providing integrated image guidance. This system is capable of delivering highly complex plans, such as the head and neck and TBI cases presented. Yet tomotherapy can also deliver simpler treatments, which can be imaged, planned, and delivered entirely on the tomotherapy unit in 15–20 min. One of the advantages of tomotherapy is that the overhead between very simple cases and very complex cases is minimal.

The integration of MVCT provides an on-line means for daily verification of not only the patient setup, but also of the internal anatomy. The interface provides tools for registering these images and repositioning the patient accordingly. Image quality depicts soft tissues and organs with sufficient contrast to reposition the patient, re-contour images, and perform other adaptive processes. The MVCT images are also ideal for dose calculations since the Hounsfield units of these images accurately represent the attenuation seen by the treatment beam.

Numerous adaptive processes are possible, and can be performed both on-line and off-line. The off-line variations involve an array of tools to perform dose reconstruction, re-contour the images, add the doses with respect to the daily deformation maps, and generate new plans that both reflect the patient's current anatomy and correct for any discrepancies in the delivered dose. The on-line corrections obviously need to be fast enough to perform in real-time, and must include options both to reposition the patient in accordance with doses and/or anatomy, and to select plans on a daily basis based on daily anatomical deformations.

As tomotherapy become increasingly prevalent in research and clinical centers, advanced tomotherapy techniques are being developed to address new and difficult problems. For example, multiple methods for lung treatment will allow for treatment using shallow breathing, optimized breath-holding, and 4D delivery. Ultimately, one of the key benefits of tomotherapy is that it combines the power of an advanced image-guided IMRT system with the simplicity of a single integrated system that can image patients, deliver a wide variety of treatments and perform integrated QA and verification.

Acknowledgements. The authors would like to thank Paul Reckwerdt, John Hughes, Tiezhi Zang, Eric Schnarr, Tim Theisen, Tim Chapman, Jason Haimerl, Bob Cravens, Carl Mauer, Quan Chen, Michael Kissick, Dan Sidney, Sam Jeswami, Jodi Pachal and Francesc Salvat for very fruitful discussion and comments that help to create this chapter.

References

1. Mackie TR, Holmes T, Swerdloff S et al. (1993) Tomotherapy: a new concept for the delivery of dynamic conformal radiotherapy. Med Phys 20:1709–1719
2. Mackie TR, Holmes TW, Reckwerdt PJ et al. (1995) Tomotherapy: optimized planning and delivery or radiation therapy. Int J Imaging Sys Technol 6:43–55
3. Yang JN, Mackie TR, Reckwerdt PJ et al. (1997) An investigation of tomotherapy beam delivery. Med Phys 24:425–436
4. Mackie TR, Balog J, Ruchala K et al. (1999) Tomotherapy. Sem Radiat Oncol 9:108–117
5. Olivera GH, Shepard DM, Ruchala K et al. (1999) Tomotherapy. In: Van Dyk J (ed) Modern technology of radiation oncology. Medical Physics Publishing, Madison

6. Mackie T, Olivera G, Kapatoes J, Ruchala K, Balog J, Tome W, Hui S, Kissick M, Wu C, Jeraj R, Reckwerdt P, Harari P, Ritter M, Forrest L, Welsh J, Mehta M (2003) In: Palata, Mackie (eds) Helical tomotherapy. Intensity-modulated radiation therapy, state of the art. AAPM Medical Physics Monograph No 29, Medical Physics Publishing, pp 247–284
7. Ruchala KJ (1999) Megavoltage computed tomography for tomotherapy verification. Dept of Medical Physics, University of Wisconsin, Madison
8. Ruchala KJ, Olivera GH, Kapatoes JM et al. (2000) Megavoltage CT image reconstruction during tomotherapy treatments. Phys Med Biol 45:3545–3562
9. Kapatoes JM, Olivera GH, Balog JP et al. (2001) On the accuracy and effectiveness of dose reconstruction for tomotherapy. Phys Med Biol 46:943– 966
10. Shepard DM, Olivera GH, Reckwerdt PJ, Mackie TR (2000) Iterative approaches to dose optimization in tomotherapy. Phys Med Biol 45:69–90
11. Moseley et al. 2004
12. Ardekani BA, Braun M, Hutton BF et al. (1995) A fully automatic multimodality image registration algorithm. J Comput Assit Tomogr 19:615– 623
13. Maes F, Collignon A, Vandermeulen D, Marchal G, Suetens P (1997) Multimodality image registration by maximization of mutual information. IEEE Trans Med Imaging 16:187–198
14. Ruchala KJ, Olivera GH, Kapatoes JM et al. (2000) Calibration of a tomotherapeutic megavoltage CT system. Phys Med Biol 45:27–36
15. Ruchala KJ, Olivera GH, Kapatoes JM (2002) Limited-data image registration for radiotherapy positioning and verification. Int J Rad Oncol Biol Phys 54:592–605
16. Yan D (1997) Adaptive radiation therapy. Phys Med Biol 42:123–132
17. Yan D, Wong J (1997) Adaptive modification of treatment planning to minimize the deleterious effects of treatment setup errors. Int J Radiat Oncol Biol Phys 38:197–206
18. Olivera G, Ruchala K, Kapatoes J, Reckwerdt P, Jeraj R, Lu W, Balog J, Mackie T (2001) Approaches to prostate patient setup including daily anatomy changes. Forty-third Annual meeting of the American Society for Therapeutic Radiology and Oncology (ASTRO), San Francisco, California, November 2001
19. Ruchala KJ, Olivera GH, Kapatoes JM et al. (2002) Multi-margin optimization with daily selection (MMODS) for image-guided radiotherapy. Int J Rad Oncol Biol Phys 54:318
20. Ruchala KJ, Olivera GH, Kapatoes J et al. (2002) Multi-margin optimization with daily selection (MMODS) for image-guided therapy. Proceedings of the ESTRO 21, Praha, CZ
21. Olivera GH, Ruchala K, Lu W, Kapatoes J, Reckwerdt P, Jeraj R, Mackie R (2003) Evaluation of patient setup and plan optimization strategies based on deformable dose registration. Int J Radiat Oncol Biol Phys 57:S188–S189
22. McNutt TR, Mackie TR, Paliwal BR (1997) Analysis and convergence of the iterative convolution/superposition dose reconstruction technique for multiple treatment beams and tomotherapy. Med Phys 9:1465–1476
23. Wu C (2002) Treatment planning in adaptive radiotherapy. PhD Thesis, University of Wisconsin
24. Wu C, Jeraj R, Olivera G, Mackie T (2002) Re-optimization in adaptive radiotherapy. Phys Med Biol 47:3181–3195
25. Lu W, Chen M, Olivera G, Ruchala K, Mackie T (2004) Fast free-form deformable registration via calculus of variations. Phys Med Biol 49:3067
26. Zhang T, Jeraj R, Keller H, Lu W, Olivera G, McNutt T, Mackie T, Paliwal B (2004) Treatment plan optimization incorporating respiratory motion. Med Phys 31:1576–1586

4D CT Simulation

George T.Y. Chen, Eike R.M. Rietzel

9

Contents

9.1 Introduction

Imaging is one of the bases of effective radiotherapy. CT and MR studies provide geometric information for the delineation of the gross target volume, and the localization of adjacent normal structures. These geometric data are used in the planning process to orient beams that simultaneously encompass the target while avoiding critical structures for complex beam orientations. CT also provides tissue density needed for radiation dose calculations.

The introduction of CT simulators and simulation software has been key to development of 3D conformal radiotherapy. Assessment of the clinical impact of CT scanning in the early era of CT based planning [1, 2] showed very significant changes in aperture design when 3D imaging was employed; 30 to 80% of plans were altered due to patient specific anatomical information provided by CT. Estimates then surmised that $\sim 40\%$ of all radiation therapy patients might benefit from CT scanning for therapy planning [3]. The percentage of patients CT scanned for treatment planning today at many institutions is close to 80%.

CT scanner manufacturers in the recent past increased the scanning capacity through helical multislice technology. Helical scanning [4] has advantages over conventional CT, including volumetric data acquisition in a single breath hold, an expected reduction of motion artifacts, high speed, improved z axis resolution [5] and excellent image quality. Within the past several years, multi-detector CT has become available, and provides two- to fourfold improvement in volume coverage speed with comparable diagnostic image quality [6].

Unlike diagnostic scans, treatment-planning scans in the thorax and abdomen are often performed with the patient breathing lightly. The rationale for this scan technique historically has been to "scan the patient the same way" he/she is treated, i.e. during light breathing. From these images, gross target volumes are outlined, and subsequently expanded to account for microscopic extension, setup uncertainty and organ motion [7, 8].

Organs in the thorax and abdomen move approximately periodically along the cranio-caudal and anterior-posterior axes during respiration. The amplitude of this motion is on the order of centimeters, with a period of $\sim$4 s [9, 10]. When imaging moving organs during CT scanning, distortions can occur [11,12]. Commonly observed distortions include discontinuities seen in the coronal multiplanar view of the diaphragm as well as artifacts in CT sampling due to breathing. Resulting images in the beam's eye viewpoint often exhibit

irregularities or "zig zags" in the assembled geometric model of the target volume. "Shrink wrapping" the observed target volume and applying a margin for motion are often assumed to be adequate to cover the clinical target volume excursions during respiration. With earlier, slower CT scanners, organ motion resulted in temporal motion artifacts, visualized as blurred edges. Increased scan speed with modern helical CT imaging appeared to decrease motion artifacts (sharper organ edges).

The accurate three-dimensional geometric modeling of an organ is a prerequisite for precision treatment planning, and directly affects both aperture shape and target center in beam's eye view based planning. The potential for distortions and deformations of organ shape must be understood in detail and strategies for mitigation developed.

In this chapter, we re-examine the process of CT simulation with the focus on how the process changes when time and motion is explicitly considered. The general outline of conventional 3D CT simulation is extensively covered elsewhere [13]. We discuss the implications of extending CT simulation into four dimensions over the respiratory time scale. Implications of shorter time scales associated with cardiac motion are not discussed, nor are changes in anatomy associated with longer time scales such as physiologic changes in organ filling (e.g. bladder) from day to day, see chapter II. 6. Table 1 lists the processes associated with CT scanning plans, and tabulates differences between 3D and 4D acquisition.

9.2 Effects of Motion on Imaging

We first examine the impact of motion on conventional CT scanning of a moving target. The magnitude of image distortion under conditions simulating respiration can be easily illustrated. Figure 1a shows a photograph of a phantom consisting of various sizes of spheres. The phantom is initially scanned by placing it on the CT table; under this condition, there is no motion. When the resulting images are surface rendered with scanner display software, they appear virtually identical to the objects in the photograph, as shown in Fig. 1b. Scans shown here were performed on a commercial CT simulator (GE Lightspeed Qx/i).

The phantom is then placed on a one-dimensional oscillating table, with amplitude of 1 cm and period of 4 s. The motion along the CT couch length is sinusoidal, and simulates the cranio-caudal motion of a target in the abdomen or thorax. Motion during the simulated breathing is along the up/down axis of Fig. 1. The next three images (Fig. 1c–e) are a series of surface renderings from helical scans, each scan begun at a slightly different initial phase of the sinusoidal motion. As can be seen by comparing the static scan (Fig. 1b) with various instances of the moving object scans, the shape and size of the object scanned can vary substantially. Simulation studies show that volumes can differ by ±35–40% of the true volume of the sphere [14]. Furthermore, note that in the surface rendered coronal views, some ob-

Table 1. Differences between 3D and 4D imaging

Process/step	3D scanning	4D scanning
Patient positioning	As currently performed	No change
Use radio-opaque seeds	As needed	No change
Scan – light breathing	Acquire ~100 slices 1 volumetric study	Acquire 1500+slices – multiple volumetric studies
Dose	~1 cGy	3–5 Times greater dose
Reconstruction	Conventional	Conventional followed by resorting/multiple sets OR projection sorting followed by conventional reconstruction
Image fusion with other studies	Complex problem	Complex problem
Contouring VOIs	Performed on single study	Performed on multiple studies; computer assistance needed
Aperture design	Standard 3D	Extract shape and trajectory; create composite ITV
Choose beam directions	BEV	Multiple/composite BEV – minimize motion effects
Generate DRRs	Conventional	At specific phase or pseudo fluoroscopic DRR movie loop
Image guided patient set up	Standard guidance by bony anatomy or clips	Guidance by gated or multiple image acquisitions (compare DRRs)

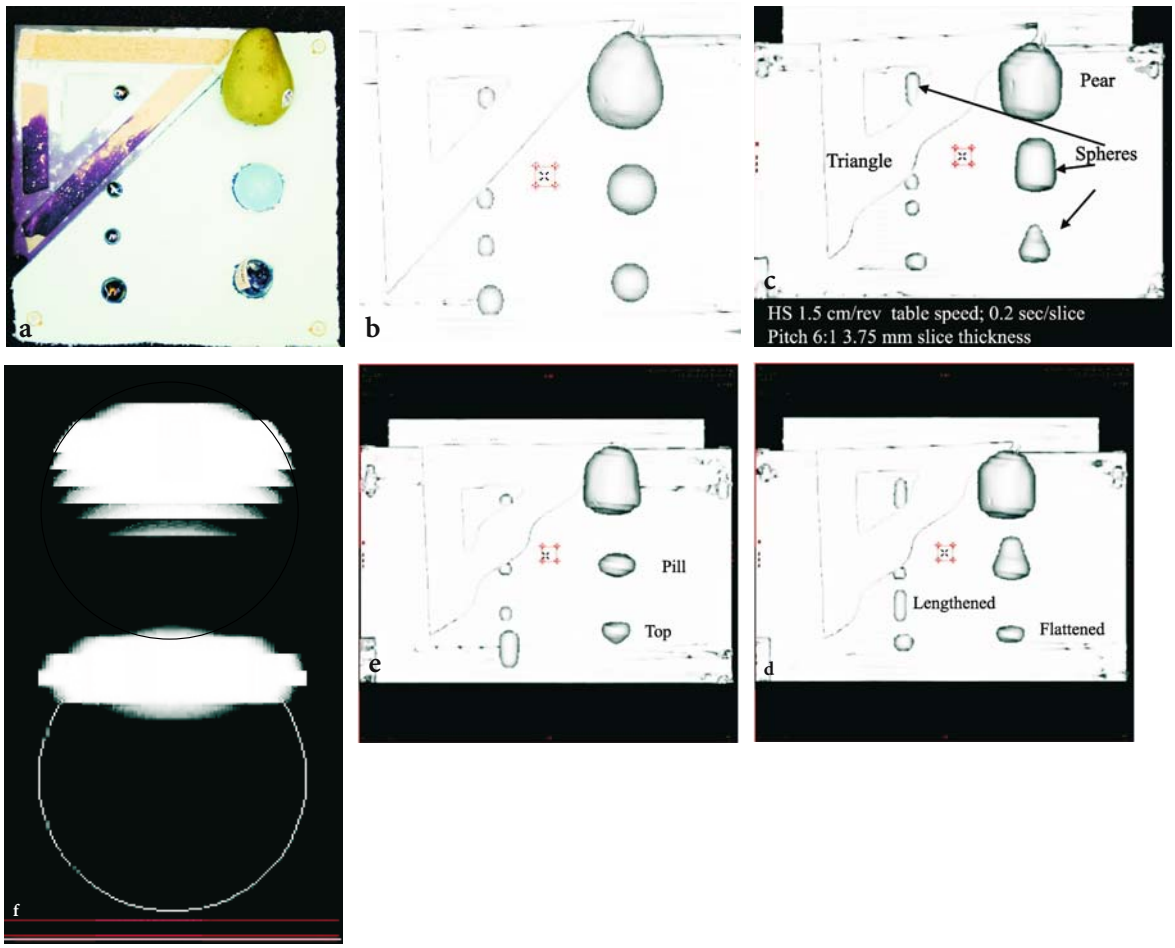

Fig. 1. (a) Photograph of phantom containing spherical objects, drafting triangle, and pear. (b) Surface rendered GE Advantage Sim image of phantom when scanned in static mode. (c)- (e) various images generated by capturing object at different initial phases of motion. All scan parameters are set at same values. (f) Simulation of scanning process showing reshuffling of imaged object (see text)

jects are shortened, while others appear elongated (see small spheres at left, which appear as tubes). This is most evident in Fig. 1e, left column, where two marbles appear elongated, and two marbles are relatively spherical. These distortions are a function of the initial location of the object as the scan plane begins imaging it. When the object moves anti-parallel to the advancing imaging plane (which moves from top to bottom of the phantom), its image becomes shortened due to the relative motion. When the object moves parallel to the direction of advancing imaging plane, it appears elongated. These studies show the distortion possible when two asynchronous motions (object motion and scan imaging/table motion) interfere with each other.

Figure 1f shows that the interaction between the CT scan plane advancing and the sinusoidal motion of the volume of interest leads not only to incomplete assessment of the range of motion, but also re-ordering of axial slices. The circles represent the two extrema of motion of a sphere. The white objects imaged represent slices of the sphere as imaged in this simulation, by a finite slice thickness of 3 mm. The object in this case is a sphere of 1.6 cm radius with an amplitude of 3 cm and period of 4 s. Scans are acquired effectively at ~ 0.2 slices/s, based on typical effective speed of helical scans. Three aspects of this simulation are apparent: 1) the sphere travels beyond the portion of the lower imaged ellipsoid, but is not imaged in this region, 2) the solid sphere is visualized as two distinctly separate objects, and 3) close inspection of the lower slices of the upper object show that the slices at the inferior portion are actually the top of the sphere, based on curvature. While this dynamic process is best understood by an animation, a single frame from the dynamic display shows significant weaknesses of scanning a moving object with standard imaging techniques.

The effects of motion can also be seen in patient studies. Figure 2a shows a coronal cut through a helical scan of a patient with a lung tumor. Note the discontinuity

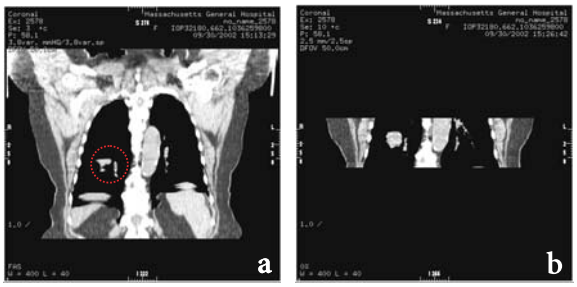

Fig. 2. (*Left*) Coronal multiplanar reconstruction during light breathing CT acquisition. (*Right*) 4D CT scan at a specific instant. This is analogous to a strobed image. Note difference in shape of tumor in right lung and diaphragm

at the diaphragm/lung interface. The tumor in the right lung is seen as a truncated spherical object above the diaphragm. Figure 2b is an image of the same patient at a specific moment of the respiratory cycle. Comparison of the two images shows substantial differences in tumor shape. Since motion is suspended in the image on the right, it represents more truthful tumor geometry.

It is the existence of such artifacts during light breathing that leads one to finding methods of acquiring images that provide improved information on the shape and trajectory of objects in motion during treatment planning scans. The implications of segmenting the tumor in Fig. 2a vs 2b in precision radiation therapy planning and delivery are obvious.

9.3 4D CT Virtual Simulation Process

In conventional 3D CT simulation, scans in the treatment position are acquired to facilitate virtual simulation. The output of this process is an understanding of the location of the tumor, location of normal structures, (quantitatively through contouring/segmentation of VOIs), apertures for geometric/dosimetric coverage, and digitally reconstructed radiographs (DRRs) to aid in the alignment of the field on the treatment unit. These objectives remain the same even in 4D acquisition and interpretation of scan data. Differences in the process of virtual simulation resulting from 4D data acquisition and analysis are discussed below.

9.4 Initial Steps in 4D-Imaging

Three-dimensional CT data acquisition begins with selecting the patient treatment position, and then reproducing it with the appropriate immobilization for scanning. Placement of radio-opaque seeds in the region of the tumor is selectively performed for patients with abdominal lesions, and under some treatment protocols in breast lesions. Currently, it is relatively uncommon to place seeds near lung tumors for the purposes of image-guided therapy, although such clips are inserted for these purposes in some centers [15–18]. If radio-opaque markers are present, they can be used to study organ motion with conventional fluoroscopy supplemented by video capture and analysis [19, 20, 45]. These data provide a more realistic estimate of the variations of target motion over treatment times. The second important use of clips is their visualization moments before treatment to guide field placement on a daily basis. Several groups have developed imaging systems on board linear accelerators that gate the radiation on when the radio-opaque marker is in the pre-determined and planned treatment position. The initial steps of patient immobilization, inclusion of clips, and other aspects are essentially unchanged between 3D and 4D scanning.

9.5 Acquisition of 4D CT Scans

The goal of a 4D CT scan is the generation of the actual volumetric spatio-temporal anatomical data set. There are several ways in which such a family of data sets at specific instants of the respiratory cycle can be acquired. The most straightforward approach is to gate CT scans at a chosen phase of respiration [21, 22]. Conceptually this is straightforward; in axial scan mode the scan is gated on at each couch position at a pre-selected instant of the respiratory cycle. Then each contiguous CT slice is taken at the same respiratory phase. On a single slice scanner, this could require a total scan time that is the product of the number of slices times the respiratory period, or about 400 s for a typical study of 100 slices and a respiratory period of 4 s. For multislice scanners this time is reduced according to the number of slices due to less data acquisition intervals. As described, this would result in only a single volumetric spatio-temporal image data set. If one wanted to capture the motion of internal anatomy at each of 10–20 points of a respiratory cycle, the procedure would need to be repeated 10–20 times and the resulting acquisition time would be prohibitively long.

In general, full 4D CT data can be obtained within a single data acquisition run by oversampling. At each couch position projection data are acquired continuously during multiple CT tube rotations over a full respiratory cycle. Reconstruction of a single image minimally requires projection data over one half tube rotation (at least 180° plus fan beam angle). By selecting a reconstruction window within the over sampled projection data, a specific motion state can be reconstructed. All motion states can be reconstructed by selection of corresponding reconstruction windows. Such reconstructions are performed at each couch position. To obtain volumetric information at a given

respiratory state, corresponding images from all couch positions are binned into different volumes.

In principle, 4D CT data acquisition can be performed with different scanning modes. At our institution 4D CT data acquisition is achieved by continuous axial cine data acquisition. A slightly different axial cine approach as been reported by Low et al. [23] where data are not acquired continuously but several independent images are obtained per couch position by individual, consecutive data acquisitions. A multislice helical approach has also been described. Vedam et al. [24] and Ford et al. [25] adapted a third generation multislice scanner to permit thoracic CT acquisition in four dimensions. These techniques were tested on phantom runs under periodic and non-periodic motion conditions. While limitations exist for all acquisition methods, the authors reported successful acquisition of 4D CT data of both phantom and patient.

9.6 4D Axial Cine-scanning

For the purposes of specificity, we describe the cine-imaging protocol used at our institution. Specifically, the scanner used is the GE Lightspeed Qx/I four slice scanner with 0.8 s rotation time. Details of the methods are described in the article by Pan et al. [26, 27]. The time required to capture about 20 cm length of anatomy is about 2 min for a four slice scanner and a respiratory period of ~4 s. For a more recent model of multislice scanner (0.5 s rotation time, eight slices), the time required is under 1 min. While we specifically describe one system, the process involved is functionally similar to that described by others [23–25].

9.6.1 Patient Breathing

Current practice at many centers is to only ask that the patient perform shallow breathing during the scan process. In this implementation, there is no difference between 3D and 4D CT data acquisition. An alternative is to provide visual or auditory breath coaching during CT data acquisition. Visual feedback of the amplitude and frequency of the ideal breathing pattern attempts to regularize these variables. The Varian RPM system (Varian Medical Systems, Palo Alto, CA) is used to monitor and record a respiratory signal, specifically the rise and fall of the anterior abdominal surface. A small plastic box with two infrared reflectors is viewed by a camera system that also emits an infrared beam. From the camera's perspective, it sees two dots moving vertically as the patient breathes lightly. The camera is anchored to the foot of the CT couch, thereby fixing the distance between the camera and reflector box as the couch translates through the CT gantry aperture. After studying the respiratory pattern for about 1 min, an average period and amplitude are determined. Limits are visually presented to the patient to guide his/her breathing during the scan.

9.6.2 Conventional Scan Parameters

Other parameters selected prior to scan include slice thickness, which is commonly set to 2.5 or 3 mm. These relatively thin slices enable finer imaging of small objects and reduced partial volume effects. Thin CT slices also improve the quality of Digitally Reconstructed Radiographs (DRRs). X-ray parameters such as kV and mA s are set to acquire good quality images. The need for diagnostic quality images at each moment of the respiratory phase to characterize target motion is debatable. We have in certain cases reduced the technique and still captured shape and trajectory of lung tumors that clinically appear acceptable. However, for 4D treatment planning (see next chapter) image quality is important for heterogeneity corrections during dose calculations.

9.6.3 4D Scan Parameters

Projection data for image reconstruction are acquired continuously for a time interval equal to the period of respiration, with a small additional time added to account for fan beam transit time. Since a typical respiratory period is on the order of 4 s, with a rotation time of 0.8 s, the time interval spent at a given couch index is approximately 5 s. During this time interval, the X-ray tube is continuously on, and projection data are gathered. At the end of the 5 s, the X-ray tube is gated off, and the couch is advanced to the next table position. The X-rays are then turned on and the next 5 s of scanning at the new table position commences. For each couch position several images (typically 15–20) are reconstructed uniformly distributed over the respiratory cycle. Typically, for a complete 4D study up to 1500 images are recon-

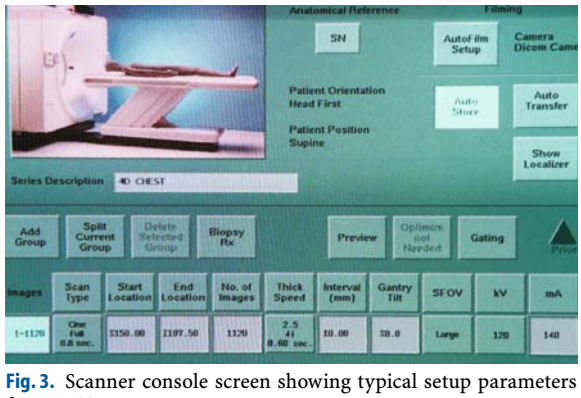

Fig. 3. Scanner console screen showing typical setup parameters for 4D CT scan

structed (e.g. 100 slices, 15 images per slice). An image of the scan parameter setup on the scanner console for a 4D CT study is shown in Fig. 3.

9.6.4 Longitudinal Extent of Scan

Scoutviews or scanograms are taken to define the craniocaudal extent of the planning scan. This would also be performed for 4D scanning, with the cautionary advice that the scan length should be sufficient to capture the anatomy of interest over the possible longitudinal dynamic range over which it travels during normal respiration. This parameter is patient dependent. In our experience, some tumors barely move; at the other extreme, a liver tumor was observed to move ~ 3 cm craniocaudally even with application of a mechanical device to limit breathing excursions.

9.6.5 Future Directions in CT Hardware

Projection data for CT reconstruction as described are acquired four slices at a time on our scanner. Newer scanners acquire 16 or even more slices per 0.35 s revolution. The quality of 4D imaging currently is dependent upon the regularity of respiration. New generation CT scanners, under development for cardiac scanning, employ area detectors, where the projection images from a cone beam of X-rays is captured simultaneously along the longitudinal direction. These new scanners, approximately five years from now, will provide 4D scans at a higher acquisition speed.

9.7 Resorting/Registering Slices

Once the 1000–1500 slices of axial scan data are reconstructed, they must be resorted into temporal bins to build 4D spatio-temporally coherent image data sets. This is done by scanner software that assigns each axial reconstructed image at a given table index to a specific respiratory phase. Both internal and external sorting approaches have been applied to resorting of 4D-CT data sets [27]. In the internal approach, the 4D images are resorted to smoothly match organ anatomy in CT images between adjacent table indices at specific respiratory cycles. The internal approach can achieve true 4D-CT imaging without an externally acquired respiratory signal, which may be compromised by the location and positioning of the sensing device to generate the respiratory signal. Currently internal sorting has to be performed manually. It is therefore extremely time consuming and limits its use in routine clinical application. Alternatively, an external signal can be used to resort CT images. The GE 4D scan system utilizes the respiratory signal generated by the RPM system as previously described. During CT data acquisition, the abdominal motion trace and CT data acquisition are precisely temporally correlated via a TTL signal. Based on the correlation, every CT image is identified with a specific respiratory phase stamp. Spatio-temporal coherent volumes are then sorted according to the externally acquired respiratory signal. The external registration approach has been implemented commercially on the GE scanner.

9.8 Qualitative Analysis of 4D Data: Viewing

9.8.1 4D Browser

Visualization and analysis of 4D CT data requires special software functionality. Exploring time dependent imaging data can be facilitated with a 4D browser. Figure 4 shows a prototype data explorer developed by E.R. at our institution. Figure 4a,b shows the inhale and exhale states as captured by 4D CT, out of a ten-phase study, where a volumetric anatomical data set is reassembled for every 0.4 s interval. This prototype data explorer shows several of the essential features of a data visualizer for 4D CT analysis and viewing. As

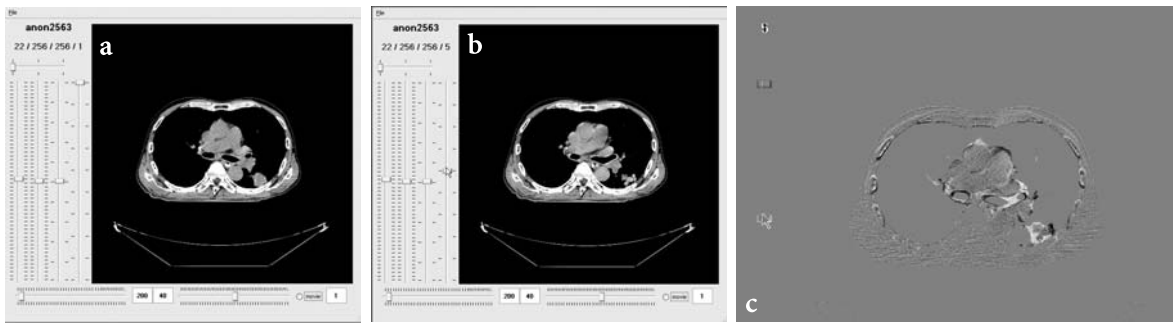

Fig. 4. (a) 4D Data Browser screen capture at inhale (respiratory phase of 0%). (b) Browser set at 50% respiratory phase corresponding to exhale. (c) Difference image between inhale and exhale

with many programs that display CT data, the volumetric data set can be viewed in multiple interactively selected principle planes (sagittal, coronal, axial) with standard window and leveling functionality. The three slider bars in the screen capture are used to select the viewing plane. The right most slider bar selects the respiratory (temporal) phase to be displayed for the given anatomical slice. A movie button initiates a video loop that dynamically cycles through the various phases of 3D data at different instants in time. The subtraction image in Fig. 4c shows the degree by which motion from one phase to another changes anatomy. Note the variations at the edges of the bronchi as well as the difference region around the tumor in the posterior portion of the left lung. Other functionality implemented for dynamic analysis includes display of composite contours and contours from individual temporal CT data sets and 4D dose. These visualizations help the viewer understand the impact of various organ motions.

9.8.2 Volume Rendering

A standard display format for three-dimensional image data is volume rendering [28]. In this process [29], a three-dimensional CT data set is projected onto a 2D image plane (computer display) with shading and perspective cues that provide the viewer with an improved understanding of the spatial relationships of anatomical structures. Three-dimensional renderings have been used extensively in diagnostic radiology [30] to aid diagnosis as well as surgical and radiation treatment planning; the authors also emphasize volume rendering as a means of communication between diagnostic radiologist and the referring clinicians [28]. Because plan design requires an understanding of the relative geometry of tumor and adjacent normal organs, such displays can also be of use in radiation treatment planning [31–33].

Two approaches to volume display are direct volume visualization and surface displays. In surface displays, the object of interest is first segmented and then surface tiles are generated to represent the constructed surface. Without surface tiles or shading, the early traditional representation of stacked wire loops was employed. In direct visualization, ray tracing through the entire volume is performed. The opaqueness of a pixel in the generated image is determined algorithmically by the cumulative ray trace operation. Motion during display (such as rotation of a rendered object) is often applied to the image to provide additional spatial cues.

An example of a volume rendering from a 4D CT data set is shown in Fig. 5. In this image, the tumor (arrow) is seen in the posterior left lung. The lung parenchyma has been rendered transparent. A cut plane is advanced to eliminate the obscuring effect of the posterior chest wall and superficial tissues. Vessels and airways in the lung are clearly visible. This image is a single frame from an animation that shows the tumor moving craniocaudally during respiration.

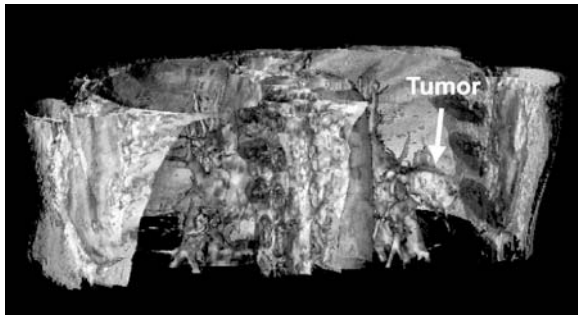

Fig. 5. Volume rendering of lung tumor, indicated by *arrow*. Lung tissue is rendered transparent; larger vessels and airways are visible at this specific window and level

9.9 Quantitative Analysis of 4D CT Data

9.9.1 Segmentation

Segmentation of 4D data is a major challenge. With 4D CT data, the number of data sets may range upwards of 20; manual contouring of normal organs and tumor would not be feasible for routine treatment planning. The development of automated contouring algorithms to track organs such as liver and lung are essential in furthering the use of dynamic medical imaging data [34–36].

One interim strategy involves limited contouring in the axial plane. The inhale and exhale data sets are contoured and the resulting GTV target contours are merged. This composite volume is then overlaid onto the dynamic CT data and visually inspected to ensure that the composite contour as defined by inhale and exhale states fully encloses all intermediate anatomical sets. A setup margin is then added to this volume. One should also consider an additional uncertainty margin associated with variations in respiration amplitude. Strictly speaking, this is not a PTV that accounts for organ motion, since internal motion is explicitly accounted for in segmentation of 4D data.

When segmentation is completed (either manually or through automated means), these volumes as a function of time provide an estimate of the trajectory of the center of mass of the target and capture deformations of the organs of interest. It should be noted that as described, 4D data is synthesized from many breathing cycles; variation of respiratory amplitude and frequency is certainly

likely over the course of a single treatment and over the entire course. Given these caveats, these contours are still useful in estimating the degree of organ deformation. Contours at different respiratory phases have been used to calculate the deformable registration vector field that describes the movement of voxels during respiration [37].

9.9.2 Quantifying Motion

The primary information to be extracted from 4D CT is the shape and trajectory of VOIs during respiration. After each of the VOIs has been segmented, the center of mass can be localized in each study set, and the trajectory assessed over the period of respiration. These contours, if sufficiently accurate, can also be utilized in assessing the degree of organ deformation [37]. Deformable registration is an active area of investigation in medical image processing [38, 39], and advances here will make complete use of 4D CT more feasible. Several software packages publicly available offer tools to deal with this technical issue [43, 44, 46].

9.9.3 Accuracy of CT Numbers

Partial volume sampling and the subsequent distortion of CT numbers is a well known artifact of finite slice thickness. An additional perturbation of CT numbers from true values is introduced by partial temporal sampling, since an object can still move within the finite X-ray tube rotation time (currently ~0.5 to 0.8 s). The uncertainty introduced in HU of a uniform object has been reported [40]. This suggests the need for care in selecting window/level to determine the geometric extent of a GTV in motion.

9.10 4D Simulation Images

9.10.1 4D DRRs

Four-dimensional CT may alter the manner in which DRRs are applied. Without motion, the DRR is utilized as a reference alignment image; images taken at treatment are compared and analyzed to determine necessary patient repositioning. In a 4D environment, consider that an aperture is designed around a specific respiratory phase, exhale for example. The aperture might still have been asymmetrically enlarged to account for motion from exhale through normal inhale, but its home position is defined at normal exhale. In this scenario, the image taken before treatment for image guidance should be acquired at the same respiratory phase and then compared with the exhale DRR.

9.10.2 4D BEV

The consequence of an aperture designed to accommodate the target trajectory during normal respiration is undoubtedly larger than for the static (or gated) aperture. This being the case, the beam's eye view process may be altered. As usual, the aperture is adjusted as a function of beam orientation to provide adequate target coverage. Some normal structures, e.g. spinal column are static, and evaluation of risk to such structures remains the same. Other structures, e.g. kidneys or liver, move approximately in synchrony with the target during respiration, but not necessarily with the same motion amplitude, vector/direction or phase.

An alternative to aperture enlargement to encompass a moving target is to identify that respiratory phase that optimally separates the target from nearby organs at risk, and choose to develop a plan to be delivered at this specific phase through gating. Four-dimensional cine mode data acquisition facilitates this by acquiring and assembling multiple data sets through the 4D simulation, each of which can be evaluated to identify the possible optimal phase.

One can envision the need for new functionality in BEV planning, where the target aperture is visualized against the envelop of an organ at risk, or an animated outline of the organ at risk over the respiratory cycle. At this point, given the early stages of clinical experience with 4D CT, these ideas are somewhat speculative. However, the fundamental principle associated with BEV, that is the design of an aperture to encompass a 3D object from the radiation source viewpoint, and avoid or minimize the irradiation of organs at risk, still remains valid, but with an additional degree of freedom associated with organ motion. Selection of beam angles that minimize motion from that viewpoint may be useful.

9.10.3 Treatment Planning

Treatment planning in the domain of 4D imaging data is covered in the following chapter. One of the primary barriers to this planning involves the calculation of voxel displacement maps that quantify the deformation of an organ during respiration [41, 42].

Preprocessing CT data for treatment planning can involve editing gas or contrast CT values to those of water. In practice, this is commonly done for charged particle treatment planning to ensure an adequate beam penetration in the presence of transient inhomogeneities (e.g. bowel gas). The task of editing these transient inhomogeneities expands significantly because of the volume of data in 4D scans.

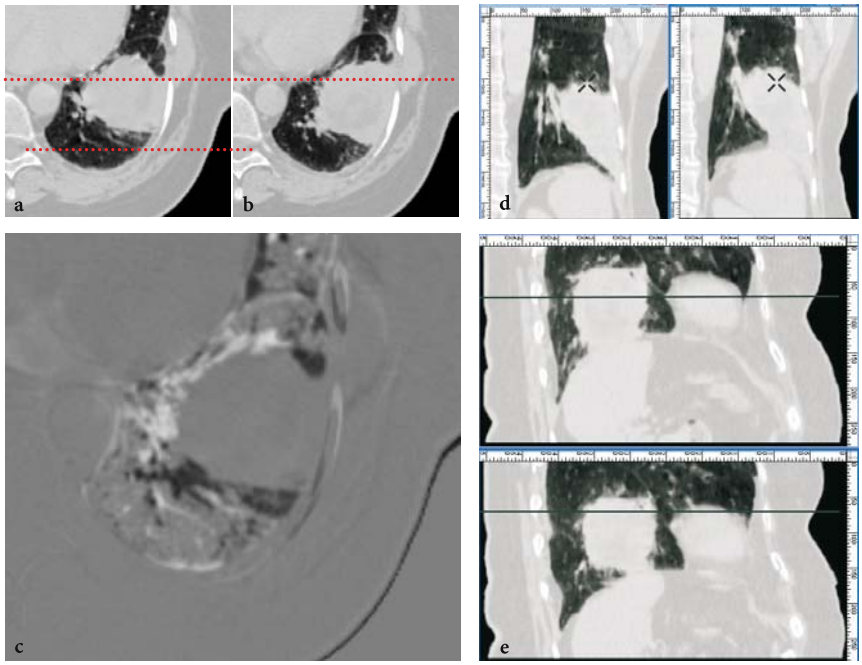

Fig. 6. (a),(b) Inhale and exhale phases of respiration of axial cut through center of large tumor in the left lung. (c) There is some shape change as indicated by the difference image. (d) Side by side coronal planes with guideline to assess cranio-caudal motion between inhale and exhale. Motion is approximately 1.5 cm (depending on region). (e) Inhale and exhale sagittal cuts through tumor (left/posterior mass in image) with reference line to indicate relative motion

9.11 Case Study

A case study of a 4D CT case is presented. The patient has a large lung tumor in the lower left lung. A free breathing helical scan was initially taken, followed by a 4D CT study. Figure 6a and b shows two axial scans from the 4D CT study; the image on the left is acquired at the moment of inhalation, on the right at the peak of exhale. The images are quite similar, although a subtraction image in Fig. 6c shows some differences at the periphery of the tumor as indicated by the dark/light areas around the tumor. Views in the coronal and sagittal planes for the inhale and exhale phases of respiration are shown in Fig. 6d,e respectively. In these planes, tumor and diaphragm motion is more evident, as seen relative to the cross/horizontal dotted guide line. Motion in the sagittal plane is approximately 1.7 cm between the inhale and exhale states through the displayed cut plane.

Figure 7a is a coronal plane through the free breathing scan taken at the same planning session; There is a small artifact at the right diaphragm/lung interface. Figure 7b shows the full view coronal cuts at inhale and exhale states. Examination of the images shows that as the free breathing helical scan is acquired, it most closely resembles the scan at exhale. Contouring the GTV on the free breathing scan and the application of symmetric margins would not be representative of the volume

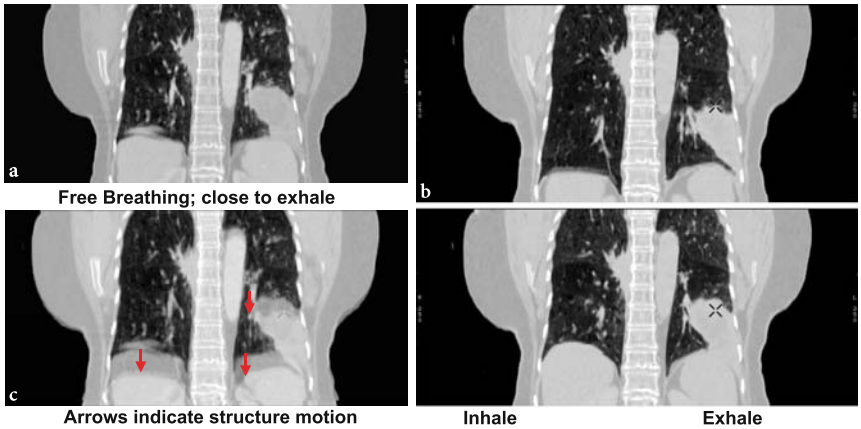

Fig. 7. (a) Free breathing coronal cut. (b) Inhale and exhale 4D CT coronal cuts through same plane. Inspection shows free breathing is quite similar in anatomy to exhale state. (c) Average image of a and inhale b. Non moving/minimally moving anatomy such as spinal column and external soft tissue contours in this plane are sharp. Significant movement of internal anatomy including left and right diaphragms and tumor are seen by the darker gray areas indicated with *red arrows*

swept out by the moving tumor over the entire respiratory cycle. Figure 7c displays the differences between free breathing and inhale anatomy. This image is the average image formed by adding Fig. 7a and Fig. 7b upper. The soft tissues of the breast, and the bony anatomy of the spinal column are in good congruence. Discrepancies in the soft tissues at the lung diaphragm and lung tumor interfaces are seen as darker gray areas. The differences in these regions are indicated by the red arrows, which measure to be about 2 cm, depending on where the distance is measured.

9.12 Summary

Four-dimensional CT is an imaging technique that provides information on organ motion during respiration. It provides a more accurate assessment of target shape and trajectory, and similar information on organs at risk. Technological advances in software and hardware for 4D simulation are likely to rapidly become available in the next few years. The ability to generate 3D CT maps of anatomy as a function of respiratory phase has important applications in treatment planning and delivery, including optimization in the presence of motion, aperture design, dose calculations to moving targets, and image guided therapy delivery.

Acknowledgements. The authors wish to acknowledge the contributions of members of the Department of Radiation Oncology at the Massachusetts General Hospital, including Christopher G. Willet, M.D. and Noah C. Choi, M.D., Karen Doppke, M.S., Jong H. Kung, Ph.D., Kevin Beaudette, M.S., Joann Pacella, RTT and Nancy Ditullio, RTT. Thanks also to Tinsu Pan, Ph.D., David Caumartin, MBA of General Electric Medical Systems, and Hassan Mostafavi, Ph.D. of Varian Medical Systems for their important work in the development of 4D CT.

References

1. Munzenrider JE, Pilepich M, Rene-Ferrero JB, Tchakarova I, Carter BL (1977) Use of body scanner in radiotherapy treatment planning. Cancer 40(1):170–179
2. Emami B, Melo A, Carter BL, Munzenrider JE, Piro AJ (1978) Value of computed tomography in radiotherapy of lung cancer. Am J Roentgenol 131(1):63–67
3. Goitein M (1982) Application of C. T. in radiotherapy treatment planning. In: Orton C (ed) Progress in medical radiation physics, vol 1. Plenum Press, NY, pp 195–293
4. Costello P (1994) Thoracic helical CT. Radiographics 14:913–918
5. Kasales C, Hopper K, Ariola D et al. (1995) Reconstructed helical CT scans: improvement in z-axis resolution compared with overlapped and nonoverlapped conventional CT scans. Am J Radiol 164:1281–1284
6. Hu H, He H, Foley W, Fox S (2000) Four multidector row helical CT: image quality and volume coverage speed. Radiology 215:55–62
7. ICRU50 (1993) Prescribing recording and reporting photon bream therapy. ICRU, Bethesda, MD
8. ICRU62 (1999) Prescribing, recording, and reporting photon beam therapy (supplement to ICRU Report 50). ICRU, Bethesda, MD
9. Langen K, Jones D (2001) Organ motion and its management. Int J Radiat Oncol Biol Phys 50:265–278
10. Booth J, Zavgorodni S (1999) Set-up error and organ motion uncertainty: a review. Austr Phys Eng Sci Med 22:29–47
11. Balter J, Ten Haken R, Lawrence T et al. (1996) Uncertainties in CT-based radiation therapy treatment planning associated with patient breathing. Int J Radiat Oncol Biol Phys 36:167–174
12. Balter J, Lam K et al. (1998) Improvement of CT-based treatment planning models of abdominal targets using static exhale imaging. Int J Radiat Oncol Biol Phys 41:939–943
13. Van Dyk J (ed) (1999) 4D CT extension of CT simulation. In: Modern technology of radiation oncology, chap 5. Medical Physics Publishing, Madison, Wisconsin, pp 131–168
14. Chen GT, Kung JH, Beaudette KP (2004) Artifacts in computed tomography scanning of moving objects. Semin Radiat Oncol 14(1):19–26
15. Shirato H, Seppenwoolde Y, Kitamura K, Onimura R, Shimizu S (2004) Intrafractional tumor motion: lung and liver. Semin Radiat Oncol 14(1):10–18
16. Shirato H, Harada T, Harabayashi T, Hida K, Endo H, Kitamura K, Onimaru R, Yamazaki K, Kurauchi N, Shimizu T, Shinohara N, Matsushita M, Dosaka-Akita H, Miyasaka K (2003) Feasibility of insertion/implantation of 2.0-mm-diameter gold internal fiducial markers for precise setup and real-time tumor tracking in radiotherapy. Int J Radiat Oncol Biol Phys 56(1):240–247
17. Kitamura K, Shirato H, Seppenwoolde Y, Shimizu T, Kodama Y, Endo H, Onimaru R, Oda M, Fujita K, Shimizu S, Miyasaka K (2003) Tumor location, cirrhosis, and surgical history contribute to tumor movement in the liver, as measured during stereotactic irradiation using a real-time tumor-tracking radiotherapy system. Int J Radiat Oncol Biol Phys 56(1):221–228
18. Harada T, Shirato H, Ogura S, Oizumi S, Yamazaki K, Shimizu S, Onimaru R, Miyasaka K, Nishimura M, Dosaka-Akita H (2002) Real-time tumor-tracking radiation therapy for lung carcinoma by the aid of insertion of a gold marker using bronchofiberscopy. Cancer 95(8):1720–1727
19. Gierga DP, Chen GT, Kung JH, Betke M, Lombardi J, Willett CG (2004) Quantification of respiration-induced abdominal tumor motion and its impact on IMRT dose distributions. Int J Radiat Oncol Biol Phys 58(5):1584–1595
20. Murphy MJ (2004) Tracking moving organs in real time. Semin Radiat Oncol 14(1):91–100
21. Wagman R, Yorke E, Ford E, Giraud P, Mageras G, Minsky B, Rosenzweig K. (2003) Respiratory gating for liver tumors: use in dose escalation. Int J Radiat Oncol Biol Phys 55(3):659–668
22. Ford E, Mageras G, Yorke E, Rosenzweig K, Wagman R, Ling C (2002) Evaluation of respiratory movement during gated radiotherapy using film and electronic portal imaging. Int J Radiat Oncol Biol Phys 52:522–531
23. Low D, Nystrom M, Kalinin E, Parikh P, Dempsey J, Bradley J, Mutic S, Wahab S, Islam T, Christensen G, Politte D, Whiting B (2003) A method for the reconstruction of four-dimensional

synchronized CT scans acquired during free breathing. Med Phys 30:1254–1263
24. Vedam S, Keall P, Kini V, Mohan R (2003) Acquiring a 4D CT data set using an external respiratory signal. Phys Med Biol 48:45–62
25. Ford E, Mageras G, Yorke E, Ling C (2003) Respiration-correlated spiral CT: a method of measuring respiratory-induced anatomic motion for radiation treatment planning. Med Phys 30(1):88–97
26. Pan T, Lee T (2003) Internal and external 4D respiratory gating on multi-slice CT images. Eur Cong Radiol 13:222
27. Pan T, Lee TY, Rietzel E, Chen GT (2004) 4D-CT imaging of a volume influenced by respiratory motion on multi-slice CT. Med Phys 31(2):333–340
28. Remy J, Remy-Jardin M, Artaud D, Fribourg M (1998) Multiplanar and 3 dimensional reconstruction techniques in CT: impact on chest diseases. Eur Radiol 8:335–351
29. Elvins TT (1998) Introduction to volume visualization: imaging multi-dimensional scientific data. SIGGRAPH 94
30. Lawler LP, Pannu HK, Corl FM, Fishman EK (2002) Multidetector row computed tomography with volume rendering – an aid to understanding pelvic anatomy and disease Curr Probl Diagn Radiol 31(6):230–243
31. Pelizzari SA, Grzeszczuk R, Chen GT, Heimann R, Haraf DJ, Vijayakumar S, Ryan MJ (1996) Volumetric visualization of anatomy for treatment planning. Int J Radiat Oncol Biol Phys 34(1):205–211
32. Lee JS, Jani AB, Pelizzari CA, Haraf DJ, Vokes EE, Weichselbaum RR, Chen GT (1999) Volumetric visualization of head and neck CT data for treatment planning. Int J Radiat Oncol Biol Phys 44(3):693–703
33. Jani AB, Pelizzari CA, Chen GT, Grzeszczuk RP (1998) Accuracy of object depiction and opacity transfer function optimization in CT volume-rendered images. J Comput Assist Tomogr 22(3):459–470
34. Bland PH, Meyer CR (1996) Robust three-dimensional object definition in CT and MRI. Med Phys 23(1):99–107
35. Gao L, Heath DG, Kuszyk BS, Fishman EK (1996) Automatic liver segmentation technique for three-dimensional visualization of CT data. Radiology 201(2):359–364
36. Mullally W, Rietzel E, Chen G, Choi N, Betke M (2004) Fast segmentation of pulmonary tumors by contour propagation in 4DCT (AAPM 2004). Med Phys 31(6):1846 (abstract)
37. Brock KK, Hollister SJ, Dawson LA, Balter JM (2002) Technical note: creating a four-dimensional model of the liver using finite element analysis. Med Phys 29(7):1403–1405
38. Liang J, Yana D (2003) Reducing uncertainties in volumetric image based deformable organ registration. Med Phys 30(8):2116–2122
39. Mackie TR, Kapatoes J, Ruchala K, Lu W, Wu C, Olivera G, Forrest L, Tome W, Welsh J, Jeraj R, Harari P, Reckwerdt P, Paliwal B, Ritter M, Keller H, Fowler J, Mehta M (2003) Image guidance for precise conformal radiotherapy. Int J Radiat Oncol Biol Phys 56(1):89–105
40. Rietzel E, Pan T, Chen GTY (2004) 4D CT: Image formation and clinical protocol. Med Phys 31(6):1778
41. Rietzel E, Chen GT, Doppke KP, Pan T, Choi NC, Willett CG (2003) 4D computed tomography for treatment planning. Int J Radiat Oncol Biol Phys57(Suppl2):S232–S233
42. Keall PJ, Starkschall G, Shukla H, Forster KM, Ortiz V, Stevens CW, Vedam SS, George R, Guerrero T, Mohan R (2004) Acquiring 4D thoracic CT scans using a multislice helical method. Phys Med Biol 49(10):2053–2067
43. http://www.itk.org/
44. http://www-ipg.umds.ac.uk/cisg/vtk-software/
45. Mageras G, Yorke E, Rosenzweig K, Braban L, Keatley E, Ford E, Leibel S, Ling C (2001) Fluoroscopic evaluation of diaphragmatic motion reduction with a respiratory gated radio-therapy system. J Appl Clin Med Phys 2(4):191–200
46. http://public.kitware.com/VTK/

4D Treatment Planning

Paul J. Keall

10

Contents

10.1 Introduction

Four-dimensional (4D) radiotherapy can be defined as the explicit inclusion of the temporal changes in anatomy during the imaging, planning and delivery of radiotherapy [1]. High precision radiation therapy of moving targets is becoming increasingly important in this era of image-guided therapy (see Bortfeld and Chen [2] and articles therein).

The anatomy and physiology of cancerous and healthy tissues change with time, both within and between treatments. For radiotherapy patients, the additional effects of radiation, potentially with concomitant chemotherapy and or/hormone therapy, can also cause anatomical changes during treatment. Though it is acknowledged that there are many sources of anatomical changes, for some sites, such as the lung, liver, pancreas, esophagus and possibly even breast, prostate and cervix, respiratory motion is a significant issue and negatively affects the imaging [3–15], planning [13, 16–19] and delivery [20–29] of radiation. Due to recent technological developments in both 4D imaging (refer to chapter II. 9) and 4D radiation delivery (refer to chapter II. 11), we are in an era in which respiratory motion can be explicitly accounted for. Reducing the deleterious effects of interfraction motion is discussed in the chapters II. 7 and II. 8.

The focus of this chapter is to discuss the process of creating a 4D plan from a 4D computed tomography (CT) image set, in which the radiation beam tracks the tumor motion during 4D radiotherapy delivery. By moving the radiation beam during treatment, the intensity is modulated. However, for the purpose of clarity, the distinction is made between 4D planning for beams in which the dynamic multileaf collimator (DMLC) motion only compensates for tumor motion (4D conformal radiotherapy) and planning for beams in which DMLC motion accounts for intensity modulation based on optimizing an objective function as well as compensating for tumor motion (4D IMRT). The rationale for 4D radiotherapy is to reduce geometric errors during imaging and treatment delivery, as well as to safely reduce the margins added for internal motion, which will spare healthy tissue and/or allow dose escalation.

There are methods to account for respiratory motion in the absence of devices that account for this motion during radiation treatment delivery. The one practiced most commonly in clinics is the simple addition of clinical target volume (CTV)-planning target volume (PTV) margins that are large enough to encompass the increased geometric uncertainties introduced by respiratory motion [16]. These increased margins result in a higher dose to normal tissue and particularly lung, for which treatment-related toxicity is strongly correlated with mean lung dose (or a similar surrogate, such as V_{20}) [30–35]. Thus, methods such as 4D radiotherapy, which can potentially reduce some of the geometric error, should result in lower treatment-related toxicity and/or tumor dose escalation.

In this chapter, some 4D treatment-planning examples are given. These plans use a 4D CT dataset acquired under an IRB-approved study at the M.D. Anderson Cancer Center [36] and the Pinnacle [3] treatment-planning system (Philips Medical Systems, Milpitas CA). The tumor is located in the upper lobe of the right lung. The center of mass of the tumor moved approximately 1 cm from exhale to inhale. The gross tumor volume (GTV)-CTV margin was 8 mm based on [37], and the CTV-PTV margin was 8 mm to account for setup error. All dose calculations shown use the collapsed cone convolution implementation of the superposition algorithm.

Throughout this chapter, it is assumed that the delivery device in motion to account for respiration is the DMLC. However, the device in motion could equally be a robotic linear accelerator [38] or the treatment couch.

10.2 4D Planning Procedure

A generalized flowchart for 4D treatment planning is shown in Fig. 1. The first step (1) of 4D treatment planning is to obtain a 4D CT scan, as described in the preceding chapter. The second step (2) is to define the anatomy for all structures of interest for dosimetric coverage (e.g. GTV, CTV) as well as the dosimetric avoidance/monitoring (e.g. spinal cord, lungs, heart, esophagus) on one of the 3D CT image sets constituting one respiratory phase of the 4D CT. The choice of which respiratory phase to use will generally be the exhale phase, as motion is less at exhale than at inhale, and the exhale position, being a passive rather than active state, is more reproducible between respiratory cycles than the inhale position.

Once the anatomy definition is complete on one 3D CT image set, deformable image registration (explained in further detail below) can be used to create automatically the anatomic structures on the other respiratory phases of the 4D CT, accounting for the movement and deformation on each structure caused by the respiratory cycle. The deformable image registration process may introduce an error that may require additional geometric margins.

Step (3) of the 4D planning process is to create a treatment plan on one of the 3D CT image sets. This treatment plan will be developed as the conventional conformal or IMRT plan, though the geometric CTV-PTV margins for respiratory motion may be reduced. However, as explained in a separate section below, other geometric uncertainties introduced by the planning process will require additional margins. Once the plan is complete for one image set, automated planning is used to reproduce the treatment plans on the other respiratory phases of the 4D CT, accounting for the changing anatomy by varying the multileaf collimator (MLC) positions. Because the MLC is being used to account for the change in the PTV with respiration, the concept of a 4D PTV is naturally introduced.

In step (4) of Fig. 1, the dose distributions are summed up through the deformable registration operator (weighted by the fraction of time spent in each respiratory phase), and the composite plan is displayed

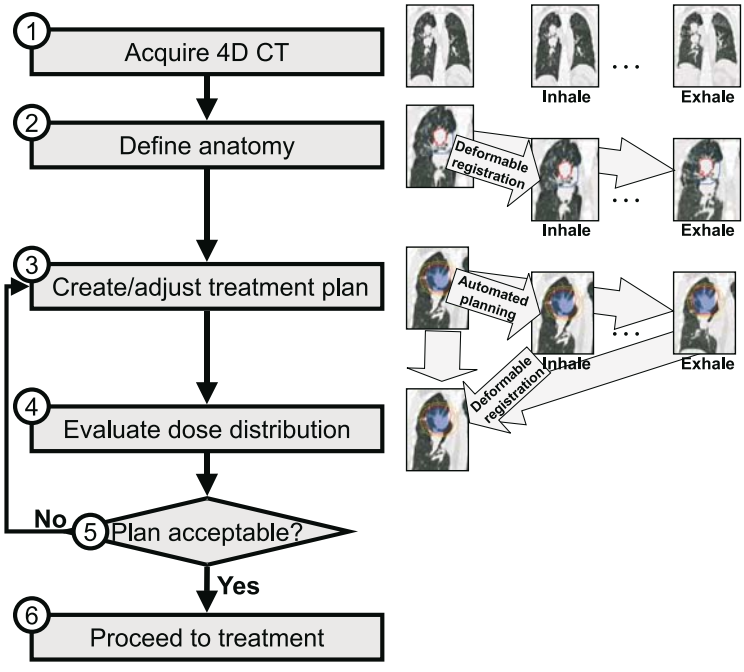

Fig. 1. A schematic showing the general 4D planning process for both conformal and intensity modulated radiation therapy (IMRT) delivery

for evaluation. Should this plan prove unacceptable, adjustments need to be made, and steps 3–5 are repeated.

10.3 The Need for Automation in 4D Planning

In Fig. 1, steps (1) to (6) are those typically performed for routine conformal or IMRT planning, except that a 3D CT scan is used as input rather than a 4D CT scan. Note that the extra procedures used to create and analyze the 4D plan on the ten or so CT image sets (totaling up to 1500 individual CT images) are automated. This automation consists of three tools: deformable image registration, automated planning and dose calculation on multiple CT image sets.

There are both logistical and fundamental reasons for using automated tools. The logistical reason is that performing all of the planning tasks manually on ten or more CT image sets would take an order of magnitude more human interaction time, which is clearly not feasible in any but the most well-staffed institutions. The fundamental reason is that to estimate the cumulative dose for the 4D plan, the dose to the moving tissues in each of the plans for each respiratory phase needs to be added. This requires an estimation of the motion for each CT voxel in each image for each respiratory phase, a process of such magnitude that automation is necessary.

10.3.1 Tools for Automation 1: Deformable Image Registration

Deformable image registration is a tool used to map each voxel from one CT image set to the new position of that voxel in the second image set, accommodating the anatomic deformation caused by respiration. Let Ω be the coordinate space of a CT image. A time index transformation, $h(x,t)$: $\Omega^t \rightarrow \Omega$, mapping the coordinate space of each of the respiratory phases of the 4D CT is estimated. There are several candidate algorithms to determine $h(x,t)$, including finite element methods, optical flow techniques and large deformation diffeomorphic image registration. It is unclear which algorithm(s) will prove to be the most accurate and generally applicable to the 4D radiotherapy planning problem.

Since the contoured structures are a subset of the volume on which the deformable registration transformations were calculated, the contoured structures can be automatically created in other CT phases by applying the appropriate transformation, as shown in step (2) of Fig. 1. Similarly, after the treatment plans have been created, the dose distributions can also be mapped between CT phases, enabling the evaluation of the composite 4D plan, as shown in steps (3) and (4) of Fig. 1.

Using these transformations, the combined or 4D dose distribution, D_{4D}, can be given by

$$D_{4D}(\boldsymbol{x}) = \sum_i w_i D_i \left(\boldsymbol{h}_i(\boldsymbol{x})\right) \quad (1)$$

where w_i is the weight of the dose distribution D_i for each of the constituent respiratory phase CT image sets. The w_i values correspond with the fraction of a breathing cycle spent in each respiratory phase.

10.3.2 Tools for Automation 2: Automated Planning

Rather than performing treatment planning on ten or so CT scans, scripts can be written to automate planning in order to transfer a plan generated at one CT phase to plans generated in other CT phases. For example, for 4D conformal planning, the beam parameters stipulated on the manually planned respiratory phase can be automatically generated on the other phases using the automatic blocking function so that the MLC conforms to the PTV for each phase and adds a margin for the penumbra. As a note of caution for this method, in some phases the beams may pass through critical serial structures such as cord and esophagus, and, in other phases, the beams may not pass through these structures. Careful assessment of the composite plan [step (4) in Fig. 1] and making appropriate adjustments are required.

10.3.3 Tools for Automation 3: Dose Calculation on Multiple CT Image Sets

Tied closely to automated planning is the ability to calculate dose on multiple CT scans within the same treatment plan. This task is mentioned explicitly here, because at the time of writing commercial treatment-planning systems do not offer this option. Dose calculation on multiple image sets is clearly important, since motion moves the anatomy and, therefore, changes the pattern of radiation interaction within the patient. The expanded lung at inhale affects the radiation dose deposition in two competing ways. First, the radiological pathlength within the patient is reduced, causing higher primary photon fluence to be expected at the same physical depth. Second, the reduced lung density increases the range of the secondary electrons, thereby increasing the electronic disequilibrium and widening the penumbra.

An example of the importance of dose calculation is given in Fig. 2, where the same structures (PTV, esophagus and lungs) are calculated for the same IMRT treatment plan, with the only variable being the CT image set on which the dose was calculated. Though in this case the DVHs for the lungs and esophagus are similar in both cases, the PTV dose calculated on the inhale CT

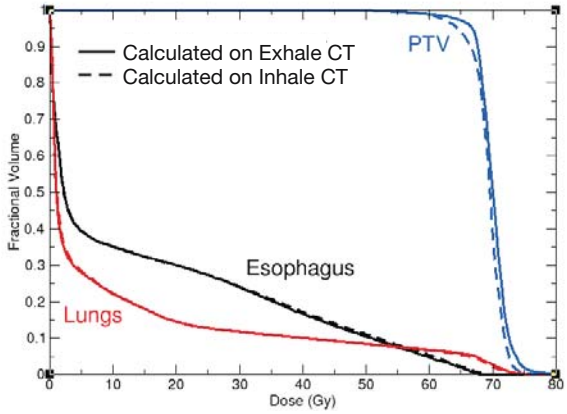

Fig. 2. Intensity modulated radiation therapy (IMRT) dose-volume histograms (DVHs) of the exhale planning target volume (PTV), lungs and esophagus calculated on the exhale and inhale CT of the same patient

scan shows a consistent underdose, particularly where IMRT prescriptions are often given, near D_{95}.

10.3.4 Addition Tools Required for 4D Planning

Four-dimensional planning introduces several issues for networking, data storage and communications. Typically, an order of magnitude more data are used for 4D planning, and data management tools need to developed to ensure these data are appropriately stored and communicated to the treatment-delivery device. At the time of writing, DICOM-RT did not support 4D radiotherapy.

10.4 4D Conformal Radiotherapy Planning

As mentioned above, the flowchart in Fig. 1 is generic to both 4D conformal radiotherapy planning and 4D IMRT, the differences being in the processes of step (3) of Fig. 1. Tumor motion is predominantly along one axis (and observed to be primarily in the superior–inferior direction [39–43]). Thus, the MLC should be aligned such that the leaf motion coincides with the major axis of the tumor motion and compensates for the tumor motion. In principal, it is possible to account for motion perpendicular to the leaf motion direction. This may be easier for 4D conformal radiotherapy than 4D IMRT, unless the leaves are synchronized.

Using one of the constituent CT sets, corresponding with a single respiratory phase from the 4D CT, a conformal treatment plan is constructed based on the anatomy drawn in that phase. Typically, the inhale or exhale phase will be used for this step. Beam angles, weights, energies and modifiers should be chosen to achieve an acceptable plan in terms of PTV coverage and critical structure doses. The plan may consist

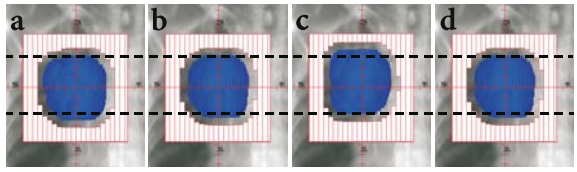

Fig. 3a–d. Four-dimensional conformal anterior beam-view images for respiratory phases: (a) inhale; (b) mid-exhale; (c) exhale; (d) mid-inhale. The planning target volume (PTV) for each phase is conformally blocked by the dynamic multileaf collimator (DMLC) with a margin for the penumbra (0.8 cm in this case). To aid comparison, *horizontal lines* are drawn at the superior edge of the PTV at inhale and the inferior PTV edge at exhale

of several stages typically used for lung cancer radiotherapy, such as anterior-posterior beams to spinal cord tolerance, followed by oblique fields. Once an acceptable plan is created for a single phase, automated planning is used to recreate the treatment plan on the other respiratory phase CT image sets, with the beams adapting to the changing PTV shape and position in the beam view, allowing for the appropriate penumbral margins. Examples of beam-view images from 4D conformal planning are given in Fig. 3. Note that the motion of the PTV is, in this case, predominantly superior-inferior, and the alignment of the collimator is in this dimension also.

Due to changes in both the anatomy and the beam geometry during each respiratory phase, the overall PTV dose in each phase will be different. However for critical structures, the variation in dose is expected to be larger, as differing fractions of the beam aperture will intersect with the different critical structures. Example 4D conformal radiotherapy dose-volume histograms (DVHs) for each constituent breathing phase and for the combined dose distribution (obtained by summing the constituent dose distributions via deformable operators) are given in Fig. 4 for the PTV, lungs, cord and heart (reproduced from [44]). The DVHs for the PTV at all phases and the combined (4D) DVH are all very similar (note the expanded x-axis scale). The lung DVHs are closely bunched, with the combined 4D DVH being closer to the end-inhale DVH due to the fact that DVHs typically use normalized rather than absolute volumes. The 4D DVHs for the cord and heart appear to be near the middle of the constituent-phase DVHs. The variation in cord and heart DVHs for the constituent phases is due to the change in beam aperture with respiratory phase and, hence, the fraction of the organ intersecting the beam passing through these structures, as the PTV deforms with respiratory phase.

10.5 4D IMRT Planning

There are many levels of complexity for 4D IMRT. The simplest assumption, that the target undergoes rigid

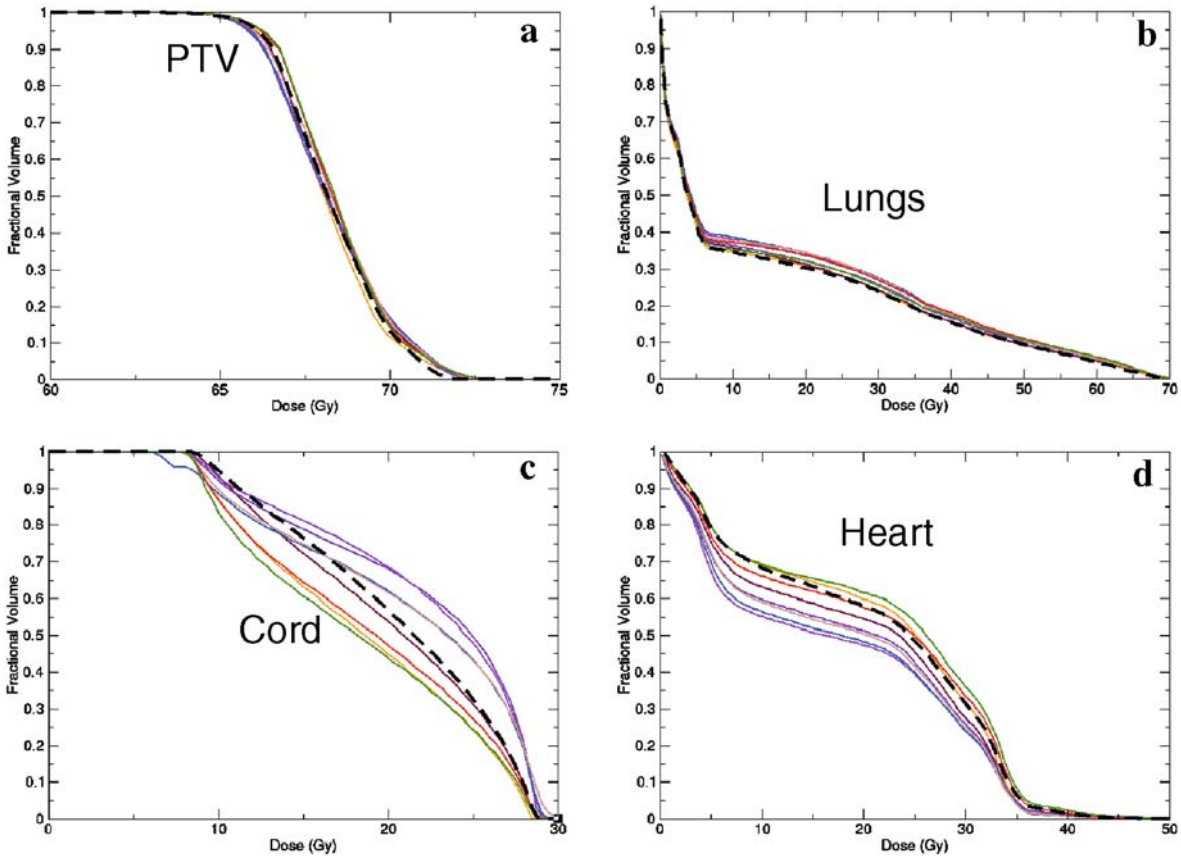

Fig. 4a–d. Four-dimensional conformal radiotherapy dose-volume histograms (DVHs) for each breathing phase (*thin solid lines*) and the combined distribution (*thick dashed line*) for the: (a) planning target volume (PTV); (b) lungs; (c) cord; (d) heart. Note the expanded dose scale for the PTV. Reprinted from [44]

body motion without deformation, is the easiest to plan and implement; however, more sophisticated models of motion including deformation will allow even greater conformality. DVHs of the PTV, lungs and esophagus for an IMRT plan optimized on the inhale CT scan and the corresponding plan at exhale, calculated assuming rigid body PTV motion, are shown in Fig. 5. This figure shows that, for this particular example, the rigid body assumption gave a uniform PTV dose; however, the dose to the lungs and esophagus was higher in the exhale phase plan in which the anatomical variations were ignored.

An example comparison of the rigid body motion assumption with a full replanned IMRT optimization in the exhale phase is shown in Fig. 6. This figure shows some benefit in the reoptimized plan, where the PTV dose is more homogeneous and a lower maximum esophageal dose is obtained, than with the plan calculated assuming rigid body motion based on the inhale IMRT plan.

Four-dimensional segmental MLC IMRT planning is a generalization of 4D conformal planning, in that if the same, or similar, segment shapes (but different positional projections) are used in the 4D IMRT plan, the 4D SMLC IMRT is an extension of the 4D conformal planning process with many apertures per beam as opposed to one. Segmental IMRT planning will be less affected by leaf velocity constraints than dynamic delivery.

Breathing will change between imaging session and delivery, thus we cannot rely on the knowledge of the patient's breathing pattern a priori on any given day of treatment (if so, 4D radiotherapy would be feasible with circa 2000 technology). Accounting for these changes can be incorporated by first improving respiration reproducibility with breathing training tools [45,46] and, second, by being flexible enough during delivery to account for deviations and, ultimately, recording the deviations from the planned treatment and reporting what was actually delivered.

For both 4D conformal planning and 4D IMRT, it is important that tumor motion tracking is within the mechanical capabilities of the DMLC. The mechanical capabilities (maximum velocity, acceleration and deceleration) should be known constraints within the planning process. This DMLC does not need to track the tumor for the entire respiratory cycle, as a beam hold can account for short time periods during which tumor motion exceeds the DMLC capabilities; however,

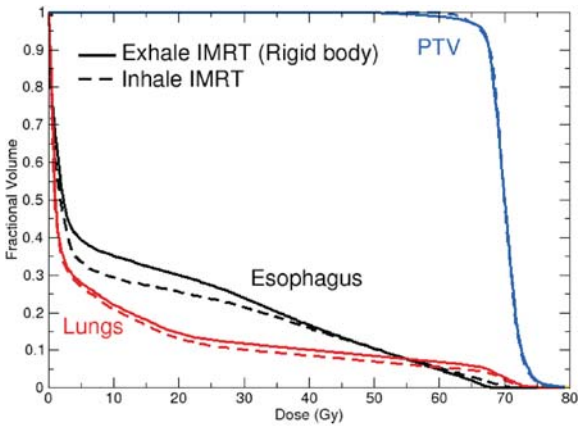

Fig. 5. Dose-volume histograms (DVHs) of the planning target volume (PTV), lungs and esophagus for an intensity modulated radiation therapy (IMRT) plan optimized on the inhale CT scan, and the corresponding plan at exhale calculated assuming rigid body PTV motion. The *solid lines* are for the IMRT plan and anatomy drawn on the exhale CT scan, and the *dashed lines* are for the IMRT plan and anatomy drawn on the inhale CT scan

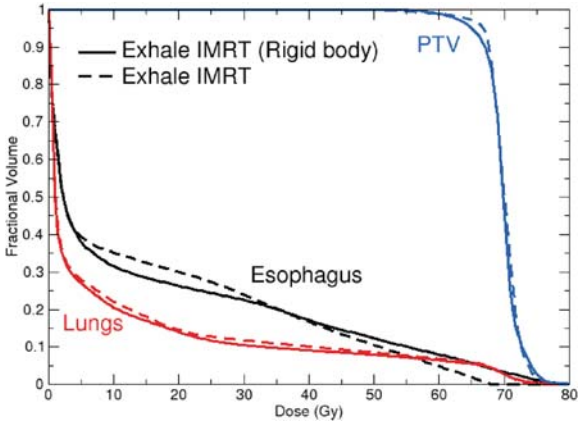

Fig. 6. Dose-volume histograms (DVHs) of the exhale planning target volume (PTV), lungs and esophagus for an intensity modulated radiation therapy (IMRT) plan optimized on the inhale CT scan, and the corresponding plan at exhale calculated assuming rigid body PTV motion. The *solid lines* are for the IMRT plan calculated assuming rigid body PTV motion from the inhale IMRT plan, and the *dashed lines* are for the IMRT plan optimized on the exhale CT scan

this should be satisfied for a significant fraction of the motion cycle to ensure efficient delivery.

10.6 Margins for 4D Planning

One of the reasons for performing 4D radiotherapy is to reduce the margins required for geometric uncertainties introduced by respiratory motion. However, during the act of accounting for respiratory motion, new geometric uncertainties are introduced.

First, the 4D CT used as input to the planning process is temporally discrete, typically separated into 8–15 individual respiratory phases. This discretization of the continuous temporal changes means that interpolation of the motion between these phases is necessary. The accuracy of this interpolation is unknown. Furthermore, the 4D CT may contain artifacts due to irregular respiration during acquisition. Second, the deformable image registration algorithm used will contain geometric errors due to limitations of either the algorithm or the artifacts in the input 4D CT data.

The correlation between the respiratory signal and the tumor motion may change with time, both between breathing cycles and between successive treatments. This variation in correlation will translate into a targeting error. If the respiratory signal is external – for example, a strain gauge, spirometer or optical signal – the relationship between the respiration signal and internal motion can be determined using a 4D CT scan, and this relationship can be checked and adjusted if necessary during the treatment course. The use of external respiration signals will not reduce the set-up error, typically 3–5 mm (1 standard deviation) for lung cancer radiotherapy [47–54], which, along with respiratory motion is a significant issue. The use of internal markers for tumor tracking [7, 10, 55–57] reduces both the set-up error and the error in the actual tumor motion/tumor motion surrogate correlation. Thus the choice of respiratory signal or tumor motion surrogate will have an impact on the margins used for 4D radiotherapy.

Finally, an additional geometric error is added during radiation delivery from the finite time delay in the DMLC response due to the acquisition of the respiratory motion, the processing of this motion, the creation of leaf-position instructions and the execution of these instructions. These time delays require future prediction of the tumor position, which for respiratory motion has proved challenging [27, 58, 59]. This error will decrease as the system response time decreases and also as improved prediction algorithms are developed.

The careful analysis of each of these errors should be performed before the clinical implementation of 4D radiotherapy to ensure that the appropriate margins are applied and indeed that the net of the geometric uncertainties introduced by 4D radiotherapy are significantly less than those required for more traditional methods.

10.7 Delivery of a 4D Treatment Plan

The output of a planning process is a series of instructions to the linear accelerator and therapy staff to ensure the correct execution of the treatment plan. Thus, the plan needs to incorporate the constraints of the treatment device and particularly those of the DMLC; otherwise, the plan may not be able to be delivered.

For conventional IMRT to a target assumed to be static during radiation delivery, the maximum leaf velocity is a constraint used in the leaf-sequencing process [60–62] if dynamic MLC delivery rather than segmental MLC delivery is used. However, for 4D conformal or IMRT planning for a target moving during radiation delivery, the ability of the MLC to respond to the temporal position changes requires knowledge of both the velocity limitations and also the acceleration limitations, since the MLC needs to be able to respond to changes in target velocity. An additional beam-hold function will be required in cases where the DMLC mechanically cannot reproduce the target motion. Initial developments of leaf sequences have been published [21, 63, 64], though further advancements in this area will be required, particularly due to the variations in respiration patterns observed on a cycle-to-cycle and day-to-day basis.

Varying breathing patterns during delivery, compared with those measured during the 4D CT imaging session used for treatment planning, mean that the planned and delivered doses may differ. For example, if the time spent within each breathing phase during treatment delivery, w_d, differs from that during planning where fraction w_i was used for the final dose calculation, the combined 4D dose will change following Eq. 1. However, using Eq. 1 with w_d means that the actual dose delivered to the moving tumor and critical structures for each treatment fraction can be calculated. A problem appears if the respiration pattern limits during delivery exceed those obtained during the 4D CT session used for planning. Should such a situation occur, either the treatment should be paused until the respiration pattern returns within the limits known from planning (the prudent approach) or until a reasonable extrapolation of the tumor position and shape based on the respiratory signal can be made.

10.8 Conclusion

Four-dimensional treatment planning is a new process and set of tools that allows the optimal use of 4D CT data and dynamic radiation delivery. The ability to account explicitly for respiratory motion means the potential to safely reduce margins, thus allowing increased tumor dose and/or a decrease in treatment-related toxicity for sites affected by respiratory motion.

Four-dimensional radiotherapy is synergistic with adaptive radiotherapy (refer to chapters II. 7 and II. 8) in that some tools developed to account for interfraction geometric variations can be applied to account for intrafraction geometric variations and vice versa. Four-dimensional planning is also appealing for Monte Carlo calculations [65], since, for a given statistical uncertainty, the number of particles (and hence calculation time) required for summed 4D dose distributions (see Eq. 1) is approximately the same as that for a 3D distribution, meaning a speed gain of $\sim N$ for Monte Carlo compared with conventional algorithms, where N is the number of constituent respiratory phases in the 4D CT image set.

Four-dimensional planning is developing, along with 4D imaging and 4D radiation delivery. The tools and algorithms used for 4D radiotherapy have yet to be fully defined. Though all of these technologies are in their infancy, it is envisaged that 4D radiotherapy will become an established clinical tool in this new era of IMRT, image-guided radiotherapy and adaptive radiotherapy.

Acknowledgements. The author wishes to acknowledge the grant support of NIH/NCI R01 CA93626. Devon Murphy carefully reviewed and significantly improved the clarity of the text. Drs. Theodore Chung, Vaughn Dill, Rohini George, Sarang Joshi, Vijay Kini, Radhe Mohan, Jeffrey Siebers, Sastry Vedam, Krishni Wijesooriya, and Jeffrey Williamson have all significantly contributed to the 4D planning project at Virginia Commonwealth University.

References

1. Keall PJ, Chen GTY, Joshi S, Mackie TR, Stevens CW (2003) Time – the fourth dimension in radiotherapy (ASTRO Panel Discussion). Int J Radiat Oncol Biol Phys 57(Suppl.2):S8–S9
2. Bortfeld T, Chen GT (2004) Introduction: intrafractional organ motion and its management. Semin Radiat Oncol 14(1):1
3. Mayo JR, Müller NL, Henkelman RM (1987) The double-fissure sign: a motion artifact on thin-section CT scans. Radiology 165:580–581
4. Ritchie CJ, Hseih J, Gard MF, Godwin JD, Kim Y, Crawford CR (1994) Predictive respiratory gating: a new method to reduce motion artifacts on CT scans. Radiology 190(3):847–852
5. Shepp LA, Hilal SK, Schulz RA (1979) The tuning fork artifact in computerized tomography. Comput Graph Image Proc 10:246–255
6. Tarver RD, Conces DJ, Godwin JD (1988) Motion artifacts on CT simulate bronchiectasis. Am J Roentgenol 151(6):1117–1119
7. Shimizu S, Shirato H, Ogura S, Akita-Dosaka H, Kitamura K, Nishioka T, Kagei K, Nishimura M, Miyasaka K (2001) Detection of lung tumor movement in real-time tumor-tracking radiotherapy. Int J Radiat Oncol Biol Phys 51(2):304–310
8. Keall PJ, Kini VR, Vedam SS, Mohan R (2002) Potential radiotherapy improvements with respiratory gating. Australas Phys Eng Sci Med 25(1):1–6
9. Ritchie CJ, Godwin JD, Crawford CR, Stanford W, Anno H, Kim Y (1992) Minimum scan speeds for suppresion of motion artifacts in CT. Radiology 185:37–42
10. Shimizu S, Shirato H, Kagei K, Nishioka T, Bo X, Dosaka-Akita H, Hashimoto S, Aoyama H, Tsuchiya K, Miyasaka K (2000) Impact of respiratory movement on the computed tomographic images of small lung tumors in three-dimensional (3D) radiotherapy. Int J Radiat Oncol Biol Phys 46(5):1127–1133

11. Vedam SS, Keall PJ, Kini VR, Mostafavi H, Shukla HP, Mohan R (2003) Acquiring a four-dimensional computed tomography dataset using an external respiratory signal. Phys Med Biol 48(1):45–62
12. Ford EC, Mageras GS, Yorke E, Ling CC (2003) Respiration-correlated spiral CT: a method of measuring respiratory-induced anatomic motion for radiation treatment planning. Med Phys 30(1):88–97
13. van Herk M, Remeijer P, Rasch C, Lebesque JV (2000) The probability of correct target dosage: dose-population histograms for deriving treatment margins in radiotherapy. Int J Radiat Oncol Biol Phys 47(4):1121–1135
14. Balter JM, Ten Haken RK, Lawrence TS, Lam KL, Robertson JM (1996) Uncertainties in CT-based radiation therapy treatment planning associated with patient breathing. Int J Radiat Oncol Biol Phys 36(1):167–174
15. Chen GT, Kung JH, Beaudette KP (2004) Artifacts in computed tomography scanning of moving objects. Semin Radiat Oncol 14(1):19–26
16. ICRU (1999) Prescribing, recording and reporting photon beam therapy. ICRU Report 62 (supplement to ICRU Report 50). International Commission on Radiation Units and Measurements, Bethesda, MD
17. Chetty IJ, Rosu M, Tyagi N, Marsh LH, McShan DL, Balter JM, Fraass BA, Ten Haken RK (2003) A fluence convolution method to account for respiratory motion in three-dimensional dose calculations of the liver: a Monte Carlo study. Med Phys 30(7):1776–1780
18. Van Herk M (2004) Errors and margins in radiotherapy. Semin Radiat Oncol 14(1):52–64
19. Keall P (2004) 4-Dimensional computed tomography imaging and treatment planning. Semin Radiat Oncol 14(1):81–90
20. Yu CX, Jaffray DA, Wong JW (1998) The effects of intra-fraction organ motion on the delivery of dynamic intensity modulation. Phys Med Biol 43(1):91–104
21. Keall PJ, Kini V, Vedam SS, Mohan R (2001) Motion adaptive X-ray therapy: a feasibility study. Phys Med Biol 46(1):1–10
22. Jiang SB, Pope C, Al Jarrah KM, Kung JH, Bortfeld T, Chen GT (2003) An experimental investigation on intra-fractional organ motion effects in lung IMRT treatments. Phys Med Biol 48(12):1773–1784
23. Bortfeld T, Jokivarsi K, Goitein M, Kung J, Jiang SB (2002) Effects of intra-fraction motion on IMRT dose delivery: statistical analysis and simulation. Phys Med Biol 47(13):2203–2220
24. Chui CS, Yorke E, Hong L (2003) The effects of intra-fraction organ motion on the delivery of intensity-modulated field with a multileaf collimator. Med Phys 30(7):1736–1746
25. George R, Keall PJ, Kini VR, Vedam SS, Siebers JV, Wu Q, Lauterbach MH, Arthur DW, Mohan R (2003) Quantifying the effect of intrafraction motion during breast IMRT planning and dose delivery. Med Phys 30(4):552–562
26. Kung JH, Zygmanski P, Choi N, Chen GT (2003) A method of calculating a lung clinical target volume DVH for IMRT with intrafractional motion. Med Phys 30(6):1103–1109
27. Murphy MJ (2004) Tracking moving organs in real time. Semin Radiat Oncol 14(1):91–100
28. Shirato H, Seppenwoolde Y, Kitamura K, Onimura R, Shimizu S (2004) Intrafractional tumor motion: lung and liver. Semin Radiat Oncol 14(1):10–18
29. Bortfeld T, Jiang SB, Rietzel E (2004) Effects of motion on the total dose distribution. Semin Radiat Oncol 14(1):41–51
30. Kwa SL, Lebesque JV, Theuws JC, Marks LB, Munley MT, Bentel G, Oetzel D, Spahn U, Graham MV, Drzymala RE, Purdy JA, Lichter AS, Martel MK, Ten Haken RK (1998) Radiation pneumonitis as a function of mean lung dose: an analysis of pooled data of 540 patients. Int J Radiat Oncol Biol Phys 42(1):1–9
31. Graham MV, Purdy JA, Emami B, Harms W, Bosch W, Lockett MA, Perez CA (1999) Clinical dose-volume histogram analysis for pneumonitis after 3D treatment for non-small cell lung cancer (NSCLC). Int J Radiat Oncol Biol Phys 45(2):323–329
32. Hernando ML, Marks LB, Bentel GC, Zhou SM, Hollis D, Das SK, Fan M, Munley MT, Shafman TD, Anscher MS, Lind PA (2001) Radiation-induced pulmonary toxicity: a dose-volume histogram analysis in 201 patients with lung cancer. Int J Radiat Oncol Biol Phys 51(3):650–659
33. Oetzel D, Schraube P, Hensley F, Sroka- Perez G, Menke M, Flentje M (1995) Estimation of pneumonitis risk in three-dimensional treatment planning using dose-volume histogram analysis. Int J Radiat Oncol Biol Phys 33(2):455–460
34. Seppenwoolde Y, Lebesque JV, de Jaeger K, Belderbos JS, Boersma LJ, Schilstra C, Henning GT, Hayman JA, Martel MK, Ten Haken RK (2003) Comparing different NTCP models that predict the incidence of radiation pneumonitis. Int J Radiat Oncol Biol Phys 55(3):724–735
35. Yorke ED, Jackson A, Rosenzweig KE, Merrick SA, Gabrys D, Venkatraman ES, Burman CM, Leibel SA, Ling CC (2002) Dose-volume factors contributing to the incidence of radiation pneumonitis in non-small-cell lung cancer patients treated with three-dimensional conformal radiation therapy. Int J Radiat Oncol Biol Phys 54(2):329–339
36. Keall PJ, Starkschall G, Shukla H, Forster KM, Ortiz V, Stevens CW, Vedam SS, George R, Guerrero T, Mohan R (2004) Acquiring 4D thoracic CT scans using a multislice helical method. Phys Med Biol 49:2053–2067
37. Giraud P, Antoine M, Larrouy A, Milleron B, Callard P, De Rycke Y, Carette MF, Rosenwald JC, Cosset JM, Housset M, Touboul E (2000) Evaluation of microscopic tumor extension in non-small-cell lung cancer for three-dimensional conformal radiotherapy planning. Int J Radiat Oncol Biol Phys 48(4):1015–1024
38. Adler JR Jr, Murphy MJ, Chang SD, Hancock SL (1999) Image-guided robotic radiosurgery. Neurosurgery 44(6):1299–1306; discussion 306–307
39. Grills IS, Yan D, Martinez AA, Vicini FA, Wong JW, Kestin LL (2003) Potential for reduced toxicity and dose escalation in the treatment of inoperable non-small-cell lung cancer: a comparison of intensity-modulated radiation therapy (IMRT), 3D conformal radiation, and elective nodal irradiation. Int J Radiat Oncol Biol Phys 57(3):875–890
40. Korin HW, Ehman RL, Riederer SJ, Felmlee JP, Grimm RC (1992) Respiratory kinematics of the upper abdominal organs: a quantitative study. Magn Reson Med 23(1):172–178
41. Ross CS, Hussey DH, Pennington EC, Stanford W, Doornbos JF (1990) Analysis of movement of intrathoracic neoplasms using ultrafast computerized tomography. Int J Radiat Oncol Biol Phys 18(3):671–677
42. Seppenwoolde Y, Shirato H, Kitamura K, Shimizu S, van Herk M, Lebesque JV, Miyasaka K (2002) Precise and real-time measurement of 3D tumor motion in lung due to breathing and heartbeat, measured during radiotherapy. Int J Radiat Oncol Biol Phys 53(4):822– 834
43. Sixel KE, Ruschin M, Tirona R, Cheung PC (2003) Digital fluoroscopy to quantify lung tumor motion: potential for patient-specific planning target volumes. Int J Radiat Oncol Biol Phys 57(3):717–723
44. Keall PJ, Joshi S, Vedam SS, Siebers JV, Kini VR, Mohan R (2005) Four-dimensional radiotherapy planning for DMLC-based respiratory motion tracking. Med Phys 32:942

45. Kini VR, Vedam SS, Keall PJ, Patil S, Chen C, Mohan R (2003) Patient training in respiratory-gated radiotherapy. Med Dosim 28(1):7–11
46. Vedam SS, Kini VR, Keall PJ, Ramakrishnan V, Mostafavi H, Mohan R (2003) Quantifying the predictability of diaphragm motion during respiration with a noninvasive external marker. Med Phys 30(4):505–513
47. Bowden P, Fisher R, MacManus M, Wirth A, Duchesne G, Millward M, McKenzie A, Andrews J, Ball D (2002) Measurement of lung tumor volumes using three-dimensional computer planning software. Int J Radiat Oncol Biol Phys 53(3):566–573
48. Rodrigus P, Van den Weyngaert D, Van den Bogaert W (1987) The value of treatment portal films in radiotherapy for bronchial carcinoma. Radiother Oncol 9(1):27–31
49. Booth JT, Zavgorodni SF (1999) Set-up error & organ motion uncertainty: a review. Australas Phys Eng Sci Med 22(2):29–47
50. Ekberg L, Holmberg O, Wittgren L, Bjelkengren G, Landberg T (1998) What margins should be added to the clinical target volume in radiotherapy treatment planning for lung cancer? Radiother Oncol 48:71–77
51. Engelsman M, Damen EM, De Jaeger K, van Ingen KM, Mijnheer BJ (2001) The effect of breathing and set-up errors on the cumulative dose to a lung tumor. Radiother Oncol 60(1):95–105
52. Essapen S, Knowles C, Norman A, Tait D (2002) Accuracy of set-up of thoracic radiotherapy: prospective analysis of 24 patients treated with radiotherapy for lung cancer. Br J Radiol 75(890):162–169
53. Halperin R, Roa W, Field M, Hanson J, Murray B (1999) Setup reproducibility in radiation therapy for lung cancer: a comparison between T-bar and expanded foam immobilization devices. Int J Radiat Oncol Biol Phys 43(1):211–216
54. Hurkmans CW, Remeijer P, Lebesque JV, Mijnheer BJ (2001) Set-up verification using portal imaging; review of current clinical practice. Radiother Oncol 58(2):105–120
55. Schweikard A, Glosser G, Bodduluri M, Murphy MJ, Adler JR (2000) Robotic motion compensation for respiratory movement during radiosurgery. Comput Aided Surg 5(4):263–277
56. Shirato H, Shimizu S, Shimizu T, Nishioka T, Miyasaka K (1999) Real-time tumour-tracking radiotherapy. Lancet 353(9161):1331–1332
57. Shirato H, Shimizu S, Kunieda T, Kitamura K, van Herk M, Kagei K, Nishioka T, Hashimoto S, Fujita K, Aoyama H, Tsuchiya K, Kudo K, Miyasaka K (2000) Physical aspects of a real-time tumor-tracking system for gated radiotherapy. Int J Radiat Oncol Biol Phys 48(4):1187–1195
58. Vedam SS, Keall PJ, Todor DA, Docef A, Kini VR, Mohan R (2004) Predicting respiratory motion for four-dimensional radiotherapy. Med Phys 31:2274
59. Sharp GC, Jiang SB, Shimizu S, Shirato H (2004) Prediction of respiratory tumour motion for real-time image-guided radiotherapy. Phys Med Biol 49(3):425–440
60. LoSasso T, Chui CS, Ling CC (1998) Physical and dosimetric aspects of a multileaf collimation system used in the dynamic mode for implementing intensity modulated radiotherapy. Med Phys 25(10):1919–1927
61. Chui CS, Spirou S, LoSasso T (1996) Testing of dynamic multileaf collimation. Med Phys 23(5):635–641
62. Litzenberg DW, Moran JM, Fraass BA (2002) Incorporation of realistic delivery limitations into dynamic MLC treatment delivery. Med Phys 29(5):810–820
63. Papiez L (2003) The leaf sweep algorithm for an immobile and moving target as an optimal control problem in radiotherapy delivery. Math Comput Modelling 37:735–745
64. Neicu T, Shirato H, Seppenwoolde Y, Jiang SB (2003) Synchronized moving aperture radiation therapy (SMART): average tumour trajectory for lung patients. Phys Med Biol 48(5):587–598
65. Keall PJ, Siebers JV, Joshi S, Mohan R (2004) Monte Carlo as a four-dimensional radiotherapy treatment planning tool to account for respiratory motion. Phys Med Biol 49(16):3639–3648

"4D" IMRT Delivery

Gig S. Mageras, Ellen Yorke, Steve B. Jiang

11

Contents

11.1 Introduction

Increased interest in interventional strategies for managing respiratory motion in radiation treatments in recent years has been prompted by several factors. First, there has been limited ability to control tumors in the thorax and abdomen with standard radiotherapy techniques. Second, anatomical movement with respiration, at least in some circumstances, limits the accuracy with which radiation can be delivered to tumor-bearing tissue. The resultant larger treatment volumes required to accommodate target mobility may limit the tumoricidal dose, owing to the larger amounts of surrounding normal tissue exposure, particularly for larger treatment volumes. Conversely, under-estimation of the required treatment margins may result in marginal misses. It therefore seems desirable to limit respiratory motion for tumor sites exhibiting large excursions. Third, technological advances have spawned new capabilities for measuring and reducing respiratory motion.

This chapter surveys different strategies for managing respiratory motion during radiation treatment. These can be divided into three categories: 1) ignore respiration during treatment; 2) freeze the motion; and 3) tumor tracking. Following a brief description of the effects of respiration on radiation treatment delivery, we discuss each of these strategies in turn.

11.2 Respiratory Motion During IMRT Delivery

Respiratory motion during radiation delivery in effect blurs the planned dose distribution, which in standard clinical practice, is calculated without explicit inclusion of motion. For statically delivered treatment fields (i.e., the treatment machine components do not move) with uniform radiation intensity within the field, respiratory motion will broaden the dose distribution in the anatomy moving near the beam edges. For IMRT delivered with physical compensators, the dose gradients in moving tissue will broaden and become less steep.

IMRT delivered with a multileaf collimator (MLC) poses additional considerations, because of the interplay between moving MLC and respiratory motion [1]. An intensity modulated field is composed of many small fields that are delivered temporally; thus the dose actually received by moving tissue may be less than, or greater than, the planned dose. This pertains to both dynamic and "step-and-shoot" MLC delivery. Initial studies reported large dose variations, exceeding 20%, for a single field [2, 3]. More recent studies show that for multiple field treatments with 30 fractions and assuming periodic tissue motion patterns which remain constant throughout treatment dose variations average out to produce dose distributions that are the same as for treatments delivered with a physical compensatory [4–6]. Consideration

of interplay effects should be given for limited fraction IMRT and with scanning particle beams, however.

11.3 Interventional Strategies

11.3.1 Ignore Respiration During Treatment

In cases of limited tumor mobility, it may be sufficient not to take any measures to control respiratory motion during treatment, provided that it is properly accounted for during imaging for treatment planning. Respiration is an important source of error in a planning CT scan of the thorax or abdomen, resulting in motion artifacts that adversely affect the accuracy of target and nontarget organ definition. The motion artifacts give rise to a systematic error in tumor position and extent, i.e., the tumor observed in the image is not the respiration-averaged position [7–9]. CT acquisition techniques are available that include the range of tumor motion with respiration, discussed in chapter II.9. Using such techniques, one can obtain an image that is representative of the respiration-averaged position of the tumor at the time of simulation. Under the assumption that systematic error is thereby removed, Van Herk has suggested that the margin for respiration during treatment is only 30% of the peak-to-peak tumor excursion [10]; see also chapter I.3. For the majority of lung tumors with peak-to-peak amplitudes of 1 cm or less, the margin for respiration is a few millimeters, which is added in quadrature with other error sources. It is important to note, however, that the average tumor position at treatment may differ from that at simulation, thus the assumption of no systematic error may break down. Studies of patients receiving respiratory gated treatments at Memorial Sloan-Kettering Cancer Center (MSKCC) have found systematic displacements in diaphragm position between simulation and treatment of up to 1 cm, and exceeding 0.4 cm in about half of the patients, although image acquisition was at the same point in the respiration cycle for both simulation and treatment [11, 12]. These results imply that some amount of systematic tumor displacement may be present during treatment despite attempts to remove it at simulation (discussed further in the section on respiratory gating), and that image-based monitoring is required to ensure that systematic error does not exceed the assumed value. If the systematic and random variations are known, e.g., through measurements from the initial treatment sessions, then to obtain a 90% probability that the 95% isodose encompasses the target, the required margin is $2.5\,\Sigma + 0.7\,\sigma$, where Σ is the total standard deviation (SD) of all systematic errors and σ is the total SD of random errors [13].

11.3.2 Freeze the Motion

Two different strategies have evolved to "freeze" respiratory motion in radiation treatments: respiratory gating of the accelerator while the patient breathes normally, and controlled patient breathing. Varying amounts of patient cooperation and staff effort are required, depending on the particular technique.

Respiratory Gating

In respiratory gated treatment, delivery of radiation occurs only during certain time intervals, synchronous with the patient's respiration. Respiratory gated radiotherapy has been in clinical use for over a decade in Japan [14–16]. Hokkaido University has developed a gated linear accelerator system using real-time fluoroscopic tracking of gold markers implanted in tumor [17, 18], described further in the section on tumor tracking. In the U.S., the University of California at Davis has reported on a gated radiotherapy system, developed jointly with Varian Medical Systems, which accepts respiratory signals from a video camera (now commercially available as the Real-Time Position Management Respiratory Gating System, or RPM) [19]. A number of centers have reported on clinical studies with the RPM system, which is described further below [20–23].

RPM System Description

The RPM system has capabilities for breathing-synchronized CT acquisition, fluoroscopy on a conventional simulator, and gated treatment on a linear accelerator. To monitor respiration, infrared light from an illuminator is reflected from a passive reflective block placed on the patient and detected by video camera (Fig. 1). A computer program processes the video signals and sends on-off control signals to the accelerator. At the start of each session, the operator places the system into a so-called tracking mode for a few breathing cycles, to allow the system to determine the minimum

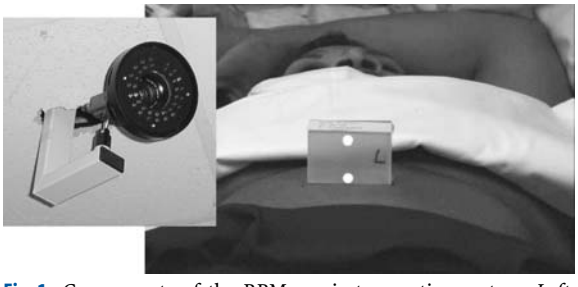

Fig. 1. Components of the RPM respiratory gating system. *Left:* video camera and infrared illuminator. *Right:* passive reflective block positioned on patient

and maximum vertical position of the upper marker. A periodicity filter algorithm checks that the breathing waveform (i.e., the marker position vs time) is regular and periodic. Once breathing is stable and regular, the operator places the system into a record mode, during which the waveform is recorded and displayed. There are two modes of producing gate signals, amplitude or phase. In the amplitude-based mode, dose is delivered only when the waveform is between user-settable thresholds (Fig. 2). In the phase-based mode, the operator specifies a phase interval of the waveform calculated by the periodicity filter algorithm. Several publications report negligible dosimetric effects of gated operation for both static and sliding window IMRT fields [24–26]. Nonetheless, users should independently commission their own RPM (or similar) system.

On a conventional simulator, the RPM system allows recording and playback of fluoroscopy images, synchronized with the waveform. Only those fluoroscopy frames occurring within the gate intervals are played back, allowing one to evaluate anatomic motion within the gate. There are two types of respiration-synchronized CT acquisition: prospective triggering and retrospective correlation. In prospective triggering, the scanner is operated in axial scan mode and a gate-enable signal from the RPM system triggers the acquisition of an axial image, followed by a table advance to the next image position. Only one image is acquired per respiratory cycle, at a single phase. In retrospective correlation (variously referred to as respiration-correlated CT or 4D-CT, see the chapter II.9), CT images are repeatedly acquired over a full respiratory cycle at each couch position while simultaneously recording respiration. The images are retrospectively correlated with respiration phase to produce three-dimensional image sets at different phases.

Clinical Implementation at MSKCC

In late 1999, MSKCC initiated clinical studies with the RPM system. As of this writing, 44 patients (28 lung, 15 liver, 1 abdominal) have received gated treatment, and of these, 19 have received gated IMRT (12 lung, 6 liver, 1 abdominal). Gated treatment with RPM is well tolerated by most patients; however, some patient effort and concentration is required, along with considerable care and patient-specific quality assurance on the part of all involved staff. This is because the RPM system – like all gating systems based on signals generated outside the tumor – makes two assumptions. The first assumption is that there is a one-to-one correspondence between the external signal (the motion of the markers on the patient's chest) and the patient's internal anatomy (tumor and critical normal tissues). Second, it is assumed that this relationship, once determined at simulation, is maintained over the entire course of treatment. In an effort to ensure the validity of these assumptions we wish to keep the breathing motion as reproducible as possible from session to session, to use frequent portal imaging to observe internal anatomy, and to make field adjustments as necessary. We use simple, repetitive verbal coaching instructions ("breathe in", "breathe out"), customized to the patient's breathing tempo, to improve breathing regularity. In the past year we have added visual prompting, in which the patient observes her waveform on a monitor, to assist the patient in maintaining consistent marker amplitude, and by inference, breathing amplitude [27,28].

Patient Selection. Patients must be able to breathe regularly and follow breathing instruction. They must also be able to tolerate the longer simulation session (overall ~2 h). For treatment of nonsmall cell lung cancer

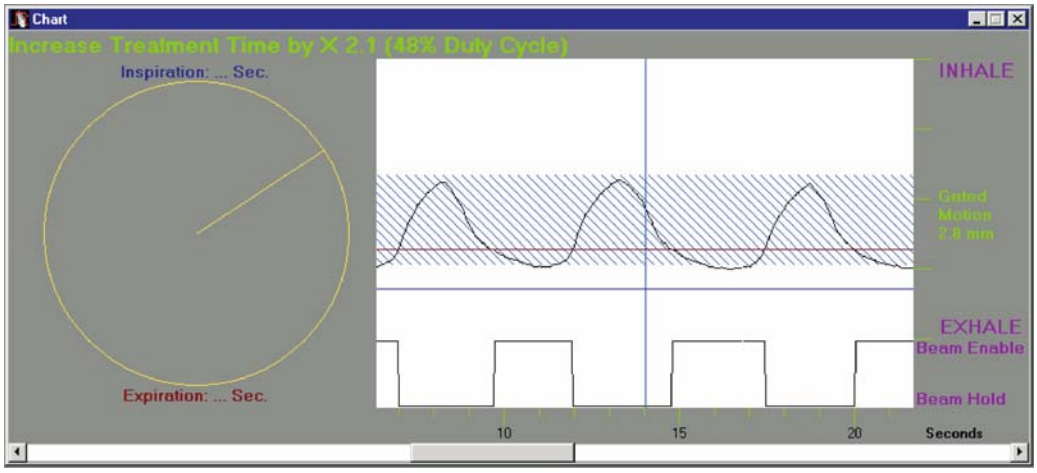

Fig. 2. A patient respiration waveform from the RPM system, with thresholds (*horizontal lines*) set for amplitude-based gating at expiration. Tick-marks on the horizontal axis are time in seconds – on the vertical axis, distance in cm. The *square wave graph* at the bottom of the display indicates when the treatment beam would be enabled. *Hashed region behind trace* indicates amplitude of waveform recorded at simulation, for verifying reproducibility

(NSCLC), gating is indicated if the physician believes that the tumor is mobile. In liver, gating is indicated for curative or long-term palliative intent, and margin reduction is a priority, such as proximity of the tumor to a kidney, impaired kidney function, or impaired liver function.

Simulation. MSKCC has RPM systems installed on a conventional simulator (Ximatron, Varian Medical Systems, Palo Alto, CA) and a CT-Simulator (AcQSim PQ5000, Philips Marconi Medical Systems, Cleveland, OH). Following patient immobilization, the marker block position is selected and its position is marked for reproducible placement. Waveform motion extent (peak to through) should be at least 0.5 cm; we find that a midline location approximately two-thirds of the way between umbilicus and xyphoid gives sufficient signal. The audio prompting is customized and the physicist trains the patient to follow the combination of audio and visual prompting. We acquire an approximately 45 s voice-instructed fluoroscopic movie and an anterior-posterior (AP) film, which includes the isocenter, ipsilateral diaphragm, any tumor shadow and spine. The superior visualization of subtle vertebral features on the kV film is helpful for comparison with port films. The gate width is tentatively established, based on observation of the waveform and the anatomical motion in the fluoroscopic playback. Conventional simulation takes 45–60 min, with physics assistance throughout.

CT simulation requires mounting the camera-infrared illuminator assembly onto the foot of the couch. In addition to the longer scan time with prospective triggered CT, irregular breathing further slows the process, requiring restarting the scanner to correct for artifacts near the target or diaphragm. If desired, a second complete CT image set is acquired to allow an estimate of reproducibility and the patient is encouraged to rest between scans. The more regular of the two image sets is used as the planning scan. Typical time for the CT simulation is 1–1.5 h, with direct physics involvement throughout.

Selection of Gate. In order to minimize residual organ motion, gated treatment at MSKCC is usually centered at end expiration, which results in a more reproducible anatomic position than at end inspiration [27]. Gated treatment at end inspiration may offer an advantage for treatment of lung carcinoma, because of the increased lung volume resulting in a lower dose to normal lung. Initial studies indicate that the average improvement for a group of patients is small [23, 69], although further studies may determine individual patients for whom there is advantage.

The choice of gate width is a trade-off between minimizing motion within the gate and treatment time – usually a 20 to 40% duty cycle in our experience. Treatment times may be reduced with higher dose rate; at MSKCC, gated treatment is normally delivered at 600 MU/min, for both static and IMRT fields. Increasing the dose rate from 300 to 600 MU/min, while not halving the gated IMRT delivery time, does decrease it by approximately 60%. Kubo et al. have used a short (5–10 s) breath-hold technique as a means of increasing the treatment duty cycle and reducing residual organ motion within the gate interval [29].

Treatment Planning. No special treatment planning measures are taken for gating patients; either static 3D conformal radiotherapy or IMRT is used, at the discretion of the physician and the planner. IMRT is preferred for a medium or larger sized planning target volume (PTV) of 100–700 cm^3, if the tumor is long or bifurcated, or if the planner cannot achieve good PTV coverage and normal tissue dose limits at the desired dose.

Small tumors (e.g., T1-NSCLC) are more easily treated with 3D conformal static fields. Some IMRT plans are treated without gating for immobile tumors, or with the deep-inspiration breath hold technique (described later in this section). For NSCLC patients, we have not reduced the PTV margin that has been used for conventional treatment, but rather assign patients to gated treatment if there is evidence of tumor mobility. Respiratory gated treatment for liver cancer patients has enabled a safe reduction of margins (GTV to PTV) from 2 cm to 1 cm, subject to continuing portal radiograph surveillance during treatment [21].

Treatment. Both audio and visual prompting is used for treatment. The therapists must carefully watch the respiration waveform during treatment, stop treatment to remind the patient or check setup if they see serious irregularity or drift, and contact a designated physicist for persistent problems. Gated treatment is well accepted by patients and therapists. Gated treatment session times are increased relative to standard treatments by 5–10 min depending on patient compliance. Routinely, for each patient we acquire AP localization films including the diaphragm and vertebral landmarks, three films per week for the first two weeks of treatment, twice per week for the next two weeks if no systematic differences are observed and at least once per week thereafter. If systematic errors in excess of 0.4–0.5 cm are observed, the physician is consulted as to the need for field adjustment. To date, field adjustments have been made in about 15% of patients.

Accuracy of External Monitors in Gated Treatment

A key issue in using external respiratory monitors for gating is their accuracy in predicting internal target position. The best correlation is expected from a direct image of tumor motion, but at present this requires the invasive implantation of radio-opaque markers into the

tumor, discussed further in the section on tumor tracking below. Fluoroscopic studies with the RPM system have demonstrated high short-term (1 min) correlation between respiratory signal (abdominal wall motion) and diaphragm motion in most cases [22, 27]. A study by Wagman et al. found good reproducibility in abdominal organ positions with prospectively triggered CT at end expiration, with average organ displacement of 0.2 cm in the superior-inferior direction in repeat CT scans at the same session [21]. However, internal-external correlation can be disturbed by transient changes in breathing [30]. Drifts of the waveform may occur, caused by patient movement, particularly if the motion amplitude is small, such as monitoring anterior chest wall motion [31]. In amplitude-based gating with the RPM system, a drift of the waveform with respect to the thresholds can result in dose delivery occurring at points at an unintended part of the breathing cycle. In both prospective triggered and retrospective correlated CT, irregular breathing can lead to motion artifacts in the images. For these reasons, patient training is important, to allow the patient to familiarize herself with the breathing technique, and to evaluate the patient's ability to achieve reproducible respiratory signals.

As mentioned earlier, another quality assurance consideration is to ensure the reproducibility of internal organ position between simulation and treatment. Although external monitors may correlate well with the respiratory organs within a single session, thus reducing intra-fractional variations, the relationship between external monitor and internal organ positions may change between sessions, which can adversely affect organ reproducibility and produce inter-fractional variations. Factors that can affect the diaphragm/respiratory signal relationship between sessions include changes in patient's respiration pattern, such as the relative amount of chest vs abdominal breathing, or changes in abdominal pressure caused by stomach contents, ascites, or changes in hepatic tumor shape and size. Inter-fractional diaphragm variations have often been observed to be larger than intra-fractional ones. Ford et al. examined portal radiographs of eight patients receiving gated treatment during tidal breathing, and separated the inter-fractional diaphragm variation into systematic (mean displacement from its planned position) and random (daily displacements about the mean) components [11]. They found that random inter-fractional and intra- fractional variations were comparable in magnitude (~0.3 cm), whereas the systematic inter-fractional variations were larger, with half the patients exceeding 0.4 cm. Our subsequent studies have found that in one-third of patients, the diaphragm position on the radiographs showed a systematic displacement of at least 0.5 cm relative to its position on the DRR constructed from the planning CT simulation [12]. A program of frequent gated portal radiographs of the surrogate organ (or target, if visible) throughout treatment is essential to measure inter-fractional variations.

Since the tumor is often not visible in fluoroscopy or portal radiographs and in the absence of implanted markers, one must rely on a surrogate such as the diaphragm or anterior chest wall. Dawson et al. have found that diaphragm movement correlates to within approximately 0.2 cm with microcoils implanted near hepatic tumors [32]. Correspondence of lung tumor motion with the diaphragm or chest wall varies and should be measured for individual patients [33, 34]. When using a surrogate, the relative magnitudes of target and surrogate motion should be measured at least during simulation, in order to infer the amount of target displacement for a given surrogate displacement. CT acquisition techniques are available that provide a measure of the range of tumor motion with respiration, discussed in chapter II.9. It is important to keep in mind that the positional relation between tumor and surrogate may change over the treatment course; thus, confirming inter-fractional constancy of surrogate position does not necessarily guarantee the same for the target.

Controlled Patient Breathing

Breath-hold Methods

Breath-hold methods exploit the anatomical immobilization to minimize the effects of breathing motion. For radiation therapy, the aim is to achieve the same breath-hold position between fields during a single treatment fraction, and between fractions. In principle, breath-hold methods appear technically simpler than respiratory gating. In practice, reproducibility of breath-hold, patient compliance and comfort need to considered, particularly for patients with compromised pulmonary status.

Because not all respiratory muscles may be involved in normal breathing and tidal volume between breaths is variable, it is difficult for patients to achieve reproducible breath-hold voluntarily during normal respiration. Instead breath-hold methods are usually applied at maximum or moderate deep inspiration [35,36], or at end of normal expiration [32]. Deep inspiration actively recruits all respiratory muscles to expand the lungs, while they are at their most relaxed state at normal end expiration.

A breath-hold procedure typically uses a nose clip and mouthpiece connected via tubing to a digital flow meter. The flow meter signal is converted to a lung volume and displayed to the treatment personnel outside the room, or to the patient as visual feedback. A predefined lung volume serves as a cue for applying breath-hold. We discuss two approaches that have been in clinical use: active breathing control (ABC), and voluntary deep inspiration breath-hold (DIBH).

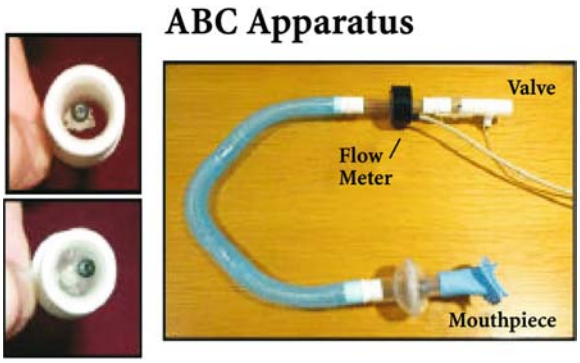

Fig. 3. Photograph of mouthpiece, digital flow meter, and balloon valve of the ABC device. *Left insets* show the balloon valve in the open (*top*) and closed state (*bottom*) when the balloon is inflated with an air compressor. (Reprinted from: Intensity-modulated radiation therapy – The state of the art, Wong J, Methods to manage respiratory motion in radiation treatment, pp 663–702, Copyright (2003) with permission from Medical Physics Publishing)

Active Breathing Control (ABC)

The ABC method was developed at William Beaumont Hospital [36] and is a commercially available product (Active Breathing Coordinator, Elekta Oncology Systems, Crawley, UK). The device suspends patient breathing at any pre-determined position in the normal breathing cycle, or at active inspiration. It consists of a digital spirometer to measure respiratory volume, which is in turn connected to a computer-controlled balloon valve (Fig. 3). With the patient normally breathing through the apparatus, the operator sets the lung volume and phase (inhalation or exhalation) at which the valve will close. The patient is coached to the pre-determined lung volume, usually after taking two preparatory breaths; at this point, the valve is inflated to actively hold the patient's breath. The breath-hold duration is patient dependent, usually 15 to 30 s, and should be well tolerated by the patient to allow for repeated (after a brief rest period) breath-holds.

Clinical experience [37, 38] shows that a moderately deep inspiration breath-hold (mDIBH) at 75% of maximum inspiratory capacity achieves substantial and reproducible internal organ displacement while maintaining patient comfort. The intended mDIBH level is calculated from the baseline at normal end expiration and is set during an initial training session with each patient. Since the baseline can vary between breath cycles, the patient is given instruction to help achieve a steady breathing pattern. In each breathing cycle, the device resets the baseline when zero flow is detected at end expiration. Once the patient achieves normal respiration in a relaxed manner, the frequency and magnitude of baseline resets becomes minimal. At this point, three measurements of maximum inspiratory capacity are made. The mDIBH threshold is set to approximately 75% of the average maximum inspiratory capacity, and the value is used for all subsequent sessions. Because of the relatively large lung volume at mDIBH, the baseline provides a sufficiently stable reference for achieving reproducible breath-holds.

Breath-hold Reproducibility at mDIBH with ABC. William Beaumont Hospital has performed extensive CT studies to assess reproducibility [38]. The study protocol includes two mDIBH scans at the same session to measure intra-fraction reproducibility, and for some patients, a scan at mDIBH one to four weeks later to measure inter-fractional reproducibility. During a CT study, breath-hold procedures are repeated to acquire the scans in smaller segments that together span the entire thorax. The scans are registered via alignment of the vertebrae, the lungs and other thoracic structures delineated to generate three-dimensional surfaces, and a closest distance-to-agreement (DTA) calculated as a measure of reproducibility. Data from 14 breast patients positioned with Alpha cradle immobilization showed mean (standard deviation) intra-fractional DTA in lung of 0.10 cm (0.11 cm), while inter-fractional DTA in eight patients was 0.14 cm (0.16 cm). The results indicate that with proper setup and immobilization, a 0.5 cm margin suffices for breathing motion in lung.

Treatment of Breast. In addition to reproducible immobilization with ABC, moderate DIBH provides the advantage of displacing organs at risk from the high dose region. In patients with left sided breast disease whose anatomy is such that partial heart irradiation may occur with a tangential field arrangement, mDIBH with ABC can move the heart away from the fields (Fig. 4) [39, 40]. Setup of ABC treatment with tangential fields requires special procedures. Each patient receives free breathing and mDIBH simulation and CT. The free breathing information is used to mark the patient for setup, while the mDIBH information is used for treatment planning and delivery. Source-to-surface distances are checked both at free breathing and with a short duration (5–10 s) mDIBH. A second set of keyboard and

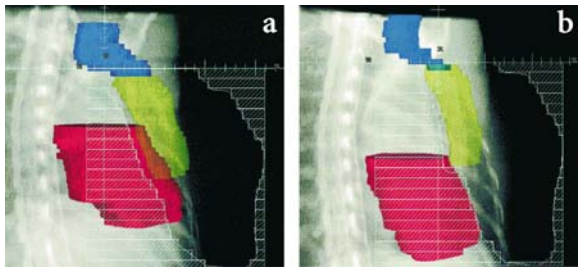

Fig. 4a,b. Beam's eye view display of: (a) tangential breast field with patient breathing normally, showing irradiation of a portion of the heart (*red*); (b) displacement of the heart from the field at mDIBH. (Reprinted from International Journal of Radiation Oncology Biology Physics, vol 55, Remouchamps FA et al., Significant reductions in heart and lung doses using deep inspiration breath hold with active breathing control and intensity-modulated radiation therapy for patients treated with locoregional breast irradiation, pp 392–406, Copyright (2003), with permission from Elsevier)

display provides convenient in-room operation of the ABC system. In the clinical implementation at William Beaumont Hospital, each IMRT tangential field segment is divided into two or three separate breath-holds. In addition, an open tangential field segment with beam-on time exceeding one breath-hold is split into two breath-holds. Electronic portal images of the open field segment serves to examine intra- and inter-fraction variation that combines both breath-hold and setup. Mean (standard deviation) variations in the first five patients studied were 0.16 cm (0.23 cm), and 0.27 cm (0.32 cm) in the transverse and superior-inferior directions, respectively. The larger variation in the superior-inferior direction owes to the larger setup error than breath hold variation. Treatments at mDIBH with ABC are well tolerated by all selected patients. With the exception of the first five patients, all treatments have been completed within 15 min.

Studies of ABC in Other Disease Sites. The University of Michigan has developed a system for daily targeting of intrahepatic tumors, using a combination of ABC and in-room diagnostic quality radiographs [41]. The ABC device suspends breathing at end expiration, at which time orthogonal radiographs are acquired. The radiographs are matched to the planning CT using the diaphragm for superior-inferior setup determination, and using the skeletal anatomy for anterior-posterior and lateral setup. Adjustments to couch positions are made for positioning errors exceeding 0.3 – 0.5 cm. Typical treatment times are 25 – 30 min. The procedure has reduced setup errors almost a factor of two, from 0.67 cm (standard deviation) to 0.35 cm in the superior-inferior direction, with similar improvement in the other directions. The reduced margins have allowed a 5 Gy average increase in the prescribed dose. In a study of the reproducibility of ABC at end expiration in eight patients, Dawson et al. found the intra-fractional variation of diaphragm and implanted microcoils near the tumor to be 0.25 cm (standard deviation in the superior-inferior direction) and 0.23 cm. However, inter-fractional variation was larger, 0.44 cm and 0.43 cm, respectively, indicating the need for daily imaging and correction if treatment margins smaller than for free breathing treatment are required.

Cheung et al. have studied the inter-fraction reproducibility of peripheral nonsmall cell lung carcinoma tumors using repeat CT scans in the first five days of radiation treatment in ten patients [42]. Because of the compromised pulmonary function in some patients, breath-hold with ABC was initiated at a comfortable, predefined lung volume during inspiration, relative to the baseline at end expiration. Total lung volumes with ABC increased an average of 42% relative to free breathing CT, resulting in an average decrease in lung mass of 18% within a standard 1.5 cm PTV margin around the GTV. The standard deviation inter-fractional variation in GTV centroid position with ABC was 0.18 cm, 0.23 cm and 0.35 cm in the lateral, anterior-posterior and superior-inferior directions (mean variation was 0.1 cm or less). The results indicate that some inter-fractional variation remains, precluding a significant reduction in margin. However, the lung volume is significantly increased, resulting in decreased amount of lung with a standard PTV. In a CT study of ten NSCLC patients using ABC set at 75% vital capacity, Wilson et al. found no significant variation in lung volume over several weeks, while the volume of lung receiving more than 20 Gy decreased in all (median 6.4%), and spinal cord dose in 80% (median 1.03 Gy) of the plans [43].

Deep Inspiration Breath-hold

A technique of voluntary maximum breath-hold (deep inspiration breath-hold or DIBH) has been developed and clinically implemented primarily for conformal radiation treatments of nonsmall-cell lung cancer (NSCLC) at MSKCC [33, 35, 44]. The technique involves verbally coaching the patient to a reproducible deep inspiration breath-hold during simulation and treatment. The patient, with a nose clip, breathes through a mouthpiece connected via flexible tubing to a spirometer. A computer program integrates the flow signal to obtain the volume of inhaled and exhaled air, which is displayed and recorded as a function of time (Fig. 5). While watching the display, the therapist coaches the patient through a modified version of the slow vital capacity maneuver, consisting of a deep inhalation, deep exhalation, second

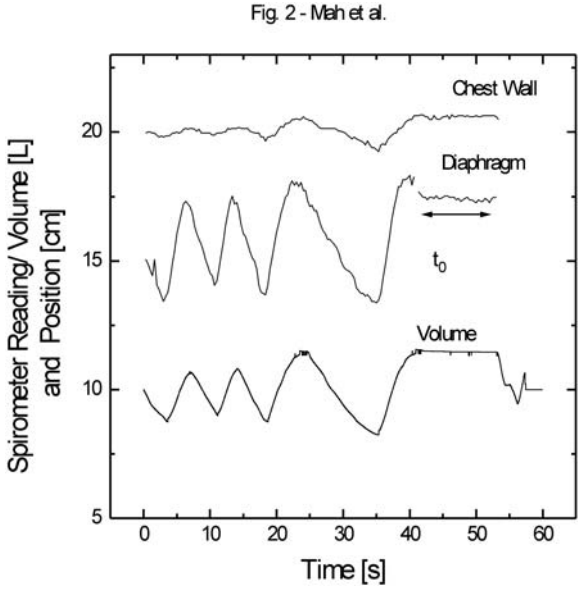

Fig. 5. Example of position of diaphragm and chest wall position compared to spirometer signal, of a DIBH maneuver. (Reprinted from International Journal of Radiation Oncology Biology Physics, vol 48, Mah D et al., Technical aspects of the deep inspiration breath hold technique in the treatment of thoracic cancer, pp. 1175–1185, Copyright (2000), with permission from Elsevier)

deep inhalation and breath-hold. At each phase of the maneuver, the therapist waits for the breathing trace to plateau before coaching the patient to the next phase. The program compares air volumes at maximum exhalation and second maximum inhalation with user-set thresholds to verify the reproducibility of the maneuver. The maneuver yields highly reproducible lung inflation at approximately 100% capacity, which can be maintained for 10–20 s (patient specific). Two features of this technique potentially reduce lung morbidity: deep inspiration expands the lung out of the high-dose region while the volume of the GTV remains largely unchanged, and breath-hold reduces tumor motion.

Patient Selection. The applicability of DIBH is limited by patient compliance. Approximately 60% of the lung cancer patients at MSKCC cannot perform the maneuver reproducibly enough to permit its use. It also calls for special staff effort, as therapists must be trained to coach and advise the patients. Because DIBH is relatively demanding for patients, it is used only for compliant patients in whom the significant lung inflation allows treatment to a higher total dose than is possible with free breathing. To familiarize the patient with the DIBH maneuver and to determine the patient's ability to perform it reproducibly, a training session with the spirometer is given a few days before simulation, which also provides initial threshold values.

Simulation. Following a brief DIBH practice session, the patient receives three helical CT scans in the treatment position: 1) with normal breathing (NB); 2) with spirometer-monitored deep inspiration (DI); and 3) with spirometer-monitored shallow inspiration (SI). The DI and SI scans are performed in four to six breath-hold segments of 10–12 s each. The NB scan provides a check that the patient's state of respiration does not alter the position of the spine, thus allowing positioning of the patient for treatment while breathing normally. It also serves as the alternative treatment plan CT if the patient cannot be completely treated with DIBH. The SI scan is used to set breath-hold tolerance levels by determining the motion extent of the GTV for a known change in breath-hold volume [33]. For treatment with DIBH, the treatment plan and DRRs are based on the DI scan. The simulation process – including immobilization, isocenter selection, practice, three CT scans and resting between scans – takes approximately 2 h.

Treatment Planning. The DIBH treatment plan usually involves two to six static conformal fields; however, sliding window IMRT, delivered dynamically with multi-leaf collimation [45] is possible with patients capable of achieving a sufficiently long breath-hold (see Treatment section below). If there is insufficient lung expansion to permit a treatment dose increase of ~10% or more, with acceptable normal tissue dose-volume histograms (DVHs) and calculated lung complication probability relative to NB [44], the patient receives NB planning and treatment. Despite the reduced respiratory motion, the GTV-to-PTV margin of 1 to 1.5 cm has not been reduced for three reasons: first, DI lung expansion allows sufficient target dose escalation with acceptable estimated lung toxicity, as described below; second, the margins protect against possible expansion of microscopic disease due to DI; and third, the treatment-planning dose-calculation algorithm at present does not handle lateral disequilibrium in low density tissue, but Monte Carlo dose-calculation studies suggest that the margins (GTV-to-aperture edge) used in NB treatment adequately cover the GTV with DIBH if 6 MV photons are used [46].

Treatment. During treatment, the therapists are instructed to turn on the beam only when the target breath-hold level has been achieved and to stop treatment if the level has fallen below a pre-set tolerance. In all imaging and treatment sessions, the therapist is instructed to wait 1 s following breath-hold before turning on the beam, to allow for transient diaphragm relaxation (Fig. 5) [33]. For static conformal treatments at 2 Gy/fraction on linear accelerators operated at 500–600 MU/min, a single breath-hold is usually sufficient for each field. More recently, IMRT in combination with DIBH has been introduced for patients able to hold their breath long enough to complete a field, approximately 20 s for a typical beam-on time of 200 MU delivered at 600 MU/min with the sliding window technique. An extra AP localization radiograph showing the entire lung is taken at least weekly to confirm that the lung inflation, as indicated by the distance from the lung apex to the dome of the diaphragm, remains constant. If the films or the graphic traces on the computer indicate that a patient is repeatedly missing or exceeding the DIBH maneuver levels, the dosimetric consequences and remedies are evaluated by the physicist and the physician. Treatment sessions usually take

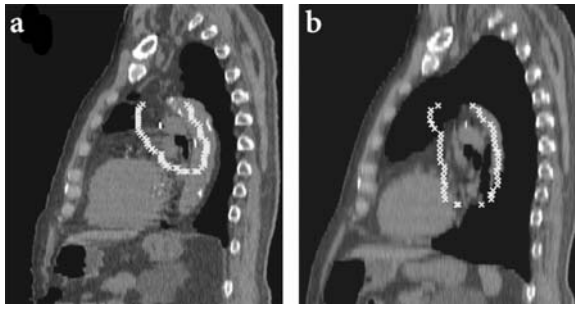

Fig. 6a,b. Sagittal section of: (a) free breathing CT; (b) deep inspiration breath hold (DIBH) CT. For some patients, the use of DIBH moves the tumor (*outline*) away from the cord. (Reprinted from Seminars in Radiation Oncology, vol 14, Mageras GS and Yorke E, Deep inspiration breath hold and respiratory gating strategies for reducing organ motion in radiation treatment, pp. 65–75, Copyright (2004), with permission from Elsevier)

5–10 min longer than a similar beam arrangement for a free-breathing patient.

Treatment and Clinical Imaging Studies. The DIBH technique has been used to treat 40 patients at MSKCC (39 with NSCLC) since February 1998; of these, three patients were treated with DIBH in combination with IMRT. For the first seven NSCLC patients treated with DIBH at MSKCC, Rosenzweig et al. found the average lung volume increased by a factor of 1.9 relative to normal breathing (Fig. 6), thus reducing the fraction of normal lung tissue irradiated [44]. The amount of reduction varies among patients, with the largest reduction seen in patients having large tumors. Since dosimetric predictors of radiation pneumonitis depend strongly on the fraction of irradiated lung, DIBH permits higher total treatment doses for the same predicted lung toxicity. A study comparing 3D conformal radiation treatment (3DCRT) plans for standard normal breathing (NB) and DIBH CT scans of these patients found that if restricting the Lyman model lung normal tissue complication probability (NTCP) to no more than 25% and maintaining the same GTV-to-PTV margin were the only dose-limiting consideration, the average prescription dose could be increased from 69.4 Gy with NB to 87.9 Gy with DIBH [44]. Deep inspiration, in some cases, increases the separation between the GTV and spinal cord, giving more freedom in the choice of beam directions [47]. The reproducible reduction of diaphragm motion presumably also results in reduced tumor motion. Fluoroscopy studies of diaphragm position in the initial five patients have shown an intra-breath-hold variation (mean±standard deviation) of 0.10 ± 0.09 cm and inter- breath-hold variation of 0.25 ± 0.16 cm [35]. Interfractional variation of the diaphragm position relative to the isocenter was measured in AP port films taken on different days over the course of treatment and was compared to the position in the treatment plan DRR; the study of 92 films found a mean±standard deviation difference of -0.1 ± 0.4 cm (range −1.2 to 1.1 cm), indicating good overall diaphragm reproducibility over the course of treatment [33].

Abdominal Compression

Abdominal compression was originally developed for stereotactic irradiation of small lung and liver lesions at the Karolinska Hospital in Stockholm [48]. The technique employs a stereotactic body frame with a flexible plate that presses against the abdomen, thereby minimizing diaphragmatic excursions while still permitting limited normal respiration. Negoro et al. have reported on the treatment of solitary lung tumors with hypofractionation [49]. At simulation, the patient is positioned and immobilized in a stereotactic body frame (Elekta Instrument AB, Stockholm, Sweden). Tumor motion is evaluated under fluoroscopy, and abdominal compression is used in cases where tumor excursion exceeds 0.5 cm. Usually the maximum pressure is used that the patient can comfortably tolerate for the treatment session duration. Fluoroscopy is repeated in orthogonal directions to assess resultant tumor excursion, followed by CT simulation. In 10 out of 20 patients requiring compression, tumor excursion was reduced from 0.8–2.0 cm without compression (mean 1.2 cm) to 0.2–1.1 cm with compression (mean 0.7 cm). On each treatment day, portal and simulation radiographs are compared, and the patient repositioned if the setup error is greater than 0.3 cm in at least one of three directions. In this study, most of the lung lesions could be identified in the portal radiographs. Of 80 verifications, patient repositioning was required in 25% of the cases. The range of 3D setup errors prior to correction was 0.4–0.8 cm (mean 0.5 cm).

11.3.3 Tumor Tracking

The third category of methods for managing respiratory motion during the treatment is *tumor tracking*, which consists of two major aspects: real-time localization of, and real-time beam adaptation to, a constantly moving tumor. Compared to the motion freezing methods, tumor tracking techniques potentially offer additional benefits such as higher delivery efficiency and less residual target motion. These factors may be particularly important in radiosurgery to thoracic and abdominal tumor sites, where a large dose is delivered during a single relatively lengthy treatment session. Delivering a large dose at one time requires high dose conformity to the target, and the lengthy treatment time demands a high degree of dose delivery efficiency and a procedure that is comfortable to patients. In addition, tumor tracking is applicable to regularly fractionated IMRT and 3DCRT treatment of mobile tumors.

It is important to note that real-time beam adaptation is not feasible without *precise* real-time localization of the tumor position in three dimensions (3D). Owing to system latency and the desire to reduce the imaging dose, predictive filters are usually required for anticipating tumor position in a coming short period of time after localizing it at one time point. Errors in the localization should be identified in real-time in order to avoid irradiating wrong target. Various aspects of tumor tracking will be discussed in the following subsections.

Real-Time Tumor Localization

Use of External Respiratory Surrogates

In most gating schemes, tumor position is derived from surrogate breathing signals such as lung volume or skin motion. As mentioned earlier in this chapter, the short

term correlation between external surrogates and internal target position may be high for some tumor sites; however, the correlation may be not stable during a long treatment fraction, owing to transient changes in breathing and waveform drifts [30, 31]. In addition, the internal-external correlation may change over the treatment course. The diaphragm may be used as a surrogate landmark for lower lobe lung tumor, liver tumor, and pancreas tumor, if fluoroscopy is available during the treatment [27]. Again, the correlation between diaphragm and target may not hold for a long treatment time and from fraction to fraction. Therefore, the prediction of tumor position from external surrogates should be used with great caution. If one decides to use this approach, the correlation between surrogate and tumor position should be established before each treatment fraction, and be checked/updated during the treatment session at a frequency depending on the tumor site or even the individual patient [31, 50]. The major advantage of this approach is the reduced radiographic dose.

Use of Implanted Radio-opaque Fiducial Markers

High-Z metal fiducial markers can be implanted in the tumor-bearing organs to help localize the tumor position in real-time. Spherical or cylindrical gold markers are often used for this purpose [17, 31, 51]. Markers can be implanted either percutaneously or endoscopically, depending on the tumor location and other medical considerations. The high radio-opacity of the markers makes them readily detectable in fluoroscopic images. Marker positions can be calculated through a simple and fast triangulation process. Therefore, fiducial marker based tumor localization is relatively straightforward from the image processing point of view and can be done in a very efficient way to facilitate real-time tumor tracking.

Fiducial marker based real-time tumor localization has been extensively used at Hokkaido University in Japan for gated treatment of lung, liver, prostate, and other tumor sites [17, 52, 53]. Markers are tracked at the video frame rate (30 Hz) using the Real-time Tumor-Tracking Radiation Treatment (RTRT) system developed by Mitsubishi and Hokkaido University. The RTRT imaging system consists of four kV X-ray units and is described in more detail in a later subsection.

Percutaneously implanting fiducial markers is an invasive procedure with potential risks of infection. Many clinicians are reluctant to use this procedure for lung cancer treatment because puncturing of the chest wall may cause pneumothorax. The effectiveness of using fiducial markers for tumor localization relies on the stability of the relationship between markers and tumor center. This relationship may change during the treatment course due to changes in tumor geometry. Additionally, markers may migrate within the tissue between the planning CT study and the treatment delivery. For these reasons, three to four markers are often implanted and any marker migration may be detected by monitoring the inter-marker spacing. Three markers also allow detection of tumor rotation [54].

Non-radiographic Tumor Tracking

Efforts have been made to track tumors non-radiographically. A miniature, implantable RF coil has been developed by Seiler et al. [55] that can be tracked magnetically in 3D from outside the patient. A new technology currently under development at Calypso Medical Technologies, Inc., Seattle, WA, is based on non-ionizing electromagnetic fields, using small wireless transponders implanted in human tissue [56]. Real-time 3D ultrasound is another possible alternative to X-ray imaging for tracking the tumor [57].

Direct Tracking of Lung Tumor Mass

Owing to the risk of pneumothorax, percutaneous implantation of fiducial markers should be avoided whenever the lung tumor can be tracked directly. Direct fluoroscopic tumor tracking is extremely difficult, if not impossible, for tumors in abdomen. In the case of lung tumors, however, the density difference between the tumor mass and normal lung tissue may be large enough to provide a good visualization in radiographic images. Berbeco et al. [58] have found that direct detection of a lung tumor mass in kV X-ray images is possible if the tumor mass is small, well-defined, and has a high-contrast edge. Early stage lung cancer patients may have tumors that fulfill these requirements, and those patients may benefit from extra-cranial radiosurgery based on precise tumor tracking. For cases where contrast between tumor and normal tissue is low, direct tumor tracking may still be feasible, if CT data taken before each treatment fraction are combined with fluoroscopic images acquired during the treatment and advanced image processing/computer vision techniques are used. This technology is still in an early investigational stage.

On-board X-Ray Imaging

There are two categories of on-board kV X-ray imaging systems: room mounted and gantry mounted. Examples of room mounted systems are the Mitsubishi/Hokkaido RTRT, Accuray CyberKnife system, and BrainLab ExacTrac systems. Gantry mounted systems include Elekta Synergy, Varian Trilogy, and IRIS systems.

Room Mounted Imaging Systems

The RTRT (Real-Time Tumor-Tracking) system was developed by Mitsubishi Electronics Co. in collaboration with Hokkaido University [17]. As shown in Fig. 7a, the

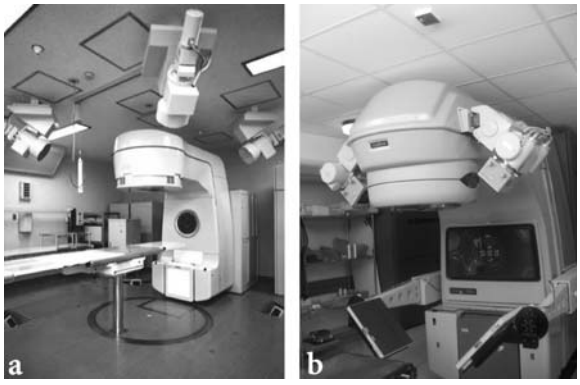

Fig. 7a,b. Photos of: (a) the Mitsubishi/Hokkaido Real-Time Tumor-Tracking (RTRT) system; (b) the Integrated Radiotherapy Imaging System (IRIS). (From: Shirato H, personal communication, with permission)

RTRT imaging system consists of four sets of diagnostic X-ray camera systems, each consisting of an X-ray tube mounted under the floor, a nine-inch image intensifier mounted in the ceiling, and a high-voltage X-ray generator. The four X-ray tubes are placed at right caudal, right cranial, left caudal, and left cranial position with respect to the patient couch at a distance of 280 cm from the isocenter. The image intensifiers are mounted on the ceiling, opposite to the X-ray tubes, at a distance of 180 cm from the isocenter, with beam central axes intersecting at the isocenter. At a given time during patient treatment, depending on the linac gantry angle, only two out of the four X-ray systems are enabled to provide a pair of orthogonal fluoroscopic images. To reduce the scatter radiation from the therapeutic beam to the imagers, the X-ray units and the linac are synchronized, i.e., the MV beam is gated off while the kV X-ray units are pulsed.

The imaging part of the CyberKnife system consists of two X-ray tubes mounted on the ceiling and two amorphous silicon (aSi) flat panel imagers mounted by each side of the treatment couch. The BrainLab ExacTrac system can also be potentially used for tumor tracking. It is similar to the Mitsubishi/Hokkaido RTRT system, using only two pairs of X-ray tubes and imagers instead of four.

Room mounted X-ray imaging systems are particularly suitable for real-time internal fiducial marker tracking during treatment. The X-ray sources and imagers are fixed on either floor or ceiling to provide high mechanic precision once calibrated. The imagers are far away from the patient (except for the CyberKnife system) so that the degradation of image quality by scattered MV photons is minimized. The downside of the large imager-patient distance is the smaller field of view and the lower imaging efficiency (which means higher imaging dose). Another weakness of room mounted systems is the unconventional imaging angles that make human interpretation of the imagers difficult.

Gantry Mounted Imaging Systems

The Synergy system was developed by Elekta Inc. in collaboration with William Beaumont Hospital. The system consists of an X-ray tube and an aSi flat panel imager mounted on the linac gantry and orthogonal to the therapy beam. A similar system (on-board imager, or OBI) has been developed by Varian Medical Systems, Inc. Both Synergy and OBI have the capability of acquiring cone beam CT scans with patients positioned on the treatment machine.

IRIS (Integrated Radiotherapy Imaging System) system has been developed by Massachusetts General Hospital and Varian Medical Systems, Inc. [58]. An earlier version of the system, developed by Varian, was first installed at Tohoku University, Japan [59]. As shown in Fig. 7b, the system consists of two gantry mounted diagnostic (kV) X-ray tubes and two flat panel aSi imagers. The central axes of the two kV X-ray beams are orthogonal to each other, 45° from the MV beam central axis, and intersecting with each other at the linac isocenter. The system was uniquely designed to integrate three main imaging functions (simultaneous orthogonal radiographs, cone-beam CT, and real-time tumor tracking) into a therapy system. Both X-ray sources are 100 cm away from the isocenter, while the imagers are at 162 cm distance from the isocenter. The fluoroscopic images can be acquired at a rate of 15 frames per second.

Gantry mounted systems can be used to acquire large field of view and conventional beam angle (anterior-posterior and lateral) radiographs, as well as cone beam CT data. The additional capability is potentially useful for difficult tracking cases such as direct lung tumor tracking. The major weakness of the gantry mounted systems is the suboptimal mechanical precision (e.g., gantry sagging) and the scatter radiation from the patient to the imagers.

Both Elekta Synergy and Varian OBI systems only have one imager. Theoretically speaking, to locate a tumor or marker in 3D, two simultaneous projection images from different directions are required, unless tumor motion is only along the cranial-caudal direction. Unfortunately, tumors often follow complex 3D trajectories and sometimes exhibit hysteresis [53]. Berbeco et al. [58] have shown that, even if one models the tumor trajectory before the treatment, one projection image still may not localize tumor position with sufficient accuracy. Combining other respiratory signals with the 2D image may improve the localization accuracy, but needs to be investigated.

System Tracking Failure Identification

Tracking radio-opaque markers in fluoroscopic imagers may seem straightforward. However, there are still technical challenges in practical scenarios, such as 1) the change of the marker shape from time to time when using a cylindrical or a wire marker; 2) the occlusion of

the markers by, or confusion with, the bony structure, air bubbles, and other objects in the image; 3) the confusion of multiple markers when they are close to each other at certain imaging angles; and 4) the poor image quality due to the MV beam interference.

Due to these practical challenges, there is no guarantee that the tracking algorithm is able to correctly localize the marker or tumor position 100% of the time. Therefore, accurate identification of system tracking failures has an important role in the clinical application of a tumor tracking system. When the tracking software fails, the treatment beam must be held off until the software resumes correct tracking. Repeated or unrecoverable tracking failures require human intervention, such as adjusting the software settings, adjusting the X-ray generator settings, etc.

Sharp et al. have developed a tracking failure detection algorithm [60]. The algorithm uses pattern-matching information such as the cross-correlation score, the 3D distance between rays that correspond to the same marker in the two images, and the regularity of the tumor motion. The method calculates the error probability from the set of available cues to decide if a tracking error has occurred.

Tumor Position Prediction

Given that one can locate and track the position of a tumor in real-time using diagnostic X-ray imaging, the delivery of a treatment plan through beam tracking (or gating, to a lesser extent, depending on the length of the gate) requires adequate consideration of treatment system latencies. Examples of the system latencies may include image acquisition, image processing, communication delays, control system processing, and for dynamic MLC based beam tracking, MLC mechanical latencies. Furthermore, the imaging dose given over long radiosurgery procedures or multiple radiotherapy fractions must be considered. Reducing the sampling rate of the imaging system can mitigate the adverse side effects of extend fluoroscopic exposure. Hence, predictive models are needed to reduce tumor localization errors that may result from the larger system latencies and slower imaging rate.

Let us assume that images are taken at a constant frequency, with a period of Δt, and the latency between image capture and treatment system response is $\Delta t'$ (see Fig. 8). For an image at time t, because of the latency, decisions made for treatment cannot be performed until time $t + \Delta t'$. Because of the imaging frequency, the image at time t (and preferably previous images) will be used for treatment until time $t + \Delta t' + \Delta t$. When both the imaging period and system latency are small enough, the tumor positions between $t + \Delta t'$ and $t + \Delta t' + \Delta t$ can be approximated using its position at time t. However, this approximation can introduce significant localization errors when system latency is not negligible, or when the X-ray imaging frequency is reduced to limit imaging dose. Figure 9 shows the kinds of errors introduced by long system latencies (a) and reduced imaging frequency (b). In these plots, the most recent measurement is shown with a dashed line, and the true position is shown with a solid line. Treatment based solely on the most recent measurement will consistently miss the target.

Preliminary results from investigations in this area suggest that improvements in targeting accuracies can be realized. Shirato et al. have used linear extrapolation to estimate the future position of a tumor, and have evaluated the accuracy on phantom measurements [18]. Murphy et al. compare two adaptive prediction meth-

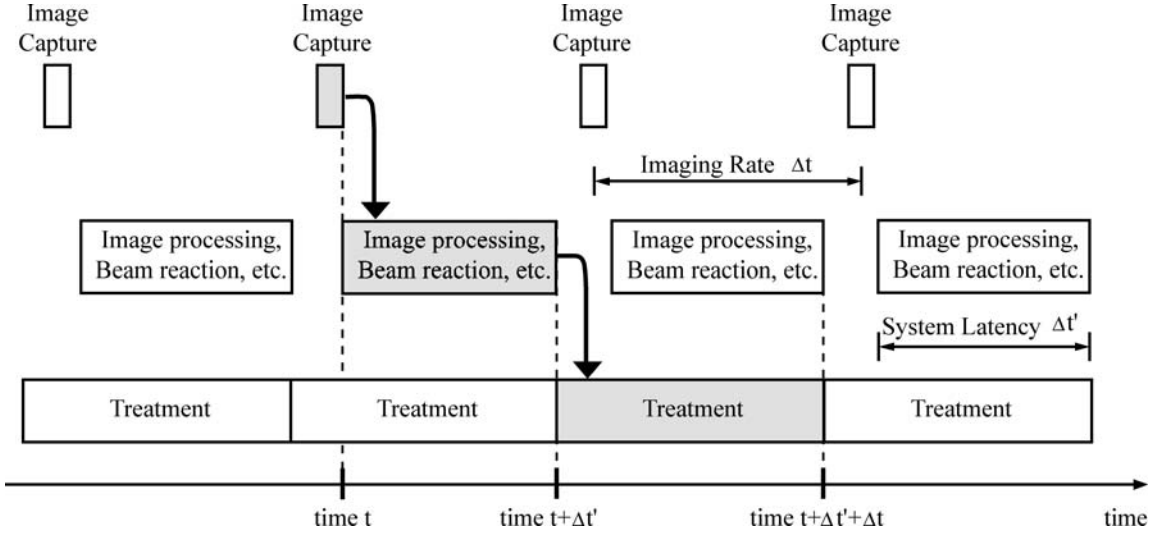

Fig. 8. A diagram illustrating the problem of tumor position prediction. For a system with an imaging period of Δt and a system latency of $\Delta t'$, an image captured at time t (*shown in grey*) must be used for treatment between time $t + \Delta t'$ and time $t + \Delta t' + \Delta t$. (Reprinted from Physics in Medicine and Biology, vol 49, Sharp GC et al., Prediction of respiratory tumour motion for real-time image-guided radiotherapy, pp 425–440, Copyright (2004) with permission from Institute of Physics and IOP Publishing)

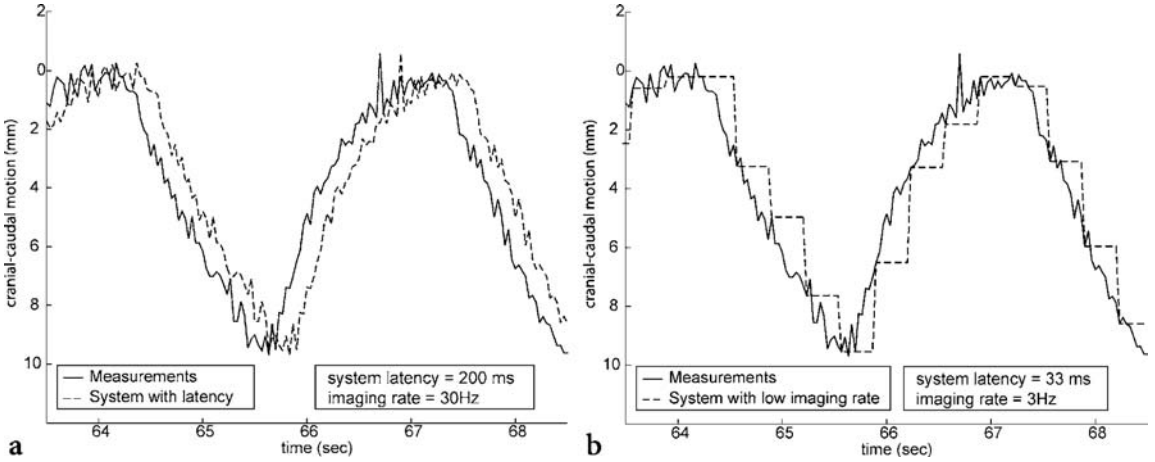

Fig. 9a,b. Effect of large system latency and slow imaging rate on tumor localization accuracy: **(a)** a system with latency of 200 ms and imaging rate of 30 Hz; **(b)** a system with latency of 33 ms and imaging rate of 3 Hz. (Reprinted from Physics in Medicine and Biology, vol 49, Sharp GC et al., Prediction of respiratory tumour motion for real-time image-guided radiotherapy, pp 425–440, Copyright (2004) with permission from Institute of Physics and IOP Publishing)

ods for overcoming system latencies using data taken from fluoroscopic simulation [61]. Sharp et al. have used measured lung tumor trajectory data to evaluate the performance of several generic prediction algorithms (linear prediction, neural network prediction, and Kalman filtering) against a system that uses no prediction [62]. At all latency intervals and image sampling rates evaluated, prediction methods improved the root-mean-squared error accuracy of tumor localization during the treatment window between $t+\Delta t'$ and $t+\Delta t'+\Delta t$. Further development is necessary in order to have clinically robust, efficient, and accurate prediction software.

Real-Time Beam Adaptation

Methods for Real-time Beam Alignment

By knowing the tumor position during the treatment, through real-time marker tracking and position predicting, the treatment delivery system can respond accordingly. One way is to gate the beam on at a particular tumor position [17], the other is to align the beam with the instantaneous tumor position. Murphy [54] has summarized four possible ways for real-time beam alignment: 1) move the patient using a remotely-controlled couch, 2) move a charged particle beam electromagnetically, 3) move a robotically mounted lightweight linear accelerator, and 4) move the aperture shaped by a dynamic multileaf collimator (DMLC).

Technically, it is feasible to shift the patient to cancel out the tumor motion by repositioning a remote-controlled couch [63]. However, to track respiratory motion, the practicality of this method is questionable, because the constant motion will cause problems of patient comfort and the non-rigidity of the human body will compromise the tracking accuracy. Within the context of IMRT with X-rays, we will address methods 3) and 4) for real-time beam alignment.

The CyberKnife system has implemented motion of a linear accelerator in real-time to follow the tumor, by means of a lightweight 6 MV X-band linac mounted on an industrial robotic arm. A real-time control loop monitors the tumor position from the imaging system and directs the repositioning of the linac [31,50,51]. The major strength of the system is that it can move and orient the X-ray beam with six degrees of freedom, so that it can adapt to the full 3D motion of the tumor. A disadvantage is that the system has limited beam output and beam size, therefore the treatment time can be lengthy for large size tumors.

Tumor tracking by means of a DMLC shaped aperture is an active area of investigation [3, 64–66]. DMLC has become a standard means of IMRT delivery on some gantry-mounted linacs. The MLC leaf travel speed can safely reach 2.5 cm/s, which is comparable with respiration induced tumor motion speed. Since it only moves the beam aperture in 2D, the approach can not compensate out-of-plane tumor motion. However, the resultant dosimetric error should be small.

Because of its potential for providing high dose conformity and high duty cycle, as well as its technical complexity, real-time beam adaptation methods are suitable for hypofractionated thoracic and abdominal cancer treatment. However, there are a number of technical hurdles before this approach becomes clinically feasible. These include treatment planning, and the accurate response of the MLC to tumor positions measured in real time. The actual tumor movement as well as its relationship to surrounding critical structures during the treatment cannot be known at the time of treatment planning. Therefore, treatment planning can only be done based on some kind of average patient geometry information or at best on 4D-CT simulation data,

and an adaptive scheme must be used throughout the treatment course.

Synchronized Moving Aperture Radiation Therapy (SMART)

Synchronized Moving Aperture Radiation Therapy (SMART), developed at Massachusetts General Hospital, is a simplified implementation of DMLC based real-time beam adaptation technology [64]. The basic assumption is that, under breath coaching or other kinds of breath regulation, the tumor motion pattern is stable and reproducible during the whole treatment course; therefore, it can be measured prior to treatment and used to modify the treatment plan. The practical implementation includes: 1) during treatment simulation and planning, tumor motion data are measured and the average tumor trajectory (ATT) is derived; then the IMRT MLC leaf sequence is modified based on the ATT to compensate for tumor motion; 2) during treatment delivery, respiratory surrogates or implanted markers are monitored and used to synchronize the treatment with tumor motion. Treatment can be interrupted and resumed if target motion differs from the average trajectory.

Studies have shown the practicality and effectiveness of breath coaching for improving the regularity and reproducibility of patient breathing [27, 28]. Another method is to control patient breathing to follow a preset pattern using a ventilator [66]. A method for deriving the ATT from the measured tumor trajectory has been developed [64]. Figure 10 shows a typical ATT. Including tumor motion into an IMRT MLC leaf sequence seems a straightforward superposition process. However, it can be very complicated when considering the hardware constraints of MLC, such as the maximum leaf travel speed, communication time delay, minimum leaf gap, and acceleration constraints.

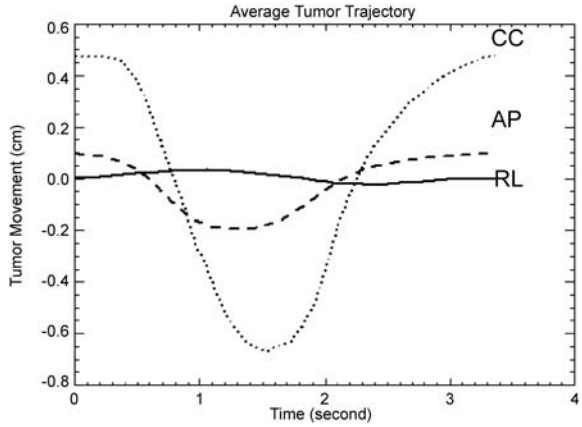

Fig. 10. A typical average tumor trajectory (ATT) derived from the measured trajectory

Instead of modifying an existing leaf sequence to include tumor motion, one can also consider the tumor motion at the leaf sequencing stage, or include the motion at the treatment planning stage, if 4D CT data are available. Papiez has developed a leaf sequencing algorithm that optimizes the leaf sequence for a moving target system [65]. When 4D CT data are available, it is possible to optimize the SMART treatment plan incorporating the tumor motion present in the images. Jiang et al. have developed an optimization scheme which does not require mapping voxel displacements between image sets at different phases [67]. The optimization results in one intensity map for each breathing phase and field. The leaf sequencing algorithm for SMART is analogous to that for Intensity Modulated Arc Therapy (IMAT), with breathing phase corresponding to the gantry angle from 0° to 360° [68]. Further studies are needed in order to make this approach clinically useful.

Table 1. Summary of intra- and inter- fractional variations for different methods of respiratory management

Reference	Technique	Organ	Intra-fraction variation (cm)	Inter-fraction variation (cm)
[42]	BH at inspiration with ABC	Lung tumor	–	SD: 0.18 LR, 0.23 AP, 0.35 SI
[32]	BH at expiration with ABC	Diaphragm	SD: 0.25	SD: 0.44
[11]	Gating at expiration with RPM	Diaphragm	Mean: 0.26 SD: 0.17	Mean: 0.0 SD: 0.39
[35]	DIBH	Diaphragm	SD: 0.25	–
[33]	DIBH	Diaphragm	–	0. 4[a]
[49]	Abdominal compression with stereotactic body frame	Lung tumor	Mean 3D: 0.7 Range: 0.2–1.1	Mean 3D: 0. 5[a] Range: 0.4–0. 8[a]
[38]	mDIBH with ABC	Diaphragm	Mean: 0.14 SD: 0.17	Mean 0.19 SD: 0.22
[21]	Gating at expiration with RPM	Abdominal organs	Mean: 0.20	–

Abbreviations: BH breath-hold, ABC active breathing control, SD standard deviation, LR left-right, AP anterior-posterior, SI superior-inferior, DIBH deep inspiration breath-hold, 3D three-dimensional error, mDIBH moderately deep inspiration breath-hold [a]Includes setup error

11.4 Summary and Conclusions

This chapter has briefly discussed the effect of respiratory motion on radiation dose delivery, and surveyed different methods to manage respiratory motion in radiation treatment. Respiratory motion during radiation delivery with static fields blurs the planned dose distribution. The interplay between respiratory motion and IMRT delivered with an MLC can produce areas of overdose and underdose in moving tissue for single fraction (and possibly hypofractionated) treatment, but for multiple field treatments with 30 fractions and assuming simple tissue motion patterns, the resultant dose distributions are similar to statically delivered treatments. Table 1 summarizes intra- and inter-fractional variations for different "freeze the motion" techniques discussed here. In cases of limited tumor mobility, it may be not be necessary to take any measures to control respiratory motion during treatment, provided that it is properly accounted for during imaging for treatment planning and in the PTV definition, and that possible changes are monitored at treatment. A common goal of "freeze the motion" strategies is to immobilize the tumor. For some disease sites, breath hold with increased lung inflation can be of additional benefit in sparing organs at risk. It is important to keep in mind that "freeze the motion" strategies described here are still in the investigational stages. The validity of an external respiration monitor in inferring internal anatomical position, and the potential for changes over the course of treatment, should be measured and taken into account through a careful program of imaging at simulation and treatment. Tumor tracking technology relies on real-time localization of 3D tumor position directly by means of on-board X-ray imaging systems, additionally requiring system tracking failure identification, tumor position prediction, and real-time beam adaptation to the moving tumor. Although much of the technology is still under development, it seems a promising tool for precisely and efficiently delivering large single or hypofractionated doses to tumors in the thorax and abdomen.

Acknowledgements. We thank Dr. John Wong for contributing material on the active breathing control studies, and Drs. Greg Sharp, Ross Berbeco, and Toni Neicu for their contribution to the tumor tracking section.

References

1. Bortfeld T, Jiang SB, Rietzel E (2004) Effects of motion on the total dose distribution. Semin Radiat Oncol 14:41–50
2. Yu CX, Jaffray DA, Wong JW (1998) The effects of intra-fraction organ motion on the delivery of dynamic intensity modulation. Phys Med Biol 43:91–104
3. Keall PJ, Kini VR, Vedam SS, Mohan R (2001) Motion adaptive X-ray therapy: a feasibility study. Phys Med Biol 46:1–10
4. Bortfeld T, Jokivarsi K, Goitein M, Kung J, Jiang SB (2002) Effects of intra-fraction motion on IMRT dose delivery: statistical analysis and simulation. Phys Med Biol 47:2203–2220
5. Chui CS, Yorke E, Hong L (2003) The effects of intra-fraction organ motion on the delivery of intensity-modulated field with a multileaf collimator. Med Phys 30:1736–1746
6. Jiang SB, Pope C, Al Jarrah KM, Kung JH, Bortfeld T, Chen GT (2003) An experimental investigation on intra-fractional organ motion effects in lung IMRT treatments. Phys Med Biol 48:1773–1784
7. Balter JM, Ten Haken RK, Lawrence TS, Lam KL, Robertson JM (1996) Uncertainties in CT-based radiation therapy treatment planning associated with patient breathing. Int J Radiat Oncol Biol Phys 36:167–174
8. Chen GTY, Kung J, Beaudette KP (2004) Artifacts in computed tomography scanning of moving objects. Semin Radiat Oncol 14:19–26
9. Mechalakos J, Yorke E, Mageras G, Hertanto A, Jackson A, Obcemea C, Rosenzweig K, Ling C (2004) Dosimetric effect of respiratory motion in external beam radiotherapy of the lung. Radiother Oncol 71:191–200
10. van Herk M (2004) Is it safe to ignore respiration during external beam radiotherapy? In: Yi BY, Ahn SD, Choi EK, Ha SW (eds) The 14th International Conference on the Use of Computers in Radiotherapy. Jeong Publishing, Seoul, South Korea, p 44
11. Ford E, Mageras GS, Yorke E, Rosenzweig KE, Wagman R, Ling CC (2002) Evaluation of respiratory movement during gated radiotherapy using film and electronic portal imaging. Int J Radiat Oncol Biol Phys 52:522–531
12. Yorke E, Rosenzweig K, Wagman R, Mageras G (2005) Inter-fractional anatomic variation in patient treated with respiration-gated radiotherapy. J Applied Clin Med Phys 6: 19-32
13. van Herk M, Remeijer P, Rasch C, Lebesque JV (2000) The probability of correct target dosage: dose-population histograms for deriving treatment margins in radiotherapy. Int J Radiat Oncol Biol Phys 47:1121–1135
14. Ohara K, Okumura T, Akisada M et al. (1989) Irradiation synchronized with respiration gate. Int J Radiat Oncol Biol Phys 17:853–857
15. Okumara T, Tsuji H, Hayakawa Y (1994) Respiration-gated irradiation system for proton radiotherapy. In: Hounsell AR, Wilkinson JM, Williams PC (eds) Proceedings of the 11th International Conference on the Use of Computers in Radiation Therapy. North Western Medical Physics Dept. Christie Hospital, Manchester, pp 358–359
16. Tada T, Minakuchi K, Fujioka T, Sakurai M, Koda M, Kawase I, Nakajima T, Nishioka M, Tonai T, Kozuka T (1998) Lung cancer: intermittent irradiation synchronized with respiratory motion – results of a pilot study. Radiology 207:779–783
17. Shirato H, Shimizu S, Kitamura K, Nishioka T, Kagei K, Hashimoto S, Aoyama H, Kunieda T, Shinohara N, Dosaka-Akita H, Miyasaka K (2000a) Four-dimensional treatment planning and fluoroscopic real-time tumor tracking radiotherapy for moving tumor. Int J Radiat Oncol Biol Phys 48:435–442
18. Shirato H, Shimizu S, Kunieda T, Kitamura K, van Herk M, Kagei K, Nishioka T, Hashimoto S, Fujita K, Aoyama H,

Tsuchiya K, Kudo K, Miyasaka K (2000b) Physical aspects of a real-time tumor-tracking system for gated radiotherapy. Int J Radiat Oncol Biol Phys 48:1187–1195
19. Kubo H, Len P, Minohara S, Mostafavi H (2000) Breathing-synchronized radiotherapy program at the University of California Davis Cancer Center. Med Phys 27:346–353
20. Ramsey CR, Scaperoth D, Arwood D (2000) Clinical experience with a commercial respiratory gating system (abstract). Int J Radiat Oncol Biol Phys 48:164–165
21. Wagman R, Yorke E, Giraud P, Ford E, Sidhu K, Mageras G, Minsky B, Rosenzweig K (2003) Reproducibility of organ position with respiratory gating for liver tumors: use in dose-escalation. Int J Radiat Oncol Biol Phys 55:659–668
22. Vedam SS, Kini VR, Keall PJ, Ramakrishnan V, Mostafavi H, Mohan R (2003) Quantifying the predictability of diaphragm motion during respiration with a noninvasive external marker. Med Phys 30:505–513
23. Butler L, Forster KM, Stevens CW, Tucker S, Starkschall G (2002) Dosimetric benefits of respiratory gating (abstract). Med Phys 29:1239
24. Ramsey CR, Cordrey IL, Oliver AL (1999) A comparison of beam characteristics for gated and nongated clinical X-ray beams. Med Phys 26:2086–2091
25. Kubo HD, Wang L (2000) Compatibility of Varian 2100C gated operations with enhanced dynamic wedge and IMRT dose delivery. Med Phys 27:1732–1738
26. Yorke E, Mageras G, LoSasso T (2000) Respiratory gating of sliding window IMRT. In: Fullerton G (eds) CD-ROM Proceedings of the World Congress on Medical Physics and Biomedical Engineering. American Association of Physicists in Medicine, Chicago, p 4
27. Mageras GS, Yorke E, Rosenzweig K, Braban L, Keatley E, Ford E, Leibel SA, Ling CC (2001) Fluoroscopic evaluation of diaphragmatic motion reduction with a respiratory gated radiotherapy system. J Appl Clin Med Phys 2:191–200
28. Kini VR, Vedam SS, Keall PJ, Patil S, Chen C, Mohan R (2003) Patient training in respiratory- gated radiotherapy. Med Dosim 28:7–11
29. Kubo HD, Wang L (2002) Introduction of audio gating to further reduce organ motion in breathing synchronized radiotherapy. Med Phys 29:345–350
30. Ozhasoglu C, Murphy MJ (2002) Issues in respiratory motion compensation during external-beam radiotherapy. Int J Radiat Oncol Biol Phys 52:1389–1399
31. Chen QS, Weinhous MS, Deibel FC, Ciezki JP, Macklis RM (2001) Fluoroscopic study of tumor motion due to breathing: facilitating precise radiation therapy for lung cancer patients. Med Phys 28:1850–1856
32. Dawson LA, Brock KK, Kazanjian S, Fitch D, McGinn CJ, Lawrence TS, Ten Haken RK, Balter J (2001) The reproducibility of organ position using active breathing control (ABC) during liver radiotherapy. Int J Radiat Oncol Biol Phys 51:1410–1421
33. Mah D, Hanley J, Rosenzweig KE, Yorke E, Braban L, Ling CC, Mageras G (2000) Technical aspects of the deep inspiration breath hold technique in the treatment of thoracic cancer. Int J Radiat Oncol Biol Phys 48:1175–1185
34. Stevens CW, Munden RF, Forster KM, Kelly JF, Liao Z, Starkschall G, Tucker S, Komaki R (2001) Respiratory-driven lung tumor motion is independent of tumor size, tumor location, and pulmonary function. Int J Radiat Oncol Biol Phys 51:62–68
35. Hanley J, Debois MM, Mah D, Mageras GS, Raben A, Rosenzweig K, Mychalczak B, Schwartz LH, Gloeggler PJ, Lutz W, Ling CC, Leibel SA, Fuks Z, Kutcher GJ (1999) Deep inspiration breath-hold technique for lung tumors: the potential value of target immobilization and reduced lung density in dose escalation. Int J Radiat Oncol Biol Phys 45:603–611
36. Wong JW, Sharpe MB, Jaffray DA, Kini VR, Robertson JM, Stromberg JS, Martinez AA (1999) The use of active breathing control (ABC) to reduce margin for breathing motion. Int J Radiat Oncol Biol Phys 44:911– 919
37. Stromberg JS, Sharpe M, Kim LH, Kini V, Jaffray DA, Martinez AA, Wong JW (2000) Active breathing control (ABC) for Hodgkin's disease: reduction in normal tissue irradiation with deep inspiration and implications for treatment. Int J Radiat Oncol Biol Phys 48:797–806
38. Remouchamps VM, Letts N, Yan D, Vicini F, Moreau M, Zielinski JA, Liang J, Kestin L, Martinez A, Wong JW (2003a) Three dimensional evaluation of intra- and inter-fraction reproducibility of lung and chest wall immobilization using active breathing control. Int J Radiat Oncol Biol Phys 57:968–978
39. Remouchamps VM, Vicini FA, Sharpe MB, Kestin LL, Martinez AA, Wong JW (2003b) Significant reductions in heart and lung doses using deep inspiration breath hold with active breathing control and intensity-modulated radiation therapy for patients treated with locoregional breast irradiation. Int J Radiat Oncol Biol Phys 55:392–406
40. Sixel KE, Aznar MC, Ung YC (2001) Deep inspiration breath hold to reduce irradiated heart volume in breast cancer patients. Int J Radiat Oncol Biol Phys 49:199–204
41. Balter JM, Brock KK, Litzenberg DW, McShan DL, Lawrence TS, Haken RT, McGinn CJ, Lam KL, Dawson LA (2002) Daily targeting of intrahepatic tumors for radiotherapy. Int J Radiat Oncol Biol Phys 52:266–271
42. Cheung PCF, Sixel KE, Tirona R, Ung YC (2003) Reproducibility of lung tumor position and reduction of lung mass within the planning target volume using active breathing control (ABC). Int J Radiat Oncol Biol Phys 57:1437–1442
43. Wilson EM, Williams FJ, Lyn BE, Wong JW, Aird EGA (2003) Validation of active breathing control in patients with non-small-cell lung cancer to be treated with CHARTWEL. Int J Radiat Oncol Biol Phys 57:864–874
44. Rosenzweig KE, Hanley J, Mah D, Mageras G, Hunt M, Toner S, Burman C, Ling CC, Mychalczak B, Fuks Z, Leibel S (2000) The deep inspiration breath hold technique in the treatment of inoperable non-small cell lung cancer. Int J Radiat Oncol Biol Phys 48:81–87
45. Spirou SV, Chui CS (1994) Generation of arbitrary intensity profiles by dynamic jaws or multileaf collimators. Med Phys 21:1031–1041
46. Yorke ED, Wang L, Rosenzweig KE, Mah D, Paoli J-B, Chui C-S (2002) Evaluation of deep inspiration breath-hold lung treatment plans with Monte Carlo dose calculation. Int J Radiat Oncol Biol Phys 53:1058–1070
47. Paoli J, Rosenzweig K, Yorke E, Hanley J, Mah D, Mageras GS, Hunt MA, Braban LE, Leibel SA, Ling CC (1999) Comparison of different phases of respiration in the treatment of lung cancer: implications for gated treatment. Int J Radiat Oncol Biol Phys 45:386–387
48. Blomgren H, Lax I, Naslund I (1995) Stereotactic high dose fraction radiation therapy of extracranial tumors using an accelerator: Clinical experience of the first thirty-one patients. Acta Oncol 34:861–870
49. Negoro Y, Nagata Y, Aoki T, Mizowaki T, Araki N, Takayama K, Kokubo M, Yano S, Koga S, Sasai K (2001) The effectiveness of an immobilization device in conformal radiotherapy for lung tumor: reduction of respiratory tumor movement and evaluation of the daily setup accuracy. Int J Radiat Oncol Biol Phys 50:889–898

50. Schweikard A, Glosser G, Bodduluri M, Murphy MJ, Adler JR (2000) Robotic motion compensation for respiratory movement during radiosurgery. Comput Aided Surg 5:263–277
51. Murphy MJ, Adler JR Jr, Bodduluri M, Dooley J, Forster K, Hai J, Le Q, Luxton G, Martin D, Poen J (2000) Image-guided radiosurgery for the spine and pancreas. Comput Aided Surg 5:278–288
52. Shimizu S, Shirato H, Ogura S, Akita-Dosaka H, Kitamura K, Nishioka T, Kagei K, Nishimura M, Miyasaka K (2001) Detection of lung tumor movement in real-time tumor-tracking radiotherapy. Int J Radiat Oncol Biol Phys 51:304–310
53. Seppenwoolde Y, Shirato H, Kitamura K, Shimizu S, van Herk M, Lebesque JV, Miyasaka K (2002) Precise and real-time measurement of 3D tumor motion in lung due to breathing and heartbeat, measured during radiotherapy. Int J Radiat Oncol Biol Phys 53:822–834
54. Murphy MJ (2004) Tracking moving organs in real time. Semin Radiat Oncol 14:91–100
55. Seiler PG, Blattmann H, Kirsch S, Muench RK, Schilling C (2000) A novel tracking technique for the continuous precise measurement of tumour positions in conformal radiotherapy. Phys Med Biol 45:N103–N110
56. Russell K, Skrumeda L, Gisselberg M, Hadford E, Humphries D, Sandler H, Roach M, Kupelian P, Mate T (2003) Biocompatibility of a wireless electromagnetic transponder permanent implant for accurate localization and continuous tracking of tumor targets. Int J Radiat Oncol Biol Phys 57:S396–S397
57. Meeks SL, Buatti JM, Bouchet LG, Bova FJ, Ryken TC, Pennington EC, Anderson KM, Friedman WA (2003) Ultrasound-guided extracranial radiosurgery: technique and application. Int J Radiat Oncol Biol Phys 55:1092–1101
58. Berbeco RI, Mostafavi H, Sharp GC, Jiang SB (2004) Tumor tracking in the absence of radiopaque markers. In: Yi BY, Ahn SD, Choi EK, Ha SW (eds) The 14th International Conference on the Use of Computers in Radiation Therapy. Jeong Publishing, Seoul, Korea, pp 433–436
59. Takai Y, Mitsuya M, Nemoto K, Ogawa Y, Matsusita H, Yamada S, Mostafavi H, Marc M, Jeung A, Manfield S (2001) Development of a new linear accelerator mounted with dual X-ray fluoroscopy using amorphous silicon flat panel X-ray sensors to detect a gold seed in a tumor at real treatment position. Int J Radiat Oncol Biol Phys 51:381
60. Sharp GC, Jiang SB, Shimizu S, Shirato H (2004) Identification of tracking failures in a real-time tumor tracking system (personal communication)
61. Murphy MJ, Jalden J, Isaksson M (2002) Adaptive filtering to predict lung tumor breathing motion during image-guided radiation therapy. In: Lemke HU, Inamura K, Vannier MW, Farman AG, Doi K (eds) Proc 16th Int Conf on Computer Assisted Radiology (CARS 2002)
62. Sharp GC, Jiang SB, Shimizu S, Shirato H (2003) Prediction of respiratory tumor motion for real-time image guided radiotherapy. Phys Med Biol 49:425–440
63. Bel A, Petrascu O, Van de Vondel I, Coppens L, Linthout N, Verellen D, Storme G (2000) A computerized remote table control for fast on-line patient repositioning: implementation and clinical feasibility. Med Phys 27:354–358
64. Neicu T, Shirato H, Seppenwoolde Y, Jiang SB (2003) Synchronized moving aperture radiation therapy (SMART): average tumour trajectory for lung patients. Phys Med Biol 48:587–598
65. Papiez L (2003) The leaf sweep algorithm for an immobile and moving target as an optimal control problem in radiotherapy delivery. Math Comput Modelling 37:735–745
66. Suh Y, Yi B, Ahn S, Kim J, Lee S, Shin S, Shin S, Choi E (2004) Aperture maneuver with compelled breath (AMC) for moving tumors: A feasibility study with a moving phantom. Med Phys 31:760–766
67. Jiang S, Bortfeld T, Trofimov A, Rietzel E, Sharp G, Choi N, Chen GTY (2004) Synchronized Moving Aperture Radiation Therapy (SMART): Treatment planning using 4D CT data. In: Yi BY, Ahn SD, Choi EK, Ha SW (eds) The 14th International Conference on the Use of Computers in Radiation Therapy. Jeong Publishing, Seoul, Korea, pp 429–431
68. Yu CX (1995) Intensity-modulated arc therapy with dynamic multileaf collimation: an alternative to tomotherapy. Phys Med Biol 40:1435–1449
69. Della Biancia C, Yorke E, Chui CS, Giraud P, Rosenzweig K, Amols H, Ling C, Mageras G (2005) Comparison of end normal inspiration and expiration for gated intensity modulated radiation therapy (IMRT) of lung cancer . Radiother Oncol 75:149-156

Part III
Clinical

IMRT for Paranasal Sinus and Nasal Cavity (Sino-Nasal) Tumors

Wim Duthoy, Wilfried De Neve

1

Contents

1.1 Clinical Problem

1.1.1 Epidemiology, Natural History and Treatment Options

The term sino-nasal tumor is used for tumors arising from the paranasal sinuses (= ethmoid, maxillary, frontal and sphenoid sinuses) and of the nasal cavity (excluding the nasal vestibulum). The estimated number of new patients with a sino-nasal tumor per physician is 1 in 50 years for a general practitioner, 1 per year for an ear-nose-throat surgeon and between 10 and 15 new patients for a center for head and neck oncology [1]. The site of origin in paranasal sinus cancer is most frequently the maxillary sinus or the ethmoid sinus complex. Tumors originating from the frontal or sphenoid sinus are extremely rare.

Most tumors are advanced at diagnosis. They commonly involve the nasal cavity and several adjacent sinuses. The presenting symptoms depend on the site(s) of involvement (nasal cavity vs ethmoid sinus or maxillary sinus), but commonly include nasal obstruction and/or discharge, intermittent epistaxis and headache. The relative banality and high prevalence of these symptoms in combination with the low prevalence of this cancer explains why the diagnosis of sino-nasal cancer is often made in an advanced stage. More severe symptoms are caused by contiguous invasion outside the sino-nasal structures. Knowledge of the routes of invasion is relevant for CTV definition. Orbital invasion occurs commonly in maxillary or ethmoid sinus tumors. Associated symptoms are tearing, diplopia and/or proptosis. The anterior cranial fossa is invaded through the cribriform plate and the roof of the ethmoid sinuses. Associated symptoms are hypo- or anosmia, headache and even personality changes.

Tumors involving the cranial part of the nasal cavity tend to destroy the septum and may invade the nasal bone and eventually the skin. Associated symptoms are deformation of the nasal bridge, swelling and skin ulcer-

ation. Tumors involving the maxillary floor may invade through the hard palate and oral mucosa or more laterally though the bone to appear at the gingivo-buccal sulcus. Associated symptoms are toothache and problems with dental prostheses. Tumors that invade through the posterior maxillary bone invade the infra-temporal fossa, and the pterygoid plates. Associated symptoms are trismus and earache. The middle cranial fossa is reached by way of the infratemporal fossa, the pterygoid plates or by lateral extension directly from the sphenoid sinus. Nasopharyngeal extension is common in tumors involving the ethmoid sinuses or the nasal cavity.

Sino-nasal mucosae contain sparse lymphatic capillary networks. Nodal involvement is infrequent in tumors of epithelial origin, less than 10% at the time of diagnosis [2]. Lymph node areas II and I are the most common sites of involvement.

A wide variety of histologies can be found in sino-nasal tumors. The most common tumor histology is squamous cell carcinoma followed by adenocarcinoma and adenoid cystic carcinoma [3]. Undifferentiated carcinomas rank fourth in incidence. Other, less frequent histologies include esthesioneuroblastoma, malignant melanoma, lymphomas and sarcomas. The reader should be noted that the subsequent discussion is mainly dealing with carcinomas, and that the treatment options for these rare histological types can differ considerably. Of interest to the radiation oncologist are high local control rates obtained by high-LET particle therapy of melanomas and adenoid cystic carcinomas [4, 5].

For carcinomas, a combined treatment of surgery and radiation therapy is generally recommended [6, 7]. Radiotherapy as the only treatment modality is usually reserved for patients who are unfit for surgery or have inoperable disease. Radical neck dissection or neck nodal irradiation is generally recommended only for patients presenting with positive nodes. The role of systemic chemotherapy in the management of these tumors remains unclear.

1.1.2 Surgery

The surgical approach to the sino-nasal tumors can be endoscopic (eg for small nasal tumors) by lateral rhinotomy or using a craniofacial fenestration (in cases of invasion of the cribriform plate). The objective of maximal debulking is balanced against the morbidity of surgery involving orbit, pterygopalatine fossa, cavernous sinus, and anterior or middle cranial fossa. In a combined approach with surgery and radiation, functional sparing is usually attempted. Enucleation is performed only in those cases with pre-existing blindness of the eye. To avoid excessive morbidity, en-block resection of tumor invading pterygoid plates, infratemporal fossa or cavernous sinus is almost never conducted.

In the combined approach, it is accepted that the vicinity of the eyes, the cranial nerves and the brain to the sino-nasal cavities hampers broad resection margins, and results in close shave resections nearby these organs at risk. The combination of conservative surgery with radiation therapy is obvious.

1.1.3 Results of Treatment

Due to the low incidence of the disease, most reported series are small and present treatment results from a (retrospectively analyzed) mixture of different histologies and treatments, often accumulated over many years. This complicates the interpretation, and certainly the comparison, of treatment results. Dulguerov conducted a review of 154 articles published including a total of 16,396 patients treated between 1960 and 1998 [3]. When classified according to the decade of treatment, the overall survival rates showed a progressive increase from $28 \pm 13\%$ in the 1960s, $36 \pm 13\%$ in the 1970s, $43 \pm 15\%$ in the 1980s to $51 \pm 14\%$ in the 1990s. In univariate analysis, histology, tumor site, tumor extension and treatment modality were significant prognostic factors. For patients treated in the 1990s ($n = 3416$), overall survival was $60 \pm 24\%$, $50 \pm 14\%$, $50 \pm 19\%$ and $28 \pm 21\%$, for adenoid cystic, adeno-, squamous cell and undifferentiated carcinoma respectively. Considering the 1990s for tumor site of origin, T-stage and treatment modality, overall survival was $66 \pm 15\%$, $51 \pm 15\%$ and $45 \pm 11\%$ for nasal cavity, ethmoid sinus and maxillary sinus respectively; $90 \pm 19\%$, $70 \pm 30\%$, $44 \pm 29\%$ and $28 \pm 18\%$ for T1, T2, T3 and T4-stage respectively; and $70 \pm 20\%$, $56 \pm 13\%$, $33 \pm 18\%$ and $42 \pm 18\%$ for surgery alone, surgery plus radiation therapy, radiation therapy alone and schedules involving chemotherapy respectively. Data on treatment modality are biased in patient selection. Patients with favorable lesions are found mainly in the surgery alone group while patients with unresectable tumors or treated with palliative intend are found in the radiotherapy alone or chemotherapy groups. No randomized study has been published. In multivariate analysis, tumor histology, extension to the pterygopalatine fossa and invasion of the dura remained significant prognostic factors [3].

1.2 Unique Anatomical Challenges

The anterior radiograph in Fig. 1a and the drawing in Fig. 1b show that the orbits are separated from the frontal, ethmoidal and maxillary sinuses by tiny bony walls. The anterior cranial fossa and the frontal lobes of the brain are at close distance from the frontal and sphenoid sinuses and from the roof of the nasal cavity (Fig. 1c) as well as from the roof of the ethmoidal sinuses

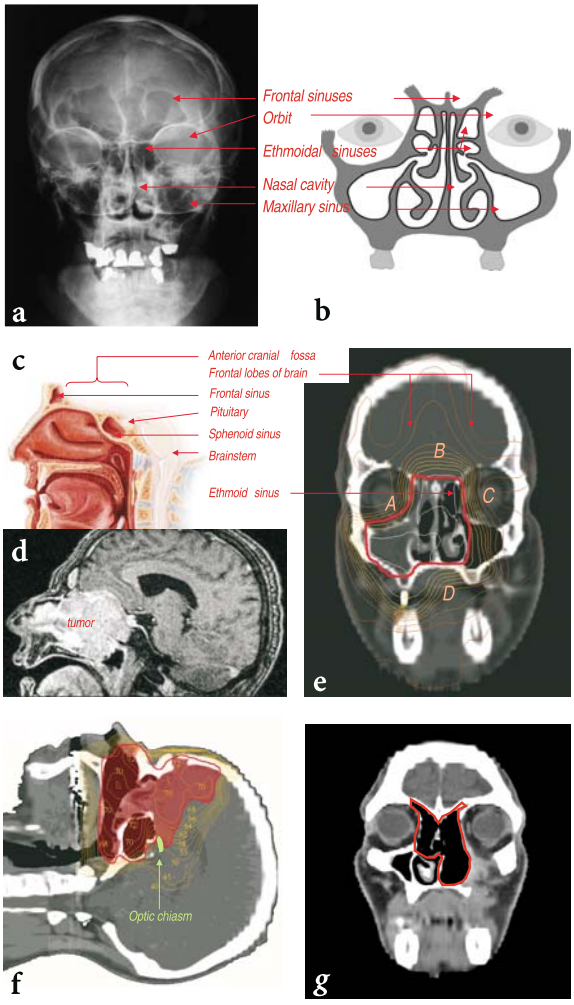

Fig. 1. (a) Anterior radiograph showing sino-nasal anatomy. (b) Drawing of the nasal cavity and the frontal, ethmoidal and maxillary sinuses. (c) Drawing of the frontal and sphenoid sinuses. (d) Advanced tumor destroying the bony septa between the sino-nasal cavities as well as the skull base. (e) Challenges for IMRT (see text). Regions A–D where steep gradients are required. (f) Steep gradients and concavities in the dose distribution may be needed posterior to spare the optic chiasm and the brain stem. (g) Large air cavities may result from surgical debulking

(Fig. 1e). Advanced tumors as shown in Fig. 1d, may destroy the bony septa between the sino-nasal cavities as well as the skull base. Challenges for IMRT (illustrated by Fig. 1e) include the creation of a concave dose distribution to keep the dose at the optic pathway structures (retina, optic nerves) and at the lacrimal apparatus within tolerance (A); the creation of a steep cranial (B), lateral (C) and caudal (D) gradient to avoid brain necrosis, to spare the optic structures at the opposite site and to limit oral cavity toxicity. Steep gradients and concavities in the dose distribution may be needed posterior to spare the optic chiasm and the brain stem as illustrated by Fig. 1f. Large air cavities may result from surgical debulking (Fig. 1g) and may lead to challenging dose computation by loss of electron equilibrium. Avoidance of re-buildup is of special concern. Considering the close-shave tumor resections that are typical in this tumor site, air-tissue surfaces should not be underdosed in regions where they are CTV. Re-buildup nearby air cavities is discussed below.

1.3 Potential Benefits of IMRT

The basic beam setup in conventional radiation techniques usually involves an anterior beam complemented by a lateral beam or by lateral opposed beams (Fig. 2). In the two-field setup, both beams are wedged while the opposed lateral beams are wedged in the three-field setup. The field outlines of the anterior beam are designed to spare one eye and most of its lacrimal glands. At the affected side, a high risk of two severe radiation-induced side effects, namely dry-eye syndrome and blindness, was often accepted. Blindness may result from injury to the retina (retinopathy), the optic nerve or chiasm (optic neuropathy).

The eye is optically equivalent to a photographic camera with a lens system, a variable aperture system (iris) and a detector plate (retina). The lens is highly radiation sensitive and cataract (opacification) may occur at doses below 10 Gy at 2 Gy/fraction). However, because of the relative ease of lens transplantation, the dose to the lens became a minor issue in planning of sino-nasal tumors. The retinal detector plate is bended to fit the inner surface of the posterior half-globe of the eye. It consists of an array of detector units (photoreceptors; rods and cones) that convert light to electrical signals, which are transported by wires (nerve endings). The nerve endings converge in the optic disc at the poste-

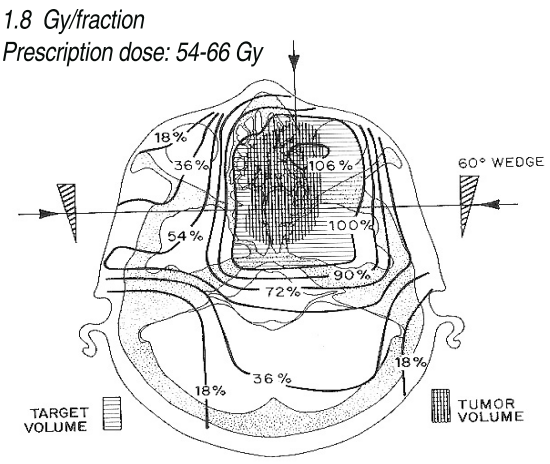

Fig. 2. Conventional radiation technique using an anterior beam complemented by lateral opposed wedged beams. The field outlines of the anterior beam are designed to spare one eye and most of the lacrimal glands at the spared side

rior retina where the optic nerve is connected to the eye-ball. When detectors or their wires are damaged by radiation the image formed by the detector plate looses functional pixels and a defect in the visual field (scotoma) or, in extended cases, global loss of vision results. The mechanism by which radiation causes loss of function of photoreceptors is uncertain but vascular damage is a prominent feature of radiation induced retinopathy [8]. Rarely, radiation induced retinopathy can lead to neovascular glaucoma and enucleating due to pain. Investigations of the dose response relation of radiation-induced retinopathy show divergent results. In a recent study on orbital irradiation for Graves' opthalmopathy, the criteria for possible retinopathy (presence of > or = 1 hemorrhages and/or microaneurysms on red-free retina photographs) were fulfilled in 24 of 159 patients after a dose of 20 Gy in 10 fractions [9]. In the control group of 86 non-irradiated patients only one patient had possible retinopathy. In five patients (all had been irradiated), definite retinopathy (i. e., more than retinal lesions) was present. Of these, three had diabetes mellitus, and one had hypertension. Diabetes was associated with both possible ($p = 0.029$) and definite ($p = 0.005$) retinopathy, with a relative risk of 21 (95% confidence interval, 3–179) [9]. A review of the literature on fractionated external photon radiotherapy for sino-nasal tumors shows a low incidence of retinopathy at doses below 45 Gy delivered with fraction sizes 2 Gy [8]. Parsons showed that, after treatment at approximately 1.8 to 2.0 Gy per fraction, the incidence of retinopathy increased steeply after dose of 50 [10]. From Parson's studies, a maximum retinal dose 50 Gy delivered in fractions 2.0 Gy can be inferred as a planning goal in IMRT protocols.

It is believed that radiation optic neuropathy [11] is caused mainly by vascular injury to the optic nerve or optic chiasm. Radiation optic neuropathy has been described at relatively low doses. The occurrence of radiation optic neuropathy after doses as low as 45–50 Gy administered in fractions of 1.67–2 Gy has been reported most often in patients with pituitary tumours, and probably reflects pre-existing optic nerve and chiasm compression and vascular compromise secondary to a mass effect or due to surgery [9]. More often referred for radiation therapy of sino-nasal tumors are the studies by Parsons et al. [12]. In a group of 131 patients from whom 84 were irradiated for sino-nasal tumors, a 15-year actuarial incidence of optic neuropathy of 11% was found at a dose of 60 Gy delivered in fractions of 1.9 Gy [12]. The incidence rapidly increased with increasing dose per fraction or total dose. A later update reviewing the results of 157 patients who were followed for a minimum of three years after radiotherapy confirmed that, at 1.8 to 2.0 Gy per fraction, the incidence of optic neuropathy increased steeply after doses $\geq$ 60 Gy [10]. For both optic nerves and for the optic chiasm, a maximum dose 60 Gy delivered in fractions $\leq$ 2.0 Gy can be considered as a planning goal in IMRT protocols.

The other feared side effect of conventional radiation of sino-nasal tumors, especially those involving the ethmoid sinus(es) or orbit(s), is severe dry-eye syndrome. Severe dry-eye syndrome is caused by irreversible damage to the lacrimal apparatus. By moistening of cornea and conjunctiva, the lacrimal apparatus provides a barrier against particles, fumes, and microorganisms, improves surface smoothness of the cornea for vision and secures motion smoothness of the eyelids. Anatomically, seven types of glands are described which functionally produce a three-layered lacrimal film. The conjunctival goblet cells (1) play a major role in the production of the mucinous deep layer. The aqueous middle layer is produced by the accessory lacrimal glands (Fig. 3a), located at the fornix superior of the upper eyelid (glands of Krause: (2) in Fig. 3a) and cranial to the tarsus of the upper eyelid (glands of Wolfring: (3) in Fig. 3a), and by the major lacrimal glands (4) located cranial-laterally of the eye in the anterior part of the orbit (Fig. 3b). The accessory lacrimal glands maintain basic secretion of watery fluid while the major lacrimal glands provide watery fluid as reflex secretion to various stimuli. The upper lipid layer is provided by the Meibomian (5), Zeiss (6) and Moll (7) glands. These glands are

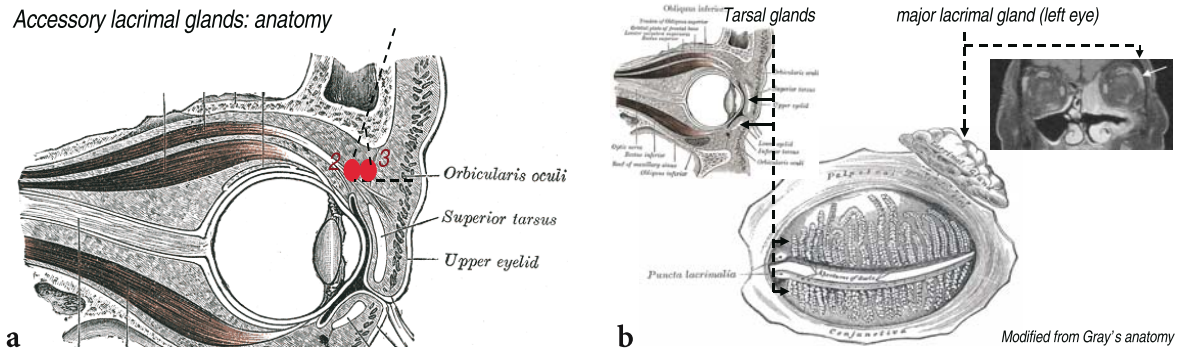

Fig. 3. (a) Accessory lacrimal glands of Krause (2) and of Wolfring (3). (b) Major lacrimal gland of the left eye indicated in the *middle* and the *right panel*. Location of the tarsus (*left panel*) and the tarsal glands (*middle panel*). Most of the glands are located in the tarsus fibrous tissue of both eyelids with orifices at the edge of the eyelid

mainly located in the tarsus fibrous tissue of both eyelids (Fig. 3b) with orifices at the edge of the eyelid. They maintain an oily secretion that spreads over the margins of the eyelids. An oily film, which is laid over the tear film as the fissure opens after a blink, improves tear film stability, reduces evaporation and the hydrophobic film at the margins of the eyelids prevents tears from spilling over the face. The individual dose-function relationships of the three types of lacrimal glands are unknown. Dose-effect relationships of severe dry-eye syndrome are based on simultaneous irradiation of the seven types of glands. A dose of less than 40 Gy to the lacrimal apparatus was inferred by Parsons [13] as a planning goal for functional sparing. Analysis of our experience (see further), using 30 Gy as a planning goal, may indicate that a maximum dose limit of 40 Gy is rather high.

The potential benefit of IMRT in sino-nasal cancer can be summarized as achieving bilateral functional sparing of lacrimal glands and optic pathway structures by limiting the maximum doses to 30–40 Gy, 50 Gy and 60 Gy or less for the lacrimal apparatus, the retina and the optic nerves and chiasm, respectively, simultaneously with achieving a target prescription doses above 60 Gy.

1.4 Target and Organ-at-risk Definition

1.4.1 Imaging

For planning purposes a CT scan in treatment (supine) position from the vertex to the sternoclavicular junction is recommended. To limit the number of slices for contouring, 2 – 3 mm thick slices can be generated in a region that widely covers the (pre-operative) tumor volume and the paranasal sinuses while adjacent 5 mm thick slices outside this region provide sufficient resolution. At Ghent University Hospital (GUH), such CT-dataset usually consists of 80–140 transverse slices (pixel resolution 512×512). An additional MRI dataset (slice thickness 1 mm) in treatment position is recommended because of its superior tumor-soft tissue contrast in patients with gross tumor and for image co-registration to delineate small organs at risk. On MRI-scans, the optic chiasm can be contoured easily while on CT-scans; it is hard or even impossible to distinguish from the adjacent tissues. CT-MRI fusion capabilities should be available for contouring.

1.4.2 CTV and PTV

General recommendations for CTV definition in sino-nasal cancer do not exist. The compartment (according to Harnsberger [14]) based contouring guidelines used at GUH are herewith described. In non-operated patients, the gross tumor volume (GTV) is defined from the MRI image. The margin around GTV to create CTV is defined as follows: In those regions where the GTV is flanked by intact bone or by cranial nerves, no margin is added. In those regions where GTV invades compartments enclosed by bone, like other paranasal sinuses, or extends up to their ostia, the whole compartment is included in the CTV contours. In those regions where GTV invades radiologically defined spaces known to resist poorly to invasion (eg masticator or parapharyngeal spaces), or where GTV invades the orbit, either the entire space or a margin of 0.5 – 1.0 cm is added. In case of minimal orbital invasion, the medial part (including the rectus medialis muscle) of the orbit was included into the CTV. When the GTV extended intracranially, we initially added 0.5 – 1.0 cm to the GTV margin. Follow-up showing relapse within eight months after treatment in eight of eight patients (with a leptomeningeal relapse component outside the CTV in five of eight) made us change this attitude. In the actual protocol, the meningeal structures of the frontal lobes are included in the CTV to a dose of 60 Gy in 35 fractions in cases of invasion of the anterior cranial fossa.

To define the CTV in patients who underwent macroscopically complete surgery for squamous cell or adenocarcinoma, the above principles are applied to the resection cavity as if the edges of the resection delineated the GTV. Thus, the postoperative CTV consists of the resection cavity plus a variable margin according to the principles of a “compartment-related CTV” as described above.

No elective irradiation of the cervical lymph nodes is performed. However, the elective irradiation of lymph node areas II and I for T3–4 squamous cell cancer of the maxillary sinus is debatable as well as for undifferentiated sino-nasal cancer. At GUH, the CTV is isotropically expanded with 3 mm to form a planning target volume (PTV).

1.4.3 PRV

The anatomical structures contoured as organs at risk (OARs) by default include the optic chiasm, the optic nerves, the retinas, the major lacrimal glands, the pituitary gland, the brainstem, the brain, the mandible, and both parotids. The delineation of the posterior part of the optic nerves, the optic chiasm and the pituitary gland is based on the MRI dataset. The optic pathway structures (optic chiasm, optic nerves and both retinas) are isotropically expanded with 2 mm to form a PRV (planning at risk volume). The brainstem is isotropically expanded with 3 mm. For all other OARs, the PRVs are identical to the respective OARs.

1.5 Planning

1.5.1 Dose Provisional Prescription and Dose Objectives for Planning

The PTV dose provisional prescription is 70 Gy median dose, delivered in 35 fractions, with an acceptable minimum dose (D_{min}) of 66.5 Gy (5% of the prescription dose). An under-dosage of more than 5% inside the PTV is accepted in the regions adjacent to or overlapping with the optic structures (PRVs), as well as in the buildup region of the 6-MV photon beams. With regard to PTV over-dosage, the ICRU guideline of 7% is followed. The three-dimensional dose maximum must be located inside the PTV. The dose limit for the 2 mm expanded optic structures (optic chiasm, optic nerves and retinas) is 60 Gy to D-95, i. e.95% of the volume of the structure has to receive 60 Gy or less. This is a hard constraint as well as the maximum dose for the brainstem, which is of 60 Gy (applied to the PRV). At GUH, no PRV-specific dose constraints are specified in the dose provisional prescription for the major lacrimal glands, the pituitary gland, the brain tissue, the mandible and both parotids glands. However, the dose maximum is controlled by constraints to unspecified imaged (normal) tissue (see further) in the dose objectives for planning. For all of these structures, biophysical constraints are used during optimization.

To avoid severe dry-eye syndrome, a median dose of 30 Gy should not be exceeded to the major lacrimal glands [15]. In the majority of cases, this constraint can be achieved without affecting the dose prescription to the PTV. If priority ranking would be imposed, we suggest giving priority to the dose objectives of the PTV.

Pituitary gland dysfunction can be adequately treated by hormone substitution. In most adult patients, substitution is not needed at doses below 50 Gy. A soft dose maximum constraint of 50 Gy seams reasonable.

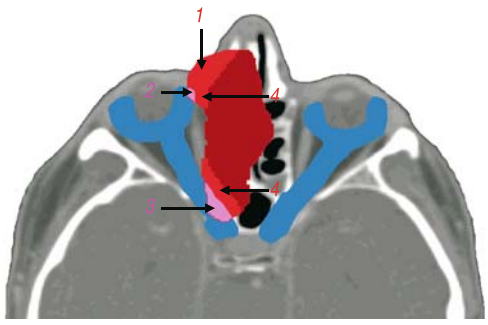

Fig. 4. Overlap between PTV and PRVs of the right retina (*arrow 2*) and optic nerve (*arrow 3*). Anteriorly, *arrow 1* points to a "buildup" region of the PTV. *Arrows 4* indicate gradient zones

The clinical picture of focal brain necrosis depends on size and location of the insult. The symptoms of small-volume necrosis in the anterior part of the frontal lobes, which are at highest risk in radiotherapy of sino-nasal cancer, are usually mild. A dose maximum constraint of 70 Gy to a 2 cm rind of brain tissue flanking the PTV, complemented by a 50 Gy dose maximum constraint for the brain tissue outside the rind can be proposed.

For the mandible, a 70 Gy dose maximum constraint is proposed after good dental care.

For the parotid glands, a 26 Gy maximum of the mean dose is consistent with preservation of function [16].

Buildup and Flash

Sino-nasal tumors may extend close to the surface or may even invade through the skin. When the PTV extends in the build-up region or in air, a challenging optimization problem occurs as described in chapter I. 5. If under-dosage of the skin is clinically unacceptable, bolus should be applied and optimization can proceed using the dose provisional prescription to the PTV as dose objectives for planning. Poor dose distributions usually result if optimization is done on a PTV volume exposed to buildup or in air. The intensity of suitable bixels will be raised to avoid under-dosage in the buildup or in-air regions of the PTV. This may result in spiky intensity profiles of some beams and hot dose spots elsewhere in the patient. The optimization result is not appropriate to compensate for under-dosage in build-up since the location of the intensity spikes is accurate only for the scanned position of the patient, i. e.the solution does not take into account set-up errors. Neither does dose calculation in air provide appropriate optimization of the flash region. A common approach to this problem involves setting the dose objectives for planning only to the part of the PTV that is located more than 4–6 mm below the patient's surface. In Fig. 4, arrow 1 points to the region where the dose objectives for planning have to be relaxed (ie lowering of the minimum requested PTV dose) in comparison to the dose provisional prescription. Typically, the apertures of three (1 vertex and 2 antero-lateral) of the seven beam directions used in our class solution [17] have to be evaluated and eventually adapted to secure flash.

PTV-PRV Overlap

Overlap with the PTV most often occurs for PRVs of the retinas, optic nerves and optic chiasm. In Fig. 4, arrow 2 points to a region of overlap between the right retinal PRV and the PTV. The overlap concerns a "buildup" region of the PTV. The minimum dose is relaxed. Since the retinal PRV has priority, the maximum dose constraint of 60 Gy applies to the overlap volume. Arrow 3 in Fig. 4 points at overlap between the PTV and the right optic

nerve PRV. The optic nerve PRV has priority over the PTV and hence, a dose maximum of 60 Gy applies to the overlap volume. Ideally both overlap volumes should receive exactly 60 Gy. In practice, a dose range of 57 – 60 Gy is technically achievable for most patients and therefore the dose objectives for planning are set to this range. Outside the overlap volume, a dose gradient zone exists, which allows for the dose increase from 60 Gy dose maximum at the retinal and optic nerve PRV to the 67 Gy dose minimum constraint of the PTV. A 3 mm wide PTV-subvolume (arrows 4 in Fig. 4) outside these PRVs is usually sufficient. In practice, no planning dose objectives are set for this part of the PTV but implicitly, the dose objective is the range between 57 and 67 Gy. The planning dose objectives for the part of the PTV outside its build-up, air, overlap and gradient subvolumes (dark red area in Fig. 4) are identical to the dose provisional prescription.

Unspecified Imaged Volume (UIV)

As described elsewhere in this chapter, the UIV is the part of the imaged volume outside the contours of PTVs and PRVs. Absence of planning dose objectives to the UIV results in two types of problems, namely high-dose spots and poor dose gradients outside the PTV. The method applied at GUH to define planning dose objectives to the UIV is the "matroska" method described in chapter I. 5.

Air Cavities

After surgical resection of sino-nasal tumors, grotesque air cavities may occur (Fig. 1g). Surgery with a tumor free margin is usually not possible without severe mutilation. Typically, the surface of the air cavity is CTV. Under-dosage of the surface due to electron non-equilibrium must be considered, especially if beam apertures are used that cover the air cavity incompletely [18,19]. Such beam apertures are commonly used in IMRT of sino-nasal cancer but abutting beam apertures of similar intensity reduces the effect of rebuild-up. Such abutting beam apertures are often present but their intensity may be vastly different. Highly modulated intensity profiles are often used so that the risk of electron equilibrium loss leading to uncompensated rebuild-up must be considered.

1.5.2 IMRT Treatment Planning at GUH

Treatment planning is based on a class solution approach [17]. The template beam set (Fig. 5a) is characterized by each beam's isocenter, gantry, table and collimator angles, linear accelerator, radiation modality and energy. The template beam set is used in a two-step procedure that makes use of two IMRT planning tools

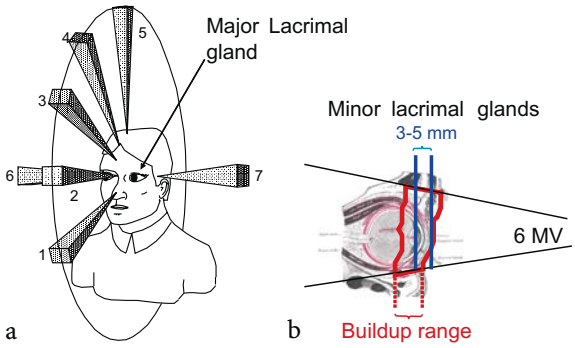

Fig. 5. **(a)** Template beam set consisting of seven beam directions. Location of the major lacrimal gland indicated by the *arrow*. **(b)** Illustration of the depth of the minor lacrimal glands in the buildup range of an anterior 6 MV photon beam

developed at GUH. For each template beam, an anatomy-based segmentation tool designs MLC-collimated beam apertures encompassing the BEV-projection of each PTV as well as MLC-collimated segments inside these beam apertures [20]. The second tool, called segment outline and weight adapting tool (SOWAT), performs a direct optimization of MLC-apertures and monitor unit counts for all beams and segments [21, 22]. SOWAT makes use of a biophysical objective function that uses a biological and a physical term for each PTV, PTV-subvolume, OAR, OAR-subvolume and UIV [17].

1.6 Delivery Issues

Immobilization is performed using a standard thermoplastic head cast and a knee cushion was used for patient comfort. Positioning is done using orthogonal green lasers. A random error of 1.5 – 2 mm was measured using electronic portal imaging (EPI) of bony landmarks. Daily EPI is performed for the first five treatment fractions; the mean of the setup error, calculated in three dimensions, is used to reduce the systematic setup errors. On-line setup corrections are performed if the setup error is 4 mm. Online corrections take approximately 4 min because the technologists have to enter the treatment room by absence of a computer controlled couch. After the first five EPI sessions, weekly or daily portal imaging was performed depending on the frequency of setup errors 4 mm. The treatment delivery time falls within a 12- or 16-min time slot (without or with on-line corrections respectively).

Given the small size of OARs like retinas, optic nerves, optic chiasm and lacrimal glands, a number of improvements at the delivery side are envisaged:

1. The absence of remote couch control (cannot be offered by major linac vendors anno 2004!) is a serious default.

2. Patient immobilization and positioning could be improved. Dose gradients are shaped nearby optic pathway structures in such a way that the maximum tolerated dose is achieved at the low-dose side of the gradient. The dosimetric impact of positioning errors depends on the steepness of the dose gradients. Improvements of the mask system using a dental offprint mouthpiece and more rigid mask materials are investigated. Volumetric X-ray imaging has potential to improve positioning accuracy in this site.
3. With improved positioning, measures to improve gradient steepness could be undertaken. To shield structures of 3–4 mm diameter like the optic nerves, smaller than 1 cm MLC leaf pitch and sharper than 6 mm penumbra 20–80% are needed. With smaller leaf width and sharper penumbra, leaf position accuracy should be better than the present 1–2 mm on some present MLCs.

The impact of internal organ motion/deformation and patient setup error on the delivered dose still remains a challenging topic of research. The variation in dose delivery, per fraction and cumulative, for each OAR makes it difficult to obtain accurate dose-toxicity relationships. Little is known about the effect of inhomogeneous irradiation of small critical structures such as the optic nerves and the optic chiasm in IMRT treatments. Dose-toxicity data are based on homogeneous irradiation of these volumes with conventional techniques. The use of image co-registration (CT-MRI) in order to delineate the optic nerves and the chiasm more precisely, and the availability of more accurate dose computation algorithms, better patient setup and more accurate delivery methods will enable us in the future to analyze more reliable NTCP values for these nervous structures.

1.7 Therapeutic Results of IMRT

At prescription doses above tolerance of the lacrimal apparatus and the optic pathway structures, conventional radiation therapy for sino-nasal cancer results in significant ocular toxicity [10] and local control rates (in combination with surgery) of 90–70% in stages T1–T2 and below 50% in stages T3–T4 [3]. Clinical trials of IMRT should answer the question if radiation-induced toxicity can be decreased at unchanged or improved local control rates. It is unlikely that answers at level I evidence (evidence generated from randomized clinical trials) will emerge in the foreseeable future given the rarity of the disease and the difficulties to obtain the patient's informed consent for randomization in trials where IMRT is compared to flat beam techniques. A PubMed search on December 8, 2004 using IMRT and PARANASAL SINUS as keywords yielded 17 publications. From these, 12 were on IMRT planning or technical issues. Of the five clinical publications, two reported on more than 11 patients, one from UCSF [23] and one from GUH [15]. We recently conducted a review of clinical outcome at GUH, we will use these data in an attempt to answer the following questions: Do local control and survival rates of IMRT-treated patients compare favorably with results obtained by conventional radiotherapy in the literature? Can IMRT avoid dry-eye syndrome, visual impairment from retinopathy, optic neuropathy and other ocular toxicity as well as non-ocular toxicity?

1.7.1 Loco-regional Control and Survival

From a group of 62 patients who received IMRT for sino-nasal tumors between July 1, 1998 and August 31, 2003, the patients with stage M0 who underwent R0-resection and postoperative IMRT for adenocarcinoma ($n = 31$) or squamous cell carcinoma (SCC: $n = 8$) were studied for analysis of outcome. The subsite of origin, as determined from the epicenter of tumor mass was the ethmoid sinus in 30 patients, the maxillary sinus in 6 (all SCC) and the nasal cavity in 3 patients (all adenocarcinoma). A history of occupational wood dust exposure was recorded in 24 patients (all adenocarcinoma). The above distribution according to subsite and histology is typical for the patient population referred to GUH and is related to the wood furniture industry that is abundant in the region of Ghent. Classification according to subsite, histology and T-stage (2002 UICC TNM classification) is shown in Table 1. All patients with T4b tumors belonged to the ethmoid sinus group and all had invasion of the dura or brain. One patient had bilateral cervical lymph nodes and underwent bi-

Table 1. T-classification and histology per subsite

	Ethmoid sinus				Maxillary sinus			Nasal cavity			
Histology	T2	T3	T4a	T4b	T2	T3	T4a	T2	T3	T4	Total
Adeno	13	3	5	7	-	-	-	3	-	-	31
SCC	-	-	1	1	-	3	3	-	-	-	8
Total	13	3	6	8	-	3	3	3	-	-	39

Adeno: adenocarcinoma
SCC: squamous cell carcinoma

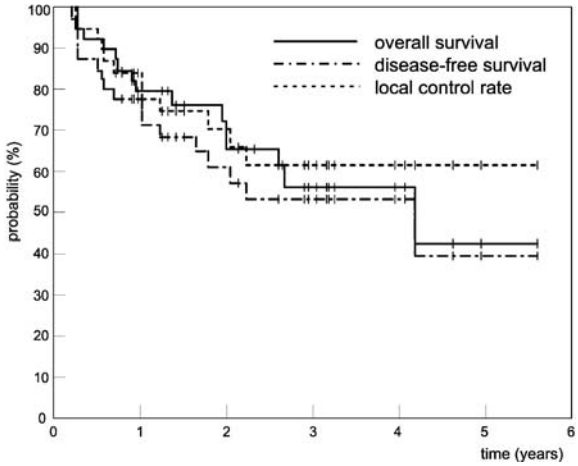

Fig. 6. Actuarial overall survival, disease-free survival and local control calculated from the date of histological diagnosis for epithelial N0M0 sino-nasal cancer treated by IMRT

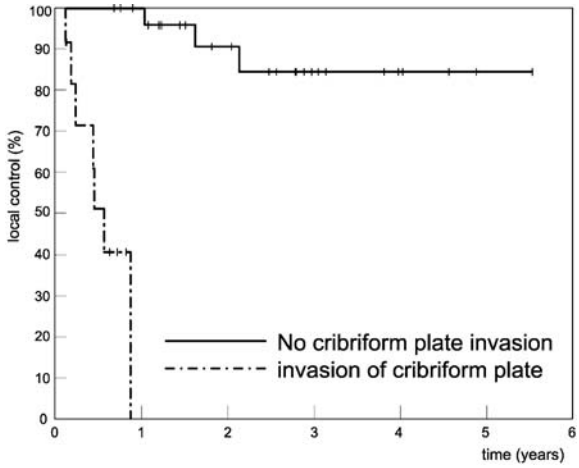

Fig. 7. Actuarial local control for patients with T1–T4 stage without cribriform plate invasion compared to patients with T4 stage and cribriform plate invasion

lateral neck dissection. For this patient, the neck was included in the CTV. Elective nodal irradiation was not performed in the 38 other patients. The type of surgery was broad resection via lateral rhinotomy in 22 patients, maxillectomy in 5, functional endoscopic resection in 4 and craniofacial resection in 8 patients. Three patients underwent orbital exenteration as part of the surgical procedure.

The PTV provisional dose prescription was 60 Gy for the first 4 patients, 66 Gy for next 6 patients and 70 Gy for the remaining 29 patients. In one patient no dose constraint was implemented for the left eye and optic nerve because of a pre-existing unilateral blindness caused by orbital tumor extension. In the first 4 patients, a maximum dose constraint of 50 Gy to the retina, optic nerves and chiasm was implemented. The optic pathway structures (retina, optic nerve and chiasm) of the remaining 34 patients were expanded by 2 mm to create PRVs and maximum dose constraints of 50 Gy (retina PRV) and 60 Gy (optic nerve and chiasm PRV) were implemented. Actuarial overall survival, disease-free survival and local control calculated from the date of histological diagnosis are shown in Fig. 6. The 3 – 5 year actuarial local control rate was 84% for patients with T1–T4 stage without cribriform plate invasion and 0% in T4 stage with cribriform plate invasion (Fig. 7). The latter patients developed local or lepto-meningeal relapses within eight months after treatment. This analysis shows that, just by excluding stage T4b patients with cribriform plate invasion, a patient group can be selected in which good local control can be achieved. Patient inclusion criteria influence prognosis much more than what could be expected from radiotherapy techniques like IMRT. Although the results compare well with literature data [3] for stages T2–T4a, no conclusions should be drawn regarding the effect of IMRT on local control as compared to conventional techniques. The present IMRT implementation was clearly not able to reverse the dismal local control rates that are known to exist in stage T4b with cribriform plate invasion.

1.7.2 Avoidance of Dry-eye Syndrome

In an earlier analysis involving 32 patients, Claus showed that severe dry eye syndrome could be avoided by IMRT [15]. In this update with longer follow-up, severe dry-eye syndrome (grade 3: persistent pain) was seen in two patients, including the patient with unilateral blindness due to orbital tumor invasion in which no attempt was made to spare the optic structures. Five patients reported mild forms of dry-eye syndrome. In two patients, the dry eyes caused minimal pain (grade 1) while three patients had grade 2 toxicity (intermittent and tolerable pain). In three more patients who had no complaints, the ophthalmologist diagnosed mild dry-eye syndrome. It is known that all patients who develop severe dry-eye syndrome are symptomatic within at one month after radiation therapy and therefore these data can be considered as mature. A cohort of 30 patients was treated between 1985 and 1998 with 2D ($n = 19$) techniques, using anterior and ipsi-lateral wedged fields, sometimes complemented with an opposed lateral field at prescription doses of 54 – 66 Gy (1.8 Gy/fraction) or with 3D-conformal non-coplanar techniques ($n = 11$: period 1995–1998) at prescription doses of 60 – 70 Gy (2 Gy/fraction). Severe dry-eye syndrome occurred in respectively five (enucleation in one patient) and two patients.

High success rates of IMRT in avoidance of severe dry-eye syndrome can be partially explained by beam arrangement used at GUH (Fig. 5). The BEV-projection of three or more of the seven beams, used by the

GUH class solution (Fig. 5a), excludes most of the major lacrimal glands. In addition, most of the minor lacrimal glands are located in the eyelids, less than 3–5 mm below the skin, in the build-up region of several of the beams (Fig. 5b). By this beam arrangement in IMRT, most of the lacrimal apparatus typically receives a dose well below 30 Gy, which seems consistent with avoidance of severe dry-eye syndrome. However, even at doses below 30 Gy median dose to the lacrimal apparatus, mild forms of dry-eye syndrome could be diagnosed.

1.7.3 Avoidance of Visual Impairment

Before the start of RT, 3 of 39 patients had a pre- existing ocular disease. There was one patient with known retinitis pigmentosa, one with pre-existing severe hypertensive retinopathy and one patient, mentioned above, with tumor-induced blindness. The patient with hypertensive retinopathy had no decrease of vision over baseline (DVoB) at 15 months after RT while the patient with retinitis pigmentosa had a significant DVoB (from grade 2 bilaterally before RT to grade 3 at 11 months after RT). In these patients, it is not clear if the deterioration of the visual acuity is due to the effects of radiotherapy, or due to the progression of the underlying ocular disease. Of the remaining 33 patients, 5 showed a decrease of vision during follow-up that seemed related to optic pathway radiation injury. One patient developed retinopathy with neovascular glaucoma (drop of visual acuity to 2/10). One patient suffered from retinal detachment (drop of visual acuity to 2/10). In three patients, drop of visual acuity to 8/10 (for all three) lead to the diagnosis of mild optic neuropathy by an experienced ophthalmologic team. Considering a median follow-up of 32 months in survivors, the data on radiation retinopathy and optic neuropathy should be considered as immature. We conclude that during this limited follow-up period and using a hard dose-maximum constraint of 50 Gy to the retina and 60 Gy to the optic nerves and chiasm, two serious retinal and three mild optic nerve events were recorded. These dose- maximum constraints at fraction sizes 2 Gy seem to be close to the maximum tolerated dose (especially for the retina) when preservation of vision is the endpoint.

1.7.4 Non-ocular Chronic Toxicity

Focal brain necrosis was an MRI diagnosis in two patients, confirmed by biopsy in one. Grade 2 xerostomia (partial but persistent mouth dryness) was present in five patients. Six patients reported alteration in taste. Although not scored, nasal crusts were present in most patients and were treated by daily nasal irrigations.

1.8 Clinical Studies and Trials

The rarity of sino-nasal tumors makes it difficult to obtain sufficient patient accrual for randomized trials. For patients with T4b tumors, loco-regional control for duration of more than one year would be a significant therapeutic achievement. Treatment strategies aiming at this goal could be tested using a single arm phase II design.

1.9 Future Directions

Loco-regional control after surgery and IMRT was above 80% at five years for patients with T1–T3N0M0 disease. Severe dry-eye syndrome could be avoided almost completely but some degree of optic pathway injury occurred in 15% of patients. We hypothesize that the maximum tolerated dose to the optic pathway structures might have been reached in the GUH protocol. Improved target coverage using steeper dose gradients nearby the optic pathway structures might be possible by micro- and mini-MLC technology. The fraction of patients who develop distant metastasis during follow-up varies according to histology and site of involvement. Trials of concurrent or adjuvant chemotherapy could be considered.

The outcome of T4N0M0 disease is poor with less than 50% loco-regional control at one year and death within months after loco-regional relapse. In the series of GUH, all patients with T4b and cribriform plate invasion developed local or lepto-meningeal relapses within eight months after treatment. Failures were early and massive, suggesting that major improvements in treatment are required. A variety of strategic approaches could be tested including the simultaneous use of systemic therapy, reversal of the sequence of radiation and surgery and image guided focused dose escalation. Considering that progress in cancer treatment occurs in small steps, there is little hope that these strategic approaches will alter the fate of loco-regionally advanced sino-nasal cancer. In our series, most T4b tumors with cribriform plate invasion were adenocarcinomas, related to occupational wood dust exposure. In other words, the target population for screening using MRI or CT-PET is known. The main objective of such screening program would be a reduction of the number of patients who present with T4b tumors for treatment by detection of disease in earlier stages.

Acknowledgements The project "Conformal Radiotherapy Ghent University Hospital" is supported by the Belgische Federatie tegen Kanker and Ghent University (GOA 12050401, BOF 01112300, 011V0497, 011B3300).

References

1. Coebergh JWW, van der Heijden LH, Janssen-Heijnen MLG (1995) Cancer incidence and survival in the Southeast of the Netherlands 1955–1994. A report from the Eindhoven Cancer Registry. IKZ Comprehensive Cancer Centre South. Eindhoven, The Netherlands
2. Robin PE, Powell DJ (1980) Regional node involvement and distant metastases in carcinoma of the nasal cavity and paranasal sinuses. J Laryngol Otol 94:301–309
3. Dulguerov P, Jacobsen MS, Allal AS, Lehmann W, Calcaterra T (2001) Nasal and paranasal sinus carcinoma: are we making progress? A series of 220 patients and a systematic review. Cancer 92:3012–3029
4. Schulz-Ertner D, Nikoghosyan A, Thilmann C, Haberer T, Jakel O, Karger C, Kraft G, Wannenmacher M, Debus J (2004) Results of carbon ion radiotherapy in 152 patients. Int J Radiat Oncol Biol Phys 58:631–640
5. Mizoe JE, Tsujii H, Kamada T, Matsuoka Y, Tsuji H, Osaka Y, Hasegawa A, Yamamoto N, Ebihara S, Konno A (2004) Dose escalation study of carbon ion radiotherapy for locally advanced head-and-neck cancer. Int J Radiat Oncol Biol Phys 60:358–364
6. Jansen EP, Keus RB, Hilgers FJ, Haas RL, Tan IB, Bartelink H (2000) Does the combination of radiotherapy and debulking surgery favor survival in paranasal sinus carcinoma? Int J Radiat Oncol Biol Phys 48:27–35
7. Physician Data Query (PDQ) of the National Cancer Institute: Treatment options for health professionals. Paranasal Sinus and Nasal Cavity Cancer. CancerNet http://cancernet.nci.nih.gov
8. Lumbroso L, Dendale R, Fourquet A, Desjardins L (2002) Radiation-induced retinopathy. Cancer Radiother 6:289–295
9. Wakelkamp IM, Tan H, Saeed P, Schlingemann RO, Verbraak FD, Blank LE, Prummel MF, Wiersinga WM (2004) Orbital irradiation for Graves' ophthalmopathy: Is it safe? A long-term follow-up study. Ophthalmology 111:1557–1562
10. Parsons JT, Bova FJ, Mendenhall WM, Million RR, Fitzgerald CR(1996) Response of the normal eye to high dose radiotherapy. Oncology (Huntingt) 10:837–847
11. van den Bergh AC, Dullaart RP, Hoving MA, Links TP, ter Weeme CA, Szabo BG, Pott JW (2003) Radiation optic neuropathy after external beam radiation therapy for acromegaly. Radiother Oncol 68:95–100
12. Parsons JT, Bova FJ, Fitzgerald CR, Mendenhall WM, Million RR (1994) Radiation optic neuropathy after megavoltage external-beam irradiation: analysis of time-dose factors. Int J Radiat Oncol Biol Phys 30(4):755–763
13. Parsons JT, Bova FJ, Fitzgerald CR, Mendenhall WM, Million RR (1994) Severe dry-eye syndrome following external beam irradiation. Int J Radiat Oncol Biol Phys 30:775–780
14. Harnsberger H (1995) Handbook of head and neck imaging, 2nd edn. Mosby, pp 339–395
15. Claus F, Boterberg T, Ost P, De Neve W(2002) Short term toxicity profile for 32 sinonasal cancer patients treated with IMRT. Can we avoid dry eye syndrome? Radiother Oncol 64:205–208
16. Eisbruch A, Ten Haken RK, Kim HM, Marsh LH, Ship JA (1999) Dose, volume, and function relationships in parotid salivary glands following conformal and intensity-modulated irradiation of head and neck cancer. Int J Radiat Oncol Biol Phys 45:577–587
17. Claus F, De Gersem W, De Wagter C, Van Severen R, Vanhoutte I, Duthoy W, Remouchamps V, Van Duyse B, Vakaet L, Lemmerling M, Vermeersch H, De Neve W (2001) An implementation strategy for IMRT of ethmoid sinus cancer with bilateral sparing of the optic pathways. Int J Radiat Oncol Biol Phys 51:318–331
18. Martens C, Reynaert N, de Wagter C, Nilsson P, Coghe M, Palmans H, Thierens H, De Neve W (2002) Underdosage of the upper-airway mucosa for small fields as used in intensity-modulated radiation therapy: a comparison between radiochromic film measurements, Monte Carlo simulations, and collapsed cone convolution calculations. Med Phys 29:1528–1535
19. De Vlamynck K, De Wagter C, De Neve W (1999) Diamond detector measurements near simulated air channels for narrow photon beams. Radiother Oncol 53:155–159
20. De Gersem W, Claus F, De Wagter C, De Neve W (2001) An anatomy-based beam segmentation tool for intensity-modulated radiation therapy and its application to head-and-neck cancer. Int J Radiat Oncol Biol Phys 51:849–859
21. De Gersem W, Claus F, De Wagter C, Van Duyse B, De Neve W (2001) Leaf position optimization for step-and-shoot IMRT. Int J Radiat Oncol Biol Phys 51:1371–1388
22. Claus F, De Gersem W, Vanhoutte I, Duthoy W, Remouchamps V, De Wagter C, De Neve W (2001) Evaluation of a leaf position optimization tool for intensity modulated radiation therapy of head and neck cancer. Radiother Oncol 61:281–286
23. Lee N, Xia P, Fischbein NJ, Akazawa P, Akazawa C, Quivey JM (2003) Intensity-modulated radiation therapy for head-and-neck cancer: the UCSF experience focusing on target volume delineation. Int J Radiat Oncol Biol Phys 57:49–60 (2003).

IMRT for Carcinomas of the Oropharynx and Oral Cavity

Rupert K. Schmidt-Ullrich, David Buck, Nesrin Dogan, Jeffrey Siebers, Monica Morris, Yan Wu

2

Contents

2.1 Introduction – The Clinical Problem

Despite significant progress over the past decade, the loco-regional control and survival rates of 50–60% for patients with locally-advanced oropharyngeal (OP) head and neck squamous cell carcinomas (HNSCC) with radiotherapy (RT) alone leave room for improvement [21] considering the limited options for salvage treatment after failure of the initial therapy. Current standards of RT have been re-defined by the RTOG-9003 trial, comparing standard fractionation (SF) of 70 Gy, delivered in 35 fractions over 47 treatment days, with three different altered fractionation RT regimens; of the latter, both pure hyperfractination (HFX) and accelerated fractionation with concomitant boost (AFX CB) produced superior outcomes [21]. This RTOG trial produced important clinical evidence for the benefit of radiation dose intensification and shortening of the overall treatment time which had been demonstrated by other trial results and institutional experiences [2, 3, 21, 23, 24, 38, 40]. However, most approaches of dose intensification to the gross tumor volume (GTV) by three-dimensional conformal radiotherapy (3D-CRT) techniques require twice-daily irradiation. This has the disadvantages of reduced biological effectiveness of the cumulative nominal daily doses, and includes the need for repeated irradiation of normal and other target tissues overlying gross tumor.

The unique power of intensity-modulated radiotherapy (IMRT) lies in its ability to deliver different radiation dose levels to tissues in close proximity, thus permitting radiation dose escalation to the GTV while delivering standard size doses, e.g., 1.8–2.0 Gy, to surrounding and electively irradiated lymph node (LN) bearing tissues. Thus, IMRT provides a means to implement radiation dose escalation in the radiotherapeutic management of HNSCCs that has been shown to be beneficial [21, 40].

Among photon RT delivery methods, IMRT represents the most currently effective form of 3D-CRT to spare normal tissues adjacent to overlying gross tumor;

this includes selective dose sparing to organs-at-risk (OAR) with highest dose conformality. This need for conformality represents a particular challenge in the H + N region because of the relative proximities of gross-tumor in the primary location and in multiple metastatic LNs, both requiring high doses, frequently linked to the required sparing of a large number of adjacent critical normal tissues.

Thus, IMRT allows the simultaneous application of two important radiobiological concepts. Dose-per-fraction escalation, i.e., delivery of doses > 2 Gy to gross tumor with enhanced biological effectiveness due to greater tumor cell killing with higher radiation doses. This form of dose escalation to gross tumor has been applied clinically (see below) and may be defined as a form of AFX with a simultaneous integrated boost (SIB), defined here as an AFX SIB-IMRT schedule [4, 8, 52]. Depending upon the fraction sizes delivered to gross tumor and the overall treatment time or number of fractions delivered, different AFX-SIB IMRT regimens may be developed. As an alternative to a previous report [4], we have established the feasibility of dose escalation to nominal doses of 68.1 to 73.8 Gy to the GTV delivered in 30 daily fractions of 2.27 and 2.46 Gy, respectively, over a period of 40 days, providing BED equivalencies exceeding currently used HNSCC radiotherapy schedules [28, 49]. Conformal avoidance, the second major advantage of IMRT, implies here the preferential delivery of fraction sizes $\leq$ 1.8 – 2.0 Gy in an effort to achieve selective normal tissue dose sparing at or beyond that expected from the nominal doses, to be applied to critical normal tissues of the central nervous system, e.g., spinal cord, brain stem, cranial nerves and brachial plexus, and other normal tissues, including larynx and major salivary glands.

At the same time, the capabilities of different IMRT systems to deliver uniform radiation doses to defined target volumes, e.g., GTV/clinical target volume (CTV), may vary substantially and needs to be carefully considered in their clinical applications (see Chap. I.1.). Relative to other 3D-CRT techniques, this is counterbalanced by the high degree of conformality that can be achieved with IMRT and represents the most important feature for dose/fraction escalation to gross tumor and conformal avoidance of critical normal tissues in a single treatment session.

This chapter is written to provide guidance regarding the application of IMRT to treatment of OP HNSCCs (with some discussion of challenges applying to SCCs of the oral cavity (OC)), including planning and delivery. The primary tumor sites include SCCs of the base of tongue (BOT), various locations in the tonsil, typically tonsillar fossa (TF), retromolar trigon (RMT) and soft palate (SP), and for the oral cavity primaries of the oral tongue (OT) and floor of mouth (FOM). Potential pitfalls regarding planning will be addressed, most importantly the expertise required of physicians in defining and editing of GTV and the margins for the GTV containing likely subclinical tumor extension, defined as CTV. Selection of the electively irradiated LN bearing tissues (ETV; [28, 49]) represents another important responsibility of the radiation oncologist. In addition, planning treatment volumes (PTV) need to be defined that consider set-up/delivery inaccuracies, critical for the ultimate success of IMRT. Since there is considerable variation in the delineation of the electively irradiated LN bearing tissues of the neck a compilation of the different published approaches is offered as used at our institution (see below).

The applications of IMRT as RT to HNSCCs of OP/(OC) is described with emphasis on the ultimate radiobiological advantages of IMRT over SF RT, i.e., the use of AFX SIB-IMRT; these approaches are currently complex and best realized with complex inverse planning approaches. However, the power of IMRT in delivering highest degree conformality through inverse planning may currently be most effectively applied by some institutionally developed systems, although some commercial systems do provide forward and inverse planning capabilities.

2.2 Unique Anatomical Challenges

The challenges of RT for HNSCCs are defined by the large number of critical and vital structures in relatively small tissue volumes that are in close proximity to normal tissues commonly invaded by these tumors. Because of the widely varied aggressiveness of these tumors, the extent of subclinical invasion of tissues immediately adjacent to gross primary tumor and the widely varied extent of spread to regional lymphatics resulted in the tradition of using wide margins on gross tumors, typically $\geq$ 2 cm. This clinical practice predates the routine use of image-based treatment planning (see below); thus, the recommendations for GTV and *OARs* definitions in a recent review [15], require, in our opinion, refinement when IMRT is applied, in particular as a dose escalation tool (see below for discussion).

HNSCCs of the OP/(OC) are typically delineated by CT scans combined with intravenous contrast; however, given the complexity of HN anatomy, margins of these tumors relative to surrounding normal tissues are often difficult to define and would benefit from complementary imaging techniques (see below). The proximities of primary tumors and their LN metastases to critical structures presents another important challenge, including spinal cord, the brain stem, optic nerves and chiasm, and brachial plexus in the presence of adjacent extensive nodal disease. All these structures need to be assigned maximum dose limits below those used in standard RT and should be additionally protected from over-dosing by appropriate auto-contoured margins.

2.3 Target Volume Delineation, Organ at Risk Definition

2.3.1 Tissue Imaging for Target Volume Definition

Because of the anatomic accuracy, CT scanning remains the primary imaging modality for target delineation and treatment planning, including the use of CT-simulators for image acquisition; in addition, CT Hounsfield numbers are required by dose calculation algorithms [20,26, 27,30].

Supplemental target localization information may be obtained from combined use of MRI and PET both of which may be fused with CT images. MRI has the potential of providing improved soft tissue resolution for the definition of soft tissue boundaries, e.g., tumor and surrounding normal tissues, when optimally applied through scanning of the immobilized patient in identical positions or through evolving methods of deformable image registration. Different challenges are faced with *PET* scanning that provides a high level of sensitivity and specificity for tumor involvement, but currently offers little benefit in improving target delineation (for more detail see Chap. I.3.).

The important issues of IMRT target volume and margin definition will be discussed in more detail in Chap. I.5. Therefore, we will only briefly introduce the concepts of GTV/CTV/ETV vs the corresponding planning treatment volumes, PTV1/2/3, respectively.

By technical application of the ICRU-50 and ICRU-62 Report nomenclature, the GTV volume definition given here corresponds to a planning target volume (PTV) for the gross disease (PTV_{GD}), the CTV to a PTV for the sub-clinical disease (PTV_{SCD}), and the ETV to a PTV for the LN volumes (PTV_{LN}).

The capabilities of different IMRT systems related to achieving conformal dose distributions and isodose coverage have raised concerns which ICRU nomenclature can and should be applied to IMRT treatment planning or delivery. Critical issues center around the ability to tightly conform dose distributions around PTVs, and the size of the added margins used in the volume definition to achieve similar PTV coverage with different IMRT planning systems. Some IMRT planning systems internally expand volumes to ensure that fluence matrix elements near the edge of target volumes receive adequate coverage. To achieve similar coverage with systems that do not internally expand volumes, users must manually expand targets to ensure that the fluence matrix will adequately cover the volume edge. Thus, IMRT in general requires better margin definitions, but in particular when SIB-IMRT is applied. In addition to clinical traditions, the concept of treatment margins to account for patient setup errors was developed in an era when treatment delivery systems could deliver only uniform or uniformly varying (wedge) shaped fluence distributions. With IMRT's ability to provide non-uniform fluence distributions, perhaps other margining strategies such as those based on probability of target coverage may be more appropriate (see Chap. I.3.).

2.3.2 Target Volumes and their Delineation

Gross Tumor Volume (GTV)

For the purpose of radiotherapy treatment planning for OP/(OC) SCCs, identical head positions should be assured for CT, MR and PET scanning which has proven feasible at our institution. Thus, CT simulations with patient immobilization should be performed first before additional imaging modalities are employed. For best CT scan quality, intravenous contrast is required, and scanning should be performed with a maximum slice thickness of 3 mm.

All target volumes need to be manually delineated and categorized by radiation dose levels to be delivered. Gross tumor, both at the primary site and grossly enlarged metastatic LNs, i.e., ≥ 1.0 cm, are coded as GTV (Fig. 1). For planning purposes, the GTVs of the primary tumor and metastatic LNs should be separated; but GTV LNs in proximity to each other are best treated as one planning volume. There is current uncertainty how to categorize LNs in the size range of < 10 mm, which are readily identified with modern CT planning equipment. If they demonstrate peripheral rim enhancement it is our policy to treat them as GTV. PET scanning may represent a useful complementary imaging tool for LNs in

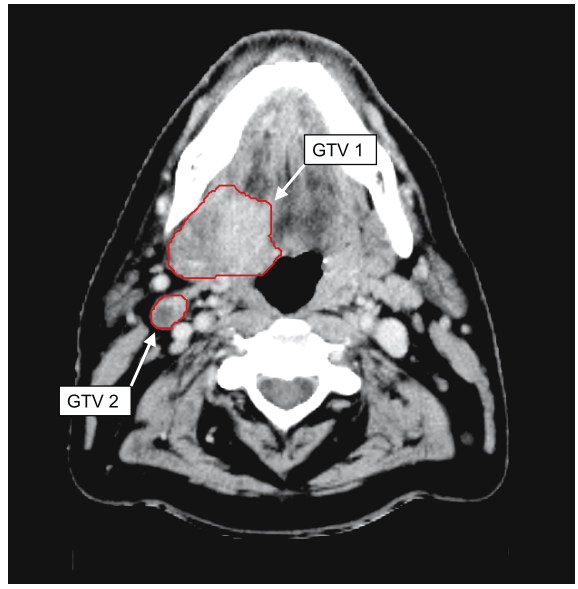

Fig. 1. GTV contour definition illustrating the primary tumor (GTV 1) and a 1 cm peripherally enhancing lymph node (GTV2). The smaller lymph node was planned to receive a minimum dose of 60 Gy

the 5 – 10 mm size range. Methods of detecting tumors in LNs < 10 mm are evolving. Because of these uncertainties we have included LNs in the 5 – 10 mm range into the CTV to assure a minimum delivered dose of 60 Gy. The GTV describing the primary tumor may be identified as GTV1. LNs may be defined collectively or individually, the latter making IMRT planning potentially more cumbersome; thus, the relative proximity of metastatic LNs should be a deciding parameter (Fig. 2).

There are currently no absolute standards of how to delineate the GTV [10, 42, 43]. It is assumed that the contrast enhancement around gross tumor defines the tumor-normal tissue boundary; thus, the GTV should fully include that boundary and should be drawn outside the contrast-enhancing rim (Fig. 1 and Fig. 2). In defining the GTV, MRI fusion may be considered, but HNSCCs have not yielded unambiguous results for improved soft tissue definition [42]. The delineation of primary carcinomas in the OP is challenging because of the common extension of tumor into adjacent soft tissues, e.g., BOT, SP and SCC of the TF with BOT, lateral pharyngeal wall or SP invasion, where rim enhancement may not be sufficiently reliable. In such cases tissue asymmetries, comparing involved and uninvolved sides in the OP, and evidence for distortion of normal tissue structures have to be employed for additional guidance. Suggestions made in a recent review on this topic may be considered as guides with caution since they reflect traditionally applied wide margins on gross tumor [15]. Such margins may be practical if IMRT is used for enhanced conformality and normal tissues sparing. They are almost certainly impractical when schedules of AFX SIB-IMRT are applied because of enhanced volume- dependent normal tissue toxicities [28]. Results from clinical studies applying different margins will be reported below.

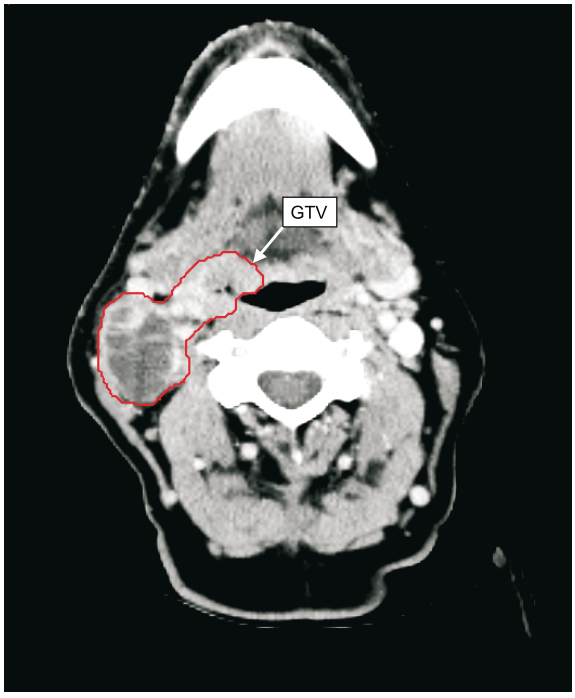

Fig. 2. GTV contour definition illustrating the primary tumor and an adjacent involved node. The close proximity of these two lesions requires one *GTV* volume for planning (GTV)

In addition to imaging data, detailed clinical evaluation of the patient remains mandatory, including inspection and palpation of the tissues involved with and immediately adjacent to gross tumor. In addition, panendoscopy including biopsies of tissues adjacent to gross tumor, is a mandatory component of this clinical evaluation. With the evolving practice of decreasing full-mouth dental extractions in patients receiving IMRT with salivary gland sparing, dental fillings may pose serious limitation for the GTV definition at some levels and require extrapolation of tumor/target volumes at those levels or the additional use of coronal or oblique images.

Similar principles of enclosing the entire contrast-enhancing region should be applied to the delineation of LNs apparently involved with gross tumor. In the cases of extensive primaries, the separation of primary tumor and metastatic LNs may be artificial and may require their treatment as a single volume (Fig. 2).

Clinical Target Volume (CTV)

The CTV is typically derived through 3D expansion of the GTV. Most commercial and institution-based IMRT treatment planning and delivery systems offer this feature for automated volume expansion (Table 1) around the GTV, typically 10 mm in three dimensions, as defined below. The volume generated by that expansion is treated as the CTV, accounting for subclinical tumor extension adjacent to the GTV. This automated GTV expansion can be problematic because it may include significant mucosal surfaces/volumes of normal tissues that will be irradiated to high doses. For example, in the setting of AFX SIB-IMRT approach with minimum prescription isodoses of the GTV > 95%, the entire CTV may receive total radiation doses in excess of 60 Gy at fraction sizes of ≥ 2 Gy. Such doses to the entire circumference of the OP have proven too toxic in our clinical experience [28] (Fig. 3A,B). In addition, invasion of primary tumors into the surrounding soft tissues may vary substantially depending on the anatomic location and biological features of the primary tumor. Thus, judgment and experience of the treating radiation oncologist is critical and has to be applied in defining the most likely sites of tumor extension by editing the CTV.

The editing of auto-contoured margins in their coverage of the mucosal surfaces of the OP/(OC) and the surrounding soft tissues is essential for the ultimate tolerance of IMRT, in particular, when integrated boosting techniques are applied. This editing process needs to include tracking the CTV definition such that it approx-

Table 1. Comparison of inverse treatment planning systems

1. Systems and Versions			
Company	**Inverse planning system**	**Version**	**Date of release**
BrainLAB	BrainSCAN	5.2	2002
CMS	XiO IMRT	4.1	July 2003
Electa	PrecisePLAN	2.0	April 2003
NOMOS	CORVUS	5.0	November 2003
Nucletron	PLATO	1.1	March 2003
Philips	Pinnacle	2.0	2003
Siemens	Konrad	2.1	July 2003
Varian	Helios	7.1.35	April 2003

[a] February 2004

Table 2. Dose-volume contraints for VCU IMRT optimization system[a]

2. Prescription (patient data)								
		Max.# of structures	**Dose objectives**	**Dose volume objectives**	**OAR D_{min}**	**Variable weights or penalties**	**DVH constraints**	**Ovelap priority**
		Target+OAR					Target+ OAR	
BrainLAB	BrainScan	16T+32 OAR	Yes	Yes	y	Yes	4 OAR	PTV
CMS	Xio	499	Yes	Ver 4.2	n	Yes	None in ver. 4.1, 5 OAR in ver. 4.2	User defined
Electa	PrecisePLAN	Unlimited	?	?	n	?	2T+l OAR+margin	Average
NOMOS	Corvus	27	No	Yes	y	No	IT (*goal*)+l OAR (*limit*)	Average
Nucletron	plato	Unlimited	?	?	n	?	5 OAR	User defined
Philips	Pinnacle	Unlimited	Yes	Yes	y	Yes	Unlimited T+OAR+EUD	Average
Siemens	Konrad	Unlimited	?	Yes	n	Yes	5 OAR	User define
Varian	Helios	Unlimited	?	?	y	Yes	Unlimited T + OAR	Average
VCU	VCU-IMRT	Unlimited	Yes	Yes	y	Yes		Defined

imates the mucosal surfaces in the OP in the cases of significant air spaces (Fig. 3C,D). While no standards have been established, a minimum of 10 mm lateral margin around the primary at the level of the mucosa should be assured [15, 28] (see below for clinical results).

In addition to defining the CTV at the mucosal surfaces, infiltrative tumors, typically those in the BOT, require more generous CTV margins, typically between 1and 2 cm into the direction of most likely soft-tissues extension, e.g., for BOT SCC into the lateral pharyngeal wall and the soft tissues of the OT. In the case of immediate proximity of gross disease in LNs with evidence of extension to or invasion into the skin, a 5-mm bolus over these areas of concern is sufficient for IMRT.

Depending upon the size, location and invasiveness of the OP primary, the routine expansion-derived CTVs of 10 mm may increase the GTV by factors between 2.5 to 7 (derived from data in [28]); this dramatic increase in volume makes apparent the potential consequences on the extent of OP/(OC) mucosal surface OP to be irradiated to daily doses $\geq$ 2 Gy and its consequences on tolerability of the treatment (see Fig. 3 and below).

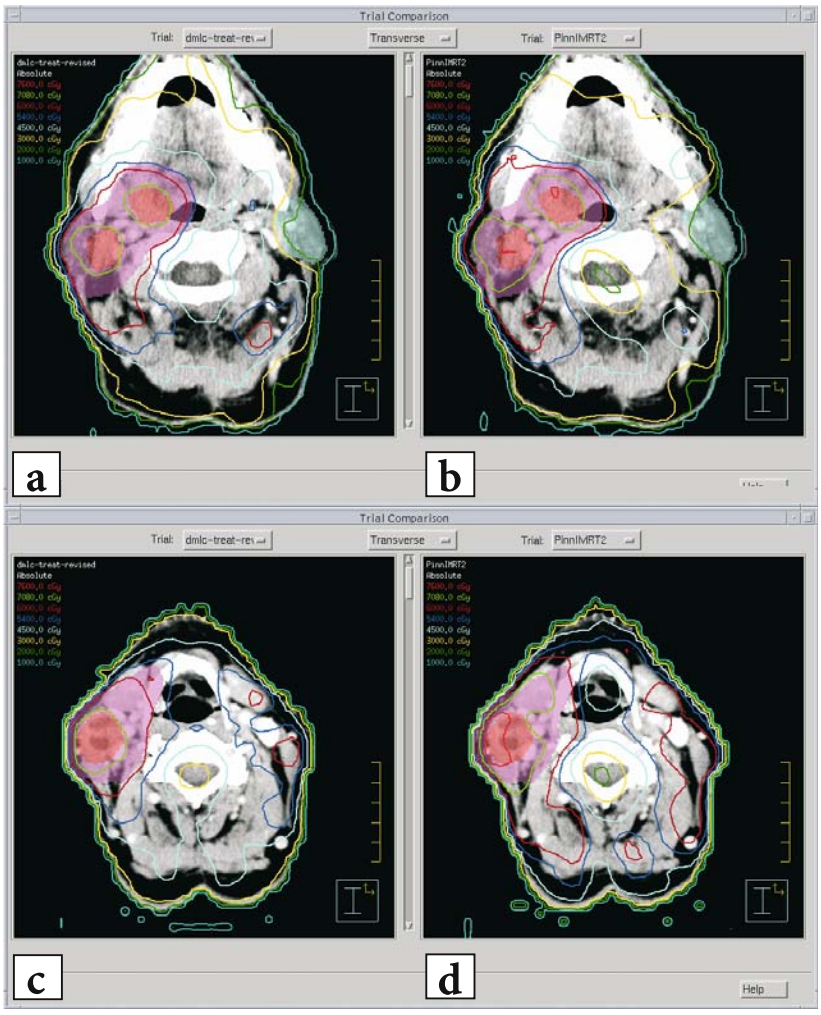

Fig. 3a–d. Trial comparison of: **(a)**, **(c)** the VCU-IMRT system; **(b)**, **(d)** the ADAC Pinnacle IMRT system. Note the improved conformality, the more homogeneous dose distribution, and the laryngeal sparing with the VCU system

For these reasons, stringent criteria should be applied to editing of the CTV with the purpose of limiting the high-dose regions in the OP/(OC) to the greatest extent possible. Extension of LN CTVs beyond the margins of the skin need to be eliminated (Fig. 4). Additional benefit may be derived by excluding an additional 2 mm of skin/subcutaneous tissues [29] in order to eliminate overdosing of the skin with formation of grade 3 radiodermatitis at the lower lateral neck in patients receiving IMRT to the entire HN region.

For generating the optimal outlines of the GTV/CTV, the following is required: (1) patient immobilization and set-up precision for IMRT with substantial improvement over traditional radiotherapy set-ups [32,45] – daily set-errors should fall in the 1 – 3 mm range and certainly not exceed 5 mm; (2) considering current standards of CT-based treatment planning, CTV volumes, comprising a 1.0 cm expansion of the GTV, should be sufficient in accounting for microscopic tumor extension below the mucosal surfaces and most adjacent soft tissues (see exceptions above); (3) when AFX SIB-IMRT approaches are employed the extent of the irradiated mucosa in the OP/(OC) must be limited to the greatest extent possible; therefore, careful editing of the CTV is essential including the use of pseudo-OAR to further enhance conformality ((see Figs. 3,and 4). These recommendations apply to all applications of IMRT but are essential when SIB-IMRT regimens are employed.

Electively Irradiated Lymph Node Bearing Target Tissues (ETV)

Considerable variation exists in the recommendations regarding delineation of electively irradiated lymph node bearing tissues in the neck [9, 22, 33] (Fig. 5). The LN groups at risk depend upon the location of the primary T and N stages and the distribution of nodal disease. Typically, bilateral level 2–5 LNs of the neck and parapharyngeal nodes are included for locally advanced carcinomas of the BOT, TF, and SP. Unilateral LN coverage may be considered for tumors of the tonsil with favorable prognosis/RMT. Depending upon the extent of LN involvement at level 2 and the invasion of tumors into structures of the oral cavity, level 1 LNs should be irradiated. More detailed recommendations

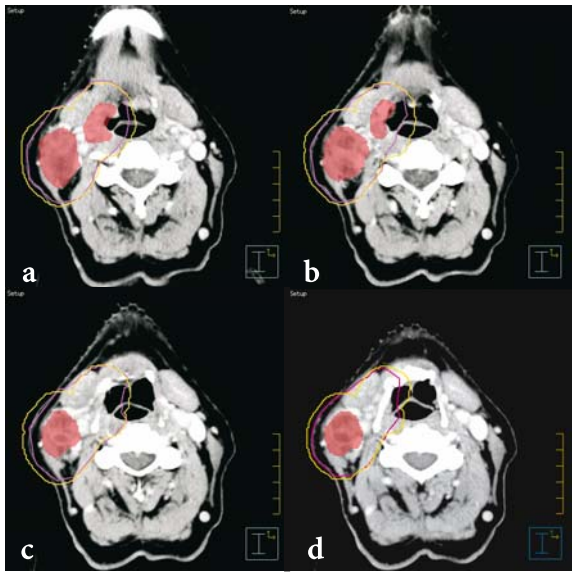

Fig. 4. Comparison of automated CTV expansion (*yellow*) and physician edited CTV expansion (*magenta*). Note the volume of posterior pharyngeal wall, epiglottis, and air outside of the patient treated with a computer ge nerated expansion

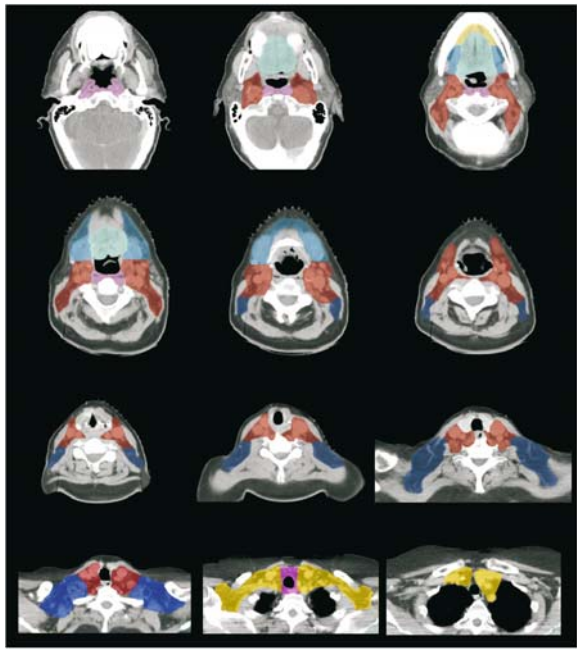

Fig. 5. Representative CT slices (3 mm thickness) of lymph node regions in a node negative neck as defined for IMRT planning. These images represent regions approximately every 1.5 cm

regarding selective LN coverage [1,15,18,39,41] may be used as a guide, but have not been confirmed by others and will have to be supported by documented failure patterns. All LN bearing tissues to be irradiated electively need to be individually contoured by the planning radiation oncologist. The LN regions to be potentially outlined, compiled from the sources listed above, are depicted in CT slices separated by 15 mm intervals as used at the MCV/VCU Department of Radiation Oncology (Fig. 5).

Organs at Risk (OAR)

OAR represent normal tissue structures that must be limited in the total and daily radiation dose or must be spared through the conformal avoidance capabilities of IMRT. In this respect, the capabilities of different IMRT planning/delivery systems vary substantially (Table 1); however, rapid improvements in these capabilities can be expected. For IMRT of OP/(OC) SCCs a number of OARs in excess of 10 will be a likely requirement. This number may increase substantially when pseudo-OARs (see below) are more widely used as conformality improvement tools (see Figs. 3,and 4 as examples). Critical OARs, e.g., spinal cord and other central nervous system structures, are delineated and expanded by a minimum of 5 mm with a dose limitation of 45 and 55 Gy for the brain stem. Experiences suggest that these dose levels could be lowered for some IMRT systems. These doses should be substantially reduced, e.g., 20%, if IMRT is combined with chemotherapy. For OP SCCs the doses to the larynx should not exceed 45 Gy. Sparing of the major salivary glands is another focus of IMRT target delineation. To date, most of the effort has been focused on sparing the parotid glands because of their importance in salivary fluid production and their relatively peripheral location. Absolute dose/volume values for the cumulative parotid gland volume and that of the gland distant from gross tumor are still being defined [1, 18, 28, 39, 41]; this may require some compromise in LN coverage on that side. Based on a recent report, sparing of submandibular glands may have significant benefit and should be considered [25]. The prioritization of overlap regions between target volumes and OAR will be discussed below.

The selection and delineation of pseudo-OAR represents another critical function of the planning radiation oncologist and most significantly influences the quality of the IMRT plan (Fig. 6A–D). These structures (volumes) are placed adjacent to GTV/CTV and are highly effective in enhancing conformality. They can also be employed to modify relative IMRT weighting for selective sparing of normal tissues. For example, multiple-beam IMRT to the OP will deliver significant doses through the OC that will facilitate delivery of AFX SIB-IMRT without treatment breaks. In addition to anatomic delineation, the experience gained with respect to relative penalties as prioritization parameters evolves as another critical variable ultimately affects the quality and deliverability of IMRT plans (see below).

Margins for Set-up Variation

Parameters for set-up variation have been defined in two ICRU reports outlined above [52] and in Chap. I.3.

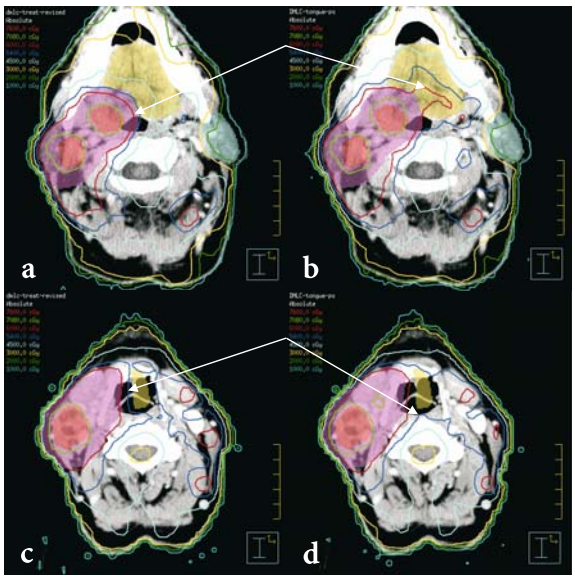

Fig. 6a–d. Isodose distribution: (a), (c)with; (b), (d)without pseudostructure (*yellow*) planning incorporation. Note the volume of the floor of mouth receiving 60 Gy and the supraglottis receiving 54 Gy without the pseudostructure in place (*arrows*)

The rigid expansion of anatomically defined volumes may interfere with goals of IMRT because of unreasonable volumes irradiated to doses in excess of 60 Gy at daily fractions sizes 2 Gy. For example, with IMRT systems that permit very high degrees of conformality and dose uniformity [51], the 98% of the GTV can be irradiated to the desired dose with $\leq 2\%$ of the volume receiving a dose $> 10\%$ of the prescribed dose (Fig. 7). Similarly, the CTV receives $\geq 95\%$ of the prescribed dose (see below) [28, 52]. In these situations the dose gradients are placed outside the prescribed GTV/CTV thus incorporating a minimum 3 mm set-up margin [28, 52]. Thus, the attention to margins on the GTV/CTV may have to vary greatly depending upon the features of the IMRT system used. This is illustrated by the comparison of dose distributions achievable, and by dose-volume histograms (DVH), using the VCU IMRT (inverse planning) vs the ADAC Pinnacle (forward planning) systems (Philips Medical Systems, Milpitas, CA), derived thereof (see below; Fig. 8). In addition, the margins of 1 – 5 mm depend on the documented accuracy in set-up variation in each center engaging in IMRT for HNSCCs. Modeling studies, using the ICRU-62 recommendations in defining planning OAR volumes (PRVs) have been quantified for parotid gland planning of HNSCCs cases and can limit the normal tissue volumes to be spared [32].

2.4 Planning

2.4.1 Patient Immobilization and Treatment Planning Imaging

Patient immobilization is critical to the success of IMRT for OP/(OC) HNSCCs. Commercial or customized head

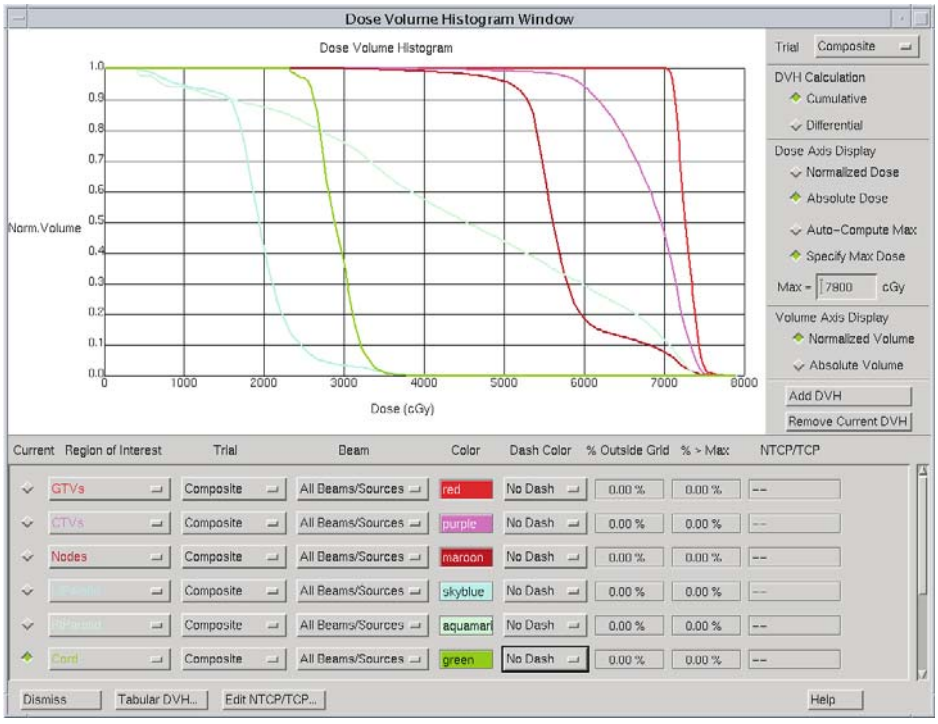

Fig. 7. Dose volume histogram (DVH) of a deliverable treatment planned with the VCU-IMRT system. Note that the entire GTV receives 70 Gy with 95% of the CTV receiving 60 Gy while sparing 95% of the contralateral parotid to less than 25 Gy

Fig. 8. Dose volume histogram (DVH) comparing the VCU-IMRT system (*no dash*) with the ADAC Pinnacle IMRT system (dash). Note that the Pinnacle system delivers generally higher doses to the target tissues with less homogeneity. The colors represent the following: GTV, CTV, elective nodes, contralateral parotid, and spinal cord

holders, including individual fitting of thermoplastic masks, have become standard [45]; ideally, this mask should also immobilize the patient's shoulders. Prior to fitting of the mask, optimal head extension of the patient has to be assured for displacement of critical normal tissues, e.g., eyes and optic chiasm, hard palate etc. This should be outside the planes of IM radiation beams to the greatest extent possible if a multi-beam coplanar delivery plan is intended. For OP/(OC) SCCs, fabrication of customized bite blocks, putty or other material, is advisable for the additional displacement of normal tissues through separation of the mandibular and maxillary alveolar ridges. Appropriate shaping of the bite-block for dental impressions and as a superior convex membrane following the contour of the hard palate will create a defined space for placement of the OT; this, with appropriate patient instruction, will reduce daily position changes of the OT/BOT for IMRT of OT, BOT and SP SCCs. For additional stability, the bite block is firmly melded to the thermoplastic mask.

The anatomic range of imaging depends on the IMRT delivery methods to be employed. Typically, coplanar fields are sufficient for irradiating locally-advanced HNSCCs. For the locally-advanced HNSCCs the planning CT scans should include the vertex of the skull and extend at least 1–2 cm below the carina. Treatment planning imaging is performed after patient immobilization. If multiple imaging methods (see Chap. I.3.) are employed, the same patient position is desired for supplemental MRI and PET imaging (which has been implemented at our institution, but may be replaced by evolving technologies of deformable image registration).

2.4.2 Beam Directions and IMRT Delivery

DMLC systems [28, 52] benefit relatively little from the use of non-coplanar beam arrangements. Similarly, the step-and-shoot methods primarily rely on co-planar beam delivery [17]. The use of co-planar beams and pre-determined equidistant gantry angles (typically 5–11 equiangular positions) combined with DMLC for generation of the IM beam profiles proves a powerful and efficient approach (see below). The VCU IMRT system [34, 36, 48], representing an automated prototype unit, and the Helios system (Varian, Medical Systems, Palo Alto, CA) are based on similar principles. Extensive studies in the HN region by our group have demonstrated that significant conformality/dose uniformity gains may be achieved with up to nine beams [28, 50–52]. Field size limitations of various DMLC delivery systems for the volumes to be irradiated with large IMRT fields, e.g., 14.5 cm for Varian MLC, require careful consideration in treatment planning. For example, these limitations have been overcome at our institution by delivering two sets of nine beams with IMRT using a modulated junction between the upper and lower neck tissues in a single treatment session. Vertical movements of the leafs reduce interleaf radiation leakage, and are the preferred form of delivery [48]. Since the delivery is pre-programmed, the delivery of 18 IMRT beams is completed within 15–20 min [28]. Alternatively, the upper neck IMRT portals may be matched with a traditional anterior supraclavicular photon portal [8].

Intensity-modulated arc therapy [13, 31, 54] combines DML collimation with moving the tumor/target tissues through variable arc rotations of the gantry. This approach represents another example of primarily single-planar IMRT delivery.

2.4.3 Optimization Strategies

Each IMRT planning/delivery system has built-in optimization features (see Chap. I.4; Table 1). In addition, there are parameters that may be controlled by the planning radiation oncologist. Based on our experience with a highly flexible system [34, 36, 51], commanding an extensive research platform, the planning system will select beam entries or shortest distances between skin surface and the GTV to be irradiated to the highest dose. For OP/(OC) HNSCCs this frequently results in preferred dose delivery through beams transgressing the OC which represents a major clinical disadvantage. Despite editing of the CTV planning systems frequently generate plans that enclose major portions of the OP mucosa uninvolved with tumor. This delivery of radiation doses in excess of 60 Gy (at daily fraction sizes > 2 Gy) produces unacceptable acute mucosal toxicities in the setting of AFX SIB-IMRT [28] (Figs. 6A,B). While this powerful method of RT dose escalation is more sensitive to the requirement discussed here and in the following Sections, any form of IMRT will benefit from and should utilize the placement of pseudo-OARs.

2.4.4 Pseudo OARs as a Method of Sparing Normal Tissues Approximating Target Tissues

Based on the planning system-derived dose intensities of different beams it is frequently necessary to modify beam entries for improved normal tissue protection. The introduction of pseudo-OARs in the OP/(OC) tissues immediately adjacent to the GTV/CTV not only improves conformality but also achieves significant dose sparing of normal tissues that markedly reduces the acute toxicity of IMRT.

These adjustments need to be directed by the planning radiation oncologist based on evaluation of the IMRT plans. At this time, generally applicable recommendations cannot not be provided at this time as different planning systems are currently too diverse due to differences in their optimization parameters, including effects on beam entries (see Table 1; see Chaps. II.1 and II.2. for more detail). Thus, the routine use of pseudo-OARs to modify the beam entry proves an effective method in our hands with broad applicability. Goals for the planning radiation oncologist should include avoiding irradiating the entire circumference of the OP to fractions > 2 Gy and avoiding similar doses to critical mobile structures of the larynx that approximate gross tumor (see Figs. 3,and 4).

2.4.5 OAR and Target Volume Overlap Priorities

Decisions regarding overlap priorities represent a major challenge in IMRT planning and delivery for HNSCCs. This important and complex problem requires close physician involvement in directing the IMRT system's handling of target priorities. Each IMRT plan also requires a physician driven definition of critical normal tissue dose limits. These priorities are typically achieved by relative weighting of penalties, considering varied features of different IMRT planning systems (Table 1), and the assigned priorities of protecting such structures; these priorities need to be balanced relative to the requirement of maximum dosing to the GTV. Absolute upper dose limits to be set for vital normal tissues, e.g., spinal cord and brain stem, may require compromise of GTV coverage.

In defining upper dose limits for OARs it is important to understand the algorithms that drive penalty-based weighting in the different IMRT systems (Table 1; Chap. II.1.2). The experience described here is based on the use of the VCU IMRT system [34, 36, 51], which may not differ that much from other systems with rapidly advancing software. A critical feature represents handling of dose gradients between critical normal tissues and GTV/CTV target volumes that are defined by automated IMRT treatment planning algorithms. While some systems have the capability of generating very steep gradients for competing priorities of target tissue coverage and the effective protection of immediately adjacent normal tissues, priority weighting, through imposed different penalty levels, does not necessarily assure adequate protection of the critical normal tissues. For example, changing the weighting of two adjacent OARs structures may sharpen the dose gradient but does not necessarily shift the gradient to create a greater margin to protect the structure assigned a higher penalty. Thus, for improved protection of a given OAR an additional margin may have to be generated around that structure. Thus, the only safe solution in such situations is to create an expansion margin around the vital critical structure(s) or a pseudo-OAR.

2.4.6 Planning Results, Criteria for Plan Evaluation and Acceptance

Dose distributions of IMRT plans may depart substantially in conformality and dose uniformity relative to conventional 3D-CRT plans. Therefore, any center engaging in IMRT for HNSCCs should define prospectively a set of plan evaluation criteria that conform with acceptable dose-volume criteria (Table 2).

Conventional tools of plan evaluation need to include isodose display on axial, coronal, sagittal digital CT images/constructions and dose-volume histograms (DVH) (Fig. 7). These parameters are useful but may be inadequate to define the quality of an IMRT plan. For quantitative evaluation of dose uniformity and dose conformality a number of parameters have proven useful using standard or SIB-IMRT [28, 49, 52].

Evaluation of the GTV

The percentage of the target volume that is covered by the prescription isodose, thus defining the minimum dose to the target, is quantitatively displayed by the DVH (Figs. 7,8). For some IMRT planning systems, this dose may be defined as the D_{98}, i.e. $\geq 98\%$ of the target volume receiving the prescription dose. More generally achievable coverage criteria by commercial systems approximate 95%. In addition to specifying the minimum dose, the DVH quantifies the degree of dose inhomogeneity in the target volume, e.g., GTV, including the fractional volumes of tumor or normal tissue being irradiated in excess of the minimum prescribed dose. Thus, the slope of the DVH above the prescribed dose displays the doses homogeneity as a percentage of the target volume (Fig. 8). This is an important parameter to be evaluated by the physician since relatively shallow slopes of the high end of the DVH (e.g., forward vs inverse planning DVH; Fig. 8) will indicate higher degrees of dose inhomogeneity with potential for significant overdosing of tissues within the target volume, such as the GTV/CTV and immediately adjacent normal tissues. Thus, in addition to the minimum dose

Table 3. (continued)

	GTVs	CTVs	LN group	Expandet cord	Expandet brainstream	Larynx	Lt. parotid	RT. parotid	Oral cavity	Ant. tongue
$Dose_1$ (Gy)	68.1	60.0	54.0	40.0	50.0	40.0	28.0	18.0	58.0	52.0
$Volume_1$ (%)	> 99. 9	> 99. 0	> 97. 0	< 0. 01	< 0. 01	< 50. 0	<40.0	40.0	<0.01	<10.0
$Penalty_1$	50.0	45.0	40.0	50.0	50.0	30.0	30.0	40.0	20.0	10.0
$Dose_2$(Gy)	73.5	64.0	57.0							
$Volume_2$(%)	< 0. 01	< 30. 0	< 10. 0							
$Penalty_2$	40.0	20.0	20.0							
$Dose_3$(Gy)		70.0	62.0							
$Volume_3$(%)		< 0. 01	< 0. 01							
$Penalty_3$		30.0	30.0							

The prescribed doses are to be delivered in 30 fractions Rx: 68.1 Gy to GTVs, 60.0 Gy to CTVs and 54.0 Gy to nodal groups. The actual volume of CTVs excludes that of the GTVs, and the actual volume of nodal groups excludes that of the CTVs. The expanded cord and expanded brainstem are both 5.0 mm 3D expansions of the cord and brainstem. The rt. parotid is the contra-lateral parotid in this case. The optimization criteria for GTVs are no less than 99.9% of the volume receives 68.1 Gy and no more than 0.01% of the volume receives 73.5 Gy. $Volume_1$ stands for the lower limit for the volume for the dose-volume constraint (e.g., for CTVs, no less than 99.9% volume receives 60 Gy). $Volume_2$ stands for the first upper limit for the volume for the dose-volume constraint (e.g., for CTVs, no more than 30% volume receives 64 Gy). $Volume_3$ stands for the second upper limit for the volume for the dose-volume constraint (e.g., for CTVs, no more than 0.01% volume receives 70 Gy) [a] [28, 52]

prescription to the GTV/CTV target volumes, the dose homogeneity of the GTV/CTV needs to be quantified by the planning radiation oncologist before approving any IMRT plan.

Frequently, highest dose regions are specified in the form of point doses. Based on our experience, we conclude that this method does not provide the best measure of the maximum dose within the prescribed volume. We have therefore introduced the term D_2, i.e., the 2% volume of the target volume receiving the maximum dose [52] with a rationale for choosing the D_{98} and D_2 to represent the minimum and maximum doses, respectively [52] (while similar criteria should be applied to other IMRT systems quantitative parameters may have to be adjusted). Therefore, the true minimum and maximum dose is typically not reliable. In addition, for target volumes < 100 cm^3, D_2 represents a more stringent constraint of maximum dose than the traditional definition of highest-dose regions, which represents the maximum dose encompassing a 2 cm^3 volume.

In addition, for each IMRT plan objective measures of dose homogeneity and conformality within the GTV target volume should be specified. In our experience, the homogeneity index (HI) represents a useful parameter which is defined as $HI = D_2 - D_{98}/D_{\text{prescription}} \times 100\%$ [28, 52]. Thus, lower HI values indicate greater target dose homogeneity. The degree of conformality may be quantified by volumetric parameters, such as the Prescription Isodose to Target (see Figs. 3 and 4) and Volume Ratio (PITV). Lower PITV values describe plans of greater conformality. As a reference value, the minimum prescription isodose, e.g., D_{98}, may be used as the Prescription Isodose Volume [52, 55]. Unfortunately, many of the currently available IMRT systems are limited in the ability to generate plans of the uniformity achieved by some institutionally developed systems [50, 52]. For this reason the D_{95} was adopted by the RTOG (H-0022) 3D-CRT/IMRT trial as the minimum prescription dose for the GTV. However, systems like NOMOS require acceptance of even greater inhomogeneity and therefore lower prescription isodoses volumes (Fig. 9). These parameters will have to be standardized once more extensive clinical experiences are available.

Evaluation of the CTV

The CTV covers the soft tissues surrounding gross tumor, likely harboring subclinical tumor, and should be irradiated to a minimum dose of 60 Gy at minimum daily fraction sizes of $\geq$ 2.0 Gy. The percentage of the CTV to be covered by the prescription dose is governed by similar principles as described for the GTV. For most IMRT systems homogeneities with minimum prescription isodose lines of 60 Gy to $\geq$ 95% of the volume should be achievable. The critical importance of editing the CTV, depending on the goals of IMRT has already been discussed.

Elective Coverage of LN Bearing Tissues

A number of groups [9, 21, 22, 33] have recommended volumes to be employed for the elective coverage of clinically uninvolved LNs. However, this aspect of IMRT remains controversial. For OP/(OC) SCCs these include, depending on the stage of disease, parapharyngeal LNs, LNs of levels I through VI and the LNs in the supraclavicular regions which have been traditionally irradiated in all patients presenting with locally-advanced HNCSSs.

Careful decisions are required regarding the coverage of the tongue lymphatics vs level II LNs since high dose irradiation to the former, without stringent indication, may cause treatment toxicities that will limit delivery of SIB-IMRT schedules or require treatment delays that have been shown to compromise outcome. Typically, 90% of the ETV should be irradiated to the prescribed dose equivalent of 50 Gy in 25 fractions or 54 Gy in 1.8 Gy fractions when SIB-IMRT schedules are employed with a fixed overall fraction size and treatment time [21]. This dose may have to be compromised for parotid gland sparing to be applied to the gland contralateral to the primary tumor with dose reduction not exceeding 10–15%. The safety of dose reductions in general, in the interest of normal tissue sparing, will remain a topic of investigation of future studies. Substantially greater compromises would be required for significant sparing of the submandibular glands in patients with locally advanced OP SCCs (see below).

Dose Specifications for OARs

Dose specifications to OARs are currently not clearly defined and depend upon the application of IMRT. Parameters to be considered are the total dose to the GTV target volume, the daily fraction size, and the degree of dose conformality and uniformity desired. Volumes of the OARs to be spared represent another obvious variable; based on our experience the dose to those OARs should be maintained at a daily dose of < 2.0 Gy, and if the risk of tumor involvement is low all OARs should be maintained at as low a dose as achievable by IMRT planning/delivery. These goals will become even more important when AFX SIB-IMRT regimens are combined with chemotherapy.

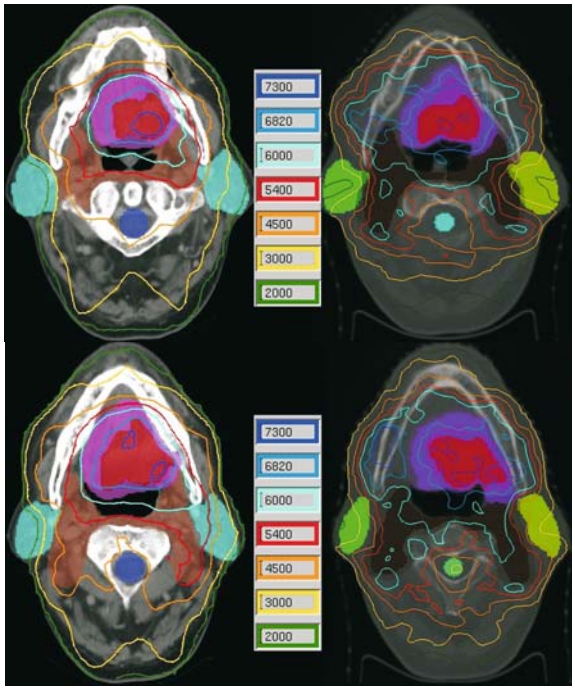

Fig. 9. Trial comparison of the VCU-IMRT system (*left*) and the Corvus system (*right*). The comparison remains qualitative because the contours are not identical. Image courtesy of Quiwen Wu, Tufts New England Medical Center.

2.4.7 Dose Prescriptions

Dose prescriptions should be formulaic based on pre-determined criteria to be established in each radiotherapy center that has established a credible IMRT Program. The physician has to approve the final prescription after careful evaluation of conformality/dose uniformity over total doses delivered to each of the tumor/target volumes. This requires coordinated evaluation of both three-dimensional isodose plans and DVHs (Figs. 3,7,8). When AFX SIB- IMRT schedules are employed dose heterogeneity to the GTV/CTV has to be considered as an important variable between different IMRT systems. For example, if by DVH criteria the D_{98} prescription criteria are met, the physician should still evaluate the total dose delivered, e.g., the doses delivered to 50 and 20% of the GTV (Figs 7 and 8). Should those doses appear too high the entire plan may have to be "down-scaled", with 1–3% being reasonable ranges to explore. This represents the easiest method of reducing segmental over-dosing within the GTV relative to re-initiating an entire new planning cycle, while also yielding greater conformality to the GTV. However, in many cases continued planning for improved conformality and dose uniformity may be required through additional inverse planning interactions (Fig. 8).

2.5 Clinical Experince/Trials Defining the Role of IMRT

2.5.1 IMRT for Normal Tissue Sparing

Since xerostomia after high-dose radiotherapy for HNSCC is one of the major treatment-related morbidities, sparing of the major salivary glands, primarily the parotid glands, has become a rationale for use of IMRT [12, 16, 19]. This experience also resulted in one of the first reports on patterns of failure analysis [14] on a heterogeneous group of 85 patients irradiated with conformal or segmental IMRT techniques in the settings of primary or post-operative irradiation. While sparing of one of the parotid glands was one of the goals of the treatment, delineation of the GTV, CTV and 5 mm expansion for the PTV was adhered to in order to assure delivery of $\geq 95\%$ of the prescribed dose to the respective volumes. The reported median radiation doses to the gross tumor, the operative bed, and the

subclinical disease were 70.4, 61.2, and 50.4 Gy, respectively. The dose delivery followed SF approaches. Based on careful position of recurrences relative to the 95% prescription isodose lines the failure patterns were categorized as infield, marginal and outside the prescribed dose. Of the 12 recurrences, 2 were marginal and 10 had an in-field component; many of these were within the post-operative bed with only two in the tumor GTVs in patients receiving primary irradiation. The reason for these recurrences my have been due to uncertainty in delineating the post-operative CTVs. No LN recurrences could be attributed to the intended sparing of the parotid glands.

A similar failure analysis was performed based on firm criteria of delineating LN bearing areas of the neck in patients who received definitive and post-operative IMRT [7, 9], again, using maximum daily fraction sizes to the GTV between 1.8 and 2.0 Gy. Of 126 patients, 52 patients underwent definitive and 74 received post-operative irradiation with IMRT. At a median follow-up of 26 months, nodal failure patterns were analyzed in these patients having level I–V LNs irradiated based on the location of the primary tumor and the probabilities of microscopic metastases in the ipsilateral and contralateral LN regions of the neck. The mean doses for the 52 definitively irradiated patients were 70.2 ± 3.4 Gy to CTV1 and 60.2 ± 2.9 Gy to CTV2; these treatments resulted in a 12% failure rate, i.e., 6 of 52 patients; a similar failure rate of 9% (7/74) was seen in the post-operative patients who received doses between 65.1 ± 4.2 and 57.8 ± 5.6 Gy to CTV1 and CTV2, respectively. This failure analysis was updated [8], and 52 patients in this experience were treated with irradiation with or with platinum-based chemotherapy using IMRT to the upper portion the head and neck region for parotid sparing. The mean doses were 72.6 ± 4.8 and 64.3 ± 5.2 Gy to the CTV1 and CTV2, respectively; doses to the equivalent regions in the postoperative cases were near 69 and 61 Gy, respectively. Of the patients irradiated definitively, ten failed, eight in the CTV1 and two in the lower neck. Considering changes in the parameters applied for the radiation tolerance of a single and the total parotid gland volume [6, 19] current clinical data support the use of IMRT as a means of parotid gland sparing. Future clinical studies will have to examine more uniform patient populations to assure that this sparing is not at the expense of increased tumor failures, not suggested by the reported failures rates or patterns by either of the experiences.

2.5.2 IMRT for Dose Escalation

The application of IMRT for dose/fraction escalation was first tested in 20 patients, most of them with locally advanced HNSCCs. The SMART (Simultaneous Modulated Accelerated Radiation Therapy) regimen utilized the NOMOS Peacock system (NOMOS Corporation, Sewickley, PA) and delivered IMRT through three to five arc treatments [4]. A total dose to the primary target was 60 Gy in 25 fractions of 2.4 Gy, delivered to the GTV; the secondary target volume, defined as tissues at risk for microscopic disease was irradiated to 50 Gy at 2 Gy fractions, a schedule that should require an overall treatment time between 33 and 35 days. Most likely due to dose inhomogeneities (inherent in the NOMOS System; Fig. 9), the median doses delivered to the primary and secondary target volumes were 64.4 and 54.7 Gy, respectively. Reported biological equivalent dose (BED) estimations deriving BED equivalence of 60 Gy to 81–83 Gy at 2 Gy fractions [4] differ from other calculations and raise the question which parameters were considered in these derivations [35]. At the same time, the median doses and sparing of critical normal tissues was explored by prospectively defined dose limits to the spinal cord, brain stem, ipsi- and contralateral parotid glands. At a mean follow-up of 15.2 months, 16 of 20 patients were free of tumor with only two patients having demonstrated isolated local recurrences. Significant acute toxicity is suggested from the report since only 80% of the patients completed the regimen within 40 days, thus implying minimum 5–7-day treatment breaks in these patients. While follow-up is relatively short, the study represents an important first attempt of dose escalation to gross tumor by IMRT while sparing OARs and has generated encouraging tumor control rates.

The RTOG is currently conducting a trial for select centers with experience in different 3D-CRT/IMRT systems. Quality assurance is established through the Advanced Technology Consortium (ATC). The trial compares 3D-CRT vs IMRT (RTOG H-0022) and uses differential dosing, following the concept of SIB-IMRT while conformally avoiding OARs. Following the dose prescription criteria of the ICRU for 3D-CRT a rigid expansion margin is prescribed around the PTV1 (GTV), PTV2 (CTV), and PTV3, i.e., LN bearing tissues at risk for microscopic disease. The dose to the GTV will be 66 Gy to $\geq 95\%$ of the volume, 60 Gy to the CTV, and 54 Gy to 90% of the PTV3.

The first prospective dose escalation trial was conducted at VCU, using the institutionally-developed IMRT system with unique capabilities and interfacing with a commercial treatment planning system (Pinnacle) [35,49,52]. The Phase I trial was designed to escalate the dose to the GTV beyond currently accepted dose levels because of the greatly improved conformality of IMRT and its capability of selective dose/fraction escalation using an AFX SIB-IMRT regimen to increase dose to the GTV while maintaining irradiation to other tissues at or below standard doses. As discussed in detail elsewhere [35], complex alpha/beta-based formulations, also considering overall treatment time and

repopulation, have been employed to compare the RBE of different SIB-IMRT schedules relative to those of standard and other established altered fractionation radiotherapy regimens [21]. We selected 6 weeks or 40 days as an acceptable overall treatment time since a one-week shortening of standard radiotherapy schedules had produced improved tumor control outcomes in several randomized clinical trials [21, 40]. Based on radiation doses of 70–72 Gy delivered during these six-week regimens, we selected the lowest GTV level for the AFX SIB-IMRT trial to be biologically equivalent to the concomitant boost regimen [2, 37, 38] which has produced very similar five-year control rates with two slightly different AFX CB regimens [3, 35, 37, 38]. The following dose levels were selected delivering 30 fractions over 40 days, always initiating IMRT on Mondays; the intended doses for level 1 were 68.1 Gy in 2.27 fractions, for dose level 2, 70.8 Gy in 2.36 Gy fractions, and, for dose level 3, 73.8 Gy in 2.46 Gy fractions. The actual average minimum dose, D_{98}, delivered to 98% of the GTV was 68.6, 70.1, and 71.1 Gy for the three dose levels, amounting to, by normalized tumor doses [35], 75.2, 77.5, and 78.9 Gy, respectively. Following this Phase I dose escalation scheme, six evaluable patients were treated on escalated dose levels, 12 on dose level 2 and 2 on dose level 3. Based on the National Cancer Institute Normal Tissue Toxicity Criteria (NCI NTTC), dose limiting toxicity (DLT) was reached at dose level 3 as indicated by significantly faster developing grade 3 mucosal toxicity during the third week of treatment; thus, the dose of 70.1 Gy over 40 days in 2.36 Gy fractions was identified as the maximum tolerable dose (MTD). The trial also established a volume-dependence of treatment-related normal tissue toxicity for both GTV and CTV that emphasized the importance of physician involvement in the planning process to minimize irradiation to mucosal and non-mucosal tissues to the greatest extent possible [28]. Compliance of patients with overall treatment time and doses delivered to target volumes, e.g., GTV/CTV and ETV, was excellent. Tumor control rates are encouraging with only 2 of 20 patients experiencing isolated local recurrences within the GTV; marginal failures were not identified. Based on recent data suggesting relatively late salivary gland function recovery between 6 and 18 month after completion of treatment [16, 18] this data has not been fully evaluated since we are also attempting to correlate clinical findings with sialochemical analyses.

2.5.3 IMRT for Unusual Volume Shaping and Re-irradiation

The value of IMRT in the re-irradiation of HNSCCs has enormous potential and has been explored in several centers [11]. In addition to conformal avoidance, re-irradiation will require the reporting of highly quantitative data sets that should be uniformly applied to these challenging clinical situations. Such parameters should include dose uniformity indices, integral radiation dose, i.e., target tissue coverage over integral dose delivered, dose to the re-irradiated volume and stringencies regarding avoidance of critical normal tissues. Definition of these parameters is currently examined at our center using a limited number of patients. Five of 11 patients achieved survival rates in excess of 7 months (M. Chang, S. Benedict, and R. K. Schmidt-Ullrich, unpublished).

2.6 Summary

The major potential advantages of IMRT have been addressed in a number of preliminary clinical investigations/trials which have generated encouraging results that salivary gland sparing can be achieved with improvements in xerostomia without risking increased failure rates. Dose escalation trials, although documenting the potential of IMRT as a tool for dose escalation, require refinement and intense physician involvement but have produced encouraging loco-regional tumor control rates. Finally, the ability of generating plans with outstanding dose conformality in the radiotherapeutic management of HNSCCs of the OP/(OC) has been clearly established.

2.7 Future Directions

The standardization of IMRT is currently a major challenge because of the diverse capabilities of different IMRT systems, institutionally developed or commercial. These systems vary widely in their capabilities for conformality of delineated target volumes and dose uniformity within these volumes. The latter has an obvious implication on minimal prescription doses to the target and, therefore, represents the critical parameter of dose uniformity and the ability of that system to be applied diversely, including the use of SIB-IMRT schedules. If dose uniformity becomes a limiting factor those systems may still produce plans that exceed conformality to defined targets over 3D-CRT [46, 47].

The use of IMRT in the setting of multimodality therapy is another potential indication for this modality over other conformal RT approaches. Limiting the volume of highest-dose irradiation should improve the tolerance of combined irradiation and chemotherapy. The relative toxicity of SIB-IMRT will require careful adjustments of the maximum radiation dose and of chemotherapeutic agents to be used. While the RTOG is exploring the feasibility of IMRT vs 3D-CRT at some institutions, our center is currently exploring the addition of weekly cis-

platinum in combination with AFX SIB-IMRT to 68.1 Gy in 40 days in a Phase I/II trial.

Set-up error standardization is an area of future study and is dependent upon the degree of patient immobilization, routine of patient set-up, patient cooperation, and experience of the radiotherapy staff. Each center engaging into IMRT needs to prospectively quantify its set-up/delivery accuracy, which at experienced centers ranges around 3 mm in cranio-caudate and/or circumferential lateral dimensions. These ranges need to be incorporated into the planning process by expanding the PTV by that value. It needs to be appreciated that significant expansion of the *PTVs* may limit the ability to deliver highest radiation doses because of tolerance reasons.

The current concepts for rigid margin definition based on 3D-CRT have not been adjusted to the unique features of IMRT (Chap. I.3.). While the elimination for systematic errors is one of the most important challenges for IMRT delivery, there is also a need to develop statistically more valid models that treat random errors other than rigidly applied PTV margins (see Chap. I.5.).

The known heterogeneity of gross tumors with respect to blood flow, extent of hypoxia and, likely, histopathology have been exploited to a limited extent for therapeutic use. Existing studies have also not been correlated, e.g., in the case of hypoxia, with response patterns to radiotherapy [5]. However, future improvement in functional imaging, before, during and after irradiation may permit IMRT to be applied as a method for intra-tumoral dose painting and/or selective boosting.

The widely varied capabilities of different commercial and institution-based systems may generate substantially different IMRT plans and delivered treatments. One major difference will be the degree of dose homogeneity achievable within the target volumes that may limit the minimum prescription isodose. As a result, significant differences in the target volume coverage and overall dosing may remain. This variance may be, at least in part, corrected by planning/delivery systems that additionally consider biological radiation effects for greater uniformity between different systems. One of the promising attempts represents the introduction of the equivalent uniform dose (EUD) concept [44, 49, 53].

References

1. Amosson CM, Teh BS, Van TJ et al. (2003) Dosimetric predictors of xerostomia for head-and-neck cancer patients treated with the smart (simultaneous modulated accelerated radiation therapy) boost technique. Int J Radiat Oncol Biol Phys 56:136–144
2. Ang KK, Peters LJ (1992) Concomitant boost radiotherapy in the treatment of head and neck cancers. Semin Radiat Oncol 2:31–33
3. Ang KK, Thames HD (2004) Altered fractionation schedules. In: Perez CA, Brady LW, Halpern EC, Schmidt-Ullrich RK (ed) Principles and practices of radiation oncology. Lippincott Williams and Wilkins, Philadelphia, PA, pp 337–356
4. Butler EB, Teh BS, Grant WH III et al. (1999) Smart (simultaneous modulated accelerated radiation therapy) boost: a new accelerated fractionation schedule for the treatment of head and neck cancer with intensity modulated radiotherapy. Int J Radiat Oncol Biol Phys 45:21–32
5. Chao KS, Bosch WR, Mutic S et al. (2001) A novel approach to overcome hypoxic tumor resistance: Cu-ATSM-guided intensity-modulated radiation therapy. Int J Radiat Oncol Biol Phys 49:1171–1182
6. Chao KS, Deasy JO, Markman J et al. (2001) A prospective study of salivary function sparing in patients with head-and-neck cancers receiving intensity-modulated or three-dimensional radiation therapy: initial results. Int J Radiat Oncol Biol Phys 49:907–916
7. Chao KS, Low DA, Perez CA et al. (2000) Intensity-modulated radiation therapy in head and neck cancers: The Mallinckrodt experience. Int J Cancer 90:92–103
8. Chao KS, Ozyigit G, Tran BN et al. (2003) Patterns of failure in patients receiving definitive and postoperative IMRT for head-and-neck cancer. Int J Radiat Oncol Biol Phys 55:312–321
9. Chao KS, Wippold FJ, Ozyigit G et al. (2002) Determination and delineation of nodal target volumes for head-and-neck cancer based on patterns of failure in patients receiving definitive and postoperative IMRT. Int J Radiat Oncol Biol Phys 53: 1174–1184
10. Chung NN, Ting LL, Hsu WC et al. (2004) Impact of magnetic resonance imaging versus CT on nasopharyngeal carcinoma: primary tumor target delineation for radiotherapy. Head Neck 26:241–246
11. Claus F, Duthoy W, Boterberg T et al. (2002) Intensity modulated radiation therapy for oropharyngeal and oral cavity tumors: clinical use and experience. Oral Oncol 38:597–604
12. De Gersem W, Claus F, De Wagter C et al. (2001) An anatomy-based beam segmentation tool for intensity-modulated radiation therapy and its application to head-and-neck cancer. Int J Radiat Oncol Biol Phys 51:849–859
13. Earl MA, Shepard DM, Naqvi S et al. (2003) Inverse planning for intensity-modulated arc therapy using direct aperture optimization. Phys Med Biol 48:1075–1089
14. Eisbruch A. (2002) Intensity-modulated radiotherapy of head-and-neck cancer: encouraging early results. Int J Radiat Oncol Biol Phys 53:1–3
15. Eisbruch A, Foote RL, O'Sullivan B et al. (2002) Intensity-modulated radiation therapy for head and neck cancer: emphasis on the selection and delineation of the targets. Semin Radiat Oncol 12:238–249
16. Eisbruch A, Kim HM, Terrell JE et al. (2001) Xerostomia and its predictors following parotid-sparing irradiation of head-and-neck cancer. Int J Radiat Oncol Biol Phys 50:695–704
17. Eisbruch A, Marsh LH, Martel MK et al. (1998) Comprehensive irradiation of head and neck cancer using conformal multisegmental fields: assessment of target coverage and noninvolved tissue sparing. Int J Radiat Oncol Biol Phys 41:559–568
18. Eisbruch A, Ship JA, Dawson LA et al. (2003) Salivary gland sparing and improved target irradiation by conformal and intensity modulated irradiation of head and neck cancer. World J Surg 27:832–837
19. Eisbruch A, Ten Haken RK, Kim HM et al. (1999) Dose, volume, and function relationships in parotid salivary glands following conformal and intensity-modulated irradiation of head and neck cancer. Int J Radiat Oncol Biol Phys 45:577–587

20. Ezzell GA, Galvin JM, Low D et al. (2003) Guidance document on delivery, treatment planning, and clinical implementation of IMRT: report of the IMRT Subcommittee of the AAPM Radiation Therapy Committee. Med Phys 30:2089–2115
21. Fu KK, Pajak TF, Trotti A et al. (2000) A Radiation Therapy Oncology Group (RTOG) phase III randomized study to compare hyperfractionation and two variants of accelerated fractionation to standard fractionation radiotherapy for head and neck squamous cell carcinomas: first report of RTOG 9003. Int J Radiat Oncol Biol Phys 48:7–16
22. Gregoire V, Levendag P, Ang KK et al. (2003) CT-based delineation of lymph node levels and related CTVs in the node-negative neck: DAHANCA, EORTC, GORTEC, NCIC, RTOG consensus guidelines. Radiother Oncol 69:227–236
23. Horiot JC, Bontemps P, van den Bogaert W et al. (1997) Accelerated fractionation (AF) compared to conventional fractionation (CF) improves loco- regional control in the radiotherapy of advanced head and neck cancers: results of the EORTC 22851 randomized trial. Radiother Oncol 44: 111–121
24. Horiot JC, Le Fur R, N'Guyen T et al. (1992) Hyperfractionation versus conventional fractionation in oropharyngeal carcinoma: final analysis of a randomized trial of the EORTC cooperative group of radiotherapy. Radiother Oncol 25: 231–241
25. Jha N, Seikaly H, Harris J et al. (2003) Prevention of radiation induced xerostomia by surgical transfer of submandibular salivary gland into the submental space. Radiother Oncol 66:283–289
26. Kalet IJ, Austin-Seymour MM (1997) The use of medical images in planning and delivery of radiation therapy. J Am Med Inform Assoc 4:327–339
27. Khoo VS, Dearnaley DP, Finnigan DJ et al. (1997) Magnetic resonance imaging (MRI): considerations and applications in radiotherapy treatment planning. Radiother Oncol 42:1–15
28. Lauve A, Morris M, Schmidt-Ullrich R et al. (2004) Simultaneous integrated boost intensity-modulated radiotherapy for locally advanced head-and- neck squamous cell carcinomas: II: Clinical results. Int J Radiat Oncol Biol Phys 60(2): 374–387
29. Lee N, Chuang C, Quivey JM et al. (2002) Skin toxicity due to intensity-modulated radiotherapy for head-and-neck carcinoma. Int J Radiat Oncol Biol Phys 53:630–637
30. Ling CC, Humm J, Larson S et al. (2000) Towards multidimensional radiotherapy (MD-CRT): biological imaging and biological conformality. Int J Radiat Oncol Biol Phys 47: 551–560
31. Ma L, Yu CX, Earl M et al. (2001) Optimized intensity-modulated arc therapy for prostate cancer treatment. Int J Cancer 96:379–384
32. Manning MA, Wu Q, Cardinale RM et al. (2001) The effect of setup uncertainty on normal tissue sparing with IMRT for head-and-neck cancer. Int J Radiat Oncol Biol Phys 51:1400–1409
33. Martinez-Monge R, Fernandes PS, Gupta N et al. (1999) Cross-sectional nodal atlas: a tool for the definition of clinical target volumes in three-dimensional radiation therapy planning. Radiology 211:815–828
34. Mohan R, Wang X, Jackson A et al. (1994) The potential and limitations of the inverse radiotherapy technique. Radiother Oncol 32:232–248
35. Mohan R, Wu Q, Manning M et al. (2000) Radiobiological considerations in the design of fractionation strategies for intensity-modulated radiation therapy of head and neck cancers. Int J Radiat Oncol Biol Phys 46:619–630
36. Mohan R, Wu Q, Wang X et al. (1996) Intensity modulation optimization, lateral transport of radiation, and margins. Med Phys 23:2011–2021
37. Morris MM, Schmidt-Ullrich R, Johnson CR (2000) Advances in radiotherapy for carcinoma of the head and neck. Surg Oncol Clin N Am 9:563–575, x
38. Morris MM, Schmidt-Ullrich RK, DiNardo L et al. (2002) Accelerated superfractionated radiotherapy with concomitant boost for locally advanced head-and-neck squamous cell carcinomas. Int J Radiat Oncol Biol Phys 52:918–928
39. Munter MW, Karger CP, Hoffner SG et al. (2004) Evaluation of salivary gland function after treatment of head-and-neck tumors with intensity-modulated radiotherapy by quantitative pertechnetate scintigraphy. Int J Radiat Oncol Biol Phys 58:175–184
40. Overgaard J, Hansen HS, Specht L et al. (2003) Five compared with six fractions per week of conventional radiotherapy of squamous-cell carcinoma of head and neck: DAHANCA 6 and 7 randomised controlled trial. Lancet 362:933–940
41. Parliament MB, Scrimger RA, Anderson SG et al. (2004) Preservation of oral health-related quality of life and salivary flow rates after inverse-planned intensity-modulated radiotherapy (IMRT) for head-and-neck cancer. Int J Radiat Oncol Biol Phys 58:663–673
42. Rasch C, Keus R, Pameijer FA et al. (1997) The potential impact of CT-MRI matching on tumor volume delineation in advanced head and neck cancer. Int J Radiat Oncol Biol Phys 39:841–848
43. Sanguineti G, Foppiano F, Marcenaro M et al. (2001) On the delineation of the gross tumor volume and clinical target volume for head and neck squamous cell carcinomas. Tumori 87:153–161
44. Thieke C, Bortfeld T, Niemierko A et al. (2003) From physical dose constraints to equivalent uniform dose constraints in inverse radiotherapy planning. Med Phys 30:2332–2339
45. Tsai JS, Engler MJ, Ling MN et al. (1999) A non-invasive immobilization system and related quality assurance for dynamic intensity modulated radiation therapy of intracranial and head and neck disease. Int J Radiat Oncol Biol Phys 43:455–467
46. Verhey LJ (1999) Comparison of three-dimensional conformal radiation therapy and intensity-modulated radiation therapy systems. Semin Radiat Oncol 9:78–98
47. Verhey LJ (2002) Issues in optimization for planning of intensity-modulated radiation therapy. Semin Radiat Oncol 12:210–218
48. Wu Q, Arnfield M, Tong S et al. (2000) Dynamic splitting of large intensity-modulated fields. Phys Med Biol 45:1731–1740
49. Wu Q, Djajaputra D, Wu Y et al. (2003) Intensity-modulated radiotherapy optimization with gEUD-guided dose-volume objectives. Phys Med Biol 48:279–291
50. Wu Q, Manning M, Schmidt-Ullrich R et al. (2000) The potential for sparing of parotids and escalation of biologically effective dose with intensity-modulated radiation treatments of head and neck cancers: a treatment design study. Int J Radiat Oncol Biol Phys 46:195–205
51. Wu Q, Mohan R (2000) Algorithms and functionality of an intensity modulated radiotherapy optimization system. Med Phys 27:701–711
52. Wu Q, Mohan R, Morris M et al. (2003) Simultaneous integrated boost intensity-modulated radiotherapy for locally advanced head-and-neck squamous cell carcinomas. I: dosimetric results. Int J Radiat Oncol Biol Phys 56:573–585
53. Wu Q, Mohan R, Niemierko A et al. (2002) Optimization of intensity-modulated radiotherapy plans based on the equivalent uniform dose. Int J Radiat Oncol Biol Phys 52:224–235

54. Yu CX, Li XA, Ma L et al. (2002) Clinical implementation of intensity-modulated arc therapy. Int J Radiat Oncol Biol Phys 53:453–463

55. Zhou J, Fei D, Wu Q (2003) Potential of intensity-modulated radiotherapy to escalate doses to head-and-neck cancers: what is the maximal dose? Int J Radiat Oncol Biol Phys 57:673–682

IMRT for Carcinomas of the Nasopharynx

Benjamin D. Rosenbluth, William W. Chou, Nancy Y. Lee

3

Contents

3.1 Introduction – The Clinical Problem and the Potential Benefits of IMRT

Nasopharyngeal carcinoma (NPC) is common among Asians, especially the Southern Chinese, and is rarely seen among the Caucasian population, representing < 1% of all cancers in the United States [1].

The nasopharynx is a cuboidal chamber located below the base of the skull and behind the nasal cavity. The posterior wall lies at the level of the first two cervical vertebrae and is continuous with the roof, which is formed by the basisphenoid, basiocciput, and the anterior arch of the atlas. The lymphoid tissue in this area forms the pharyngeal tonsil (adenoids). Each lateral wall contains a eustachian tube orifice, which is surrounded by the torus tubarius, a prominence in the cartilaginous portion of the tube. Behind the torus tubarius is a recess called Rosenmüller's fossa (Fig. 1). The lateral walls, including Rosenmüller's fossa, are the most common sites of origin of nasopharyngeal carcinoma. The floor of the nasopharynx consists of the upper surface of the soft palate and communicates with the oropharynx via the pharyngeal isthmus.

Lymphatic spread to the ipsilateral nodes is common in NPC and is present in 85–90% of cases [2]. Bilateral spread occurs in about 50% of cases. Metastasis to the contralateral nodes only is uncommon. Spread to the lateral and posterior retropharyngeal lymph nodes occurs early and is frequently seen on MRI or CT scans, although the nodes are not palpable (Fig. 1D). Metastasis to the jugulodigastric and superior posterior cervical nodes is also common. From these first echelon nodes, further metastasis to the midjugular and posterior cervical, lower jugular, and posterior cervical and supraclavicular nodes can occur. Occasionally, spread to the submental and occipital nodes occurs as a result of lymphatic obstruction due to extensive cervical lymphadenopathy. Spread to the parotid nodes can occur via the lymphatics of the eustachian tube. Metastasis to the mediastinal lymph nodes may occur when supraclavicular lymphadenopathy is present. Distant lymph node metastasis is often reported in autopsy series. Survival decreases as cervical lymph node involvement progresses from the upper to the middle and lower nodes [3].

Both MRI and CT scans are useful in radiotherapy treatment planning. However, MRI is capable of multiplanar display of tumor extent and is superior to CT scans in delineating muscle and other soft tissue involvement. In post-treatment follow-up examinations, MRI can help differentiate radiation fibrosis from persistent or recurrent tumor based on T2-weighted signal intensities and with gadolinium enhancement and fat suppression [4]. MRI and CT scans can also detect lymph node metastasis that may not be evident on clinical examination (see Fig. 1D) [5]. CT, however, is superior to MRI in the detection of early bone invasion [6, 7], and a CT scan with bone windows is useful to demonstrate the extent of invasion of the base of the skull or the cervical vertebrae. The major limitation of CT is its poor tissue differentiation. Thus, ideally both CT and MRI should be used in planning radiation treatment for patients with NPC.

The standard treatment for nasopharyngeal carcinoma is definitive radiotherapy, +/– chemotherapy, with chemotherapy reserved for more advanced le-

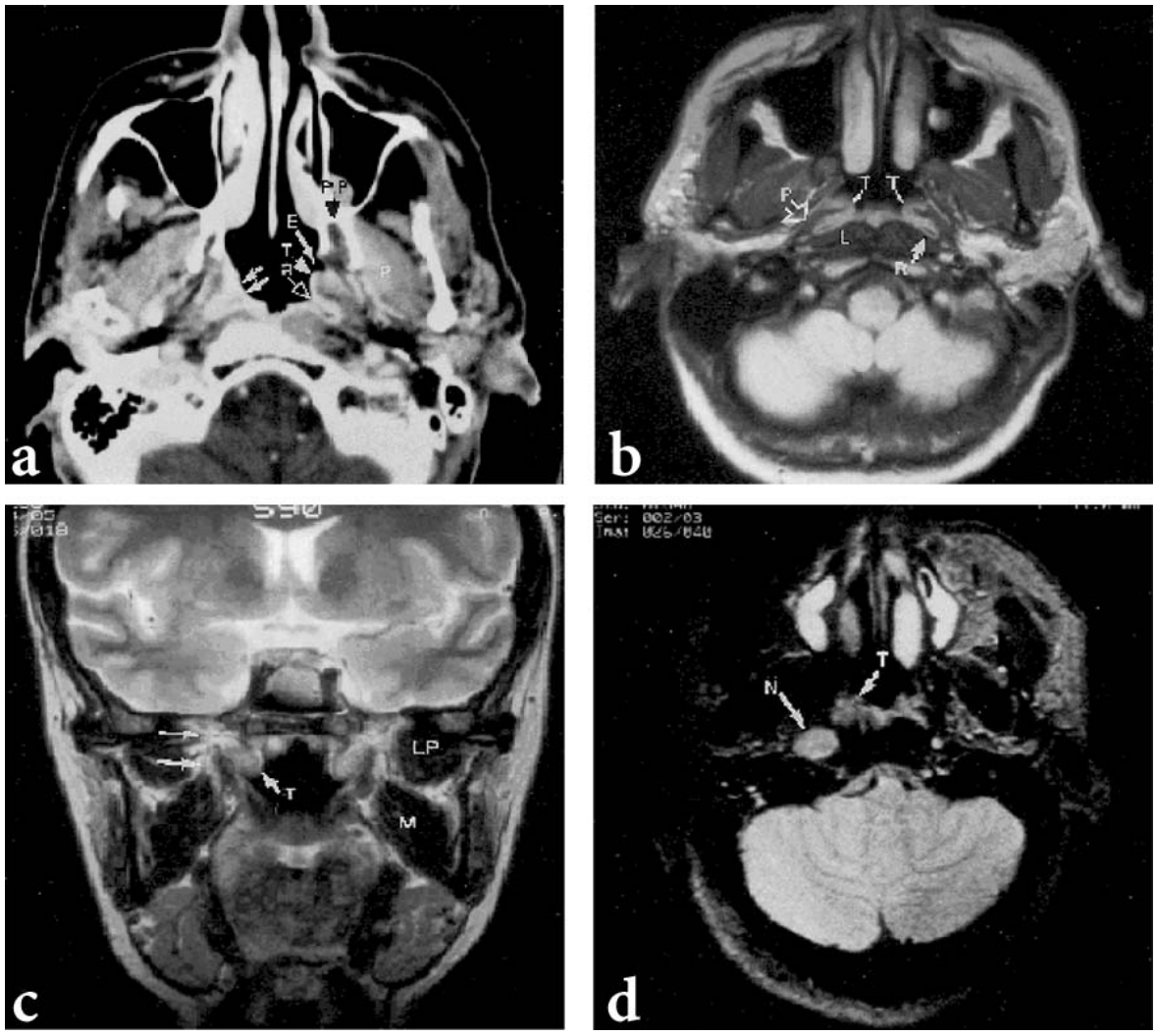

Fig. 1a–d. Normal computed tomography (CT) and magnetic resonance imaging (MRI) images of the nasopharynx: **(a)** axial postcontrast CT scan of the mid- nasopharynx. Just posterior to the medial pterygoid plate (PP), there is a small recess representing the orifice of the eustachian tube (E). Posterior to this and separating the fossa of Rosenmüller (R) from the eustachian orifice is a protuberance extending into the nasopharyngeal airway, the torus tubarius (T). Lateral to the pterygoid plates is the lateral pterygoid muscle (P). Note the normal asymmetry of the fossa of Rosenmüller (*double white arrows*), which can occasionally simulate early carcinoma. Also of importance is the symmetrical parapharyngeal space that contains branches of the internal maxillary artery and small veins of the pterygoid plexus. The parapharyngeal space separates the deep lobe of the parotid gland from the soft tissues of the nasopharynx and serves as a landmark for deep invasion from carcinoma of the nasopharynx; **(b)** axial proton density-weighted MRI scan through the nasopharynx showing soft tissue contrast achieved with MRI scanning in this region. Note the higher-signal-intensity mucosal adenoidal tissue, which is easily separated from the underlying musculature of the deep pharyngeal soft tissues. Also note the musculature of the masticator space, including the masseter muscle, deep head of the temporalis muscle, lateral and medial pterygoid muscles, and the tensor veli and levator veli palatini muscles. Note the symmetrical convex appearance of the longus capitis muscles (L) positioned directly behind the mucosa of the nasopharynx and Rosenmüller's fossa (R). Posterior and lateral to the torus tubarius (T) is the parapharyngeal space (P), containing fat and separating the deep structures from the deep lobe of the parotid gland; **(c)** coronal T2-weighted MRI scan demonstrating the close relationship of the superior recess of the nasopharynx to the skull base, the torus tubarius (T), the levator veli palatini muscle (*double arrows*), the medial pterygoid muscle (M), the lateral pterygoid (LP) muscle, the mandible, and the masseter muscle. Positioned in the midline are the tongue and the soft palate; **(d)** axial T2-weighted MRI scan through the midnasopharynx showing the presence of a metastatic right lateral retropharyngeal lymph node (N). Note its location lateral and posterior to the tumor (T) in the right fossa of Rosenmüller

sions [8, 9]. Radiotherapy's use as primary therapy for nasopharyngeal carcinoma is largely attributable to the nasopharynx's anatomical location, as well as the propensity of NPC for early bilateral lymph node metastases and involvement of the lateral retropharyngeal node of Rouvière , which usually cannot be surgically removed. Furthermore, cervical lymph node metastases from nasopharyngeal carcinoma, even when they are bulky, are very radioresponsive and locally radiocurable.

Utilizing conventional radiation, the local control rate for T1 and T2 tumors ranges from 64 to 95%; however, the control rate drops to 44–68% in more advanced T3/T4 lesions. Five-year survival is reported to be between 36 and 58% [11–17].

Tumor control for carcinoma of the nasopharynx has been highly correlated with the dose delivered to the tumor [18, 19]. In a series of 107 patients with NPC treated with conventional radiation, local control was significantly improved when > 67 Gy was delivered to the tumor target. In another series of 118 patients, the improvement of tumor control was not only attributed to the prescription of higher doses of radiation, but also to improvements in technical accuracy. Technical accuracy is desirable in the treatment of NPC for another reason: as mentioned above, the nasopharynx is surrounded by many normal critical structures, including the brainstem, optic chiasm, optic nerves, and the spinal cord [20–29].

It is therefore apparent why intensity modulated radiation therapy (IMRT) has gained its popularity in the treatment of head and neck cancers. With this technique, multiple radiation beams can be modulated and shaped, such that a high dose can be delivered to the tumor while significantly reducing the dose to the surrounding normal tissue. The proximity of NPC to critical normal tissues, its dose responsiveness, and its improved control with greater technical accuracy all argue for the use of IMRT in obtaining good local control for these tumors. Also, due to the relative lack of organ motion within the head-and-neck region, accurate reproduction of daily patient setups is quite feasible, provided adequate immobilization is utilized.

This ability of IMRT to safely and effectively treat primary tumor which may approximate critical normal structures, is predominantly manifest in the treatment of more advanced NPC tumors, namely T3 and T4 tumors.

Another major benefit of IMRT in the treatment of NPC, and one which benefits patients with all T stages, is its ability to spare the parotids and maintain salivary function (see next section). This benefit is applicable to the treatment of both early and locally invasive tumors, as all patients previously required opposed lateral radiation fields, which inevitably treated the parotid glands to toxic doses. Thus, for patients with T1 and T2 disease, while treatment with IMRT provides target coverage and control which may not differ significantly from that with conventional radiation, it is superior in sparing the parotid glands. On the other hand, for patients with T3 and T4 disease, IMRT can help us accomplish two goals, namely parotid sparing and adequate dose to the GTV without significant normal-tissue toxicity.

As mentioned previously, chemotherapy has been shown to play a role, along with radiation, in the management of more advanced lesions. A recent phase III trial by the Head and Neck Intergroup in the United States compared radiotherapy alone to radiotherapy plus concurrent and adjuvant chemotherapy for stage III and IV disease. Chemotherapy consisted of cisplatin 100 mg/m^2 on days 1, 22 and 43 during radiotherapy. Following completion of radiotherapy, treatment continued with cisplatin 80 mg/m^2 on day 1 plus 5-fluorouracil (5-FU) 1,000 mg/m^2/day on days 1 to 4 every four weeks for three courses. Radiotherapy in both arms was conventional, given as 1.8 to 2.0 Gy per fraction per day, five days a week, to a total dose of 70 Gy. At five years, the overall survival was 37% vs 67% ($P < 0.001$) and progression-free survival was 29% vs 58% in favor of the chemotherapy arm ($P < 0.001$) [30]. These results have been confirmed by several other studies, including four meta-analyses [31–38].

It should be noted, however, that, although the intergroup trial demonstrated an improvement in local control and survival, about 1/3 of the patients did not complete the prescribed therapy due to toxicity. As IMRT may also decrease the toxicities associated with radiation therapy, it may therefore improve patient compliance with combined modality therapy. This theory is currently being tested in an ongoing phase II trial (RTOG 0225), examining IMRT +/- chemotherapy for NPC.

Yet another role for IMRT in NPC treatment is in the re-treatment of patients with recurrent disease. Patients with recurrences have often already received very high doses of radiation and are usually not considered surgically resectable. Therefore, their only chance of control frequently lies in the radiation oncologist's ability to delimit with extreme precision the volume which receives additional radiation. Close collaboration with one's physics department can help determine the extent to which a patient can be re-treated, and can offer these patients their best chances of salvage.

3.2 Unique Anatomical Challenges in the Treatment of Nasopharyngeal Carcinoma

Many of the common acute and late side effects of conventional radiation for NPC are directly related to the proximity and radiosensitivity of multiple normal tissues in the area of the tumor. Many of these organs, while not critical for survival, are extremely important when it comes to quality of life for these patients. Among the more common side effects are xerostomia, temporal lobe necrosis, hearing loss and pituitary hypofunction. Less commonly seen in recent data are oral and dental complications, neuro-ophthalmologic complications, and soft or hard-tissue complications.

One of the major complaints of patients undergoing conventional external beam radiation therapy to the nasopharynx is xerostomia. Standard radiation delivers a high dose to the bilateral major salivary glands.

Salivary flow is markedly reduced following 10–15 Gy of radiation delivered to most of the gland [39, 40]. The recovery of the salivary function is possible over time even with doses up to 40–50 Gy. However, higher doses to most of the gland will result in irreversible and permanent xerostomia. The degree of xerostomia is largely dependent on the radiation dose and the volume of the salivary gland that is in the radiation field. As a result, patients' quality of life is compromised as they experience changes in speech and taste. The oral dryness also predisposes the patients to fissures, ulcers, dental caries, infection, and even in worst cases, osteoradionecrosis [41–44]. Thus, IMRT has the potential to reduce the dose to the salivary glands while simultaneously delivering a high dose to the tumor target.

In the cases of locally advanced NPC, there is often involvement of critical intracranial structures, especially once margin is added to the gross tumor volume (GTV). If there is any chance of toxicity to these organs, they must be contoured and monitored for toxic doses. The organs particularly at risk for radiation damage include the temporal lobes, spinal cord, cochleae, optic nerves, optic chiasm and mandible (including the mandibular horns). Usually the brainstem is the area of greatest concern, given the usual areas involved by NPC. For further details, including dose specifications to the organs at risk, see "Planning Goals" below.

3.3 Target Volume Delineation – Definition of Organs at Risk

One of the most important issues in the application of IMRT is the accurate and adequate definition of target volumes. The precise delineation of these volumes, especially the subclinical volumes, is crucial in treatment planning. When compared to standard techniques, the very tight and conformal isodose curves around the outlined target volumes in IMRT increase the risk of missing areas containing subclinical disease if the treatment volumes are not drawn accurately. Consequently, there is an increased risk of marginal or out-of-field recurrence. As there is significant variation among physicians regarding the definitions of head and neck nodal volumes, efforts to define accurately the location of lymph nodes in the head and neck, using cadaver CT scans, have been described [45–48].

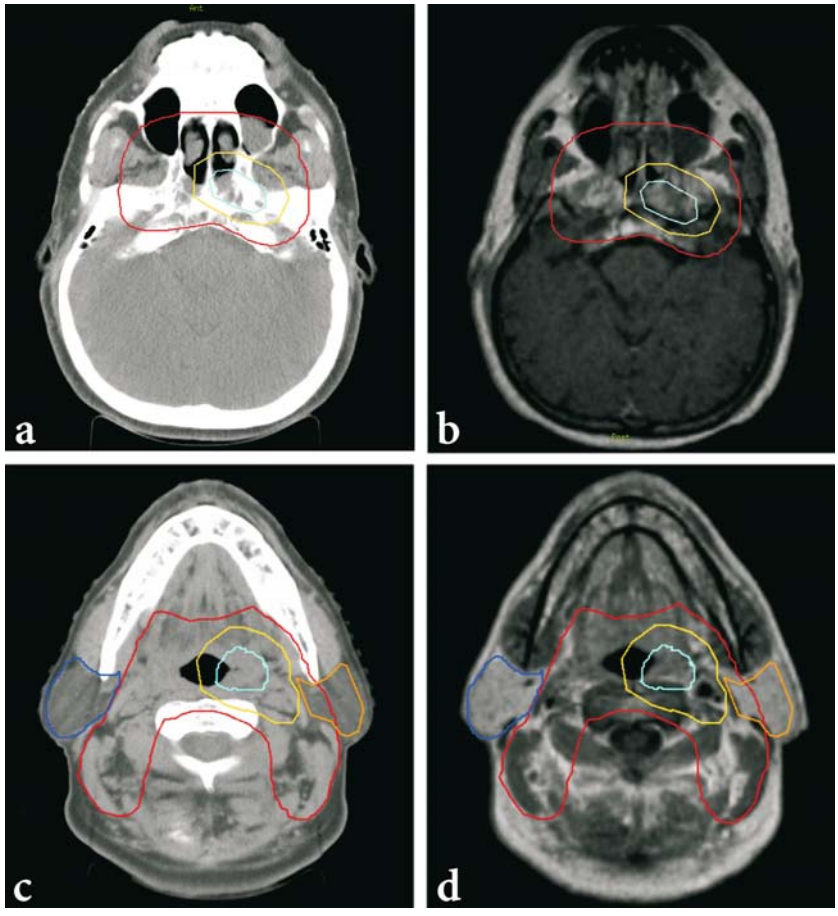

Fig. 2. CT delineation of tumor volume with correlating MR images. GTV, *light blue*; PTV1, *yellow*; PTV2, *red*; right parotid gland, *dark blue*; left parotid gland, *orange*

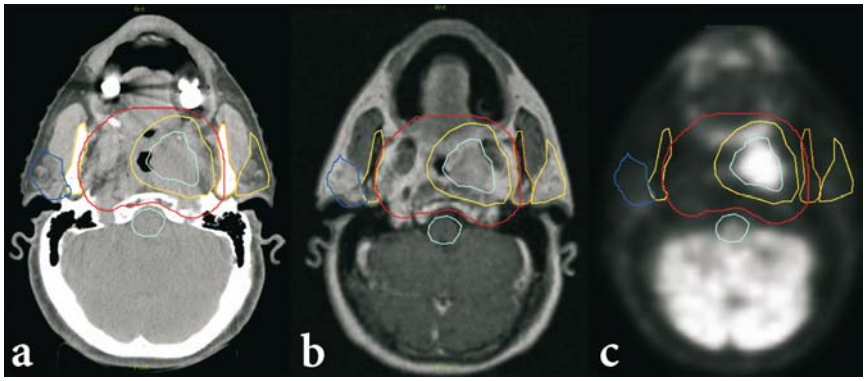

Fig. 3. CT and MRI supplemented by PET information. GTV, *light blue*; PTV1, *yellow*; PTV2, *red*; right parotid gland, *dark blue*; left parotid gland, *orange*

Since precise delineation of both the tumor and normal structures is crucial in treatment planning [37, 49, 50], fusion of MRI and/or PET images may be performed to supplement CT for better determination of gross tumor volume (GTV) and the surrounding normal tissue (Fig. 2). Information from the PET scan may further supplement MRI findings, especially regarding additional tumor manifestations (Fig. 3) [51]. All available imaging modalities should be used when outlining the gross extent of the disease. For example, PET scans may help ensure that a GTV outlined with the aid of MRI truly encompasses the entire area of high-metabolic activity, as detected on PET. Conversely, one must be sure not to make the GTV too small by basing contours only on the areas of high uptake on PET, as an MRI will often reveal abnormalities which a PET scan is too insensitive to detect.

In addition, target volumes should be delineated slice by slice on the treatment CT axial images in conjunction with a neuroradiologist (Fig. 4). GTV is defined as all known gross disease determined from clinical information, endoscopic findings, and imaging studies. This essentially includes the nasopharyngeal primary with any local extension, gross retropharyngeal lymphadenopathy, and any gross nodal disease greater than 1.0 cm or with a necrotic center. Close attention must be paid to the retropharyngeal nodal regions to detect any abnormal nodes. When in doubt, nodes in these regions should be considered GTV and should be outlined as such.

Table 1. Suggested target volumes and margins

Target	Definition	Margin (prescription dose)
GTV	CTV1 = Nasopharyngeal primary and Gross nodal disease+at least 5 mm margin (see CTV2: CTV1 should be encompassed by CTV2) except in areas adjacent to critical structure, i.e. brainstem, where margin can be as small as 1 mm	PTV1 (70 Gy)* = 5 mm in all directions from CTV1 except for areas adjacent to critical structures, i.e. brainstem, where margin can be as small as 1 mm *GTV will have at least a 1 cm margin in all directions, except for regions near critical structures.
High risk subclinical disease	CTV2 = Adjacent soft tissue/structures , i.e., entire nasopharynx, clivus, skull base, retropharyngeal nodal regions, pterygoid fossae, parapharyngeal space, sphenoid sinus, and posterior third of maxillary sinus and up to posterior 1/2 of nasal cavity (CTV2 should encompass CTV1) High risk nodal groups a. Upper deep jugular b. Subdigastric c. Midjugular d. Posterior Cervical e. Retropharyngeal f. Submandibular (may omit at discretion of treating physician if T1N0)	PTV2 (59.4 Gy*)= 5 mm in all directions of CTV2 except when near brainstem where margin can be as small as 1 mm *PTV2 should encompass PTV1 in all directions
Low risk subclinical disease	CTV3 = lower jugular nodes, supraclavicular lymph nodes	PTV3 (50.4 Gy)= low anterior AP field Alternatively, if PTV3 is encompassed in the IMRT field and there is no low anterior AP field, the prescription for PTV3 should be 54 Gy (see text under dose specification)

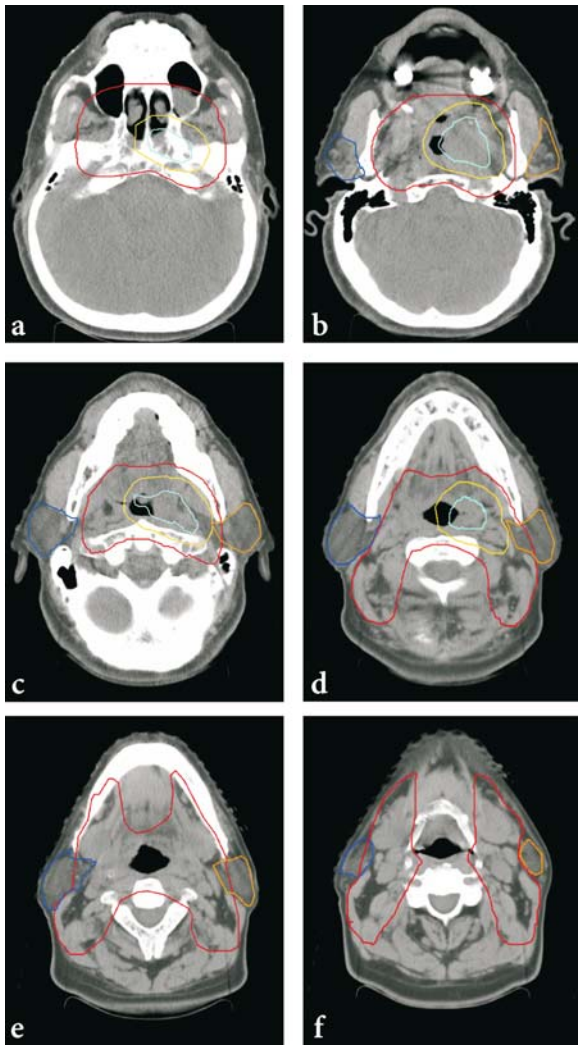

Fig. 4. CTV delineation for a T2bN0M0 nasopharyngeal carcinoma receiving definitive IMRT. GTV, *light blue*; PTV2, *red*; right parotid gland, *darkblue*; left parotid gland, *orange*

Clinical tumor volume (CTV) is defined as the GTV plus areas with potential microscopic spread as determined by the treating physician. A margin of at least 5.0 mm on the GTV should be used in all directions; this may be reduced to 1.0 mm in situations where the GTV is adjacent to the brainstem, such as in the event of clivus infiltration. Three different CTVs are defined, namely CTV1 for gross tumor volume, CTV2 for high-risk nodal regions and adjacent soft tissue, and CTV3 for low-risk nodal regions (Table 1).

At-risk adjacent tissues, defined by the CTV2, include the entire nasopharynx, clivus, skull base, retropharyngeal nodal regions, pterygoid fossae, parapharyngeal space, sphenoid sinus, posterior third of maxillary sinus and up to the posterior one-half of the nasal cavity. High-risk lymph-node groups in NPC include upper deep jugular (junctional, parapharyngeal), subdigastric (jugulodigastric), midjugular, posterior cervical, retropharyngeal lymph nodes, and submandibular lymph nodes [46, 52].

Elective treatment of all cervical lymph nodes should be performed due to the high likelihood of cervical metastases including clinically N0 patients. This generally held approach is challenged by a randomized study by Ho demonstrating that survival of N0 patients receiving elective irradiation of the cervical lymphatics was not better than that of N0 patients not receiving neck irradiation [53]. Lee et al., however, reported that in 384 NPC patients with clinically negative necks, 11% (44 patients) of those receiving elective neck irradiation had regional failure compared with 40% (362 of 906) of those not electively treated [15]. (At the discretion of the treating physician, patients with stage T1N0 may be spared treatment of the level I nodes.) Lower risk lymph node groups such as lower neck and supraclavicular lymph nodes bilaterally are included in CTV3, which may be included in the AP field.

The planning target volume (PTV) provides a margin around the CTV to compensate for internal organ motion and treatment-setup uncertainty. Studies should be performed by each institution to define the appropriate magnitude of compensation necessary for the variables related to the PTV. In our institution, 5.0 mm expansion around the CTV is utilized, except for situations where the CTV is adjacent to the brain stem, in which case the margins are reduced to 1.0 mm. Figure 4 shows serial GTV, PTV1, and PTV2 axial delineation in a T2bN0M0 NPC patient receiving definitive IMRT.

Critical normal structures, including the brain stem, spinal cord, optic nerves, optic chiasm, temporomandibular (T-M) joints, mandible, and brain must be outlined in three dimensions. The spinal cord contours should be 5.0 mm larger in the radial dimension than the spinal cord (i.e., the cord diameter on any given slice should be 10 mm larger than the cord itself). The brain stem and chiasm should be defined as at least 1.0 mm larger in all directions than the corresponding structure. Important but less critical normal structures such as parotid gland, eyes, lens, middle and inner ears, tongue and glottic larynx should also be included.

3.4 Planning and Dose Prescriptions – Optimization Strategies

The fundamental sequential steps involved in IMRT planning, from simulation to treatment delivery, are illustrated in Fig. 5.

Target volumes and normal anatomy must be defined by CT simulation to allow for accurate target definition, digital reconstruction and three-dimensional planning. Fusion of MR images may be used to supplement CT imaging for better delineation of gross

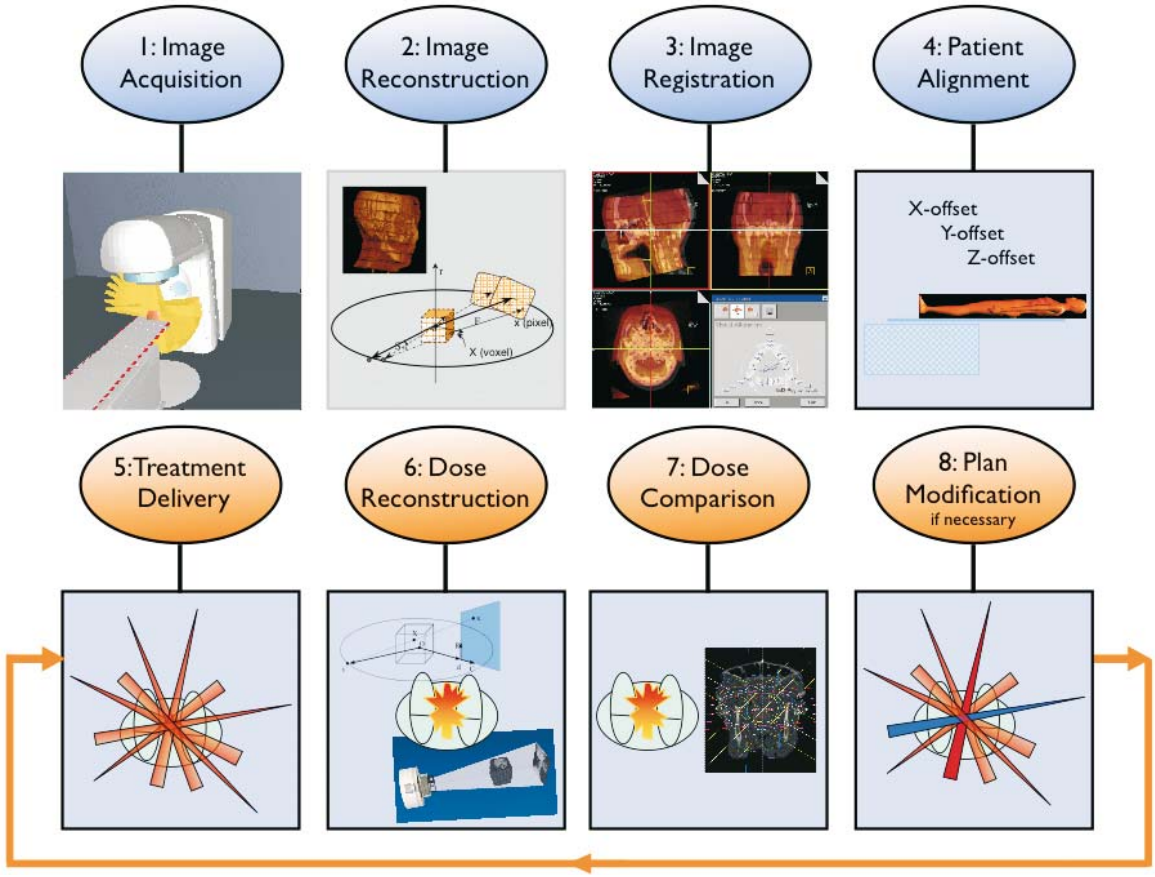

Fig. 5. Flow chart of IMRT planning from simulation to plan evaluation and modification

tumor and surrounding normal tissue. IMRT plans are sensitive to setup errors and patient movement, and therefore, they require stringent patient immobilization and daily setup reproducibility [37]. Special considerations during the simulation are required to address these concerns.

For immobilization, the head and neck should be immobilized using a thermoplastic mask; neck support may be needed if a thermoplastic head mask alone is not sufficient for neck immobilization. Immobilization can be achieved with a headboard (Timo S-type, MEDTEC) for attachment of an Aquaplastic mask (Aquaplast, Wycoff Heights, NJ) that extends from the vertex of the scalp to the shoulders [25, 54]. The treatment immobilization device can also be used for MRI fusion scans. Due to the size of the head rest and the immobilization setup, diagnostic MRI with the head coil may not be compatible with these devices; however, in such cases, MRI with body coil setup should accommodate the immobilization devices and allowed for duplication of the CT simulation process with good image resolution. Alternatively, image-registration methods may be employed to correlate diagnostic MRI with CT simulations.

The patient's head should be hyperextended at the simulation to provide adequate separation between the primary lesion/retropharyngeal lymph node and the upper neck field [27]. The tip of the uvula and the base of the occiput should be parallel to the beam axis [55]. A pair of orthogonal radiographs should be taken for isocenter localization at the initial simulation. A treatment planning CT scan in serial 3.0 mm thickness slices should be obtained from the head down to the clavicles, with a minimum margin of 5–10 cm above and below the target. CT scan slice thickness for the GTV should be 3.0 mm or less while regions above and below the target volume can have slice thicknesses of 5.0 mm.

An isocenter for the conformal IMRT field is chosen based on the patient's anatomy and disease distribution. Currently, at our medical center, the primary tumor and upper neck are treated with conformal IMRT field while the lower neck is treated with a conventional anterior field. These two fields are matched with a split-beam technique and the match line is set above the vocal cords. Multiple radiotherapy techniques as well as IMRT methods in defining the isocenter and match line have been described [55].

An older technique only used IMRT for the primary tumor and retropharyngeal region, while the upper neck above the vocal cords was irradiated with opposed-lateral fields and the lower neck and supraclavicular fossae were treated with a single anterior field using conventional radiotherapy. In these cases, the IMRT field is matched with the opposed-lateral neck field using a split-beam technique. The opposed-lateral neck field is also matched to the lower neck and supraclavicular field with a split-beam technique.

At some centers, a third technique has evolved, stemming from concerns about dose uncertainties at the match lines. This technique uses an extended-field IMRT (EF-IMRT), which treats the primary tumor as well as all regional lymph nodes, including the supraclavicular nodes (see next section). However, due to the extended field size, application of this EF-IMRT technique may be limited by the field-size constraints of the available linear accelerators. General indications, as well as advantages and disadvantages for each of the three techniques (IMRT for the primary tumor alone, IMRT for the primary plus upper neck nodes, and IMRT for the entire tumor and neck volume) are presented in Table 2.

Regardless of the technique used, the aim of treatment is to deliver sufficient radiation to the PTVs while excluding the non-involved tissue. The treatment plan is based on an analysis of the volumetric dose, including a dose-volume histogram (DVH) analyses of the PTVs and critical normal structures. Due to the complexity and variations in clinical presentation, treatment plans should be customized for each patient. The method of inverse planning should be utilized to determine intensity optimizations and beam configurations. The number of fields should be determined by treatment planning to produce the best conformal plan. For the intensity optimization, the prescribed dose should encompass at least 95% of the involved and electively irradiated sites of disease.

Megavoltage machines, usually using a 6-MV photon beam, should be used for the irradiation of the primary tumor. Energy greater than 6 MV should not be used for the irradiation of cervical lymph nodes. Treatment must be delivered with megavoltage equipment capable of delivering dynamic intensity modulation with computer controlled auto-sequence multi-leaf collimators. Other techniques, including the use of partial block transmission blocks and sequential tomotherapy, have been previously described and are acceptable, as long as dose specifications and constraints are met [37].

3.4.1 Dose Specification

The prescription dose is the isodose surface that encompasses at least 95% of the PTV. The gross tumor and involved lymph nodes along with margin for set-up error and organ motion (PTV1) should receive 70 Gy in 33 fractions at 2.12 Gy per fraction. PTV2 with high risk cervical lymph nodes or dissected neck area containing lymph node metastasis should receive 59.4 Gy in 33 fractions at 1.8 Gy per fraction. If possible, no more than 20% of any PTV1 should be treated with 110% of the prescribed dose and no more than 1% of any PTV1 and PTV2 should exceed 93% of the prescribed dose. Dose greater than 110% of 70 Gy should be limited to 1% or 1.0 cc of the tissue outside the PTVs. Examples of dose distribution and coverage are presented in Fig. 6–8.

This dose distribution or dose painting may allow for a differential radiobiologic advantage. GTV receives a higher dose per fraction when compared to CTV and all surrounding normal tissues potentially may benefit from a greater radiobiologic effect. Other investigators have reported encouraging results from the differential dose delivery and minimization of toxicity [21, 22].

Table 2. Indications and advantages for different IMRT planning techniques

IMRT for the primary tumor alone	IMRT for the primary plus upper neck nodes	IMRT for the entire tumor and neck
Suitable for cases with no lymph node involvement	For cases when upper neck nodes are involved	Simple in treatment setup
No need to contour lymph nodes	Lower neck nodes can be treated at a lower dose but still at a standard fractionation	No match-line problem
Lymph nodes can be treated at a lower dose (i.e., 54 Gy) but still at a standard dose fractionation	Simpler treatment setup	Suitable for cases with lymph node involvement
Improved dose conformity and uniformity	Dose uncertainties at match line	Longer field lengths required: 20 – 24 cm (for oropharynx); 22 – 28 cm (for nasopharynx); 26 – 32 cm (for sinus)
Complex treatment setup Sensitive to patient movement during treatment Dose uncertainties at match lines	Sensitive to patient motion during the treatment	

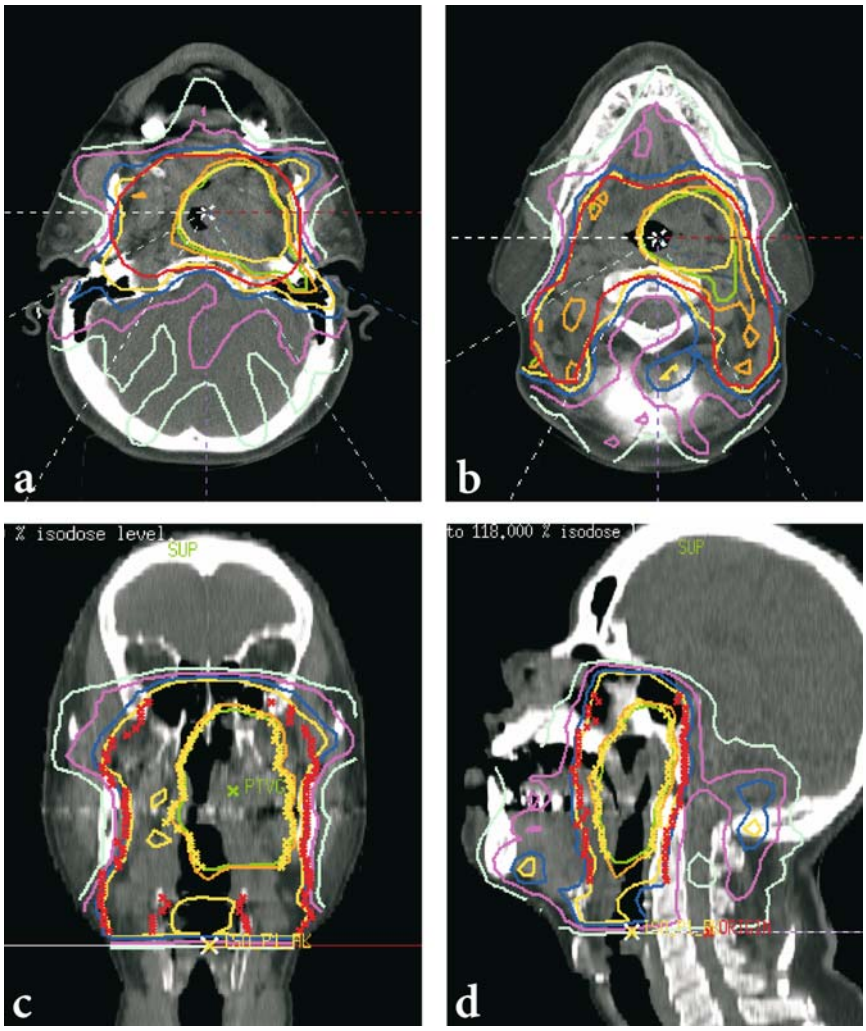

Fig. 6a–d. IMRT dose distribution for a patient with a T2bN0 NPC: **(a)** superior axial; **(b)** inferior axial; **(c)** coronol; **(d)** sagittal. PTV1, *yellow*; PTV2, *red*; 118% isodose line (70 Gy), *green*; 114%, *orange*; 100% (59.4 Gy), *yellow*; 90%, *dark blue*; 70%, *magenta*; 50%, *light blue*

At our center, the lower neck and supraclavicular field (PTV3) is treated with a conventional AP field, beam split to the IMRT fields, as discussed previously. The conventional AP field is generally prescribed to a depth of 3 cm from the anterior surface and receives 50.4 Gy in 28 fractions of 1.8 Gy per fraction. As mentioned above, dose uncertainty at the match line has led to the use of extended-field IMRT that treats the primary tumor with all the regional lymph nodes including the supraclavicular nodes. A head, neck, shoulder immobilization device must be used in these situations. In these situations, the dose per fraction in PTV3 is 1.64 Gy; in order to compensate for fractionation lower than conventional fractionation of 1.8 Gy, the low neck and supraclavicular fields are treated to a higher total dose of 54.0 Gy in the IMRT plan (see Fig. 9). A third alternative is to plan to treat the low neck in the IMRT plan, defining the low neck/supraclavicular fossae as part of the PTV2 and, after 28 fractions, to close these fields and complete the remainder of the treatments using the same IMRT plan, following reoptimization and replanning.

3.4.2 Planning Goals

Conforming to the critical normal structure constraints followed by prescription goals must be the main treatment-planning priorities. Other planning goals include obtaining a low mean parotid dose, a reduced dose to submandibular glands and oral cavity, and meeting dose constraints for other normal structures. DVHs

Table 3. Dose constraints for critical normal structures (RTOG 0225)

Critical normal structure	Dose constraints
Brainstem	54 Gy or 1 cc volume 60 Gy
Optic chiasm/optic nerves	54 Gy or 1 cc volume 60 Gy
Spinal cord	45 Gy or 1 cc volume 50 Gy
Mandible/T-M joint	70 Gy or 1 cc volume 75 Gy
Temporal lobes	60 Gy or 1% volume 65 Gy

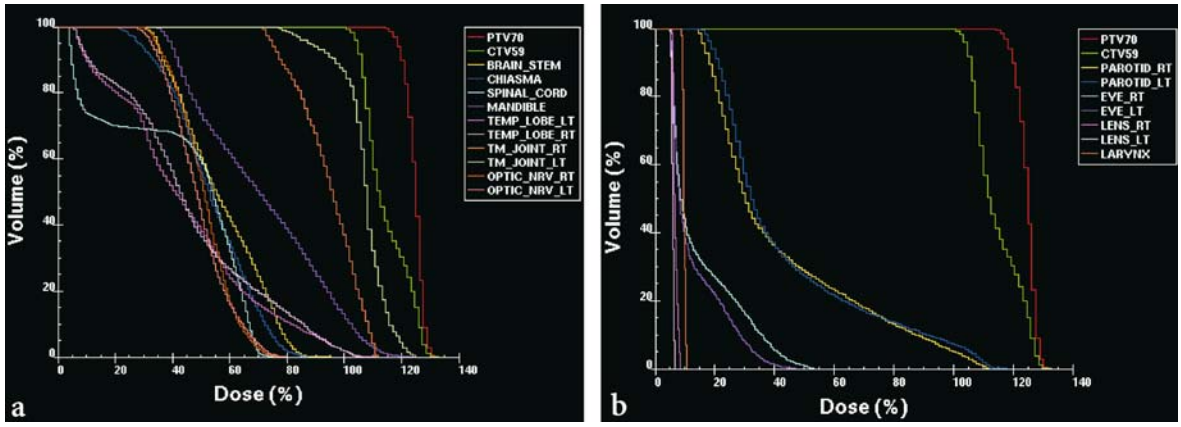

Fig. 7a,b. Dose volume histogram for the patient in Fig. 15: (a) critical normal structures; (b) lower priority normal structures

should be generated for all target volumes, critical normal structures and other unspecified tissues (Fig. 7 and 8). No more than 5% of the non-target tissue should receive more than 70 Gy, including all transmitted and scattered doses.

Dose constraints for critical normal structures are presented in Table 3. In cases where constraints to critical structures lead to under-dosing the tumor, these limits can be exceeded, at the discretion of the treating physician, but patients should be fully consented for the anticipated risk of injury to these normal structures. Dose restraints for other normal structures, including tongue, inner/middle ear, eyes and glottic larynx, may be of lower priority and should not compromise the GTV or CTV coverage. Table 4 lists recommended dose for these lower-priority normal structures.

For the parotid glands, a mean dose of 26 Gy should be achieved in at least one gland; alternatively, at least 20 cc of the combined volume for both parotid glands should receive less than 20 Gy. The degree of xerostomia is largely dependent on the radiation dose and the volume of the salivary gland irradiated. Salivary flow is markedly reduced following 10–15 Gy of radiation delivered to most of the gland. Recovery of salivary function is possible over time with doses up to 40–50 Gy, although irreversible xerostomia occurs with higher doses [39, 56, 57]. Doses to the submandibular and sublingual glands should be as low as possible, without compromising target coverage.

Treatment Delivery Issues

Treatment is delivered once daily for a total of five fractions per week until completion. All targets are treated simultaneously, except for the supraclavicular area, which is usually stopped after 28 fractions when treated with a conventional low neck field. During treat-

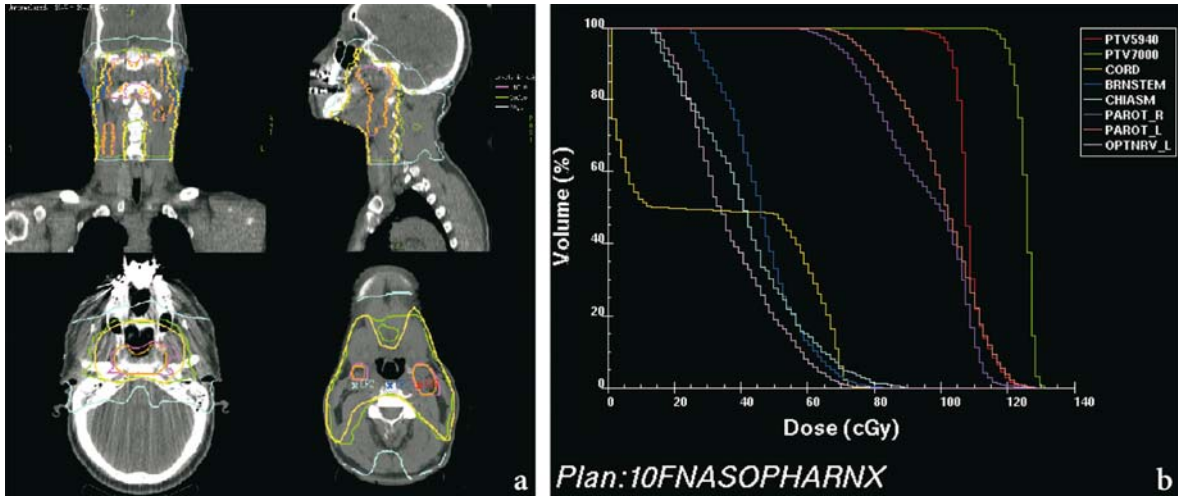

Fig. 8a,b. Patient with a T4N2 NPC treated using an IMRT plan with a separate supraclavicular field: (a) isodose distribution. GTV, *orange*; PTV2, *yellow*; parotid glands, *dark blue*; 59.4 Gy isodose line, *green*; 70 Gy isodose line, *pink*; (b) dose-volume histogram for the same patient. (Courtesy of Louise E. Braban, Ph.D., and Linda X. Hong, Ph.D.)

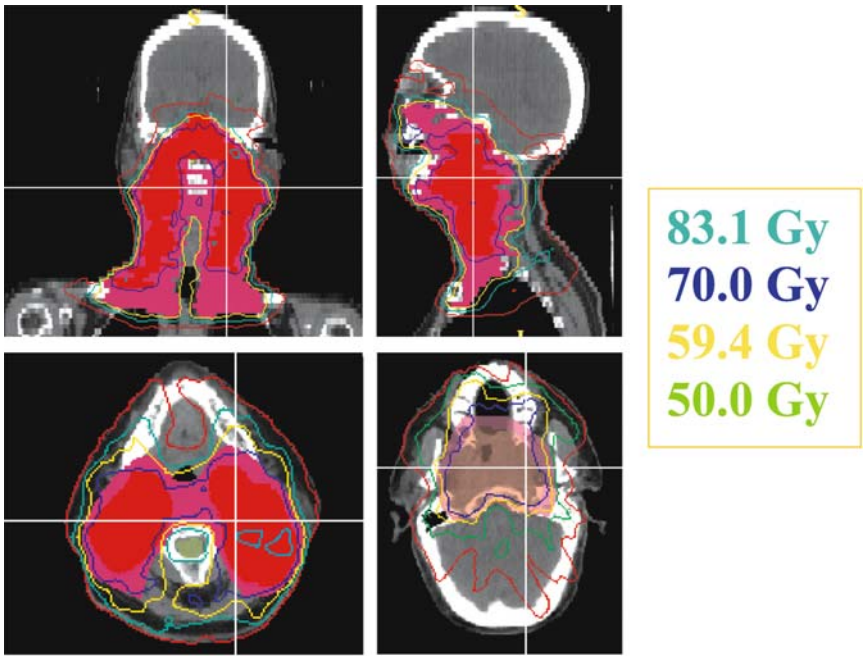

Fig. 9. Patient with a T3N3 NPC treated using an IMRT-only plan. Because the patient had bilateral and supraclavicular gross LNs, the decision in this case was made to increase the subclinical dose from 54 Gy to 59.4 Gy to the low neck. (Courtesy of Ping Xia, Ph.D.)

ment, port films (including an orthogonal pair) should be taken for each field on a weekly basis, to ensure accurate location of the isocenter. Patient position and MLC aperture should be monitored by weekly verification films.

For pre-treatment patient-specific quality assurance (QA), a thorough plan check and independent monitored unit (MU) calculations are performed, as is the case with conventional treatment. During radiation delivery, accelerator MLC position readout and the record and verify (RV) system should be monitored to verify the start- and stop-leaf positions of each field for the daily treatments. Routine film dosimetry for pretreatment delivery verification has been eliminated at our institution after long-term comparison between film and calculation consistently demonstrated agreement to within 2%. Film dosimetry is now reserved for new treatment sites, unusual intensity profiles or MU verification checks with discrepancies in excess of 3%.

Table 4. Recommended dose limits for lower priority normal structures (RTOG 0225)

Normal structures	Recommended constraints
Parotid glands	Mean dose 26 Gy in at least one gland or 20 cc of both 20 Gy
Tongue	55 Gy or 1% volume 65 Gy
Inner/middle ear	Mean dose 50 Gy
Eyes	Mean dose 35 Gy
Lens	As low as possible
Glottic larynx	Mean dose 45 Gy

3.5 Clinical Experiences Defining the Role of IMRT

While the role of IMRT for the treatment of NPC continues to be defined, multiple studies over the last few years have helped explicate the specific benefits of IMRT, both on a technical/theoretical basis as well as on a clinical/practical basis.

Cheung et al. demonstrated that target coverage of the primary tumor was maintained and that nodal coverage was improved in 17 NPC patients planned with IMRT, as compared with conventional beam arrangements [58]. The ability of IMRT to spare the parotid glands was noted as well. Similar results were reported by Hunt et al. in 23 patients with primary NPC [27]. However, no attempt was made in their series to spare the parotids, and, as a result, the mean parotid dose was quite high, at 60.5 Gy. Subsequently, with the use of proper normal-tissue dose constraints, substantial improvements have been noted.

Xia et al. compared IMRT treatment plans with conventional treatment plans for a case of locally advanced nasopharyngeal carcinoma [25]. In their series, the coverage to the GTV a well as the CTV was superior with the inverse-planned IMRT plans. Also, with the use of proper normal-structure dose constraints, inverse-planned IMRT plans achieved the least dose delivered to the brain stem, chiasm, optic structures, and parotid. In fact, the mean parotid dose was reduced to as low as 21.4 Gy. The authors concluded that IMRT provided improved tumor target coverage with significantly better sparing of sensitive normal tissue structures in the treat-

ment of locally advanced nasopharyngeal carcinoma. A similar conclusion was reached in a study by Wolden et al., in which, due to a lack of major benefit with conventional three-dimensional treatment planning used only during the boost phase of treatment for nasopharyngeal carcinoma, the authors recommend using IMRT to deliver the entire course of radiation [59]. It is worth noting that, although this study only investigated the use of a three-dimensional boost, the same lack of efficacy would likely be found if an IMRT boost had been used. This is because, in such a situation, the conventional portion of the treatment would already have treated certain critical structures (e.g., the spinal cord) to significant enough doses, such that further treatment with an IMRT plan would be compromised. It is therefore highly preferable to perform the entire treatment course using IMRT.

At UCSF, IMRT has been used for treatment of nasopharyngeal carcinoma since 1995. In their series, patients were treated with both forwardly planned as well as inversely planned IMRT. Radiation beams were delivered using partial transmission blocks, computer controlled auto-sequencing static multileaf collimator (MLC), or the Peacock system using a dynamic multivane intensity-modulating multileaf collimator, called the MIMiC. An update of their experience by Lee et al. reported that, in 87 patients treated with IMRT, the 4-year local progression-free survival, regional progression-free survival, distant metastasis-free survival, and overall survival were 94, 98, 66, and 73%, respectively, with a median follow up of 31 months [60]. IMRT achieved excellent locoregional control, provided excellent tumor coverage, and allowed the delivery of a high dose to the target with significant sparing of the salivary gland and other nearby critical normal tissues (see Fig. 10).

Kwong et al., from Queen Mary Hospital in Hong Kong, presented their data on 50 patients with T1–2N0–1M0 NPC treated with IMRT. With a median followup of 14 months after completion of radiotherapy, the 2-year nasopharynx, neck, and distant failure-free survival rates were 100, 94.4, and 94.1%, respectively [61]. Again, good parotid-sparing was achieved in these patients.

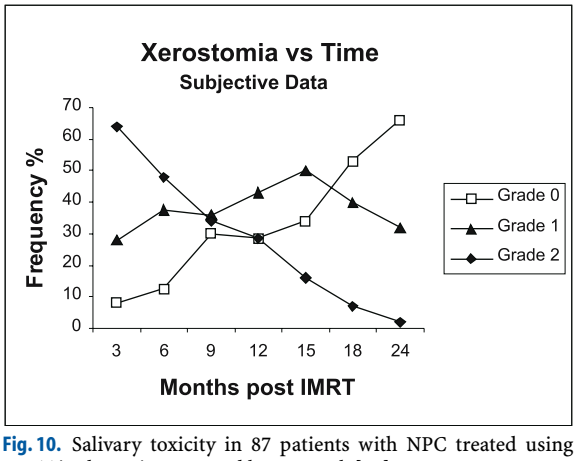

Fig. 10. Salivary toxicity in 87 patients with NPC treated using IMRT in the series reported by Lee et al. [60]

In a recent report, Ozyigit and Chao provide an updated report of the Washington University-Mallinckrodt experience. Twelve patients with NPC were treated with IMRT between February 1997 and December 2000 [62]. T stages included one T1, three T2, three T3, and five T4; N stages included one N0, three N1, four N2, and four N3. The patients received chemotherapy according to the Intergroup 0099 regimen. With a median follow-up time of 31 months (range 19–52 months), one neck recurrence was observed. Three patients developed distant metastases, and one patient dies of distant metastasis. There were no failures in the nasopharynx.

3.6 Future Directions

While the potential benefits of IMRT for treatment of NPC are well understood, the practical aspects of its implementation as well as the potential further minimization of treatment-related toxicities continue to be explored.

RTOG 0225 is a phase II study of IMRT +/– chemotherapy for stage I–IVB squamous cell carcinoma of the nasopharynx. The primary purpose of this study is to test the feasibility and transportability of delivering IMRT in a multi-institutional setting for the treatment of nasopharyngeal carcinoma. The rate of late xerostomia associated with the treatment regimen will also be assessed. The rationale of this study is that a potential reduction in radiation side effects using IMRT will increase patient compliance to combined therapy without compromising local-regional control. The study is on-going and the results are eagerly awaited at this time.

With the development of new technology comes the need for re-evaluation of older data. In 1991, Emami et al. collected and amended information on radiation tolerance of multiple normal tissues, with a special emphasis on partial volume effects [63]. At the time, the authors acknowledged that the work obviously was not and could not be comprehensive. We now know that, as the information collected in this seminal study was drawn from sources utilizing techniques which pre-dated IMRT, it is quite certain that the dosimetric analyses performed to arrive at those tolerance doses are not as accurate as the dosimetric analyses which can be performed using a computer-generated IMRT plan. Emami and colleagues studied two-dimensional data for their study, and had no access to computer-derived dose-volume histograms; as a result, many of their outcomes were necessarily a result of close estimates. Now, as clinical data is collected and evaluated in the context

of newer IMRT plans, it will become possible – and necessary – to validate, and perhaps amend, much of the vital data that Emami and colleagues have given us.

One area in which more accurate tissue-tolerance data would be particularly useful is in reirradiation of recurrent NPC. Five-year actuarial survival of select patients reirradiated for recurrent NPC, using conventional radiotherapy, has ranged from 20 to 45% [64–69]. However, long-term local control was noted in only 14–60% of the retreated patients. Five-year actuarial survival ranged from 13% (in patients who recurred within two years following initial radiotherapy) to 66% (in patients who recurred later than two years following initial radiotherapy) [65]. Again, a dose-responsive element was noted: five-year actuarial survival was 45% with doses greater than or equal to 60 Gy and 0% with doses less than 60 Gy, although most patients treated with lower doses had more advanced disease at recurrence [65]. Severe complications following reirradiation occurred in 4–48% of the patients reported in the literature [19, 64–68, 70]. The incidence of severe complications from reirradiation increased with increasing

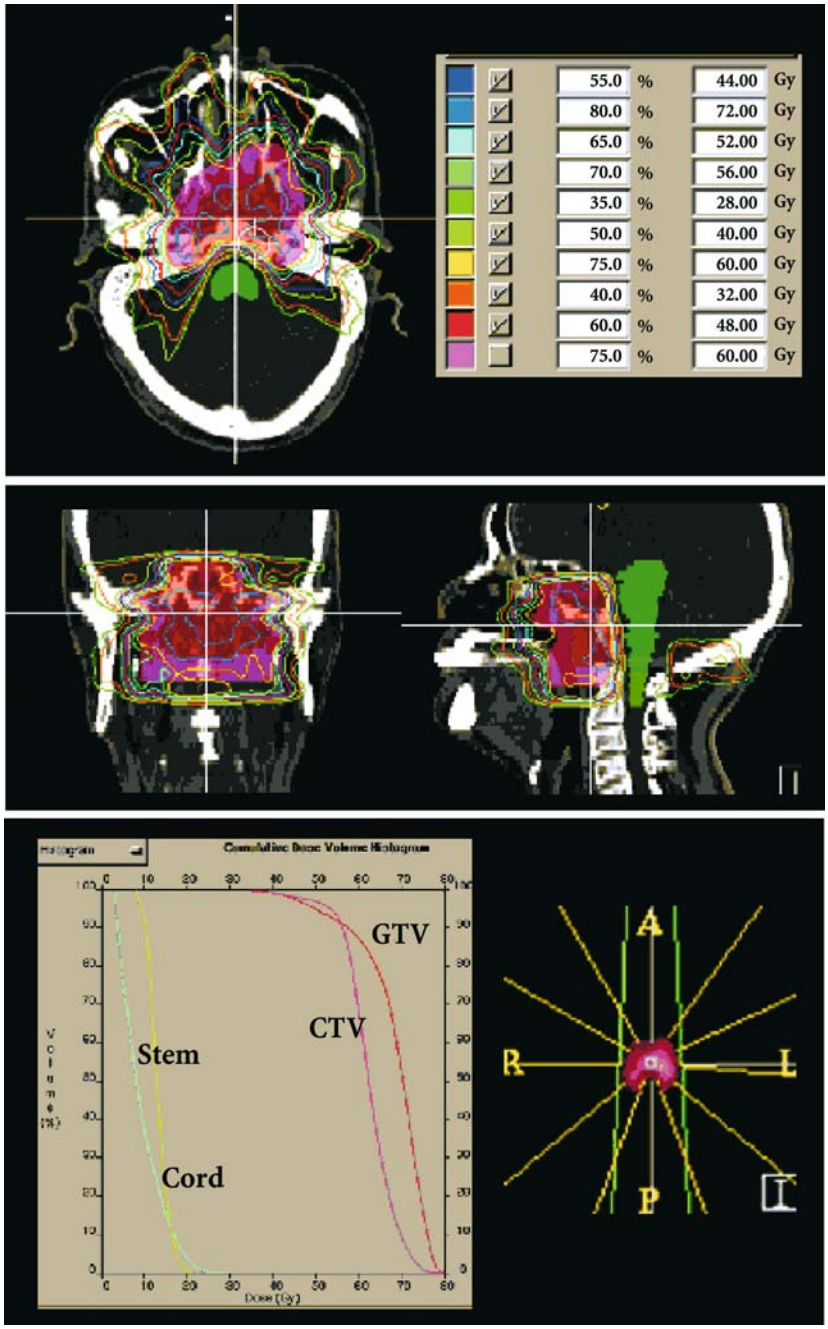

Fig. 11. IMRT plan for a patient with recurrent NPC. Patient previously received full-dose radiation therapy. (Courtesy of Ping Xia, Ph.D.)

total cumulative dose: incidence was 4% with doses less than or equal to 100 Gy, vs 39% with doses greater than 100 Gy [66]. The use of IMRT in these patients would theoretically lower the rate of late normal-tissue complications, allow better targeting of tumor, and ultimately enable the delivery of at least 60 Gy to tumors, even in advanced cases.

The practice at UCSF is to treat recurrent NPC patients with IMRT to a dose of 60 Gy at 1.44 Gy/fraction, twice-daily, 6 h apart, five days per week to the GTV, with concurrent cisplatin chemotherapy, while the CTV receives a dose of 50 Gy at 1.2 Gy/fraction twice-daily. Alternatively, once-daily fractionation using IMRT to a dose of 60 Gy, with concurrent chemotherapy, can be used if an appropriate plan is formulated. An example of an IMRT plan for recurrent NPC is shown in Fig. 11. Treatment for NPC recurrences must be evaluated on a case-by-case basis, in close collaboration with ones physics staff. Often, it is necessary to "recreate" previous treatment fields, especially when a conventional plan was used previously, to approximate the cumulative dose which will be delivered to the target as well as to adjacent critical structures. Such a three-dimensional "recreation" entails a thorough anatomic analysis of prior treatment fields, as well as a detailed knowledge of the treatment techniques used.

One area in the treatment for NPC which is not intrinsic, but is often complementary, to IMRT is chemotherapy. As mentioned earlier, the addition of chemotherapy to radiation improves locoregional control, distant metastasis-free rates, disease-free survival, and overall survival. These positive effects have especially been seen in patients treated with concurrent, as opposed to adjuvant, chemoradiotherapy. However, compliance has been a problem: there was only a 53–73% compliance rate in patients treated with concurrent cisplatin-based chemotherapy and radiotherapy, and only a 55–76% compliance rate seen in radiation-treated patients who received adjuvant cisplatin-based therapy. This poor compliance is in large part due to the toxicity associated with combined- modality therapy. While IMRT has decreased this toxicity, improvements in the toxicity profiles of the chemotherapeutic regimens being used would further improve compliance rates.

Moreover, while local-control rates will improve with the higher radiation doses enabled by IMRT, further improvements in chemotherapy will result in improved distant-metastasis and overall-survival rates. High distant-metastasis rates continue to be a problem for patients with NPC; this is especially apparent as patients' tumors have a more effective local response to IMRT. As systemic chemotherapy for NPC continues to evolve, especially with the development of targeted chemotherapeutic agents (e.g., C225 [cetuximab], Iressa [gefitinib] and COX-2 inhibitors), the distant manifestations of NPC will be addressed. When delivered in combination with IMRT, these agents will help maximize control of both local and distant disease in these patients. The result will undoubtedly be further improvement in quality of life and overall survival for patients with NPC.

References

1. Yu MC (1990) Diet and nasopharyngeal carcinoma. FEMS Microbiol Immunol 2(4):235–242
2. Lindberg R (1972) Distribution of cervical lymph node metastases from squamous cell carcinoma of the upper respiratory and digestive tracts. Cancer 29(6):1446–1449
3. Qin DX et al. (1988) Analysis of 1379 patients with nasopharyngeal carcinoma treated by radiation. Cancer 61(6): 1117–1124
4. Gong QY, Zheng GL, Zhu HY (1991) MRI differentiation of recurrent nasopharyngeal carcinoma from postradiation fibrosis. Comput Med Imaging Graph 15(6):423–429
5. Som PM (1992) Detection of metastasis in cervical lymph nodes: CT and MR criteria and differential diagnosis. AJR Am J Roentgenol 158(5):961–969
6. Mancuso AA, Dillon WP (1989) Nasopharynx, parapharyngeal space, skull base, cranial nerves V and IX–XII, and sympathetics. In: Grayson TH (ed) Workbook for MRI and CT of the head and neck. Williams & Wilkins, Baltimore, p 123
7. Dillon WP, Harnsberger HR (1991) The impact of radiologic imaging on staging of cancer of the head and neck. Semin Oncol 18(2):64–79
8. Al-Sarraf M et al. (1998) Chemoradiotherapy versus radiotherapy in patients with advanced nasopharyngeal cancer: phase III randomized Intergroup study 0099. J Clin Oncol 16(4):1310–1317
9. Cooper JS et al. (2000) Improved outcome secondary to concurrent chemoradiotherapy for advanced carcinoma of the nasopharynx: preliminary corroboration of the intergroup experience. Int J Radiat Oncol Biol Phys 47(4):861–866
10. Ozyar E et al. (1999) Comparison of AJCC 1988 and 1997 classifications for nasopharyngeal carcinoma. American Joint Committee on Cancer. Int J Radiat Oncol Biol Phys 44(5):1079–1087
11. Chu AM et al. (1984) Irradiation of nasopharyngeal carcinoma: correlations with treatment factors and stage. Int J Radiat Oncol Biol Phys 10(12):2241–2249
12. Hoppe RT, Goffinet DR, Bagshaw MA (1976) Carcinoma of the nasopharynx. Eighteen years' experience with megavoltage radiation therapy. Cancer 37(6):2605–2612
13. Mesic JB, Fletcher GH, Goepfert H (1981) Megavoltage irradiation of epithelial tumors of the nasopharynx. Int J Radiat Oncol Biol Phys 7(4):447–453
14. Sanguineti G et al. (1997) Carcinoma of the nasopharynx treated by radiotherapy alone: determinants of local and regional control. Int J Radiat Oncol Biol Phys 37(5): 985–996
15. Bailet JW et al. (1992) Nasopharyngeal carcinoma: treatment results with primary radiation therapy. Laryngoscope 102(9):965–972
16. Vikram B et al. (1984) Improved survival in carcinoma of the nasopharynx. Head Neck Surg 7(2):123–128
17. Wang CC (1990) Carcinoma of the nasopharynx. In: Wang CC (ed) Radiation therapy for head and neck neoplasms: indications, techniques, and results. Year Book Medical Publishers, Chicago, pp 261–283

18. Marks JE et al. (1982) Dose-response analysis for nasopharyngeal carcinoma: an historical perspective. Cancer 50(6):1042–1050
19. Vikram B et al. (1985) Patterns of failure in carcinoma of the nasopharynx: I. Failure at the primary site. Int J Radiat Oncol Biol Phys 11(8):1455–1459
20. Intensity Modulated Radiation Therapy Collaborative Working Group (2001) Intensity-modulated radiotherapy: current status and issues of interest. Int J Radiat Oncol Biol Phys 51(4):880–914
21. Mohan R et al. (2000) Radiobiological considerations in the design of fractionation strategies for intensity-modulated radiation therapy of head and neck cancers. Int J Radiat Oncol Biol Phys 46(3):619–630
22. Butler EB et al. (1999) Smart (simultaneous modulated accelerated radiation therapy) boost: a new accelerated fractionation schedule for the treatment of head and neck cancer with intensity modulated radiotherapy. Int J Radiat Oncol Biol Phys 45(1):21–32
23. Eisbruch A et al. (1996) Parotid gland sparing in patients undergoing bilateral head and neck irradiation: techniques and early results. Int J Radiat Oncol Biol Phys 36(2):469–480
24. Nutting C, Dearnaley DP, Webb S (2000) Intensity modulated radiation therapy: a clinical review. Br J Radiol 73(869):459–469
25. Xia P et al. (2000) Comparison of treatment plans involving intensity-modulated radiotherapy for nasopharyngeal carcinoma. Int J Radiat Oncol Biol Phys 48(2):329–337
26. Chao KS et al. (2000) Intensity-modulated radiation therapy in head and neck cancers: the Mallinckrodt experience. Int J Cancer 90(2):92–103
27. Hunt MA et al. (2001) Treatment planning and delivery of intensity-modulated radiation therapy for primary nasopharynx cancer. Int J Radiat Oncol Biol Phys 49(3):623–632
28. van Dieren EB et al. (2000) Beam intensity modulation using tissue compensators or dynamic multileaf collimation in three-dimensional conformal radiotherapy of primary cancers of the oropharynx and larynx, including the elective neck. Int J Radiat Oncol Biol Phys 47(5):1299–1309
29. Claus F et al. (2002) Intensity modulated radiation therapy for oropharyngeal and oral cavity tumors: clinical use and experience. Oral Oncol 38(6):597–604
30. Al-Sarraf M, Giri PGS et al. (2001) Superiority of five year survival with chemo-radiotherapy (CT-RT) vs radiotherapy in patients (pts) with locally advanced nasopharyngeal cancer (NPC). Intergroup (0099) (SWOG 8892, RTOG 8817, ECOG 2388) Phase III Study: Final Report. Proc Am Soc Clin Oncol 20:227a
31. Wee J, Tai BC et al. (2004) Phase III randomized trial of radiotherapy versus concurrent chemo-radiotherapy followed by adjuvant chemotherapy in patients with AJCC/UICC (1997) stage 3 and 4 nasopharyngeal cancer of the endemic variety. Proc Am Soc Clin Oncol 23:487
32. Chan AT, Teo P et al. (2004) Final results of a phase III randomized study of concurrent weekly cisplatin-RT versus RT alone in locoregionally advanced nasopharyngeal carcinoma (NPC). Proc Am Soc Clin Oncol 23:492
33. Lin JC et al. (2003) Phase III study of concurrent chemoradiotherapy versus radiotherapy alone for advanced nasopharyngeal carcinoma: positive effect on overall and progression-free survival. J Clin Oncol 21(4):631–637
34. Lee AW, Tung SY et al. (2004) Prospective randomized study on therapeutic gain achieved by addition of chemotherapy for T1–4N2–3M0 nasopharyngeal carcinoma (NPC). Proc Am Soc Clin Oncol 2004
35. Huncharek M, Kupelnick B (2002) Combined chemoradiation versus radiation therapy alone in locally advanced nasopharyngeal carcinoma: results of a meta-analysis of 1,528 patients from six randomized trials. Am J Clin Oncol 25(3): 219–223
36. Thephamongkhol K et al. (2003) Does the addition of chemotherapy to radiotherapy improve the survival of patients with locally advanced nasopharyngeal cancer? A systematic review and meta-analysis of randomized controlled trials. Int J Radiat Oncol Biol Phys 57(Suppl2):S247–S248
37. Langendijk JA et al. (2003) A meta-analysis of the addition of chemotherapy to radiotherapy in locally advanced nasopharyngeal carcinoma. Int J Radiat Oncol Biol Phys 57(Suppl2):S246–247
38. Thephamongkhol K, Browman G (2004) Chemo- radiotherapy versus radiotherapy alone for nasopharyngeal carcinoma: a meta-analysis of 78 randomized controlled trials (RCTs) from English and non-English databases. Proc Am Soc Clin Oncol 23:491
39. Leslie MD, Dische S (1994) The early changes in salivary gland function during and after radiotherapy given for head and neck cancer. Radiother Oncol 30(1):26–32
40. Mira JG et al. (1981) Some factors influencing salivary function when treating with radiotherapy. Int J Radiat Oncol Biol Phys 7(4):535–541
41. Harrison LB et al. (1997) Detailed quality of life assessment in patients treated with primary radiotherapy for squamous cell cancer of the base of the tongue. Head Neck 19(3):169–175
42. Balogh JM, Sutherland SE (1989) Osteoradionecrosis of the mandible: a review. J Otolaryngol 18(5):245–250
43. Cooper JS et al. (1995) Late effects of radiation therapy in the head and neck region. Int J Radiat Oncol Biol Phys 31(5):1141–1164
44. Shannon IL, Starcke EN, Wescott WB (1977) Effect of radiotherapy on whole saliva flow. J Dent Res 56(6):693
45. Nowak P et al. (1997) Treatment portals for elective radiotherapy of the neck: an inventory in The Netherlands. Radiother Oncol 43(1):81–86
46. Nowak PJ et al. (1999) A three-dimensional CT-based target definition for elective irradiation of the neck. Int J Radiat Oncol Biol Phys 45(1):33–39
47. Som PM, Curtin HD, Mancuso AA (1999) An imaging-based classification for the cervical nodes designed as an adjunct to recent clinically based nodal classifications. Arch Otolaryngol Head Neck Surg 125(4):388–396
48. Dawson LA et al. (2000) Patterns of local-regional recurrence following parotid-sparing conformal and segmental intensity-modulated radiotherapy for head and neck cancer. Int J Radiat Oncol Biol Phys 46(5):1117–1126
49. Chao KS et al. (2002) Determination and delineation of nodal target volumes for head-and-neck cancer based on patterns of failure in patients receiving definitive and postoperative IMRT. Int J Radiat Oncol Biol Phys 53(5):1174–1184
50. Eisbruch A et al. (2002) Intensity-modulated radiation therapy for head and neck cancer: emphasis on the selection and delineation of the targets. Semin Radiat Oncol 12(3):238–249
51. Rahn AN et al. (1998) Value of 18F fluorodeoxyglucose positron emission tomography in radiotherapy planning of head-neck tumors. Strahlenther Onkol 174(7):358–364
52. Som PM, Curtin HD, Mancuso AA (2000) Imaging-based nodal classification for evaluation of neck metastatic adenopathy. Am J Roentgenol 174(3):837–844
53. Jian JJ et al. (1998) T classification and clivus margin as risk factors for determining locoregional control by radiotherapy of nasopharyngeal carcinoma. Cancer 82(2):261–267

54. Thornton AF Jr et al. (1991) A head immobilization system for radiation simulation, CT, MRI, and PET imaging. Med Dosim 16(2):51–56
55. Lee N et al. (2003) Intensity-modulated radiation therapy for head-and-neck cancer: the UCSF experience focusing on target volume delineation. Int J Radiat Oncol Biol Phys 57(1):49–60
56. Eisbruch A et al. (1999) Dose, volume, and function relationships in parotid salivary glands following conformal and intensity-modulated irradiation of head and neck cancer. Int J Radiat Oncol Biol Phys 45(3):577–587
57. Roesink JM et al. (2001) Quantitative dose-volume response analysis of changes in parotid gland function after radiotherapy in the head-and-neck region. Int J Radiat Oncol Biol Phys 51(4):938–946
58. Cheng JC, Chao KS, Low D (2001) Comparison of intensity modulated radiation therapy (IMRT) treatment techniques for nasopharyngeal carcinoma. Int J Cancer 96(2):126–131
59. Wolden SL et al. (2001) Failure of a 3D conformal boost to improve radiotherapy for nasopharyngeal carcinoma. Int J Radiat Oncol Biol Phys 49(5):1229–1234
60. Lee N et al. (2002) Intensity-modulated radiotherapy in the treatment of nasopharyngeal carcinoma: an update of the UCSF experience. Int J Radiat Oncol Biol Phys 53(1):12–22
61. Kwong DL et al. (2003) Intensity-modulated radiotherapy for early stage nasopharyngeal carcinoma: preliminary results on parotid sparing. Int J Radiat Oncol Biol Phys 57(Suppl2):S303
62. Ozyigit G, Chao KS (2002) Clinical experience of head-and-neck cancer IMRT with serial tomotherapy. Med Dosim 27(2):91–98
63. Emami B et al. (1991) Tolerance of normal tissue to therapeutic irradiation. Int J Radiat Oncol Biol Phys 21(1):109–122
64. Wei WW, Lan KH et al. (1993) Surgical resection for nasopharynx cancer. In: Johnson JT (ed) Head and neck cancer. Elsevier Science, Hong Kong, p 465
65. Wang CC (1987) Re-irradiation of recurrent nasopharyngeal carcinoma–treatment techniques and results. Int J Radiat Oncol Biol Phys 13(7):953–956
66. Pryzant RM et al. (1992) Re-treatment of nasopharyngeal carcinoma in 53 patients. Int J Radiat Oncol Biol Phys 22(5): 941–947
67. Hwang JM, Fu KK, Phillips TL (1998) Results and prognostic factors in the retreatment of locally recurrent nasopharyngeal carcinoma. Int J Radiat Oncol Biol Phys 41(5):1099–1111
68. Yan JH, Hu YH, Gu XZ (1983) Radiation therapy of recurrent nasopharyngeal carcinoma. Report on 219 patients. Acta Radiol Oncol 22(1):23–28
69. Lee AW et al. (1997) Reirradiation for recurrent nasopharyngeal carcinoma: factors affecting the therapeutic ratio and ways for improvement. Int J Radiat Oncol Biol Phys 38(1):43–52
70. Vikram B et al. (1986) Patterns of failure in carcinoma of the nasopharynx: failure at distant sites. Head Neck Surg 8(4): 276–279

Intensity Modulated Radiotherapy in Cancer of the Larynx

M.T. Guerrero Urbano, C.H. Clark, M. Bidmead, D.P. Dearnaley, K.J. Harrington, C.M. Nutting

4

Contents

4.1 Introduction

The larynx is the organ of speech and tumours of this area and their treatment have a big impact on speech, swallowing and respiration. Most tumours arising in this area are squamous cell carcinomas that display a clear radiation dose-response relationship, with both the probability of tumour control and the risk of radiation-induced normal tissue damage increasing with radiation dose. Treatment with radiotherapy is curative for many patients with localized disease but, with current radiation techniques, dose is limited by both acute and late side effects. Locally advanced tumours are associated with poorer survival and manoeuvers introduced to improve results, such as accelerated radiotherapy fractionation and concomitant chemo-radiation schedules can result in significant morbidity.

Intensity-modulated radiotherapy (IMRT) is a new development in three-dimensional conformal radiotherapy (3DCRT) that by combining several beams of varying intensity achieves improved dose homogeneity with highly conformal dose distributions. In tumors of the larynx, the organs at risk (OAR) often lie very close to the target volume, which commonly has an irregular concave shape. Partial reductions of the volume of normal tissue irradiated, such as those offered by 3DCRT, often do not reduce the risk of late toxicity. This is because the slopes of the clinical dose-response curves are quite steep [19] and the most critical OAR (spinal cord) has in-series organization of functional subunits. This means that little extra dose can be given to the smaller high dose volumes resulting from the use of conformal techniques, without exceeding the complication rates produced when conventional tissue volumes are irradiated to conventional dose-levels. Because of this, the dose to the planning target volume (PTV) sometimes has to be compromised. IMRT allows more conformal dose distributions, and plans can be produced with the aim of conformal avoidance of critical OAR or dose escalation of the PTV.

4.2 Clinical Problem, Patterns of Dissemination and Recurrence

The larynx is an important organ in vocal, swallowing and respiratory functions. Alterations by disease or by anti-cancer treatment will have a significant impact on the patient's quality of life. Most laryngeal squamous cell carcinomas result from long-term exposure to carcinogens, with tobacco smoking and alcohol being the two most important factors. These habits lead

to a number of concurrent medical problems, such as respiratory, cardiac, vascular and hepatic dysfunction that can all influence the patient's ability to tolerate treatment.

The three anatomical laryngeal sub-sites (glottis, supraglottis and subglottis) have different lymphatic patterns: the true vocal cords have little or no lymphatic drainage, the supraglottis has profuse lymphatic drainage to level II and III nodes and the subglottis drains to level III nodes. Laryngeal cancer is staged using the UICC TNM system [29].

4.2.1 Glottis

Glottic tumors are the commonest of all laryngeal cancers, with most lesions located on the free edge of the anterior vocal cord. They tend to present early, as small alterations of the mucosal wave produce a persistent and early change in voice quality. Spread is initially mucosal, but later spread into the para-glottic space and underlying tissues may affect vocal cord motion. The anterior commissure initially acts as a barrier to tumour spread, but once breached tumours can spread anteriorly into the pre-epiglottic space and/or laterally into the thyroid cartilage. The likelihood of occult disease in the neck nodes for T1 tumours is deemed to be close to zero and very low (2–7%) for T2 tumours [46], with the risk increasing with higher T stage. Table 1 shows the anatomical distribution of cervical metastases from glottic cancers [58].

4.2.2 Supraglottis

Supraglottic lesions tend to present at a more advanced stage as symptoms (voice changes, referred ear pain and odynophagia) are produced late in the course of the disease. Tumours arising in the supra-hyoid epiglottis can spread into the tongue base once the pre-epiglottic space has been invaded. Aryepiglottic fold cancers tend to follow a pattern similar to piriform sinus tumors, with a more diffuse local spread and a higher tendency to metastasize. Lymphatics in the supraglottis are abundant and the incidence of clinically positive nodes at the time of diagnosis is 55%, of which 16% are bilateral. The risk of nodal metastases increases with higher tumour stage: T1 63%, T2 70%, T3 79% and T4 73% [41]. The anatomical distribution of cervical node metastases in supraglottic tumors is shown in Table 2 [37, 41].

Table 1. Anatomical distribution of cervical nodal metastases for glottic tumours

Level of involvement	Larynx (glottic)	
	Ipsilateral	Contralateral
I	9.3%	0%
II ($a+b$)	50.5%	50%
III	21.5%	25%
IV	0%	0%
V	6.5%	0%
VI	12.3%	25%

Tomik et al.(2001)

Table 2. Anatomical distribution of cervical node metastases for supraglottic tumours

Level of involvement	Larynx (supraglottic)			
N0	45%[a]			
N+	Ipsilateral		Contralateral	
	a	b	a	b
I	1%	10%	0%	0%
II ($a+b$)	38%	48%	12%	13%
III	26%	41%	5%	12%
IV	8%	7%	3%	4%
V	5%	5%	3%	1%

[a] Lindberg (1972) [b] Johansen et al.(2002)

4.2.3 Subglottis

Primary subglottic carcinomas are rare [55] and most present late. Their spread is infiltrative with early invasion of the cricoid cartilage and cricothyroid membrane due to lack of tissue barriers. Often these tumours invade the vocal cords, making it difficult to determine where they are primary glottic tumours with subglottic spread or vice versa.

4.3 Control Rates of Conventional RT

Survival of laryngeal cancer sufferers decreases with increasing tumor stage. Early glottic cancer (T1-T2) is often successfully treated with radiation or surgery. Local control rates for T1 tumours following radiotherapy are close to 90%, increasing to 98% with surgical salvage [20]. Local control rates at five years with radiotherapy alone have been reported at 80% for T2 glottic tumors [44]. Larger doses per fraction [7,24] and hyperfractionated accelerated regimes with reduced overall treatment times [44] have been associated with response rates of 69–93% in T1 and T2 tumours. Response rates in patients with T3 and T4 glottic tumours are markedly poorer with local control rates of 53% after once-daily fractionation and 71% after twice-daily fractionation for T3 [45] and 56% for T4 tumors, with an overall five-year survival after radiotherapy and surgical salvage of 49% for T4 N0 tumors [28].

For subglottic tumors, local control with radiotherapy alone has been reported at 56% for all stages and 81.3% with surgical salvage for an overall five-year survival rate of 50% [51].

Reported five-year disease specific survival rates for T1-T2 supraglottic tumors with radiation or surgery (primary or salvage) are similar, from 72 to 79% [56], but radiotherapy is associated with better organ function and preservation of natural speech. The incidence of histopathologically positive nodes in clinically node negative patients treated with surgery alone has been reported as 30% [30] and the risk of occult contralateral metastases about 40% when an ipsilateral node was present [23]. Recurrence rates for the electively irradiated neck have been reported as 3% [27]. Advanced supraglottic lesions respond less well to radiotherapy alone. Surgical management of these patients usually involves a total laryngectomy followed by post-operative radiotherapy to the primary site and the neck. In an attempt to preserve the larynx, accelerated radiotherapy and combination chemo-radiotherapy protocols have been evaluated reserving surgery for salvage [1, 4, 17, 21, 22, 32, 50, 52, 57]. A large multicentre randomised trial of laryngeal preservation showed two-year laryngeal preservation rates of 64% and two-year survival 68% in both the surgical and radiation group [57]. A meta-analysis of chemotherapy added to the loco-regional treatment of head and neck cancer showed a statistically significant absolute improvement in survival at five years of 8% with concomitant chemotherapy [52]. A meta-analysis of laryngeal preservation showed a non-statistically significant reduction in survival in patients with laryngeal tumours treated with organ-sparing approaches compared with those treated by surgery, but 23% of the patients who were alive at five years had preserved their larynx [52]. Other meta-analyses have also shown this benefit in local control and survival, but unfortunately, at the expense of significant morbidity [1, 17]. Forastiere et al. [21] reported the results of a randomised trial comparing induction Cisplatin plus Fluorouracil followed by radiotherapy, radiotherapy with concomitant Cisplatin or radiotherapy alone (70 Gy in 35 daily fractions of 2 Gy to the primary and 50 Gy to the elective neck). Despite improved local control on the concomitant chemo-radiotherapy arm, there was no significant difference in overall survival between the three arms (75% at two years). However, 88% patients in the concomitant chemo-radiotherapy arm had maintained their larynx at median FU 3.8 years, vs 75% ($p = 0.005$) in the neoadjuvant and RT arm and 70% ($p < 0.001$) in the radiotherapy alone arm. These data translated to an absolute reduction in the rate of laryngectomy of 43%. Toxicity was more severe in the concomitant arm, with a marked increase of mucositis and esophageal toxicity.

Another approach to improve the therapeutic ratio is altered fractionation. There is evidence that prolongation of overall treatment time is associated with reduced loco-regional disease-free survival [42] and that this is due to accelerated repopulation of tumor clonogens [61]. Fu et al. [22] reported an 8% increase in loco-regional tumor control with a hyperfractionated schedule or acceleration by concomitant boost technique (1.8 Gy/fraction/day, five days/week and 1.5 Gy/fraction/day to a boost field as second daily treatment for the last 12 treatment days to 72 Gy/42 fractions/6 weeks) when compared with standard fractionation (70 Gy in 35 fractions) or accelerated radiotherapy with a two-week treatment gap. Other randomized studies have also shown significantly improved tumour control and voice preservation with altered fractionation schedules [32, 50]. An ongoing meta-analysis of hyperfractionated/accelerated schedules has also shown increased responses at the expense of increased toxicity [4]. Both accelerated regimes and combination chemo-radiotherapy are associated with significant acute and potentially late toxicity.

4.4 Potential Benefits of IMRT and Indications

The main advantages of IMRT are more conformal and homogeneous dose distributions and sparing of normal tissues. This is particularly relevant where matching fields are required in the context of conventional radiotherapy. Conventional radiotherapy for locally advanced tumours of the larynx usually involves two opposed lateral fields to include the primary tumour and upper neck and a matched anterior (or an anterior and a posterior) neck field for the lower neck, including the stoma where appropriate. In patients where the posterior neck is electively treated, the anatomical position of the tumor and regional lymph nodes relative to the spinal cord precludes the delivery of radiotherapy in a single phase, and requires the matching of photon and electron fields to keep the spinal cord within the dose tolerance of 46–48 Gy. This leads to dose inhomogeneities close to the tumor or lymph nodes in the neck. With conventional radiotherapy planning studies have shown doses as low as 38 Gy within the nodal PTV [13]. These doses are considerably lower than those required to achieve tumor cell kill and may contribute to local recurrence. Using IMRT, treatment can be delivered in a single phase without the need to match photon/photon and/or photon/electron fields, re-

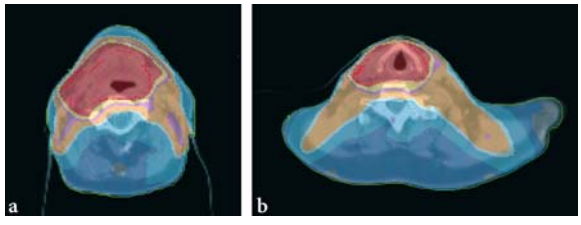

Fig. 1. (a), (b) Larynx and nodal dose distributions with IMRT. The *red color* denotes the 95–105% of the primary dose. The *orange color* denotes the 95–105% of the nodal dose. The *pale blue* is the cord tolerance

sulting in more homogeneous dose distributions and spinal cord sparing to below 40 Gy [13] (Fig. 1). These improved and more homogeneous dose distributions should theoretically be associated with a reduced risk of loco-regional recurrence. Additionally, the increased acute and late toxicity associated with accelerated radiotherapy and concomitant chemotherapy might also be reduced by virtue of reducing the radiation dose in normal tissues.

IMRT techniques such as simultaneous integrated boost (SIB) [48, 62] or simultaneous modulated accelerated radiotherapy (SMART) techniques [8], characterised by the delivery of a different dose-per-fraction to different targets within the head and neck region, have the radiobiological advantage of delivering both a higher total dose and a higher dose per fraction to the primary tumor and allow overall treatment times to be kept short [47].

Where bilateral nodal irradiation is indicated, radiotherapy using parallel-opposed fields is often associated with xerostomia, even when treatment is limited to an elective dose of 46–50 Gy. This adverse event is due to irradiation of substantial parts of both the parotid and submandibular salivary glands, located in close proximity to level II neck nodes. IMRT allows unilateral and, in some cases (such as in N0 patients where the superior limit of level II nodes for the electively irradiated neck is set at the inferior aspect of the transverse process of C1 [25]), bilateral parotid gland sparing [5]. The posterior border of the submandibular gland represents the anterior boundary of level II neck nodes, making them difficult to spare even with IMRT.

Other potential future applications include selective dose escalation of biological gross tumor volumes and/or hypoxic areas identified by PET scanning.

Early glottic cancer has good cure rates with either organ conserving surgical approaches or radiation therapy alone. The standard technique uses two parallel-opposed fields or two anterior oblique fields and often requires wedges to improve dose homogeneity and compensate for changes in the contour of the neck. Since there is no need for elective nodal irradiation, the field sizes required are very small and we feel that IMRT at its current stage of development has no role to play in the treatment of early laryngeal tumors.

4.5 Target Volume Delineation – OAR Definition

Accurate target volume definition and, therefore, knowledge of CT-based anatomy is essential when using IMRT to ensure all the involved areas and those at risk are included in the target volume. Consensus guidelines for the clinical target volume definition of the node negative neck have been recently published and were endorsed by DAHANCA, EORTC, GORTEC, NCIC, RTOG [25]. A CT atlas of the head and neck region is available on the following websites:

- http://www.dshho.suite.dk/dahanca/guidelines.htlm
- http://groups.eortc.be/radio/EDUCATION.htm
- http://www.rtog.org/hnatlas/main.htm

There is, however, no such consensus applicable to target volume definition of the primary tumor and the involved and post-operative neck. ICRU 50 and 62 guidelines provide the basis for defining the different target volumes [35, 36].

4.5.1 Gross Tumor Volume

The extent of the primary tumour and nodal Gross Tumor Volumes (GTV) can be difficult to determine, even on intravenous contrast-enhanced computed tomography (CT). Clinical assessment and careful examination under anaesthetic will help to assess the extent of disease. New imaging modalities (magnetic resonance imaging – MRI, positron emission tomography – PET and PET-CT) are currently being evaluated as an adjunct to conventional radiotherapy planning. MRI provides better soft tissue definition than CT and is helpful in determining invasion of the pre-epiglottic space/tongue base in supraglottic tumours and determining cartilage invasion. However, it is not suitable for radiotherapy planning alone due to lack of electron density information and inherent geometric inaccuracies.

4.5.2 Clinical Target Volume (CTV)

High/Radical Dose CTV

The primary CTV should encompass the primary and nodal GTVs and those areas at high risk of microscopic spread that will be treated to a radical dose. Chao et al. [12] proposed a CTV, for patients who receive definitive IMRT, that encompassed the GTV and region adjacent but not directly involved, based on clinical findings and CT or MR imaging. Involved nodes were included with 2-cm margin.

As a general principle, uninvolved barriers to tumor spread, such as bone and fasciae and, of course, air can be excluded from this CTV. At our institution we add a minimum 1-cm margin to both the primary and nodal GTV, where no obvious anatomical barrier exists, to obtain a CTV.

Partial organ sparing in radiotherapy treatment of early tumours is an exciting possibility, analogous to partial pharyngectomy or partial laryngectomy. At present, however, organ motion on swallowing and the steep dose gradients created with IMRT in a small volume would make geographical miss a real possibility and, therefore, it is not advised at present. We believe that

any reduction in the volume treated with radiotherapy should only be contemplated in the context of clinical studies, and suggest the inclusion of the entire larynx, including the thyroid cartilage, in the primary CTV. Other authors, however, have suggested the inclusion of only the ipsilateral hemi-hypopharynx and hemi-larynx in piriform fossa and lateral pharyngeal wall tumors [18].

For locally advanced tumours, at our institution, the entire larynx/hypopharynx complex is included within the radical CTV, from the tip of the epiglottis to the cricoid cartilage or 2 cm above or below the superior and inferior extent of the tumour, whichever is larger.

Clinical Target Volume in the Node Positive Neck

Where cervical nodes are involved, the probability of extra-capsular spread rises with increasing nodal size [2, 11, 31, 38], and this is linked to an increased probability of recurrence [33]. Chao et al. advocated a 2-cm margin around involved nodes [12]. Where there is infiltration of adjacent structures (i. e. muscle), it has been suggested to treat it in its entirety at least up to an elective dose [25].

The high dose CTV should be tailored to each specific case, taking into consideration the tumor and nodal stage and involved anatomical areas. Considering the volume that would have been treated with conventional radiotherapy usually provides good guidance. Since IMRT is a new technique, it is advisable to be conservative to avoid increased recurrence rates in untreated areas.

The Postoperative Neck

In the post-operative patient the high dose CTV includes any residual disease and/or the surgical bed of the primary tumour and involved nodes. Chao et al. [12] advocated a postoperative CTV that encompassed the pre-operative GTV plus a 2-cm margin, including the resection bed of the area of soft tissue invasion by the tumor or metastatic nodes. The nodal volume will vary according to the type of neck dissection performed.

The Elective Neck CTV

Many studies suggest that the neck should be irradiated electively when the risk of occult cervical metastases is >5% [3,9,10,41,43,54]. The consensus guidelines for the node negative neck are an essential tool in delineating the elective CTV. However, the supraclavicular nodes, commonly treated in many UK centres, are not included. Gregoire et al. [25] reported that few surgical dissections extend down to the clavicle and that they definitely do not reach the medial portion of the clavicle at the level of the sterno-clavicular joint. However there is some local variation in surgical practice, and in some centers neck dissections do extend down to this level.

4.5.3 Planning Target Volume (PTV)

A margin to account for patient motion, organ motion and set up inaccuracies is added to the CTV to obtain the PTV. Movement of the hypopharynx and larynx was estimated as 7 mm in the supero-inferior direction [59].

Different immobilization systems are in use in the head and neck region and an assessment of the degree of accuracy will determine the margin to be used in each centre. Such a study was performed at the Royal Marsden Hospital and a margin of 3 mm is added to obtain a PTV [34].

4.5.4 Organs at Risk (OARs) and Planning Risk Volume (PRV)

In this setting, the organs at risk are the spinal cord, brain stem, parotid glands, submandibular glands, mandible, and esophagus. A margin is added to spinal cord and brain stem to obtain a PRV according to ICRU 62 [36].

4.6 Planning, Dose Prescriptions and Optimization Strategies

The IMRT plans produced with SIB and SMART [8, 48, 62] techniques have concave dose distributions that include the midline primary tumor (e.g. larynx or hypopharynx) and lymph nodes on both sides of the neck, eliminating the use of electron fields to treat lymph nodes in the posterior triangle. This reduces dose inhomogeneity in the PTV, and higher minimum doses offer the potential for improved tumor control [13]. This technique is used in a Phase I dose escalation study currently conducted at the Royal Marsden Hospital, where

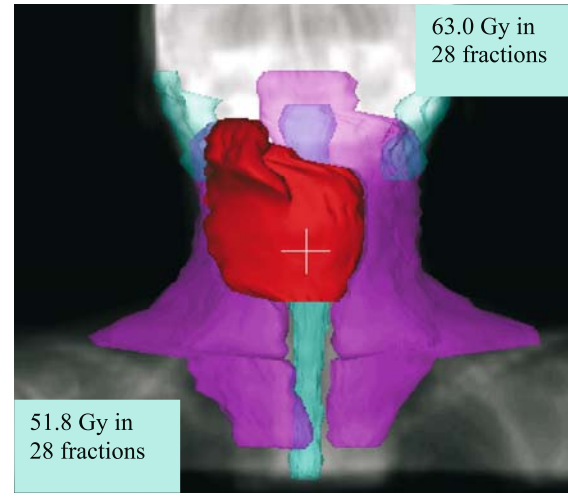

Fig. 2. SMART technique diagram

a dose of 2.25 Gy per fraction is delivered to the primary tumour site, and involved lymph nodes, and 1.8 Gy per fraction to elective lymph node groups. After 28 fractions the primary tumor and involved lymph nodes have received a total of 63 Gy, and the elective lymph nodes 51.8 Gy (Fig. 2).

The advantage of the SIB or SMART techniques is that the whole treatment course is planned in a single phase, with savings in simulation, planning, delivery and verification time compared to conventional multiphase plans [47]. Radiobiologically, SIB and SMART techniques represent accelerated fractionation schedules that may reduce accelerated repopulation of tumour clonogens and have shown improved tumour control. Theoretically, the use of larger doses per fraction may be associated with increased late normal tissue radiation toxicity to structures with a low α/β ratio (e.g. peripheral or cranial nerves) within the high-dose PTV. Long-term follow up of patients will indicate if this is a significant clinical problem.

IMRT planning modules are now commonly available in treatment planning systems. The current planning techniques in IMRT can be divided into two methods, forward planned (i. e. the user determines the relative beam weights) and inverse planned (the user defines an ideal dose volume histogram and the optimization algorithm defines the beam weights). Forward planning can produce some excellent dose distributions [14, 16, 60]; however we will focus on inverse planning techniques.

4.6.1 Prescription Dose Volume Histograms

Inverse planning depends fundamentally on the initial design of the prescription dose-volume histogram. In order to do this it is essential to delineate a full 3D set of volumes of interest including all structures that will be analyzed in the plan approval (i. e. radical and elective PTVs, spinal cord, parotid glands, etc.). Acceptable dose levels to be delivered to or avoided by those volumes must also be prescribed before the planning process can begin. Laryngeal cancer is treated at the Royal Marsden Hospital within a phase I/II dose escalation study. The dose levels are shown in Table 3. Examples of dose constraints used are 46 Gy for the spinal cord and 24 Gy mean dose to the parotids.

Table 3. Dose levels of phase I dose escalation IMRT study

Larynx/ hypopharynx	Current IMRT dose	Dose escalation
Primary tumour site	63.0 Gy in 28# (2.25 Gy per fraction)	67.2 Gy in 28# (2.4 Gy per fraction)
Elective nodal areas	51.8 Gy in 28# (1.85 Gy per fraction)	56 Gy in 28# (2 Gy per fraction)

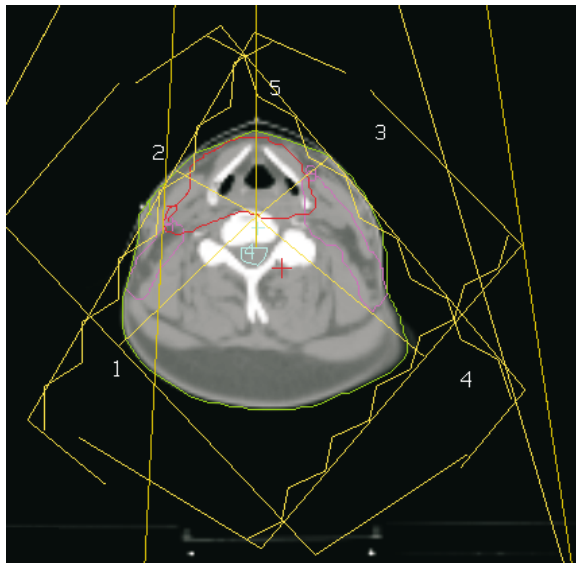

Fig. 3. The IMRT beam arrangement consisting of two anterior and two posterior oblique fields and an anterior field which has been tilted by 10° in the caudal direction

4.6.2 Field Parameters

The choice of beam parameters plays an important role in inverse planning. Gantry angle orientations can have significant effects on isodose shaping, normal tissue orientation and sparing of critical organs. This is especially true if a limited number of fields are used (e.g. 5). Most commercial inverse planning systems do not include gantry or collimator angle as part of the optimisation and therefore these basic field parameters need to be defined before the inverse planning begins. There has been much work done on finding class solutions for IMRT plans. This includes defining standard numbers of beams and their respective angles and energy as well as sets of predefined dose constraints. Initially the general consensus was that an odd number of equi-spaced beams was optimal and that more gantry angles was superior to fewer. However more recent work has suggested that for some sites equi-spaced fields may not be the optimal solution [6]. A modest number of appropriately selected beam orientations (Fig. 3) can sometimes provide dose distributions as satisfactory as those produced by a large number of unselected equi-spaced orientations [13, 15, 49, 53]. Considerations regarding whether the beam is entering the patient through the couch or immobilization system should be taken into account as attenuation factors cannot always be easily applied, especially if they only apply to part of the field. As with all 3D planning, gantry orientations that unnecessarily irradiate tissue should be avoided, such as entry through the shoulder for treatment of larynx tumors (equi-spaced fields may produce this problem).

The position of the isocentre for individual patients will determine the exact angles available.

Non-coplanar beam orientations can help with avoiding treating through normal tissue. An anterior beam tilted in the cranial direction can irradiate the upper neck without passing through the anterior oral cavity. This also causes the separation between the primary target and parotid glands to increase, thus improving the sparing of the glands. A judicious choice of collimator angles can also improve sparing of the parotid glands by ensuring that the jaw is blocking the maximum amount of gland in the beam's eye view of each field. Variation of collimator angle between the fields also ensures that any effects of tongue and groove are smeared out across the entire treated volume.

4.6.3 Additional Volumes

During the inverse planning process the optimisation algorithm will only attempt to cover or spare those volumes that have been fully outlined and that have a DVH to direct the optimisation process. It may be necessary to outline extra volumes where although strict dose sparing is not required it is still important to avoid "hot spots".

Examples of this are the esophagus and the oral cavity, where it is preferable to reduce the dose if possible in order to avoid toxicity. A volume that does not strictly relate to the anatomy can be drawn so that a dose constraint can be applied, with a relative low priority, that will help to avoid dose 'overspill' in this area. Such extra volumes can also be used to help shape the dose distributions. This is especially helpful where a lower number of gantry directions are used and therefore the shaping of the dose distributions is more difficult.

Expanded volumes (i. e. extra margins for planning purposes only) can be used to ensure coverage of targets. Depending on the leaf widths and motions this may require differing margins in different directions. This technique can also be used to ensure sparing of organs at risk.

Target volumes which extend to near the skin surface can cause the planning system to increase the dose in a tangential field in order to compensate for the build-up of dose in a directly incident field and cause skin necrosis [39]. A clinical decision needs to be made as to the appropriate skin dose. Creation of a volume for planning purposes with the volume edited away from the skin surface [39] helps reduce excessive skin treatment. The original volume can then be used for plan analysis.

4.6.4 Dose Constraints

The clinical prescription and dose limits form the goals of the inverse planning process. However, direct entry of these values into the optimization function does not always produce the optimal planning result. Inverse planning modules require dose volume points with associated penalties or priorities. These often need to vary from the clinical prescription in order to take into account effects in the planning system such as the calculation of the leaf motions and radiation leakage. If this occurs after the optimization process then user knowledge of the effects need to be included in the initial constraints such that the final solution is close to the clinical prescription.

4.6.5 Optimization Strategies

Some planning systems allow interaction with the optimization function parameters during the process, whereas others use a more closed system. If interaction is available the changes to the dose/volume/priority values may be used to 'drive' the system towards the optimal solution. Gradient descent algorithms have a tendency to get stuck in a local minimum if the constraints are so 'tight' that only small steps may be taken in the optimiza-

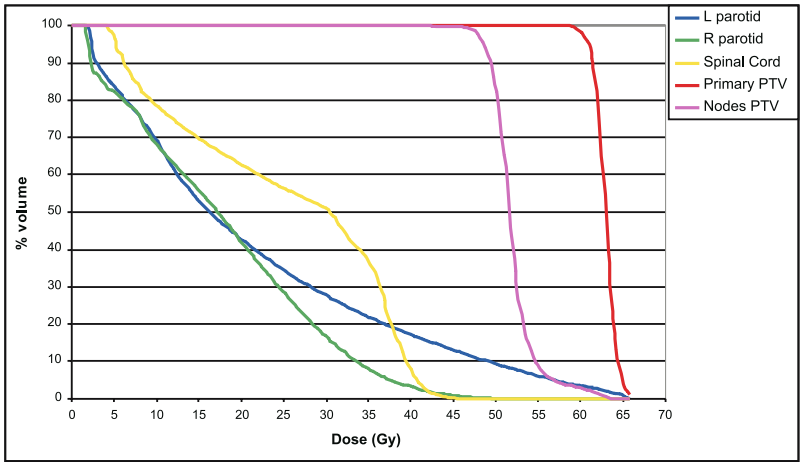

Fig. 4. A typical dose volume histogram for an IMRT treatment

tion iteration process. To avoid this, 'looser' constraints can be used in the early stages of the function, which are then 'tightened' as the function approaches the global minimum.

4.6.6 Analysis of Plans

Plans are analysed primarily based on comparison of the prescription constraints with the relevant points on the dose volume histogram (Fig. 4). Following this, dose distributions are checked in transverse, sagittal and coronal slices, as untoward hot and cold spots may not be immediately obvious in the dose volume histogram due to the lack of spatial information.

4.7 Clinical Experiences/Trials to Define the Role of IMRT

There is little clinical experience in laryngeal cancer IMRT. The UCSF group reported having treated two larynx patients as part of their overall experience with head and neck IMRT [40]. Patients with stage T2–4, N1–3, M0 squamous cell carcinoma of the larynx and hypopharynx are currently being recruited into a phase I dose escalation study at the Royal Marsden Hospital. The dose levels are shown on Table 3 and patients receive concomitant Cisplatin, 100 mg/m^2 on weeks 1 and 5. To date 15 patients have been treated to the first dose level and 5 patients have been recruited to the dose escalated level. A report of toxicity following treatment of the first 11 larynx/hypopharynx patients with median follow up of 6 months (range 2–24) showed no grade 4 toxicity. Mean PTV1 D95 was 60.3 Gy (range 57.8–61.42) and mean PTV 2/3 D95 48.14 Gy (range 47.2–49.1). Thirty seven percent of all patients developed skin toxicity grade 3. A typical pattern of widespread erythema with dry and/or moist desquamation over the neck creases was observed (Fig. 5). Half of the patients required nasogastric or gastrostomy tube feeding. Most patients experienced mucositis and pain grades 1–2, with 44% reporting grade 3. A positive correlation was found with maximum oral cavity dose ($R = 0.7$, 95% CI 0.3–0.9; $p = 0.002$) [26].

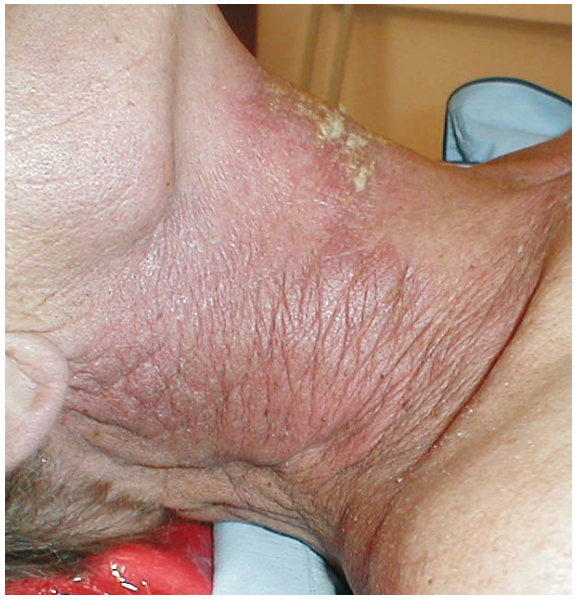

Fig. 5. Typical skin reaction

4.8 Future Directions

IMRT has a defined role in improving the therapeutic ratio in laryngeal cancer. Its ability to spare normal tissues can be exploited to design studies that evaluate conventional and accelerated fractionation radiation regimes in conjunction with concomitant chemotherapy, hypoxic sensitisers, biological agents (i. e. Iressa) and/or gene therapy. Another exciting area of study is the boosting of hypoxic areas and/or biological gross tumour volumes as identified on PET scanning and re-treatment of small recurrences.

The increasing use of IMRT in the clinic will provide us with new data which will allow us to maximise its potential with the dual aim of improving patient's survival and quality of life.

References

1. Adelstein DJ (1998) Recent randomised trial of chemoradiation in the management of locally advanced head and neck cancer. Curr Opin Oncol 10:213–218
2. Annyas AA et al. (1979) Prognostic factors of neck node metastasis: their impact on planning a treatment regimen. American Society of Head and Neck Surgeons, Los Angeles
3. Bataini JP et al. (1985) Natural history of neck disease in patients with squamous cell carcinoma of oropharynx and pharyngolarynx. Radiother Oncol 3:245–255
4. Bourhis J et al. (2002) Conventional versus modified fractionated radiotherapy: meta-analysis based on individual data of patients with head and neck squamous cell carcinoma (HNSCC). Radiother Oncol 64(suppl.1):S23
5. Braaksma MMJ et al. (2003) Optimisation of conformal radiation therapy by intensity modulation: cancer of the larynx and salivary gland function. Radiother Oncol 66:291–302
6. Bragg CM et al. (2002) The role of intensity-modulated radiotherapy in the treatment of parotid tumors. Int J Radiat Oncol Biol Phys 52(3)729–738
7. Burke LS et al. (1997) Definitive radiotherapy for early glottic carcinoma: prognostic factors and implications for treatment. Int J Radiat Oncol Biol Phys 38:37–42
8. Butler EB et al. (1999) Smart (simultaneous modulated accelerated radiation therapy) boost: a new accelerated fractionation

schedule for the treatment of head and neck cancer with intensity modulated radiotherapy. Int J Radiat Oncol Biol Phys 45:21–32
9. Byers et al. (1988) Rationale for elective modified neck dissection. Head Neck Surg 10:160–167
10. Candela et al. (1998) Patterns of cervical node metastases from squamous cell carcinoma of the oropharynx and hypopharynx. Head Neck 12:197–203
11. Carter et al. (1987) Radical neck dissections for squamous carcinomas: pathological findings and their clinical implications with particular reference to transcapsular spread. Int J Radiat Oncol Biol Phys 13:825–832
12. Chao KS et al. (2002) Determination and delineation of nodal target volumes for head and neck cancer based on patterns of failure in patients receiving definitive and postoperative IMRT. Int J Radiat Oncol Biol Phys 53(5):1174–1184
13. Clark CH et al. (2004) Intensity modulated radiotherapy improves target coverage, spinal cord sparing and allows dose escalation in patients with locally advanced cancer of the larynx. Radiother Oncol 70(2):189–198
14. Claus F et al. (2001) Evaluation of a leaf position optimisation tool for intensity modulated radiation therapy of head and neck cancer. Radiother Oncol 61:281–286
15. Das S et al. (2003) Beam orientation selection for intensity-modulated radiation therapy based on target equivalent uniform dose maximization. Int J Radiat Oncol Biol Phys 55(1):215–224
16. De Neve W et al. (1996) Planning and delivering high doses to targets surrounding the spinal cord at the lower neck and upper mediastinal levels: static beam-segmentation technique executed by a multileaf collimator. Radiother Oncol 40: 271–279
17. El-Sayed S, Nelson N (1996) Adjuvant and adjunctive chemotherapy in the management of squamous cell carcinoma of the head and neck region: a meta-analysis of prospective and randomised trials. J Clin Oncol 14:838–847
18. Eisbruch et al. (2002) Intensity modulated radiation therapy for head and neck cancer: emphasis on the selection and delineation of targets. Semin Radiat Oncol 12(3):238–249
19. Emami B et al. (1991) Tolerance of normal tissue to therapeutic irradiation. Int J Radiat Oncol Biol Phys 21(1):109–122
20. Fletcher GH, Goepfert H (1980) Larynx and hypopharynx. In: Fletcher G (ed) Textbook of radiotherapy. Lea & Febiger, Philadelphia, pp 330–363
21. Forastiere AA et al. (2003) Concurrent chemotherapy and radiotherapy for organ preservation in advanced laryngeal cancer. N Engl J Med 349(22):2091–2098
22. Fu KK et al. (2000) Radiation Therapy Oncology Group (RTOG) phase III randomised study to compare hyperfractionation radiotherapy for head and neck squamous cell carcinomas: first report of RTOG 9003. Int J Radiat Oncol Biol Phys 48:7–16
23. Gallo O et al. (2000) Treatment of the contralateral negative neck in supraglottic cancer patients with unilateral node metastases (N1–N3). Head Neck 22:386–392
24. Gowda RV et al. (2003) Three weeks radiotherapy for T1 glottic cancer: the Christie and Royal Marsden Hospital experience. Radiother Oncol 68:105–111
25. Gregoire et al. (2003) CT-based delineation of lymph node levels and related CTVs in the node negative enck: DAHANCA, EORTC, GORTEC, NCIC, RTOG consensus guidelines. Radiother Oncol 69:227–236
26. Guerrero Urbano MT, Nutting CM (2004) Clinical use of intensity-modulated radiotherapy: part I. Br J Radiol 77(914):88–96
27. Harwood A et al. (1983) Supraglottic laryngeal carcinoma: an analysis of dose-time-volume factors in 410 patients. Int J Radiat Oncol Biol Phys 9:311
28. Harwood A et al. (1979) Management of advanced glottic cancer: a 10-year review of the Toronto experience. Int J Radiat Oncol Biol Phys 5:899
29. Hermanek P et al. (1997) UICC TNM atlas, 4th edn
30. Hicks WL et al. (1999) Patterns of nodal metastasis and surgical management of the neck in supraglottic laryngeal carcinoma. Otolaryngol Head Neck Surg 121:57–61
31. Hirabayashi et al. (1991) Extracapsular spread of squamous cell carcinoma in the neck lymph nodes: prognostic factor of laryngeal cancer. Laryngoscope 101:502–506
32. Horiot JC et al. (1997) Accelerated fractionation (AF) compared to conventional fractionation (CF) improves locoregional control in the radiotherapy of advanced head and neck cancers: results of the EORTC 22581 randomised trial. Radiother Oncol 44:111–121
33. Huang et al. (1992) Postoperative radiotherapy in head and neck carcinoma with extracapsular lymph node extension and/or positive resection margins. A comparative study. Int J Radiat Oncol Biol Phys 23:737–742
34. Humphreys M et al. (2003) Assessment of treatment accuracy for head and neck intensity modulated radiotherapy (IMRT) and conventional radiotherapy using amorphous silicon portal imaging. Radiother Oncol 68:S65
35. ICRU 50 (1993) Prescribing, recording and reporting photon beam therapy ICRU report 50. International Commission on Radiation Units and Measurement, Bethesda
36. ICRU 62 (1999) Prescribing, recording and reporting photon beam therapy (supplement to ICRU Report 50). International Commission on Radiation Units and Measurement, Bethesda
37. Johansen LV et al. (2002) Supraglottic carcinoma: patterns of failure and salvage treatment after curatively intended radiotherapy in 410 consecutive patients. Int J Radiat Oncology Biol Phys 53:948–958
38. Johnson et al. (1981) The extracapsular spread of tumours in cervical node metastasis. Arch Otolaryngol 107:725–729
39. Lee N et al. (2002) Skin toxicity due to intensity modulated radiotherapy for head-and-neck carcinoma Int J Radiat Oncol Biol Phys 53(3)630–637
40. Lee N et al. (2003) Intensity-modulated radiation therapy for head-and-neck cancer: the UCSF experience focusing on target volume delineation. Int J Radiat Oncology Biol Phys 57(1):49–60
41. Lindberg R (1972) Distribution of cervical lymph node metastases from squamous cell carcinoma of the upper respiratory and digestive tracts. Cancer 29:1446–1449
42. Maciejewski B et al. (1983) The influence of the number of fractions and of overall treatment time on local control and late complication rate in squamous cell carcinoma of the larynx. Int J Radiat Oncol Biol Phys 9:321–328
43. McLaughlin et al. (1995) Retropharyngeal adenopathy as a predictor of outcome in squamous cell carcinoma of the head and neck. Head Neck 17:190–198
44. Mendenhall WM et al. (2001) T1-T2 squamous cell carcinoma of the glottic larynx treated with radiation therapy. J Clin Oncol 19:4029–4036
45. Mendenhall W et al. (1992) Stage T3 squamous cell carcinoma of the glottic larynx: a comparison of laryngectomy and irradiation. Int J Radiat Oncol Biol Phys 23(4):725–732
46. Mendenhall WM et al. (1989) Is elective neck treatment indicated for T2N0 squamous cell carcinoma of theglottic larynx? Radiother Oncol 14:199–202

47. Miles EA et al. (2003) How routine can IMRT become in daily clinical practice? Radiother Oncol 68:S121
48. Mohan R et al. (2000) Radiobiological considerations in the design of fractionation strategies for intensity-modulated radiation therapy of head and neck cancers. Int J Radiat Oncol Biol Phys 46:619–630
49. Nutting CM et al. (2001) Optimisation of radiotherapy for carcinoma of the parotid gland: a comparison of conventional, three-dimensional conformal and intensity-modulated techniques Radiother Oncol 60:163–172
50. Overgaard J et al. (2003) Five compared with six fractions per week of conventional radiotherapy of squamous cell carcinoma of the head and neck: DAHANCA 6 and 7 randomised controlled trial. Lancet 362:933–940
51. Paisley S et al. (2002) Results of radiotherapy for primary subglottic squamous cell carcinoma. Int J Radiation Oncol Biol Phys 52:1245–1250
52. Pignon JP et al. (2000) Chemotherapy added to locoregional treatment for head and neck squamous cell carcinoma: three meta-analyses of updated individual data. MACH-NC Collaborative Group. Meta- analysis of chemotherapy on head and neck cancer. Lancet 355:949–955
53. Rowbottom CG et al. (2001) Beam-orientation optimization of intensity-modulated radiotherapy: clinical application to parotid gland tumors. Radiother Oncol 59:169–177
54. Shah et al. (1990) The patterns of cervical lymph node meatastases from squamous carcinoma of the oral cavity. Cancer 66:109–113
55. Sessions DG et al. (1975) Carcinoma of the subglottic area. Laryngoscope 4:618–636
56. Spriano G et al. (1997) Conservative management of T1-T2N0 supraglottic cancer: a retrospective study. Am J Otoralyngol 18:299–305
57. The Department of Veteran Affairs Laryngeal Cancer Study Group (1991) Induction chemotherapy plus radiation compared with surgery plus radiation in patients with advanced laryngeal cancer. N England J Med 324:1685–1690
58. Tomik J et al. (2001) Evaluation of cervical lymph node metastasis of 1400 patients with cancer of the larynx. Auris Nasus Larynx 28:233–240
59. van Asselen B et al. (2002) The dose to the parotid glands with IMRT for oropharyngeal tumors: the effect of reduction of positioning margins. Radiother Oncol 64:197–204
60. van Dieren EB et al. (2000) Beam intensity modulation using tissue compensators or dynamic multileaf collimation in three dimensional conformal radiotherapy of primary cancers of the oropharynx and larynx, including the elective neck. Int J Radiation Oncology Biology and Physics 47(5): 1299–1309
61. Withers HR et al. (1988) The hazard of accelerated tumour clonogens repopulation during radiotherapy. Acta Oncol 27:131–146
62. Wu Q et al. (2000) The potential for sparing of parotids and escalation of biologically effective dose with intensity-modulated radiation treatments of head and neck cancers: a treatment design study. Int J Radiat Oncol Biol Phys 46:195–205

Central Nervous System, Skull Base and Paraspinal Tumors

Anita Mahajan, Eric L. Chang

5

Contents

5.1 Introduction

Central nervous system (CNS) tumors represent a diverse group of neoplasms that require special consideration for benign, malignant, primary or metastatic lesions. The CNS has a large number of critical tissues that have specific concerns that must be evaluated in any form of radiotherapy planning. Intensity modulated radiotherapy (IMRT) is an ideal form of treatment to minimize the risk of morbidity while maintaining target volume coverage.

5.2 Anatomic Considerations

CNS tumors can occur anywhere within the head or spine. In general, all diagnostic information, including the pre-operative, post-operative radiographic imaging, the operative note, physical examination and history, must be considered when developing an IMRT treatment plan. The tumor geometry and its relationship to the surrounding normal structures are optimally evaluated by radiographic studies. The operative note may help in determination of the extent of surgery, the extent of subclinical disease and identification of normal structures. The patient's history and physical examination may give information as far as specific risks that may be increased or dose allowances that may be acceptable to facilitate planning. Previous or concomitant chemotherapy with its potential toxicity to normal structures is important to identify the additional risk that is taken with the addition of radiotherapy. In a similar fashion, previous surgical interventions may also alter the susceptibility of normal tissue.

The anatomic considerations vary according to the location of the tumor. One must always consider the surrounding normal brain. The function of the adjacent brain, for example: temporal lobes with respect to memory should be considered when designing IMRT plans. An effort to minimize dose to the contralateral cerebral hemisphere should be made if there is no evidence of gross or subclinical disease. In frontal and temporal lesions, the optic pathway including the optic nerves and optic chiasm commonly become critical tissue that must be identified and be considered for treatment planning. In central lesions, the brain stem may be the normal tissue that limits dose. Infratentorial lesions may be adjacent to the middle ear and brainstem. In paraspinal lesions, the spinal cord and retroperitoneal structures such as the kidney must be identified and considered during treatment planning.

The cranial nerves, brainstem, temporal lobes, neuro-endocrine and ocular apparatus are important to identify in patients with skull base tumors. Usually these tumors have an irregular shape and can abut and

Table 1. Current institutional guidelines for target volume delineation for selected intracranial diagnosis

Tumor type	Gross tumor volume (GTV)	Clinical target volume (CTV)	Planning target volume (PTV)	Physical penumbra[a]	Dose
High-grade primary tumors	T1C, CT+C, surgical bed, suspicious T2	(1) GTV + 2 cm (2) CTV = GTV	(1) CTV + 0.3 – 0.5 cm (2) GTV + 0.3 – 0.5 cm	0.3 – 0.5 cm	(1) 50 Gy/25 (2) 10 Gy/5 SIB (1) 48 Gy & (2) 60 Gy/30
Low grade primary tumors	T2, T1C, CT + C, surgical bed	*GTV* + 0.5 – 1.5 cm	(1) *CTV* + 0.2 – 0.3 cm (2) *GTV* + 0.2 – 0.3 cm (optional)	As above	(1) 45 – 54 Gy/ 25–30 (2) 5 – 10 Gy/3 – 5 (after 45 Gy)
Chordoma, chondrosarcoma	T1C, T2, CT + C, consider surgical bed	None	*GTV* + 0.3 – 0.5 cm	As above	66 – 78 Gy /33 – 39
Meningioma	T1C & CT + C dural/ bony extension	None	*GTV* + 0.2 – 0.3 cm	As above	50 – 54 Gy /25 – 30
Vestibular schwannoma	T1C, CT + C	None	*GTV* + 0.2 – 0.3 cm	As above	45 – 50 Gy /25 – 30 25 Gy /5
Pituitary adenoma	T1C, CT + C	None	*GTV* + 0.2 – 0.3 cm	As above	45 – 50 Gy /25 – 30

[a] The physical penumbra, i. e. additional distance to the block edge is generated automatically by the planning software, but does depend on multileaf collimator size. In our current software, this distance can be manually adjusted after the plan has been generated to optimize further the dose distribution T1C: T1 weighted MRI with contrast; T2: T2 weighted; CT + C: CT with contrast; SIB: simultaneous integrated boost

displace surrounding normal structures without infiltration. The diagnostic imaging should be reviewed with a neuro-radiologist and neurosurgeon to determine the location, if possible, of the distorted structures. Infratentorial tumors can involve the cerebellar hemispheres, brainstem, skull, spinal cord or cranial nerves and these structures should be identified during IMRT planning in this area.

Paraspinal tumors include vertebral lesions, extra vertebral lesions in close proximity to the spine and intra-spinal tumors. The anatomy of the vertebral body, and its posterior elements, and spinal cord, lends itself well and is exquisitely suited to treatment by intensity-modulated radiation therapy (IMRT) to create a "horseshoe" shaped dose distribution around the vertebral body, and its pedicles while sparing the spinal cord itself. Stereotactic body radiotherapy (SBRT) with IMRT to spinal tumors has the potential to expand treatment options available to the patient afflicted with spinal metastases. For patients with mechanically stable spinal metastases without spinal cord compression, a non-invasive treatment alternative to surgery is attractive. Potential indications for SBRT to the spine include primary treatment for a single or oligometastases in the spine, the postoperatively setting, postoperative salvage treatment, and salvage therapy after previous irradiation. The primary concern in all cases is the spinal cord. Pulmonary dose should be evaluated in thoracic lesions and oropharyngeal anatomy should be noted in cervical spine disease. Retroperitoneal structures such as the kidneys should be considered for upper lumbar lesions. In lower lumbar planning gonadal doses should be considered because of their inherent sensitivity to radiation dose.

5.3 Histologic Considerations

In general, neoplasms within the CNS can be categorized into primary or metastatic. The primary neoplasms can be subdivided into benign or malignant. Within the primary neoplasms, any tissue within the CNS may give rise to a tumor development. When planning IMRT for CNS malignancies, knowledge of the neoplasm's natural history, probability and direction of subclinical extension and inherent radiosensitivity becomes crucial for optimal treatment design. The gross tumor volume, clinical target volume and planning target volume (GTV, CTV and PTV) are tumor specific and vary according the histology, location, other therapies and normal tissues (Table 1).

5.3.1 Malignant

The most common types of primary malignant CNS tumors are of astrocytic origin, which are classified by the WHO system in which nuclear atypia, mitotic rate, presence of necrosis and neovascularization are evaluated. In general, tumors are assigned a grade from I to IV with grade I being the least aggressive. Higher- grade tumors (i. e. glioblastoma) usually have a greater probability of subclinical extension and patients benefit from

higher doses of radiation (60 Gy) [1]. Low-grade malignant tumors can be treated with smaller margins and dose is limited to 45–54 Gy [2, 3]. Other primary malignant CNS tumors can be treated, for radiotherapy planning purposes, similar to their astrocytic counterpart as long as there is no specific risk of dissemination within the cerebrospinal fluid (CSF). Uncommon tumors such as chordomas or chondrosarcomas of the skull base have significant radioresistance and though the risk of direct brain infiltration is low, aggressive high dose radiotherapy is recommended for optimal local control.

5.3.2 Benign

Benign tumors of the CNS can originate from any tissue within the cranium and spine. In general, these tumors grow through local extension usually without evidence of infiltration into the brain parenchyma. When planning IMRT for these neoplasms, one should consider tissue planes, the direction of tumor extension, the pre-operative and post-operative tumor volumes and the possibility of microscopic residual at the surfaces of the surgical bed to identify the GTV, CTV and PTV. For non-infiltrative tumors where there does not appear to be a risk of post-operative surgical bed contamination, a CTV is not usually necessary.

5.3.3 Metastatic

Metastatic disease to the CNS can involve the bone, dura or the parenchyma within the cranium or spine. Metastatic tumors commonly remain localized with limited invasiveness; therefore, margins for subclinical extension can be small. Of the approximately half million cancer-related deaths that occur each year, 40% involve

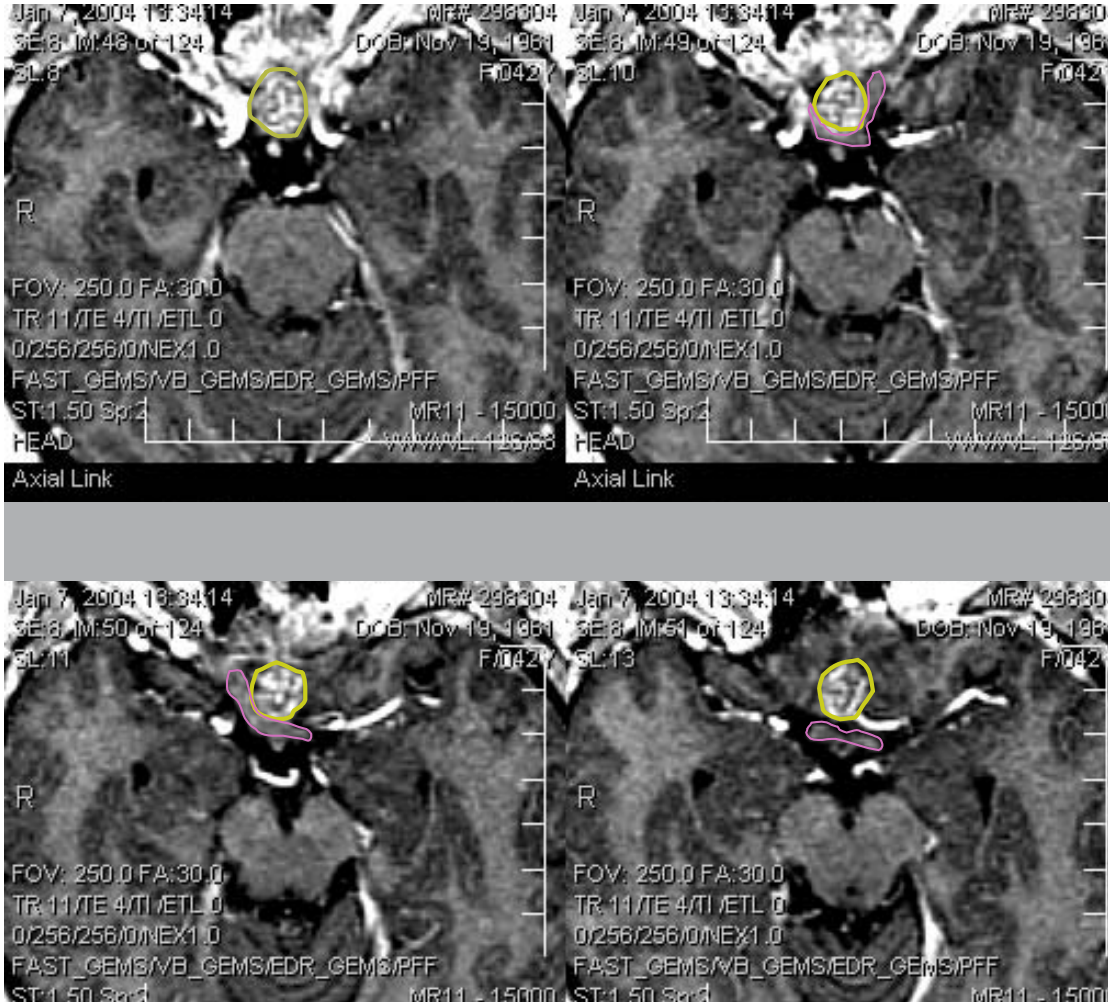

Fig. 1. T1 weighted gadolinium enhanced volumetric MRI of patient with recurrent pituitary adenoma. Tumor is outlined in *green*; optic chiasm is identified in *pink*. This MRI was obtained for planning purposes and was done with 1.5-mm slice thickness to identify the normal critical structures and tumor volume accurately

patients with spinal metastases, making the spine the most common site for bone metastases where radiotherapy is frequently used for palliation of pain, and neurologic symptoms.

5.3.4 Recurrent

Patients who have progressive disease despite previous irradiation may be candidates for conformal, carefully planned radiotherapy. Time and dose considerations from the previous radiotherapy treatment as well as normal tissue repair and the cost benefit ratio require evaluation. Other treatments, including chemotherapy and surgery as well as patient's co-morbidities will impact on the final therapeutic decision.

5.4 Target Volume Delineation, Organ at Risk Definition

5.4.1 Computerized Tomography

Computerized tomography (CT) best evaluates bony involvement of tumors, in particular those that involve the skull base, but it does not identify soft tissue components of neoplastic processes as well as magnetic resonance imaging (MRI) [4]. Additional information with respect to the tumor contents, including hemorrhage, calcification can be obtained from CT scan imaging. The spatial accuracy of CT scan has been better than that of MRI; therefore, it has benefit in radiotherapy planning to achieve precise delivery of treatment [5, 6]. Current dosimetry algorithms also rely on information from CT scans to perform heterogeneity corrections based on tissue density data from the planning CT scans [7]. For appropriate identification of the spinal cord in a patient who has undergone surgical instrumentation a CT myelogram can be done in the treatment position for better delineation of the tumor volumes and the spinal cord.

5.4.2 Magnetic Resonance Imaging

Magnetic Resonance Imaging technology has improved detection and diagnosis of CNS tumors immensely. The various sequences can be used to optimally define area of gross tumor involvement in a three dimensional fashion. Subclinical extension for high grade and low grade gliomas may be better defined with the use of newer magnetic resonance spectroscopic (MRS) software [8,9]. Diffusion imaging may play a role in further identification of high risk areas for infiltrative tumors [10]. Thin slice axial MRIs with high resolution are invaluable for target and normal tissue delineation when fused with planning CT scans as shown in Fig. 1.

5.4.3 Positron Emission Tomography

^{11}C-methionine (Met) and ^{18}F-fluorodeoxy-glucose (FDG) positron emission tomography (PET) imaging is being evaluated for tumor characterization. Reports have suggested the Met-PET may be very sensitive in distinguishing between neoplastic tissue and normal brain [11, 12]. This technology may prove to useful in target volume delineation for IMRT planning for identification of the clinical target volume.

5.5 Dose Requirements

There appears to be some benefit in treating some tumors to high doses: i. e. skull base chordomas, chondrosarcomas and high-grade glial tumors. Many other less aggressive histologic variants have do not appear to benefit from dose escalation. Two prospective randomized studies did not support dose escalation in low grade glioma and doses as low as 45 Gy can be used if normal tissue toxicity is of concern [2, 3]. For benign meningioma and vestibular schwannoma, doses of 50 – 54 Gy have greater than 85% progression free survival at five to ten years [13–16]. The optimal dose with good long-term control for other low grade or benign neoplasms such as functioning or non-functioning pituitary adenomas appears to be 45 – 50 Gy delivered to the GTV [17,19]. With IMRT the benefit in tumor control will not be evident but patients will benefit overtime with a potential reduction in toxicity [20]. In Fig. 2, the tumor volume and IMRT plan for a patient with a vestibular schwannoma demonstrates the potential benefit of the reduction of dose to the brainstem, even though the prescribed dose was only 45 Gy.

For higher-grade or radioresistant tumors IMRT can be useful in delivering the desired dose to the neoplasm while respecting normal tissue tolerances. Current recommended doses for high-grade glial tumors is 60 Gy over six weeks. Previously reported investigations researching further dose escalation has not indicated a significant benefit [21, 22]. The Radiation Therapy Oncology Group (RTOG 9803) has recently completed a study with conformal radiotherapy with a final dose of 84 Gy to newly diagnosed glioblastoma. The results have not been published thus far. There appears to be a benefit of dose escalation in other radioresistant histologies including skull base chordomas and chondrosarcomas. Fractionated doses of 66 up to 79.2 Gy have been delivered to skull base chordomas with five-year control rates of 44 – 59%. It appears that the minimum dose delivered to the tumor volume can impact the local control rate

and IMRT may be a technology to deliver the prescribed dose to a higher proportion of the tumor [23, 24]. In Fig. 3 and IMRT plan of a young patient with a skull base chordoma is demonstrated. IMRT allowed a higher proportion of the GTV to be treated with the prescription dose. In this situation, the brainstem tolerance was increased because of the nature and the prognosis of the disease process. Other recurrent, radioresistant primary or metastatic neoplasms to the CNS may also benefit with the use of IMRT.

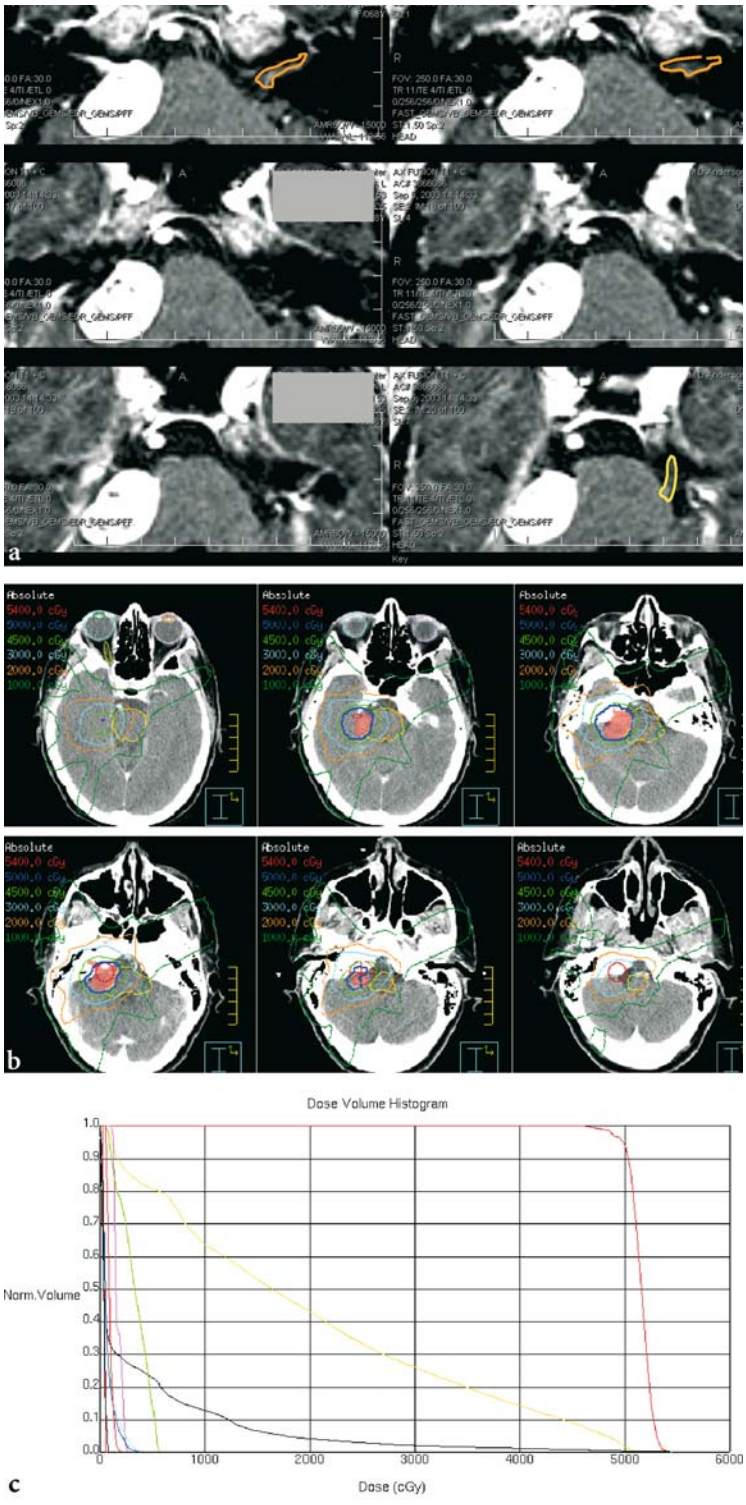

Fig. 2. **(a)** T1 weighted 1.5 mm planning volumetric MRI in a patient with a right vestibular schwannoma. The contralateral VII/VIII cranial nerve complex is outlined in *orange*. The left cranial nerve V is identified in *yellow*. Care was taken to limit dose the brainstem that is compressed by the tumor and the contralateral normal tissues to preserve function. The ipsilateral cochlea was identified on the planning CT scan. **(b)** Isodose curves with six-field IMRT plan generated with GTV in *red*. Brain stem is outlined in *yellow*. Additional normal tissues that were outlined were: optic apparatus, cochlea, parotid glands, and uninvolved brain. A dose of 45 Gy was given in 25 fractions over 5 weeks. **(c)** Dose volume histogram of right vestibular schwannoma, six-field plan. GTV is noted in *red*. Brainstem is *yellow*. Normal brain is in *black*. Remaining structures received negligible doses

Since SBRT for spinal metastases is given in the context of palliation, and avoiding spinal cord damage is paramount, we initially chose to prescribe doses in a hypofractionated yet conservative fashion to a total dose of 30 Gy in five fractions on alternating days to allow for sufficient repair, while limiting the spinal cord dose to 10 Gy. A typical dose distribution and dose volume histogram are shown (Fig. 4). In so doing, this would permit re-irradiation of the spine if necessary. In terms of biologic equivalence, the BED2 Gy is 40 Gy for early responding tissues assuming an a/b of 10 Gy, and 54–64 Gy assuming an a/b of 1.5–3 Gy for the spinal cord. With the increased confidence of our safety and setup data, we have proceeded to shorten our treatments to a total dose of 27 Gy in three fractions on alternating days while limiting the spinal cord dose to 9 Gy.

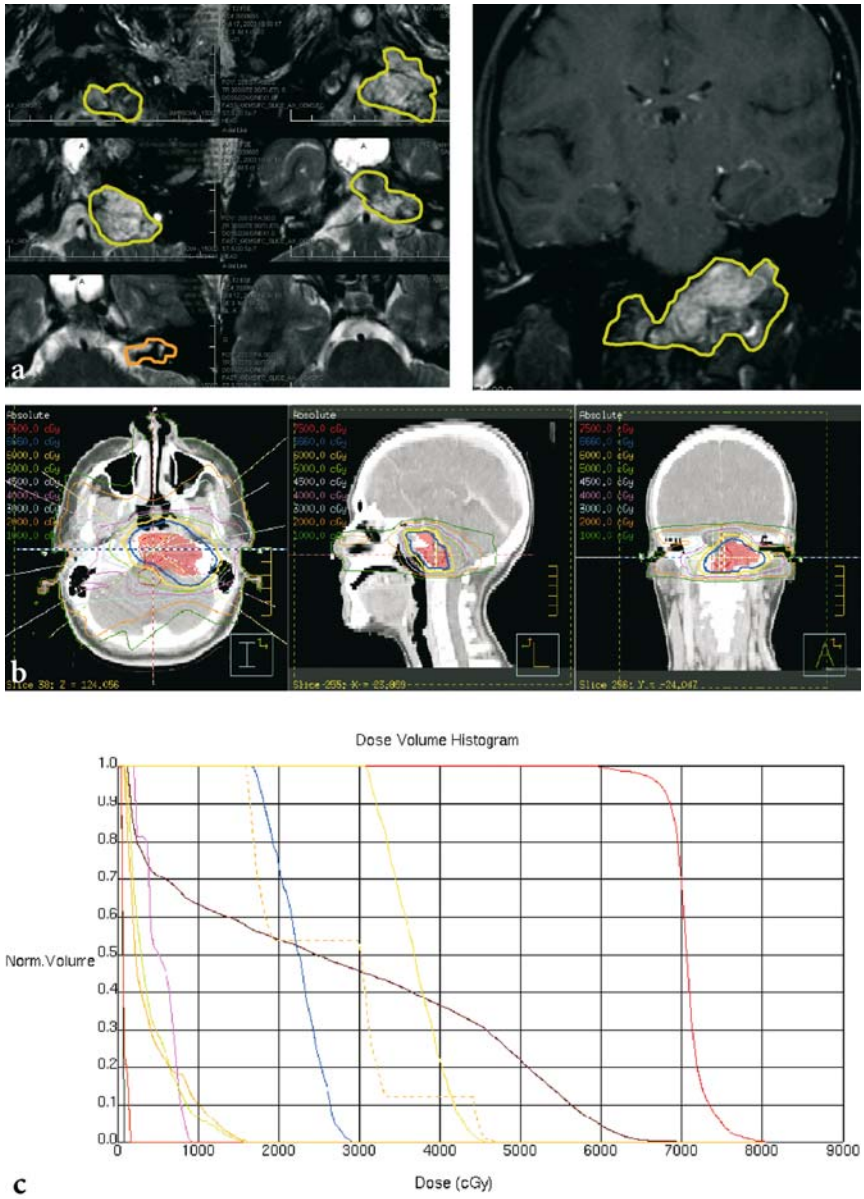

Fig. 3. (a) 12-year-old girl with skull base chordoma status post sub-total resection. The residual tumor (*green*) was identified after discussion with the surgeon. Critical structures including the brain stem, left acoustic apparatus (*orange*), lower cranial nerves, optic apparatus, temporal lobes, eyes were identified for planning purposes and an IMRT plan was used for treatment. (b) Axial, sagittal and coronal reconstructions of planning CT with isodose lines of seven-field IMRT plan with a planar arrangement with a final dose of 66.6 Gy given in 37 fractions of 1.8 Gy each. The GTV is identified in *red*; the brainstem is outlined in *brown*. (c) Dose volume histogram with prescription dose of 66.6 Gy. GTV is noted in *red*. Brainstem in *brown*, left cochlea in *yellow*, right cochlea in *blue*, pituitary gland in *dashed orange*. Other structures include the chiasm (*fuchsia*), optic nerves (*right and left, lime green and light orange*) and lens (*right and left in forest and dark orange*). A small volume of brain stem exceeded 60 Gy, the absolute dose and the distribution of the dose was evaluated carefully

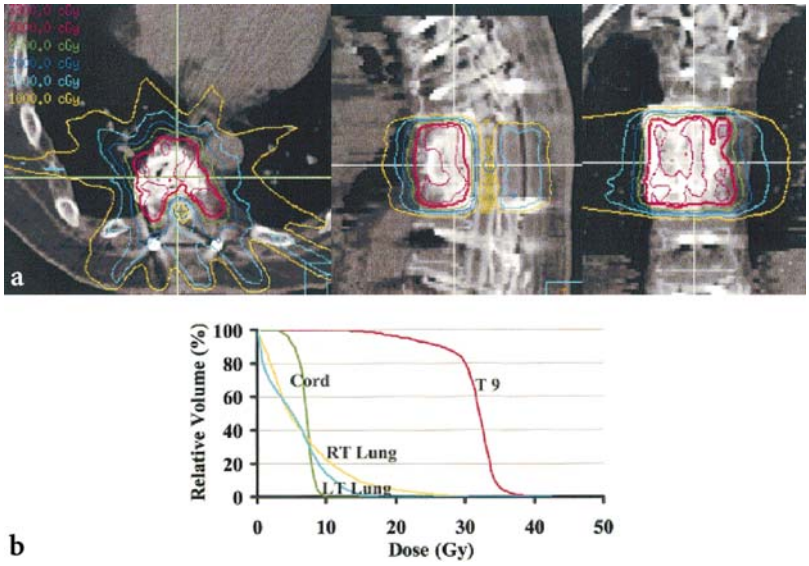

Fig. 4. Axial, sagittal and coronal reconstructions with isodose lines and a DVH of a stereotactic spinal IMRT plan with the T9 verterbral body as the target. 30 Gy (*red*) was given in ten fractions of 3 Gy each to the GTV with restrictions placed on the spinal cord (*yellow*) and the lungs (*blue and green*)

We intend to deliver conservatively and exclusively hypofractionated SBRT. After completing our prospective phase I trial for various hypofractionated schedules with adequate follow-up, we will proceed to single fraction SBRT. It is postulated that "radioresistant" histologies such as renal cell carcinoma, and melanoma may require higher doses, but this must be balanced against the greater volumes of normal surrounding tissues (kidneys, esophagus, bowel, heart, lung) that must be necessarily irradiated to higher doses.

5.6 Optimization Strategies

The benefit of IMRT is the improved ability to sculpt or paint the dose distribution into the optimal shape to improve the therapeutic ratio. Technical challenges involving immobilization, treatment planning, and real-time image image-guidance of SBRT are being addressed through investigations involving recent advances in imaging, treatment planning software, and computational power.

One of the major concerns is the correct determination of both the normal tissues and target volumes. Good diagnostic and planning imaging software with excellent quality assurance will help attain this goal. The radiographic images use for planning, either MRI and/or CT, should be performed with 3 mm or less slice thickness. Intravenous contrast should be used, in particular if the lesion enhances on previous diagnostic studies. In addition, the use of radiographic contrast material may help to identify normal structures. Image fusion of the CT and MRI images, and if appropriate, PET or MRS should be considered and if done, quality assurance of the fusion process and accuracy of the resulting images should be evaluated.

Patient immobilization is important since it may reduce the PTV if done well. The patient's head and upper neck should be immobilized in a thermoplastic mask with adequate rigidity that will minimize inter and intra-fraction patient motion [25, 26]. Other systems for head immobilization have been used in the past, but they require surgical interventions or an very co-operative patient for optimal use [27–29]. The PTV margin that is added is dependent on the reliability of the patient set up and should be realistic when developing an IMRT plan. Rotational and translational errors should be considered [30]. In general our PTV margin is in the 2–5 mm range but it depends on the equipment parameters, institutional limitations and clinical situation. All potential external parameters for positioning errors should be considered: patient immobilization, patient co-operation, machine and couch quality assurance, etc. Currently, at our institution, for conventionally fractionated cranial IMRT a rigid aquaplast mask with melded reinforcements strips is used for patient immobilization. The additional strips increase the mask stability and decrease potential rotational positional error. A PTV of 2–3 mm is the optimal margin used for potential positioning variation in most situations [30]. If patient set up and normal tissue tolerance is critical, then more frequent port films are taken or fractionated stereotactic setup using a Gill-Thomas-Cosman (GTC) relocatable head frame will be used with a set up error of less than 1 mm. In this situation the block edge is placed at 2–4 mm which includes the 1 mm for the PTV margin and 2–3 mm for the dosimetric penumbra.

SBRT has advantages, such as the ability to give higher doses to the spinal tumor while minimizing dose to the spinal cord. Dose painting is a technique of IMRT that can be used to give differential doses to a spinal tumor and the vertebral body containing it. Before

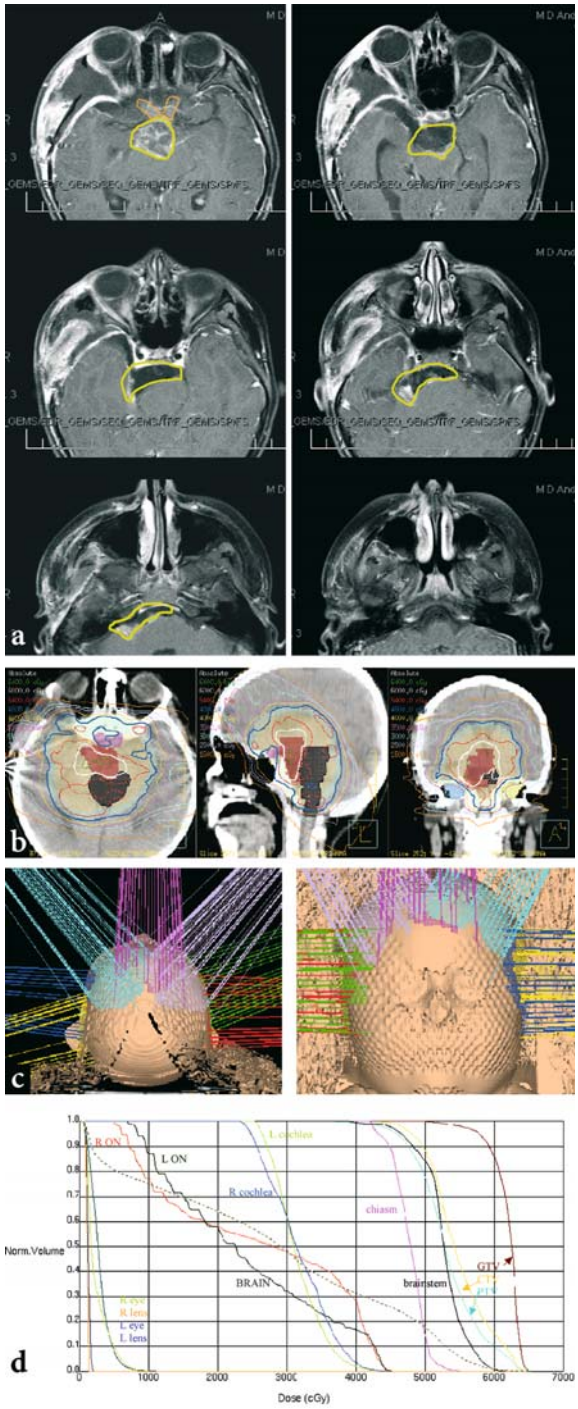

Fig. 5. **(a)** Postoperative T1 weighted MRI scan of six-year-old patient with a glioblastoma in an unusual location. The GTV is outlined in *green* and represents the residual disease as well as the surgical bed. Additional margins were added for the CTV (1.5 cm) and PTV (0.5 cm). Critical structures that required attention were the brain stem, optic chiasm (*orange*), optic apparatus, temporal lobes, and cochlea. The goal was to deliver 60 Gy in 30 fractions. **(b)** The GTV (*red*) was identified as the surgical bed and residual tumor. A CTV (tan) was generated with the addition of a 2 cm margin that was adjusted according the anatomic tissue planes. A 0.5-cm margin was added to delineate the PTV (aqua). 60 Gy and 48 Gy were prescribed to the GTV and CTV respectively. Normal tissues demonstrated here include the chiasm (*fuchsia*), brainstem (*black*) and the cochlea (*blue, lime green*). The isodose lines were reviewed in all views and the hotspot position was carefully evaluated and restricted to the GTV. **(c)** 3 D view of the beam arrangement for the seven-field IMRT plan is shown here. Three couch positions each with 34–48 control points were used. **(d)** Dose volume histogram for the seven-field IMRT plan. The DVHs for the critical structures were reviewed. The final dose to the GTV was limited because of tolerance of the brainstem. The dose above 54 and 60 Gy was carefully evaluated to confirm that no normal tissues were overlapping the with tumor volumes, to reduce the risk of unacceptable toxicity. L: left, R: right, R ON: right optic nerve, L ON: left optic nerve, GTV: gross tumor volume, CTV: clinical target volume, PTV: planning target volume

SBRT to the spine can be considered a viable treatment, clinical safety, which is predicated upon accurate and precise treatment, must be demonstrated. At our institution a targeting system that integrates a CT-on-rails scanner with a linear accelerator (LINAC) is used for SBRT. Patients are immobilized in a supine position by a moldable body cushion vacuum wrapped with a plastic fixation sheet. A Planning CT and immediately repeated CT were performed on the LINAC/CT-on-rails unit to assess respiratory-related vertebral body motion. A coplanar IMRT using seven to nine beams is generated and daily pre-treatment CT scans are fused with the planning CT scans to correct the target isocenter by accounting for any translational and roll (axial) rotational discrepancies from the planning CT [31].

The CTV is not added as a uniform margin around the GTV, but is modified based on natural anatomic barriers, such as the tentorium, orbital bone or falx cerebrum. It may also be reduced in areas that critical structures exist if the clinical situation allows. The uncertainty of tumor identification and image resolution and spatial accuracy should be considered when generating CTV volumes. Additional planning margins around normal structures such as the optic chiasm can be considered if there is a particular concern with respect to its tolerance to radiotherapy or if the dose to the tumor volume that is abutting that area can be reduced. It is important to know how the planning software manages overlapping structures and margins and one must develop a prescription that reflects that understanding when using inverse planning. If the tumor volumes overlap a normal structure, the dose delivered to the "hidden" structure should be evaluated and modified if necessary (Fig. 5a–d).

At the time of planning, optimization of the plan is performed by the planning system under the planner's guidelines. Overall, smaller the multi-leaf collimator (MLC) leaves, i. e. 5 mm vs 10 mm may provide better conformality. Zinkin et al. identified a dosimetric benefit with the use of a smaller aperture for MIMIC based IMRT [32]. A number of reports have suggested different techniques for beam angle choice, in general, there are five to nine different beam entry points which are chosen either by the planner or by a computer algorithm [33, 35]. The beams eye view (BEV) and three-dimensional reconstruction are useful in development of optimal IMRT plans because one can identify critical structures in the path and optimize the plan by possibly avoiding entry through these organs. When entering prescriptions, normal tissue dose limitations and positional uncertainty have to be realistic but also should be at the level where appropriate conformality is achieved. The treating physician has to be prepared to determine where radiation dose can be pushed and where dose should be limited at all costs.

Because of the inherent inhomogeneity that is seen in IMRT planning in comparison to conventional 3D planning, the concept of the simultaneous integrated boost (SIB) or concomitant boost technique has been developed [36–38]. With this strategy the relative inhomogeneity can be used to one's advantage by creating a GTV, which could potentially benefit from a higher dose per fraction per day and a second area (for example the CTV with a high-grade glioma) for which a lower daily dose is prescribed. In doing so, the GTV may receive up to 2 – 2.2 Gy per day whereas the CTV could receive 1.6 – 1.8 Gy per day that would theoretically improve the biologic effect where the tumor density is highest.

Additional artificial avoidance structures may be drawn during the planning to facilitate sparing of certain critical structures such as the oral or nasal cavity when treating skull base or posterior fossa tumors. The planning system will then be forced to push the extra dose in another direction that may have less morbidity. Once a plan has been generated, final optimization can take place by manually adjusting the MLC leaves to cover critical structures at selected beam angles to "fine tune" the plan. This technique currently is not available with MIMIC based treatment systems.

In all cases, careful dose volume histogram (DVH) analysis as well as evaluation of the isodose lines with respect to the normal regions of interest should take place. At this time, the risk/benefit ratio between tumor control and normal tissue toxicity is considered. Further adjustments by adjusting the planning parameters or reconsideration of the plan objectives may be required. The isodose lines should be evaluated in all planes, including the reconstructed sagittal and coronal planes, to determine the distribution of dose. The areas of high dose and dose inhomogeneity in both the normal and target tissues should be evaluated and manipulated if the "hot spots" are in the tumor but close to critical structures. The DVHs should be evaluated with the absolute volume of the structure kept in mind as well as the relative amount, if the entire structure has not been outlined, then the percent volume is of less importance.

Pre-treatment verification films and weekly orthogonal port films are taken to ensure appropriate patient positioning. If the patient port films are not within 5 mm of the digital reconstructed radiographs (DRR) from the planning system, then a fluoroscopic simulation may be indicated to verify all parameters to duplicate the planned geometry. Radiation therapists may use electronic portal imaging (EPID) systems for daily set up verification by use of internal bony landmarks and DRRs. External fiducials placed on the patient or the immobilization devices can be used for real time patient position verification for robotic treatment delivery systems where the external markers are tracked. This system may be useful for single fraction or hypofractionated treatments where intra-fraction or internal motion is noted and where treatment times may be prolonged. In general, with conventional fractionation for cranial IMRT this feature does not usually add much benefit at this time.

Normal tissue tolerance is multi-factorial but volume and dose are highly correlated with toxicity outcomes. The absolute maximal dose as well as volume of tissue receiving the specified dose should be considered in the overall clinical plan [39–44]. For temporal lobe necrosis, for example, a variety of other factors may also contribute to outcomes. Santoni et al.reported that radiation dose, volume of normal brain, age and sex of the patient and the number of surgical procedures were independently related to temporal lobe necrosis [45]. There is a complex interaction of many biologic and physical factors that are not completely understood, but in general

conservative doses are suggested in particular if the patient is expected to have a long life expectancy. Table 2 summarizes the experience of several centers with a variety of normal tissues and our institutional guidelines. Concern has been voiced regarding the potential toxicity to other critical neuro-vascular structures such as the carotid artery or nerves within the cavernous sinus. There has been a long history of treatment of small volumes of vascular structures with high doses of single fraction radiation with stereotactic radiosurgery (SRS). At this time, there does not appear to be convincing evidence of specific toxicities related to this type of treatment. With fractionated radiotherapy, the biologic dose may have less chance for morbidity; however, the volume of the structure will generally be larger. Again, there have been no specific concerns noted, except, in some patients, such as patients with connective tissue disorders, ataxia telangectasia or neurofibromatosis, who may be at higher risk for vascular changes. In general, dose to such structures are evaluated and an effort is made to reduce dose if there is a particular concern or risk factors that are identified.

5.7 Clinical Experience and Trials

There have been many reports of dose comparisons between IMRT plans and other planning strategies including stereotactic radiotherapy, proton radiotherapy and conventional radiotherapy. Overall, each system has both advantages and disadvantages. IMRT planning has generally been able to deliver conformal treatment to complex shapes with low doses to surrounding normal tissues [4, 46–51]. Most studies have identified a benefit of IMRT to conventional conformal radiotherapy. IMRT allows the possibility of the delivery of higher dose of radiation to radioresistant tumors that are in close relationship to normal tissues [52,53]. IMRT has been found to be feasible and advantageous by delivering a higher radiation dose to the GTV with the same dose to normal surrounding tissue in these studies. Pirzkall et al. reported that the use of IMRT increased target coverage an average of 36% and conformality by 10%. Where dose escalation was a goal, IMRT increased the mean dose by 4 – 6 Gy and target coverage by 19% with the same degree of conformality [47]. The combination of stereotactic tools with IMRT may provide further benefit by the ability to decrease PTV and maintain conformality as shown by Fuss et al. In this study, eight patients with small vestibular schwannomas were treated with a fractionated stereotactic IMRT strategy. The PTV was reduced to 2 mm, and the median conformality and homogeneity indices were 1.69 and 1.12, respectively. Short-term follow up has indicated excellent outcome thus far [54]. Voynov et al. reported their experience with ten patients who have recurrent high-grade glioma (median volume 35 cc) who were treated with fractionated stereotactic IMRT with a median dose of 30 Gy in 5-Gy fractions. The median overall survival in this group was ten months, which is comparable to other studies with aggressive re-irradiation (SRS or brachytherapy) for recurrent malignant brain tumors [55]. IMRT technology is also being applied to SRS treatments [46, 56, 57].

Several groups have reported their experience with the SIB approach for high-grade glioma and it has been found to be feasible and safe [37, 48]. There appears to be a reduction in dose to the surrounding brain and

Table 2. Summary of selected modern neurotoxicity publications and our current institutional guidelines, which can be modified depending on the clinical situation

Organ	Toxicity	Other factors	References	Guidelines
Optic chiasm	VF & VA changes	Mean > 55, max > 59, DM, age, HTN	[41, 43, 63]	Max ≤ 54 Gy, + factors mean ≤ 45 – 50 Gy
Optic nerves	< 20/100 VA	Age, fraction size	[41, 43, 63]	Max ≤ 60 Gy, mean ≤ 54 Gy
Pituitary gland	Endocrinopathies	Min dose > 50	[40]	45 Gy
Hypothalamus	Endocrinopathies	Max dose 50 Gy	[40]	45 Gy
Temporal lobe	Necrosis	Volume > 66 Gy Gender, age, surgery	[45]	Max < 70 Gy; keep normal brain low
Brainstem	Brainstem/CN RTOG tox 1–5	Volume > 55 & 60 Gy, DM, HTN, surgery	[39]	Max 54 Gy, ≤ 0.5 cc 60 Gy
Spinal cord	RTOG/EORTC Grade 3	Surgery, fraction size, length of cord	[44]	Max point 50 – 55 Gy, mean < 45 Gy
Cochlea	SN hearing loss	Age, chemotherapy, shunt, original status	[64, 65]	Mean < 40 Gy, + factors < 36 Gy

VF: visual field, VA: visual acuity, CN: cranial nerve, RTOG: Radiation Therapy Oncology Group, tox: toxicity, EORTC: European Organization for Research and Treatment of Cancer, SN: sensorineuronal, Max: maximum, Min: minimum, DM: diabetes mellitus, HTN: hypertension

possibly better sparing of normal tissues. The potential benefit of this was might allow hypofractionation and overall shorter time for treatment for patients who have a limited life span. Sultanem et al. reported their experience with SIB technique and hypofractionation in which 3 Gy per day was delivered to the GTV and 2 Gy per day was delivered to the PTV (GTV with 1.5 cm margin) for a final dose of 60 Gy to the GTV and 40 Gy to the PTV. In this group of 25 patients with newly diagnosed glioblastoma, the treatment was tolerated well with no unexpected toxicity and survival outcomes were comparable to other techniques. The added benefit was the reduction of the overall treatment duration by two weeks [58].

Huang et al. noted reduction of toxicity where IMRT planning was used to decrease cochlear radiation dose in children receiving cisplatinum-based chemotherapy in conjunction with radiotherapy for medulloblastoma. In this study follow up audiograms documented less hearing loss and the ability to deliver more cisplatinum in children treated with IMRT with no difference in tumor control or overall survival [59].

Overall, it appears the reported literature supports the feasibility and safety of IMRT for CNS tumor indications. The clinical benefit should emerge over time as the reduction of normal tissue toxicity and maintenance of tumor control is confirmed with clinical follow up. In patients requiring high doses of radiation, such as chordomas and chondrosarcomas, the clinical benefit may be noted as experience increases with these rare tumors [60].

Our group at M. D. Anderson Cancer Center reported on 15 consecutive patients with metastatic spinal disease who underwent 75 treatments involving 90 isocenter setups on a Phase I clinical trial involving intensity-modulated, computed tomographic image-guided SBRT. Patients uniformly received 30 Gy in five fractions, while constraining the spinal cord to a maximum dose of 10 Gy. The procedure was technically feasible to perform in all patients and no neurologic toxicity was observed in any patient with a median follow-up time of nine months (range 6–16). Axial CT scans taken immediately after each treatment without moving the patient from the treatment position showed that the positional setup error was within 1 mm of planning isocenter (Fig. 6) [61].

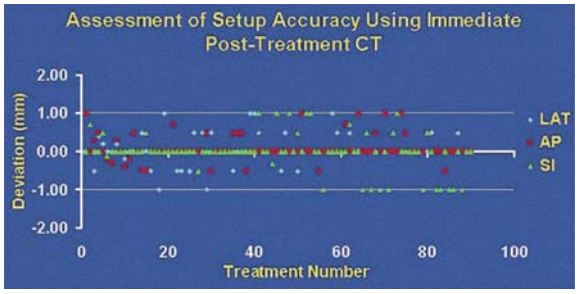

Fig. 6. The set up accuracy for hypofractionated spinal IMRT in 15 patients with 75 set up verification CT scans. Overall less than 1 mm corrections were required in any one direction with current immobilization techniques.

5.8 Future Directions

Clinical experience and longer term follow up with patients treated with IMRT for CNS tumors are increasing. At this time, there does not appear to be a documented disadvantage to the use of IMRT to intracranial and spinal tumors where patients could benefit from dose limitation to normal structures. The area of dose escalation or hypofractionation has not been explored significantly; however, at this time with the increased use of systemic agents with possible neurotoxicity, this direction may be limited. Improvement in diagnostic imaging, for anatomic, functional and biologic information will improve the delineation of target and normal tissue and could improve the therapeutic index. Biologic modeling to help predict the presence of tumor cells as well as the risk of normal tissue toxicity would be helpful to help quantify the risk and benefits of treatment. Constant quality assurance and impeccable radiation delivery is extremely important as efforts carry on to reduce the amount of radiated tissue.

The American Society for Therapeutic Radiology and Oncology, and American College of Radiology practice guideline [62] define SBRT as a "newly emerging radiotherapy treatment method to deliver a high dose of radiation to the target, utilizing either a single dose or small number of fractions with a high degree of precision within the body." Since SBRT uses either a hypofractionated regimen or a single fraction, there is little to no opportunity to adjust or correct for errors once treatment has been initiated. Thus, at its inception, and during the formative years of our SBRT program at M. D. Anderson. It is our philosophy that with any new procedure, there is a learning curve that must be climbed for all members of the team. It is our opinion that single fraction SBRT should be deferred until the entire team has demonstrated confidence in the entire procedure through experience, and clinical outcomes data demonstrating safety of hypofractionated SBRT to the spine.

References

1. Walker MD, Strike TA, Sheline GE (1979) An analysis of dose-effect relationship in the radiotherapy of malignant gliomas. Int J Radiat Oncol Biol Phys 5:1725–1731
2. Karim AB, Maat B, Hatlevoll R et al. (1996) A randomized trial on dose-response in radiation therapy of low-grade cerebral glioma: European Organization for Research and Treatment

of Cancer (EORTC) Study 22844. Int J Radiat Oncol Biol Phys 36:549–556
3. Shaw E, Arusell R, Scheithauer B et al. (2002) Prospective randomized trial of low- versus high-dose radiation therapy in adults with supratentorial low-grade glioma: initial report of a North Central Cancer Treatment Group/Radiation Therapy Oncology Group/Eastern Cooperative Oncology Group study. J Clin Oncol 20:2267–2276
4. Khoo VS, Oldham M, Adams EJ et al. (1999) Comparison of intensity-modulated tomotherapy with stereotactically guided conformal radiotherapy for brain tumors. Int J Radiat Oncol Biol Phys 45:415–425
5. Alexander E III, Kooy HM, van Herk M et al. (1995) Magnetic resonance image-directed stereotactic neurosurgery: use of image fusion with computerized tomography to enhance spatial accuracy. J Neurosurg 83:271–276
6. Borden JA, Tsai JS, Mahajan A (2002) Effect of subpixel magnetic resonance imaging shifts on radiosurgical dosimetry for vestibular schwannoma. J Neurosurg 97:445–449
7. Chu JC, Ni B, Kriz R et al. (2000) Applications of simulator computed tomography number for photon dose calculations during radiotherapy treatment planning. Radiother Oncol 55:65–73
8. Pirzkall A, Li X, Oh J et al. (2004) 3D MRSI for resected high-grade gliomas before RT: tumor extent according to metabolic activity in relation to MRI. Int J Radiat Oncol Biol Phys 59:126–137
9. Pirzkall A, Nelson SJ, McKnight TR et al. (2002) Metabolic imaging of low-grade gliomas with three-dimensional magnetic resonance spectroscopy. Int J Radiat Oncol Biol Phys 53:1254–1264
10. Price SJ, Burnet NG, Donovan T et al. (2003) Diffusion tensor imaging of brain tumours at 3T: a potential tool for assessing white matter tract invasion? Clin Radiol 58:455–462
11. Pirotte B, Goldman S, Massager N et al. (2004) Combined use of 18F-fluorodeoxyglucose and 11C-methionine in 45 positron emission tomography-guided stereotactic brain biopsies. J Neurosurg 101:476–483
12. Kracht LW, Miletic H, Busch S et al. (2004) Delineation of brain tumor extent with [11C]L-methionine positron emission tomography: local comparison with stereotactic histopathology. Clin Cancer Res 10:7163–7170
13. Miralbell R, Linggood RM, de la Monte S et al. (1992) The role of radiotherapy in the treatment of subtotally resected benign meningiomas. J Neurooncol 13:157–164
14. Wenkel E, Thornton AF, Finkelstein D et al. (2000) Benign meningioma: partially resected, biopsied, and recurrent intracranial tumors treated with combined proton and photon radiotherapy. Int J Radiat Oncol Biol Phys 48:1363–1370
15. Varlotto JM, Shrieve DC, Alexander E III et al. (1996) Fractionated stereotactic radiotherapy for the treatment of acoustic neuromas: preliminary results. Int J Radiat Oncol Biol Phys 36:141–145
16. Darrouzet V, Maire JP, Guerin J et al. (2000) Fractionated radiation therapy long-term effectiveness in the treatment of cerebello-pontine angle schwannomas: 12 years of experience in 30 cases. Ann Otolaryngol Chir Cervicofac 117: 267–273
17. Becker G, Kocher M, Kortmann RD et al. (2002) Radiation therapy in the multimodal treatment approach of pituitary adenoma. Strahlenther Onkol 178:173–186
18. Tsang RW, Brierley JD, Panzarella T et al. (1996) Role of radiation therapy in clinical hormonally-active pituitary adenomas. Radiother Oncol 41:45–53
19. Sasaki R, Murakami M, Okamoto Y et al. (2000) The efficacy of conventional radiation therapy in the management of pituitary adenoma. Int J Radiat Oncol Biol Phys 47:1337–1345
20. Abayomi OK (2002) Pathogenesis of cognitive decline following therapeutic irradiation for head and neck tumors. Acta Oncol 41:346–351
21. Coughlin C, Scott C, Langer C et al. (2000) Phase II, two-arm RTOG trial (94–11) of bischloroethyl-nitrosourea plus accelerated hyperfractionated radiotherapy (64.0 or 70.4 Gy) based on tumor volume (>20 or = 20 cm^2, respectively) in the treatment of newly-diagnosed radiosurgery-ineligible glioblastoma multiforme patients. Int J Radiat Oncol Biol Phys 48: 1351–1358
22. Souhami L, Seiferheld W, Brachman D et al. (2004) Randomized comparison of stereotactic radiosurgery followed by conventional radiotherapy with carmustine to conventional radiotherapy with carmustine for patients with glioblastoma multiforme: report of Radiation Therapy Oncology Group 93–05 protocol. Int J Radiat Oncol Biol Phys 60:853–860
23. Igaki H, Tokuuye K, Okumura T et al. (2004) Clinical results of proton beam therapy for skull base chordoma. Int J Radiat Oncol Biol Phys 60:1120–1126
24. Terahara A, Niemierko A, Goitein M et al. (1999) Analysis of the relationship between tumor dose inhomogeneity and local control in patients with skull base chordoma. Int J Radiat Oncol Biol Phys 45:351–358
25. Tsai JS, Engler MJ, Ling MN et al. (1999) A non-invasive immobilization system and related quality assurance for dynamic intensity modulated radiation therapy of intracranial and head and neck disease. Int J Radiat Oncol Biol Phys 43:455–467
26. Gilbeau L, Octave-Prignot M, Loncol T et al. (2001) Comparison of setup accuracy of three different thermoplastic masks for the treatment of brain and head and neck tumors. Radiother Oncol 58:155–162
27. Salter BJ, Fuss M, Vollmer DG et al. (2001) The TALON removable head frame system for stereotactic radiosurgery/radiotherapy: measurement of the repositioning accuracy. Int J Radiat Oncol Biol Phys 51:555–562
28. Saw CB, Yakoob R, Enke CA et al. (2001) Immobilization devices for intensity-modulated radiation therapy (IMRT). Med Dosim 26:71–77
29. Leybovich LB, Sethi A, Dogan N et al. (2002) An immobilization and localization technique for SRT and IMRT of intracranial tumors. J Appl Clin Med Phys 2002;3:317–322
30. Parker BC, Shiu AS, Maor MH et al. (2002) *PTV* margin determination in conformal SRT of intracranial lesions. J Appl Clin Med Phys 3:176–189
31. Shiu AS, Chang EL, Ye JS et al. (2003) Near simultaneous computed tomography image-guided stereotactic spinal radiotherapy: an emerging paradigm for achieving true stereotaxy. Int J Radiat Oncol Biol Phys 57:605–613
32. Zinkin HD, Rivard MJ, Mignano JE et al. (2004) Analysis of dose conformity and normal-tissue sparing using two different IMRT prescription methodologies for irregularly shaped CNS lesions irradiated with the Beak and 1-cm MIMiC collimators. Int J Radiat Oncol Biol Phys 59:285–292
33. Li Y, Yao J, Yao D (2004) Automatic beam angle selection in IMRT planning using genetic algorithm. Phys Med Biol 49:1915–1932
34. Djajaputra D, Wu Q, Wu Y et al. (2003) Algorithm and performance of a clinical IMRT beam-angle optimization system. Phys Med Biol 48:3191–3212
35. Pugachev A, Xing L (2001) Computer-assisted selection of coplanar beam orientations in intensity-modulated radiation therapy. Phys Med Biol 46:2467–2476

36. Wu Q, Manning M, Schmidt-Ullrich R et al. (2000) The potential for sparing of parotids and escalation of biologically effective dose with intensity-modulated radiation treatments of head and neck cancers: a treatment design study. Int J Radiat Oncol Biol Phys 46:195–205
37. Suzuki M, Nakamatsu K, Kanamori S et al. (2003) Feasibility study of the simultaneous integrated boost (SIB) method for malignant gliomas using intensity-modulated radiotherapy (IMRT). Jpn J Clin Oncol 33:271–277
38. Chan MF, Schupak K, Burman C et al. (2003) Comparison of intensity-modulated radiotherapy with three-dimensional conformal radiation therapy planning for glioblastoma multiforme. Med Dosim 28:261–265
39. Debus J, Hug EB, Liebsch NJ et al. (1997) Brainstem tolerance to conformal radiotherapy of skull base tumors. Int J Radiat Oncol Biol Phys 39:967–975
40. Pai HH, Thornton A, Katznelson L et al. (2001) Hypothalamic/pituitary function following high- dose conformal radiotherapy to the base of skull: demonstration of a dose-effect relationship using dose- volume histogram analysis. Int J Radiat Oncol Biol Phys 49:1079–1092
41. Martel MK, Sandler HM, Cornblath WT et al. (1997) Dose-volume complication analysis for visual pathway structures of patients with advanced paranasal sinus tumors. Int J Radiat Oncol Biol Phys 38:273–284
42. Grill J, Couanet D, Cappelli C et al. (1999) Radiation-induced cerebral vasculopathy in children with neurofibromatosis and optic pathway glioma. Ann Neurol 45:393–396
43. Habrand IL, Austin-Seymour M, Birnbaum S et al. (1989) Neurovisual outcome following proton radiation therapy. Int J Radiat Oncol Biol Phys 16:1601–1606
44. Marucci L, Niemierko A, Liebsch NJ et al. (2004) Spinal cord tolerance to high-dose fractionated 3D conformal proton-photon irradiation as evaluated by equivalent uniform dose and dose volume histogram analysis. Int J Radiat Oncol Biol Phys 59:551–555
45. Santoni R, Liebsch N, Finkelstein DM et al. (1998) Temporal lobe (TL) damage following surgery and high-dose photon and proton irradiation in 96 patients affected by chordomas and chondrosarcomas of the base of the skull. Int J Radiat Oncol Biol Phys 41:59–68
46. Sankaranarayanan V, Ganesan S, Oommen S et al. (2003) Study on dosimetric parameters for stereotactic radiosurgery and intensity-modulated radiotherapy. Med Dosim 28:85–90
47. Pirzkall A, Carol M, Lohr F et al. (2000) Comparison of intensity-modulated radiotherapy with conventional conformal radiotherapy for complex-shaped tumors. Int J Radiat Oncol Biol Phys 48:1371–1380
48. Thilmann C, Zabel A, Grosser KH et al. (2001) Intensity-modulated radiotherapy with an integrated boost to the macroscopic tumor volume in the treatment of high-grade gliomas. Int J Cancer 96:341–349
49. Baumert BG, Norton IA, Davis JB (2003) Intensity-modulated stereotactic radiotherapy vs. stereotactic conformal radiotherapy for the treatment of meningioma located predominantly in the skull base. Int J Radiat Oncol Biol Phys 57:580–592
50. Cardinale RM, Benedict SH, Wu Q et al. (1998) A comparison of three stereotactic radiotherapy techniques; ARCS vs. noncoplanar fixed fields vs. intensity modulation. Int J Radiat Oncol Biol Phys 42:431–436
51. Breen SL, Kehagioglou P, Usher C et al. (2004) A comparison of conventional, conformal and intensity-modulated coplanar radiotherapy plans for posterior fossa treatment. Br J Radiol 77:768–774
52. Pirzkall A, Debus J, Haering P et al. (2003) Intensity modulated radiotherapy (IMRT) for recurrent, residual, or untreated skull-base meningiomas: preliminary clinical experience. Int J Radiat Oncol Biol Phys 55:362–372
53. Uy NW, Woo SY, Teh BS et al. (2002) Intensity-modulated radiation therapy (IMRT) for meningioma. Int J Radiat Oncol Biol Phys 53:1265–1270
54. Fuss M, Salter BJ, Sadeghi A et al. (2002) Fractionated stereotactic intensity-modulated radiotherapy (FS-IMRT) for small acoustic neuromas. Med Dosim 27:147–154
55. Voynov G, Kaufman S, Hong T et al. (2002) Treatment of recurrent malignant gliomas with stereotactic intensity modulated radiation therapy. Am J Clin Oncol 25:606–611
56. Benedict SH, Cardinale RM, Wu Q et al. (2001) Intensity-modulated stereotactic radiosurgery using dynamic micro-multileaf collimation. Int J Radiat Oncol Biol Phys 50: 751–758
57. Shiu A, Parker B, Ye JS et al. (2003) An integrated treatment delivery system for CSRS and CSRT and clinical applications. J Appl Clin Med Phys 4:261–273
58. Sultanem K, Patrocinio H, Lambert C et al. (2004) The use of hypofractionated intensity- modulated irradiation in the treatment of glioblastoma multiforme: preliminary results of a prospective trial. Int J Radiat Oncol Biol Phys 58:247–252
59. Huang E, Teh BS, Strother DR et al. (2002) Intensity-modulated radiation therapy for pediatric medulloblastoma: early report on the reduction of ototoxicity. Int J Radiat Oncol Biol Phys 52:599–605
60. Thilmann C, Schulz-Ertner D, Zabel A et al. (2002) Intensity-modulated radiotherapy of sacral chordoma – a case report and a comparison with stereotactic conformal radiotherapy. Acta Oncol 41:395–399
61. Chang EL, Shiu AS, Lii MF et al. (2004) Phase I clinical evaluation of near-simultaneous computed tomographic image-guided stereotactic body radiotherapy for spinal metastases. Int J Radiat Oncol Biol Phys 59:1288–1294
62. Potters L, Steinberg M, Rose C et al. (2004) American Society for Therapeutic Radiology and Oncology and American College of Radiology practice guideline for the performance of stereotactic body radiation therapy. Int J Radiat Oncol Biol Phys 60:1026–1032
63. Parsons JT, Bova FJ, Fitzgerald CR et al. (1994) Radiation optic neuropathy after megavoltage external-beam irradiation: analysis of time-dose factors. Int J Radiat Oncol Biol Phys 30:755–763
64. Honore HB, Bentzen SM, Moller K et al. (2002) Sensori-neural hearing loss after radiotherapy for nasopharyngeal carcinoma: individualized risk estimation. Radiother Oncol 65:9–16
65. Merchant TE, Gould CJ, Xiong X et al. (2004) Early neuro-otologic effects of three-dimensional irradiation in children with primary brain tumors. Int J Radiat Oncol Biol Phys 58:1194–1207

IMRT Lung

Kenneth E. Rosenzweig

6

Contents

6.1 Introduction

Lung cancer remains one of the most common cancers in the United States and the most common cause of cancer death. Approximately 174,000 people are diagnosed with lung cancer annually with approximately 160,000 deaths per year [1, 2]. There are more female deaths from lung cancer than breast, ovarian, and cervical cancers combined. Despite some progress with the use of chemotherapy [3–5], radiation therapy (RT) remains the main curative modality for inoperable non-small cell lung cancer (NSCLC). However, the treatment of lung cancer with RT is one of the most technically challenging procedures in radiation oncology, with five-year survival rates ranging from 5–10% and median survival approximately ten months [6–8]. In patients receiving 65 Gy without chemotherapy, only 15% are disease free one year after treatment when assessed by bronchoscopy [3].

Previous studies have demonstrated the value of dose-escalation in radiation therapy. Protocol 73–01 of the Radiation Therapy Oncology Group (RTOG) reported a decrease in in-field local failure as dose increased from 40 to 60 Gy [6]. Armstrong et al. have shown that three-dimensional conformal RT (3D-CRT) provides improved tumor coverage while decreasing the dose to the ipsilateral and contralateral lung [9]. At the University of Michigan 3D-CRT has been used to deliver localized doses as high as 102.9 Gy to small solitary lung tumors [10]. RTOG 93–11 is currently treating small lesions to 90.3 Gy and intermediate sized tumors to 77.4 Gy [11]. A Phase I dose-escalation trial at MSKCC found the maximum tolerated dose (MTD) of 3D-CRT for NSCLC to be 84 Gy, regardless of tumor size [12].

The focus of this chapter is to explore the feasibility of further dose escalation for NSCLC via the use of intensity modulated radiation therapy (IMRT) and other advanced RT techniques. Patients with newly diagnosed stage T1–4, N0–3, M0 and recurrent NSCLC are most suitable for IMRT dose escalation. Generally, there are three patient populations referred for definitive thoracic RT:

1. Early stage (T1–2 N0) lung tumors. This subgroup is expected to increase significantly due to the renewed popularity and efficacy of early lung cancer screening [13]. Although surgical resection is the standard of care for these patients, for those who are inoperable due to medical co-morbidities RT is the main curative treatment option.
2. Locally advanced disease (T3–4 N0, T1–4 N1–3) receiving sequential chemotherapy and RT. These patients frequently receive induction chemotherapy in the hopes of undergoing surgical resection. However, if they remain unresectable then RT is the standard of care. RT is also used for patients in this category unable to tolerate concurrent chemotherapy/RT.
3. Locally advanced disease receiving concurrent chemotherapy and RT. Recent studies [4, 14] show that for unresectable patients, concurrent chemotherapy/RT has improved outcome as compared to sequential chemotherapy/RT.

Escalation to higher doses with conventional RT, and even with 3D-CRT, is often impossible because radiation pneumonitis becomes a serious treatment complication when mean lung doses exceed 20 Gy [15, 16]. For patients receiving concurrent chemotherapy esophagitis may also occur at organ doses as low as 50–60 Gy [4]. Spinal cord dose must also be limited to less than 50 Gy.

If IMRT is to be successful in improving the RT of NSCLC, it must be used in conjunction with other emerging technologies to address not only these problems of dose escalation, but also those of geographic miss caused by poor initial identification of the gross target volume (GTV) and errors caused by respiratory motion. The integration of Positron Emission Tomography (PET) scanning using the tracer FDG (^{18}F-2-Fluoro-2-deoxy-d-glucose) and CT simulation, for example, has recently emerged as a useful tool to augment tumor detection and treatment planning. The extent of many lung tumors is not fully visible on CT scans, and inadequate delineation of the GTV contributes to geographic miss, which limits the success of RT. Using surgery as the gold standard, FDG-PET imaging has been shown to have a higher sensitivity, specificity, and accuracy than CT (76–92% sensitivity for PET vs 56–75% for CT; 81–100% specificity for PET vs 73–87% for CT; and 80–100% accuracy for PET vs 77–82% for CT) [17–20].

Respiratory motion is another serious source of error for RT of NSCLC in many patients, and the integration of other technologies such as respiratory gated radiotherapy and electronic portal imaging systems (EPID) for verification of patient set-up and IMRT beam delivery are important components of IMRT for the lung [21–23].

To summarize, the limited success in local control of NSCLC with RT stems primarily from two factors:

1. Inability to escalate to tumoricidal doses because of limits imposed by normal tissue complications.
2. Geographic miss of tumor caused by the limited sensitivity and accuracy of CT for initial tumor definition, plus errors in treatment delivery caused by respiratory motion.

The first factor can potentially be mitigated via IMRT, which enables the delivery of higher tumor doses, conformed to the tumor geometry, with a concomitant reduction in the volume of normal tissues irradiated (particularly the lung itself, but for patients receiving RT + chemotherapy, also esophagus). Errors of the second nature may be reduced via the incorporation of improved imaging modalities (such as FDG-PET), and control of respiratory motion during both imaging scans and radiation therapy delivery. These issues are the focus of this chapter. Specifically, approaches for each of the following will be discussed:

1. Inverse treatment planning (ITP) and IMRT for delivery of improved dose distributions.
2. Respiratory gating (RG) for IMRT delivery, and for CT and PET imaging studies.
3. Implementation of FDG-PET and CT image registration in RT treatment planning.
4. Application of EPIDs for improved treatment verification.

6.2 IMRT Treatment Planning for NSCLC

At MSKCC, there has been focus on the sliding window technique of IMRT which permits continuous variations in beam intensity via customized, uninterrupted motion of the individual leaf pairs of a dynamic MLC (DMLC) [24, 25]. Presented here is a brief summary with particular reference to NSCLC. Central to IMRT are the following steps:

1. Three-dimensional (3D) CT simulation, often augmented with FDG-PET images (as described in the section on PET scanning).
2. Selection of beam angles and definition of the planning target volume (PTV), normal lung, spinal cord, and esophagus from fused PET-CT images.
3. Specification of dose-volume constraints for each relevant tissue in the treatment plan. Typically, fraction of functional lung units damaged (fdam) less than 0.28 or mean lung dose less than 20 Gy, maximum spinal cord less than 50 Gy, and for patients receiving concurrent chemotherapy esophageal dose less than 40 Gy.
4. Definition of an objective function (OF), or mathematical expression quantifying the differences between the planners' specified dose-volume constraints and the computed dose distribution, with the goal of the ITP process being to minimize the numerical value of the OF.
5. Computer controlled linear accelerator (or linac) and MLC for delivery of IMRT, plus respiratory gating system for beam delivery.
6. Treatment verification using EPID.

Different types of NSCLC tumors may require different strategies for treatment plan optimization and beam delivery. Small Stage I tumors, for example, may prove relatively simple to treat, especially for tumors in the periphery of the lung. For these tumors the field sizes may be small enough to permit meeting normal tissue dose-volume tolerances with only minimal intensity modulation. Respiratory gating for these patients may also be less beneficial than it might be for larger tumors. Stage II and III tumors present greater challenges because larger treatment volumes usually result in higher lung toxicity. Similarly, patients receiving concurrent chemotherapy present the additional challenge of including esophageal toxicity as a dose-volume constraint, plus the added complication of both lung and esophageal motion within the respiratory cycle. It is expected that RG and IMRT will be particularly beneficial to this group of patients.

A key aspect of safe dose-escalation often incorporates one or another of various biological indices for estimating lung toxicity such as fdam, effective volume (V_{eff}), normal tissue complication probability (NTCP), or mean lung dose [26, 27]. At MSKCC the f_{dam} model is

Table 1. Comparison of 3DCRT and IMRT plans

Case	PTV (cc)	Lung (cc)	Maximum dose I MRT 3DCRT	IMRT	IMRT gain (Gy)
1	462	2500	62	80	18
2	311	3500	66	76	10
3	556	1940	80	86	6
4	490	3730	88	88	0
5	312	2280	64	88	24
6	229	3110	80	98	18
Average	393	2843	73.3	86.0	13

used, which is based on the assumption that lung functions as a 'parallel' tissue with radiation pneumonitis being correlated with the *fraction* of lung volume subject to radiation damage rather than the mean or integral dose (although they are obviously correlated).

Patients are simulated and treated in the supine position, hands over head, immobilized via custom alpha cradle body molds. Consecutive CT images with 3 mm slice thickness are obtained from the larynx to L2 to encompass the entire thoracic cavity. Currently patients for whom respiratory gated RT is deemed beneficial are scanned with slightly larger slice thickness of 4–5 mm in order to reduce total scanning times, although improved CT gating techniques are expected to reduce the slice thickness back to 3 mm in the near future (see section on respiratory gating).

The physician identifies and outlines the GTV on the scans. The PTV is defined by a physician-specified margin of approximately 10–15 mm beyond the GTV to allow for microscopic tumor extension, treatment set-up errors, organ motion, and other uncertainties. Tumors probably extend microscopically 6–8 mm beyond what is visible on imaging studies [28] which, we believe, justifies a 10–15 mm margin. The PTV margin for IMRT can likely be the same as that for a 3D-CRT plan, as Chui et al. report similar effects of organ motion on delivered dose for both treatment approaches [29]. There is not yet enough clinical data to determine whether or not respiratory gating will permit a reduction in field margins. In theory, this should be possible, as gating reduces the effect of tumor movement, which in turn should reduce the need to expand the PTV beyond the GTV and clinical target volume (CTV); however, without definitive clinical demonstration of this hypothesis we are currently using the conventional field margins described above, with or without respiratory gating-assisted RT.

The carina is outlined as a landmark which is useful for comparing digitally reconstructed radiographs (DRR) to portal images. The lungs, heart, esophagus, spinal cord and body surface are all contoured. Complete contouring of all normal tissues is particularly important when biological dose-response models are being used to predict treatment toxicity, as these models are based on dose-volume effects and require accurate information regarding tissue and organ volumes. Selection of beam directions is similar to conventional 3D-CRT planning and is usually made with the aid of beam's-eye view (BEV) computer display. Typically three to five coplanar treatment beams are used, occasionally with the addition of non-coplanar beams. Treatment beams are almost exclusively 6 MV photons, and dose distributions include pixel-by-pixel inhomogeneity corrections.

Treatment planning criteria are specified via dose-volume constraints, with typical constraints being a maximum spinal cord dose constraint of 50 Gy, and an f_{dam} lung constraint of 0.28. This f_{dam} constraint is not *explicitly* incorporated into the treatment planning, but is rather 'faked' by specifying dose-volume constraints for the lung, followed by a calculation of f_{dam} from the ensuing dose-volume histogram (DVH) (i. e., after the dose distribution has been calculated). If the f_{dam} constraint is not met then the planner modifies the dose-volume constraints and runs the ITP optimization again. If this fails several times then the physician must consider decreasing the prescription dose in order to meet normal tissue tolerance limits. For patients receiving concurrent chemotherapy, an esophageal dose constraint of 40–50 Gy is also incorporated into the optimization process. It should be noted that frequently it is necessary to set dose constraints lower than what is actually desired, and/or to adjust penalties and dose-volume constraints during planning optimization to achieve acceptable plans. Both PTV coverage and normal tissue doses are evaluated by examining isodose distributions and DVHs. Dose distributions are usually renormalized such that the isodose contour covering the PTV is defined to be 95%.

The advantages of ITP and IMRT for NSCLC were demonstrated in a pilot study at MSKCC of six patients previously treated with 3D-CRT who were retrospectively replanned using ITP and IMRT [30, 31]. 3D-CRT and IMRT plans were calculated using identical dose volume constraints. Comparisons were made between the maximum dose achievable using the treatment plan-

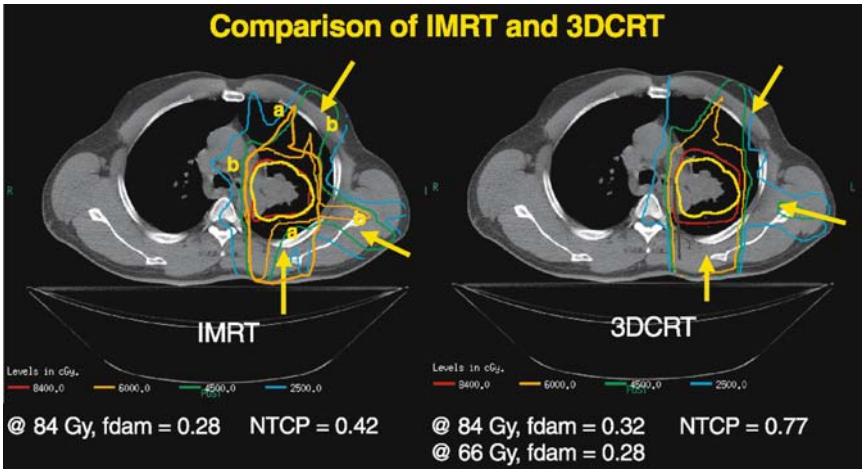

Fig. 1. Comparison between IMRT and 3DCRT using the same beam direction. The reduced f_{dam} and NTCP of the IMRT plan can be explained by a smaller beam aperture and by a superior distribution of unwanted dose in the IMRT plan. The smaller beam aperture leads to i) a tighter conformality of the 84 Gy isodose (*red*) with the outline of the PTV (*yellow*) and ii) a reduction of integral dose. Intensity modulation results in a different distribution of unwanted dose: less in lung (regions indicated by a); more in mediastinum, thoracic wall and subscapular soft tissue (regions indicated by b)

ner's best 3D-CRT plan (typically three to five wedged fields), and an IMRT plan using the same or similar beam orientations. For all plans the prescription dose was escalated until the biological dose constraint for lung was violated ($f_{\text{dam}} > 0.28$). For the six patients, PTV ranged from 229 to 556 cm^3, and total lung volumes from 1940 to 3,730 cm^3. The results are summarized in Table 1 and Figs. 1–3. Table 1 demonstrates that in five of six cases the prescription dose could be increased with IMRT, on average by 13 Gy. In Fig. 1a comparison between IMRT and 3D-CRT treatment plans using three coplanar beams is displayed. Note the decreased lung and spinal cord doses with almost similar PTV uniformity for the IMRT plan, which is also evident in the DVHs of Fig. 2. This reduced lung dose enabled escalation of the prescription dose for this patient to 84 Gy using IMRT, as compared to only 66 Gy using 3D-CRT (for the same f_{dam} constraint of 0.28). The capability of sparing normal lung irradiation using IMRT is more graphically illustrated in Fig. 3 where we compare the same two treatment plans in the coronal and sagittal planes. In a related study of ten patients we found that IMRT also reduced the maximum and mean dose to the esophagus by 11 and 7% respectively, with a corresponding decrease in NTCP from 41% to 19%. In a more recent comparison of RT techniques for NSCLC, Grills et al. found that in node-positive cases, IMRT reduced the lung V_{20} and mean dose by approximately 15% and lung NTCP by 30%, compared to 3D-CRT [32]. A study by Liu et al. compared the ability of IMRT to reduce the irradiated volumes of normal lung and critical structures to that of 3D-CRT. Ten distinct cases of NSCLC were chosen to represent a range of common disease presentations. 3D-CRT plans were designed based on the patients' prior 3D-CRT treatments, prescribed to cover 95% of the PTV with 63 Gy in 35 fractions, using 4 beams. IMRT plans were designed using ITP, with the goals of delivering a minimum of 90% and a maximum of 120% of the prescribed dose to the PTV and to minimize the V_{10} and V_{20} of normal lung, the V_{45} of esophagus and to keep dose to spinal cord < 45 Gy. Most of the beam configurations involved nine 6-MV coplanar beams. They found statistically significant differences in the V_{20}, V_{30}, V_{eff} and MLD between the two

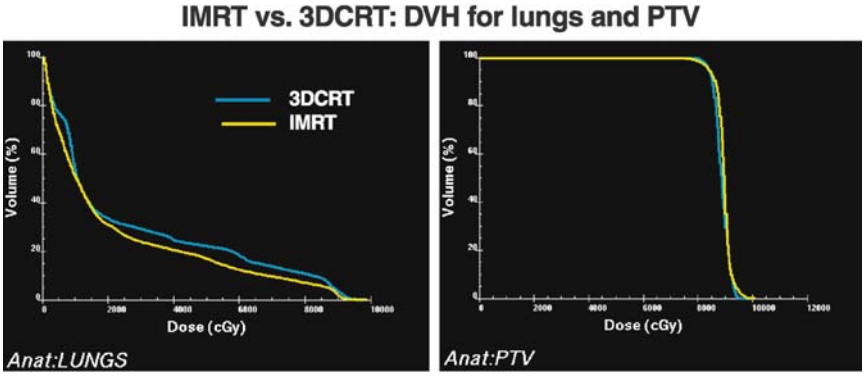

Fig. 2. DVH of lungs and PTV for the same plans as in Fig. 1. In the *left panel*, note the decreased dose to lungs in the IMRT plan. The *right panel* shows an almost equal dose homogeneity for the PTV in the IMRT plan

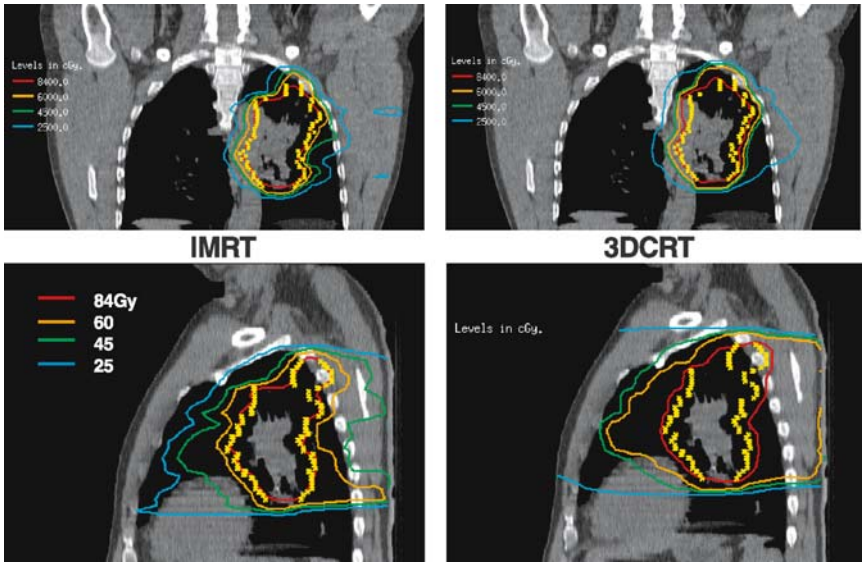

Fig. 3. Coronal (*upper panels*) and sagittal (*lower panels*) planes of the same plans as in Figs. 1 and 2; illustrating the better sparing of lung tissue in the IMRT plan. Note the shape of the 25 Gy isodose (*blue*) in the upper panels and the shape of the 25, 45 (*green*) and 60 (*orange*) Gy isodoses in the lower panels

plans, with those of the IMRT being lower. In most cases, the IMRT plans also resulted in lower V_{10} for the total lung, but a higher V_5. The benefits of lung-sparing with IMRT plans appeared more pronounced in those cases with medium to large PTVs. They also demonstrated the ability of IMRT to decrease or maintain the V_{45} of the heart and esophagus seen in the 3D-CRT plans [33].

Using the aforementioned advanced treatment planning techniques at MSKCC, the prescription dose has been escalated from conventional levels of 60–70 Gy to 81, 84, and 90 Gy for selected patients. Fractionation was initially at the conventional value of 1.8 Gy per day, but the lengthy duration of the 81 Gy treatment course resulted in patient dissatisfaction. Therefore, the daily doses were increased to 2 Gy per fraction (typically normalized to the D_{95},) to facilitate a more timely completion of treatment. Eight patients have been treated to 90 Gy, but unacceptable toxicity was observed, due in part to the poor general health of most of these patients. Maximum prescribed doses have subsequently been restricted to 84 Gy.

As with other treatment sites, the experience for NSCLC has been that IMRT treatment planning requires both the physicist and the radiation oncologist to embark on something of a new learning curve, in that treatment planning strategies are sometimes different between IMRT and 3D-CRT. In particular, the determination of suitable dose-volume constraints and penalty functions to be used as input to the optimization program will require some trial and error.

6.3 Respiratory Gating

Geographic miss is a major contributing factor in the failure of RT to control NSCLC. Most obviously, geographic miss can result from incorrect initial identification of the GTV, but also from respiration-induced tumor motion during RT beam delivery which can be 1 cm or more, and in some cases up to 2.5 cm. Numerous studies have demonstrated the importance of respiratory motion in patients with intrathoracic tumors [34–38]. Prescribing larger radiation fields can circumvent geographic miss due to respiratory motion, but this also increases toxicity, usually to unacceptable levels. Thus, control of respiratory motion during treatment may be a key factor in improving RT results. Two approaches have been proposed to reduce respiratory motion. One is coached or assisted patient breath hold such as the Active Breathing Control method [39] or deep inspiration breath hold (DIBH) [34]. The other is respiratory gated (RG) beam delivery. All of these methods have been restricted to use in a few research protocols, although RG is now commercially available and has been applied clinically at many institutions [35, 40].

All respiratory gating systems are designed to circumvent respiratory motion via correlating RT beam delivery to a specific phase within the breathing cycle rather than via increasing field margins to 'cover' the motion. The benefits of reducing the volume of normal tissues irradiated via control of respiratory motion can be as much as 30% when compared with free breathing [34]. This in turn permits an increase of prescription doses by as much as 18 Gy above conventional prescriptions for the same level of lung toxicity [37, 38].

In order to achieve maximum benefit, care must be given to the selection of the optimum phase within the respiratory cycle in which to treat, although it turns out that compromises must be made towards this end. For most patients the mean lung dose is minimized by gating at end inspiration, due to displacement of normal lung tissue outside of the high dose volume. However,

in many patients, tumor and organ position is more reproducible at expiration rather than at inspiration. Fluoroscopic images can be useful in measuring the magnitudes and directions of diaphragm and chest wall motion, to determine the optimal point in the breathing cycle for radiation treatment.

DIBH was first implemented at MSKCC in February 1998 expressly to control the respiratory motion. DIBH permits:

1. Expansion of lung volume to reduce the amount of normal lung within the treatment field.
2. Synchronization of beam delivery to a fixed phase of the breathing cycle to reduce geographic miss caused by respiratory motion.
3. Increased separation between tumor and normal tissues (in some patients).

DIBH, however, requires active participation by the patients, as many techniques require that they breathe through a spirometer and hold their breath for extended periods of time [41]. The DIBH technique used at MSKCC also required that the treatment technologist manually gate the linac X-ray beam on and off for treatment via observation of spirometer readings indicating when the patient is in the correct breathing phase. Typically one or two breath holds of 10–15 s duration are required per treatment portal with the therapist gating the linac beam off and on.

While the DIBH method is quite beneficial, it is already somewhat cumbersome to use in practice, even for conventional RT beam delivery. With the addition of IMRT, respiratory gated beam delivery using DIBH becomes even more problematic, principally because such treatments require substantially increased treatment times as compared to 3D-CRT. IMRT typically increases total beam-on time (or monitor units) by a factor of 2–3 depending on the degree of intensity modulation required. Treating patients with the combination of IMRT plus DIBH would therefore require as many as five or six breath holds per treatment field, or more than a dozen breath holds per treatment fraction. Such a requirement would be beyond the physical capacity of most NSCLC patients. Thus, even though the clinical advantages of DIBH in achieving reductions in mean lung dose as compared with free-breathing treatments have been demonstrated, DIBH is not really practical for many patients. In fact, because of their poor performance status at initial presentation, only about one-third of patients referred for definitive lung RT are capable of performing DIBH. With the addition of IMRT, this proportion would likely be even smaller.

Similarly, the use of DIBH for respiratory control of PET scanning would also create prohibitively long scanning times and would require multiple breath holds that are beyond the physical capacity of most patients. Thus, a more adaptable system for control of respiratory motion is needed. In 1999 a new commercially available RG system designated as 'real-time position management system' (RPM) (Varian Oncology Systems) was installed at MSKCC. The RPM system, shown in Fig. 4, achieves many of the clinical advantages of DIBH, but with only passive input from the patient. This is achieved via the use of an infrared camera system, which tracks a reflective marker placed on the patient's chest to monitor respiratory motion. Video images of the marker position are computer analyzed to determine when the patient is in a specific user-defined phase of the breathing cycle, at which time the computer generates a gating signal that is sent to the linac to enable RT delivery. The patient need only maintain a reasonably regular breathing pattern for the system to work reliably. The simplicity of this system increases patient comfort and accrual rates as compared with DIBH. The RPM system is also easily adaptable to CT and PET scanning, thus facilitating the acquisition of respiratory gated diagnostic and radiation therapy treatment scans [42]. This capability is crucial, because patient simulation, CT and PET scanning, treatment planning, and RT beam delivery must all be carried out using identical methods of controlling, or synchronizing with respiratory motion.

Pilot studies have established that the RPM system functions nearly as well as DIBH for synchronization of beam delivery to patient breathing cycle. Some of the lung expansion benefits of DIBH are lost with RPM, but much of this loss is regained via IMRT, which is not compatible with DIBH. Another method for recovering some of the lung expansion benefits of DIBH when using the RPM system is via patient coaching. When patients are given verbal instructions for when to inhale and exhale, they tend to inhale more deeply and breathe more consistently as compared with normal breathing. Coaching also improves the correlation between the external marker and diaphragm positions, as assessed during simulation sessions using fluoroscopic images. Upgraded versions of the RPM system include in-room video displays that provide the patients with real-time video feedback of breathing pattern to aid them in maintaining regular breathing.

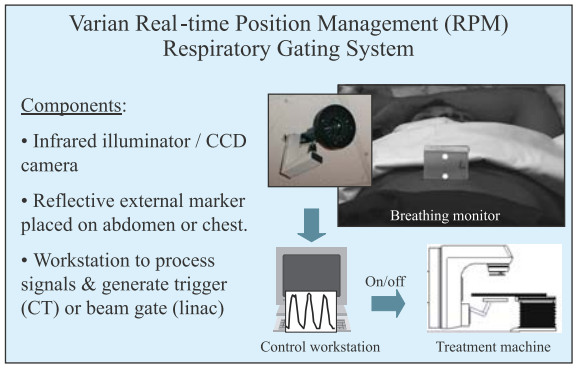

Fig. 4. A schematic illustrating the components of a commercially available respiratory gating system

Thus, even though the combination RPM plus IMRT increases the number of monitor units by a factor of 2–3 above conventional RT, and the total treatment time by a factor of 6–12, the system is well suited to patient comfort and reproducibility (Note: although respiratory gating increases the total time of treatment by a factor of 3–4 above that of IMRT alone, it does not additionally increase the total number of monitor units, as the X-ray beam is gated off when the patient is not in the desired phase of the breathing cycle). As an example, consider the delivery of a 2 Gy daily fraction of radiation at 300 MU/min, which would require approximately 300 total MU or 1.00 min total treatment time for conventional RT beam delivery. A similar treatment delivered with IMRT alone would require approximately 600–900 MU, or 2–3 min total treatment time. With the addition of respiratory gating, and assuming that beam on occurred during approximately one quarter of the total respiratory cycle this treatment would still require 600–900 monitor (i. e., the same as IMRT alone), but would require a total treatment time of approximately 8–12 min. While this is not an excessive period of time, it does raise questions about patient comfort, other types of intrafraction motion, patient immobilization techniques, and overall efficiency of resources.

These issues aside, the application of the RPM respiratory gating system to CT and PET imaging will be discussed next. A more detailed discussion of the special advantages of FDG-PET imaging for NSCLC is reserved for the next section on PET scanning.

The RPM system can be integrated with CT data acquisition in two very different modes. The first mode, which is easier both in implementation and concept is designated as *respiration-triggered CT* (RTCT). In RTCT mode, the RPM system interfaces with the CT scanner in a manner almost identical to its operation on the linear accelerator. During CT simulation the physician *pre-selects* a phase in the breathing cycle during which imaging and treatment will occur. A reflective marker, identical to that used for linear accelerator treatments, is placed on the patient's skin, and during CT scanning the RPM records the motion of the reflective marker and sends a trigger signal to the CT scanner each time the patient enters this designated phase of the breathing cycle. The trigger signal initiates the acquisition of a *single* axial CT slice, which is followed by a table advance to the next couch position, at which point the CT scanner waits for the next trigger signal. Since modern CT scanners can acquire a single axial slice in 1–2 s or less, and since a typical respiratory cycle has a period of 4–5 s, there is ample time during each trigger signal to acquire the CT data, and there is also ample time between trigger signals to translate between couch positions. However, since only one slice is acquired per respiratory cycle (assuming one has access only to a single slice CT scanner), a data set of 100 slices requires 9–10 min. Multislice CT scanners, of course, decrease the total time required for image acquisition. Nonetheless, the relatively long acquisition times can result in artifacts from patient movement due to discomfort, or an irregular breathing pattern. This can be seen in Fig. 5 which shows several different coronal CT reconstructions obtained using the RTCT techniques. The free-breathing scan shown in the leftmost panel shows artifacts (arrows) near the diaphragm resulting from respiratory motion between axial slices. An RTCT scan taken at end expiration (center panel) shows virtually no artifacts, as expected. The right panel, however, also taken using RTCT but taken at end inspiration, shows some small

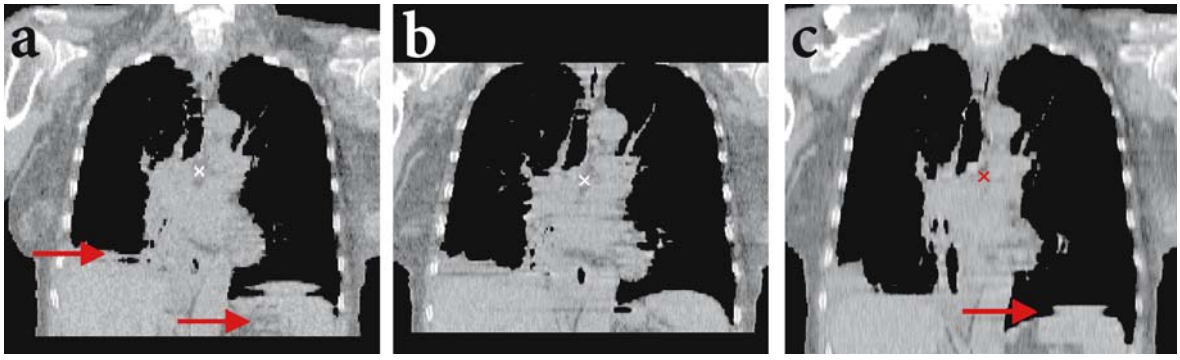

Fig. 5a–c. Elements of the Real-Time Position Management (RPM) respiratory gating system. A reflective marker placed on the patient and detected by video camera reflects infrared light from an illuminator. A computer program processes the video signals and sends on-off control signals to the accelerator. At the start of each session, the operator places the system into the tracking mode for a few breathing cycles, to allow the system to determine the minimum and maximum vertical position of the upper marker. A periodicity filter algorithm checks the frequency and regularity of the breathing waveform. Once breathing characteristics are stable, the operator places the system into a record mode, during which the waveform is recorded and displayed. There are two modes of producing gate signals, amplitude or phase. In the amplitude-based mode, dose is delivered only when the waveform is between user-settable thresholds. In the phase-based mode, the operator specifies a phase interval of the waveform calculated by the periodicity filter algorithm: (a) a free-breathing scan shows artifacts (*arrows*) near the diaphragm resulting from respiratory motion between axial slices; (b) a respiration-triggered CT-scan (RTCT) taken at end-expiration shows only small artifacts; (c) a RTCT taken at end-inspiration shows larger artifacts than the end-expiration RTCT

artifacts indicating that the RTCT system is not working perfectly.

A second limitation of the RTCT method is the need to pre-select the desired point in the respiratory phase for RTCT. This restriction precludes, for example, a quantitative assessment of the preferred phase for each particular patient, or determination of the maximum width of the respiratory window to be used for beam delivery. Some patients, for example, might be best treated at end inspiration owing to the increased lung inflation and separation between tumor and normal tissues; but for many patients we have found that position reproducibility is better at end expiration. Hence, assessment of the ideal portion of the respiratory cycle over which it is *safe* to treat (i. e., during which there is minimal respiratory motion) also cannot easily be assessed with RTCT. Another factor to be considered in using the RPM system is the fact that some patients have a tendency to lapse into irregular breathing patterns. The earlier version of the RPM system, which only measured respiratory amplitude, could not detect this. Improved software, however, now records both amplitude and phase, which does permit detection of irregular breathing patterns.

For these reasons, a more sophisticated method of gating CT scans, designated as *Respiration-correlated spiral CT* (RCCT), has been developed at MSKCC. Implementation of RCCT requires a spiral (rather than an axial) CT scanner, with the CT scanner operating in a near-normal acquisition mode. The only change to normal spiral CT scanning with the addition of RCCT is that all CT images are time-labeled to designate the phase of the respiratory cycle at which the scan was acquired. This is achieved by recording a data file of RPM readings (i. e., phase and amplitude of the reflective respiratory marker) simultaneously with CT image acquisition. In this manner, each reconstructed axial CT slice can be retrospectively labeled, and binned according to its appropriate phase within the respiratory cycle. RCCT scanning must be done using a very small couch pitch (i. e., slow couch speed during scanning) to ensure that there is an overlap between CT slices which ensures that any desired slice can be reconstructed at whatever respiratory phase one chooses. Thus, with RCCT it becomes possible to obtain a complete CT data set for *all* respiratory phases in a single spiral acquisition sequence, yielding a 4D data set. From such a 4D data set the physician can choose, after CT scanning is completed, the ideal position within the respiratory cycle for each particular patient. RCCT also enables the treatment planner to select the optimum window width for beam delivery which is a compromise between accuracy of treatment and absolute reduction of motion (i. e., narrow window width), and practicality of total treatment time (i. e., broad window width).

If PET scanning is to be used along with CT to aid in definition of the CTV, then the thoracic PET scans used for simulation must also be respiratory gated. Thoracic PET scans often require 45–60 min total scanning time, and patient motion can result in overestimation of lesion size, reduction in signal to noise ratio and reduction in specific uptake value (SUV) [Note: SUV = (decay corrected ^{18}F activity/lesion weight)/(injected activity/patient weight)]. An example of the changes in apparent PET lesion size with and without respiratory gating corrections is shown in Fig. 6. At present the RPM system cannot directly gate PET scan data acquisition. Instead, for the scans shown in Fig. 6, the RPM system was used to generate a gating signal at the start of each patient breathing cycle (as per used with the linear accelerator and CT scanner) which was retrospectively used to bin all PET events, which are already labeled with the manufacturers data acquisition software, into different time bins within the respiratory cycle. This is similar in concept to RCCT data acquisition described previously, except for the fact that at present the RPM system does not directly label PET events with an exact time signature, although modifications to the system to enable this are in progress.

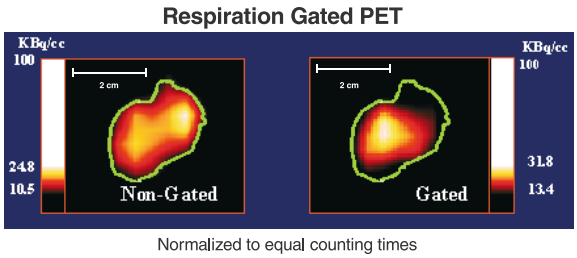

Fig. 6. Changes in apparent PET lesion size without and with respiratory gating

Nonetheless, in Fig. 6 it is evident that respiratory gating can have a significant impact on improving the accuracy of PET scanning, with reductions in the measured GTV of 20–30% as compared to standard mode. Thus, gating aids in more accurate definition of GTV and reduction in PTV size. Gating both CT and PET scans in a similar manner also facilitates more accurate fusion of image data sets.

6.4 PET Scanning

To date, radiological imaging has been largely anatomical, based on physical properties of tissue such as X-ray attenuation (CT imaging) or magnetic susceptibility (MR imaging). New imaging modalities based on the biological, metabolic, or chemical properties of tissues are beginning to provide new dimensions in tumor diagnosis [43]. At present, the most promising vis-a-vis NSCLC is FDG-PET. With the approval of FDG-PET for staging lung cancer by the Food and Drug Administration, its role in cancer detection has increased

dramatically [44], as the tracer FDG enables PET detection of increased glucose metabolism in cancer cells. Approximately 85000 lung cancer patients per year will benefit from FDG-PET [45]. PET is a valuable complement to CT scanning, which has known limitations for detecting the full extent of many lung tumors. PET often identifies involved lymph nodes not identified by CT, as shown in Fig. 7. Conversely, PET sometimes shows overdefinition of GTV by CT scan alone especially in areas of atelectasis [46]. The impact of PET images on PTV definition can be profound. Prospective and retrospective studies have shown that FDG-PET images influence the design of radiation treatments in 23–65% of all cases [17,47,48] and many patients are re-staged as a result of PET.

The use of registered PET/CT images has gained favor in recent years, having been demonstrated as a superior staging tool to visual correlation or either modality alone [49]. The addition of registered PET-CT images for treatment planning will allow more accurate definition of the GTV, thereby reducing geographic miss. A number of studies have shown that the use of registered images can result in smaller target volumes due to distinction of atelectasis from tumor, or larger volumes due to detection of lymph node metastases not seen on CT [28, 50–53]. In a small study at MSKCC, it was found that inter-observer and intra-observer variability in tumor volumes was decreased when registered PET-CT images were used rather than CT with separate PET images as a reference [54].

Despite these observations, with current technology the fusion of CT and PET images for treatment planning purposes can be problematic. PET emission scans contain only limited structural anatomy with little density information, making them difficult to correlate with CT images that are entirely density based. The PET transmission scans do contain anatomical details and are currently used to register the emission scans to CT, but even the transmission scans are of poor quality, with only bony landmarks and very low density structures being well visualized, although for lung this is often sufficient. PET-CT image registration is still in its development phases [20, 55]. Many centers still rely on manual registration techniques, wherein the user must translate and/or rotate images on a computer screen to obtain the best visual match, although automated registration is currently being developed by several groups [56,57].

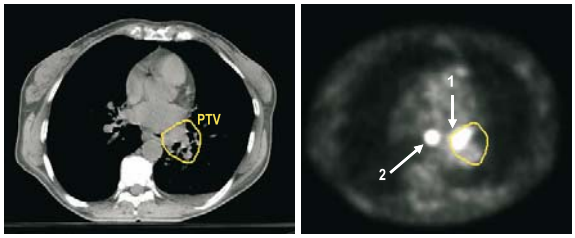

Fig. 7. *Left panel:* planning CT scan; *right panel:* FDG-PET scan. CT-defined PTV projected on PET image suggest insufficient margin (1) towards the mediastinum. Para-oesophageal lymph node not contoured using the planning CT scan exhibits high PET signal (2)

For virtually all image registration techniques the CT image is used as the reference scan. In the manual method the user contours several anatomical structures that are visible in both CT and PET image sets. These contours are observed on orthogonal image planes that are reconstructed for both CT and PET, allowing the user to translate and/or rotate the PET images in three dimensions to best match the reference CT images. Once the best match has been achieved, a transformation matrix is calculated and the PET images are reformatted to best match the CT scans. One serious problem vis-a-vis image registration is that patient positioning can differ between scanning units. The recent introduction of combined PET/CT machines should greatly reduce many of these image registration difficulties.

These caveats of image registration not withstanding, at MSKCC 30–60 min of ungated PET scan acquisition are performed, usually in 3–4 segments due to the 14 cm field of view (FOV) of the current PET scanner. A 'rest and stretch' follows, followed by a 16-min respiratory-gated scan sequence. The gated scan is usually focused in on the single FOV strip containing the PTV, and thus requires less scanning time. For the gated PET, each recorded PET event is placed in its appropriate time bin (based on the time lapse between the PET event and the start trigger signal from the RPM as described above), in the same manner as a multichannel analyzer operating in time scaling mode. At the completion of image acquisition one can reconstruct the individual PET emission images from each time bin, as well as the integrated image (which is the equivalent of a free breathing scan).

6.5 EPID Based Treatment Verification

Recent improvements in EPIDs such as amorphous silicon (aSi) detectors now provide an attractive alternative to conventional portal films. Their speed and convenience coupled with the advantages of digital image processing make them a useful tool for on-line treatment verification and transit dosimetry measurements of IMRT treatments, in addition to being simply a replacement for conventional static portal films [21, 58–60]. The additional complications in treatment delivery introduced by the combination of IMRT plus respiratory gating render treatment verification even more important. Future advances may even make possible 3D rather than 2D treatment verification. In particular, real-time 3D megavoltage cone beam imaging is currently being investigated as new generation aSi EPID technology

[61–64] brings this approach within the realm of possibility.

ASi EPIDs also have the potential for verification of IMRT and RG, wherein the EPID can be used as a movie camera, capturing as many as five images per second, which may be used to record MLC leaf positions and internal anatomy as a function of time.

6.6 Summary and Conclusions

IMRT offers exciting potential for improving the radiation therapy of NSCLC, a disease that generally responds poorly to conventional RT. NSCLC is in many aspects a textbook example of a treatment site for which IMRT was designed, as it is a disease for which dose-escalation is clearly required, but for which improved normal tissue dose sparing is also critically important. It is also a site where significant improvements over conventional RT are clearly needed, being the most common cause of cancer death in the US. Even with implementation of IMRT, however, there are still many technical details that could mitigate any possible benefits of increased radiation doses. In particular, conventional RT does poorly in NSCLC in large part because of poor initial identification of the tumor volume, and errors associated with respiratory motion. Thus, this chapter has highlighted that the application of IMRT to NSCLC must be clinically tested in conjunction with other cutting edge technologies such as FDG-PET imaging, respiratory gating, and EPID-based treatment verification. Such a multi-faceted approach represents the best, and perhaps the only possibility for improved outcome in the treatment of this disease with radiation.

References

1. Greenlee RT et al. (2001) Cancer statistics, 2001. CA Cancer J Clin 51:15–36
2. Jemal A et al. (2004) Cancer statistics, 2004. CA Cancer J Clin 54:8–29
3. Arriagada R et al. (1991) ASTRO (American Society for Therapeutic Radiology and Oncology) plenary: Effect of chemotherapy on locally advanced non-small cell lung carcinoma: a randomized study of 353 patients. GETCB (Groupe d'Etude et Traitement des Cancers Bronchiques), FNCLCC (Federation Nationale des Centres de Lutte contre le Cancer) and the CEBI trialists. Int J Radiat Oncol Biol Phys 20:1183–1190
4. Furuse K et al. (1999) Phase III study of concurrent versus sequential thoracic radiotherapy in combination with mitomycin, vindesine, and cisplatin in unresectable stage III non-small-cell lung cancer. J Clin Oncol 17:2692–2699
5. Pisters KM (2000) The role of chemotherapy in early-stage (stage I and II) resectable non-small cell lung cancer. Semin Radiat Oncol 10:274–279
6. Cox JD et al. (1990) A randomized phase I/II trial of hyperfractionated radiation therapy with total doses of 60.0 Gy to 79.2 Gy: possible survival benefit with greater than or equal to 69.6 Gy in favorable patients with Radiation Therapy Oncology Group stage III non- small-cell lung carcinoma: report of Radiation Therapy Oncology Group 83–11. J Clin Oncol 8:1543–1555
7. Emami B (1996) Three-dimensional conformal radiation therapy in bronchogenic carcinoma. Semin Radiat Oncol 6:92–97
8. Perez CA et al. (1987) Long-term observations of the patterns of failure in patients with unresectable non-oat cell carcinoma of the lung treated with definitive radiotherapy. Cancer 59:1874–1881
9. Armstrong JG et al. (1993) Three-dimensional conformal radiation therapy may improve the therapeutic ratio of high dose radiation therapy for lung cancer. Int J Radiat Oncol Biol Phys 26:685–689
10. Narayan S et al. (2004) Results following treatment to doses of 92.4 or 102.9 Gy on a phase I dose escalation study for non-small cell lung cancer. Lung Cancer 44:79–88
11. Graham MV et al. (1995) Preliminary results of a prospective trial using three dimensional radiotherapy for lung cancer. Int J Radiat Oncol Biol Phys 33:993–1000
12. Rosenzweig KE et al. (2003) Results of a phase I dose escalation study in the treatment of inoperable non-small cell lung cancer. Int J Radiat Oncol Biol Phys 57:S417–S418
13. Henschke CI et al. (1999) Early Lung Cancer Action Project: overall design and findings from baseline screening. Lancet 354:99–105
14. Curran W et al. (2003) Long-term benefit is observed in a phase III comparison of sequential vs. concurrent chemo-radiation for patients with unresected stage III nsclc: RTOG 9410. Proc ASCO 22:621
15. Emami B et al. (1991) Tolerance of normal tissue to therapeutic irradiation. Int J Radiat Oncol Biol Phys 21:109–122
16. Kwa SL et al. (1998) Radiation pneumonitis as a function of mean lung dose: an analysis of pooled data of 540 patients. Int J Radiat Oncol Biol Phys 42:1–9
17. Kiffer JD et al. (1998) The contribution of 18F-fluoro-2-deoxy-glucose positron emission tomographic imaging to radiotherapy planning in lung cancer. Lung Cancer 19:167–177
18. Sasaki M et al. (1996) The usefulness of FDG positron emission tomography for the detection of mediastinal lymph node metastases in patients with non-small cell lung cancer: a comparative study with X-ray computed tomography. Eur J Nucl Med
19. Vansteenkiste JF et al. (1998) Lymph node staging in non-small-cell lung cancer with FDG-PET scan: a prospective study on 690 lymph node stations from 68 patients. J Clin Oncol 16:2142–2149
20. Wahl RL et al. (1994) Staging of mediastinal non-small cell lung cancer with FDG PET, CT, and fusion images: preliminary prospective evaluation. Radiology 191:371–377
21. Chang J et al. (2000) Relative profile and dose verification of intensity-modulated radiation therapy. Int J Radiat Oncol Biol Phys 47:231–240
22. Kubo HD et al. (1999) Potential and role of a prototype amorphous silicon array electronic portal imaging device in breathing synchronized radiotherapy. Med Phys 26:2410–2414
23. Mageras G et al. (2000) Initial clinical evaluation of a respiratory gated radiotherapy system. Med Phys 27:1419
24. Chui CS et al. (1994) Dose calculation for photon beams with intensity modulation generated by dynamic jaw or multileaf collimations. Med Phys 21:1237–1244

25. Spirou SV, Chui CS (1996) Generation of arbitrary intensity profiles by combining the scanning beam with dynamic multileaf collimation. Med Phys 23:1–8
26. Jackson A et al. (1993) Probability of radiation-induced complications for normal tissues with a parallel architecture subject to non-uniform irradiation. Med Phys 20:613–625
27. Jackson A et al. (1995) Analysis of clinical complication data for radiation hepatitis using a parallel architecture model. Int J Radiat Oncol Biol Phys 31:883–891
28. Giraud P et al. (2001) CT and (18)F-deoxyglucose (FDG) image fusion for optimization of conformal radiotherapy of lung cancers. Int J Radiat Oncol Biol Phys 49:1249–1257
29. Chui C-S et al. (2003) The effects of intra-fraction organ motion on the delivery of intensity-modulated field with a multileaf collimator.Med Phys 30:1736–1746
30. Yorke E (2001) Advantages of IMRT for dose escalation in radiation therapy for lung cancer. Med Phys 28:1291
31. Yorke E et al. (2001) Optimization with both dose-volume and biological constraints for lung IMRT. Med Phys 28(6):1261
32. Grills IS et al. (2003) Potential for reduced toxicity and dose escalation in the treatment of inoperable non-small-cell lung cancer: a comparison of intensity-modulated radiation therapy (IMRT), 3D conformal radiation, and elective nodal irradiation. Int J Radiat Oncol Biol Phys 57:875–890
33. Liu HH et al. (2004) Feasibility of sparing lung and other thoracic structures with intensity-modulated radiotherapy for non-small-cell lung cancer. Int J Radiat Oncol Biol Phys 58:1268–1279
34. Hanley J et al. (1999) Deep inspiration breath-hold technique for lung tumors: the potential value of target immobilization and reduced lung density in dose escalation. Int J Radiat Oncol Biol Phys 45:603–611
35. Kubo HD, Hill BC (1996) Respiration gated radiotherapy treatment: a technical study. Phys Med Biol 41:83–91
36. Ohara K et al. (1989) Irradiation synchronized with respiration gate. Int J Radiat Oncol Biol Phys 17:853–857
37. Rosenzweig KE et al. (2000a) The deep inspiration breath-hold technique in the treatment of inoperable non-small cell lung cancer. Int J Radiat Oncol Biol Phys 48:81–87
38. Rosenzweig KE et al. (2000b) Final report of the 70.2 Gy and 75.6 Gy dose levels of a phase I dose escalation study using three dimensional conformal radiotherapy in the treatment of inoperable lung cancer. Cancer J 6:82–87
39. Wong JW et al. (1999) The use of active breathing control (ABC) to reduce margin for breathing motion. Int J Radiat Oncol Biol Phys 44:911–919
40. Wagman R et al. (2003) Respiratory gating for liver tumors: use in dose escalation. Int J Radiat Oncol Biol Phys 55:659–668
41. Mah D et al. (2000) Technical aspects of the deep inspiration breath-hold technique in the treatment of thoracic cancer. Int J Radiat Oncol Biol Phys 48:1175–1185
42. Nehmeh SA et al. (2001) Gated positron emission tomography in lung cancer: a novel technique to reduce lung tumor motion effect for radiotherapy. 43rd Annual AAPM Meeting abstract MO-D-BRB-01 28:1232
43. Ling CC et al. (2000) Towards multidimensional radiotherapy (MD-CRT): biological imaging and biological conformality. Int J Radiat Oncol Biol Phys 47:551–560
44. Coleman RE, Tesar RD (1997) Clinical PET: are we ready? J Nucl Med 38:16 N, 24 N
45. Gambhir SS et al. (1998) Analytical decision model for the cost-effective management of solitary pulmonary nodules. J Clin Oncol 16:2113–2125
46. Nestle U et al. (1999) 18F-deoxyglucose positron emission tomography (FDG-PET) for the planning of radiotherapy in lung cancer: high impact in patients with atelectasis. Int J Radiat Oncol Biol Phys 44:593–597
47. Hebert ME et al. (1996) Positron emission tomography in the pretreatment evaluation and follow-up of non-small cell lung cancer patients treated with radiotherapy: preliminary findings. Am J Clin Oncol 19:416–421
48. Munley MT et al. (1999) Multimodality nuclear medicine imaging in three-dimensional radiation treatment planning for lung cancer: challenges and prospects. Lung Cancer 23:105–114
49. Lardinois D et al. (2003) Staging of non-small cell lung cancer with integrated positron-emission tomography and computed tomography. N Engl J Med 348:2500–2507
50. Bradley J et al. (2004) Impact of FDG-PET on radiation therapy volume delineation in non-small-cell lung cancer. Int J Radiat Oncol Biol Phys59:78–86
51. Erdi YE et al.(2002) Radiotherapy treatment planning for patients with non-small cell lung cancer using positron emission tomography (PET). Radiother Oncol 62:51–60
52. Mah K et al. (2002) The impact of (18)FDG-PET on target and critical organs in CT-based treatment planning of patients with poorly defined non-small-cell lung carcinoma: a prospective study. Int J Radiat Oncol Biol Phys 52:339–350
53. Ung YC et al. (2000) Fusing 18flourodeoxyglucose (FDG)-hybrid PET to CT images significantly alters treatment planning in the radical treatment of non-small cell carcinoma of the lung. Int J Radiat Oncol Biol Phys 48:327–328
54. Fox J et al. (2004) Does the registration of PET and planning CT images decrease inter- and intra-observer variation in delineating tumor volumes for non-small cell lung cancer (NSCLC)? Int J Radiat Oncol Biol Phys (under review)
55. Tai Y et al. (1997) Utilization of 3D elastic transformation in the registration of chest X-ray CT and whole body PET. IEEE Trans Nucl Sci 44:1606–1612
56. Erdi YE et al. (2000) Using mutual information (MI) for automated 3D registration in the pelvic and lung region for CT images. Proc SPIE 3979:416–425
57. Maes F et al. (1997) Multimodality image registration by maximization of mutual information. IEEE Trans Nucl Sci 16:187–198
58. Curtin-Savard AJ, Podgorsak EB (1999) Verification of segmented beam delivery using a commercial electronic portal imaging device. Med Phys 26:737–742
59. Pasma KL et al. (1999) Dosimetric verification of intensity modulated beams produced with dynamic multileaf collimation using an electronic portal imaging device. Med Phys 26:2373–2378
60. Vieira SC et al. (2002) Fast and accurate leaf verification for dynamic multileaf collimation using an electronic portal imaging device. Med Phys 29:2034–2040
61. Jaffray DA et al. (1999) A radiographic and tomographic imaging system integrated into a medical linear accelerator for localization of bone and soft-tissue targets. Int J Radiat Oncol Biol Phys 45:773–789
62. Midgley S et al. (1998) A feasibility study for megavoltage cone beam CT using a commercial EPID. Phys Med Biol 43:155–169
63. Mosleh-Shirazi MA et al. (1998) A cone-beam megavoltage CT scanner for treatment verification in conformal radiotherapy. Radiother Oncol 48:319–328
64. Swindell W et al. (1983) Computed tomography with a linear accelerator with radiotherapy applications. Med Phys 10:416–420

Breast IMRT

Douglas W. Arthur, Monica M. Morris,
Frank A. Vicini, Nesrin Dogan

7

Contents

7.1 The Clinical Problem

The radiation oncologist is involved in the management of breast cancer patients throughout the spectrum of the disease: from adjuvant treatment of early and locally advanced stage to palliative treatment of metastasis. In the adjuvant setting there are two distinct clinical situations; (1) treatment of the breast only following breast conserving surgery for early stage disease and (2) treatment to the breast/chest wall and regional nodes for locally advanced disease. The use of radiotherapy in these clinical settings has been shown to improve local, local-regional control and overall survival [1–4]. When radiotherapy was first introduced into these clinical settings, broad field designs were used. These original broad fields were simplistic in design, and limited by the planning and treatment delivery systems available. However, because of their simplicity, success in reducing disease recurrence, and ease of implementation, these treatment techniques quickly became widely adopted. In fact, the majority of treatment centers today continue the same general disease management principles and treatment approaches originally designed and practiced in the 1970s and 1980s. Although upgraded field matching techniques and CT based treatment planning have been incorporated in many centers, minimal modifications have been made until recently with the emergence of image based treatment planning and advanced, intensity modulated radiotherapy delivery techniques. Intensity Modulated Radiotherapy (IMRT) in the treatment of breast cancer offers improved dose conformality and homogeneity. Only through appropriate investigation will we be able to determine whether this improvement in dose delivery actually translates into a clinical benefit and, therefore, justify widespread adoption of this treatment technology.

7.1.1 Isolated Breast Treatment

Treatment of the whole breast following lumpectomy to achieve in-breast disease control has been documented to be successful in both local control and cosmetic outcome [1, 2, 5]. The use of parallel opposed tangential fields, with varying levels of mechanical compensation, has become the standard whole-breast treatment approach due to its straight-forward simplicity, and familiarity of use from large randomized trials. The need for improvements in these simple but effective treatment approaches has been challenged and, therefore, it is appropriate to evaluate what improvements can be realized with IMRT [6–8]. As local control rates are primarily dependent on appropriate surgical resection followed by modest doses of adjuvant radiotherapy, improved dose coverage of the breast target or dose escalation for tumor control may not be necessary. It has been suggested that the application of IMRT forces physicians to focus attention on target delineation and target coverage therefore possibly yielding an improvement in disease control [9]. However, this advantage would not be a result of treatment delivered with IMRT technology but rather a result of the target-focused planning process which can also be achieved through appropriate application of conventional treatment techniques. The potential

advantages that IMRT technique may have over conventional 3D and non-3D techniques are (1) the ability to achieve dose uniformity throughout the breast target and (2) the potential to reduce the dose to underlying heart and lung. These abilities are expected to translate into an improved cosmetic outcome and reduced toxicity.

Although it is recognized that, in many women, appropriate use of mechanical wedges produces acceptable homogeneity, management of moist desquamation in the inframammary fold and low axilla is often necessary and late breast fibrosis (inframammary fold fibrosis), breast edema and costochondral discomfort are frequently encountered. Possibly due to the ease of standard tangential treatment, the successful local control rates and the significant improvement of life quality over mastectomy, these toxicities have been accepted as a part of the standard of care. Initially, it was common to follow the treatment guidelines used in NSABP B-06, where uncompensated tangential fields (i. e., no wedge filters used) were prescribed to midplane at a point two-thirds the distance from the skin to the base of the tangent at central axis [10]. As a result, the anterior aspect of the treated breast received a daily dose and total dose that exceeded the prescription dose, masking the fact that doses higher than 50 Gy to the surgical bed were often delivered. The degree of this inhomogeneity would have been variable as it is dependent on the size and shape of the breast. In the absence of dosimetric information, the effect is difficult to quantitate. Recognizing the varying level of inhomogeneity with such an approach, wedge filters have since been universally adopted to compensate for the difference in breast width encountered. However, wedges do not compensate for three-dimensional changes and toxicity related to dose inhomogeneity is still encountered. Mechanical lead compensators have been described as a method of providing customized compensation that achieves a highly homogeneous dose distribution [11]. This approach has been adopted in some centers but has never achieved widespread use as planning, compensator construction and treatment delivery times have been viewed as excessive, despite dosimetric benefits. The emergence of IMRT and multi-leaf collimation has provided an electronic method of 3D compensation that addresses these difficulties by providing an automated method of delivering a homogeneous dose. For this and other reasons, IMRT has the potential to become the preferred method of radiation delivery for breast cancer.

In the treatment of breast-only, IMRT is unlikely to make a great improvement in the already-low normal tissue complication probability. In whatever manner the breast target is defined, it remains a concave structure with lung and, if left sided, heart tissue directly adjacent. Avoiding dose to the underlying lung and heart has been the goal of some IMRT techniques; however, the dose reductions are marginal and of questionable clinical benefit when standard tangential field arrangements are used [12]. Creative multi-field arrangements have also been attempted, but the added complexity and associated increase in integral dose without the obvious potential for clinical benefit has prevented acceptance into clinical use [13–15]. The proper design of standard breast-only tangential fields limits the dose delivered to the heart and ipsilateral lung to an acceptable level in the majority of women. Although patients are encountered that present with a unique chest wall shape leading to an excessive amount of lung and/or heart in the field, these rare cases can usually be managed with minimal changes in tangential beam entry angle or the addition of a small heart block that reduces dose to these critical structures. Alternative methods of reducing the dose to neighboring lung and heart have been studied, but not yet widely accepted and include field arrangements and controlled breath hold techniques [16–18]. Review of the late heart and lung clinical toxicity data following treatment with standard tangential fields supports the idea that further reduction of dose to the heart and lung beyond that achieved with standard tangential field is not necessary [19–21]. Therefore, the benefits of IMRT in isolated breast treatment should be focused on delivering a homogeneous dose distribution throughout the breast in a population of patients with varying breast size and shape with the promise of reducing acute and late soft tissue toxicity.

7.1.2 Loco-Regional Breast/Chest Wall Treatment

Despite limited publications on use of IMRT in the setting of breast/chest wall and regional lymphatics, it is in this clinical setting of locally advanced disease that there is a real potential role for IMRT due to the undeniable need for improvement in the ability to achieve dose coverage of target with maximal normal tissue avoidance. The comprehensive coverage of the breast, chest wall, supraclavicular nodes, internal mammary nodes, and possibly the axilla presents a complicated target volume that wraps around the immediately adjacent lung, heart, mediastinum and brachial plexus. Many conventional techniques have been devised and investigated for local-regional coverage in both the settings of intact breast and post-mastectomy treatment [22, 23]. Although many of these techniques offer improved dosimetric coverage of this complex target volume and a reduction in normal tissue exposure, the partially wide tangent technique offers the best balance between target coverage and reduction in heart and lung dose [24]. However, it is recognized that there is no universally successful technique in a population presenting with widely varying thoracic structure and breast dimensions. One of the more obvious concerns with the inclusion of the internal mammary nodes is the resultant increase in dose

received by the heart. This concern is augmented with the knowledge that most of these patients will receive cardiotoxic agents as a part of their chemotherapy regimen and further validates the role of IMRT if techniques are shown to reduce cardiac dose.

7.1.3 Simultaneous Integrated Boost (SIB)

Several studies have indicated that delivering a boost dose to the tumor bed plus margin, typically with electrons, following conventional whole breast radiotherapy results in improved in-breast control rates [25, 26]. Despite the documented local control benefit, the design of these boost fields in many practices remains a clinical process based on mammograms, clinical exam and site of surgery. CT-based planning has opened the eyes of radiation oncologists, revealing the potential for boost field design error if image guidance is not incorporated into the boost field planning process. With the advanced planning process of IMRT, there emerges the potential for incorporating the boost dose into the whole breast dose delivery, therefore simultaneously delivering the boost dose – simultaneous integrated boost, SIB. This would facilitate shortening the treatment course delivery time by one to two weeks while potentially improving the conformance of the boost dose to the boost target. Minimal investigational work has been completed in this area, possibly related to the high rates of local control seen with present boosting techniques and because shortening the treatment course to five to five-and-a-half weeks is not remarkable compared to achievements with newer techniques accelerating the overall treatment course further and completing in three- and-a-half weeks or even in five days [27, 28]. It is uncertain at this time whether SIB can be incorporated into standard practice and further investigation is needed to address several questions. These questions include the design of reliable field arrangements that would allow SIB dose delivery and avoid increase dose delivery to surrounding normal tissue and critical organs. SIB is based on the ability to deliver an incremental daily dose increase to the boost target while continuing delivery of standard doses to the remainder of the breast. The amount of dose increase that will result in equivalent tumor control and breast tissue toxicity rates experienced with present techniques has not yet been determined. Lastly, additional daily treatment time will be required to deliver this treatment approach. Whether the benefit of applying IMRT technology in this situation justifies the additional time needed to plan and deliver treatment with a SIB is unknown and requires additional investigation.

An example of early investigation into the use of SIB with whole breast irradiation is described by Singla et al. [29]. They investigated the feasibility of SIB-IMRT for treatment of ten early stage left-sided invasive breast carcinoma patients. They compared target volume coverage and normal tissue dose using SIB-IMRT using six-field non-coplanar fields to traditional tangential fields optimized with wedges or compensating filters with an en-face electron lumpectomy bed boost. Their results showed that there was no difference seen in the coverage of left breast and lumpectomy bed using SIB-IMRT vs conventional 3D CRT. However, the plans generated with SIB-IMRT were significantly more conformal than all other plans. Their study also showed that SIB-IMRT significantly reduced the maximum dose to the left lung by ~22%. However, this benefit came at the expense of increased left breast dose outside of the lumpectomy bed, a direct result of the simultaneous boost. They concluded that although the use of a simultaneous integrated boost to the lumpectomy bed seems feasible, the clinical consequences of the increased ipsilateral breast dose remains unknown and therefore should be investigated further.

7.2 Unique Anatomical Challenges

7.2.1 Lung and Heart Avoidance

As modern treatment techniques allow us the luxury of working not only for a five-year cure in breast cancer, but also an avoidance of premature death [30], the toxicity of treatment becomes an increasingly important consideration. In breast cancer, early techniques, such as the hockey stick approach, were effective, though the improvement in survival was offset by excess treatment-related cardiac morbidity. More modern techniques (tangents) continue to demonstrate an improved disease control with acceptable normal tissue toxicity [19–21]. The goal of IMRT is to decrease further treatment toxicity while concurrently maintaining early stage disease control and/or increasing locally advanced disease control.

Current standard treatment techniques typically entail full-dose treatment to at least 10–15% ipsilateral lung volume and 3–6% of the heart volume for breast-only tangents [31, 32]. Greater treated volumes on the order of 15–25% for lung and 10–25% for heart can be expected for treatment involving the regional nodes (internal mammary chain, supraclavicular fossa, axilla). Marks et al. have attempted to quantify lung injury after radiotherapy using SPECT imaging [33]. They demonstrated that for most patients there was a statistically significant, dose-dependent reduction in regional blood flow at all time points following pulmonary irradiation, developing within three to six months post therapy at doses above 5–10 Gy. Such treatment has a reported clinical pneumonitis rate of between 1 and 4% [34].

Similar studies with regard to cardiac injury after radiotherapy demonstrate dose-dependent cardiac perfusion defects in 60% of patients at six months [35, 36]. Preliminary findings indicate that patients with cardiac perfusion defects shortly after therapy are more likely to experience transient chest pain in the two years following [37]. The long-term, clinically relevant effects of such changes are unknown. Geynes et al. noted that the early randomized trials in breast cancer which demonstrated excess cardiac morbidity also utilized treatment techniques likely to deliver at least 25 Gy to 25% or more of the cardiac volume; whereas modern techniques typically deliver this dose to 5–12% [31]. This same group analyzed the cardiac and myocardial DVHs for tangential therapy in left-sided stage I breast cancer and estimated the mean excess cardiac risk at 2% using a relative seriality model; however, there remained patients whose excess risk was as high as 9–12%, for whom intensity modulated radiotherapy was suggested [37].

As mentioned above, breast-only tangent radiotherapy is associated with a quite low but real risk of pneumonitis and cardiac disease. A number of studies of isolated breast IMRT have consistently demonstrated improved target volume dose homogeneity, a modest improvement in normal tissue sparing, with an associated increase in the mean doses to the contralateral breast and lung [14, 38, 39]. Isolated breast IMRT has been successfully implemented in the clinic with excellent cosmetic and acute complication results [39]; however, it will take lengthy follow-up of many more patients thus treated to demonstrate any incremental improvement in an already-low toxicity profile.

As opposed to simple tangents, the use of IMRT in the setting of locally advanced disease, with treatment of the regional nodes, may prove to be more compelling and will certainly be more technically challenging. Considerably fewer studies have been done in this setting, and all are planning studies. The lack of clinical use of IMRT for local-regional breast cancer treatment likely relates to concerns about set-up accuracy, organ motion and increased integral dose. Increased integral dose, as is consistently demonstrated in IMRT planning studies, may be associated with a near-doubling of the induced malignancy rate [40]. While the risk of second malignancy with radiotherapy is so low as to be statistically insignificant 15 years post-therapy, it does remain a real consideration, particularly amongst our younger patients [41, 42].

Kreuger et al. conducted a planning study of chest wall and regional nodal IMRT with the CTs of ten post-mastectomy patients with left sided stage II–III breast cancer [43]. They demonstrated increased dose uniformity with minimum doses to chest wall and internal mammary chain improved from 31 and 22 Gy to 44 and 43 Gy, respectively. Cardiac normal tissue complication probability (NTCP) was unchanged with IMRT, while ipsilateral lung NTCP was decreased. However, the mean dose to contralateral lung and breast increased. Johansson et al. present similar findings in their planning study of standard photons, IMRT and proton therapy for node positive left-sided breast cancer treatment [44]. In this study, mean NTCP for heart decreased from 7% with standard tangents to 2% and to 0.5% with IMRT and protons, respectively. NTCP for the left lung remained 28% for both tangents and IMRT and decreased to 0.6% for protons.

Table 1. Conservative normal tissue constraints presently applied at VCU

Normal tissue	Dose limit
Ipsilateral lung	< 5 Gy to < 30% of lung < 20 Gy to < 10% of lung 0 Gy to < 50% of lung
Contralateral lung	0 Gy to 100% of lung
Heart	< 5 Gy to < 50% of total heart volume < 10 Gy to < 33% of total heart volume < 20 Gy to < 10% of total heart volume 40 Gy to < 3% of total heart volume

Most of the data used to set lung and heart dose constraints is generated from patients treated for lung cancer and other malignancies where the disease process frequently outpaces the development of late normal tissue toxicity. Therefore, when treating young patients, setting definitive normal tissue constraints is difficult as the late effects of treating large volumes of normal tissue to low doses are not known. When constraints are set, they tend to be conservative, see Table 1, which often becomes restrictive and may limit or potentially inhibit the ability of the IMRT planning process to achieve the desired dose conformality. Until additional data is available, a reasonable approach to setting normal tissue constraints and determining cost functions is to use normal tissue dose tolerances derived from data observed in other organ sites or to use clinically acceptable dose/volume data generated from standard plans/techniques that have resulted in acceptable rates of local control and complications.

7.2.2 Inter- and Intra-Fraction Motion

With the generous tangential fields and target definition used with breast-only treatment, inter- and intra-fraction motion is not a significant factor. It is assumed that any movement of the true target, which lies within the confines of the breast tissue, moves within the fields as defined by the previously discussed conventional methods. However, that assumption cannot be extrapolated to local-regional treatment. The internal mammary lymph nodes are located in immediate proximity to the lung and heart and the dose is tightly conformed to the target structure in order to minimize normal tissue dose and avoid toxicity. Because of the

sharp dose fall-off at the field edge and the tight conformality of dose, intra-fraction movement, as a result of breathing, may be a factor confounding accurate dose delivery. Studies exploring this potential pitfall indicate that normal breathing motion results in approximately 5 mm of position change and that this movement has little effect on dose homogeneity within the clinical target volume (CTV) [45, 46]. Fraction to fraction differences can be seen; however, due to the interplay between respiratory motion and multi-leaf collimator motion during treatment delivery. Over a full course of treatment, however, there are no statistical differences between the planned and expected dose distributions. An effect of breathing motion that may require attention when treating a local-regional target is the resultant degradation of the planning target volume (PTV) dose uniformity that requires an increase in CTV to PTV expansion [45]. In addition, lung and heart doses also increase. Breath-hold, respiratory gating and 4D techniques can limit motion effect and remove the need for additional CTV-PTV expansion.

7.3 Breast Volume Delineation

In keeping with the IMRT planning principles used in other treatment sites, the planning of breast-only IMRT begins with the accurate delineation of target and critical normal tissue volumes. In breast-only treatment, conformal coverage of the breast immediately becomes problematic because of the inability to reliably define the extent of breast tissue and, therefore the target, to be treated. Many publications discussing IMRT for breast cancer simply state that the breast volume was entered for planning, and the volumes depicted in publication vary widely. However, in reality breast tissue extent cannot be reliably defined on CT scan and therefore this process translates into the entry of a breast target contour that is manually delineated relying on knowledge of breast anatomy, external skin contour and often external markers that are placed prior to CT to delineate breast tissue extent based on palpation. This approach results in the uncomfortable situation of planning the delivery of a highly conformal treatment to a target that is subjectively delineated. One solution has been to recognize that treatment using standard tangential fields has historically resulted in excellent local control, and so to assume that the clinical methods of defining these fields reliably covers the target and, therefore, can also be used to define the target for IMRT. As a result of this thinking, many of the various published IMRT techniques define the breast tissue by designating all tissue within standard tangential fields, excluding lung, as the breast target. Others have developed dose optimization approaches that simply assure dose uniformity to all tissue within the tangential fields.

7.4 Planning and Dose Prescriptions

7.4.1 Isolated Breast

Although it is recognized that there are physicians who prefer to have the breast volume contour entered freehand on each CT cut, at the Virginia Commonwealth University we have found that the contouring of the target volume is efficient and consistent when the contour is automated and guided by standard tangential field borders. Using tangential field borders, designed with clinical and CT guidance, the planning system can be programmed to auto-contour the target by including all tissue within the tangential field borders excluding lung. Although the chest wall is included within the breast reference volume, this has little impact on the final dose distribution due to the effect of the lung/chest wall interface on the final dose distribution. We additionally retract the contour 5 mm from the skin surface to account for dose build up. The IMRT plans are generated to be delivered with the step-and-shoot technique that employs the segmented multi leaf collimator (sMLC). All treatments are planned using 6-MV photon beams. The inverse planning optimization is performed using the Pinnacle [3] planning system (Philips laboratories, Milpitas, CA). A pencil beam calculation algorithm is used during optimization and the final dose is calculated, with heterogeneity corrections, using a superposition/convolution algorithm after the leaf sequencing is determined. The dosimetric goal for isolated breast IMRT is to achieve 95% target volume coverage with 100% of the prescription dose. Lung and heart volumes are not considered when optimizing the dose distribution as it is assumed that the volumes included

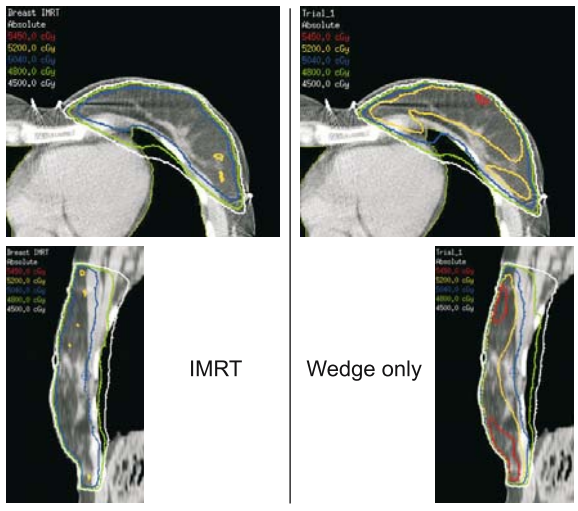

Fig. 1. Isolated breast treatment – dosimetric comparison of IMRT and Wedge only dosimetry

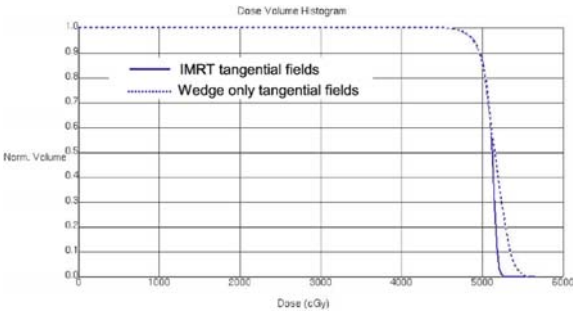

Fig. 2. Breast volume dose volume histogram

reflect the acceptable volumes included in standard tangential fields based on the methods used for breast target volume delineation.

Treating with standard tangential fields, where wedges are the only form of tissue compensation used, often results in significant areas inhomogeneity that are typically 10–15% greater than the prescribed dose. The degree of inhomogeneity is dependant on breast size and shape. Acute and late breast and overlying skin toxicity are typically experienced, most commonly in the infra-mammary fold. These normal tissue effects manifest as moist desquamation with subsequent risk of telangiectasia and/or degree of fibrosis. With IMRT planning and dose delivery these areas of increased dose can be reduced with a correlative improvement in toxicity. Figures 1 and 2 illustrate the improvements in dose distribution that can be achieved with IMRT planning as compared with results from standard planning using wedge compensation.

7.4.2 Loco-Regional Breast/Chest Wall IMRT

Treating the breast/chest wall and nodal regions as a contiguous volume with an IMRT planned and delivered approach, constructed for dose conformality with the generation of sharp dose gradients to protect organs at risk, has not yet been adopted into routine clinical use. An acceptable method of approaching this treatment challenge has not yet been devised. Remouchamps et al. have presented improvements in internal mammary node coverage with reduction in dose to lung and heart through their methods of moderate Deep Inspiration Breath Hold combined with IMRT [17, 18]. The form of IMRT described delivers a homogeneous dose with a standard tangential field arrangement. In this approach, dose conformality constructed to avoid organs at risk is not applied, but rather, the improvement in dose delivery achieved by optimizing the geometric positioning between the target and the organs at risk by utilizing the breath hold technique.

The spatial relationship between the loco-regional target and the underlying lung and heart is challenging and presently described approaches either compromise

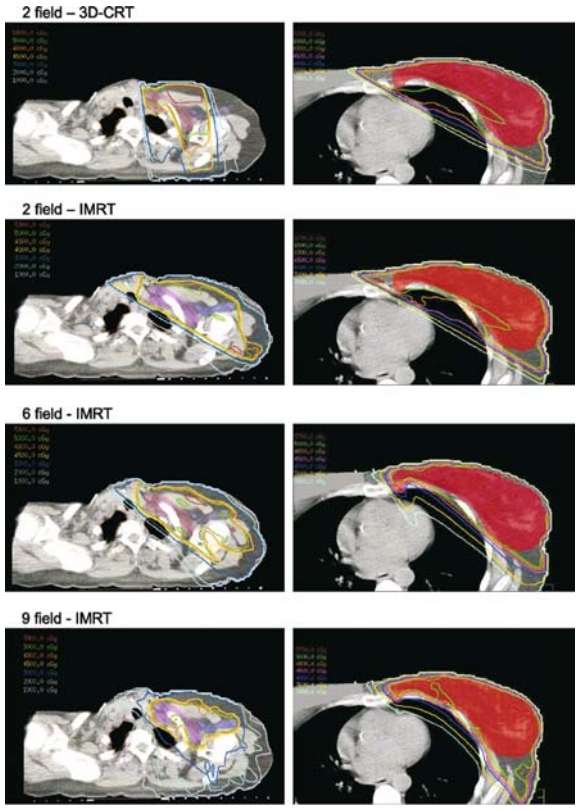

Fig. 3. Isodose comparison between field arrangements for loco-regional coverage – supraclavicular target *shaded purple* – breast and internal mammary node target *shaded red*

on target coverage or accept an increase in dose to normal structures. In our preliminary investigation, we have evaluated a two-field 3D-CRT, and a two-, six- and nine-field IMRT approach and compared dose distributions as they relate to loco-regional target coverage and normal tissue avoidance. Initially, we set conservative normal tissue constraints, Table 1. Plans covering the breast and internal mammary nodes (IMN) were generated and optimized with the goal of covering 95% of the

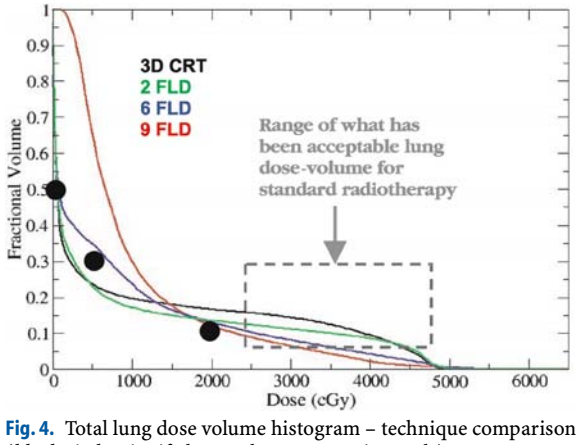

Fig. 4. Total lung dose volume histogram – technique comparison (*black circles* signify lung volume constraint goals)

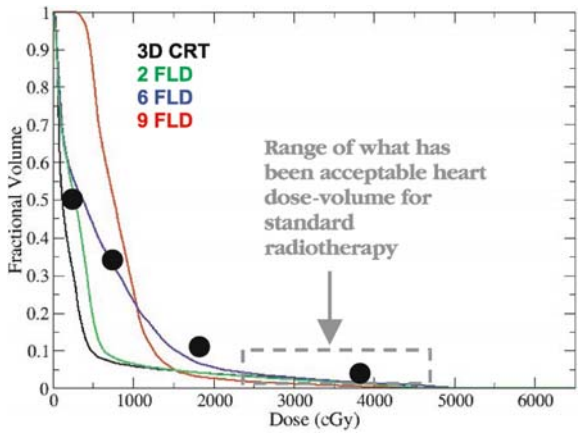

Fig. 5. Heart dose volume histogram – technique comparison (*black circles* signify lung volume constraint goals)

breast target volume with 100% of the prescribed dose. A two-field tangential 3D-conformal plan was compared to a two-field IMRT plan, a six-field non-coplanar beam IMRT plan, and an IMRT plan using nine equally spaced coplanar beams. The gantry angles used for the six-beam arrangement were designed such that the sparing of organs at risk was maximized and fields were positioned at angles of 305, 125, 325, 145, 105, and 345°. Plans were optimized for breast target coverage and normal tissue avoidance. Single CT cut dose distribution comparison of these four-field arrangements is depicted in Fig. 3. The spatial relationship between the loco-regional target and critical organ structures changes from superior to inferior and therefore a three-dimensional dose comparison is needed to understand fully the differences between treatment approaches. The Dose Volume Histograms comparing the four techniques for both lung and heart are seen in Figures 4 and 5. Note that all treat within a range that is acceptable by known criteria. The dose received by percent of organ at risk for the evaluated techniques is displayed in tabular format in Tables 2 and 3 and the ability of each technique to cover the IMN target volume detailed in Table 4. This preliminary study suggests that the best balance between target coverage, as signified by internal mammary node coverage and normal tissue avoidance, appears to be achieved with a two-field IMRT approach.

Table 2. Dose received by percent lung volume

Goal dose to % lung vol	Actual lung volume receiving dose			
	Control 3DCRT	2 Fld IMRT	6 Fld IMRT	9 Fld IMRT
*V*1 Gy < 50%	35	22	39	97
*V*5 Gy < 30%	18	9	14	23
*V*20 Gy < 10%	13	5	6	5

Table 3. Dose received by percent heart volume

Goal dose to % heart vol	Actual heart volume receiving dose			
	Control 3DCRT	2 Fld IMRT	6 Fld IMRT	9 Fld IMRT
*V*5 Gy < 50%	10	5	29	32
*V*10 Gy < 33%	6	3	4	4
*V*20 Gy < 10%	4	2	2	1
*V*40 Gy < 3%	1	0	0	0

Table 4. Internal mammary node (IMN) dose coverage

IMN volume covered by the % of the prescription dose	Treatment technique			
	Control 3DCRT (%)	2 Fld IMRT (%)	6 Fld IMRT (%)	9 Fld IMRT (%)
*V*100% (50 Gy)	71	85	0	34
*V*95% (47.5 Gy)	80	98	22	50
*V*90% (45 Gy)	91	99	80	67
*V*80% (40 Gy)	95	100	100	91

7.5 Clinical Experience

7.5.1 Isolated Breast IMRT

Many institutions have investigated breast-only IMRT with the goal of improving dose homogeneity. The majority of publications are dosimetric studies, with rare clinical experiences reported. All studies report improved homogeneity of dose throughout the breast target with IMRT techniques as compared to standard wedged tangential fields. Most investigators report techniques using standard tangential field arrangements with differences existing in the methodology used to define the treatment target, to obtain the desired dose distribution, and to deliver the planned dose. Inverse planning and various forms of forward planning have been used to generate homogeneous treatment plans that can be delivered with mechanical compensators, with computer controlled multi-leaf collimation (MLC) utilizing multiple static fields, or with dynamic IMRT treatment delivery.

Three institutions have described IMRT techniques that incorporate multiple static fields delivering low dose to enhance the dose homogeneity of standard wedged tangential fields [47–49]. Starting with the majority of the dose delivered with fields optimized with wedges

only, Zackrisson et al. and Lo et al. fashioned additional fields which deliver a portion of the dose to the target excluding the higher dose regions [48, 49]. These additional fields were created with a 3D treatment planning system through an iterative process. Similarly, Evans et al. began the treatment delivery design with wedged fields and augmented the dose delivery with a set of low-dose shaped fields based on thickness maps obtained with an electronic portal imaging device [47]. All three studies demonstrated a reduction of the high dose regions within the breast. Chang et al. evaluated eight different intensity modulated approaches using anthropomorphic phantoms and compared dose homogeneity, contra-lateral breast dose and treatment delivery time [50]. They have concluded that superior dose uniformity is achieved when treatments are generated by dose optimization algorithm and delivered via the compensator and MLC techniques. They have also reported that the contralateral breast dose is maximally reduced with collimator generated techniques, i. e. MLC or virtual wedge. However, the MLC technique requires the longest treatment irradiation time.

With several publications demonstrating improved dose uniformity with IMRT, the importance of reducing treatment planning and delivery time becomes an issue if the use of IMRT for breast cancer is to be practical enough to be used in a busy clinic. This conversion to a practical, time efficient approach is exemplified in the publications from Memorial Sloan Kettering Cancer Center. Hong et al., initially presented a dosimetric study of five patients with right and five patients with left breast involvement [12]. They presented an inverse planning IMRT technique utilizing set target and critical organ optimization criteria and compared this to standard wedged tangential fields. They reported an improvement in dose homogeneity, with an 8% dose reduction in the superior and inferior aspects of the breast target and 4% in the medial and lateral, as well as a reduction in the dose delivered to the coronary artery region, ipsilateral lung and contra-lateral breast. Although improvements in normal tissue doses and target dose homogeneity were evident, the concern was raised that these improvements may not be on a large enough scale to justify the huge increase in planning effort required for such inverse methods. In response to this report, a simplified and efficient IMRT technique for the breast, referred to as simplified IMRT (sIMRT), was developed [51]. The standard tangential beam arrangement was used and contours, except the automated external contour, were eliminated. The PTV was defined as all tissue within the tangential fields, less 5 mm beam penumbra and 5 mm from skin. For each field, a pencil beam grid was created and the optimal intensity of each pencil beam determined as proportional to the inverse of the midpoint dose from an open beam. The intensity distribution was then converted to a deliverable plan utilizing multi-leaf collimation. In fifteen patients the sIMRT planning technique was compared to the standard wedged pair tangential field technique and volume based IMRT technique (vIMRT). They reported that the target dose homogeneity and normal tissue dose limitation was equivalent between sIMRT and vIMRT planning. However, the planning time for sIMRT was significantly less than that for vIMRT and equivalent to the planning time for standard wedged fields, thus converting the planning technique to one which can be adopted in clinics treating high volumes of patients.

Similarly, two additional methods have been described, both delivering the majority of the intended dose with open fields and supplementing with shaped low dose fields to optimize dose homogeneity throughout the field. The technique first described by van Asselen et al., delivers approximately 88% of the dose with open fields [52]. The remaining dose is given with multiple shaped fields, or segments, that are obtained from an equivalent path length map of the irradiated volume. Kestin et al. has described a similar technique, developed at the William Beaumont Hospital, where multi-leaf segments are designed based upon isodose surfaces that result from an open set of tangent fields, with each segment weight-optimized using a computerized algorithm [53]. Limitations are placed on the volume of tissue that can exceed the prescription and a set of rules is then used to derive a sequence of field apertures, with the weights of these apertures the free parameters in the optimization. This approach is referred to as "limited parameter set" optimization, because the number of free parameters is small compared to pixel-based, or fluence map optimizations. Others have referred to this as aperture-based inverse planning, or segmental IMRT (sIMRT). This approach (an optimized combination of open fields and customized field apertures) allows one to compensate precisely for the changing breast contour. With treatment planning and treatment delivery times reported as less than 60 min and 10 min, respectively, we now have the tools to achieve superior dose homogeneity in a time efficient manner [39].

Limited data is available regarding any clinical experience with IMRT-based treatment of breast cancer. The largest clinical experience with whole-breast IMRT was recently published by the William Beaumont Hospital group [39]. Two hundred and eighty one patients, with early stage breast cancer and electing breast conserving therapy, received whole breast radiotherapy after lumpectomy using an sIMRT technique. The technical and practical aspects of implementing this technique on a large scale in the clinic were analyzed, as well as the acute toxicity and cosmetic outcome of the patients. Treatment time was equivalent to conventional wedged-tangent treatment techniques. The median volume of breast receiving 105% and 110% of the prescribed dose was 11% (range 0–68%) and 0% (range 0–39%), re-

spectively. No or mild acute skin toxicity was noted in 56% of patients. Forty three percent experienced moderate, grade II, acute skin toxicity, and only three patients (1%) had significant, grade III toxicity. Cosmetic result at year one in the 95 evaluable patients was rated as excellent or good in 94 (99%). No skin telangiectasias, significant fibrosis or persistent breast pain were noted. The authors concluded that the use of intensity modulation using their static multi-leaf collimator technique for tangential whole breast radiotherapy was an efficient method for achieving a uniform and standardized dose throughout the whole breast.

7.5.2 Loco-Regional Breast/Chest Wall IMRT

In the work published on IMRT technique for treatment of breast/chest wall and regional nodes, there is a divergence in methods used to approach the challenge of balancing target coverage and normal tissue avoidance. One direction has been to use multiple fields shaped to conform to the target, while the other continues to use deep tangential fields, but with IMRT planning and respiratory gating.

All multi-field target-conformal approaches that have been described report improved coverage of the target and a reduction in the volume of normal tissue receiving high doses [14, 43, 54, 55]. Kreuger et al. reported on a ten-patient comparison between a multiple field IMRT technique and a partially wide tangential field approach planned with conventional methods [33, 43]. All patients chosen for study had undergone a left-sided modified radical mastectomy for stage II or III disease. The chest wall, defined by anatomic boundaries, supraclavicular and internal mammary target volumes and relevant normal tissue structures were contoured. A general nine-field arrangement of equally spaced fields around the patient was used. Each beam aperture was opened to include the target volume plus 1 – 2 cm and an in-house inverse planning system used to determine the intensity of each beamlet. In comparison to the partially wide tangential field approach, considered the optimal conventional technique to avoid cardiac dose, their nine-field approach improved chest wall coverage, achieved comparable low cardiac doses, improved internal mammary node coverage and reduced the left lung mean dose and normal tissue complication probability. This technique was successful over a range of body habitus. Despite the apparent superiority of this approach, the authors cautioned that to achieve these results, there is an associated penalty of increased volume of heart, lung and contralateral breast receiving low doses (i. e., increased integral dose) and suggested that, before clinical implementation, a reduction in these volumes is necessary. Lomax et al. completed a similar study of techniques comparing a conventional photon/electron technique to a nine-field IMRT approach but also compared a proton technique [55]. They reported similar improvement in target coverage and normal tissue avoidance with the IMRT technique that was surpassed by the proton plan with respect to non-target integral dose and potential risk of carcinogenesis. Cho et al. compared IMRT and non-IMRT techniques in the treatment of the left breast and internal mammary nodes in twelve patients and demonstrated superior breast and internal mammary chain target coverage [54]. Tangential IMRT fields were used, thus removing the concerns of increased integral dose. Whether this technique achieves the same results over a range of body habitus was not addressed. In a similar study, an inversely planned 12-beam IMRT technique proved superior in target coverage and high dose reduction to normal structures but re-iterated the associated increase in integral dose [56]. These techniques have yet to be clinically tested. It remains unknown whether the high dose reduction to the underlying heart and lung is clinically relevant and whether the increased volume of lung, heart and contralateral breast will become clinically relevant.

The alternate approach to this treatment problem has been the focus of study at the William Beaumont Hospital. Their approach is based on the continued use of deep tangential fields with IMRT-enhanced dosimetry in conjunction with active breathing control (ABC) using a moderately deep inspiration breath hold (mDIBH) technique [17, 18]. The application of tangential fields avoids the concerns of increased integral dose and the associated concerns of late toxicity. The mDIBH technique improves the geometry of the normal tissue and critical organ anatomical relationship, thus allowing improved breast/chestwall and internal mammary node coverage while reducing high dose regions to the underlying heart.

7.6 Future Directions/Conclusion

The use of IMRT in the treatment of breast cancer is increasing across the U.S. as a result of the improvements provided in dose homogeneity and normal tissue avoidance. The application of IMRT offers reduced soft tissue toxicity in isolated breast treatment and the potential for improved local-regional control without an increase in lung and heart toxicity in those requiring loco-regional treatment. When standard tangential fields are used to define the target volume, the focus of IMRT is primarily to optimize dose homogeneity. Although long term outcome studies are needed to make definitive statements, many have already accepted this treatment approach as a preferred method of treatment delivery. However, when dose conformality becomes a primary focus, many uncertainties arise that require additional study prior to widespread adoption. By generating highly conformal fields with severe dose gradients, the accuracy of

treatment delivery becomes increasingly dependant on set up error and breathing motion. This is not an issue when standard tangents are used for isolated breast treatment as the generous field design allows the target to remain in the field despite inter or intra-fraction motion. However, this is a critical issue when dose shaping with the goal of maximizing target coverage and normal tissue avoidance. Future investigation will need to address these challenges before IMRT can be considered for widespread adoption. Additionally, long term follow-up is needed to determine whether the improvements in dose homogeneity and conformality will translate into improvements in disease control and/or a reduction in toxicity.

References

1. Fischer B, Anderson S, Bryant J et al. (2002) Twenty-year follow-up of a randomized trial comparing total mastectomy, lumpectomy, and lumpectomy plus irradiation for the treatment of invasive breast cancer. N Engl J Med 347: 1233–1241
2. Veronesi U, Cascinelli N, Mariani L et al. (2002) Twenty-year follow-up of randomized study comparing breast-conserving surgery with radical (Halstead) mastectomy for early breast cancer. N Engl J Med 347:1227–1232
3. Overgaard M, Hansen PS, Overgaard J et al. (1997) The Danish Breast Cancer Cooperative Group 82b Trial. New Eng J Med 337:949–955
4. Ragaz J, Jackson SM, Le N et al. (1997) Adjuvant radiotherapy and chemotherapy in node-positive premenopausal women with breast cancer. New Eng J Med 337:956–962
5. Wazer DE, Dipetrillo T, Schmidt-Ullrich R et al.(1992) Factors influencing cosmetic outcome and complication risk after conservative surgery and radiotherapy for early stage breast carcinoma. J Clin Oncol 10:356–363
6. Potters L, Steinberg M, Wallner P et al. (2003) How one defines intensity-modulated radiation therapy. Int J Radiat Oncol Biol Phys 56:609–610
7. Glatstein E (2003) The return of the snake oil salesmen. Int J Radiat Oncol Biol Phys 55:561–562
8. Glatstein E (2002) Intensity-modulated radiation therapy: the inverse, the converse, and the perverse. Semin Radiat Oncol 12:272–281
9. Strom EA (2002) Breast IMRT: new tools leading to new vision. Int J Radiat Oncol Biol Phys 54:1297–1298
10. Fischer B, Bower M, Margolese R et al. (1985) Five year results of a randomized clinical trial comparing total mastectomy and segmental mastectomy with or without radiation in the treatment of breast cancer. N Engl J Med 312:665–673
11. Carruthers LJ, Redpath AT, Kunkler IH (1999) The use of compensators to optimize the three dimensional dose distribution in radiotherapy of the intact breast. Radiother Oncol 50:291–300
12. Hong L, Hunt M, Chui C et al. (1999) Intensity-modulated tangential beam irradiation of the intact breast. Int J Radiat Oncol Biol Phys 44:1155–1164
13. Li JG, Williams SS, Goffinet DR et al. (2000) Breast-conserving radiation therapy using combined electron and intensity-modulated radiotherapy technique. Radiother Oncol 56: 65–71
14. Thilmann C, Zabel A, Nill S et al. (2002) Intensity-modulated radiotherapy of the female breast. Med Dosim 27:79–90
15. Korevaar EW, Hutzenga H, Lof J et al. (2002) Investigation of the added value of high-evergy electroms in intensity-modulated radiotherapy: four clinical cases. Int J Radiat Oncol Biol Phys 52:236–253
16. Fogliatta A, Bolsi A, Cozzi L (2002) Critical appraisal of treatment techniques based on conventional photon beams, intensity modulated photon beams and proton beams for therapy of intact breast. Radiother Oncol 62:137–145
17. Remouchamps VM, Vicini FA, Sharpe MB et al. (2003) Significant reductions in heart and lung doses using deep inspiration breath hold with active breathing control and intensity-modulated radiation therapy for patients treated with locoregional breast irradiation. Int J Radiat Oncol Biol Phys 55:392–406
18. Remouchamps VM, Letts N, Vicini FA et al. (2003) Initial clinical experience with moderate deep-inspiration breath hold using an active breathing control device in the treatment of patients with left-sided breast cancer using external beam radiation therapy. Int J Radiat Oncol Biol Phys 56:704–715
19. Gyenes G, Rutqvist LE, Liedberg A et al. (1998) Long-term cardiac morbidity and mortality in a randomized trial of pre- and postoperative radiation therapy versus surgery alone in primary breast cancer. Radiother Oncol 48:185–190
20. Cuzick J, Stewart H, Rutqvist L et al. (1994) Cause-specific mortality in long-term survivors of breast cancer who participated in trials of radiotherapy. J Clin Oncol 12:447–453
21. Whelan TJ, Julian J, Wright J et al. (2000) Does locoregional radiation therapy improve survival in breast cancer? A meta-analysis. J Clin Oncol 18:1220–1229
22. Pierce LJ, Butler JB, Martel MK et al. (2002) Postmastectomy radiotherapy of the chest wall: dosimetric comparison of common techniques. Int J Radiat Oncol Biol Phys 52:1220–1230
23. Arthur DW, Arnfield MR, Warwicke LA et al. (2000) Internal mammary node coverage: an investigation of presently accepted techniques. Int J Radiat Oncol Biol Phys 48:139–146
24. Marks LB, Hebert ME, Bentel G et al. (1994) To treat or not to treat the internal mammary nodes: A possible compromise. Int J Radiat Oncol Biol Phys 29:903–909
25. Romestaing P, Lehinge Y, Carrie C et al. (1997) Role of a 10-Gy boost in the conservative treatment of early breast cancer: results of a randomized clinical trial in Lyon, France. J Clin Oncol 15:963–968
26. Bartelink H, Horiot JC, Poortmans P et al. (2001) Recurrence rates after treatment of breast cancer with standard radiotherapy with or without additional radiation. N Engl J Med 345:1378–1387
27. Whelan T, MacKenzie R, Julian J et al. (2002) Randomized trial of breast irradiation schedules after lumpectomy for women with lymph node-negative breast cancer. J Natl Cancer Inst 94:1143–1150
28. Arthur DW (2003) Accelerated partial breast irradiation: a change in treatment paradigm for early stage breast cancer (guest editorial). J Surg Oncol 84:185–191
29. Singla R, King S, Albuquerque K, Creech S, Dogan N (2003) Simultaneous integrated IMRT boost in the treatment of early stage left-sided breast carcinoma, presented at 2003 RSNA meeting in Chicago, IL. Abstract 1512, p 694, RSNA meeting proceedings (2003)
30. Sasieni PD, Adams J, Cuzick J (2002) Avoidance of premature death: a new definition for the proportion cured. J Cancer Epidemiol Prev 7:165–171
31. Gyenes G, Gagliardi G, Lax I et al. (1997) Evaluation of irradiated heart volumes in stage I breast cancer patients treated with

postoperative adjuvant radiotherapy. J Clin Oncol 15:1348–1353
32. Das IJ, Cheng EC, Freedman G et al. (1998) Lung and heart dose volume analysis with CT simulator in radiation treatment of breast cancer. Int J Radiat Oncol Biol Phys 42:11–19
33. Marks LB, Munley MT, Spencer DP et al. (1997) Quantification of radiation-induced regional lung injury with perfusion imaging. Int J Radiat Oncol Biol Phys 38(2):399–409
34. Lind P, Marks LB, Hardenbergh PH et al. (2002) Technical factors associated with radiation pneumonitis after local plus or minus regional radiation therapy for breast cancer. Int J Radiat Oncol Biol Phys 52(1):137–143
35. Hardenbergh PH, Munley MT, Bentel GC et al. (2001) Cardiac perfusion changes in patients treated for breast cancer with radiation therapy and doxorubicin: preliminary results. Int J Radiat Oncol Biol Phys 49(4):1023–1028
36. Lind PA, Pagnanelli R, Marks LB et al. (2003) Myocardial perfusion changes in patients irradiated for left-sided breast cancer and correlation with coronary artery distribution. Int J Radiat Oncol Biol Phys 55(4):914–920
37. Gagliardi G, Lax I, Soderstrom S et al. (1998) Prediction of excess risk of long-term cardiac mortality after radiotherapy of stage I breast cancer. Radiother Oncol 46(1):63–71
38. Landau D, Adams EJ, Webb S et al. (2001) Cardiac avoidance in breast radiotherapy: a comparison of simple shielding techniques with intensity-modulated radiotherapy. Radiother Oncol 60:247–255
39. Vicini FA, Sharpe M, Kestin L et al. (2002) Optimizing breast cancer treatment efficacy with intensity-modulated radiotherapy. Int J Radiat Oncol Biol Phys 54:1336–1344
40. Hall EJ, Wu CS (2003) Radiation-induced second cancers: the impact of 3D-CRT and IMRT. Int J Radiat Oncol Biol Phys 56:83–88
41. Obedian E, Fischer DB, Haffty BG (2000) Second malignancies after treatment of early-stage breast cancer: lumpectomy and radiation therapy versus mastectomy. J Clin Oncol 18:2406–2412
42. Taghian A, de Vathaire F, Terrier P et al. (1991) Long-term risk of sarcoma following radiation treatment for breast cancer. Int J Radiat Oncol Biol Phys 21:361–367
43. Kreuger EA, Fraass BA, McShan DL et al. (2003) Potential gains for irradiation of chest wall and regional nodes with intensity modulated radiotherapy. Int J Radiat Oncol Biol Phys 56:1023–1037
44. Johansson J, Isacsson U, Lindman H et al. (2002) Node-positive left-sided breast cancer patients after breast-conserving surgery: potential outcomes of radiotherapy modalities and techniques. Radiother Oncol 65:89–98
45. George R, Keall PJ, Kini VR et al. (2003) Quantifying the effect of intrafraction motion during breast IMRT planning and dose delivery. Med Phys 30:552–562
46. Hector CL, Evans PM, Webb S (2001) The dosimetric consequences of inter-fractional patient movement on three classes of intensity-modulated delivery techniques in breast radiotherapy. Radiother Oncol 59:281–291
47. Evans PM, Donovan EM, Partridge M et al. (2000) The delivery of intensity modulated radiotherapy to the breast using multiple static fields. Radiother Oncol 57:79–89
48. Zackrisson B, Arevarn M, Karlsson M (2000) Optimized MLC-beam arrangements for tangential breast irradiation. Radiother Oncol 54:209–212
49. Lo YC, Yasuda G, Fitzgerald TJ et al. (2000) Intensity modulation for breast treatment using static multi-leaf collimators. Int J Radiat Oncol Biol Phys 46:187–194
50. Chang SX, Deschesne KM, Cullip TJ et al. (1999) A comparison of different intensity modulation treatment techniques for tangential breast irradiation. Int J Radiat Oncol Biol Phys 45:1305–1314
51. Chui CS, Hong L, Hunt M et al. (2002) A simplified intensity modulated radiation therapy technique for the breast. Med Phys 29:522–529
52. van Asselen B, Raaijmakers CP, Hofman P et al.(2001) An improved breast irradiation technique using three-dimensional geometrical information and intensity modulation. Radiother Oncol 58:341–347
53. Kestin LL, Sharpe MB, Frazier RC et al. (2000) Intensity modulation to improve dose uniformity with tangential breast radiotherapy: initial clinical experience. Int J Radiat Oncol Biol Phys 48:1559–1568
54. Cho BC, Hurkmans CW, Damen EM et al. (2002) Intensity modulated versus non-intensity modulated radiotherapy in the treatment of the left breast and upper internal mammary lymph node chain: a comparative planning study. Radiother Oncol 62:127–136
55. Lomax AJ, Cella L, Weber D et al. (2003) Potential role of intensity-modulated photons and protons in the treatment of the breast and regional nodes. Int J Radiat Oncol Biol Phys 55:785–792
56. Thilmann C, Sroka-Perez G, Krempien R et al. (2004) Inversely planned intensity modulated radiotherapy of the breast including the internal mammary chain: a plan comparison study. Technol Cancer Res Treat 3:69–75

IMRT for Malignancies of the Upper Abdomen and Retroperitoneum

Jerome C. Landry, Christopher G. Willett, Natia Esiashvili, Mary Koshy

8

Contents

8.1 General Introduction

Radiation therapy is indicated for different upper abdominal tumors, but is often associated with substantial gastrointestinal or genitourinary side-effects. With conventional radiotherapy, the most commonly applied techniques are two or four fields with custom-made blocks to exclude portions of normal structures. Even then, patients are still at risk for both acute and long-term side effects. Clinical applications of IMRT for treatment of upper abdominal tumors may allow the minimizing of serious acute and long-term complications while increasing cure probability by dose escalation.

Despite advancements in diagnostic tools, understanding cellular mechanisms, and invention of novel systemic therapies, pancreatic cancer remains one of the greatest challenges for clinicians. Pancreatic cancer is the fourth leading cause of cancer-related death with less then 5% of patients surviving at five years after diagnosis [1]. Improved radiation treatment delivery can have great impact on this disease, as local regional failure is the one of the most predominant patterns of progression for pancreatic tumors with local recurrence in up to 30–86% of patients after surgery alone [2–4]. Efforts to escalate radiation dose in pancreatic cancer patients are hampered by the proximity of dose-sensitive adjacent normal structures and increased risk for serious complications [5, 6]. Combined chemotherapy and radiation further increases the risk of significant acute and long-term complications [7–10].

Retroperitoneal sarcomas account for 14% of all soft tissue sarcomas and 0.7% of all cancers diagnosed in the United States [11]. Surgical resection has been and remains the only curative modality for this disease [12]. Because of the large tumor size at presentation and intimate involvement with adjacent organs, it is difficult to obtain resection with negative margins. Historically, rates of complete surgical resectability have varied from 38 to 65% with local recurrence rates as high as 70–90% [13–15]. Local recurrence in retroperitoneal sarcoma is the primary cause of mortality in patients with this disease. Clearly, this is a disease in which improvements in local control have the potential to significantly impact survival [16, 17]. Retroperitoneal sarcoma has been responsive to radiation dose escalation [18–22], yet efforts to achieve this with external beam radiation alone (EBRT) have been hampered by OAR (organs at risk) toxicity. IMRT can be used as a means to minimize dose to OAR and concurrently maximize tumor dose coverage.

The introduction of 3D-CRT (3D conformal radiotherapy) has led to progress in objective evaluation of dose-to-target volumes and critical structures. IMRT, as the most advanced form of conformal therapy, can improve even further the dose conformity to the tumor targets and minimize the dose to organs at risk. This strategy may give the oncologist and physicist more freedom to push the radiation dose to the tumor itself.

8.2 Unique Anatomic Challenges

There are several serious challenges in the treatment of abdominal tumors. The upper abdomen is one of the most complex anatomical sites in terms of number and proximity of normal structures with the lowest radiation dose tolerance. Liver, kidneys, and spinal cord

surround the pancreas and its regional lymph nodes in almost all directions and limit the radiation field design and optimal dose delivery to the target. Even with 3D-CRT, it is difficult to achieve good dose conformity. By employing inverse radiation treatment planning techniques and setting dose constraints to normal organs, IMRT can potentially achieve the most optimal beam angles and shape and give us the best conformal dose distribution.

The most critical step in designing IMRT plans for upper gastrointestinal malignancies is the precise identification of the tumor volume and normal structures. In some cases, collapsed hollow organs, such as segment of small bowel or stomach, can be difficult to differentiate from tumor extension or adenopathy. Another consideration is to evaluate organ motion in the upper abdomen. Based on data from Massachusetts Hospital, the pancreas can move during different phases of respiration up to 5–7 mm anterior to posterior, 2–3 mm medial to lateral, and < 5 mm cranio-caudal direction [23]. Other investigators have reported movement with the respiratory cycle as much as 23.7 ± 15.9 mm [24]. Obtaining CT images in static exhalation phase may limit this motion [25]. In one study, when patients were tested at static exhalation, which would represent differential gastrointestinal distention, CTV (clinical tumor volume) expansion for the pancreatic head was required to be at least 4 mm in right-left, and 3.5 mm in antero-posterior and cranio-caudal directions to compensate for organ motion [26]. Accurate delineation of regional lymph nodes is also crucial and requires good knowledge of CT anatomy. We are evaluating pancreatic motion by scanning patients with our 4D CT simulator allowing an evaluation of tumor motion during all phases of the respiratory cycle.

Accurate delineation of regional lymph nodes in the treatment of pancreatic cancer is crucial. There is substantial evidence of disease spread to the celiac axis, porta hepatis, and pancreato-duodenal and splenic hilum for tail and body lesions according to surgical pathology and patterns of failure data [27–30]. The celiac axis is typically located at T11–T12 and one can often visualize the celiac trunk. During contouring, the celiac axis should be drawn on approximately three to five CT slices. The porta hepatis is located at the level of the hepatic duct bifurcation. A study at our institution indicated that if one uses a reference point derived as 4.5 cm to the right of and 4.7 cm cephalic to the inferior end plate of L-1 vertebral body, and constructs a 10×10-cm portal that is 6 cm superior, 4 cm inferior, 4 cm to right lateral, and 6 cm to left lateral direction, the porta hepatic nodes will be covered in about 80% of cases [19].

The pancreato-duodenal lymph nodes are difficult to visualize on CT. Data from the Mayo clinic show that there is a change in location of celiac axis, porta hepatic, and superior mesenteric artery after Whipple resection, with only minimal anterior-posterior variation in the celiac axis (median 2 mm), and more prominent change in the portal vein, up to 2 cm in the lateral-medial direction and 1.9 cm in the anterior-posterior direction [32]. Physicians must keep this variability in mind while designing the margins around the treatment volumes. Treatment volumes must be individualized based on the volume and location of the primary tumor mass.

Treatment of retroperitoneal sarcomas with radiation also has been limited due to the close proximity of these tumors to small bowel, liver, and kidney. To avoid critically overdosing these organs at risk, the total dose delivered to the tumor is often compromised and consequently, the risk of local recurrence is increased. Although the kidneys and liver are dose-limiting structures when treating retroperitoneal sarcomas, the small bowel as an OAR poses the greatest challenge. Radiation doses beyond 45–50 Gy have been associated with small bowel obstruction; this is often the rate-limiting factor in dose escalation to a variety of tumors in the abdominal region [5]. Historically, these tumors have been treated with a 3–5-cm margin around the gross tumor volume (*GTV*) to include the anatomy of the involved tissues [20, 21, 33]. To treat with tighter margins than previously described in order to achieve dose escalation may potentially underdose the peritoneal cavity, where the risk of local recurrence is the greatest. We believe that the use of IMRT and intent of dose escalation does not give one a mandate to compromise the margin that would normally be employed in the treatment of retroperitoneal sarcoma. The use of IMRT throughout treatment, from the beginning, allows for optimal dose minimization to OAR and maximization to tumor volume.

8.3 Target Volume Delineation and Organs at Risk Definition

IMRT planning starts with good simulation techniques. To assure accurate visualization of the small bowel, all patients are given three to four glasses of radiopaque gastrografin oral contrast and placed supine in a rigid foam cradle. Approximately 30 min after drinking the oral contrast, treatment planning computer tomography (CT) scans of the abdomen and pelvis are obtained. The planning volume is scanned with 3-mm increments. The next step is to create a treatment plan based on CT images, with precise outlining of all the volumes of interest. The gross tumor volume is defined as all known gross disease determined from comparing the diagnostic with the treatment planning CT. Both GTV and lymph node groups are included in the clinical tumor volume (CTV) for pancreatic cancers. The Planning Target Volume (PTV) in non-resected pancreatic cancers provides 2–3-cm margins in all directions around the CTV to compensate for set-up and organ motion. In some cases,

the PTV at the vertebral column and/or skin may be too generous, in which case PTV can be modified. Incorporation of functional image fusion techniques in radiation treatment planning potentially can help radiation oncologists in modifying CTV. Additionally, newer techniques for definition of organ motions such as onboard imaging and gating will give us an opportunity to farther minimize the margins around CTV. The PTV for retroperitoneal sarcoma ultimately included the GTV plus a 5-cm margin in the superior and inferior dimensions and a 2-cm margin in the anterior/posterior and medial/lateral dimensions. Because the main advantage of IMRT is sparing of the normal organs adjacent to the CTV from receiving excessive doses of radiation, IMRT planning routinely includes outlining the normal organs, including kidneys, liver, small intestines, and spinal cord. The literature supports the fact that small bowel obstruction increases when radiation doses above 45 to 50 Gy are delivered. IMRT allows one to decrease the dose to the small bowel and other critical structures.

8.4 Planning Dose Prescription and Optimization Strategies

Target volumes and contours are transferred to the 3D treatment planning computer station and used to generate 3D conformal and IMRT plans (Fig. 1). A four-field conventional arrangement was utilized for the 3D planning process. Usually six to ten nonopposing beams with 0.25×0.5 cm minimum beam resolution are employed for IMRT. The IMRT plans are generated using inverse treatment planning techniques. In our institution originally we used CAD plan (Helios) and later Eclipse (Varian Medical Systems) treatment planning software for generation of IMRT plans (Fig. 2).

The PTV is specified to receive uniformly 100% of the dose and no more than 110% inhomogeneity within the target volume. Inverse planning (optimization process) may generate larger (than we are accustomed to) dose gradients across the PTV; Generally, high degrees of dose conformity and constraints on critical organs will cause large dose gradients within the PTV. The PTV of both plans is designed to receive 100% uniformity of dose with the 95% isodose line encompassing the CTV + 2.5 cm and no more than + 110% inhomogeneity within the target volume.

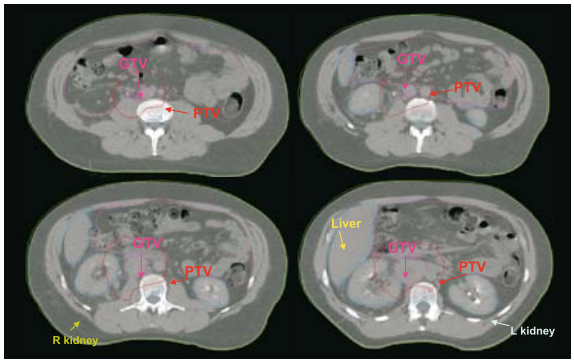

Fig. 1. Axial CT images demonstrating GTV (gross tumor volume), PTV (planning target volume) and organs at risk (kidneys, liver)

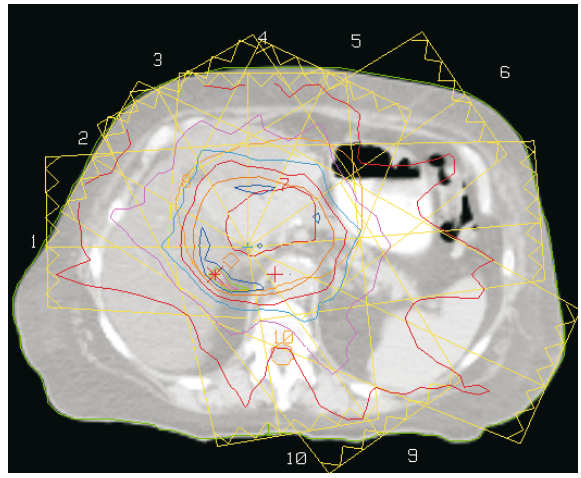

Fig. 2. CT axial image demonstrates multiple IMRT beam angles and dose-distribution for pancreatic tumor

In respect to pancreatic cancer, after a dose of 45 Gy, the treatment margins are reduced to include GTV with 1.5–2-cm margins in all dimensions except at the interface of the small bowel and GTV. For IMRT plans for retroperitoneal sarcomas, after 45 Gy the treatment margins are also reduced to 2 cm around the GTV in all dimensions. If there are MLC (multi-leaf collimator) restrictions and field widths larger than 15 cm, it is necessary to employ the technique of "beam splitting" [34, 35].

The GTV and OAR were all assigned an optimal dose, constraints, and priority. Tables 1 and 2 illustrate the various dose volume constraints and priorities for IMRT plans for pancreatic and retroperitoneal tumors. The PTV and GTV are usually assigned a constraint of 90% or greater while small bowel and other OAR were assigned a priority of 80% or greater. Isodose distributions, field arrangements, and DVHs (dose volume histogram) are calculated.

According to the treatment planning method introduced by the Emory group, clinical tumor volume as well as the nodal and soft tissue volumes are defined by the 3D outlining process and designated as the volume at risk approach, or VaRA. The description of this technique has been reported [36]. Instead of defining conventional field borders, the physician demands that the VaRA receive a certain minimum isodose coverage, in most cases 98% or greater. In employing the VaRA approach, the boost field margin at the in-

Table 1. IMRT inverse treatment planning algorithm constraint template for pancreatic cancer

Structure	Volume(%)	IMRT Constraint criteria (*Gy*)
Planning treatment volume (PTV)	100	Prescription dose: 50.4
		Minimum dose: 45
		Priority: 90%
Gross tumor volume (GTV)	100	Prescription dose: 61.2
		Minimum dose: 59.4
		Priority: 90%
Small bowel	100	Maximum dose: 45
	75	Maximum dose: 48
	50	Maximum dose: 50
	25	Maximum dose: 55
		Priority: 80%

Table 2. IMRT inverse treatment planning algorithm constraint template for retroperitoneal sarcoma

Structure	Volume(%)	IMRT Constraint(*Gy*)
Planning treatment volume	100	Prescription dose: 45–50.4
		Minimum dose: 45
		Priority: 90%
Gross tumor volume (GTV)	100	Prescription dose: 50.4
		Minimum dose: 45
		Priority: 90%
Small bowel	100	Maximum dose: 45
	75	Maximum dose: 48
	50	Maximum dose: 50
	25	Maximum dose: 55
		Priority: 80%
Kidney	100	Maximum dose: 12
	50	Maximum dose: 15
		Priority: 80%
Liver	100	Maximum dose: 30
	50	Maximum dose: 40
		Priority: 80%

terface between the small bowel and PTV is defined as the 95% or greater isodose level. This strategy allows a decrease in the volume of small bowel that is treated.

8.5 Clinical Experience and Trials to Define the Role of IMRT

After introduction of 3D-CRT and IMRT, radiation oncologists looked for ways to further minimize the doses to organs at risk (OAR) and improve dose conformity to the tumor and regional lymph nodes [37]. Clinical applications of IMRT strategies may allow us to minimize serious acute and long-term complications while increasing cure probability in cancer patients. Although anatomical variations must be taken into account, there are data to demonstrate superior dose conformity with IMRT plans for delivering dose to PTV and also less dose to the normal organs. A study from Emory University has considered several parameters when comparing treatment plans for IMRT and 3D conformal radiation in ten randomly selected patients treated for pancreatic cancer [36]. There was superior outcome in minimizing the dose to the small bowel and right kidney when employing the IMRT technique. The average dose delivered to small bowel was lower with the IMRT plan compared to 3D-CRT. Using Lyman-Kutcher models, normal tissue complication probability (NTCP) was 9.3 ± 6% with IMRT compared to 24.4 ± 18.9% with 3D-CRT ($P = 0.021$) (Table 3). The median volume of small bowel that received greater than either 50 or 60 Gy was also reduced with IMRT. The median volume of small bowel that exceeded 50 Gy was 19.2 ± 11.2% (range 3–45%) compared to 31.4 ± 21.3% (range 7–70%) for 3D-CRT ($P = 0.048$). The median volume of small bowel that received greater than 60 Gy was 12.5 ± 4.8% from IMRT compared to 19.8 ± 18.9% for 3D-CRT ($P = 0.034$). A comparison of DVHs between 3D-CRT and IMRT is presented in Fig. 3. The Emory group also reported treatment related toxicities from utiliza-

Table 3. Analysis of DVHs for small bowel comparing IMRT and 3D-CRT treatment plans for ten patients with adenocarcinoma of the pancreatic head

	IMRT Mean ±S D (*range*)	3D-CRT Mean ± SD (*range*)	*P*-value
Percent of SBV > 50 Gy	19.2 ± 11.2 (3.0–45.0)	31.4 ± 21.3 (7.0– 70)	0.048
Percent of SBV > 60 Gy	12.5 ± 4.8 (0.0–17.0)	19.8 ± 18.6 (4.0–62.0)	0.034
Dose to 1/3 of SB (Gy)	30.0 ± 12.9 (5.0–50.0)	38.5 ± 14.2 (8.0–56.0)	0.006
Percent of SB NTCP	9.3 ± 6.0 (0.3–23.2)	24.4 ± 18.0 (3.8–68.0)	0.021

SBV = small bowel volume
7 SB = small bowel
NTCP = normal tissue complication probability

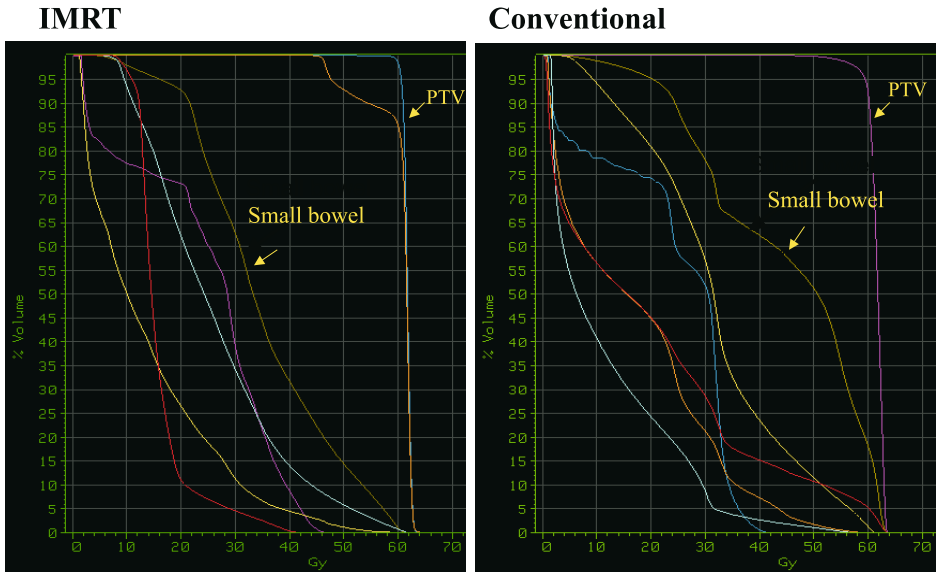

Fig. 3. Comparison of small bowel DVHs of IMRT and 3D-CRT plans

tion of IMRT for pancreatic cancer in a separate study. Most patients were treated with preoperative combined regimen with concomitant continuous infusion 5-FU. Dosimetric parameters were favorable for sparing normal organs. Based on the RTOG toxicity scale, most patients experienced only grade I or II gastrointestinal symptoms [38].

Bai et al. from China reported on dose-escalation with IMRT and concurrent chemotherapy for locally advanced pancreatic cancer [39]. Tolerable dose with their dose-fractionation regimen (60 Gy in 25 fractions) achieved good palliative effect. All patients had less then grade II gastrointestinal toxicity. There were no late gastrointestinal complications.

A phase I study of gemcitabine dose escalation in conjunction with hypofractionated radiotherapy for unresectable pancreatic tumors was tested by Crane and colleagues from MD Anderson Cancer Center [40]. Radiotherapy was started at 33 Gy in 11 fractions treating the primary tumor and lymphatics with an IMRT technique that included escalating the dose by 3 Gy. Patients also received concurrent gemcitabine starting at a dose of 350 mg/m^2. Because of dose-limiting toxicity due to myelosuppression and upper gastrointestinal symptoms, the regimen did not permit either radiation dose or gemcitabine dose escalation.

Ringash et al. from Princess Margaret Hospital in Canada had retrospectively re-planned 20 cases of gastric cancer and had physicians compare them with 3D-CRT plans [41]. IMRT plans were preferred in most cases based on better dose-volume histogram (DVH) data, which showed better target volume coverage and sparing of critical organs. Chen et al. [23] also retrospectively designed their study to compare 3D-CRT plans with IMRT for patients treated for hepato-cellular carcinoma. The IMRT plan was superior in limiting the dose to the spinal cord, but it had diverse dosimetric effects on the liver itself with reduction of normal tissue complication probability based on their model, but increase in mean dose as compared with 3D-CRT.

Hong et al. recently reported the use of IMRT for whole abdomen radiation and found bone marrow dose reduction and improved tumor coverage when compared to traditional whole abdomen treatment [34]. A five-field arrangement was used and the volume of pelvic bones receiving a dose > 21 Gy was reduced by 60% and tumor coverage improved by 11.8% with the use of IMRT. Clearly, the use of large fields, sometimes necessary for retroperitoneal sarcoma does not preclude employment of IMRT. The Emory University group reported their institutional experience with IMRT in the treatment of retroperitoneal sarcoma. They analyzed the benefits of IMRT with respect to the reduction of dose to critical OAR and enhanced tumor coverage: three patients presented with tumors < 10 cm, seven patients had tumors between 10 and 20 cm, and one patient had a tumor > 20 cm. Eight of the patients had primary tumors while the remaining three presented with recurrence of disease. Of the 11 patients, 2 had pelvic involvement and 9 of the 11 patients were treated with preoperative radiation followed by resection. Two patients were treated postoperatively.

Dose-volume histograms of patients planned and treated with IMRT to 50.4 Gy were compared with 3D-CRT treatment plans to the same dose. For all 11 patients, the IMRT plans with the VaRA approach were generated and compared with 3D-CRT. Tumor coverage, tumor dose received, and OAR toxicity are further illustrated in comparative DVHs in Figs. 4 and 5. For the same dose constraints assigned to liver, small bowel, kidney, and PTV, IMRT resulted in improved coverage of the PTV and reduced dose to critical organs at risk. The dif-

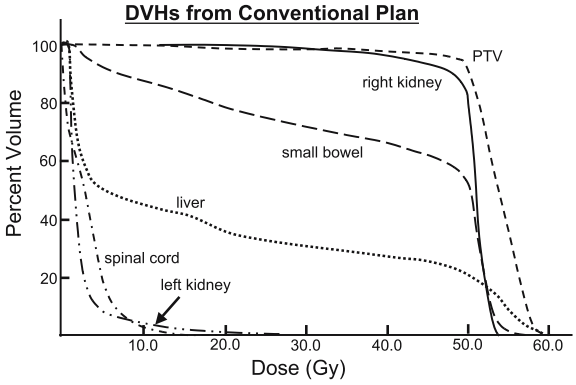

Fig. 4. Composite dose volume histogram (DVH) for 3D-CRT for retroperitoneal sarcoma for patient no. 8

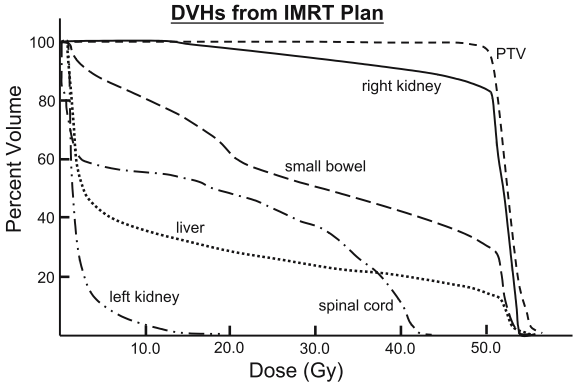

Fig. 5. Composite DVH of IMRT for retroperitoneal sarcoma for patient no. 8

Table 4. Analysis of DVHs for small bowel, left kidney, and liver comparing IMRT and 3D-CRT treatment plans for patients with retroperitoneal sarcoma

	IMRT Mean ± SD (*range*)	3D-CRT Mean ± SD (*range*)	*P*-value
Percent of small bowel > 30 Gy	43.1 ± 20.6 (20–92)	63.5 ± 25.2 (20–97)	0.043
Percent of small bowel > 50 Gy	8.8 ± 12.1 (0–31)	23.5 ± 34.4 (0–85)	0.073
Dose to 33% of small bowel	31.3 ± 7.9 (2–48)	40.6 ± 11.5 (2–54)	0.098
Percent of left kidney > 15 Gy	50.3 ± 43.9 (1–100)	55.1 ± 39.3 (3–100)	0.422
Percent of left kidney > 25 Gy	37.0 ± 40.6 (0–97)	49.0 ± 41.9 (0–100)	0.312
Dose to 33% of eft kidney	27.0 ± 19.0 (2–47)	28.7 ± 18.6 (2–47)	0.442
Percent of liver > 30 Gy	33.3 ± 26.3 (1–60)	49.6 ± 37.5 (13–100)	0.201
Percent of liver > 40 Gy	26.8 ± 23.1 (0–50)	46.0 ± 38.1 (11–99)	0.158
Dose to 33% of liver	27.0 ± 19.0 (10–48)	33.3 ± 19.2 (11–55)	0.289

ference was statistically significant for dose received to the small bowel and for the maximum and minimum dose received to the tumor volume. For the prescription dose to 50.4 Gy, both the maximum and minimum doses delivered to the PTV were significantly increased by 6 and 22%, respectively ($P = 0.011$, $P = 0.055$) resulting in better dose distribution within the tumor volume. In addition, tumor coverage as measured by the V95 (volume receiving 95% of the dose) was improved from 95.3% with conventional treatment to 98.6% with IMRT, although this value did not reach statistical significance. The mean average dose to the small bowel decreased from 36 Gy with conventional 3D conformal treatment to 27 Gy using IMRT. Furthermore, the mean dose to left kidney, liver, and spinal cord were all decreased with the use of IMRT. Although the difference in mean dose to the left kidney, liver, and spinal cord structures was not statistically significant due to the small sample size and large standard deviation, the overall trend favors IMRT. The doses received by clinically significant volumes of small bowel, liver, and kidney with both IMRT and 3D-CRT were also analyzed (Table 4). The volume of small bowel receiving >30 Gy was significantly decreased from 63.5 ± 25.2% (range 20–92%) to 43.1 ± 20.6% (range 20–92%) with IMRT compared with conventional treatment ($P = 0.043$). In addition, the median volume of small bowel that received a dose greater than 50 Gy and the dose delivered to one-third of the bowel volume was reduced with IMRT. The median volume of small bowel that received a dose greater than 50 Gy was 8.8 ± 12.1% with IMRT compared to 23.5 ± 34.4% for 3D-CRT ($P = 0.073$). The volume of left kidney that received a dose greater than 25 Gy decreased from 49 to 37% with the use of IMRT.

For patients with recurrent disease, recurrence varied from three to six years and on average was 4.3 years. The majority of the resected tumors were liposarcoma and most patients presented with Stage III disease. Only two patients did not present with Stage III disease; one had Stage I, and one had Stage II tumor. All 11 patients had complete excision of gross tumor. On review of pathologic specimens, four patients had microscopic positive margins and the remaining seven patients had negative margins. A total of eight patients required some element of organ removal (defined as removal of the kidney, spleen, pancreas, adrenals, or colon) with nephrectomy the most common. RTOG scoring was used to measure both acute and chronic toxicities for all patients. The most common symptoms were nausea and vomiting and less frequently diarrhea. Seven patients developed grade 2 nausea, three developed grade 2 diarrhea, and one pa-

tient with primary groin involvement experienced grade 2 skin toxicity. One patient, who had extensive liver involvement and received 3D-CRT, developed grade 3 liver toxicity six months after his radiation and was hospitalized for management of ascites. This patient had approximately 85% of his liver involved with gross tumor and consequently 67% of the whole liver received 30 Gy while 60% received 40 Gy with 3D-CRT. Currently, his ascites and hepatitis resolved and he remains free of disease recurrence. Other than this patient, there have been no other delayed toxicities related to radiation. No genitourinary or wound toxicities were observed and no treatment breaks were necessary. At a median follow-up of 58 weeks, there were no local recurrences and only one patient developed disease progression with distant metastasis in the liver.

At the University of Alabama, 14 patients with retroperitoneal sarcomas were treated with preoperative IMRT with PTV (GTV +1 to 1.5 cm), initially receiving 45 Gy in 25 fractions [42]. The tumor volume that was judged to be at highest risk for positive margins at surgical resection received a higher "boost" dose of 57.5 Gy. Of the 12 patients undergoing surgery, 11 had negative margins at resection and only one patient experienced grade III or greater toxicity. At a median follow up of 48 weeks there were no late toxicities and although 3 of the 11 patients developed disease progression, only 1 of these patients had a local recurrence. From a treatment planning perspective, the boost dose could theoretically have been escalated to 75.2 – 82.8 Gy while continuing to respect the OAR tolerance. These data as well as data from Princess Margaret on the use of IMRT in retroperitoneal sarcoma have shown encouraging clinical results and demonstrated feasibility of dose escalation [42, 43].

8.6 Future Directions

Additional studies with a larger number of patients and longer follow-up may be necessary to clearly demonstrate the benefit of IMRT for upper abdominal and retroperitoneal tumors in respect to superior tumor coverage and lowering treatment toxicity, as well as the potential for dose escalation for certain tumors. Dose escalation is a potential area of investigation for GI tumors as well as retroperitoneal sarcomas. Differential dose rate delivery with altered fractionation is another potential area that can be explored in the future. Studies evaluating IMRT in combination with novel chemotherapeutic and molecular agents are warranted because of the potential for IMRT to reduce GI toxicity and allow escalation of both the chemotherapy and radiation dosage. Organ motion studies along with incorporation of gated radiotherapy techniques may find have an important role in IMRT delivery for abdominal tumors.

References

1. Jemal A, Tiwari RC, Murray T et al. (2004) American Cancer Society. Cancer statistics, 2004. CA Cancer J Clin 54:8–29
2. Gastrointestinal Tumor Study Group (1987) Further evidence of effective adjuvant combined radiation and chemotherapy following curative resection of pancreatic cancer. Cancer 59:2006–2010
3. Whittington R, Bryer MP, Haller DG et al. (1991) Adjuvant therapy of resected adenocarcinoma of the pancreas. Int J Radiat Oncol Biol Phys 21:1137–1143
4. Willett CG, Lewandrowski K, Warshaw AL et al. (1993) Resection margins in carcinoma of the head of the pancreas. Implications for radiation therapy. Ann Surg 217:144–148
5. Coia LR, Mayerson RJ, Tepper JE (1995) Late effects of radiation therapy on the gastrointestinal tract. Int J Radiat Oncol Biol Phys 31:1213–1236
6. Emami B, Lyman J, Brown A et al. (1991) Tolerance of normal tissue to therapeutic irradiation. Int J Radiat Oncol Biol Phys 21:109
7. Talamonti MS, Catalano PJ, Vaughn DJ et al. (2000) Eastern Cooperative Oncology Group Phase I trial of protracted venous infusion fluorouracil plus weekly gemcitabine with concurrent radiation therapy in patients with locally advanced pancreas cancer: A regimen with expected early toxicity. J Clin Oncol 18:3384–3389
8. Andre T, Balosso J, Louvet C et al. (2000) Combined radiotherapy and chemotherapy (cisplatin and 5-fluorouracil) as palliative treatment for localized unresectable or adjuvant treatment for resected pancreatic adenocarcinoma: results of a feasibility study. Int J Radiat Oncol Biol Phys 46:903–911
9. Whittington R, Neuberg D, Tester WJ et al. (1995) Protracted intravenous fluorouracil infusion with radiation therapy in the management of localized pancreaticobiliary carcinoma: a phase I ECOG trial. J Clin Oncol 13:227–232
10. Hoffman PH, Lipitz S, Pisansky T (1998) Phase II trial of preoperative radiation therapy and chemotherapy for patients with localized, resectable adenocarcima of the pancreas: an Eastern Cooperative Oncology Group Study. J Clin Oncol 16:317–323
11. Brennan MF, Casper ES, Harrison LB et al. (1991) The role of multimodality therapy in soft-tissue sarcoma. Ann Surg 214:328–338
12. Stoeckle E, Coindre JM, Bonvalot S et al. (2001) Prognostic factors in retroperitoneal sarcoma: a multivariate analysis of a series of 165 patients of the French Cancer Center Federation Sarcoma Group. Cancer 92:359–368
13. Zhang G, Chen KK, Manivel C, Fraley EE (1989) Sarcomas of the retroperitoneum and genitourinary tract. J Urol 141:1107–1110
14. Storm FK, Mauve DM (1991) Diagnosis and management of retroperitoneal soft-tissue sarcoma. Ann Surg 214:2–10
15. van Doorn RC, Gallee MP, Hart AA et al. (1994) Resectable retroperitoneal soft tissue sarcomas. The effect of extent of resection and postoperative radiation therapy on local tumor control. Cancer 73:637–642
16. McGrath PC, Neifeld JP, Lawrence W Jr et al. (1984) Improved survival following complete excision of retroperitoneal sarcomas. Ann Surg 200:200–204
17. Heslin MJ, Lewis JJ, Nadler E et al. (1997) Prognostic factors associated with long-term survival for retroperitoneal sarcoma: implications for management. J Clin Oncol 15:2832–2839
18. Glenn J, Sindelar WF, Kinsella T et al. (1985) Results of multimodality therapy of resectable soft-tissue sarcomas of the retroperitoneum. Surgery 97:316–325

19. Jaques DP, Coit DG, Hajdu SI, Brennan MF (1990) Management of primary and recurrent soft-tissue sarcoma of the retroperitoneum. Ann Surg 212:51–59
20. Catton CN, O'Sullivan B, Kotwall C et al. (1994) Outcome and prognosis in retroperitoneal soft tissue sarcoma. Int J Radiat Oncol Biol Phys 29:1005–1010
21. Fein DA, Corn BW, Lanciano RM et al. (1995) Management of retroperitoneal sarcomas: does dose escalation impact on locoregional control? Int J Radiat Oncol Biol Phys 31:129–134
22. Tepper JE, Suit HD, Wood WC et al. (1984) Radiation therapy of retroperitoneal soft tissue sarcomas. Int J Radiat Oncol Biol Phys 10:825–830
23. Chen GT, Jiang SB, Kung J et al. (2001) Abdominal organ motion and deformation: Implications for IMRT. Int J Radiat Oncol Biol Phys 51:210
24. Bussels B, Goetals L, Feron M et al. (2003) Respiration-induced movement of the upper abdominal organs: a pitfall of the three-dimensional conformal radiation treatment of pancreatic cancer. Radiother Oncol 68:69–74
25. Batler JM, Lam KL, McGinn CJ et al. (1998) Improvement of CT-based treatment planning models of abdominal targets using static exhales imaging. Int J Radiat Oncol Biol Phys 41:939–943
26. Horst E, Micke O, Moustakis C et al. (2002) Conformal therapy for pancreatic cancer: variation of organ position due to gastrointestinal distention-implications for treatment planning. Radiology 222:681–686
27. Tepper J, Nardi G, Sutt H (1976) Carcinoma of the pancreas: review of MGH experience from 1963 to 1973. Analysis of surgical failure and implications for radiation therapy. Cancer 37:1519–1524
28. Cubilla AL, Fortner J, Fitzgerald PJ (1978) Lymph node involvement in carcinoma of the head of the pancreas area. Cancer 41:880–887
29. Griffin JF, Smalley SR, Jewell W et al. (1990) Patterns of failure after curative resection of pancreatic carcinoma. Cancer 66:56–61
30. Johnstone PA, Sindelar WF (1993) Lymph node involvement and pancreatic resection: correlation with prognosis and local disease control in a clinical trial. Pancreas 8:535–539
31. Smith RG, Keller JW, Landry JC et al. (1996) Anatomic variation of extrahepatic biliary tree structures: importance in treatment planning for radiation therapy. Radiology 201:271–273
32. Kresl J, Bonner JA, Bender CE et al. (1997) Postoperative localization of porta hepatic and abdominal vasculature in pancreatic malignancies: Implications for postoperative radiotherapy planning. Int J Radiat Oncol Biol Phys 39:51–56
33. Willett CG, Suit HD, Tepper JE et al. (1991) Intraoperative electron beam radiation therapy for retroperitoneal soft tissue sarcoma. Cancer 68:278–283
34. Hong L, Alektiar K, Chui C et al. (2002) IMRT of large fields: whole-abdomen irradiation. Int J Radiat Oncol Biol Phys 54:278–289
35. Wu Q, Arnfield M, Tong S et al. (2000) Dynamic splitting of large intensity-modulated fields. Phys Med Biol 45:1731–1740
36. Landry JC, Yang GY, Ting JY et al. (2002) Treatment of pancreatic cancer tumors with intensity-modulated radiation therapy (IMRT) using the volume at risk approach (VaRA): employing dose-volume histogram (DVH) and normal tissue complication probability (NTCP) to evaluate small bowel toxicity. Med Dosim 27:121–129
37. Fine RM, Elshaikh R, Pelley MR et al. (2001) Treatment outcome of 3D non-coplanar conformal radiotherapy and 5FU for resected pancreatic carcinoma. Int J Radiat Oncol Biol Phys 51(suppl 1)1:269
38. Landry J, Esiashvili N, Ting J, Staley C (2001) Intensity modulated radiation therapy employing the volume at risk approach to minimize small bowel and renal toxicity when treating patients with locally advanced pancreatic carcinomas. Int J Radiat Oncol Biol Phys 51(suppl 1):270
39. Bai YR, Wu GH, Guo WJ, Wu XD, Yao Y, Chen Y, Zhou RH, Lu DQ (2003) Intensity modulated radiation therapy and chemotherapy for locally advanced pancreatic cancer: results of feasibility study. World J Gastroenterol 9:2561–2564
40. Crane CH, Antolak JA, Rosen II et al. (2001) Phase I study of concomitant gemcitabine and IMRT for patients with unresectable adenocarcinoma of the pancreatic head. Int J Gastrointest Cancer 30:123–132
41. Ringash J, Perkins G, Lockwood G et al. (2003) IMRT for adjuvant radiation in gastric cancer: A preferred plan? Int J Radiat Oncol Biol Phys 57(suppl 2):S381–S382
42. Fiveash JB, Hyatt MD, Caranto J et al. (2002) Preoperative IMRT with dose escalation to tumor subvolumes for retroperitoneal sarcomas: initial clinical results and potential for future dose escalation. Int J Radiat Oncol Biol Phys 54(suppl 1):140
43. Haycocks T, Kelly V, Islam M, O'Sullivan B, Swallow CJ, Catton CN (2001) High resolution, intensity modulated radiation therapy (IMRT) for retroperitoneal soft tissue sarcoma (RPS). CTOS Annual Meeting Posters. Radiation Oncology 2001

Prostate IMRT

Mark K. Buyyounouski, Eric M. Horwitz, Robert A. Price Jr, Steve J. Feigenberg, Alan Pollack

9

Contents

9.1 Clinical Problem

To achieve the greatest local control with minimal toxicity is the chief objective in the treatment of clinically localized prostate cancer. Dose escalation, first recognized with conventional techniques [1–4], has been shown to improve local control using three- dimensional conformal radiation therapy (3D-CRT). Subsequently, objective parameters for determining normal tissue complication risk have been defined with computed tomography based treatment planning. With dose well established as a strong determinant of biochemical control (freedom from a rising prostate specific antigen level), intensity modulated radiation therapy (IMRT) has been the next step in the pursuit of greater conformality to enable further dose escalation and sparing of normal tissues. Preliminary results with IMRT suggest that the gains in disease control and toxicity reduction may be significant. To be effective, however, the implementation of IMRT requires accurate targeting of the prostate and the selection of appropriate treatment parameters.

9.1.1 Dose Escalation

A benefit in disease control has been demonstrated in several sequential dose escalation studies of 3D-CRT and IMRT [5–10], using biochemical failure as the surrogate end-point. Biochemical failure, or a rising PSA profile, has been standardized by the American Society for Therapeutic Radiology and Oncology (ASTRO) as three consecutive rises in prostate specific antigen (PSA) in three to six month intervals with backdating to the midpoint in time between the PSA nadir and the first rise [11]. Biochemical failure appears to be a robust correlate of distant metastasis and disease-specific death [12]. The correlation of biochemical failure with overall survival has been less clear [9, 13, 14]; the competing risk of death from intercurrent illness is most likely the cause. In light of the long natural history of clinically localized prostate cancer, biochemical failure is a valid early endpoint for use in dose escalation studies. Overall, these studies have shown an improvement in freedom from biochemical failure (FFBF) with dose escalation for men treated with external beam radiation therapy. When subdividing men into low, intermediate and high risk groups based on clinical features, the results suggest that the benefit is not universal for all dose levels.

Two commonly used three-tier risk stratification schemes are shown in Table 1. The single factor high risk model used at Fox Chase Cancer Center (FCCC) (modeled after D'Amico et al. [15]) classifies those with Gleason Score 8 to 10, initial PSA (iPSA) >20 ng/ml orT3/T4 disease (based on digital rectal exam) as high

Table 1. The single and double high risk factor models

	Single Factor	Double Factor
Low risk	PSA ≤ 10 GS 2–6 T1–T2c[a]	PSA ≤ 10 GS 2–6 T1–T2c
Intermediate risk	Presence of 1 or more[b]	Presence of 1
	PSA > 10 to 20 GS 7	PSA > 10 GS ≥ 7 ≥ T3
High risk	Presence of 1 or more	Presence of 2 or 3
	PSA > 20 GS 8 – 10 ≥ T3	PSA > 10 GS ≥ 7 ≥ T3

The single and double factor high risk models are patterned after that described by D'Amico et al. [15] and Zelefsky et al. [39] [a]T2b has sometimes been considered intermediate risk and T2c has sometimes been considered intermediate or high risk (see [5, 15]). In the Fox Chase database, these patients have about the same prognosis as patients with T2a disease in univariate and multivariate analysis, and so have been grouped in a favorable category here; [b]No high risk factors present. Modified from Chism et al. [25], with permission

risk. Included as intermediate risk are those with an iPSA 10 to 20 ng/ml or Gleason 7 disease, as long as no high risk factors are present. An alternative three-tier system used at Memorial Sloan- Kettering is the double factor high risk model [7]. In a comparison of these models by Chism et al. [16] the FCCC model resulted in more homogeneous groups. Table 2 summarizes the results of some of the dose escalation studies that subdivide patients by risk group. The greatest benefit is observed for intermediate risk patients when doses are escalated above 70 Gy. Men with low risk disease appear to benefit from doses as high as 70 Gy. Doses above 70 Gy in favorable patients has not consistently improved outcome. When a dose response in favorable patients has been observed and doses ≥ 75.6 Gy were used, the comparison group contained patients treated to < 70 Gy. The MSKCC sequential dose escalation series was recently presented by Zelefsky et al. [17] and with longer follow-up suggests that favorable risk patients benefited from an increase in dose from 70 to > 75.6 Gy. Perhaps with longer follow-up and, more importantly, randomized trials, others will confirm the importance of dose above 70 Gy in favorable prostate cancer patients. Patients with high risk features also benefit less than intermediate risk patients from purely increasing the dose from 10 Gy to ≥ 75.6 Gy [7, 8].

Unfortunately, sequential dose escalation trials are sensitive to other changes over time unbeknownst to investigators. For example, there is stage migration. There has been a shift towards more favorable disease as PSA and ultrasound have been used to direct prostate biopsies [18–20]. Similarly, imaging modalities such as ultrasound and magnetic resonance imaging (MRI) used for staging can cause stage migration [21–24]. Gleason scoring has also been shown to have shifted to higher values over time [25] while T-stage and initial PSA (iPSA) have decreased. The year of treatment itself has been shown to be a predictor of FFBF throughout the PSA era independent of age, race, clinical T stage, pretreatment PSA, biopsy Gleason score, use of

Table 2. Dose escalation studies

Author (institution)	Year	n	Risk	Five-year results % FFBF (Dose)	% FFBF (Dose)	*p*
Lyons et al. (Cleveland Clinic)	2000	738	Low High	81 (< 72 Gy) 41 (< 72 Gy)	98 (≥ 72 Gy) 75 (≥ 72 Gy)	0.02 0.001
Hanks et al. (FCCC)	2000	618	Low[b] Int High	86 (< 70 Gy) 29 (< 71.5 Gy) 8 (< 71.5 Gy)	80 (≥ 70 Gy) 66 (≥ 71.5 Gy) 29 (≥ 71.5 Gy)	NS < 0.05 < 0.05
Pollack et al.[a] (MDACC)	2000	1213	Low Low Int Int High High	84 (< 67 Gy) 91 (> 67 – 77 Gy) 55 (≤ 67 Gy) 79 (> 67 – 77 Gy) 27 (≤ 67 Gy) 47 (> 67 – 77 Gy)	91 (> 67 – 70 Gy) 100(> 77 Gy) 79 (> 67 – 76 Gy) 89 (> 77 Gy) 47 (> 67 – 77 Gy) 67 (> 77 Gy)	NS NS 0.0001 NS 0.0001 0.016
Zelefsky et al. (MSKCC)	2001	1100	Low Int High	77 (≤ 70 Gy) 50 (≤ 70 Gy) 21 (≤ 70 Gy)	90 (≥ 75.6 Gy) 70 (≥ 75.6 Gy) 47 (≥ 75.6 Gy)	0.05 0.001 0.002

[a]Four year results (published in a book chapter) [b]Based on pre-treatment PSA Int = intermediate; MSKCC = Memorial Sloan-Kettering Cancer Center; FCCC = Fox Chase Cancer Center; MDACC = M.D. Anderson Cancer Center; bFFF = biochemical freedom from failure Modified from The prostate: In: Radiation oncology, rationale, technique, results, 8th edn. JD Cox, KK Ang (eds), Mosby, St. Louis, MO 2003, with permission

AD, and radiation dose [26]. Together, these factors have a great impact upon the interpretation of sequential dose escalation studies. Randomized dose escalation trials eliminate such time dependent factors.

An early randomized dose escalation trial was conducted at the Massachusetts General Hospital comparing 67.2 Gy to 75.6 CGE (Cobalt-Gray Equivalent) utilizing a proton boost. This was a pre-PSA era trial that showed a significant increase in local control for the high dose arm but did not show a significant improvement in disease freedom or survival. Subgroup analysis revealed improved disease freedom in the Gleason 8–10 subset that received a higher dose. Most of the patients in the trial would be considered to have high-risk prostate cancer. Recently, an interim analysis was presented of a randomized dose escalation trial conducted by the Proton Radiation Oncology Group (PROG) in the PSA era for men with low and intermediate risk prostate cancer [151]. In this trial and previous studies, dose escalation has the greater effect on those with intermediate risk factors. The favorable-risk patients in the PROG trial did worse than described in retrospective series, casting some doubt about the extent of the gains observed in this risk group.

A trial from M.D. Anderson Cancer Center is the only modern randomized trial in the PSA era that has reached maturity and has been published [9]. Three-hundred and one assessable patients were randomized, with 150 receiving 70 Gy and 151 receiving 78 Gy (dose prescribed to isocenter). The CTV consisted of the prostate and seminal vesicles. The 70 Gy patients were treated with a conventional four-field box, with a field reduction after 46 Gy. The 78 Gy patients also received a four-field box to 46 Gy and then a six-field conformal boost to 78 Gy. The margins (CTV to block edge) on the conformal boost were 0.75 – 1.0 cm posteriorly and superiorly, and 1.25 – 1.5 cm anteriorly and inferiorly. The freedom from failure results (based mainly on biochemical criteria) supported the conclusions of the sequential dose escalation trials. The freedom from biochemical failure (FFBF) rates were significantly higher for those randomized to 78 Gy (70 vs 64% at six years, $p = 0.03$). The greatest benefit was observed in men with a pretreatment PSA > 10 ng/mL who had a 19% absolute gain in FFBF at six years when treated to 78 Gy (Fig. 1). This translated into a borderline reduction in distant metastasis (2 vs 12% at six years, $p = 0.056$), although there were only eight patients with distant metastasis at the time of the analysis. For patients with a pretreatment PSA 10 ng/mL, no dose-related difference in FFBF or any other endpoint were observed. Larger clinical trials powered to detect differences in clinical disease and survival endpoints, such as distant metastasis and cause specific death are needed.

The application of the ASTRO definition has led to many advances in understanding and treating prostate cancer because it has provided a much needed standardization of PSA as an endpoint. At the same time, much has been learned regarding the PSA profiles of men following treatment with radiotherapy and some deficiencies in the ASTRO definition have come to attention. The ASTRO definition is based on three consecutive rises at follow-up of three- to six-month intervals, with backdating of the failure to the midpoint between the nadir and the first rise in PSA [11]. Under these conditions, 20 – 30% of patients who receive neoadjuvant or adjuvant androgen deprivation therapy are misclassified as biochemical failures because of a transient rise in PSA prior to stabilization after stopping androgen deprivation [27]. Backdating distorts the shape of Kaplan-Meier curves causing a flattening at later time points, resulting in falsely high estimates of FFBF

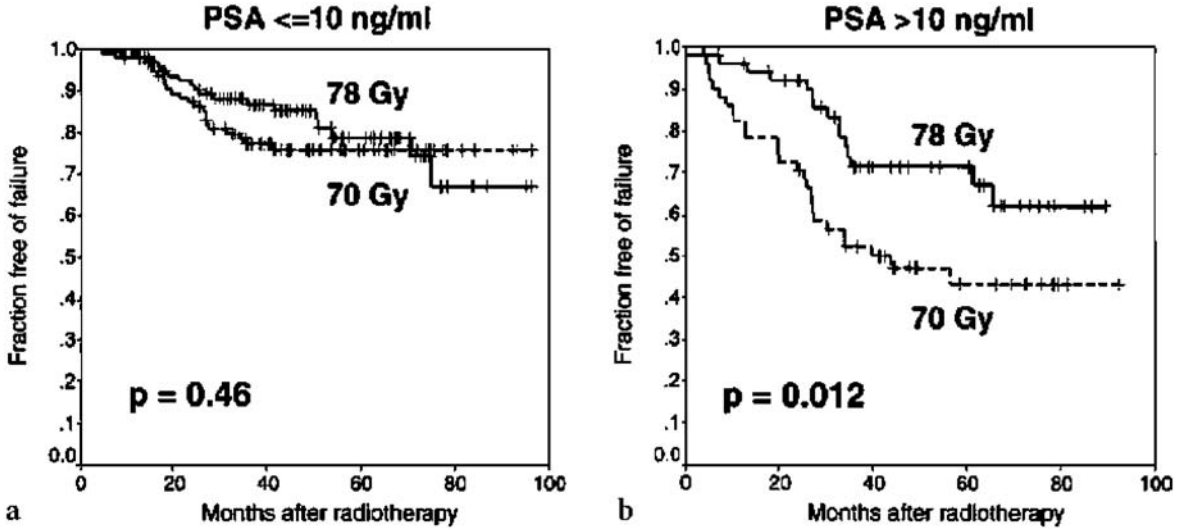

Fig. 1. (a),(b) Freedom from biochemical failure Kaplan-Meier results of the M.D. Anderson randomized trial. The *left and right figures* display the patients with a pretreatment PSA ≤ 10 and > 10 ng/ml, respectively. From Pollack et al. [9], with permission

that is exacerbated by short follow-up [28, 29]. These concerns have prompted investigations of alternative definitions [13, 29–34]. The nadir plus 2 ng/ml definition requires a PSA rise of 2 ng/ml above the PSA nadir and eliminates the effects of backdating and appears to be a better correlate of clinical outcome, as compared to the ASTRO definition [13, 32, 33].

9.1.2 Dose Escalation and Morbidity

The close relationship of dose and volume to late rectal toxicity are well-established [9, 35–45]. It has been more difficult to demonstrate a well-defined bladder dose-volume relationship for morbidity, probably due to the inconsistent volume of the bladder at simulation, day-to-day (interfraction) variation during treatment, and the requirement for long follow- up due to the late onset of symptoms [46]. Radiation dose to the erectile tissues, the penile bulb and corporal bodies, may also correlate with the development of erectile dysfunction following treatment [47,48] but, large prospective series using standardized measures of erectile function are needed.

The associations of radiation dose to rectal toxicity are summarized in Table 3. Higher radiation dose is related to increased grade 2 or higher rectal reactions. Remarkably similar conclusions have been drawn by multiple groups. Only the recently described randomized trial results from the Netherlands [45] has yet to show an effect of dose because follow-up has been short. The significant increase in the rectal complication risk found in patients who received the higher dose in the MDACC randomized trial was not demonstrated until the median follow-up was five years (Fig. 2).

Table 3. Dose and rectal toxicity

Author	Year	Dose	GI Toxicity
Smit	1990	≤ 70 Gy	22%
		$>70-75$ Gy	20%
		>75 Gy	60%
Shipley	1995	≤ 67.2 Gy	12% (10-year act)
		>75.6 CGE	32%
Lee	1996	<72 Gy	7%
		72–76 Gy	16%
		>76 Gy	23%
Zelefsky	1998	≤ 70.2 Gy	6%
		>75.6 Gy	17%
Pollack	2002	70 Gy	12%
		78 Gy	26%
Peeters	2005	68 Gy	23%
		78 Gy	27% (3-year cumulative)

Act = actuarial Reproduced from IMRT for Prostate cancer: In: Intensity modulated radiation therapy: a clinical perspective. AJ Mundt, JC Roeske (eds), BC Decker Inc, Hamilton, Ontario, Canada 2004, with permission

The effect of rectal volume on the associations of radiation dose to rectal toxicity is displayed in Table 4. These findings demonstrate that the volume of the rectum exposed to a specific radiation dose level is as important as the dose prescribed. For a given dose, rectal complications are lower for smaller volumes irradiated. The implication is that high radiation doses (≥ 75.6 Gy) may be used when specific dose-volume criteria are applied

Table 4. Rectal volume and rectal toxicity

Author	Year	Dose	Rectum	GI Toxicity
Benk	1993	67 – 76 CGE	$V76_{CGE} < 40\%$ ARW	19% (40 mo Act)[a]
		67 – 76 CGE	$V76_{CGE} \geq 40\%$ ARW	71%
Lee	1996	74 – 76 Gy	Rectal Block	10% (18 mo Act)
		74 – 76 Gy	No Block	19%
Boersma	1998	70 Gy	$\leq 30\%$	0% (crude)
		70 Gy	$>30\%$	9%
Daernaley	1999	64 Gy	3D-CRT	8% (5 yr Act)
		64 Gy	Conventional RT	18%
Pollack	2002	70 – 78 Gy	$V70_{Gy} \leq 25\%$	16% (6 yr Act)
		70 – 78 Gy	$V70_{Gy} > 25\%$	46%
Kupelian	2002	78 Gy	≤ 15 cc	5% (24 mo Act)
		78 Gy	>15 cc	22%
Fiorino	2003	70 – 78 Gy	$V50_{Gy} \leq 66\%$	8%
		70 – 78 Gy	$V50_{Gy} > 66\%$	32%
		70 – 78 Gy	$V70_{Gy} \leq 30\%$	8%
		70 – 78 Gy	$V70_{Gy} > 30\%$	24%

mo = months; Act = actuarial; ARW = anterior rectal wall; [a]Any rectal bleeding Reproduced from IMRT for Prostate Cancer: In Intensity Modulated Radiation Therapy: A Clinical Perspective. AJ Mundt, JC Roeske (eds), BC Decker Inc, Hamilton, Ontario, Canada 2004, with permission.

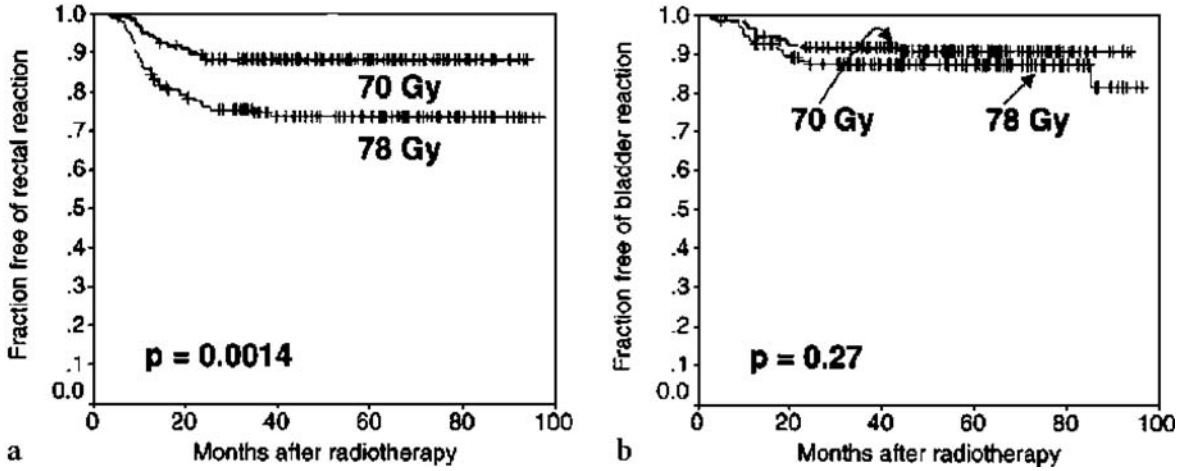

Fig. 2a,b. Kaplan-Meier plots of the risk of grade 2 or higher: (a) rectal toxicity; (b) bladder toxicity. From Pollack et al. [9],with permission

to limit the rectal exposure. The formulation of such criteria has been essential for prostate cancer dose escalation with IMRT. The adoption of universal thresholds that should be used in IMRT planning, however, has not occurred; the rectal dose-volume criteria vary from one series to another. In implementing planning constraints that have been published by a particular investigative team, one must carefully attempt to mimic all aspects of the features used in the planning process. These features include, for example, how the normal structures were identified (i.e. whole rectum vs rectal wall; entire rectal length vs a smaller segment).

The potential for erectile dysfunction is an important consideration for many men when selecting treatment for favorable, clinically localized prostate cancer [49]. As many as 80% of the 230000 new prostate cancer cases estimated in the United States for 2004 will be low or intermediate risk for distant disease [50, 51]. Approximately 30% of these cases (55000 men) will be treated with radiation therapy [52]. Erectile dysfunction (ED) or "the inability to attain and/or maintain penile erection sufficient for satisfactory sexual performance" [53], occurs in over 50–60% of men following treatment with external beam radiotherapy [54,55]. This translates into roughly 33000 new cases of ED in the United States related to radiation therapy for prostate cancer. For many men this is important. When asked if they would rather choose a treatment with a 90% five-year survival and 90% risk of developing ED or a 80% survival with a 40% risk of ED, 68% of men in a study by Singer et al. [49] would choose the latter.

Escalating radiation doses received by erectile tissues, the penile bulb and corporal bodies (Fig. 3), have been suggested to contribute to the development of post-radiation erectile dysfunction following treatment for prostate cancer [47, 48, 56–58]. Normal erectile function is multifactorial, dependent upon endocrinologic, neurologic and vascular mechanisms [59], but can be briefly summarized as follows. During sexual stimulation the neurotransmitters (i.e. nitric oxide) cause an increase in arterial flow to the penile bulb and corporal bodies via smooth muscle relaxation in penile arterioles. This in turn causes mechanical compression and venous occlusion, increased intracavernosal pressures, and an erect state. A reduction of nitric oxide synthase-containing nerve fibers in the smooth muscle of penile arterioles [60] together with corporal fibrosis and vasculopathy [61] are likely for the arteriogenic

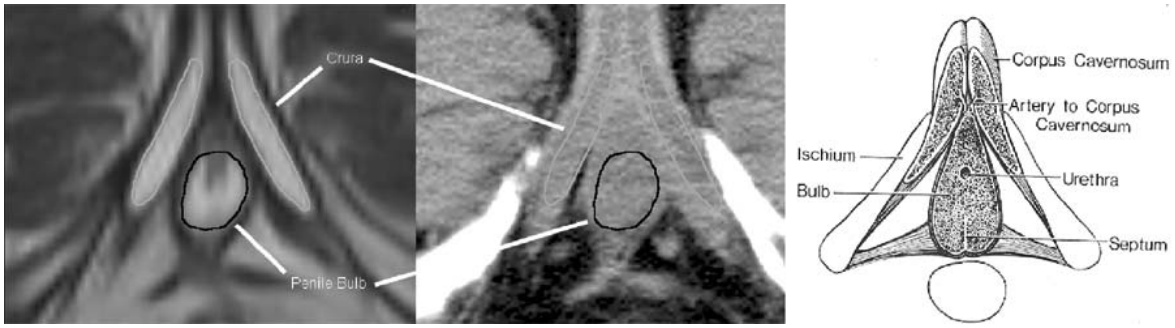

Fig. 3. Penile bulb and corporal body anatomy. Modified from Buyyounouski et al. [150] and Hricak et al. [137], with permission

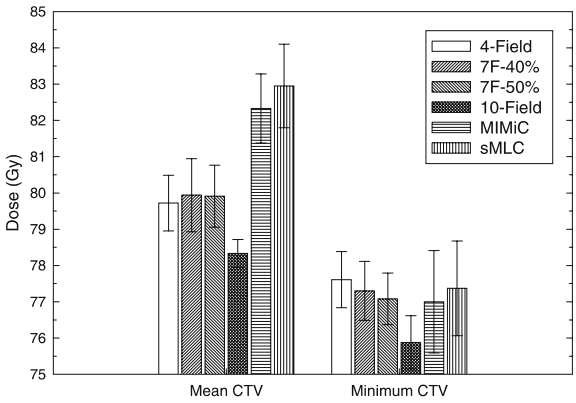

Fig. 4. Comparison of mean and minimum CTV doses in six different plans, four 3D-CRT and two IMRT. The CTV included the prostate and proximal seminal vesicles and was identical for all of the different plans. The prescription for five of the plans was for the PTV to receive 75.6 Gy; the ten-field plan was prescribed to 78 Gy to the isocenter, as was done in the MDACC randomized trial. Abbreviations: 4-field = four-field conventional; 7-field 40% = seven-field technique with 40% weighting of laterals; 7-field 50% = seven-field technique with 50% weighting of laterals; 10-field=four- field conventional followed by a six-field conformal boost; MIMiC = Peacock MIMiC system IMRT; sMLC = ten-field segmented multileaf collimation IMRT; CTV clinical target volume. Reproduced from IMRT for prostate cancer: In: Intensity modulated radiation therapy: a clinical perspective. AJ Mundt, JC Roeske (eds), BC Decker Inc, Hamilton, Ontario, Canada 2004, with permission

nature of erectile dysfunction following radiation therapy [62].

As discussed, with the use of dose-volume histograms (DVH) constraints, IMRT has been shown to reduce rectal toxicity compared to 3D-CRT [7,63]. Similarly, IMRT may improve ED rates by lowering both the volume of

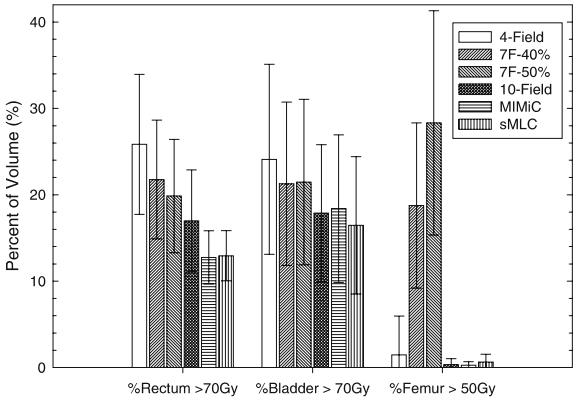

Fig. 5. Comparison of the percentages of the rectum treated to $\geq$ 70 Gy, bladder treated to $\geq$ 70 Gy, and femoral heads treated to $\geq$ 50 Gy. The prescription for five of the plans was for the PTV to receive 75.6 Gy; the ten-field plan was prescribed to 78 Gy to the isocenter, as was done in the MDACC randomized trial. Abbreviations as in Fig. 3. Reproduced from IMRT for prostate cancer: In: Intensity modulated radiation therapy: a clinical perspective. AJ Mundt, JC Roeske (eds), BC Decker Inc, Hamilton, Ontario, Canada 2004, with permission

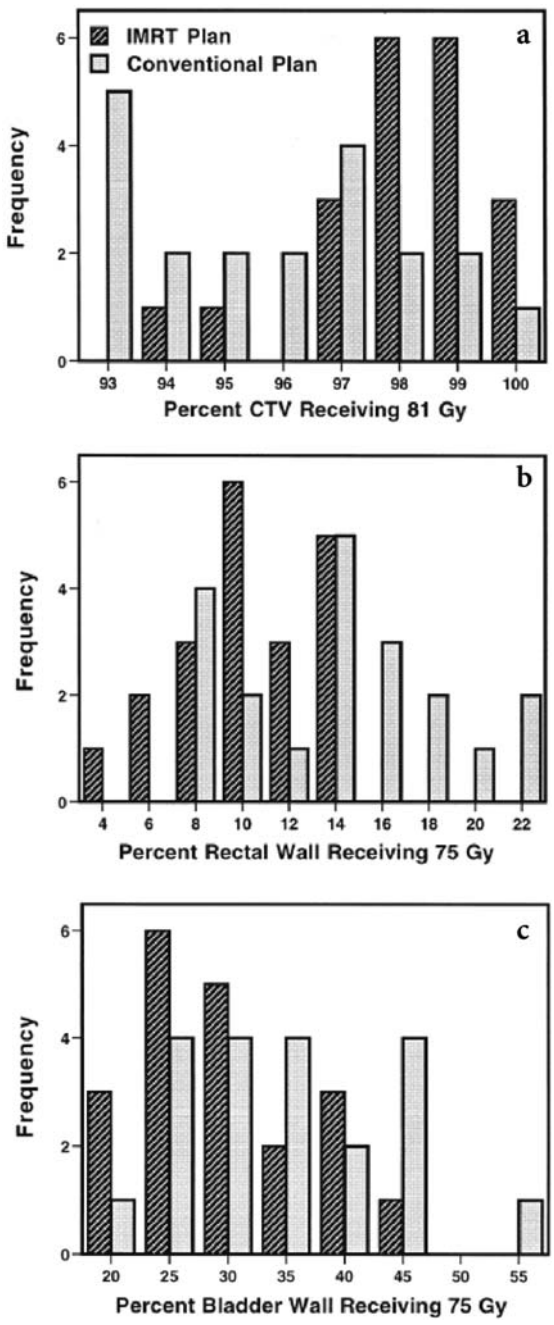

Fig. 6a–c. Histograms of: (a) the percent clinical target volume (CTV) receiving 81 Gy; (b) the percentages of the rectal wall carried to 75 Gy; (c) the percentages of the bladder wall receiving 75 Gy. Data were derived from dose volume histograms generated from treatment plans of 20 randomly selected patients planned simultaneously from conventional 3D-CRT and IMRT. Differences in the frequency distributions shown in (a), (b) and (c) are significant ($P < 0.01$). Reproduced from Zelefsky et al. [69], with permission

erectile tissue irradiated and the dose delivered compared to 3D-CRT [64, 65, 152, 153]. We have described a technique, discussed in detail below, that limits the doses received by the penile bulb and corporal bodies

using IMRT without compromising prostate coverage, dose homogeneity, rectal DVH criteria or overall treatment time [66]. The clinical significance of erectile tissue constraints is being tested in a randomized clinical trial at Fox Chase Cancer Center.

9.1.3 Target Dose Conformality

IMRT offers the greatest gains over 3D-CRT for the treatment of unsymmetrical, complex volumes. From an anatomical perspective, the benefit of IMRT in the treatment of the prostate may be low because it is a nearly elliptical structure. Dong and colleagues [63] systematically investigated this question in patients with favorable risk prostate cancer that did not have much of the seminal vesicles outlined. They rationalized that the inclusion of the seminal vesicles in this test might give IMRT an advantage. The conditions used, therefore, were heavily weighted in favor of 3D-CRT. The same CTV/PTV margins were used in all plans. Two different IMRT delivery methods, Peacock serial tomotherapy technique via a binary multileaf collimator (MIMiC) system and a ten-field step-and-shoot multileaf collimator (sMLC) system, were compared to four conformal plans. The conformal plans included a four-field technique, two seven-field techniques with different weightings from the laterals (40% and 50%) and the ten-field conformal boost technique used in the MDACC randomized dose escalation trial (four-field conventional followed by a six-field conformal boost). The prescription to the PTV was 75.6 Gy, with the exception of the MDACC protocol method, which was prescribed to 78 Gy to the isocenter as was done in the original trial. The 78 Gy isocenter plan actually had a lower CTV mean dose (Fig. 4). Figure 4 shows that the highest mean CTV doses were achieved in the two IMRT plans. Figure 5 demonstrates that the IMRT plans also resulted in the lowest percentages of the rectum treated to over $\geq$ 70 Gy, bladder treated to $\geq$ 70 Gy, and femoral heads $\geq$ 50 Gy. The two IMRT plans were nearly identical in terms of the DVH parameters. The benefit of IMRT over 3D-CRT was both in the achievement of higher doses to the CTV and limitation of exposure of the nearby normal tissues to the higher radiation doses. Others have come to similar conclusions [67–70].

Zelefsky et al. [69] from Memorial Sloan-Kettering found a similar benefit to IMRT over 3D-CRT. Twenty randomly selected patients were planned with both 3D-CRT and IMRT to compare target conformality and normal tissue sparing using DVH analysis. Figure 6A shows that significantly larger volumes of the CTV received the prescribed dose of 81 Gy with IMRT with only one plan receiving < 95% of the prescribed dose compared to seven 3D-CRT plans. Overall, $98 \pm 2\%$ of the CTV received 81 Gy with IMRT compared to $95 \pm 2\%$ with 3D-CRT plan ($p < 0.01$). With results similar to that

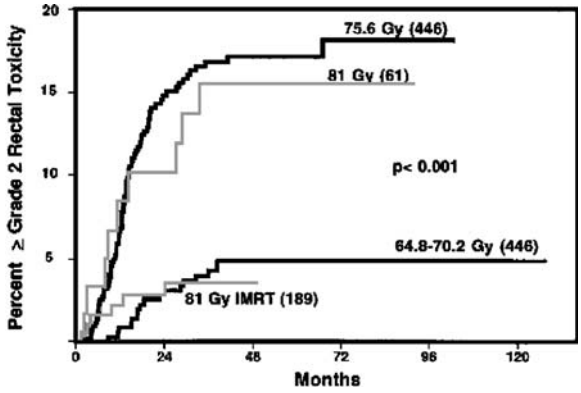

Fig. 7. Effect of IMRT on grade 2 or higher rectal complications. These data are from the MSKCC group sequential prospective dose escalation study. The ≥grade 2 rectal reactions are shown for patients treated with 3D-CRT to 64.8 – 70.2 Gy, 75.6 Gy and 81 Gy, and with IMRT to 81 Gy. From Zelefsky et al. [7], with permission

of Dong et al. [63], the percentages of the rectal wall (Fig. 6B) and bladder wall (Fig. 6C) volumes receiving high doses (75 Gy) were significantly decreased with IMRT ($p < 0.01$). The clinical results from Memorial Sloan-Kettering [7, 71] further substantiate their dosimetric conclusions that IMRT is superior to 3D-CRT in reducing rectal toxicity at 81 Gy (Fig. 7), while maintaining high levels of freedom from biochemical failure (Fig. 8).

IMRT has the potential to treat the pelvic lymph nodes with greater sparing of the bladder, rectum and small bowel than conventional and 3D conformal whole pelvic techniques [72–74]. Radiobiologic model predictions of normal tissue complication probability (NTCP) for rectum, bladder and small bowel following treatment designed to treat the prostate and pelvic lymph nodes with IMRT have been shown to be significantly lower compared to 3D-CRT [74]. Nutting and colleagues [72] compared the normal tissue dosimetry with conventional, 3D-CRT and IMRT plans also designed to treat

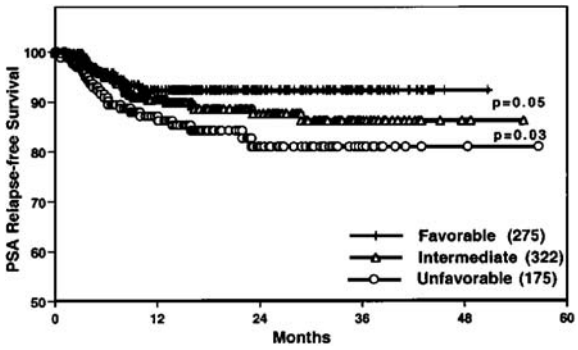

Fig. 8. Kaplan-Meier freedom from biochemical failure for men with prostate cancer treated at MSKCC with IMRT. Six hundred and ninety eight were treated to 81 Gy and 74 to 86.4 Gy. A total of 426 received 3 months of neoadjuvant androgen deprivation. The double factor risk stratification scheme (Table 1) was used. From Zelefsky et al. [71], with permission

the prostate and pelvic lymph nodes. Using IMRT, the mean percentage volume of small bowel and colon receiving > 45 Gy was significantly reduced to as little as 5.3% compared to 18.3% for 3D-CRT plans and 21.4% for conventional plans. The rectal volume irradiated > 45 Gy was significantly reduced from 50.5% with 3D-CRT to 5.8% with nine-field IMRT and bladder from 52.2 to 7%. Recently, Nutting et al. discussed the implementation of IMRT for treatment of the prostate and pelvic lymph nodes for high risk patients on a Phase I trial pelvic lymph node dose escalation trial [73]. The first dose level will treat the prostate to 70 Gy and pelvic lymph nodes to 50 Gy in 35 fractions with 3 years of androgen deprivation. Subsequent dose levels will escalate the dose to the pelvic lymph nodes 5 Gy in the same number of fractions.

9.1.4 Tumor-targeted Therapy

Numerous imaging tools have been investigated for the purpose of guiding treatment for prostate cancer. Anatomical modalities, such as computed tomography (CT) and transrectal ultrasound (TRUS), can be used to distinguish target structures from normal structures. Magnetic resonance imaging (MRI), also an anatomical imaging modality, is superior to CT and TRUS for defining prostatic and periprostatic soft tissue anatomy [75–79]. In addition, functional imaging reveals information about the biologic characteristics of the tissues to better direct therapy. Magnetic resonance spectroscopy imaging (MRSI) is one functional imaging technique that combines MRI with a proton signal intensity map to identify regions with altered tissue metabolism. The ratio of choline plus creatine-to-citrate levels has been shown to correlate with Gleason score and to be incrementally prognostic for men with intermediate and high risk tumors [79]. In a study by Coakley et al. [80], combined MRI and MRSI findings correlated with histopathological tumor volume but, not with MRI alone. Because a high level accuracy is difficult to achieve for small tumors, this correlation was statistically significant for tumors measuring 5 cc.

Investigators at the University of California-San Francisco have demonstrated it is technically feasible to concurrently treat single or multiple selected high-risk regions within the prostate, defined by MRI/MRSI, to 90 Gy and the remaining prostate above 70 Gy, without compromising rectal and bladder sparing [81, 82]. More recently, Pickett et al. [83] observed declines in metabolic activity from cancerous levels to normal levels following IMRT in patients receiving > 80 Gy to areas identified by as suspicious by MRSI. MRSI appears to be a reliable measure of tumor metabolism, which may be used to target tumor areas in need of higher doses and to monitor response post-treatment.

9.1.5 Combination Brachytherapy

Small retrospective series have demonstrated some efficacy for the combination external-beam radiation therapy (EBRT) and brachytherapy. Prostate brachytherapy has been performed with ^{125}I or ^{103}Pd given before or after external-beam therapy [84–87], ^{198}Au plus external-beam therapy (with the implant usually given first), or temporary high dose rate (HDR) ^{192}Ir given before, during, or after external-beam therapy [88–91]. Each method has technical advantages and disadvantages, and at present comparisons among them are not available. However, results from small retrospective series have been promising. Ragde et al. [87] have shown that after long follow-up, the results after prostate send implant plus external-beam therapy were slightly, but not significantly, better than results with prostate seed implant alone even though the patients treated with seed implant alone had more favorable risk features.

As has been found for external-beam monotherapy [5, 6, 17, 39, 92] and prostate seed implant monotherapy [93], a dose response relationship seems to exist for the combination therapy as well. Martinez et al. [94] have escalated the biological equivalent dose from HDR ^{192}Ir implants given during external-beam therapy to 46 Gy. They have slowly escalated the biological equivalent dose from 80.2 Gy ($\alpha/\beta = 1.2$, derived from their own clinical data [95]) to 136.3 Gy using either two or three HDR implants given during the course of external beam therapy for 207 men. Their results suggest an improvement in FFBF for patients with intermediate and high risk features who received higher biologic equivalent doses with the combination therapy. With a median follow-up of 4.7 years the 5-year FFBF rate was 74%. Biological equivalent dose (> 92 Gy), Gleason score and PSA nadir were associated with biochemical failure on multivariate analysis. MRSI guided brachytherapy in combination with IMRT would be another reasonable approach to test further dose escalation for intermediate and high risk disease [96, 97].

While the results with EBRT and brachytherapy have been promising, no benefit over EBRT alone (RT dose 72 Gy) was observed in a contemporary series recently reported by Kupelian and colleagues [98]. There were 2991 clinical Stage T1 and T2 patients treated consecutively between 1990 and 1998 at the Cleveland Clinic Foundation or Memorial Sloan Kettering at Mercy Medical Center with a median follow-up of 56 months. There was no statistically significant difference between seven-year FFBF rates for men treated with radical prostatectomy, EBRT alone (RT dose 72 Gy, prostate implant alone, or EBRT in combination with a prostate implant (seven-year FFBF: 76% for RP ($n = 1034$), 82% for EBRT 72 Gy ($n = 301$), 76% for prostate implant ($n = 950$), and 77% for combined external beam RT with a prostate implant ($n = 222$), Fig. 9). However, men

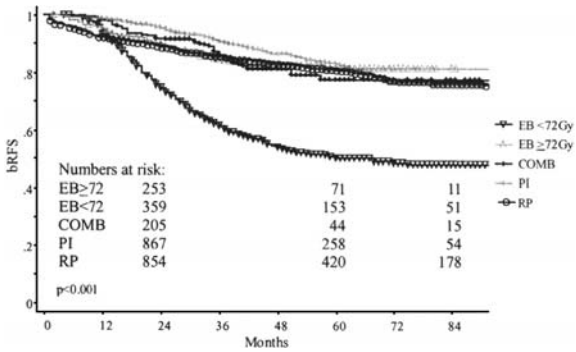

Fig. 9. Biochemical relapse-free survival by treatment modality. RP = radical prostatectomy; EBRT = external beam radiation therapy; PI = prostate implant; COMB = external beam radiation therapy and prostate implant. Reproduced from Kupelian et al. [98], with permission

treated with EBRT to a dose less than 72 Gy had a significantly lower FFBF rate of 47% at seven years. Excluding the external beam RT< 72 Gy group, treatment modality (surgery, external beam RT, implant alone or external beam RT with an implant) was not an independent predictor of FFBF. Prostate implants are not offered with EBRT at FCCC outside of a protocol because, as these data suggest, there is no apparent benefit to the combination therapy and there may be additional or greater toxicity.

9.2 Unique Anatomical Challenges

9.2.1 Motion and Margin Considerations

Despite a location deep in the pelvis, bladder and rectal volume changes result in prostate motion that warrants consideration. Day-to-day, or interfraction, motion is more influenced by rectal volume than by bladder volume changes in the majority of studies [99–104]. Antolak et al. [103] estimated that the *PTV* margin required to contain the *CTV* within the *PTV* 95% of the time was 1.1 cm in the anterior-posterior, 0.7 cm in the superior-inferior, and 0.7 cm in the left-right planes. The major limitation of adhering to the 1.1 cm *PTV* anterior-posterior margin has been rectal toxicity, mainly in the form of increased rectal bleeding. Lee et al. [37] have shown in patients treated with conformal radiotherapy that when the fields extended 1.5 cm from the prostate to the block edge (PTV = prostate + 1.0 cm) that rectal bleeding was substantial. Results were improved by reducing off of the rectum (rectal block) at 61 – 65 Gy. Although the FCCC results have held up over time in patients who had such blocking [105], the margin is insufficient to adequately ensure coverage of the posterior aspect of the prostate where the majority of prostate cancers arise. Ideally, interfraction motion is best corrected using tighter margins throughout the entire treatment in such a way that toxicity-based, rectal planning constraints are met while ensuring adequate coverage of the prostate.

Prostate motion during treatment, or intrafraction motion, from respiration and changes in rectal or bladder filling should also be considered because an IMRT treatment can last 15 min or more. Displacement of the prostate during a typical 15-min treatment is usually minimal [106–109, 112]. However, there are situations in which intrafraction motion may be more significant. Examples are the pronounced respiratory motion when patients are treated prone and/or with a thermoplastic shell over the pelvis [106, 110–112]. Prostate motion from respiration is minor when the patient is positioned supine without a thermoplastic shell. In our experience at FCCC, where patients undergo sequential CT and MRI simulations, extremes in bladder filling effects when the bladder is either near empty or full can influence the position of the prostate considerably.

Several techniques for localizing the prostate prior to the delivery of each fraction have been described. The two most popular methods for imaging the prostate on a daily basis prior to treatment are: (1) transabdominal ultrasound [109, 113, 114] and (2) the implantation of metallic (usually gold) seed markers and localization using electronic portal imaging [100, 106, 112, 115, 116]. The former is the most commonly used system with the longest clinical experience.

The first commercially available ultrasound imaging device designed specifically to adjust for interfraction motion was the NOMOS BAT ultrasound system (Sewickley, PA). The initial reports described a close correlation of the corrections from transabdominal ultrasound with pelvic CT-scan measurements [113, 117]. Although patients who can not maintain fluid in the bladder or are obese are more difficult to image, the quality of the images and the accuracy of the shifts by the therapists are usually acceptable [109]. The success of ultrasound imaging for the correction of interfraction prostate motion hinges on diligent quality assurance by the team of treating physicians, medical physicists and radiation therapists. Review and agreement on policies regarding the shifts can better insure consistent and accurate positioning. The physicians must also check each daily ultrasound-based shift and give feedback to the therapists on a regular basis. Without such practices, the value of the ultrasound method has been questioned [118].

New approaches to this problem continue to be explored. Rectal balloons have been used in the past to reduce prostate motion by immobilizing the prostate against the pubic symphysis [119]. Although limited by the variability of where exactly the prostate in pinned against the pubic bone each day, combing this with daily transabdominal ultrasound may provide a precise

localization technique [120]. Daily CT-scan measurements in the linear accelerator treatment room are now possible [121, 122]. Soon cone beam CT reconstructions using images created from the megavoltage beam or from a gantry mounted kilovoltage device will be available [123, 124].

9.3 Target Volume Delineation

When implementing any IMRT strategy from published studies, careful attention to the details specific to that technique are necessary to achieve similar dose distributions. They include: (1) definition of target and normal tissue structures, (2) the daily localization procedure, (3) dose prescription, (4) normal tissue constraints, and (5) method for determining plan adequacy. While the following sections detail how IMRT is delivered at FCCC, the successful implementation of any one of the published series is possible when these factors are considered. Each single institution protocol is unique and methods should not be interchanged. Considerations for target/normal tissue definition, motion uncertainties, and tolerance criteria are often interdependent and central to the treatments success. With that in mind, target/normal tissue DVH criteria for the purpose of determining plan adequacy should always be in the context of the target/normal tissue volume delineation method used.

9.3.1 Prostate, Seminal Vesicles and Lymph Nodes

The gross tumor volume (GTV) for adenocarcinoma of the prostate is not visualized well and therefore is not

Table 5. Treatment planning and evaluation scheme at Fox Chase Cancer Center

		Constraints		Comment
Volume	Target	Absolute (hard)	Relative (soft)	
CTV1	Prostate Proximal Seminal vesicles[a] Gross extracapsular extension	$D_{100\%} \geq 100\%$ prescription dose†	None	
PTV1	CTV1 +8 mm, except 5 mm posteriorly	$D_{95\%} \geq 100\%$ prescription dose† $D_{max} < 17\%$ prescription dose† $V_{<65\,Gy} < 1\%$	Effective PTV: the slice-by-slice distance from the posterior edge of the prostate (CTV1) to the prescription isodose line is ~ 3 mm to 8 mm	The PTV is a 3D structure and the distance between the CTV and prescription line varies
PTV2	Distal seminal vesicles (CTV2 +8 mm), except 5 mm posteriorly	$D_{95\%} \geq 100\%$ prescription dose‡	None	The distal SVs are only treated in high risk patients
PTV3	Lymph nodes (CTV3)+8 mm, except 5 mm posteriorly	$D_{95\%} \geq 100\%$ prescription dose‡		If the bladder dose is too high, the lateral margins are reduced to 6 mm
Rectum	Entire rectal volume (empty) from the ishial tuberosities to the sigmoid flexure	$V_{<65\,Gy} < 17\%$ $V_{<40\,Gy} < 35\%$	The 90% dose line encompasses no more than the half-width of the rectum on any axial cut. The 50% dose line does not encompass the full rectum width	The soft constraints are a way of ensuring a rapid dose gradient across the rectum
Bladder	Entire bladder volume (partially full)	$V_{<65\,Gy} < 25\%$ $V_{<40\,Gy} < 50\%$	None	Often times, bladder constrains are not met. These are poorly defined and the least important
Femoral heads	Right and left femoral heads to a level between the greater and lesser trochanters	$V_{50\,Gy} < 10\%$ for each	None	

CTV = clinical target volume; PTV = planning target volume; D_{XX} = the dose received by XX% of the volume; V_{XX} = the volume receiving *XX* Gy; Int = intermediate[a]For T3b disease, most, if not all of the seminal vesicles are treated to the full dose. [b]Delivered in 38 to 39 fractions. †Prescription dose: low risk = 76 Gy; intermediate/high risk = 76 – 78 Gy. ‡Prescription dose: low/intermediate risk = N/A; high risk = 56 Gy

contoured separately. Some investigators use functional imaging to distinguish bulky tumor volume areas for dose escalation with MR spectroscopy [81, 125] as discussed above or Prostascint scans [126], but clearly these are investigational. The clinical target volume (CTV) is determined by the patient's respective risk group (low, intermediate or high, Table 1) using a combination of subvolumes (i.e. CTV1, CTV2, etc.). In general, the CTV includes the prostate, any gross extracapsular extension and proximal seminal vesicles (CTV1) with or without the distal seminal vesicles (CTV2) and lymph nodes (CTV3) (Table 5).

For low and intermediate risk patients at FCCC the CTV (listed as CTV1 in Table 5) includes the prostate and proximal seminal vesicles (Table 5 and Fig. 10). While the probability of proximal seminal vesicle involvement is low, this region is included in the CTV1 because it is difficult to identify accurately the prostate-seminal vesicle interface. Our experience using fused CT-MRI images routinely in treatment planning has been that MRI is superior to CT for defining the CTV; this is particularly true at the bladder-prostate interface at the base of the prostate and the urogenital diagram-prostate interface at the apex. Adequate coverage of the apex is of particular concern because it can be involved by tumor in over 30% of men [127]. Lying in close proximity to the neurovascular bundles, the apex is common site of perineural invasion which provides a direct route of extracapsular extension. Extracapsular extension typically can extend to 4 mm beyond the prostatic capsule [128, 129]. For these reasons, the CTV1 should extend about 6 mm below where the prostate apex is believed to end. The planning target volume (PTV) for the CTV1, or PTV1, incorporates 8 mm of margin in all directions except posteriorly where the margin is 5 mm to limit the dose received by the rectum.

The CTVs for high risk disease at FCCC includes the prostate, seminal vesicles (SVs), periprostatic and

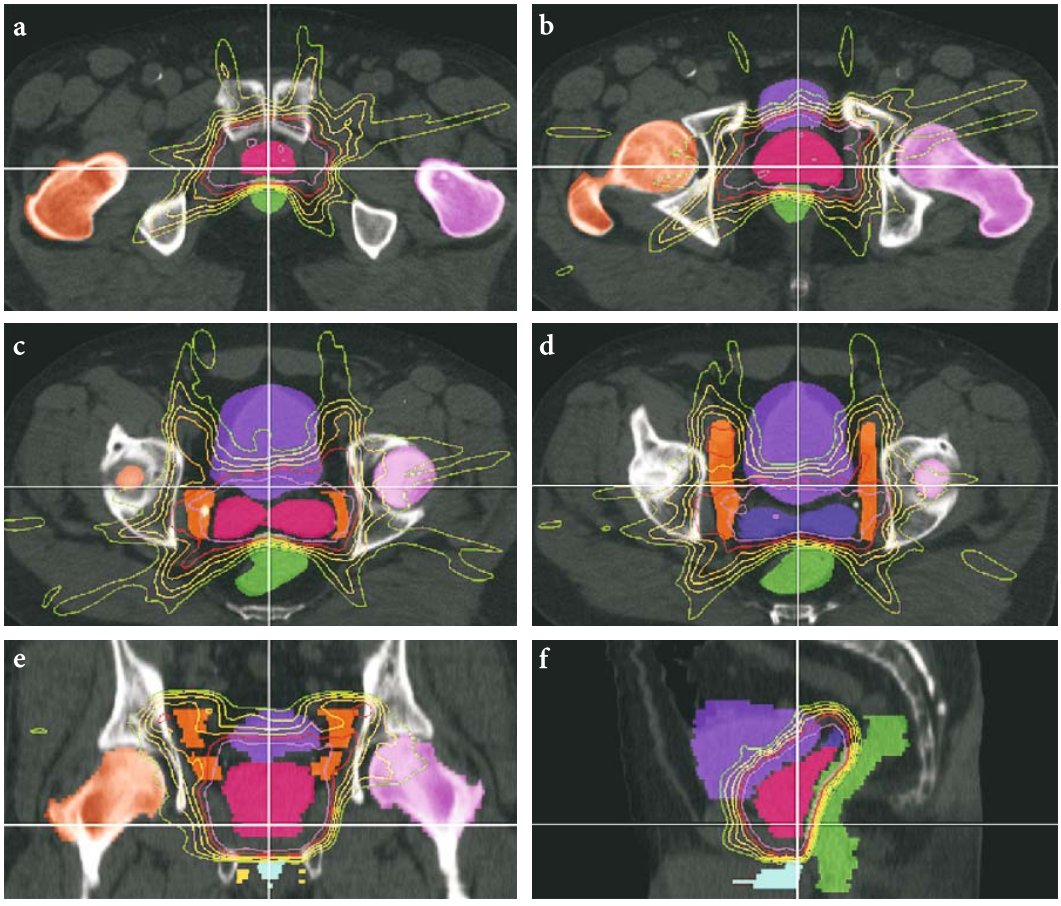

Fig. 10a–f. MRI defined target and normal tissue volumes shown on selected CT planning images for a patient with high risk prostate cancer planned to receive 70.2 Gy in 26 fractions on protocol. Clinical target volume (CTV) definitions as in Table 5: **(a)** mid prostate with prostate (CTV1) shown in *pink* and rectum in *green*; **(b)** prostatic base with bladder shown in *purple*; **(c)** the proximal seminal vesicles contoured as CTV1 (*pink*) and periprostatic lymph node regions (CTV3) shown in *orange*; **(d)** the distal seminal vesicles (CTV2) shown in *dark purple*; **(e)** a coronal representation with the penile bulb shown in *light blue* and corporal bodies shown in *yellow*; **(f)** a sagittal slice showing the proximal seminal vesicles contoured together with the prostate as CTV1. Isodose lines shown represent the 100% (*purple*) through the 50% (*green*) prescription dose regions in 10% increments

pelvic lymph nodes (Table 5). Each is contoured separately; CTV1 is the prostate and proximal SVs, CTV2 is the distal SVs and CTV3 the lymph nodes (Fig. 10). The proximal and distal seminal vesicles are defined separately because the proximal SVs receive the full dose, while the distal SVs are given the same dose as the lymph nodes. The added PTV margins to for CTV2 and CTV3 are the same as for CTV1. While it is possible for a portion of CTV3, the obturator, external iliac and internal iliac lymph nodes, to lie outside *PTV*3 when shifts are made, this should not occur often.

The coverage of lymph nodes outside the periprostatic and periseminal vesicle regions should be considered in CTV3 in men with high risk disease, based on the recent results from RTOG 94–13 [130]. This adds considerable complexity to the construction of treatment volumes and dose calculations. At Fox Chase, the extent of pelvic lymph node coverage and the dosimetric parameters are in a state of flux at the present time. We are planning to include in the CTV3 the periprostatic, periseminal vesicle and pelvic lymph nodes typically included in a staging lymphadenectomy. They are contoured together extending along the obturator, external iliac and internal iliac vessels from the level of the prostate inferiorly to the bifurcation of the bifurcation of the common iliac vessels superiorly. Volume expansion to define a PTV3 is somewhat problematic because prostate motion is independent of the lymph nodes; prostate motion corrected using transabdominal ultrasound will result in a shift of the PTV3 away from the lymph nodes, assuming the isocenter remains aligned with the bony anatomy. Thus, the PTV3 should utilize a larger margin than the PTV1. However, this would lead to compromise in the treatment of the prostate in terms of achieving high target doses and sparing of the bladder and rectum. We are using the same margins as for the other PTVs (8 mm everywhere and 5 mm posteriorly), although we have found that sometime 6 mm lateral margins are necessary to limit bladder dose. Since lateral interfraction prostate displacement is typically small, this seems reasonable. Presacral lymph nodes have not been treated at FCCC with IMRT, although disease could certainly spread to this region. Our goal is to treat as much of the lymph node regions as possible without compromising the delivery of high doses to the PTV1. Our results suggest that dose is of primary importance [131].

9.3.2 Rectum

Rectal toxicity is the chief limiting factor in the treatment of prostate cancer with radiation. Pollack et al. [9] and Huang et al. [132] using data from MDACC observed a strong association of complication risk with the percentage of the rectum treated to certain threshold doses, which serve the basis of the rectal tolerance criteria for IMRT at FCCC. In these reports, the rectum was outlined from the ischial tuberosities, superiorly for an 11-cm segment. The 11-cm length was done because the initial fields extended 11 cm in the superior-inferior dimensions. Pollack et al. [9] found that when $\leq 25\%$ of the rectal volume received ≥ 70 Gy, grade 2 or higher rectal morbidity was 16% at five years vs 46% when $> 25\%$ of the rectal volume received ≥ 70 Gy (Fig. 11). Huang et al. [132] extended these observations by testing multiple rectal dose-volume (absolute and percentage) relationships. The percentage of rectal volume correlated significantly with the incidence of rectal complications at multiple RT dose levels, whereas the absolute rectal volume criteria were only significant at the higher RT doses (70, 75.6 and 78 Gy). Fiorino et al. [42, 44] also found that the percentage of the rectum treated to specified dose levels was a robust determinant of rectal complication risk; they outlined from the anal verge to the sigmoid flexure superiorly. This is the volume of rectum that has been used in RTOG protocols, at FCCC, and is the volume most commonly used. Patients should be simulated with an empty rectum because rectal distention at the time of simulation, which can lead to a systematic errors in target localization during treatment, has been shown to correlate with rectal toxicity, as well as biochemical and local control [154].

In contrast to the relative volume method, Kupelian and colleagues [43] from the Cleveland Clinic defined the rectum as a segment extending from just above and below the prostate and found that the absolute volume that received the prescription radiation dose or higher was a more significant predictor of grade 2 or higher toxicity than the percentage of the rectum. When > 15 cc of the rectum received greater than the prescription dose (78 Gy in 2-Gy fractions or 70 Gy in 2.5-Gy fractions) the risk of rectal bleeding was 22%, whereas the risk was 5% when ≤ 15 cc received greater than the prescrip-

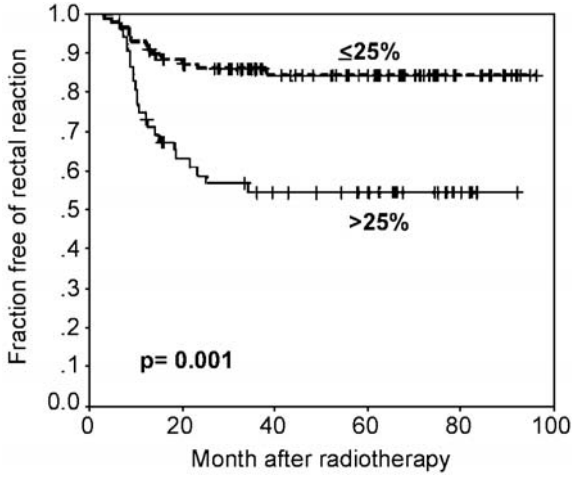

Fig. 11. Relationship of the percentage of rectum ($\leq 25\%$ *vs* $> 25\%$) treated to ≥ 70 Gy to grade 2 or higher rectal morbidity. From Pollack et al. [9], with permission

tion dose. As a result, the investigators have adopted a 10 cc limit to the volume of rectum receiving the prescribed dose in hopes of further reducing the risk of rectal bleeding [133].

When using rectal wall volume, rather than the entire rectum, the results of Skwarchuck et al. [134] and Jackson [40] from MSKCC were mixed in terms of whether an absolute or percentage volume should be used. In those reports, the rectal wall was defined from just above the anal verge to just below the sigmoid flexure. They found that the rectal Dmax and the rectal wall volume (a smaller volume implies a higher percentage exposed to significant dose) were both correlates of $\geq$ grade 2 rectal bleeding. They also found that enclosure of the rectum by the 50% line at isocenter, age and diabetes were predictive of rectal morbidity. The significance of age and diabetes was small in comparison to the DVH factors [40]. Of note, diabetes has been described by others to be a risk factor previously [134,135]. Recently Feigenberg et al. [136] found that a history of diabetes was primarily a correlate of grade 3, but not grade 2, complications. Diabetes was not a factor in the MDACC study reported by Huang et al. [132].

9.3.3 Bladder

The relationship of radiation dose to bladder complication risk has not been established, due in part to the dramatic variability in volume that occurs and the need for long term follow-up to observe toxicity. The bladder volume has been defined as the entire bladder and its contents by FCCC, MDACC and Cleveland Clinic groups while those at MSKCC use just the bladder wall. Prior to simulation and each treatment patients should be asked to ensure their bladders are not empty (to reduce the volume of bladder treated) nor too full (to minimize prostate displacement and discomfort). Adequate bladder distention also better enables adequate transabdominal imaging to correct for interfraction motion.

9.3.4 Penile Bulb and Corporal Bodies

The corporal bodies and penile bulb (Fig. 10) are currently under investigation at FCCC for their role in the development in post-treatment erectile dysfunction. The penile bulb is defined as the bulbous, proximal portion of the corpora spongiosum and typically measures 1–2 cm in length. The corporal bodies are paired structures defined as the divergent, proximal portions of the corpora cavernosa and typically measure 2–3 cm in length before their departure from the ischial tuberosities.

Magnetic resonance imaging is superior to CT for defining these structures [78] as both appear as high signal intensity on T2-weighted images [78,137] (Fig. 3). When using CT alone, identification of the urogenital diaphragm using a urethragram can also be used to aid in identifying the superior extent of the penile bulb [138]. IMRT has been shown to reduce doses to these structures compared to 3D-CRT [65] and enable further dose escalation [64].

9.4 Planning and Dose Prescriptions

Inverse planning is a powerful method for escalating dose and reducing toxicity. Central to obtaining this goal is the adoption of strict normal tissue constraints. The latest inverse planning software allows for exceptional dose conformality, but to achieve an optimal plan requires an understanding of such constraints on several levels and the intricacies of the planning system in use. The latter is almost as important as the constraints because there are methods for forcing dose into the PTV and reducing dose to the surrounding normal tissue such that constraints are met with fewer segments and shorter treatment times [139].

9.4.1 Absolute (Hard) PTV Constraints

The absolute conditions for plan acceptance should include that 95–100% of the PTV receives the prescription dose. At FCCC, the dose received by 95% of the volume (D_{95}) for the PTV is used. The CTV should receive very close to 100% of the prescription dose. The maximum dose to the PTV should not exceed 17% of the prescribed dose and $< 1\%$ of the PTV should receive less than 65 Gy (it is usually $< 0.5\%$). These constraints have been easier to maintain with the newer software versions. However, the inclusion of the pelvic lymph nodes in planning makes it more difficult to adhere to the 17% maximum dose constraint. Treatment plans should also be evaluated on a slice by slice basis in two dimensions in order to ensure margin adequacy at each level.

9.4.2 Effective (Soft) PTV Constraints

The effective or soft PTV constraints are those that are not put into the planning system, but are still viewed important for plan acceptance. The prescription line (the effective PTV) does not encompass the desired PTV on every axial slice. The physician should evaluate every transverse slice to determine the relationship between the prescription line and the PTV. If the prescription line deviates into the PTV on several slices or deviates into the CTV on any slice, the physician may opt to have the plan redone.

9.4.3 Absolute (Hard) Normal Tissue Constraints

Normal tissue complication risk in the management of prostate cancer is well established and related to radiation dose and volume for grade 2 and 3 late rectal bleeding [35–43, 140]. Rectal side effects are manifest by two to four years [9], while bladder side effects mature over a much longer time course [46, 141]. Thus, the rectal constraints that have been implemented are based on sound data. In contrast, bladder constraints are less well-defined. As a consequence of this and the considerable variability in interfraction bladder volume, bladder planning restrictions have in general been less strict.

Rectum

The FCCC hard normal tissue constraints are derived in part from the MDACC randomized trial discussed above [9]. In that study there was a very dramatic increase in $\geq$ grade 2 rectal reactions when $\geq 25\%$ of the rectal volume received ≥ 70 Gy (Fig. 11). The rectum was outlined from the ischial tuberosities to 11 cm superiorly. The prescription was 78 Gy in 2-Gy fractions to the isocenter. Since that time, a number of changes have been made that make the constraints now used much stricter. First, a shorter segment is outlined, extending superiorly from the ischial tuberosities to the sigmoid flexure (about 10 cm on average). Second, the prescription has changed to give 74–78 Gy to the PTV at 2 Gy per fraction and so the cut-point was reduced from 70 to 65 Gy. Third, the percentage of rectum that receives the cut-point dose was lowered from 25 to 17% because the risk of complications is a continuous function and we found that we could consistently meet this stricter constraint.

The analysis by Jackson et al. [40] revealed that the most significant relationship between rectal toxicity and dose was with the percentage of the rectal wall exposed to intermediate doses of 40–50 Gy. They recommended DVH constraints of $\leq 60\%$ rectal wall volume treated to ≥ 40 Gy and $\leq 30\%$ rectal wall volume treated to ≥ 75.6 Gy. Although they have used rectal wall volumes rather than the entire rectum, the DVH data in aggregate indicate that a single dose-volume constraint is not optimal for minimizing rectal reactions. Our rectal tolerance DVH criteria now include a second cut-point at 40 Gy range. The hard constraints for the rectum are now that $\leq 17\%$ and $\leq 35\%$ of the rectum receives ≥ 65 Gy and ≥ 40 Gy, respectively.

Bladder

No well-defined bladder constraints have been identified. We have initiated constraints that seem reasonable and serve as a guide. The hard constraints for the bladder are that $\leq 25\%$ and $\leq 50\%$ of the rectum receives ≥ 65 Gy and ≥ 40 Gy, respectively. Some plans, however, do not meet the constraints because the bladder was not sufficiently full during simulation.

Femoral Heads

There is infrequently a problem limiting the dose to the femoral heads, such that $\leq 10\%$ receives over 50 Gy. The femoral heads are outlined down to the level between the greater trochanters and lesser trochanters.

9.4.4 Effective (Soft) Normal Tissue Constraints

Examining the isodose lines on a slice by slice basis is critical to implementing effectively IMRT. If the 90% dose line encompasses more than the half-width of the rectum or the 50% dose line encompasses the full-width of the rectum on any slice, the plan should be better optimized. Sometimes these constraints are subject to the discretion of the physician. For example, there may be some cuts where the rectum is very small and these soft constraints are violated. The goal is to have relatively sharp fall-off in dose. These constraints are a surrogate measure of dose fall-off.

9.4.5 Beam Energy, Number and Arrangement

Reasonable IMRT plans are obtained with 6, 10 or 18-MV photons. With 18 MV there is greater neutron production through photonuclear interactions and at FCCC a precautionary age limit of ≥ 65 has been set for the use of this energy. The optimal energy at FCCC is considered to be 10 MV.

At FCCC, the beam number and arrangement have not been standardized; while at other institutions standard five or six field arrangements have been used. We usually start with six beams and then add beams as needed to meet the above described constraints. The use of nine beams is not uncommon. Our typical six-beam configuration consists of the following directions and associated beam angles: LPO (gantry 135), LPO (gantry 105), LAO (gantry 75), AP (gantry 0), right lateral (gantry 270), and RPO (gantry 225). Additional beam directions are added in an iterative manner while attempting to meet our acceptance criteria for normal structures and maximize dose conformity to the target. The use of parallel opposed beams is avoided. The collimator angle is evaluated through each beam's eye view (BEV) in order to achieve geometric separation between target and normal structures where possible. Five intensity levels are used in all plans, resulting in approximately 45–110 total segments given over 10–25 min for 6 MV and 7–18 min for 10 and 18 MV on a Siemens Primus. The inclusion of the pelvic lymph nodes greatly enhances the number of segments and overall treatment time.

When confronted with difficulty in meeting the planning criteria, non-coplanar beam arrangements are explored [142]. We now use on a routine basis a planning technique that has resulted in a significant reduction in the number of segments used. Tissue regions outside of the target and normal tissues normally outlined have been defined by concentric rings, each with dose constraints added. This maneuver results in an increased control over the dose gradient outside the target boundaries. We have built standardized templates for input parameters for each specific dose scheme for the treatment of prostate cancer at FCCC. Some of these parameters including gantry angles, number of beam directions, and collimator angles, are varied in an iterative manner on a case-by-case basis in an attempt to arrive at the best plan for each individual. Target conformity, normal tissue sparing, and efficient delivery time are the primary endpoints for plan acceptance.

9.4.6 Penile Bulb and Corporal Bodies

The effect of employing dose constraints for the erectile tissues in treatment planning on prostate coverage and rectal sparing has been studied [66]. Twenty-three patients with palpation stage T1c-2b N0 M0 prostate cancer who received IMRT alone were planned with and without dose constraints for the erectile tissues. The dose prescribed to the planning target volume (PTV) was 74–78 Gy. All patients underwent CT and MRI simulation to define target and normal structures. Three plans with identical beam arrangements and energy were generated for each patient with varying dose constraints for the penile bulb and corporal bodies: no dose constraint, intermediate dose constraint (20 and 15 Gy, respectively) and low dose constraint (15 and 7 Gy, respectively). All plans were normalized such that 95% of the prostate received at least 100% of the prescribed dose. For each plan, the ability to meet prostate dose homogeneity criteria (prostate $D_{\max} \leq 120\%$ prescribed dose) and rectal tolerance dose-volume histogram criteria (the proportion of the rectum treated to ≥ 40 Gy is limited to $\leq 35\%$ and the proportion of the rectum treated to ≥ 65 Gy is limited to $\leq 17\%$) was determined.

Figure 12 illustrates that when treatment planning dose constraints for the penile bulb are used the penile bulb D_{90} (the dose received by 90% of the volume) can be limited to 15 Gy in approximately 80% of patients for either an intermediate (20 Gy) or low dose (15 Gy) treatment planning constraint. For the corporal bodies, the D_{90} can be limited to 7 Gy or less in approximately 80% of patients when applying either constraint (intermediate = 15 and low = 7 Gy). These reductions were achieved without compromising prostate homogeneity criteria, rectal DVH toxicity criteria or treatment duration. Comparing the intermediate to low dose constraints, the penile bulb and corporal bodies' volumes receiving high doses were significantly smaller with a low dose constraint, although D_{90} values were not significantly reduced and there was reduced prostate coverage and rectal sparing.

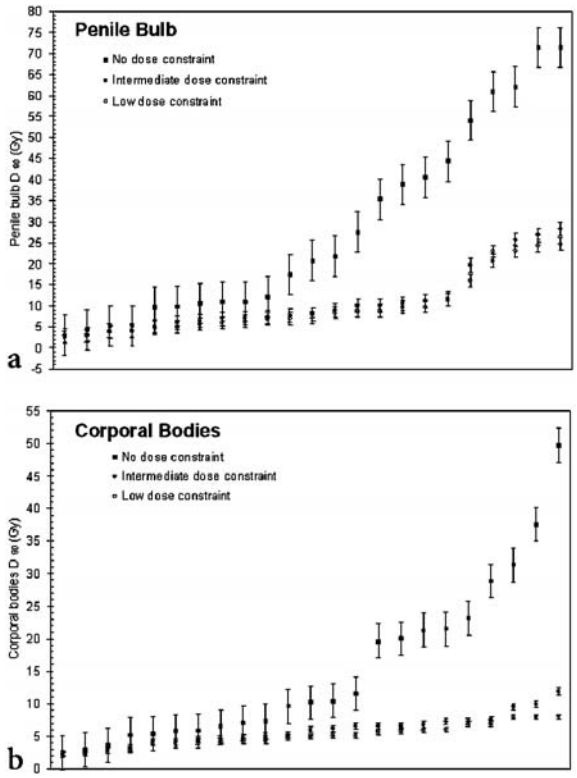

Fig. 12a,b. Ordered sequences of: (a) penile bulb; (b) corporal bodies D_{90} values for each level of dose constraint. Modified from Buyyounouski et al. [66] with permission

In a report by Fisch et al. [47], the median penile bulb D_{95} in men who had no decline in erectile function following 3D-CRT was 14 Gy compared to 33.2 Gy in men with a slight decline and 51.1 Gy in men with a marked decline ($p = 0.05$). Our ability to limit the penile bulb D_{90} to 15 Gy in 80% of men is the basis for a single blind, FCCC randomized trial comparing IMRT with and without erectile tissue sparing. The trial will better elucidate the important dose-volume relationships for the erectile tissues.

9.5 Future Directions

An increase in radiation dose from < 70 to 75.6 Gy results in a substantial increase in FFBF. Some data indicate that ultimately this translates into an increase in cause specific survival [143]. The documentation of DVH parameters associated with rectal complication risk was an important step in the application of IMRT to the problem of escalating dose without increasing rectal morbidity. With the definition of absolute (or hard) DVH con-

straints, it has become possible to push dose escalation to greater levels and to reduce morbidity of treatment. Even with the gains realized there is room for further improvement.

Another approach that has received much attention lately is the use of higher doses per fraction (hypofractionation). Brenner and Hall [95, 144], and others [145,146], have pooled patient outcome data from prostate implant and external beam radiotherapy series, and estimated the a/b ratio to be low at 1.5–3.0. An α/β ratio in the 1.5 range would indicate that prostate cancer behaves like a late reacting tissue. There were a number of assumptions that were made in these derivations of α/β and, as a result, the confidence limits of the estimate are wide [147]. If the α/β is low, then hypofractionation would result in an advantage biologically. The reason that hypofractionation has been avoided is that normal tissue late effects may be worse. However, if one considers that the α/β ratios for the rectum and bladder are estimated to be > 3.0, there may be an advantage to hypofractionating prostate treatments if prostate cancer has a lower α/β.

Kupelian and colleagues [148, 149] have been treating prostate cancers at 2.5 Gy per fraction to 70 Gy using IMRT. This dose is biologically equivalent to 80 Gy at 2 Gy per fraction, considering the α/β to be 1.5. They have described a trend toward improved FFBF over that observed in patients ($n = 166$) treated to similar biologic doses with 3D-CRT. There was no significant increase in toxicity. At Fox Chase Cancer Center there is a randomized dose escalation trial using hypofractionation in progress. Intermediate to high risk patients are being randomized between 76 Gy in 2-Gy fractions and 70.2 Gy in 2.7-Gy fractions. It should be noted that the high risk patients also receive two years of androgen deprivation. The latter hypofractionated regimen is biologically equivalent to 84.4 Gy at 2 Gy per fraction assuming an α/β of 1.5. This and similar studies will provide much needed data for more precisely determining the α/β for prostate cancer.

There is every reason to believe that dose escalation using 3D-CRT or IMRT will have a substantial effect on prostate cancer patient outcome. Those with intermediate risk features stand to benefit the most. The trial from M.D. Anderson supports this concept, but is a rather small experience based mainly on FFBF. There are several trials in progress that hopefully will strengthen the conclusions drawn from the M.D. Anderson experience.

References

1. Hanks GE, Leibel SA et al. (1985) Patterns of care studies: dose-response observations for local control of adenocarcinoma of the prostate. Int J Radiat Oncol Biol Phys 11: 153–157
2. Hanks GE (1988) External-beam radiation therapy for clinically localized prostate cancer: patterns of care studies in the United States. NCI Monogr 75–84
3. Hanks GE, Martz KL et al. (1988) The effect of dose on local control of prostate cancer. Int J Radiat Oncol Biol Phys 15:1299–1305
4. Perez CA, Pilepich MV et al. (1988) Definitive radiation therapy in carcinoma of the prostate localized to the pelvis: experience at the Mallinckrodt Institute of Radiology. NCI Monogr 85–94
5. Lyons J, Kupelian P et al. (2000) Importance of high radiation doses (72 Gy or greater) in the treatment of stage T1–T3 adenocarcinoma of the prostate. Urology 55:85–90
6. Pollack A, Smith L et al. (2000) External beam radiotherapy dose-response characteristics of 1127 men with prostate cancer treated in the PSA era. Int J Radiat Oncol Biol Phys 48:507–512
7. Zelefsky MJ, Fuks Z et al. (2001) High dose radiation delivered by intensity modulated conformal radiotherapy improves the outcome of localized prostate cancer. J Urol 166:876–881
8. Hanks GE, Hanlon AL et al. (2002) Dose response in prostate cancer with 8–12 years' follow- up. Int J Radiat Oncol Biol Phys 54:427–435
9. Pollack A, Zagars GK et al. (2002) Prostate cancer radiation dose response: results of the M. D. Anderson phase III randomized trial. Int J Radiat Oncol Biol Phys 53: 1097–1105
10. Bey P, Carrie C et al. (2003) French study of dose escalation from 66 to 80 GY with 3D-CRT in prostate cancer: results at 5 years. Int J Radiat Oncol Biol Phys 57:S272
11. Cox G (1997) American Society for Therapeutic Radiology and Oncology Consensus Panel. Consensus statement: Guidelines for PSA following radiation therapy. Int J Radiat Oncol Biol Phys 37:1035–1041
12. Pollack A, Hanlon AL et al. (2003) Biochemical failure as a determinant of distant metastasis and death in prostate cancer treated with radiotherapy. Int J Radiat Oncol Biol Phys 57:19–23
13. Kestin LL, Vicini FA et al. (2002) Practical application of biochemical failure definitions: what to do and when to do it. Int J Radiat Oncol Biol Phys 53:304–315
14. Kupelian PA, Buchsbaum JC et al. (2002) Impact of biochemical failure on overall survival after radiation therapy for localized prostate cancer in the PSA era. Int J Radiat Oncol Biol Phys 52:704–711
15. D'Amico A, Whittington R et al. (1998) Biochemical outcome after radical prostatectomy, external beam radiation therapy, or interstitial radiation therapy for clinically localized prostate cancer. JAMA 280:969–974
16. Chism DB, Hanlon AL et al. (2004) A comparison of the single and double factor high-risk models for risk assignment of prostate cancer treated with 3D conformal radiotherapy. Int J Radiat Oncol Biol Phys 59:380–385
17. Zelefsky M, Fuks Z et al. (2003) Ten- year results of dose escalation with 3-dimensional conformal radiotherapy for patients with clinically localized prostate cancer. Int J Radiat Oncol Biol Phys 57:S149–S150
18. Amling CL, Blute ML et al. (1998) Influence of prostate-specific antigen testing on the spectrum of patients with prostate cancer undergoing radical prostatectomy at a large referral practice. Mayo Clin Proc 73:401–406
19. Jhaveri FM, Klein EA et al. (1999) Declining rates of extracapsular extension after radical prostatectomy: evidence for continued stage migration. J Clin Oncol 17:3167–3172

20. D'Amico AV, Chen MH et al. (2002) Changing prostate-specific antigen outcome after surgery or radiotherapy for localized prostate cancer during the prostate-specific antigen era. Int J Radiat Oncol Biol Phys 54:436–441
21. Pinover WH, Hanlon A et al. (1996) Prostate carcinoma patients upstaged by imaging and treated with irradiation. An outcome-based analysis. Cancer 77:1334–1341
22. Liebross RH, Pollack A et al. (1998) Relationship of ultrasound staging and bilateral biopsy positivity to outcome in stage T1c prostate cancer treated with radiotherapy. Urology 52:647–652
23. Iyer RV, Hanlon AL et al. (1999) Outcome evaluation of the 1997 American Joint Committee on Cancer staging system for prostate carcinoma treated by radiation therapy. Cancer 85:1816–1821
24. Liebross RH, Pollack A et al. (1999) Transrectal ultrasound for staging prostate carcinoma prior to radiation therapy: an evaluation based on disease outcome. Cancer 85:1577–1585
25. Chism DB, Hanlon AL et al. (2003) The Gleason score shift: score four and seven years ago. Int J Radiat Oncol Biol Phys 56:1241–1247
26. Khuntia D, Reddy CA et al. (2004) Recurrence-free survival rates after external-beam radiotherapy for patients with clinical T1–T3 prostate carcinoma in the prostate-specific antigen era: what should we expect? Cancer 100:1283–1292
27. Buyyounouski MK, Hanlon AL et al. (2003) The temporal kinetics of PSA after 3D-conformal radiotherapy with androgen deprivation. Int J Radiat Oncol Biol Phys 57(Suppl):S147–S148
28. Vicini F, Kestin L et al. (1999) The importance of adequate follow-up in defining treatment success after external beam irradiation for prostate cancer. Int J Radiat Oncol Biol Phys 45:553–561
29. Horwitz EM, Thames HD et al. (2003) Definitions of biochemical failure that best predict clinical failure in prostate cancer patients treated with external beam radiation alone-a multi-institutional pooled analysis. Int J Radiat Oncol Biol Phys 57:S147
30. Kestin LL, Vicini FA et al. (1999) Defining biochemical cure for prostate carcinoma patients treated with external beam radiation therapy. Cancer 86:1557–1566
31. Horwitz EM, Uzzo RG et al. (2003) Modifying the ASTRO definition of biochemcical failure to minimize the influence of backdating in patients with prostate cancer treated with 3D Conformal radiation therapy alone. J Urol 169: 2153–2159
32. Kuban DA, Thames HD et al. (2003) Failure definition-dependent differences in outcome following radiation for localized prostate cancer. can one size fit all? Int J Radiat Oncol Biol Phys 57:S146–S147
33. Pickles T, Kim-Sing C et al. (2003) Evaluation of the Houston biochemical relapse definition in men treated with prolonged neoadjuvant and adjuvant androgen ablation and assessment of follow-up lead-time bias. Int J Radiat Oncol Biol Phys 57:11–18
34. Thames H, Kuban D et al. (2003) Comparison of alternative biochemical failure definitions based on clinical outcome in 4839 prostate cancer patients treated by external beam radiotherapy between 1986 and 1995. Int J Radiat Oncol Biol Phys 57:929–943
35. Benk VA, Adams JA et al. (1993) Late rectal bleeding following combined X-ray and proton high dose irradiation for patients with stages T3-T4 prostate carcinoma. Int J Radiat Oncol Biol Phys 26:551–557
36. Shipley WU, Verhey LJ et al. (1995) Advanced prostate cancer: the results of a randomized comparative trial of high dose irradiation boosting with conformal protons compared with conventional dose irradiation using photons alone. Int J Radiat Oncol Biol Phys 32:3–12
37. Lee WR, Hanks GE et al. (1996) Lateral rectal shielding reduces late rectal morbidity following high dose three-dimensional conformal radiation therapy for clinically localized prostate cancer: further evidence for a significant dose effect. Int J Radiat Oncol Biol Phys 35:251–257
38. Boersma LJ, van den Brink M et al. (1998) Estimation of the incidence of late bladder and rectum complications after high-dose (70–78 GY) conformal radiotherapy for prostate cancer, using dose-volume histograms. Int J Radiat Oncol Biol Phys 41:83–92
39. Zelefsky M, Leibel S et al. (1998) Dose escalation with three-dimensional conformal radiation therapy affects the outcome in prostate cancer. Int J Radiat Oncol Biol Phys 41:491–500
40. Jackson A, Skwarchuk MW et al. (2001) Late rectal bleeding after conformal radiotherapy of prostate cancer. II. Volume effects and dose-volume histograms. Int J Radiat Oncol Biol Phys 49:685–698
41. Wachter S, Gerstner N et al. (2001) Rectal sequelae after conformal radiotherapy of prostate cancer: dose-volume histograms as predictive factors. Radiother Oncol 59:65–70
42. Fiorino C, Cozzarini C et al. (2002) Relationships between DVHs and late rectal bleeding after radiotherapy for prostate cancer: analysis of a large group of patients pooled from three institutions. Radiother Oncol 64:1–12
43. Kupelian PA, Reddy CA et al. (2002) Dose/volume relationship of late rectal bleeding after external beam radiotherapy for localized prostate cancer: absolute or relative rectal volume? Cancer J 8:62–66
44. Fiorino C, Sanguineti G et al. (2003) Rectal dose-volume constraints in high-dose radiotherapy of localized prostate cancer. Int J Radiat Oncol Biol Phys 57:953–962
45. Lebesque J, Koper P et al. (2003) Acute and late GI and GU toxicity after prostate irradiation to doses of 68 Gy and 78 Gy; results of a randomized trial. Int J Radiat Oncol Biol Phys 57:S152
46. Gardner BG, Zietman AL et al. (2002) Late normal tissue sequelae in the second decade after high dose radiation therapy with combined photons and conformal protons for locally advanced prostate cancer. J Urol 167:123–126
47. Fisch BM, Pickett B et al. (2001) Dose of radiation received by the bulb of the penis correlates with risk of impotence after three-dimensional conformal radiotherapy for prostate cancer. Urology 57:955–959
48. Merrick GS, Butler WM et al. (2002) The importance of radiation doses to the penile bulb vs crura in the development of postbrachytherapy erectile dysfunction. Int J Radiat Oncol Biol Phys 54:1055–1062
49. Singer PA, Tasch ES et al. (1991) Sex or survival: trade-offs between quality and quantity of life. J Clin Oncol 9:328–334
50. Miller DC, Hafez KS et al. (2003) Prostate carcinoma presentation, diagnosis, and staging: an update form the National Cancer Data Base. Cancer 98:1169–1178
51. American Cancer Society (2004) Cancer facts and figures 2004
52. Mettlin CJ, Murphy GP et al. (1998) The National Cancer Data Base report on prostate carcinoma after the peak in incidence rates in the U.S. The American College of Surgeons Commission on Cancer and the American Cancer Society. Cancer 83:1679–1684

53. NIH Consensus Development Panel on Impotence (1993). NIH Consensus Conference on Impotence. JAMA 270:83–90
54. Incrocci L, Slob AK et al. (2002) Sexual (dys)function after radiotherapy for prostate cancer: a review. Int J Radiat Oncol Biol Phys 52:681–693
55. Little DJ, Kuban DA et al. (2003) Quality-of-life questionnaire results 2 and 3 years after radiotherapy for prostate cancer in a randomized dose-escalation study. Urology 62:707–713
56. Beard CJ, Propert KJ et al. (1997) Complications after treatment with external-beam irradiation in early-stage prostate cancer patients: a prospective multiinstitutional outcomes study. J Clin Oncol 15:223–229
57. Roach M III, Winter K et al. (2000) Mean dose of radiation to the bulb of the penis correlates with risk of impotence at 24 months: Preliminary analysis of Radiation Therapy Oncology Group (RTOG phase I/II dose escalation trial 9406. Int J Radiat Oncol Biol Phys 48:316
58. Wernicke AG, Pequignot E et al. (2003) Radiation dose delivered to the proximal penis as a predictor of the risk of erectile dysfunction after three-dimensional conformal radiotherapy for localized prostate cancer. Int J Radiat Oncol Biol Phys 57:S274– S275
59. Shetty S, Farah RN (1999) Erectile dysfunction. In: Textbook of erectile dysfunction. Isis Medical Media, Spain, pp 25–30
60. Carrier S, Hricak H et al. (1995) Radiation-induced decrease in nitric oxide synthase-containing nerves in the rat penis. Radiology 195:95–99
61. Hall SJ, Basile G et al. (1995) Extensive corporeal fibrosis after penile irradiation. J Urol 153:372–377
62. Zelefsky MJ, Eid JF (1998) Elucidating the etiology of erectile dysfunction after definitive therapy for prostatic cancer. Int J Radiat Oncol Biol Phys 40:129–133
63. Dong L, O'Daniel JC et al. (2001) Comparison of 3D conformal and intensity-modulated radiation therapy for early-stage prostate cancer. Int J Radiat Oncol Biol Phys 51:320
64. Sethi A, Mohideen N et al. (2003) Role of IMRT in reducing penile doses in dose escalation for prostate cancer. Int J Radiat Oncol Biol Phys 55:970–978
65. Kao J, Turian J et al. (2004) Sparing of the penile bulb and proximal penile structures with intensity-modulated radiation therapy for prostate cancer. Br J Radiol 77: 129–136
66. Buyyounouski MK, Horwitz EM et al. (2004) Intensity-modulated radiotherapy with mri simulation to reduce doses received by erectile tissue during prostate cancer treatment. Int J Radiat Oncol Biol Phys 58:743–749
67. Oh CE, Antes K et al. (1999) Comparison of 2D conventional, 3D conformal, and intensity- modulated treatment planning techniques for patients with prostate cancer with regard to target-dose homogeneity and dose to critical, uninvolved structures. Med Dosim 24:255–263
68. Fiorino C, Broggi S et al. (2000) Conformal irradiation of concave-shaped *PTV*s in the treatment of prostate cancer by simple 1D intensity- modulated beams. Radiother Oncol 55:49–58
69. Zelefsky MJ, Fuks Z et al. (2000) Clinical experience with intensity modulated radiation therapy (IMRT) in prostate cancer. Radiother Oncol 55:241–249
70. Corletto D, Iori M et al. (2003) Inverse and forward optimization of one- and two-dimensional intensity-modulated radiation therapy-based treatment of concave-shaped planning target volumes: the case of prostate cancer. Radiother Oncol 66:185–195
71. Zelefsky MJ, Fuks Z et al. (2002) High-dose intensity modulated radiation therapy for prostate cancer: early toxicity and biochemical outcome in 772 patients. Int J Radiat Oncol Biol Phys 53:1111–1116
72. Nutting CM, Convery DJ et al. (2000) Reduction of small and large bowel irradiation using an optimized intensity-modulated pelvic radiotherapy technique in patients with prostate cancer. Int J Radiat Oncol Biol Phys 48:649–656
73. Adams EJ, Convery DJ et al. (2004) Clinical implementation of dynamic and step-and-shoot IMRT to treat prostate cancer with high risk of pelvic lymph node involvement. Radiother Oncol 70:1–10
74. Luxton G, Hancock SL et al. (2004) Dosimetry and radiobiologic model comparison of IMRT and 3D conformal radiotherapy in treatment of carcinoma of the prostate. Int J Radiat Oncol Biol Phys 59:267–284
75. Roach M III, Faillace-Akazawa P et al. (1996) Prostate volumes defined by magnetic resonance imaging and computerized tomographic scans for three-dimensional conformal radiotherapy. Int J Radiat Oncol Biol Phys 35:1011–1018
76. Kagawa K, Lee WR et al. (1997) Initial clinical assessment of CT-MRI image fusion software in localization of the prostate for 3D conformal radiation therapy. Int J Radiat Oncol Biol Phys 38:319–325
77. Milosevic M, Voruganti S et al. (1998) Magnetic resonance imaging (MRI) for localization of the prostatic apex: comparison to computed tomography (CT) and urethrography. Radiother Oncol 47:277–284
78. Wallner KE, Merrick GS et al. (2002) Penile bulb imaging. Int J Radiat Oncol Biol Phys 53:928–933
79. Coakley FV, Qayyum A et al. (2003) Magnetic resonance imaging and spectroscopic imaging of prostate cancer. J Urol 170:S69–S75; discussion S75–S76
80. Coakley FV, Kurhanewicz J et al. (2002) Prostate cancer tumor volume: measurement with endorectal MR and MR spectroscopic imaging. Radiology 223:91–97
81. Pickett B, Vigneault E et al. (1999) Static field intensity modulation to treat a dominant intra-prostatic lesion to 90 Gy compared to seven field 3-dimensional radiotherapy. Int J Radiat Oncol Biol Phys 44:921–929
82. Xia P, Pickett B et al. (2001) Forward or inversely planned segmental multileaf collimator IMRT and sequential tomotherapy to treat multiple dominant intraprostatic lesions of prostate cancer to 90 Gy. Int J Radiat Oncol Biol Phys 51:244–254
83. Pickett B, Kurhanewicz J et al. (2003) Use of magnetic resonance imaging and spectroscopy in the evaluation of external beam radiation therapy for prostate cancer. Int J Radiat Oncol Biol Phys 57:S163–S164
84. Dattoli M, Wallner K et al. (1996) 103Pd brachytherapy and external beam irradiation for clinically localized, high-risk prostatic carcinoma. Int J Radiat Oncol Biol Phys 35: 875–879
85. Zeitlin SI, Sherman J et al. (1998) High dose combination radiotherapy for the treatment of localized prostate cancer. J Urol 160:91–95; discussion 95–96
86. Critz, FA, Williams WH et al. (1999) Post-treatment PSA <or = 0.2 ng/mL defines disease freedom after radiotherapy for prostate cancer using modern techniques. Urology 54:968–971
87. Ragde H, Korb LJ et al. (2000) Modern prostate brachytherapy. Prostate specific antigen results in 219 patients with up to 12 years of observed follow-up. Cancer 89: 135–141
88. Borghede G, Hedelin H et al. (1997) Combined treatment with temporary short-term high dose rate Iridium-192

brachytherapy and external beam radiotherapy for irradiation of localized prostate cancer. Radiother Oncol 44: 237–244
89. Deger S, Dinges S et al. (1997) High-dose rate iridium192 afterloading therapy in combination with external beam irradiation for localized prostate cancer. Tech Urol 3: 190–194
90. Mate TP, Gottesman JE et al. (1998) High dose-rate afterloading 192Iridium prostate brachytherapy: feasibility report. Int J Radiat Oncol Biol Phys 41:525–533
91. Martinez AA, Kestin LL et al. (2000) Interim report of image-guided conformal high-dose-rate brachytherapy for patients with unfavorable prostate cancer: The William Beaumont Hospital phase II dose-escalating trial. Red J 47:343–352
92. Pollack A, Zagars GK et al. (2000) Preliminary results of a randomized radiotherapy dose- escalation study comparing 70 Gy with 78 Gy for prostate cancer. J Clin Oncol 18:3904–3911
93. Stock RG, Stone NN et al. (1998) A dose-response study for I-125 prostate implants. Int J Radiat Oncol Biol Phys 41: 101–108
94. Martinez A, Gonzalez J et al. (2003) Conformal high dose rate brachytherapy improves biochemical control and cause specific survival in patients with prostate cancer and poor prognostic factors. J Urol 169:974–979; discussion 979–980
95. Brenner DJ, Martinez AA et al. (2002) Direct evidence that prostate tumors show high sensitivity to fractionation (low alpha/beta ratio), similar to late-responding normal tissue. Int J Radiat Oncol Biol Phys 52:6–13
96. Zelefsky MJ, Cohen G et al. (2000) Intraoperative conformal optimization for transperineal prostate implantation using magnetic resonance spectroscopic imaging. Cancer J 6:249–255
97. DiBiase SJ, Hosseinzadeh K et al. (2002) Magnetic resonance spectroscopic imaging-guided brachytherapy for localized prostate cancer. Int J Radiat Oncol Biol Phys 52:429–438
98. Kupelian PA, Potters L et al. (2004) Radical prostatectomy, external beam radiotherapy < 72 Gy, external beam radiotherapy $>$ or $= 72$ Gy, permanent seed implantation, or combined seeds/external beam radiotherapy for stage T1–T2 prostate cancer. Int J Radiat Oncol Biol Phys 58:25–33
99. Schild SE, Casale HE et al. (1993) Movements of the prostate due to rectal and bladder distension: implications for radiotherapy. Med Dosim 18:13–15
100. Crook JM, Raymond Y et al. (1995) Prostate motion during standard radiotherapy as assessed by fiducial markers. Radiother Oncol 37:35–42
101. van Herk M, Bruce A et al. (1995) Quantification of organ motion during conformal radiotherapy of the prostate by three dimensional image registration. Int J Radiat Oncol Biol Phys 33:1311–1320
102. Beard CJ, Kijewski P et al. (1996) Analysis of prostate and seminal vesicle motion: implications for treatment planning. Int J Radiat Oncol Biol Phys 34:451–458
103. Antolak J, Rosen I et al. (1998) Prostate target volume variations during a course of radiotherapy. Int J Radiat Oncol Biol Phys 42:661–672
104. Zelefsky MJ, Wallner KE et al. (1999) Comparison of the 5-year outcome and morbidity of three- dimensional conformal radiotherapy versus transperineal permanent Iodine-125 implantation for early-stage prostatic cancer. J Clin Oncol 17:517–522
105. Pollack A, Hanlon AL et al. (2004) Prostate cancer radiotherapy dose response: an update of the fox chase experience. J Urol 171:1132–1136
106. Kitamura K, Shirato H et al. (2002) Three-dimensional intrafractional movement of prostate measured during real-time tumor-tracking radiotherapy in supine and prone treatment positions. Int J Radiat Oncol Biol Phys 53:1117–1123
107. Mah D, Freedman G et al. (2002) Measurement of intrafractional prostate motion using magnetic resonance imaging. Int J Radiat Oncol Biol Phys 54:568–575
108. Nederveen AJ, van der Heide UA et al. (2002) Measurements and clinical consequences of prostate motion during a radiotherapy fraction. Int J Radiat Oncol Biol Phys 53: 206–214
109. Chandra A, Dong L et al. (2003) Experience of ultrasound-based daily prostate localization. Int J Radiat Oncol Biol Phys 56:436–447
110. Dawson LA, Litzenberg DW et al. (2000) A comparison of ventilatory prostate movement in four treatment positions. Int J Radiat Oncol Biol Phys 48:319–323
111. Malone S, Crook JM et al. (2000) Respiratory-induced prostate motion: quantification and characterization. Int J Radiat Oncol Biol Phys 48:105–109
112. Kitamura K, Shirato H et al. (2002) Registration accuracy and possible migration of internal fiducial gold marker implanted in prostate and liver treated with real-time tumor-tracking radiation therapy (RTRT). Radiother Oncol 62:275–281
113. Lattanzi J, McNeeley S et al. (1999) A comparison of daily CT localization to a daily ultrasound-based system in prostate cancer. Int J Radiat Oncol Biol Phys 43:719–725
114. Huang E, Dong L et al. (2002) Intrafraction prostate motion during IMRT for prostate cancer. Int J Radiat Oncol Biol Phys 53:261–268
115. Nederveen AJ, Lagendijk JJ et al. (2001) Feasibility of automatic marker detection with an a-Si flat-panel imager. Phys Med Biol 46:1219–1230
116. Wu J, Haycocks T et al. (2001) Positioning errors and prostate motion during conformal prostate radiotherapy using on-line isocentre set-up verification and implanted prostate markers. Radiother Oncol 61:127–133
117. Lattanzi J, McNeeley S et al. (2000) Ultrasound-based stereotactic guidance of precision conformal external beam radiation therapy in clinically localized prostate cancer. Urology 55:73–78
118. Langen KM, Pouliot J et al. (2003). Evaluation of ultrasound-based prostate localization for image-guided radiotherapy. Int J Radiat Oncol Biol Phys 57:635–644
119. Teh BS, McGary JE et al. (2002) The use of rectal balloon during the delivery of intensity modulated radiotherapy (IMRT) for prostate cancer: more than just a prostate gland immobilization device? Cancer J 8:476–483
120. Patel RR, Orton N et al. (2003) Rectal dose sparing with a balloon catheter and ultrasound localization in conformal radiation therapy for prostate cancer. Radiother Oncol 67:285–294
121. Uematsu M, Shioda A et al. (2001) Computed tomography-guided frameless stereotactic radiotherapy for stage I non-small cell lung cancer: a 5-year experience. Int J Radiat Oncol Biol Phys 51:666–670
122. Hua C, Lovelock M et al. (2003) Development of a semi-automatic alignment tool for accelerated localization of the prostate. Int J Radiat Oncol Biol Phys 55:811–824
123. Jaffray DA, Siewerdsen JH et al. (2002) Flat-panel cone-beam computed tomography for image-guided radiation therapy. Int J Radiat Oncol Biol Phys 53:1337–1349
124. Sidhu K, Ford EC et al. (2003) Optimization of conformal thoracic radiotherapy using cone-beam CT imaging

for treatment verification. Int J Radiat Oncol Biol Phys 55: 757–767
125. Roach M III, Kurhanewicz J et al. (2001) Spectroscopy in prostate cancer: hope or hype? Oncology (Huntingt) 15:1399–1410; discussion 1415–1416, 1418
126. Ellis RJ, Vertocnik S et al. (2003) Four-year biochemical outcome after radioimmunoguided transperineal brachytherapy for patients with prostate adenocarcinoma. Int J Radiat Oncol Biol Phys 57:362–370
127. Ohori M, Abbas F et al. (1999) Pathological features and prognostic significance of prostate cancer in the apical section determined by whole mount histology. J Urol 161:500–504
128. Sohayda C, Kupelian PA et al. (2000) Extent of extracapsular extension in localized prostate cancer. Urology 55:382–386
129. Teh BS, Bastasch MD et al. (2003) IMRT for prostate cancer: defining target volume based on correlated pathologic volume of disease. Int J Radiat Oncol Biol Phys 56:184–191
130. Roach M III, DeSilvio M et al. (2003) Phase III trial comparing whole-pelvic versus prostate-only radiotherapy and neoadjuvant versus adjuvant combined androgen suppression: Radiation Therapy Oncology Group 9413. J Clin Oncol 21:1904–1911
131. Jacob R, Hanlon AL et al. (2003) Role of prostate dose escalation in patients with $> 15\%$ risk of pelvic lymph-node involvement. Int J Radiat Oncol Biol Phys 57:S150
132. Huang EH, Pollack A et al. (2002) Late rectal toxicity: dose-volume effects of conformal radiotherapy for prostate cancer. Int J Radiat Oncol Biol Phys 54:1314–1321
133. Kupelian PA (2004) Personal communication on the rectal volume limit for IMRT
134. Skwarchuk MW, Jackson A et al. (2000) Late rectal toxicity after conformal radiotherapy of prostate cancer (I): multivariate analysis and dose-response. Int J Radiat Oncol Biol Phys 47:103–113
135. Schultheiss TE, Lee WR et al. (1997) Late GI and GU complications in the treatment of prostate cancer. Int J Radiat Oncol Biol Phys 37:3–11
136. Feigenberg SJ, Hanlon AL et al. (2003) Androgen deprivation increases late morbidity in prostate cancer patients treated with 3D conformal radiation therapy. Int J Radiat Oncol Biol Phys 57:S176
137. Hricak H, Marotti M et al. (1988) Normal penile anatomy and abnormal penile conditions: evaluation with MR imaging. Radiology 169:683–690
138. Plants BA, Chen DT et al. (2003) Bulb of penis as a marker for prostatic apex in external beam radiotherapy of prostate cancer. Int J Radiat Oncol Biol Phys 56:1079–1084
139. Price RA, Murphy S et al. (2003) A method for increased dose conformity and segment reduction for SMLC delivered IMRT treatment of the prostate. Int J Radiat Oncol Biol Phys 57:843–852
140. Ryu JK, Winter K et al. (2002) Interim report of toxicity from 3D conformal radiation therapy (3D-CRT) for prostate cancer on 3DOG/RTOG 9406, level III (79.2 Gy). Int J Radiat Oncol Biol Phys 54:1036–1046
141. Zelefsky MJ, Cowen D et al. (1999) Long term tolerance of high dose three-dimensional conformal radiotherapy in patients with localized prostate carcinoma. Cancer 85:2460–2468
142. Price R, Hanks GE et al. (2002) Advantages of using non-coplanar vs axial beam arrangements when treating prostate cancer with intensity modulated radiation therapy and the step-and- shoot delivery method. Int J Radiat Oncol Biol Phys 53:236–243
143. Hanks G, Hanlon A et al. (1999) Survival advantage for prostate cancer patients treated with high dose 3D conformal radiation. Cancer J Sci Am 5:152–158
144. Brenner DJ, Hall EJ (1999) Fractionation and protraction for radiotherapy of prostate carcinoma. Int J Radiat Oncol Biol Phys 43:1095–1101
145. Fowler J, Chappell R et al. (2001) Is alpha/beta for prostate tumors really low? Int J Radiat Oncol Biol Phys 50: 1021–1031
146. King CR, Fowler JF (2001) A simple analytic derivation suggests that prostate cancer alpha/beta ratio is low. Int J Radiat Oncol Biol Phys 51:213–214
147. D'Souza WD, Thames HD (2001) Is the alpha/beta ratio for prostate cancer low? Int J Radiat Oncol Biol Phys 51:1–3
148. Kupelian PA, Reddy CA et al. (2001) Short-course intensity-modulated radiotherapy (70 GY at 2.5 GY per fraction) for localized prostate cancer: preliminary results on late toxicity and quality of life. Int J Radiat Oncol Biol Phys 51: 988–993
149. Kupelian PA, Willoughby TR (2001) Short-course, intensity-modulated radiotherapy for localized prostate cancer. Cancer J 7:421–426
150. Buyyounouski M, Horwitz EM, Uzzo RG, Price RA, McNeeley SW, Azizi D, Hanlon AL, Milestone BN, Pollack A (2005) Using MRI-simulation to define radiation dose to the penile bulb and corporal bodies for prostate cancer patients treated with intensity modulated radiation therapy or iodine-125 brachytherapy alone. Int J Radiat Oncol Biol Phys
151. Zietman AL, DeSilvio M, Slater JD et al. (2004) A randomized trial comparing conventional dose (70.2 GyE) and high-dose (79.2 GyE) conformal radiation in early stage adenocarcinoma of the prostate: results of an interim analysis of PROG 95-09. Int J Radiat Oncol Biol Phys 60:S131–S132
152. Roach M, Winter K, Michalski JM et al. (2004) Penile bulb dose and impotence after three-dimensional conformal radiotherapy for prostate cancer on RTOG 9406: findings from a prospective, multi-institutional, phase I/II dose-escalation study. Int J Radiat Oncol Biol Phys 60:1351–1356
153. Wernicke AG, Valicenti R, Dieva K et al. (2004) Radiation dose delivered to the proximal penis as a predictor of the risk of erectile dysfunction after three-dimensional conformal radiotherapy for localized prostate cancer. Int Radiat Oncol Biol Phys 60:1357–1363
154. De Crevoisier R, Tucker SL, Dong L et al. (2005) Increased risk of biochemical and local failure in patients with distended rectum on the planning CT for prostate cancer radiotherapy. Int J Radiat Oncol Biol Phys 62:965–973

Intensity-modulated Radiation Therapy for Carcinomas of the Uterine Cervix and Endometrium

Patricia J. Eifel

10

Contents

10.1 Introduction – The Clinical Problem

Radiation therapy plays an important role in the treatment of most patients with invasive cervical cancer and in many patients with uterine cancer. These cancers are usually confined to locoregional sites at the time of diagnosis, and locoregional recurrence is a dominant component of recurrence after definitive treatment, particularly for patients with cervical cancer. For these reasons, accurate determination of the radiation target volume and delivery of a sufficiently high dose of radiation to sterilize locoregional disease are necessary to achieve high cure rates. However, the intimate relationship between the uterus, pelvic lymph nodes, and adjacent critical structures frequently limits the dose of radiation that can safely be delivered. Radiation therapy may be used as a single local modality for locoregionally advanced disease, after surgical resection for more limited cancers, as salvage treatment for recurrent disease, or for palliation.

10.1.1 Radiation Therapy for Locoregionally Advanced Disease

The primary treatment for women who have bulky stage IB or stages IIB–IVA cervical cancer is usually radical radiation therapy, often given with concurrent chemotherapy. Brachytherapy is key to the successful management of intact cervical cancers; in particular, intracavitary radiation therapy (ICRT) permits delivery of a high dose of radiation to the cervix and paracervical tissues while usually sparing adjacent bladder and bowel from severe injury. In most cases, intravaginal packing displaces portions of the bladder and rectum away from the radiation sources; the rapid fall-off of dose with distance from the radiation sources contributes to a favorable therapeutic ratio. Because the ICRT applicators and radiation sources are placed within the target tissue (in the uterus and vagina), the importance of internal organ motion is diminished. Modern treatment with external-beam radiation therapy, ICRT, and concurrent chemotherapy achieves high pelvic disease control rates that range from 70% for patients with stage III disease to more than 85% for patients with bulky ($\geq$ 5 cm diameter) stage IB2 or II disease [1].

However, pelvic disease recurrence continues to be a problem, particularly for patients who have bulky regional disease that falls outside the high-dose range of ICRT; with standard techniques, bowel tolerance limits the dose deliverable to regional nodes. Intensity-modulated radiation therapy (IMRT) may be a means of increasing the radiation dose and the probability of tu-

mor control. Preliminary studies suggest that IMRT may be particularly useful as a tool to deliver high doses of radiation to gross regional metastases without causing an unacceptable risk of serious normal tissue toxicity [2,3].

Some investigators have also speculated that IMRT might be used as an alternative to ICRT in patients with intact cervical cancer [4,5]. The techniques used to deliver optimal ICRT are highly specialized, and because cervical cancer is rare in most developed countries, radiation oncologists may have little experience with these techniques and find them challenging; the capital costs of maintaining the equipment and sources needed for ICRT also provide an incentive to find alternative ways of treating intact cervical cancer. However, as will be discussed, features that make cervical cancer an ideal target for ICRT may be impediments to successful IMRT, and this application of IMRT remains particularly controversial.

10.1.2 Pelvic Radiation Therapy After Hysterectomy

More attention has been given to the postoperative use of IMRT to treat the pelvis. Patients who have early cervical cancers or primary carcinomas of the uterus are usually treated with an initial hysterectomy and lymph node dissection; however, if findings in the surgical specimen suggest a high risk of pelvic recurrence, postoperative radiation therapy is often recommended. Randomized trials have demonstrated that pelvic radiation therapy reduces the rate of pelvic disease recurrence in patients who have undergone hysterectomy for uterine or cervical cancer. However, most studies of high-risk disease still show a significant incidence of pelvic recurrence after delivery of 45–50 Gy of radiation using conventional anteroposterior-posteroanterior or four-field techniques. Ideally, clinicians would like to be able to deliver safely more than 50 Gy to at-risk tissues in the retroperitoneum; clinical data from other sites (e.g., carcinomas of the head and neck) suggest that 50–60 Gy may be needed to prevent recurrence in some patients who have a high of recurrence after radical surgery. However, even the modest doses of radiation that are usually given after radical pelvic surgery can significantly increase the risk of serious complications. Although several studies have suggested that genitourinary side effects may be increased, the most consistent finding has been a marked increase in the incidence of small bowel complications in patients who receive pelvic radiation therapy after radical hysterectomy [6–8].

The most important potential advantage of IMRT over standard two-field or four-field treatment of the whole pelvis is the ability to shape a dose distribution that delivers a lower dose to intraperitoneal pelvic contents (e.g., small and large bowel) than to the surrounding pelvic lymph nodes (Fig. 1). This should make it possible to increase the dose of radiation to the target (to improve pelvic disease control rates) or reduce the acute and late side effects of treatment.

10.1.3 Radiation Therapy for Recurrent Disease

Most of the early studies of IMRT in patients with gynecologic cancer focused on its use to treat the whole pelvis; however, the complex, tightly focused dose distributions that can be achieved with IMRT also make it a powerful tool in the treatment of locoregionally recurrent disease. Integrated boosting of gross disease, differential assignment of avoidance criteria to previously treated normal tissues, and increased conformality of the dose distribution make IMRT particularly helpful in the treatment of patients who have recur-

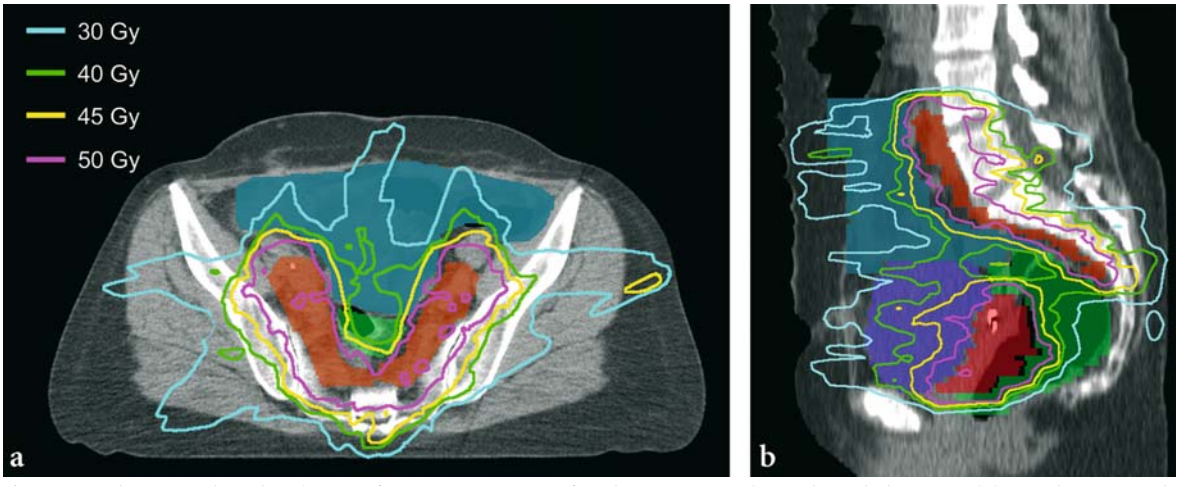

Fig. 1a,b. Radiation isodose distributions for IMRT treatment of the vagina, paravaginal tissues and pelvic lymph nodes in a patient treated after hysterectomy for cervical cancer. Two views show: **(a)** an axial view through the external iliac nodes; **(b)** a midline sagittal view through the vagina, presacral, and common iliac lymph nodes

rences within or marginal to previously treated radiation fields.

10.2 Unique Anatomical Challenges

The radiotherapeutic management of uterine cancers poses special challenges because of the close proximity of internal reproductive organs and their regional draining lymph nodes to critical structures. In addition, the unique anatomy of the uterus and its supporting ligaments permits dramatic shifts in organ position between radiation fractions, complicating accurate target volume definition.

The uterus is suspended in the pelvis by pairs of fibromuscular ligaments – most importantly the broad ligaments, which pass from the sides of the uterus to the lateral walls of the pelvis, and the uterosacral ligaments, which extend backwards from the cervix around both sides of the rectum and attach to the front of the sacrum. The uterosacral and broad ligaments are important routes of gross and microscopic spread of cancer from the cervix. The normal purpose of these elastic structures is to support the uterus while maintaining the extensive mobility needed for coitus and pregnancy. They also permit the uterus to move with variations in bladder and rectal filling and with changes in uterocervical conformation; in patients with cancer, changes in conformation can result from gross expansion of the uterus or cervix by cancer or by fluid that may be trapped in the uterus when tumor blocks the endocervical canal. Although the anatomy of the female reproductive organs is well adapted to their normal function, the variations in internal organ position with time can be dramatic and complex; this factor must be carefully considered in the design of highly conformal IMRT plans.

The uterus, cervix, and vagina are very close to several critical structures. The supravaginal portion of the cervix and superior vagina are separated from the bladder only by a thin layer of connective tissue. Posteriorly, the supravaginal cervix is covered by peritoneum. With the uterus and broad ligaments, the peritoneum forms a septum across the pelvis, creating a space posteriorly that contains the rectum, part of the sigmoid colon, and, frequently, the terminal ileum. These structures are usually in or immediately adjacent to the clinical target volume (CTV) during irradiation of uterine or cervical cancers. If the target is expanded to accommodate internal organ motion, large portions of these structures may lie within the target volume.

When the pelvis is irradiated with the uterus in situ, the uterus and bladder (if filled) frequently displace most of the small bowl out of the pelvis (Fig. 2a), and major enteric complications are rare [9]. When serious small bowel injury does occur after radical radiation treatment of cervical cancer, the terminal ileum is most

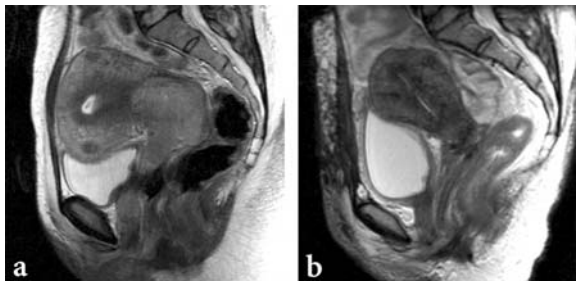

Fig. 2a,b. Midline sagittal MRI views of a patient with cervical cancer: (a) before; (b) after treatment with 45 Gy of external beam irradiation with concurrent chemotherapy. Before treatment, the bulky tumor protrudes into the sacral hollow; the tumor and uterus fill most of the pelvis displacing small bowel superiorly even when the bladder is relatively empty. After external irradiation there has been a dramatic change in the anatomy. The remaining tumor is much smaller, and the positions of the uterus, bladder and rectum have shifted dramatically

frequently affected [9]. Although this may suggest an inherently greater susceptibility to radiation injury, it probably also reflects the frequent anatomical location of the terminal ileum in the posterior cul de sac, a region that may receive a high dose of radiation from brachytherapy or external-beam treatments.

After hysterectomy, bowel tends to fill the space formerly occupied by the uterus; although some bowel can be displaced by encouraging the patient to be treated with a full bladder or by applying external pressure, a substantial portion of small bowel often remains in the pelvis. For patients who require postoperative external-beam irradiation after hysterectomy, the volume at risk usually includes the external iliac, common iliac, and internal iliac lymph nodes as well as the vagina, paravaginal tissues, and posterior bladder wall; for patients with cervical cancer, the presacral nodes may also be included in the CTV. These structures form a cup that contains intraperitoneal small and large intestine. With standard two-field and four-field radiation techniques, it is impossible to treat the walls of the cup without including its contents. IMRT makes it possible to conform the dose distribution to the walls with relative sparing of enclosed intraperitoneal structures.

Highly conformal radiation therapy delivery can only be successful if it is planned with an accurate understanding of the tissues at risk. Simple two- or four-field techniques that treat the entire pelvic contents leave relatively little opportunity for marginal recurrence; nevertheless, careful analysis of patterns of recurrence suggest that even generous lateral fields sometimes miss microscopic tumor within the pelvis (Fig. 3). Our understanding of the tissues at risk after hysterectomy is imperfect. With the advent of routine computed tomography (CT)-based treatment planning, we have discovered a higher than expected incidence of post-lymphadenectomy lymphocysts; we do not yet know whether or when these fluid-filled spaces are at risk for containing disease. Also, our appreciation of the im-

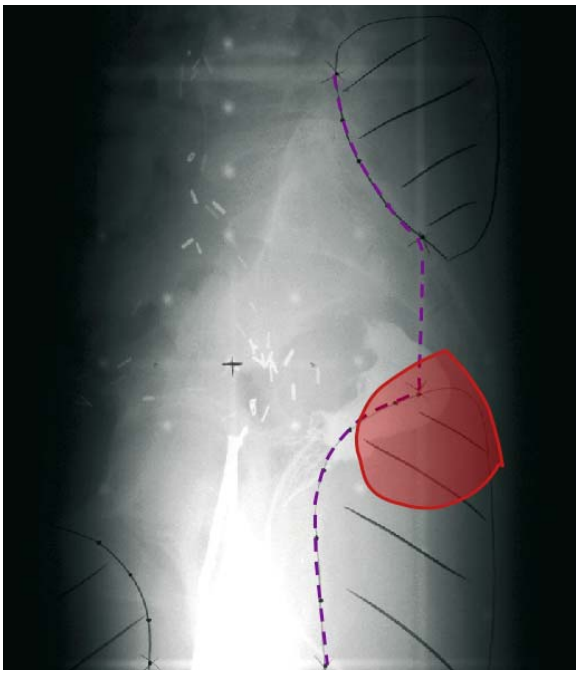

Fig. 3. Site of tumor recurrence in a patient who was initially treated with radiation therapy using antero-posterior, postero-anterior, and two lateral fields after radical hysterectomy for cervical cancer. In this case, the patient experienced an isolated pre-coccygeal recurrence of cancer four years after treatment. The recurrent disease was contoured and superimposed on the original lateral fields demonstrating this to be a marginal recurrence under blocks used to shield the inferior rectum

pact of internal organ motion on the delivered dose is incomplete. IMRT demands detailed, time-consuming evaluation of the target volume anatomy in every case. We routinely review target volumes with our colleagues in diagnostic imaging to verify and improve our understanding of the CT anatomy. Ultimately, detailed analysis of recurrences matched with volumetric radiation dose distributions will be needed to determine whether these target volumes have been sufficient.

10.3 Target Volume Delineation and Organ-at-risk Definition

10.3.1 Tissue Imaging and Clinical Evaluation for Target Volume Definition

Local and regional sites that contain gross or possible subclinical disease usually can be accurately delineated using a combination of diagnostic and treatment planning CT. However, magnetic resonance imaging (MRI) and positron emission tomography (PET) are very helpful in selected cases.

Some clinicians advocate administration of oral, intravenous, or rectal contrast agents during CT simulation for IMRT. If contrast is administered, inhomogeneity corrections must be turned off during the treatment planning process. In our experience, we have not found that rectal contrast adds sufficient information to justify the added patient discomfort and possible anatomical distortion from the administration. Timed intravenous contrast may clarify the position of the great vessels along which lymph node chains are situated; however, we have found that the path of the vessels and node-bearing tissues can also be identified without using contrast by alternating between coronal, sagittal, and axial views and by comparing planning CT images with diagnostic images. MRI scans, which usually yield very clear images of the pelvic vessels, can be particularly helpful.

We do recommend insertion of small radiopaque marker seeds to identify the vaginal apex (in patients who are treated after hysterectomy) or the distal extent of gross disease in the vagina. The vaginal apex is poorly visualized on CT, and even MRI often fails to detect vaginal disease that is readily apparent on clinical examination. Applicators can be purchased to insert marker seeds into the vaginal soft tissue; markers that distend or otherwise alter the vaginal anatomy are not recommended.

If the uterus or upper vagina is included in the CTV, two sequential planning CT scans should be obtained in the treatment position, first with the patient's bladder full and then after the patient has voided. The two scans should be fused to delineate an integrated target volume (ITV) that encompasses the positions of the vagina and paravaginal tissues under both conditions. Although full-bladder CT scans should be used for treatment planning, we have not found that patients can reliably maintain a full bladder throughout a course of pelvic radiation therapy; for this reason, IMRT plans are generated using the vaginal ITV. For shorter courses of IMRT (e.g., for vaginal boosts at the end of pelvic radiation therapy), the bladder may be catheterized, drained, and filled with a fixed volume of saline (usually 150–200 mL) at the time of simulation and immediately before each radiation treatment to decrease daily variations in the position of the vagina.

Diagnostic-quality CT with intravenous contrast or an MRI scan should be used in conjunction with planning CT to identify gross lymphadenopathy for delineation of the gross tumor volume (GTV). However, CT and MRI are able to detect regional metastases only when there is sufficient disease to cause significant lymph node enlargement. Lymph nodes that are heavily infiltrated by tumor but that are not sufficiently enlarged to be considered positive may require more than the 40–50 Gy that is usually given for subclinical disease. Recent studies have demonstrated that PET is a more sensitive method than CT for detecting regional metastases. PET can be a very useful tool in identi-

fying involved nodes that should be treated to more than 50 Gy or that lie outside the true pelvis. The role of PET in the delineation of local disease is less well established; in particular, the possible confounding influence of pelvic infection is unknown. MRI can be very helpful in determining the extent of local disease in the cervix, uterus, and paracervical tissues. However, MRI is less accurate in identifying areas of vaginal extension and should always be supplemented by a careful pelvic examination.

10.3.2 Patient Positioning, Immobilization, and Treatment Planning Imaging

Patients are usually imaged and treated in a supine position. As with all IMRT, external immobilization is a critically important factor in accurate treatment delivery. The magnitude of the margin required for planning target volume (PTV) definition is closely related to the consistency of patient positioning; in turn, the degree of normal tissue sparing achievable with IMRT is closely related to the size of the PTV margin. Patients should at least be immobilized in an immobilization cradle that fixes the position of the upper body, trunk, and proximal legs. If the target volume necessitates treatment of the distal vagina, patients may be positioned with their legs separated or in a frog-leg position to reduce the radiation dose to the vulvar skin. When this is done, the immobilization cradle should extend to include the distal lower extremity to permit reproducible positioning of the hips.

Treatment planning CT should be performed with a maximum slice thickness of 3 mm. The range of imaging depends on the intended target volume. If the target is limited to the true pelvis, the cephalad extent of image acquisition should be to L3–4 or above. If the treatment field will extend to include paraaortic nodes, images should be acquired up to the level of the diaphragms to include the entire kidney volume and, if the upper paraaortic nodes require treatment, to include the entire liver. Distally, the scan should usually include the introitus. If the patient has received previous treatment that overlaps with the new target volume, the entire anatomical range of the previous treatment field should be imaged.

If PET images are obtained specifically for treatment planning purposes, these should ideally be acquired with the patient in the treatment position.

10.3.3 Delineation of Target Volumes

Gross Tumor Volume (GTV)

Tissues that are known or suspected to contain gross disease should be carefully contoured, with separate GTV

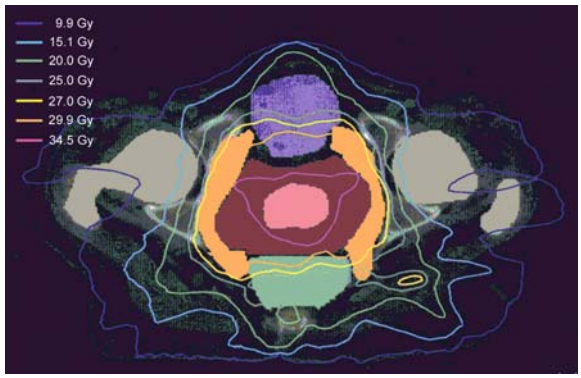

Fig. 4. IMRT radiation isodose distribution for a patient treated with IMRT for stage *IVA* cervical cancer with a vesico-vaginal fistula. Because the patient required emergent treatment, she began with two weeks of external beam irradiation using anterior and posterior fields. Then, using nested target volumes, IMRT was used to give the nodes, GTV, and an internal GTV additional doses of 27, 30, and 34.5 Gy, respectively. Although she had an excellent response to initial treatment, a large fistula persisted, precluding intracavitary therapy. She was then treated with a second IMRT plan, bringing the total dose to the cervix to between 70 and 80 Gy without exposing rectum and small bowel to excessive dose. In this case, only the anterior bladder was contoured as an avoidance structure because the posterior bladder was included in the primary target volume. Two years after treatment the patient has no evidence of cancer but has a persistent fistula

structures contoured for each intended treatment dose level. For example, large lymph nodes are often treated to higher doses than smaller suspicious nodes and should be contoured separately. In some cases, separate, nested GTVs are contoured within a structure to create a gradient of dose within the structure (Fig. 4). In some cases, we have defined multiple GTVs within a lateral-pelvic-wall target structure that requires boost treatment after ICRT for cervical cancer; the contours are then used to generate a plan that mirrors the gradient dose distribution from brachytherapy (Fig. 5). Ideally, this should be done by fusing the treatment planning CT scan with a CT scan of the pelvis with the intracavitary applicator in place (and with superimposed isodose contours from the brachytherapy treatment); unfortunately, incompatibilities between current brachytherapy and external treatment planning systems currently make this difficult to do.

Brachytherapy is often used to deliver boost treatment to gross disease at the primary tumor site in patients with cervical or endometrial cancer. However, in selected cases of cervical or recurrent endometrial cancers that are not amenable to curative brachytherapy, IMRT may be used to treat gross disease at the primary tumor site. Whenever IMRT is used to treat central disease, the effect of possible internal organ motion should be carefully considered (see below). CT usually provides inadequate detail for accurate delineation of the GTV in central structures (cervix, vagina, and paracentral tissues). MRI is an important source of supplementary information in most cases. The extent of

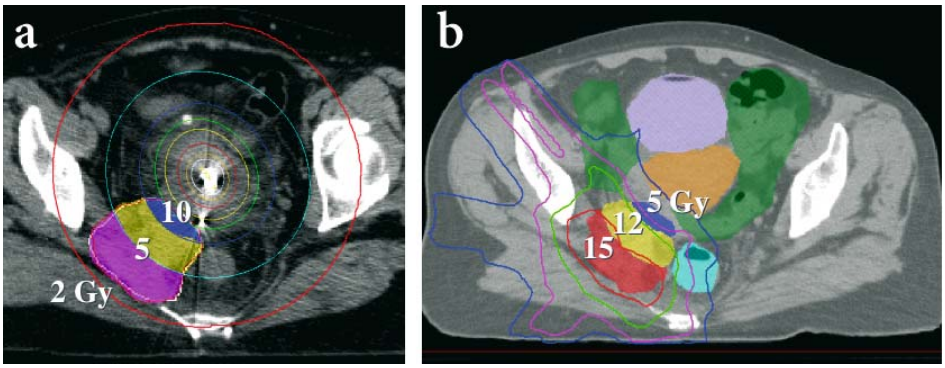

Fig. 5. (a), (b) IMRT used to boost disease that was inadequately treated with intracavitary radiation. This patient initially had a 10-cm cervical cancer that was fixed to the pelvic wall. After 45 Gy and chemotherapy, she had had an excellent response but had gross residual disease invading the uterosacral ligaments surrounding the rectum to the piriformis muscle. The patient underwent low dose-rate intracavitary therapy. She underwent CT with the intracavitary applicator in place for volumetric dosimetry (*left*). This CT with superimposed isodose distributions was fused with a second treatment planning CT. IMRT planning was then used to generate an IMRT plan that would supplement the gradient dose from the intracavitary application bringing the total dose to the uterosacral disease to between 65 and 70 Gy. Because the tumor was firmly fixed to the pelvic wall, uterine motion was not a major concern

vaginal involvement should be carefully defined using marker seeds placed during clinical examination before simulation.

For patients who have bulky central disease, nested GTVs may be used to produce a gradient of radiation dose within the target volume. The value of this approach is not known. However, the extreme gradient produced by ICRT of cervical cancer is highly successful and suggests that delivery of a high dose to the center of a large mass may be of value. Nevertheless, the influence of these additional high- dose targets on dose to adjacent critical structures should be carefully weighed against the theoretical benefit.

Clinical Target Volume (CTV)

The CTV encompasses the GTV as well as any tissues within the treatment volume that are at risk for containing microscopic disease. This should include lymph nodes that drain the involved site and adjacent perinodal soft tissue. The CTV should also include paracervical and paravaginal soft tissues that are at risk for tumor involvement. Tissues that are unlikely to harbor disease, such as intraperitoneal bowel or pelvic bone, should be excluded from the CTV in most cases. However, portions of the bladder, rectum, and pararectal tissue may be included, particularly after internal organ motion is considered (see below).

For most cases of intact or surgically resected endometrial or cervical cancer, the internal (hypogastric and obturator), external, and common iliac lymph nodes are included in the CTV. If the cervix is involved, presacral lymph nodes and soft tissue are usually included, and in selected cases, inguinal or paraaortic lymph nodes may require treatment. Because the lymph nodes lie along the paths of the iliac vessels, identification of the CTV usually begins with identification of these vessels. The regional CTV should include the vessels with surrounding perivascular soft tissue and lymph nodes. Mundt et al. [10] recommend that the contour encompass the common iliac, external iliac, and hypogastric vessels with a 2-cm margin. Bone and intraperitoneal small bowel should be excluded from the CTV; also, ileopsoas muscle that lies adjacent to clinically negative lymph nodes can usually be excluded from the CTV. Approximately 1 – 2 cm of tissue anterior to the S1, S2, and S3 sacral segments is usually added to the CTV to include the presacral lymph nodes and uterosacral ligaments in patients who have cervical cancer. Although most of the external iliac lymph nodes are at risk for metastases from cervical or endometrial cancer, the most anterolateral external iliac lymph nodes that lie just proximal to the inguinal canal (and are usually excluded from conventional anteroposterior-posteroanterior pelvic fields) are rarely involved with cancer from these sites and can probably be excluded from the CTV, particularly if the more proximal nodes are negative. The CTV also must include the uterus and cervix (if present) and at least the upper half of the vagina with adjacent paravaginal and parametrial tissues. However, we usually contour central structures separately at an ITV.

In some cases, it may be desirable to contour multiple CTVs according to the level of risk in various portions of the treatment volume. For, example, in some postoperative cases, central tissues in the vagina and paravaginal space may be considered to have a higher risk of harboring disease, or a region where there was known to have been microscopic paranodal soft tissue extension may be contoured separately to allow prescription of a higher dose to that region.

In patients who have recurrences that straddle previously treated regions, the CTV may be contoured separately within and outside the previous field to provide maximum flexibility in the treatment planning process.

Integrated Target Volume (ITV)

Internal organ motion must be carefully considered any time the radiation target volume includes the uterus or upper vagina. As has been discussed, these structures are suspended on elastic ligaments that often permit far-ranging and unpredictable movement within the pelvis. Although, at least for patients who receive postoperative pelvic radiation therapy, it is usually desirable to treat with a full bladder to reduce the volume of small intestine within the pelvis, we have found that patients are not able to maintain constant levels of bladder filling despite careful counseling. For this reason, we routinely perform planning CT while the patient has a full bladder (the patient is instructed to drink 32 ounces of fluid 60–90 min before simulation) and then perform CT again after the patient has voided (Fig. 6). The two scans are then fused to generate an ITV that encompasses both vaginal positions. If the rectum is filled with gas, some anterior rectal wall may also need to be included within the ITV to ensure coverage of the vagina throughout treatment. For short treatment courses, catheterizing the bladder and filling it with a constant volume of saline daily can reduce variations in vaginal position. Because the vaginal target motion may be large and is independent of the rest of the target volume (e.g., lymph nodes), use of a transabdominal ultrasound system (e.g., BAT) is generally not useful.

The magnitude and complexity of internal organ motion are even greater when the uterus and cervix are present than after hysterectomy. Variations in bladder and rectal filling can cause dramatic translations and rotations in the axis of the uterus; in addition, the positions of the target and normal tissue structures can change significantly with the tumor regression that typically occurs during treatment (Fig. 2). Low et al. [4] have suggested that the problem of internal organ motion could be controlled by internally fixing the uterus using a device similar to an intracavitary applicator; even with this method, though, sequential treatment plans would still be needed to address major changes in the target volume due to tumor regression. Although these authors posed a hypothetical solution to the problem, this technique would be as invasive as ICRT and could be practical only if radiation were delivered in large doses per fraction. Although it is possible to create IMRT dose distributions that have a pear-shaped contour to the dose at point A, the internal dose gradients are less than those achieved with ICRT, and it not know whether they would be equally effective.

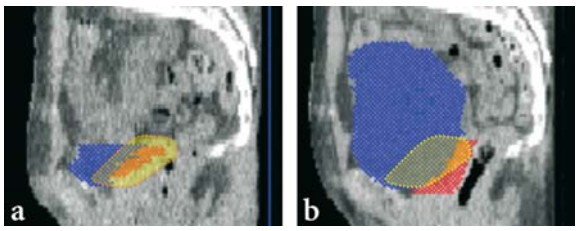

Fig. 6a,b. Sequential planning CT scans taken with: (a) full; (b) empty bladder in a patient who had had a hysterectomy for cervical cancer. The *yellow dotted line and shading* IMRT plan used to treat a patient who experienced a painful recurrence in a right common iliac lymph node six years after treatment with 45 Gy pelvic and paraaortic external beam irradiation for cervical cancer. The patient experience excellent pain relief form more than two years until she developed progression in several other sites indicate a planning target volume that might be drawn from the empty bladder CT scan. With the bladder full, the vagina has moved significantly and is now outside of the original target volume. Failure to consider internal organ motion can result in significant underdosage of the vaginal target volume

Organs at Risk (OAR)

The conformality of pelvic and abdominal IMRT treatments is strongly dependent on the methods used to identify normal tissue structures and on the criteria used to define acceptable normal tissue dose parameters. The processes used to define these avoidance parameters involve a little bit of science and quite a bit of art. As experience with IMRT has grown, clinicians have developed a variety of methods that can be used to drive the computer to generate dose distributions that maximize the difference between the doses to target structures and the doses to OARs. Delineation of avoidance structures for inverse planning requires an understanding of the structure of OARs, their sensitivity to radiation, and the effects of volume irradiation on late effects.

Most of the major complications of high-dose pelvic radiation therapy involve bladder, rectum, or small bowel, and IMRT plans are usually designed to minimize the radiation dose to these structures. These structures should always be delineated on CT scans used for treatment planning. However, it should be recognized that organ contours that are derived from a single CT scan are only approximations of their situation during a course of radiation treatment. Investigators have not yet defined the most useful methods for describing and summarizing dose-volume data for hollow viscera such as the bladder or rectum. In studies of conformal prostate cancer treatment, authors have reported their data in terms of whole organ volumes (including the wall and its contents), organ wall volumes, or mucosal surface areas [11–13]. Because whole-organ contours are simplest to define and have not yet been demonstrated to be less useful than other designations of hollow viscera, rectal and bladder contours are usually defined to include the organ wall and contents. For IMRT treatment planning for gynecologic tumors, the entire rectum is usually contoured up to the level of the splenic flexure.

We usually request that patients have a full bladder during simulation and treatment. The bladder wall is contoured for use as an avoidance structure during treatment planning. However, the posterior bladder wall is usually included in the CTV and is almost al-

ways covered in the ITV as described above. Some treatment planning systems (i.e., Corvus) exclude regions of overlap with the target from normal-tissue dose-volume calculations; with these systems, dose-volume histograms always underestimate the volume of bladder irradiated. It should also be remembered that bladder contours are, in large part, fictitious unless the bladder volume is being artificially controlled (by daily catheterization). Because patients do not consistently maintain a full bladder during treatment, the space occupied by the bladder dome during full- bladder simulation is usually occupied by bowel during at least some of the patient's treatments; this should be considered during specification of avoidance parameters.

The bowel-containing intraperitoneal space is usually contoured as a single structure. All bowel should be contoured within and 1–2 cm above and below the target volume structures; additional bowel may need to be contoured if noncoplanar beam arrangements are being considered, although this is rarely required in gynecologic treatments. No attempt should be made to outline individual loops of small bowel separately; doing so is labor-intensive and unrealistic because bowel moves freely within the peritoneal cavity. For the same reasons, we do not attempt to differentiate between small and large bowel within the peritoneal cavity. However, bowel that lies within or on the margin of a previous radiation treatment field is contoured separately to permit assignment of different avoidance parameters to bowel that is more or less likely to have been affected by previous irradiation (Fig. 7).

Other normal tissue structures should be defined if they are within the plane of radiation treatment. The kidneys, spinal cord, and liver should be contoured if the target volume extends to abdominal structures. The femoral heads and necks should be delimited; other pelvic bones may be contoured for use as avoidance structures, particularly if they have received previous treatment. Because anterior bowel is often given high priority as an avoidance structure, it is often necessary to place a "pseudo-OAR" in posterior bone or soft tissue to avoid hot spots in this region and to encourage a more conformal treatment arrangement.

Planning Target Volume (PTV): Margins for Set-up Variation

Day-to-day variations in patient set-up must be carefully considered in designing highly conformal IMRT treatment plans. Some expansion of the CTV is usually required to account for these variations; this expanded volume is referred to as the planning target volume (PTV). The amount of expansion and the priorities set for coverage of the PTV should take into careful account the reproducibility of the patient's set-up, the critical structures within the expanded volume, and the impact of target volume expansion on the normal tissue sparing relative to more conventional treatment techniques. Ahamed et al. [14] have shown that the normal tissue sparing achieved with IMRT vs conventional four-field conformal pelvic irradiation may be significantly reduced with expansion of the CTV [14]. Also, appropriate parameters for designation of the PTV should vary according to the type of IMRT planning system used. In particular, heterogeneity within the target volume and the steepness of the gradient at the edges of the target volume should be considered in designating a minimum set-up margin. Additional margin depends on documented set-up accuracy achieved within a given institution. However, the most common upper and lower body cradle system with isocenter tattoos usually can achieve 3- to 5-mm accuracy in patients who have an average body habitus. In most cases, a PTV margin of 5–10 mm is needed unless the patient is being repositioned with daily pretreatment imaging.

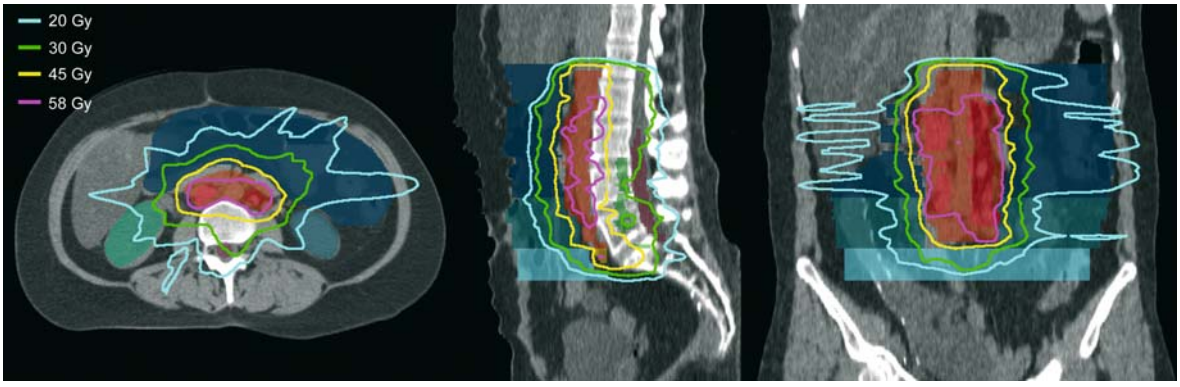

Fig. 7. *Axial*, *sagittal*, and *coronal* views of IMRT plan used to treat a patient who had recurrence in the paraaortic nodes after receiving previous pelvic irradiation for cervical cancer. Details of her previous pelvic treatment were unavailable, so MRI was used to determine the pattern of fatty marrow replacement; this indicated that the entire sacrum had been treated and possibly the L5 vertebral body. To plan this case, the bowel was contoured in three sections corresponding to regions that were more or less likely to have been treated in the past. Different avoidance priorities were set for the three sections. The patient was treated in 25 fractions, receiving 58 Gy (at 2.32 Gy per fraction) to the gross tumor and 45 Gy to clinically uninvolved nodes in the region

10.4 IMRT Treatment Planning

10.4.1 Treatment Prescription Parameters

Target Volume Dose Prescription

The dose of radiation required for tumor eradication depends heavily on the volume of disease. Within a single patient, there are often regions of low risk and regions of small or bulky gross disease that require different doses to achieve tumor control. With standard treatment techniques, this dose variation is usually accomplished with sequential shrinking fields, delivering all treatment with the same daily radiation fraction size. Although conformal field-within-field techniques can also be used, their complexity is limited by the time required to plan and deliver treatments. With IMRT, different doses can quite easily be concurrently delivered to several portions of a target. However, variations in the daily fraction size within the target and adjacent normal tissue must be carefully considered. Hypofractionation of gross tumor may be highly desirable if a steep gradient outside the target results in a reduced dose and fraction size to adjacent normal tissues; in such cases, the therapeutic ratio between tumor and normal tissue effects may be particularly favorable. On the other hand, large daily fractions should be avoided if bowel, bladder, or other critical structures fall within the high-dose volume. The unpredictable motion of central structures (e.g., apex of the vagina, cervix) and intertreatment regression tend to make these regions poor targets for hypofractionation – unless they are firmly fixed, the risk of including bladder or rectum in the high-dose region is high. Larger daily doses of radiation may be advantageous in treatment of bulky lymph nodes if there is reliable patient set-up permitting a sharp dose gradient between lymph node and adjacent bowel.

Prescriptions should be determined after careful consideration of the range of fraction sizes that will be produced and the proximity of critical structures to targets that will receive the highest doses. A range of doses should be selected that does not excessively protract treatment to low-risk tissues and also avoids possible exposure of critical structures to very large fraction size. We usually try to select treatments that can be given with fractions ranging from 1.75 to 2.2 Gy. This still permits a considerable range of doses to different portions of the target: for example, a course of 27 fractions may be prescribed with doses ranging from 47.25 Gy at 1.75 Gy per fraction to 59.4 Gy at 2.2 Gy per fraction. However, this flexibility requires advance planning. It is often tempting to begin treatment with a simpler two-field or four-field technique while time-consuming contouring and IMRT planning are being performed. However, even one or two weeks of such treatment dramatically increases the range of fraction sizes that must be used to achieve effective treatments to microscopic and gross disease.

Hypofractionation of gross tumor may be advantageous in some cases, particularly for patients who are treated for a nodal recurrence within a previously treated field (Fig. 8). When large fraction sizes are used, the total nominal dose required to achieve an effect on tumor is less. If the dose gradient outside the target is steep enough to expose little or no bowel to the larger fraction size, hypofractionation may achieve a more favorable ratio between the effective dose to tumor and normal tissue that a more standard fractionation scheme.

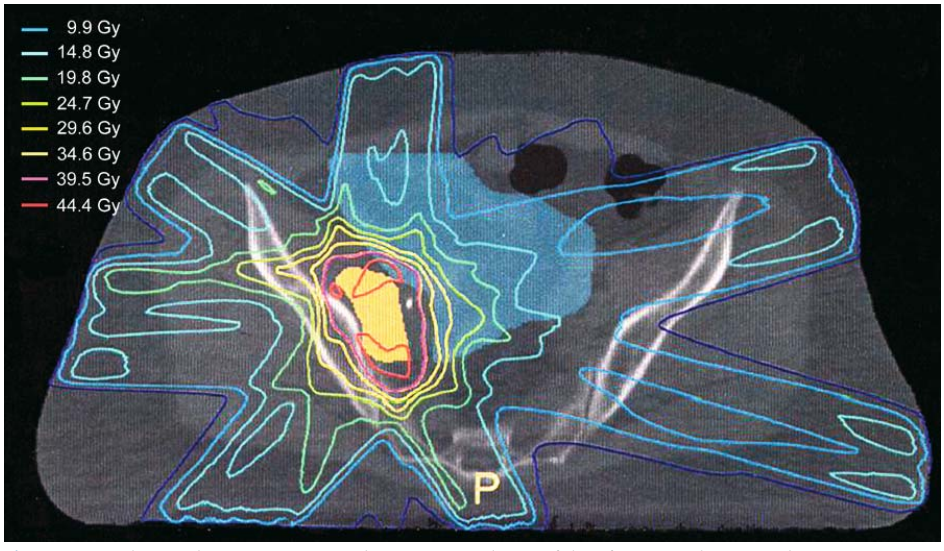

Fig. 8. IMRT plan used to treat a patient who experienced a painful recurrence in a right common iliac lymph node six years after treatment with 45 Gy pelvic and paraaortic external beam irradiation for cervical cancer. The patient experience excellent pain relief for more than two years until she developed progression in several other sites

Selection of Normal Tissue Constraints

All IMRT treatment planning systems require that a set of normal tissue constraints be assigned before plan optimization. However, the methods used to specify and prioritize dose constraints vary markedly between treatment planning systems. Some systems permit the planner to request more detailed dose and volume limits on OARs than other systems. In most systems, very strict limits on the maximum dose to approximating OARs will tend to lead to greater heterogeneity of dose within the target and to areas of possible underdosage within the target. Systems also vary in their consideration of tissues within overlap regions. Optimization of these relationships is often an iterative process, requiring an excellent understanding of the treatment planning system that is in use.

Small and large bowel are frequently the most important dose-limiting structures in patients who receive pelvic radiation. Radiation-induced bowel obstructions are usually caused by exposure of one or more loops of small bowel to a high dose of radiation. The risk of small bowel injury rises steeply and the dose of radiation is increased between 40 and 70 Gy [15]. An effort should always be made to limit the volume of intestine exposed to high doses > 50 Gy. However, it may also be important to limit the volume of bowel exposed to intermediate doses of radiation between 35 and 50 Gy. Although it may be impossible to eliminate the risk of small bowel injury if there is a loop of bowel fixed in close association with the target, the ease of repair and magnitude of long-terms sequelae will be influenced by the health of bowel surrounding the stricture.

10.4.2 Beam Selection

The relatively large target volumes required for many gynecologic treatments are usually best addressed with a coplanar beam arrangement. Eight equally spaced beams often provide a good starting point, particularly for relatively midline or symmetrical target volumes. Beams that pass through a high-priority avoidance structure before reaching the target may be shifted or eliminated, particularly if they are opposite a relatively peripheral target (Fig. 8). Noncoplanar arrangements can be very useful in selected situations, particularly in the treatment of localized recurrences within a previously irradiated field.

A number of factors may influence the number of fields needed to achieve an acceptable plan; in particular, the speed of the delivery system may constrain the number of fields or segments that can be delivered during a reasonable length of time. The groups at the University of Chicago [16] and at The University of Texas M. D. Anderson Cancer Center [14] found that eight or nine coplanar fields were needed to achieve optimal IMRT treatment plans for posthysterectomy treatment of the pelvic lymph nodes, upper vagina, and operative bed. Treatment plans tend to be less conformal when fewer than seven fields are used, and there is usually very little improvement achieved with more than nine fields. Mundt et al. [17] recommend use of nine evenly spaced beams placed at 40° intervals. The treatment protocol used at M. D. Anderson Cancer Center [14] uses eight beams positioned at 20, 85, 120, 150, 210, 240, 275 and 340°. Treatments are usually delivered using 6-MV beams; in our experience, 18-MV beams rarely produce plans for this volume superior to the plans produced with 6-MV beams, and 18-MV beams generate more potentially harmful neutron exposure than do 6-MV beams.

Optimization systems tend to favor beams that pass from the skin surface to the target in relatively short distances, particularly if the beams do not pass through a critical structure with a particularly high avoidance priority. Treatment of eccentrically positioned targets (e.g., pelvic wall lymph nodes) usually favors fields that enter from the ipsilateral side, while more central targets (e.g., paraaortic lymph nodes) are usually treated with more evenly distributed concentric beam arrangements.

10.4.3 Prioritization and Optimization and Evaluation of Treatment Plans

Optimization strategies and methods of prioritization must be tailored to the treatment planning system that is being used. Optimal IMRT planning requires some understanding of a treatment planning program's response to changes in normal tissue constraints and prioritization; because these responses vary according to the treatment planning system, parameters cannot always be generalized from one system to another.

After delineation of the target volumes and initial beam selection, avoidance criteria must be set for critical structures. Assignment of priorities is often an iterative process that requires careful, critical evaluation of the dose distribution to the target and normal tissues and particularly to normal tissue structures in regions of overlap with the target.

The primary theoretical advantage of IMRT of the postoperative pelvis is to reduce the radiation dose to small bowel deep within the pelvis. Criteria should be set to minimize the volume of bowel receiving more than 30–40 Gy. However, criteria should be sufficiently flexible to permit adequate coverage of the CTV and PTV. If very strict criteria are placed on the maximum small bowel dose, optimization systems tend to cut into these anterior protruding portions of the target. To avoid this, it may be necessary to expand the target slightly in this region or to relax small bowel avoidance criteria. The greatest sparing of bowel is achieved when treatment is delivered while the patient has a full bladder. However, patients cannot achieve consistent bladder filling

during treatment, and treatment planning CT may be performed with a full or empty bladder. If the patient had a full bladder for treatment planning CT, OAR dose limits should be assigned, keeping in mind that space occupied by the bladder will sometimes contain small bowel during treatment delivery.

Careful attention should also be paid to dose heterogeneities within the target volume. The CTV and PTV usually overlap with OARs, particularly bowel. A modest volume of small bowel can usually tolerate a dose of 45–50 Gy at standard daily doses; however, depending on the planning systems, optimized plans can produce regions of higher dose within the target. If these overlap with critical structures, they can be a source of potential side effects. It is particularly easy to miss these hot spots when using treatment planning systems that exclude overlap regions from the OAR dose-volume histograms. It is important to scrutinize the dose distributions where bowel is located within the periphery of the GTV or CTV, particularly if the target is treated with high doses or large daily doses.

Very strict constraints on one OAR can cause regions of excess dose to concentrate in unconstrained bone or soft tissues. For example, during planning for posthysterectomy pelvic RT, constraints on small bowel dose can drive the optimization to place heaving weightings on posterior fields; it is often necessary to place constraints on the sacral dose or to add a pseudo-OAR in the region of the sacrum to prevent excess dose in this region. Hot spots may also occur within the margin of tissue assigned as part of the PTV. If this is unacceptably high, the PTV margin or its priority can be reduced; however, set-up reproducibility should be carefully considered when making these adjustments. Also, in some cases a considerable volume of normal tissue may be irradiated to cover the vaginal ITV. This can be reduced by treating the patient with a fixed volume of saline instilled by catheterization of the bladder, but this approach may not be acceptable to the patient during long treatment courses.

It is also important not to compromise coverage of the target to maintain overly strict avoidance of normal tissues. Target structures that protrude into or surround a critical structure create particularly challenging optimization problems. In the pelvis, increased anterior coverage of the external iliac nodes tends to reduce sparing of intrapelvic bowel. Strict bowel constraints may cause the optimization program to reduce coverage in this area. In some cases, this can be improved by increasing constraints on PTV coverage; alternatively, coverage can be improved by selectively expanding the CTV in this region.

Forward and inverse planning systems are highly responsive to alterations in target volume delineation and planning constraints. With experience, clinicians and dosimetrists learn to anticipate many of these responses to achieve excellent plans, often with relatively few iterations. However, careful plan evaluation is always a critical part of the planning process. In many cases, the first step is to evaluate dose-volume histograms for overall coverage of the targets, the irradiated volumes, and doses received by OARs. However, this should always be followed by careful scrutiny of the radiation dose distributions to determine whether the inevitable compromises are acceptable and to perform final assessment of the adequacy of the target volume definition and coverage.

10.5 Clinical Experience/Trials Defining the Role of IMRT

Until recently, IMRT was still a very scarce resource in most centers and many of the clinical protocols focused on a limited number of sites, particularly prostate, or head and neck neoplasms. Although the use of IMRT in gynecologic applications is expanding, there have as yet been few clinical reports of results in patients who were treated with IMRT for cervical or endometrial cancers. Most published studies have included fewer than 50 patients and have had short durations of follow-up after treatment. However, a few studies have provided early indications that the acute side effects of pelvic radiation therapy may be reduced with IMRT when compared with more conventional two- or four-field techniques.

The largest clinical experiences have been reported by investigators at the University of Chicago [10,16–18]. In several recent papers, these authors have reported results in 36 patients who received pelvic IMRT for cervical or uterine cancer between February 2000 and August 2001. Their study group was heterogeneous; most were treated with RT after hysterectomy although about one-third had a uterus at the time of pelvic IMRT; 53% received concurrent chemotherapy with RT; 61% underwent ICRT. Acute and subacute toxicity were compared between these patients and a group of historical control patients who were treated with a standard four-field approach. Although the characteristics of patients in these two groups appeared to be similar, their follow-up durations differed and subtle differences between patients and data collection methods could have biased comparisons. However, the results do suggest that patients may have benefited from IMRT; only 60% of patients experienced grade 2 or greater gastrointestinal toxicity during pelvic IMRT vs 91% of patients treated with a four- field technique ($p = 0.002$); the rates of urinary tract toxicity were not significantly different between the two groups [16]. In a subsequent report [10] the authors compared chronic gastrointestinal toxicity in the two groups; although follow-up of patients in the IMRT group was short, the results suggested that patients treated with IMRT had a lower rate of chronic gastrointestinal side effects that those treated with four

fields. In a more recent paper [18], these authors have suggested that hematological toxicity may also be reduced with IMRT, particularly if pelvic bone marrow is designated as an avoidance structure. However, efforts to spare bone marrow may increase the doses to other normal tissue structures and the dose heterogeneity within the target volume [19].

Overall, these early studies of pelvic IMRT are very encouraging, but longer follow-up will be needed to fully evaluate the risks of late toxicity and recurrence and, ultimately, prospective randomized comparisons will be needed to determine whether IMRT of the whole pelvis is better than less expensive conventional radiation techniques.

Potential uses of IMRT to increase the deliverable dose of radiation to gross disease in regional lymph nodes are of particular interest because recurrence in these sites is a major source of failure with standard techniques. In a study of regional disease control in patients with cervical cancer, Grigsby et al. [20] have demonstrated that high regional control rates may be achieved if advanced imaging techniques are used to determine the risk of tumor involvement and if adequate doses of radiation are delivered to sites of regional metastasis. In preliminary studies, Esthappan et al. have demonstrated how CT and PET may be used to guide IMRT treatment plans that would tailor radiation dose to the volume of disease while minimizing the risk of serious late toxicity. This kind of approach is likely to be an important subject of future clinical studies.

References

1. Eifel PJ, Winter K, Morris M et al. (2004) Pelvic irradiation with concurrent chemotherapy versus pelvic and para-aortic irradiation for high-risk cervical cancer: an update of radiation therapy oncology group trial (RTOG) 90–01. J Clin Oncol 22:872–880
2. Esthappan J, Mutic S, Malyapa RS et al. (2004) Treatment planning guidelines regarding the use of CT/PET-guided IMRT for cervical carcinoma with positive paraaortic lymph nodes. Int J Radiat Oncol Biol Phys 58:1289–1297
3. Mutic S, Malyapa RS, Grigsby PW et al. (2003) PET-guided IMRT for cervical carcinoma with positive para-aortic lymph nodes-a dose-escalation treatment planning study. Int J Radiat Oncol Biol Phys 55:28–35
4. Low DA, Grigsby PW, Dempsey JF et al. (2002) Applicator-guided intensity-modulated radiation therapy. Int J Radiat Oncol Biol Phys 52:1400–1406
5. Schefter TE, Kavanagh BD, Wu Q et al. (2002) Technical considerations in the application of intensity-modulated radiotherapy as a concomitant integrated boost for locally-advanced cervix cancer. Med Dosim 27:177–184
6. Corn BW, Lanciano RM, Greven KM et al. (1994) Impact of improved irradiation technique, age and lymph node sampling on the severe complication rate of surgically staged endometrial cancer patients: a multivariate analysis. J Clin Oncol 12:510–515
7. Landoni F, Maneo A, Colombo A et al. (1997) Randomised study of radical surgery versus radiotherapy for stage Ib–IIa cervical cancer. Lancet 350:535–540
8. Sedlis A, Bundy BN, Rotman MZ et al. (1999) A randomized trial of pelvic radiation therapy versus no further therapy in selected patients with stage IB carcinoma of the cervix after radical hysterectomy and pelvic lymphadenectomy: a Gynecologic Oncology Group study. Gynecol Oncol 73:177–183
9. Eifel PJ, Levenback C, Wharton JT et al. (1995) Time course and incidence of late complications in patients treated with radiation therapy for FIGO stage IB carcinoma of the uterine cervix. Int J Radiat Oncol Biol Phys 32:1289–1300
10. Mundt AJ, Mell LK, Roeske JC (2003) Preliminary analysis of chronic gastrointestinal toxicity in gynecology patients treated with intensity-modulated whole pelvic radiation therapy. Int J Radiat Oncol Biol Phys 56:1354–1360
11. Jackson A, Skwarchuk MW, Zelefsky MJ et al. (2001) Late rectal bleeding after conformal radiotherapy of prostate cancer. II. Volume effects and dose-volume histograms. Int J Radiat Oncol Biol Phys 49:685–698
12. Koper PC, Heemsbergen WD, Hoogeman MS et al. (2004) Impact of volume and location of irradiated rectum wall on rectal blood loss after radiotherapy of prostate cancer. Int J Radiat Oncol Biol Phys 58:1072–1082
13. Huang EH, Pollack A, Levy L et al. (2002) Late rectal toxicity: dose-volume effects of conformal radiotherapy for prostate cancer. Int J Radiat Oncol Biol Phys 54:1314–1321
14. Ahamed A, D'Souza W, Salehpour M, Iyer R, Tucker SL, Jhingran A, Eifel PJ (2005) Intensity-modulated radiation therapy after hysterectomy: Comparison with conventional treatment and sensitivity of the normal-tissue-sparing effect to margin size. Int J Radiat Oncol Biol Phys 62(4):1117–1124
15. Eifel PJ, Jhingran A, Bodurka DC et al. (2002) Correlation of smoking history and other patient characteristics with major complications of pelvic radiation therapy for cervical cancer. J Clin Oncol 20:3651–3657
16. Mundt AJ, Lujan AE, Rotmensch J et al. (2002) Intensity-modulated whole pelvic radiotherapy in women with gynecologic malignancies. Int J Radiat Oncol Biol Phys 52:1330–1337
17. Mundt AJ, Roeske JC, Lujan AE et al. (2001) Initial clinical experience with intensity-modulated whole-pelvis radiation therapy in women with gynecologic malignancies. Gynecol Oncol 82:456–463
18. Brixey CJ, Roeske JC, Lujan AE et al. (2002) Impact of intensity-modulated radiotherapy on acute hematologic toxicity in women with gynecologic malignancies. Int J Radiat Oncol Biol Phys 54:1388–1396
19. Lujan AE, Mundt AJ, Yamada SD et al. (2003) Intensity-modulated radiotherapy as a means of reducing dose to bone marrow in gynecologic patients receiving whole pelvic radiotherapy. Int J Radiat Oncol Biol Phys 57:516–521
20. Grigsby PW, Singh AK, Siegel BA et al. (2004) Lymph node control in cervical cancer. Int J Radiat Oncol Biol Phys 59: 706–712

Integration of IMRT and Brachytherapy

Jeffrey F. Williamson

11

Contents

11.1 Introduction

Combinations of external beam radiotherapy and interstitial or intracavitary brachytherapy have been effectively used in variety of clinically settings since the introduction of megavoltage beam therapy in the 1950s. Generally, brachytherapy is used to administer high doses to unresected or residual primary tumor while external beam radiotherapy is used to deliver more modest doses to larger volumes of adjacent tissue or regional lymph nodes at high risk for microscopic invasion. Conventionally, relatively simple external beam field arrangements are used to administer uniform doses to the region treated by brachytherapy. The dose conformality and normal tissue avoidance needed to make the high total tumor dose tolerable is generally provided by the brachytherapy component of treatment. Usually, the brachytherapy and external beam components of treatment are planned independently of one another.

With the advent of intensity-modulated radiation therapy (IMRT), it is now possible for external beam therapy to deliver topologically complex dose distributions that conform to target volumes of arbitrary shape (including concavities and involutions) with rapid dose falloff outside the target volume comparable to brachytherapy. Brachytherapy also is able to realize highly conformal dose distributions for treating nonconvex target volumes. These two conformal treatment modalities have somewhat complimentary strengths and weaknesses. IMRT is able to produce more homogeneous dose distributions, while brachytherapy avoids much of the geometric uncertainty characteristic of current external-beam delivery techniques that effectively limits the conformality and normal tissue sparing achievable by IMRT. The many possible ways of combining these two modalities provides new opportunities for improving well-established brachytherapy-external beam regimens, but also expands the possibilities for delivering more aggressive radiotherapy regimens to extended loco-regional target volumes. This chapter reviews the published clinical literature on combined IMRT-brachytherapy regimens. In addition, the clinical and technical challenges that arise in integrating these two modalities are discussed along with the research initiatives designed to address these problems.

11.2 Comparative Merits and Disadvantages of Brachytherapy and IMRT

11.2.1 Dose Distribution Characteristics

Both brachytherapy and IMRT produce highly conformal dose distributions, although few quantitative analyses comparing the two modalities have been published. Using a quantitative index of conformality, the "conformation number (*CN*)", Van't Riet et al. [1] have compared prostate brachytherapy and 3D conformal radiation therapy (3D-CRT) plans. *CN* is defined as the

product of two ratios: the fraction of the target receiving a dose equal to or greater than the prescribed dose, D_{ref}, and the ratio of target volume receiving a dose $\geq D_{ref}$ to the total tissue volume receiving a dose $\geq D_{ref}$. Both ratios are unity when the D_{ref} isodose surface exactly covers the target volume without including any normal tissue. For ^{125}I permanent seed prostate implants and 3D-CRT plans, respectively, Van't Riet found *CN* values of 0.72 and 0.65. Using the same index, Zelefsky [2] found conformality values for IMRT prostate plans of 0.63 and 0.82 for prescribed doses of 81 and 75.6 Gy, respectively. Thus, available evidence suggests that comparable dose conformality can be realized by the two treatment modalities.

However, as illustrated in Fig. 1, normal tissue sparing, which is governed by the steepness of the dose-gradient outside the target volume, is not well predicted by the conformality number, which describes the dose distribution shape for a single dose level. Because of inverse square law, ^{103}Pd and HDR ^{192}Ir brachytherapy dose distributions fall off isotropically (equally in all radial directions away from the target volume surface) reducing the dose to 25% and 37% 1 cm outside of the 95% isodose (Fig. 1d). This falloff varies slowly with implanted volumes. The IMRT dose distribution falls off more slowly in the transverse plane (falling to 57% 1 cm outside the 95% isodose), where extra-target tissue is contained within the intersection of several converging beams. However, on the superior and inferior boundaries of the CTV, where the dose is collimated by the beam edges, the dose falloff is comparable to the ^{103}Pd implant (see Fig. 1e). While the additional degrees of freedom provided by intensity modulation dramatically increases the planner's dose-shaping capabilities, both IMRT and conventional radiation therapy (RT) still rely on positioning the target tissue within the intersection of multiple converging beams to spare normal tissue surrounding the target volume. For unmodulated rotational beam therapy, Fig. 2 demonstrates that, as the field size increases, extra-target dose gradients decrease, and the magnitude of dose sparing achievable in the transverse plane rapidly diminishes. While intensity modulation can create tissue sparing and dose gradients comparable to brachytherapy in any specified local region along the target circumference, IMRT cannot provide brachytherapy-like dose falloff around the entire target volume surface. Due to the less rapid fall off in the transverse and the 10-mm margin required by IMRT, the volume of tissue treated by IMRT to 75% of the prescribed dose is approximately five times that of brachytherapy (See Fig. 1f).

Generally, IMRT is able to achieve much superior dose homogeneity within the target volume. A well-optimized HDR interstitial implant may limit the magnitude of the high dose region receiving at least 150% of the prescribed dose to 20–25% of the target volume. In

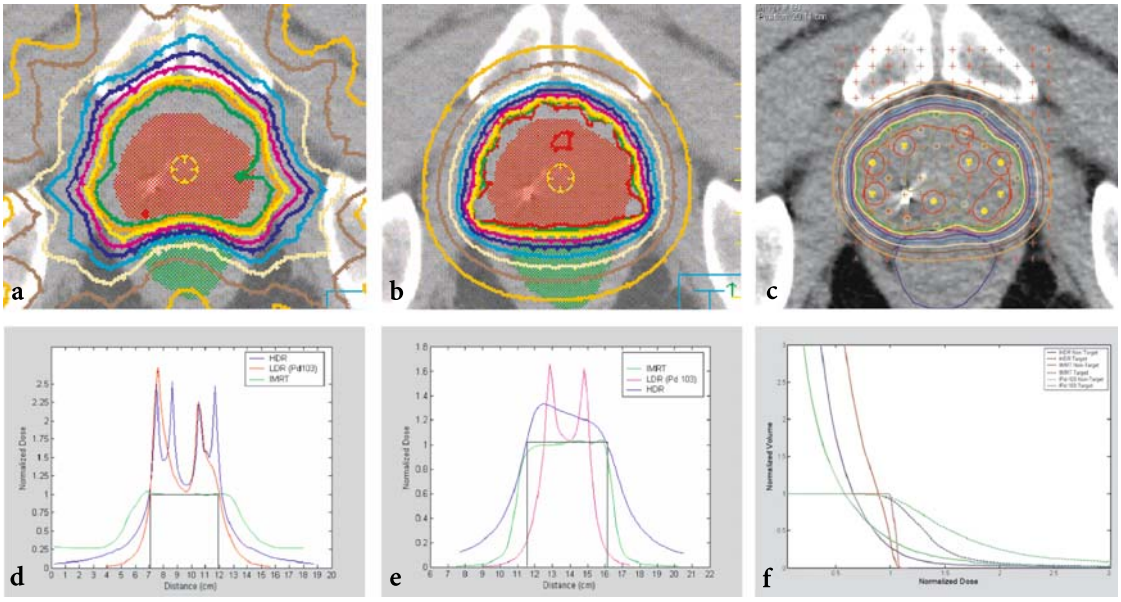

Fig. 1a–f. Isodose plots of: (a) a nine field coplanar IMRT plan; (b) an HDR ^{192}Ir interstitial implant; (c) an LDR ^{103}Pd permanent seed implant. The isodoses are normalized so that 100% (*Green isodose*) denotes the prescribed dose (for IMRT, D_{98} to PTV prostate +10-mm margin (6 mm posteriorly) and for implants, D_{90} (LDR) and D_{98} (HDR) to prostate capsule. For HDR and IMRT, the following isodose lines are shown: 110%, 100%, 95%, and lines from 90% to 30% in decrements of 10%. For the LDR implant (c), the following isodoses lines are shown: 200%, 130%, and lines from 100% to 30% in decrements of 10%; (d),(e) transverse (right-to-left) and axial (caudad-to-cephalod) 1-D normalized dose (dose/prescribed dose) profiles, respectively, passing through the center of the prostate. The *black rectangles* indicate the boundary of the prostate gland; (f) dose-volume histograms evaluated for the prostate gland and all extra-prostatic tissue. Dose is expressed in multiples of the prescribed dose and volume in terms of multiples of the prostate gland volume (47 cm^3 in this case)

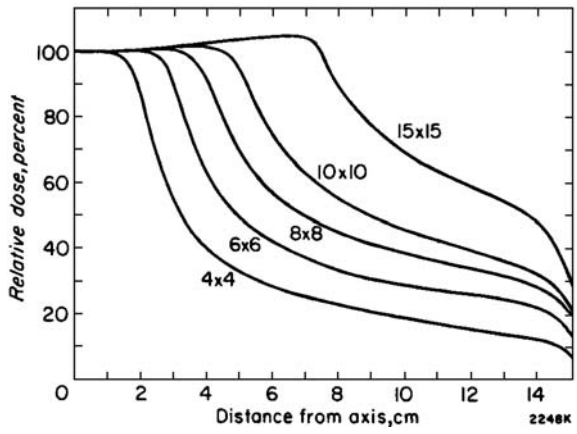

Fig. 2. Dose profiles for 360° rotation about a 30 cm diameter cylindrical phantom for field sizes from 4 × 4 to 15 × 5 cm. From [77] with permission

contrast, VCU's IMRT planning guidelines for head and neck limit the volume receiving more than 10% of the prescribed dose to no more than 2% of the GTV volume.

In summary, IMRT and interstitial brachytherapy both support creation of highly conformal dose distributions. However, optimization software for identifying optimal brachytherapy source locations, needle trajectories, and dwell weights to create user-specified dose distributions is much less well developed compared to IMRT. IMRT dose homogeneity is inherently superior to that of brachytherapy. Except for very small target volumes, brachytherapy dose fall-off outside the target tissue is superior that achievable with IMRT, in that rapid dose falloff is, in principle, uniformly distributed around the target surface rather than limited to user-specified focal regions adjacent to the target surface.

11.2.2 Geometric Delivery Uncertainties

For both brachytherapy and IMRT, assuring adequate coverage of the target volume and avoiding geometric miss present challenges. While both modalities are affected by geometric uncertainties, their origins and management techniques differ. Assuming that an adequate quality assurance program is in place, IMRT dose distributions can be delivered with mm or even sub-mm accuracy within the accelerator frame of reference. However, using conventional setup, immobilization, and weekly port film verification techniques, soft-tissue targeting accuracy achievable in practice is substantially reduced. As reviewed in more detail elsewhere in this volume, using surface or bony landmarks to align the patient with the accelerator coordinate system on a daily basis along with conventional verification techniques results in errors in alignment of the isocenter relative to bony anatomy (setup errors) and in alignment of the soft-tissue target volume relative to bony structures (internal motion errors). These errors have both systematic (a displacement that persists through a course of therapy) and random (fluctuates fraction-to-fraction about the patient's systematic error) components. For prostate cancer, estimates of standard deviation for random and systematic setup error range from 3 to 4 mm and, 2–3 mm per axis, respectively [3–8]. This corresponds to 26–36% of the patients having an offset > 5 mm. Interfraction internal motion errors of 3–4 mm have been reported [9]. These errors are managed by a combination of generous CTV delineation and contouring practices and the explicit addition of a PTV margin. ICRU reports 50 [10] and 62 [11] recommend that the prescribed dose should be delivered to the expanded PTV in order to assure adequate dose delivery to the CTV. According to the probabilistic margin recipes of Stroom [6] and Van Herk [12], margins of 8 mm for internal motion and 11 mm for internal plus setup error, are required to ensure that prostate CTVs are adequately covered for 90% of the patients. These additional margins significantly increase the volume of tissue irradiated to high doses and correspondingly reduce the potential for normal tissue sparing. For a 60-cc prostate, an 11-mm margin corresponds to a threefold increase in the volume of tissue receiving the prescribed dose.

The uncertainties described above are characteristic of conventional immobilization and verification techniques. By quantitatively analyzing daily orthogonal setup images, acquired by means of electronic portal imaging devices (EPID), and implementing online [13] or offline [14] setup corrections, it is possible to reduce setup error significantly, resulting in systematic setup error standard deviations as low as 1–2 mm. Similarly, by using five serial daily CT images to estimate a corrected CTV during the first week of treatment, Yan et al. [15] demonstrated that the PTV margin needed to ensure adequate prostate coverage due to internal motion errors could be reduced from 10 to 6–7 mm. In-room 3D imaging systems – such as CT-on-rails [16] and linac-mounted kilovoltage cone-beam CT [17] – offer the possibility of even larger reductions of geometric uncertainty for IMRT and other forms of external beam radiotherapy.

Brachytherapy seeds, needles, and other applicators are inserted directly into the target tissue either using image guidance, as in the case of prostate brachytherapy, or by direct visualization and palpation of the target. Thus systematic shifts of the delivered dose distribution relative to the target tissue are unlikely in the hands of an experienced brachytherapist since external landmarks are not used to guide seed or applicator insertion. Indeed, for interstitial brachytherapy, ICRU Report 58 [18] does not recommend adding a PTV margin to the CTV. Moreover, no margins for tissue motion are thought to be needed, since implanted sources will be displaced along with the local tissue.

While the clinical success achieved by experienced brachytherapists supports the practice of implanting

margin-free CTVs, there is little published data available to quantify the geometric precision with which brachytherapy dose distributions can be delivered to target volumes delineated on pre-treatment images. One factor that limits the brachytherapy delivery accuracy are limits on the accuracy with which the operator can implant a seed or applicator at an intended location due to needle deflection, target- tissue deformation, and seed migration. Published analyses quantifying source-positioning errors are few and are largely limited to permanent prostate seed implants. Roberson [19], Yu [20], and Taschereau [21] have compared intended locations (based upon pre- procedure TRUS volume images) with seed coordinates extracted from post-procedure CT images for small patient samples. These authors reported average seed displacements from their preplanned locations, a metric which ignores the displacement direction, of approximately 0.5 cm. This corresponds to a standard deviation (averaged over all seed positions within a given patient) of approximately 3 mm per orthogonal axis. None of these studies rigorously distinguishes between systematic and random error, although some of the data suggest that random errors dominate. It must be noted that these studies compare intended treatment plans with realized plans. Therefore, they do not distinguish between true positioning errors and legitimate adaptations of the intended plan undertaken to accommodate the average 60% discrepancy between prostate CTVs derived from TRUS volume studies and post- implant CT images [22], relatively poor definition of the prostate capsule by X-ray CT [23], edema and deformation of the prostate by the implant procedure, inability to reproduce exactly the preplan anatomy, and a host of other factors. The accuracy with which stainless steel HDR interstitial applicators can be inserted appears to be about 2 mm, based upon the measured of image-guided biopsy needle localization; several [24, 25] have studied the accuracy of MRI-guided intraprostatic placement of gold fiducial markers and prostate biopsy needles.

Two studies [20, 26] have assessed the influence of random errors in seed positioning on dose-delivery accuracy by means of stochastic simulations. Both studies demonstrate that clinically validated dose- specification indices are quite insensitive to random error. Both studies found that D_{90} and V_{95} varied by less than 5% for seeds normally distributed about their reference locations with $\sigma = 0.4–0.6$ cm. However, minimum dose to the prostate (*mPD*) was much more sensitive, ranging from 10% for larger implants to 30% for small implants [20]. These theoretical results are supported by Merrick's [22] analysis of 60 patients, in which quality indices derived from preoperative planning, based on TRUS volume studies, were compared to those derived from post-implant CT imaging. The average post-implant D_{90} and D_{100} values were 108 and 68%, respectively, of the prescribed preplan *mPD* ($= D_{100}$) while the post-implant V_{100} was 0.94. The corresponding pre-implant D_{100} and V_{100} values were 100% and 0.995, respectively. As predicted, experienced operators achieve excellent coverage of the prostate despite the many factors, described above, that invalidate the target-volume geometry extracted from pre-implant imaging procedures.

Besides needle and seed insertion accuracy, brachytherapy delivery precision is compromised by other factors that depend on the implant modality. For example, permanent implant dose delivery is affected by prostate edema, which increases the prostate volume by 30–50%, and slowly resolves with a 4–25-day half life [27] and increases D_{90} by 15% on average [28]. The accuracy with which implanted seeds or applicators track soft-tissue target volumes in the face of intrafraction internal motion (LDR brachytherapy) or interfraction tissue motion (fractionated HDR) affect has not been quantitatively studied. From this perspective, intraoperatively image-guided single-fraction HDR interstitial brachytherapy is perhaps the most geometrically and dosimetrically precise of all extracranial radiotherapy delivery modalities [29]. In this setting, the dwell positions relative to the CTV surface visualized intraoperatively accurately describe their locations during treatment. In addition, intraoperative dwell-weight optimization can be used to compensate for deviations in the planned vs treated needle locations.

In summary, available data suggest that the standard deviation of seed and needle placement errors is about 0.4–0.5 cm (corresponding to 3 mm/axis), that systematic error remains to be quantified accurately, that prognostically-significant indices such as D_{90} and V_{100} are relatively insensitive to random source positioning errors, but can significantly underdose the periphery of the target volume, rendering D_{100} an unstable quality index unsuitable for prescribing brachytherapy doses. Single-fraction intraoperatively imaged and planned HDR interstitial brachytherapy currently represents the ultimate in "what you see is what you get" radiotherapy. Like IMRT and external-beam radiotherapy, research aimed at improving the geometric accuracy of brachytherapy is underway at a number of centers. These developments include use of a single intraoperative imaging modality (MR [30] or TRUS [31]) to plan and evaluate permanent implants, intraoperative planning [32, 33], intraoperative implant optimization to reduce the impact of seed positioning errors [34], and robot-assisted seed and needle positioning [35].

11.2.3 The Role of 3D Imaging in Treatment Planning

IMRT is inherently an image-based radiation therapy modality. A full 3D model of the target and normal-tissue anatomy is used to specify the desired dose distribution in terms of DVH, dose, and biological

model endpoints and constraints, all defined with reference to underlying anatomy. Brachytherapy, on the other hand, historically is a surgical modality: image-guided applicator and source insertion are relatively recent innovations. The extent to which imaging is integrated into the planning and evaluation of brachytherapy dose delivery is highly dependent upon the brachytherapy procedure and the implanted site. Intracavitary brachytherapy for locally advanced cervical carcinoma represents one extreme. Other than using orthogonal radiographs to identify bladder and rectal references and to check the quality of the placement, imaging is rarely used to plan or place intracavitary applicators. Among the reasons are inability of CT imaging to define cervical cancer GTV [36, 37] and significant deformation of the soft tissues due to applicator insertion, tumor regression, and other factors [38]. At the other extreme, technology for transrectal ultrasound (TRUS)-guided transperineal prostate implants is well developed for both permanent seed implants and HDR temporary interstitial boosts. The growing acceptance of image-based evaluation of brachytherapy dose distributions offers the prospect of integrating brachytherapy and IMRT in new and innovative ways since the possibility of registering brachytherapy and IMRT dose distributions in a single anatomic frame of reference now exists.

11.2.4 Accelerated Fractionation

Brachytherapy is a well-established modality for delivering large dose fractions to small and medium volumes. With classical low dose-rate delivery, intracavitary doses as large as 32.5 Gy over 40 h to volumes ranging from 100 to 200 cm^3 are well tolerated [39]. Classical LDR brachytherapy is able to administer large and well-tolerated total doses given over a short overall treatment time in part because of therapeutic ratio advantage conferred by sublethal damage repair [40]. However, HDR brachytherapy can deliver biologically equivalent doses in two to six fractions with fraction sizes ranging from 6 to 10 Gy. HDR brachytherapy as monotherapy has been used to deliver biologically equivalent doses (*BED*) as large as 96 Gy_{10} (6×10 Gy) to oral cavity tumors [33] and as large as 120 Gy_3 (4×9.5 Gy) for low-risk prostate cancer [41]. With the exception of large fraction therapy to very small targets using radiosurgical localization and collimation devices, brachytherapy is clearly the modality of choice for administering large fraction therapy to surgically accessible sites. While IMRT is a promising approach for delivering accelerated fractionation regimens [42, 43], both to GTVs and regional CTVs, its capability of administering HDR-size fractions without exceeding normal tissue tolerance remains to be validated by clinical investigation. One can hypothesize that such large fractions to moderate volumes are well tolerated in part because of the increased normal-tissue avoidance due to the small PTV margins needed for HDR interstitial brachytherapy.

11.3 Clinical Applications of Combined IMRT- Brachytherapy

Efforts to integrate brachytherapy and IMRT fall into one of several categories:

1. IMRT as a replacement for brachytherapy
2. Supplementary IMRT for improving implant quality
3. IMRT as a complement to brachytherapy for treating extended target volumes

11.3.1 IMRT as a Replacement for Brachytherapy

Low and colleagues at Washington University [44, 45] have investigated an external beam modality, "applicator-guided IMRT" or AGIMRT as a potential replacement for HDR intracavitary brachytherapy. The basic idea is to implant a radio-opaque "applicator substitute" into the patient's uterus and vagina prior to imaging the patient for treatment planning. The applicator substitute remains in the patient throughout treatment delivery, and is used on a daily basis to align the external fields with the PTV. The investigators assume that primary tumor volume and the critical anatomy (anterior rectal and posterior bladder walls) are rigid structures rigidly attached to the applicator. Thus the applicator substitute serves as a radiographically visible surrogate for localization of this anatomy. Such an applicator substitute has not actually been constructed and applied clinically. Instead, the authors have compared CT imaging studies of first and second LDR intracavitary insertions using a CT-compatible shielded applicator [46] to assess the accuracy with which the applicator tracks motion of central pelvic anatomy. PET FDG images, acquired with conventional shielded Fletcher-Williamson applicators in place, were used to assess the potential benefits of AGIMRT against HDR brachytherapy in a later study [45].

The results (see Fig. 3 for an example) demonstrate that AGIMRT produces far superior and more uniform coverage of the GTV then conventional HDR intracavitary brachytherapy. For the ten patients investigated, AGIMRT consistently covers 90% of the pretreatment PTV (PET-FDG abnormality +5-mm margin) compared to 58% for conventional brachytherapy [45]. AGIMRT also reduces the volumes of bladder and rectal tissue (a 1-cm critical structure margin was used for IMRT planning but not for DVH endpoint evaluation) exceeding the specified tolerance doses by factors of 2 and 3 respectively, indicating that IMRT is able produce steep

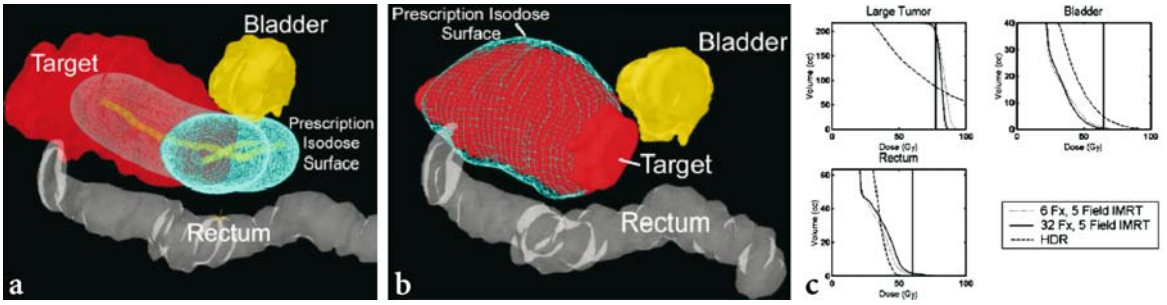

Fig. 3a–c. Comparison of coverage of the PET-FDG defined GTV (red structure) by: (a) the HDR intracavitary brachytherapy prescription isodose; (b) the AGIMRT prescription isodose. (c) compares the GTV, bladder, and rectal DVHs achieved by HDR brachytherapy, and AGIMRT using 6 6.5 Gy fractions and 32 1.8 Gy fractions. Doses are plotted in terms of total dose delivered via 1.8-Gy fractions (nominal tumor dose, $NTD_{1.8\,Gy}$). Only the brachytherapy component is shown (prescribed dose of 39 Gy in six fractions to point A). *Vertical lines* denote the prescribed NTD (77.6 Gy), and the bladder (65 Gy) and rectal (60 Gy) tolerance NTDs. The DVHs are not identical for the two IMRT fractionations, because the tolerance doses are larger fractions of the prescribed dose for 6.5 Gy fractions than for 1.8 Gy fractions). From [45] with permission

gradients outside the target volume that are competitive with, if not superior to, intracavitary brachytherapy.

There are several difficult issues that must be addressed before AGIMRT can be implemented clinically, many of which are challenges to any significant departure from current practice patterns in definitive treatment of locally advanced cervical cancer. Because conventional radiotherapy practices are not based on delivering a minimum dose to an anatomically specified soft-tissue target volume, it is not clear what dose needs to be delivered to the pretreatment GTV, how tumor regression affects dose prescription, and whether the high doses (more than twice that of point A) delivered to mucosal surfaces in contact with the intracavitary applicators provide a therapeutic benefit. In addition, the highly nonuniform external-beam dose distribution, consisting of 20 Gy whole pelvis and up to 40 Gy parametrial boost at Washington University, was not considered. The most important technical issue specific to AGIMRT is whether tracking the applicator substitute on a daily basis provides sufficiently accurate localization of the CTV and OARs. Low's comparison of two sequential insertions in three patients suggested that their procedure localizes the anterior rectal and posterior bladder walls with root-mean-square accuracies of 6–13 mm. However, their study compared two independently inserted sets of LDR applicators. Christensen [38], who used a biomechanical model to register deformably serial 3D imaging studies with and without applicators to the CT imaging studied acquired immediately after the first insertion, found large variations even in the way serial external beam images mapped to the reference 3D image set. Relative to the optimal rigid alignment (equivalent to applicator substitute alignment), two of the three patients studied revealed > 5 mm (5–25 mm) variations in the mean voxel displacement of bladder, rectum, and uterus-cervix tissue among the three external-beam images mapped to the intracavitary images. The assumption that a large cervical tumor with extensive parametrial involvement or sidewall extension, the lateral aspects of which maybe constrained by the peripheral anatomy, moves rigidly with midline pelvic structures is implausible. Thus, it is possible that the PTV and critical structure margins are inadequate for AGIMRT and excessive for HDR brachytherapy. Nor was the influence of random and systematic setup and internal motion errors (presumably much larger for AGIMRT than individually inserted intracavitary insertions) on the dosimetric comparison evaluated. Hence the advantage of AGIMRT relative to brachytherapy maybe overstated. While this line of research is very promising, a comprehensive investigation of geometric uncertainties, based upon serial 3D imaging, is needed to develop optimal techniques for daily alignment of the IMRT dose distribution with the applicator substitute and an objective basis for assigning uncertainty margins.

A recent study by King et al. [47] comparing CyberKnife to conventional IMRT for low risk prostate cancer illustrates the potential of IMRT-like modalities to compete with brachytherapy. The CyberKnife is a compact 6-MV photon linear accelerator mounted on a computer controlled robotic arm and is intended for stereotactic radiosurgery of extra-cranial sites. An integral component of this device is an orthogonal pair of digital X-ray imaging systems used to monitor the position of fiducial markers (three gold seeds implanted into the prostate) implanted in the target structure. The imaging system is coupled to the robotic delivery system so that the beam orientation can be automatically corrected prior to initiating treatment to compensate for interfraction setup error and can be continuously adapted during treatment to compensate for intrafraction motion of the target structure. The vendor claims that their tracking hardware and software can reduce geometric errors, relative to the markers, to less than 1 mm. King et al. compared conventional IMRT (using an 8–10-mm margin to accommodate setup and tissue motion errors) with CyberKnife step-and-shoot plans (using a 3–5-mm *PTV* margin). Not surprisingly, they found

that equivalent prostate coverage could be obtained with substantially improved bladder and rectal sparing with the CyberKnife plan. Because delivery times are of the order of 1 h per fraction, the authors introduce the device as an alternative to HDR brachytherapy, in which four to eight fractions of 5 – 10 Gy are administered when used for monotherapy [41]. The major lesson conveyed by this study is that marker-based daily target motion and possibly intrafraction error tracking are needed for any external-beam modality to safely treat with brachytherapy-like margins.

11.3.2 Supplementary IMRT for Improving Implant Quality

Less than optimal seed or source positioning, especially for permanent seed implants, is a common outcome of brachytherapy. Pubic arch interference, seed migration, resolution of prostate edema, operator inexperience, and limited accuracy with which seeds can be positioned are just a few of the factors that can compromise implant quality. Potters et al. [48] found that 42 and 48% of their ^{103}Pd and ^{125}I implants, respectively, had D_{90} doses less than 90% of the prescribed dose on post-procedure CT-based dose evaluation. As D_{90} has been found to be predictive of relapse-free survival, developing accurate, well-tolerated supplementary treatments to compensate for poor-quality implants is an important problem in radiotherapy. Similar problems arise in other brachytherapy applications, e.g., intracavitary brachytherapy. As noted above, one argument for AGIMRT is that conventional implants cannot deliver adequate doses to the periphery of large primary tumors.

IMRT is an attractive option for providing such supplementary treatment. In principle, small cold areas of the implanted target volume can be boosted while minimizing the volume of surrounding normal tissue receiving high doses. The group at University of Maryland [49, 50] has described a process for planning supplementary IMRT on a voxel-by-voxel basis. In their abstract, they note that daily image-based localization is necessary to limit the geometric error with which the highly nonuniform brachytherapy and IMRT dose distributions are combined.

11.3.3 IMRT as a Complement to Brachytherapy for Treating Extended Target Volumes

Perhaps the most promising IMRT-brachytherapy combination is use of brachytherapy to treat or boost the primary tumor component with the highest clonogen density, and IMRT for treatment of the periphery of the primary tumor or surrounding lymph node CTVs that are not adequately treated by the implant. The most widely published example of this approach is the work of Mundt et al. [51] at University of Chicago, who have proposed replacing conventional whole pelvis irradiation with IMRT for locally advanced carcinoma of the cervix (Fig. 4). Their CTV consisted of the internal, external and common iliac nodes; the presacral nodes; upper vagina; cervix; and any parametrial tumor extension. Treatment goals included uniform delivery of 45 Gy to 98% of the PTV in 1.8-Gy fractions, and no more than 40, 40, and 32 Gy to 40% of the bladder, rectum, and small bowel, respectively. No modifications to the intracavitary dose prescription or planning procedure were introduced. The authors have treated and evaluated 50 patients with whole pelvis IMRT technique. Compared to a historical control group treated with conventional fields, IMRT reduced the volume of small bowel receiving 45 Gy from 600 to 300 cm^3 on average. This was accompanied by a statistically significant decrease of grade I–III GI toxicity from 50 to 11.1% [52]. A statistically significant correlation between grade II acute GI toxicity and absolute volume of small bowel receiving >45 Gy was reported [53]. No effort was made to incorporate the intracavitary dose distributions into the IMRT planning nor to deviate from conventional pelvic and brachytherapy dose prescriptions.

The major goal of Mundt's IMRT whole-pelvis technique is to reduce the toxicity associated with conventional definitive radiotherapy. However, despite the addition of platinum-based concomitant chemotherapy to definitive radiotherapy, local and regional recurrence remains a significant problem with locally advanced disease [54,55]. Thus, an additional motivation for utilizing IMRT in treatment of cervical cancer is to improve local control by increasing BED to selected target volumes by some combination of the following techniques: dose escalation, accelerated fractionation, or reduction of overall treatment time. For example, Mutic et al. [56] described treatment planning simulations suggesting that IMRT can deliver doses of 50.4 and 59.4 Gy to the paraaortic lymph node (PALN) bed and PALN GTV (defined as region of abnormal PET-FDG uptake), respectively, without exceeding their guidelines for normal tissue toxicity. In contrast, the maximum dose that can be

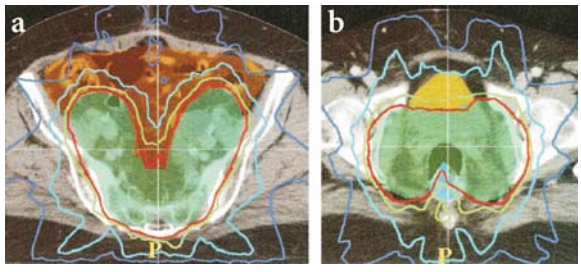

Fig. 4. IMRT whole pelvis as implemented by Mundt et al. [51] for cross sections in the upper (*left panel*) and lower (*right panel*). The CTV, small bowel, bladder and rectum are illustrated by the *green, brown,yellow and blue structures*, respectively. From [51] with permission

safely delivered by conventional AP-PA ports is 45 Gy. At Virginia Commonwealth University (VCU), we have implemented an IMRT simultaneous integrated boost (SIB) technique to designed to boost the dose to primary tumor using accelerated fractionation while simultaneously treating the clinically negative pelvic lymph nodes with conventional fractionation and doses [57]. In this technique, the boost volume, PTV_{cervix}, consists of a 1-cm margin around the GTV, which includes all primary gross disease, any contiguous lymph node involvement, and the remainder of the uterus. The generously delineated PTV_{pelvis} includes all lymph nodes at risk, the parametria, and proximal vagina. In this protocol, 25 fractions of 1.95 and 1.8 Gy are delivered to the PTV_{cervix} and PTV_{pelvis}, respectively, in conjunction with unmodified conventional intracavitary therapy. Orthogonal EPID images are used to align the treatment fields on a daily basis with gold marker seeds previously implanted in the cervix.

Application of combined IMRT-brachytherapy to treatment of intermediate and high-risk prostate cancer illustrates another combined modality strategy: using HDR interstitial brachytherapy, rather than external beam irradiation, to escalate the primary tumor dose. Two institutions (William Beaumont Hospital [58] and Kiel University [59]) have combined whole pelvic doses of 46–50 Gy with 2–3 HDR interstitial brachytherapy fractions. Both groups progressively increased fraction sizes in order to assess the efficacy and safety of dose escalation to the prostate, achieving HDR brachytherapy doses of 23–30 Gy in two fractions. Galalae [59] and colleagues used intensity modulation to limit the prostate CTV dose to 40 Gy when delivering 50 Gy to the pelvic lymph node PTV. Total combined NTDs ($\alpha/\beta = 3$) to the prostate CTV range from 76 to 113 Gy and in the case of Kiel University patients, a cumulative NTD of 145 Gy is delivered to the peripheral zone of the prostate [58–60]. Excellent eight-year bNEDs and late toxicity rates were reported.

The combined IMRT-brachytherapy protocol at VCU uses both IMRT and interstitial brachytherapy to escalate doses to the prostate CTV. An IMRT simultaneous integrated boost technique (see Fig. 5) delivers conformal radiotherapy (50 Gy in 28 fractions) to the pelvic lymph node PTV (vascular bundles expanded by 1 cm with an additional 0.5 cm *PTV* expansion) while simultaneously delivering 61 Gy to the prostate PTV. In addition, IMRT is preceded by a single 6-Gy fraction of HDR brachytherapy [61]. This corresponds to pelvic lymph node and prostate total NTDs of 48 and 74 Gy respectively. As described above, EPID imaging is used to align the delivery isocenter with the plan isocenter on a daily basis.

An interesting but unexplored application of combined IMRT-brachytherapy is use conformal IMRT to escalate the dose to lymph node CTVs in patients with intermediate and high risk disease. Interest in this treatment strategy has been stimulated by a recent phase III clinical trial demonstrating [62] that whole pelvic treatment (50 Gy) significantly improves progression-free survival relative to patients receiving treatment to the prostate only. At this time, the volumes and doses needed to produce optimal clinical outcomes are not known. In this setting, use of HDR interstitial brachytherapy to boost the primary tumor and conformal IMRT to treat the pelvic lymph node bed more aggressively than permitted by conventional whole pelvis fields is attractive option.

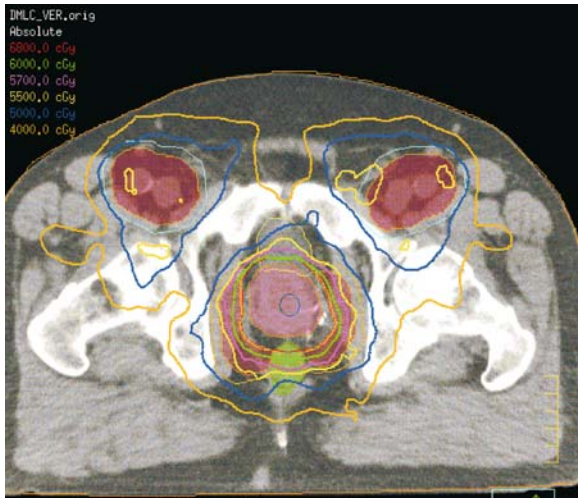

Fig. 5. Isodose illustrating VCU combined IMRT-HDR brachytherapy protocol. Only the IMRT component of treatment is illustrated

11.4 Challenges Posed by Integration of IMRT and Brachytherapy

A number of innovative combinations of IMRT and brachytherapy have been proposed in the literature. Of these, only use of brachytherapy to treat the primary tumor PTV supplemented by IMRT conformal therapy of the pelvic lymph nodes in cervical and prostate cancer have been clinically implemented and evaluated. Limited single-institution studies show that using combined modality treatment to administer conventional doses reduces some forms of acute and moderate late morbidity compared to conventional field arrangements. The combined conventional external beam-HDR brachytherapy literature for prostate cancer shows that very large biologically effective doses can be safely administered to limited volume targets. At this time, brachytherapy and IMRT components are planned independently of one another with little attempt to add anatomy-registered dose or BED distributions to one another. Biological planning is limited to adding average or point BEDs or EUDs calculated separately for the individual treatment components.

The "nonintegrated" approach to combined modality planning significantly limits the potential for improving clinical outcome by integrating brachytherapy and IMRT. For example, an IMRT plan cannot be optimized to deliver a uniform dose distribution to large cervical tumor that invades the parametrium, without accounting for the previously administered or anticipated intracavitary insertion that delivers significant but inadequate doses to the lateral margin of the primary tumor. Pelvic nodes near the primary tumor will receive significant dose contributions from either interstitial or intracavitary brachytherapy, which should be reflected in the final composite dose distribution. However, point-by-point addition of brachytherapy and IMRT doses as the basis of combined plan optimization and prescription requires solution of two fundamental problems: accommodating large variations in temporal dose delivery and managing tissue deformation arising from the applicator insertion procedure.

11.4.1 Radiobiological Modeling

The inadequacy of using physical absorbed dose as a surrogate for the biological effectiveness of combined dose distributions is an important conceptual issue confronting the integration of brachytherapy and IMRT. Large differences in temporal delivery (fractionated vs continuous), relative biological effectiveness (RBE), and potentially different partial coverages of dose-limiting anatomic and target structures undermine confidence in dose additivity as a guide to planning and prescribing combined modality treatment. In conventional radiotherapy practice, rigidly fixed combinations of brachytherapy and external beam are used, often supported by decades of clinical experience. However, individually optimized combinations of IMRT and brachytherapy confront the radiation oncologist with a potentially unlimited number of combinations to choose from.

The University of Maryland group [49, 50, 63] has proposed using global radiobiological surrogates, separately calculated for the IMRT and brachytherapy components, as a means of optimizing the entire course of therapy. One such quantity, for specifying dose intensity to the tumor [63] is equivalent uniform dose (EUD) [64]. EUD is defined as the uniform tumor dose producing the same tumor cell survival as the given nonuniform dose distribution (see elsewhere in this volume for a more complete description of is a global parameter characterizing the response of the entire tumor, accounting for fractionation, repopulation, dose-rate effects, and dose heterogeneity. Most importantly for combined modality therapy, EUD is additive. Suppose brachytherapy and external beam irradiation separated by the time T' give rise to surviving fractions S_1 and S_2, respectively. Then the overall surviving fraction is $S = S_1 \cdot S_2 \cdot e^{\gamma T'}$ and EUD is given by

$$EUD \propto -\log(S)/\alpha = -\left(\log(S_1) + \log(S_2) + \gamma T'\right)/\alpha \quad (1)$$
$$= EUD_1 + EUD_2 - \gamma T'/\alpha$$

where γ is the effective tumor cell repopulation rate and α is the usual linear-quadratic parameter. As a mathematically global additive quantity, EUD can in principle quantify tradeoffs between brachytherapy and external beam. Using the EUD formalism, Wang [63] argues that underdosing of 25 Gy by ^{125}I brachytherapy can be compensated by an external beam NTD of 12.5 Gy. Note that EUD as defined assumes that both modalities fully cover the tumor. To facilitate partial volume irradiation to compensate for localized brachytherapy underdoses, Li et al. [49, 50] have proposed calculating EUD for each voxel.

The Maryland group has extended the EUD concept to normal tissue [49, 50], defining EUD as the uniform whole-organ dose that gives the same NTCP as the given non-uniform dose distribution. They show that this definition leads to the generalized EUD harmonic mean dose formula of Niemierko [65] if the Lyman [66] NTCP formula is used in conjunction with the Kutcher-Burman [67] effective volume DVH reduction scheme. However, in contrast to the tumor EUD, the normal tissue EUD does not appear to possess the formal property of additivity, and hence is of limited value in estimating complications for combined modality treatment.

The value of EUD or other global parameters for guiding combined brachytherapy-IMRT planning, regardless of its additivity properties, can be questioned on fundamental grounds. Suppose that the medial half of a primary cervix tumor is adequately treated by brachytherapy and its lateral aspect boosted by complimentary IMRT. Taken separately, the IMRT will given therapeutic doses to the lateral aspect of the tumor and subtherapeutic to its medial aspect, while the dose gradient is reversed for brachytherapy. Because each modality undertreats the tumor, each plan taken separately will have very small EUDs yielding a cumulative EUD that significantly understates the therapeutic efficacy of the combined dose distribution. Clearly, the sum of parameters describing the response of a whole organ to a partial treatment is meaningful only if hot and cold spots in the corresponding partial 3D dose distributions are highly correlated. Unfortunately, many practical combined planning situations fail to meet this condition.

A more principled approach is to convert separately brachytherapy and IMRT doses, point-by-point, to an isoeffective quantity that is locally additive. Consider a hypothetical combined-modality course of therapy where the brachytherapy and IMRT components are described by 4D dose distributions, $D_1(x, y, z, t)$ and $D_2(x, y, z, t)$, where D represents the cumulative physical dose delivered at each voxel (x, y, z) prior to time, t.

Combined-modality treatment planning requires voxel-by- voxel conversion of these dose distributions into time- independent, additive isoeffective quantities by means of the linear-quadratic model. One such quantity is BED (biologically effective dose). In the case of complete sublethal damage repair between fractions, BED is given by

$$BED_2(x,y,z) = D_2(x,y,z,T_2)\cdot\left[1+\frac{d_2(x,y,z)}{(\alpha/\beta)}\right]-\frac{\gamma T_2'}{\alpha} \quad (2)$$

where $d_2(x,y,z)$ is the daily fraction size, T_2 is the time at completion of the last fraction, and T_2' is the overall IMRT treatment time. It is assumed that the various L-Q parameters (α, α/β, and γ in (2)) also depend on position. Extensions of (2) to continuous LDR brachytherapy and other examples of incomplete repair have been reviewed by many authors. Assuming that appropriate adjustments have been made for any treatment gaps, one can easily calculate the total BED distribution, ($BED_T(x,y,z)$), as follows:

$$BED_T(x,y,z) = BED_1(x,y,z) + BED_2(x,y,z) \quad (3)$$

This distribution, along with volume fraction plots, v (BED_T) (differential or cumulative DVHs) for various organs, can be utilized to plan the combined treatment. In addition, NTCP or TCP models can be evaluated given organ-specific v (BED_T) distributions. While the voxel-based biological planning philosophy has been described in the combined brachytherapy-IMRT literature (see [68] for example) and is certainly widely used in other radiotherapy applications, there is almost no published literature that rigorously applies this approach to combined brachytherapy-external beam treatment planning.

Biological modeling is a promising approach for rationally planning combinations of two highly conformal modalities with different partial organ coverages and large differences in time-dose-fractionation patterns. However, practitioners should bear in mind that biological models have large uncertainties and questionable mechanistic bases. Thus planners should deviate only incrementally and cautiously from brachytherapy-external beam combinations that have been clinically validated.

11.4.2 Image Registration and Fusion

Because insertion of sources and applicators applies external forces to the target anatomy and activates physiological processes such as edema, brachytherapy procedures may cause extensive soft-tissue deformation and displacement relative to the unperturbed anatomy characteristic of external-beam radiotherapy. Thus brachytherapy and IMRT dose distributions are registered to potentially different 3D representations of the patient's anatomy. Consequently, neither the total cumulative dose nor derived surrogate biological responses administered to each tissue voxel can be accurately estimated simply by adding the two dose or BED matrices together as indicated by (3).

Several papers document the variation of pelvic anatomy from one intracavitary insertion to another. By quantifying applicator displacements from one insertion to the next relative to bony anatomy visualized on orthogonal radiographs, linear shifts as large as 26 mm [39, 69] have been found. Helleburst and colleagues [70] performed 4–6 serial CT scans following HDR intracavitary insertions on 13 patients and found that the coefficient of variation of the bladder and rectal volumes (standard deviation of organ volume/mean volume, averaged over multiple fractions) ranged from 4 to 51% from patient-to-patient. Christensen et al. [38] studied three cervix patients who underwent serial X-ray CT examination during external beam therapy, as well as after each of two LDR intracavitary insertions (see Fig. 6 for an example). On each patient, they used deformable image registration (described below) to map each of the four serial imaging studies to the 3D imaging study acquired immediately after the first intracavitary insertion. For each mapping and organ illustrated by Fig. 6, they evaluated the distribution and mean of voxel displacements due to soft-tissue deformation relative to rigid registration based on bony anatomy. The mean voxel displacement ranged from 3 to 28 mm. The patient illustrated by Fig. 6 exhibited tissue displacements as large as 50 mm relative to rigid registration based on bony landmarks. Clearly, for gynecological brachytherapy, tissue deformation and displacement can be so extensive as to make meaningful addition of brachytherapy and IMRT doses impossible using rigid image registration technology.

For prostate cancer, the author could find no published data documenting tissue deformation or gland displacement, relative to the external beam planning anatomy, arising from the implant procedure. Although available studies do not address anatomical registration

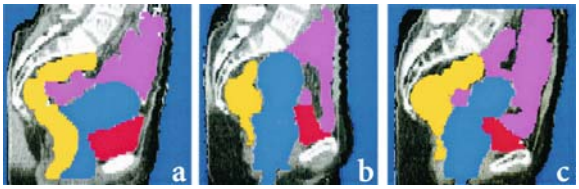

Fig. 6. (a)- (c) Midline sagittal images reconstructed from serial X-ray CT studies of a patient receiving definitive radiotherapy for stage IIIB cervix cancer. The three images represent, *from left to right*, the patient geometry upon initiating external beam therapy, after insertion of the first LDR intracavitary system, and after insertion of the second intracavitary system. The *yellow, blue, red and pink structures* illustrate the rectum, the vagina and uterus, the bladder and the small bowel. These images show that in extreme cases, not only are organs deformed and displaced, but can be completely rearranged. From [38] with permission

of brachytherapy to external beam dose distributions, they do demonstrate that significant prostate deformation during brachytherapy does occur. For example, Hirose et al. [71] examined the effect of the large endorectal receiving coil (about 4 cm diameter) used for MRS imaging on the much smaller diameter rectal obdurator used for stabilizing the interstitial needle template for MR-guided brachytherapy. They found significant changes in prostate shape, thickness of peripheral zone, and relative dimensions of the prostate. For example the median change in anterior-posterior and transverse diameters was −5 mm and +5 mm, respectively (range −16. 0 to 8.8 mm). For HDR interstitial boosts to be combined with IMRT, comparable gland distortion and significant displacement relative to bony landmarks relative to the external beam anatomy would not be unexpected, since the HDR plan is delivered with the patient in the lithotomy position and with the TRUS probe in place. In addition, prostate edema, following transperineal insertion of permanent interstitial sources, increases the immediate post-procedure volume of the prostate by 50% relative to pre-implant imaging studies [27]. For permanent implants this significantly complicates brachytherapy dose estimation, since the rate at which edema resolves varies significantly from patient-to-patient [72]. While not as well documented for HDR interstitial brachytherapy, probable prostate edema increases the uncertainty of combined IMRT-brachytherapy dose distributions.

The impact of soft tissue registration errors should be considered when designing combined IMRT-brachytherapy protocols. Soft-tissue displacement can be mitigated by number of strategies. These include attempting to reproduce the patient's external-beam treatment position during HDR interstitial brachytherapy, using post-implant CT images or permanently implanted seeds to align the brachytherapy dose distribution with the IMRT planning images, and localizing implanted markers by daily EPID imaging to ensure that the treatment isocenter is aligned at least approximately correctly with respect to the brachytherapy treatment volume. Another strategy is to plan IMRT dose distributions so as to minimize dose summation uncertainty, e.g., by employing relatively uniform IMRT dose distributions in high gradient regions of the brachytherapy dose distribution.

A promising general approach for dealing with soft-tissue deformation in combined modality planning is non-rigid or deformable image registration. Using the notation of the previous section consider two images, $I_1(x,y,z)$ and $I_2(x,y,z)$, which specify the image intensity I of the IMRT and brachytherapy anatomies, respectively, such that their coordinate systems are in one-to-one correspondence with the associated dose distributions, $\mathrm{BED}_1(x,y,z)$ and $\mathrm{BED}_2(x,y,z)$. Currently available image registration assumes that a brachytherapy image set (or subvolume therein) can be brought into voxel-to-voxel alignment with the external beam planning imaging by applying an appropriate rigid translation and rotation to the brachytherapy image set. In contrast, the goal of nonrigid registration is to estimate a vector-valued transformation $\boldsymbol{h}_{2-1} : (x,y,z)_2 \rightarrow (x,y,z)_1$ that defines the point-wise correspondence between voxels in study 1 and those in study 2. Thus given, for a given tissue voxel located at (x,y,z) in the brachytherapy image, $I_2(x,y,z)$, $\boldsymbol{h}_{2-1}(x,y,z)$ specifies its location in the IMRT image, $I_1(x,y,z)$. Assuming that the transformation is correct and the two images are obtained from the same modality,

$$I_1\left(\boldsymbol{h}_{2-1}(x,y,z)\right) = I_2(x,y,z) \tag{4}$$

Thus using $\boldsymbol{h}_{2-1}$ to transform the coordinate system of the IMRT planning image effectively warps it so that it is in voxel-to-voxel correspondence to its brachytherapy counterpart. Because each voxel is independently transformed by this approach, highly localized tissue displacements can be accounted for. As proposed by Christensen and Williamson [38], $\boldsymbol{h}_{2-1}$ can also be used to warp the IMRT dose distribution so that a 3D cumulative dose distribution registered to the image 2 anatomy can be computed:

$$BED_T(x,y,z) = BED_1\left(\boldsymbol{h}_{2-1}(x,y,z)\right) + BED_2(x,y,z) \tag{5}$$

Deformable image registration is an active area of research within the biomedical engineering community and has been applied to radiation oncology problems by relatively few investigators. At this point, a number of different techniques are under investigation. All nonrigid algorithms seek to estimate the transformation $\boldsymbol{h}_{2-1}$ that maximizes the similarity between the target image $I_2(x,y,z)$ and the deformed source image $I_1\left(\boldsymbol{h}_{2-1}(x,y,z)\right)$. Computational anatomy techniques under investigation [73] differ according to the image features to be forced into spatial correspondence (gray-scale intensity, landmark points, or contoured volumes), the similarity metric used (RMS mean difference, mutual information), the deformation process model used (biomechanical model vs parametric model), and the mathematical formulation of the optimization problem (finite element, finite difference). A global review of this field is beyond the scope of this chapter: only a few applications to radiation oncology will be mentioned. In the approach proposed by Christensen and colleagues [38], the deformation process (Fig. 7) is modeled as a viscous fluid flow problem, in which the force acting on the deforming source image to bring it into correspondence with the target image is proportional to discrepancy between the two image sets. This physical process was described in terms of a simplified Navier-Stokes partial differential equation, which was solved by conventional techniques. Their volume-registration technique allowed matching based upon matching gray-

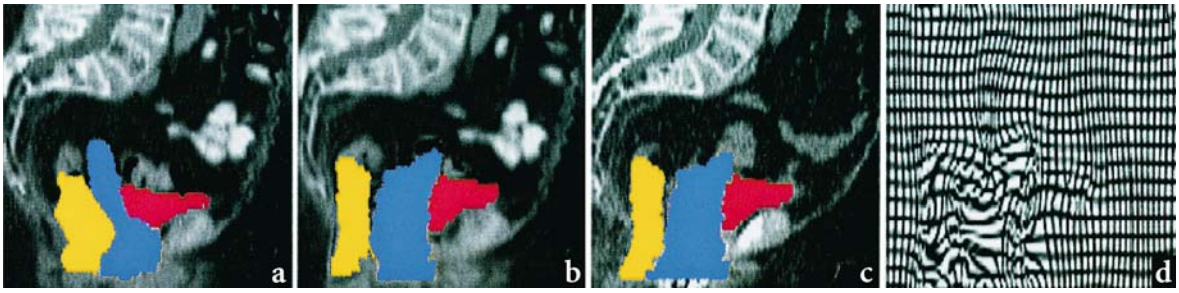

Fig. 7. (a)- (d) An example of the viscous fluid nonrigid registration method of Christensen. The first panel is sagittal image showing the patient's anatomy prior to initiating external beam therapy (source), the third image illustrates the anatomy with the second intracavitary insertion in place (target image), and the second shows the source image deformed to match the image set with the Fletcher-Suit applicator system in place. The fourth panel illustrates a rectangular grid deformed by the corresponding transformation, illustrating the large local voxel displacements. From [38] with permission

scale signal intensity, coincidence of contoured structures, or a weighted combination of the two. Figure 7 shows a sample of Christensen's results. Their method worked well so long as the deformations are not too topologically complex. Their method encountered difficulty when organs separated or moved along common boundaries (see Fig. 6), introducing discontinuities in $\boldsymbol{h}_{2-1}$ which cannot be described by differential equations operating on a single finite-difference grid.

Several authors have applied nonrigid registration techniques to the matching pre-procedure prostate MRS images to intraoperative prostate MR images used to guide permanent seed implantation. Bharatha et al. [74] successfully applied a finite element technique, in which the peripheral and central prostate zones in the target image were represented as tetrahedral meshes and the prostate modeled as a linear elastic medium. The algorithm derives a surface tension map by matching the prostate surfaces on the two imaging studies (both previously manually contoured) and estimates the transformation by requiring equilibrium between internal elastic and external forces everywhere in the gland. This example illustrates the power of finite element techniques (ability to represent irregularly shaped structures by meshes and to model organ boundary discontinuities) and disadvantages (requiring manual contouring and not using image intensity information). Wu and colleagues [75] solved the same problem using a parametric representation of $\boldsymbol{h}_{2-1}$ (linear combination of basis functions, e.g., thin plate splines [76] or polynomials [75]) in conjunction with image intensity matching via the mutual information metric and the linear elastic model to enforce continuity. Their technique did not require the matched structures to be manually contoured.

Non-rigid registration is a promising approach for managing tissue deformation in brachytherapy and radiotherapy more generally. If judiciously applied, the result is likely to be more accurate than the conventional approaches of either ignoring tissue motion or approximating its effects by rigid registration techniques. However, the use of computational anatomy techniques in radiotherapy planning is in its infancy as a research area. Serious questions about the uniqueness and geometric verity of the estimated transformations have yet to be answered.

11.5 Conclusion

Integrated courses of IMRT-brachytherapy treatment offer many clinical advantages. These range from reducing the toxicity profile associated with standard combinations of external beam therapy and brachytherapy to achieving dose intensification or accelerated fractionation to an extent not possible by either modality alone. However, combined modality treatment presents several challenges that currently available brachytherapy and IMRT planning technology are ill equipped to manage. One challenge is evaluation of composite dose distributions derived from individual treatment plans that differ significantly in partial organ coverage and fractionation. Another challenge is significant differences in soft-tissue organ locations and shapes between the brachytherapy and IMRT treatment geometries. Clinical application of surrogate biological endpoints and non-rigid image registration techniques, currently active areas of research, are promising general solutions to these problems. In the absence of suitable planning and treatment verification tools, these sources of uncertainty should be considered in designing combined modality treatment protocols.

Acknowledgements. The author would like to thank Drs. Nesrin Dogan and Dorin Todor for performing the dosimetric comparison shown in Fig. 1.

References

1. vant Riet A, Mak ACA, Moerland MA, Elders LH, van der Zee W (1997) A conformation number to quantify the degree of conformality in brachytherapy and external beam irradiation:

application to the prostate. Int J Radiat Oncol Biol Phys 37:731–736
2. Zelefsky M, Fuks Z, Happersett L, Lee H, Ling C, Burman C, Hunt M, Venkatraman E, Jackson A, Leibel S (1999) Improved conformality and reduced toxicity with high-dose intensity modulated radiation therapy (IMRT) for patients with prostate cancer. Int J Radiat Oncol Biol Phys 45(Suppl 1):170
3. Bel A, van Herk M, Lebesque JV (1996) Target margins for random geometrical treatment uncertainties in conformal radiotherapy. Med Phys 23:1537–1545
4. de Boer JC, Heijmen BJ (2002) A new approach to off-line setup corrections: combining safety with minimum workload. Med Phys 29:1998–2012
5. Meijer GJ, Rasch C, Remeijer P, Lebesque JV (2003) Three-dimensional analysis of delineation errors, setup errors, and organ motion during radiotherapy of bladder cancer. Int J Radiat Oncol Biol Phys 55:1277–1287
6. Stroom JC, de Boer HC, Huizenga H, Visser AG (1999) Inclusion of geometrical uncertainties in radiotherapy treatment planning by means of coverage probability Int J Radiat Oncol Biol Phys 43:905–919
7. Van Herk M (2004) Errors and margins in radiotherapy. Semin Radiat Oncol 14:52–64
8. Yan D, Ziaja E, Jaffray D, Wong J, Brabbins D, Vicini F, Martinez A (1998) The use of adaptive radiation therapy to reduce setup error: a prospective clinical study. Int J Radiat Oncol Biol Phys 41:715–720
9. Langen KM, Jones DTL (2001) Organ motion and its management. Inter J Radiat Oncol Biol Phys 50:265–278
10. ICRU (1993) Prescribing, recording, and reporting photon beam therapy. Report No 50, International Commission on Radiation Units and Measurements
11. ICRU (1999) Prescribing, recording, and reporting photon beam therapy (supplement to ICRU Report No 50). Report No 62, International Commission on Radiation Units and Measurements
12. van Herk M, Remeijer P, Rasch C, Lebesque JV (2000) The probability of correct target dosage: dose-population histograms for deriving treatment margins in radiotherapy Int J Radiat Oncol Biol Phys 47:1121–1135
13. Van de Steene J, Van den Heuvel F, Bel A, Verellen D, De Mey J, Noppen M, De Beukeleer M, Storme G (1998) Electronic portal imaging with on-line correction of setup error in thoracic irradiation: clinical evaluation. Int J Radiat Oncol Biol Phys 40:967–976
14. Bel A, Vos PH, Rodrigus PT, Creutzberg CL, Visser AG, Stroom JC, Lebesque JV (1996) High-precision prostate cancer irradiation by clinical application of an offline patient setup verification procedure, using portal imaging. Int J Radiat Oncol Biol Phys 35:321–332
15. Yan D, Lockman D, Brabbins D, Tyburski L, Martinez A (2000) An off-line strategy for constructing a patient-specific planning target volume in adaptive treatment process for prostate cancer. Int J Radiat Oncol Biol Phys 48:289–302
16. Shiu AS, Chang EL, Ye JS, Lii M, Rhines LD, Mendel E, Weinberg J, Singh S, Maor MH, Mohan R, Cox JD (2003) Near simultaneous computed tomography image-guided stereotactic spinal radiotherapy: an emerging paradigm for achieving true stereotaxy. Int J Radiat Oncol Biol Phys 57:605–613
17. Jaffray DA, Siewerdsen JH, Wong JW, Martinez AA (2002) Flat-panel cone-beam computed tomography for image-guided radiation therapy. Int J Radiat Oncol Biol Phys 53:1337–1349
18. ICRU (1997) Dose and volume specification for reporting interstitial therapy. Report No 58, International Commission on Radiation Units and Measurements
19. Roberson PL, Narayana V, McShan DL, Winfield RJ, McLaughlin PW (1997) Source placement error for permanent implant of the prostate. Med Phys 24:251–257
20. Yu Y, Waterman FM, Suntharalingam N, Schulsinger A (1996) Limitations of the minimum peripheral dose as a parameter for dose specification in permanent 125I prostate implants. Int J Radiat Oncol Biol Phys 34:717–725
21. Taschereau R, Roy J, Pouliot J (1999) Monte Carlo simulations of prostate implants to improve dosimetry and compare planning methods. Med Phys 26:1952–1959
22. Merrick GS, Butler WM, Dorsey AT, Lief JH (1999) Potential role of various dosimetric quality indicators in prostate brachytherapy. Int J Radiat Oncol Biol Phys 44:717–724
23. McLaughlin PW, Narayana V, Drake DG, Miller BM, Marsh L, Chan J, Gonda R Jr, Winfield RJ, Roberson PL (2002) Comparison of MRI pulse sequences in defining prostate volume after permanent implantation. Int J Radiat Oncol Biol Phys 54:703–711
24. Deurloo E, Gilhuijs K, Schultze Kool L, Muller S (2001) Displacement of breast tissue and needle deviations during stereotactic procedures. Invest Radiol 36:347–353
25. Susil RC, Krieger A, Derbyshire JA, Tanacs A, Whitcomb LL, Fichtinger G, Atalar E (2003) System for MR image-guided prostate interventions: canine study. Radiology 228:886–894
26. Lindsay PE, Van Dyk J, Battista JJ (2003) A systematic study of imaging uncertainties and their impact on 125I prostate brachytherapy dose evaluation. Med Phys 30:1897–1908
27. Waterman FM, Yue N, Corn BW, Dicker AP (1998) Edema associated with I-125 or Pd-103 prostate brachytherapy and its impact on post-implant dosimetry: an analysis based on serial CT acquisition. Int J Radiat Oncol Biol Phys41:1069–1077
28. Waterman FM, Dicker AP (2002) Impact of postimplant edema on V(100) and D(90) in prostate brachytherapy: can implant quality be predicted on day 0? Int J Radiat Oncol Biol Phys 53:610–621
29. Vicini F, Vargas C, Gustafson G, Edmundson G, Martinez A (2003) High dose rate brachytherapy in the treatment of prostate cancer. World J Urol 21:220–228
30. Cormack RA, Kooy H, Tempany CM, D'Amico AV (2000) A clinical method for real-time dosimetric guidance of transperineal 125I prostate implants using interventional magnetic resonance imaging. Int J Radiat Oncol Biol Phys 46:207–214
31. Todor DA, Cohen GN, Amols HI, Zaider M (2002) Operator-free, film-based 3D seed reconstruction in brachytherapy. Phys Med Biol 47:2031–2048
32. Martin T, Baltas D, Kurek R, Roddiger S, Kontova M, Anagnostopoulos G, Dannenberg T, Buhleier T, Skazikis G, Tunn U, Zamboglou N (2004) 3-D conformal HDR brachytherapy as monotherapy for localized prostate cancer. A pilot study. Strahlenther Onkol 180:225–232
33. Nag S, Cano ER, Demanes DJ, Puthawala AA, Vikram B (2001) The American Brachytherapy Society recommendations for high-dose-rate brachytherapy for head-and-neck carcinoma. Int J Radiat Oncol Biol Phys 50:1190–1198
34. Lee EK, Zaider M (2003) Intraoperative dynamic dose optimization in permanent prostate implants. Int J Radiat Oncol Biol Phys 56:854–861
35. Wei Z, Wan G, Gardi L, Mills G, Downey D, Fenster A (2004) Robot-assisted 3D-TRUS guided prostate brachytherapy: system integration and validation. Med Phys 31:539–548
36. Burghardt E, Hofmann HMH, Ebner F, Haas J, Tamussino K, Justich E (1989) Magnetic resonance imaging in cervical cancer: a basis for objective classification. Gynecol Oncol 33:61–67

37. Greco A, Mason P, Leung AWL, Dische S, McIndoe GAJ, Anderson MC (1989) Staging of carcinoma of the uterine cervix: MRI-surgical correlation. Clin Radiol 40:401–405
38. Christensen GE, Carlson B, Chao KS, Yin P, Grigsby PW, Nguyen K, Dempsey JF, Lerma FA, Bae KT, Vannier MW, Williamson JF (2001) Image-based dose planning of intracavitary brachytherapy: registration of serial-imaging studies using deformable anatomic templates. Int J Radiat Oncol Biol Phys 51:227–243
39. Eisbruch A, Williamson JF, Dickson R et al. (1993) Estimation of tissue volume irradiated by intracavitary implants. Int J Radiat Oncol Biol Phys 25:733–744
40. Brenner DJ, Huang Y, Hall EJ (1991) Fractionated high dose-rate versus low dose-rate regimens for intracavitary brachytherapy of the cervix: equivalent regimens for combined brachytherapy and external irradiation. Int J Radiat Oncol Biol Phys 21:1415–1423
41. Martinez AA, Pataki I, Edmundson G, Sebastian E, Brabbins D, Gustafson G (2001) Phase II prospective study of the use of conformal high-dose-rate brachytherapy as monotherapy for the treatment of favorable stage prostate cancer: a feasibility report. Int J Radiat Oncol Biol Phys 49:61–69
42. Kupelian PA, Reddy CA, Klein EA, Willoughby TR (2001) Short-course intensity-modulated radiotherapy (70 GY at 2.5 GY per fraction) for localized prostate cancer: preliminary results on late toxicity and quality of life. Int J Radiat Oncol Biol Phys 51:988–993
43. Wu Q, Mohan R, Morris M, Lauve A, Schmidt-Ullrich R (2003) Simultaneous integrated boost intensity-modulated radiotherapy for locally advanced head-and-neck squamous cell carcinomas. I: Dosimetric results. Int J Radiat Oncol Biol Phys 56:573–585
44. Low DA, Grigsby PW, Dempsey JF, Mutic S, Williamson JF, Markman J, Chao KS, Klein EE, Purdy JA (2002) Applicator-guided intensity-modulated radiation therapy. Int J Radiat Oncol Biol Phys 52:1400–1406
45. Wahab SH, Malyapa RS, Mutic S, Grigsby PW, Deasy JO, Miller TR, Zoberi I, Low DA (2004) A treatment planning study comparing HDR and AGIMRT for cervical cancer. Med Phys 31:734–743
46. Weeks KJ, Montana GS (1997) Three-dimensional applicator system for carcinoma of the uterine cervix. Int J Radiat Oncol Biol Phys 37:455–463
47. King CR, Lehmann J, Adler JR, Hai J (2003) CyberKnife radiotherapy for localized prostate cancer: rationale and technical feasibility. Technol Cancer Res Treat 2:25–30
48. Potters L, Cao Y, Calugaru E, Torre T, Fearn P, Wang XH (2001) A comprehensive review of CT-based dosimetry parameters and biochemical control in patients treated with permanent prostate brachytherapy. Int J Radiat Oncol Biol Phys 50:605–614
49. Li X, Wang JZ, Amin PP, Earl M, Shepard D (2003) Using IMRT to repair unacceptable dose distributions of prostate implants. Int J Radiat Oncol Biol Phys 57:S434
50. Li XA, Wang JZ, Stewart RD, DiBiase SJ (2003) Dose escalation in permanent brachytherapy for prostate cancer: dosimetric and biological considerations. Phys Med Biol 48:2753–2765
51. Mundt AJ, Lujan AE, Rotmensch J, Waggoner SE, Yamada SD, Fleming G, Roeske JC (2002) Intensity-modulated whole pelvic radiotherapy in women with gynecologic malignancies. Int J Radiat Oncol Biol Phys 52:1330–1337
52. Mundt AJ, Mell LK, Roeske JC (2003) Preliminary analysis of chronic gastrointestinal toxicity in gynecology patients treated with intensity- modulated whole pelvic radiation therapy. Int J Radiat Oncol Biol Phys 56:1354–1360
53. Roeske JC, Bonta D, Mell LK, Lujan AE, Mundt AJ (2003) A dosimetric analysis of acute gastrointestinal toxicity in women receiving intensity-modulated whole-pelvic radiation therapy Radiother Oncol 69:201–207
54. Morris M, Eifel PJ, Lu J, Grigsby PW, Levenback C, Stevens RE, Rotman M, Gershenson DM, Mutch DG (1999) Pelvic radiation with concurrent chemotherapy compared with pelvic and para-aortic radiation for high-risk cervical cancer. N Engl J Med 340:1137–1143
55. Rose PG, Bundy BN, Watkins EB, Thigpen JT, Deppe G, Maiman MA, Clarke-Pearson DL, Insalaco S (1999) Concurrent cisplatin-based radiotherapy and chemotherapy for locally advanced cervical cancer. N Engl J Med 340:1144–1153
56. Mutic S, Malyapa RS, Grigsby PW, Dehdashti F, Miller TR, Zoberi I, Bosch WR, Esthappan J, Low DA (2003) PET-guided IMRT for cervical carcinoma with positive para-aortic lymph nodes-a dose-escalation treatment planning study. Int J Radiat Oncol Biol Phys 55:28–35
57. Schefter TE, Kavanagh BD, Wu Q, Tong S, Newman F, McCourt S, Arnfield M, Benedict S, Mohan R (2002) Technical considerations in the application of intensity-modulated radiotherapy as a concomitant integrated boost for locally-advanced cervix cancer. Med Dosim 27:177–184
58. Galalae RM, Martinez A, Mate T, Mitchell C, Edmundson G, Nuernberg N, Eulau S, Gustafson G, Gribble M, Kovacs G (2004) Long-term outcome by risk factors using conformal high-dose-rate brachytherapy (HDR-BT) boost with or without neoadjuvant androgen suppression for localized prostate cancer. Int J Radiat Oncol Biol Phys 58:1048–1055
59. Galalae RM, Kovacs G, Schultze J, Loch T, Rzehak P, Wilhelm R, Bertermann H, Buschbeck B, Kohr P, Kimmig B (2002) Long-term outcome after elective irradiation of the pelvic lymphatics and local dose escalation using high-dose-rate brachytherapy for locally advanced prostate cancer. Int J Radiat Oncol Biol Phys 52:81–90
60. Martinez AA, Gustafson G, Gonzalez J, Armour E, Mitchell C, Edmundson G, Spencer W, Stromberg J, Huang R, Vicini F (2002) Dose escalation using conformal high-dose-rate brachytherapy improves outcome in unfavorable prostate cancer. Int J Radia Oncol Biol Phys 53:316–327
61. Wu Q, Arthur D, Benedict S, Tong S, Wu Y, Hagan M (2002) Intensity-modulated radiotherapy for prostate cancer treatment with nodal coverage. Int J Radiat Oncol Biol Phys54:321
62. Roach M III, DeSilvio M, Lawton C, Uhl V, Machtay M, Seider MJ, Rotman M, Jones C, Asbell SO, Valicenti RK, Han S, Thomas CR Jr et al. (2003) Phase III trial comparing whole-pelvic versus prostate-only radiotherapy and neoadjuvant versus adjuvant combined androgen suppression: Radiation Therapy Oncology Group 9413. J Clin Oncol 21:1904–1911
63. Wang JZ, Li XA (2003) Evaluation of external beam radiotherapy and brachytherapy for localized prostate cancer using equivalent uniform dose. Med Phys 30:34–40
64. Niemierko A (1997) Reporting and analyzing dose distributions: a concept of equivalent uniform dose. Med Phys 24:103–110
65. Niemierko A (1999) A generalized concept of equivalent uniform dose (EUD) (Abstract). Med Phys 26:1100
66. Lyman JT (1985) Complication probability as assessed from dose volume histograms. Radiat Res Suppl 104:S13–S19
67. Kutcher GJ, Burman C (1989) Calculation probability factors for non-uniform normal tissue irradiation: the effective volume method. Int J Radiat Oncol Biol Phys 16:1623–1630
68. Dale E, Hellebust TP, Skjonsberg A, Hogberg T, Olsen DR (2000) Modeling normal tissue complication probability from repetitive computed tomography scans during fractionated

high-dose-rate brachytherapy and external beam radiotherapy of the uterine cervix. Int J Radiat Oncol Biol Phys 47:963–971
69. Grigsby PW, Georgiou A, Williamson JF, Perez CA (1993) Anatomic variation of gynecologic brachytherapy prescription points. Int J Radiat Oncol Biol Phys 27:725–729
70. Hellebust TP, Dale E, Skjonsberg A, Olsen DR (2001) Inter fraction variations in rectum and bladder volumes and dose distributions during high dose rate brachytherapy treatment of the uterine cervix investigated by repetitive CT-examinations. Radiother Oncol 60:273–280
71. Hirose M, Bharatha A, Hata N, Zou KH, Warfield SK, Cormack RA, D'Amico A, Kikinis R, Jolesz FA, Tempany CM (2002) Quantitative MR imaging assessment of prostate gland deformation before and during MR imaging-guided brachytherapy Acad Radiol 9:906–912
72. Yue N, Dicker AP, Nath R, Waterman FM (1999) The impact of edema on planning 125I and 103Pd prostate implants. Med Phys 26:763–767
73. Thompson P (2002) A framework for computational anatomy. Comput Visual Sci 5:13–34
74. Bharatha A, Hirose M, Hata N, Warfield SK, Ferrant M, Zou KH, Suarez-Santana E, Ruiz-Alzola J, D'Amico A, Cormack RA, Kikinis R, Jolesz FA et al. (2001) Evaluation of three-dimensional finite element-based deformable registration of pre- and intraoperative prostate imaging. Med Phys 28:2551–2560
75. Wu X, Dibiase SJ, Gullapalli R, Yu CX (2004) Deformable image registration for the use of magnetic resonance spectroscopy in prostate treatment planning. Int J Radiat Oncol Biol Phys 58:1577–1583
76. Brock KM, Balter JM, Dawson LA, Kessler ML, Meyer CR (2003) Automated generation of a four- dimensional model of the liver using warping and mutual information. Med Phys 30:1128–1133
77. Johns HE, and Cannigham JR (1983), The Physics of Radiology, 4th edition, Charles C. Thomas, Springfield, Ill.

High Precision and Unconventional Fractionation IMRT

Stanley H. Benedict, John Purviance, Danny Song, David E. Wazer

12

Contents

12.1 Introduction

Dynamic multileaf collimation and intensity modulated radiotherapy (IMRT) produce dose distributions that are superior to conventional radiotherapy planning and may be exploited in a number of anatomic sites and clinical circumstances. In this chapter we report on techniques which combine the spatial accuracy of stereotactic positioning with the dose delivery capabilities of IMRT to treat small critically located targets. To date, the majority of studies demonstrating improvement in dose distribution with IMRT have been for broad field sizes using relatively large multileaf collimation systems, generally with leaves 1.0 cm in width. The recent introduction of micro-multileaf collimator systems have allowed the advantages of IMRT to be further extended to small intra- and extra-cranial targets. The dosimetric advantages seen with IMRT coupled with high precision localization systems have allowed the clinician to explore dose escalation and hypofractionation as a means to improve both tumor control and patient convenience.

12.2 Unique Anatomic Challenges and Target Volume Delineation

The application of small field high precision IMRT requires an extraordinary degree of spatial accuracy. In fact, for a complete understanding of the potential and limitations of small field IMRT, one must briefly review the concepts that underlie stereotactic radiosurgery and the more recently introduced stereotactic body radiotherapy (SBRT).

Stereotactic radiosurgery (SRS) was a term originally used to describe an approach for radiotherapy of brain tumors using rigid invasive immobilization, precise localization via a stereotactic coordinate system, multiple convergent beams, and single fraction treatments [1]. The spatial precision afforded by the use of an invasive stereotactic immobilization frame practically necessitated single fraction irradiation, but in return allowed for treatment with a minimal margin of surrounding tissue. Stereotactic precision coupled with circular collimator diameters generally less than 2 cm resulted in small volumes of irradiated tissue and the consequent delivery of very high radiation doses. Clinical experience accumulated over the past two decades has validated SRS as achieving a high rate of control with acceptably low rates of complication for a variety of intra-cranial tumors [2–5].

The anatomical characteristics of the skull and stability of cranial contents made SRS readily feasible for intra-cranial tumors, but the lack of a similar fixed bony reference structure as well as target and normal tissue movement created difficulty for the application of a similar treatment approach outside of the cranium. Initial progress in addressing this problem was presented by Lax et al. [6] who described a method for performing stereotactic body radiotherapy (SBRT) for abdominal malignancies. In a subsequent report, Blomgren and Lax [7] reported the clinical application of this technique to a series of patients with tumors of the lung, liver, and abdomen treated to a mean dose of 30 Gy delivered in one to four fractions.

As a consequence of these studies, there has been increasing interest to develop similar approaches of SBRT, that is, spatially precise, hypo-fractionated treatment as applied to several different extra-cranial locations. The general principles that have been used in the selective application of SBRT mirror those of SRS: treatment is limited to a small to moderate volume target with a minimal margin of surrounding tissue and dose distributions are chosen that minimize exposure to surrounding normal tissue. Prophylactic coverage of clinically uninvolved areas is not performed, thereby maintaining a simple volume and avoiding dose gradients between spatially distinct target structures. A target is generally chosen within or adjacent to anatomic structures with parallel architecture, such that small volumes of normal tissue can receive a high dose of radiation without clinical sequelae due to the functional reserve of the non-irradiated organ.

Sophisticated three-dimensional conformal treatment planning and IMRT has improved dose sculpting such that normal tissue avoidance is both more practical and achievable. However, aggressive dose escalation or hypofractionated treatment regimens have seen limited application in extra-cranial sites due primarily to the complexity of ensuring precise and reproducible targeting of small and often mobile tumors. A long appreciated limitation of conventional external beam radiotherapy derives from the inherent difficulty of reproducibility for both inter- and intra-fractional set-up. Specifically, clinicians must recognize that, at many anatomic sites, there is a relative independence of target tumor position from bony anatomy. Further, intra-fractional target movements may occur due to patient movement on the treatment couch or normal physiologic processes such as respiration and peristalsis. Traditional radiation therapy planning methods have compensated for these factors with the use of generous margins around clinical target volumes. However, due to the constraint of normal tissue toxicity, such an approach severely limits the extent to which dose escalation or hypofractionation can be explored.

Therefore, a basic requirement of small field high precision IMRT is a high degree of confidence in tumor targeting throughout treatment delivery. For tumors of the cranium and upper neck, stereotactic localization can be readily applied and immobilization can be accomplished with both invasive [8] and non-invasive [9–12] techniques. Invasive immobilization with rigid fixation to the treatment couch can achieve sub- millimeter positional accuracy [8,13] but severely limits the number of treatment fractions that can be practically employed. Non-invasive immobilization will result in positional reproducibility within approximately 2 mm [14, 15] but has the advantage of less discomfort for the patient and is readily amenable to more extended fractionation.

For extra-cranial tumors, a number of positional verification and immobilization systems are under development. The initial report by Lax et al. [6] described a body cast within a rigid box frame with radio-opaque

Table 1. Stereotactic body radiotherapy immobilization techniques

Author	Site	Immobilization/repositioning	Reported accuracy
Lax-1994 [6]	Abdomen	Woodframe/stereotactic coordinates on box to skin marks	3.7 mm lat 5.7 mm long
Hamilton-1995 [43]	Spine	Screw fixation of spinous processes to box	2 mm
Tokuuye-1997 [44]	Liver	Prone position/jaw and arm straps	5 mm
Murphy-1997 [45]	Spine	Frameless/implanted fiducial markers with real time imaging and tracking	1.6 mm radial
Sato-1998 [46]	Abdomen	Frameless/combination CT, X-ray, and linac	N/A
Lohr-1999 [47]	Body cast with stereotactic $\leq$ 3.6 mm coordinates	mean vector	
Wulf-2000 [48]	Lung, liver	Elekta^{T}M body frame	3.3 mm lat 4.4 mm long
Nakagawa-2000 [49]	Thoracic	Megavoltage CT on linac	N/A
Herfarth-2001 [50]	Liver	Leibinger body frame	1.8 – 4.4 mm
Nagata-2002 [51]	Lung	Elekta body frame	2 mm
Fukumoto-2002 [52]	Lung	Elekta^{T}M body frame	N/A
Hara-2002 [53]	Lung	Custom bed transferred to treatment unit after confirmatory scan	2 mm
Hof-2003 [54]	Leibinger body frame	1.8 – 4 mm	
Timmerman-2003 [55]	Lung	Elektabody frame	Approx 5 mm

scale markers for imaging data acquisition. The scales mounted on the frame corresponded with fiducial points and were used to set up the isocenter co-ordinates in the treatment room. Diaphragmatic movement was limited by using a plate to apply pressure to the anterior abdominal musculature. A number of similar systems have been subsequently described that have relied upon some method of body stereotaxis, rigid immobilization, respiratory gating, or some combination thereof (Table 1). Overall, the reported positional accuracy is within 5 mm for the various methods utilized.

An alternative method for achieving precise tumor localization and to guide correction for organ movement is to implant radio-opaque markers. This allows for setup verification on a daily basis, correction of both translational and rotational errors [16], and the potential for tracking organ motion in real time. For example, the Cyberknife system (Accuray, Sunnyvale CA) employs a combination of implanted fiducials and skeletal landmarks for real-time beam positioning via fluoroscopic monitors. The use of this method has been described for targets in multiple organs including the spine [17], pancreas [18], brain [19], and lung [20].

Positional verification of tumors within mobile organ structures has also been described at Kyoto University where 2.0-mm gold spheres were placed through a bronchoscope into the airways of patients with lung tumors [21]. A real-time tumor tracking system consisting of dual fluoroscopic detectors was used to activate the treatment beam when the markers were within pre-defined coordinates.

Radio-opaque markers may also be implanted into the prostate to correct for inter-fractional positional variability due to differences in rectal and bladder volume [22, 23]. Although current electronic imaging technology does not allow for intra-fractional real- time tracking, portal images may be taken immediately prior to treatment and guide positional corrections [24, 25].

Techniques to place radio-opaque markers in the liver have employed intravascular as well as intraparenchymal approaches. Dawson et al. described the use of intra-arterial hepatic microcoils (5×0.46 mm platinum) placed through a hepatic artery catheter for liver localization [26]. Kitamura et al. used an interstitial technique to implant 2.0-mm gold markers into patients with liver tumors and found minimal migration with follow-up CT scans [27].

12.3 Planning Dose Prescription and Optimization

In general, the sequence of events for patients undergoing small field high precision IMRT include:

1. Immobilization
2. CT simulation
3. Planning
4. Repositioning
5. Re-localization
6. Treatment delivery

To ensure a reproducible set-up, immobilization typically includes a custom-fit device to minimize motion. The CT simulation is used to assess the size, location, and range of motion of the tumor as well as to determine if the patient can tolerate the planned immobilization. The measurement of motion of the tumor provides the necessary data to determine the PTV and to assess if respiratory gating should be incorporated in the treatment delivery. The treatment planning must address the complexity of small field dosimetry [28] and, when appropriate, inhomogeneity corrections (e.g., the lung) [29]. A critical parameter in treatment planning is the volume of normal tissue exposed to threshold doses that will vary according to the organ that either surrounds or is adjacent to the target. The normal tissue complication probabilities are intimately related to these dose-volume relationships [30–32]. Repositioning addresses the accurate set up of the patient in the planned treatment position while re- localization addresses the specific identification of the tumor and planned isocenter in the treatment field. Finally, treatment delivery is performed using an assortment of high precision beam delivery techniques, including micro-multileaf collimation (MLC), gantry mounted linear accelerators, and combined imaging and treatment units.

The accepted limit for accurate dose delivery for an SRS linear accelerator is < 1 mm for the gantry, couch, collimator angles, and the mechanical isocenter. This degree of tolerance places a very strict accuracy requirement on the design of any multileaf collimator system that may be used for small field high precision IMRT. While most commercially available multi-leaf collimators have a leaf positioning accuracy of approximately 1 mm and are acceptable for standard fractionated large

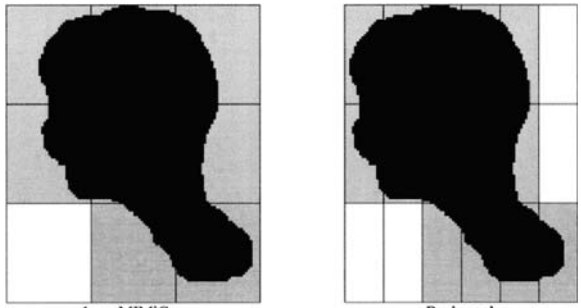

Fig. 1. Geometric advantage of the beak intensity modulated sequential tomotherapy (BIMST) vs 1- cm MIMiC for irradiation of irregularly shaped small lesions. The identical black region represents the clinical target volume for comparison between both modalities. Reproduced with permission from Elsevier [38]

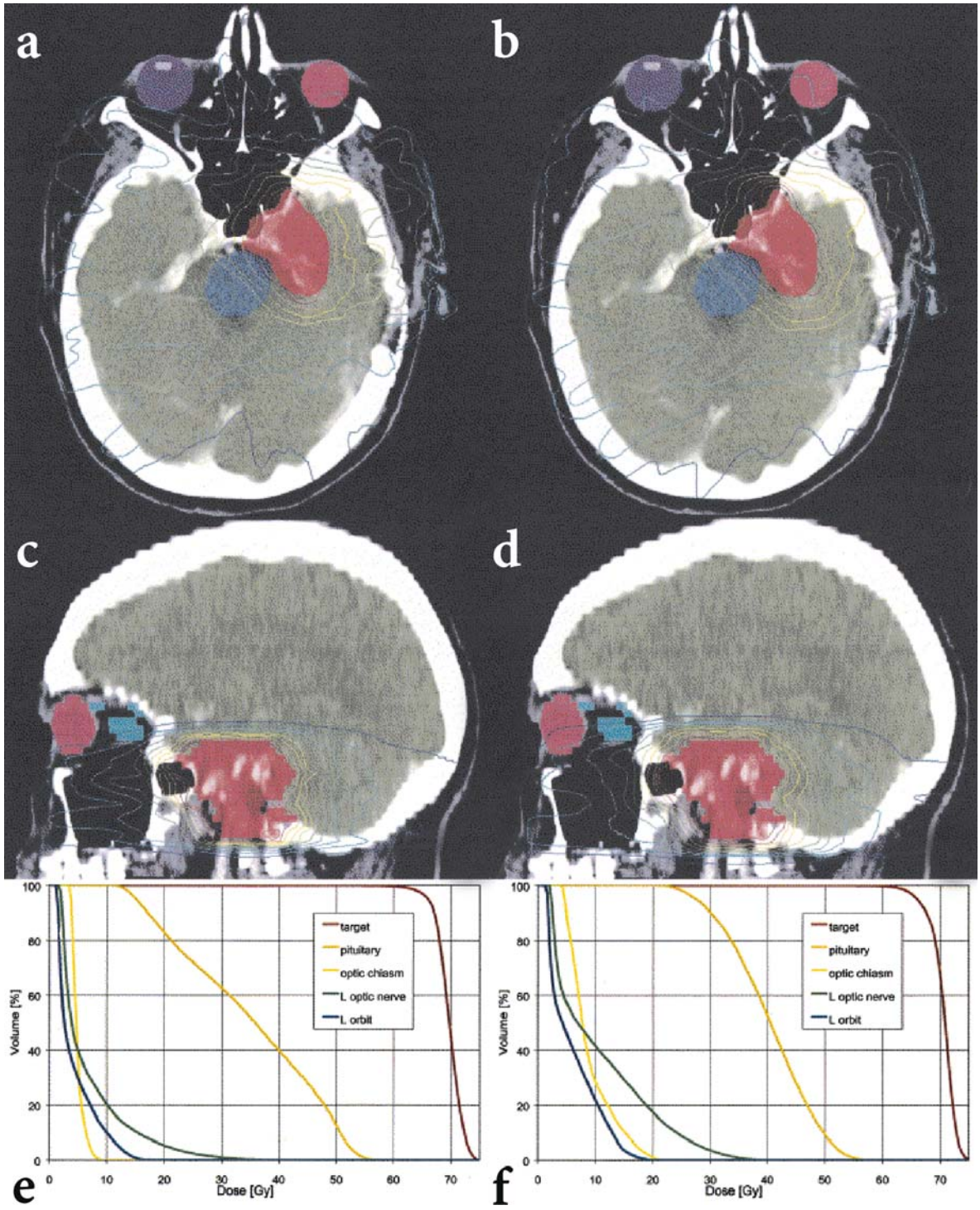

Fig. 2a–f. The influence of 0.39 cm vs 0.85 cm leaf width on dose distribution for a small intracranial irregularly shaped target: **(a)** beak intensity modulated sequential tomotherapy (BIMST) axial view; **(b)** 1-cm MIMiC axial view; **(c)** BIMST sagittal view; **(d)** 1-cm MIMiC sagittal view. The *purple* isodose line corresponds to the prescription line (84%), and the 90, 70, and 50% isodose lines are *red*, *yellow*, and *green*, respectively; **(e)**, **(f)** BIMST and 1-cm MIMiC DVHs for various clinical target volumes. Reproduced with permission from Elsevier [38]

field radiotherapy, they do not meet the general clinical accuracy standard for SRS. Therefore, in order to provide small field high precision IMRT, substantial hardware development was required to develop the "mini and micro" multi-leaf (mMLC) collimator technology.

High precision and a steep dose gradient (rapid dose fall-off) are the two requirements that must be met by any conformal SRS or SBRT system. These critical criteria can now be achieved with mMLC collimators. Standard MLC devices that are components of commercial linear accelerators have leaf widths that range from 0.5 to 1.0 cm. In contrast, the leaf width of an mMLC is narrower which greatly influences the beam penumbra and is the determinant parameter for how sharply the dose gradient extends beyond a target boundary. The physical characteristics of the mMLC leaf tips have been specifically designed to satisfy the rigorous requirements for SRS and SBRT. A conventional MLC has a penumbra width between 6 and 8 mm (measured from the 80 to −20% isodose line), whereas the penumbra width of an mMLC ranges between 2.5 and 3.5 mm.

The relevance of leaf width for small field high precision IMRT is illustrated in Fig. 1 and Fig. 2 [33]. In this example, a geometrically complex target sits in immediate proximity to several radiosensitive critical normal structures. One can readily appreciate that the mMLC with the leaf width of 0.39 cm results in a significant enhancement of dose conformity as compared to the MLC with a leaf width of 0.85 cm. This is associated with an improvement in the normal tissue dose-volume relationships. These seemingly modest changes in dose distribution may be of particular clinical importance when treatment is delivered by a high dose hypofractionated treatment scheme.

Several mMLC systems are now commercially available that can deliver highly conformal treatment using fixed static fields, dynamic conformal arcing, and IMRT. The MIMiC, manufactured by NOMOS Corporation, is a multileaf collimator driven by the CORVUS inverse treatment planning software component of the PEACOCK System. The MIMiC provides a 40-leaf binary temporal modulator specifically with a leaf width of 0.85 cm designed for the delivery of sequential tomotherapy and was the first MLC developed to deliver IMRT. The device directs thousands of pencil-thin radiation beams at a tumor target, each of which may be varied in intensity as the linear accelerator gantry rotates about the patient. For small field IMRT, NOMOS developed the mMLC BEAK collimator with a leaf width of 0.39 cm. The BrainLAB m3 mMLC (BrainLAB AG, Heimstetten, Germany) was designed specifically for radiosurgery with 3-mm center leaves for an effective penumbra of < 3.0 mm for all SRS field sizes. In a field size dimension of 10×10 cm, the m3 leaves are of variable width, including 14 pairs of 0.3 cm, 6 pairs of 0.45 cm, and 6 pairs of 0.55 cm leaves [34, 35]. The Radionics (Radionics – Tyco Healthcare, Burlington, MA) MMLC has 31 pairs of 4-mm leaves, with a total field size of 10×12 cm and a leaf height of 7 cm of tungsten. The leaf geometry of the MMLC is a divergent lock and key design in order to minimize radiation leakage and transmission. Planning for the MMLC is with the XKnife software [36]. The mMLC manufactured by 3DLINE (3DLINE USA Inc., Reston, VA) is called DMLC (Dynamic Multi Leaf Collimator) and is an auto-controlled dual focused system. This mMLC is designed as an accessory for all models of liner accelerator and consists of 24 tungsten leaf pairs providing a maximum field size of 10.8×12 cm. The dual focused characteristic of the DMLC is a unique feature and provides a penumbra that is field size independent.

12.4 Clinical Experience and Trials to Define the Role of IMRT

Small field high precision IMRT has been applied to a number of anatomic sites. In general, the studies reported to date have represented small institutional experiences that have focused on innovations in patient immobilization, target definition and tracking, treatment planning, and mMLC applications. Table 2 presents a summary of trials that have specifically employed small field high precision and unconventionally fractionated IMRT techniques. Many of the relevant related technologies of patient immobilization, tumor localization, and physiological gating have been reported in detail in studies of SBRT which are beyond the scope of this chapter but have been extensively reviewed elsewhere [37].

The interpretation of existing clinical literature is made complicated by the small number of treated patients, the different anatomic sites addressed, and the variety of fractionation schemes that were used. As such, it is difficult to draw definitive conclusions or to make explicit treatment recommendations for the application of small field high precision IMRT. Therefore, to assist the reader better in understanding the concepts explored in this chapter as applied to actual patient treatment, two case examples are presented.

12.5 Intracranial: Meningioma

This case is presented to demonstrate the issues related to the application of small field high precision IMRT to a highly irregular target volume in proximity to radiosensitive critical normal structures. In this case a patient received a partial resection for a left cavernous sinus meningioma that extended into the suprasellar

Table 2. Clinical trials for high precision and unconventionally fractionated IMRT

Anatomic site	Immobilization/ Localication	Collimation/Planning	Dose(Gy)	Fraction Size (Gy)	Patient #	Median Field Size (range)	Clinical Endpoints
Glioblastoma Floyd NS, et al. [56]	Aquaplast mask Coordinaticsystem	Peacock IMRT system (NOMOS)	60	3 Gy	20	Not reported	Median time to disease progression six months. Median survival seven months Minimal grade 0–1 acute neurtoxicity. Brain necrosis in three patients.
Glioblastoma Sultanem, K et al. [57]	Thermoplastic mask Coordinate system	MLC "step-and-shoot" with multiple co-/non-coplanar beams	60	3 Gy	25	Post-op tumor volume $\leq$ 110 cc	Disease progression in 21 patients, 16 deaths at 8.8 months. No improvement in Overall Survival or Time to Disease Progression.
High Grade Glioma Chang, IL et al. [58]	Thermoplastic mask Coordinate system (CT/MRI fusion)	Segmental IMRT via non-coplanar beams	90	2 Gy	34	Not reported	67.6% developed radiographic recurrence. 91% of recurrences predominantly within high dose field (PTV).
Meningoma Pirzkall, A et al. [59]	Custom head mask Coordinate System	Static MLC KonRad or Corvus	55.8–58.2	1.8 Gy	20	108 cc	60% improvement of neurologic symptoms. 40% tumor shrinkage.
Trigeminal Neuralgia Romanelli, P et al. [60]	Custom head mask with CT cisternography for localization	Cyberknife	XXX		10	XXX	Pain relief achived in 7 patients.
Paraspinal Bilsky, MH et al. [17]	Memorial Body Cradle/Electronic Portal Image Device with metallic implants or Memorial Stereotactic Body Frame with CT based localization	Cyberknife	Primary Tumors: median dose 70 Gy in 33–37 fractions. Metastatic tumors: 20 Gy in 4–5 fractions after conventional EBRT to tolerance of normal tissue.		16	Median tumor volume 7.8 cc (8.1–385.3)	No interval growth for 13 of 15 patients. Improvement in pain for all 11 symptomatic patients. Improved radiculopathy in 4 of 4 patients.

Table 2. (continued)

Anatomic site	Immobilization/ Localication	Collimation/Planning	Dose(Gy)	Fraction Size (Gy)	Patient #	Median Field Size (range)	Clinical Endpoints
Spine Gerszten, PC et al. [61]	Aquaplast Face Mask (cervical) Tracking of Implanted Fiducials (thoracic, lumbar, sacral)	Cyberknife with Dynamic Tracking System 3.0	Single Fraction of 12–20 Gy to the 80% isodose line (median 14 Gy)		115	Mean tumor volume 27.8 cc (0.3–232)	No new acute radiation toxicity or neurological symptoms. Pain improved in 74 of 79 symptomatic patients.
Spine Milker-Zabel et al. [62]	Custom made body cast/head mask Coordinate system	MLC "step-and-shoot" KonRad	All patients underwent EBTR (median dose 38 Gy) Median total dose for re-irradiation 39.6 Gy in 2 Gy fractions		14	Median target volume 111.2 cc (20.8–734.9)	94% local control at 12 months- 81.2% recieved pain relief. Tumor size unchanged in 84.2%.
Lung Timmerman, RD et al. [55]	Stereotactic Body Frame (Elekta Oncology) with Abdominal Compression Coordinate System	7 non-coplanar, non-opposing beams with milled attenuation compensators RenderPlan 3D planning system	24–60 Gy in 3 fractions. Dose escalation performed with cohorts receiving 3 fractions of 8,10,12,16,18 or 20 Gy		37	22.5 cc	27% complete tumor response. 60% partial tumor response. All 6 patients with local failure received < 18 Gy/fraction.
Lung Whyte, RI et al. [20]	Alpha Cradle Implanted metal Fiducials Tumor tracking with light-emitting diodes/diagnostic x-ray	Cyberknife	15 Gy	Single fraction of 15 Gy	23	Tumor diameter 1–5 cm	Radiographic tumor response: complete in 2 patients, partial in 15 patients, stable in 4, progressive in 2. No grade 3–5 radiation related complications.
Mesothelioma Munter, MW et al. [63]	Custom body cask/face mask (Scotchcast) Coordinate system	MLC "step-and-shoot" KonRad or CORVUS	Median tumor dose 40 Gy for 3 patients, 48 Gy for 1 and 50 Gy for 3 patients Fraction size not reported		7	2,314 cc (1006–3981)	28% actuarial overall survival at 1 year. No significant acute side effects according to RTOG criteria.

Table 2. (continued)

Anatomic site	Immobilization/ Localication	Collimation/Planning	Dose(Gy)	Fraction Size (Gy)	Patient #	Median Field Size (range)	Clinical Endpoints
Pancreas Koong, AC et al. [64]	Alpha Cradle Implanted Gold Fiducials	Cyberknife	Single Fraction: 15 Gy (3 patients) 20 Gy (5 patients) 25 Gy (7 patients)		15	Median GTV 29.0 cc (19.2–71.9)	No grade ≥ 3 GI toxicity observed. Local control achieved in all patients who received 25 Gy.
Pancreas/Bile Duct Milano, MT et al. [65]	Alpha Cradle Coordinate system	Dynamic MLC	50.4 – 59.4 Gy	1.8 Gy	25	Not reported	Median survival was 13.4 months. No resected patients had local failure and 1 unresectable patient had disease progression at 10 months. 1 Patient surviving > 5 years had grade 4 liver toxicity.
Prostate Kupelian, PA et al. [66]	Minimal immobilization Daily transabdominal ultrasound (BAT) prostate localication	5 static fields using dynamic MLC intensity modulation Corvus planning system	70 Gy	2.5 Gy	166	Not reported	Biochemical relapse-free survival at 30 months 94%. Late rectal toxicity (grade 2-3) was 5%. Late urinary toxicity in 4 patients.
Prostate Zelefsky, MJ et al. [67]	Minimal immobilization Localization based on CT simulation/skin fiducials	5 field sliding window technique Inverse planning system	81.0 Gy(698 patients) 86.4 Gy (74 patients)	1.8 Gy	722	Not reported	3-year PSA relapse-free survival for favorable, intermediate, and unfavorable risk groups were 92%, 86%, 81% respectively. 4% risk of late ≥ grade 2 rectal toxicity at 3 years. 15% risk ≥ late grade 2 urinary toxicity at 3 years.
Oropharynx Chao, KSC et al. [68]	Thermoplastic mask Coordinate system	MIMiC Peacock planning system (NOMOS)	70 Gy (average dose prescribet to GTV in primary cases) 66 Gy (dose to GTV in post-op cases)	1.9 – 2.0 Gy Daily	74	Mean GTV 30.5 cc±22.3	87% locoregional control at 4 years. 81% Disease free survival at 4 years. 87% overall survival at 4 years 32 patients with grade 1 xerostomia. 9 patients with grade 2 xerostomia.

Table 2. (continued)

Anatomic site	Immobilization/ Localication	Collimation/Planning	Dose(Gy)	Fraction Size (Gy)	Patient #	Median Field Size (range)	Clinical Endpoints
Head and Neck Lee, N et al. [69]	Thermaplastic mask Coordinate system	Manually cut partial transmission blocks, segmental MLC or MIMiC Corvus planning system	70 Gy (average dose prescribet to GTV in primary cases) 66 Gy (dose to GTV in post-op cases)	2.12 Gy Daily	150	Not reported	Local freedom from progression rate for primary treated group 95% at 3 years. Local freedom from progression rate for post-op group 82% at 2 years. Average of 3% of definitive treatment group received ≤95% of prescribed dose to GTV and CTV. Average of 6% of post-op treatment received 95% of prescribed dose to GTV and CTV.
Nasopharynx Lee, N et al. [70]	Thermaplastic mask Coordinate system	Manually cut partial transmission blocks, segmental MLC or MIMiC Corvus planning system	65–70 Gy prescribed to GTV 60 Gy to CTV 50–60 Gy to clinically negative neck	2.12–2.25 Gy to GTV 1.8 Gy to CTV	67	Mean GTV volume 104 (10–669.2) Mean CTV volume 301 cc (82–1248)	Locoregional progression-free survival 98% at 4 years. Distant metastases-free survival 66% with grade 0 xerostomia.
Nasopharynx (recurrent) Lu, TX et al. [71]	Immobilization not reported Coordinate system	MIMiC Corvus planning system (NOMOS)	Median dose for initial conventional EBRT 70 Gy to the nasopharynx. Re-irradiation prescribed dose to nasopharynx 68–70 Gy in 2.2–2.3 Gy daily fractions.		49	Mean GTV 47.2 cc (7.0–158.9)	100% Locoregional control at 9 months. Xerostomia: 53% with grade 1, 47% with grade 2.

Table 3. Sphenoid wing meningioma. A comparison of doses delivered with fixed field uniform intensity to intensity-modulated plans. All plans prescribed to 10 Gy to 99% of PTV

Plan type	PITV	Volume	Volume	Volume	Brainstem	Brainstem
		9.0 Gy	8.0 Gy	5.0 Gy	9.0 Gy	5.0 Gy
IMRT	2.86	14.32	18.48	38.31	0.19	1.13
FIXED FLDS	3.05	13.88	17.87	37.73	0.25	1.37

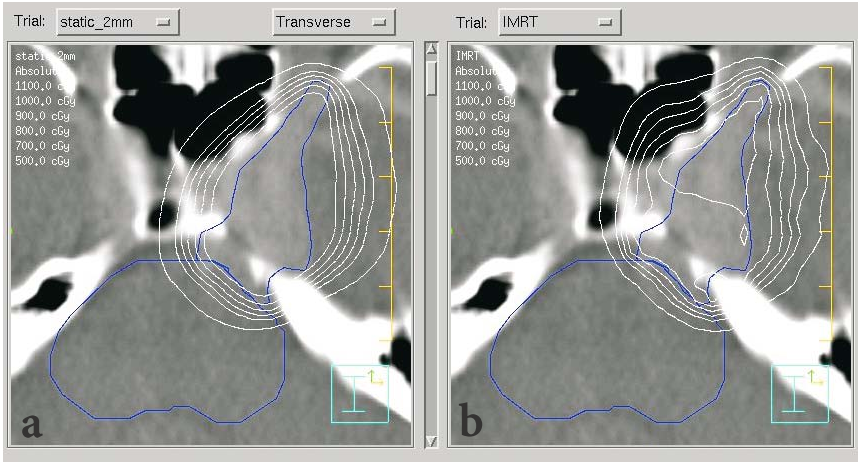

Fig. 3. Dose distributions for treatment of a sphenoid wing meningioma. Transverse CT of isodose lines through the PTV, comparing a plan with 15 fixed- gantry uniform intensity fields (*left*) and the same fixed-field arrangement with intensity modulation (*right*). Both plans were normalized to deliver 10 Gy to 99% of the PTV. The lesion and brainstem are the dark contours and the dose lines surrounding the lesion are 11, 10, 9, 8, and 5 Gy respectively

region. The patient was referred for radiotherapy to include a hypofractionated boost dose of radiation as gross residual disease remained within the left cavernous sinus and sella turcica. Clinically, the patient presented with post-operative cranial nerve deficits on the ipsilateral side. A treatment planning goal was to minimize the dose of radiation to the intact and functioning right optic apparatus. The patient was immobilized with the BrainLab invasive stereotactic cranial frame system. This consists of a rigid fixation frame with four pins inserted into the outer table of the skull. The frame was mounted to the treatment couch resulting in repositioning and reproducibility accuracy < 1 mm. A plan was generated with 15 beams (3 fixed fields equidistant along 5 conventional SRS arcs) and optimized for open static fields. This was followed by an alternate plan using the same fixed beams but with IMRT.

Figure 3 shows a transverse CT slice for comparison of the open static field and IMRT techniques. Each plan was normalized to deliver the prescription dose of10 Gy per fraction to 99% of the target volume. The IMRT plan provided a modest improvement as compared to the open static field plan as reflected in higher dose conformity. This is quantified in Table 3, which shows the dose-volume data for the total brain, including the PITV, and volume enclosed in the 9.0, 8.0, and 5.0-Gy isodose surfaces. These data demonstrate that the optimization available with IMRT applied to the fixed beam configuration provides additional tumor conformity and sparing of the adjacent brainstem.

The maximum to minimum dose ratios for the tumor were 1.48 (13.0/8.8 Gy) for the open static fields and 1.41 (12.7/9.0) for the IMRT plan. The open static field plan and IMRT plan resulted in similar dose homogeneity.

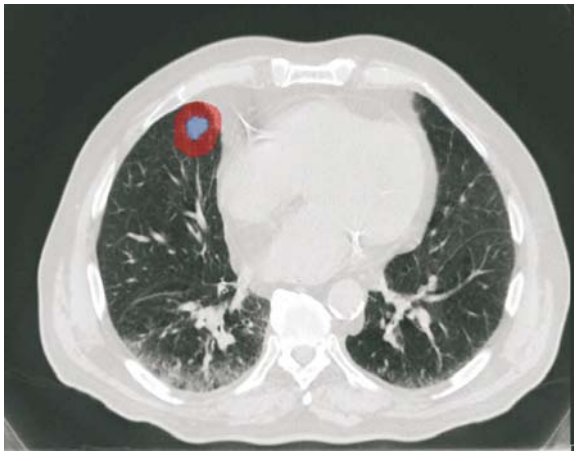

Fig. 4. CT transverse slice of an NSC RLL lung lesion treated with a small field IMRT plan with the gross tumor volume (GTV-*blue*), and the expanded planning target volume (PTV-*red*) (see text for details)

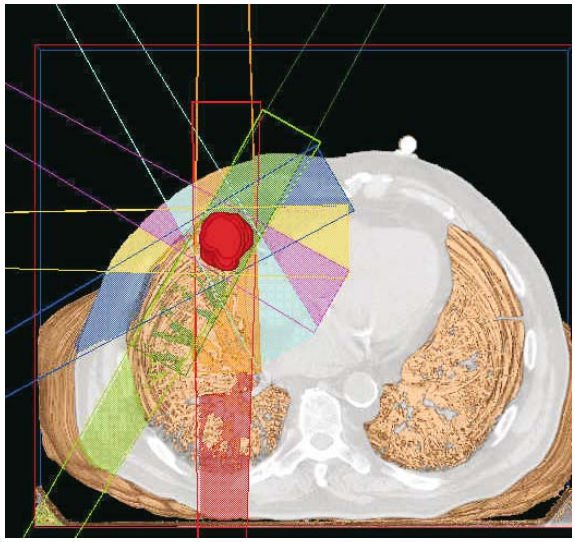

Fig. 5. A 3D animation of the multiple fixed field coplanar beam arrangement for the RLL lung lesion treated with a small field IMRT plan (see text for details)

12.6 Extracranial: Lung Tumor

This case is presented to demonstrate the issues relevant to the application of small field high precision IMRT in an extracranial location where target movement presents a particular challenge. An 81-year-old male presented with a history of heavy tobacco abuse and long-standing severe emphysema. A routine chest X-ray revealed multiple right-sided pulmonary nodules. After a work-up that included a CT scan, PET imaging, and biopsy, the patient was diagnosed with a TxN0M1 Non-Small Cell Lung Carcinoma. The patient was initially managed with carboplatin and taxol chemotherapy. He was followed with CT scans of the chest every three months and had no evidence of disease progression for two years. After 26 months of follow- up, he was found to have a new site of metastasis manifesting as a right lower lobe pulmonary nodule that measured 1.7×1.2 cm (Fig. 4). This lesion was clearly defined on CT scan and was noted in immediate proximity to the anterior chest wall and right ventricle. Serial CT scans demonstrated that this mass was enlarging and threatened to cause imminent symptoms. The patient was referred for SBRT.

The patient underwent a CT simulation and was immobilized with the BrainLab ExacTrac system. As the target was subject to significant movement with each breathing cycle, expiratory respiratory gating was employed. The treatment plan was developed with forward planned IMRT that resulted in an eight beam configuration. In accordance with an institutional protocol, the dose was prescribed to the 80% isodose line at 10 Gy per fraction for a total of 30 Gy (Fig. 4,Fig. 5,Fig. 6,Fig. 7). The patient tolerated the treatment well, and on subsequent follow-up the lesion decreased in size.

12.7 Future Directions

The central future clinical application of small field high precision IMRT is dose escalation achievable through increased target conformity, improved target coverage, and decreased dose to adjacent organs-at- risk. These same characteristics may also allow hypofractionated treatment schemes to replace the standard six to seven week course of radiation therapy. Progress in imaging (e.g., spectroscopic magnetic resonance, ^{1}1C-choline or -acetate positron emission tomography) may help to improve further the definition of tumor extent and allow for radiation delivery tailored to specific three-dimensional metabolic tumor maps based on regions of hypoxia, proliferation, and distribution of clonogens. This extent of functional and physiological data would support the application of small field IMRT to intentionally inhomogeneous dose distributions to high density or high risk tumor- bearing areas.

Small field high precision IMRT has been currently established to be particularly advantageous for small,

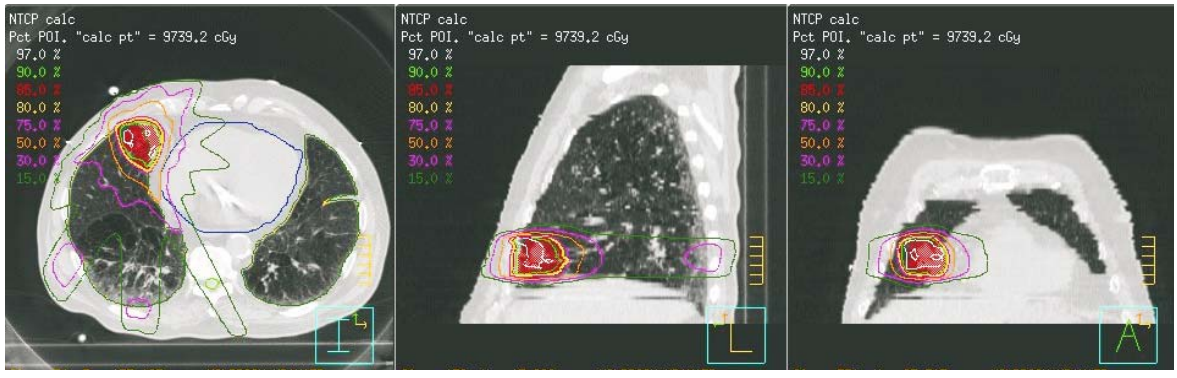

Fig. 6. Transverse, saggital and coronal views of the NSC RLL lung lesion with overlay of resultant isodose curves from small field IMRT plan: the prescription was to the 80% isodose line

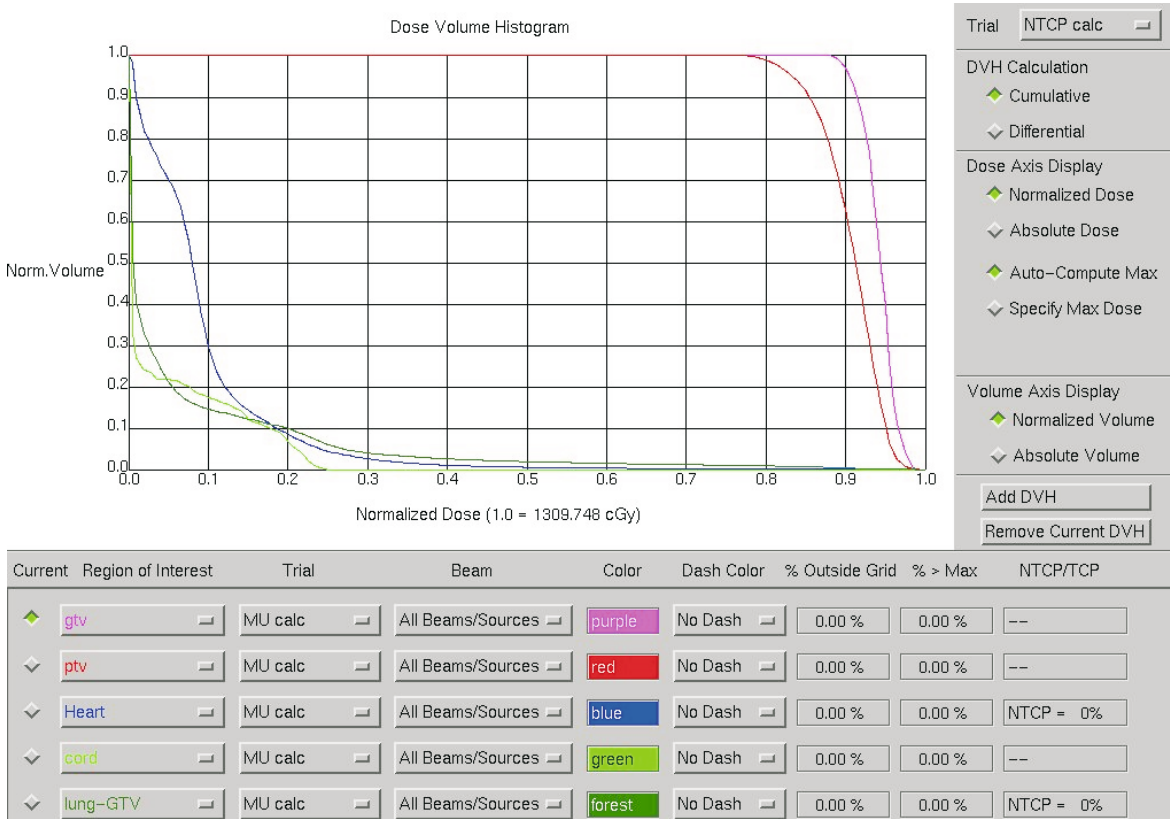

Fig. 7. The dose volume histogram of the NSC RLL lung lesion treated with a small field IMRT plan: GTV (*blue-right*), PTV (*red*), heart (*blue-left*), spinal cord (*green*), and ipsilateral lung (*dark green*)

irregularly shaped lesions of the brain particularly when compared to complex, multi-isocenter linac-based stereotactic arc or uniform-intensity fixed static field techniques [38–41]. Its application to extracranial tumor locations is still in development and will require further advancement in techniques that allow for patient immobilization, target localization, target tracking, and physiological gating. Recent linear accelerator designs provide technological solutions to each of these issues by incorporating stereotactic head and body localization, cone beam tomographic imaging, high-resolution real-time portal imaging, tracking software, and mMLCs into a fully integrated system.

The potential for further improvements in small field shaping with the application of IMRT is possible using dynamic mMLC collimation. In addition to enhanced dose conformity, small field high precision IMRT allows for the selective prioritization of dose to adjacent critical areas. Small field high precision IMRT has the potential to achieve superior dose distributions as compared to uniform-intensity fixed-field, arc-based methods with circular collimators, and even gamma knife radiosurgery [33]. Future research challenges in this field are related to the fact that while IMRT has been demonstrated to produce significant dosimetric improvements for large tumors, its application and utility for small tumors may be limited due to the lateral transport of radiation [42]. Further investigation of the dosimetry inherent to small leaf collimation must include automated beam configurations, automated beam weight optimization, and the use of conformal arcs with dynamic collimation.

References

1. Bova FJ, Buatti JM, Friedman WA, Mendenhall WM, Yang CC, Liu C (1997) The University of Florida frameless high-precision stereotactic radiotherapy system. Int J Radiat Oncol Biol Phys 38(4):875–882
2. Hartford AC, Loeffler JS (2001) Radiosurgery for benign tumors and arteriovenous malformations of the central nervous system. Front Radiat Ther Oncol 35:30–47
3. Kondziolka D, Niranjan A, Lunsford LD, Flickinger JC (1999) Stereotactic radiosurgery for meningiomas. Neurosurg Clin N Am 10(2):317–325
4. Lopez BC, Hamlyn PJ, Zakrzewska JM (2004) Stereotactic radiosurgery for primary trigeminal neuralgia: state of the evidence and recommendations for future reports. J Neurol Neurosurg Psychiatry 75(7):1019–1024
5. Young RF (1998) Radiosurgery for the treatment of brain metastases. Semin Surg Oncol 14(1):70–78

6. Lax I, Blomgren H, Naslund I, Svanstrom R (1994) Stereotactic radiotherapy of malignancies in the abdomen. Methodological aspects. Acta Oncol 33(6):677– 683
7. Blomgren H, Lax I, Naslund I, Svanstrom R (1995) Stereotactic high dose fraction radiation therapy of extracranial tumors using an accelerator. Clinical experience of the first thirty-one patients. Acta Oncol 34(6):861–870
8. Ganslandt O, Mueller R, Mueller W, Borchert H, Grabenbauer GG (2003) Simple invasive fixation device for fractionated stereotactic LINAC based radiotherapy. Acta Neurochir (Wien) 145(4):289– 294
9. Gill SS, Thomas DG, Warrington AP, Brada M (1991) Relocatable frame for stereotactic external beam radiotherapy. Int J Radiat Oncol Biol Phys 20(3):599–603
10. Kalapurakal JA, Ilahi Z, Kepka AG, Bista T, Goldman S, Tomita T et al. (2001) Repositioning accuracy with the Laitinen frame for fractionated stereotactic radiation therapy in adult and pediatric brain tumors: preliminary report. Radiology 218(1):157- -161
11. Alheit H, Dornfeld S, Dawel M, Alheit M, Henzel B, Steckler K et al. (2001) Patient position reproducibility in fractionated stereotactically guided conformal radiotherapy using the BrainLab mask system. Strahlenther Onkol 177(5):264–268
12. Schlegel W, Pastyr O, Bortfeld T, Gademann G, Menke M, Maier-Borst W (1993) Stereotactically guided fractionated radiotherapy: technical aspects. Radiother Oncol 29(2): 197–204
13. Gliemroth J, Gaebel C, Kehler U, Grande- Nagel I, Missler U, Arnold H (2002) An in vitro study to evaluate the accuracy of stereotactic localization using magnetic resonance imaging by means of the Leksell stereotactic system. Minim Invasive Neurosurg 45(1):1–5
14. Gerszten PC, Ozhasoglu C, Burton SA, Vogel W, Atkins B, Kalnicki S et al. (2003) Evaluation of CyberKnife frameless real-time image-guided stereotactic radiosurgery for spinal lesions. Stereotact Funct Neurosurg 81(1/4):84–89
15. Yenice KM, Lovelock DM, Hunt MA, Lutz WR, Fournier-Bidoz N, Hua CH et al. (2003) CT image- guided intensity-modulated therapy for paraspinal tumors using stereotactic immobilization. Int J Radiat Oncol Biol Phys 55(3):583–593
16. Onimaru R, Shirato H, Aoyama H, Kitakura K, Seki T, Hida K et al. (2002) Calculation of rotational setup error using the real-time tracking radiation therapy (RTRT) system and its application to the treatment of spinal schwannoma. Int J Radiat Oncol Biol Phys 54(3):939–947
17. Bilsky MH, Yamada Y, Yenice KM, Lovelock M, Hunt M, Gutin PH et al. (2004) Intensity-modulated stereotactic radiotherapy of paraspinal tumors: a preliminary report. Neurosurgery 54(4):823–830
18. Murphy MJ, Adler JR Jr, Bodduluri M, Dooley J, Forster K, Hai J et al. (2000) Image-guided radiosurgery for the spine and pancreas. Comput Aided Surg 5(4):278–288
19. Shimamoto S, Inoue T, Shiomi H, Sumida I, Yamada Y, Tanaka E et al. (2002) CyberKnife stereotactic irradiation for metastatic brain tumors. Radiat Med 20(6):299–304
20. Whyte RI, Crownover R, Murphy MJ, Martin DP, Rice TW, DeCamp MM Jr et al. (2003) Stereotactic radiosurgery for lung tumors: preliminary report of a phase I trial. Ann Thorac Surg 75(4):1097–1101
21. Harada T, Shirato H, Ogura S, Oizumi S, Yamazaki K, Shimizu S, et al. (2002) Real-time tumor- tracking radiation therapy for lung carcinoma by the aid of insertion of a gold marker using bronchofiberscopy. Cancer 95(8):1720–1727
22. Balter JM, Sandler HM, Lam K, Bree RL, Lichter AS, ten Haken RK (1995) Measurement of prostate movement over the course of routine radiotherapy using implanted markers. Int J Radiat Oncol Biol Phys 31(1):113–118
23. Soete G, Van de Steene J, Verellen D, Vinh-Hung V, Van den Berge D, Michielsen D et al. (2002) Initial clinical experience with infrared- reflecting skin markers in the positioning of patients treated by conformal radiotherapy for prostate cancer. Int J Radiat Oncol Biol Phys 52(3):694–698
24. Wu J, Haycocks T, Alasti H, Ottewell G, Middlemiss N, Abdolell M et al. (2001) Positioning errors and prostate motion during conformal prostate radiotherapy using on-line isocentre set-up verification and implanted prostate markers. Radiother Oncol 61(2):127–133
25. Hurkmans CW, Remeijer P, Lebesque JV, Mijnheer BJ (2001) Set-up verification using portal imaging; review of current clinical practice. Radiother Oncol 58(2):105–120
26. Dawson LA, Brock KK, Kazanjian S, Fitch D, McGinn CJ, Lawrence TS et al. (2001) The reproducibility of organ position using active breathing control (ABC) during liver radiotherapy. Int J Radiat Oncol Biol Phys 51(5):1410–1421
27. Kitamura K, Shirato H, Shinohara N, Harabayashi T, Onimaru R, Fujita K et al. (2003) Reduction in acute morbidity using hypofractionated intensity-modulated radiation therapy assisted with a fluoroscopic real-time tumor-tracking system for prostate cancer: preliminary results of a phase I/II study.Cancer J 9(4):268–276
28. Bayouth JE, Morrill SM (2003) MLC dosimetric characteristics for small field and IMRT applications. Med Phys 30(9):2545–2552
29. Orton CG, Chungbin S, Klein EE, Gillin MT, Schultheiss TE, Sause WT (1998) Study of lung density corrections in a clinical trial (RTOG 88–08). Radiation Therapy Oncology Group. Int J Radiat Oncol Biol Phys 41(4):787–794
30. Burman C, Kutcher GJ, Emami B, Goitein M (1991) Fitting of normal tissue tolerance data to an analytic function. Int J Radiat Oncol Biol Phys 21(1):123–135
31. Spanos WJ Jr, Shukovsky LJ, Fletcher GH (1976) Time, dose, and tumor volume relationships in irradiation of squamous cell carcinomas of the base of the tongue. Cancer 37(6):2591–2599
32. Emami B, Lyman J, Brown A, Coia L, Goitein M, Munzenrider JE et al. (1991) Tolerance of normal tissue to therapeutic irradiation. Int J Radiat Oncol Biol Phys 21(1):109–122
33. Benedict SH, Cardinale RM, Wu Q, Zwicker RD, Broaddus WC, Mohan R (2001) Intensity-modulated stereotactic radiosurgery using dynamic micro-multileaf collimation. Int J Radiat Oncol Biol Phys 50(3):751– 758
34. Cosgrove VP, Jahn U, Pfaender M, Bauer S, Budach V, Wurm RE (1999) Commissioning of a micro multi-leaf collimator and planning system for stereotactic radiosurgery. Radiother Oncol 50(3):325– 336
35. Xia P, Verhey LJ (2001) Delivery systems of intensity-modulated radiotherapy using conventional multileaf collimators. Med Dosim 26(2):169–177
36. Shiu AS, Kooy HM, Ewton JR, Tung SS, Wong J, Antes K et al. (1997) Comparison of miniature multileaf collimation (MMLC) with circular collimation for stereotactic treatment. Int J Radiat Oncol Biol Phys 37(3):679–688
37. Song D, Kavanagh B, Benedict S, Schefter T (2004) Stereotactic body radiation therapy: rationale, techniques, applications, and optimization. Oncology 18(11):1419–1430
38. Zinkin HD, Rivard MJ, Mignano JE, Wazer DE (2004) Analysis of dose conformity and normal-tissue sparing using two different IMRT prescription methodologies for irregularly shaped CNS lesions irradiated with the Beak and 1-cm MIMiC collimators. Int J Radiat Oncol Biol Phys 59(1):285–292

39. Woo SY, Grant WH III, Bellezza D, Grossman R, Gildenberg P, Carpentar LS, Carol M, Butler EB (1996) A comparison of intensity modulated conformal therapy with a conventional external beam stereotactic radiosurgery system for the treatment of single and multiple intracranial lesions. Int J Radiat Oncol Biol Phys 35(3):593–597
40. Ma L, Xia P, Verhey LJ, Boyer AL (1999) A dosimetric comparison of fan-beam intensity modulated radiotherapy with Gamma Knife stereotactic radiosurgery for treating intermediate intracranial lesions. Int J Radiat Oncol Biol Phys 45(5):1325–1330
41. Nakamura JL, Pirzkall A, Carol MP, Xia P, Smith V, Wara WM et al. (2003) Comparison of intensity-modulated radiosurgery with gamma knife radiosurgery for challenging skull base lesions. Int J Radiat Oncol Biol Phys 55(1):99–109
42. Mohan R, Wu Q, Wang X, Stein J (1996) Intensity modulation optimization, lateral transport of radiation, and margins. Med Phys 23(12):2011–2021
43. Hamilton AJ, Lulu BA, Fosmire H, Stea B, Cassady JR (1995) Preliminary clinical experience with linear accelerator-based spinal stereotactic radiosurgery. Neurosurgery 36(2):311–319
44. Tokuuye K, Sumi M, Ikeda H, Kagami Y, Murayama S, Nakayama H et al. (1997) Technical considerations for fractionated stereotactic radiotherapy of hepatocellular carcinoma. Jpn J Clin Oncol 27(3):170–173
45. Murphy MJ (1997) An automatic six-degree- of-freedom image registration algorithm for image- guided frameless stereotaxic radiosurgery. Med Phys 24(6):857–866
46. Sato M, Uematsu M, Yamamoto F (1998) Feasibility of frameless stereotactic high-dose radiation therapy for primary or metastatic liver cancer. J Radiosurg 1(1):233–238
47. Lohr F, Debus J, Frank C, Herfarth K, Pastyr O, Rhein B et al. (1999) Noninvasive patient fixation for extracranial stereotactic radiotherapy. Int J Radiat Oncol Biol Phys 45(2):521–527
48. Wulf J, Hadinger U, Oppitz U, Thiele W, Ness-Dourdoumas R, Flentje M (2001) Stereotactic radiotherapy of targets in the lung and liver. Strahlenther Onkol 177(12):645–655
49. Nakagawa K, Aoki Y, Tago M, Terahara A, Ohtomo K (2000) Megavoltage CT-assisted stereotactic radiosurgery for thoracic tumors: original research in the treatment of thoracic neoplasms. Int J Radiat Oncol Biol Phys 48(2):449–457
50. Herfarth KK, Debus J, Lohr F, Bahner ML, Rhein B, Fritz P et al. (2001) Stereotactic single-dose radiation therapy of liver tumors: results of a phase I/II trial. J Clin Oncol 19(1):164–170
51. Nagata Y, Negoro Y, Aoki T, Mizowaki T, Takayama K, Kokubo M et al. (2002) Clinical outcomes of 3D conformal hypofractionated single high-dose radiotherapy for one or two lung tumors using a stereotactic body frame. Int J Radiat Oncol Biol Phys 52(4):1041–1046
52. Fukumoto S, Shirato H, Shimzu S, Ogura S, Onimaru R, Kitamura K et al. (2002) Small-volume image-guided radiotherapy using hypofractionated, coplanar, and noncoplanar multiple fields for patients with inoperable Stage I nonsmall cell lung carcinomas. Cancer 95(7):1546–1553
53. Hara R, Itami J, Kondo T, Aruga T, Abe Y, Ito M et al. (2002) Stereotactic single high dose irradiation of lung tumors under respiratory gating. Radiother Oncol 63(2):159–163
54. Hof H, Herfarth KK, Munter M, Hoess A, Motsch J, Wannenmacher M et al. (2003) Stereotactic single-dose radiotherapy of stage I non-small-cell lung cancer (NSCLC). Int J Radiat Oncol Biol Phys 56(2):335- -341
55. Timmerman R, Papiez L, McGarry R, Likes L, DesRosiers C, Frost S, et al. Extracranial stereotactic radioablation: results of a phase I study in medically inoperable stage I non-small cell lung cancer. Chest 124(5):1946–1955
56. Floyd NS, Woo SY, Teh BS, Prado C, Mai WY, Trask T, Gildenberg PL, Holoye P, Augspurger ME, Carpenter LS, Lu HH, Chiu JK, Grant WH III, Butler EB (2004) Hypofractionated intensity-modulated radiotherapy for primary glioblastoma multiforme. Int J Radiat Oncol Biol Phys 58(3):721–726
57. Sultanem K, Patrocinio H, Lambert C, Corns R, Leblanc R, Parker W et al. (2004) The use of hypofractionated intensity-modulated irradiation in the treatment of glioblastoma multiforme: preliminary results of a prospective trial. Int J Radiat Oncol Biol Phys 58(1):247–252
58. Chan JL, Lee SW, Fraass BA, Normolle DP, Greenberg HS, Junck LR et al. (2002) Survival and failure patterns of high-grade gliomas after three- dimensional conformal radiotherapy. J Clin Oncol 20(6):1635–1642
59. Pirzkall A, Debus J, Haering P, Rhein B, Grosser KH, Hoss A et al. (2003) Intensity modulated radiotherapy (IMRT) for recurrent, residual, or untreated skull-base meningiomas: preliminary clinical experience. Int J Radiat Oncol Biol Phys 55(2):362–372
60. Romanelli P, Heit G, Chang SD, Martin D, Pham C, Adler J (2003) Cyberknife radiosurgery for trigeminal neuralgia. Stereotact Funct Neurosurg 81(1/4):105–109
61. Gerszten PC, Ozhasoglu C, Burton SA, Vogel WJ, Atkins BA, Kalnicki S et al. (2004) CyberKnife frameless stereotactic radiosurgery for spinal lesions: clinical experience in 125 cases. Neurosurg 55(1):89–99
62. Milker-Zabel S, Zabel A, Thilmann C, Schlegel W, Wannenmacher M, Debus J (2003) Clinical results of retreatment of vertebral bone metastases by stereotactic conformal radiotherapy and intensity- modulated radiotherapy. Int J Radiat Oncol Biol Phys 55(1):162–167
63. Munter MW, Nill S, Thilmann C, Hof H, Hoss A, Haring P et al. (2003) Stereotactic intensity- modulated radiation therapy (IMRT) and inverse treatment planning for advanced pleural mesothelioma. Feasibility and initial results. Strahlenther Onkol 179(8):535–541
64. Koong AC, Le QT, Ho A, Fong B, Fisher G, Cho C et al. (2004) Phase I study of stereotactic radiosurgery in patients with locally advanced pancreatic cancer. Int J Radiat Oncol Biol Phys 58(4):1017–1021
65. Milano MT, Chmura SJ, Garofalo MC, Rash C, Roeske JC, Connell PP et al. (2004) Intensity- modulated radiotherapy in treatment of pancreatic and bile duct malignancies: toxicity and clinical outcome. Int J Radiat Oncol Biol Phys 59(2):445–453
66. Kupelian PA, Reddy CA, Carlson TP, Altsman KA, Willoughby TR (2002) Preliminary observations on biochemical relapse-free survival rates after short-course intensity-modulated radiotherapy (70 Gy at 2.5 Gy/fraction) for localized prostate cancer. Int J Radiat Oncol Biol Phys 53(4):904–912
67. Zelefsky MJ, Fuks Z, Hunt M, Yamada Y, Marion C, Ling CC et al. (2002) High-dose intensity modulated radiation therapy for prostate cancer: early toxicity and biochemical outcome in 772 patients. Int J Radiat Oncol Biol Phys 53(5): 1111–1116
68. Chao KS, Ozyigit G, Blanco AI, Thorstad WL, Deasy JO, Haughey BH et al. (2004) Intensity- modulated radiation therapy for oropharyngeal carcinoma: impact of tumor volume. Int J Radiat Oncol Biol Phys 59(1):43–50
69. Lee N, Xia P, Fischbein NJ, Akazawa P, Akazawa C, Quivey JM (2003) Intensity-modulated radiation therapy for head-and-neck cancer: the UCSF experience focusing on target volume delineation. Int J Radiat Oncol Biol Phys 57(1):49–60
70. Lee N, Xia P, Quivey JM, Sultanem K, Poon I, Akazawa C et al. (2002) Intensity-modulated radiotherapy in the treatment of

nasopharyngeal carcinoma: an update of the UCSF experience. Int J Radiat Oncol Biol Phys 53(1):12–22
71. Lu TX, Mai WY, Teh BS, Zhao C, Han F, Huang Y, Deng XW, Lu LX, Huang SM, Zeng ZF, Lin CG, Lu HH, Chiu JK, Carpenter LS, Grant WH III, Woo SY, Cui NJ, Butler EB (2004) Initial experience using intensity- modulated radiotherapy for recurrent nasopharyngeal carcinoma. Int J Radiat Oncol Biol Phys 58(3):682–687

Subject Index